Indian Institute of Metals Series

A. K. Tyagi
Raghumani S. Ningthoujam *Editors*

Handbook on Synthesis Strategies for Advanced Materials

Volume-III: Materials Specific Synthesis Strategies

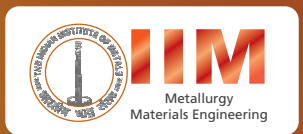

Springer

Indian Institute of Metals Series

About the Book Series:

The study of metallurgy and materials science is vital for developing advanced materials for diverse applications. In the last decade, the progress in this field has been rapid and extensive, giving us a new array of materials, with a wide range of applications, and a variety of possibilities for processing and characterizing the materials. In order to make this growing volume of knowledge available, an initiative to publish a series of books in Metallurgy and Materials Science was taken during the Diamond Jubilee year of the Indian Institute of Metals (IIM) in the year 2006. Ten years later the series is now published in partnership with Springer.

This book series publishes different categories of publications: textbooks to satisfy the requirements of students and beginners in the field, monographs on select topics by experts in the field, professional books to cater to the needs of practicing engineers, and proceedings of select international conferences organized by IIM after mandatory peer review. The series publishes across all areas of materials sciences and metallurgy. An eminent panel of international and national experts acts as the advisory body in overseeing the selection of topics, important areas to be covered, and the selection of contributing authors.

More information about this series at https://link.springer.com/bookseries/15453

A. K. Tyagi · Raghumani S. Ningthoujam
Editors

Handbook on Synthesis Strategies for Advanced Materials

Volume-III: Materials Specific Synthesis Strategies

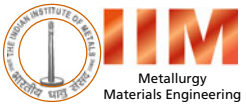

Springer

Editors
A. K. Tyagi
Chemistry Division, Bhabha Atomic Research Centre, Mumbai, Maharashtra, India

Homi Bhabha National Institute, Mumbai, Maharashtra, India

Raghumani S. Ningthoujam
Chemistry Division, Bhabha Atomic Research Centre, Mumbai, Maharashtra, India

Homi Bhabha National Institute, Mumbai, Maharashtra, India

ISSN 2509-6400 ISSN 2509-6419 (electronic)
Indian Institute of Metals Series
ISBN 978-981-16-1891-8 ISBN 978-981-16-1892-5 (eBook)
https://doi.org/10.1007/978-981-16-1892-5

This Springer imprint is published by the registered company Springer Nature Singapore Pte Ltd.
The registered company address is: 152 Beach Road, #21-01/04 Gateway East, Singapore 189721, Singapore

Series Editor's Preface

The Indian Institute of Metals Series is an institutional partnership series focusing on metallurgy and materials science and engineering.

About the Indian Institute of Metals

The Indian Institute of Metals (IIM) is a premier professional body (since 1947) representing an eminent and dynamic group of metallurgists and materials scientists and engineers from R&D institutions, academia, and industry, mostly from India. It is a registered professional institute with the primary objective of promoting and advancing the study and practice of the science and technology of metals, alloys, and novel materials. The institute is actively engaged in promoting academia–research and institute–industry interactions.

Genesis and History of the Series

The study of metallurgy and materials science and engineering is vital for developing advanced materials for diverse applications. In the last decade, the progress in this field has been rapid and extensive, giving us a new array of materials, with a wide range of applications and a variety of possibilities for processing and characterizing the materials. In order to make this growing volume of knowledge available, an initiative to publish a series of books in metallurgy and materials science and engineering was taken during the Diamond Jubilee year of the Indian Institute of Metals (IIM) in the year 2006. IIM entered into a partnership with Universities Press, Hyderabad, and, as part of the IIM book series, 11 books were published, and a number of these have been co-published by CRC Press, USA. The books were authored by eminent professionals in academia, industry, and R&D with outstanding background in their respective domains, thus generating unique resources of validated expertise of interest in metallurgy. The international character of the authors' and editors has

enabled the books to command national and global readership. This book series includes different categories of publications: textbooks to satisfy the requirements of undergraduates and beginners in the field, monographs on selected topics by experts in the field, and proceedings of selected international conferences organized by IIM, after mandatory peer review. An eminent panel of international and national experts constitutes the advisory body in overseeing the selection of topics, important areas to be covered, in the books and the selection of contributing authors.

Current Series Information

To increase the readership and to ensure wide dissemination among global readers, this new chapter of the series has been initiated with Springer in the year 2016. The goal is to continue publishing high-value content on metallurgy and materials science and engineering, focusing on current trends and applications. So far, four important books on state of the art in metallurgy and materials science and engineering have been published and, during this year, three more books are released during IIM-ATM 2021. Readers who are interested in writing books for the Series may contact the Series Editor-in-Chief, Dr. U. Kamachi Mudali, Former President of IIM and Vice Chancellor of VIT Bhopal University at ukmudali1@gmail.com, vc@vitbhopal.ac.in or the Springer Editorial Director, Ms. Swati Meherishi at swati.meherishi@springer.com.

About the Three Volumes of Handbook on Synthesis Strategies for Advanced Materials

The Handbook on "Synthesis Strategies for Advanced Materials" is aimed to provide information on (i) Variety of synthetic methods to prepare advanced materials (stable and metastable hitherto unknown materials, chemically and crystallographically designed materials and assemblies) and their structure, micro-structure, and morphology; and (ii) Functional properties like soft to hard, insulators to superconductors, crystalline to amorphous like glass or polymeric, nano- to thin films to bulk single crystals. Keeping in mind the interests of students and young researchers, and senior faculty members, the basic concepts of synthesis, processing and materials aspects, and their recent developments are covered in three volumes.

The Editors Dr. A.K. Tyagi, Director, Chemistry Group, and Dr. S.R. Ningthoujam, Scientific Officer-F, Chemistry Group, from Bhabha Atomic Research Centre have meticulously edited the three volumes with 20 each chapters for Vols. I and II, and 18 chapters for Vol. III. These chapters have been prepared by the editors as well as well-experienced authors from academia, R&D, and industry. This handbook will

be a treasure for those who are interested in learning everything about advanced materials and pursue a career and study in the area of advanced materials. The editors and authors are gratefully acknowledged for their excellent chapters covering wide range of information on the subject matter.

Dr. U. Kamachi Mudali
Editor-in-Chief
Series in Metallurgy and Materials Engineering

Preface

The ever-developing human civilization thrives on materials which may be of technological, health, environmental or geological relevance. The development of materials has, thus, been a constantly evolving process both in nature and by human efforts. Over time immemorial, a continuous evolution of materials for the fulfilment of the needs of healthy living or advanced lifestyle has been witnessed and that makes the twenty-first century a century of materials. This is recognized by the surge in advanced materials in engineering, electronics and communications as well as in healthcare, medicine and societal sectors. The fascinating and ever-growing world of materials extends from soft materials to super-hard materials, insulators to superconductors, extended solids to molecular solids, self-assembled materials, catalysts, materials with tailored thermal expansion, composites and hybrid materials, materials with multi-functionality, ceramics and glasses, metals–alloys–intermetallics, drugs and drugs delivery systems, polymers, biomaterials, nuclear materials, optical materials, fast ionic conductors, soft and hard magnets, etc. Still the quest of humanity for developing better and more efficient materials remains never-ending. The development of materials depends on the ability to synthesize them or to find a more cost- and energy-efficient synthesis methodology or design newer materials with appropriate constituents and functionalities to make them usable. Thus, the synthesis methods play a pivotal role in the materials research. Although the synthesis or synthetic materials chemistry originated just after the Stone Age, the understanding of chemistry and physics of materials with the progress of time only could lead to the discovery of newer materials as well as the targeted materials for desired purposes. This, in turn, resulted in the development of state-of-the-art synthesis procedures. Further, new functional materials are also being designed by the interplay of synthesis methodologies, crystallographic structures, morphologies and dimensionality for desired functional properties. Many a time, thermodynamics and kinetic parameters are controlled to overcome the barriers to achieve the desired materials. Thus, the methodologies for the synthesis of materials became multi-disciplinary which include the approaches from chemists, biologists, physicists, metallurgists and engineers. This has been witnessed as the development of several unconventional synthetic routes that involve parameters such as extremely high temperature, high pressure, radiation, mechanical attrition and unusually reactive intermediates. Some non-traditional synthesis

routes have also been developed that follow a gentle chemical reaction favoring an intermediate or alternate pathway to bypass hindrance to reach the targeted material or utilizing the memory of the materials to introduce functionalities. The unconventional synthesis methodologies play important roles in the direction of many new and metastable materials which otherwise were not possible to prepare. Similarly, the multi-functional materials, i.e., the materials which can perform two or more synergistic or antagonistic functionalities, are being achieved by judicious adoption of synthesis methods. In addition, varieties of soft chemical methods have emerged that play important roles in the field of functional materials, in particular medicine and healthcare products, to design materials for desired technological applications. Thus, the material synthesis assumes an unprecedented role in this endeavor and remains a challenge as well as an opportunity to chemists and materials scientists. The synthesis methods and their scopes have been discussed in varieties of monographs as well as compilations and proceedings from time to time. Usage for various synthetic methods for the preparation of newer and exotic materials as well as recent modifications and their potentials as handy information is essentially a need for researchers in today's times and that has been achieved in this present compilation "Handbook on Synthesis Strategies for Advanced Materials," Volumes I, II and III.

This handbook series on "Synthesis Strategies for Advanced Materials" is aimed to provide information on varieties of synthetic methods being adopted by researchers to prepare different kinds of advanced materials covering from the viewpoints of structure, microstructure and morphology of materials, stable and metastable hitherto unknown materials, chemically and crystallographically designed materials and assemblies, as well as from the viewpoints of functional properties like soft to hard, insulators to superconductors, crystalline to amorphous like glass or polymeric, nano- to thin films to bulk single crystal. These have been achieved by adoption, alteration or judicious selection of synthesis methods. Keeping in mind the interests of students and young researchers, and senior faculty members, the basic concepts of synthesis, processing and materials aspects and their recent developments are covered in three volumes, namely Volume I: *Techniques and Fundamentals*, Volume II: *Processing and Functionalization of Materials* and Volume III: *Materials Specific Synthesis Strategies*. Each volume is made independent by taking care of minimal overlap of the topics. Volume I is primarily focused on the principles and procedures of various synthesis methods. The basic principles and scope/limitations of various synthetic methods, like solid-state reaction to gentle molecular aggregation methods and chimie douce, synthesis under high temperature, hot-injection, method, polyol method, metal-organic frameworks, electrochemical method, mechanochemistry, hydro/solvothermal reaction, high-pressure and high-temperature reactions, arc melting, induction heating, melt-quench method, ion exchange process, microwave and visible to gamma radiations, green methods of synthesis, thermolysis, bio-inspired synthesis, etc., are discussed along with the inputs from authors' hands-on experience and expertise. In Volume II, various processing methodologies for the preparation of various types of functional materials or functionalization of materials by chemical, structural or microstructural alterations are presented. This volume

covers processing of nanomaterials, porous or sintered materials, composite materials, low dimensional like 1D to 2D materials, thin films, single crystals, template method, self-assembly, biomaterials, inkjet printing, 3D printing, size and shape engineering, etc., in a lucid manner. Volume III is focused on the synthesis aspects of materials like hybrid inorganic–organic, metal oxide frameworks, intermetallics, hydrides, borides, carbides, nitrides, phosphides, silicide, selenides, fluorides, various biomaterials, materials for sensors and detectors, optical materials, carbon-based materials, colloids, noble gas compounds, lithium-based ceramics, materials with unusual oxidation state, organo-selenium and platinum compounds, silicon-based materials and lithium-based ceramics. The evolution and state-of-the-art synthesis methods for practical requirements as well as new concepts with the most recent literatures dealing with their synthesis are presented in this volume. These volumes are expected to serve as handy guides for synthesis and processing of advanced materials of wide range and category.

The editors are immensely thankful to all the authors for their rich contributions toward this book. Although due efforts have been taken to make the book as error-free as possible, some may have crept in as unnoticed. We shall be thankful to the readers for bringing such unintentional errors to our notice. Finally, we sincerely hope that our efforts will be of use to both new and experienced researchers in the field.

Mumbai, India
October 2021

A. K. Tyagi
Raghumani S. Ningthoujam

Contents

About the Editors

Dr. A. K. Tyagi obtained his M.Sc. (Chemistry) degree in 1985 from Meerut University, Meerut, India and joined 29th batch of BARC Training School, Mumbai in the same year. After completing one year orientation course, he joined Chemistry Division, Bhabha Atomic Research Centre (BARC), Mumbai in 1986. Presently, he is Director, Chemistry Group, BARC, Mumbai, and a Senior Professor of Chemistry at Homi Bhabha National Institute (HBNI), Mumbai. His research interests are in the field chemistry of materials, which includes functional materials, nanomaterials, nuclear materials, energy materials, metastable materials, hybrid materials and structure-property correlation. He has published more than 600 papers in journals, several books and has supervised 30 Ph.D. students.

He was awarded Ph.D. by Mumbai University, Mumbai in 1992. He did postdoctoral research at Max-Planck Institute for Solid State Research (MPI-FKF), Stuttgart, Germany during 1995–1996 on a Max-Planck Fellowship. Subsequently, he regularly visited MPI-FKF, Stuttgart as a visiting scientist. In addition, he has also visited Institute of Superior Technology, Portugal; Institute for Chemical Process and Environmental Technology, Ottawa, Canada; Dalhousie University, Halifax, Canada; Moscow State University, Moscow, Russia; Institute for Materials, Nantes, France; University of Malay, Malaysia; National Institute of Materials Science, Tsukuba, Japan; National University of Singapore, Singapore; Royal Institute of Technology, Stockholm, Sweden; Rice University, Houston, USA; Shanghai, China; University of Valencia, Valencia,

Spain; Weizmann Institute of Science, Israel; University of Queensland, Brisbane, Australia; US-Air Force Research Lab, Dayton, USA, Institute for Studies of Nanostructured Materials, Palermo, Italy and iThemba Labs, Cape Town, South Africa.

In recognition of his significant contributions to the field of chemistry of materials, he has been conferred with many prestigious awards, such as Dr. Lakshmi award by the Indian Association of Solid State Chemists and Allied Scientists (2001); Rheometric Scientific-Indian Thermal Analysis Society Award (2002); Gold Medal of Indian Nuclear Society (2003); Materials Research Society of India's Medal (2005); Chemical Research Society of India's Bronze Medal (2006); DAE-Homi Bhabha Science and Technology Award (2006); IANCAS-Dr. Tarun Datta Memorial Award (2007); Rajib Goyal Prize in Chemical Sciences (2007); RD Desai Memorial Award from Indian Chemical Society (2008) and DAE-SRC Outstanding Research Investigator Award (2010); CRSI-Prof. CNR Rao National Prize in Chemical Sciences (2012); ISCB Award for Excellence in Chemical Sciences (2013); MRSI-ICSC Materials Science Senior Award (2014); Coastal Chemical Research Society's Award (2014); Platinum Jubilee Lecture Award in Materials Science from Indian Science Congress Association (2015); Metallurgist of the Year Award (2017), from Ministry of Steel, Government of India; Chemical Research Society of India's Silver Medal (2018); Materials Research Society of India's Prof. C. N. R. Rao Prize in Advanced Materials (2018); JNCASR's National Prize in Solid State and Materials Chemistry (2018) and Acharya PC Ray Memorial Award from Indian Science Congress Association (2020).

He is an elected Fellow of the Indian Academy of Sciences (FASc); National Academy of Sciences, India (FNASc); Maharashtra Academy of Sciences (FMASc); Royal Society of Chemistry, UK (FRSC) and Asia Pacific Academy of Materials.

Dr. Raghumani S. Ningthoujam obtained M.Sc. in Chemistry from Manipur University, Imphal, Manipur, India in 1994. He was awarded Ph.D. in Chemistry from IIT Kanpur in area of superconductivity, electron transport and magnetic properties of nanostructured transition metal nitrides in 2004. He joined BARC (Bhabha Atomic Research Centre), Mumbai as Scientific Officer (D) in 2006 after completion of Dr. K. S. Krishnan Research Associate Fellowship. Presently, he is working in area of Luminescent and Magnetic Nanomaterials and their applications in sensors, imaging, diagnosis and therapy. He did Post-Doctoral Fellowship at University of Victoria, Canada in the area of quantum dots. Presently, he is ScientificOfficer (F) at Chemistry Division, BARC, Mumbai. He is recognized for Guideship of Ph.D. at Homi Bhabha National Institute (HBNI), Mumbai and Mumbai University, Mumbai. Many research scholars and students finished their projects under his guidance. He has published about 150 Papers in the refereed journals, five review articles and four book chapters. In recognition of his significant contributions to the chemical science, he has been awarded DAE-Scientific & Technical Excellence Award in 2012 and Young Achiever Award, SSPS 2010. He has been elected as a Fellow, The National Academy of Sciences, India (FNASc) in 2016 and Fellow, Maharashtra Academy of Sciences (FMASc) in 2013.

Chapter 1
High-Performance Polymer-Matrix Composites: Novel Routes of Synthesis and Interface-Structure-Property Correlations

K. A. Dubey and Y. K. Bhardwaj

Abstract No single material or a class of material meets the diverse set of properties required for different applications. Inherent advantages and disadvantages of metals, ceramics, or polymers have made it necessary to develop combinatorial approaches, wherein their functional advantages are maximized and drawbacks are abridged. Composites are the materials comprising two or more constituent materials with significantly different physical, mechanical, electrical, or thermal attributes. Composites offer material characteristics that are different from the individual components and can be engineered to entail synergistic advantages such as high strength, corrosion resistance, electrical or thermal conductivity, and low cost. Notably, in composites, the individual components may remain separate and distinct within the finished structure. The composite material is generally defined by the matrix such as metal-matrix composite, ceramic-matrix composites, and polymer-matrix composites, or by the type and morphological arrangement of the filler such as particle reinforced, fiber reinforced, unidirectional, random, laminates, or honeycombs. Fabrication of composite materials is accomplished by a wide variety of techniques such as melt compounding, in situ polymerization, tufting, tailored fiber placement and filament winding. Depending on the matrix and the filler, different synthetic strategies are adopted. Further with the advent of nano-sized fillers, new class of composites has emerged which have significant important advantages over the conventional composites. This chapter provides details on the synthesis strategies of different polymer-matrix composite materials. A detailed account of the strategies to tailor interfacial adhesion, dispersion, filler asymmetry, filler orientation, and high loading is made, and specific details on the synthesis of nanocomposites and the morphology-interface-property correlation are presented. Recent advances in the theoretical frameworks and the specific applications of the composites are also discussed.

K. A. Dubey (✉) · Y. K. Bhardwaj
Homi Bhabha National Institute, Mumbai 400094, India
e-mail: abhinav@barc.gov.in

Radiation Technology Development Division, Bhabha Atomic Research Centre, Trombay, Mumbai 400085, India

A. K. Tyagi and R. S. Ningthoujam (eds.), *Handbook on Synthesis Strategies for Advanced Materials*, Indian Institute of Metals Series,
https://doi.org/10.1007/978-981-16-1892-5_1

Keywords Polymer composites · Interface · Mechanical properties · Percolation

Abbreviations

3D	Three dimensional
AlN	Aluminum nitride
BS	Barium sulfate
BT	Barium titanate
$CaCO_3$	Calcium carbonate
CF	Carbon fiber
CNF	Conducting nano-fiber
CNT	Carbon nanotube
CPC	Conducting polymer composites
DVB	Divinylbenzene
EB	Electron beam
EPDM	Ethylene propylene diene monomer
EPR	Electron paramagnetic resonance
Epoxy-Br	Brominated epoxy
ER	Epoxy resin
EVA	Ethylene vinyl acetate
FCE	Fluorocarbon elastomer
FRPs	Fiber-reinforced plastics
GO	Graphene oxide
MA	Maleic anhydride
MCFs	Microcrystalline cellulose fibers
MMT	Montmorillonite
MWCNT	Multi-walled carbon nanotube
NCB	Nano carbon black
NR	Natural rubber
PAN-g-PDMS	Polyacrylonitrile-graft-poly(dimethyl siloxane)
PB	Polybutadiene
PBA	Poly(butyl acrylate)
PC	Polymer composites
PDMS	Poly(dimethyl siloxane)
PP	Polypropylene
PTFE	Poly(tetra fluoro ethylene)
PVDF	Polyvinylidene fluoride
PVP	Poly(vinyl pyrrolidone)
SBR	Styrene-butadiene rubber
SEM	Scanning electron microscopy
SWCNT	Single-walled carbon nanotube
T_g	Glass transition temperature
TPC	Thermoplastic composites

TSCs	Thermoset composites
TiO_2	Titanium dioxide
TMPTA	Trimethylolpropane triacrylate

1.1 Introduction

Polymer composites (PC) are materials consisting of two or more physically and/or chemically different phases separated by an interface. Synthesis of PC aims at developing advanced materials through a synergistic combination of components with significantly different properties. A judicious combination of fillers and polymer matrices results in PC of bulk properties significantly different from those of any of the constituents. Irrespective of the type of PC, interactions at the interface significantly influence the PC properties. At the interface region of PC, the load is transmitted between the filler and the matrix; hence, it is at the interface that stresses develop during processing or during the service life of the PC. The interface may act as a site for adsorption and nucleation as well. Application of PC particularly advanced polymer composites in high-tech sectors such as aircraft and aerospace manufacturing has brought "interface" at the focus both for the industry and academia. Thus, in the last two to three decades, there has been an increased interest in understanding the filler–polymer interface and its modification [1–3]. The interface was initially visualized as the two-dimensional boundary between adjacent phases in composites where an abrupt change in properties was mandatory. However, now it has been realized that it is not two-dimensional, but a three-dimensional zone where a gradual change in properties from one phase to other phase is observed and a more appropriate term "interphase" has been coined to describe it [4]. This chapter describes various strategies devised and adopted for the synthesis of PC. Choice of fillers and polymers, processing strategies, and interface modification particularly through modification of filler surface for various applications have been discussed in detail.

1.2 PC Constituents and Their Modification

1.2.1 Fillers

Fillers have different key properties like particle size and shape, density, purity, surface chemistry, thermal, electrical, and optical properties. They were initially employed in PC to reduce material costs and to improve processability. However, the observation that they also alter properties provided an impetus to research on the effect of filler properties on PC. The fillers can be of organic or inorganic origin with geometries like particulates, spheres, fibers, ribbons, flakes, and platelets. Continuous fillers like fibers or ribbons extend throughout the PC in a regular pattern while

discontinuous fillers like flakes, short fibers, and spheres are dispersed throughout the matrix. As the continuous fillers are arranged in a particular pattern/sequence in the matrix, they are also termed as reinforcing fillers. Reinforcing fillers are characterized by the relatively high aspect ratio (*length/diameter*) for fiber or the ratio of diameter to thickness for flakes and platelets. Reinforcing fillers are primarily added to enhance the mechanical properties of the PC, but they may significantly affect other properties such as transparency and thermal stability. Reinforcing fillers sometimes are a major component of the PC. Discontinuous fillers are randomly dispersed in the matrix, and their orientation is governed by the processing and shaping methods. Irrespective of the filler type (continuous or discontinuous), properties of PC are highly dependent on key properties of fillers, the extent of filler loading in PC, type, and extent of interaction with the polymer matrix, and fabrication protocol followed for PC synthesis [5].

1.2.1.1 Types and Geometry of Fillers

A wide range of materials like talc, fly ash, glass, inorganic carbonates, synthetic polymer fiber, carbon fiber, sisal fiber, banana fiber, conducting fillers, and agricultural wastes such as crop husk, sawdust, groundnut shell, and aquatic animals shell powder have been used as fillers in PC. An important parameter for evaluating the effectiveness of filler is the ratio of its surface area (A) to its volume (V). Higher the ratio, the better is the reinforcement [6]. The size of the filler drastically affects the properties of PC. Figure 1.1 illustrates that maximizing A/V and particle/matrix interaction through the interface requires $\alpha >> 1$ for fibers and $\alpha << 1$ for platelets[7]. A report on the effect of addition of micro- and nano-size aluminum nitride (AlN) on properties of brominated epoxy (Epoxy-Br) has clearly shown that nano-AlN

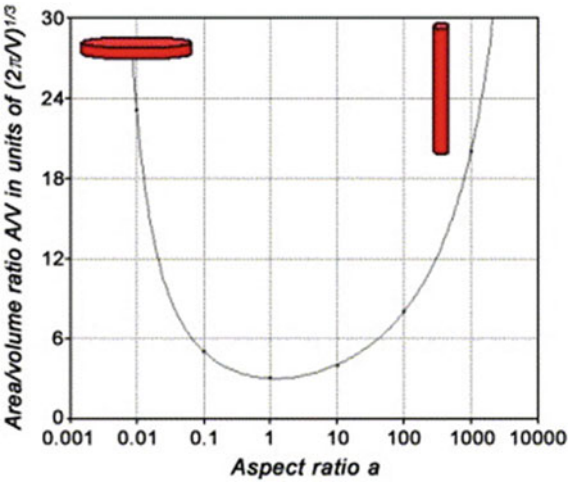

Fig. 1.1 Plot of the surface area-to-volume ratio (A/V) versus aspect ratio (α = length/diameter) for cylindrical particle. "Reproduced with the permission of Elsevier" [7]

decreases T_g while micro-AlN enhances the T_g of the matrix. The decrease in T_g has been attributed to effective aggregation of nano-AlN and voids in the composites and to decrease in the cross-link density of the epoxy-Br matrix in presence of nano-AlN [8]. Another interesting study on the effect of incorporating micron- and nanometer-sized aluminum particles in polyester resin established that overall fracture toughness increased monotonically with the volume fraction of aluminum particles, for the given particle size, provided particle remains de-agglomerated and dispersed. Also, nanoparticles led to a greater increase in fracture toughness for a given particle volume fraction. Elastic modulus was in accordance with the rule-of-mixtures [9]. Fu et al. critically reviewed the effect of particle size, particle/matrix adhesion, and particle loading on composite stiffness, strength, and toughness of a range of composites having micro and nano-fillers [10]. They report diverse trends of the effect of particle loading on composite strength and toughness are observed due to the interplay between these three factors. However, composite stiffness depends on particle loading, not particle/matrix adhesion. There is also a critical particle size (usually in nanoscale) below which the composite stiffness is greatly enhanced (by the much larger surface area) imparting a nano-effect.

1.2.1.2 Filler Surface Modification and Its Effects on Composite Properties

Surface modification of fillers is an easy and reliable method to bring out desired changes at the interface and thus to improve the overall macroscopic properties of composites [11]. The method employed for filler synthesis markedly changes the surface energy. The widely used method for surface modification of inorganic filler is by silane-coupling. The chemistry involved in this modification is a generation of reactive silanol group which undergoes a condensation reaction with other silanol groups to form siloxane linkages. In a recent report on styrene-butadiene (SBR)-based formulation for passenger car tires with ultra-low rolling resistance and high wet-grip performance, it has been shown that the pyrogenic and precipitated silica results in composites of very different properties. On the basis of structural phenomenological modeling using layered fiber model (LFM), it was noted that depending on the filler surface properties in one class of composites, during deformation, polymer chain slips-off from the polymer interphase around the filler particles into the gaps between aggregates, resulting in uniaxially oriented high-strength polymer fibers and significantly high tensile strength of composites [12]. In another investigation, the problem of increasing the adsorptive and adhesive interaction at the phase boundary between a matrix and reinforcing fibrous filler has been successfully addressed by modifying the surface of carbon-reinforcing fillers through plasma treatment [13]. An interesting work on the ferroelectric-relaxor behavior of nano-spun fiber of $Ba(Zr_{0.3}Ti_{0.7})O_3$ (BZT-NF)-polyvinylidene fluoride (PVDF) composite reports enhanced dielectric constant and reduced loss tangents at a low volume fraction of BZT-NF surface modified with poly(vinyl pyrrolidone) (PVP) [14]. Both high-energy gamma radiation and electron beam (EB) irradiation have

been used to modify filler surfaces to overcome organophobic character of inorganic fillers and enhance filler–matrix compatibility. Radiation-induced surface modification of fillers is a chemical-free, clean room temperature process. Thus, no residual chemicals are left for post-modification and also temperature-sensitive fillers can be modified using this method. In a study on radiation-modified fillers, maleic anhydride (MA) was adsorbed on montmorillonite (MMT) surface through ionic interaction. The modified filler was dispersed in polypropylene (PP) followed by EB irradiation. It has been postulated that EB irradiation leads to a covalent linkage between radicals generated on MA (of MMT surface) and PP matrix leading to a significant increase in mechanical properties [15]. The EB irradiation of fillers enhances mechanical properties and tribological properties of composites. It has been reported that the introduction of EB irradiated PTFE in ethylene–propylene–diene–monomer (EPDM) not only enhances mechanical properties but also tribological properties of composites. The friction and wear processes (shown in Fig. 1.2) change drastically for EPDM through breaking adhesive bonds on boundary layers, plastic deformation of the contacting area zones, and plowing due to roughness peaks and wear debris and elastic hysteresis due to damping on the incorporation of irradiated PTFE. The coefficient and specific wear rate of irradiated PTFE-filled EPDM increased with an absorbed dose of PTFE. Increase in absorbed dose also increases the energy dissipation (tan δ) of the composite [16]. Recent work on radiation vulcanization of styrene–butadiene rubber (SBR) silica composites reports use of γ-ray for grafting of polybutadiene (PB) oligomer on the silica surface. The radiation-grafted silica was

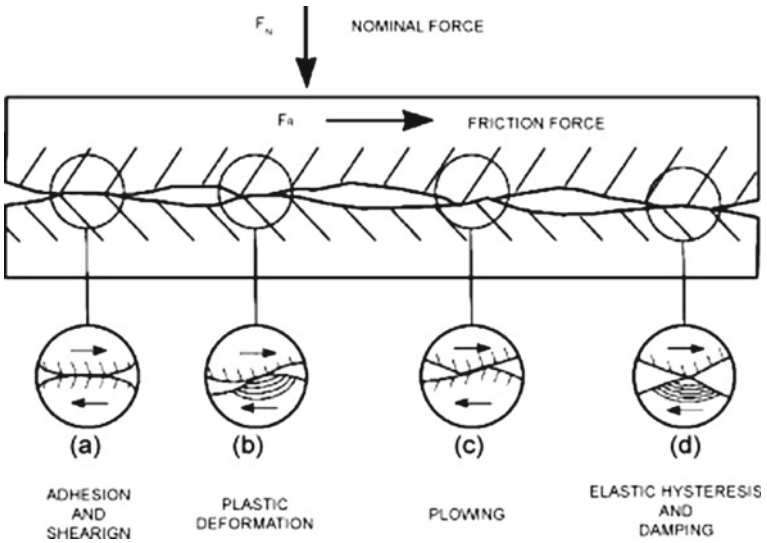

Fig. 1.2 Friction and wear mechanisms involved in viscoelastic solid bodies sliding against a rough counter surface. "Reproduced with the permission of Elsevier" [16]

dispersed in the SBR matrix. The electron paramagnetic resonance (EPR) investigation indicated that PB coating on silica is effective in enhancing the mechanism of formation of filler SBR covalent links [17]. Gamma-ray irradiation technique was used to functionalize graphene oxide (GO) with alkylamines of various alkyl chain lengths. Scanning electron microscopy (SEM) analysis showed an increase in surface roughness with an increase in alkyl chain length. The addition of alkyl chains on GO surfaces also improved the thermal stability of the GO [18].

1.2.2 Polymer Matrix

The polymer matrix is the continuous component of the composite. Its primary function is to hold the dispersed phase and is usually softer and ductile than the filler. Choice of polymer matrix for the composite depends on the intended application of the composite. The major advantages of polymers, as the matrix, are lightweight, low cost, easy processability, and good chemical resistance. Low modulus and high thermal sensitivity limit their applications [19].

1.2.2.1 Types of Polymer for the Composite Synthesis

Almost all type of polymers, thermosetting, thermoplastic, elastomers, or their blends can be used for preparing composites. Thermosetting polymers, e.g., epoxies, phenolics, and melamines, form covalently cross-linked polymer network structures. They decompose on heating instead of softening. Thermosets are commonly used in fiber-reinforced plastics. As initial viscosity of these mixes is low, they are easy to handle. However, as thermoset resins undergo chemical reaction to cross-link the polymer to form three-dimensional (3D) network, a single monolith of filler embedded in 3D polymer network is formed. The 3D network provides dimensional stability, high-temperature resistance, and good solvent resistance. The inherent synthesis process of thermoset composites (TSCs) leads to some design considerations of the finished product. The TSCs are highly anisotropic. As the cured composite itself takes the final structural form, there is poor scope for post-synthesis modification. Recycling of TSCs is energy-intensive and difficult [20]. Thermoplastic polymers are either semicrystalline or amorphous polymers consisting of linear or branched chain molecules. Polyethylene, polypropylene, polystyrene, nylons, polycarbonate, polyether ether ketone (PEEK), etc., fall in this class of polymer. They are characterized by strong intramolecular interactions but weak intermolecular interactions. Elastomers are highly amorphous polymers with glass transition temperature (T_g) well below ambient temperature and are thus soft and flexible. They find application as flexible molded parts, sealants, and adhesives. Natural rubber (NR), ethylene propylene diene rubber (EPDM), butyl rubber, polysiloxanes, and fluoroelastomers fall under the elastomer category [21]. A fast-evolving use of elastomers in composites is for electromagnetic (EM) shielding [22], where the introduction of conducting

fillers like graphene and nano carbon black (NCB) negates its insulating behavior and enhances its electromagnetic interference-shielding effectiveness, attenuation, and reflection of electromagnetic waves. The fillers like graphene and carbon nanotube (CNT) could also drastically improve the low stiffness of elastomers. Large volumes of elastomer composite find use as automobile tires. Technologies have been now developed for complete retrieval of different components of used tires leaving the minimal environmental effect of waste tires [23].

1.2.3 Interface in Composites

The interactions between filler and polymer matrix at the interface vary considerably from one combination of reinforcement/matrix to others. Interactions at interface have been a debatable proposition. Some groups speculate the formation of primary bonds (covalent and/or ionic) between two phases while others feel that secondary bonding (weak van der Waals interactions) or hydrogen bonding has an important role to play in adhesion of two phases. The interface being a key factor in the performance of composite, rigorous efforts is still on to modify, characterize, and understand it. For a filler–matrix combination, interface is tailored depending on the desired properties of the composite. Interfacial interactions are sometimes so strong that lead to the formation of a distinct phase termed as "interphase." Figure 1.3 illustrates composite interphase [24]. Interphase is as a result of and controls the interaction between filler and the polymer matrix. Strong chemical bonding and relatively weak interfacial bonding would contribute to the improvement in different properties, e.g., in case of structural composites, strong bonding between fiber and polymer leads to increased tensile strength and stiffness, whereas weak interfacial bonding results in better

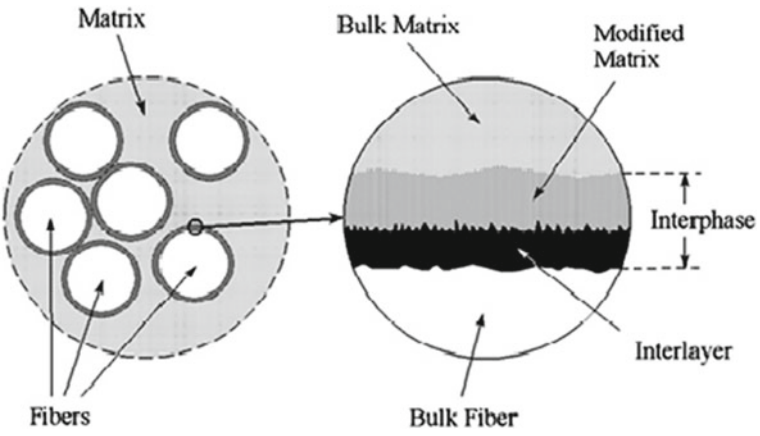

Fig. 1.3 Schematic representation of composite interphase. "Reproduced with the permission of Elsevier" [24]

damping characteristics. Interphase no doubt is the fulcrum of the properties of PCs; however, the constituents of PC, the processing protocol followed, and morphology and size of filler are equally important variables that decide final properties of PC. The effect of these variables has been well understood and documented [25–31].

1.2.3.1 Interface Modification by Filler Treatment

Certain strategies are adopted to modify the filler surface. The interface tailoring for reinforcing fibers is mainly done by (i) polymer deposition on fiber surface (ii) nanostructuring of fiber surface, and (iii) sizing/coating of fiber [2]. The polymer coating on reinforcing fiber surface results in gradient structure at interface, i.e., in such cases the properties gradually change from fiber surface toward the bulk of the matrix (as shown in Fig. 1.3). The polymer coating on fiber surface can be done by polymer grafting, plasma polymerization, or through self-assembly. As the name suggests, polymer grafting involves growing polymer chains on the filler surface. Conventional thermochemical grafting and radiation-induced grafting have been adopted for grafting purpose. Bayley et al. have used a copolymer, polyacrylonitrile-graft-poly(dimethylsiloxane) (PAN-g-PDMS), as fibrous filler for poly(dimethylsiloxane) (PDMS). The graft copolymer was electrospun to produce the fiber filler. It was shown that the PDMS content of the graft copolymer provides increased compatibility with silicone matrices and excellent dispersion of the fiber fillers throughout the silicone matrix. Presence of PAN-g-PDMS as filler further aided the incorporation of multi-walled carbon nanotubes (MWNT) in the composites. The inclusion of PAN-g-PDMS in PDMS in non-woven and aligned forms resulted in significantly different mechanical properties [32]. In another interesting work, microcrystalline cellulose fibers (MCFs), extracted from sisal fibers, were treated with functional end-group hyperbranched liquid crystals (HLP). The treated HLP-MCFs was used for synthesizing HLP-MCFs co-epoxy composites. Even at as low as 1.0 wt% of HLP-MCFs content flexural strength, tensile strength, impact strength, and flexural modulus increased by 60%, 69%, 130%, and 192%, respectively, for the composite [33]. Filler grafted by mutual radiation grafting technique or post-irradiation grafting technique has also shown an effective improvement in many composite systems. Chao et al. report γ-irradiation grafting of poly(butyl acrylate) (PBA) onto pretreated nano-sized calcium carbonate ($CaCO_3$). The melt compounding of PP with grafted $CaCO_3$ resulted in a synergistic effect, due to the interlayer of grafted PBA between PP and $CaCO_3$. The composite displayed a significant increase in notch impact strength and elongation to break of PP at a rather low content of grafted nano-$CaCO_3$ [34]. An interesting study on EB grafting of fillers reports grafting of trimethylolpropane triacrylate (TMPTA) onto titanium dioxide (TiO_2). The effect of modified and unmodified TiO_2 onto PP composites revealed, a modified filler not only enhances the mechanical properties significantly but also the reinforcing effect of filler is fully felt even at low filler loading for treated nanoparticles. The EB modification of fillers has many advantages, like a simple process, low cost, ease of control, and having broader applicability [35].

Sizing of filler alters the filler surface and hence the interface. Qing Wu et al. reported the effects of sizing of carbon fiber (CF) using acetone at elevated temperature on the CF-epoxy composite interface. It was shown that up to certain temperature (200 °C), interfacial shear strength of CF-epoxy composite improved markedly post sizing reaction. The interface modulus also increased with a thinner gradient distance. Further increase in surface roughness and a decrease in fiber wettability with epoxy were observed [36]. In other research article influence of sizing components, coupling agents and film formers of glass fiber on the interface of reinforced polyurethane (PU) composites have been reported. The interfacial adhesion properties of untreated, extracted, heat-treated glass fibers, and polyurethane resin were measured through the micro-droplet test. The results showed that the interfacial shear strength of the glass fiber-reinforced PU composite mainly depends on the coupling agents, in which the N-containing groups play a dominant role [37].

1.2.3.2 Interface Modification by Matrix Treatment

Altering the interactions at the interface by treatment of matrix is also another potential strategy to enhance filler matrix compatibility. The matrix modification is preferred over filler modification particularly when the filler surface modification conditions are too demanding. It has been reported that compared to conditions for filler modification, the matrix modification involves fewer solvent-based processes [38]. In a recent study, wood polypropylene composites were prepared using polypropylene (PP) modified using divinyl benzene (DVB) and MA to improve interfacial compatibility. It was noted that compared to unmodified PP, composites containing coupling agent or MA modified PP or PP modified by both (DVB and MHA) improved the tensile, flexural, and impact strengths to a greater extent. Interestingly, adding a small amount of DVB (0.4%) resulted in a significant increase in impact strength in comparison with that of the composites modified with only MA [39]. Lai et al. report high permittivity of barium titanate/epoxy resin (BT/ER) composite through graft modification on the ER matrix. Polyether polyols were employed to enhance the molecular polarity of epoxy, which brought more polar oxygen atoms and produced more ester groups in the cured epoxy resin. The permittivity of the composite films containing the same amount of BT fillers improved from 18.91 to 28.73, while the dielectric loss remained nearly unchanged [40]. An excellent article by Gutowski on theoretical principles of macromolecular design of interfaces provides deep insight into contemporary theories on macromolecular "connector molecules." It explains how the chains grafted onto solid polymer surfaces effectively improve adhesion and fracture performance of interfaces. The crux of the investigation is that the interaction between polymers and adjacent material happens through one or both of the following mechanisms (i) chemical reaction/cross-linking with the adjacent material and (ii) interpenetration into adjacent phase. It has been shown that the effectiveness of the interface reinforcement by surface-grafted connector molecules depends on the surface density of grafted molecules, length of individual

chains of grafted molecules, and optimum surface density in relation to the length of connector molecules [41].

1.3 Fabrication, Assembly, and Processing of Composites

The fabrication and shaping of composites into finished products often combine the formation of the material itself during the fabrication process. The primary manufacturing methods used to produce composites include manual and automated layup, spray-up, filament winding, pultrusion, and resin transfer molding.

Manual layup is the oldest and simplest method for manufacturing of reinforced products. It involves cutting the reinforcement material to the desired size. The cut pieces are impregnated with a wetting matrix material and spread over a mold surface pre-coated with a release agent. The impregnated reinforcement material is then hand-rolled to ensure uniform distribution and to remove trapped air. More reinforcement material is added until the desired thickness of part has been built up. Manual layup can also be performed using pre-impregnated reinforcement material, called "prepreg." The use of prepreg material eliminates separate handling of the reinforcement and resin. It improves final composite quality but requires stringent process control to prevent premature curing. The throughputs of the manual layup can be increased through machine automation. There is virtually no limit to the size of the work that can be tape-rolled (particularly through automation), but the shape has to be relatively flat to butt each successive layer without gaps or wrinkles [42].

In spray-up, the resin is sprayed onto a prepared mold surface using a specially designed spray gun. This gun simultaneously chops continuous reinforcement into suitable lengths as it sprays the resin. It is suitable for making tub, boats, tanks, and transportation components in a variety of shapes and sizes. Through spray-up, the chopped laminate has a good conformability. It is faster to hand layup method particularly when complex molded shapes are desired. After layup, the composite parts can be cured at room temperature, with hot air, by oven baking, using heated plates or in autoclaves. The curing time depends on the heating method and may range from an hour to a day. Curing can also be accomplished by bag molding in which a non-adhering plastic film is sealed around the layup material and mold plate. Curing is done with heat and pressure, and vacuum is slowly created under the bag forcing it against the layup as a result of which integrated molded part shaped to the desired configuration is obtained [42].

Filament winding is used for the manufacturing of curved/circular surfaces such as pipes, tubes, spheres, cylinders, and construction of large tanks and pipework for the chemical industry. Filament winding is typically applied using either hoop or helical winding. High-speed precise laydown of continuous reinforcement in pre-described patterns is the basis of the filament winding method [42].

Pultrusion is a continuous process used to produce long, straight shapes of constant cross section. Pultrusion is similar to extrusion except that the composite material is pulled, rather than pushed, through a die. Pultrusions are produced using continuous

reinforcing fibers that provide longitudinal as well as transverse reinforcement in the form of mat or cloth materials. These reinforcements are resin impregnated by drawing through a resin mix and shaped within a guiding or performing system. They are then subsequently shaped and cured through a preheated die or set of dies [42].

Resin transfer molding (RTM) has proven to be the most economic process for the fabrication of large, integrated, and high-performance products. In this process, a set of mold halves are loaded with dried, cut reinforcement material shaped into a preformed piece (called preform), and then clamped together. The resin is then pumped or gravity fed into the mold infusing the reinforcement material. Once the mold is filled with resin, it is plugged and allowed to cure. After curing, the mold halves are separated and the part is removed for final trimming and finishing. Reaction injection molding (RIM) is similar to the injection molding except that here those thermosetting polymers are used, which requires a curing reaction to occur within the mold. Here the two parts of the polymer are mixed together, and the mixture is then injected into the mold under high pressure using an impinging mixer. Among polymers, polyurethane (PU) is the most common RIM processable material. If reinforcing agents are added to the mixture of RIM, then the process is known as reinforced reaction injection molding (RRIM). A subset of RRIM is the structural reaction injection molding (SRIM), where meshes are a reinforcing agent. The fiber mesh is first arranged in the mold, and then the polymer mixture is the injection molded over it [42].

Cured composites may be sawed, drilled, or machined to desired dimensions and shape using sharp tools. In view of high abrasiveness of composites, the use of coolant is preferred to avoid heat buildup during machining. Composite parts can be assembled using suitable adhesives producing strong permanent joints. Curing and setting with the pressing of workpieces in a fixture at room temperature or elevated temperature are common practice for composite assembly. Mechanical fastening of joint configurations like a lap, double lap, overlays, and scarf joints using rivets, screws, nut and bolts pins, and other fasteners is also adopted for multi-component composite assembly [42].

1.4 Composites and Their Applications

Polymer composites were initially envisaged for lightweight high-strength material but in last two decades, and another genre of composites, namely conducting composites has been the area of active research due to their application as chemiresistive sensors, strain sensors, piezoresistive sensors, electromagnetic interference (EMI) shielding, radio frequency (RF) shielding microelectronics, and antistatic protectors. Conducting polymer composites (CPC) score over intrinsic conducting polymers (polymer with a backbone of π–conjugated electrons) in terms of pronounced mechanical and environmental stability as well as the option of tunable conductivity [43]. Polymers like poly(ethylene) (PE), PP, poly(urethane) (PU), elastomers, conducting polymers, their blends, and fillers like electrically conductive functional

materials like carbon black (CB), carbon fiber (CF), carbon nano-fiber (CNF), single-walled carbon nanotube (SWCNT) and multi-walled carbon nanotube (MWCNT), graphene, graphite, metals and metal oxides, and conjugated polymers have been used for composite preparation. Solvent-based as well as solvent facile methods have been practiced for preparing CPC [44]. Preferential percolation is a fast-evolving promising strategy to develop conducting composites at a lower loading of conducting filler. In an interesting development, recently synthesis and characterization of acrylonitrile butadiene styrene (ABS)-polycaprolactam (PCL)-NCB-based conducting composites were reported. It was found that in the composites, ABS and PCL exist as two separate non-interacting phases in which NCB selectively percolates at the interface. The electrical conductivity of the composites as a function of polymer ratio in the composites is shown in Fig. 1.4. Thermal investigation (Fig. 1.5) of these composites established that an optimum composition of composite results in sudden disruption of conductivity depending on T_g of the polymer matrices. Such composites may find application as effective overcurrent protection devices [45].

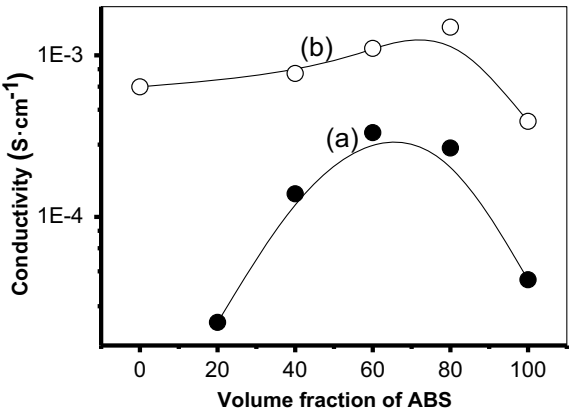

Fig. 1.4 Variation of DC conductivity with blend (ABS-PCL) composition for (**a**) 30 wt% NCB and (**b**) 50 wt% NCB. "Reproduced with the permission of John Wiley and Sons" [45]

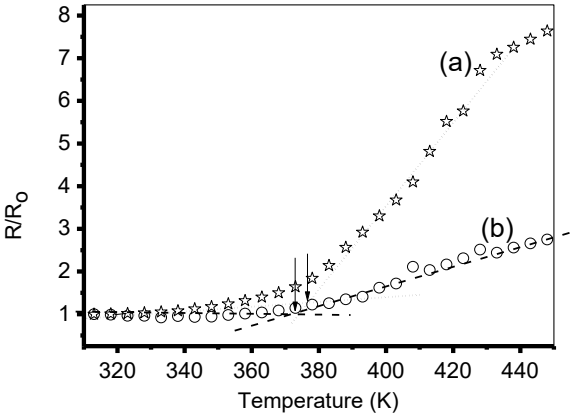

Fig. 1.5 Abrupt changes in the electrical conductivity of (**a**) ABS/NCB 30 wt% and (**b**) ABS/NCB 50 wt% binary composites; dotted lines represent linear fit in two regions (before and after T_g) of ABS and intersection of two slopes that have been shown by arrows. "Reproduced with the permission of John Wiley and Sons" [45]

Radiation has proven to be an effective tool for the synthesis and processing of CPC due to its inherent advantages. Dubey et al. recently reported strain sensing behavior of fluorocarbon elastomer (FCE)-nanocarbon black (NCB) nanocomposites of different network densities [44]. Different extent of cross-linking was achieved by irradiating with high-energy radiation from Co-60 gamma source for different doses. Figure 1.6 shows a synthesis protocol for these composites. The effect of network density on AC, DC conductivity, and electromechanical performance has been reported. Network density was found to have a profound effect on the sensing range as well as on the gauge factor (GF) of the composites (Fig. 1.7). Cyclic strain sensing response was also found to be affected by network density, and the best results were observed for a network density of 73.2 μmol/g. At higher network density (290 μmol/g), two peaks were observed for each strain cycle, and the sensing response was not stable (Fig. 1.8). For 5 and 10% cyclic strains, the gauge factor was around 14, and no change in gauge factor was observed within 2–5 mm/min strain rates [46]. Mondal et al. explored the development of FCE-NCB composite-based novel stand-alone radiation processed chemiresistive sensor with high sensitivity and selectivity for 2-propanone. They report significant, radiation absorbed dose-dependent change

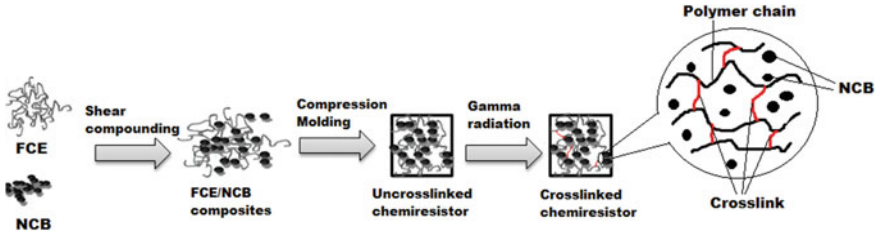

Fig. 1.6 Schematic of FCE/NCB strain sensor/chemiresistor synthesis protocol (red lines depict cross-linking). "Reproduced with the permission of Elsevier" [48]

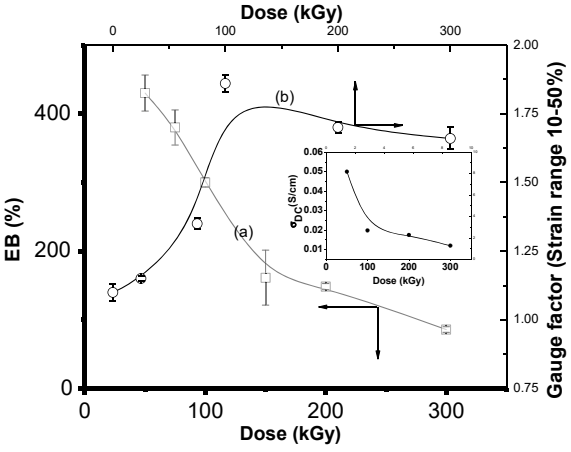

Fig. 1.7 Variation in elongation at break (EB) and gauge factor for nanocomposite with 0.35 weight fraction of NCB with dose. (**a**) Elongation at the break. (**b**) Gauge factor. Inset: change in DC conductivity with the dose for nanocomposite with 0.35 weight fraction of NCB. "Reproduced with the permission of Elsevier" [48]

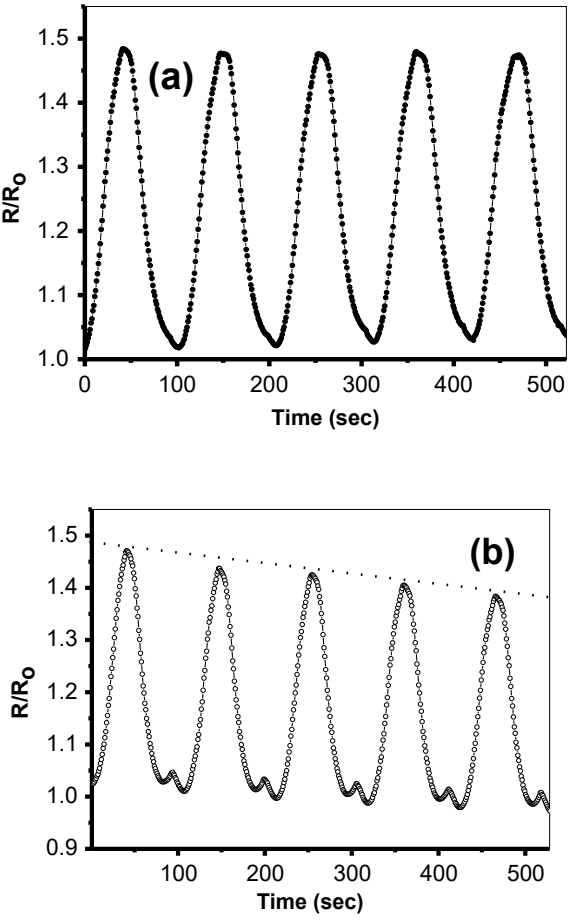

Fig. 1.8 Sensing response (R/R_o) of nanocomposite (FCE-NCB) with 0.35 weight fraction of NCB irradiated to different doses at 5% strain at a strain rate of 1 mm/min. (**a**) 50 kGy, (**b**) 200 kGy. "Reproduced with the permission of Elsevier" [48]

in relative change in resistance (A_r) and sensing kinetics of chemiresistive sensors. As shown in Fig. 1.9, the chemiresistor showed linear response with 2-propanone concentration and also highly selective response for 2-propanone in comparison with others like benzene, toluene, xylene, ethanol, methanol, and water (Fig. 1.10) [47].

Certain studies report the synergistic effect of two fillers on composite properties. Hybrid nano-carbons have been reported to have synergetic advantages on several mechanical and electrical applications. Recently, the development of PDMS-CNT-NCB-based novel chemiresistive sensors through a solvent-free route was reported. These sensors demonstrated high sensitivity and reversible response against benzene, toluene, ethylbenzene, and xylene (BTEX) (Fig. 1.11). The sensing response had a strong correlation with BTEX–PDMS interaction parameters (χ). Introduction of CNT in PDMS-NCB composite affected detection of each analyte differently. The principal component analysis using an array of four chemiresistors with different CNT content demonstrated distinct pattern only for benzene. The sensitivity and

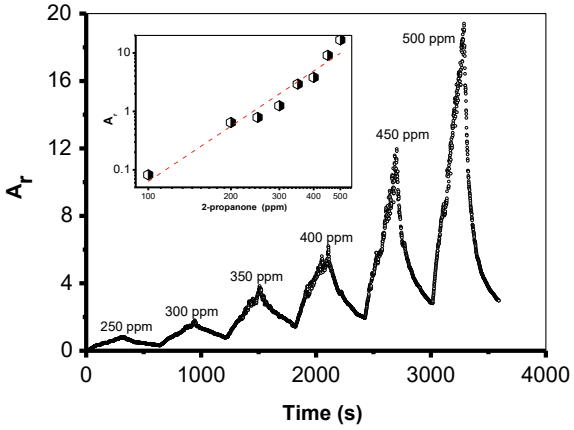

Fig. 1.9 Variations in the A_r (relative change in resistance; $\Delta R/R_o$) with an increase in 2-propanone concentration (ppm), 2-propanone field nitrogen cycles are shown at each concentration to highlight reversibility [static setup]; inset shows log–log linear fitting. For composite FCE:NCB (65:35) irradiated to an absorbed dose of 100 kGy. "Reproduced with the permission of Elsevier" [47]

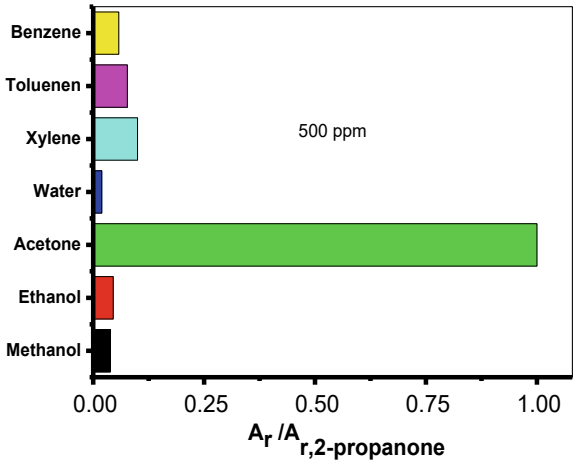

Fig. 1.10 Variation in the relative change in resistance for chemiresistors {FCE:NCB (65:35)} irradiated to an absorbed dose of 100 kGy; [volatile organic compound] = 500 ppm, static setup. "Reproduced with the permission of Elsevier" [47]

the temperature coefficient of resistance of chemiresistors decreased; whereas, the detection range increased considerably with the addition of CNT [49]. Majji et al. report radiation degradation of Teflon scrap to micro-fine powder and utilization of this polytetrafluoroethylene micro-powder (PTFEMP) for the synthesis of EB cross-linked PDMS-PTFEMP composites [47]. A linear increase in modulus up to an optimum cross-linking dose is reported. As shown in Fig. 1.12, the introduction of PTFEMP did not affect the surface energy of PDMS but significantly reduced the coefficient of friction of the composites [50]. Exceptional synergistic effects between organic–inorganic dual filler in ethylene-vinyl acetate (EVA) composites have been

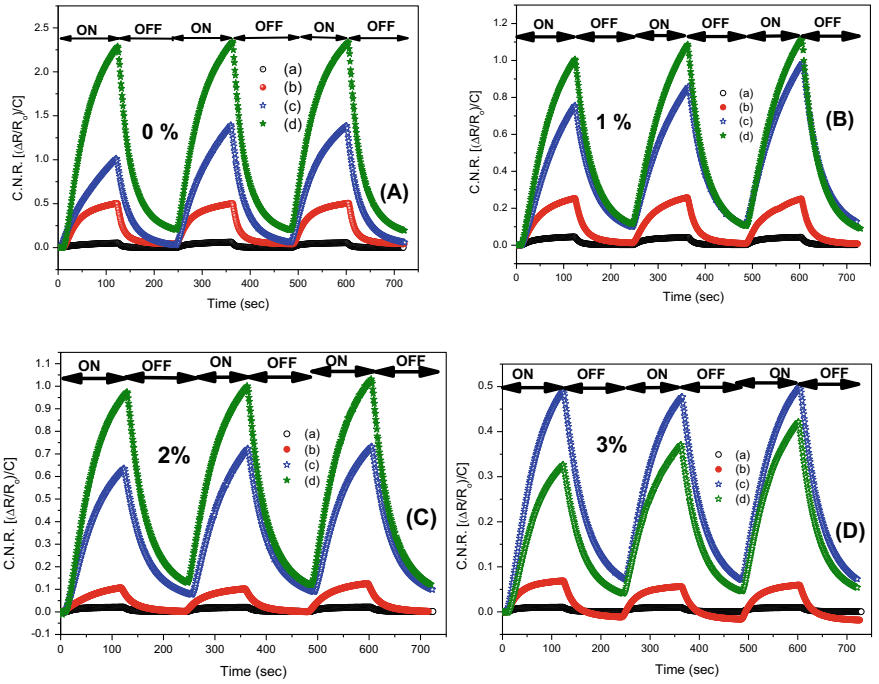

Fig. 1.11 Concentration normalized relative change in the resistance [CNR = $(\Delta R/R)/C$, μL/L] for PDMS-NCB: 70:30 nanocomposites (**a**) Benzene. (**b**) Toluene. (**c**) Ethyl benzene, (**d**) Xylene. (**A**) 0 wt% CNT, (**B**) 1 wt % CNT, (**C**) 2 wt% CNT, (**D**) 3 wt% CNT BTEX flow rate = 100 ml/min. "Reproduced with the permission of Elsevier" [49]

Fig. 1.12 Coefficient of friction PDMS-PTFEMP composites

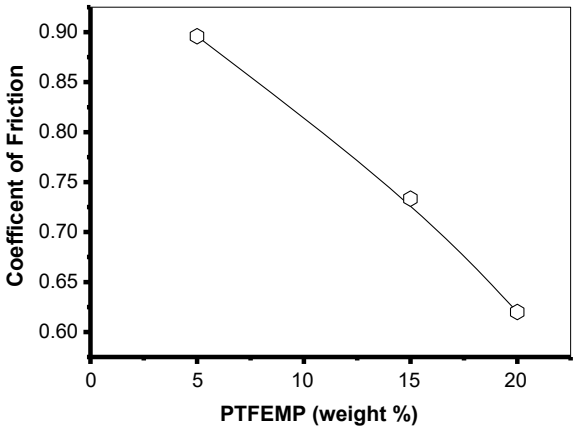

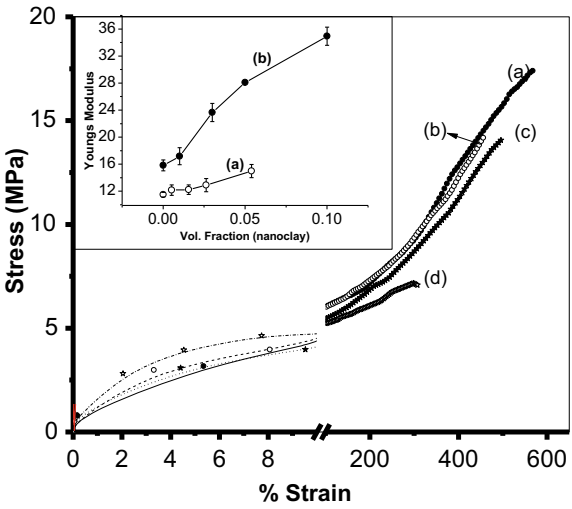

Fig. 1.13 Stress–strain profiles for EVA/organoclay (5%) composites having different loading of PTFEMP (**a**) 5%, (**b**) 10%, (**c**) 20%, (**d**) 50% inset: effect of organoclay loading on modulus (**a**) EVA, (**b**) EVA/PTFEMP (15%) composites. "Reproduced with the permission of Elsevier" [51]

observed. Composites of EVA containing PTFEMP and organoclay were prepared by melt compounding. The exceptional increase in the mechanical properties of ternary composites demonstrated high synergy between fillers, leading to a manifold increase in the modulus of dual filler-filled composites in comparison with single filler-filled systems (Fig. 1.13). X-ray diffraction studies revealed ~10% intergallery expansion in organoclay, in the composites having a high loading of PTFEMP; though no significant change in the crystallinity of EVA was observed [51].

Composites are not confined to applications like improvement in mechanical properties or electrical applications. They have been extensively investigated for other applications particularly biomedical applications. $MgSO_4$-EVA composites were found to function as a wide range (15–4000 Gy) absorbed dose dosimeter for industrial radiation processing (Fig. 1.14). During post-irradiation, the electron paramagnetic resonance (EPR) signal of the composite dosimeters faded by ~20% in a month's period. The energy dependence response of the dosimeter was within acceptable limits [52, 53]. Composites of high-density fillers have been investigated for applications involving high-energy attenuation. Recently, interesting findings on EVA-$BaSO_4$ (EVA-BS) composite as highly radiopaque flexible polymer composites for X-ray imaging application have been reported. As shown in Fig. 1.15a, 0.7-mm-thick sheet of EVA-BS composites had markedly higher gray value (radiopacity) than 1 mm sheet of aluminum while retaining more >1200% elongation at break and complete flexibility [54]. On similar lines, Dubey et al. reported studies on radiation cross-linked PDMS-Bi_2O_3 composites. As shown in Figs. 1.16 and 1.17, the composites were highly flexible and showed effective attenuation of low-energy (Am-241; 59.9 keV) γ-rays [55].

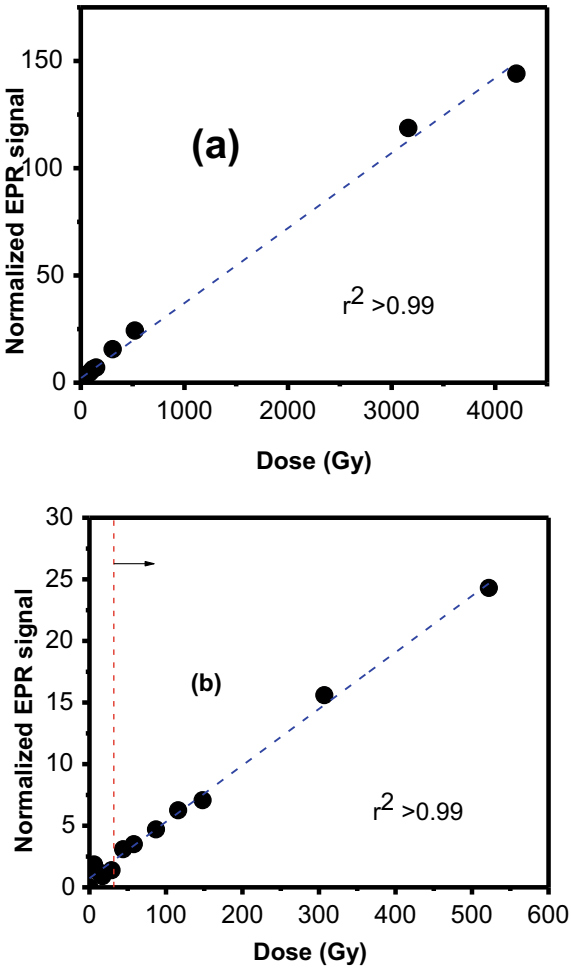

Fig. 1.14 Effect of the absorbed radiation dose on the peak-to-peak amplitude of the EPR signal (A_{pp}) of the composite (EVA:$MgSO_4$: 50:50): (**a**) 500 Gy to 4 kGy, (**b**) 10 Gy to 500 Gy. "Reproduced with the permission of Elsevier" [52]

1.5 Smart Composites

The current focus of composite research is on the composites which would mimic biological composites. These composites in addition to the desired role (say the increase in mechanical properties) would also be able to sense the damage and undergo self-healing. Thus, in this approach self-sensing of damage in composites employs the reinforcing fibers as the sensing element, obviating the need for the addition of sensing elements to the composite. The concept involves monitoring overall strain in the composite unit in terms of overall resistance or conductivity in the form of an electrical signal. An interesting investigation on this concept is of laminate composites of fiber-reinforced plastics (FRP) proposed for a high-end application like aerospace. Zhang et al. have reported the utility of an embedded CNTs network in

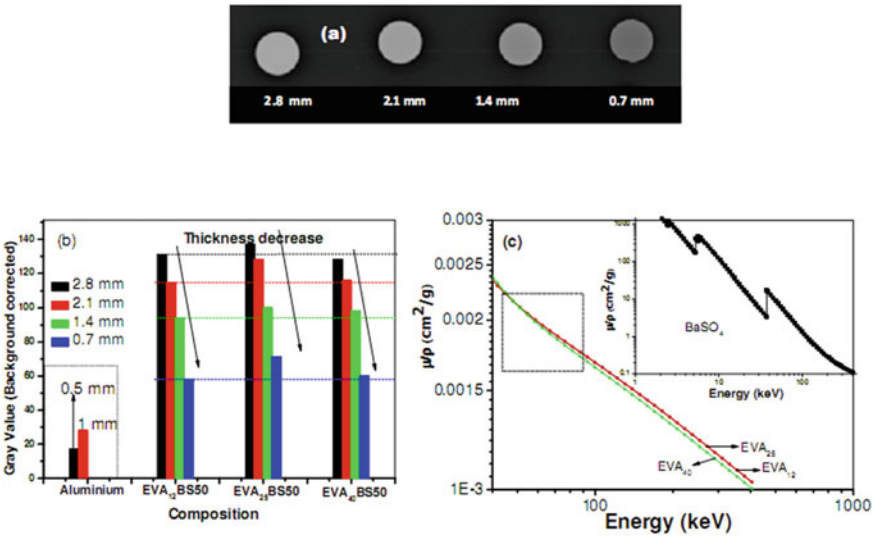

Fig. 1.15 Radiopacity of the composites. (**a**) Actual X-ray radiographs of EVA_{25}:BS (50:50) composites of different thicknesses. (**b**) Variation in gray values for composites with composition; dotted block presents gray values for aluminum sheets. (**c**) Variation in mass attenuation coefficient variation of EVA_{12}, EVA_{25}, and EVA_{40} with X-ray energy (inset: variation in the mass attenuation coefficient of BS with X-ray energy). "Reproduced with the permission of Elsevier" [54]

Fig. 1.16 Flexible radiation shield composite of PDMS-Bi_2O_3 (30:70). "Reproduced with the permission of John Wiley and Sons" [55]

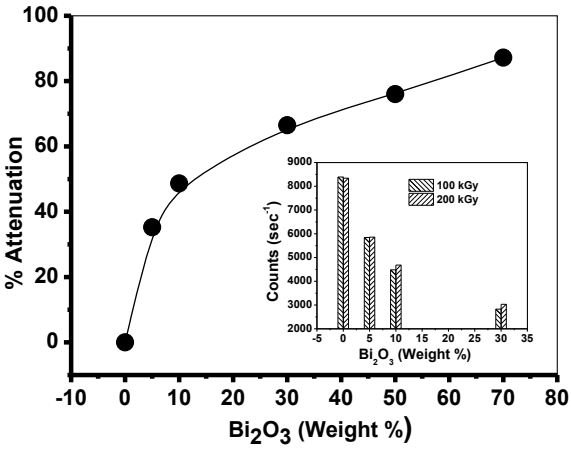

Fig. 1.17 Variation in attenuation of different composites irradiated to different doses. Inset: variation in counts with Bi_2O_3 (weight %) at two different radiation doses. "Reproduced with the permission of John Wiley and Sons" [55]

FRP for sensing wear and tear in FRP. It was shown that change in the propagating wear and tear (displacement) with applied stress disturbs the continuity of embedded CNT network proportionately which is reflected as change is resistance of the FRP. Thus, such introduction of CNT into FRP composite provides not only integrated damage sensing capability but also leads to additional mechanical reinforcement [56]. Another study on self-sensing composites for impact damage detection reports the use of commercially available *E*-glass fabric as sensing as well as reinforcing agent for commercial resin-based composite. The extent of damage induced in the panel can be monitored visually or by light transmission. The system is capable of detecting low-energy impacts within the panel. The progression of damage could also be monitored, and multiple impact damage events could also be observed. It was shown that this system is capable of not only identifying and locating the impact but can also quantify the extent of damage within the composite [57]. A notable feature of assemblies/components made from such composites is that non-destructive (NDT) inspection is required which otherwise results in significant reduction in downtime of the system.

Irrespective of the composite application once cracks or faults have formed, the integrity of the structure is significantly compromised. Therefore, to avoid drastic deterioration in properties, the next logical step would be the initiation of a self-repair mechanism on sensing the fault. In fact, the autonomic healing concept was successfully demonstrated at the beginning of the twenty-first century by incorporating a microencapsulated healing agent and a catalytic chemical trigger within an epoxy matrix [58]. An excellent review on the topic appeared recently [59]. As the interface is often the weakest region in composites where failure starts, therefore, it is obvious that self-healing action originates from the filler–matrix interface. In this respect, two distinct approaches are generally followed [2].

(i) **Capsule-based healing systems**: In capsule-based self-healing systems, the healing agent is in the form of discrete capsules. The damage to composite

ruptures these capsules to release the contents at the interface. Thus, if debonding between filler and matrix causes weak load transfer, the repair mechanism rejuvenates bonding and hence the efficient load transfer.

(ii) **Intrinsic self-healing behavior**: Here reversible physical and chemical reactions are exploited to bring out the repair. These physical/chemical reactions are triggered by damage itself or some time by an external stimulus. Predominantly, processes like reversible polymerization, hydrogen or ionic bonding, molecular diffusion causing entanglements, and melting of a thermoplastic phase are involved in self-healing. The healing processes may happen in conjunction also as all of them are reversible events.

1.6 Outlook and Future Trends

Composite materials have boundless engineering application where the strength-to-weight ratio, low cost, and ease of fabrication are required. For certain applications, the use of composite materials as compared to metals has in fact resulted in savings of both weight and cost. Polymer composites have been considered among the five synthetic materials that will shape the future of the world. Presently, among the different materials used by the aerospace industry, a large proportion represents fiber-reinforced composites. It is believed that as the cost of these composites decreases, they will find wider applications in automobile and other sectors. Nanocomposites would also not remain confined to presently envisaged applications like lightweight sensors, wind turbine blades, powerful batteries, body scaffolds, etc., because they still are crude in comparison with natural composites which possess incredibly complicated and intricate structure. As the nanocomposite synthesis processes become more refined, it will be possible to design them in a very controlled manner.

Acknowledgements The authors sincerely thank Dr. P. K. Pujari, Director, Radiochemistry and Isotope Group, for his constant encouragement and a keen interest in this work.

References

1. DiBenedetto AT (2001) Tailoring of interfaces in glass fiber reinforced polymer composites: a review. Mater Sci Eng, A 302(1):74–82
2. Karger-Kocsis J, Mahmood H, Pegoretti A (2015) Recent advances in fiber/matrix interphase engineering for polymer composites. Prog Mater Sci 73:1–43
3. Kumre A, Rana RS, Purohit R (2017) A review on mechanical property of sisal glass fiber reinforced polymer composites. Mater Today: Proc 4((2, Part A)):3466–3476
4. Sharpe LH (1998) Some fundamental issues in adhesion: a conceptual view. J Adhes 67(1–4):277–289
5. Park S-J, Seo M-K (2011) Element and processing (chapter 6). In: Park S-J, Seo M-K (eds) Interface science and technology. Elsevier, pp 431–499

6. Rothon R, DeArmitt C (2017) Fillers (including fiber reinforcements) (chapter 8). In: Gilbert M (ed) Brydson's plastics materials, 8th edn. Butterworth-Heinemann, pp 169–204
7. Fischer H (2003) Polymer nanocomposites: from fundamental research to specific applications. Mater Sci Eng, C 23(6):763–772
8. Yung KC, Zhu BL, Yue TM, Xie CS (2009) Effect of the filler size and content on the thermo-mechanical properties of particulate aluminum nitride filled epoxy composites. J Appl Polym Sci 116(1):225–236
9. Singh RP, Zhang M, Chan D (2002) Toughening of a brittle thermosetting polymer: effects of reinforcement particle size and volume fraction. J Mater Sci 37(4):781–788
10. Fu S-Y, Feng X-Q, Lauke B, Mai Y-W (2008) Effects of particle size, particle/matrix interface adhesion and particle loading on mechanical properties of particulate–polymer composites. Compos B Eng 39(6):933–961
11. Dubey KA, Bhardwaj YK, Chaudhari CV, Sarma KSS, Goel NK, Sabharwal S (2011) Electron beam processing of LDPE/EVA/PCR ternary blends: radiation sensitivity evaluation and physico-mechanical characterization. J Polym Res 18(1):95–103
12. Stöckelhuber KW, Svistkov AS, Pelevin AG, Heinrich G (2011) Impact of filler surface modification on large scale mechanics of styrene butadiene/silica rubber composites. Macromolecules 44(11):4366–4381
13. Sidorina AI, Gunyaeva AG (2017) Modification of surface of reinforcing carbon fillers for polymeric composite materials by plasma treatment (review). Fibre Chem 49(1):24–27
14. Liu S, Xue S, Xiu S, Shen B, Zhai J (2016) Surface-modified $Ba(Zr0.3Ti0.7)O_3$ nanofibers by polyvinylpyrrolidone filler for poly(vinylidene fluoride) composites with enhanced dielectric constant and energy storage density. Sci Rep 6:26198
15. Nowicki A, Przybytniak G, Kornacka E, Mirkowski K, Zimek Z (2007) Radiation-induced modification of montmorillonite used as a filler in PP composite. Radiat Phys Chem 76(5):893–900
16. Khan MS, Franke R, Gohs U, Lehmann D, Heinrich G (2009) Friction and wear behaviour of electron beam modified PTFE filled EPDM compounds. Wear 266(1):175–183
17. Dondi D, Buttafava A, Palamini C, Pepori F, Lostritto A, Giannini L, Nahmias M, Conzatti L, Faucitano A (2011) γ-Radiation induced functional modification of silica and radiation vulcanization of SBR-silica composites. Macromol Symp 301(1):90–95
18. Daud NA, Chieng BW, Ibrahim NA, Talib ZA, Muhamad EN, Abidin ZZ (2017) Functionalizing graphene oxide with alkylamine by gamma-ray irradiation method. Nanomaterials 7(6):135
19. Landel RF, Nielsen LE (1993) Mechanical properties of polymers and composites, 2nd edn. Taylor & Francis
20. Peng W, Riedl B (1995) Thermosetting resins. J Chem Educ 72(7):587
21. Pazat A, Barrès C, Bruno F, Janin C, Beyou E (2018) Preparation and properties of elastomer composites containing "graphene"-based fillers: a review. Polym Rev 58(3):403–443
22. Sýkora R, Babayan V, Ušáková M, Kruželák J, Hudec I (2015) Rubber composite materials with the effects of electromagnetic shielding. Polym Compos 37(10):2933–2939
23. Linhua P, Guilin W (2015) The research of scrapped automobiles recycling and disassembling industry development based on auto industry chain. In: MATEC web of conferences, vol 26
24. Cech V, Palesch E, Lukes J (2013) The glass fiber–polymer matrix interface/interphase characterized by nanoscale imaging techniques. Compos Sci Technol 83:22–26
25. Rodriguez-Uicab O, May-Pat A, Aviles F, Toro P, Yazdani-Pedram M (2013) Influence of processing method on the mechanical and electrical properties of MWCNT/PET composites. J Mater 2013:10
26. Li X, Coleman MR (2014) Impact of processing method and surface functionality on carbon nanofiber dispersion in polyimide matrix and resulting mechanical properties. Polym Compos 35(8):1473–1485
27. Lin-Gibson S, Sung L, Forster AM, Hu H, Cheng Y, Lin NJ (2009) Effects of filler type and content on mechanical properties of photopolymerizable composites measured across two-dimensional combinatorial arrays. Acta Biomater 5(6):2084–2094

28. Kim K-H, Ong JL, Okuno O (2002) The effect of filler loading and morphology on the mechanical properties of contemporary composites. J Prosthet Dent 87(6):642–649
29. Kim YH, Kim DH, Kim JM, Kim SH, Kim WN, Lee HS (2009) Effects of filler characteristics and processing conditions on the electrical, morphological and rheological properties of PE and PP with conductive filler composites. Macromol Res 17(2):110–115
30. Jesson DA, Watts JF (2012) The interface and interphase in polymer matrix composites: effect on mechanical properties and methods for identification. Polym Rev 52(3):321–354
31. Gan XY (2009) Effect of interface structure on mechanical properties of advanced composite materials. Int J Mol Sci 10(12)
32. Bayley GM, Hedenqvist M, Mallon PE (2011) Large strain and toughness enhancement of poly(dimethyl siloxane) composite films filled with electrospun polyacrylonitrile-graft-poly(dimethyl siloxane) fibres and multi-walled carbon nanotubes. Polymer 52(18):4061–4072
33. Luo QY, Lu SR, Song LF, Li YQ (2016) Fabrication of sisal fibers/epoxy composites with liquid crystals polymer grafted on sisal fibers. In: IOP conference series: materials science and engineering, vol 137, issue 1, pp 012052
34. Ma CG, Rong MZ, Zhang MQ, Friedrich K (2005) Irradiation-induced surface graft polymerization onto calcium carbonate nanoparticles and its toughening effects on polypropylene composites. Polym Eng Sci 45(4):529–538
35. Madani M (2009) Mechanical properties of polypropylene filled with electron beam modified surface-treated titanium dioxide nanoparticles. J Reinf Plast Compos 29(13):1999–2014
36. Wu Q, Li M, Gu Y, Wang S, Wang X, Zhang Z (2015) Reaction of carbon fiber sizing and its influence on the interphase region of composites. J Appl Polym Sci 132(18)
37. Guo X, Lu Y, Sun Y, Wang J, Li H, Yang C (2018) Effect of sizing on interfacial adhesion property of glass fiber-reinforced polyurethane composites. J Reinf Plast Compos 37(5):321–330
38. Pracella M, Chionna D, Anguillesi I, Kulinski Z, Piorkowska E (2006) Functionalization, compatibilization and properties of polypropylene composites with Hemp fibres. Compos Sci Technol 66(13):2218–2230
39. Yi S, Xu S, Fang Y, Wang H, Wang Q (2017) Effects of matrix modification on the mechanical properties of wood-polypropylene composites. Polymers 9(12):712
40. Lai M, Yu S, Sun R (2014) Ceramic/polymer composites with enhanced permittivity and low dielectric loss through grafting modification of polymer matrix by polyethylene glycol. Mater Lett 122:45–48
41. Gutowski WS (2003) Interface/Interphase engineering of polymers for adhesion enhancement: part I. Review of micromechanical aspects of polymer interface reinforcement through surface grafted molecular brushes. J Adhes 79(5):445–482
42. Tapan BA, Piyush PG, Vijaykumar C (2018) Primary manufacturing processes for fiber reinforced composites: history, development & future research trends. In: IOP conference series: materials science and engineering, vol 330, issue 1, pp 012107
43. Calvert O, Duggal D, Patra P, Agrawal A, Sawhney A (2008) Conducting polymer and conducting composite strain sensors on textiles. Mol Cryst Liq Cryst Sci 484(1):291/[657]-302/[668]
44. Sarath CC, Shanks RA, Thomas S (2014) Polymer Blends (chapter 1). In: Thomas S, Shanks R, Chandrasekharakurup S (eds) Nanostructured polymer blends. William Andrew Publishing, Oxford, pp 1–14
45. Mondal RK, Dubey KA, Bhardwaj YK, Panicker L, Varshney L (2016) Acronitrile butadiene styrene/polycaprolactam/nano carbon black composites: selective percolation, glass transition and temperature dependence of electrical conductivity. Polym Compos 37(2):481–487
46. Dubey KA, Mondal RK, Grover V, Bhardwaj YK, Tyagi AK (2015) Development of a novel strain sensor based on fluorocarbon–elastomeric nanocomposites: effect of network density on the electromechanical properties. Sens Actuators, A 221:33–40
47. Mondal RK, Kumar J, Dubey KA, Bhardwaj YK, Melo JS, Varshney L (2018) Network density tailored standalone-flexible fluorocarbon elastomer/nanocarbon black chemiresistors for 2-propanone field detection. Sens Actuators, B Chem 265:193–203

48. Jamdar V, Kathalewar M, Jagtap RN, Dubey KA, Sabnis A (2015) Effect of -irradiation on glycolysis of PET waste and preparation of ecofriendly coatings using bio-based and recycled materials. Polym Eng Sci 55(11):2653–2660
49. Mondal RK, Dubey KA, Bhardwaj YK, Varshney L (2016) Novel hybrid nanocarbons/poly(dimethylsiloxane) composites based chemiresistors for real time detection of hazardous aromatic hydrocarbons. Carbon 100:42–51
50. Majji S, Dubey KA, Mondal RK, Bhardwaj YK, Acharya S (2014) Development of electron beam cross-linked PDMS/PTFEM composites with low coefficient of friction and high elastic modulus. Polym-Plast Technol Eng 53(5):435–441
51. Dubey KA, Majji S, Sinha SK, Bhardwaj YK, Acharya S, Chaudhari CV, Varshney L (2013) Synergetic effects of radiolytically degraded PTFE microparticles and organoclay in PTFE-reinforced ethylene vinyl acetate composites. Mater Chem Phys 143(1):149–154
52. Suman SK, Kadam RM, Mondal RK, Murali S, Dubey KA, Bhardwaj YK, Natarajan V (2017) Melt-compounded composites of ethylene vinyl acetate with magnesium sulfate as flexible EPR dosimeters: mechanical properties, manufacturing process feasibility and dosimetric characteristics. Appl Radiat Isot 121:82–86
53. Suman SK, Dubey KA, Mishra BB, Bhardwaj YK, Mondal RK, Seshadri M, Natarajan V, Varshney L (2015) Synthesis of a flexible poly(chloroprene)/methyl red film dosimeter using an environment-benign shear compounding method. Appl Radiat Isot 98:60–65
54. Suman SK, Mondal RK, Kumar J, Dubey KA, Kadam RM, Melo JS, Bhardwaj YK, Varshney L (2017) Development of highly radiopaque flexible polymer composites for X-ray imaging applications and copolymer architecture-morphology-property correlations. Eur Polymer J 95:41–55
55. Dubey KA, Chaudhari CV, Suman SK, Raje N, Mondal RK, Grover V, Murali S, Bhardwaj YK, Varshney L (2016) Synthesis of flexible polymeric shielding materials for soft gamma rays: physicomechanical and attenuation characteristics of radiation crosslinked polydimethylsiloxane/Bi_2O_3 composites. Polym Compos 37(3):756–762
56. Zhang H, Bilotti E, Peijs T (2015) The use of carbon nanotubes for damage sensing and structural health monitoring in laminated composites: a review. Nanocomposites 1(4):167–184
57. Rauf A, Hand RJ, Hayes SA (2012) Optical self-sensing of impact damage in composites using E-glass cloth. Smart Mater Struct 21(4):045021
58. White SR, Sottos NR, Geubelle PH, Moore JS, Kessler MR, Sriram SR, Brown EN, Viswanathan S (2001) Autonomic healing of polymer composites. Nature 409:794
59. Mphahlele K, Ray SS, Kolesnikov A (2017) Self-healing polymeric composite material design, failure analysis and future outlook: a review. Polymers 9(10):535

Chapter 2
Synthesis of Advanced Nanomaterials for Electrochemical Sensor and Biosensor Platforms

Anu Prathap M. Udayan and Shilpa N. Sawant

Abstract Advent of advanced analytical techniques for nanoscale characterization complemented by novel synthesis methodologies has led to a plethora of functional nanomaterials. These nanomaterials have opened avenues for application of electrochemical sensors in medical diagnostics, biotechnological, environmental monitoring, wellness monitoring and food markets. This chapter presents an overview of the accomplishments of electrochemical sensor devices based on carbon nanomaterials, noble metals, nanostructured polymers, and metal/metal oxides/composite nanostructures. Also, attempt is made to address several concerns around the selection of appropriate nanomaterials, their characterization and means to utilize the interesting chemistry they offer, especially from the point of view of electrochemical sensing.

Keywords Chemically modified electrodes · Mesoporous nanomaterials · Electroanalysis · Conducting nanomaterials · Nanoscale characterization · Nanobioelectronics

2.1 Introduction

Nanomaterials could be wide term given to the materials having at least one dimension in nanoscale regime of 1–100 nm [1]. There are two broad categories of techniques commonly proposed for synthesizing nanomaterials, the bottom-up approach and the top-down strategy [2]. In the bottom-up approach, the nanoparticles are at atomic scale to begin with, and later grow to the nanoscale level [1, 2]. The top-down strategy begins with a bulk material at the macroscopic degree followed by

A. P. M. Udayan · S. N. Sawant (✉)
Chemistry Division, Bhabha Atomic Research Centre, Trombay, Mumbai 400085, India
e-mail: stawde@barc.gov.in

S. N. Sawant
Homi Bhabha National Institute, Anushaktinagar, Mumbai 400094, India

A. K. Tyagi and R. S. Ningthoujam (eds.), *Handbook on Synthesis Strategies for Advanced Materials*, Indian Institute of Metals Series,
https://doi.org/10.1007/978-981-16-1892-5_2

trimming of the material to the required nanoparticles [1, 2]. Significant advancements in nanotechnology in the previous years have offered numerous electrochemical devices consisting of fuel cells, batteries, supercapacitors and sensors, to name a few [3]. In contrast to traditional bulk-scale materials, nanomaterials have the capacity for better performance due to their high surface-to-volume ratio [3, 4]. One of the foremost impressive accomplishments has been to utilize nanoscale materials for detection of trace analytes such as environmental pollutants, heavy metals, and biomolecules, employing tracking strategies based on electrical, optical, and thermal measurements [5, 6]. Among these, electroanalytical strategies are getting special attention for detection of analytes as a result of its simplicity, cost-effective devices, and field-portability [7]. Conventional electrodes have problems as a result of their slow electron kinetics which seriously impacts the level of sensitivity along with selectivity of the electrodes [8]. Among the various types of sensing systems, nanomaterial-based sensors presently generate highest possible performance owing to their high surface-to-volume ratio which provides ample active sites for electrocatalytic transformation [9]. With considerable growth in the area of nanotechnology over the past few years, conducting nanomaterials based on noble metals, carbon and conducting polymers (CPs) have been integrated into electrochemical device [7–9]. The marvellous electrical properties of nanomaterials have permitted the advancement of brand-new and enhanced electrical detecting platforms, mostly based upon capacitance and cyclic voltammetry (CV), which respond to changes in resistance or current [10]. Hence, the progression of electrochemical sensors has attracted a lot of interest due to their high level of sensitivity and selectivity, and are being increasingly utilized in many areas, including biological science investigation, biomedical and environmental science research [11].

This chapter presents an overview of various kinds of conducting nanomaterials-based electrochemical sensors. The chapter is organized based on the type of functionalized electrode modifiers used to accomplish robust electrochemical sensing units. Attempt is made to selectively concentrate on some materials which have lately demonstrated tremendous success in design of electrochemical sensors having high potential for real life application. A viewpoint on the possible future advancements in electrochemical sensing by boosting the sensitivity for detection of trace analytes using appropriate nanomaterials is also presented.

2.2 Nanomaterials and Nanostructures Relevant to Electrochemical Sensing

Amperometric, potentiometric, conductometric and impedance-based electrochemical sensing units, provide limitless opportunities for the selective and sensitive detection of chemicals and as well as biological targets [12, 13]. Conventional electrodes such as gas electrode, ion selective electrode and chemically modified screen-printed

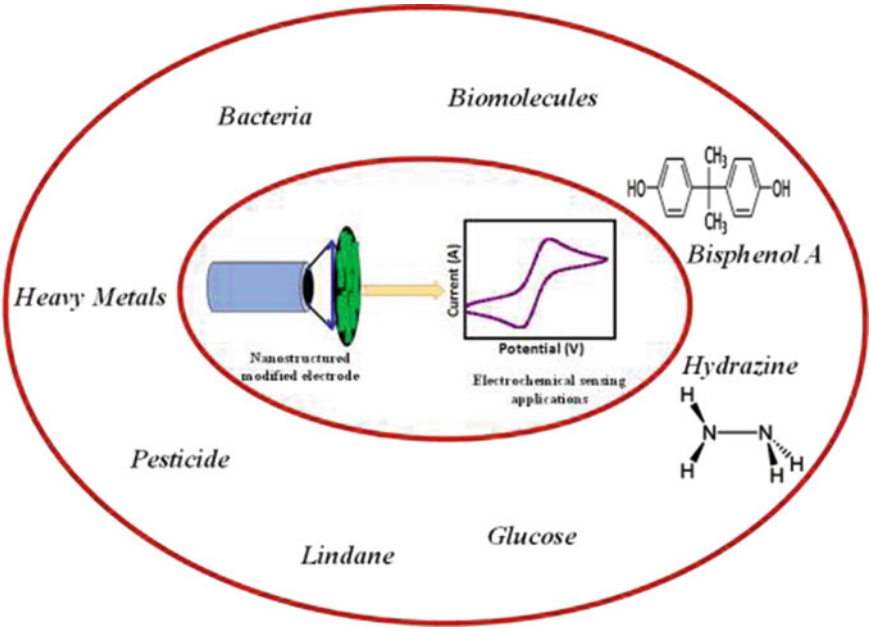

Fig. 2.1 Electrochemical detection of analytes based upon nanostructured modified electrodes

electrode (SPE) or glassy carbon electrode (GCE) based on low surface area materials generally suffer from high over potentials and slow electron transfer kinetics. To get over these constraints, electrode materials with a wide potential window and high electrocatalytic activities are needed. Nanomaterials play a vital role in the fabrication of selective electrodes for detection of analyte of interest. In current times, nanomaterials modified electrodes are attracting lot of attention as an active element in electrochemical sensor for a plethora of analytes ranging from metal ions, small organic molecules to biomolecules and whole cell (Fig. 2.1) [7, 11–21]. For modification of electrodes with nanomaterials, four routes are commonly followed namely, adsorption, covalent binding, polymer film coating and composite [22, 23]. In adsorption, the material is either physiosorbed by drop casting/spin coating or chemisorbed on the surface of the electrode to obtain monolayer accumulation. This technique has the benefit of speed and simplicity, unfavourable orientations and decreased functionality are likely. Covalent binding method utilizes chemical agents which link the desired nanomaterial with functional groups present on the electrode via covalent bonds, thus eliminating desorption issue [22, 23]. However, uncontrolled covalent binding of an enzyme to surface of the nanomaterial can hinder access to active site or even denature the enzyme. Polymer film coating method involves spreading a polymer solution on the electrode and drying, which can be accomplished by dip coating, solvent evaporating or spin coating. Polymer film coating can also be obtained by electropolymerization on the electrode surface. For composite modification, chemical modifier is mixed with electrode matrix material. For example, electron transfer mediator can be

mixed with carbon particles to prepare a carbon paste electrode. The modified electrode with nanomaterials helps in fast electron transfer and afford enhanced sensitively compared to other modified and unmodified electrodes. Substantial interest has been drawn towards application of metal nanoparticles as active sensing material in chemically modified electrodes due to their low cost, excellent electron transfer kinetics, and biocompatibility. Since metal nanoparticles are zero-dimensional nanomaterials, they exhibit quantum tunnelling effects and have good electrical conductivity [24]. While looking in recent published articles in the area of electroanalytical chemistry, most of the scientists suggested use of metal nanoparticles modified electrodes for pharmaceutical drug detection purpose. For instance, Sildenafil citrate was detected by using gold nanoparticles modified electrode [25], antituberculosis drug (Isoniazid) detection by utilizing rhodium-based nanomaterial modified electrode [26], metal praseodymium hexacyanoferrates modified electrode for sulphite detection [27], samarium hexacyanoferrates for the catechol detection, to name a few [28]. Metal nanoparticle modified electrodes are extremely simple to make and these chemically modified electrodes will certainly play a vital function in the area of electrochemical biosensors in future. Centring on the recent activity being pursued in this area by scientists worldwide, this chapter provides an outline of electrochemical sensors and biosensors based on various nanostructured materials.

2.3 Noble Metal Nanomaterials

Nanoscale form of gold (Au), silver (Ag), platinum (Pt), palladium (Pd), and their alloys have been extensively utilized for the development of electrochemical sensing systems for environmental monitoring as well as for in vivo and in vitro sensing in biological systems [29]. Compared to other nanoscale scale-based system, noble metal nanoparticles (NP) are more stable and less hazardous. NP finds applications in immunoassay for improving signal for binding of macromolecules (i.e. RNA and DNA), proteins, etc. Further, NP-based electrochemical sensing units have an extraordinary ability to improve level of sensitivity and selectivity by signal boosting [29]. This chapter mainly focuses on the intriguing qualities of noble metal nanoparticles for electrochemical detection of organic molecules, inorganic species and biomolecules.

2.3.1 Gold Nanoparticles

Gold nanoparticles (GNP) have received significant focus due to excellent chemical stability, oxidation resistance, electrical conductivity, good biocompatibility, wide electrochemical window and high surface-to-volume ratio [30]. Noble metal-based catalysts, particularly Au, is one of the most appealing due to high abundance and environmental benignity. Presently, the common strategies for synthesis

of gold nanoparticles entail the reduction of gold chloride ($HAuCl_4$) under aqueous conditions. Reduction of $HAuCl_4$ with common reducing reagents, such as sodium borohydride ($NaBH_4$) or sodium citrate enables to produce spherical nanoparticles. However, this approach is not preferred as it results in gold nanoparticles with large size distribution and are sensitive to presence of salts. The sol-gel route is one of the preferred methods for the synthesis of gold nanoparticles. Interest to make use of gold nanoparticles in recognition events with signal transduction is of great interest because on modification of biological recognition elements with Au NP, its sensitive and selective binding to the specific target molecules leads to large change in electrical properties. GNPs are material of choice for the detection of mercury ion (Hg^{2+}) by anodic stripping voltammetry (ASV) since it can form amalgam with Hg giving a large change in the output signal. It is carried out in two steps; first step involves the pre-concentration step in which Hg^{2+}ions are adsorbed at the electrode surface. Second step involves striping of the adsorbed Hg^{2+} [31]. GNP modified with streptavidin has been used for sensitive detection of blood clotting protein, Factor IX in human serum. The sensor showed a limit of detection (LOD) of 99.2 fM [32]. GNP-conjugated antibody sensing unit has been reported for influenza virus utilizing genosensor technology, which is based on measuring the voltammetric reduction signal of an intercalator label, Meldola's Blue (MDB). The magnitude of hybridization reactions between a single strand DNA probe and its complementary target strain was established by utilizing differential pulse voltammetric signals of MDB [33]. In another work, gold microwire electrode has been used for the electrochemical detection of Cu^{2+} and Hg^{2+} in seawater employing anodic stripping voltammetry [34]. Likewise, making use of a gold microwire electrode integrated with stripping voltammetry, a rapid and affordable sensing unit was made for the electrochemical detection of As^{3+}, Cu^{2+}, Hg^{2+} and Hg^{2+} in freshwater [35]. Ding et al. proposed dealloying of nanoporous gold leaf from Au/Ag alloy by depletion of Ag, which results in nanoporous structure entirely comprising of Au [36]. The process involves interfacial phase separation in which Au does not dissolve from the alloy thereby forming cluster. The efficiency of the nanoporous gold leaf electrode showed amazing electrocatalytic ability towards nitrite oxidation with much higher peak current compared to glassy carbon electrode. The enhanced activity is ascribed to the expanded 3D nanoporous material. In a recent study, an electrochemical sensor was developed by electrodeposition of GNP@polypyrrole(PPy) nanowires onto a GCE surface [37]. The GNP having size of 15.0 nm was uniformly dispersed in PPy nanowires. XPS examination revealed FCC framework for GNP. The SEM images depict the nanoporous framework of the Au microelectrode and shows up a favourable 3D framework with pore dimensions of 200–400 nm. The 3D nanoporous framework boosted sensing abilities and selectivity towards the oxidation of hydrazine, sulphite, and nitrite, simultaneously. Kaur et al. have outlined GNP modified nanocrystalline ZSM-5 zeolite (GNP-Nano-ZSM-5) for detection of cysteine (CySH) and glutathione (GSH) simultaneously in nanomolar concentration range [38]. The SH bonds in CySH and GSH can be oxidized at the electrode surface but the drawback is that the process is very slow and it requires a large potential. Hence, surface of Nano-ZSM-5 was functionalized with propylamine and protonated with acetic acid to generate positive charge on

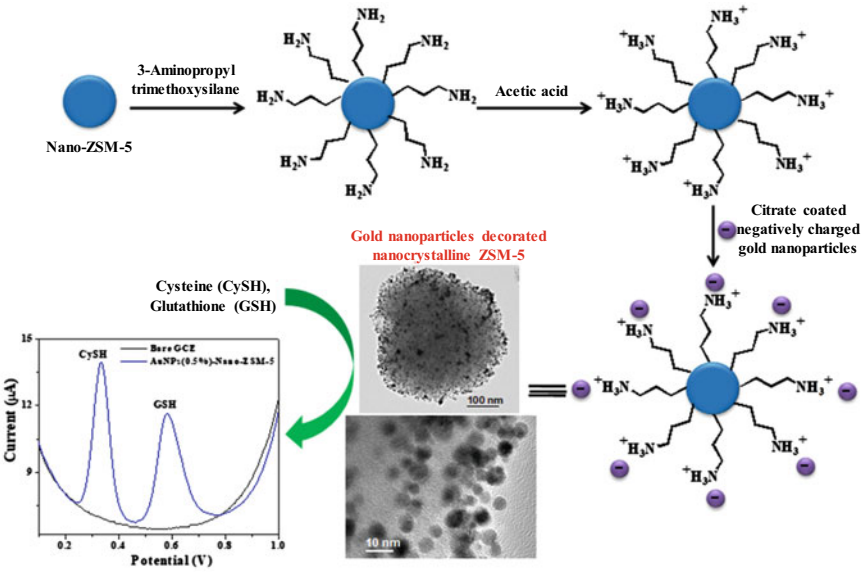

Fig. 2.2 Illustration for the preparation of GNP decorated Nano-ZSM-5, and the represented TEM images of GNP@Nano-ZSM-5 for the detection of (CySH) and glutathione (GSH). Reproduced from Ref. [38] with permission of RSC Publishing

the surface. Further, negatively charged citrate coated GNP was immobilized on the Nano-ZSM-5 surface by electrostatic interactions (Fig. 2.2) [38]. The TEM images demonstrated that 3–5 nm spherical GNP was upheld on the surface of Nano-ZSM-5 (Fig. 2.2). The size of Nano-ZSM-5 was found to be 300–500 nm from the HRTEM image (Fig. 2.2). EDS mapping from the high angular dark field (HAADF) imaging proved the incorporation of GNP inside the Nano-ZSM-5. The nanocomposite unit revealed a linear response from 2 nm-800 μM and 3 nM-800 μM with LOD of 0.3 nM and 0.6 nM for CySH and GSH, respectively. The application of the GNP-based nanocomposite sensing unit was examined in drugs like CySH syrup and GSH injections. The authors proposed that the nanostructured zeolite can increase the electrode stability where GNP acted as redox mediator for the electro-oxidation of –SH group.

2.3.2 Platinum Nanoparticles

Platinum nanoparticles (PtNPs) have been used in numerous areas counting electrochemical sensor, biomedical chemistry, neurochemistry, and diagnostic research [39]. Recently, PtNPs with high surface-to-volume ratio has received much interested because they provide better electrochemical performances compared to the

bulk PtNPs. These NPs can be synthesized through hydrothermal method, electrochemical synthesis, sol-gel synthesis, template synthesis, and electrochemical dealloying. Ideally, PtNPs should be synthesized by simple method, free from chemical contaminant. However, the above-mentioned methods are complicated and involve multiple steps. Substantial initiatives have been taken to lower the quantity of platinum use by broadening the catalytic efficiency of Pt catalysts considering the fact that their electrocatalytic sensitivity depends on their morphology [40]. The chemical composition, crystal framework, crystallographic axis, etc. are critical criteria for PtNPs that enhances electron transport [41]. PtNPs are involved in many biomedical applications through exploitation of these impressive properties such as PtNPs therapies, which appear to fix a broad collection of human problems within the scientific setup [42]. PtNPs have broad possible applications in pharmacogenomic discovery, pharmaceutical assessment, diagnostics, microbial affirmation, disclosure of bio-warfare and bioterrorism drivers [42]. In a study, PtNPs were used in combination with multi-walled carbon nanotubes (MWNTs) for the development of an electrochemical DNA identifying device [43]. The LOD obtained was 1.0×10^{-11} M. The advancement of non-enzymatic glucose sensor is one of the wonderful steps towards the advancement of sensing units for diabetic individuals. Detailed studies have revealed the mechanistic aspects of the electrochemical oxidation of α-glucose in addition to β-glucose on Pt surface in phosphate buffer where gluconic acid and H_2O_2 are formed as the product. Unique glucose sensing unit based upon 3D Pt/Pb and Pt/Ir nanostructures on titanium substratum have also been reported [44]. CV was used to study glucose oxidation at pH = 7 in the presence of chloride ions, which revealed that the sensor current response for chloride ions was negligible. The interference studied show that nanoporous PtPb electrode has negligible interference with uric acid (UA), 4-acetamidophenol, and ascorbic acid (AA) [44]. In an another study, a sensing unit was created for bisphenol A (BPA) using dendritic platinum nanoparticles (DPNs) with high surface area modified on AuNPs/SPE, with the deposition of a polyethyleneimine-phosphatidylcholine (PEI-PC) layer (Fig. 2.3) [45]. The HRTEM images of DPNs showed particles with size of 2–4 nm (Fig. 2.3a). The XRD revealed *fcc* crystal structure (Fig. 2.3b) and the HAADF-STEM analysis showed {111} and {200} facets confirming *fcc* crystal structure (Fig. 2.3c). The SEM image of PEI-PC/DPNs/AuNPs electrode showed uniformly distributed DPNs on the electrode surface (Fig. 2.3d). The CVs of DPNs and Pt black were recorded in 0.5 H_2SO_4 to find the electroactive surface area (ECSA). The DPNs showed more hydrogen adsorption peak compared to the Pt black electrode. The electrochemical surface area (ECSA) for DPNs electrode and AuNPs were found to be 5.46 m^2/g and 3.78 m^2/g, respectively (Fig. 2.3e). The electro-oxidation of Bisphenol A (BPA) was carried out by CV in phosphate buffer saline solution at PEI-PC/DPNs/AuNPs electrode and at Pt black/AuNPs electrode (Fig. 2.3f,g). In the absence of BPA, no oxidation peak was obtained at both the electrodes. With the addition of BPA, a sharp oxidation peak at +0.27 V was obtained (Fig. 2.3f,g). The voltammetric peak height and sensitivity at PEI-PC/DPNs/AuNPs electrode was found to be twice that of Pt black/AuNPs electrode which can be seen from the calibration plot (Fig. 2.3 h). The PEI-PC layer secures the sensor against common interferents such as from AA,

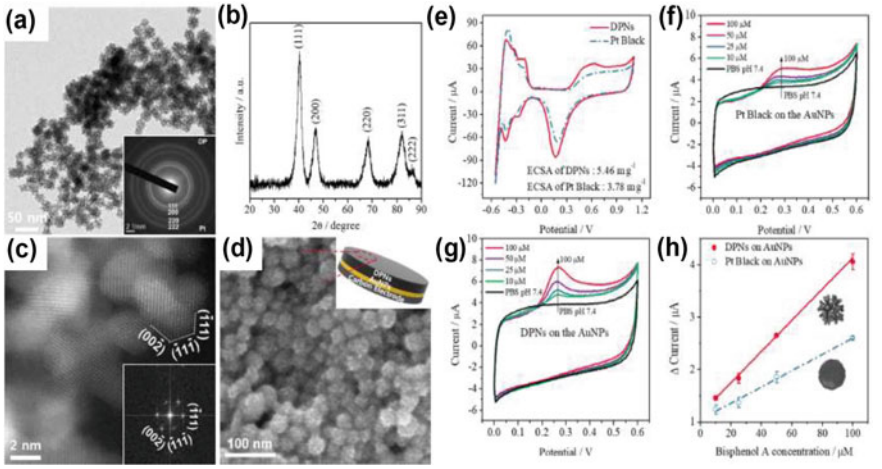

Fig. 2.3 Characterizations: **a** TEM image of the prepared DPNs, **b** XRD pattern **c** HAADF-SAED image (inset: magnified image), **d** SEM image of the PEI-PC/DPNs/AuNPs electrode (inset: photo of the electrode), **e** determination of ECSA for DPN and Pt black **f** determination of various concentration of BPA at Pt black/AuNPs electrode, **g** determination of various concentration of BPA at PEI-PC/DPNs/AuNPs electrode, and **h** calibration curves for Pt black/AuNPs electrode and DPNs/AuNPs for BPA. Reproduced from Ref. [45] with permission of Elsevier

acetaminophen, UA, and DA. The sensing unit under the optimized test condition gave two wide linear range of 0.01–1.0 and 1.0–300 μM having LOD of 6.63 nM. These promising results open the door for tailoring of the novel biosensing platforms with platinum nanoparticles.

2.3.3 Silver Nanoparticles

Silver nanoparticles (AgNPs) have made tremendous progress within the globe of nanoscience [46]. Specific and sensitive detection units based upon AgNPs have truly opened the opportunity of making detection systems for screening of infectious disease because of its biocompatibility and high conductivity [27]. AgNPs, with their excellent catalytic activity, reduced poisoning, high conductivity and antibacterial activity, are made use in biological sensing, clinical and environmental applications [47]. The stable and non-aggregated AgNPs are preferred, for this objective [48]. Lindane is an organochlorine pesticide that has been extensively used in agriculture as well as for the treatment for head and crab lice, and nits [49]. Kaur et al. reported silver nanoparticles (5%) modified conductive polyaniline (PANI)-nanocrystalline zeolite ZSM-5 for the nanomolar detection of lindane having a linear range from 10 nM-900 uM and a LOD of 5 nM (Figs. 2.4, and 2.5) [50]. The TEM image of

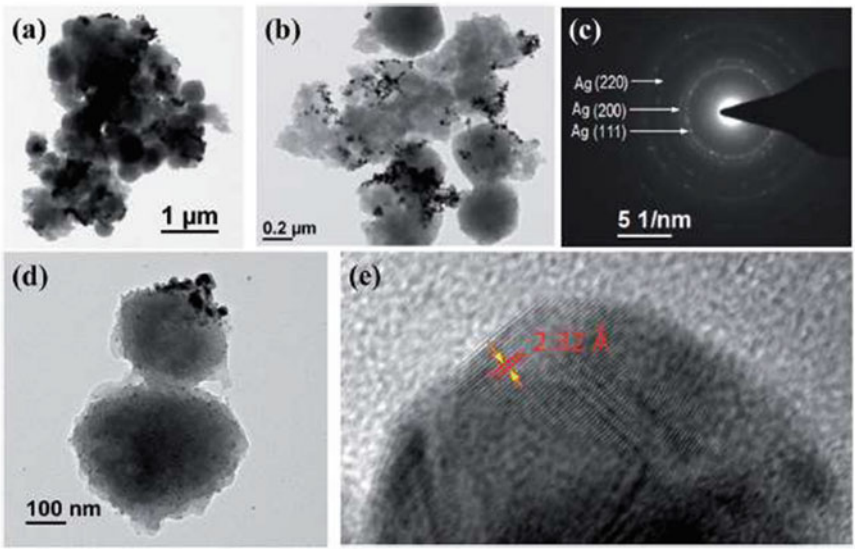

Fig. 2.4 **a**, **b** Low magnification TEM images, **c** SAED pattern, **d** HRTEM image of AgNPs(5%)-PANI-Nano-ZSM-5, and **e** HRTEM image of a single crystal of AgNP. Reproduced from Ref. [50] with permission of RSC Publishing

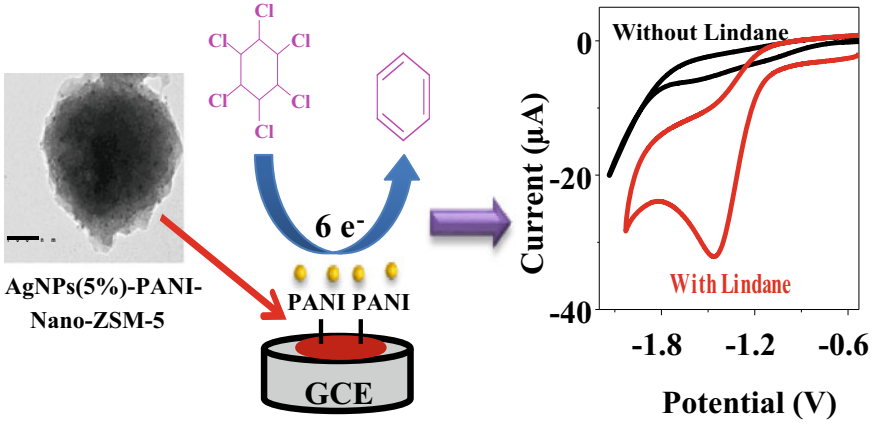

Fig. 2.5 Schematic illustration showing the construction processes of AgNPs(@PANI@Nano-ZSM-5/GCE for the detection of lindane. Reproduced from Ref. [50] with permission of RSC Publishing

the composite showed that AgNPs are uniformly distributed over PANI-Nano-ZSM-5 (Fig. 2.4a,b,d). SAED pattern showed concentric circle with diffraction patterns corresponding to *fcc*-Ag with a measured d-spacing of 2.32 A^{o} corresponding to (111) interplanar spacing (Fig. 2.4c,e). The size of AgNPs varies from 5–20 nm from the HRTEM image (Fig. 2.4d).

Electrochemical reduction of lindane has been carried out using AgNPs(5%)-PANI-Nano-ZSM-5/GCE (Fig. 2.5), PANI-Nano-ZSM-5/GCE, PANI/GCE and Nano-ZSM-5/GCE modified electrodes. The ECSA was found to be 1.32, 0.86, 0.34, and 0.32 cm^2, respectively. The higher ECSA obtained at AgNPs(5%)-PANI-Nano-ZSM-5/GCE was due mesoporosity and high surface area. Here, AgNPs and PANI provided electrons required for lindane reduction. The conductive polyaniline on nanocrystalline ZSM-5 facilitated transport of electrons. The CV results indicated that the electrochemical reduction of lindane at modified electrode can be a dissociative electron exchange transfer process. In another strategy, electrochemical synthesis of AgNPs@GCE with modification of p-isopropyl calixarene was proposed for H_2O_2 detection. The sensor evaluation confirmed that the H_2O_2 reduction under optimum condition lead to a linear range of 5.0×10^{-5} to 6.5×10^{-3} M having LOD of 2.7×10^{-5} M. A recent study showed a sensing system in which hybrid AgNPs-DNA nanoparticles were electrodeposited onto a GCE. The DNA prevented accumulation of AgNPs and the sensor displayed remarkable electrochemical reduction of H_2O_2 [51].

Hydroxyapatite (HAP) nanoparticles spread on Ag ion-exchanged ZSM-5 for the detection of Cd^{2+}, Pb^{2+}, As^{3+}, and Hg^{2+} in water bodies was reported by Kaur et al. (Fig. 2.6) [52]. HAP@Ag-Nano-ZSM-5 was synthesized by incubating AgNPs-Nano-ZSM-5 in simulated body fluid (SBF). Ag-Nano-ZSM-5 has a significant surface area silanol groups to ion-exchange, which assist the adsorption of calcium and phosphate. Physico-chemical characterization verified that a substantial quantity of hydroxyapatite with nanosheet morphology settled within the Ag-Nano-ZSM-5 structure when it was kept in SBF for 20 days. The elemental composition of HAP@Ag-Nano-ZSM-5 was estimated using HAADF (Fig. 2.6a). EDS mapping confirmed presence of elements such as Ag, Ca, Si, O, Al, and P (Fig. 2.6b) and successful anchoring of Ag-Nano-ZSM-5 with HAP (Fig. 2.6c,d). It was reported that no hydroxyapatite nanoparticles were formed on Nano-ZSM-5 which indicates that Ag^+ is needed for its growth. Larger number of silanol in the Nano-ZSM-5 is responsible for growth of HAP in the HAP@Ag-Nano-ZSM-5. Square wave stripping voltammetry (SWSV) studies revealed excellent performance of the sensor for detection of heavy metals such as Cd^{2+}, Pb^{2+},As^{3+}, and Hg^{2+} (Fig. 2.7) due to high adsorbing capability and mesoporosity of HAP@Ag-Nano-ZSM-5 [52].

2.3.4 Palladium Nanoparticles

Palladium nanoparticle (PdNPs) based catalysts show prominent capability for hydrogen absorption and are extensively used in hydrogenation reactions, hydrogen

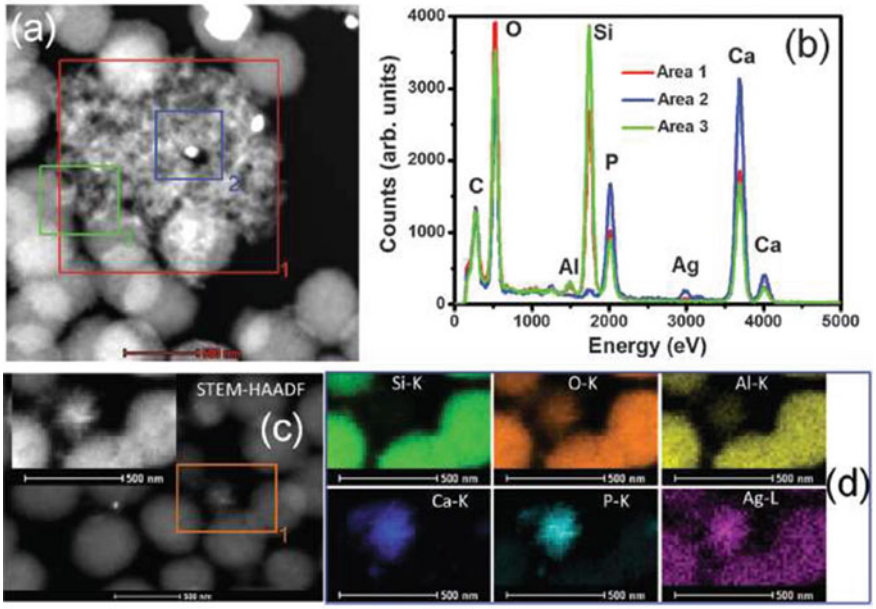

Fig. 2.6 **a** TEM-HAADF image of Ag-Nano-ZSM-5. **b** EDX spectra from different areas of Ag-Nano-ZSM-5. **c** STEM-HAADF image of HAP/Ag-Nano-ZSM-5. **d** The chemical maps of HAP/Ag-Nano-ZSM-5. Reproduced from Ref. [52] with permission of RSC Publishing

purification, and more [53]. They have shown excellent electrocatalytic performance in the oxidation of formic acid, methanol, ethanol, and hydrazine [54]. Palladium nanomaterials have played an essential role in fuel cell innovation. In all these applications, the shape and size of PdNPs is one of the essential criteria in order to achieve optimum efficiency. Consequently, different nanostructures are required for various catalytic applications. PdNPs have also shown application in the area of electrochemical biosensor [55]. The relatively massive plenitude of PdNPs over other noble metals makes it a more economical substitute in numerous electrochemical biosensing applications. Owing to one-of-a-kind electronic properties, upgraded catalytic, a variety of PdNPs and its derivatives have been investigated. Brucellosis, a transmittable disease is impacted by the genus *Brucella* and this illness can be transmitted to humans via microbes spotted pets or pet dog. A genosensor for *Brucella* was reported utilizing PdNPs exchanged on an Au surface [56]. This detecting device showed a linear calibration from 1.0 pM to 0.1 aM and a LOD as low as 27 zM. An electrochemical sensor based on rGO/PdNPs nanocomposite was proposed for detection of chloramphenicol (CAP). In a typical synthesis, sonication of GO was carried out for 3 h in deionized water till uniform and homogeneous solution was obtained. The GO was reduced by utilizing ethylenediamine as a reducing agent. $PdCl_2$ was gradually added to homogenous rGO suspension with consistent stirring. The mixture

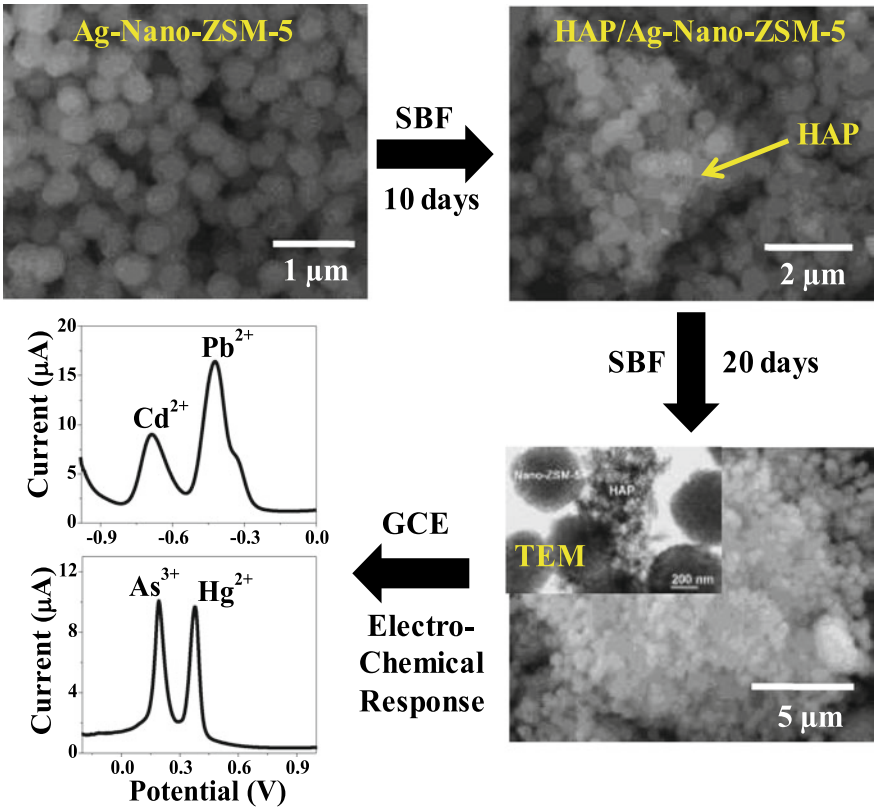

Fig. 2.7 Schematic representation of the electrochemical sensor for the sensing of Cd^{2+}, Pb^{2+}, As^{3+}, and Hg^{2+} based on HAP/Ag-Nano-ZSM-5. Reproduced from Ref. [52] with permission of RSC Publishing

was washed and dried in air. The schematic for synthesis procedure and electrochemical detection are shown in Fig. 2.8 [57]. The nanocomposite was characterized by TEM, UV-Vis, FT-IR, and XPS analysis. The textural characterization proved the successful formation of the nanocomposites. Electrochemical characterization of the rGO/PdNPs nanocomposite modified electrode was carried out using chronocoulmetric studies. A plot of Q vs. $t^{1/2}$ gave a slope from which effective surface area for GCE (0.408 cm^2) and rGO/PdNPs nanocomposites (0.95 cm^2) was obtained. In another study rGO/PdNPs nanocomposite modified electrode was used as an electrochemical sensor for chloramphenicol (CAP) (Fig. 2.8). The appealing sensing unit revealed high level of sensitivity, good stability, reproducibility, and excellent recovery rate for CAP in real sample. The electrochemical attributes of the sensing unit were evaluated by DPV and CV, where a linear range from 50 to 1000 nM with an LOD of 50 nM was obtained for detection of CAP.

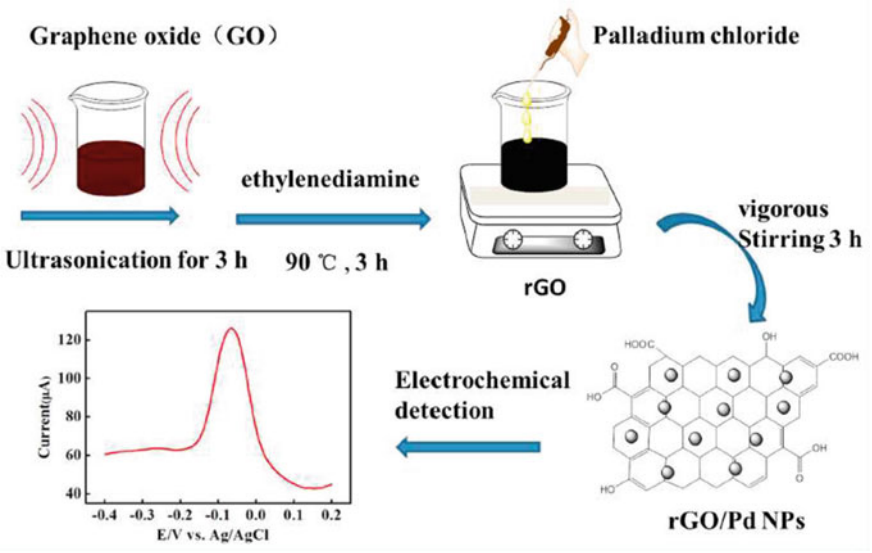

Fig. 2.8 Schematic illustration of preparation procedures of rGO/PdNPs nanocomposite for its use in electrochemical detection for CAP. Reproduced from Ref. [57] with permission of Elsevier

2.4 Metal Oxide Nanomaterials

Metal oxide nanomaterials have been taken advantage of a credible electrocatalyst for detecting numerous analytes in the area of clinical research and biomedicine [58]. Semiconducting metal oxides are the most popular nanomaterial explored in chemical and biosensing because of their tunable redox and conducting properties, high degree of sensitivity, fast response/recovery time, as well as ability to recognize a significant wide array of analyte/biomolecules. Transition metal oxides are actually much more attractive compared to silicate because of tunable redox activity. Sol–gel method is widely employed for the synthesis of micro-/nanostructured metal oxides. Semiconducting metal oxide are classified into two types: n-type (consisting of ZnO, SnO_2, TiO_2, and many others) and p-type (e.g. NiO, Fe_3O_4, etc.). Cost-effective metal oxide-based, enzyme-free glucose sensors based on NiO, MnO_2, Ag_2O, Cu_2O, and CuO have been extensively explored. Metal oxide with high adsorption ability and electron affinity has been used for organic molecule sensing such as pesticide, herbicide, and phenolic compound. These metal oxides have reduced detection limit and increased the sensitivity of the sensor. Metal oxides have high isoelectric points (IEP) therefore immobilization of enzymes is easier. Some of the metal oxides have electrocatalytic capacity for oxidation of glucose with high selectivity. A selection of metal oxide nanoparticles has been made use of in electroanalysis.

An electrochemical sensing unit for the detection of bisphenol A (BPA) has been reported using ZrO_2 nanoparticles (Fig. 2.9) [59]. A coordinate, one-step procedure was utilized to get nanocrystalline ZrO_2 using F127 tri-block copolymer, a mix

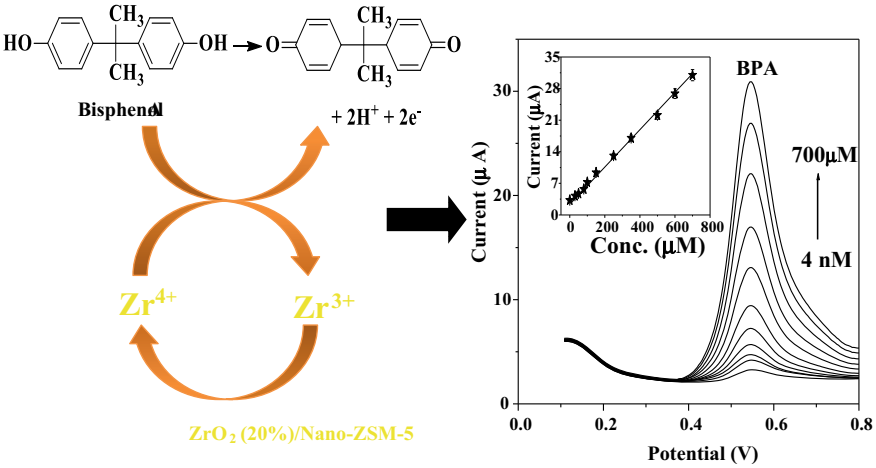

Fig. 2.9 Schematic representation of electro-oxidation of bisphenol A at ZrO_2/Nano-ZSM-5. Reproduced from Ref. [59] with permission of RSC Publishing

of phloroglucinol, formaldehyde, and additionally zirconylnitrate. The DPV results show that BPA was oxidized at lower oxidation potential (Fig. 2.9) [59]. Zr^{4+} at the electrode surface helps in the oxidation of BPA with a linear range of 6 nM-600 μM and LOD of 3 nM. A comparison of overall results of this work with numerous other published works confirmed the sensing system was able to distinguish BPA with higher sensitivity. The abundant Si–OH and Al–OH group in Nano-ZSM-5 helps to interact with –OH (hydroxyl group) in BPA due to hydrogen bonding which resulted in faster electro-oxidation of BPA. Also, inter-crystalline mesoporosity in Nano-ZSM-5 facilitated diffusion of reactants/products. In another work, an electrochemical H_2O_2 sensor based upon the composite of single-walled carbon nanohorns (SWCNH) with CeO_2 (CeO_2/SWCNH) was reported. The produced CeO_2/SWCNH electrode showed efficiency for H_2O_2 detection having LOD of 100 μM. The sensor showed good performance in other matrix like milk and cleaning fluid, giving an extraordinary selectivity. CuO-based nanomaterials have also been proficiently utilized in many biosensing applications. A non-enzymatic glucose sensor is demonstrated by Yang et al. utilizing nanoneedle-like CuO on N-doped rGO (CuO/N-rGO). The CuO/N-rGO-based sensor showed oxidation to glucose at 0.6 V with a linear range of 0.5–639.0 μM [60]. Li et al. have developed Cu_2O@CeO_2-Au sensor for the detection of prostate antigen (PSA). The sensor showed higher H_2O_2 reduction efficiency compared to Cu_2O, AuNPs, and Cu_2O@CeO_2 [61]. A protein sensing unit based on choline oxidase (ChO) immobilized externally on α-Fe_2O_3 nanoparticles and poly(3,4-ethylenedioxythiophene) (PEDOT)-rGO nanocomposites were made use for sensing of acetylcholine, a neurotransmitter [62]. This biosensor showed a linear range of 4.0 nM-800.0 μM with a LOD of 4.0 nM for detection of acetylcholine.

Various advancements based upon metal oxides and their nanocomposites have been reported. Anu Prathap et al. described a novel electrochemical lindane sensors

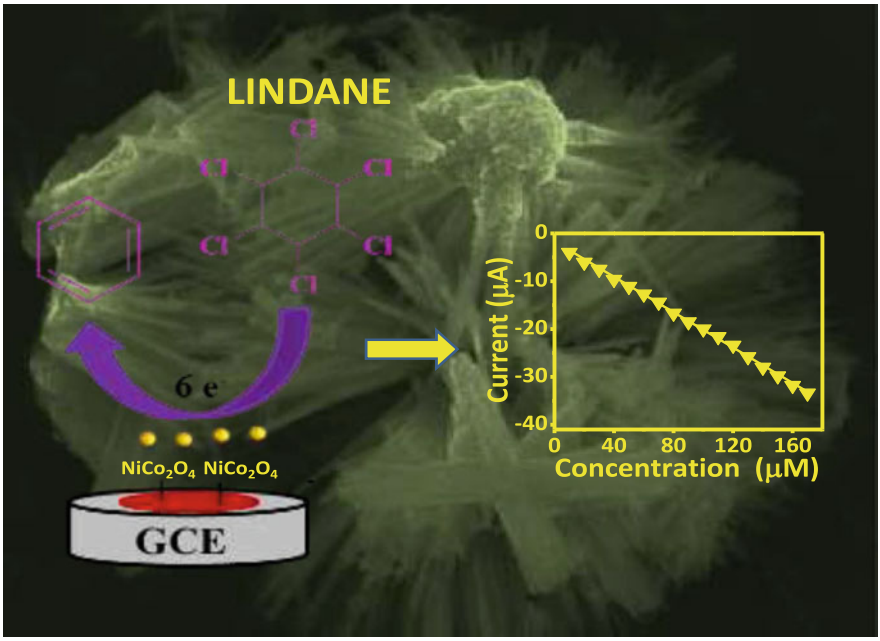

Fig. 2.10 $NiCo_2O_4$ modified electrode for selective detection of lindane. Reproduced from Ref. [19] with permission of Elsevier

based on $NiCo_2O_4$ nano-microstructures (Fig. 2.10). Direct reduction of lindane in aqueous solution is very difficult task because of its insolubility and high reduction potential [19]. The reported work was performed in 60:40 (v/v) methanol–water electrolyte. Polarographic examination of lindane revealed a six-electron irreversible reduction. A linear range from 10–170 μM and a LOD of 3.6 μM was obtained (Fig. 2.10) [19]. $NiCo_2O_4$exhibited electrochemical activity as a result of the contributions offered by Ni^{2+} and Co^{2+}ions existing in $NiCo_2O_4$, as compared to the individual oxides namely, NiO and Co_3O_4.

2.5 Carbon-Based Nanomaterial Modified Electrodes

Electroanalysts are constantly looking for next finest electrode materials. The electroanalytical qualities looked for are substantial enhancement in the voltammetric peak height and enhancement in the analytical level of sensitivity [63]. Carbon nanomaterials are being thoroughly investigated to see if they fulfil these standards. Carbon is without doubt one of the most frequently used electrode material in electroanalysis and also, according to the level of graphitization, carbon is morphologically diverse and a selection of frameworks exists in a plethora of micro- and also nanostructures such as GCE, carbon fibre, nanotubes, Buckminster fullerenes and graphene

(Fig. 2.11) [64]. Carbon electrodes are much more extensively used over metal electrodes because of their large potential windows in aqueous medium. Carbon electrodes display low background currents, high electric conductivity, plentiful surface chemistry and relative chemical inertness. Additionally, low cost of carbon nanomaterials has given further impetus to widespread use of these electrodes. One key architectural distinction between carbon electrodes that considerably affects their electrochemical performance is the relative percentage of edge plane over that of basal plane. This affects its electrochemical sensitivity and it is well established that electron transfer process occurs mainly at edge plane sites while the basal plane is electrochemically inert. Thus, a carbon electrode or carbon nanomaterials containing a high thickness of edge plane sites will certainly show a reversible voltammetric signature while if it is composed mainly of basal sites it will show irreversible behaviour [65]. This is certainly one of the most crucial specifications when choosing carbon-based nanomaterials as electrode modifier.

Objective of this section is to illustrate relevant examples of carbon nanomaterials used in electroanalysis by researchers with the sole objective to improve the electroanalytical performance. As a result of the large variety of available carbon nanomaterials, it is impossible to overview every material without creating a committed book on the topic, as a result, only essential examples are discussed here.

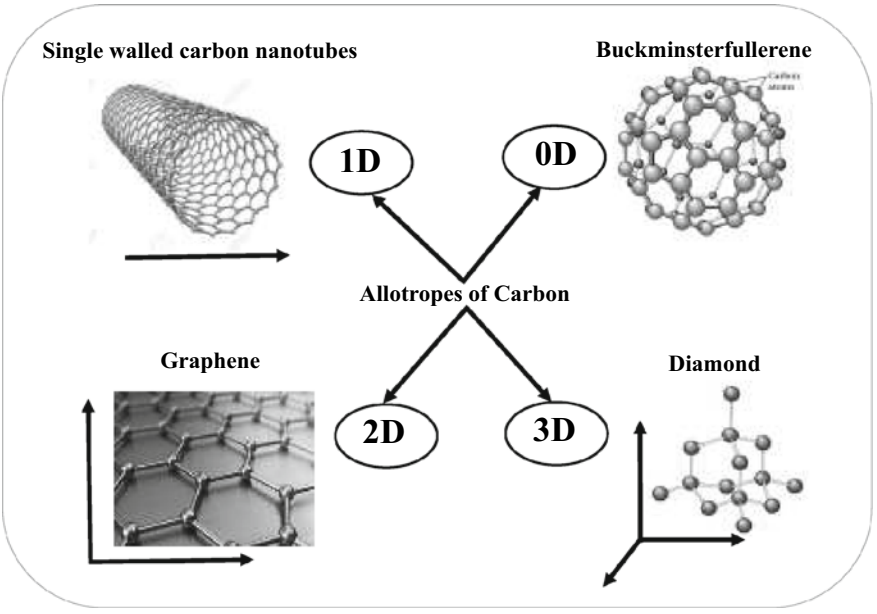

Fig. 2.11 Various allotropes of carbon. Reproduced from Ref. [64] with permission of Elsevier

2.5.1 Carbon Nanotubes

Carbon nanotubes (CNTs) are sp^2 hybridized carbon particles which were discovered as a by-product during fullerene synthesis. Carbon nanotubes are divided into two common categories types: single-walled carbon nanotubes (SWCNTs) and multi-walled carbon nanotubes (MWCNTs) and have at least one dimension within the nano range. Particularly, CNTs have been used in biosensing systems as a result of their properties such as high conductivity and ease of functionalization for biomolecules immobilization. A variety of CNT have been reported used for immobilization of biomolecules (protein, nucleic acid, and carbohydrate). Acid treatment of CNT introduces oxide group at the tube end and at defective sites on the nanotube. Thus, CNT can be covalent immobilized with biomaterial through covalent linkage chemistry.

2.5.2 Single-Walled Carbon Nanotubes

There has been a big interest in single-walled carbon nanotubes (SWNTs) as electrode as they are pure and free from metal contamination. Their high electric conductivity combined with diminutive dimension makes them perfect as nanoelectrodes. This ability prevents the need of costly electronic tools; leading to ultrasensitive electrochemical sensing units for the detection of chemical along with organic analytes in addition enhances the S/N ratio, for the detection of analytes. Functionalized carbon nanotubes render interesting properties that might help in clinical applications comprising of treatment of cancer cells, transmittable sickness, and central nervous system disorders. Diabetes mellitus is a chronic disease that has influenced 171 million people around the globe. Hyperglycaemia, or raised blood sugar, is a consequence of unchecked diabetes and in time brings about major damages to organs, particularly the eyes, kidneys, and nerves. As a result, the standard screening of physiological glucose levels is critical. Various electrochemical biosensors have been applied successfully for the detection of glucose. A needle microsensor based on SWNT-GOx for the detection of glucose inside a 21-gauge needle was reported to have a wide linear range of 35 mM [66]. Monitoring of lactate is fundamental for continuous surveillance in surgery, sports medication, medical diagnostics, and food assessment. Rubianes and Rivas employed SWNT-mineral-oil adhesive immobilized lactate oxidase for electrochemical detection of lactate [67]. The efficient electron transfer of hydrogen peroxide at the SWNT electrode resulted in fast detection of the analyte at a low potential (−0.10 V). Similarly, enzymatic biosensors obtained by incorporation of polyphenol oxidase for the detection of polyphenolic substances were also reported. High sensitivity was observed, which showed that SWNT exhibited electrocatalytic activity for enzymatically generated catechol–quinone redox couple. Dopamine is a catecholamine neurotransmitter which plays important function as an extracellular chemical messenger. Inadequate levels of dopamine can result in neurological disorders such as schizophrenia and Parkinson's disease. However,

one essential concern for the detection of dopamine in blood is its reduced concentration level, which is further complicated by the interference signal from various other constituents such as glucose, ascorbic acid (AA) and uric acid (UA). SWNT modified electrode have been used to solve this inconvenience. For example, in a recent study, poly(3-methylthiophene) was covered with Nafion-SWNTs for selective detection of DA in the presence of other biological molecules such as AA and UA. Nafion worked as a dispersant and helped in uniform distribution of SWNTs over the electrode to form an even film which served as a barrier for the interfering species [68]. This electrode combined the benefits of P3MT, CNTs and Nafion thus exhibiting dramatic effect on the electrocatalytic oxidation of DA with high selectivity. A SWNT-polymer composite consisting of poly(styrenesulfonic acid) sodium salt, was cast onto the surface of glassy carbon electrode and the electrochemical behaviour of the modified electrode was investigated. The negative charged poly(styrenesulfonate) ions attracted positively charged dopamine at pH 7 which rendered selectively for DA in the presence of other interfering biomolecules. An Au@SWNTs modified electrode was used for the electrochemical detection of rutin, which involved an electrochemical reaction with two electrons transfer [69]. A linear range from 2.0×10^{-8} to 5.0×10^{-6} M with a LOD of 1.0×10^{-8} M was obtained. The sensor was used for estimation of rutin in Chinese medications. Magnetic nanoparticles (MPs) of unique dimensions with an electroactive tag, Fc (ferrocene), in conjugation with SWCNT electrical wiring can act as an electrochemical sensor of non-electroactive targets (Fig. 2.12) [70]. Modification with Fc was performed by EDC/NHS chemistry (Fig. 2.12). A sensing unit could be used for the detection of detergents and antibodies. In these initial experiments, binding of Tween 20 onto sensor could be traced by DPV. In addition, affinity capture of biotinylated antibody by streptavidin MP-Fc could be determined in much less than 30 min.

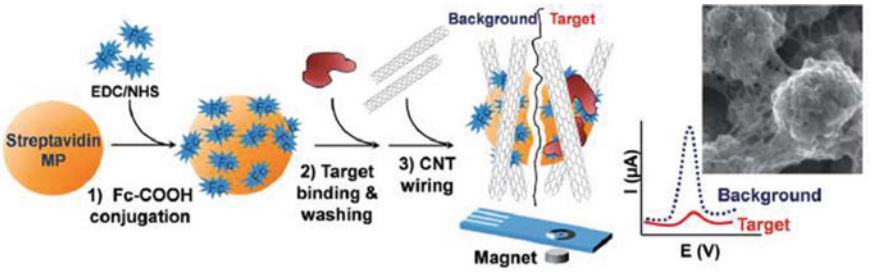

Fig. 2.12 Schematic of fabrication process for fabrication magnetic nanoparticles-based sensing system for electrochemical assay performance. **1** EDC/NHS chemistry was used for conjugation of Fc-COOH. **2** Target binding and washing with Tween followed by SWCNTs mixing. **3** Electrochemical detection by SWCNT. Reproduced from Ref. [70] with permission of RSC Publishing

2.5.3 Multi-walled Carbon Nanotubes

Multi-walled carbon nanotubes (MWCNTs) are lengthened cylindrical nanoobjects crafted from sp^2 carbon. Their diameter is typically in the range of 3–30 nm but their length can extend to a few cm, thereby their aspect ratio can easily vary between 10 and ten million. Multi-walled carbon nanotubes have outer diameter between 2 and 100 nm relying on number of coaxial tubes present. MWNTs are generally mesoporous in nature and find biomedical applications. MWCNTs are one of the most fascinating nanomaterials from the nanotechnology revolution. MWCNTs offer several functions such as boosted electron transfer kinetics, mechanical toughness, electrical conductivity, biocompatibility, and electrocatalytic activity. Additionally, MWCNTs can be integrated with other nanomaterials to boost sensor performance in terms of level of sensitivity and specificity. It is well known that electrocatalytic activity of nanomaterials can be increased by making a composite material. Nanomaterials with large surface area, such as CNT, graphite, graphene, and carbon nanofibers are the appropriate choice, of which MWCNTs are most used. A DNA electrochemical sensor based on self-assembled MWCNT@Au surface has been reported where the DNA was grafted to MWCNTs by utilizing diimide. Hybridization between probe and target DNA was detected by monitoring the alteration in current. Another study describes Ag-4-ATP-MWCNT nanocomposite modified with a double-stranded DNA (dsDNA) to detect daunorubicin-DNA interactions making use of DPV [71]. This sensing unit displayed amazing selectivity in the range from 0.10×10^{-8} to 1.0×10^{-5} mol L^{-1}, with the LOD of 3.0×10^{-10} mol L^{-1}. A novel and sensitive electrochemical DNA biosensor having a LOD of 7.5×10^{-11} mol L^{-1} was fabricated by immobilizing oligonucleotides on MWNTs@nanoZrO_2@chitosan@GCE [72]. The hybridization reaction on the electrode was monitored by DPV analysis using electroactive daunomycin as an indicator. In another study, CNT paste electrode for adsorption and electrochemical oxidation of nucleic acids was reported wherein incorporation of MWNT into the carbon paste matrix supplied 29 and 61-fold increase in current values for ss-DNA and 21-mer oligonucleotide, respectively. Epinephrine (EP), a cis-diol compound present in the mammalian nervous system can bring about glycogenolysis in the liver as well as skeletal muscle. Various diseases depend upon the concentration of EP, such as Parkinson's disease, Alzheimer's disease, high blood pressure, and multiple sclerosis. A study shows a strategy for the detection of AA, EP and UA making use of a composite film of functionalized MWNTs with Nafion, which incorporated Pt and AuNPs. All the analytes showed well-separated oxidation peaks for these three compounds, thus enabling their simultaneous detection. Cholesterol is a waxy sterol in mammalian cells membrane which plays a crucial role in brain synapses, body immune system and protection against cancer. However, higher concentration of cholesterol in blood, particularly reduced thickness lipoprotein (LDL), leads to high blood pressure, heart diseases, and nephrosis. Therefore, monitoring of cholesterol level in the blood is an essential criterion for the diagnosis and prevention of a variety of diseases. A sensor based on SPE@MWNT immobilized with cholesterol

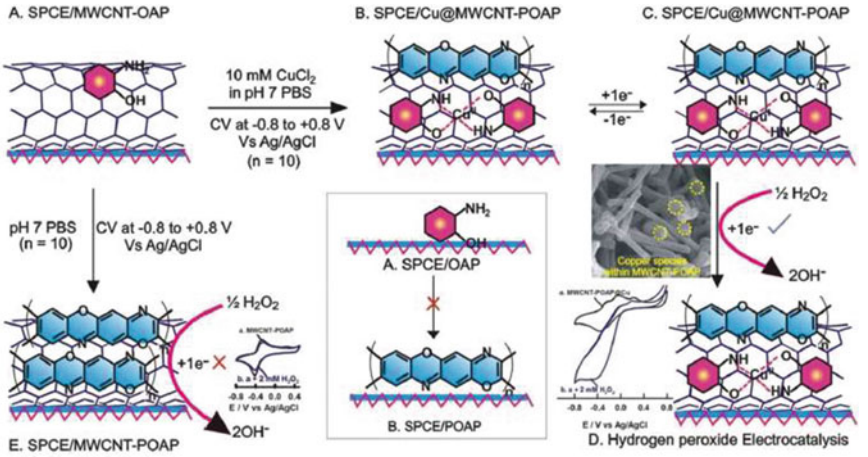

Fig. 2.13 Schematic representation of Cu@MWCNT-POAP preparation and detection principle for H_2O_2. Reproduced from Ref. [73] with permission of RSC Publishing

oxidase had the capability for the detection of cholesterol in blood. The MWCNT facilitated electron transfer and increased sensitivity providing good result for clinical assays of blood. A unique electrochemical sensing method for H_2O_2 making use of Cu@MWCNT-POAP was proposed where the composite was prepared by electrochemically depositing Cu nanospheres on the MWCNT (Fig. 2.13) [73]. After the electrochemical polymerization, both copper (Cu) and poly(o-aminophenol) (POAP) are deposited on the MWCNT. The result suggests that Cu is chelated with oxygen and nitrogen functional groups of aminophenol and stably anchored in between the MWCNT. The excellent performance could be attributed to the stable immobilization of copper species on the surface of POAP dispersed MWCNT. The electrochemical sensor showed excellent electrochemical response to H_2O_2 in the concentration range of 20–360 μM due to significant amplification capacity of MWCNT thin layer (Fig. 2.13). The sensor showed good performance even in the presence of common interfering agents such as dopamine, ascorbic acid, NaCl, and uric acid.

2.5.4 Carbon Nanohorns

Carbon nanohorns (CNHs) are cone-shaped carbon nanostructures derived from a sp^2 carbon sheet and have typical size of 30–50 nm with 2–5 nm diameter [74]. SWCNHs can be prepared via CO_2 laser ablation of a graphite target. Unlike CNTs, nanohorns call for no metal catalyst in their synthesis [75]. They provide a realistic and beneficial choice to SWCNTs due to their protracted shape. SWCNHs are a new material, comparable to SWCNTs and are categorized into three variations, namely,

dahlia, bud and seed [76]. SWCNHs have internal and interstitial nanopores. Therefore, they find applications in gas adsorption, catalysis and electroanalysis. Though SWCNHs have not been extensively utilized in electroanalysis, unlike their CNT counterparts, yet as a result of the similar architectural properties, insights from CNTs may be applied to this potential electrode material. From the structure of SWCNHs, the proportion of edge plane sites is reduced with a high percentage of basal plane sites, suggesting that an electrode modified with SWCNHs will certainly offer an inadequate voltammetric reaction. Nevertheless, among the first examples of their uses was reported in the direction of the electroanalytical determination of UA, DA, and AA [77]. Linear sweep voltammetric response was acquired at a bare GCE where no signals were obtained, however when the electrode is modified with SWCNHs, three distinct and well-resolved peaks are observed. Such a modification in feedback was credited to the boost in edge plane density and adsorption ability of the SWCNHs, which is rather surprising. The authors reported peak separations between uric acid-dopamine, and dopamine-ascorbic acid as 152 mV and 221 mV, respectively. The calibration curve for UA, DA and AA were in the range of 0.06–10 mM, 0.2–3.8 mM, and 30–400 mM, with detection limits of 20 nM, 60 nM, and 5 mM respectively. The sensing approach was applied for the determination of uric acid, dopamine, and ascorbic acid in urine samples. Zhao et al. made use of SWCNHs modified with GNP to offer a disposable immunosensor and utilized α-fetoprotein as a design target analyte and demonstrated its applicability for detection in serum samples. Valentini et al. [75] used oxidized single-walled carbon nanohorns that were immobilized onto SCE. These electrodes were explored for the electrochemical detection of epinephrine, in the presence of serotonine-5-HT, DA, epinephrine, AA, acetaminophen, and UA. A linear range of 2–2500 μM was obtained for epinephrine with a LOD of 0.1 mM [75]. A CNHs/β-CD nanohybrid was reported for sensing 1-chloro-4-nitrobenzene (CNB) (Fig. 2.14) [78]. The β-CD formed by partly unzipping CNHs give abundant active sites, additional rise in surface area along with enhanced dispersibility of the CNHs/β-CD which resulted in fast electron transportation. TEM, FT-IR spectroscopy, Raman spectroscopy, XRD, and electrochemical methods were used to characterize the structure and morphology of CNHs/β-CD. The results show that the sensor exhibits excellent electrochemical sensing performance (linear response range of 2–2500 mM and a LOD of 0.1 mM) to CNB.

2.5.5 Fullerene

The fullerene (C_{60}) is a unique electron pool of π-conjugated systems that has gotten noteworthy attention as electrode modifier [79]. The derived nanostructures of fullerene with different morphologies have produced huge amount of progress in nanotechnology due to their physical properties [79]. 1D fullerene nanorods stemmed out of 0D C_{60} have special physical properties including large surface and outstanding electron accepting properties. Covalent immobilization of fullerenes

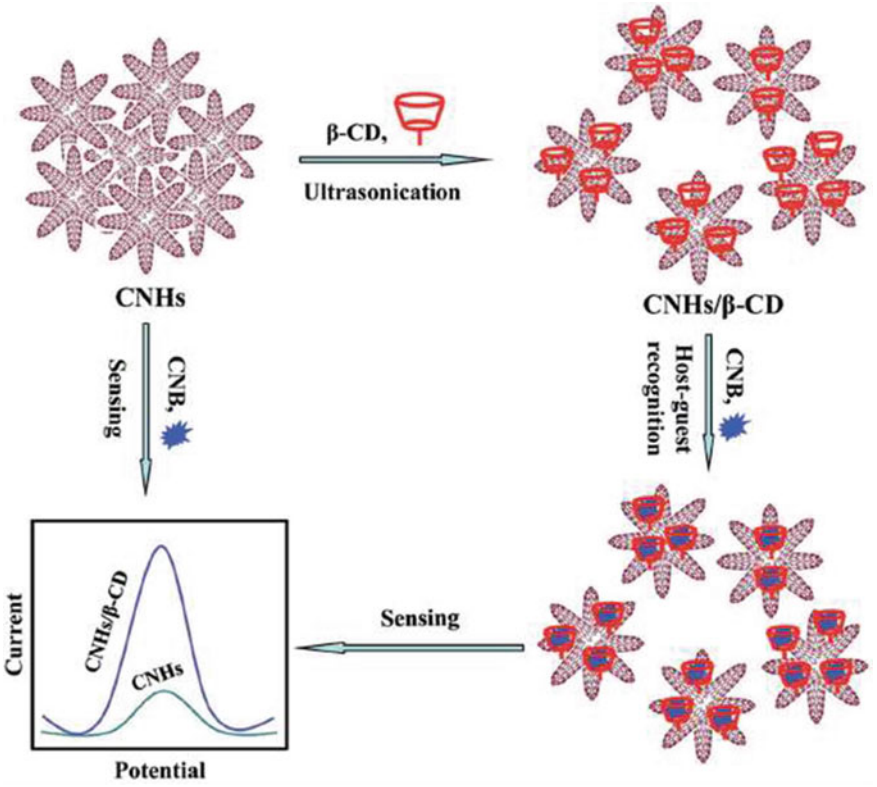

Fig. 2.14 Preparation of the CNHs/β-CD nanohybrids electrode for CNB detection. Reproduced from Ref. [78] with permission of RSC Publishing

onto solid surface and films is being persuaded to understand their chemistry at the interface for future applications in electronic gadgets [80]. Undoubtedly, composite of C_{60} with nanomaterials such as nitrogen-doped carbon nanotubes, AuNPs and PdNPs has been shown to be helpful for incorporating the special physical properties of these materials which results in novel applications [81]. Moreover, C_{60} exhibited inner redox activity, reproducible catalytic reaction, and high chemical stability which have brought about considerable interest in scientists to explore the possibilities of utilizing this material in biosensing devices. Biomolecules bearing NH groups are anticipated to bond chemically to the C_{60} molecule, leading to the formation conjugates. Therefore, functionalization of fullerene to prepare water-soluble derivatives and conjugates with enzymes urease, glucose oxidase, haemoglobin, myoglobin, has been reported. The dispersion of the functionalized C_{60}@AuNPs modified electrode revealed excellent catalytic activity for the non-enzymatic detection of glucose [82]. C_{60} groups functionalized with hydroxyl groups can be mediators in biosensor applications. A recent study used antibody immobilized C_{60} to identify immunoglobulin G (IgG) and haemoglobin (Hb) [83]. The carboxylic acid functional

group also plays remarkably imperative component to make a contact in between fullerene and biomolecules thus improving the level of sensitivity of the biosensor. A potentiometric urea biosensor was constructed by immobilizing urease enzyme onto C_{60}-COOH for sensing urea in urine samples. In this study, urease enzyme was immobilized the C_{60}-COOH [84]. Real sample analysis of diluted urine solution has shown promising results.

2.5.6 Graphene

The Nobel Prize in Physics was awarded to Geim and Novoselov in the year 2010, for their simple yet ingenious method to fabricate graphene from highly oriented pyrolytic graphite (HOPG), the so-called "Scotch tape" method, where graphene layers are mechanically cleaved which resulted in graphene and few-layer graphene [85]. Graphene is an indeterminately extended two-dimensional (2D) carbon network with a hexagonal lattice resembling a honeycomb structure which exhibit high sensitivity, great selectivity, good stability, low overpotential, wide potential window, negligible capacitive current, and excellent electrocatalytic activity. The first instances reporting graphene to be potentially utilized as an electrode material was towards the detection of NADH and dopamine. The authors reported that via the addition of graphene onto an electrode surface the voltammetric peak heights increased at reduced overpotentials. Such work was the beginning of the graphene where scientists anxiously modified electrodes, analysed these towards target analytes and reported electrocatalysis compared with the unmodified electrode. Porous graphene (PG), as a new kind of graphene derivatives, has good dispersibility in aqueous medium, because of π-π stacking of graphene [86]. As a result, PG possesses high surface area and mechanical stability contrasted to graphene. Furthermore, the pore framework in PG facilitates quick movements of charge, which Renders electrical conductivity to this material. PG has been widely utilized in the area of electrochemical sensor. A glucose sensor based on $CuCo_2O_4$ polyhedron/porous reduced graphene oxide (PrGO) composite with hollow structure have high sensitivity for glucose. A novel electrochemical sensor making use of PG prepared by chemical vapour deposition for the detection of dopamine showed no interferences of UA and DA. A recent work compared the electrochemistry of graphene making use of CV and DPV. The DPV result showed that several electroactive substances AA, serotonin (ST), and DA were very well resolved, because of quick electron transfer in graphene. Hybrid nanocomposites of 3D graphene with NPs have pulled in consideration for the advancement of H_2O_2 sensors. Cheng et al. reported Cu_2O microcrystals embedded porous 2D and 3D graphene aerogel (GA) by hydrothermal and filtration strategies for the electrochemical detection of H_2O_2 (Fig. 2.15) [87]. Textural characterization proves that Cu_2O is uniformly distributed over the GA. Electrochemical sensing performance of 3D Cu_2O-rGO-P is higher compared that of its 2D analogue. Both sensors based on 3D Cu_2O-GA and 2D Cu_2O-rGO-P nanocomposites appeared good selectivity towards the detection of

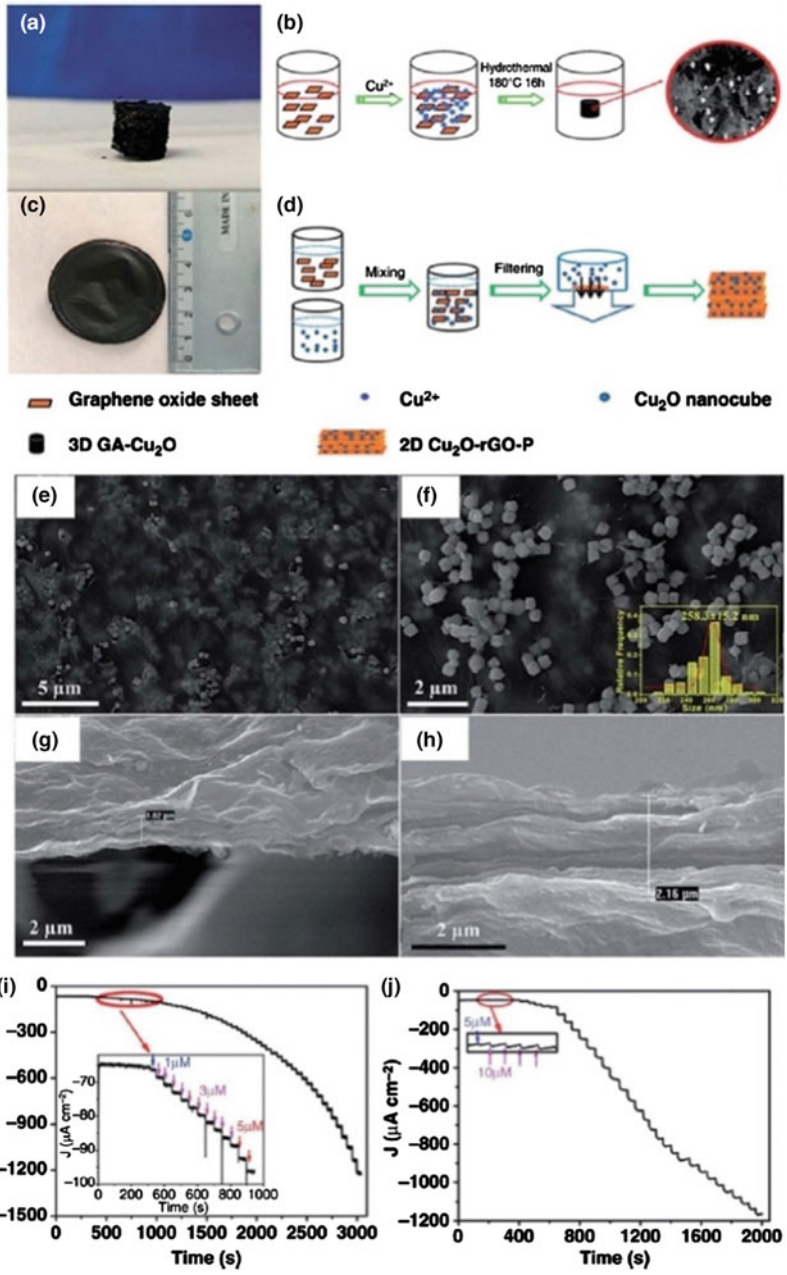
(a)
(b)
Cu2+
Hydrothermal
180°C 16h
(c)
(d)
Mixing
Filtering
Graphene oxide sheet
Cu2+
Cu2O nanocube
3D GA-Cu2O
2D Cu2O-rGO-P
(e)
5 µm
(f)
2 µm
(g)
2 µm
(h)
2 µm
(i)
1µM
3µM
5µM
J (µA cm-2)
Time (s)
(j)
5µM
10µM
J (µA cm-2)
Time (s)

◀**Fig. 2.15** Image of 3D-Cu_2O-GA (**a**).The obtained 2D Cu_2O-rGO-P nanostructure after filtration (**c**). Schematic diagrams of the synthesis of 3D Cu_2O-GA composite (**b**) and 2D Cu_2O-rGO-P (**d**). (**e** and **f**) SEM images obtained at different magnifications of the 2D Cu_2O-rGO paper without thermal annealing. Inset in (**f**) shows size distribution histogram. SEM images of the 2D Cu_2O-rGO paper before (**g**) and after (**h**) thermal annealing. The insets in (**i**) and (**j**) show the magnified cathodic current response for low H_2O_2 concentrations. Reproduced from Ref. [87] with permission of American Chemical Society

H_2O_2 having no interference. The high electrocatalytic activity of the 3D Cu_2O-GA is due to the large surface area provided by the rGO and good conductivity which helps the transfer of electrons.

2.6 Conducting Polymer Nanomaterials

Typically, plastics are associated with excellent electric resistivity and are often used as protection for electrical cables [88]. However, lately with the advent of conducting polymers, plastics have been associated as semiconducting or even conducting materials for various applications ranging from electrocatalyst to product oriented scientific research [88]. Conductivity of these polymers increases on addition of dopant (Fig. 2.16). For all intents and objectives, CPs can be called Nobel Prize-winning materials, given the fact that they find real life application in various fields such as

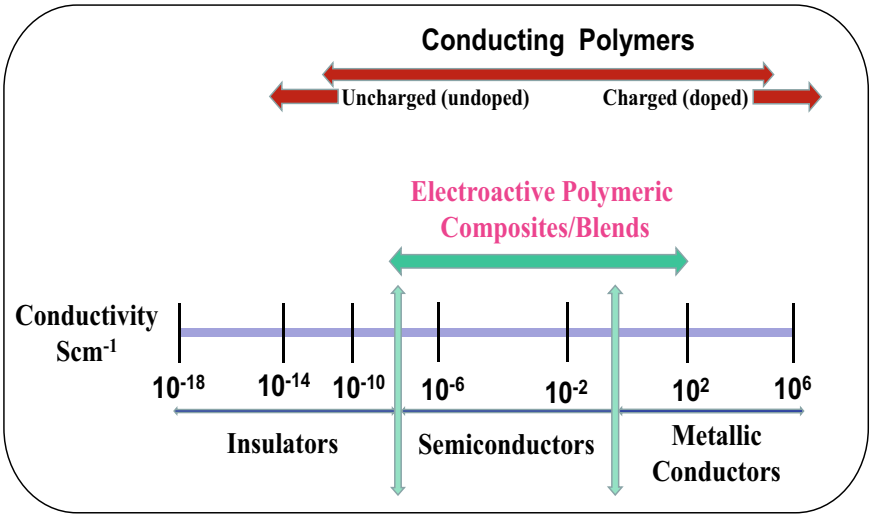

Fig. 2.16 Conductivity range of CPs and conductive polymeric composites. Reproduced from Ref. [85] with permission of Elsevier

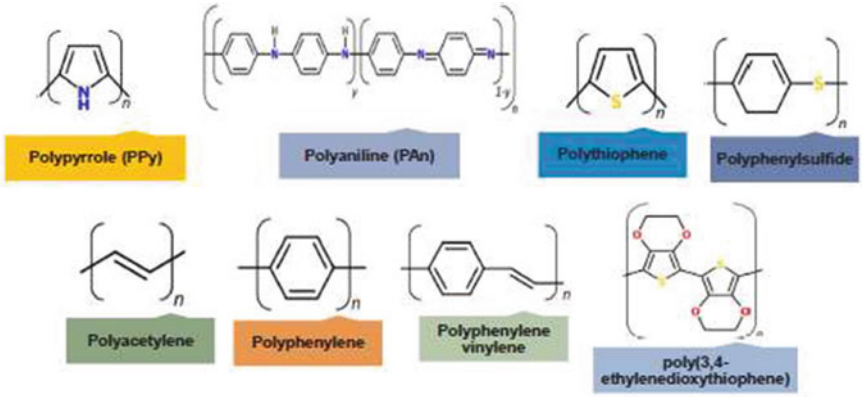

Fig. 2.17 Various conducting polymer reported in the literature. Reproduced from Ref. [88] with permission of Elsevier

rechargeable batteries, capacitors, sensors, and electrochromic devices. Three scientists, Alan J. Heeger, Alan G. MacDiarmid and Hideki Shirakawa were awarded Nobel Prize in Chemistry in the year 2000 for the discovery of conducting polymers [88].

In this section, an overview of a few prominent conducting polymer (Fig. 2.17) based nanomaterials for electrochemical sensing applications is presented. Polyacetylene, the first polymer discovered to have intrinsic conductivity on doping, has the most basic molecular framework [88]. However, its insolubility and inadequate stability restricts its technological applications. Among CPs, the highly appropriate front runners belong to essentially three families: polyaniline (PANI), polypyrrole (PPy), and polythiophene (PT). The various strategies for synthesis of CPs include (i) templates method (hard-template and soft-template), template-free approaches and (ii) polymerization methods (dispersion polymerization, interfacial polymerization, vapour polymerization, and also electrochemical polymerization) (Fig. 2.18) [88]. Soft templating method includes use of surfactants for generating porosity in the nanostructured material. The hard-templating method uses the pore structure of mesoporous material (e.g. mesoporous silica) to create a new material (also known as nanocasting). A precursor to the desired end material can infuse into the mesoporous structure of the silica. This is then heated to a suitable temperature for thermal degradation to form the required product. Chemical synthesis is carried out by polymerization of the monomer in acidic medium using oxidants such as ammonium persulphate ($(NH_4)_2S_2O_8$), and $FeCl_3$. Electrochemical synthesis can be carried out in three ways: (1) potentiostatic (constant potential) method; (2) galvanostatic (constant current) method; (3) potentiodynamic (potential scanning or cyclic voltammetric) method. In the interfacial polymerization technique, the radical reaction occurs at the interface of two immiscible solvents and the result is polymer nanofibers. Dispersion polymerization (DP) is a heterogeneous polymerization process carried out using

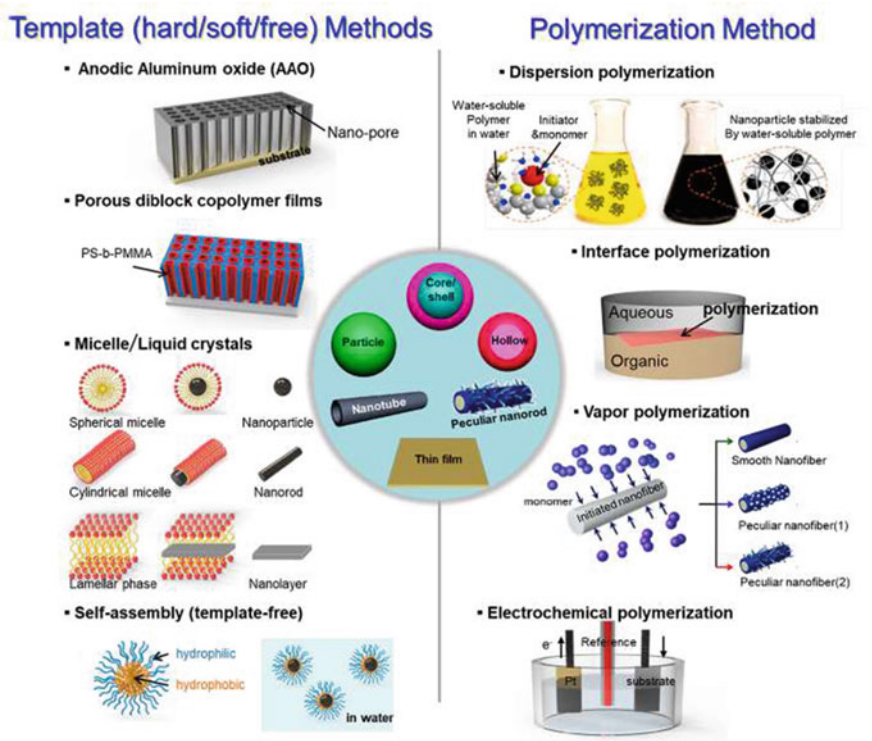

Fig. 2.18 Route of CP nanomaterial synthesis by using the template method and polymerization methods. Reproduced from Ref. [88] with permission of American Chemical Society

polymeric stabilizer in the reaction medium. Dispersion polymerization is a convenient method to obtain bigger solid particles. Uniform-sized polymer beads with diameters between 0.1 and 10 μm are obtained by this method which finds application in coatings, biomedical, electronics and microelectronics. In vapour phase polymerization, monomer vapour is introduced to the oxidant coated substrate and the polymerization happens at the oxidant vapour interface. The above methods can also be used for synthesis of polymer-based nanomaterials.

2.6.1 Polypyrrole

Among conducting polymers, polypyrroles (PPy) is without doubt the most thoroughly examined polymer due to its water solubility, low oxidation potential, and reasonably priced monomer pyrrole [89] PPy along with its derivatives are typically made use of as immobilizing substrate for biomolecules. Ability to be polymerized in aqueous media, one-step electrodeposition on the electrode surface, extremely

simple enzyme entrapment, long-lasting ecological environmental stability are all favourable highlights that allow them to be used in chemical sensing units, biosensors, and solar batteries [89]. PPy has been efficiently made use of in fabricating transistors for sensing purpose. For the synthesis of polypyrrole, electrochemical polymerization is an often-made use of technique considering that it demands small amount of monomer and enables examination of in-situ growth during polymerisation [89]. The technique is easy, and it gives direct grafting of the polymer onto electrode surface area without the requirement of doping after synthesis. Even though polypyrrole was one of the very first conducting polymer to be electrochemically synthesized, there is an ongoing controversy concerning its polymerization mechanism [89]. Regardless, the polymerisation is considered to include formation of cation which is observed through either radical cation coupling or reaction of a radical cation with a neutral monomer [89]. A new sort of bio-nanohybrid product consisting of functionalized multiwall carbon nanotubes and PPy was proposed for an enzymatic amperometric biosensor [90]. It is produced by enveloping the enzyme GOx by electrochemical polymerization where PPy grows in the sites of the functionalized-MWCNTs giving enough space for enzyme immobilization (Fig. 2.19) [90]. Nafion was used for dispersion of MWCNTs which also prevented leaching of GOx from the electrode. The enhanced glucose biosensor electrode showed a wide detection range spanning upto

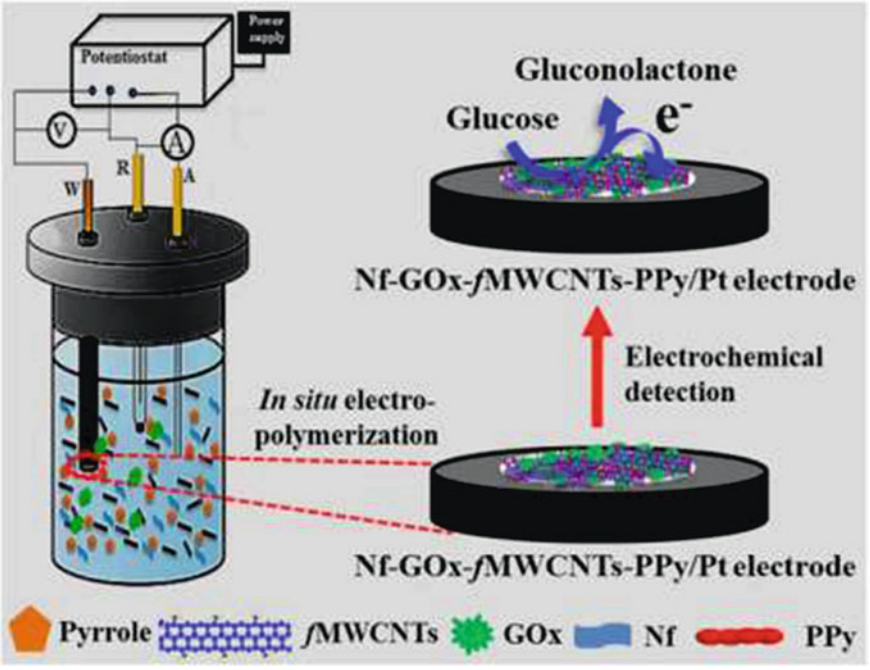

Fig. 2.19 Glucose detection scheme using ternary Nf-GOx-fMWCNTs-PPy/Pt electrode. Adapted and reproduced from Shrestha et al. [90] under a Creative Commons Attribution 4.0 International

4.1 mM, with a response time less than 4 s. The applicability of the biosensor was examined for the determination of a real serum sample. The high performance of the sensor is due to π-stacking of MWCNTs with PPy which increases the electrical conductivity of the composite. Nafion, having a negative charge due to hydrophilic anion, helps to repel most of the negatively charged interfering analytes such as AA, DA, and UA, thus rendering good selectivity to the biosensor [90]. An organic electrochemical transistor (OECT) consisting of an interdigitated microarray electrode coated with Nano-PPy and a penicillinase membrane layer was reported. Pencilline-G in contact with device is converted to pencillonic acid on hydrolysis by enzyme. The enzyme reaction acidifies the PPy membrane, causing an increase in the electric conductivity of Nano-PPy. In a recent report, an electrochemical sensing unit with exceptionally high selectivity for detection of p-nitrophenol (p-NP) has been demonstrated using nanoPPY@sodium dodecyl sulphate@GCE. The biosensor showed a good detection range from 0.1 nM-100 μM for estimation of p-NP with LOD of 0.1 nM [91]. The pores of the thin layer can serve as minicells which can also act as capillary tubes for the diffusion of p-NP right into the electrode surface area [91]. In another study, nanofiber PPy(PPyNFs) film was grown on n-type silicon substrate by electropolymerisation to fabricate Schottky junction diode for detection of m-dihydroxybenzene by CV [92]. The introduction of Pt layer on p-aligned PPy NFs/n-Si film resulted in non-linear I-V curves due to the development of Schottky barrier between PPyNFs/n-Si and Pt layer.

A highly sensitive electrochemical sensor for nitrate and nitrite ions was reported using copper nanoparticles, zinc superoxide dismutase (SOD1) modified with nitrate reductase (NaR) co-immobilized on a CNT-polypyrrole (PPy) nanocomposites (Fig. 2.20) [93]. The electrochemical behaviour of nitrate and nitrite ions on the sensor was investigated. The high surface area provided by PPy helps to bind CNT. The PPy also provides enough porous structure for the immobilization of two enzymes (SOD1) and (NaR) [93]. The CNT acted as a molecular wire which helped in accelerating the electron transfer. The sensor showed best selectivity against interfering agents because of the cellulose acetate membrane. The results showed that the sensor exhibited electrocatalytic activity for nitrite oxidation at +0.8 V and at −0.76 V for nitrate ions (Fig. 2.20). The findings show that CNT–PPy nanocomposites helped co-immobilization of SOD1 and NaR which enhanced the sensitivity of the biosensor [93]. Lin et al. described biosensor transducer of carboxyl capped overoxidized PPy nanowire electrode for sensing tripeptide (Gly-Gly-His) cognitive of Cu^{2+} [94]. Result from the electrochemical sensor showed to be extremely specific to Cu^{2+} within the concentration range of 20–300 nM [94].

2.6.2 Polythiophene

Polythiophenes (PThs) nanomaterials are conjugated polymers which are environmentally and thermally stable. The density of polymer film can be tuned by altering the polymerization time using electropolymerization technique [89]. PThs forms

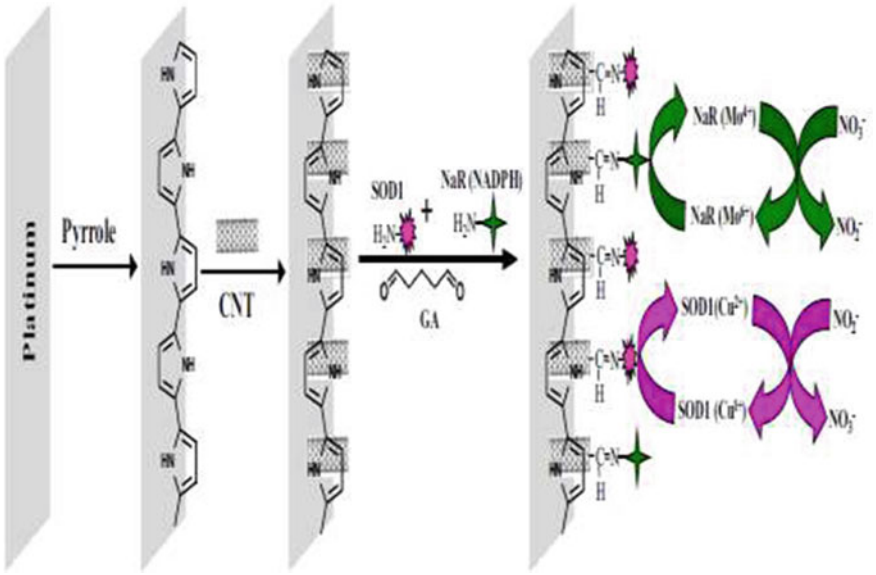

Fig. 2.20 Construction of a NaR–SOD1–CNT–PPy–Pt electrode for the detection of NO_2^- and NO_3^-. Reproduced from Ref. [93] with permission of Elsevier

films with good adhesion to the substrate and also help in transmission of signals between the substrate and the biomolecules. PThs finds application in various areas, such as electric gadgets, sensing units, batteries, electro-magnetic material, artificial noses, muscular tissues, solar batteries, microwave absorbing products, memory gadgets, nano-switches, and polymer digital interconnects [95]. Earlier, the non-substituted polythiophene was rarely used due to its insolubility in common organic solvents as a result of its extended π-conjugated structure. Hence, alkyl chains are introduced into the thiophene systems using functionalized monomers to synthesize soluble polymers [95, 96]. Electropolymerization utilizing monomers can be a fast, useful and well-understood approach. An electrochemical sensor with poly(3-thiopheneacetic acid) as a nanostructure has actually been produced by linking cholesterol oxidase, for detection of cholesterol [97]. Even though fluorescent tag and surface plasmon resonance have actually been made use as hybridization transduction, these techniques might be expensive and lengthy [97]. There are reports such as DNA hybridization immobilization of oligonucleotide. The development of hydrogen bonds in between corresponding regions of DNA but also the functionalized PThs has altered their electrochemical characteristic which creates the exploration of particular DNA in PThs-based biosensors. A label-free electrochemical sensing unit for DNA was prepared by electrochemical polymerization of Poly(4-hydroxyphenyl thiophene-3-carboxylate) (PHPT) onto GCE (Fig. 2.21) [98]. In the hybridization process, DNA labelled oligonucleotides (ODN) complementary to another target were combined in equivalent quantities (Fig. 2.21) [98]. A biological recognition can

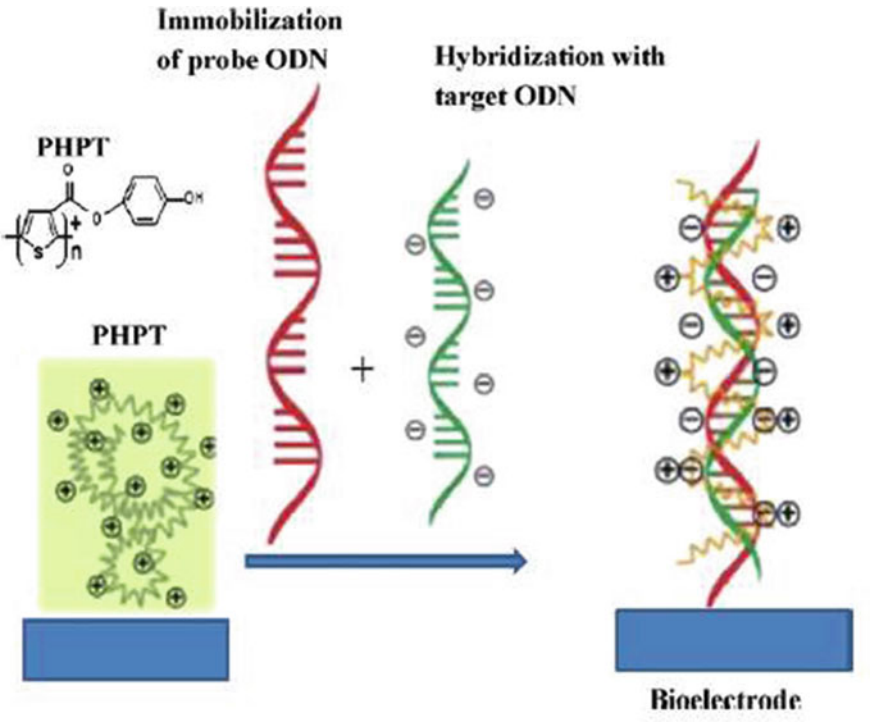

Fig. 2.21 Schematic representation of the fabrication of PHPT/ODN bioelectrode. Reproduced from Ref. [98] with permission of Elsevier

be checked by comparing CV of single and double-stranded oligonucleotide. The double strand oligonucleotide has lower oxidation current than that of single strand, which leads to decrease of PHPT electroactivity due to stiffness of the polymer chain. One of the reasons is probe and target in the polymer chain caused restricted movement and rotation of the polymer chain which result into decrease in conductivity. The sensitivity of the electrochemical sensing unit was 0.02 μA/ nmol with an LOD of 1.49 nmol [98].

2.6.3 Polyaniline (PANI)

Among CPs, polyaniline (PANI) is well-known semi-flexible rode-like CP, having high conductivity, ease of synthesis, and environmental stability. PANI with different nanostructures ranging from nanoplates, tubes, fibres to brain-like structures are reported (Fig. 2.22) [89]. PANI and its derivatives have a remarkable number of active sites for immobilization of enzyme without any additional treatment. The nanostructured PANI also finds applications as matrix material in microelectronic

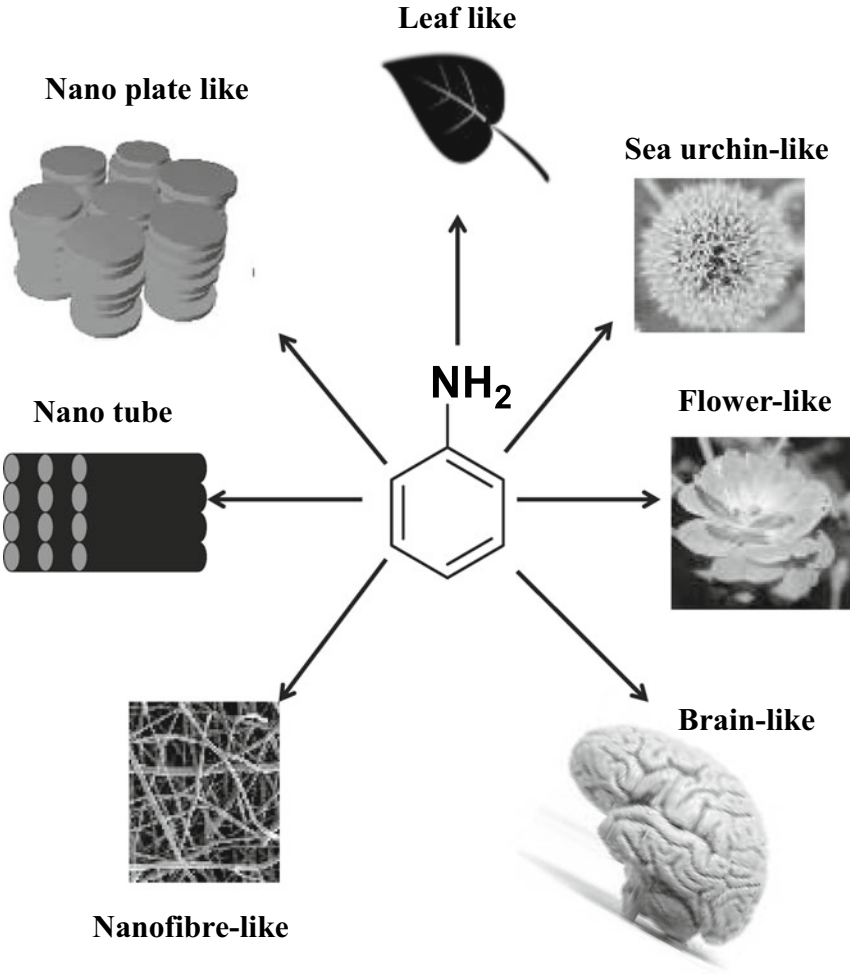

Fig. 2.22 Morphology of different PANI structures

devices. PANI has been generally made use of in numerous biosensors applications such as biomedical gadgets and biosensors for detection of biomolecules such as glucose [22, 63, 99–101]. Commonly, PANI is synthesized through electrochemical, chemical oxidation of the aniline monomer in acid solution, vapour-phase deposition polymerizations, plasma polymerizations, technique, photochemical polymerization, inverse emulsion polymerization, and enzymatic polymerization. PANI has several structural forms among which the emeraldine salt (ES) form is the highest conducting form. ES is formed by protonation of the emeraldine base, which takes place preferentially at the imines N atoms creating radical cations accompanied by an increment in conductivity by several orders of magnitude. Early mechanism used

for biosensor developed in the 1980s depended on the pH alterations which stem from chemical responses, though with poor LOD. In a much more sensitive methodology, reduction of oxidized PANI was coupled with the oxidation of glucose by GOx [11, 23, 99]. The greater surface area and ease of incorporation of biological materials are some of the main advantages for the nanofibers type of polyaniline over traditional dense films. Polyaniline has been used in DNA sensing considering that the redox activity of the polymer comes with oligonucleotide binding occasions likewise provides signal increasing. Whereas PANI is identified for being a lot more chemically and mechanically stable than various other conducting polymers, its utilization was restricted in biological sensing applications which typically need neutral pH range. This is because electropolymerisation generally requires acidic pH whereas most of the biomolecules are known to lose their activity in low pH range. This problem can be overcome by making use of self-doped polyaniline. For example, doping polyaniline with polyacid such as poly(styrenesulfonate) can help to maintain electroactivity of PANI even in neutral pH range. The sulfonate groups on the polyacid retain local acidity even in neutral electrolytes. Lee et al. suggested use of poly(aniline-co-metanilic acid) copolymer for detecting progesterone [102]. Sulfonate group in the metanilic acid form hydrogen bond with progesterone. Progesterone is imprinted into the poly(aniline-co-metanilic acid) on the working electrode surface. In another study electropolymerization method was carried out to produce a PANI nanotube cluster that had an extremely reduced LOD of 1.0 fM conjointly, illustrated the capacity to set separated single base pair mismatches. The ultrasensitivity was due to oriented nanotubes having high conductivity. Sawant et al. established a highly sensitive microbial biosensor for electrochemical detection of pesticide lindane utilizing PANI nanofibers immobilized with genetically modified *E.coli* cells overexpressing γ-hexachlorocyclohexane dehydrochlorinase (LinA2) gene (Fig. 2.23) [103]. Results showed that the LinA2 gene present in the genetically modified cells helps degrade lindane to produce HCl causing protonation of PANI microenvironment and an enhancement in its conductivity, which was determined

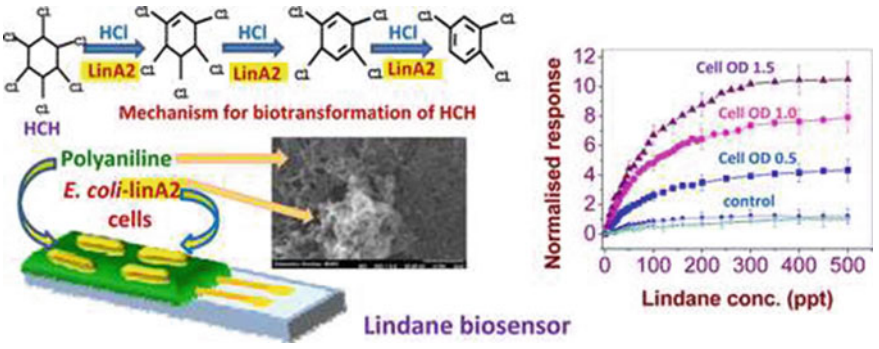

Fig. 2.23 Scheme of enzymatic biotransformation of HCH by step-by-step dehydrochlorination making use of the LinA2 HCH dehydrochlorinase. Reproduced from Ref. [103] with permission of American Chemical Society

by pulsed amperometry. The biosensor detects lindane at part-per-trillion concentration range having a linear range from 2 to 45 ppt (Fig. 2.23) [7]. Over the last few years, electrochemical immunosensors based upon different electrochemical analytical methods has been widely applied in biochemistry and biology, clinical chemistry and ecological surveillance. The detection selectivity of electrochemical immunosensors relies on molecular recognition between antigens and antibodies. The label-free immunosensor becomes an appealing and promising method due to its simplified working procedure, high sensitivity and selectivity, reduced instrumentation expense, simplicity of usage and rapidity of the assay. Detection of circulating tumour cells (CTCs) in the bloodstream of patients diagnosed with Stage III cancer and undergoing treatment is important for monitoring the effectiveness of the treatment and to implement any additional intervention necessary towards a cure. However, identifying and enumerating very few CTCs present among billions of normal blood cells remains a challenge. Melanoma (melanotic carcinoma) is a kind of deadly cutaneous cancer which is metastatic in nature. The incidence of cutaneous cancer malignancy has proliferated over the last few decades, making it a leading cause of death. Realizing the lethality of cancer malignancy, scientists have developed varied techniques to diagnose the primary as well as metastatic cancer malignancy. Anu Prathap et al. reported antibody MC1R-functionalized PANI@SPE-based microfluidic device (PANI@SPE-MFD) for the detection of cancer malignancy skin CTC (Figs. 2.24, and 2.25) [104]. The polyaniline nanofibers (PANI-NFs) were prepared by interfacial polymerization technique. XRD confirmed the formation PANI having high crystallinity (Fig. 2.24a). Electron microscopy showed that the nanofibers having a size of ~95 nm (Fig. 2.24b). XPS analysis confirmed the presence of that C1s, N1s, and O1s, respectively (Fig. 2.24c). N_2 adsorption shows type IV isotherm indicating presence of mesopores (Fig. 2.24d). PANI-NFs modified electrode was used as a sensor for melanoma cells (Fig. 2.25).The fabricated device shows LOD of 1 cell/1 mL and an excellent linearity with cell concentration ranging from 10 to 9000 melanoma cells/10 mL [104]. The high electrochemical activity of the sensor was due to high surface area and amine nitrogen linkages in PANI-NFs which facilitated the antibody immobilization. Moreover, the biocompatibility and non-cytotoxicity makes the PANI matrix easier for higher amount antibody loading which lead to higher linear range of detection and lower limit of quantification (LOQ) compared to reported literature [105]. Sawant et al. have reported a very sensitive electrochemical strategy for monitoring the extracellular acidity (pH_e) in the microenvironment of cells in real-time (Fig. 2.26) [106]. The mechanism includes doping of PANI by the acidic metabolites released by the cells which bring about conversion of the emeraldine base of PANI to salt form (Fig. 2.26) [106]. This triggers an increase in conductivity of the sensing unit, which is evaluated by amperometry. Various cell types (MCF7, DU145, PC3, and PBMC) are used in this study. By innovative layout of the electrodes, it was possible to detect as low as 5 cells. The sensor could also be used to examine the effectiveness of glycolysis inhibiting drugs on cancer cells. It is anticipated that further information and comprehensive research on nanobiosensors will lead to their application in personalized clinical diagnosis, which could eventually decrease the health problems and improve quality of human life.

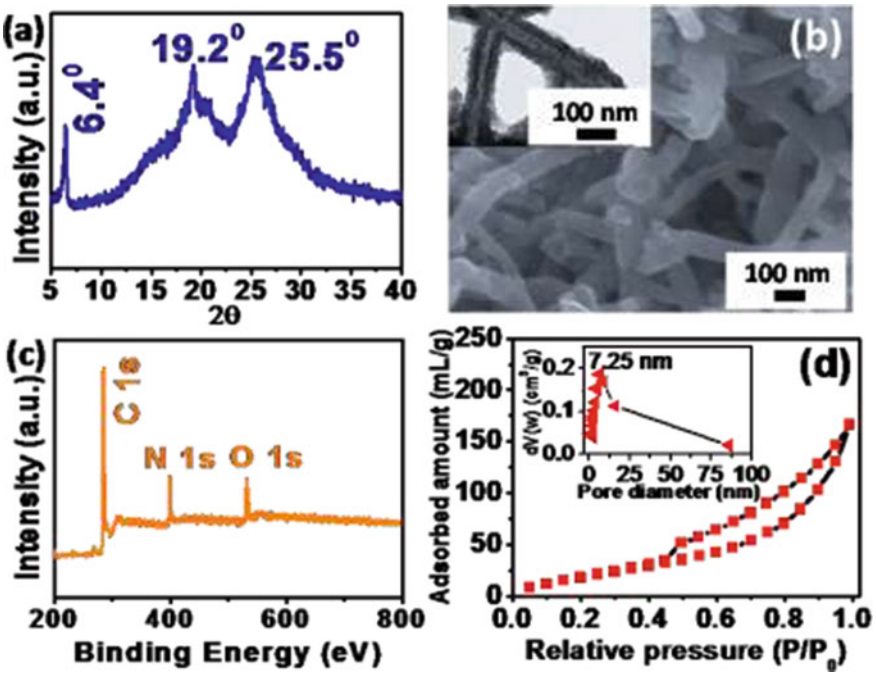

Fig. 2.24 Characterization of PANI-NFs: **a** XRD pattern, **b** SEM image (inset: HRTEM image), **c** XPS spectra, and **d** N_2 adsorption isotherm (inset: pore size distribution). Reproduced from Ref. [104] with permission of Elsevier

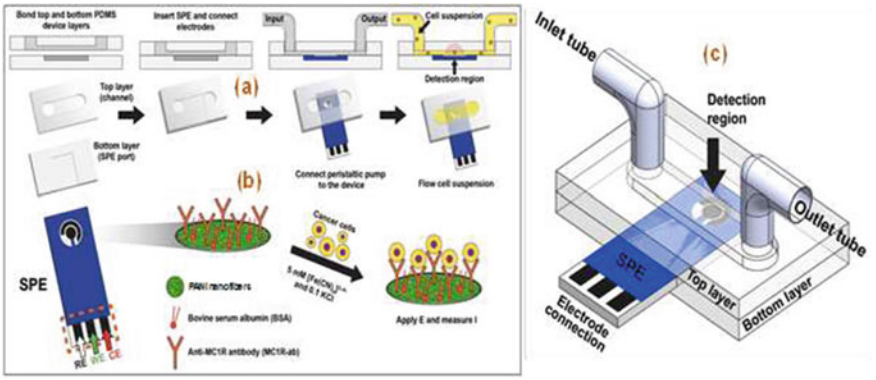

Fig. 2.25 **a** Schematic drawing of parts of the gadgets. **b** Electrochemical detection scheme for CTC. **c** Schematic of fully constructed device. Reproduced from Ref. [104] with permission of Elsevier

Fig. 2.26 Schematic for conversion of the emeraldine base form of polyaniline to emeraldine salt form on interaction with acidic metabolites with concomitant increase in its conductivity. Reproduced from Ref. with permission of Royal Society of Chemistry. Adapted and reproduced from Sawant et al. [106] under a Creative Commons Attribution 3.0 Unported License

2.7 Conclusions and Outlook

Introduction of electroanalytical technologies based on unique functional nanomaterials implies a significant opportunity for the development of electrochemical sensor and biosensor devices for a wide range of applications. Property of nanostructured materials can be further enhanced with introduction of porosity. Nanostructured materials with porosity are very important for catalytic and electrochemical sensing applications. In this chapter, the relevance of nanomaterials-based electrochemical sensor as well as biosensor systems for environmental and biomedical applications is highlighted. Detailed electrochemical sensing and biosensing strategies based

on vast array of nanomaterials including semiconducting metal oxide nanomaterials, noble metals, conducting polymer nanomaterials, carbon nanomaterials, as well as their nanocomposites are described. Applications of these nanomaterials for single and simultaneous multiple analyte detection using electrochemical sensor were discussed. Compared to other techniques such as mass spectrometric and optical techniques, the electrochemical measurements are more affordable, simple and easier for miniaturization, which makes it better for online detection. Nanomaterials with small size, high surface area, inter-crystalline mesoporosity and high dispersion of active metal species on the porous materials were some of the key feature for displaying high catalytic activity and electrochemical sensitivity. The promising results obtained using nanomaterials provides scope for future development of several new class of tailored nanomaterials targeting specialized applications. Although remarkable advances have been obtained in exploring nanomaterial-based signal boosting techniques for the progression of ultrasensitive biosensing approaches, the nanomaterials-based biosensors utilizing biomolecules often suffer from problems of poor stability and reusability. The detection of cancer cells and specific proteins at ultra-low levels in real sample is particularly challenging. Hence, substantial effort is still an urgent demand to boost the reproducibility and practicability of the nanomaterials-based signal boosting strategies. However, with further advancement in nanotechnology, innovative sensing platforms will certainly be developed to detect trace target analytes with enhanced sensitivity and selectivity.

Acknowledgements Anu Prathap M. Udayan is grateful to Department of Biotechnology (DBT), Government of India for Ramalingaswami Re-entry Fellowship (BT/HRD/35/02/2006; BT/RLF/Re-entry/30/2017) and financial support.

References

1. Whitesides GM (2005) Nanoscience, nanotechnology, and chemistry. Small 1:172–179. https://doi.org/10.1002/smll.200400130
2. Friedman RS, McAlpine MC, Ricketts DS, Ham D, Lieber CM (2005) High-speed integrated nanowire circuits. Nature 434:1085–1085. https://doi.org/10.1038/4341085a
3. Nalwa HS (2014) A special issue on reviews in biomedical applications of nanomaterials, tissue engineering, stem cells, bioimaging, and toxicity. J Biomed Nanotechnol 10:2421–2423
4. Mazzola L (2003) Commercializing nanotechnology. Nat Biotechnol 21:1137–1143. https://doi.org/10.1038/nbt1003-1137
5. Colvin VL (2003) The potential environmental impact of engineered nanomaterials. Nat Biotechnol 21:1166–1170. https://doi.org/10.1038/nbt875
6. Chen X, Mao SS (2007) Titanium dioxide nanomaterials: synthesis, properties, modifications, and applications. Chem Rev 107:2891–2959. https://doi.org/10.1021/cr0500535
7. Thakur B, Amarnath CA, Mangoli SH, Sawant SN (2015) Polyaniline nanoparticle based colorimetric sensor for monitoring bacterial growth. Sens Actuators, B Chem 207:262–268. https://doi.org/10.1016/j.snb.2014.10.045
8. Pandey PC, Singh S, Sawant SN (2018) Functional alkoxysilane mediated controlled synthesis of Prussian blue nanoparticles, enabling silica alginate bead development; nanomaterial for

selective electrochemical sensing. Electrochim Acta 287:37–48. https://doi.org/10.1016/j.electacta.2018.05.003
9. ChellachamyAnbalagan A, Sawant SN (2016) Brine solution-driven synthesis of porous polyaniline for supercapacitor electrode application. Polymer 87:129–137. https://doi.org/10.1016/j.polymer.2016.01.049
10. Pumera M, Ambrosi A, Bonanni A, Chng ELK, Poh HL (2010) Graphene for electrochemical sensing and biosensing. TrAC, Trends Anal Chem 29:954–965. https://doi.org/10.1016/j.trac.2010.05.011
11. Anu MP, Kaur B, Srivastava R (2019) Electrochemical sensor platforms based on nanostructured metal oxides, and zeolite-based materials. Chem Rec 19:883–907. https://doi.org/10.1002/tcr.201800068
12. Sawant S (2017) Development of biosensors from biopolymer composites. In: Biopolymer composites in electronics, pp 353–383. https://doi.org/10.1016/B978-0-12-809261-3.00013-9
13. Thakur B, Amarnath CA, Sawant SN (2014) Pectin coated polyaniline nanoparticles for an amperometric glucose biosensor. RSC Adv 4:40917–40923. https://doi.org/10.1039/C4RA05264A
14. Prathap MUA, Wei C, Sun S, Xu ZJ (2015) A new insight into electrochemical detection of eugenol by hierarchical sheaf-like mesoporous $NiCo_2O_4$. Nano Res 8:2636–2645. https://doi.org/10.1007/s12274-015-0769-z
15. Prathap MUA, Sun S, Wei C, Xu ZJ (2015) A novel non-enzymatic lindane sensor based on CuO–MnO_2 hierarchical nano-microstructures for enhanced sensitivity. Chem Commun 51:4376–4379. https://doi.org/10.1039/C5CC00024F
16. Prathap MUA, Gunasekaran S (2018) Rapid and scalable synthesis of zeolitic imidazole framework (ZIF-8) and its use for the detection of trace levels of nitroaromatic explosives. Adv Sustain Syst 2:1800053. https://doi.org/10.1002/adsu.201800053
17. Prathap MUA, Srivastava R (2013) Synthesis of $NiCo_2O_4$ and its application in the electrocatalytic oxidation of methanol. Nano Energy 2:1046–1053. https://doi.org/10.1016/j.nanoen.2013.04.003
18. Thakur B, Sawant SN (2013) Polyaniline/prussian-blue-based amperometric biosensor for detection of uric acid. ChemPlusChem 78:166–174. https://doi.org/10.1002/cplu.201200222
19. Prathap MUA, Srivastava R (2013) Electrochemical reduction of lindane (γ-HCH) at $NiCo_2O_4$ modified electrode. Electrochim Acta 108:145–152. https://doi.org/10.1016/j.electacta.2013.06.122
20. Prathap MUA, Thakur B, Sawant SN, Srivastava R (2012) Synthesis of mesostructured polyaniline using mixed surfactants, anionic sodium dodecylsulfate and non-ionic polymers and their applications in H_2O_2 and glucose sensing. Colloids Surf B: Biointerfaces 89:108–116. https://doi.org/10.1016/j.colsurfb.2011.09.002
21. Prathap MUA, Rodríguez CI, Sadak O, Guan J, Setaluri V, Gunasekaran S (2018) Ultrasensitive electrochemical immunoassay for melanoma cells using mesoporous polyaniline. Chem Commun 54:710–714. https://doi.org/10.1039/C7CC09248B
22. Prathap MUA, Srivastava R, Satpati B (2013) Simultaneous detection of guanine, adenine, thymine, and cytosine at polyaniline/MnO_2 modified electrode. Electrochim Acta 114:285–295. https://doi.org/10.1016/j.electacta.2013.10.064
23. Prathap MUA, Satpati B, Srivastava R (2014) Facile preparation of β-$Ni(OH)_2$-$NiCo_2O_4$ hybrid nanostructure and its application in the electro-catalytic oxidation of methanol. Electrochim Acta 130:368–380. https://doi.org/10.1016/j.electacta.2014.03.043
24. Ma Y, Li H, Bridges D, Peng P, Lawrie B, Feng Z, Hu A (2016) Zero-dimensional to three-dimensional nanojoining: current status and potential applications. RSC Adv 6:75916–75936. https://doi.org/10.1039/C6RA15897H
25. Gaffar S, Udamas D, Hartati YW, Subroto T (2018) Gold modified screen printed carbon electrode (SPCE) with steptavidin-biotin system for detection of heart failure by using immunosensor. AIP Conf Proc 2049:030017. https://doi.org/10.1063/1.5082518

26. Cheemalapati S, Chen S-M, Ali MA, Al-Hemaid FM (2014) Enhanced electrocatalytic oxidation of isoniazid at electrochemically modified rhodium electrode for biological and pharmaceutical analysis. Colloids Surf B, Biointerfaces 121:444–450. https://doi.org/10.1016/j.colsurfb.2014.06.035
27. Devadas B, Sivakumar M, Chen SM, Cheemalapati S (2015) An electrochemical approach: Switching Structures of rare earth metal Praseodymium hexacyanoferrate and its application to sulfite sensor in Red Wine. Electrochim Acta 176:350–358. https://doi.org/10.1016/j.electacta.2015.07.022
28. AnithaKumary V, Divya J, Nancy TEM, Sreevalsan K (2013) Voltammetric detection of paracetamol at cobalt ferrite nanoparticles modified glassy carbon electrode. Int J Electrochem Sci 8:6610–6619
29. Smith BR, Gambhir SS (2017) Nanomaterials for in vivo imaging. Chem Rev 117:901–986. https://doi.org/10.1021/acs.chemrev.6b00073
30. Masitas RA, Allen SL, Zamborini FP (2016) Size-dependent electrophoretic deposition of catalytic gold nanoparticles. J Am Chem Soc 138:15295–15298. https://doi.org/10.1021/jacs.6b09172
31. Rajkumar C, Thirumalraj B, Chen S-M, Palanisamy S (2016) Novel electrochemical preparation of gold nanoparticles decorated on a reduced graphene oxide–fullerene composite for the highly sensitive electrochemical detection of nitrite. RSC Adv 6:68798–68805. https://doi.org/10.1039/C6RA10690K
32. Niemeyer CM, Adler M, Pignataro B, Lenhert S, Gao S, Chi L, Fuchs H, Blohm D (1999) Self-assembly of DNA-streptavidin nanostructures and their use as reagents in immuno-PCR. Nucleic Acids Res 27:4553–4561
33. Cheng MS, Toh C-S (2013) Novel biosensing methodologies for ultrasensitive detection of viruses. Analyst 138:6219–6229. https://doi.org/10.1039/C3AN01394D
34. Salaün P, van den Berg CMG (2006) Voltammetric detection of mercury and copper in seawater using a gold microwire electrode. Anal Chem 78:5052–5060. https://doi.org/10.1021/ac060231+
35. Bi Z, Salaün P, van den Berg CMG (2013) Study of bare and mercury-coated vibrated carbon, gold and silver microwire electrodes for the determination of lead and cadmium in seawater by anodic stripping voltammetry. Electroanalysis 25:357–366. https://doi.org/10.1002/elan.201200446
36. Ding Y, Kim Y-J, Erlebacher J (2004) Nanoporous gold leaf: "ancient technology"/advanced material. Adv Mater 16:1897–1900. https://doi.org/10.1002/adma.200400792
37. Li J, Lin X (2007) Electrocatalytic oxidation of hydrazine and hydroxylamine at gold nanoparticle—polypyrrole nanowire modified glassy carbon electrode. Sens Actuators, B Chem 126:527–535. https://doi.org/10.1016/j.snb.2007.03.044
38. Kaur B, Srivastava R, Satpati B (2015) A novel gold nanoparticle decorated nanocrystalline zeolite based electrochemical sensor for the nanomolar simultaneous detection of cysteine and glutathione. RSC Adv 5:95028–95037. https://doi.org/10.1039/C5RA19249H
39. Shen Y, Sheng Q, Zheng J (2017) A high-performance electrochemical dopamine sensor based on a platinum–nickel bimetallic decorated poly(dopamine)-functionalized reduced graphene oxide nanocomposite. Anal Methods 9:4566–4573. https://doi.org/10.1039/C7AY00717E
40. Liu X, Chen X, Ju J, Wang X, Mei Z, Qu H, Xu Y, Zeng X (2019) Platinum-nickel bimetallic nanosphere-ionic liquid interface for electrochemical oxygen and hydrogen sensing. ACS Appl. Nano Mater. 2:2958–2968. https://doi.org/10.1021/acsanm.9b00380
41. Huang H, Hu X, Zhang J, Su N, Cheng J (2017) Facile fabrication of platinum-cobalt alloy nanoparticles with enhanced electrocatalytic activity for a methanol oxidation reaction. Sci Rep 7:45555. https://doi.org/10.1038/srep45555
42. McNamara K, Tofail SAM (2017) Nanoparticles in biomedical applications. Adv Phys: X 2:54–88. https://doi.org/10.1080/23746149.2016.1254570
43. Zhu N, Chang Z, He P, Fang Y (2005) Electrochemical DNA biosensors based on platinum nanoparticles combined carbon nanotubes. Anal Chim Acta 545:21–26. https://doi.org/10.1016/j.aca.2005.04.015

44. Cui H-F, Ye J, Liu X, Zhang W-D, Sheu F-S (2006) Pt–Pb alloy nanoparticle/carbon nanotube nanocomposite: a strong electrocatalyst for glucose oxidation. Nanotechnology 17:2334. https://doi.org/10.1088/0957-4484/17/9/043
45. Shim K, Kim J, Shahabuddin M, Yamauchi Y, Hossain MdSA, Kim JH (2018) Efficient wide range electrochemical bisphenol-A sensor by self-supported dendritic platinum nanoparticles on screen-printed carbon electrode. Sens Actuators, B Chem 255:2800–2808. https://doi.org/10.1016/j.snb.2017.09.096
46. Zahed FM, Hatamluyi B, Lorestani F, Es'haghi Z (2018) Silver nanoparticles decorated polyaniline nanocomposite based electrochemical sensor for the determination of anticancer drug 5-fluorouracil. J Pharm Biomed Anal 161:12–19. https://doi.org/10.1016/j.jpba.2018.08.004
47. Sandeep S, Santhosh AS, Swamy NK, Suresh GS, Melo JS, Chamaraja NA (2018) A biosensor based on a graphene nanoribbon/silver nanoparticle/polyphenol oxidase composite matrix on a graphite electrode: application in the analysis of catechol in green tea samples. New J Chem 42:16620–16629. https://doi.org/10.1039/C8NJ02325E
48. Arkan E, Shamsipur M, Saber R, Karimi Z, Majnooni M (2014) A novel electrochemical sensor based on a silver nanoparticle modified carbon ionic liquid electrode for selective and sensitive determination of levetiracetam in pharmaceutical tablets and blood plasma samples. Anal Methods 6:2197–2204. https://doi.org/10.1039/C3AY42295J
49. Prathap MUA, Sun S, Xu ZJ (2016) An electrochemical sensor highly selective for lindane determination: a comparative study using three different α-MnO_2 nanostructures. RSC Adv 6:22973–22979. https://doi.org/10.1039/C5RA26771D
50. Kaur B, Srivastava R, Satpati B (2015) Silver nanoparticle decorated polyaniline–zeolite nanocomposite material based non-enzymatic electrochemical sensor for nanomolar detection of lindane. RSC Adv 5:57657–57665. https://doi.org/10.1039/C5RA09461E
51. Abdelwahab A, Shim Y-B (2014) Nonenzymatic H_2O_2 sensing based on silver nanoparticles capped polyterthiophene/MWCNT nanocomposite. Sens Actuators, B Chem 201:51–58. https://doi.org/10.1016/j.snb.2014.05.004
52. Kaur B, Srivastava R, Satpati B (2015) Ultratrace detection of toxic heavy metal ions found in water bodies using hydroxyapatite supported nanocrystalline ZSM-5 modified electrodes. New J Chem 39:5137–5149. https://doi.org/10.1039/C4NJ02369B
53. Rahi R, Fang M, Ahmed A, Sánchez-Delgado RA (2012) Hydrogenation of quinolines, alkenes, and biodiesel by palladium nanoparticles supported on magnesium oxide. Dalton Trans 41:14490–14497. https://doi.org/10.1039/C2DT31533E
54. Datta A, Kapri S, Bhattacharyya S (2015) Enhanced catalytic activity of palladium nanoparticles confined inside porous carbon in methanol electro-oxidation. Green Chem 17:1572–1580. https://doi.org/10.1039/C4GC02052A
55. Sefid-sefidehkhan Y, Nekoueian K, Amiri M, Sillanpaa M, Eskandari H (2017) Palladium nanoparticles in electrochemical sensing of trace terazosin in human serum and pharmaceutical preparations. Mater Sci Eng, C 75:368–374. https://doi.org/10.1016/j.msec.2017.02.061
56. Rahi A, Sattarahmady N, Heli H (2016) An ultrasensitive electrochemical genosensor for brucella based on palladium nanoparticles. Anal Biochem 510:11–17. https://doi.org/10.1016/j.ab.2016.07.012
57. Wang C-H, Yang C-H, Chang J-K (2017) High-selectivity electrochemical non-enzymatic sensors based on graphene/Pd nanocomposites functionalized with designated ionic liquids. Biosens Bioelectron 89:483–488. https://doi.org/10.1016/j.bios.2016.03.071
58. Prathap MUA, Anuraj V, Satpati B, Srivastava B (2013) Facile preparation of Ni(OH)2–MnO2 hybrid material and its application in the electrocatalytic oxidation of hydrazine. J Hazard Mater 262:766–774. https://doi.org/10.1016/j.jhazmat.2013.09.050
59. Kaur B, Satpati B, Srivastava R (2016) ZrO_2 supported nano-ZSM-5 nanocomposite material for the nanomolar electrochemical detection of metol and bisphenol A. RSC Adv 6:65736–65746. https://doi.org/10.1039/C6RA08391A

60. Yang S, Li G, Wang D, Qiao Z, Qu L (2017) Synthesis of nanoneedle-like copper oxide on N-doped reduced graphene oxide: a three-dimensional hybrid for nonenzymatic glucose sensor. Sens Actuators, B Chem 238:588–595. https://doi.org/10.1016/j.snb.2016.07.105
61. Li F, Li Y, Feng J, Dong Y, Wang P, Chen L, Chen Z, Liu H, Wei Q (2017) Ultrasensitive amperometric immunosensor for PSA detection based on Cu_2O@CeO_2-Au nanocomposites as integrated triple signal amplification strategy. Biosens Bioelectron 87:630–637. https://doi.org/10.1016/j.bios.2016.09.018
62. Chauhan N, Chawla S, Pundir CS, Jain U (2017) An electrochemical sensor for detection of neurotransmitter-acetylcholine using metal nanoparticles, 2D material and conducting polymer modified electrode. Biosens Bioelectron 89:377–383. https://doi.org/10.1016/j.bios.2016.06.047
63. Sadak O, Prathap MUA, Gunasekaran S (2019) Facile fabrication of highly ordered polyaniline–exfoliated graphite composite for enhanced charge storage. Carbon 144:756–763. https://doi.org/10.1016/j.carbon.2018.12.062
64. Sekar M, Pandiaraj M, Bhansali S, Ponpandian N, Viswanathan C (2019) Carbon fiber based electrochemical sensor for sweat cortisol measurement. Sci Rep 9:1–14. https://doi.org/10.1038/s41598-018-37243-w
65. Yuan W, Zhou Y, Li Y, Li C, Peng H, Zhang J, Liu Z, Dai L, Shi G (2013) The edge- and basal-plane-specific electrochemistry of a single-layer graphene sheet. Sci Rep 3:1–7. https://doi.org/10.1038/srep02248
66. Wang J, Musameh M (2003) Enzyme-dispersed carbon-nanotube electrodes: a needle microsensor for monitoring glucose. Analyst 128:1382–1385. https://doi.org/10.1039/B309928H
67. Rubianes MD, Rivas GA (2005) Enzymatic biosensors based on carbon nanotubes paste electrodes. Electroanalysis 17:73–78. https://doi.org/10.1002/elan.200403121
68. Wang H-S, Li T-H, Jia W-L, Xu H-Y (2006) Highly selective and sensitive determination of dopamine using a nafion/carbon nanotubes coated poly(3-methylthiophene) modified electrode. Biosens Bioelectron 22:664–669. https://doi.org/10.1016/j.bios.2006.02.007
69. Zeng B, Wei S, Xiao F, Zhao F (2006) Voltammetric behavior and determination of rutin at a single-walled carbon nanotubes modified gold electrode. Sens Actuators, B Chem 115:240–246. https://doi.org/10.1016/j.snb.2005.09.007
70. Herrasti Z, Olivé-Monllau R, Muñoz-Pascual FX, Martínez F, Baldrich E (2014) Electrochemical biosensing of non-electroactive targets using ferrocene-labeled magnetic particles and CNT wiring. Analyst 139:1334–1339. https://doi.org/10.1039/C3AN02276E
71. Saljooqi A, Shamspur T, Mostafavi A (2017) Ag-4-ATP-MWCNT electrode modified with dsDNA as label-free electrochemical sensor for the detection of daunorubicin anticancer drug. Bioelectrochemistry 118:161–167. https://doi.org/10.1016/j.bioelechem.2017.08.003
72. Li X-M, Zhan Z-M, Ju H-Q, Zhang S-S (2008) Label-free electrochemical detection of short sequences related to the hepatitis B virus using 4,4'-diaminoazobenzene based on multiwalled carbon nanotube-modified GCE. Oligonucleotides 18:321–328. https://doi.org/10.1089/oli.2008.0143
73. Barathi P, Thirumalraj B, Chen S-M, Subramania A (2017) One-pot electrochemical preparation of copper species immobilized poly(o-aminophenol)/MWCNT composite with excellent electrocatalytic activity for use as an H_2O_2 sensor. Inorg Chem Front 4:1356–1364. https://doi.org/10.1039/C7QI00259A
74. Ortolani TS, Pereira TS, Assumpção MHMT, Vicentini FC, Gabriel de Oliveira G, Janegitz BC (2019) Electrochemical sensing of purines guanine and adenine using single-walled carbon nanohorns and nanocellulose. Electrochim Acta 298:893–900. https://doi.org/10.1016/j.electacta.2018.12.114
75. Valentini F, Ciambella E, Conte V, Sabatini L, Ditaranto N, Cataldo F, Palleschi G, Bonchio M, Giacalone F, Syrgiannis Z, Prato M (2014) Highly selective detection of Epinephrine at oxidized Single-Wall Carbon Nanohorns modified Screen Printed Electrodes (SPEs). Biosens Bioelectron 59:94–98. https://doi.org/10.1016/j.bios.2014.02.065

76. Zhu G, Sun H, Zou B, Liu Z, Sun N, Yi Y, Wong K (2018) Electrochemical sensing of 4-nitrochlorobenzene based on carbon nanohorns/graphene oxide nanohybrids. Biosens Bioelectron 106:136–141. https://doi.org/10.1016/j.bios.2018.01.058
77. Zhu S, Li H, Niu W, Xu G (2009) Simultaneous electrochemical determination of uric acid, dopamine, and ascorbic acid at single-walled carbon nanohorn modified glassy carbon electrode. Biosens Bioelectron 25:940–943. https://doi.org/10.1016/j.bios.2009.08.022
78. Kingsford OJ, Qian J, Zhang D, Yi Y, Zhu G (2018) Electrochemical sensing for 1-chloro-4-nitrobenzene based on β-cyclodextrin/carbon nanohorn nanohybrids. Anal Methods 10:5372–5379. https://doi.org/10.1039/C8AY01892H
79. Sherigara BS, Kutner W, D'Souza F (2003) Electrocatalytic properties and sensor applications of fullerenes and carbon nanotubes. Electroanalysis 15:753–772. https://doi.org/10.1002/elan.200390094
80. Das S, Presselt M (2019) Progress and development in structural and optoelectronic tunability of supramolecular nonbonded fullerene assemblies. J. Mater. Chem. C. 7:6194–6216. https://doi.org/10.1039/C9TC00889F
81. Palanisamy S, Thirumalraj B, Chen S-M (2015) Electrochemical fabrication of gold nanoparticles decorated on activated fullerene C_{60}: an enhanced sensing platform for trace level detection of toxic hydrazine in water samples. RSC Adv 5:94591–94598. https://doi.org/10.1039/C5RA17197K
82. Sutradhar S, Patnaik A (2017) A new fullerene-C_{60}—nanogold composite for non-enzymatic glucose sensing. Sens Actuators, B Chem 241:681–689. https://doi.org/10.1016/j.snb.2016.10.111
83. Sheng Q, Liu R, Zheng J (2013) Fullerene-nitrogen doped carbon nanotubes for the direct electrochemistry of hemoglobin and its application in biosensing. Bioelectrochemistry 94:39–46. https://doi.org/10.1016/j.bioelechem.2013.05.003
84. Saeedfar K, Heng LY, Ling TL, Rezayi M (2013) Potentiometric urea biosensor based on an immobilised fullerene-urease bio-conjugate. Sensors 13:16851–16866. https://doi.org/10.3390/s131216851
85. Klunder KJ, Nilsson Z, Sambur JB, Henry CS (2017) Patternable solvent-processed thermoplastic graphite electrodes. J Am Chem Soc 139:12623–12631. https://doi.org/10.1021/jacs.7b06173
86. Sun B-L, Cai J-Y, Li D, Gou X-D, Gou Y-Q, Li W, Hu F-D (2019) Fabrication of electrochemical sensor modified with porous graphene for determination of trace calycosin. Chin J Anal Chem 47:271–279. https://doi.org/10.1016/S1872-2040(19)61141-2
87. Cheng C, Zhang C, Gao X, Zhuang Z, Du C, Chen W (2018) 3D Network and 2D paper of reduced graphene oxide/Cu_2O composite for electrochemical sensing of hydrogen peroxide. Anal Chem 90:1983–1991. https://doi.org/10.1021/acs.analchem.7b04070
88. Kwon OS, Song HS, Park TH, Jang J (2019) Conducting nanomaterial sensor using natural receptors. Chem Rev 119:36–93. https://doi.org/10.1021/acs.chemrev.8b00159
89. Zamani FG, Moulahoum H, Ak M, OdaciDemirkol D, Timur S (2019) Current trends in the development of conducting polymers-based biosensors. TrAC Trends Anal Chem 118:264–276. https://doi.org/10.1016/j.trac.2019.05.031
90. Shrestha BK, Ahmad R, Shrestha S, Park CH, Kim CS (2017) Globular shaped polypyrrole doped well-dispersed functionalized multiwall carbon nanotubes/nafion composite for enzymatic glucose biosensor application. Sci Rep 7:1–13. https://doi.org/10.1038/s41598-017-16541-9
91. Arulraj AD, Vijayan M, Vasantha VS (2015) Highly selective and sensitive simple sensor based on electrochemically treated nano polypyrrole-sodium dodecyl sulphate film for the detection of para-nitrophenol. Anal Chim Acta 899:66–74. https://doi.org/10.1016/j.aca.2015.09.055
92. Ameen S, Akhtar MS, Seo H-K, Shin HS (2015) High sensitivity Schottky junction diode based on monolithically grown aligned polypyrrole nanofibers: broad range detection of m-dihydroxybenzene. Anal Chim Acta 886:165–174. https://doi.org/10.1016/j.aca.2015.05.038

93. Bagheri H, Hajian A, Rezaei M, Shirzadmehr A (2017) Composite of Cu metal nanoparticles-multiwall carbon nanotubes-reduced graphene oxide as a novel and high performance platform of the electrochemical sensor for simultaneous determination of nitrite and nitrate. J Hazard Mater 324:762–772. https://doi.org/10.1016/j.jhazmat.2016.11.055
94. Madasamy T, Pandiaraj M, Balamurugan M, Bhargava K, Sethy NK, Karunakaran C (2014) Copper, zinc superoxide dismutase and nitrate reductase coimmobilized bienzymatic biosensor for the simultaneous determination of nitrite and nitrate. Biosens Bioelectron 52:209–215. https://doi.org/10.1016/j.bios.2013.08.036
95. Wang F, Li M, Wang B, Zhang J, Cheng Y, Liu L, Lv F, Wang S (2015) Synthesis and characterization of water-soluble polythiophene derivatives for cell imaging. Sci Rep 5:7617. https://doi.org/10.1038/srep07617
96. Liu R, Liu Z (2009) Polythiophene: synthesis in aqueous medium and controllable morphology. Chin Sci Bull 54:2028–2032. https://doi.org/10.1007/s11434-009-0217-0
97. Nien P-C, Chen P-Y, Ho K-C (2009) Fabricating an amperometric cholesterol biosensor by a covalent linkage between poly(3-thiopheneacetic acid) and cholesterol oxidase. Sensors (Basel). 9:1794–1806. https://doi.org/10.3390/s90301794
98. Nie G, Bai Z, Yu W, Chen J (2013) Electrochemiluminescence biosensor based on conducting poly(5-formylindole) for sensitive detection of Ramos cells. Biomacromol 14:834–840. https://doi.org/10.1021/bm3018802
99. Prathap MUA, Satpati B, Srivastava R (2013) Facile preparation of polyaniline/MnO_2 nanofibers and its electrochemical application in the simultaneous determination of catechol, hydroquinone, and resorcinol. Sens Actuators B: Chem 186:67–77. https://doi.org/10.1016/j.snb.2013.05.076
100. Prathap MUA, Srivastava R (2013) Tailoring properties of polyaniline for simultaneous determination of a quaternary mixture of ascorbic acid, dopamine, uric acid, and tryptophan. Sens Actuators B: Chem 177:239–250. https://doi.org/10.1016/j.snb.2012.10.138
101. Prathap MUA, Srivastava R (2011) Morphological controlled synthesis of micro-/nano-polyaniline. J Polym Res 18:2455–2467. https://doi.org/10.1007/s10965-011-9662-y
102. Lee M-H, O'Hare D, Guo H-Z, Yang C-H, Lin H-Y (2016) Electrochemical sensing of urinary progesterone with molecularly imprinted poly(aniline-co-metanilic acid)s. J Mater Chem B 4:3782–3787. https://doi.org/10.1039/C6TB00760K
103. Prathap MUA, Chaurasia AK, Sawant SN, Apte SK (2012) Polyaniline-based highly sensitive microbial biosensor for selective detection of lindane. Anal Chem 84:6672–6678. https://doi.org/10.1021/ac301077d
104. Anu Prathap MU, Castro-Pérez E, Jiménez-Torres JA, Setaluri V, Gunasekaran S (2019) A flow-through microfluidic system for the detection of circulating melanoma cells. Biosens Bioelectron 142:111522. https://doi.org/10.1016/j.bios.2019.111522
105. Prabhakar PK, Raj S, Anuradha PR, Sawant SN, Doble M (2011) Biocompatibility studies on polyaniline and polyaniline–silver nanoparticle coated polyurethane composite. Colloids Surf, B 86:146–153. https://doi.org/10.1016/j.colsurfb.2011.03.033
106. Thakur B, Jayakumar S, Sawant SN (2015) Probing extracellular acidity of live cells in real time for cancer detection and monitoring anti-cancer drug activity. Chem Commun 51:7015–7018. https://doi.org/10.1039/C5CC01445J

Chapter 3
Synthesis of Noble Gas Compounds: Defying the Common Perception

Adish Tyagi

Abstract Although they were not assigned a place in original Mendeleev periodic table, noble gases found a special place in popular science history. Their discovery, prediction about their reactivity, and preparation of first compound of noble gases are a display of utter determination, innovation, scientific temperament, and conviction. Since discovery, noble gases have been considered as inert or rare gases that are unable to react with other elements. This notion was shattered in 1962 when Bartlett prepared first noble gas compound. Subsequently, a flurry of synthetic and structural work ensued in hundreds of noble gas compounds. This chapter will take the readers on a journey of how the noble gases were discovered from the 0.1% discrepancy in assigning the density of nitrogen. Moving further, the chapter will shine light on how a 60 years long dogma related to the inertness of noble gases was overthrown in one master stroke. In addition to this, the chapter will also provide the discussion on the synthesis of compounds of noble gases and how the compounds which are almost impossible to prepare under ambient conditions become reality under high pressure. Furthermore, an enigma related to missing xenon phenomenon and proposed models to explain this paradox has also been included in this chapter. In the last, the chapter would like to draw the attention of the readers toward a question; was coaxing reactivity from these intractable elements not remarkable?

Keywords Noble gases · Neil Bartlett · Missing xenon · Noble gas compounds · Xenon oxides

3.1 Introduction

Noble gases were believed to be inert gases but they are not; many of noble gas compounds have been prepared and isolated since 1962. They were labeled as lazy elements however they are not; once they were provided them suitable conditions,

A. Tyagi (✉)
Chemistry Division, Bhabha Atomic Research Centre, Mumbai 400085, India
e-mail: tyagia@barc.gov.in

A. K. Tyagi and R. S. Ningthoujam (eds.), *Handbook on Synthesis Strategies for Advanced Materials*, Indian Institute of Metals Series,
https://doi.org/10.1007/978-981-16-1892-5_3

they will surprise with the unusual chemical behavior, intriguing structures, and unexpected properties. Calling them as noblesse oblige is imprecise and misleading [1]. These elements work diligently and exhibit several applications. Helium (He) plays a pivotal role in space, defense, and energy program encompassing pressurization of liquid propellants, weapons development, and nuclear fusion experiments. Furthermore, liquid helium is used for cooling the magnets of NMR instruments, biological, climate and weather forecast, and superconductivity research. In combination with neon (Ne), it produces powerful He-Ne laser with immense applications. Ne, apart from being utilized in lasers, also finds application as lightening arresters. Argon (Ar) is extensively used by chemists for creating inert atmosphere in round bottom flask or glove boxes. Xenon (Xe) and krypton (Kr) find significance in electronics and medical field. Xenon-131 is used in CT scans and MRI as a contrasting agent. Being NMR active xenon-129 is extensively used to understand the bonding in Xe compounds and recently as a probe to understand the biological processes. Furthermore, xenon ion thrusters are used to propel spacecrafts whereas krypton flashes enable photographers to capture images at high speed [2]. Diversified applications of noble gases are depicted in Fig. 3.1.

Fluorides of xenon and krypton are considered as powerful oxidizing agents and also used for fluorination of compounds. Xenon difluoride finds utility in synthetic organic chemistry and is used for preparing the intermediate for the syntheses of ^{18}F-labeled radiopharmaceuticals like L-[^{18}F]6-fluorodopa which finds application in positron emission tomography [3].

Apart from above-mentioned applications, the most predictable and recognizable use of these gases is in illuminated signs, light bulbs, and lamps (Fig. 3.2). Their lack of chemical reactivity helps to preserve filaments in light bulbs and grants distinctive colors when used in gas-discharge lamps.

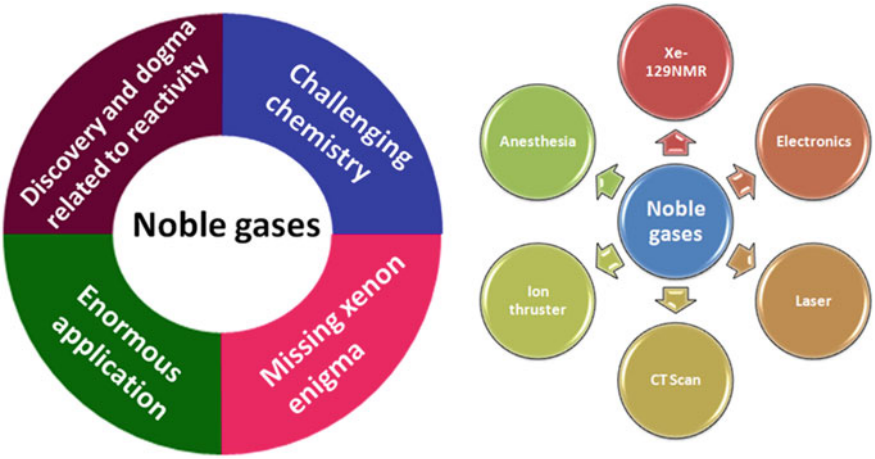

Fig. 3.1 Fascinating noble gases and their application

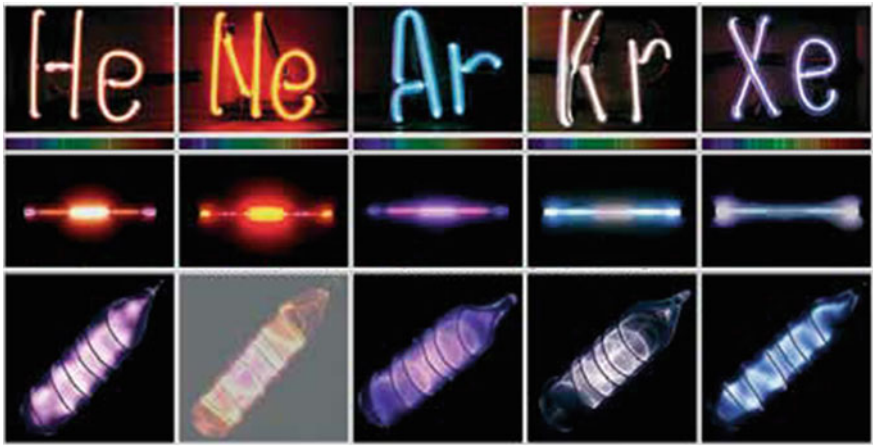

Fig. 3.2 Colors of electric discharge in noble gases (Credit Wikipedia)

From the brief introduction, it can be realized that noble gases and their compounds have the potential to find space in both fundamental and applied fields. On the one hand, synthesis of novel compounds and their fascinating structures has garnered the attraction in basic science, while on other hand, their utilization in various fields has cemented their place in applied sciences. In this chapter, the strategies which compelled noble gases to lose their identity if inertness and types of noble gas compounds formed are discussed. However, prior to that it will be interesting to know about their discoveries.

3.2 Discovery of Noble Gases

The discovery of noble gases is one of the most interesting events in the history of science. It is the story of creativeness and intuition, as well as scientific adventure and determination. It is also a real showcase of fundamental and applied science working in concert.

Rare gases or noble gases constitute a group of elements which form about one percent of the volume of earth's atmosphere. It can be visualized, in a room which is 12 feet long 12 feet wide and 8 feet high than this room is likely to contain inert gases of about 11.5 cubic feet. In universe, helium is the second most abundant gas after hydrogen, while in earth's atmosphere, argon is the most abundant gas among all noble gases. It is approximately 800 times more abundant than neon, the second most common. It will be interesting to know that whenever a normal human being takes a deep breath it is likely to inhale about $5cm^3$ of argon. So calling argon as rare gas is rather unfair. Nevertheless, while apparently so accessible, the existence argon in earth's atmosphere remained unknown till 1890s, when physical methods, especially

spectroscopy and liquification of gases, became sufficiently well developed. It was not correct to say that scientists had not earlier encountered them. It was documented that in 1785, Cavendish had actually isolated argon during his "Experiments on air." Cavendish was trying to convert atmospheric nitrogen into nitrous acid but could not do so. He was always left out with a bubble of air as unconverted. He called it as mysterious bubble [4]. However, he did not realized that this residue as a new element and the matter was rested for almost 100 years, when Lord Rayleigh in 1892 had observed 0.1% discrepancy in the density of nitrogen obtained from air [5]. Prior to this, something interesting had happened in Guntur, India in 1868 which marks the discovery of helium.

Discovery of Helium: Noble gases were unknown till 1868, when a total solar eclipse took place in Guntur, Andhra Pradesh, India. During the solar eclipse, sun central fire ball is totally obscured leaving the incandescent gases in its vicinity clearly visible. Pierre Janssen, a French astronomer, had visited India in 1868 to measure the solar spectrum during the solar eclipse through his rudimentary spectroscope. He made a careful investigation of the sun's spectrum and observed a yellow line at wavelength of 587.49 nm emanating from chromosphere (sun's atmosphere) of the sun where no yellow line was expected. This indicated the existence of an element that is not yet discovered [6]. Same line was observed by English astronomer Norman Lockyer through London smog, just two months after Janssen. Lockyer along with English chemist named this element *helios*, a Greek word for the sun [7]. Later, both Jenssen and Lockyer unraveled a new way of observing the chromosphere without actually waiting for eclipse to happen and had made a similar observation. Coincidently both communicated their result to French Academy of Sciences which arrived on the same day. Consequently, the discovery of Helium was credited to both Jenssen and Lockyer (Fig. 3.3).

However, helium was considered to be a celestial element as no trace of helium was found on earth. Some even thought that the yellow line from the chromospheres could be due to previously undetected emission of hydrogen. Famous among non-believers was a rather intimidating opponent, Dmitrii Mendeleev (Fig. 3.3a) who brought periodic table into existence.

Discovery of argon and other noble gases: During 1880s, Lord Rayleigh endeavored to assign accurate densities to the gases than had ever been made before. He calculated the accurate densities of oxygen and hydrogen. However, in case of nitrogen, he found 0.1% discrepancy [8]. Nitrogen he got from air appears to be 0.1% denser than the nitrogen obtained from ammonia. This discrepancy was enough to attract the attention of Prof. William Ramsay, an English chemist. With the permission of Rayleigh, Ramsay begins experiments to discover the unknown thing which was responsible for 0.1% error in density of nitrogen. Ramsay removed all the known components from a sample of air, i.e., oxygen, carbon dioxide, and nitrogen. After doing this, he was left with an unknown gas which is 20 times heavier than hydrogen and no matter what he did to it he could not alter its density further. He investigated the gas with spectroscopy and found that its spectrum did not match with that of any

Fig. 3.3 Images of **a** Pierre Janssen and **b** Norman Lockyer (Credit Wikimedia Commons)

known element [9]. Ramsay and Rayleigh made the joint announcement about their discovery in August 1894 and the new gas was named as argon [10].

Mendeleev and Ramsay (Fig. 3.4) were not on the same side over the discovery of Argon. Mendeleev claimed that argon was actually triatomic nitrogen N_3. However, spectroscopic evidence and specific heat measurement clearly indicated that argon consisted of single atom and convinced the scientific fraternity that argon was an element which does not belong to any group in the Mendeleev periodic table. This became a major setback for the Mendeleev as there was no space for argon in the original periodic table. Nevertheless, more relevant question at that time was, if argon belongs to a group not mentioned in periodic table, then where were the other members of that group. Whether they exist and not discovered yet? Ramsay was also aware of this and decided to discover other elements of this group.

Ramsay came to know that Dr. Hillebrand in 1888 obtained an unreactive gas from the reaction of uranium ore with boiling H_2SO_4 [11]. The gas was initially thought to be nitrogen. However, Ramsay, based on his previous experience, wondered that Hillebrand's gas might be argon. Spectroscopic evidences indicated that the gas was neither nitrogen nor argon. Instead its spectrum closely matched with helium, previously detected in chromosphere. All efforts to combine helium with any other substance failed which led Ramsay to conclude that helium is the second member of noble gases [12]. After the discovery of helium and argon, Ramsay predicted that there were at least two more inert gas elements to be discovered. Subsequently, he along with his coworker Morris Travers discovered neon, krypton, and xenon [13] while radon was discovered by a German Physicist, Friedrich Dorn from radium emanation and is radioactive. Radon was initially named as *niton*, but since 1923 it

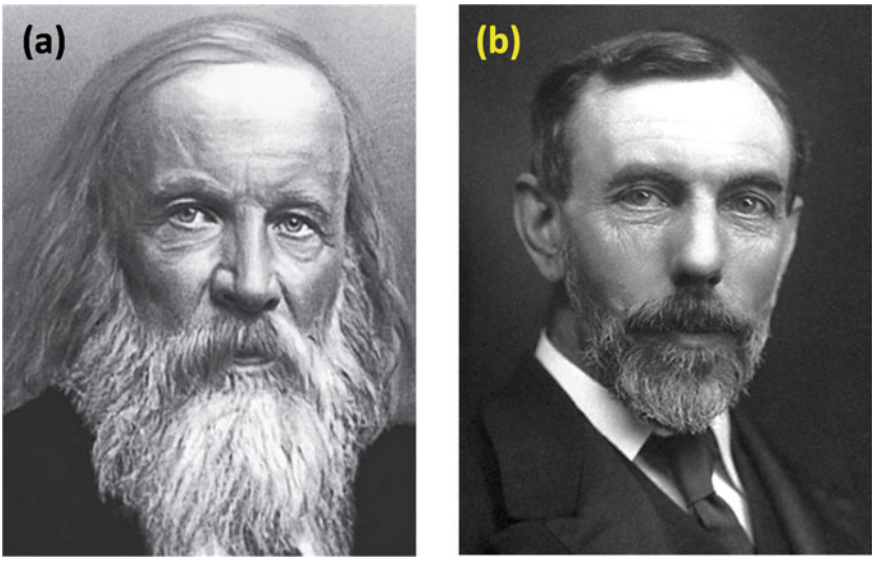

Fig. 3.4 Images of **a** Dmitri Mendeleev and **b** William Ramsay (Credit Wikimedia Commons)

has been known as *radon* (named after his original source radium) [14]. Apart from discovering the noble gases, Ramsay determined their properties such as density as well (Table 3.1). The phenomenal effort put for the discovery of inert gases was appreciated and recognized in 1904 when Rayleigh was awarded Nobel prize in Physics for his "investigations of the densities of the most important gases and for his discovery of argon" while William Ramsay was awarded Nobel prize in Chemistry "in recognition of his services in the discovery of the inert gaseous elements in air, and his determination of their place in the periodic system."

Although the discovery of noble gases was a major bolt to Mendeleev Periodic Table, these gases also follow the Mendeleev periodic law which was a kind of sigh of

Table 3.1 Properties of the noble gases (Credit: Wikipedia of individual gases)

Noble gas (symbol)/atomic no.	Greek/Latin meaning	Atomic mass	Abundance ppm by volume	Density at 0 °C	Specific gravity	Polarizability (Å3)
Helium (He)/2	Sun element	4.003	5	0.178	0.138	0.205
Neon (Ne)/10	New	20.183	18	0.899	0.696	0.396
Argon (Ar)/18	Lazy or inactive	39.944	9430	1.783	1.379	1.641
Krypton (Kr)/36	The hidden one	83.8	1	3.745	2.896	2.484
Xenon (Xe)/54	Strange	131.3	0.1	5.897	4.561	4.044
Radon (Rn)/86	Shining	222	6×10^{-14}	9.73	7.526	5.3

relief for Mendeleev. The astute observation of Rayleigh and the phenomenal work by William Ramsay led to the addition of a new group called *zero group* comprising of noble gases to the Mendeleev table.

Recently a new member having atomic number 118 has been added to this group. The element was named as Oganesson (Og) in the honor of Yuri Oganessian who played a leading role in the discovery of the heaviest element. The element was synthesized in year 2002, however it was recognized as a new element in 2015 by international scientific bodies IUPAC and IUPAP. This element although belongs to group 18 is predicted to have reactivity considerably higher than the rest of the group members. Under ambient conditions, it is predicted to be a solid due to relativistic effects.

3.3 Reactivity of Noble Gases and Discovery of First Noble Gas Compound

In a milestone paper, Ramsay and Rayleigh also reported their unsuccessful attempts to chemically combine argon with other element/group [10]. They found that new element was unaffected by elements of very opposite characters ranging from alkali/alkaline elements on the one hand to oxygen and chlorine on the other. Further they wrote that it will be interesting to see whether fluorine also remains without action. On the basis of above observation, they wrote in conclusions that; *we do not claim to have exhausted the possible reagents. But this much is certain; that the gas deserves the name "argon," for it is a most astonishingly indifferent body*. The reaction of argon with fluorine was tried by Henry Moissan (1906, Noble prize in chemistry for isolation of fluorine) but without any success. These failures only helped the traditional scientific wisdom that noble gases elements are so noble that they could not form compounds owing to their extremely stable electronic structure. G. N. Lewis in his monumental and revolutionary paper "The atoms and the molecule" and Kossel explained the concept of bonding on the basis noble gas electronic configuration known as "Octet Rule." They postulated that atoms lose, accept, or share electrons to attain noble gas configuration. However, few chemists raised doubts over the absolute non-reactive behavior of noble gases. These included Walther Kossel himself and two times Nobel Prize winning chemist Linus Pauling. They postulated that highly electronegative fluorine might induce reactivity in krypton and xenon because their electrons were not as tightly held as those of the lighter noble gases. Kossel, based on the first ionization potential of xenon, made an astute observation that xenon was most likely to have the ability to combine with oxygen and fluorine [15]. Pauling had even predicted the existence of H_4XeO_6, and of KrF_6 and XeF_6 in his paper published in 1933 [16]. Gaining inspiration from this, Prof. Yost and coworkers attempted to combine xenon and fluorine by passing electric discharge [17]. They came close to preparing xenon fluoride compound; however, they were unsuccessful in isolating measurable amounts. Prior to them many researchers like Andreas von Antropoff,

Otto Ruff, Menzel [18, 19], etc., had also endeavored to prepare noble gas compounds but all in vain. Ruff and Menzel were fantastic chemist and when fluorine is considered they were among the best, but unfortunately they tried to induce reactivity in argon and krypton by reacting them with fluorine instead of xenon which is least noble among noble. All these failures only strengthened the perception that noble gases are indeed un-reactive, and this became a dogma which was embraced in all common science textbooks of the time and up until 1962.

However, the dogma, that noble gases were absolutely inert, was abandoned when Neil Bartlett announced the synthesis of $Xe[PtF_6]$ compound (Eq. 3.1) on March 23, 1962, nearly 30 years after Yost and Kaye's attempts to induce chemical reactivity in xenon [20, 21]. Nonetheless, the discovery was not so straightforward. It was the result of sheer acumen and observation of Bartlett that led to the discovery. He was synthesizing PtF_2 by reducing PtF_4. So for the experiment Bartlett was requiring pure PtF_4. He attempted the purification of PtF_4 by heating it in the presence of dilute fluorine gas and obtained a red sublimate which he initially thought was platinum fluoride oxide, PtF_4O, but subsequently recognized correctly that an oxidation reaction had occurred and dioxygen hexafluorplatinate, $O_2^+PtF_6^-$was formed. Interestingly, in above reaction, oxygen was oxidized by PtF_6. While the discovery was accidental, Bartlett subsequent reasoning and experiments were phenomenal. He realized that the first ionization potential of oxygen (12.075 eV) and xenon (12.129 eV) is comparable and if PtF6 can oxidize molecular oxygen then it can oxidize Xe also. This reasoning convinced Bartlett to react xenon gas with PtF_6 and it did in a visually rapid dramatic fashion (Fig. 3.5). A non-stoichiometric amorphous product of composition $[Xe][PtF_6]_x$ was isolated whose structure is still not well understood. It is widely believed that PtF6 oxidizes xenon to form xenon cation (Xe+) which subsequently underwent fluorine transfer and redox reaction to form different fluoroxenon fluoroplatinum salts [22].

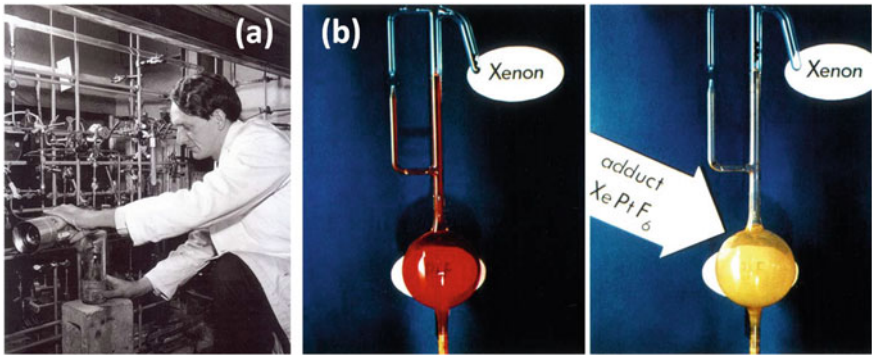

Fig. 3.5 **a** Neil Bartlett and **b** innovative experiment that led to the preparation of first noble gas compound (With the permission from Springer publisher, Ref. [22])

$$Xe + PtF_6 \xrightarrow[\text{Temperature}]{\text{Room}} Xe(PtF_6)_x$$

- x depends upon reactant ratio
- Sticky, redtinged yellow solid (3.1)

Neil Bartlett discovery ignited a worldwide interest in this area and many new compounds of noble gases were reported in subsequent years. Large amount of synthetic and structural work pertaining to behavior of xenon and krypton is appeared in literature in the following years which revealed their true nature.

3.4 Initial Progress in the Synthesis of Other Xenon Compounds

Year 1962, in which Neil Bartlett had demolished the common belief about the inertness of noble gas elements, will also be remembered for the synthesis of different composition of xenon fluorides. A report by Howard H. Claasen, Henry Selig, and John G. Malm, at Argonne National Laboratory on the synthesis of xenon tetrafluoride (XeF_4) by fluorination of xenon with F_2 under high temperature (400 °C) and high pressure (6 atm) conditions appeared in literature [23]. In the same year, Prof. Rudolf Hoppe (Fig. 3.6) announced the synthesis of xenon difluoride (XeF_2) by electric discharge method and this synthesis was not accidental. It was a result of many years of studies and analyses. Hoppe and his team were working on this problem since 1949 and from preliminary thermodynamic analysis, and they were convinced that

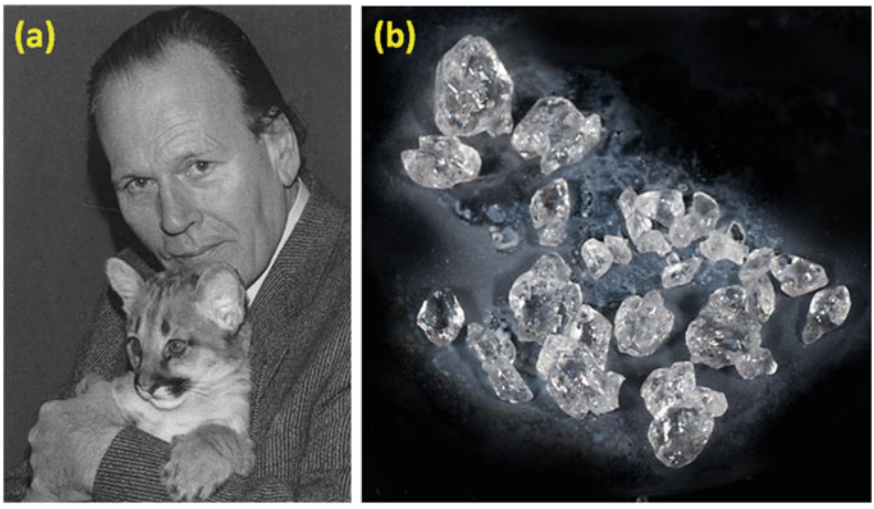

Fig. 3.6 **a** Prof. Rudolf Hoppe and **b** crystal of XeF_2 (Credit Wikimedia Commons)

XeF_2 and XeF_4 would be thermodynamically stable. Their study led to the conclusion that the formation of these compounds would be exothermic. Furthermore, the synthesis of XeF_4 confirmed Hoppe that his forecasts about noble gas fluorides were correct, a vindicated Hoppe synthesized colorless crystalline XeF_2 solid by simple electrical discharge method and at ambient pressure condition. The paper was an experimental verification of his decade old prediction [24].

Hoppe confirmed the absence of higher fluorinated xenon species in the product by mass spectrometric analysis. Moreover, he had also investigated the room temperature stability of XeF_2 as well as its chemical reactivity with various chemicals including acids, bases, water, alcohols, etc. Later Weissenberg obtained the photographs of XeF_2 crystals and found that they belong to monoclinic crystal system. Experiments revealed that, Xe combines with fluorine in different ratios usually under high pressure to form di, tetra, and hexa fluorides (Fig. 3.7).

Unlike direct fluorination of xenon, direct combination of xenon and oxygen was not possible. Xenon fluorides particularly XeF_2 constitute the only starting materials for Xe-O compounds and compounds of other elements also. Thus, monumental work of Rudolf Hoppe which led to synthesis of XeF_2 under ambient conditions had served

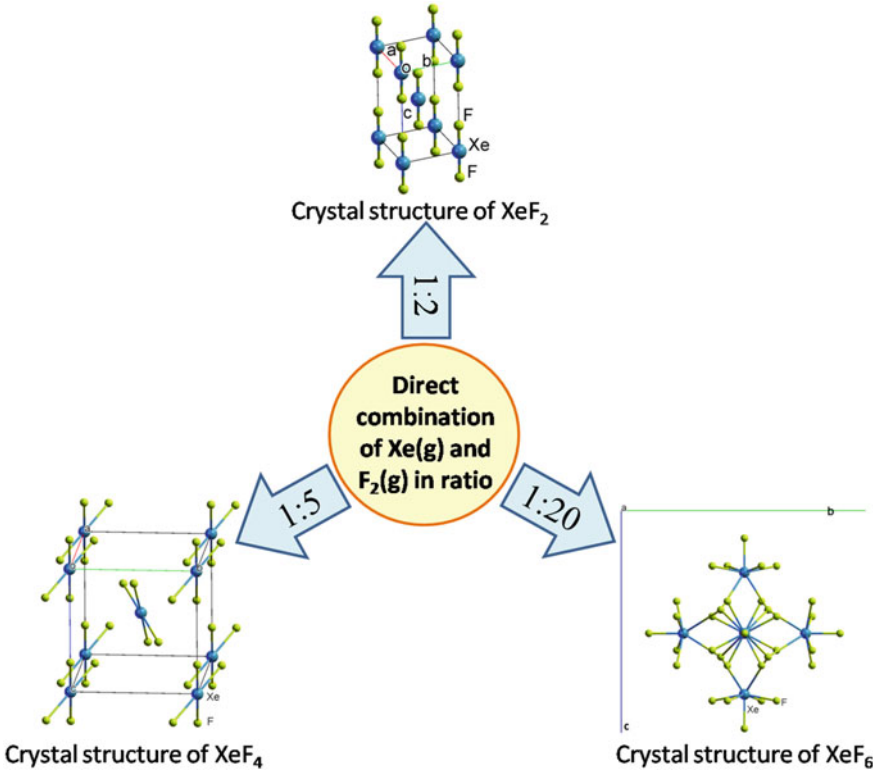

Fig. 3.7 Different fluorinated products of Xe and F_2 reaction

as an impetus for the synthesis of a plethora of compounds having Xe-O, Xe-N, Xe-C, Xe-Xe bonds. In basic inorganic chemistry, XeF_2 acts as a convenient fluorinating agent. Moreover, XeF_2 being room temperature stable and least strongly oxidizing and air-sensitive noble gas fluoride was easy to handle and found applications as an electrophilic fluorinator to generate ^{18}F labeled radiopharmaceuticals for use in imaging through positron emission tomography (PET). It is also extensively used in electronic industry as a dry gas phase etchant [3].

3.5 Synthesis of Compounds of Noble Gases

This section will present a brief chemical perspective of noble gases highlighting the important developments. Since xenon is the most reactive among noble gases (radon being radioactive gas, so excluded from the discussion), "synthesis of compounds of noble gases" is mainly emphasized on the compounds of xenon. Least noble among noble gases, xenon frequently forms bond with highly electronegative elements like fluorine, oxygen, etc., and exhibit oxidation states +2, +4, +6, +8 (Fig. 3.8). Apart from the fluorine and oxygen elements, xenon has enjoyed a good chemistry with powerful oxidizing agent as well. This section is dedicated to the compounds of xenon and other noble gases with different elements.

Oxides: Discovery of noble gas reactivity by Bartlett was followed shortly thereafter by the discovery of XeO_3 [25] which is white solid at room temperature and XeO_4 [26] which is gas at room temperature and exist as yellow solid only at lower temperature. Pitzer [27] predicted that xenon oxides would be unstable as well as explosive in nature. The prediction was verified by Bartlett and Rao who had

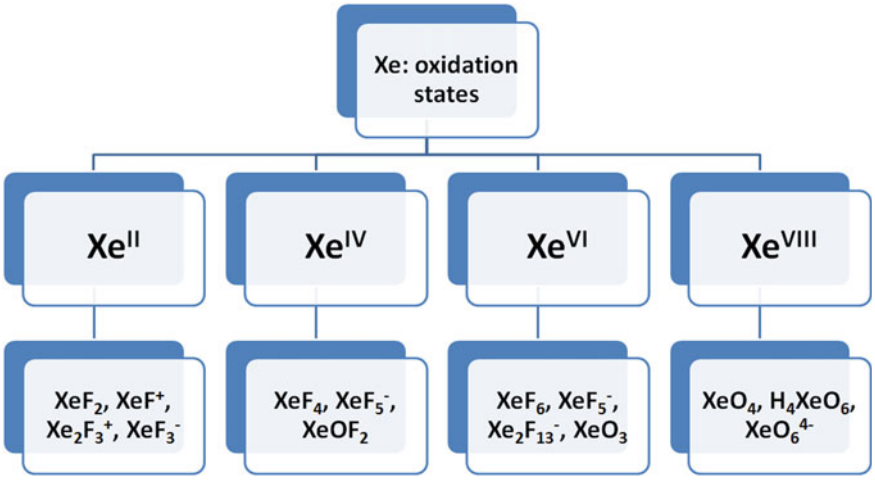

Fig. 3.8 Xenon compounds in different oxidation states

isolated XeO_3 white powder evolved from the hydrolysis of XeF_4 (Eqs. 3.2 and 3.3). Unfortunately, the powder gets exploded which led to the hospitalization of both the researchers [28].

$$4XeF_4 + 8H_2O \rightarrow 2XeO_3 + 2Xe + O_2 + 16HF \tag{3.2}$$

$$XeF_6 + 3H_2O \rightarrow XeO_3 + 6HF \tag{3.3}$$

$$Na_4XeO_6 + 2H_2SO_4 \rightarrow XeO_4 + 2Na_2SO_4 + 2H_2O \tag{3.4}$$

Bartlett and Rao initially analyzed the hydrolysis product as $Xe(OH)_4$ of $XeO_2 \cdot 2H_2O$. However, later with the help of infrared spectroscopy and single crystal analyses, it was unambiguously established that the solid was xenon trioxide instead of xenon hydroxide or xenon dioxide dihydrate [25, 29]. The geometry of XeO_3 was found to be trigonal pyramidal which was same as predicted by valence shell electron pair repulsion theory (VSEPR). Recently, it was established that XeO_3 exhibits crystallization condition-dependent polymorphism. When crystallized by the slow evaporation of HF solution of XeO_3, α-phase (orthorhombic, $P2_12_12_1$) was formed, while slow evaporation of aqueous solution resulted in β-phase (rhombohedral, R3) and γ-phase (rhombohedral, R3c) respectively (Fig. 3.9). All three polymorphs exhibit Xe = O-Xe bridge interactions among XeO_3 molecules resulted from the amphoteric donor–acceptor nature of XeO_3 in extended forms and are consistent with σ-hole bonding. This Xe-O-Xe bridge is responsible for the kinetic instability of XeO_3. The bridge interaction provides an efficient channel to propagate the detonation shock wave across the crystal lattice [30].

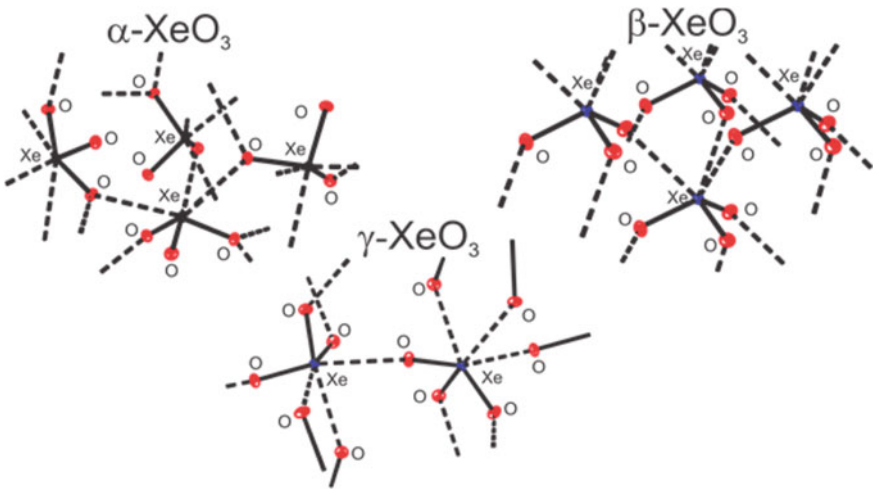

Fig. 3.9 Crystal structure of α, β and γ phase of XeO_3. (With the permission of ACS Ref. [30])

XeO_3 is a potent oxidizer and has an ability to oxidize primary and secondary alcohols to CO_2 and H_2O in aqueous medium. However, its shock-sensitive nature has limited its practical utility. Adduct formation by lewis base is an efficient way to improvise the stability of XeO_3 to an extent where its potential can harnessed [31]. With this perspective, Prof. Schrobilgen et al. prepared the first ever stable crown ether complex of XeO_3 and characterized it structurally (Fig. 3.10) and from theoretical calculations. The crystal structure revealed that XeO_3 core is bonded through five oxygen atoms from crown ether molecule. The bonding between polydentate crown ether and XeO_3 proved to be instrumental in significantly reducing the detonating ability of XeO_3 [31].

On the other hand, XeO_4 was prepared by the reaction of xenate salts (Na_4XeO_6 or Ba_2XeO_6) with concentrated H_2SO_4 and has a tetrahedral shape (Eq. 3.4). From infrared spectroscopy it is found that Xe-O bond length in XeO_3 (176 pm) is slightly

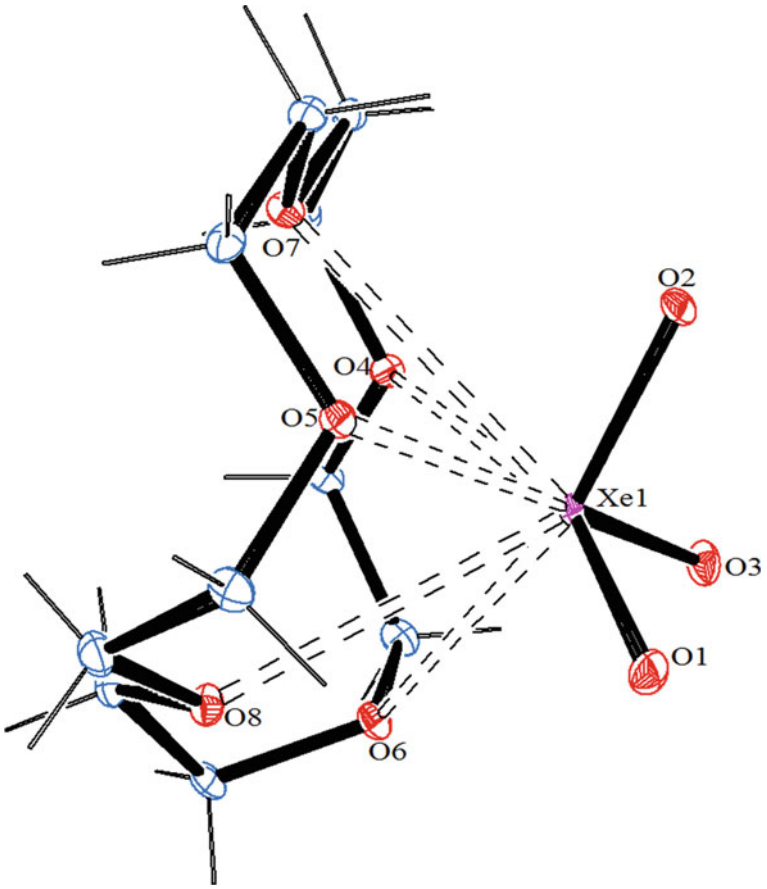

Fig. 3.10 Crystal structure of $(CH_2CH_2O)_5XeO_3$ formed by the reaction of XeO_3 and 15-crown-5. Redrawn from Marczenko Ref. [31]

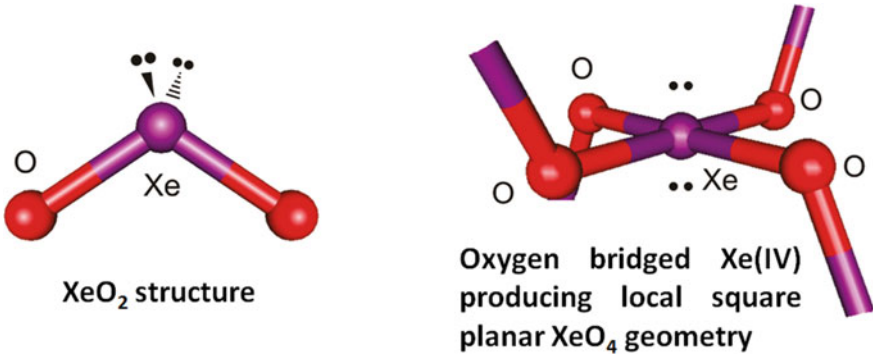

Fig. 3.11 Monomeric and extended structure of XeO_2. (With the permission of ACS, Ref. [33])

longer than that in XeO_4 (173 pm). Solution phase purity of XeO_4 has also been evaluated from low-temperature ^{17}O, ^{129}Xe, and ^{131}Xe NMR spectroscopy. Just like XeO_3, XeO_4 is also deliquescent, extremely shock and temperature sensitive. XeO_3 and XeO_4 upon decomposition releases 402 and 642 kJ/mol of energy, respectively, on slightest of mechanical provocation [3].

Immediately after the discovery of reactivity of noble gas, Xe(VI) and Xe(VIII) oxides were prepared whereas the Xe(II) and Xe(IV) oxides, i.e., XeO and XeO_2 were missing from the list. Theoretical prediction suggested that XeO will have unstable ground state which limits its prospects to exist as monomer [32]. XeO_2, although predicted theoretically, experimentally it was never successfully synthesized in laboratory. Nevertheless, there were incidents when researchers suspect that XeO_2 was formed in chemical reaction. Once such incident was the synthesis of XeO_3 where the product was initially assumed to be hydrated XeO_2. However, recently research group of Schrobilgen succeeded in the preparing XeO_2 compound by the hydrolysis of XeF_4 at 0 °C and in presence of 2 M conc. H_2SO_4 [33]. The structure of XeO_2 (Fig. 3.11) was established on the basis of Raman spectroscopy and $^{16/18}O$ isotopic enrichment investigations which indicate that Xe(IV) in XeO_2 is bonded to four neighboring oxygen atoms giving rise to square planar XeO_4 geometry.

In another study by Zhu and coworkers [34], it was concluded that the xenon which is not very reactive at room temperature shed its inertness under high pressure. Furthermore, they predicted on the basis of theoretical calculations that it can forms mono, bi, and tri oxides under high pressure (Fig. 3.12).

Apart from thermodynamic stability of XeO, XeO_2, and XeO_3 at high pressure, a separate experimental study discloses that xenon can directly react with oxygen at high pressure (above 50 GPa) to form two oxides having xenon in mixed valence state, viz. Xe_3O_2 and Xe_2O_5 under oxygen-deficient and oxygen-rich environment, respectively [34]. The oxidation state of xenon is 0 and +4 in Xe_3O_2 and +4 and +6 in Xe_2O_5. The three-dimensional morphology of Xe_3O_2 reveals that it consists of XeO_4 planar chain having Xe in +4 oxidation state while unoxidized xenon is sandwiched between the parallel chains. On the other hand, extended network of Xe_2O_5 consists

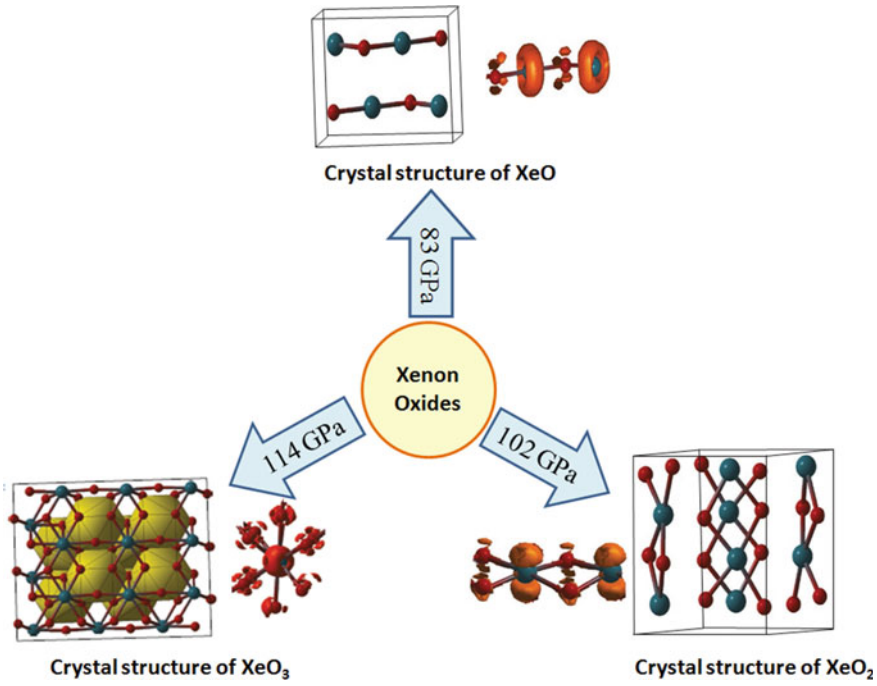

Fig. 3.12 Existence of xenon oxides under high pressure. (With the permission from Nature publishing group, Ref. [34])

of oxygen sharing XeO_5 pyramids in addition to XeO_4 chains. Theoretical studies looking at the highest molecular orbitals indicate that Xe_2O_5 is likely be an insulator while Xe_3O_2 has characteristics close to small bandgap semiconductor.

Halides and compounds derived from them: As previously discussed, xenon reacts with different moles of fluorine to form XeF_2, XeF_4, and XeF_6 (Fig. 7). XeF_2 is a linear symmetrical molecule; XeF_4 is square planar while XeF6 adopts distorted octahedral structure. The distortion in the latter molecule arises due to the interaction among the extra pair of non-bonding electrons in xenon valence shell [35]. Solid-state existence of XeF_6 is even more interesting, where it crystallizes in at least seven different crystal systems, most of them features tetrameric and hexameric rings of nearly undistorted square pyramidal XeF_5^+ joined by fluoride ion bridges [36]. Apart from fluorides, higher halides (Cl, Br) of xenon ($XeCl_2$, $XeBr_2$, $XeCl_4$) were also prepared mostly by photochemical or electric discharge method [37]. However, due to the thermodynamic instability, no neutral halide of xenon other than XeF_2 has been isolated in large quantity. XeF_2 is a colorless solid in which individual XeF_2 molecules are linearly arranged with strong electrostatic interaction between the XeF_2 molecules. The strong interaction among the XeF_2 molecules explains its high heat of sublimation [38]. It exhibits strong fluoride donor ability and coordinates very well with fluoride acceptor molecules like AsF_5, SbF_5, and BiF_5. This highlights

the ligand properties of XeF_2 which can be coordinated to metal center [39]. First compound where XeF_2 was acting as a ligand was prepared in 1991 with silver metal center to form $[Ag(XeF_2)_2]$ (AsF_6) [40]. Realizing this ability of XeF_2, researchers coordinated XeF_2 with different metal centers appearing in different oxidation states like M(I) Ag, Li; M(II) Mg, Cu, Zn, Ca, Cd, Hg, Sr, Pb, Ba; M(III) Ln (Ln = La, Nd, Sm, Eu, Gd) stabilized with fluorinated counter anions like AsF_6, PF_6, SbF_6, NbF_6, etc., center [39]. Few representative examples of such complexes are shown in Fig. 3.13.

Monohalides of xenon XeE (E = F, Cl, Br, I) have been prepared by electron bombardment method or irradiation method. Although they are thermodynamically unstable and short lived in gas phase, these monohalides of xenon are of significant interest owing to their usage as light emitting species in gas lasers (qv) [41, 42].

Xenon also forms variety of oxidefluoride compounds such as $XeOF_2$, $XeOF_4$, XeO_2F_2, XeO_3F_2, and XeO_2F_4. The latter two are thermodynamically unstable containing xenon in +8 oxidation state and their existence were confirmed mainly by ^{129}Xe and ^{19}F NMR spectroscopy and mass spectrometric technique [43]. On the other hand, xenon oxide fluorides, featuring xenon in lower oxidation state, were relatively well explored and were prepared from xenon fluorides. Their shapes/geometries were explained on the basis of valence shell electron pair repulsion theory (VSEPR theory). $XeOF_2$, $XeOF_4$, XeO_2F_2; possess V-shape geometry, square pyramidal geometry, and triagonal bipyramidal geometry, respectively.

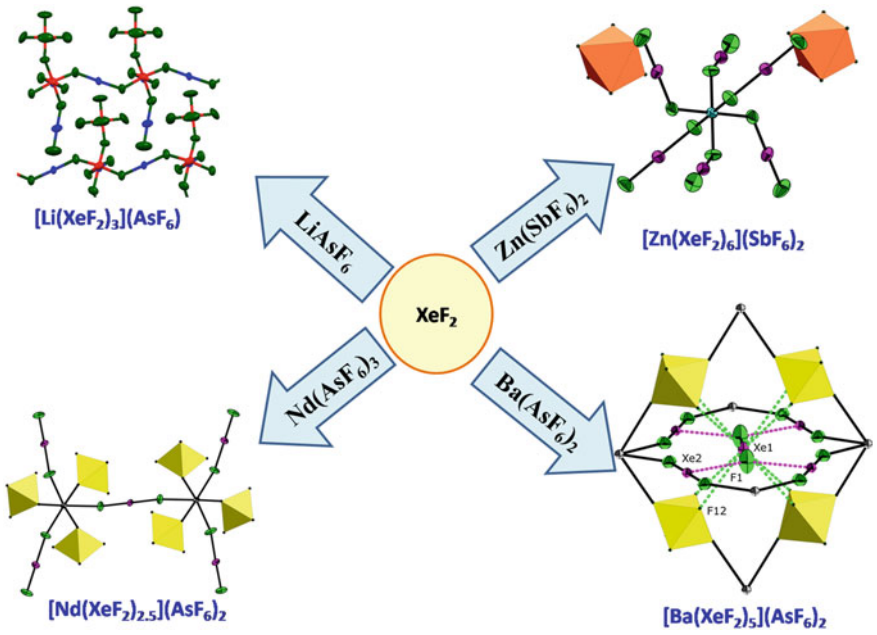

Fig. 3.13 Compound formed by coordinating XeF_2 ligand with different metal centers. (With the permission from Elsevier, Ref. [39])

Xenon is also known to form alkali metal xenates (XeO_4^{2-}) and perxenates (XeO_4^{2-}) compounds. The xenates salts were prepared by freeze drying xenon trioxide, and alkali metal hydroxides in 1:1 mixture while perxenates salts were synthesized by the hydrolysis of XeF_6 in strong alkali solution where some portion of xenon is evolved as gas while rest precipitated as perxenate salts. Xenates are unstable and explosive while perxenates are a stable compound which gradually loses water of hydration on heating. Apart from alkali, several transition metal and actinide perxenates have also been prepared and characterized. In chemistry, perxenates solution is known as powerful oxidizing agents capable of oxidizing iodate ion to periodate, manganous ion to permanganate, etc. [44].

Other than xenon, krypton is the only noble gas known to form isolable in macroscopic quantities. The chemistry of krypton, unlike xenon is limited to +2 oxidation state. The simplest and most explored of krypton compounds is krypton difluoride (KrF_2). It is thermodynamically unstable and strong oxidizing agent which has potential to oxidize xenon to xenon hexafluoride, metallic silver to AgF_3, and metallic gold to AuF_6^-. Moreover, it can also oxidize chlorine, bromine, and iodine to their +5 oxidation state. Due to thermodynamically unstable ($\Delta H_f = 60$ kJ/mol), KrF_2 cannot be prepared following strategy of high-temperature high-pressure strategy used for the preparation of thermodynamically stable xenon fluorides (ΔH_f for XeF_2, XeF_4, and XeF_6 are −162, −267, −338 kJ/mole, respectively) [45, 46]. KrF_2 was prepared by electric discharges, UV-photolysis, hot wires reactor, and by use of high energy particle (electron, proton, or alpha particle) bombardment method, which can atomize fluorine at low temperatures [47]. In spite of its aggressive chemical behavior, KrF_2 has been studied extensively by using variety of spectroscopic techniques like UV-vis, UV-PES, IR, Raman, rotational, XANES, ^{19}FNMR, and Mossbauer techniques. These studies not only revealed information about the electronic structure but also the molecular structure of KrF_2. Moreover, KrF_2 exists in two different crystallographic forms which is unambiguously established by X-ray crystallography in solid state and by electron diffraction in gaseous state (Fig. 3.14).

3.6 Missing Xenon Paradox

The earth atmosphere contains 90% less xenon than meteorites similar to the rocky material that constitute the earth [48]. The surprisingly strong depletion of xenon compared to light noble gases from the earth's atmosphere has become one of the most challenging puzzles for the researchers across the science disciplines spanning planetary, mineralogical, geological, nuclear, and other physical sciences as well as theoretical and computational sciences. Therefore, various alternative models have been proposed to explain the xenon missing enigma. These include possibility of xenon hydrodynamic escaping from the earth atmosphere into the space. This explanation, however, does not explain scarcity of xenon compared to argon because the xenon being heavier than argon would be less affected by this process. An alternative hypothesis is that xenon may be hidden in the earth atmosphere. Then there are

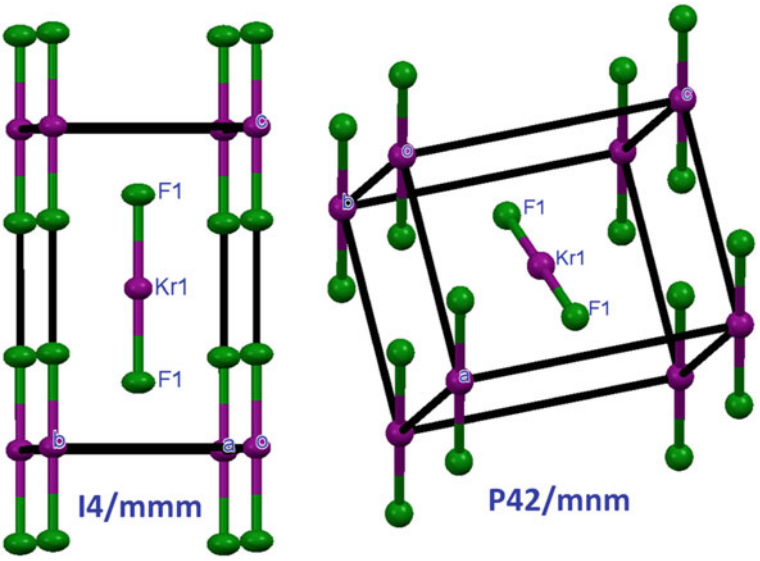

Fig. 3.14 Two crystallographic forms of KrF_2 (redrawn from ICSD database)

researchers having strong consensus that the missing xenon are entrapped in ices, water clathrates, and sediments [49]. However, no such xenon rich pool has been identified in nature. Furthermore, a study had predicted the reactivity of xenon with water ice but under a pressure and temperature conditions around 50 GPa and 1500 K which will be available in the interiors of giant planets like uranus and neptune only [50]. It has also been postulated that xenon might have displaced silicon from quartz (SiO_2) under high temperature and pressure conditions. Such types of conditions are encountered in the continental crust. It indicates that xenon may be captured within silicates as XeO_2 instead of SiO_2 [51]. Although there were indications and a subsequent experiment reported the synthesis of XeO_2, first principle calculations have excluded this possibility as incorporation of Xe in SiO_2 matrix would be requiring very high positive formation energy which is energetically unfavorable [52]. Application of high pressure on xenon not only causes structural transition from face centered cubic (fcc) to hexagonal close packed (hcp) structure but also instigate behavioral changes from insulator to metallic xenon by bandgap closure [53]. Such structural and behavioral transformation in xenon is the basis of next hypothesis which suggested that xenon may be concentrated in Earth's core by forming intermetallic compounds with Fe and Ni, the main constituents of the earth core, in different stoichiometries ($XeFe_3$, $XeFe_4$, $XeFe_5$, $XeFe_6$ or $XeNi_3$, $XeNi_4$, $XeNi_5$, $XeNi_6$). Moreover, through DFT studies, it was predicted that under high pressure there will be negative electron transfer from xenon to Fe(Ni) contrary to the expected behavior [48]. However, high-pressure experiments up to 155 GPa did not provide evidence for a chemical reaction between Xe and Fe. Furthermore, the difference between the atomic sizes of Xe and Fe is more than 30%, formation of solid solution is unlikely event according

to Hume-Rothery rule, although both Xe and Fe have same hexagonal close pack structure under high pressure.

Overall, so many hypothesis have been put forward to explain the xenon missing paradox. They were proposed on the basis of theoretical predictions while few of them were found to be true in certain set of conditions, however none of them could be able to explain this enigma completely and still the origin of xenon depletion is poorly understood. Nevertheless, the above-mentioned theoretical predictions and experiments have shined some light on the probable explanation for xenon missing mystery and quite possible that researchers will unravel this paradox shortly.

3.7 Summary and Outlook

This chapter provides an overview of the discovery of noble gases and their journey from being non-reactive as per conventional scientific wisdom to form thousands of compounds. Synthetic strategies adopted to prepare and stabilize the noble gas compounds as discussed in this chapter clearly indicates that making noble gas compounds is not for the faint of heart. Since electrons in noble gases are comfortable and do not have an urge to interact with other elements, the researchers had gone and have to go to the extreme conditions to make them dislodge from where they are. Synthesizing the first noble compound was like discarding the decades old belief, shattering the basic fundamentals of chemistry that noble gases which have eight electrons in the valence shell do not react. Already many compounds of noble gases have been synthesized but many more have been theoretically predicted which are yet to be experimentally verified, thus providing ample scope of research for the chemists. Moreover, the paradox related to xenon depletion is still not fully understood and this could be an opportunity for the researchers to solve the puzzle created by nature.

References

1. Pyykko P (2000) Noblesse oblige. Science 290:64–65
2. Hallford B (2019) To get noble gases to forge bonds, chemists go to extremes. 97:22. https://cen.acs.org
3. Schrobilgen GJ, Brock DS, Mercier HPA Noble gas compounds. https://doi.org/10.1002/0471238961.0315131619030818.a01.pub3
4. Grandinetti F (2018) Noble gas chemistry, Wiley-VCH Verlag GmbH & Co. KGaA, Boschstr. 12, 9469 Weinheim, Germany, Print ISBN: 978-3-527-34180-1
5. Cavendish H (1785) Experiments on air. Philos Trans R Soc Lond 75:372–384
6. Janssen P (1868) Discovery of helium. Compt Rend 67:839
7. Lockyer JN (1896) The story of helium. Nature 53:319–22
8. Rayleigh (1894) Proc R Soc Lond 55:40–344
9. Ramsay W (1915) Macmillan and Co., London
10. Rayleigh L, Ramsay W (1895) Argon, a new constituent of the atmosphere philosophical transactions. Philos Trans R Soc Lond Ser A Math Phys Eng Sci 186:187–241

11. Hillebrand W (1891) Am J Sci 42:390
12. Ramsay W, Collie JN, Travers M (1895) On the behaviour of argon and helium when submitted to the electric discharge. J Chem Soc Trans 67:684–701
13. Ramsay W, Travers MW (1900) Argon and its companions. Proc R Soc Lond 67:329–333
14. Partington JR (1957) Discovery of radon. Nature 179:912
15. Christe KO (2008) Neil Bartlett (1932–2008). Nature 455:182
16. Neil Bartlett and the Reactive Noble Gases commemorative booklet produced by the National Historic Chemical Landmarks program of the American Chemical Society in 2006
17. Yost DM, Kaye AL (1933) An attempt to prepare a chloride or fluoride of xenon. J Am Chem Soc 55:3890–3892
18. Antropoff A (1924) Die Wertigkeit der Edelgase und ihre Stellung im periodischen System. Angew Chem 37:217 and 695
19. Ruff O, Menzel W, Anorg Z (1933) Neue Sauerstofffluoride: O_2F_2 and OF. Allg Chem 213:206
20. Bartlett N (1962) Xenon hexafluoroplatinate(V) Xe+(PtF6)−. Proc Chem Soc 218
21. Christe KO (2013) Bartlett's discovery of noble gas fluorides, a milestone in chemical history. Chem Commun 49:4588–4590
22. Hargittai I (2009) Neil Bartlett and the first noble-gas compound. Struct Chem 20:953–959
23. Claasen HH, Selig H, Malm JG (1962) Xenon tetrafluoride. J Am Chem Soc 84:3593
24. Hoppe R, Dähne W, Mattauch H, Rödder KM (1962) Fluorination of xenon. Angew Chem Int Ed 1:599
25. Smith DF (1963) Xenon trioxide. J Am Chem Soc 85:816–817
26. Selig H, Classen HW, Chernick CL, Malm JG, Huston JL (1964) Xenon trioxide: preparation and some properties. Science 143:1322–1323
27. Pitzer KS (1963) Bonding in xenon fluorides and halogen fluorides. Science 139:414
28. Bartlett NR, Rao PR (1963) Xenon hydroxide: an experimental hazard. Science 139:506
29. Templeton DH, Zalkin A, Forrester JD, Williamson SM (1963) Crystal and molecular structure of xenon trioxide. J Am Chem Soc 85:817
30. Goettel JT, Schrobilgen GJ (2016) Solid-State Structures of XeO_3. 55:12975–12981
31. Marczenko KM, Mercier HPA, Schrobilgen GJ (2018) A stable crown ether complex with a noble-gas compound. Angew Chem 57:12448–12452
32. Szarek P, Grochala W (2015) Noble gas monoxides stabilized in a dipolar cavity: a theoretical study. J Phys Chem A 119:2483–2489
33. Brock DS, Schrobilgen GJ (2011) Synthesis of the missing oxide of xenon, XeO_2, and its implications for earth's missing xenon. J Am Chem Soc 133:6265–6269
34. Zhu Q, Zung DY, Oganov AR, Glass CW, Gatti C, Lyakhov AO (2013) Stability of xenon oxides at high pressures. Nat Chem 5:61–65
35. Rupp HH, Seppelt K (1974) Struktur von Xenonhexafluorid in Lösung: Xe_4F_{24}. Angew Chem Int Ed Engl 13:612
36. Burbank RD, Jones GR (1971) Xenon hexafluoride: structural crystallography of tetrameric phases. Science 171:485
37. Howard WF Jr, Andrews L (1974) Synthesis of noble-gas dihalides by laser photolysis of matrix-isolated halogens. J Am Chem Soc 96:7864
38. Jortner J, Wilson EG, Rice SA (1963) The heats of sublimation of XeF_2 and XeF_4 and a conjecture on bonding in the solids. J Am Chem Soc 85:814–815
39. Tavcar G, Tramsek M (2015) J Fluorine Chem 174:14–21
40. Hagiwara R, Hollander F, Maines C, Bartlett N (1991) The crystal structure of [Ag $(XeF_2)_2$]AsF_6 formed in the oxidation of Xe by $AgFAsF_6$. J Eur Solid State Inorg Chem 28:855–866
41. Brau CA, Ewing JJ (1975) Emission spectra of XeBr, XeCl, XeF, and KrF. J Chem Phys 63:4640
42. Ault BS, Andrews L (1976) Absorption and emission spectra of matrix-isolated XeF, KrF, XeCl, and XeBr. J Chem Phys 65:4192
43. Huston JL (1971) Xenon dioxide tetrafluoride. J Am Chem Soc 93:5255
44. Malm JG, Appelman EH (1969) At Energy Rev 7:3

45. Gunn SR (1967) Heat of formation of krypton difluoride. J Phys Chem 71:2934
46. Johnson GK, Malm JG, Hubbard WN (1972) The enthalpies of formation of XeF_6(c), XeF_4(c), XeF_2(c), and PF_3(g). J Chem Thermodyn 4:879
47. Lehmann JF, Mercier HPA, Schrobilgen GJ (2002) The chemistry of krypton. Coord Chem Rev 233–234:1–39
48. Zhu L, Liu H, Pickard CJ, Zou G, Ma Y (2014) Reactions of xenon with iron and nickel are predicted in the Earth's inner core. Nat Chem 6:644–648
49. Wacker JF, Andres E (1984) Where is the Earth's missing xenon. SAO/NASA Astrophysics Data System (ADS) 48:2373–2380
50. Sanloup C, Bonev SA, Hochalf M, Casley HEM (2013) Reactivity of xenon with ice at planetary conditions. Phy Rev Lett 110:265501
51. Sanloup C, Schmidt BC, Perez EMC, Jambon A, Gregoryanz E (2005) Retention of xenon in quartz and Earth's missing xenon. Science 310:1174
52. Probert MIJ (2010) Retention of xenon in quartz and Earth's missing xenon. J Phys 22:025501
53. Cynn H, Yoo CS, Baer B, Herbei VL, McMahan AK, Nicol M, Carlson S (2001) Martensitic fcc-to-hcp transformation observed in xenon at high pressure. Phys Rev Lett 86:4552

Chapter 4
Synthesis of Inorganic Fluorides

S. N. Achary, S. J. Patwe, and A. K. Tyagi

Abstract In this chapter, a brief introduction to fluorine and fluorides with an emphasis on their preparation is presented. The general procedures for preparation of fluorides, in particular inorganic fluorides, are explained. Preparation of F_2 and HF, and their properties are discussed in light of their importance to fluoride chemistry. Since the fluorine and fluorides are hazardous, corrosive and reactive materials, the need for special experimental conditions are explained. In addition to F_2 and HF, other fluorinating reagents are also briefly mentioned. The common experimental procedures used for fluorides and oxyfluorides, like solid-state reactions, solid–liquid and solid–vapor reactions as well as non-conventional fluorides preparation methods like sol–gel, hydrothermal, displacement and precipitation reactions are presented. The specific examples of preparation and properties of fluorides and oxyfluorides are presented at the end. The chapter is concluded with a mention of the scope of innovative needs in preparative fluorine chemistry.

Keywords Fluorine · Fluoride · Oxyfluorides · Inorganic fluoride · Preparative chemistry

4.1 Introduction

Inorganic fluorides find wide range of applications as optical, ionic conducting materials and in metallurgical processes. Low melting temperature coupled with high reactivity of fluorides render high metallurgical values to fluoride and fluorine chemistry. In particular, high pure metals, especially nuclear materials, like U, Th, Pu as

S. N. Achary (✉) · S. J. Patwe · A. K. Tyagi
Chemistry Division, Bhabha Atomic Research Centre, Mumbai 400085, India
e-mail: sachary@barc.gov.in

A. K. Tyagi
e-mail: aktyagi@barc.gov.in

S. N. Achary · A. K. Tyagi
Homi Bhabha National Institute, Mumbai 400094, India

A. K. Tyagi and R. S. Ningthoujam (eds.), *Handbook on Synthesis Strategies for Advanced Materials*, Indian Institute of Metals Series,
https://doi.org/10.1007/978-981-16-1892-5_4

well as refractory metals like Zr, Hf, Ta, etc. are conveniently obtained from their corresponding fluorides. Also due to their wide band gap and low phonon loss, they are often used as host materials for luminescent ions and laser crystals. In general, fluorides of most of the elements have electrostatic interactions and hence they form non-molecular crystals with more symmetric structures than oxides. In the field of solid inorganic fluorides, significant efforts have been paid on the synthesis of metal fluorides by fluorination of the oxides and metals with various fluorinating agents. Due to wide practical applications and rich fundamental chemistry, preparative chemistry of inorganic fluorides has been of interest since long. The preparative chemical reactions for fluorides in general are carried out by homogenous or heterogeneous media using solid, liquid and gas phases. The preparation conditions are often dependent on the materials to be synthesized as well as their final applications.

Since the discovery of fluorides, which predates to the preparation of fluorine itself, wide varieties of materials having relevance either for fundamental chemistry or applied chemistry have been prepared in the laboratories. Many fluorides and their preparations methods have been extensively investigated and also extended to industrial scale productions for various practical applications. Though the fluorides have tremendous scope for applications, they are always less preferred compared to oxides for practical applications due to their challenging synthesis procedures and limited stabilities in normal environmental conditions. However, several applications need only fluorides because of their superior properties and also non-availability of materials in other system to meet them. Thus, solid fluorides have occupied unique places in both inorganic and organic materials due to their specific physical as well as chemical properties. Though wider and highly specific applications are known for fluorides, they remain as lesser investigated research area compared to oxides till date. The limited investigations in fluorides can be due to the higher reactivity, stringent preparation conditions, availability of limited preparation facilities and involvement of toxicity of the reactants to be used for preparations. Also, the preparation of fluorides needs a special source for F_2 or F^- for reactions, and the availabilities of these reactants limit the rapid growth of fluoride chemistry. Later developments on the large-scale industrial production of F_2 and HF, materials and alloys as well as availability sophisticated machineries and equipments widened the research opportunity in fluorine and fluoride chemistry. The developments of fluorine chemistry and preparation of fluorides have been documented from time to time in many monographs, chapters and reviews [1–11]. Of late, the research activities in organic fluorides surpass the inorganic fluorides, due to the demand of organic fluoro-compounds for chemical and medical applications. The widely used typical fluoro-pharmaceuticals, like flurocortisones, 5-fluorouracil, varieties of fluoro-glucose, are to name a few. Presently, a number of fluoro-pharmaceuticals are available in market, and they form a separate branch of fluorine chemistry. However, the inorganic fluorides are still remaining as a challenge in materials chemistry due to their need as advanced synthetic optical and ionic conducting materials, like doped CaF_2, PbF_2, $PbSnF_4$, $LiYF_4$, $LiCaAlF_6$, BaY_2F_8, etc. and materials with unusual functional properties

like superconducting (like AFeAsF (A = Sr, Eu and Ca) [12, 13], magnetic, dielectric and multi-ferroelectric properties (examples: $BaMnF_4$, $Pb_8Fe_3F_{24}$, $Pb_5Al_3F_{19}$, etc.) [14, 15].

In this chapter a brief overview on the progress and general methodologies of the preparative fluoride chemistry and preparation of novel fluorides and oxyfluorides are presented. The chapter initially explains the preparation of F_2 and HF and their importance in preparative fluoride chemistry, and subsequently general preparation methods are explained with typical examples.

4.2 Fluorine

Fluorine is a unique element which forms compounds with all known elements except helium, neon and argon, and is the 13th most abundant element in earth crust. The abundance of fluorine in earth crust (540 ppm) is more than that of chlorine (170 ppm), and it exists in various rock minerals. The principle minerals for fluorine source are fluorspar (CaF_2), cryolite (AlF_3–3NaF) and fluorapatite ($Ca_5(PO_4)_3F$). Besides these several other secondary minerals, namely, topaz (Al_2SiO_4(F, OH)$_2$), amblygonite ($LiFePO_4$(F, OH)), etc. are also the known fluorine sources. But the later minerals are not used for extraction of fluorine due to lesser fluorine content and limited commercial benefits. Due to the higher reactivity of fluorine, it is widely accepted that all the fluorine in earth crust exist as fluorides, even though there had been claims of existence of molecular fluorine before the isolation or preparation of molecular fluorine. The claims of existence of molecular fluorine in nature were based on the smell produced by the crystal of fluorites occurring near radioactive sources [16]. Only recently the existence of molecular fluorine in such fluorite crystals had been confirmed by NMR [17]. The β-ray induced reduction of Ca^{2+} ions of fluorite has been attributed to the formation of trapped F_2 and precipitated elemental Ca in CaF_2 [17].

The discovery of fluorine and its characterization was a result of continuous efforts from the seventeenth century onwards till it got its preliminary unraveling by Gay-Lussac in nineteenth century and its identity as *fluorine* by Sir Humphry Davy (1813). The isolation attempts on fluorine and research on fluorine and fluorides bear a long tragic history, like severely injured and fatalities [18]. Thus, fluorine had been considered as one of the most dangerous elements to work with. However, the studies physical and chemical properties of fluorine and fluorides have got impetus after Prof. Henri Moissan (1886) demonstrated large-scale production of fluorine by electrolyzing dry KHF_2 in anhydrous HF [18]. Moissan used a typical U type electrolysis cell made from platinum and platinum or iridium electrodes for electrolytic separation of H_2 and F_2 from HF. He had carried out the electrolysis of anhydrous HF containing KHF_2at lower temperature (around 250 K) to separate H_2 and F_2 at cathode and anode, respectively [19]. He confirmed the isolated gas as molecular F_2byitscombustion reaction with silicon.

The reactivity of fluorine due to its anion like character or as neutral radical and small ionic radius have been the key features in the fluorine chemistry. The low dissociation energy of F_2 (the bond energy of fluorine molecule (F–F) is only 157 kJ/mol, lower than the bond energies of hydrogen H–H (434 kJ/mol) and chlorine Cl-Cl (242 kJ/mol), https://labs.chem.ucsb.edu/zakarian/armen/11---bonddissociationenergy.pdf) makes it highly reactive. Due to its smaller ionic and atomic radii, fluoride chemistry shows similarity with oxide chemistry and hydride chemistry, and also with chemistry of other halides due to one electron deficient inert gas electronic configuration of F. Thus, fluorine forms compounds similar to oxides, hydrides and other halides. Also, it can replace hydrogen of organic compounds forming *fluoro-organic* compounds and *fluorocarbon* stable compounds. Due to high electronegativity and low polarizability, most of the fluorides in general crystallize in highly ionic lattice, and have very high band gap and weak phonon loss. Very commonly fluorides are more stable compared to other analogous halides. The oxidation state of fluorine is always −1 and the anion is named as fluoride, which is analogous to other halides. F_2 is a pale greenish yellow color gas with highly pungent and penetrating odor. A detailed description of the general properties of fluorine and their compounds are available as monographs [7–10]. Some of the typical properties of fluorine are given in Table 4.1, and its comparisons with other elements are given in

Table 4.1 Some general information on fluorine[a]

Symbol	F (Fluorine)
Atomic number	9 ($1s^2 2s^2 2p^5$)
Mass number	19 (100% abundance)
	18 (artificial)*
Melting point	54 K
Boiling point	85 K
Atomic radius	0.71 Å
Ionic radii (F^{1-})	1.33 Å
Dissociation energy of F_2	37.8 kcal/mole
F–F bond distance in F_2	1.42 Å
Electronegativity	4.10 (Allred-Rochow), 3.98 (Pauling)
Electron affinity	−79 kcal/mol (−3.6 eV/g atom)
Ionization potential	404 kcal/mol (17.4 eV/g atom)
Polarizability	0.81×10^{-24} cm^3

[a]Compiled from data from CRC hand book for Chemistry and Physics; and webpage: http://hyperphysics.phy-astr.gsu.edu/hbase/pertab/pertab.html#c1

*^{18}F (half-life: 1.83 h) is generally produced by irradiation of ^{16}O or ^{18}O by ^{2}H (deuterium) or ^{1}H (proton). The Accelerated $^{2}H^{+}$ and $^{1}H^{+}$ from a cyclotron are bombarded on the target containing the desired isotopes of oxygen. The nuclear reactions for production ^{18}F are below

Table 4.2 Comparison of electronic properties of F with other nonmetallic elements[a]

	Pauling electrnegativity	Electron affinity (kcal/mol)	1st IP (eV)	covalent radius (Å)	Atomic volume (cm^3/mol)
H	2.20	17.7	13.598	0.32	14.4
F	3.98	79.5	17.422	0.72	17.1
Cl	3.16	83.3	12.967	0.99	22.7
Br	2.96	72.6	11.814	1.14	23.5
I	2.66	70.6	10.451	1.33	25.7
C	2.55	29.0	11.260	0.77	4.58
N	3.04	−6.2	14.534	0.75	17.3
O	3.44	33.8	13.618	0.73	14.0

[a]Compiled from data from CRC hand book for Chemistry and Physics; and webpage: http://hyperphysics.phy-astr.gsu.edu/hbase/pertab/pertab.html#c1

Table 4.2. In addition to the high reactivity, fluorine and fluorides also pose potential toxicity, and can form varieties of products and complicate the biological and chemical systems. The chemical toxicities of fluorine are mainly arising from its potential to replace hydrogen or OH of biological molecules and strong bonding with metal ions in biological system.

$$^{16}_{8}\mathrm{O} + {}^{2}_{1}\mathrm{H} \rightarrow {}^{18}_{9}\mathrm{F};$$

$$^{18}_{8}\mathrm{O} + {}^{1}_{1}\mathrm{H} \rightarrow {}^{18}_{9}\mathrm{F} + {}^{1}_{0}\mathrm{H}$$

Besides, ^{18}F, at least there are 16 other isotopes which are produced by various nuclear reactions. All these istopes are highly unstable and radioactive.

Though the preparation of fluorine knowingly or unknowingly has been documented from seventeenth century onwards, the credit for its preparation goes to the Prof. Henri Moissan due to his proper characterization and scalable method production. The redox potential for F–F is 2.85 eV and thus the electrochemical method is the best and adopted method for production of fluorine. Early trials for electrolysis with anhydrous HF were unsuccessful due to the poor electrical conduction of HF. However, the early method of Moissan was expensive for commercial and large-scale productions of F_2. Thus, several modifications in electrolysis cell and electrolyte composition as well as optimization of power have been carried out in later periods. These successive developments in the electrochemical cell resulted in commercial and economical methods for large-scale production of F_2. Effect of composition of electrolyte for viable production of F_2 has been investigated by Caddy before the world war-II [20]. Electrolysis of the compositions containing KF with about 42 wt % of HF produces about 40 wt % F_2 at temperature 120 °C [21]. Commercial production of F_2 is usually carried out from KF-HF mixture, molar ratio 1:2–1:2.2, where the mixture provides suitable melting temperature (60–150 °C) for

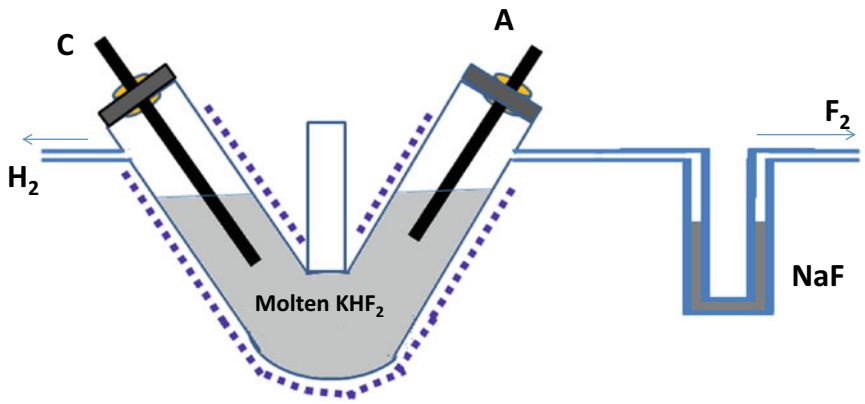

Fig. 4.1 Typical sketch of early electrolysis cell used for fluorine preparation. A and C are anode and cathode. Central column is reservoir of electrolyte. The figure is not to be scaled for real experiments and based on Dennis' methods for fluorine production. For more details, refer: L. M. Dennis, J. M. Veeder and E. G. Rochow, The preparation of fluorine by electrolysis, J. Am. Chem. Soc., 53 (1931) 3263–3269

carrying out electrolysis. Such intermediate electrochemical cells are best suited due to necessary conductivity arising from the KF in the molten mass and electrolysis of HF produces H_2 and F_2 [20–23]. In common the electrochemical reaction for electrolysis of HF is carried out in a non-reactive container using various types of electrodes, viz. noble metals like platinum, or graphite and the containers are made from fluorine and fluoride compatible materials like cupper, graphite, nickel or monel. The materials compatible with F_2 and fluorides have been explained in other sections of this chapter. The entire reaction chamber needs to be free from moisture and air or oxygen. The electrochemical reactions are given below and a schematic of a typical electrochemical cell used for electrolysis of HF is shown in Figs. 4.1 and 4.2. The representative phase diagram of KF-HF relevant for HF electrolysis is shown in Fig. 4.3. The electrolysis is carried out by applying potential between electrodes while the electrolyte is maintained in molten state. Typical operation voltage ranges in between 7 and 12 V and current density 1.0–1.5 kA/m^2 for yield of F_2 in the range of 90–98% [20]. The F_2 is purified from the contaminated HF by passing over dry NaF, where the HF is trapped by forming $NaHF_2$.

$$KHF_2 \rightarrow KF + HF$$

$$HF \rightarrow H^+ + F^-$$

$$2H^+ + 2e^- \rightarrow H_2 \text{ (At cathode)}$$

$$2F^- - 2e^- \rightarrow F_2 \text{ (At anode)}$$

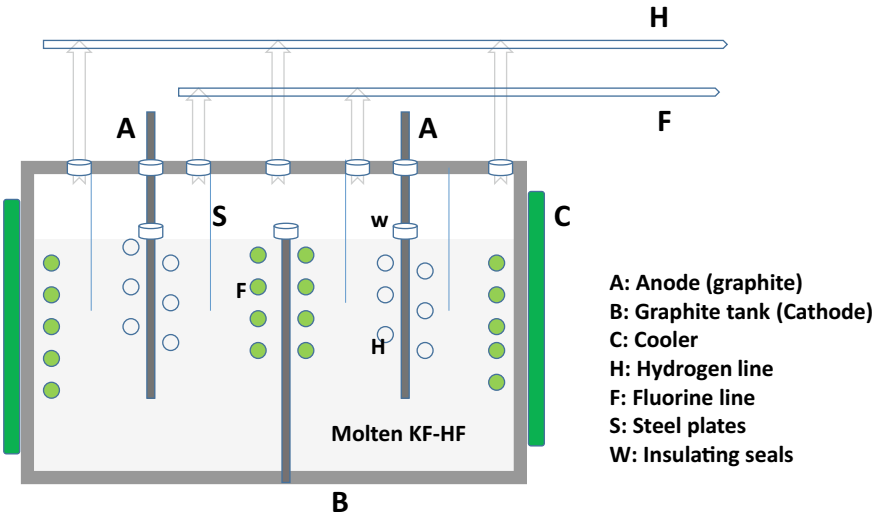

Fig. 4.2 Schematic diagram of a modern electrolysis cell for fluorine production. The exact design and materials are decided by the operation mode and capacity of fluorine production

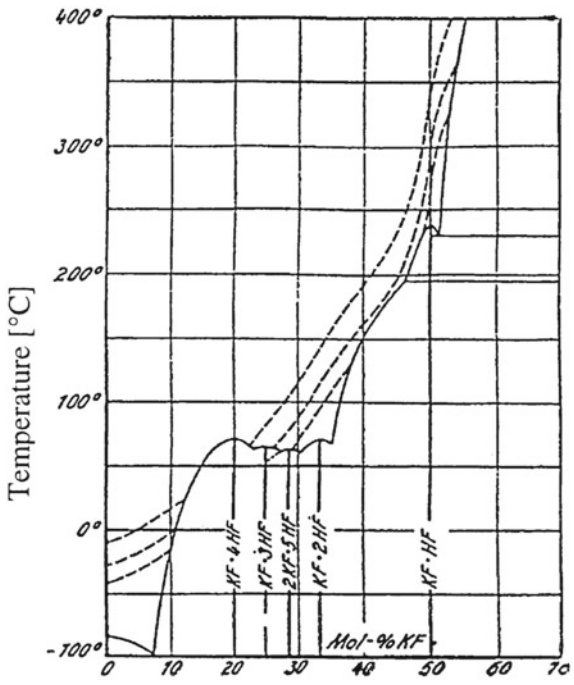

Fig. 4.3 KF–HF phase diagram. Reproduced from Ref. [24] with permission of American Chemical Society

Besides this electrochemical reaction, a number of other chemical reactions are also used for production of F_2 in laboratory. The common mode of F_2 productions is based on the decomposition of fluorides of high oxidation state transition metal ions or their complex fluorides [25, 26]. Although there are large number possible materials like CeF_4, UF_6, CF_3NF_2, N_2F_3, etc. which can decompose to produce F_2, they are not generally considered for preparation of F_2. This can be attributed to the difficulty to prepare such materials as well as high exothermicity and violent process where the produced fluorine often reacted with the reactor itself. Decomposition of K_3PbF_7 producing detectable amount of fluorine is the first well documented procedure for preparation of molecular fluorine [27]. The most common preparation methods are decomposition of K_2NiF_6, $CaNiF_4$, MnF_4, NiF_4, etc. [25–27]. The reaction of K_2MnF_6 with SbF_5 for lab scale production of fluorine is known for long time. K_2MnF_6 can be prepared by interaction of KF with $KMnO_4$ in aqueous HF in presence of hydrogen peroxide as oxidizing agent. The controlled reduction of Mn^{7+} to Mn^{4+} is achieved by a mild oxidizing medium of H_2O_2 [28].

$$K_2MnF_6 + 2SbF_6 \xrightarrow{40\%\ \text{aq HF}} 2KSbF_6 + MnF_4$$

$$2KMnO_4 + 2KF + 10HF_{aq} + 3H_2O_2 \xrightarrow{\text{aq HF}} 2K_2MnF_6 + 8H_2O + 3O_2$$

$$MnF_4 \xrightarrow{380\,^\circ\text{C}} MnF_3 + \frac{1}{2}F_2$$

MnF_4 can also be prepared by action of F_2 gas under high pressure with MnF_2 at relatively lower temperature, viz. around 70 °C or by action of KrF_2 with MnF_2 [29]. Also, the fluorides of tetravalent Mn and its complex derivatives can be obtained by controlled reductive fluorination of $KMnO_4$ in aqueous HF and H_2O_2 [30]. Analogous NiF_4 has been prepared from $NiF_2$by the reaction with KrF_2, XeF_2, AsF_5, BF_3, SbF_5, etc. at lower temperature [31]. Some typical reactions for preparation of NiF_4 are as below

$$K_2NiF_6 + 2AsF_5 \xrightarrow{\text{anhydrous HF at} -65\,^\circ\text{C}} 2KAsF_6 + NiF_4$$

$$K_2NiF_6 + 2BF_3 \xrightarrow{\text{anhydrous HF at} -65\,^\circ\text{C}} 2KBF_4 + NiF_4$$

$$NiF_4 \xrightarrow{-55\,^\circ\text{C}} NiF_3 + \frac{1}{2}F_2$$

In addition, the catalytic electrochemical methods of oxidation of F^- to F_2 are also known [32]. The photo-generated holes of suitable semiconducting oxides and oxyfluorides can oxidize F^- to F^0. Wang et al. have produced molecular fluorine using semiconducting n-type TiO_2 as catalyst for electrolysis of anhydrous HF-NaF solution [32] while illuminating the assembly with light of 365 nm light (band edge

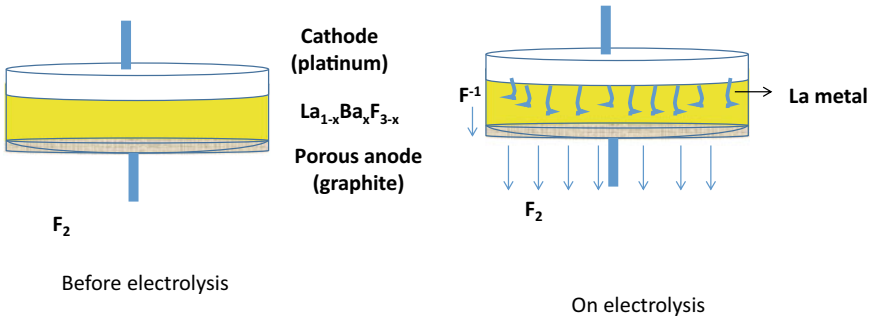

Fig. 4.4 Schematic of a solid electrochemical electrolyser for F_2 production. Adapted from Ref. [33] with permission of Elsevier

of TiO_2). The corrosion product $TiO_{2-x}F_x$ also serves the similar purpose for oxidation of F^-. The electrolysis of anhydrous HF-NaF using Pt as cathode and TiO_2 or $TiO_{2-x}F_x$ as reference electrode produces $F_2$with photochemical yield of about 55%. Additionally, electrochemical methods for productions of molecular fluorine using solid electrolytes are also reported in literature [33]. Electrolysis of solid electrolytes, like Ba doped LaF_3 (as $La_{1-x}Ba_xF_{3-x}$, where $0.03 \leq x \leq 0.10$; high fluoride ionic conductivity ~4–8 $\times$ 10^{-5} S/cm at 20 °C and relatively higher stability in air or moisture) can liberate F_2. Usually the solid electrolyte is placed in between two electrodes (generally a porous graphite anode and thin layer of noble metal as cathode) and the electrolysis is carried out by applying electric field higher than the equilibrium decomposition potential of LaF_3 (5.81 V). The electrolysis of $La_{1-x}Ba_xF_{3-x}$ leads to migration of La^{3+} toward the cathode while F^- ions toward the anode. The La^{3+} reduces to a metal at the cathode and forms dendrite like metal deposits on the surface of cathode. The F^- ions migrate through the electrolyte to the anode and oxidize to F, and that escapes through the porous anode as F_2. The schematic of an electrochemical F_2 generator is shown in Fig. 4.4.

Although there can be many methods for preparation of molecular fluorine, the laboratory scale preparations are mainly carried out by decomposition of MnF_4 and NiF_4.

4.3 Hydrogen Fluoride

The preparation and properties of hydrogen fluorides have been realized much before identity of fluorine. Hydrogen fluoride (HF) is the most widely used primary reagent for preparation of fluoride and source for industrial scale production of F_2. It is also one of the most commonly used laboratory reagents. Some of the properties of HF are given in Table 4.3. Both pure anhydrous HF and diluted aqueous HF are commercially produced in large scale.

Table 4.3 Some of the general information on HF[a]

Chemical formula	HF
Molar mass	20.01 g mol^{-1}
BP	19.5 °C
Density	1.15 g/L, gas (25 °C) 0.99 g/mL, liquid (19.5 °C) 1.663 g/mL, solid (–125 °C)
Melting point	−83.6 °C
Boiling point	19.5 °C (67.1 °F; 292.6 K)
Solubility in water	Completely miscible
Vapor pressure	783 mmHg (20 °C)

[a]Compiled from data from CRC hand book for Chemistry and Physics, and Wikipedia sources

The commercial preparation of HF is based on the reaction of fluorspar and fluoroapatite with concentrated sulfuric acid. However, the commercial production of HF is relied only on the fluorspar and sulfuric acid reaction [34, 35] and typical chemical reaction is as below

$$CaF_2 + H_2SO_4 \xrightarrow{600\,K} CaSO_4(solid) + 2HF(g)$$

A typical flow sheet for HF production is shown in Fig. 4.5. Usually fine powder fluorspar is mixed with anhydrous and preheated concentrated sulfuric acid in a rotary retort made of iron. Hot concentrated sulfuric acid and fluorspar powder are continuously fed from reservoirs into the retort. The temperature of the retort is maintained at around 600 K and the gaseous products are collected from another end of the retort. The purity of the HF produced depends on the purity of the fluorspar and corrosion from the reactor. The common impurities in HF are fluorosilicic acid and sulfates, and they are produced from the impurities in raw materials and corrosion of reactor. The gaseous products are passed through scrubbers to remove sulfuric acid vapor, and gaseous SiF_4 and H_2SiF_6. The purification of gaseous HF is generally carried out by repeated distillation. The gaseous SiF_4 which originates from the silica impurity in the fluorspar reacts with water producing H_2SiF_6, which is collected as a byproduct from HF plants. The concentrated HF free from these impurities is finally collected in a copper, lead or steel vessel. Hydrogen fluoride of purity of >99.9% can be achieved by distillation in copper or steel vessels.

Aqueous hydrofluoric acid is obtained by dissolving HF in water. HF and water form a miscible liquid in all proportions at certain temperature, and the solutions of different concentration of HF in water is used as aqueous HF. Typical concentrations of HF in water used for technical applications are between 42 and 85%. Aqueous solutions and liquid HF are stored in gutta-percha, a natural rubber material or polythene bottles and also large tanks of stainless steel with rubber-linings. Aqueous solutions of HF stored in plastic bottles are used as a common laboratory reagent.

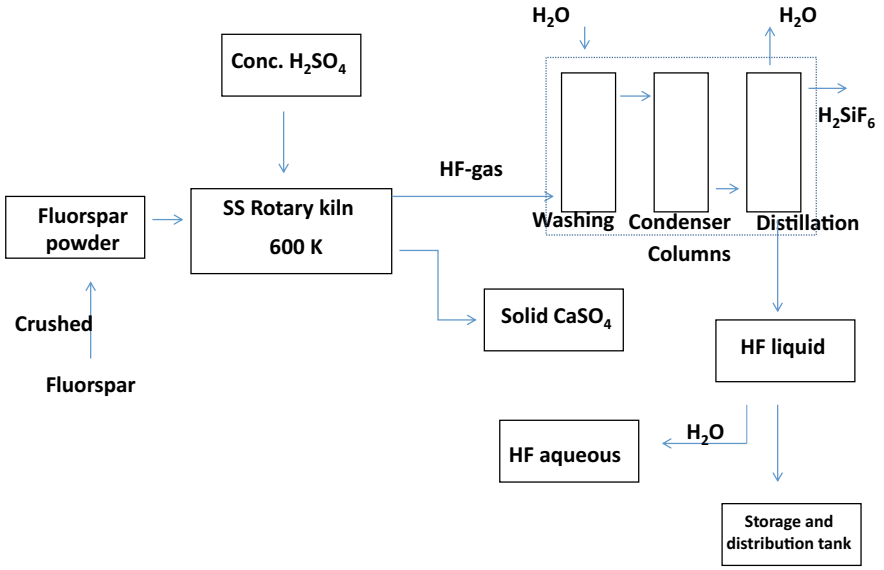

Fig. 4.5 Typical flow sheet for HF production from fluorspar and concentrated H_2SO_4. Schematic is based on the method of HF production in fluorspar plants. For more details, see references 23 and 35

Anhydrous HF is also prepared by direct reaction of H_2 and F_2. The H_2 and F_2 reacts exothermically producing HF with large amount of heat and a self-sustaining flame under a condition of continuous feed of H_2 and F_2 but the reaction needs to be activated. Presence of small amount of impurity gases, like HF or ignition by a spark or heating can initiate the reaction violently. The reaction of H_2 and F_2 produces heat about 540 kJ/g-mol. Thus, this reaction is often useful for carrying out fluorination reactions where this excess heat and HF are simultaneously used. The mechanism of the H_2 and F_2 reaction has been a subject of debate while it is accepted that the reaction proceeds through a chain and branching reaction involving several radicals and molecules in vibronically exited states. The rate constant of the H_2 and F_2 reaction have been investigated in several literatures and they are reported in the order of 10^{-11}–10^{-20} cm^3/s at around 300 K and the activation energy is around 50–60 kJ mol^{-1} [36]. The typical chemical reaction and mode of chemical progress of chain reactions [36] are summarize mentioned below.

$$H_2 + F_2 \rightarrow H + HF + F$$

$$H + F_2 \rightarrow HF + F$$

$$F_2 + H_2 \rightarrow HF + H$$

$$H_2 + F_2 \rightarrow 2HF$$

Thus, it can be mentioned here that H_2 and F_2 react spontaneously producing pure anhydrous HF gas. However, this reaction is rarely used for preparation of HF unless it is required to use for specific chemical reaction. As an example, preparation of UF_4 from UF_6 gas is carried out by using H_2 and F_2 mixture, where H_2 reduces the UF_6 in presence of excess heat of H_2 and F_2 reaction.

The laboratory synthesis of HF is commonly based on the decomposition of NH_4HF_2, NH_4F or KHF_2 [34]. The widely used method is decomposition of Fremy's salt (KHF_2). KF also absorbs HF forming KHF_2 and thus used to trap HF form fluorine line and residual HF from HF reactors. The dry KHF_2 is generally decomposed in a steel, copper or platinum retort at around 573 K to produce gaseous HF. The HF vapor is cooled to lower temperature by using freezing mixture to get anhydrous HF. The quality of HF depends on the moisture content in the KHF_2 and the reactors. Similarly, the decomposition reactions of NH_4HF_2 and NH_4F also used for production of HF, but usually the gaseous products are accompanied with ammonia. So often they form complex fluorides containing the NH^{4+} ions.

$$KHF_2 \xrightarrow{\Delta} KF + HF$$

$$NH_4F \xrightarrow{\Delta} NH_3 + HF$$

$$NH_4HF_2 \xrightarrow{\Delta} NH_3 + 2HF$$

The hydrous HF can be dehydrated by reaction with thionyl chloride. The reaction can be represented as

$$HF \cdot H_2O + SOCl_2 \xrightarrow{\Delta} 2HCl + SO_2 + HF$$

As mentioned earlier, apatite type silicate and phosphate minerals can also be used for preparation of HF. Usually fluorosilicic acid (H_2SiF_6) is the produced as the main aim and subsequently that is used for preparation HF as a side product. Similarly, apatite type phosphates are used for phosphate production and HF is obtained as a side product. Silica reacts with in situ formed HF forming H_2SiF_6 and that is decomposed to HF in presence of moisture. The fluorosilicic acid is commonly prepared as a byproduct in phosphoric acid production from fluorapatite ore.

Depleted UF_6 is also used as HF source, where the UF_6 is hydrolyzed by Steam-H_2 mixture to defluoridize the uranium producing gaseous HF and solid U_3O_8. Mostly such plants are used for their need and to maximize the HF or F_2 utilization.

$$3(H_2 \cdot nH_2O)(g) + 3UF_6(g) \xrightarrow{\Delta} U_3O_8 + 6HF + 3mH_2O$$

4.4 Inorganic Fluorides and Oxyfluorides

4.4.1 Fluorides of Metals

As explained earlier, under certain conditions fluorine reacts with almost all elements in periodic table except lighter inert gases, and usually form compounds with F^- ions. Depending on the electronic configuration of the metal ions, they can form compounds with their different oxidation states. The compounds of fluorine with variable oxidations state elements are commonly similar to their oxide counterparts but their structure and properties are often different due to the nature of bonding, unit oxidation state of F^- and no back-bonding probability. The preparation of fluorides of metal ions depends on the nature of the metal as well as stability, reactivity and solubility of the products. Depending on these properties, the preparations of such metal fluorides are carried out by reaction of HF, F_2 or some suitable fluorinating agents. Preparation procedures for such fluorides are explained in the later sections. In this section, the general crystal chemistry and structure of such metal fluorides are explained.

4.4.2 Binary Fluorides

Among the binary fluorides, alkali and alkaline earth metals form stable fluorides with A^IX and $A^{II}X_2$ (A^I = monovalent alkali ions and A^{II} = divalent alkaline earth ions) compositions. All the AX type fluorides have rock salt type structure where both the A^I and F^-ions have octahedral coordination polyhedra. Except, Be^{2+} and Mg^{2+}, all the alkaline earth metal ions forms fluorite type structure where the A^{II} have cubic eight coordinated polyhedra while F^- ions have tetrahedral coordination polyhedra. Due to smaller ionic radius of Be^{2+} ions, they form tetrahedral coordination polyhedra with F^-ions and SiO_2 type chain structures while Mg^{2+} forms octahedral coordination with F^-ions and that in turn leads to rutile type structures. However, structures of the MF_2 are susceptible to thermodynamic parameters, like temperature and pressure. Thus, most of them show polymorphism under pressure while all have congruent melting temperature. Rutile type MgF_2 is the only thermodynamically stable polymorphs of MgF_2, and analogous to TiO_2 no other polymorphs are known. Only temperature induced structural transition has been known for BeF_2. However, the divalent fluorides, with cations containing lone pairs, like Sn^{2+} and Pb^{2+} form distorted polyhedra with fluoride ions and they exhibit polymorphism. SnF_2 and HgF_2 have distinct square pyramid type coordination polyhedra around the divalent cations and they form relatively open structure or layered structure. These structures of such fluorides depend on temperature, pressure and also on preparation methods.

The structural diversities in fluorides of trivalent cations originate from the ionic radii of the cations. The coordination polyhedron for the trivalent cations varies from 3 to 11 and hence they form wide varieties of structures. Additionally, they exhibit

extensive temperature and pressure induced transitions as well as polymorphism depending on preparation conditions. B^{3+} ions form triangular coordination with F^- ions and the BF_3 units show structural and vibrational properties similar to the carbonatesand nitrates in oxides. The larger coordination polyhedra are formed with larger ionic radii cations, like trivalent lanthanides, actinides, Bi^{3+}, Tl^{3+}, etc. and they form distinct class crystals with trigonal prismatic, cubical, capped triangular prismatic or capped cubical polyhedra around the cation. MF_4 type fluorides are widely encountered as stable or unstable depending on the stabilities of the tetravalent ions. The structural features of most of the tetravalent cations are originated from the MF_6, MF_7 or MF_8 type polyhedra. Also, tetrahedral coordination polyhedra (MF_4) are observed for smaller cations, like Si^{4+}, Ge^{4+} while the octahedral MF_6 units are observed in case of ions like Ti^{4+}, Mn^{4+}, Ni^{4+}, Ge^{4+}, Te^{4+}, Ru^{4+}, etc. In MF_3 or MF_4 materials the electronic configuration also plays crucial role for their structure, stability as well as properties. The higher valent cations, Nb^{5+}, Ta^{5+}, Mo^{6+} andW^{6+} are formed mostly with coordination number 6 and they can sublime easily due to the less binding interaction between the polyhedral units. Different coordination polyhedra around the metal ions in some binary metal fluorides are shown in Fig. 4.6a, b. Compared to oxides, the back-bonding form F^- to M^{n+} ion is not observed and thus the M–F bonding is mostly ionic in nature, and hence fluorides show lower meltingand boiling temperature. These properties were extensively exploited in recovery, production and purification process in metallurgical and electronic industries.

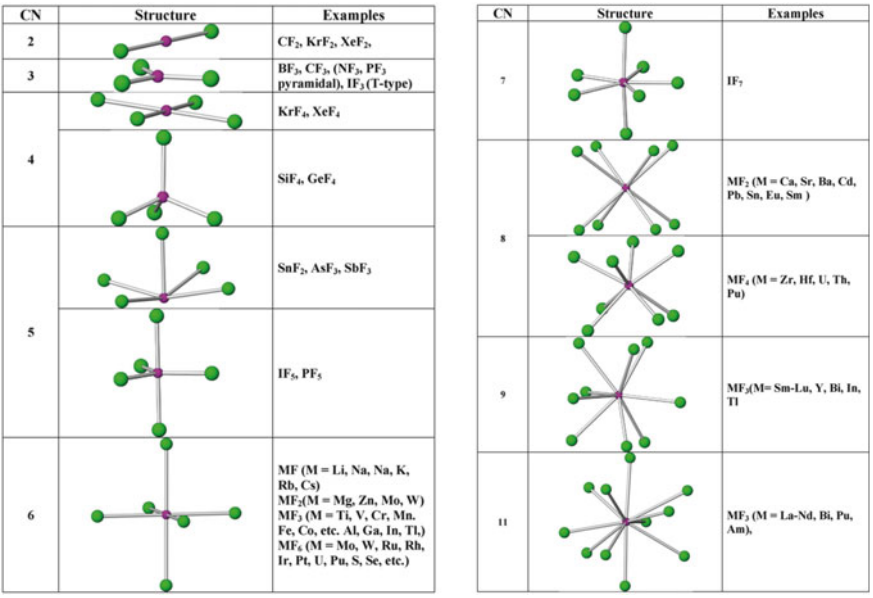

Fig. 4.6 Local structure of some binary fluorides with different coordination number (CN) of metal ions

4.4.3 Nonmetal Fluorides

Among the nonmetal fluorides, the HF shows distinct and interesting structure in solid and also in liquid states due to strong intermolecular hydrogen bonding between H and F from different molecules. HF molecules arrange as a zigzag chain in solid HF due to such strong hydrogen bonding. Due to same reason, they show higher boiling points than other halides of hydrogen. A comparison of some typical properties of HF with other halides of hydrogen is given in Table 4.4. Typical structure of HF in solid state is shown in Fig. 4.7.

Almost all nonmetals form compounds with fluorine which can be treated mostly as molecular crystal where the fluorine oxidizes them to lager oxidation states. Due to high reactivity and high electronegativity of F, it also forms diversified inter-halogen compounds and compounds with O, and noble gases too. Unusual and common oxidation state cations like Kr^{2+}, Xe^{2+}, Xe^{4+}, Xe^{6+}, P^{5+}, S^{6+}, Se^{4+}, Se^{6+}, etc. are known in fluorides. However extended structures are also formed in most of the nonmetal fluorides. The coordination polyhedra around the cations varies from 2 to 8, depending on the ionic radii, electronic structure and composition of the fluorides, and they

Table 4.4 Comparison of some physical properties of halides of hydrogen[a]

	$d_{H\text{-}X}$ Å	μ (Debye)	MP (°C)	BP (°C)	Acidity (pKa)
HF	0.92	1.86	−83.6	19.5	3.17
HCl	1.27	1.11	−114.22	−85.05	− 5.9
HBr	1.41	0.788	−86.9	−66.8	− 8.8
HI	1.61	0.382	−50.80	−35.36	−9.5

[a]Compiled from data from CRC hand book for Chemistry and Physics, and Wikipedia sources

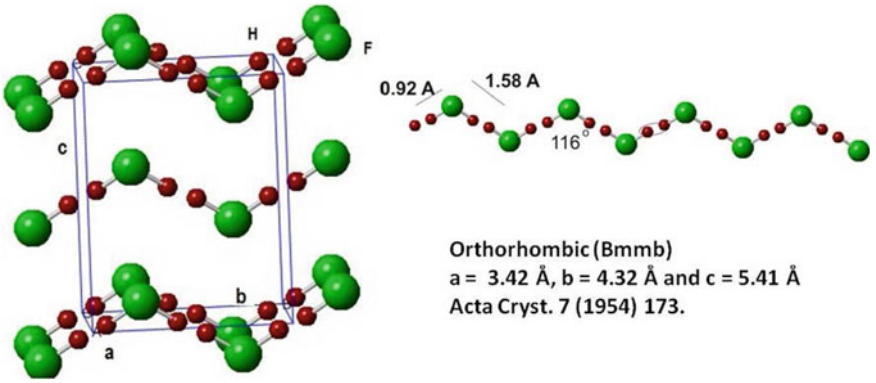

Fig. 4.7 Crystal structure of solid HF. The strong hydrogen bonding gives intermolecular interaction and hence the H^+ site becomes disordered in between two F^- ions (Redrawn with structural details reported by M. Atoji and W. N. Lipscomb, The crystal structure of hydrogen fluoride, Acta. Cryst. 7 (1954) 173)

Table 4.5 Typical inter-halogen compounds

	F	Cl	Br	I
F	F_2(g)	ClF(*g*) ClF_3(*g*) ClF_5(*g*)	BrF(*g*) BrF_3(*l*) BrF_5(*l*)	IF(*s*) IF_3(*s*) IF_5(*l*) IF_7(*g*)
Cl		Cl_2(g)	BrCl(*g*)	
Br		BrCl(*g*)	Br_2(l)	
I		ICl(*l*) ICl_3(*s*)	IBr(*s*)	I_2(s)

are included in Fig. 4.6. Extended network structures in these are also encountered depending on the temperature, pressure and compositions. Compounds with highest oxidation state of halogens are formed only in fluorides. (viz. I is oxidized to 7 + while Cl and Br are oxidized to maximum 5 + state). Some of the examples of inter-halogen compounds are given in Table 4.5. For example, IF_3 has T-shaped, IF_5 has trigonal pyramidal while IF_7 has pentagonal bi-pyramidal structure. Some of the shapes of such molecular fluorides are included in Fig. 4.6. Inter-halogen compounds are formed with one heavier halogen atoms combining with odd number of lighter halogen atoms and their structure depend on electronic configuration, oxidation state of heavier halogen and compositions. They are unstable and strongly oxidizing and hence used as fluorinating reagents.

4.4.4 Complex Fluorides

Similar to oxides chemistry, diversified complex fluorides with more number of cations are also known. The possibilities of diversified compositions of complex fluorides render wide varieties of compounds with distinct physical and chemical properties, and hence they provide an opportunity to tune their functional properties. Such complex fluorides are formed with the polyhedral suitable for the respective cations or with altogether different polyhedra depending on the composition and ionic radii of the cations. In such cases, the structure building principles govern their coordination polyhedra. As an example, in BaF_2 the Ba^{2+} ion is coordinated with eight fluorides ions and forms regular cubical polyhedra, and in LiF, Li^+ is octahedrally coordinated with F^- ions. But, in $BaLiF_3$, which is analogous to perovskite ($CaTiO_3$). In this composition, the octahedral LiF_6 units build the structure and the interstitial spaces are occupied by Ba^{2+} ions. Thus, in such cases, the Ba^{2+} is surrounded by 12 F^- ions with identical Ba-F bond lengths.

Though large varieties of complex fluorides are formed with different combinations of cations analogous to complex oxides, they are still less diversified than complex oxides. This can be attributed to the nature of F^- ions and high ionic characters of M-F bonds. Since F^- is less polarizable, due to small size with complete

filled octet electronic configuration, the structures of complex fluorides are more symmetric compared to the oxides. The complex fluorides provide more opportunity for substitution of aliovalent ions as well as ions of different ionic radii and hence they have been extensively synthesized for introducing various functional properties, and in particular optical and ionic conduction properties. As a general rule, the complex fluorides with distinct structure are formed when the cations have different ionic radii, charge and electronic configuration. Also, fluorides of smaller cations as well as higher charge can form complex anionic fluoride species in the structure. This is a parallel situation to the complex oxides. The disordering of cations in general occurs with cations with similar size and charge, and they form a solid solution or totally disordered structure as glass. It may be noted that the randomization of cations leading to amorphous state is less commonly observed due to their highly ionic nature and strong interaction to next nearest neighbors and relatively weaker M–F bonds compared M–O bonds. Thus, the fluoride glasses are mainly prepared by arresting the molten liquid by rapid quench methods, which otherwise undergoes phase separation to different crystalline phases. Also, it can be mentioned here that complex fluorides can form crystalline structures easily compared to the complex oxides. Some of the cases of complex fluorides are explained later section while dealing their preparations.

4.4.5 Oxyfluorides

Apart from fluorides, oxyfluorides form a large class material and they are formed with both O^{2-} and F^{-} ions together as anions. Despite the charge difference, the fluorides ions of fluorides can be replaced by oxide ions or oxide ions of oxide can be replaced by fluoride ions provided the charge neutrality is appropriately maintained. Also, oxide and fluoride ions may be randomly distributed or may also arrange in an ordered manner. Usually at lower concentration of the substituent (F^{-} or O^{2-}) concentrations these anions are randomly arranged in the parent structure while they are orderly arranged in the higher concentration forming district crystal structures. Additionally, the hydrolysis of the certain fluorides forms oxyfluorides through intermediate hydroxyl group substituted phase. Owing to the close similarity of the radius of F^{-}, O^{2-} and OH^{-} ions, the O^{2-} and OH^{-} are easily incorporated in the fluorides lattice, and that often hinders the preparation of pure fluoride, i.e., fluorides devoid of the minor O^{2-} and OH^{-} ions.

Oxyfluorides exhibits wide range of functional properties, like fast oxide or F^{-} ions conductions, tunable electrical and optical band gaps, or unusual accentricity leading to ferroelectric or piezoelectric properties. Even though the incorporation of fluorine into La_2CuO_{4+x} does not exhibit any drastic change in crystal structure, it alters the electronic properties, viz. they induce superconductivity in $La_2CuO_{4+x}F_y$ [37]. A large number of high temperature superconducting materials in oxide fluorides systems have been reported in literature [38].

The crystal chemistry of oxyfluorides can be formed by involving polyhedra with oxide ions or fluoride ions or both ions together. Varieties of oxyfluorides exist in nature, and they are either formed from oxides by the interactions of fluoride ions in ground water or from fluorides by the process of hydrolysis. A variety of silicate and phosphate minerals exists in earth crust as oxyfluorides'topaz ($Al_2SiO_4F_2$) and apatite ($Ca_5(PO_4)_3F$ are the representative examples. Bastnasite, a fluoro carbonate mineral ($Ln(CO_3)F$) is a rich source of rare-earths, usually mined for rare-earth. A number of mica group minerals contain fluoride ions in the structure and in general they existas disordered fluoro and hydroxyl groups. In analogy of hydroxide minerals, a number of oxyfluorides have also been prepared in laboratory by different experimental methods, like hydrothermal, solvothermal and controlled hydrolysis or by fluorination reactions with F_2 or HF. Some examples are explained in later sections. The oxyfluorides with almost all metallic cations except with alkali and alkaline earth metal ions are formed, while with more cationic species, more possible number of oxyfluorides can be expected. In some of the compounds, fluoride ions also exist as anion (F^-) centered coordination polyhedra which are classed as "naked F^-" containing oxides. Usually the structures of oxyfluorides are relatively complex due to the variations in the nature of bonding of O^{2-} and F^-, and difficult to characterize by technique like X-ray diffraction due to similar scattering power of these anions.

4.5 Preparative Strategies

The preparation of fluorides always needs special attentions compared to oxides which are due to.

(i) Reactivity and stability of the reactants to be used for fluorine source
(ii) Reactivity of container materials with fluorine or F^- ions
(iii) Uncontrolled side reactions and incorporation or unwanted elements (cations and anions) and
(iv) Hazardous effect of fluorine or F^- to health and environment.

All these special needs arise from the fundamental properties of F_2 and F^- ions. Thus, judicious selection of appropriate reactants and experimental equipments as well as physical and chemical environments are extremely important in preparative chemistry of fluorides. It also needs to mention here that there are a large number of organic molecules of technological and medical relevance being prepared in laboratories and industries in present time. However, the experimental setup and environmental conditions are more or less similar, except they use mild fluorinating agents and require lower temperature as well as a medium suitable for final products, reactants and F^- ions. For controlled fluorine release, mostly organic fluoride while some time inorganic fluorides are used. In this chapter the details of fluororganic and fluoropolymeric materials are not covered in the aim to restrict this compilation to the inorganic fluoride materials. Some of the important aspects of experimental conditions and methods are explained in subsequent sections.

4.5.1 Fluorinating Reagents and Common F^- Ion Sources

In general, F_2 and HF serve as most common reactants for preparation of fluorides. However, a large number of inorganic or organic fluorides can also be used for preparation of fluorides. Often organic fluorides are prepared using the solid fluorides, like NaF, AlF_3, PVDF, etc. or suitable reagents, like fluorinated organic acids, alcohol or esters as fluorinating and/or reactants. These reagents provide F radicals or F^- ions under certain thermodynamic conditions and they react with other reactants forming fluorides. In additions some of the fluorinating reagents, like NH_4F, NH_4HF_2, KHF_2, etc. can also form a complex fluoride or oxyfluorides depending on their nature and they subsequently decompose to fluorides or oxyfluorides. However, some of the fluorinating the reagents can also change the oxidation state of the metal or nonmetal during the course of the reactions. Such redox properties of the fluorinating reagents are governed by the other ion or radical produced by them. For example, the reagents like BrF_3, XeF_2, NF_3, etc. have strong tendency to oxidize other elements due to the strong electron affinity of Br^+, Xe^{2+} and N^{3+} ions. Similarly, hydrazine fluoride acts as a mild reducing agent due to the formation of native H radicals during the fluorination process. Some of the fluorinating reagents commonly used for fluoride preparation and their reaction process are summarized in Table 4.6.

4.5.2 Materials Compatibility

It has been mentioned earlier that F_2 or HF reacts with almost all the elements except a few rare gases under some conditions, and hence the working equipments with these reactants need special attention. Because of their high reactivities, only limited materials are used as reaction equipments, like container, storage and flow lines in preparative fluoride chemistry using F_2 or HF. But the reactivity other fluorides, like metal or nonmetal solid fluorides are less compared to F_2 and HF and thus a relatively wider choice of materials exist. However, still the choice is limited due to the corrosive nature of the F^- ions as well as their hydrolysis and subsequent corrosion from the generated HF. The F_2 can also oxidize water giving a mixture of O_2, O_3 and HF. At ambient conditions, F_2 reacts slowly with metals except higher electropositive ones, but at higher temperature it reacts vigorously with all metals. This can be attributed to higher free energy of formation of metal fluorides. The equilibrium constant between the metal to fluorine or fluoride reactions and free energy of formation of fluorides govern the suitability of that metal as container for fluoride preparation. The typical temperature dependent free energy traces for metal fluorine reactions are also used for extraction of metal from fluorides.

Depending on the temperature, nature of reactants and products, different types of materials are selected for container and other accessories for proportion. Some of the materials and their usability are summarized in Table 4.7. All the equipments need to be free from moisture as well as OH^- groups while using F_2, HF as well as fluorides

Table 4.6 Typical fluorinating agents used for fluoride preparation and fluorination of materials

Reagents	Physical state	Process
F_2	Gas, liquid	Oxidation and fluorination
HF	Liquid, Aq. Soln., gas	Acid–Base and halide exchange
BrF_3	Pale yellow liquid	Oxidation, Fluorination
AgF_2	Solid	Oxidative fluorination
AsF_3	Liquid	Oxidative fluorination
ZnF_2, CdF_2, PbF_2	Solid	Displacive fluorination
SF_4	Gas	Moderate fluorination
SbF_5	Colorless oily liquid	Oxidative fluorination
NF_3	Colorless gas	Oxidative fluorination
XeF_2	Colorless solid	Oxidative fluorination
NH_4F	Colorless solid	Fluorination
NH_4HF_2	Colorless solid	Fluorination
$N_2H_6F_2$	Colorless solid	Reductive fluorination
NaF, KF, RbF, CsF	Solutions	Displacive fluorination
Metal fluorides	Solid	Additive or displacement
Teflon	Solid	Mild fluorination
CF_3COOH	Liquid	Mild fluorination
PVDF	Solid	Mild fluorination

for preparing fluorides by moderate or high temperature reactions. Platinum is practically inert to fluoride salts up to very high temperature while the presence of oxygen and water also limits their repeated usability. At lower temperature, below 100 °C, Teflon and Teflon-like polymeric materials are best suited for fluoride preparation reactions. Common laboratory glassware free from hydroxyl group and moisture may be used to carry out reactions with fluorine gas under low pressure and lower temperature. Glassy carbon coating on glassware can provide some protection while working with fluoride salts.

Table 4.7 Typical reactor and container materials for fluorine chemistry[a]

Material	Composition	Compatibility					Max. Temp. (°C)
		Solid fluoride	Molten fluoride and HF	Gases fluoride	F_2	HF	
Nickel	Ni	Yes	Yes	Yes	Yes	Yes	650
Monel	67% Ni, Cu	Yes	Yes	Yes	Yes	Yes	550
Copper	Cu	Yes	Yes	Yes	Yes	No	400
Brass	Cu (50–65%), Zn	Yes	Yes	Yes	Yes	Yes	200
Stainless steel	Fe Cr 11–20%	Yes	Yes	Yes	Yes	Yes	<200
Aluminum	Al	Yes	No	No	Yes	No	400
Platinum	Pt	Yes	Yes	Yes	Yes	Yes	1000
Hasteloy	Ni Mo-15–17%, Cr 14–17, Fe 4–7, W 3–5	Yes	Yes	Yes	Yes	Yes	800
Teflon	$(C_2F_4)_n$	Yes	Yes	Yes	Yes	Yes	100
Graphite	C	Yes	Yes	Yes	Yes	Yes	800
Glassy carbon	C	Yes	Yes	Yes	Yes	Yes	800

[a]Compositions of alloys are compiled from various Internet sources

4.5.3 Toxicological Effects

The fluorine and fluorides have hazard potential to health and environment which are related to their high reactivity. Due to their hazardous natures for long time the fluorine was considered as a "devils' element" to work with. It is now accepted that fluoride ions have dual health effect, like at lower concentration they have beneficial effect to human, particularly on tooth and bone formation, while at higher concentration they become hazardous. From a number of case studies as well as from the knowledge on chemistry and biochemistry of fluorine and fluorides, safety limits for exposure or intake have been formulated and guidelines for their usage have been documented. With the advancement of materials and infrastructure as well as safety guidelines for handling, the fluoride chemistry becomes more popular and usable in common laboratories. But it needs to mention here that the careful handling and safety precaution are essential to remain within the tolerance limits. The compounds of fluorides are readily absorbed by the stomach and intestines, and excreted through the urine. Urine tests have been used to follow the F_2 or F^-exposure and to set upper limits for exposure to them.

Apart from toxicity of other associated elements in fluorides, the chemical toxicity issues in fluorine chemistry are due to molecular fluorine, F^- ion and acidic HF. The toxic effect of fluoride salts is in general due to HF or F- produced by hydrolysis.

Toxicity of fluoride (F^-) ions

The contact of high concentrations of any fluoride salts to skin or eye is dangerous. Due to higher electronegativity of fluoride ions, they are attracted to calcium ions of teeth and bones. The toxic levels of fluoride have been associated with the weakening of bones and increasing risk for hip and wrist fractures due to precipitation of CaF_2 in bone from apatite. Dental fluorosis, skeletal fluorosis and deformation of bones are the results of excess fluoride ions in animals. In the high dosage, F^- ions can also interfere with the metabolism of carbohydrates, lipids, protein, vitamins, enzymes and minerals. Skeletal deformation and weakening of joints in plant and animals are typical for the high levels fluoride intake. About 0.5–1.0 mg/L in drinking water has been recommended by World Health Organization (WHO) for optimal dental health. Bureau of Indian Standards (BIS) has recommended 1.0 ppm (maximum tolerable limit is 1.5 ppm) in drinking water in India.

Toxicity of HF

Apart from all the F^- ion induced hazards, HF also has additional hazardous potential due to its acidic and corrosive properties. The threshold limit value (TLV) for HF intake is 3 ppm (parts per million). HF produces fume which can directly go to body through inhalation and forms an aqueous HFsolution. HF_{aq} reacts with biochemically important ions like Ca^{2+} and Mg^{2+} of human body and at higher concentration these ions are precipitated as CaF_2 or MgF_2. Thus, HF in animals primarily causes hypocalcaemia and hypomagnecia. Severe or over-exposure can cause death also. HF_{aq} also interacts with many other metal oxides in the body, forming fluoride compounds. Exposure of HF to skin causes itching, scaling, reddening, blistering, etc. Exposure of HF in low concentration (<20 ppm) shows delayed effect, like the symptoms are realized in about 24 h. However, all effects are immediately felt in exposure of high concentration of HF (above 50 ppm). Severe or over-exposure HF can cause death within few hours also.

Toxicity of F_2

The toxic effect of F_2 is due to its strong oxidizing nature and also due to its transformation of HF by reacting with water. Fluorine is accepted as a toxic gas (LC_{50} = 185 ppm). Fluorine is the most powerful oxidizing material and hence it enhances the burning rate, and also can cause ignition. A leak of pure fluorine will usually cause a fire. Also, F_2 can produce ozone, hydrogen peroxide and oxygen fluoride with water and they are also strong oxidants. The corrosive and oxidizing actions of F_2can burn soft tissues. Fluorine has a low odor and hence can be easily sensed by nose.

Due to the chemical and biochemical reactivities, fluorine and fluorides need to be handled with care. Thus, appropriate hand gloves and gas masks as well as goggles are required while working with fluorine or fluorides. The preliminary remedies for

fluoride exposures are: dipping or washing with lime solutions or application $CaCl_2$ or $Ca(OH)_2$ solutions or slurries or paste. These solutions usually counter the effect of F^- ions on tissues. Lotions containing Ca^{2+} and Mg^{2+} ions are also used for minor contaminations. Solutions of calcium gluconate also injected for remedy of internal F^- ion contaminations. Any exposure of F^- ions needs a consultation from doctor.

4.6 General Preparation Chemistry

4.6.1 Gas–Gas

Several fluorides can be prepared by reaction of gaseous mixture of reactants where at least one of them needs to be a fluorinating agent. Usually gaseous F_2, HF, PtF_6, XeF_4, etc. are used as fluorinating agent. Such reactions are often violent and exothermic, and spontaneous or self-propagating. Depending on the nature of reactants, it may require external parameters like ignition, heating or irradiation to initiate the reaction and the reaction completes spontaneously or the reaction continues as a chain reaction.

The preparation of HF can be done by simple mixing of H_2 and F_2 gases. However, the reaction of liquid H_2 with F_2 is more spontaneous than the gaseous mixture, which can be attributed to higher stability of H_2 to dissociate as in the case H_2 and O_2 reaction. The reactions proceed through the interaction of atomic hydrogen and molecular F_2. Thus, irradiation with light, presence of smaller impurity or catalyst and temperature activate the F_2or break hydrogen molecules. Mostly the gas phase reactions are carried out in closed container or a container with provisions to feed the gases and to collect products. The gas phase reactions involving F_2 can be carried out in pyrex or quartz glass rector, but they corrode very fast. These reactions can be carried out in monel, inconel or nickel reactors.

Similar homogeneous gas phase reactions have been used to prepare noble gas compounds. A number of ionic salts of Xe and PtF_6, like $[XeF]^+[PtF_5]^-$, $[XeF]^+[Pt_2F_{11}]^-$, and $[Xe_2F_3]^+[PtF_6]^-$ have been prepared at room temperature by the reaction of Xe and PtF_6 gases in a gaseous medium of SF_6 [39]. Also, XeF_2, XeF_4 and XeF_6 are also prepared by gas phase reaction of PtF_6 and Xe [39]. Xe and F_2 also react under high pressure at room temperature to form xenon fluoride compounds and the XeF_6 is favored with the increase in pressure and decreasing temperature while XeF_2 is favored with decreasing pressure and increasing temperature [40]. At room temperature a mixture Xe and F_2 exposed to day light also produces XeF_2 [41]. However, reaction of Kr with F_2 is not favorable in gas phase, but can occur fast on the interaction of F_2 with liquid Kr. Similarly, reaction of NF_3 with BF_3, AsF_3, PF_5, etc. occur in gas phase at low temperature under the UV or γ-ray irradiation or electric spark. Compounds like NF_4BF_4, NF_4AsF_6, etc. have been prepared by such processes [42]. The gas phase reactions involving F_2, PtF_6, SF_6, etc. are usually free radical reactions and thus they occur on exposure to different radiations, including the visible lights.

4.6.2 Liquid/Solid–Gas

Preparative fluorine chemistry has also been extensively exploited by using gaseous fluorinating agents with solid/liquid materials. It has been mentioned earlier that KrF_2 can be conveniently prepared by reacting liquid Kr and gaseous F_2. Such reactions depend on the pressure of fluorinating gas and temperature. The reaction of liquid H_2 with F_2 gas is spontaneous and forms liquid HF. Gaseous HF and F_2react with organic materials by displacement or additive reactions. Unsaturated hydrocarbons form fluoro or polyfluoro hydrocarbon by the interaction of F_2 gas. Varieties of fluoropolymers have been prepared by such solid gas reactions. These reactions again proceed by homolytic cleavage of bonds forming radical.

Highly pure metal fluorides are prepared by reaction of HF with solids where the elimination of oxygen occurs by fluorine substitution. The reaction involving F_2 can be oxidative fluorination while with HF they are usually substitution reaction. As an example, UO_2 reacts with HF forming UF_4 while with F_2 gives UO_2F_2 or UF_6. U_3O_8 reacts with H_2–F_2 mixture to produce UF_4 while with only F_2 it transforms to UF_6. Solid UF_4 powder on mixing with F_2 at temperature above 300 °C explosively form UF_6 gas.

Most commonly fluorides are non-reactive to fluorinating agents, however, fluorides with cations of higher oxidation can be prepared by the reaction of gaseous fluorine (F_2), PtF_6, MoF_6, etc. with their stable fluorides. For example, TiF_3, CeF_3, MoF_4, SnF_2 can be transformed to TiF_4, CeF_4, MoF_5, SnF_4, etc. by reacting them with F_2 gas. Thus, such oxidative fluorination by gaseous F_2 is becoming popular for purification of materials, managements of wastes, and in particular nuclear waste. The volatile nature of fluorides of metals in high oxidation state are used for separation of actinides, noble metals, transitions metals, like Mo, W, etc. in nuclear waste. Ti metal under red hot condition reacts with gaseous HF to produce TiF_4 while Ti metal can react with F_2 gas faster to form TiF_4. The reducing atmosphere created by H_2 generated Ti-HF reaction prevents the highest oxidations state of Ti [43, 44]. Zr metal can be reacted with both HF and F_2 to produce ZrF_4 by high temperature fluorination. However, pure ZrF_4, TaF_5, NbF_5, etc. are usually prepared by reaction of their hydrides with F_2 gas at high temperature. ZrO_2 reacts with gaseous F_2 or HF forming wide varieties of oxyfluorides rather than ZrF_4, while at high temperature complete ZrF_4 is formed [45]. Similarly, reductive fluorination of fluorides or oxides can also be carried out using HF and H_2or H_2 and F_2 mixture. For example: TiOF, CeOF type oxyfluorides can be prepared by reaction TiO_2 and CeO_2 with H_2 and F_2 mixture.

4.6.3 Solid/Liquid–Liquid

Liquid HF and aqueous HF are common reagents for fluorination and preparation of fluorides. Almost all metals react with liquid HF and aqueous HF analogous to

metal acid reactions producing salt. Similarly, metal oxides or carbonates also react with the HF producing metal fluorides. All the metal fluorides of electropositive elements, like alkali, alkaline earth and rare-earths, can be prepared by reacting their oxides, carbonates or hydroxides with liquid as well as aqueous HF. Depending on the natures of the metal ions, like electro-positivity and charge they may form a homogenous solution from which the fluorides can be crystallized by evaporating the solution. Also, in several cases, pure fluorides can be directly precipitated from aqueous solutions due to their low solubility in water. For example, all the alkali metal fluorides can be separated from reaction medium by evaporating the solvent. Alkaline earth metal as well as rare-earth fluorides are less soluble in water and thus they precipitate out from the aqueous medium. In general fluorides are less soluble compared to their corresponding chlorides, and thus they can be prepared even from chlorides. Solution and solid liquid methods of preparation of fluorides can be grouped as precipitation, solution crystallization, and controlled crystallization as in hydrothermal and sol–gel processes.

4.6.3.1 Solid–Liquid

The solid and liquid HF reaction methods for preparation for fluorides can be acid–base type or diffusion of F^- into the solid. The reactions of metal and liquid and aqueous HF have been investigated widely to study corrosion behavior as well as for preparation of fluorides [44]. In a diffusion assisted reaction, the reaction occurs only at surfaces in the initial stage and then propagates slowly to the interior. The etching of crystal surfaces as well as cleaning of crystal or film surfaces can be carried out by such process.

For preparation, such reactions are usually carried out at higher temperature and/or higher pressure. Since the diffusion-controlled reactions are slow processes, they are exploited to grow single crystals of fluoride and oxyfluorides. BiOF, LnOF (Ln = Lanthanide ion) type oxyfluorides though can be prepared by such liquid solid reactions, like Bi_2O_3/Ln_2O_3 + HF = BiOF/LaOF, the stoichiometry is difficult to ascertain by such reaction, as they are usually controlled by time and nature of solid materials. The morphology and structure of oxides are also dominating features for such reactions; viz. Al_2O_3 is less reactive to both liquid and gaseous F_2 and HF but the oxides of alkali, alkaline earth and rare-earths are more reactive. Al_2O_3 reacts with aqueous HF forming $Al_2O_xF_y$ (where $x + y = 3$) and gradually ended with gamma AlF_3 and finally to alpha AlF_3 on prolonged reactions. Also by controlling the fluorination time and temperature varieties of porous AlF_3 structures can be obtained by such solid Al_2O_3 and HF reactions.

4.6.3.2 Liquid–Liquid

Liquid phase fluorinations are the most commonly used method for preparation of fluorides. This can be carried out by reaction of reactants with at least one of

them as fluoride ion source. Commonly the soluble salts of fluorides, like NaF, KF, RbF, CsF, NH_4F, NH_4HF_2, $NaHF_2$, KHF_2, as well as salts of PtF_6, SF_6, BF_3, SiF_4, XeF_6, KrF_4, etc., and solutions of HF are used as fluoride ion sources. Also a number of fluoro-organic compounds, like trifluoroacetic acids, fluoroalcohols, 4-iodotoluene difluoride, silver trifluoro methane sulfonate, HF-amine complexes, like HF-pyridine, etc. are used for mild fluorination of organic compounds. Some of the organic synthesis use intermediate fluoride during the path for the desired product. Typically, such reactions are carried out in open Teflon containers or closed Teflon, Ni, monel or inconel lined autoclaves. The solvent can be aqueous or organic liquids while the environment can be inert or air, depending on the stability and reactivity of the products. Some of the examples of liquid–liquid reactions for preparations are explained below.

In general, the fluorides are less soluble compared to chlorides and nitrates, and thus they can be precipitated from the solution by adding soluble fluoride salt to the medium. For precipitating fluorides, soluble salts, like HF, NaF, KF, NH_4F, NH_4HF_2, etc. are added to the homogenous solution of metal ions. Temperature and pH of media have importance in such precipitation processes. Wide varieties of binary fluorides, in particular fluorides of heavier ions and higher charge ions can be precipitated from solutions. SrF_2, BaF_2, LnF_3 (Ln—lanthanides), PbF_2, BiF_3, etc. can be easily prepared by treating their nitrate solutions with aqueous HF. Often incorporation of OH^- in fluorides is encountered due to similar charge and size. On subsequent heat treatment they can also lead to formation of oxyfluorides. $TiF_{2-x}(OH)_x$ type hydroxide fluorides prepared by such process for catalytic and photocatalytic applications. Several types of complex fluorides can also be prepared by precipitation or slow crystallization of solutions. Cubic $NaYF_4$ can be precipitated by treating YCl_3 or $Y(NO_3)_3$ solution with NaF solution. Similar complex fluorides of other lanthanides can be conveniently prepared by analogousreactions. Some cases of such preparations are explained in later section.

Complex fluorides, like Na_3MF_6 (M = Al. Ga, Fe, etc.) can be prepared from solution containing Na^+, M^{3+} and F^- ions by slow crystallizations. Such process may also crystallize their hydrated compounds. The small cations usually form anionic fluoride units and they remain in solutions. Thus, slow evaporation of solvent leads to crystallization of the stoichiometric complex fluorides. In an analogous procedure, the molten mixture of fluorides on slow cooling crystallizes the stoichiometric complex fluorides. The formations and cooling procedure form the basis of crystal growth of complex fluoride and they are mainly guided by the phase diagram. However, complex fluoride salts of NH^{4+} ions need to be prepared by slow evaporations of their homogenous solutions.

From the homogenous solutions, simpler or complex fluorides can also be crystallized by using hydrothermal or solvo thermal procedures. Salts of desired cations and some fluoride ion sources are dissolved in suitable solvent and filled in a Teflon-lined stainless steel autoclave or directly in monel or inconel autoclaves. Water, alcohols, or their mixtures are in general used as solvent in such processes. The autoclave is heated at different temperature and time to optimize the conditions for formation of desired products. Size and shape-controlled preparation of complex fluorides

can be achieved by this method. The vapor pressure generated from the solvent at higher temperature generate pressure due to closed reactor assembly, and the reaction proceeds analogous to high temperature and high pressure or variation of solubility and reactivity of the components under simultaneous pressure and temperature condition. In such hydrothermal process, even colloidal solutions, solid and liquid mixture can also be used as reactants. Often dissolution of insoluble solid is enhanced due to the increasing corrosive nature of F^- ions. Further additional salts can also be used as mineralizer to enhance the solubility of reactants. The basic procedure and principles are closely similar to those used for oxides except the medium contains F^- ion or some fluorinating reagent.

Sol–gel methods for synthesis of fluorides are also carried from homogeneous liquid medium. Depending on the medium, method of hydrolysis, presence of additional ions and nature of the final fluorides, the method can lead to fluoride or oxyfluorides. This procedure is extensively used to prepare fluoride or oxyfluorides with controlled morphology, like, nanosized, porous, particles with large surface area. Stable binary fluorides, of alkaline earth, rare-earth, and several transition metal fluorides, like Fe, Co, Zn, Cd and Al, Ga, Pb, Bi, etc. can be prepared by aqueous sol–gel process due to the higher stabilities of their fluorides. However, the aqueous sol–gel process for fluorides of Fe, Ti, Zr, Hf, etc. may lead to fluoro hydroxy compounds. Non-aqueous sol–gel process, using alcohol or alcoholic solutions are used to prepare pure nanosized fluorides.

In general, the sol–gel processes for preparation of fluorides are two types, one involves synthesis nano metal oxides followed by fluorination while the other is preparation of a fluorinated gel followed by thermolysis. In the first process, the procedure is similar to sol–gel chemistry adopted for oxides while in the second process, a gelating agent which acts as a fluorinating agent and a non-aqueous medium are used. The second process of preparation can also be carried out by hydrolyzing metal alkoxides in a medium containing F^- ions. The controlled hydrolysis of the alkoxides leadsto the formation of a clear sol, which on slight heating form a gel. The metal ions are encapsulated inside gel where the precipitation of the metal ions either as fluoride or oxide is prevented. On decomposition, the metal fluoride is separated out from the gel. The fluoro-acids are often used as gel forming agent so that the network structure of gel is stabilized. Sol–gel synthesis for MF_2 or MF_3 are carried out by using metal alkoxides (M^{2+} = Zn, Cd, Mg, etc.; M^{3+} = Al, Ga, Fe, etc.) in an alcoholic mixture of trifluroaceteic acid. A complex gel containing alkoxide groups, trifluroacetate groups and metal ions is formed on slow evaporation of the solvent. The fluorination of metal ions occurs inside the gel by the trifluoroacetic acid and on thermolysis they separate out.

4.6.4 Solid–Solid

Solid-state reactions of fluorides have been exploited extensively to prepare complex fluorides with more than one cation. Such reactions are carried out by heating

homogenous mixture of component fluorides at higher temperature. Owing to the limited stabilities of fluorides these solid-state reactions need to be carried out under controlled atmosphere or in vacuum. These are diffusion-controlled reactions, and owing to higher mobility and lower melting points of fluorides, these reactions can occur at relatively lower temperature compared to oxides. Also, to avoid the incorporation of moisture or hydroxyl groups in the reactants, all the preprocesses like weighing and homogenization of the reactants are carried out in argon filled glove box with permissible moisture and oxygen content. This is essential to prepare as well as to use hygroscopic reactants, like RbF, CsF, etc.

In this method, pellets of homogeneous mixture of reactants are placed in platinum tube or foil and placed inside a quartz tube and sealed under vacuum or inert atmosphere like argon. Such double sealed ampoules are commonly used for preparation of complex fluorides free from oxide impurities. A typical double sealed ampoule used for preparation of fluorides is shown in Fig. 4.8. Also, some of the complex fluorides can be prepared by heating the mixture of fluorides under a flowing inert atmosphere.

Similar to the preparative oxide chemistry, the fluoride preparation by solid-state reactions are also affected by external thermodynamic parameters, like pressure and temperature. Mechanical pressure on solid fluorides also shows polymorphic transitions like oxides and the high pressure phase may or may not revert back to the original ambient pressure phase. Simultaneous application of pressure and temperature is also used to prepare single and multi-component fluorides with unusual and metastable structures. For example, cubic PbF_2 which is metastable under ambient pressure and temperature, can transform to stable orthorhombic PbF_2 under pressure, and retains the stable structure on releasing the pressure. Similarly, mechanical mixing with high energy milling can cause the reactions of the fluorides, where the local temperature and stress under grinding favor for the formation of products. FeF_3, LaF_3, UF_4, etc. can be prepared by mechanical mixing of their corresponding oxides and excess of NH_4F or NH_4HF_2 in high energy ball mill.

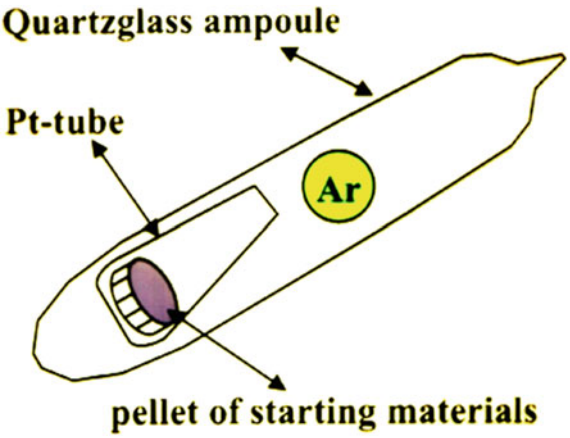

Fig. 4.8 A double sealed sample ampoule used for preparation of fluorides by high temperature solid-state reaction

High temperature solid-state reactions are also carried out to prepare oxyfluorides using desired amounts of component oxide and fluorides. As mentioned earlier, the O^{2-} and F^{-} in oxyfluorides can form an anion disordered lattice due to closely similar ionic radius. The desired reaction and ordering of oxide and fluoride ions depend on the nature of the final products as well as heating and cooling procedures. However, the anion ordering can be easily observed with the multiple cations having different bond strengths of M–O and M-F bond and the preference for oxide or F^{-} ions. Oxyfluorides show rich composition-structure relations and exhibit diversified crystal structures depending the O:F stoichiometry and degree of ordering of the anions. As an example, Bi_2O_3–BiF_3, ZrO_2–ZrF_4, Ln_2O_3–LnF_3 and so many others with different metal oxides and fluorides can form different structures with different degrees of O^{2-} and F^{-} ion ordering. These reactions can be carried out by using desired amounts of oxides and fluorides at same or different temperatures.

A variety of fluorides and oxyfluorides can also be prepared by using NH_4F, NH_4HF_2, KHF_2, $NaHF_2$, etc. which can act as both fluorinating agent as well as reactant. The reactions of these materials are fast as the reaction can occur by solid–solid, solid–liquid and solid–gas. In presence of moisture, they form a concentrated solution of HF and hence the reactions become faster like solid–liquid HF reaction. In addition, these materials have lower melting point and thus the molten materials can fluorinate and react in a similar solid–liquid reaction mode. However, the solid–solid reactions proceed very slowly at ambient or just above ambient temperature. Most commonly a little excess of NH_4HF_2 or NH_4F is used to compensate any loss due to sublimation and/or decomposition. These reactions proceed through intermediate complex fluorides of NH_4^{+} and metal ions, and subsequently they decompose to metal fluorides or oxyfluorides oxides. Thus, these reactions provide a simper pathway to prepare complex fluorides and oxyfluorides of transition metal and rare-earth ions, but not limited only to them. A complex oxyfluorides of V^{5+} with both NH^{4+} and K^{+} ions has been prepared by reacting desired amounts of NH_4HF_2 and $KHF_2$with V_2O_5at RT which has been explained in later section.

4.6.5 Fluorides of Cations with Unusual Oxidation State

As mentioned earlier, fluorides can be prepared with metal and no metal ions with their highest oxidations states. F_2 itself can oxidize the metals and nonmetal to the highest possible oxidation states while fluorinations with F_2. Several instances for high oxidization cation fluorides have been explained earlier and they are subsequently used as a F_2 source or strong fluorinating reagents. The preparation of such high oxidation may require high pressure of F_2 and a suitable temperature. Complex fluorides with Pr^{4+}, like $BaPrF_6$ and Li_2CaPrF_8 have been prepared by fluorinating reaction of F_2 gas at high pressure [46]. However, the fluorides with lower oxidation state of metal ions can also be prepared under suitable conditions. In such cases, the oxidation states are controlled by using metal or strong reducing agents. The stabilities of low valent fluorides are less compared to their analogous compositions

with other halides. Example, CeF_2 is extremely difficult to prepare while CeI_2 can be easily prepared by metallic Ce end I_2 reactions. A large number of binary fluorides of divalent rare-earths ions, like Eu, Sm, Tm, Yb can be prepared by using rare-earth metal and LnF_3 reactions [47, 48]. Also, reduction of LnF_3 by graphite or H_2 at higher temperature can also be used for preparation of LnF_2 [48, 49]. Among the lanthanides, EuF_2 has higher stability and can be prepared by interaction of $EuSO_4$ with alkaline solution of NaF [49] Similarly, FeF_2, MnF_2 can be prepared by reaction of metal with gaseous or liquid/aqueous HF. $InBF_4$, a complex fluoride with monovalent In^+ has been prepared by interaction of In metal with anhydrous HF and BF_3 [50]. Series of fluorides with In^+ and Tl^+ ions as $InPF_6$, $InAsF_6$, $TlPF_6$ and $TlAsF_6$ have been prepared by solvothermal reaction of In or Tl metal with PF_6 or AsF_6 in anhydrous HF medium [51]. TlF can be prepared by reaction of Tl_2CO_3 and aqueous HF. Fluorinating reactions of oxides or carbonates of lower valent metal ions with aqueous HF under mild conditions generally retain the oxidation states of the metal ions.

4.7 Representative Examples

a. Preparation of $LiBaF_3$ and $LiEuF_4$

$LiBaF_3$ and $LiEuF_4$ are the examples of simpler perovskite and scheelite type compounds which show significant interest as optical material. These fluorides are stable and almost insoluble in water under normal conditions. Thus, they can be prepared by a wide variety of methods, like crystallization from solvent, hydrothermal or solvothermal, sol–gel processes or conventional solid-state reactions. BaF_2 and LiF are immediately formed when the aqueous solutions containing Ba^{2+} and Li^+ ions (either as nitrate or chlorides) ions are treated with aqueous solutions of HF. Since LiF is more soluble than BaF_2, the solution of LiF progressively reacts with solid $BaF_2$to crystallize $BaLiF_3$. In hydrothermal process, aqueous or alcoholic solution or colloid containing Ba^{2+}, $Li^+$and F^- ions is heated in an autoclave under autogenously generated pressure of water vapor. In such process, slow crystallization of $LiBaF_3$ occurs from the solutions. Solid-state reaction of LiF and BaF_2 occurs around 600 °C giving the $LiBaF_3$ phase. In all these process, $LiEuF_4$, $LiYF_4$, etc. can also be prepared. Since these materials are congruently melting solids, slow crystallization of melt can produce their singe crystals. Large crystals of $LiEuF_4$, $LiYF_4$, etc. are grown by Bridgeman crystallization method from molten solutions LiF and BaF_2 orYF_3/EuF_3, etc. [52]. The composition dependent phase evolutions in LiF-BaF_2 system (Fig. 4.9) have been studied by heating different compositions at 750 °C followed by cooling to room temperature [53].

Compared to $LiYF_4$, preparation of $NaYF_4$ has interesting behavior due to its polymorphic nature. Different polymorphs of $NaYF_4$can be prepared by controlling the preparation conditions [54, 55]. The cubic (c) fluorite type phase of $NaYF_4$is the high temperature polymorph and exists as a metastable phase at ambient conditions.

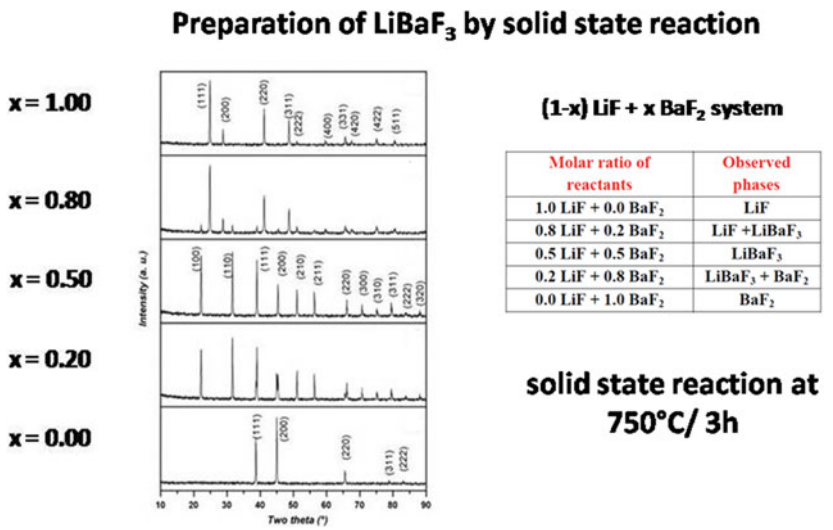

Fig. 4.9 Evolution of phases in LiF-BaF_3 system with composition at 750 °C and preparation of phase pure $LiBaF_3$. Reproduced from Ref. [52] with permission of Elsevier

The cubic $NaYF_4$ can be prepared by suitable low temperature synthesis procedures. $NaYF_4$ precipitated from YCl_3 solution by aqueous solution NaF has cubic fluorite type structure, while sample prepared by solid-state reaction at higher temperature has hexagonal (P-6) structure. Typical reaction for preparation of c-$NaYF_4$ by precipitation method is given below

$$YCl_{3,\,aq.} + 4NaF_{aq.} \xrightarrow{H_2O,\,RT} c - NaYF_4 \downarrow + 3NaCl$$

The precipitate is washed with water to remove NaCl and the dried around 100 °C to get cubic fluorite type $NaYF_4$. In this Na and Y are disordered and eight coordinated as in the fluorite lattice. The solid-state reaction of NaF and YF_3 can lead to hexagonal $NaYF_4$ phase and the conditions for reaction are written below

$$YF_3 + NaF \xrightarrow{930\,^\circ C,\,24\,h} h - NaYF_4 \equiv Na_{1.5}Y_{1.5}F_6$$

In the hexagonal structure, the cations are ordered as well as partially intermixed. In this (P-6) lattice, there are three sites for the cations. Two cation sites are nine coordinated, one of them occupied by Y^{3+} while the other one is occupied equally by Y^{3+} and Na^+. The third cation site is half occupied by only Na^+ and is coordinated with six F^- ions.

The cubic $NaYF_4$ on heating at higher temperature and pressure forms another hexagonal ($P6_3/m$) polymorph, which is related to ambient hexagonal (P-6) phase. The preparation of high pressure hexagonal phase from cubic $NaYF_4$ is reported in references 53 and 54. The typical procedure is briefly mentioned here. Cubic $NaYF_4$

sample is placed inside a platinum tube of 2 mm in diameter and 3.5 mm in height and placed in an octahedral geometry pressure transmitting medium made from MgO–Cr_2O_3 (w/w = 95/5). The pressure is applied along the eight faces of octahedral pressure transmitting medium by a multi-anvil press. $LaCrO_3$ is used as heating elements to heat the sample while the assembly is under pressurized condition. The time and temperature and pressure are usually varied to optimize for preparation of desired sample.

$$c - NaYF_4 \xrightarrow{P,T} h' - Na_{1.5}Y_{1.5}F_6$$

$$P(\text{pressure}) = 11\,\text{GPa},\ T(\text{temperature}) = 873-1373\,\text{K}.$$

Crystalline single phase hexagonal ($h' - NaYF_4$; $P6_3/m$) phase could be obtained by heating at 1373 GPa and pressure 11 GPa. This phase is closely similar to ambient condition stable hexagonal h-$NaYF_4$phase except both the nine coordinated sites are intermixed with Na^+ and Y^{3+} ions.

Nanosized hexagonal h-$NaYF_4$can also be prepared by using yttrium nitrate and NaOH in acetic acid medium. A clear solution of Na^+ and Y^{3+} in acetic acid is prepared and isopropyl alcohol ($(CH_3)_2CHOH$) and trifluoroacetic acid (CF_3COOH) are added to this solution. The solution is stirred continuously at 50 °C to form a clear gel, which on heating in protective atmosphere gives $NaYF_4$ [56, 57].

b. **Preparation of phases in between SrF_2–YF_3**

Solid-state reaction of SrF_2 and YF_3 in the complete range of stoichiometry has been investigated by heating the homogenous mixture at temperature 1073 K [58]. Pellets of homogenous mixture of predried YF_3 and SrF_2 (dried under flowing argon around 300 °C) were wrapped in a platinum foil and then placed inside a quartz tube as an ampoule shown in Fig. 4.8. The tube is evacuated to a vacuum of the order of 10^{-6} bar and then sealed under vacuum. The tubes containing different nominal compositions were heated in air. Since the materials are not in contact with air, they remain well protected from air or moisture at high temperature. The obtained products have been analyzed by powder XRD to study the evolution of phases. A systemic evolution of phases with increasing Y^{3+} content has been delineated and it is shown in Fig. 4.10. The evolution phases have been attributed to the cation disordering and ordering of cations and anions.

Single crystal of the complex fluorides suitable for crystal structure analyses can be prepared by a similar solid-state reaction but at relatively higher temperature. Single crystal of rhombohedral phase observed in SrF_2–YF_3 has been prepared by heating homogeneous mixture of well dried SrF_2 and YF_3, in 7:6.1 molar ratio [59]. A pellet of the homogenous mixture was placed inside a tantalum tube and crimped at the ends and then heated in a stream of dry argon atmosphere at 1300 °C, for 18 h followed by cooling to 900 °C in a span of 12 h and then by putting off the furnace. The tantalum ampoule is allowed to cool to room temperature under same flowing argon atmosphere. Colorless single crystal of the rhombohedral phase has

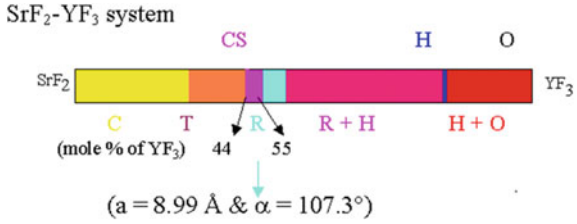

Fig. 4.10 Evolutions of phases in SrF_2–YF_3 system with YF_3 concentration; C: Cubic fluorite type, CS: Cubic super structure of fluorite, R: Rhomhohedral, H: hexagonal LaF_3 type phase, O: orthorhombic YF_3 phase (Plotted with the information presented in reference 57)

been investigated by single crystal XRD analysis. The analysis of crystal structure revealed that the sample is an oxyfluorides and the composition is concluded as $Sr_7Y_6F_{30}O$. This indicates the traces of moisture or oxygen lead to the incorporation of O^{2-} ions into lattice of fluoride. Typical crystal structure of $Sr_7Y_6F_{30}O$ is shown in Fig. 4.11.

$$7SrF_2 + 6YF_3 \xrightarrow{1300\,^{\circ}C/18\,h} Sr_7Y_6F_{32}$$

Final confirmed composition is $Sr_7Y_6F_{30}O$ as against the expected $Sr_7Y_6F_{32}$ indicates incorporation of O^{2-} from air or moisture present in the medium. The compound

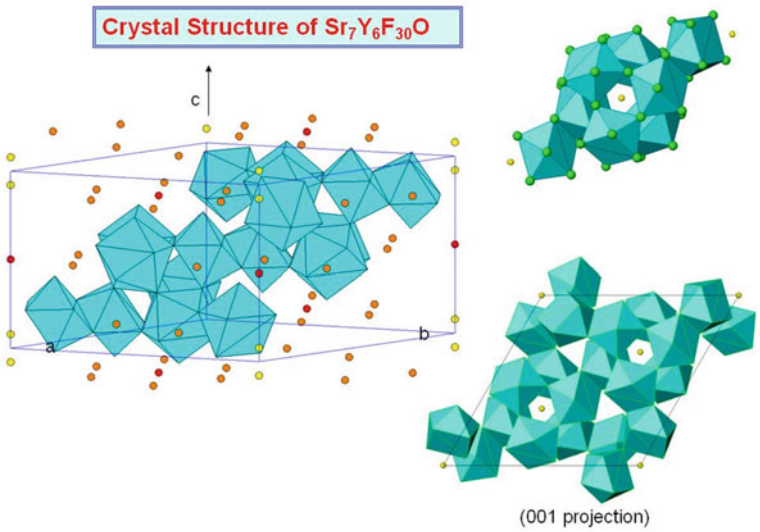

Fig. 4.11 Typical crystal structure of $Sr_7Y_6F_{30}O$. YF_8 polyhedra are shown in the figure. A cluster of Y_6F_{36} and their linkages are shown in right hand side figures. The isolated yellow spheres are incorporated O^{2-} ions inside the clusters of Y_6F_{36}. Adapted from Ref. [59] with permission of Elsevier

has a rhombohedral structure (Space group; R-3; a = 14.498(2) Å and c = 9.926(1) Å) which is closely related to fluorite (SrF_2) type structure [59]. The structure is built by arrangements of Y_6F_{36}clusters which are formed from six square anti-prismatic YF_8 polyhedra. The interstitials formed by the arrangements of these Y_6F_{36} are occupied by Sr^{2+} ions. The Sr^{2+} ions have 10 and 11 coordinated polyhedra with F^- ions. More details on such structures are available in the reference [59, 60] and references cited therein. Similar solid-state reactions have been used to prepare a number of cation and anion ordered fluorite-related anion rich fluorides in the EuF_2-EuF_3, SmF_2-SmF_3, YbF_2-YbF_3 systems [48, 49]. Anion excess fluorite-related complex fluorides, like $Ba_4Er_3F_{17}$, $Pb_4Y_3F_{17}$, $Ba_4Nd_3F_{17}$, etc. have been prepared by solid-state reaction of alkaline earth and rare-earth fluorides at high temperature [60–65].

c. Preparation of tysonite type $Sr_{0.25}Yb_{0.75}F_{2.75}$

Pure rare-earth fluorides can be prepared by a number of methods, like reaction of metal and oxides with liquid, aqueous and gaseous HF. They can also be prepared by reaction of oxides or metals with NH_4HF_2 at around 400 °C. As mentioned earlier, the structure of trivalent rare-earth fluorides (LaF_3, tysonite) form two types of structures, hexagonal ($P6_3/mmc$) or rhombohedral (P-3c1) for larger trivalent cations (La^{3+}–Nd^{3+}) while orthorhombic (Pnma) for all heavier rare-earth ions. Thus, increasing the average ionic radii of the cationic sites by substitution of cations of larger size transform the orthorhombic structures of smaller lanthanide trifluorides to hexagonal or rhombohedral structures. However, such structures usually have higher symmetric $P6_3/mmc$ due to the anion disorder in the lattice. The structures of such cationic substituted compositions depend on the nature of the cations. Also, they are formed in an optimum range of composition only, as can be seen from Fig. 4.10 for SrF_2–YF_3 phase relations. The hexagonal tysonite type phases with heavier lanthanides fluorides have been prepared by heating MF_2 (M = Ca, Sr) and MF_3 (M = Sm, Eu, Gd, Er, Yb, Y, etc.). These solid-state reactions are fast and most of the time rehomogenization and reheating are not required for completion of reaction.

$$xMF_2 + (1 - x)M'F_3 \rightarrow^{T} M_xM'_{1-x}F_{3-x}$$

M = Divalent cation and M' = Trivalent lanthanides ions from Sm^{3+} to Lu^{3+} and Y^{3+}.

The temperatures of reactions are usually above 750 °C and higher up to 1200 °C. Such solid solution samples have cation disordered tysonite type (hexagonal) structure and no ordering of cations has been observed even on cooling slowly and annealing at 1200 °C for longer time. This phase has also been prepared by heating the pellets of homogenous mixture of SrF_2 and YbF_3 at 1100 °C for 8 h followed by quenching in cold water. Typical XRD pattern and structure of tysonite type phase formed at $Sr_{0.25}Yb_{0.75}F_{2.75}$ prepared by solid-state reaction under vacuum are shown in Fig. 4.12 (hexagonal: $P6_3/mmc$, a = 3.9606(4) Å and c = 6.9731(5) Å [66, 67]).

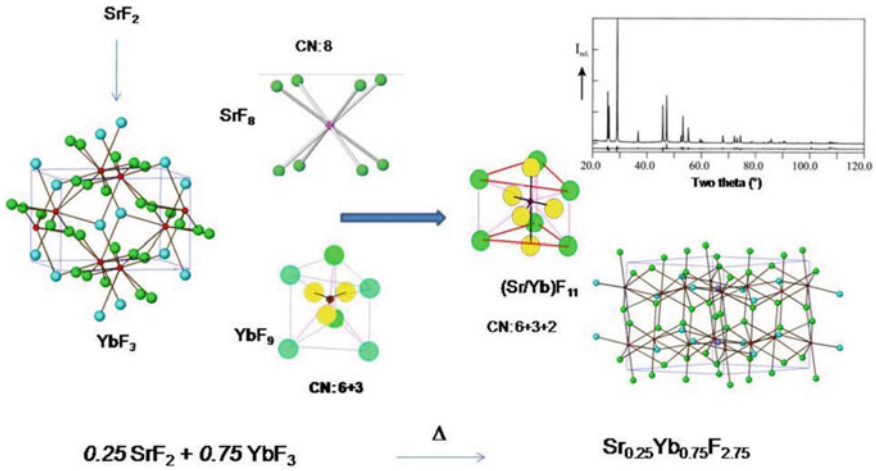

Fig. 4.12 Preparation mode and crystal structure of $Sr_{0.25}Yb_{0.75}F_{2.75}$. Adapted from Ref. [52] with permission of Elsevier

d. **Preparation of Li_3TiF_6**

Similarly, the solid-state reaction of LiF and TiF_3 in argon atmosphere or vacuum has been used to prepare Li_3TiF_6 [68]. TiF_3 can be prepared by using gas–solid reaction between gaseous HF and TiH_2 at 700 °C. Granulated or fine powder of TiH_2 is placed on a graphite or tantalum crucible and then heated under flowing HF atmosphere. This process can give high pure TiF_3 without any oxygen impurity. Pellets of homogenous mixture of LiF and TiF_3 in 3:1 molar ratio was heated at 820 °C and then cooled slowly to room temperature. The platinum used as sample container and sealed inside a quartz tube under vacuum. Purple colored single crystals are formed within the polycrystalline aggregate of cooled sample. The compound has a monoclinic lattice with unit cell parameter, a = 14.452(2) Å, b = 8.798(1) Å, c = 10.113(1) Å and β = 96.30(1)° (space group: C2/c) and is isostructural to β-Li_3VF_6. Typical crystal structure of $Li_3TiF_6$is shown in Fig. 4.13. Similarly, Li_3ScF_6 can also be prepared by solid-state reactions of ScF_3 and LiF [69]. Almost all the Li_3VF_6 type fluorides and other similarcomplex fluorides can be prepared by such method [7, 68–71].

$$2TiH_2 + 6HF_{(g)} \xrightarrow{700\,^{\circ}C} 2TiF_3 + 5H_2$$

$$TiF_3 + 3LiF \xrightarrow{820\,^{\circ}C} \beta - Li_3TiF_6$$

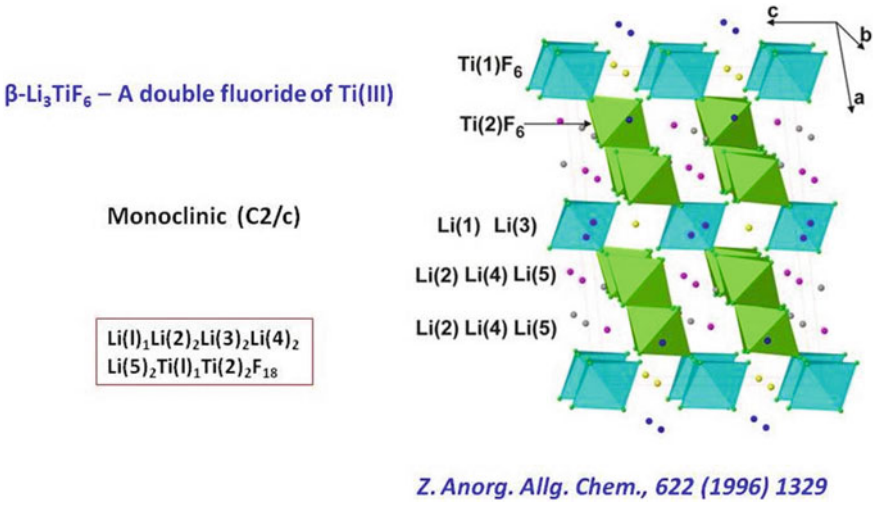

Fig. 4.13 Crystal structure of Li_3TiF_6 as observed from single crystal XRD studies (Crystal structure is redrawn with the details reported in reference [68])

e. Preparation of $BaMgF_4$

This material can be prepared by conventional solid-state reaction of BaF_2 and MgF_2 at high temperature above 800 °C in a protective atmosphere as well as by simple precipitation from aqueous solution of $Ba(NO_3)_2$ and $Mg(NO_3)_2$ using aqueous HF or solutions of NH_4F, NH_4HF_2 or NaF and subsequent suitable heat treatment [15, 72–76]. Hydrothermal method can be conveniently used to prepare this material at lower temperature. Pure $BaMgF_4$ has been prepared by hydrothermal method using aqueous solution of $Ba(NO_3)_2$, $Mg(NO_3)_2$, and NH_4HF_2 in a Teflon-lined autoclave [73]. A typical flow sheet adopted for its preparation and details of crystal structure are shown in Fig. 4.14. Judicious optimization of initial stoichiometry of Ba^{2+} and Mg^{2+} ions in solution and amount of NH_4HF_2 as well as duration and temperature are important in the formation of phase pure $BaMgF_4$. Using Ba^{2+}:Mg^{2+} as 1:1.5 (molar ratio) and excess NH_4HF_2 (~9.4 mol), pure $BaMgF_4$ can be prepared by a hydrothermal reaction at 160 °C for 60 h. Similar method can also be used to prepare analogous materials but all need an optimized ratio of reactants as well as time and temperature.

f. High pressure-high temperature synthesis of $LiScF_4$

Solid-state reactions of LiF and ScF_3 in the LiF–ScF_3 system show only one stable phase Li_3ScF_6 [69]. Li_3ScF_6can be prepared by solid-state reaction of LiF and ScF_3 at 820 °C in argon atmosphere. Li_3ScF_6 prepared under ambient condition has a rhombohedral lattice (P-3c1) with unit cell parameters: a = 8:783(1) Å, c = 9:518(1) Å. However, reaction of these two reactants (in 1:1 molar ratio) under high pressure and

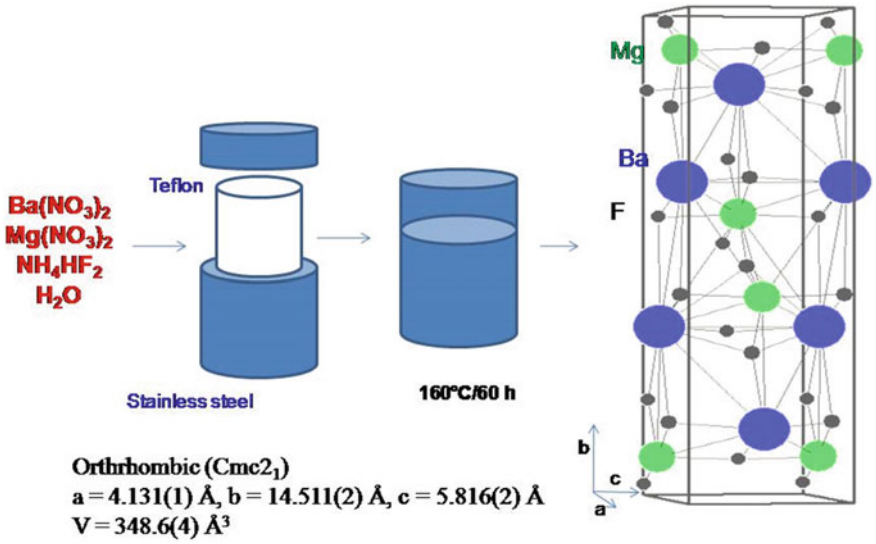

Fig. 4.14 Hydrothermal reaction for preparation of $BaMgF_4$ and its crystal structure. The reaction parameters and unit cell details are based on reference [73]

high temperature shows the formation of $LiScF_4$ phase. $LiScF_4$prepared under such condition has a scheelite type structure where Li and Sc, respectively, have tetrahedral and cubic coordination with F^- ions. This difference in phase formation can be attributed to effect of pressure, where the smaller trivalent (Sc^{3+}) ions form cubic eight coordinated ScF_8 polyhedra which otherwise favor for six coordinated ScF_6 polyhedra. In a typical experiment, homogenous mixture of LiF and ScF_3 is filled in a platinum tube and closed with a platinum cap. The tube is encapsulated inside a $LaCrO_3$ resistive heater and then placed in octahedral MgO pressure transmitting medium of a belt press. The optimization of synthesis temperature and pressure need to be carried out by trials and single phase $LiScF_4$ could be prepared at pressure and temperature of 5.5 GPa and 775 °C, respectively for 4 h. Typical structure of scheelite type $LiScF_4$and the flow sheet of preparation are shown in Fig. 4.15.

Thus, pressure and temperature are simultaneously used to prepare unusual oxidation and unusual coordination polyhedra around the cations and anions as well as denser structures. By such high pressure and high temperature reactions, a number of unusual fluorides can be prepared, which is a less explored area of fluoride chemistry.

g. **Preparation of complex mixed cation oxyfluorides**

The oxyfluorides can be conveniently prepared by solid-state reaction of oxides and fluorides. These reactions occur by the diffusion of ions through the bulk grains of reactants. Preparation oxyfluorides by high temperature reactionsare carried out in protective environments to control the O^{2-} and F^- stoichiometry. For example, LnOF (Ln—Lanthanide ions) can be prepared by heating mixture Ln_2O_3–LnF_3 above

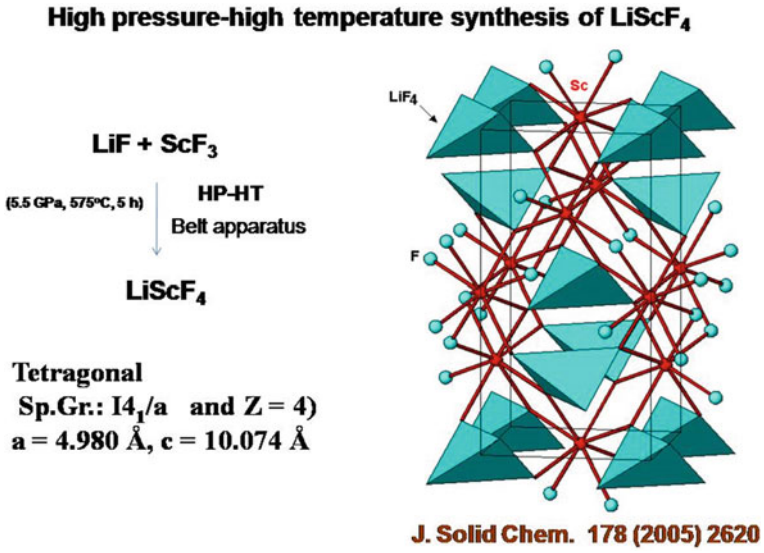

Fig. 4.15 The flow sheet for preparation of $LiScF_4$ and its crystal structure (Crystal structure is redrawn with the details reported in reference [69])

600 °C in flowing argon or in vacuum-sealed quartz ampoule [77, 78]. $V_2GeO_4F_2$, an oxyfluorides of V^{3+}ion has been prepared by heating V_2O_3, VF_3 and GeO_2 in vacuum-sealed ampoule at high temperature (700 °C/18 h) [79]. Similarly, $Cd_4Si_2O_7F_2$, a mineral analogous oxyfluorides with Cd^{2+} can be prepared by heating CdF_2, CdO and SiO_2 in sealed platinum tube at 650 °C for 24 h [80].

The oxyfluorides which has limited stability with temperature need to be prepared by alternate routes, like fluorination with reactive fluorides. In particular preparation of oxyfluorides and fluorides with NH_4^+ ion, $N_2H_6^+$ ions can be prepared by reactions of fluoride salts of ammonium or hydrazinium ions. $(NH_4)_3TiOF_5$, $(NH_4)_2TiOF_4$, and NH_4TiOF_3 type oxyfluorides can be prepared by controlled hydrolysis of $(NH_4)_3TiF_6$ in water containing NH_4OH and NH_4F [81]. The hydrolysis products depend on the pH and different oxyfluorides can be prepared controlling the pH followed by slow crystallization from the solution. Similarly, a number of oxyfluorides like $(NH_4)_3VO_2F_4$, $Na(NH_4)_2VO_2F_4$, and $(NH_4)_3NbOF_6$, etc. have been prepared by reactions of NH_4HF_2 at ambient or little above ambient temperature or evaporating solutions of containing soluble salts and NH_4HF_2 [82–84].

Preparation procedure of $(NH_4/K)_3VO_2F_4$, a typical example oxyfluorides with mixed cations has been explained here [85]. This complex oxyfluorides of V^{5+} with both NH_4^+ and $K^+$is prepared by reacting desired amounts of NH_4HF_2 and KVO_3 at ambient temperature. The homogeneous mixture of the reactants was kept in polyethene bag and stored for 2 days inside a desiccator having silica gel as desiccant. The mixture was ground after each 12 h and the progress of reaction was monitored by powder XRD. The absence of peaks due to NH_4HF_2 and KVO_3in

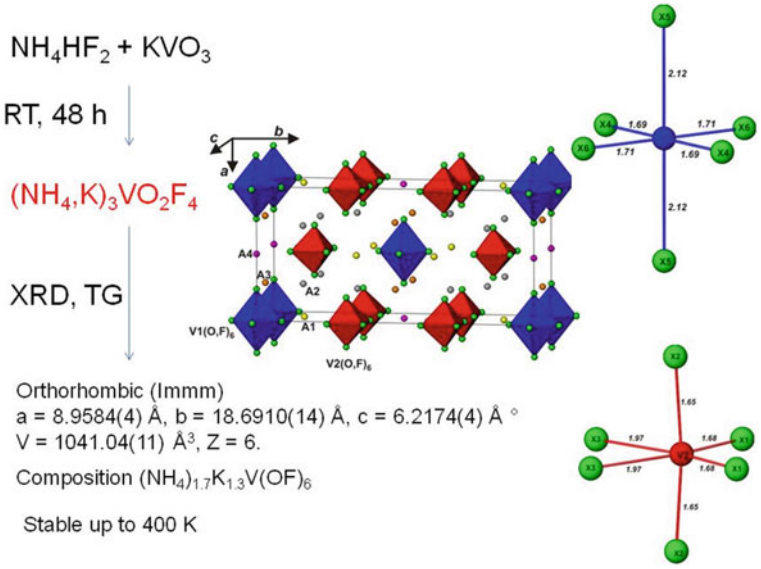

Fig. 4.16 Preparation procedure and crystal structure of $(NH_4/K)_3VO_2F_4$. The exact concentration of NH^{4+} ions has been obtained from thermogravimetric studies. The crystal structure is redrawn from the data reported in Ref. [85]

XRD pattern of sample and no further change in XRD pattern with time were used to monitor the progress of reaction and product formation. Slow diffusion of F^- ions from NH_4HF_2 transforms oxide to oxyfluorides and the negative anionic oxyfluorides group finally forms a stable complex with K^+ and NH_4^+ ions. The V^{5+} ion form an anionic $[VO_2F_4]^{3-}$ species with the F^- and O^{2-} ions and they are arranged periodically as in elpasolite type structures. The K^+ and NH_4^+ ions are statistically occupied in lattice to provide charge neutrality. Typical flow sheet for preparation and crystal structure of $(NH_4/K)_3VO_2F_4$ is shown in Fig. 4.16. Often such preparations also lead to formation of hydrated complex fluorides, and degree and stoichiometry of hydration can be controlled by the moisture content in the atmosphere.

Usually such reactions are slow but can be used to prepare complex fluorides with NH_4^+ ions as they are usually unstable at higher temperature. Also, a small excess of NH_4HF_2 are desired to avoid the loss of NH_4HF_2. These reactions need several trials to get the desired product. The compositions of such oxyfluorides need to be supported from complementary techniques, like elemental analysis, thermal analyses and other spectroscopic methods like IR, Raman, etc.

4.8 Summary and Conclusions

In this chapter a brief overview of inorganic fluorides is explained with an emphasis on their preparation and stabilities. The chapter begins with an introduction to fluorine and hydrofluoric acid, and subsequently other metal and nonmetal fluorides have been explained. The general methods for preparation which can be adopted are explained with different type chemical reactions, reactants and targeted products. The fluorides and their crystal chemistry are also touched upon. Different preparation methods have been explained with selected examples. A brief overview on preparation oxyfluorides is also presented. The fluorine chemistry, once considered as devils' chemistry, is becoming a frontier research area due to the advancement of technology, materials and technological applications. Wide varieties of fluorides and oxyfluorides prepared in recent times have shown interesting properties while many others have been tuned to obtain desired functional properties. Fluoride crystal chemistry is a growing field of research for discovery of newer materials and understanding their formation conditions. The non-conventional preparative chemistries like solvothermal, hydrothermal and high pressure-high temperature methods are still to be exploited for finding unusual and novel materials. Undoubtedly, the functional properties and applications of fluorides range in a wide spectrum and they have not been covered in this chapter to focus only on the preparative chemistry. Also, fluorine chemistry occupied a major space in the field of organic and polymer chemistry which are not covered in this chapter. Also, this chapter does not deal with fluoride glasses, which is also a reverent part in inorganic fluorides. The preparation of fluoride glasses is a highly specialized and a subject by itself, and hence deliberately spared in this chapter.

References

1. Cady GH (1950) Fluorine chemistry. In: Simons JH (ed). Academic Press, New York.
2. Peacock RD (1960) Some Fluorine Compounds of the Transition Metals. Prog Inorg Chem 2:193
3. Simons JH (1954) Fluorine chemistry, vol 2. Academic Press, New York
4. Simons JH (1964) Fluorine chemistry, vol 5. Academic Press, New York
5. Vasile D (2006) Fluorine chemistry: past, present and future. Rev Roum Chim 51:1141
6. Gouverneur V, Seppelt K (2015) Introduction: fluorine chemistry. Chem Rev 115:563
7. Tressaud A (2010) Functionalized inorganic fluorides, synthesis, characterization & properties of nanostructured solids (eds). Wiley, United Kingdom.
8. Hagenmuller P (1985) Inorganic solid fluorides, chemistry and physics, (eds). Academic Press. Inc., London
9. Paul RC, Bhasin KK, Batu RS (1995) Fluorine chemistry, an introduction, new age international, New Delhi
10. Haszeldine RS, Sharpe AG (1951) Fluorine and its compounds. Methuen Publisher, London
11. Emeleus HJ (1969) The chemistry of fluorine and its compounds. Academic Press
12. Chen TY, Tesanovic Z, Liu RH, Chen XH, Chien CL (2008) A BCS-like gap in the superconductor SmFeAsO 0.85 F 0.15. Nature 453:1224

13. Kamihara Y, Watanabe T, Hirano M, Hosono H (2008) Iron-Based Layered Superconductor La[O1-xFx]FeAs (x = 0.05−0.12) with Tc = 26 K. J Am Chem Soc 130:3296
14. Scott JF, Blinc R (2011) Multiferroic magnetoelectric fluorides: why are there so many magnetic ferroelectrics? J Phys Condens Matter 23:113202
15. Ederer C, Spaldin NA (2006) Origin of ferroelectricity in the multiferroic barium fluorides BaMF4: A first principles study. Phys Rev B 74:024102
16. Braithwaite RSW, Flowers WT, Haszeldine RN, Russell M (1973) The Cause of the Colour of Blue John and other Purple Fluorites. Min Mag 39:401
17. der Gruenne S, Mangstl M, Kraus F (2012) Occurrence of Difluorine F_2 in Nature- in situ Proof and Quantification by NMR Spectroscopy. Angew Chem Int Ed 51:7847
18. Toon R, The discoverer of fluorine. https://eic.rsc.org/feature/the-discovery-of-fluorine/2020249.article
19. Wisniak J, Moissan H (2002) The discoverer of fluorine. EducaciónQuímica 13:267
20. Cady GH, Rogers DA, Carlson CA (1942) Preparation of fluorine industrial and engineering chemistry. Ind Eng Chem 34:443
21. Crassous C, Groult H, Lantelme F, Devilliers D, Morel B (2009) Preparation of fluorine. J Fluorine Chem 130:1080
22. Hough PT (1997) Electrochemistry in the preparation of fluorine and its compounds, PV97-15, The electrochemical society proceedings series, Pennington, NJ, p 113
23. Rudge AJ (1971) Industrial electrochemical processes. In: Kuhn AT (ed) Elsevier, Amsterdam, p 17 (Chapter 1)
24. Cady GH (1934) Freezing points and vapor pressures of the system potassium fluoride—hydrogen fluoride. J Am Chem Soc 56:1431
25. Christe KO (1986) Chemical synthesis of elemental fluorine. Inorg Chem 25:3721
26. Sokolov VB, Spirin SN, Chaivanov BB (1989) Researches in the field of inorganic fluorine chemistry, preprint IAE-4936/13. Atominform, Moscow
27. Ruff O (1907) Über das Fluor und einige neuere Fluoride, Angew Chem 20:1217; Ruff O (1916) Über die Darstellung von Fluor aus Fluorwasserstoff oder anderen Fluoriden auf chemischem Weg. Z Anorg Chem 98: 27
28. Hans H, Jenssen H, Bandte F (1953) About a new representation of potassium hexafluoromanganate (IV). Angew Chem 65:304
29. Adelhelm M, Jacob E (1991) MnF4: preparation and properties. J Fluorine Chem 54:21
30. Hofmann B, Hoppe R (1979) To know the $(NH_4)_3SiF_7$ type. New metal fluorides A3MF7 with M = Si, Ti, Cr, Mn, Ni and A = Rb, Cs, Z Anorg Allg Chem 458:151
31. Zemva B, Lutar K, Chacon L, Fele-Beuermann M, Allman J, Shen C, Bartlett N (1995) Thermodynamically unstable fluorides of nickel: NiF_4 and NiF_3 syntheses and some properties. J Am Chem Soc 117:10025
32. Wang CM, Mir QC, Maleknia S, MalloukJ TE (1988) Photoelectrochemical evolution of elemental fluorine at titanium dioxide electrodes in anhydrous hydrogen fluoride solutions. Am Chem Soc 110:3710
33. Bezmelnitsyn VN, Bezmelnitsyn AV, Kolmakov AA (1996) New solid-state electrochemical source of pure fluorine. J Fluorine Chem 77:9
34. Aigueperse JA (2005) Hydrofluoric acid, chapter 1, fluorine compounds, inorganic. In: Ullmann's 'encyclopaedia of industrial chemistry'; part 11, Wiley-VCH Verlag Weinheim
35. Gall JF (1980) In: Kirk-Othmer (ed) Encyclopedia of chemical technology, 3rd edn, vol 10. Wiley, New York, pp 733–753
36. Matsugi A, Takayanagi T (2014) Mode selective dynamics and kinetics of the $H_2 + F_2 \rightarrow H + HF + F$ reaction. Phys Chem Chem Phys 16:22517
37. Chevalier B, Tressaud A, Lepine B, Amine K, Dance JM, Lozano L, Hickey JE (1990) Stabilization of a new superconducting phase by low temperature fluorination of La_2CuO_4 Physica C 167:97
38. Chevalier B, Tressaud A, Lepine B, Robin C, Etourneau (1999) Stabilization of a new superconducting phase by low temperature fluorination of La_2CuO_4. J Less-Comm Metals 164–165:832

39. Bartlett N (1962) Xenon hexafluoroplatinate (V) Xe+[PtF6]−. Proc Chem Soc 6:197
40. Hoppe R, Dahne W (1962) Die Kristastrukiur von SnF_4 und PbF_4. Naturwissenschaften 49:254
41. Streng LV, Streng AG (1965) Formation of xenon difluoride from xenon and oxygen difluoride or fluorine in pyrex glass at room temperature. Inorg Chem 4:1370
42. Christe KO, Guertin JP, Pavlath AE (1966) Complex fluoro cations. II. Tetrafluoronitrogen(V) cation, NF^{4+}. Synthesis and Properties of $NH^{4+}AsF^{6-}$. Inorg Chem 5:1921
43. Sidowick NV (1950) The chemical elements and their compounds, vol 1. Oxford University Press, London, p 637
44. Mueferties EL, Castle JE (1961) Reactors of hydrogen fluoride with metals and metalloids. J lnorg Nucl Chem 18:148
45. McNamara B, Scheele R, Kozelisky A, Edwards M (2009) Thermal reactions of uranium metal, UO_2, U_3O_8, UF_4, and $UO_2F_2$with NF_3 to produce UF_6. J Nucl Mater 394:166
46. Apprey LB, Coleman JS, Reisfeld MJ (1967) Preparation, structure and spectra of some tetravalent praseodymium compounds. Adv Chem Ser 71:122
47. Petzel T, Greis O (1973) About phase studies and saturation vapor pressure measurements on europium difluoride. Z Anorg Allg Chem 396:95
48. Greis O, Bevan DJM (1978) Electron diffraction from LaF_3 single crystals. J Solid State Chem 24:113
49. Pink H (1968) Über eine einfache Darstellung von Europium(II)-fluorid. Z Anorg Allg Chem 356:319
50. Fitz H, Mueller BG (1997) InBF4, das erste komplexe Fluorid mit Indium(I). Z Anorg Allg Chem 623:579
51. Goreshnik E, Mazej Z (2008) Single crystal structures of InPF6, InAsF6, TlPF6 and TlAsF6, Solid State Sci 10:303
52. Daniel DJ, Ramasamy P, Ramaseshan R, Kim HJ, Kim S, Bhagavannarayan G, Cheon J–K (2017) Crystal growth, structural, low temperature thermoluminescence and mechanical properties of cubic fluoroperovskite single crystal ($LiBaF_3$). Opt Mater 72:559
53. Achary SN, Tyagi AK, Seshagiri TK, Natarajan V (2006) Synthesis, powder XRD studies on LiF-BaF_2/EuF_3 systems and thermo-stimulated luminescence (TSL) of Eu^{3+} doped $LiBaF_3$. Mater Sci Eng B 129:256
54. Grzechnik A, Bouvier P, Crichton WA, Farina L, Köhler J (2002) Metastable $NaYF_4$ fluorite at high pressures and high temperatures. Solid State Sci 4:895
55. Grzechnik A, Bouvier P, Mezovar M, Mathews MD, Tyagi AK, Köhler J (2002) Hexagonal Na1. 5Y1. 5F6 at high pressures. J Solid State Chem 165:159
56. Park H, Yoo GY, Kim M-S, Kim K, Lee C, Park S, Kim W (2017) Thin film fabrication of upconversion lanthanide-doped $NaYF_4$ by a sol-gel method and soft lithographical nanopatterning. J Alloys Comp 728:927
57. Gao X, Wang N, Shi T, Wang S, Zhang M, Zhang W, Zhong J, Tong H, Zhang X (2016) Sol-gel synthesis of β-$NaYF_4$: Yb^{3+}/Nd^{3+}/Tm^{3+}/Mn^{2+} nanophosphors and color-tunable upconversion luminescence. J Fluorine Chem 188:23
58. Patwe SJ, Achary SN, Tyagi AK, Moorthy PN (1999) Synthesis and characterization of mixed fluoride $Y^{1-}xSr^{2+}1.5xF_7$ (-1.0 < x < 0.5). Mater Res Bull 34:761
59. Achary SN, Tyagi AK, Kohler J (2004) Single crystal structural study of Sr7Y6F30(O): An example of anion-rich fluorite derived structure with a cuboctahedron cluster, Mater Chem Phys 88:207
60. Tyagi AK, Köhler J (2001) Preparation and structural elucidation of the new anion-excess fluorite variant $Ba_4Er_3F_{17}$. Solid State Sci 3:689
61. Achary SN, Mahapatra S, Patwe SJ, Tyagi AK (1999) Synthesis and characterization of mixed fluorides $Y^{1-}xBa^{2+}1.5xF_7(-1.33 \leq x \leq 1.0)$. Mater Res Bull 34:1535
62. Achary SN, Patwe SJ, Tyagi AK (2002) Powder XRD study of $Ba_4Eu_3F_{17}$: a new anion rich fluorite related mixed fluoride. Powder Diffr 17:225
63. Grover V, Achary SN, Patwe SJ, Tyagi AK (2002) Synthesis and structural elucidation of $Ba_4Nd_3F_{17}$: A powder XRD study. Powder Diffr 17:326

64. Grover V, Achary SN, Patwe SJ, Tyagi AK (2003) SSynthesis and characterization of $Ba^{1-}xNdxF^{2+}$ x (0.00≤ x≤ 1.00). Mater Res Bull 38:1101
65. Tyagi AK, Patwe SJ, Achary SN, Mallia MB (2004) Phase relation studies in $Pb^{1-}xM'xF^{2+}x$ systems (0.0 ≤ x ≤ 1.0; M′= Nd^{3+}, Eu^{3+} and Er^{3+}). J Solid State Chem 177:1746
66. Achary SN, Tyagi AK (2001) Synthesis and characterization of high symmetric tysonite type non-stoichiometric compounds $SrYb^{3-}XErXF_{11}$ (0.0 ≤ X ≤ 1.0). Mater Res Bull 36:1441
67. Achary SN, Tyagi AK, Köhler J (2001) Stabilization of high temperature tysonite type compounds in the Sr-Yb-F systemsynthesis and rietveld refinement. Mater Res Bull 36:1109
68. Tyagi AK, Pöttgen R, Köhler J (1996) Preparation, crystal structure and magnetic properties of β- Li_3TiF_6 = Li[4]$_2$Li[6]$_7$(TiF_6)TiF_6)$_2$ – a Double Fluoride? Z Anorg Allg Chem 622:1329
69. Tyagi AK, Kohler J, Balog P, Weber J (2005) Syntheses and structures of Li_3ScF_6 and high pressure $LiScF^{4-}$, luminescence properties of $LiScF_4$, a new phase in the system LiF–ScF_3. J Solid State Chem 178:2620
70. Tyagi AK, Kohler J (1997) Preparation and Rietveld refinement of the structure of β-Li_3AlF_6. Mater Res Bull Mater Res Bull 32:1683
71. Köhler J, Tyagi AK (1999) Crystal structure of ß-lithium hexafluorogallate, Li_3GaF_6Z. Kristallogr. 214:25
72. Kannan CV, Shimamura K, Zeng HR, Kimura H, Villora EG, Kitamura K (2008) Ferroelectric and anisotropic electrical properties of $BaMgF_4$ single crystal for vacuum UV devices. J Appl Phys 104:114113
73. Sayed FN, Mandal BP, Jayakumar OD, Arya A, Kadam RM, Dixit A, Naik R, Tyagi AK (2011) Rare examples of fluoride-based multiferroic materials in Mn-substituted $BaMgF_4$ systems: experimental and theoretical studies. Inorg Chem 50:11765
74. Zhou S, Wang Ji, Chang X, Wang S, Qian B, Han Z, Qingyu Xu, Jun Du, Wang P, Dong S (2015) Magnetoelectricity coupled exchange bias in $BaMnF_4$. Sci Rep 5:18392
75. Cox DE, Shapiro SM, Cowley RA, Eibschütz M, Guggenheim HJ (1979) Magnetic and structural phase transitions in $BaMnF_4$. Phys Rev B 19:5754
76. Prevost H, Moret J, Anderson L, Lindqvist O (1982) Hydrothermal synthesis of fluorated single crystals: $BaMnF_4$ and BaF_2·HF. J Fluorine Chem 21:31
77. Juneja JM, Tyagi AK, Chattopadhyay G, Seetharaman S (1995) Sub-solidus phase equilibria in the NdF3-Nd2O3 system. Mater Res Bull 30:1153
78. Achary SN, Ambekar BR, Mathews MD, Tyagi AK, Moorthy PN (1998) Study of phase transition and volume thermal expansion in a rare-earth (RE) oxyfluoride system by high-temperature XRD (RE= La, Nd, Sm, Eu and Gd). Thermochim Acta 320:239
79. Achary SN, Tyagi AK, Köhler J (2002) Preparation, Structure, and Properties of V2GeO4F2—Chains of VO4F2 Octahedra in the First V (III) Metallate Fluoride. J Solid State Chem 165:74
80. Achary SN, Tyagi AK, Gupta MK, Mittal R, Bhattacharya K, Rao R (2017) Preparation, crystal structure, vibrational and electronic properties of $Cd_4Si_2O7F_2$. J Alloys and Comp. 702:573
81. Laptash NM, Maslennikova IG, Kaidalova TA (1999) Ammonium oxofluorotitanates, J Fluorine Chem 99:133
82. Patwe SJ, Wani BN, Rao URK, Venkateswalu KS (1989) Synthesis and thermal study of tris (ammonium) hexafluoro metallates (III) of some rare earths. Can J Chem 67:1815
83. Wani BR, Rao URK, Venkateswarlu KS, Gokhale AS (1982) Thermal behaviour of (NH4) 3VO2F4 and Na (NH_4) $2VO_2F_4$. Thermochim Acta 58:87
84. Fokina VD, Flerov IN, Gorev MV, Bogdanov EV, Bovina AF, Laptash NM (2007) Thermophysical studies of the phase transitions in (NH4)3NbOF6 crystals. Phys Solid State 49:1548
85. Patwe SJ, Achary SN, Girija KG, Pillai CGS, Tyagi AK (2010) Ferroelectric and proton conducting behavior of a new elpasolite-related vanadium oxyfluoride (NH^4, K) $3VO_2F_4$. J Mater Res 25:1251

Chapter 5
Synthesis of Materials with Unusual Oxidation State

S. N. Achary and A. K. Tyagi

Abstract Materials having ions in unusual oxidation states have been of interest for long time due to their relevance in understanding the oxidation–reduction process of various physicochemical phenomena, fundamental ionization process of elements as well as their challenging chemistry to prepare them. The ions in unusual oxidation states are usually unstable, and in turn they transform to stable state under ambient conditions or by feeble alteration of thermodynamic parameters or chemical environments. Since attaining such oxidation states is energetically unfavourable, they are generally achieved by either extreme or non-equilibrium thermodynamic conditions or diagonally opposite mild reactions where alternate paths are adopted. The varieties of unusual oxidation states can be conveniently obtained in solutions, but they are extremely reactive and short-lived, and are often encountered as intermediates in various chemical reactions. Cations with such oxidation states can also be stabilized by a variety of organic ligands. However, this chapter is mainly focussed on solid materials where the ions are stabilized primarily by inorganic counter ions and have significantly higher stability for further studies. In this chapter, a brief overview on preparation of materials having unusual oxidation state is presented. The chapter initially explains about the unusual oxidation state and their interest, and then the modes of their stabilization. There are several case studies explaining the process of stabilization of lower and higher valent states, and the role of judicious chemical and thermodynamic conditions, and crystal structure to stabilize them are presented.

Keywords Unusual oxidation state · Unusual compounds · Synthesis · Metastable materials · High oxidation state · Low oxidation state · Redox reaction · Crystal structure

S. N. Achary (✉) · A. K. Tyagi
Chemistry Division, Bhabha Atomic Research Centre, Mumbai 400085, India
e-mail: sachary@barc.gov.in

Homi Bhabha National Institute, Mumbai 400094, India

A. K. Tyagi
e-mail: aktyagi@barc.gov.in

A. K. Tyagi and R. S. Ningthoujam (eds.), *Handbook on Synthesis Strategies for Advanced Materials*, Indian Institute of Metals Series,
https://doi.org/10.1007/978-981-16-1892-5_5

5.1 Introduction

It is known that the property of material, whether it is physical or chemical, is predominantly arising from the elements constituting it, and in turn from the electronic configurations of the constituent elements. The electronic configuration of elements plays the guiding role for their existence either as elemental form or as compounds of elements in various oxidation states. A large number of solid elemental materials whether metal or non-metals like Fe, Al, Ti, Au, Ag, Pt, Si, Ge, W, Mo, Ta, P, I, etc., have been used by humankind, and most commonly, they exist as compounds in nature. Only few elements like Au and Pt are known to exist in nature in elemental state as well as compound state. But the elemental state (i.e. oxidation state 0) is stable state only for the noble or inert gases. For example, iron exists as Fe_2O_3 or Fe_3O_4 in nature, while the elemental form of Fe (Fe^0) is also practically used everywhere. However, zero oxidation state is not the stable oxidation state of iron under ambient environmental conditions. Hence, with time, the elemental Fe gradually transforms to Fe_3O_4 or Fe_2O_3 in a normal environmental condition, which is known as rusting. Thus, it can be understood as Fe is stable in Fe^0 state only under a given thermodynamic and environmental conditions, while the Fe^{2+} and Fe^{3+} are the favoured oxidation states of iron in earth's atmospheric or under geological conditions. The elemental Fe on heating also transforms to FeO and Fe_3O_4, and then to Fe_2O_3, while all these FeO, Fe_2O_3, Fe_3O_4 phases are abundantly occurring in nature. This indicates that both Fe^{2+} and Fe^{3+} states have significant stability under ambient conditions. Similarly, the elemental Au and Pt do not tend to rust in earth's atmospheric conditions, which suggests that the Au^0 and Pt^0 are the stable oxidation states for them. Thus, increasing oxidation state of Au or Pt is not a favourable chemical process and hence needs an alteration of chemical or thermodynamic conditions to achieve them. Thus, a terminology like *"common oxidation states"* is being used to indicate commonly observed oxidation states of elements in nature.

5.2 Oxidation States

The oxidation state of an atom means a formal or hypothetical charge on it when it is ionically bonded with other atoms or ligands, and is a relative measure of energy required to remove further electron from it or energy released on addition of an electron to it. It is a description of the degree of oxidation occurred in an atom in bonded system or compound. It can be a positive or negative number or zero. In a chemical or electrochemical process, if an increase in oxidation number from the initial oxidation number occurs, then it is known as oxidation process, while if there are decreases of oxidation number then it is called as reduction process. This is equivalently reflected in the change in oxidation number in other atoms in the system.

The driving force for the stable oxidation state can be attributed to the tendency of element to achieve stable electronic configuration, i.e. completely filled electronic shells like noble gas electronic configurations. The occurrence of different oxidation states of atoms is generally explained as a first course in general inorganic chemistry and can be referred to general inorganic chemistry textbooks [1–3]. The electrons from outermost orbitals are relatively easy to remove than that in inner orbitals. Also, once an electron is removed, the increasing attraction due to effective nuclear charge makes it difficult to remove the further electrons. Similarly, the unpaired electrons in outermost orbitals tend to accept an electron for making stable paired electronic configuration, and thus, such atoms have tendency to form negatively charged ions. Typical electronic configurations of Ar, Fe and Pt are compared in Fig. 5.1. It can be seen that Ar has stable filled configuration and thus does not have any tendency to accept or lose electrons. Fe can lose two outermost electrons easily to form Fe^{2+} state, while the loss of one additional electron can make it Fe^{3+} with half-filled ($3d^5$) outermost electronic configuration. In the case of Pt, the $5d^9 6s^1$ outermost electronic configuration makes it amenable for varieties of oxidation state ranging from -2 to $+10$, while experimentally Pt^{-3} to Pt^{6+} are observed. Typical experimentally observed oxidation states for some of the elements are compiled in Table 5.1.

The formation of stable or common oxidation states is also evident from the redox potentials or enthalpy of formation of element in particular oxidation state, which is representative for energy required to change the oxidation state. This can be simply understood from the ionization energy, the energy required to remove an electron for making positively charged ion of the element. The ionization energy progressively increases with increasing the charge of the ions and beyond certain oxidation state the ionization energy becomes extremely high, and that limits for further oxidation. Typical variation of enthalpy of formation of different oxidation states of some

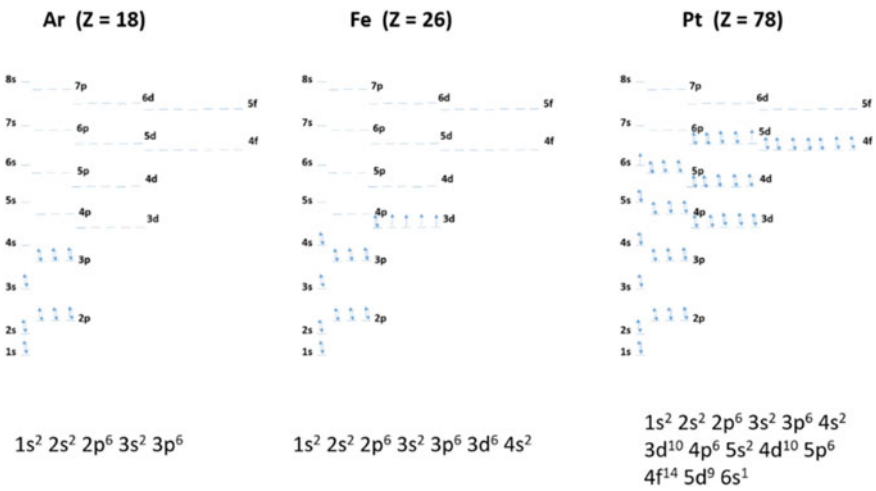

Fig. 5.1 A comparison of electronic configuration of argon, iron and platinum

Table 5.1 Oxidation states of some of the common elements[a]

Element	At. no. Z	Negative oxidation states						Positive oxidation states								
		−5	−4	−3	−2	−1	0	+1	+2	+3	+4	+5	+6	+7	+8	+9
H	**1**					−1	0	1								
B	**5**	−5				−1	0	+1	+2	+3						
C	**6**		−4	−3	−2	−1	0	+1	+2	+3	+4					
N	**7**			−3	−2	−1	0	+1	+2	+3	+4	+5				
S	**16**				−2	−1	0	+1	+2	+3	+4	+5	+6			
Cl	**17**					−1	0	+1	+2	+3	+4	+5	+6	+7		
Mn	**25**			−3	−2	−1	0	+1	+2	+3	+4	+5	+6	+7		
Ru	**44**		−4		−2		0	+1	+2	+3	+4	+5	+6	+7	+8	
Xe	**54**						0	+1	+2		+4		+6		+8	
Ir	**77**			−3		−1	0	+1	+2	+3	+4	+5	+6	+7	+8	+9
Pt	**78**			−3	−2	−1	0	+1	+2	+ 3	+4	+5	+6			

[a]Compiled from the list reported in the website https://en.wikipedia.org/wiki/Oxidation_state (for all the elements, the list of known oxidation states can be seen from given site)

elements is shown in Fig. 5.2. From the figure, it is evident the ionization enthalpy for Ar, Fe and Pt though not significant at lower oxidation states, and the final stability of even Ar^{+} and Ar^{2+} are not supported by any matrices. Hence, high electric field discharge or high energy radiations like X-ray or γ-ray only can produce Ar ions in gaseous state, and this approach is used in argon ion laser or Ar gas-filled radiation detectors.

5.3 Unusual Oxidation States

Although the unusual oxidation state materials have less stability and difficulty to attain, they bear significant fundamental and practical relevancies. Thus, the chemistry for preparation or stabilization of compounds with atoms in unusual oxidation state bears significant interest to chemist, physicist and technologist. Most commonly, such unusual oxidation states are observed as intermediate stage in oxidation–reduction process and they are short-lived. It is known that the atoms in unusually high oxidation state act as strong oxidizer while those on unusually low oxidation state act as strong reductant. Thus, they are potentially exploited in redox processes in chemical and biological reactions. Because of their affinity to undergo changes in oxidation states, they also play crucial roles in various catalytic reactions, synthetic chemistry and separation sciences. The electron transfer reactions in organic synthesis and biological processes often rely on the oxidation states of the metal ions [4]. However,

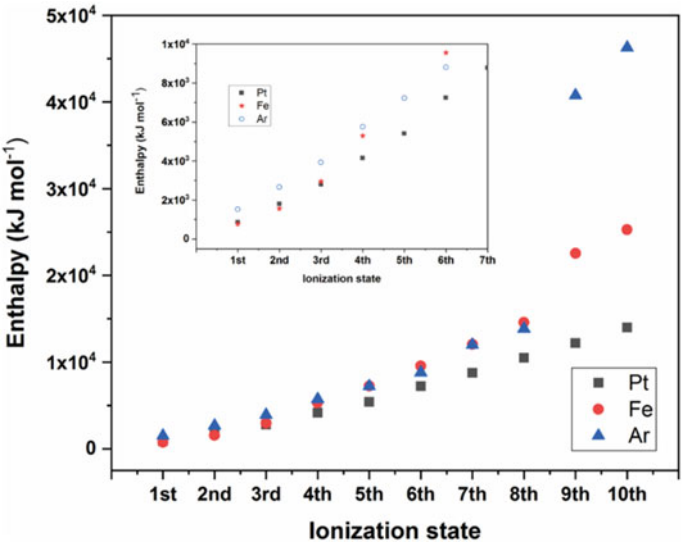

Fig. 5.2 Variation of enthalpy of formation of elements in different oxidation states. The plot is based on the data reported in WebElements data (https://www.webelements.com/)

in spite of their short lives, they are effective for several biological processes like transfer of oxygen in blood, photosynthesis in green plants, abetment of toxic pollutants, etc. [5]. Because of tremendous application potential of the compounds with such unusual oxidation states, the investigations on preparation and properties of such compounds became a challenging and interesting field in synthetic organic, organometallic and inorganic chemistry. Further, these compounds also play a crucial role for selective separation and segregation of ions from mixtures. Thus, they are used as highly desired chemicals in separation and management wastes, in particular in nuclear and mineralogical or industrial waste treatment as well as water purification processes. In addition, these materials also exhibit novel physical properties, like electrical conductivity, magnetic properties and optical properties. As an example, it can be mentioned here Cr_2O_3 is an antiferromagnetic material, while CrO_2 is a ferromagnetic material [6]. V_2O_5 shows semiconducting behaviour, while the oxides in lower oxidation state of vanadium show metallic or insulating behaviour and metal to insulator transitions [7].

The change in oxidation state of atoms is reflected in several of their crystallographic properties, like ionic radius, bond lengths and coordination numbers and also in their chemical properties. It is expected that a gradual decrease in ionic radii occurs with increasing oxidation state and vice versa for any atom due to the columbic attraction between nucleus and electron cloud. Hence, the coordination number can decrease with increasing oxidation state. Typical examples are oxides of uranium which may have coordination numbers of 8 (in UO_2) or 6 (in UO_3) depending upon the oxidation states of uranium. Similarly, the stability of higher

oxidation states of atoms decreases with deceasing atomic radii. Thus, highly positive charged ions can be obtained relatively easily with larger atoms. Also, the acidic character of an ion increases with increasing oxidation state; for example, MnO is basics, while $Mn_2O_7^{2-}$ and MnO_4^- are acidic ions and the oxides with Mn^{3+} and Mn^{4+} have amphoteric natures. Further, the oxidation state of an element can be positive or negative or zero depending on the nature of the compound and also can vary in a wider range than that expected from the stable electronic configurations. For example, oxidation state of hydrogen ($Z = 1$) can be -1, manganese can be -3 to $+7$ and iodine can be -1 to $+7$. The negative oxidation state of metal and metalloids is usually observed in intermetallic samples [8]. The highest oxidation state of $+9$ has been reported for iridium in IrO_4^+ [9].

5.4 Preparation and Stabilization of Materials with Unusual Oxidation States

As the materials with unusual oxidation state are usually unstable and stabilization of unusual oxidation states in applied materials is not energetically favourable, a careful and challenging chemistry is often involved in their preparation. The challenge and application potential of such materials have been pointed out by Jørgensen as "*One of the major goals of inorganic chemistry is to prepare compounds of elements in unusual oxidation states*" [10]. Subsequently, wide varieties of preparation strategies and theoretical analyses have been devoted to stabilize unusually charged ions in the matrices of organic and inorganic moieties as well as to understand their stability and properties. Such studies not only make way to prepare them but also lead to discovery of unusual structural and electronic effects in materials. Based on wide experimental and theoretical understanding, the typical approaches to prepare materials with unusual oxidation states can be understood as some guidelines. Some of the guidelines for preparation of unusual oxidation state material are mentioned below [11].

1. Use of strong oxidizer or reductants in suitable chemical environment and temperature.
2. Extreme temperature and pressure conditions, like high-pressure and high-temperature anvils, laser bombardment-induced ionization, accelerated ion collision, etc.
3. High gas pressure, like F_2, O_2, H_2, CO, moist gas mixtures, etc., for increasing or decreasing oxidation states.
4. Electrochemical process.
5. Free radical, energetic electron or gamma radiation.

Unusual oxidation states of varieties of elements can be stabilized as organometallics using suitable organic ligands, which may be either electron donating or accepting. In addition, variation of bulkiness of ligand can suitably alter the steric hindrance and stabilizes the unusual oxidation states. These approaches have been

exploited in stabilization of higher as well as lower valent states of transition metals in organometallics. Due to structural complexity and bulkiness of organic ligands, stabilization of unusual oxidation state materials is relatively common in organometallics compared to other types of inorganic compounds. Some of the typical stabilization methods are as follows:

1. Stabilization through coordination (p-electron-accepting ligand like CO or electron-donating ligands such as pyridine can stabilize the cations in the lowest oxidation states).
2. Highly bulky ligands render sterically hindered surrounding around the cations and help them to saturate coordination. Such ligands can stabilize the cations in low oxidation states as well as high oxidation states. Ligand like $[(RN)_2CNR'_2]$ where (R, R' = alkyl, aryl, silyl, etc.) can stabilize monovalent states of Al, Mg, Mn, etc., by coordinated bonds through the N atoms.
3. Synthesis of materials under non-ambient conditions can retain the unusual compounds as metastable phase where the high energy state materials are formed bypassing the hindrance from the thermodynamically stable phases.
4. Matrix stabilization approach is an efficient method to stabilize the unusual oxidation state. The desired oxidation state for the crystal structure and coordination number requirement of a given structure facilitates the cation in unusual oxidation states. Also, the judicious selection of counter ions on the basis of coordination saturation, acidity, electronegativity or electro-positivity provides a guiding role for stabilization of unusual oxidation states. The criterias of coordination polyhedra, packing density and counter group effect are useful for stabilizations of cations or anions in unusual oxidation states.
5. Synthesis of materials under extremely low temperature where the excess energy for obtaining other normal oxidation states is prevented.

Some of the examples of preparation of materials with elements in their unusual oxidation states are explained in subsequent sections. In particular, the focus of this chapter is made for inorganic materials and molecules. The organometallics and clusters with unusual oxidation states are excluded in this chapter.

Before discussing to the specific preparations, it may be noted that the unusual oxidation state of any atom can be achieved by applying desired amounts of energy. However, they may not be stable in a compound. Thus, stabilization of such oxidation state is essentially related to the counter species present in the compounds. As a general rule, to stabilize the high oxidation state of cation it is desired to have highly electronegative and low polarizable counter ions or species. Thus, most commonly higher cationic charge can be easily stabilized as fluorides and then as oxides. For example, UF_4 and UF_6 have higher stability than UO_2 and UO_3. Because of similar reason, TbF_4 and PbF_4 have higher stability compared to TbO_2 and PbO_2. Elements like Pt, Os, Rh, Ir can be stabilized with exceptionally higher oxidation states, like $+7$, $+8$, $+9$, etc., in fluoride matrices. Such higher oxidation states cannot be easily obtained with any other anionic species. However, there may be several exceptions and they are due to structural and steric reasons; viz. CeF_3 has higher stability compared to CeF_4, while Ce_2O_3 is less stable compared to CeO_2. Similarly,

the cations with low oxidation states are stabilized by lower electronegative and highly polarizable anions. Tl and Bi in +1 oxidation states can be easily stabilized by I^- ion. Also, varieties of reactions are being carried out by using different types of reducing agents, like CO, C, Si, H_2, metals, etc. or by electrochemical processes to obtain materials with lower oxidation states ions. In metallurgical process, such reactions are commonly used to extract metals from ores. The molecular anions or molecules having HOMO level just below the lowest occupied level of the cations can easily stabilize the higher oxidation by electron transfer from LUMO of cation to LUMO of counter species. Further, a preferential coordination of a cation in a structure, availability of space for additional anions or expansion of coordination polyhedra to reduce steric and inter-anion repulsion plays significant roles in stabilization of cations in higher oxidation states. Typical examples are $CaCrO_4$ and $YCrO_4$ in which structural requirements coupled with high electro-positivity of counter cations lead to the stabilization of 6+ and 5+ oxidation states of Cr. Most of silicates can stabilize Cr, Mn, etc., in +4 states. In case of solutions, the stabilities of the unusual oxidation states depend on the nature of solvent, like its oxidation potential and stability, pH, the electron-donating functional groups and tendency to form solvation are important parameters. As an example, Ce^{4+} and Tb^{4+} easily transform to Ce^{3+} and Tb^{3+} in acidic media compared to the alkaline media. Thus, most commonly higher oxidation states of transition metal ions are obtained from alkaline solutions. In alkaline medium, Mn can reach up to +7, while in acidic medium the stable oxidation states are mostly +2 or +3. Cr in hexavalent state can be obtained as $K_2Cr_2O_7$ and $Na_2Cr_2O_7$, and also in acidic conditions like concentred HCl as CrO_2Cl_2. $Cr_2O_7^{2-}$ can be obtained by reacting with Na_2CO_3 at high temperature in air. In weakly acidic solutions, like phosphoric acids, both Ce^{4+} and Tb^{4+} can also be stabilized. Thus, it is essential to have judicious lattice or molecular structure architect and suitable counter species for stabilization of unusual oxidation states of desired elements.

As mentioned earlier, the compounds with unusual oxidation state are in general metastable and will transform to their stable counterpart(s) on alteration of chemical environments like medium, solvent, pH, mixing with other materials or physical environments, like change in atmosphere, temperature or pressure. This can be understood as the compounds with unusual oxidation states are metastable and in higher energy states compared to their counter stable counterparts and hence need to be prepared by judicious thermodynamic and chemical environments.

5.5 Preparation Strategies for Materials with Unusual Oxidation States

5.5.1 High Temperature Reactions

High-temperature solid-state reaction with strong elemental reducing agents, like metals, carbon, silicon, etc., is effective to obtain compounds with lower oxidation

states. Such reactions need to be carried out in either vacuum or protective gaseous environments to prevent oxidation by air. Often, He, Ar, N_2 can provide efficient protective environment. N_2 beyond certain temperature (>1500 °C) becomes reactive and thus hinders the reduction; instead, it undergoes chemical reactions or oxidizes the system. Several metals like, Al, Ti, Zr, Hf, etc., are oxidized by N_2 gas at high temperature. Additionally, elemental reactions in a definite composition can also be a method for synthesizing materials in lower oxidation states. Some of the typical examples are given below.

Divalent rare-earth ions

Divalent rare-earth iodides can be prepared by high-temperature reduction using rare-earth metal as reductant. Alternatively, a slow oxidation or controlled chemical reaction composition can stabilize the elements in lower and unstable oxidation states. In a usual procedure, an intimate mixture of LnI_3 and Ln metal is placed in evacuated or argon-filled quartz or tantalum tube, and then heated at desired temperature for prolonged time to complete the reaction and to increase the crystallinity. The crystal structure of the product is similar to tetragonal $SrBr_2$.

$$2NdI_3 + Nd \xrightarrow{540\ ^\circ C,\ 3\ days\ (evacuated\ Ta\ ampoule)} 3NdI_2$$

The divalent states of rare-earth ions in fluorides are known only for Eu, Sm and Yb. However, the divalent states of most of the rare-earth ions can be retained as iodides [12]. The divalent rare-earth fluorides or chlorides disproportionate at certain temperature with an exception of EuF_2 and $EuCl_2$ which are congruently melting solids [13]. The thermal instability of trihalides of rare-earth ions like Sm^{3+}, Eu^{3+} and Yb^{3+} as chloride, bromide or iodide also offers a method to prepare them as dihalides. Thus, SmI_2, EuI_2 and YbI_2 can be prepared in pure form by thermal decomposition of trihalides (LnI_3) [14].

For stabilization of divalent lanthanides in halides, a variety of methods has been reported in literatures. A number of complex fluorides of Sm, Eu and Yb with different concentrations of +2 and +3 states have been prepared by high-temperature solid-state reaction of trivalent fluorides and metal [15–19]. Divalent Eu^{2+} can also be stabilized as oxide or halides by high-temperature reduction using gaseous hydrogen [15]. Most commonly, Eu^{2+}-doped complex oxides and fluorides are prepared by reaction in reducing Ar-H_2 atmosphere. Among the Ln^{2+} ions, Eu^{2+} has higher stability due to half-filled f^7 electronic configuration. Hence, it can be prepared relatively easily than other divalent rare-earth ions. EuF_3 can be reduced to EuF_2 using calciothermic reaction, at moderate temperature like around 400 °C in sealed ampoule [15]. However, for practical synthesis of EuF_3 is most commonly carried out by metallothermic reduction using Eu metal or by reductive reactions using Si or H_2 as reductants [15, 19]. Highly pure EuF_2 can be obtained by using Si which is due to easier separation of Si as SiF_4 gas. Sobolev et al. have adopted such silicothermic reduction to prepare complex fluorides of Eu, Sm, etc. [19]

$$EuF_3 \xrightarrow{1000\ ^\circ C,\ 24h\ \text{under flowing pure}\ H_2} EuF_2 + HF(g)\uparrow$$

$$4\ EuF_3 + Si\ (\text{powder}) \xrightarrow{900-1100\ ^\circ C} 4\ EuF_2 + SiF_4(g)\uparrow$$

Single crystals of YbF_2 have been prepared by reaction of Yb metal with Teflon $(C_2F_2)_x$. The Yb metal and Teflon in 4:3 molar ratio are heated at 1100 °C for 3 days in welded Nb tube to get YbF_2 single crystal with leftover amorphous unreacted or decomposed products of Teflon [20]. Solid-state metathesis or exchange reactions also provide a method to prepare the halides, in particular iodides of lower valent rare-earth ions. DyI_2 and YbI_2 can be prepared by reaction of stoichiometric HgI_2 with Dy or Yb metal [21, 22]. It can be mentioned here that stabilization of La^{2+} as LaO or LaF_2 is not achievable experimentally while they can be obtained as LaI_2 either by elemental La and I reaction or LaI_3 and La metal reactions. The reactions are often facilitated by application of high pressure [14, 15, 19].

Tetravalent rare-earth ions

Tetravalent halides of the rare-earth ions are conveniently prepared for Ce, Pr and Tb due to their higher stabilities dictated by their electronic structures. However, they also transform to trihalides due to higher stabilities of Ln^{3+} ions in fluoride lattices. Among these rare-earth ions, the CeF_4 has better stability and hence can be prepared easily. Metallic Ce and Tb or CeF_3 and TbF_3 can be oxidized by F_2 gas at 300–500 °C to CeF_4 and TbF_4 [23]. Also, CeF_4 and TbF_4 can be obtained by reaction of CeO_2 or Tb_4O_7 reaction of F_2, XeF_4 or ClF_3 gases at temperature around 500 °C [24–26]. Preparation of compounds with Pr^{4+} ions is usually carried out by taking the advantages of lattice stabilities. The stability of Pr^{4+} in fluorite-type Pr_6O_{11} lattice is well known. Similarly, the Pr^{4+} has substantial stability in the crystalline lattices as Na_2PrF_6 or $Na_7Pr_6F_{31}$, but these compounds need to be prepared by high F_2 gas pressure. PrF_4 in pure form can be obtained by leaching Na^+ ions from such lattices by anhydrous HF [26]. Higher valent Pr^{4+} as chlorides, bromides and iodides is never conclusively prepared. However, existence of Pr^{5+} as PrO_2^+ has been reported in gas phase and deposition of vapour species in noble gas cages [9, 27].

Due to higher Lewis acidic characteristics of PO_4^{3-} and VO_4^{3-}, the +3 oxidation state of cerium has higher stability in phosphate and vanadate matrices than Ce^{4+}. CeP_2O_7 is the only complex cerium phosphate with Ce^{4+} which has appreciably higher thermal stability [28]. As mentioned earlier, the nature of counter ions and ligands, like ionic or molecular dimensions, electronegativity, bulkiness and rigidity as well as structural stabilities play important roles in stabilization of the oxidation states of rare-earth elements. As a case, Clearfield has investigated a variety of compositions with P_2O_5 and observed that only stable phase with Ce^{4+} is observed as CeP_2O_7 [29]. Later, it has been observed that the Ce^{4+} can also be stabilized as complex phosphates [29, 30], they remain stable up to significantly higher temperature, viz. around 900 °C, and then they decompose to $Ce^{3+}PO_4$ with evolution of oxygen. The Ce^{4+} ion can be stabilized using larger counter cations with high electropositivity. $K_2Ce(PO_4)_2$ can be prepared using CeO_2, K_2HPO_4 and $(NH_4)_2HPO_4$ at

around 700° in air [31, 32]. The stabilization of Ce^{4+} has been confirmed from XPS and XANES spectra (Fig. 5.3).

Transition metal ions

Compounds of transition metals in lower oxidation state can also be obtained by reducing lower oxygen partial pressure atmosphere using CO, CO-H_2O mixture, hydrogen, etc., or by metallothermic reductions. As an example, the FeO and MnO can be obtained by heating Fe_2O_3 and Mn_2O_3 or MnO_2 in inert or reducing atmosphere [33]. Complete transformation of Fe_2O_3 or Mn_2O_3 to FeO or MnO usually requires mild reducing atmosphere like CO than the inert atmosphere or reductants like C or dilute H_2 to avoid the formation of Fe_3O_4 and Mn_3O_4. The formations of these later compounds hinder the completion of reactions. The easier formation of the intermediate Fe_3O_4 and Mn_3O_4 phases is due to their higher structural stabilities. However, FeF_2 and MnF_2 can be easily prepared by reaction of metal with dilute HF solutions. Similarly, high oxidation states of the transition metal can be obtained by heating in oxidizing atmosphere and in some cases higher gas pressure may be required to facilitate the oxidation process [34, 35]. High oxygen pressure is commonly used to stabilize higher oxidation states of transition metals. Stabilization of Ni^{3+}, Fe^{4+}, Mn^{4+}, etc., has been carried out by such approach. Mn can be easily stabilized in oxidation state of Mn^{4+}, Mn^{5+} and Mn^{6+} by oxidation in alkaline media [36]. In addition, the structural stability often drives the stabilization of higher oxidation states and such concepts are extensively used for preparation and stabilization of unusual oxidation state compounds of transition metal ions. Some of them are explained below.

High temperature reaction or controlled reduction methods are used to prepare compounds with lower oxidation state of V, Mo, W, etc. For example, V_2O_3 can be prepared by reduction of V_2O_5 in dilute H_2 atmosphere [7, 37, 38]. However, formation of oxidation states lower than +3 often requires strong chemical reductants like metal or electrochemical reductions [39, 40].

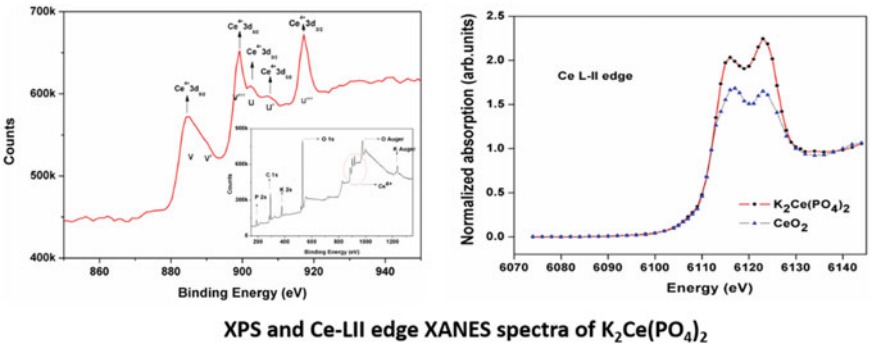

Fig. 5.3 XPS and XANES spectra of $K_2Ce(PO_4)_2$. The XANES L-II edge of Ce in CeO_2 is shown for comparison (Reproduced from Bevara et al. [31] with permission from Royal Society of Chemistry)

$$V_2O_5 \xrightarrow{800-900\ ^\circ C,\ \text{flowing pure } H_2-Ar\ \text{gas}} V_2O_3 + H_2O(g)\uparrow$$

Controlled reduction by H_2 (in H_2-Ar mixture) can also be used to obtain tetravalent V^{4+} compounds, but often they reduce to +3 states. Hence most often, pure VO_2 is prepared by solid-state reaction of V_2O_5 and V_2O_3. V_2O_3 is a common reactant to prepare compounds with V^{3+} and V^{4+} ions. Several of compounds with V^{3+} and V^{4+} ions show significantly higher-temperature stabilities, but only in non-oxidizing or inert atmosphere. Vanadium in +4 oxidation state can be prepared easily by mild reductions using mildly reducing agents like oxalic acid or phosphoric acid. Addition of V_2O_5 to aqueous solutions of oxalic acids or mild heating with H_3PO_4 transforms the solutions of V^{5+} or VO_2^+ ions to solutions of V^{4+} ions. $V(oxalate)_2$ is air stable complex of V^{4+} ions, and its thermal decomposition in inert atmosphere leads to the formation of pure VO_2. Dark blue-coloured VP_2O_7 (Fig. 5.4) with V^{4+} ions shows exceptional high-temperature stability in air; i.e. it remains stable even up to 900 °C, and it can be easily prepared from the reaction of V_2O_5 and $(NH_4)_2HPO_4$ [38]. The formation is assisted by a mild reducing effect from decomposed ammonia and stabilization effect from the lattice structure.

$$V_2O_5 + 4(NH_4)_2HPO_4 \xrightarrow{200\ ^\circ C\ (2h) + 650\ ^\circ C\ (6h)} 2VP_2O_7 + 2NH_3(g)\uparrow + 3H_2O\uparrow$$

Solid-state reactions using reactants having trivalent vanadium are carried in protective or inert gas environments or in vacuum, and usually, they need higher temperature. Solid-state reaction of V_2O_3, VF_3 and GeO_2 at 700 °C for 18 h, in argon-filled platinum ampoule, has been used to prepare $V_2GeO_4F_2$ (dark green coloured, Fig. 5.5) an oxyfluoride of V^{3+} [37]. $V_2GeO_4F_2$ is stable in air and water once prepared and remains stable up to 700 °C in inert atmosphere [37, 41].

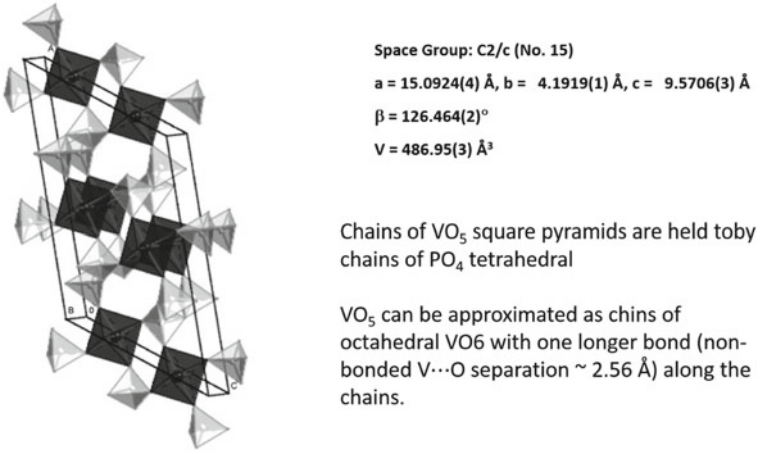

Fig. 5.4 Crystal structure of VP_2O_7 (α-$VO(PO_3)_2$) prepared by reaction of V_2O_5 and $(NH_4)_2HPO_4$ in air (Adapted from Ref. [38] with permission of Elsevier)

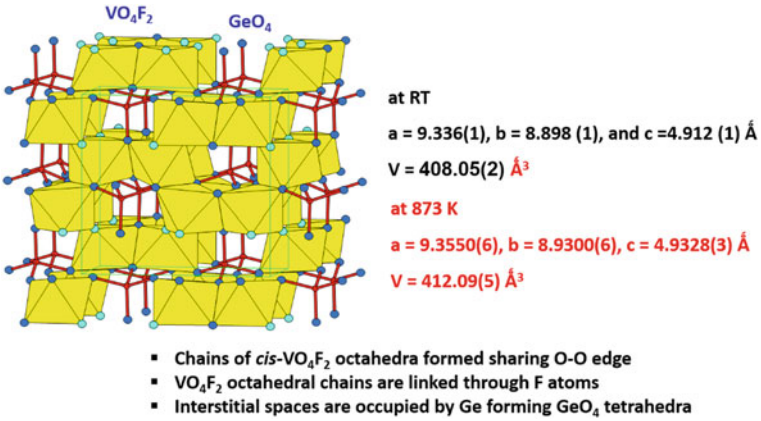

Fig. 5.5 Crystal structure of $V_2GeO_4F_2$ prepared by reaction of V_2O_3, VF_3 and GeO_2 in inert atmosphere (Adapted from Ref. [37] with permission of Elsevier)

$$2V_2O_3 + 2VF_3 + 3GeO_2 \xrightarrow{700\ ^\circ C\ (18h)\ (argon\text{-}filled\ sealed\ Pt\ ampoule)} 3V_2GeO_4F_2$$

P-block cations

The unusual oxidation states of p-block metals and metalloids can also be prepared by suitable reactions at higher temperature. Some of the cases are explained here. Ge and Si as such have stable oxidation state +4 and widely occur as GeO_2 or SiO_2 and germanates (GeO_4^{2-}) or silicate (SiO_4^{2-}). But, GeO with unstable +2 oxidation state of Ge can be prepared by reduction of GeO_2 using elemental Ge or also other weaker reducing agents, while such reductions are not feasible for preparation of SiO [42]. At extremely higher temperature, like laser or H_2-O_2 flame heating SiO_2 or GeO_2 is ablated with such species in vapour phase. Similarly, in vapour phase AlO is produced by flame ablation. Also, Al_2O_3 reacts with Si at around 1800 °C in high vacuum to form SiO (g) and Al_2O (g) [43]. Typical chemical reactions and reaction conditions are given below. The latter is essentially an adduct of Al and AlO. However, the stability of GeO, SiO and AlO is limited, and they either oxidize or disproportionate to metal and stable oxides, like GeO_2, SiO_2 and Al_2O_3.

$$GeO_2 + Ge \xrightarrow{540\ ^\circ C,\ 3\ days\ (evacuated\ Ta\ ampoule)} 2GeO$$

$$GeO_2 + CO \xrightarrow{>700\ ^\circ C} GeO + CO_2$$

$$Al_2O_3 + Si \xrightarrow{1800\ ^\circ C\ (high\ vaccum)} SiO + Al_2O$$

Although formation of Sn(III) in Sn_3O_4 prepared from reaction of SnO, SnO_2 and Sn is reported [44], the confirmation of Sn^{3+} is still debatable. The +

3 oxidation state of Sn is never confirmed in literature; rather, it has been suggested to be the average of Sn^{2+} and Sn^{4+}, and the similar arguments have been made for Sn^{3+} in SnN also [45]. However, Jensen et al. have suggested that certain organometallics, (bis(2-1,4,7-tris(4-*t*-butyl-2-mercaptobenzyl)-1,4,7-triazacyclononane)diiron-tin bis(tetraphenylborate) acetonitrile solvate) and (bis(2–1,4,- tris(4-*t*-butyl-2-mercaptobenzyl)-1,4,7-triazacyclononane)-diiron-tin triperchlorate acetone solvate) are likely to have Sn^{3+} species [45].

Similarly, In^{+} exists as InF only in gas phase, while it disproportionates to In^{0} and In^{3+} states in solids [46]. However, it can be stabilized in suitable crystalline lattice but needs to be prepared under controlled thermodynamic and chemical environments [47]. Crystalline lattices of $InBF_4$, $InMF_6$ (for M = P, As, Sb), $InHfF_4$, etc., can stabilize the In^{+} ion due to the Lewis acidic characteristics of BF_4^-, HfF_4^- or MF_6^- ions [48, 49]. $InHfF_4$ can be prepared by solid-state reaction of InF_3, HfF_4 and In metal at 750 °C, and the product once formed remains stable in air and moisture. The structure is stabilized by sheets of HfF_8 bisdisphenoids having a net negative charge of −1 (Fig. 5.6) [47].

$$InF_3 + 3HfF_4 + 2In \xrightarrow{750^{\circ}C\ (\text{in Ar filled platinum ampoule})} 3InHfF_5$$

Often, low temperature reactions are also useful to stabilize the unusually lower or higher oxidation states. Lower temperature plays an important role in preventing the decomposition of the materials by disproportionation of unusual oxidation states. A number of examples are known where ions with higher oxidation state have been prepared by using strong oxidants and lower temperature. Higher valence states of Pt, Au, Ru, Mn, Fe can be obtained by fluorinating F_2 gas or liquid fluorine. Noble gases like Kr, Xe and Rn can react with molecular fluorine liquid at low temperature by oxidizing then to +2, +6 states [50]. Compounds Kr^{2+}, Xe^{2+}, Xe^{4+}, Xe^{6+}, P^{5+}, S^{6+}, Se^{4+}, Se^{6+}, etc., can be obtained by reacting their elements with liquid or

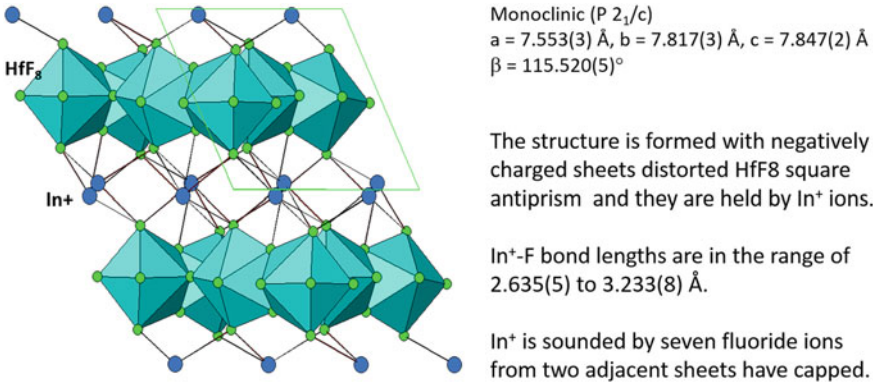

Fig. 5.6 Crystal structure of $InHfF_8$ (projected along <010>). Reference [47] (Authors' unpublished work)

gaseous F_2 at low or ambient to moderate temperature. Xe can be oxidized to +2, +4 and +6 states by F_2 gas at moderate temperature, like 120, 150 and 200 °C, respectively. Once the products like XeF_2, XeF_4 and XeF_6 are formed, they remain stable at ambient conditions [51, 52]. Iodine can be oxidized to +7 state using state obtained by F_2 gas to form IF_7 gas. Even cation with halogens can be achieved by the reacting them with fluorine. Usually, high electronegativity of fluorine plays an important role to stabilize the higher oxidation states. Number examples of fluorides with cations in high oxidation states are explained in another chapter on "inorganic fluorides" in this book. Similarly, several cations in higher oxidation states in oxides are stabilized by oxidation of O_2 gas or strong oxidizer like $KClO_3$, $KClO_4$, $KMnO_4$, K_2MnO_4, etc.

5.5.2 *High Pressure and High Temperature Reactions*

High pressure and high temperature reactions have been quite often used to stabilize the unusually higher oxidation states. The typical experimental set-ups used for such reactions are closely similar to the conventional high pressure and high temperature reactions presented in another chapter on "high pressure synthesis" in this book. Mn^{4+}, Fe^{4+} and Ni^{3+} can be stabilized in oxide lattices by high temperature reactions in high oxygen pressure. MnO or FeO can be transformed to Mn_2O_3 or Fe_2O_3 by heating in air or O_2 atmosphere, while the formation of MnO_2 or FeO_2 is not feasible. However, MnO_2 is also a naturally occurring mineral known as pyrolusite. The formation of MnO_2 mineral in nature has been attributed to the oxidation of lower valent Mn ions in alkaline conditions. MnO_2 can also be prepared by interacting the salts of Mn^{2+} with strong oxidizers like $KMnO_4$, while the freshly precipitated hydroxides $Mn(OH)_2$ in alkaline medium can be transformed to MnO_2 at ambient or lower temperature (Fig. 5.7) [36]. The extent of oxidation is reflected by the incorporation of additional cationic species in the structure.

Perovskite-type $LnNiO_3$ (for Ln = Y, La, Nd, Sm, Eu, Gd, Ho, Tm, Yb, Lu) with Ni^{3+} ion has been prepared by reaction of Ln_2O_3 and NiO in the presence of $KClO_3$ in belt apparatus [34, 35]. The authors have indicated that a temperature around 950 °C is desired to create oxygen pressure of 60 bar, where the Ni^{2+} is oxidized to Ni^{3+}. Once the Ni^{3+} state is formed in the perovskite structure, it remains stable even up to appreciably higher temperature. Demazeau et al. have prepared a number of double perovskite-type materials with iridium in unusually higher oxidation state, up to Ir^{6+}, by using high O_2 pressure generated by $KClO_3$ decomposition in a belt apparatus or compressed O_2 gas pressure in closed environments [34]. Pressurized F_2 gas has been used to stabilize Pr^{4+} in several fluoride lattices [53]. Several complex fluorides, like $Na_7Pr_6F_{31}$, $K_7Pr_6F_{31}$, K_2PrF_6, K_3PrF_7, etc., have been prepared by solid-state reaction under high F_2 gas pressure.

$$7Na/KF + 6PrF_3 + F_2 \xrightarrow{350\ ^\circ C,\ F_2\ \text{pressurized cell}} Na/K_7Pr_6F_{31}$$

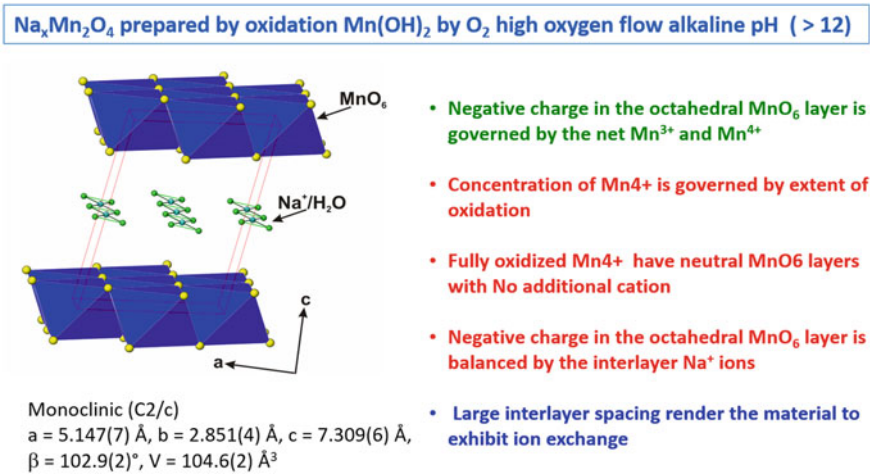

Fig. 5.7 Crystal structure of Birnessite-type phyllomangante $Na_xMn_2O_4$ xH_2O (Adapted from Ref. [36] with permission from John Wiley and Sons)

$$2KF + PrF_3 + \frac{1}{2}F_2 \xrightarrow{350\ ^\circ C,\ F_2\ \text{pressurized cell}} K_2PrF_6$$

The iron can be stabilized in highest oxidation states, up to +6, by suitable experimental conditions, appropriate crystalline lattice and using additional electropositive cations. However, the oxidization of Fe beyond +3 state needs high oxygen pressure, high temperature and pressure or electrochemical means. The compounds or ions with hexavalent iron are being routinely prepared in laboratory by electrochemical methods, and they find extensive applications owing to its strong oxidizing nature and environmental-friendly residuals. A number of materials, like $A^I_2FeO_4$ and $A^{II}FeO_4$, are prepared by high pressure of oxygen [54, 55].

5.5.3 *Reaction at Lower or Moderate Temperature and Stepwise Reactions*

Strong oxidizers like F_2, XeF_4, KrF_2, etc., can also fluorinate and oxidize Ce^{3+}, Pr^{3+} and Tb^{4+} easily to +4 state. PrF_4 has limited stability with temperature and decomposes to PrF_3 and F_2 at around 90 °C. However, it can be stabilized at lower to moderate temperature in compound states. There are several oxide matrices known to stabilize Pr^{4+} easily. Usually, perovskites with larger cations like Ba^{2+} can stabilize by solid-state reaction in oxygen atmosphere or decomposition of nitrates in oxygen atmosphere. They are the convenient precursors for preparation of complex fluorides of Pr^{4+} ions, but usually they are unstable and sensitive to moisture. Typical

procedures adopted for preparation of $BaPrF_6$ are given below [56].

$$6BaCO_3 + Pr_6O_{11} \xrightarrow{3 \text{ aqueous HCl or } HNO_3} 6BaPrCl_5 \text{ or } 6BaPr(NO_3)_5 \text{ (aqueous)}$$

$$BaPr(NO_3)_5(\text{solid}) \xrightarrow{800\ ^\circ C,\ 24h,\ O_2\ \text{flow}} BaPrO_3$$

$$BaPrO_3 \text{or} BaPrCl_5 \xrightarrow{350\ ^\circ C,\ 24h,\ F_2\ \text{gas 1 bar}} BaPrF_x \xrightarrow{500\ ^\circ C,\ 24h,\ F_2\ \text{gas 500 bar}} BaPrF_6$$

It has been observed that crystal structure of several oxides drives the stabilities of unusually higher oxidation ions. Such structures are used as intermediates for preparation of materials with unusual oxidation states. As an example, Fe in 4+ oxidation state can be achieved while preparation of Fe-doped Li_2MnO_3. Li_2MnO_3 can be prepared by conventional low-temperature sol–gel method using $LiNO_3$, $Mn(II)(NO_3)_2$ and citric acid [57]. The decomposed gel products on heating at around 750 °C in air can produce phase pure Li_2MnO_3 with complete Mn^{4+} ions. Similar preparations with the gel precursors containing Fe^{2+} ions result in the formation of Fe^{4+} ions in the lattice. The presence of appreciable fractions of Fe^{4+} and Fe^{5+} has been shown in the $Li_3Mn_{0.7}Fe_{0.3}O_4$ lattice prepared from its corresponding gel [54]. Tetravalent Fe can also be stabilized in the lattices of Na_4FeO_4 and $AFeO_3$ (A = Ca, Sr and Ba). Such materials are generally prepared by using high oxygen gas pressure and commonly inside a high pressure and temperature apparatus [54, 55].

$$2CaCO_3 + Fe_2O_3 \xrightarrow{900-1100\ ^\circ C,\ \text{in air}} Ca_2Fe_2O_5 \xrightarrow{900\ ^\circ C,\ CrO_3/CrO_2\ \text{at} > 15\ \text{kbar pressure}} CaFeO_3$$

However, the Na_4FeO_4 can be easily prepared by solid-state reaction using Na_2O_2 as oxidizer even in high vacuum [55].

$$2Na_2O_2 + FeO \xrightarrow{400\ ^\circ C,\ \text{in sealed or static vacuum}} Na_4FeO_4$$

Cr^{4+} is easily stabilized in silicate glasses where the Si^{4+} of SiO_4 is replaced by Cr^{4+} forming CrO_4 tetrahedra [58]. The stable $LnCrO_4$ with Cr^{5+} can be obtained by reactions of Ln_2O_3 and CrO_3 in air at moderate temperature (less than 850 K). Pyrolysis of rare-earth nitrates and Cr(III) nitrates in air or decompositions of $LnCr(C_2O_4)nH_2O$ and citrate gel products in air can also produce the $LnCrO_4$ with Cr^{5+} states [59–61]. In these, the areal oxidation of Cr^{3+} to Cr^{5+} leads to the formation of tetrahedral CrO_4 ions. The tetrahedral CrO_4 ions are held by the Ln^{3+} ions and hence stabilize the Cr^{5+} oxidation state of chromium. Depending on the ionic radii of rare-earth ions, they form stable lattices with either monazite or zircon-type structures.

5.5.4 Electrochemical Reactions

Additionally, preparation of materials with unusual oxidation states has also been demonstrated by using electrochemical oxidation or reduction of ions in suitable medium and temperature. Often, the solutions or molten salts are used as electrolytes, while the pH, counter ions in the medium and electrodes play important roles. The reactors, electrodes and species are considered depending on the potential desired, while their stabilities depend on the reactivity of the medium (electrolyte) or species being generated in the medium. Such electro-oxidation and reductions are routinely used for extractive metallurgy, electrolytic degradation and removal of toxic species and ions from medium.

By controlling the potential between suitable electrodes, extremely high energy can be applied to reduce or oxidize a specific ion to the desired oxidation states. The species formed can be stabilized by the counter ions present in the medium or treating them with addition reactants to get a desired stable product. Formations of several unusual oxidation states of number of d block elements like Cr, Ti, Nb, Ta, Zr, Hf, Re and Ir, viz. Ti^{2+-4+}, Cr^{2+-6+}, Zr^{2+-4+} or Hf^{2+-4+}, Nb^{4+-5+} or Ta^{4+-5+}, Re^{3+-7+}, etc., have been observed by electrochemical redox reactions in molten fluoride, chloride or oxyfluoride medium [58, 62]. In addition, it has been pointed out that higher oxidation states of the cations can be stabilized by changing the oxygen concentration of electrolyte or by using molten oxyfluoride or fluoride electrolytes.

Complex oxides with high oxidation cations, like PbO_2, TbO_2, $KBiO_3$, $NaNiO_2$, $NaBaCu_3O_5$, $SrNiPtO_6$, can be crystalized by electro-crystallization from hydroxide melts [63, 64]. In such methods, the voltage across the electrodes is applied at the maximum current state using other sacrificial cation electrolytes where the cations with oxidation states are deposited as complexes at the anodes while sacrificial cation deposited as metal at cathode; viz. $KBiO_3$ can be crystalized at the anode using molten mass of Bi_2O_3 and $ZnCl_2$ in KOH by application of 1.1 V across the cathodes [64, 65]. However, the time and temperature and sacrificial electrolyte components need to be optimized for the electrochemical oxidation. Electrochemical reduction is also carried out by using the materials itself as either electrode in a desired medium of or electrolysis in suitable medium. Reduction of vanadium from V^{5+} to V^{2+} and subsequent stabilization as complexes like V(II)-EDTA and V(II) (picolinate) or V(II) formate are known by electrochemical process [39, 40]. The progressively decreasing oxidation state from 5+ to 2+ of V is reflected in change in colour of the solutions from yellow to blue to green and purple [40].

5.5.5 Electron or γ-radiation-Induced Redox Reactions

Several elements with unusually low oxidation states are also obtained by electron irradiation or by utilization of in situ generated electrons or radicals formed by gamma radiolysis of water or liquid medium. The aqueous solution of ions on irradiation with

γ-radiation or electron causes radiolysis of water to produce species like OH, H, e−, e_{aq}−. Though these species have shorter life, they are highly reactive. The reducing species generated by radiolysis can reduce the cations or molecules present in the solution to lower oxidation states. The reduced species are generally transient and need to be stabilized by solvation. The life of the reduced species can be increased by either additional stabilizing species, lowering temperature or solidifying the solutions. Large number of studies have been reported in scattered literature indicating the formation of diversified cations like Zn^{1+}, Cd^{1+}, Hg^{1+}, Ga^{2+}, In^{2+}, Tl^{2+}, Ge^{3+}, Sn^{3+}, Pb^{3+}, Sb^{4+}, Bi^{4+}, etc. [66, 67].

Similarly, the glasses containing various cations on irradiation with electron or gamma ray also cause reduction. These reduced species have sufficient stability and may revert to stable oxidation states only after prolonged time or upon heating or irradiation with lights [68]. As an example, lead borosilicate glasses containing Zn, Ge, Sb, Sn, Ti, etc., on gamma irradiation show the presence of Zn^{+}, Ge^{3+}, Sn^{3+}, Sb^{4+}, Ti^{2+} ions [68, 69]. Glasses prepared using highly oxidizing species can also stabilize Cr^{4+} and Fe^{4+} in the glass matrix or also oxidized during the normal glass preparation conditions. Li_4SiO_4 and Li_2ZnSiO_4 glass ceramics containing Cr^{3+} ions can partially oxidize Cr^{3+}–Cr^{4+}, and the Cr^{4+} ions are occupied at tetrahedral Si sites of the ceramics or glasses [70, 71]. However, the concentrations of the oxidized species are often low and suitable for optical applications [58].

Besides these methods, there are procedures like laser flash and high energy electron beam and high energy plasma interactions can also produce highly positive charged cations. However, often they are stable only in gas phases. However, such species are difficult to stabilize or need special care experimental conditions to trap and stabilize. Most commonly used methods are stabilization by organic ligands, and they are extensively being investigated to stabilize lower valent oxidation states for synthetic organic chemistry. However, these methods are excluded from this chapter as they are extensively available in the literatures dealing with organic and organometallic chemistry.

5.6 Conclusions

From the details presented in this chapter, it can be concluded the preparation of materials with unusual oxidation states is not favourable energetically while a judicious preparation condition can stabilize them. A wide variety of experimental procedure can be used to achieve these oxidation states in laboratory, while the stabilization is predominantly dependent on the lattice structure, composition and counter ionic species present in the stabilizing matrices. In addition, it can be mentioned that though the high positive charge or high negative charge can be obtained by applying extremely high energy they may not be stabilized due to their strong oxidizing or reducing nature. Such species may alter the compound or decompose the compound, or they themselves may disproportionate to other stable oxidation states. It can be

added here that the unusual oxidation states once stabilized can be exploited for varieties of applications using their chemical and physical properties. Hence, it remains as a challenge for chemists to prepare them as well as to understand and utilize them.

References

1. Lee JD (1997) Concise inorganic chemistry. General properties of elements, 5th edn. Blackwell Science Ltd. Oxford, London
2. Greenwood NN, Earnshaw A (1994) Chemistry of the elements. Chemical periodicity and the periodic table, 2nd edn. Butterworth-Heinemann
3. Huheey JE, Keiter EA, Keiter RL (1973) Inorganic chemistry, principles of structure and reactivity. The structure of the atom, 4th edn. HarperCollins College Publishers
4. Tsukahara K, Okada M, Asami S, Nishikawa Y, Sawai N, Sakurai T (1994) Photoinduced electron-transfer reactions of zinc and magnesium myoglobins. Coord Chem Rev 132:223
5. Weaver MJ (1992) Dynamical solvent effects on activated electron-transfer reactions: principles, pitfalls, and progress. Chem Rev 92:463
6. Coey MD, Venkatesan M (2002) Half-metallic ferromagnetism: example of CrO. J Appl Phys 91:8345
7. Stefanovich G, Pergament A, Stefanovich D (2000) Electrical switching and Mott transition in VO_2. J Phys Condens Matter 12:8837
8. Corbett JD (1985) Zintl anions of the post-transition elements. Chem Rev 85:383
9. Wang G, Zhou M, Goettel JT, Schrobilgen GJ, Su J, Li J, Schlöde T, Riedel S (2014) Electrical switching and Mott transition in VO_2. Nature 514:475
10. Jørgensen CK (1976) New understanding of unusual oxidation states in the transition groups. Naturwissenschaften 63:292
11. Ting W, Chan K, Wong W-T (2013) A brief introduction to transition metals in unusual oxidation states. Polyhedron 52:43
12. Corbett JD (1973) Reduced halides of the rare earth elements. Rer Chim Mineral 10:239
13. Druding LF, Corbett JD, Ramsey BW (1963) Rare earth metal-metal halide systems. VI. Praseodymium chloride. Inorg Chem 2:869
14. Corbett JD (1966) Metal halides in low oxidation states. In: Jolly WL (ed) Preparative inorganic reactions. Interscience, New York, pp 1–33
15. Greis O, Haschke JM (1982) Rare-earth halides. In: Gscheidner KA, Eyring LR (eds) Handbook on the physics and chemistry of rare earths, vol 5. North_Holland, Amsterdam, p 387
16. Petzel T, Greis O, Anorg Z (1973) Über die Anwendung eines neuartigen Reduktionsverfahrens zur Reindarstellung von SmF_2, EuF_2, YbF_2, SmS, YbS und EuO. Allg Chem 396:95
17. Adachi G, Nishihata T, Uchijama K, Shiokawa J (1976) New preparation method of europium difluoride. Chem Lett 5:189
18. Petzel T (1985) The thermodynamics of fusion of europium(II) fluoride. J Less-Common Metals 108:241
19. Sobolev BP, Turkina TM, Sorokin NI, Karimov DN, Komar'kova ON, Sulyanova EA (2010) Crystallography Reports 55:657
20. Reckeweg O, DiSalvo FJ (2017) Single-crystal structure refinement of YbF_2 with a remark about YbH_2. Z Naturforsch 72:995
21. Asprey LB, Kruse H (1960) Divalent thulium. Thulium di-iodide. J lnorg Nucl Chem 13:32
22. Baernighausen H, Warkentin E (1973) Rev Chim Mineral 10:14l
23. Cunningham BB, Feay DC, Rollier MA (1954) Terbium tetrafluoride: preparation and properties. J Am Chem Soc 76:3361
24. Asker WJ, Wylie AW (1964) Cerium tetrafluoride. I. Preparation and reactions. Aust J Chem 18:959

25. Bratsanova LR, Zakharv YV, Opalovskii AA (1973) Russ J Inorg Chem 18:476
26. Soriano J, Givon M, Shamir J (1966) The preparation of praseodymium tetrafluoride. Inorg Nucl Chem Lett 2:13
27. Zhang Q, Hu S-X, Qu H, Su J, Wang G, Lu J-B, Chen M, Zhou M, Li J (2016) Pentavalent lanthanide compounds: formation and characterization of praseodymium (V) oxides. Angew Chem Int Ed 55:6896
28. Achary SN, Bevara S, Tyagi AK (2017) Recent progress on synthesis and structural aspects of rare-earth phosphates. Coord Chem Rev 340:266
29. Clearfield A (1982) Inorganic ion exchange materials. CRC Press Inc, Boca Raton, Florida, p 4
30. Vaivada M, Konstants Z (1979) Formation of condensed phosphates during solid-phase reaction of CeO_2 with $NH_4H_2PO_4$. Inorg Mater 12:647
31. Bevara S, Achary SN, Patwe SJ, Sinha AK, Tyagi AK (2016) Preparation and crystal structure of $K_2Ce(PO_4)_2$: a new complex phosphate of Ce (IV) having structure with one-dimensional channels. Dalton Trans 45:980
32. Bevara S, Mishra KK, Patwe SJ, Ravindran TR, Gupta MK, Mittal R, Krishna PSR, Sinha AK, Achary SN, Tyagi AK (2017) Phase transformation, vibrational and electronic properties of $K_2Ce(PO_4)_2$: a combined experimental and theoretical study. Inorg Chem 56:3335
33. Terayama K, Ikeda M (1983) Study on thermal decomposition of MnO_2 and Mn_2O_3 by thermal analysis. Trans Jpn Inst Met 24:754
34. Demazeau G, Marbeuf A, Pouchard M, Hagenmuller P (1971) Sur une série de composés oxygènes du nickel trivalent derivés de la perovskite. J Solid State Chem 3:582
35. Demazeau G, Jung DY, Largeteau A, Choy JH (1998) High oxygen pressures and the stabilization of unusual oxidation states of transition metals: application to iridium oxides. Rev High Pressure Sci Technol 7:1025
36. Chakravarty R, Bevara S, Bahadur J, Chakraborty S, Sarma HD, Achary SN, Dash A, Tyagi AK (2018) Birnessite: a new-generation and cost effective ion exchange material for separation of clinical-grade 90Y from 90Sr/90Y mixture. ChemistrySelect 3:10670
37. Achary SN, Tyagi AK, Kohler J (2002) Preparation, structure, and properties of $V_2GeO_4F_2$—chains of VO_4F_2 octahedra in the first V (III) metallate fluoride. J Solid State Chem 165:74
38. Achary SN, Patwe SJ, Tyagi AK (2008) Crystal structure and thermal expansion studies of α-$VO(PO_3)_2$. J Alloys Comp 461:474
39. Manjanna J, Venkateswaran G (2001) Dissolution of chromium-substituted iron oxides in V(II) formulations. Hydrometallurgy 61:45
40. Tripathi VS, Manjanna J, Venkateswaran G, Gokhale BK, Balaji V (2004) Electrolytic preparation of vanadium(II) formate in pilot-plant scale using stainless steel mesh electrodes: dissolution of α-Fe_2O_3/$Fe_{1.6}Cr_{0.4}O_3$ in an aqueous VII-NTA complex. Ind Eng Chem Res 43:5989
41. Achary SN, Tyagi AK, Kohler J (2005) Lattice thermal expansion studies of $V_2GeO_4F_2$: a topaz type oxide-fluoride. Mater Res Bull 40:1143
42. von Gastinge E (1956) Über die Darstellung von Germanium(II)-oxyd. Z Anorg Allg Chemi 285:103
43. Grube G, Schneideur A, Eschand U, Flad M (1949) The formation of aluminum suboxide. Z Anorg Chem 260:120
44. Von Spandau H, Ksohlmeyer EJ (1945) Über Zinnmonoxyd und sein Verhalten bei hohen Temperaturen. Z Anorg Chem 254:65
45. Jensen WP, Palenik GJ, Tiekink ERT (2001) Bond valence sums in coordination chemistry. Sn(II), Sn(III), and Sn(IV) complexes containing Sn-S and/or Sn-N bonds. Polyhedron 20:2137
46. Jennifer A, Pardoe J, Downs AJ (2007) Development of the chemistry of indium in formal oxidation states lower than +3. Chem Rev 107:2
47. Tyagi AK, Achary SN, Köhler J Synthesis and structure of $InHfF_5$–a new monovalent In containing fluoride with layers of the lone pair atoms $[In]^+$. Private communication
48. Fitz H, Müller BG, Anorg Z (1997) $InBF_4$, das erste komplexe Fluorid mit Indium(I). Allg Chem 623:579

49. Koller D, Mueller BG, (2002) Synthese und Struktur von $RbHfF_5$, $Rb_2Zr_3F_{12}O$ und $Rb_2Hf_3F_{12}O$ — zwei Oxidfluoride mit zentraler trigonal-planarer $[M_3O]$-Gruppe. Allg Chem 628:575
50. Chernick CL, Claassen HH, Fields PR, Hyman HH, Malm JG, Manning WM, Matheson MS, Quarterman LA, Schreiner F, Selig HH, Sheft I, Siegel S, Sloth EN, Stein L, Studier MH, Weeks JL, Zirin MH (1962) Fluorine compounds of xenon and radon. Science 138:136
51. Slivnik J, Smalc A, Zemva B, Mosevic AN (1968) On the synthesis of xenon di-, tetra-, and hexafluoride. Croat Chem Acta 40:49
52. Claassen HH, Selig H, Malm JG (1962) Xenon tetrafluoride. J Am Chem Soc 84:3593
53. Avignat J, Cousson D (1978) Synthesis and radiocrystallographic study of fluorides of alkali metal elements and tetravalent terbium or praseodymium. Rev Chim Mineral 15:360
54. Tabuchi M, Tatsumi K, Morimoto S, Nasu S, Saito T, Ikeda Y (2008) Stabilization of tetra- and pentavalent Fe ions in Fe-substituted Li_2MnO_3 with layered rock-salt structure. J Appl Phys 104:043909
55. Takeda Y, Naka S, Takano M, Shinjo T, Takada T, Shimada M (1978) Preparation and characterization of stoichiometric $CaFeO_3$, Mater Res Bull 13:61
56. Asprey LB, Coleman JS, Reisfeld MJ (1967) Preparation, structure and spectra of some tetravalent praseodymium compounds. Adv Chem Ser 71:122
57. Tabuchi M, Nabeshima Y, Shikano M, Ado K, Kageyama H, Tatsumi K (2007) Optimizing chemical composition and preparation conditions for Fe-substituted Li_2MnO_3 positive electrode material. J Electrochem Soc A 154:638
58. Izumitani T, Peng B, Richardson K (1966) Spectroscopic investigation of Cr-doped silicate and aluminate glasses. Rev Laser Eng 24:689
59. Leutkina EV, Puretskii NA, Bobylevand AP, Komissarova LN (2007) Solid-phase synthesis and characterization of rare-earth chromates. Theor Found Chem Eng 41:567
60. Devi PS, Rao MS (1993) Low-temperature preparation and characterization of phase-pure lanthanide chromates (V) by the citrate gel process. Mater Lett 16:14
61. Thakur J, Shukla R, Raje N, Ghonge D, Bagla H, Tyagi AK (2011) Synthesis, structural characterization and thermal stability of nanocrystalline rare-earth chromates ($RECrO_4$) and rare-earth chromites ($RECrO_3$). Nanosci Nanotechnol Lett 3:648
62. Kuznetsov SA (2016) Electrochemical study of stabilization higher oxidation states of d- and f-metals in molten salts. Int J Electrochem Sci 11:6580
63. Malchus M, Jansen M (2000) Electrocrystallization of PrO_2 and TbO_2-x from alkali hydroxide melts and characterization of the fluorite-related TbO_2-x. Solid State Sci 2:65
64. Nguyen TN, Zurloye H-C (1997) Electrosynthesis in hydroxide melts. J Crystal Grow 172:183
65. Nguyen TN, Giaquinta DM, Davis WM, Zurloye H-C (1993) Electrosynthesis of $KBiO_3$ (potassium bismuth oxide): a potassium ion conductor with the $KSbO_3$ (potassium antimony oxide) tunnel structure. Chem Mater 5:1273
66. Ershov BG, Aleksandrov AI (1977)Production and study of Ge, Sn and Pb in the unusual oxidation states (I) and (III) after low-temperature radiolysis of aqueous solutions of their salts. Int J Radiat Phys Chem 10:327
67. Aleksandrov AI, Ionova GV, Ershov BG (1979) Metal ions of (I-IV) B-groups in unstable oxidation states (electron state $^2S_{12}$) in γ-irradiated aqueous solutions at 77° K. Radiat Phys Chem 13:199
68. Aleksandrov AI, Prokof'ev AI, Bubnov NN (1996) Stabilisation of metal ions in unusual oxidation states and electron dynamics in oxide glasses. Russ Chem Rev 65:479
69. Batchelor C, Chung WJ, Shen S, Jha A (2003) Enhanced room-temperature emission in Cr^{4+} ions containing alumino-silicate glasses. Appl Phys Lett 82:4035
70. Zhuang Y, Teng Y, Luo J, Zhu B, Chi Y, Wu E, Zeng H, Qiu J (2009) Broadband optical amplification in silicate glass ceramics containing Li2ZnSiO4:Cr^{4+} nanocrystals. Appl Phys Lett 95:111913
71. Ju H, Zhao S, Wang H, Li C (2010) Broadband near-infrared emission from Cr^{4+}-doped transparent glass–ceramics based on lithium silicate. Chem Phys Lett 486:126

Chapter 6
Up-Converting Lanthanide Ions Doped Fluoride Nanophosphors: Advances from Synthesis to Applications

Chandresh Kumar Rastogi

Abstract The up-converting nanophosphors are the nano-crystalline materials that produce luminescence by converting low-energy radiation (e.g., infrared or near-infrared) into high energy radiation (ultraviolet and visible) via an anti-Stokes shift process. These can be prepared by incorporating up-converting luminescent centers such as lanthanide ions (Ln^{3+} ions, where Ln = Nd, Ho, Er, and Tm) and/or transition metal ions (e.g., Mn^{2+}, Ti^{2+}, Ni^{2+}, Mo^{3+}, Re^{4+}, and Os^{4+}) into a suitable nano-crystalline host material. The choice of dopant–host combination is decisive in determining the luminescence characteristics of a nanophosphor. Inorganic fluoride hosts such as $ALnF_4$ and LnF_3 (where A and Ln refer to alkali metal ions and lanthanide ions, respectively) and BF_2 (B stands for Ca and Sr) are found suitable for up-converting Ln^{3+} ions as they exhibit; (i) low phonon energy, (ii) promising doping conditions, (iii) favorable electronic structure, and (iv) excellent chemical, thermal, and photo-stability. Ln^{3+} ions doped fluoride nanophosphors (where Ln = Ho^{3+}, Er^{3+}, and Tm^{3+}) exhibit unique up-conversion luminescence characteristics such as strong emission in visible window, substantial anti-Stokes shifts (>600 nm), prolonged luminescence lifetimes (up to several milliseconds), and sensitization under infrared (IR) or near-infrared (NIR) irradiation. Due to these fascinating luminescence properties, they find potential applications in bio-imaging, drug delivery, tumor targeting, solid-state lighting, energy harvesting. Interestingly, their luminescence characteristics can be altered by varying the doping concentration, dopant–host combination, morphology, crystal structure, and the functional group present over the surface of the nanoparticles. This has given prime focus toward developing novel synthesis techniques that are promising in preparing the fluoride-based nanophosphors of desired morphological, compositional, structural, and optical characteristics. The solution-based synthesis methods or *wet chemical methods* are very promising in producing

C. K. Rastogi (✉)
Chemistry Division, Bhabha Atomic Research Centre Mumbai, Mumbai 400085, India
e-mail: chandresh@cas.res.in

Homi Bhabha National Institute, Anushaktinagar, Mumbai 400094, India

Centre for Advanced Studies, Dr. A.P.J. Abdul Kalam Technical University, Lucknow 226031, India

A. K. Tyagi and R. S. Ningthoujam (eds.), *Handbook on Synthesis Strategies for Advanced Materials*, Indian Institute of Metals Series,
https://doi.org/10.1007/978-981-16-1892-5_6

nanophosphors of controlled size–shape, phase, and chemical composition. Several solution-based methods were developed in past for the preparation of fluoride-based nanocrystals, with each of them having some merits and demerits. Therefore, a prior understanding of each method is essential before adapting it for material preparation. In this regard, this chapter provides a brief description about a few of solution-based synthesis methods such as hydrothermal, co-precipitation, and thermolysis, which are most versatile in the controlled preparation of a variety of Ln^{3+}-doped fluoride nanophosphors (e.g., $ALnF_4$, BF_2, and LnF_3, where A, B, and Ln stand for alkali metal, alkaline earth metal, and lanthanide ions, respectively).The critical role of reaction parameters such as pH of the reaction medium, precursor amount, ligands, reaction temperature and time on the controlled preparation of Ln^{3+}-doped fluoride nanophosphors will be discussed in light of available literature. Further, the impact of morphological, structural, and compositional characteristics of the nanophosphors on their luminescence behavior will be discussed in regard to their biomedical, energy harvesting, and lighting applications.

Keywords Morphology · Crystal structure · Fluorides · Lanthanides · Up-conversion · Luminescence

Abbreviations

CT	Computed tomography
CTAB	Hexadecyltrimethylammonium bromide
EDTA	Ethylenediaminetetraacetic acid
EMU	Energy migration up-conversion
Er	Erbium
ESA	Excited-state absorption
ETU	Energy transfer up-conversion
FITC-BSA	Fluorescein isothiocyanate-bovine serum albumin
FRET	Förster resonance energy transfer
GSA	Ground-state absorption
LbL	Layer-by-layer
Ln	Lanthanide
Ln-NPs	Lanthanide-doped nanoparticles
MRI	Magnetic resonance Imaging
NCs	Nanocrystals
NPs	Nanoparticles
PAH	Polyallylamine hydrochloride
PDADMAC	Polydiallyldimethylammonium chloride
PDDA	Poly(diallydimethylammonium)
PDT	Photodynamic therapy
PEG	Polyethylene glycol
PET	Positron emission tomography

PSS	Polystyrene sulfonate
PTT	Photothermal therapy
PVA	Polyvinyl alcohol
PVP	Polyvinylpyrrolidone
QDs	Quantum dots
TEOS	Tetraethoxysilane
Tm	Thulium
UC	Up-conversion
UCNPs	Up-converting nanoparticles or up-converting nanophosphor
UV	Ultraviolet
Vis	Visible
Y	Yttrium
Yb	Ytterbium

6.1 Introduction

Luminescence is a phenomenon of producing light from the substance upon excited with some sort of energy. It is to be distinguished from incandescence, which is a type of emission from a substance by virtue of it being at a high temperature. The luminescence can be considered as cold emission which involves two processes, viz. (i) the electronic excitation of a solid material to a higher energy state and (ii) subsequent emission of photons due to their de-excitation. Different types of luminescence are distinguished depending upon the source of excitation. As an instance, if a light source is used for excitation, the phenomenon is referred to as photo-luminescence. Lanthanide ions (e.g., Eu^{3+}, Tb^{3+}, Dy^{3+}, Er^{3+}, Tm^{3+}) and transition metal (TM) ions (e.g., Mn^{2+}, Ti^{2+}, Ni^{2+}, Mo^{3+}, Re^{4+}) are the important luminescent centers for inorganic host materials. Such luminescent centers are known as *activator* ions and produce a variety of luminescence upon excitation with suitable radiation. Lanthanide ions exhibit novel luminescence properties such as emissions over a wide wavelength range (200–2400 nm), narrow line-like emission bands, and longer luminescence lifetime due to photo-physical phenomena such as *up-conversion, down-conversion* and *Stokes shift* (vide infra). Due to these fascinating luminescence properties, they find potential applications in lighting, displays, lasers, photo-catalysis, drug delivery, bio-imaging, photo-thermal therapy, and so forth [1–4].

Though, the Ln^{3+} ions produce fascinating luminescence characteristics, however, it is difficult to excite them as they poorly absorb the radiation. To circumvent this issue, Ln^{3+} ions are introduced into a suitable host which excites them using mechanisms like "energy transfer or charge *transfer."* Furthermore, the host plays a vital role in keeping Ln^{3+} ions separated from each other to minimize their self-interaction related luminescence quenching. In case the host too has limited absorption capacity over the desired wavelength region, the excitation of the Ln^{3+} ion can be realized with the help of another type of ions (known as *sensitizer*) which have

strong absorption characteristics. Such sensitizer ions are co-doped with activator Ln^{3+} ions and provide efficient sensitization to activator ions *via* charge transfer, energy transfer, and cross-relaxation processes. As an instance, the Yb^{3+} ions can efficiently absorb near-infrared radiation of wavelength ~980 nm and are, therefore, used as the sensitizer for Er^{3+} ions incorporated into crystals of low phonon energy.

The selection of host is important for obtaining desired luminescence from Ln^{3+} ions. A host is said to be suitable for the incorporation of Ln^{3+} ions if it qualifies the following criteria: (i) low phonon energy, (ii) favorable electronic and geometric structures, (iii) good photo-stability, and (iv) improved crystallinity. Generally, fluoride-based inorganic compounds such as LnF_3 [5], $ALnF_4$, [6–8], and LnOF [9] (where A and Ln stand for alkali metal ions and lanthanide ions, respectively), BF_2 (B = Sr, Ca, and Ba) [10] are considered to be most suitable hosts for Ln^{3+} ions. As a result, they display unique luminescence properties and are potentially useful for lasers, displays, general lighting, bio-imaging, drug delivery, and bio-labeling [1–4]. In particular, to the biological applications of Ln^{3+}-doped nanophosphors, it is essential that they must qualify certain additional criteria such as (i) particle size must be small enough (lower than few microns) so that they can be internalized into the biological cells, (ii) stability in biological media (iii) minimized non-specific binding with cells, and (iv) non-toxicity.

The up-converting luminescent materials are very suitable for biomedical applications as they exhibit: (i) near-infrared (NIR) excitation which is beneficial in minimizing radiation-induced tissue damage and auto-fluorescence, (ii) several sharp emission peaks which enable new options for multiplexed encoding, (iii) large conventional anti-Stokes shift which allows differentiating between excitation and emission signals, (iv) biocompatibility and non-toxicity over wide-ranging cell lines, and so forth. Most of the practical applications of these materials rely on their ability of dispersion in aqueous, biological, or other organic media. The nano-crystalline luminescent materials have a stronger dispersion ability compared to that of their bulk counter phase. Therefore, they are of high demand despite the inferior luminescence characteristics compared to that of the bulk phase of the same composition. Further, the surface functionality of the nano-crystalline material can be significantly altered to improve its physico-chemical properties. In the present context, the terms "up-converting nanoparticles" or the "up-converting nanophosphors" are interchangeably used and an acronym UCNPs are used to denote either of them.

Most of the biomedical applications require UCNPs of desired size, shape, uniformity, and functionality. Despite the recent advancement in materials synthesis techniques, the formation of UCNPs with desired structural features and chemical composition is still very challenging due to complexity involved in synthesis monodispersed nanoparticles. The solution-based synthesis methods (also known as wet chemical methods) are found to be very promising for UCNP preparation as a number of process parameters (e.g., reaction temperature [11], reaction time [12], pH [13], ligands [14], additives [15, 16], and precursor salts) can be modulated simultaneously so as to alter the reaction kinetics and produce a variety of nanostructure [17, 18, 20–22]. In past, wet chemical synthesis employing hydrothermal, co-precipitation, thermal decomposition, sol–gel, and microemulsion methods were developed for

the controlled preparation of a variety of up-converting NPs (e.g., LnF_3, $ALnF_4$, and MF_2, where A = alkali metal ions, M = alkaline earth ions, and Ln = lanthanide ions [7, 17, 23–27]. In this direction, the current chapter describes a few of the most commonly used wet chemical methods for the preparation of fluoride-based up-converting nanophosphors. The role of various synthesis parameters (e.g., reaction temperature–time, pH, ligands, and so forth) on the morphological, structural and compositional characteristics of UCNPs, will also be discussed. The detailed discussion about the effect of doping concentration, choice of dopant, morphology and crystal structure of host on the luminescence properties of up-converting LnF_3, MF_2, and $ALnF_4$ NPs will also be presented in the light of the information available in the existing literature. The scope of this chapter is limited to the solution-based synthesis methods for the controlled preparation of fluoride-based UCNPs, and is not, intended to provide a comprehensive review on nanomaterials synthesis.

6.2 Luminescence from Lanthanides Ions

6.2.1 Lanthanides

Lanthanide (Ln) elements belong to period 6 in periodic table. The atomic number (Z) for Ln ranges from Z = 58–71, following lanthanum (La) in series, and, their 4f shell is successively filled (Fig. 6.1). Scandium (Z = 21), yttrium (Z = 39), and lanthanum (Z = 57) are also included in lanthanide series due to their similar

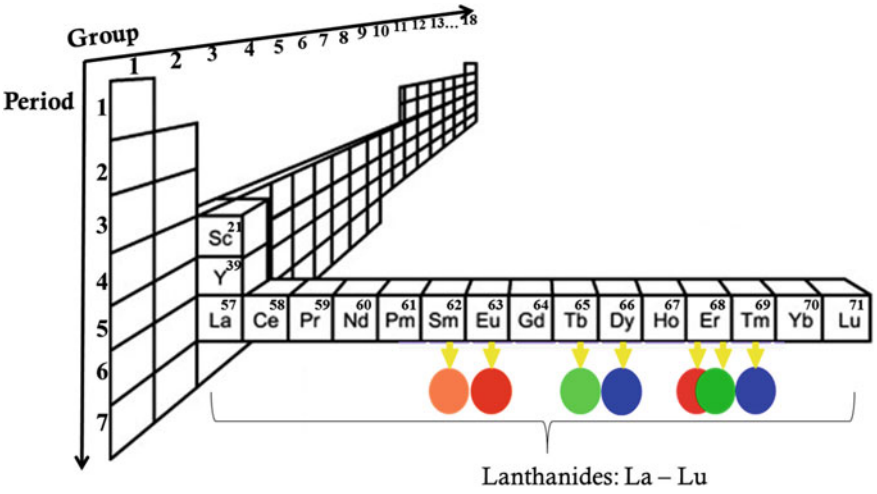

Fig. 6.1 Modified periodic table displaying different elements of the lanthanide (Ln) series. The spheres represent the luminescence colors that can be produced by various Ln^{3+} ions across the lanthanide series

chemical behavior. A majority of lanthanides exhibit 3 + oxidation state as the stable state with a few existing as divalent (Sm, Eu, and Yb) and tetravalent (Ce, Pr, and Tb) ions as well. The ionic radii of lanthanides decrease with an increase in atomic number (Table 6.1). For example, the sizes of cerium (Z = 58) and lutetium (Z = 72) ions are 1.143 Å and 0.977 Å, respectively, for coordination eight [28]. The trend of decrease in size of lanthanides with an increase in atomic number is popularly known as *lanthanide contraction* and arises due to a progressive increase in attraction by nucleus because of weak shielding of 4f electrons caused by their complicated shape of orbitals. The electrons in (4f) shell give rise to useful electronic, magnetic and optical properties in the solid state. They possess close-packed structures (fcc and hcp) with a few exceptions (Sm-rhombohedral, Eu-bcc).

6.2.2 Origin of Luminescence

Luminescence in Ln^{3+} ions arise due to intra-configurational transitions within their 4f shell. Their 4f shell is shielded by filled 5 s and 5p orbitals, and consequently, their absorption and emission characteristics are not influenced by the ligand environment. Accordingly, they exhibit sharp spectral line similar to those of free atoms or ions with high color purity. Moreover, Ln^{3+} ions exhibit low molar absorption coefficient ($10\ cm^{-1}$) but long luminescence lifetime as the transitions involved conserve parity and therefore forbidden by Laporte selection rule [29]. However, these transitions may occur via mixing with allowed $4f^{N-1} \rightarrow 5d^1$ transitions [30]. Table 6.1 lists some important data of trivalent lanthanide ions such as ionic radius, term symbol for ground state configuration, and the electronic transition responsible for producing a variety of emissions.

Figure 6.2 shows an energy-level illustration of trivalent lanthanide ions (Ln^{3+}). The ions (Eu^{3+}, Er^{3+}, Tb^{3+}, Dy^{3+}, Tm^{3+} ions) have well-defined discrete excitation states and so produce sharp emissions, while a few (e.g., Eu^{2+} and Ce^{3+}) exhibit bands in excitation states and give rise to broad emission spectra. The energy states of ions with a given electronic configuration is described by the term symbol ($^{2S+1}L_J$) notation. The letters *L, S*, and *J* represent the total orbital, spin, and angular momentum, respectively.

6.2.3 Photo-Physical Mechanism

Lanthanide ions (Ln^{3+}) doped inorganic materials exhibit novel luminescence properties such as emissions over a wide wavelength range (200–2400 nm), narrow line-like emission bands, and longer luminescence lifetime due to photo-physical phenomena such as up-conversion, down-conversion, and Stokes shift.

Table 6.1 Important data of trivalent lanthanide (Ln^{3+}) ions with their ground state configuration [Xe] $4f^N$

Z	Element (Ln)	Ionic radius[a] (Å)	N[b]	TS[c]	Transition	Emission (nm)	Application
57	Lanthanum (La)	1.16	0	$^1S_0$	–	–	–
58	Cerium (Ce)	1.14	1	$^2F_{5/2}$	$5d^1 \rightarrow 4f^1$	570–630	Phosphor
59	Praseodymium (Pr)	1.13	2	$^3H_4$	$^1G_4 \rightarrow {}^3H_5$	1300	Optical amplifier
60	Neodymium (Nd)	1.11	3	$^4I_{9/2}$	$^4F_{3/2} \rightarrow {}^4I_{11/2}$	1064	Solid-state lasers
61	Promethium (Pm)	1.09	4	$^5I_4$	$^5F_1 \rightarrow {}^5I_5$	930	Laser
62	Samarium (Sm)	1.08	5	$^6H_{5/2}$	$^4G_{5/2} \rightarrow {}^6H_{11/2}$	652	Lighting
63	Europium (Eu)	1.07	6	$^7F_0$	$^5D_0 \rightarrow {}^7F_2$	615	Display, lighting
64	Gadolinium (Gd)	1.05	7	$^8S_{7/2}$	$^6G_{11/2,\ 9/2,\ 5/2} \rightarrow {}^6P_J$	550–650	Bio-imaging
65	Terbium (Tb)	1.04	8	$^7F_6$	$^5D_4 \rightarrow {}^7F_5$	545	Lighting
66	Dysprosium (Dy)	1.03	9	$^6H_{15/2}$	$^6F_{11/2}, {}^6H_{9/2} \rightarrow {}^6H_{15/2}$	1300	Optical amplifier
67	Holmium (Ho)	1.01	10	$^5I_8$	$^5F_5 \rightarrow {}^5I_7$	966	Tele-communication
68	Erbium (Er)	1.00	11	$^4I_{15/2}$	$^4I_{13/2} \rightarrow {}^4I_{15/2}$	1530	Optical amplifier
69	Thulium (Tm)	0.99	12	$^3H_6$	$^3H_4 \rightarrow {}^3F_4$	1480	Optical Amplifier
70	Ytterbium (Yb)	0.98	13	$^2F_{7/2}$	$^2F_{5/2} \rightarrow {}^2F_{7/2}$	980	Sensitizer for Ln^{3+} ions
71	Lutetium (Lu)	0.98	14	$^1S_0$	–	–	–

[a]The ionic radii data correspond to a coordination number of 8; Xe stands for Xenon; [b]N = number of electrons in f-shell, [c]TS = term symbol

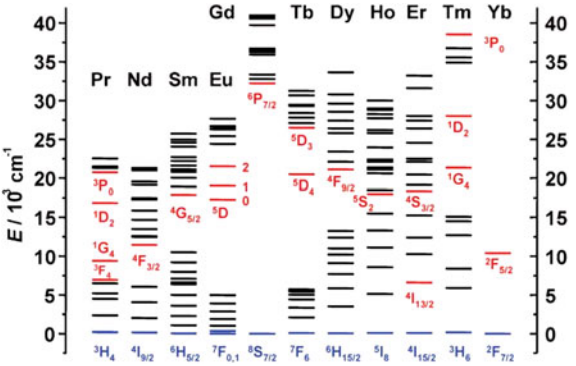

Fig. 6.2 Energy-level diagram of a few of trivalent lanthanide (Ln^{3+}) ions. Reprinted (adapted) with permission from Ref. [31]. Copyright (2005) Royal Society of Chemistry

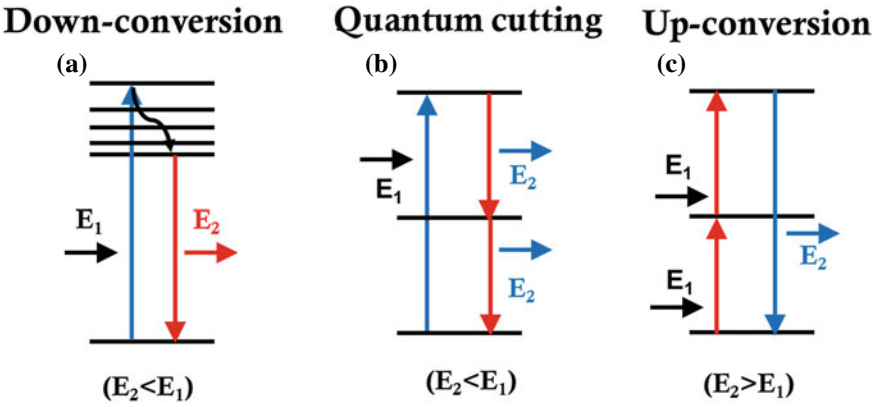

Fig. 6.3 Schematic representation of **a** Stokes shift, **b** quantum cutting, and **c** up-conversion photoluminescence

6.2.3.1 Down-Conversion

Stokes Shift Emission

Down-conversion is a photo-physical process of absorption of a higher energy photon to produce photon(s) of lower energy (Fig. 6.3a). The Stokes shift emission is an example of a down-conversion process in which the excess energy (difference of the absorption and emission energies) is liberated as heat. For example, (i) Eu^{3+}, Tb^{3+}, Tm^{3+}, Sm^{3+} ions emit red, green, blue, and orange colors emission, respectively, when excited with UV light [32, 33], and (ii) Nd^{3+}, Er^{3+}, Yb^{3+}, Pr^{3+}, Sm^{3+}, Dy^{3+}, Ho^{3+}, and Tm^{3+} ions produce near-infrared luminescence with irradiation of UV or visible light [34, 35].

Quantum Cutting

Quantum cutting is a type of down-conversion process that involves absorption of a single photon of higher energy and emission of two or more photons of lower energy. Accordingly, the theoretical efficiency of quantum cutting process is considered to be more than 100%. The process of photo-absorption and emission involved in a typical quantum cutting phenomenon is displayed in Fig. 6.3b.

6.2.3.2 Up-Conversion

This is a nonlinear optical process that involves sequential absorption of two or more photons of lower energy (via an intermediate metastable energy state) followed by the emission of a photon of higher energy (Fig. 6.3c). The general concept of an up-conversion process was first formulated by Auzel [36]. A variety of lanthanide ions (Ln^{3+} where Ln = Er, Tm, Ho, and Pr) exhibit up-conversion. Upon excitation with 980 nm near-infrared radiation, Er^{3+} ions in $NaYF_4$: Er^{3+}, Yb^{3+} produce green and red color emissions *via* two photon up-conversion process, while Tm^{3+} ions in $NaYF_4$: Tm^{3+}, Yb^{3+} produce blue color emission due to both two and three photon up-conversion mechanism [37, 38]. Depending upon the excitation mechanism, there are five different types of up-conversion processes proposed so far, namely,(a) ground-state and excited-state absorption (GSA and ESA), (b) energy transfer up-conversion, (c) cooperative up-conversion, (d) photon avalanche up-conversion, and (e) energy migration up-conversion. The detailed description of the mechanism involved in these up-conversion processes can be found in the existing literature [39–42].

6.3 Photoluminescence Measurement Technique

A fluorimeter equipped with a continuous or pulsed laser source is used to record the up-conversion luminescence spectra. A brief discussion on the basic principles, operation and various component of a fluorimeter is discussed in this section. However, the detailed description of a fluorimeter can be found elsewhere [43].

6.3.1 Instrumentation

The major components of a fluorimeter include an excitation source (e.g., 980 nm continuous laser), emission monochromator, sample chamber, detectors, and a monitoring computer. Figure 6.4 shows the simplified layout of a typical fluorimeter. A brief note about the important components of a fluorimeter is given below.

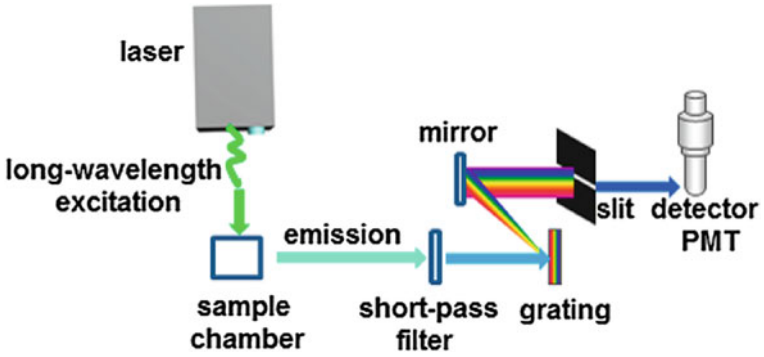

Fig. 6.4 Schematic layout of a typical fluorimeter set up demonstrating the basic components involved in fluorescence measurement. Reprinted (adapted) with permission from Ref. [44]. Copyright (2015) American Chemical Society

6.3.1.1 Excitation Source

Continuous or pulsed laser source working in infrared (IR) or near-infrared window can be used as an excitation source. Typically, a continuous wave (CW) diode laser (operating at 980 nm wavelength) is used as an excitation source. A pulsed source such as Nd: YAG laser can be utilized for carrying out time-resolved studies.

6.3.1.2 Monochromators

A fluorimeter consists of two monochromators, namely emission and excitation monochromators. The most important component of a monochromator is a reflection grating that has an ability to disperse the incident light due to the presence of vertical grooves (nearly 1200 grooves/mm). A spectrum is recorded by rotating the grating.

6.3.1.3 Slits and Shutters

In a fluorimeter, a monochromator has adjustable slits at both the excitation and emission ports that determine the resolution by controlling the range of transmitted light. These slits control the intensity of excitation and emission beams. The widening of excitation slit may allow irradiation of more light on the sample; however, a wider slit opening may cause limited resolution. The role of the shutter is to protect the sample from photo-degradation (or photo-bleaching) due to extended exposure to an intense light beam.

6.3.1.4 Detectors

The fluorimeters generally use photomultiplier tubes (PMT) as detectors. The detector must detect photons of all wavelengths with equal efficiency. There are two detectors in a fluorimeter, i.e., reference and signal detectors. A reference detector is a silicon photo-diode placed just before the sample compartment, while a signal detector is a type of PMT that directs the signal to a photon counting segment.

6.3.2 Photoluminescence Measurement

6.3.2.1 Sample Preparation

A photoluminescence (PL) measurement can be performed on three different types of samples, i.e., solid (powder phase), liquid phase (luminescent particles dispersed in some solvent), and film (composed of luminescent materials). The choice of sample preparation method depends upon the nature of the sample under study and/or the accessories or attachment available to the instrument. As an instance, for liquid phase measurement, the luminescent particles are dispersed in some solvent using vortex mixing and sonication processes. The dispersed particles are then transferred into a cuvette (preferably composed of quartz). The cuvette is then placed inside the sample chamber of the fluorimeter for the measurement. In case the particles cannot be dispersed in any solvent, the solid samples can be ground well using a mortar and pestle to yield fine powder. The powder sample is then uniformly spread over the grove of the powder sample holder. In case of the measurement using a film, initially, a film is fabricated employing deposition techniques (such as pulsed layer deposition, e-beam evaporation, spin coating, and so forth). The film is then attached to the sample holder and placed inside the sample chamber for measurement. The fluorescence measurement is sensitive to the measurement conditions. The important parameters that can influence the PL properties are the colloidal concentration, choice of solvent, film thickness, uniformity of the film, and so forth. Therefore, for the sake of high-quality measurement, meaningful analysis, and correct data interpretation, special care is needed for the sample preparation.

6.3.2.2 Measurement

As shown in Fig. 6.4, the radiation produced from an excitation source is allowed to fall on a sample under study (i.e., luminescent material) via passing it through a number of optical components such as mirrors, excitation monochromator (grating), and slits. The excitation monochromator selectively allows the radiation of a particular wavelength while blocking the other wavelengths. Upon irradiation, the luminescent material gets excited due to absorption of incident radiation, and upon de-excitation, it produces emission. The emitted light passes through the emission

monochromator which is positioned at a right angle to the excitation beam. A cut-off filter is employed in front of the emission slit and monochromator to minimize the scattered light. This arrangement also avoids the excitation beam to reach the emission detector. The detector measures the emitted light, displays the fluorescence value, and produces the fluorescence signature of the sample.

6.3.2.3 Photoluminescence Quantum Efficiency

The photoluminescence quantum yield (QY) or quantum efficiency (QE) can be defined as the ratio of the number emitted photons to the number of absorbed photons and can be expressed as follows:

$$\mathrm{QE} = \frac{\text{No. of emitted photons}}{\text{No. of absorbed photons}} \tag{6.1}$$

Quantum efficiency (QE) can be defined in many ways and have been coined with different names (viz. internal QE, external QE, and absolute QE) in the literature. The quantum efficiency estimated using the radiative luminescence lifetime (τ_{rad}) and observed lifetime (τ_{obs}) of the luminescent materials is defined as intrinsic quantum efficiency. The external quantum efficiency (QE_{ext}) can be calculated by considering the number of incident photons rather than the number of absorbed photons.

$$\mathrm{QE}_{int} = \tau_{obs} / \tau_{rad} \tag{6.2}$$

where τ_{obs} and τ_{rad} are the observed and radiative lifetime of the luminescent material, respectively.

Quantum efficiency of up-converting $NaLnF_4$ nanophosphors has been estimated by various research groups [45–48]. Table 6.2 displays the experimentally calculated QE values for various $NaLnF_4$ (Ln = Gd, Er, Y, Yb, and Lu)-based nanophosphors. Van Veggel and co-worker have estimated the absolute QE of β-$NaYF_4$: 20% Yb^{3+}, 10% Er^{3+} UCNPs using a fluorimeter equipped with an integrating sphere. An absolute QE of 0.1% is reported for 30 nm β-$NaYF_4$: 20% Yb^{3+}, 10% Er^{3+} NPs [48]. Liu et al. have reported that β-$NaLuF_4$: Gd^{3+}, Yb^{3+}, Er^{3+} NPs of size ~ 10 nm produce strong luminescence with a QE of 0.47 ± 0.06% [49].

6.4 Critical Factors that Influence Luminescence Characteristics

The luminescence characteristic of UCNPs is synergistically influenced by various factors including choice of activator/sensitizer ions and their concentration, crystallinity, morphology, and crystal structure of host containing up-converting Ln^{3+}

Table 6.2 Luminescence efficiency of a few fluoride-based up-converting nanophosphors

S. No	$NaLnF_4$ nanophosphor (Ln = Er, Gd, Y, Yb, and Tm)	Crystal structure	Particle Size (nm)	Quantum efficiency	References
1	$NaY_{0.78}Yb_{0\cdot20}Er_{0.02}F_4$	Hexagonal	100	0.30^e	[48]
2	$NaY_{0.78}Yb_{0\cdot20}Er_{0.02}F_4$	Hexagonal	30	0.10^e	[48]
3	$NaY_{0.78}Yb_{0\cdot20}Er_{0.02}F_4$	Hexagonal	8	0.005^e	[48]
4	$NaY_{0.78}Yb_{0\cdot20}Er_{0.02}F_4@NaYF_4$	Hexagonal	30	0.30^e	[48]
5	$NaGd_{0\cdot78}Yb_{0\cdot20}Er_{0.02}F_4@NaYF_4$	Hexagonal	100	0.50^e	[50]
6	$NaLu_{0.55}Yb_{0.2}Gd_{0\cdot24}Tm_{0.01}F_4$	Hexagonal	10	0.47^e	[49]
7	$NaTm_{0.005}Yb_{0.995}F_4@CaF_2$	Cubic	27	0.60^e	[51]
8	$Ca_{0.995}Er_{0.005}F_2$	Cubic	50	0.51^i	[52]
9	$La_{0.995}Er_{0.005}F_3$	Hexagonal	10	0.95^i	[52]

The superscripts *i* and *e* are used over the values of QE referring to external and internal quantum efficiency, respectively.

ions. It is vital to comprehend the influence of the above-mentioned factors on the luminescence properties UCNPs. The list of these parameters is exhaustive, and it is difficult to cover each of them in a single section; therefore, the discussion will be selective covering the parameters which are closely related to the structural and chemical features of UCNPs (e.g., crystal structure, morphology, doping concentration of activator, and sensitizer ions).

6.4.1 Choice of Activator

The choice of a suitable activator is the most important factor that governs the light emission characteristics of UCNPs. The activator ions are usually characterized by long-lived metastable excited states. Lanthanide ions ($Ln^{3+,}$ where Ln = Er, Tm, Pr, and Ho) ions can produce up-conversion luminescence if incorporated into suitable inorganic fluoride hosts. Figure 6.5 shows a typical energy-level diagram of these up-converting lanthanide ions that describes various excitation and emission processes involved in the luminescence process. A variety of blue, green, and red light emissions can be produced by the choice of activator ion. Table 6.3 displays various possible combinations of red, green, and blue light-emitting Ln^{3+} ions that can produce a variety of luminescence over the visible span of the electromagnetic spectrum.

6.4.2 Choice of Sensitizer

Several lanthanide ions (Ln^{3+}, where Ln = Er, Ho, Tm, Nd, and Pr) are suitable to produce up-conversion luminescence; however, they suffer from an inefficient

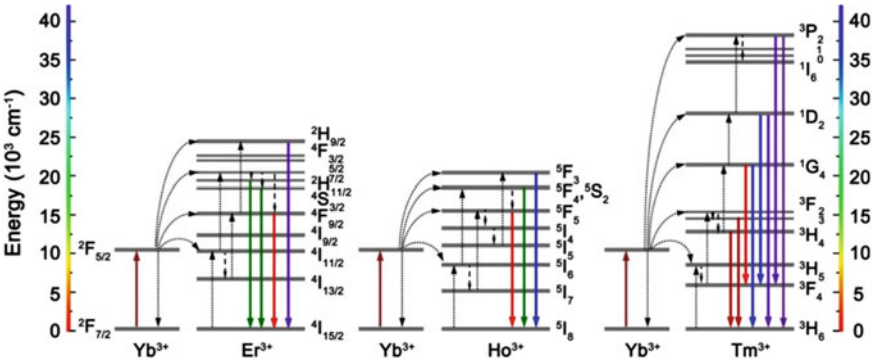

Fig. 6.5 Schematic diagram depicting various excitation and emission mechanisms responsible for up-conversion in **a** $Yb^{3+} - Er^{3+}$, **d** $Yb^{3+} - Ho^{3+}$, and **e** $Yb^{3+} - Tm^{3+}$ lanthanide ion pairs [67]. Reprinted with permission from Ref. [67]. Copyright 2015 American Chemical Society

Table 6.3 Various dopant–host combinations for up-converting lanthanide ions doped fluoride nanophosphors and the strength of their emission over the visible region of electromagnetic spectrum

Activator	Sensitizer	Host	Crystal structure	Major emission			References
				Red	Green	Blue	
1.6% Ho^{3+}	98.4% Yb^{3+}	α-$NaYbF_4$	Cubic	–	540 (S)	–	[56]
2% Er^{3+}	20% Yb^{3+}	α -$NaYF_4$	Cubic	660 (S)	540 (M)	411 (W)	[26]
2% Er^{3+}	20% Yb^{3+}	β-$NaYF_4$	Hexagonal	656 (M)	523, 542 (S)	–	[57]
2% Tm^{3+}	20% Yb^{3+}	α -$NaYF_4$	Cubic	647 (W)	–	450,475 (S)	[26]
2% Tm^{3+}	20% Yb^{3+}	β-$NaYF_4$	Hexagonal	–	–	450 & 475 (S)	[57]
2% Er^{3+}	20% Yb^{3+}	$LiYF_4$	Tetragonal	653 & 667 (W)	542 & 551 (S)	–	[58]
2% Er^{3+}	20% Yb^{3+}	CaF_2	Cubic	654 (M)	541 (S)	410 (W)	[59]
3% Er^{3+}	12% Yb^{3+}	LaF_3	Hexagonal	659 (W)	521 & 545 (S)	410 (W)	[60]
1% Ho^{3+}	20% Yb^{3+}	LaF_3	Hexagonal	645 & 658 (S)	542 (W)	–	[60]
1% Tm^{3+}	10% Yb^{3+}	LaF_3	Hexagonal	800 (S)	–	475 (S)	[60]

direct excitation owing to their lesser absorption capability. In case the host and activators, Ln^{3+} ions themselves are not capable of participating in the excitation of activator ions, and the second type of ions (having a large absorption cross-section) is co-doped into the host crystal to facilitate an efficient and indirect excitation to

Ln^{3+} ions. Accordingly, these co-dopants are known as a sensitizer. The sensitizer must exhibit strong absorption capacity of near-infrared radiation and have favorable electronic structure to transfer the absorbed radiation to activator ions. The sensitizer species not only assist in excitation of activator ions but also keep them separated so as to avoid cross-interaction among themselves. As an instance, Yb^{3+} is used as the sensitizer for various up-converting Ln^{3+} ions due to their high absorption capacity (~9.11×10^{-21} cm^{-2}) for 980 nm radiation. The Yb^{3+} ions have only one excited state (i.e., $^2F_{5/2}$) which is resonant with the excited states of many of the activator Ln^{3+} ions (e.g., Er^{3+}, Ho^{3+}, and Tm^{3+}) that can easily be populated using 980 nm laser radiation.

The energy gap between $^2F_{7/2}$ and $^2F_{5/2}$ of Yb^{3+} ions has a good match with the energy difference between certain excited states of commonly used up-converting Ln^{3+} ions (Fig. 6.5). Although Yb^{3+} doping results in an increase in up-conversion efficiency, the requirement of 980 nm excitation source limits its biological applications as the water can absorb 980 nm radiation to cause overheating of the tissues. As an alternative, Nd^{3+} ions can be used as a potential candidate; however, they exhibit inferior absorption capacity compared to the Yb^{3+} ions.

The electronic structure of the activator ions plays a vital role in determining the luminescence properties of $NaLnF_4$-based nanophosphors as they govern the energy transfer pathways to curb the excitation and emission processes. Commonly, the efficient up-converting nanomaterials developed so far relies on Er^{3+}/Yb^{3+} and Tm^{3+}/Yb^{3+} ion pairs due to the possibility of reduced non-radiative transitions in these cases owing to their well-separated excited states. The rate of non-radiative multi-phonon relaxation within luminescent ions affects the population of intermediate and higher excited states and, accordingly, defines the luminescence efficiency. The rate constant of multi-phonon relaxation k_{nr} for lanthanide ions can be expressed as follows [2]:

$$k_{nr} \propto \exp^{-\beta \Delta E/\hbar\omega} \tag{6.3}$$

where ΔE is the energy gap between the excited state and the adjacent energy level of Ln^{3+} ion, β is an empirical constant of the host, and $\hbar\omega$ is the maximum vibrational energy of the host material. The energy gap law states that the rate of multi-photon relaxation continuously drops exponentially with an increase in the energy gap.

6.4.3 Choice of a Host Material

The choice of a host material is vital for the development of an efficient lanthanide ions doped up-converting nanophosphors. The host material is found suitable for incorporation of Ln^{3+} ions if it exhibits low phonon energy, favorable electronic/geometric structures, and excellent photo-stability. In past, various inorganic host materials such as oxides, vanadates, molybdates, tungstates of alkali metal,

alkaline earth, transition metal, or lanthanides have been used as a host for Ln^{3+} ions [58–61]. Among all, the fluoride-based compounds such as LnF_3 [5], $ALnF_4$ [6–8], LnOF [62], and BF_2 [10] have been given special attention as they generally fulfil above-mentioned criteria (A, B, and Ln here stands for alkali metal ions, alkaline earth metal ions, and lanthanide ions, respectively). As mentioned in Table 6.3, various guest–host combinations are feasible for up-converting lanthanide ions (i.e., Er^{3+}, Tm^{3+}, and Ho^{3+}) incorporated into fluoride-based hosts (e.g., $NaYF_4$, LaF_3, and CaF_2) to produce strong emission over the different portion of the visible portion of the electromagnetic spectrum.

6.4.4 Doping Concentration

For the development of efficient UCNPs, the control over the energy transfer process is very important which is synergistically dependent on various factors such as the distance between the activator and sensitizer ions, the electronic structure of the materials, crystallinity, and so forth. The emission intensity of Ln^{3+}-doped nanoparticles initially increases with an increase in the doping concentration of activator ions up to a certain optimum concentration and decreases afterward. An increase in dopant concentration results in a decrease in the distance between sensitizer and activators, thereby facilitating energy transfer to produce strong emission. However, beyond a certain optimum doping concentration, self-interactions among activator ions took place that causes a decrease in luminescence intensity. Such a decrease in luminescence because of concentration effect is known as concentration quenching or self-quenching. Therefore, it is indispensable to figure out an optimum loading concentration (X_c) at which the emission intensity is maximum. For a given Ln^{3+} ion, the value of X_c differs from host to host as it depends upon structural parameters such as cell volume and number of available sites for Ln^{3+} ions besides the doping concentration. The critical distance *(R_c)* between the two luminescent centers in a crystal can be expressed as:

$$R_c = 2*(3V/4\pi X_c N)^{1/3} \tag{6.4}$$

where X_c, N, and V are the critical doping concentration, an effective number of luminescence centers in a unit cell and cell volume, respectively.

The UCNPs with an optimum loading amount of sensitizer (Yb^{3+}) and activator ions (Er^{3+}, Tm^{3+}, or Ho^{3+}) yield improved luminescence characteristics. For example, at most of the instances for $NaY_{1\text{-}x\text{-}y}Er_xYb_yF_4$ UCNPs, the luminescence is found to be brightest for a composition corresponding to $x = 0.02$ and $y = 0.18$. The optimal doping condition of sensitizer and activator ions into the host ensures the occurrence of an efficient excitation of activator ions besides avoiding non-radiative transfer between them [63–66].

6.4.5 Morphology

The light emission characteristics of UCNPs are strongly influenced by their particle size, shape, size distribution, and ligands present over the surface of nanoparticles. A brief discussion about the effect of these parameters on the luminescence behavior of UCNPs is provided herein the light of available literature.

6.4.5.1 Particle Size

The behavior of size-dependent photoluminescence from lanthanide ions doped UCNPs differs from that of semiconductor quantum dots (QDs) due to the differences in the photo-physical mechanism of excitation and emission. In lanthanide ions doped materials, luminescence is dependent upon the asymmetry around Ln^{3+} ions, the number of ligands and solvent moieties present at the NP surface, and the number of Ln^{3+} ions residing at the surface or in the bulk of the nanoparticles. All these factors affect the Ln^{3+} ions luminescence in a synergistic fashion. For example, an increase in asymmetry around surface Ln^{3+} ions is advantageous for the improvement of their emission, while the impurities or ligand may offer quenching sites that can suppress the luminescence intensity. In past, morphology-dependent light emission characteristics of UCNPs have been investigated thoroughly [58, 68, 69]. Lu et al. have prepared two different sizes of $NaLuF_4$: Gd, Yb, Er nanoparticles and studied the size effect on the up-conversion light emission behavior [27]. The emission spectra of $NaLuF_4$: Gd, Yb, ErNPs ($\lambda_{ex} = 980$ nm) shown in Fig. 6.6 show that the emission was much weaker for the particle of size 4 nm, and the trend of relative emission intensities at 542 (I_{542}) and 655 nm (I_{655}) is reversed in this case as compared to those for 14 nm UCNPs [27]. The variation in the intensity ratio (I_{542}/I_{655}) was related to the differences in the effective number of ligand adsorbed at the surface of NPs. For a smaller size NP, the S/V ratio increases that resulted in a more number of adsorbed oleate ligands (OA^-) at the surface of NPs. The vibrational energies of the $-CH_2$ and –OH bonds of the OA^- have a good match with the energy gap between the $^4S_{3/2}$ and $^4F_{9/2}$ excited states of Er^{3+} ions. This led to promotion of the non-radiation relaxations and caused the quenching of the green light emission [27]. The confinement of energy migration due to size effect is studied by Chen et al. for up-converting $NaYbF_4$: Tm system [70]. They have reported that the size effect can be harnessed to enhance the multi-phonon up-conversion in $NaYbF_4$: Tm [70]. Their investigations suggested that the confinement of energy migration due to size effect has provided a generic approach to manipulate the multi-photon up-conversion process. They established an efficient five-photon up-conversion mechanism in $NaYbF_4$: Tm NPs to produce very strong emission from Tm^{3+} ion. The strength of the emission was 100 times stronger as compared to that of a conventional Yb/Tm-based phosphor($\lambda_{em} = 650$ nm and $\lambda_{ex} = 980$ nm) [70].

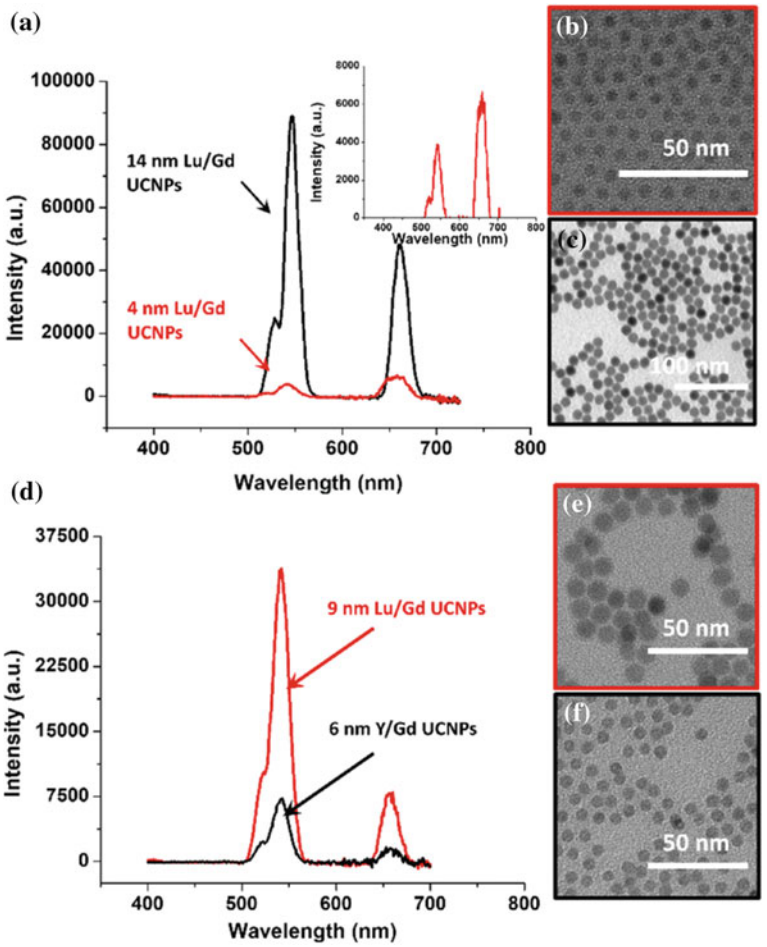

Fig. 6.6 **a** Up-conversion (UC) emission spectra (using $\lambda_{ex} = 978$ nm) of (**a**) $NaLuF_4$: Gd, Yb, Er UCNPs Lu/Gd-4 and Lu/Gd-14. The emission spectrum of Lu/Gd-4 on an expanded scale is shown in the inset of Figure a. The TEM images of the 4 nm NPs (Lu/Gd-4) is shown in (**b**) and TEM images of the 14 nm NPs (Lu/Gd-14) is shown in (**c**). **d** The emission spectra of $NaLuF_4$: Gd, Yb, Er for with Lu/Gd-9 and $NaYF_4$: Gd, Yb, ErNPs with Y/Gd6. The TEM image of Lu/Gd-9 NPs is shown in (**e**), and TEM image of Y/Gd-6 NPs is shown in (**f**). Reprinted with permission from Ref. [27]. Copyright 2017, American Chemical Society

6.4.5.2 Surface Passivation

Nanoparticles (NPs) possess a higher surface area-to-volume ratio (S/V). Accordingly, for ultra-small UCNPs, there is a significant contribution of the Ln^{3+} ions present at the surface of the nanoparticles on the light emission properties of UCNPs. At the NP surface, there exist different types of quenching sites (e.g., surface defects, free ligands, solvent moieties, etc.) that are detrimental to Ln^{3+} ion luminescence.

To obtain improved luminescence from UCNPs, the surface related non-radiative relaxation must be minimized. This can be done by the surface modification of UCNPs. The most popular approaches for their surface engineering include passivation of UCNPs with an optically inert layer and modification of the functional group present over the surface of NPs. Using the surface passivation approach, Chow et al. have demonstrated 30 fold increment in luminescence intensity of $NaYF_4$: Yb/Tm nanocrystals (size ~8 nm) by coating with an inert shell of $NaYF_4$ (1.5 nm thickness) [71]. The surface modification using ligand exchange mechanism can alter the functional group present at the surface of the UCNPs, thereby affecting their ability of dispersion in a particular solvent and the overall luminescence characteristics. Generally, the UCNPs prepared in organic media (e.g., oleic acid, octadecence, oleylamine, etc.) are hydrophobic due to the presence of ligands at their surface. Nacchache et al. reported an improvement in the up-conversion intensity of oleic acid capped $NaGdF_4$: Ho^{3+}/Yb^{3+} nanoparticles after ligand exchange with polya crylic acid (PAA) [72]. Though the luminescence properties of hydrophobic Ln-NPs are superior, however, to render them in aqueous or biological media, their surface must be hydrophilic in nature.

6.4.5.3 Core–Shell Structure

The rational design of a core–shell structure can able to produce intriguing up-conversion luminescence. Recently, Wang et al. have suggested that bright luminescence from UCNPs can be realized by the architecting of layer-by-layer assembly of nanoparticles, in which each layer contains different set of NPs loaded with distinct types of Ln^{3+} ions. They achieved this by gadolinium sub-lattice-facilitated energy migration mechanism for a variety of activator Ln^{3+} ions [73]. This mechanism has enabled fine-tuning of up-conversion emission due to the trapping of the migrating energy by the activator species [73]. The core–shell design assists in avoiding cross-talking between activator species, thereby minimizing the cross-relaxation processes, resulting in brighter luminescence. Interestingly, a 40-fold enhancement in emission intensity was noticed in case of $NaYF_4$: Yb^{3+}, Er^{3+}@ CaF_2 NPs as compared to that of bare core NPs [74].

Recently, core–shell design is proven to be useful in producing down-conversion (DC) and up-conversion (UC)-based dual-mode luminescence with improved efficiency. Zhao and co-workers have developed a $NaLnF_4$ (Ln = Er, Gd, Nd, Yb, and Y)-based core–shell architecture to realize a dual-mode emission. The graphics of such a layer-by-layer core–shells arrangement is demonstrated in Fig. 6.7a. In such a core–shell design, the two luminescent layers are separated by an optically inactive layer. The corresponding energy-level diagram depicting various processes involved in the luminescence process is shown in Fig. 6.7b. As per the scheme presented, the Nd^{3+} ions initially absorb the incident radiation (λ_{ex} = 800 nm) and transfer the absorbed energy to Er^{3+} with the assistance of Yb^{3+} ions within the shell that was composed of $NaGdF_4$: Nd^{3+}, Yb^{3+}, and Er^{3+}.They also reported an enhancement in the emission intensity of Er^{3+} ions upon co-doping of Nd^{3+} ions (Fig. 6.8a). At the

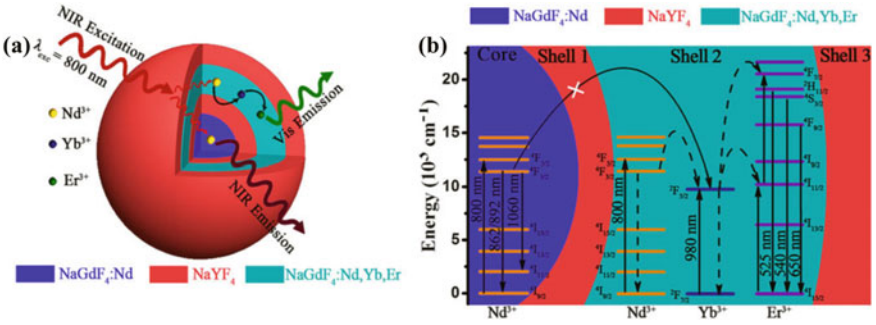

Fig. 6.7 Schematic representation demonstrating **a** the core–shell arrangement of up-converting $NaLnF_4$ (where Ln = Y, Nd, Gd, Yb, and Er) with multiple shells each composed of un doped and Ln^{3+} ion doped materials alternatively [75]. Reprinted with permission from Ref. [75]. Copyright 2013, Springer Nature

same time, the core material composed of $NaGdF_4$: Nd^{3+} produces down-conversion luminescence due to the presence of Nd^{3+} ions. An improvement in emission intensity of Nd^{3+} ions in case of a core–shell structure can be seen (as compared to that of bare NPs of the same composition as shown in Fig. 6.8b) [75].

The variation in spectral profiles of different compositions of the core and core–shell $NaLnF_4$ (Ln = Er, Gd, Nd, Yb, and Y) NPs shown in Fig. 6.8c demonstrates an improvement in the emission intensity of both the Er^{3+} and Nd^{3+} ion emissions due to the formation of an alternate shell of optically inert $NaYF_4$ over it. The comparison of the relative luminescence intensity at wavelength positions ~524, 546, 585, 650, and 862 nm (due to Er^{3+} and Nd^{3+} ions) for various compositions of core and core–shell $NaLnF_4$ (Ln = Er, Gd, Nd, Yb, and Y) NPs is shown in Fig. 6.8d.

6.4.6 Crystal Structure

The crystal structure of luminescent materials determines the distance between luminescent species in a crystal (i.e., activator–activator, sensitizer–activator, and sensitizer–sensitizer ion pairs), and the local chemical environment around Ln^{3+} ions. Therefore, it is of great interest to investigate the structure–property relationship and develop synthesis techniques to obtain NPs of desired phase. As an instance, the luminescence properties of Ln^{3+} ions incorporated in hexagonal (β) $NaYF_4$ [25] are superior in comparison to that of the cubic (α) phase. For hexagonal $NaLnF_4$ system, there are three cationic sites; i.e., first type of site is fully occupied by lanthanide ions (Ln site), and second one is randomly occupied by both lanthanide and sodium ions (1f site), while the third type of site is fully occupied by Na^+ ions. Further, the hexagonal phase belongs to P_6 space group, both lanthanide sites having C_{3h} or D_{3h} symmetry. Kramer et al. found that the green color luminescence of β-NaY (Yb, Er)

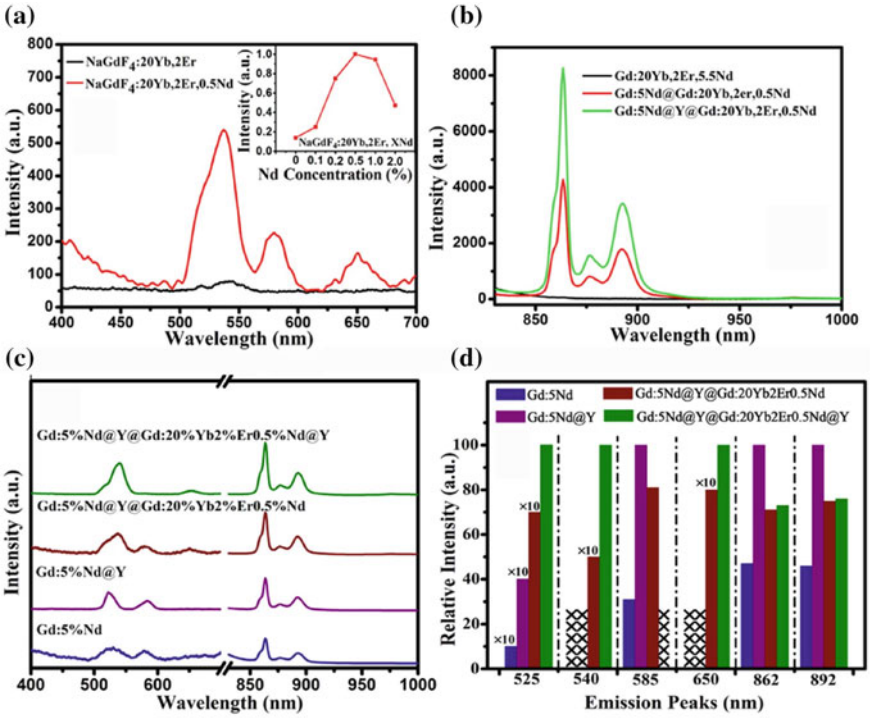

Fig. 6.8 **a** Up-conversion emission spectra of $NaGdF_4$: 20 Yb, 2 Er and $NaGdF_4$: 0.5 Nd, 20 Yb, 2 Er core and core–shell upon excitation with 800 nm radiation. The inset shows the variation in the UC emission intensity of $NaGdF_4$: 0.5Nd, 20Yb, 2Er NCs as a function of Nd^{3+} ion concentration **b** DC emission spectra of $NaGdF_4$: 0.5Nd, 20Yb, 2Er ($\lambda_{ex} = 800$ nm) **c** and **d** UC and DC emission spectra of $NaGdF_4$ core, $NaGdF_4$: Nd/$NaYF_4$, $NaGdF_4$: Nd/NaYF4/$NaGdF_4$: Nd, Yb, Er, and $NaGdF_4$: Nd/$NaYF_4$/$NaGdF_4$: Nd, Yb, Er/$NaYF_4$ NCs and corresponding comparison of the relative emission intensity at different emission position. Reprinted with permission from Ref. [75]. Copyright 2013, Springer Nature

F_4 UCNPs was 10 times more intense than that of α-phase particle of the same composition [76]. It is well known that the disordered crystallographic sites are generally useful for lanthanide ion luminescence as it favor of f-f transitions. Therefore, for a polymorphic material, the crystallographic phase which offers non-centrosymmetric sites is more useful from luminescence point of view. As an instance, erbium oxyfluoride (ErOF) is found to exist in orthorhombic and rhombohedral crystal phases. The orthorhombic structure contains three crystallographic sites to activator Er^{3+} ions such as Er1 at C_1 site (i.e., coordinated with 4 oxygen (O) and 4 fluorine (F) ions), Er2 in at C_1 site (where Er species are coordinated with 2O, 4F, and 2O/F), and Er3 at C_s site (surrounded with 4O and 4O/F). The diverse and the low symmetric sites for activator Er^{3+} ions are favorable for the occurrence of f-f transitions in ErOF to produce bright luminescence. On the other hand, the rhombohedral ErOF offers highly ordered crystallographic sites to Er^{3+} ions. Wen et al. have synthesized

orthorhombic and rhombohedral erbium oxyfluorides (ErOF) using a controllable fluorination route and reported that the variation in the luminescence behavior of the orthorhomic and rhombohedral ErOF was associated with the differences in the crystal structure-dependent energy transfer processes [77].

6.5 Controlled Preparation of Up-Converting Fluoride-Based Nanophosphors

As the luminescence properties of UCNPs are correlated with their crystal structure, morphology, and chemical composition; therefore, it is indispensable to vary these parameters to obtain desired luminescence characteristics. The reaction conditions and the method of preparation are vital for synthesizing UCNPs of desired phase and composition. In past, various methods have been developed for the controlled preparation of UCNPs [54, 69, 78–81]. The colloidal synthesis methods or *wet chemical* methods are very promising in obtaining UCNPs of desired dimensionality and crystal phase. These methods permit the manipulation of matter at molecular level and provide better homogeneity in terms of dopant distribution and composition. The additional benefits of colloidal methods include (i) successful doping of suitable Ln^{3+} ions, (ii) preparation NPs of desired size, shape, and uniformity, and (iii) simple and robust method of preparation that does not require costly equipment.

For the synthesis of nanomaterials using wet chemical methods, prior understanding of crystal chemistry, thermodynamics, phase equilibrium, and reaction kinetics can be advantageous. A better understanding of these can provide guidelines that can be useful in optimizing the synthesis parameters to control the reaction kinetics in a predetermined fashion and produce uniform NPs. The colloidal method for the preparation of fine NPs employs the precipitation of solids by the reaction of the dispersed or soluble precursor salts in non-aqueous or aqueous solutions. The synthesis process of nanoparticles experiences two stages, viz. nucleation and growth.

6.5.1 Nucleation and Growth

As soon as precursors are added into the reaction medium, formation of a new crystalline entity took place in solution due to the rearrangement of reactant species into the cluster. This process is known as *"nucleation,"* and the as developed clusters are known as *"nuclei"* which acts as a template to initiate the crystallization process. The nucleation may be termed as homogenous if the nuclei formation took place uniformly throughout the parent phase in the absence of any foreign entity. On the other hand, if the nucleation occurs at structural inhomogeneity such as impurities, container surfaces, grain boundaries, and dislocations, the process is termed as

heterogeneous nucleation. The NP growth occurs *via* a diffusion process in which the growth rate is controlled by the synthesis parameters (especially temperature and concentration gradient). NPs with narrow particle size distribution can be prepared if all the nuclei formation took place simultaneously. Besides, the nucleation must be completely stopped once the growth of particles begins and no further nucleation took place during this stage. This is the essence of burst nucleation; otherwise, if the nucleation is extended throughout the growth regime, the growth history of the NPs differs significantly from each other. Consequently, a better control over the particle size distribution would be far challenging to achieve.

LaMer and co-workers have described that the nucleation and growth processes are strongly dependent to each other; however, for the sake of simplicity, these two are discussed separately. The different stages of both processes are demonstrated in Fig. 6.9a. The nucleation theory states that the energy required to form a cluster of radius r (with n number of the molecule) is the difference between the free energy of the systems in its final and initial states plus a surface energy term (γ) related to the formation of an interface between nucleus and solution.

$$\Delta G = -n\Delta\mu + 4\pi r^2\gamma \tag{6.5}$$

The variation of the cluster free energy with the cluster size is expressed by the above equation as described by classical nucleation theory (Fig. 6.9b), [83] where

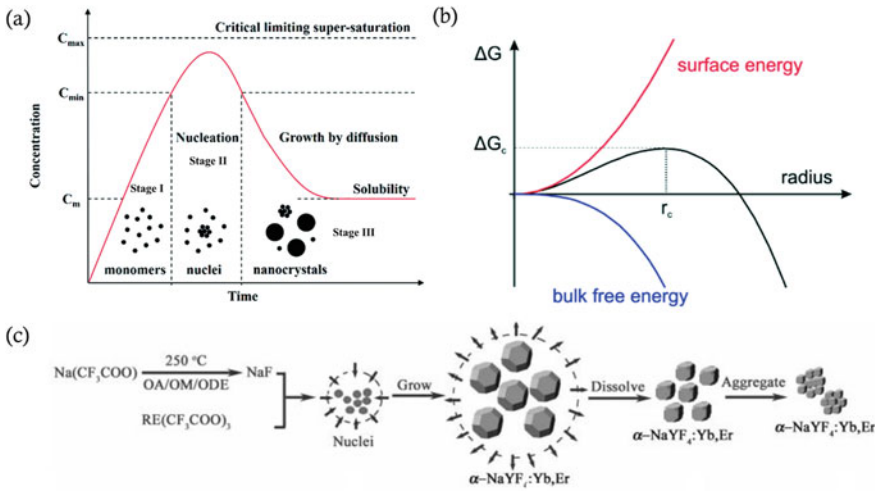

Fig. 6.9 **a** LaMer diagram demonstrating different stages involved in nucleation and growth of nanoparticles [82], **b** dependence of cluster free energy, ΔG_c on cluster size r according to classical nucleation theory [83], and **c** scheme demonstrating different steps involved in the preparation of uniform α-$NaYF_4$: Er, Yb NPs by delayed nucleation mechanism [25]. a-Reprinted with permission from Ref. [83]. Copyright 2015, Royal Society of Chemistry, b-Reprinted with permission from Ref. [82]. Copyright 2014, Royal Society of Chemistry, and c- Reprinted with permission from Ref. [25]. Copyright 2007, American Chemical Society

term $\Delta\mu$ is the difference in chemical potential between a molecule in solution (μ_s) and that in the bulk of the crystal phase (μ_c) which is a major driving force required for the nucleation and growth of a crystal and is referred to as super-saturation. The nucleation is possible once the solution becomes supersaturated, i.e., $\Delta\mu > 0$, while for $\Delta\mu < 0$, the solution becomes unsaturated and only the dissolution will take.

If the volume of each molecule is V, then the number of molecules associated with each nucleus will be $\frac{4}{3}\pi r^3/V$. The above thermodynamic equation can be rewritten as:

$$\Delta G = \frac{4}{3}\pi r^3 \Delta G_v + 4\pi r^2 \gamma = -\frac{4}{3}\pi r^3 \left(RTlnS/V_m\right) + 4\pi r^2 \gamma \qquad (6.6)$$

where ΔG_v is the free energy of the bulk crystal.

6.5.2 *Synthesis Methods*

For the synthesis of uniform nanoparticles (NPs) with a narrow particle size distribution, the nucleation and growth processes must proceed in a predetermined fashion. The control over these processes can possibly be made by modulating the reaction kinetics which is further determined by the synthesis parameters (e.g., temperature [11], reaction time [12], pH [13], ligands [14], additives [15, 16], and precursor salts [17, 18, 20–22]). Among the established methods for nanoparticle synthesis, solution-based methods can precipitate NPs directly from solution and are promising in precisely controlling the rate of nucleation, growth, and ageing that influence the particle size and their distribution. The above-mentioned reaction parameters can be systematically varied to obtain UCNPs of desired size, shape, crystal phase, and composition. Therefore, prior knowledge about the influence of each and individual parameter on the reaction kinetics may be helpful in controlling the nucleation and growth of nanoparticles. This section will provide a brief description of a few wet chemical methods that are widely used for UCNPs preparation.

6.5.2.1 Thermal Decomposition

This method involves surfactant-assisted thermal disintegration of organometallic precursors in organic solvents at high temperature. A typical scheme describing the procedure involved in NP preparation using a thermal decomposition method is shown in Fig. 6.10. This method offers burst nucleation which is an important criterion for the synthesis of uniform NPs. Typically, for the preparation of inorganic fluoride-based nanoparticles, metal trifluoroacetate is thermally decomposed in solvents with the high boiling point such as oleic acid (OA), octadecene (ODE), and oleylamine (OM) to produce metal and fluoride species in the reaction medium.

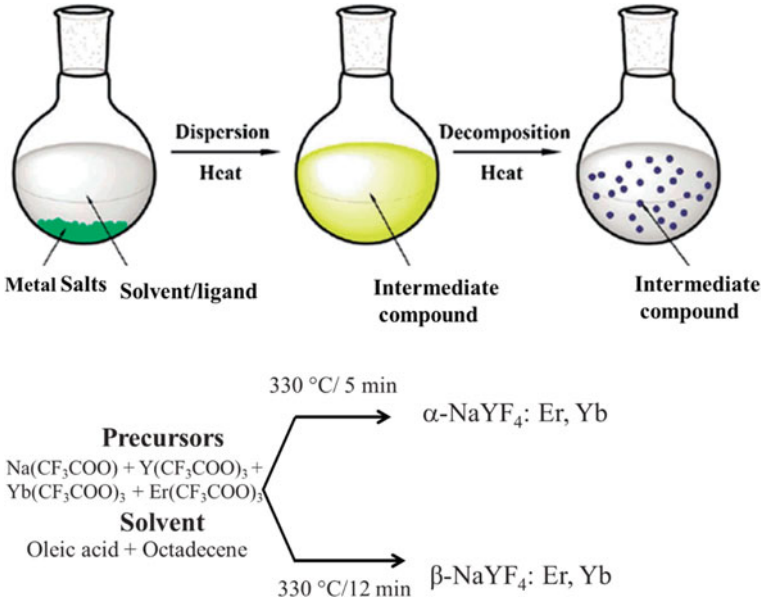

Fig. 6.10 Scheme demonstrating the steps involved in the preparation of $NaYF_4$: Er, YbNPs using thermal decomposition method [84]

These species are then combined into new nuclei at high temperature. The reaction further proceeds and results in the formation of nanoparticles precipitate in solution.

In past, thermal decomposition method is used for the preparation of diverse morphologies of lanthanide-doped nanocrystals [62, 85–89]. Usually, in the preparation of $NaLnF_4$ NPs, oleic acid (OA) is employed as ligands which control the growth of the NPs by selectively adsorbing on the particular facet of the NPs. Such a preferential growth along a particular direction can give a possibility for the preparation of NPs of diverse morphologies and crystal phases. Mai et al. have obtained mono-dispersed $NaLnF_4$ *via* the thermal decomposition of sodium trifluoroacetate and lanthanide trifluoroacetate precursors in a reaction medium that is composed of organic solvents such as oleic acid (OA) and octadecene (micrographs are shown in Fig. 6.11) [84]. Shan et al. have proposed one-pot synthesis of β-$NaYF_4$: Er^{3+}, Yb^{3+} up-converting nanophosphor by the thermal decomposition of precursor salts. They reported that NPs of diverse sizes can be produced by varying the relative amounts of the Na^+ and Ln^{3+} precursors. A higher ratio of Na^+/Ln^{3+} preferred cubic-to-hexagonal ($\alpha \rightarrow \beta$) phase transition and promoted the growth of smaller size β-UCNPs [90].

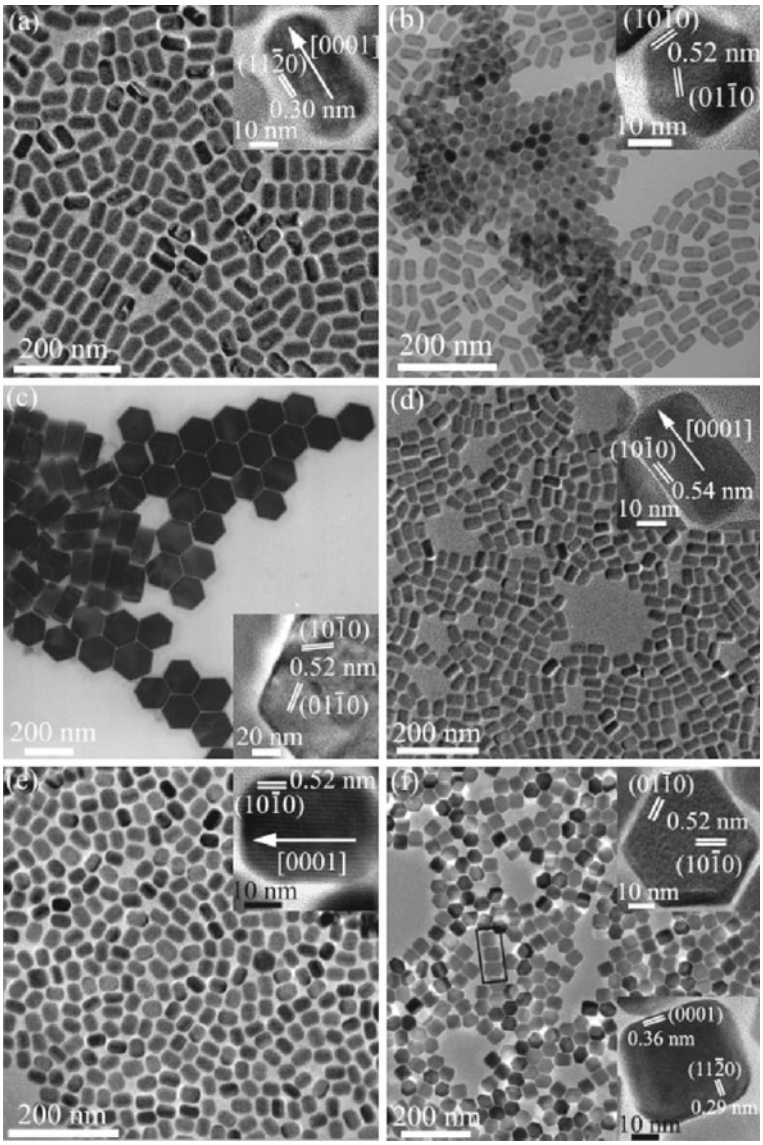

Fig. 6.11 TEM and HRTEM (inset) images of **a** β-$NaYF_4$ nanorods re-dispersed in a mixture of toluene and hexane (1:1), **b** β-$NaYF_4$ nanoplates re-dispersed in a mixture of toluene/hexane/ethanol (1:1:0.48), **c** β-$NaYF_4$ nanoplates, (β-$NaNdF_4$ nanorods, **e** β-$NaEuF_4$ nanorods, and **f** β-$NaHoF_4$ hexagonal plates. Reprinted with permission from Ref. [84]. Copyright 2006, American Chemical Society

6.5.2.2 Solvothermal

A solvothermal reaction is carried out in a reactor under an elevated temperature and pressure conditions using a steel pressure vessel known as an *autoclave*. A typical autoclave reactor should have few important characteristics such as it should be (i) resistant to deterioration under harsh chemical conditions, (ii) easily assembled and dissembled, (iii) large enough to attain the preferred temperature gradient, (iv) resistant to leak under operating conditions, and (v) capable of maintaining high-pressure and temperature conditions for prolonged duration. Figure 6.12 demonstrates a typical scheme for NP synthesis employing hydrothermal method. In a solvothermal synthesis method, the NPs in the reaction medium is precipitated using some solvent that facilitates the interaction between the precursors at a temperature above the boiling point of the solvent. In particular, this method is known as a *hydrothermal method* if the water is used as a solvent to serve as reaction medium. The unique combinations of pressure–temperature parameters allow the preparation of different phases with diverse morphologies and improved crystallinity which is challenging to obtain under other experimental conditions. The NPs prepared using this method are usually crystalline in nature and do not require further heat treatment. This essentially avoids the agglomeration of the nanoparticles caused due to heat treatment. This method is very promising in producing both the metastable and thermodynamically stable phase(s) with narrow size particle distribution for a wide range of inorganic NPs.

In past, diverse morphologies of a range of lanthanide ions doped fluoride nanoparticles were synthesized using the solvo/hydrothermal method [22, 91]. Hu et al. produced uniform LaF_3: Yb^{3+}, Er^{3+} nanoplates with an average diameter of ~15 nm

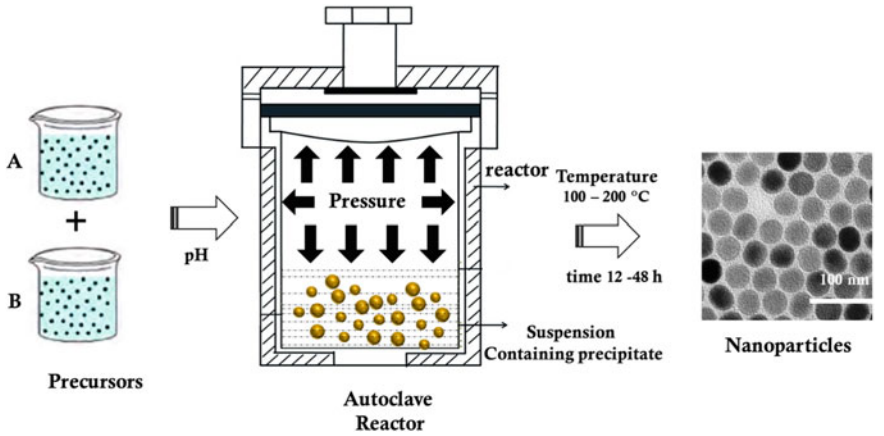

Fig. 6.12 Scheme depicting a pictorial representation for hydrothermal synthesis of inorganic nanoparticles. Reprinted with permission from Ref. [94], Copyright 2019, American Chemical Society

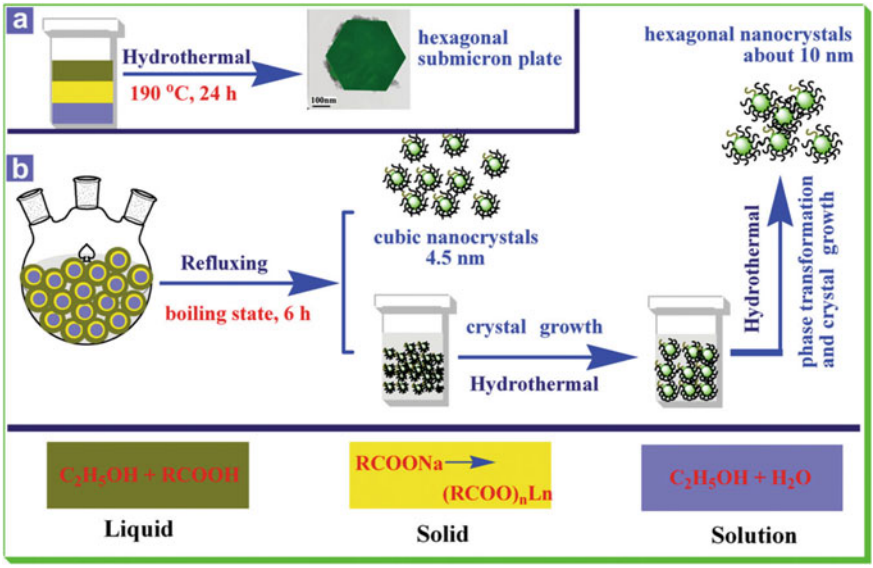

Fig. 6.13 Scheme demonstrating synthesis procedure and mechanism involved in $\alpha \rightarrow \beta$ phase transition in $NaLnF_4$ NPs (Ln stands for lanthanides). **a** Hexagon-shaped $NaYF_4$: Yb^{3+}, Er^{3+} sub-micrometer plates are obtained through only hydrothermal treatment. **b** α-phase UCNCs were produced by only reflux treatment; the $\alpha \rightarrow \beta$ phase transformation can be achieved by hydrothermal treatment. The liquid, solid, and solution phases in the Teflon bottle and three-neck flask reaction system are denoted by three different colors at the bottom. Reprinted with permission from Ref. [93]. Copyright © 2012 Wiley-VCH Verlag GmbH & Co. KGaA, Weinheim

[92]. They found that the coating reagent, reaction temperature, and time greatly influence themorphology of the final product. Recently, Ren et al. have produced different morphologies of $NaLnF_4$ nanocrystal employing a hydrothermal synthesis method by varying organic surfactant, reaction temperature, and dopant concentration [91].

Ultra-small hexagonal (β) $NaYF_4$: Yb^{3+}, Er^{3+} NPs are very demanding for biological applications due to their strong up-conversion luminescence and greater ability of dispersion in biological media. However, it is challenging to prepare small β-phase particles [93]. Wang et al. have developed a synthesis method that combine a reflux process with hydrothermal treatment as demonstrated in Fig. 6.13. Employing this method, mono-disperse $NaYF_4$: Yb^{3+}, Er^{3+} NPs of α-phase were first synthesized using a reflux process. Subsequent heat treatment under hydrothermal conditions of these α-phase NPs resulted in transformation to β-phase particles [93].

6.5.2.3 Co-precipitation

This method involves the dissolution of inorganic salts (such as nitrate, chloride, and sulfate) in water or any other suitable medium to form a homogeneous solution containing clusters of different types of ions. These clusters are simultaneously

precipitated as hydroxides, hydrous oxides, or oxalates under certain reaction conditions, i.e., at optimized pH, reaction temperature, and time. The collected precipitate is then washed several times to eradicate the by-product and non-reacted precursors. The purification and drying procedures used for the extraction of NPs sometimes result in their aggregation. Therefore, these processes must be executed carefully for the preparation of uniform NPs. If the precipitation does not proceed in a controlled fashion, the reaction may yield non-uniform and uncontrolled particle morphology. To obtain NPs with well-defined stoichiometry and composition, it is essential that the product should be insoluble in the reaction medium and the precipitation kinetics must be fast enough to precipitate the product rather than getting dissolved into the reaction medium. Special care must be taken as the precipitation rate of different reactant species varies in reaction media. To circumvent this issue, surfactants or ligands are added into the reaction medium to synchronize the co-precipitation process. Surfactants usually get adsorbed at the surface of nanoparticles and prevent their aggregation. Co-precipitation synthesis is facile, robust, and does not demand expensive apparatus, harsh reaction conditions, and complicated procedures. In few cases, NPs can be directly synthesized during co-precipitation itself and do not require further calcination or heat treatment at higher temperatures.

A variety of lanthanide-based up-converting nanoparticles (NPs) were prepared using a co-precipitation method [78]. Yi et al. have synthesized nearly uniform α-$NaYF_4$: Yb, ErNPs over a broad range of particle sizes (~37–166 nm) using a co-precipitation method. Ethylenediaminetetraacetic acid (EDTA) was used as a ligand that makes a stable metal–surfactant complex and controls the growth of the nanoparticles [78].

6.5.2.4 Sol–gel

Sols are colloidals composed of nanoscopic solid particles in a continuous liquid medium. A few examples of sols are paint, blood, and pigment ink. Sols are generally stable and display the Tyndall effect. When the solid particulate in sols interacts in the presence of large amounts of the liquid, they can form a 3D network. Eventually, the network grows in size to form a bigger 3D network which is known as a gel. Inorganic sols are prepared by sol–gel method. The sol–gel technique utilizes hydrolysis and poly-condensation reactions of molecular precursors to produce a new sol [95]. By introducing a base to sol, a large macromolecular network phase is formed which is dried and ground to yield nano-crystalline powder. The NPs prepared using this method suffer from poor crystallinity. Therefore, a post-synthesis heat treatment at elevated temperatures is required. Georgescu et al. have prepared CaF_2: Er^{3+}/Yb^{3+} doped glass-ceramics using a controlled crystallization of the (Yb^{3+}/Er^{3+}) co-doped CaF_2–SiO_2 xerogels at 650 °C [96]. The steps involved in a typical sol–gel synthesis are described using a schematic shown in Fig. 6.14.

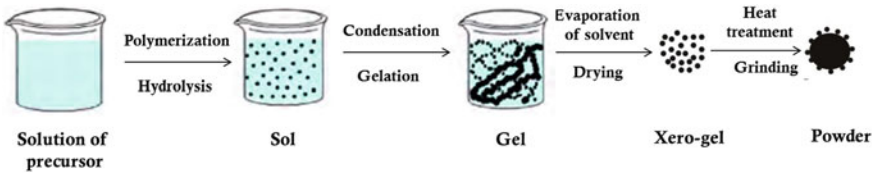

Fig. 6.14 Schematic diagram depicting various steps involved in the sol–gel process for the preparation of nano-powder. Reprinted with permission from Ref. [95], Copyright 2010, Elsevier

Advantages

A sol–gel synthesis method offer few advantages such as: It (i) can provide a better homogeneity and phase purity, (ii) does not require sintering at very high temperature, (iii) can yield small size particles (in nm range) can be prepared, (iv) can allow for doping of dissimilar species due to the development of a continuous network between dopant and host species, and (iv) does not require very costly equipment. The phosphor materials synthesized using sol–gel method exhibit high luminescence efficiency due to the improved crystallinity of the material.

Disadvantages

As far as the synthesis of nanoparticles is concerned, sol–gel method has a disadvantage in terms of poor control over the morphology that leads to aggregation of nanoparticles. Further, the synthesis is influenced by several reaction parameters that affect the reaction in a complicated manner. This makes it difficult to monitor and control the synthesis process. This causes poor control over the size, shape, and uniformity of the nanoparticles.

6.5.2.5 Microemulsion

A microemulsion is defined as an isotropic liquid mixture of non-polar (oil), polar (water), and surfactants. The surfactant species creates an interfacial film separating polar and the non-polar domains. The formation of the interfacial layer gives rise to distinct microstructures that extend from droplets of water dispersed in a continuous oil phase (W/O-microemulsion) to oil dispersed in a continuous water phase (O/W-microemulsion). The former can be used as nano-reactors for the preparation of uniform NPs. This method offers good control over the particle size, shape, and uniformity of the nanophosphor. The choice and amount of the surfactant plays a vital role in the formation of the emulsion and, thereby controlling the growth of nanoparticles. Typically, a microemulsion synthesis is carried out at a relatively lower temperature (preferably below 100 °C). Gunaseelan et al. proposed a novel scheme for the synthesis of Yb^{3+}, Er^{3+} doped $NaYF_4$ nanoparticles using a reverse microemulsion (μE_s) method in which CTAB, 1-butanol, and isooctane were used as a surfactant, co-surfactant and oil phase, respectively (Fig. 6.15). The amount of surfactant was varied to control the particle size of microemulsion over a wide range

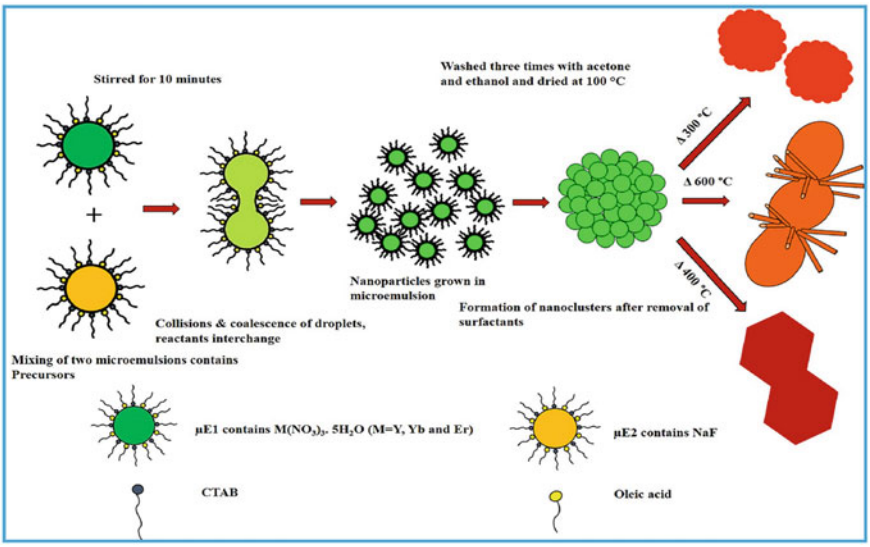

Fig. 6.15 Schematic demonstrating various steps involved in the formation of microemulsion droplet, up-converting nanoclusters, and nanorods. Reprinted with permission from Ref. [97]. Copyright 2018, Elsevier

(i.e., ~ 14 to 220 nm), which eventually, determines the particle size, shape, and crystal structure of $NaYF_4$: Yb^{3+}, Er^{3+} NPs.

In summary, several methods are well established for the controlled preparation of UCNPs. Each method has a few merits and demerits. The comparison between different methods for UCNPs synthesis is made in terms of control over the morphology, crystallinity, scalability, and the as produced information is given in Table 6.4. In general, co-precipitation synthesis, thermolysis, and hydrothermal methods have better control over the morphology; however, these methods suffer from the issue of scalability. Besides, the hydrothermal synthesis requires an autoclave reactor for carrying out the reaction. On the other hand, the combustion method is very efficient and facile in synthesizing material in the bulk phase; however, it does not have good control over size, shape, and crystal phase. The sol–gel synthesis is good in terms of scalability, and crystallinity, however, it requires post-synthesis treatment such as annealing at high temperature. A variety of fluoride-based up-converting nanocrystal has been produced in past using chemical routes. The detailed information about the synthesis protocol used for UCNP preparation can be found in the available literature [6, 7, 49, 55, 69, 98–101].

Table 6.4 Typical synthesis routes for the preparation of up-converting nanoparticles (UCNPs)

Methods	Control over morphology	Crystallinity	Heat treatment required	Scalability	Remarks	References
Thermolysis	Yes	Poor	No	Poor	(i) Uniform nanoparticles, (ii) release of toxic gases, and (iii) small yield	[84]
Hydro-thermal	Yes	Average	No	Poor	(i) Cost-effective precursors, (ii) no post-heat treatment and (iii) an autoclave reactor is needed	[91]
Co-precipitation	Yes	Poor	Yes	Poor	(i) Does not require costly equipment, (ii) complex procedures, and (iii) useful in producing uniform NPs	[78]
Sol–gel	No	Good	Yes	Good	(i) Cost-effective precursor, and (ii) postsynthesis calcinations required	[102]
Combustion	No	High	Yes	High	(i) Robust, quick, and time-effective and (ii) considerable particle aggregation	[63]
Reverse-micelle	Yes		No	Poor	(i) Does not require extreme pressure and temperature conditions, and (ii) flexibility in preparing different size and shape	[103]
Microwave-assisted	Yes	Good	None	Poor	(i) Simple, inexpensive, and rapid synthesis and (ii) can yield ultra-small NPs	[69]

6.6 Critical Parameters that Influence Morphology and Phase

There are several reaction parameters (e.g., reaction time, temperature, precursor ratio, ligands, and pH) that influence the reaction kinetics in a synergistic fashion, thereby affecting the synthesis of nanoparticles. By systematically varying these parameters, UCNPs of diverse size, shape, narrow size distribution, and desired crystal phase can be prepared. The effect of these parameters on the morphological, structural, and compositional characteristics of fluoride UCNPs is briefly described in this section with few examples.

6.6.1 Reaction Temperature and Time

The reaction temperature significantly controls the action kinetics, and, hence, the growth of the NPs. Generally, the synthesis carried out at high temperature favors the formation of bigger size particles due to an increase in the rate of reaction. For the preparation of uniform NPs, aggregation of NPs must be avoided. In a solution-based synthesis of nanoparticles, the major culprits for the broader distribution of NPs are Ostwald ripening and oriental attachment of nanoparticles. Ostwald ripening is a growth process in which the bigger particles grow at the expense of smaller size particles to minimize their surface energy. In particular to $NaLnF_4$ (Ln stands for lanthanide) NP synthesis, the broadening in particle size distribution associated with Ostwald ripening of NPs is correlated with the presence of the relative amounts of cubic (α) and hexagonal (β) phases in the reaction medium at any time during synthesis [104]. The formation of α and β phases, and $\alpha \rightarrow \beta$ phase transition characteristics are strongly dependent on the reaction temperature and time. This suggests that for the preparation of uniform NPs under a given set of reaction conditions, the choice of synthesis temperature and reaction time are essentially the two main parameters.

The influence of reaction temperature and time is vital in selectively precipitating particular phases of nano-crystalline materials. The metastable phase can be arrested at a nanoscale size range due to the predominance of the surface energy of the system. Therefore, under certain experimental conditions, preferably at lower synthesis temperature and shorter reaction time, a metastable phase can be selectively prepared. Liu et al. have systematically investigated the role of synthesis temperature and reaction time on the size, shape, uniformity, and phase purity of $NaGdF_4$: Er^{3+}/Yb^{3+} UCNPs [105]. The reaction time and temperature are coupled variables; i.e., under a given experimental condition if the synthesis temperature increases, it is possible to obtain the thermodynamically stable phase for lesser reaction time. As an instance, a higher reaction temperature of 280 °C results in the formation of the thermodynamically stable hexagonal phase (β) of $NaGdF_4$ particles despite a shorter reaction time of 15 min. On the other hand, the synthesis carried out at a

lower temperature of 200 °C yields only metastable cubic (α) phase of $NaGdF_4$ and does not form β-phase particles despite a long reaction time of 5 h [104].

6.6.2 Ligand, additives, and Solvents

The influence of ligand, additives, and surfactants on the growth of up-converting nanoparticles is extensively studied in past to produce uniform NPs of distinct sizes, shapes, and phases [62]. The addition of ligand to reaction medium results in the formation of a metal complex and retards the nucleation and growth rate. Furthermore, because of the presence of functional groups at the NP surface, they can preferentially adsorb on the specific facet of growing crystal and influence the growth rate in particular crystallographic directions. The preferential adsorption of the ligand on high energy facets hinders the evolution of those surfaces leading to the formation of distinct morphologies. The interaction of the ligand with the surface is controlled by the solvent polarity and pH of the reaction medium. Generally, the long chain surfactants such as oleic acid (OA), trioctylphosphine oxide (TOPO), cetyltrimethylammonium bromide (CTAB), polyvinylpyrrolidone (PVP), and ethylenediaminetetraacetic acid (EDTA) are employed as ligands for the controlled synthesis of $NaLnF_4$ NPs in organic media [68, 80, 106].

Similar to the ligand, solvents can affect the rate of the reaction; however, they too do not participate in the reaction itself. The reaction will proceed in a controlled fashion if the synthesis is carried out in a non-polar organic solvent, and the precursors are introduced in a reaction medium using a polar solvent. In past, the organic solvents with high boiling point (e.g., 1-octadecene, oleylamine, and oleic acid) and their mixtures were used as a solvent for carrying out the size and shape-controlled synthesis of nano-materials. Shan et al. have synthesized different morphologies (e.g., spherical, rectangular parallelepiped, and cuboidal) of $NaYF_4$ with cubic (α), hexagonal (β), and a mixture of both ($\alpha + \beta$) phase(s) by varying the ratio of the solvent [106]. An α-phase particle was formed when either TOP or OA was used solely while β-$NaYF_4$ started forming with an increase of the relative amount of TOP [106]. The formation of ligand between the Lewis base TOP and oleic acid give rise an entirely different coordinating enviroment, thereby promoting $\alpha \rightarrow \beta$ phase transition in $NaYF_4$ [106].

6.6.3 Precursor Salts

The ionic character, steric, and electronic effect of precursor species in the reaction medium can affect the reaction kinetics and, therefore, determine the growth rate of nano-crystals in solution [18–22]. The changes in precursor ratio control the reactivity of the species in the reaction medium. The electronic and steric interaction among precursor anions/cations with ligands are the main factors that govern surface

coverage and regulates the reaction kinetics at the surface of the nanoparticles [107]. Further, the reactivity of reactant species can be altered by changing the precursor salts as they have a different ionic character in the same reaction medium. Shang et al. have investigated the role of precursor amount (i.e., F^-/Ln^{3+}) on the crystal structure and morphology of $NaY_{0.78}Nd_{0.10}Yb_{0.10}Er_{0.02}F_4$ NPs. The variation in the precursor ratio (F^-/Ln^{3+}) results in nano- and micro-crystals of different shapes. When the molar ratio of F^-/Ln^{3+} was 1:1, the synthesized crystals were spherical in shape with coarser crystal facets. An increase in F^-/Ln^{3+} ratio to 2:1 and 3:1 resulted in the formation of hexagonal prism shape morphology. A further increase in the molar ratio of these ions to 5:1 resulted in the formation of rod shape morphology. Schematic shown in Fig. 6.16 describes the influence of change in the ratio of OA/Ln and F^-/Ln^{3+} on the final morphology of $NaY_{0.78}Nd_{0.10}Yb_{0.10}Er_{0.02}F_4$ NPs. The variation in the morphology with the change in the molar ratio of precursors is related to the preferential adsorption of the F^- ions on the particular facets of $NaYF_4$ microcrystals that causes a preferred growth along different directions to produce distinct morphology [108].

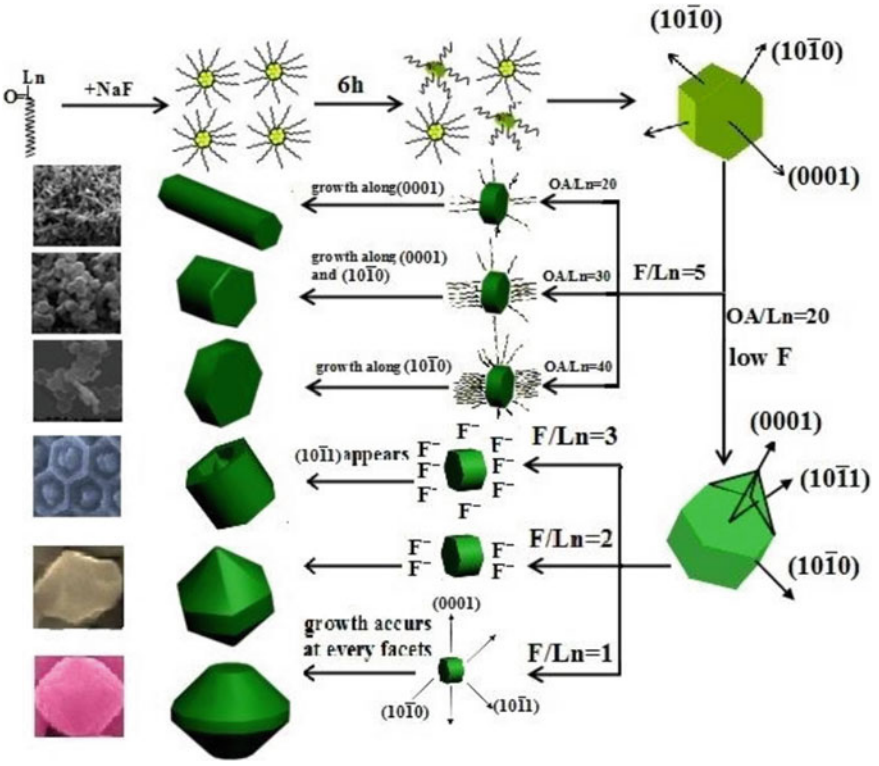

Fig. 6.16 Schematic demonstrating the formation of distinct morphologies under different OA/Ln^{3+} and F^-/Ln^{3+} molar ratio conditions. Reprinted with permission from Ref. [108]. Copyright 2015, Multidisciplinary Digital Publishing Institute

6.6.4 PH Parameter

The pH parameter of the reaction medium plays a vital role in the synthesis of nanomaterials. It can be varied by introducing acid or base in the reaction medium. Li et al. have reported that the addition of sodium hydroxide (NaOH) into the reaction solution during the synthesis effectively promoted the $\alpha \rightarrow \beta$ phase transition in NaY (Yb, Er) F_4. Addition of an excessive amount of NaOH favored the formation of α-phase particles [81]. The addition of NaOH facilitated the deprotonation of OA, leading to the formation of oleate (OA^-). However, if an excessive amount of NaOH is used, it preferred to form α-phase of $NaYF_4$: Yb^{3+}, Er^{3+} [81]. Moreover, the morpholy of NPs varied from irregular nanobranchs to uniform nanorods with an increase in NaOH amount.

6.6.5 Incorporation of Foreign Species

Doping of suitable foreign species into nanocrystal is proven to be a promising approach for producing UCNPs of desired compositional, structural and morphological characteristics that can display unique photo-physical properties [44]. Very often, the dopants get segregated over the grain boundaries and hinder the growth of the crystals, thereby influencing the particles growth. The dopant may also induce crystallization of a particular phase which is difficult to produce under particular experimental conditions [109]. As an instance, Ren et al. have incorporated Gd^{3+} and Tm^{3+} ions into $NaYbF_4$ NPs and investigated the influence of dopant ions on the morphological variation of the NPs [91]. With an increase in doping concentration of Gd^{3+}, the shapes of NaYb (Gd, Tm) F_4 NPs were varied from uniform nanocubes to a mixture of nanorods and spherical particles (Figs. 6.17b and d) and eventually to short and flat nanorods (Fig. 6.17e). The crystal structure of NPs also gets changed upon Gd^{3+} ions incorporation. Ren et al. reported that a doping concentration of ~ 60–75% led to the formation of a mixture of hexagonal (β) $NaYbF_4$ nanorods and cubic (α) $NaYbF_4$ spherical NPs [91]. Further, an increase in the doping concentration to 90% led to formation of pure β-phase. This demonstrate that an increase in loading amount of Gd^{3+} ions favors the formation of hexagonal phase NPs. Wang et al. have investigated the influence of Li^+ addition on the crystal structure and morphology of up-converting $NaLnF_4$ (Ln = Y, Er, and Yb) nanocrystals [44]. They have used distinct sources of Li^+ such as LiOA and LiOH and varied the Li^+ ions doping concentration from 0 to 100 mol%. They observed that under the identical experimental conditions used for the preparation of undoped and Li^+-doped $NaYF_4$, the undoped composition preferred to form thermodynamically stable β-phase in contrast to α-phase for doped composition. The variations in the morphological and structural characteristics of the NPs upon Li^+ doping are displayed in Fig. 6.18 [44].

Ren et al. have systematically synthesized a series of $NaLnF_4$ (La—Lu and Y) NPs and established a correlation between the ionic radius of Ln^{3+} ions to the morphology

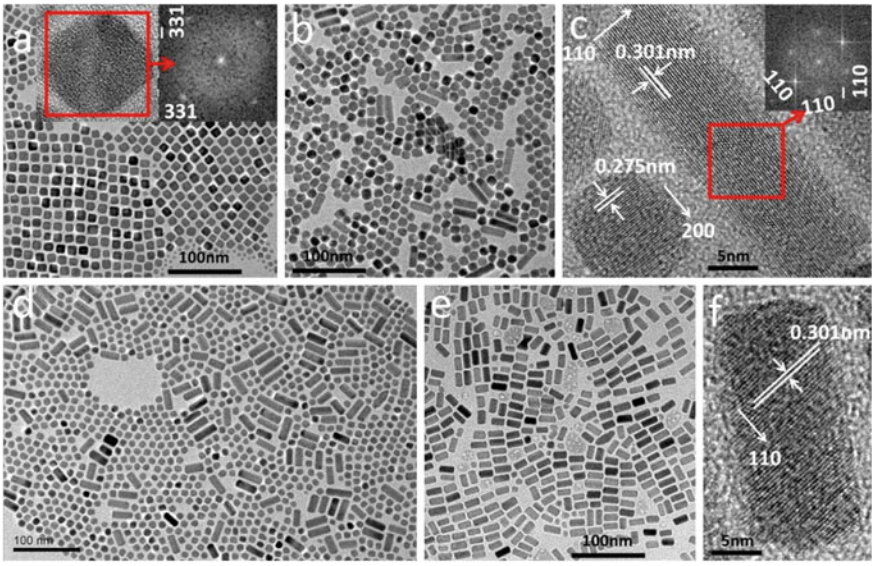

Fig. 6.17 Morphological variations of $NaYbF_4$ NPs upon Gd^{3+} and Tm^{3+} ions doping. TEM and HRTEM images of $NaYbF_4$ NPs doped with **a** 10% Gd^{3+}, 0.3% Tm^{3+}, **b**, **c** 60% Gd^{3+}, 0.3% Tm^{3+}, (**d**) 75% Gd^{3+}, 0.3% Tm^{3+}, **e**, **f** 95% Gd^{3+}, 0.3% Tm^{3+}. The arrows in (**c**) and (**f**) refer to the orientation of the planes of crystal lattice planes. Insets in (**a**) and (**c**) exhibit the HRTEM image of $NaYbF_4$ NPs and the corresponding FFT pattern of the selected area. Reprinted with permission from Ref. [91]. Copyright 2016, American Chemical Society

and crystal structure of NPs. As an instance, lighter lanthanides (i.e., La and Ce) preferred to form hexagonal LaF_3 and CeF_3 NPs rather than $NaLnF_4$ (Fig. 6.19). The pioneering work of Ren et al. has suggested that lanthanide series-based fluoride NPs can be categorized into five subgroups based on their phase formation and final morphology such as (I): β-LnF_3 (Ln = La and Ce), (II) β-$NaLnF_4$ (Ln = Pr and Nd; spherical particles), (III) β-$NaLnF_4$ (Ln = Tb, Eu, Sm, and Gd; nanorod), (IV) α-$NaLnF_4$ (Ln = Y, Ho, and Dy; nanocubes), and (V) α-$NaLnF_4$ (Ln = Yb, Tm, Er, and Lu; spherical dot). The crystallization behavior for each of the group was dependent on the size of Ln^{3+} ions.

The scheme shown in Fig. 6.20 demonstrates the variation in the morphology and crystal structure of LnF_3 and $NaLnF_4$ NPs as a function of the polarizability and ionic radii of lanthanides across the series [91]. $NaLnF_4$ NPs (where Ln = Pr and Nd) preferred to form β phase and display spherical morphology; however, the heavy lanthanide (Dy to Lu) $NaLnF_4$ NPs preferred to form cubic phase under similar reaction conditions. Dong et al. have prepared a series of citrate-stabilized lanthanide fluoride NPs (LnF_3: where Ln = La, Ce, Nd, Gd, and Eu) at 75 °C using a colloidal method. They observed that the nanocrystals of LnF_3 (Ln = La, Ce, and Nd) exhibited trigonal crystal structure similar to corresponding bulk LnF_3, while GdF_3 or EuF_3 exhibited a mixture of trigonal and orthorhombic phases (Fig. 6.21a).

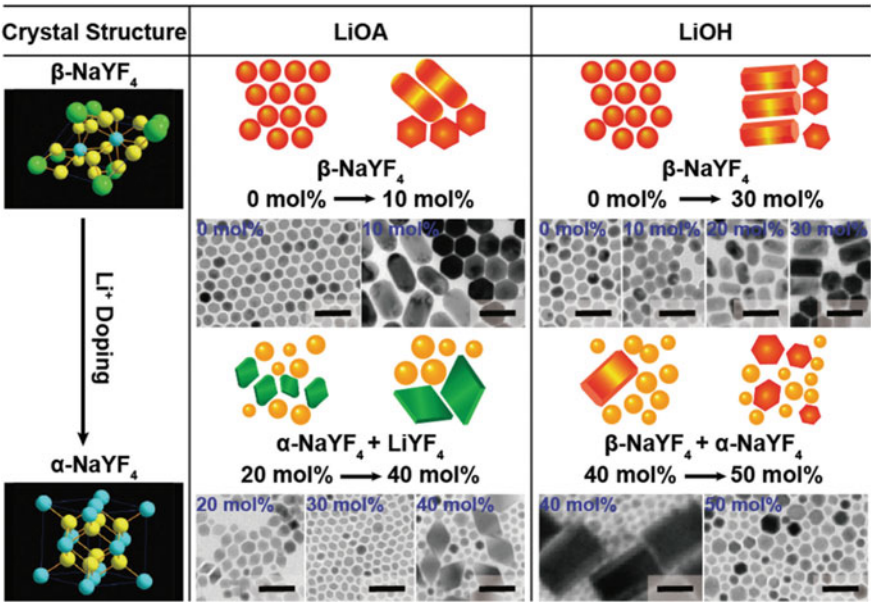

Fig. 6.18 TEM images of $NaYF_4$: Yb/Er, LiNPs with varying Li^+ concentrations. The two precursors used for Li^+ ions doping were LiOA and LiOH. Scale bar: 50 nm. The color used in the crystal structure graphics: Li atoms: pink, Y atoms: green, Na/Y atoms: blue, F atoms: yellow. The schematic shapes that correspond to the TEM images are cubic $NaYF_4$ (yellow) and hexagon $NaYF_4$ (red). Reprinted with permission from Ref. [44]. Copyright 2017, Royal Society of Chemistry

In light of this observation, they have stabilized GdF_3 nanocrystal in the trigonal phase by incorporating 15% La^{3+} ions as demonstrated in the XRD patterns shown in Fig. 6.21b [110]. These results demonstrated that the morphology and phase of lanthanide ions doped NPs can be altered by varying the type of impurity and their concentrations.

6.7 Applications

The up-converting lanthanide ions doped nanoparticles (UCNPs) produce a variety of fascinating luminescence which offer a range of applications such as in lighting industry, energy harvesting, and medical sciences. Graphics shown in Fig. 6.22 demonstrate a few of the possible applications of Ln^{3+}-doped up-converting nanoparticles (UCNPs) in various domains. A brief discussion about the same is also made in this section in light of available literature.

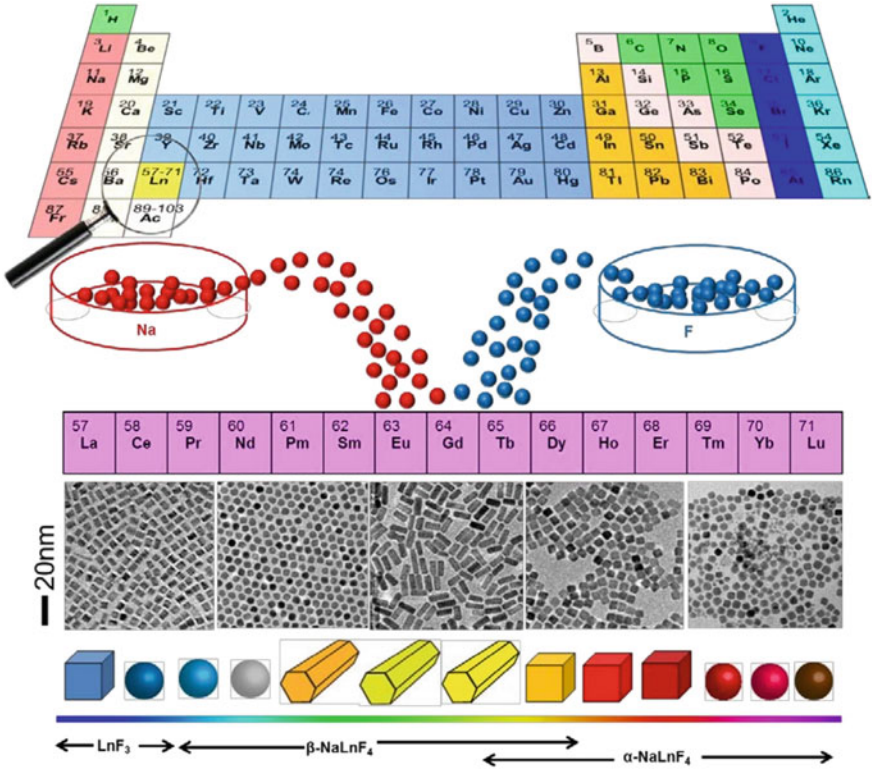

Fig. 6.19 Illustration demonstrating the formation of different morphologies of fluoride NPs (e.g., β-LaF_3, α-$NaLnF_4$, and β-$NaLnF_4$). TEM images: from left to right: CeF_3, β-$NaPrF_4$, β-$NaGdF_4$, α-$NaDyF_4$, and α-$NaYbF_4$. Reprinted with permission from Ref. [91]. Copyright 2016, American Chemical Society

6.7.1 Bio-Imaging

The bio-imaging technique has attracted much attention in the field of medical and biological sciences due to its ability of visualization of biological processes in real time. Fluorescence imaging, magnetic resonance imaging (MRI), and computed tomography (CT) are the most versatile imaging techniques. Typically, organic dyes are used as visualization tools for various imaging applications. There is a huge demand for the synthesis of other bright fluorescent materials such as quantum dots (QDs) and lanthanide ions doped up-converting nanoparticles (UCNPs). The organic dyes and quantum dots generally produce luminescence *via* the down-conversion process (i.e., emit light of larger wavelength by absorbing high-energy UV or visible radiation). Upon exciting with UV light, the biological samples often induce auto-fluorescence which causes a reduced signal-to-noise (S/N) ratio. Also, the prolonged exposure to UV radiation is detrimental to the biological samples.

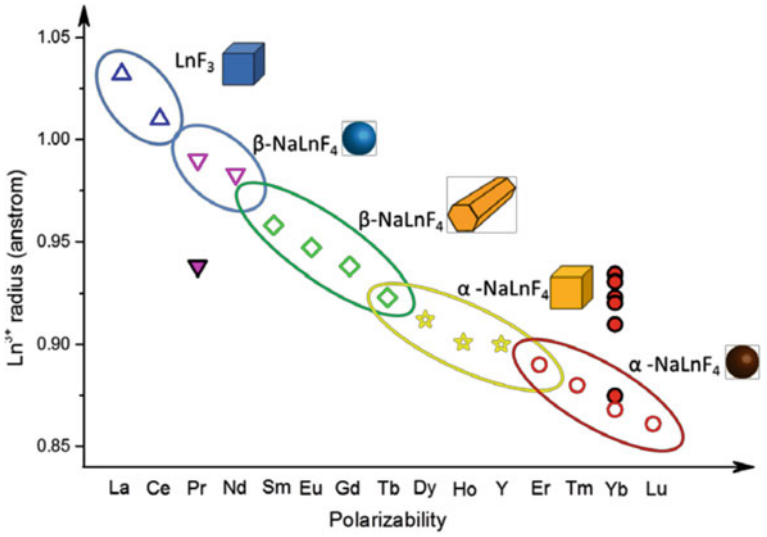

Fig. 6.20 Schematic showing variation in the morphology and crystal structure of LnF_3 and $NaLnF_4$ NPs as a function of the polarizability and ionic radius of Ln^{3+} ions across the lanthanide series. Reprinted with permission from Ref. [91]. Copyright 2016, American Chemical Society

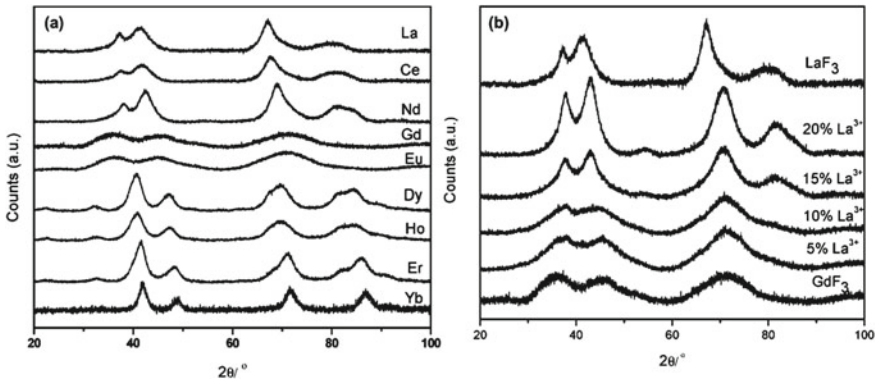

Fig. 6.21 XRD patterns of **a** LnF_3 NPs (where Ln = La, Ce, Nd, Gd, Eu, Dy, Ho, Er, and Yb), and **b** GdF_3 NPs with different La^{3+} ions doping concentration. Reprinted with permission from Ref. [110]. Copyright 2009, American Chemical Society

In contrast to quantum dots and fluorescent dyes, up-converting nanoparticles (UCNPs) exhibit certain interesting features such as: (i) excellent luminescent properties and high photo-stability, (ii) near-infrared (NIR) excitation which is beneficial in minimizing radiation-induced tissue damage and auto-fluorescence, (iii) several sharp emission peaks which enable new options for multiplexed encoding, (iv) large conventional anti-stokes shift which allows differentiating between excitation and

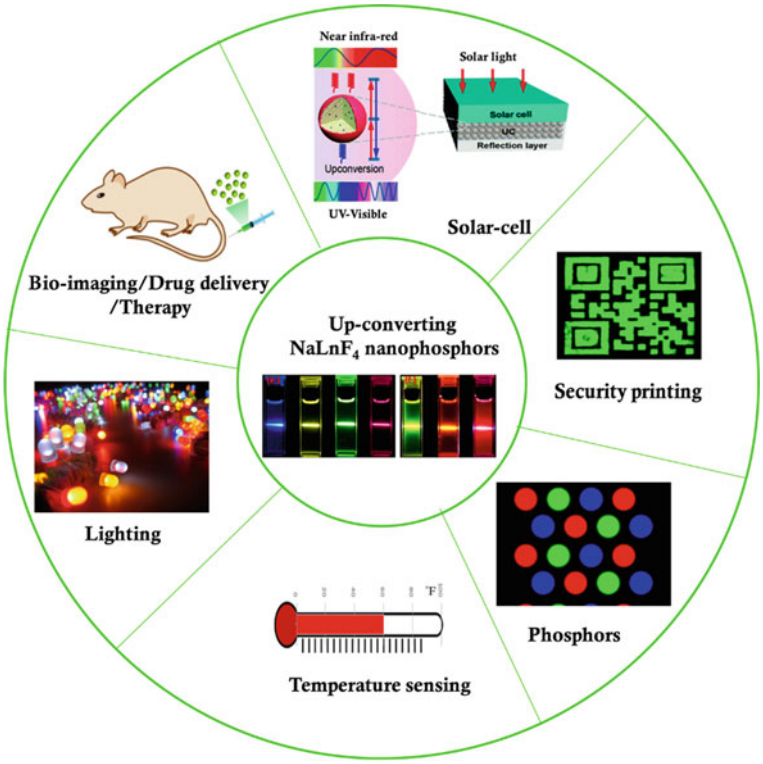

Fig. 6.22 Schematic showing applications of up-converting nanoparticles in various fields

emission signals, and (v) biocompatibility and non-toxicity for a broad range of cell lines. All the aforementioned unique photo physical characteristics of UCNPs make them useful for a variety of biomedical and diagnostic applications (e.g., bio-labels, cell imaging and targeting, bioassays, and biosensors).

Features of Up-Converting Fluoride-Based Nanophosphors

The up-converting fluorides nanoparticles qualify all of the above-mentioned essential conditions for biomedical applications. A brief note about each of the aspect is presented in this section based on the information available in the existing literature.

(i) Reduced auto-fluorescence

The up-converting nanoparticles (UCNPs) perform under near-infrared (NIR) excitation at which the biological tissues itself do not produce any emission. Therefore, the up-conversion-based luminescence techniques minimize the auto-fluorescence and produce the luminescence exclusive of the signals from biological tissue, making them an efficient probe for bio-imaging techniques. As an

instance, HeLa cells co-labeled with organic dye DiI (1,1′-dioctadecyl-3,3,3′,3′-tetramethylindocarbocyanine perchlorate) and Er^{3+}; Yb^{3+}-doped $NaYF_4$ UCNPs do not exhibit any fluorescence signal from DiI under 980 nm excitation [111].

(ii) Biocompatibility

There are several well-established methods to check the biocompatibility of the UCNPs for various types of biological cells. The cytotoxicity measurements on lanthanide-based up-converting fluoride nanoparticles generally exhibit a low level of toxicity [101, 112]. Dong et al. have studies the cell viability and cytotoxicity of HeLa cancer cells using CaF_2: Tm^{3+}, Yb^{3+} UCNPs. They used MTT assays for cytotoxicity measurements and did not notice any signal of toxicity after incubation of HeLa cells with UCNPs for 18 h [101]. Further, the toxicity measurement of CaF_2 UCNPs for mesenchymal stem cells did not show any toxic influence on the cells [101]. Naczynski et al. have developed a strategy to design a biologically targetable, water-dispersible, and biocompatible complexes of up-converting $NaYF_4$ NPs encapsulated within human serum albumin [112]. The other fluoride NPs such as $NaYbF_4$, $NaGdF_4$, LaF_3, and so forth, exhibited a very low level of cytotoxicity and were found to be bio-compatible based on the cytotoxicity measurements for various cell lines [113–115].

(iii) Non-blinking and low photo-bleaching tendency

UCNPs do not display any ON/OFF luminescence characteristics. In other words, luminescence from UCNPs is persistent over a millisecond timescale, and consequently, they exhibit non-blinking characteristics [116]. The non-blinking characteristics of up-converting NPs can contribute to the minimization of artifacts in prolonged imaging testing. In addition, the fluoride-based UCNPs offer greater photo-stability in NIR-visible window [117]. The lack of blinking and photo-bleaching tendency of UCNPs greatly improves signal-to-background (S/B) and signal-to-noise (S/N) information, permitting one to accurately and rapidly locate the exact position of distinct NPs with high precision. Further, it is possible to imprint cellular proteins for a prolonged duration with great precision [116]. Wu et al. have synthesized β-$NaYF_4$: Yb^{3+}, Er^{3+} UCNPs of particle size ~27 nm using thermal decomposition method and coated the nanoparticles using an amphiphilic polymer to make them water-dispersible. They found that under continuous excitation condition, the luminescence intensity of these UCNPs was not degrading upto an hour of time and an individual nanoparticles displayed no on/off emission (non-blinking) characteristics [116].

(iv) Improved penetration depth

The optical excitation and emission wavelengths involved in an up-conversion phenomenon positioned within the “optical transmission window” of biological tissues. Therefore, in vivo bio-imaging using UCNPs as the labels offer an improved penetration depth. As an instance, up-converting Tm^{3+}, Yb^{3+}-doped $NaYF_4$ NPs perform well over the wavelength region of 980–800 nm; therefore, these have been

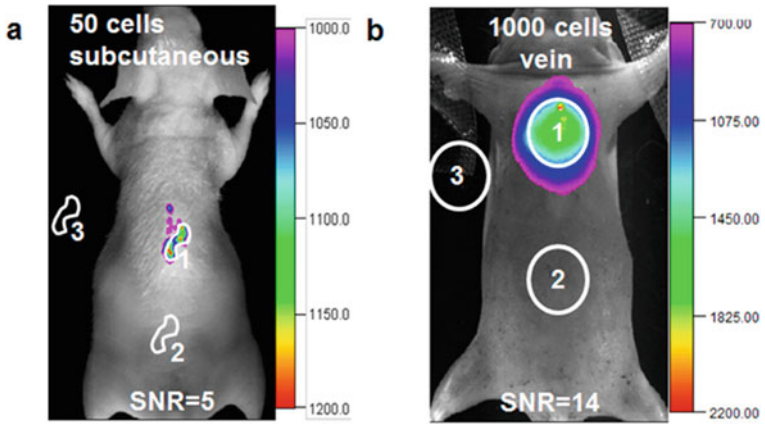

Fig. 6.23 Up-conversion luminescence-based imaging (in vivo) of athymic nude mice after subcutaneous injection of **a** 50 and **b** 100 NaLu(Gd) F_4: Tm, Yb, Tm NPs treated with KB cells. The cells were incubated with 200 $\mu g\ mL^{-1}$ citrate-coated NPs for 2 h. Reprinted with permission from Ref. [49]. Copyright 2011, American Chemical Society

used for various bio-imaging applications. Liu et al. reported the high-contrast up-conversion imaging of a black mouse using 8 nm β-$NaLuF_4$: Yb, Tm NPs as a probe where the depth of penetration was around 2 cm [49].

In brief, the fluoride-based UCNPs exhibit very interesting photo-physical and biological properties such as non-bleaching and non-blinking tendency, biocompatibility, reduced auto-fluorescence, and improved penetration depth in biological tissue. Because of these fascinating applications, UCNPs are useful for various bio-imaging applications. The available literature pertains to synthesis, surface modification, and investigation of up-conversion light emission for a variety of imaging applications [7, 49, 51, 67, 75, 118, 119]. Li and co-worker have developed a (Gd^{3+}, Yb^{3+}, Tm^{3+}) doped $NaLuF_4$ UCNPs based luminescent label and demonstrated a whole-body luminescent imaging of a mouse. Figure 6.23 shows the in vivo imaging of athymic nude mouse upon subcutaneous injection of two dissimilar doses of UCNPs treated with KB cells. Such UCNPs combined with other imaging modalities such PET, MRI, CT scan, and therapies involving PDT or PTT, or drug delivery can act as excellent theranostics platform. The detailed information about these applications of UCNPs is not covered here; however, they can be found elsewhere [1, 49, 67, 75, 119, 120].

6.7.2 Tumor Targeting

Tumor-targeted has attracted great attention toward the diagnosis and therapy of tumors. In recent years, various UCNP-based nano-bio-conjugates have been

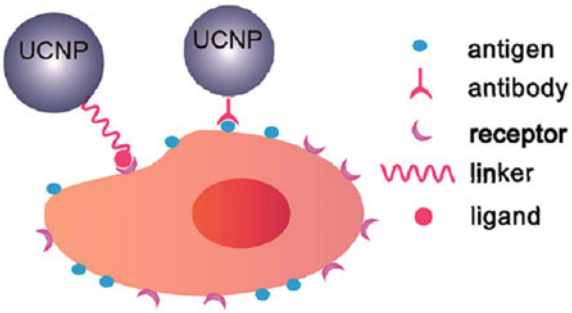

Fig. 6.24 Schematic demonstrating the design of UCNP-bio-conjugate for targeted imaging. Reprinted with permission from Ref. [117]. Copyright 2015, American Chemical Society

designed based on the interaction of UCNPs with peptides, folic acid (FA), and antibodies for targeted imaging [121, 122]. Figure 6.24 shows an illustration that demonstrates a design of UCNP bioconjugates that can be formed on the basis on ligand-acceptor or antibody-antigen interactions. Xiong et al. have developed a FA-modified $NaYF_4$: Yb, ErNPs based optical probe for the targeted in vivo up-conversion imaging of small animals [121]. Yu et al. reported that the chlorotoxin peptide-modified $NaYF_4$: Yb, Er/Ce NPs-bio-conjugate could be able to target and allow imagining of tumors in alive animals due to its efficient binding to specific tumor [122].

6.7.3 Energy Harvesting

Up-converting nanomaterials can absorb near-infrared (NIR) radiation to convert it into visible or ultraviolet light. This unique facility can provide broader absorption of solar radiation to photo-voltaic devices. Roh et al. have incorporated β-$NaYF_4$: Yb^{3+}, Er^{3+} nano-prisms into $CH_3NH_3PbI_3$ perovskite solar cells (PSCs) for energy harvesting applications [123]. The UC nano-prisms caused an improvement in the absorption characteristics of the PSC due to UC photoluminescence phenomenon that has resulted in further improvement in the power conversion efficiency. Their estimated efficiency was ~16% which was higher as compared to that of ~14% as reported for conventional TiO_2 NP-based PSCs [123]. A novel architecture composed of a different layer of $NaGdF_4$: Ln such as active core ($NaGdF_4$: Er^{3+})/active shell ($NaGdF_4Ho^{3+}$)/inert shell ($NaGdF_4$) was designed for solar energy applications, as shown in Fig. 6.25. Employing this design, the intermediate shell provides passivation between active core and outer shell to enhance the emission intensity of erbium ions incorporated into the core. This arrangement also assisted in improving Ho^{3+} ions UC luminescence [124].

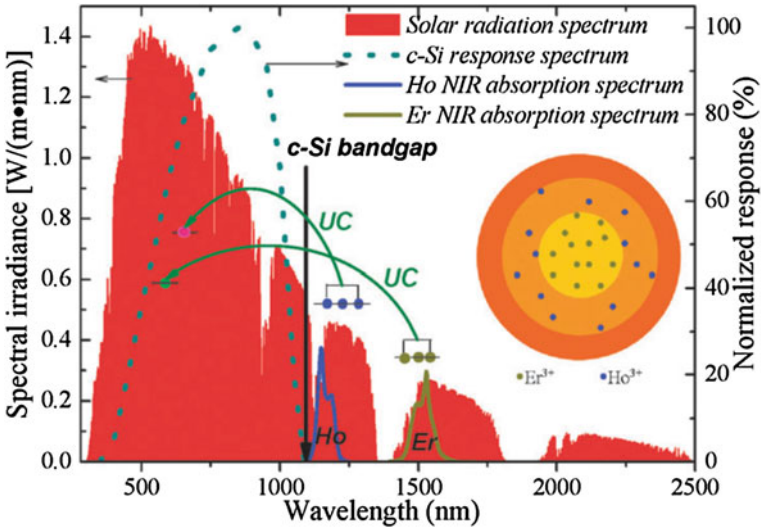

Fig. 6.25 Graphics showing how NIR radiation (transparent to c-Si) can be converted to Vis-NIR light above the forbidden gap of c-Si using ($NaGdF_4Er^{3+}$)/active shell ($NaGdF_4Ho^{3+}$)/inert shell ($NaGdF_4$) nano-architecture. Red region represents AM1.5 terrestrial solar spectrum; dotted graph belongs to c-Si response spectrum; band gap of c-Si is denoted by a vertical arrow. Reprinted with permission from Ref. [124]. Copyright 2012, Royal Society of Chemistry

6.7.4 Temperature Sensing

Most of the biological cells survive and nurture within a narrow thermal range. Therefore, the treatment methods for various diseases can be possible using a technique that depends on the localized thermal increase, such as in case of hyperthermia that refers to a heat controlled condition described by an unusually high body temperature. A change of 5 °C temperature beyond the standard body temperature is enough to destroy biological cells. If the exposure remains maintained for a longer time it may cause permanent damage to cells. These facts have given importance to develop an optical probe that can accurately sense the temperature around biological environments. Such a smart probe is an indispensable tool for medical treatment and diagnosis. UCNPs can induce localized hot spots upon excitation with near-infrared radiation. However, designing a UCNP-based temperature sensor demands for the development of a single phase light-emitting nanomaterial that exhibit some specific biological and photo-physical properties such as biocompatibility, high emission intensity, improved chemical stability and photo-stability in biological media, and measurement of temperature with high precision. Besides, the material must be performing over the biological transparency windows such that it can minimize invasiveness and maximize the depth of penetration. UCNP-based optical probes are useful for such applications. In this direction, Quintanilla et al. have developed CaF_2: Nd^{3+}, Y^{3+} UCNPs for thermometry application. These UCNPs worked well within

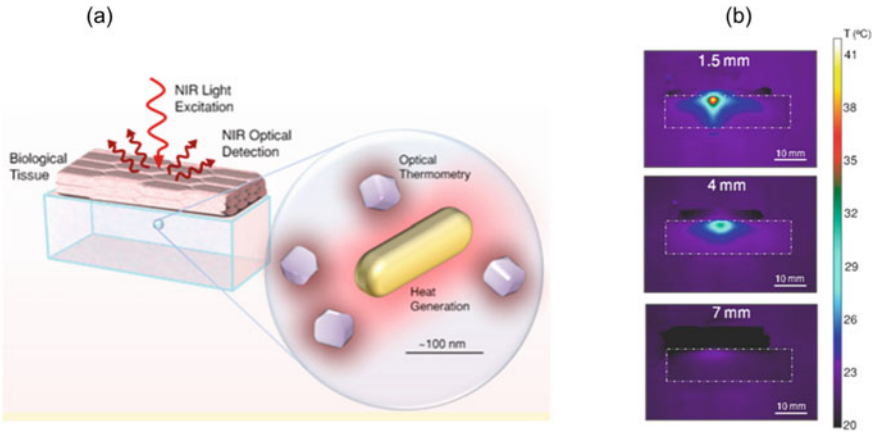

Fig. 6.26 **a** Schematic demonstrating the application of UC light-emitting material as probe for optical thermometry **b** thermographs of a cuvette containing gold nanorods and CaF_2: Nd^{3+}, Y^{3+} NPs illuminated using a laser beam of 808 nm wavelength after the beam passed a piece of tissue of 1.5, 4, or 7 mm. Reprinted with permission from Ref. [98]. Copyright 2018, American Chemical Society.

the biological windows (i.e., emission at ~1050 nm and excitation at ~808 nm) [98]. Figure 6.26a shows a schematic that demonstrated the application of UCNPs as a probe for optical thermometry. The thermal probes were optimized through the incorporation of Y^{3+} and gold species to further enhance the luminescence intensity and thermal sensitivity [98]. Figure 6.26b shows the thermographs of a cuvette holding luminescent CaF_2: Nd^{3+}, Y^{3+} NPs and gold nanorods (laser radiation of 808 nm passed through a piece of tissue under study was used for excitation of NPs). The thermal resolution depends on the thickness of tissue and other experimental parameters. Further descriptions about experimental techniques can be found in existing literature [98].

6.7.5 Anti-counterfeiting

Anti-counterfeiting has extensively useful in applications that demand noteworthy significance for personal and property safety. Lanthanide-doped up-converting nanoparticles (UCNPs) exhibit high photochemical stability and excellent luminescence properties under NIR excitation and are promising for various security-related applications. The UCNPs can over whelm background luminescence interference and provide a clearer image of the fingerprint. Yuan and co-workers designed a lysozyme-binding aptamer-functionalized UCNPs to detect fingerprints based on molecular recognition [125]. Kim et al. have developed a photo-patternable ink using

t-butoxycarbonyl-coated with α-$NaLnF_4$ (Ln = Y/Yb/Er and Y/Yb/Tm) UCNPs that can be useful for security applications [126].

6.8 Conclusions

The fluoride-based inorganic nanoparticles (NPs) area suitable host for the incorporation of luminescent up-converting lanthanide ions (e.g., Er^{3+}, Ho^{3+}, Tm^{3+}, Nd^{3+}, and Pr^{3+}) due to their low phonon energy (<350 cm^{-1}), favorable doping conditions, the possibility to synthesize optimized size, shape and phase. The light emission characteristics of up-converting fluoride-based nanoparticles (NPs) are synergistically influenced by various factors such as dopant–host combination, doping concentration, crystal structure, morphology, and so on. A wide range of emissions can be produced by changing the structural and chemical features of fluoride-based up-converting nanoparticles (UCNPs). Wet chemical synthesis methods such as hydrothermal, thermolysis, and co-precipitation are very promising for the controlled preparation of UCNPs with desired size, shape, phase, and composition. The up-converting lanthanide ions doped fluoride nanophosphors such as LnF_3, $ALnF_4$, and LnOF, BF_2 exhibit fascinating luminescence properties in a biological window, excellent dispersion in various organic and aqueous media, and bio-compatibility. These characteristics make them suitable for various biomedical applications such as bio-imaging, tissue engineering, drug delivery, and tumor targeting. Besides, their biomedical applications, they are widely utilized in the phosphor industry, solid-state lighting devices, energy harvesting, and anti-counterfeiting.

References

1. Bünzli JCG (2010) Lanthanide luminescence for biomedical analyses and imaging. Chem Rev 110:2729–2755
2. Wang F, Liu X (2009) Recent advances in the chemistry of lanthanide-doped upconversion nanocrystals. Chem Soc Rev 38:976–989
3. Phillips JM, Coltrin ME, Crawford MH, Fischer AJ, Krames MR, Mueller Mach R, Mueller GO, Ohno Y, Rohwer LES, Simmons JA, Tsao JY (2007) Research challenges to ultra efficient inorganic solid-state lighting. Laser Photon Rev 1 307–333
4. Ronda CR, Jüstel T, Nikol H (1998) Rare earth phosphors: fundamentals and applications. J Alloy Comp 275–277:669–676
5. Sivakumar S, van Veggel FCJM, Raudsepp M (2005) Bright white light through up-conversion of a single NIR source from sol−gel-derived thin film made with Ln^{3+}-Doped LaF_3 Nanoparticles. J Am Chem Soc 127:12464–12465
6. Hong AR, Kim SY, Cho S-H, Lee K, Jang HS (2017) Facile synthesis of multicolor tunable ultrasmall $LiYF_4$:Yb,Tm,Er/$LiGdF_4$ core/shell upconversion nanophosphors with sub-10 nm. Size Dyes Pigm 139:831–838
7. Shin J, Kim Y, Lee J, Kim S, Jang HS (2017) Highly bright and photostable $Li(Gd,Y)F_4$:Yb,Er/$LiGdF_4$ core/shell upconversion nanophosphors for bioimaging applications. Part Part Syst Charact 34:1600183

8. Jingning Shan XQ, Yao N, Ju Y (2007) Synthesis of monodisperse hexagonal $NaYF_4$:Yb, Ln (Ln = Er, Ho and Tm) upconversion nanocrystals in TOPO. Nanotechnol. 18:1–7
9. Höppe HA (2009) Recent developments in the field of inorganic phosphors. Angew Chem Int Ed 48:3572–3582
10. Jouart JP, Bouffard M, Klein G, Mary G (1994) Red-to-Blue up-conversion spectroscopy of Tm^{3+} in SrF_2, CaF_2, BaF_2 and CdF_2. J Lumin 60–61:93–96
11. Liu L, Zhuang Z, Xie T, Wang YG, Li J, Peng Q, Li Y (2009) Shape control of cdse nanocrystals with zinc blende structure. J Am Chem Soc 131:16423–16429
12. Huang S, Wang D, Li C, Wang L, Zhang X, Wan Y, Yang P (2012) Controllable synthesis, morphology evolution and luminescence properties of $NaLa(WO_4)_2$ microcrystals. Cryst Eng Comm 14:2235–2244
13. Li P, Zhao X, Jia CJ, Sun H, Li Y, Sun L, Cheng X, Liu L, Fan W (2012) Mechanism of morphology transformation of tetragonal phase Lavo4 nanocrystals controlled by surface chemistry: experimental and theoretical insights. Cryst Growth Des 12:5042–5050
14. Peng ZA, Peng X (2001) Mechanisms of the shape evolution of cdse nanocrystals. J Am Chem Soc 123:1389–1395
15. Deng H, Liu C, Yang S, Xiao S, Zhou ZK, Wang QQ (2008) Additive-mediated splitting of lanthanide orthovanadate nanocrystals in water: morphological evolution from rods to sheaves and to spherulites Cryst Growth Des 8:4432–4439
16. Siegfried MJ, Choi KS (2006) Elucidating the effect of additives on the growth and stability of Cu_2O surfaces via shape transformation of pre-grown crystals. J Am Chem Soc 128:10356–10357
17. Zhu L, Li Q, Liu X, Li J, Zhang Y, Meng J, Cao X (2007) Morphological control and luminescent properties of CeF_3 Nanocrystals. J Phys Chem C 111:5898–5903
18. Wang M, Huang QL, Hong JM, Chen XT, Xue ZL (2006) Controlled synthesis and characterization of nanostructured EuF_3 with different crystalline phases and morphologies. Cryst Growth Des 6:2169–2173
19. Filankembo A, Giorgio S, Lisiecki I, Pileni MP (2003) Is the anion the major parameter in the shape control of nanocrystals? J Phys Chem B 107:7492–7500
20. Wang M, Jiang G, Tang Y, Shi Y (2013) LaF_3 and LaF_3:Ln^{3+} (Ln = Eu, Tb) hierarchical microstructures: synthesis, characterization and photoluminescence. Cryst Eng Comm 15:1001–1006
21. Li C, Quan Z, Yang P, Yang J, Lian H, Lin J (2008) Shape controllable synthesis and upconversion properties of $NaYbF_4$/$NaYbF_4$:Er^{3+} and YbF_3/YbF_3:Er^{3+} microstructures. J Mater Chem 18:1353–1361
22. Li C, Yang J, Quan Z, Yang P, Kong D, Lin J (2007) Different microstructures of β-$NaYF_4$ fabricated by hydrothermal process: effects of pH values and fluoride sources. Chem Mater 19:4933–4942
23. Heer KKS, Gudel HU, Haase M (2004) Highly efficient multicolour upconversion emission in transparent colloids of lanthanide-doped $NaYF_4$ nanocrystals. Adv Mater 16:2102
24. Liu C, Chen D (2007) Controlled synthesis of hexagon shaped lanthanide-Doped LaF_3 Nanoplates with Multicolor Upconversion fluorescence. J Mater Chem 17:3875–3880
25. Mai HX, Zhang YW, Sun LD, Yan CH (2007) Size- and phase-controlled synthesis of monodisperse $NaYF_4$:Yb,Er nanocrystals from a unique delayed nucleation pathway monitored with upconversion spectroscopy. J Phys Chem C 111:13730–13739
26. Mahalingam V, Vetrone F, Naccache R, Speghini A, Capobianco JA (2009) Colloidal Tm^{3+}/Yb^{3+}-doped $LiYF_4$ nanocrystals: multiple luminescence spanning the UV to NIR regions via low-energy excitation. Adv Mater 21:4025–4028
27. Lu E, Pichaandi J, Arnett LP, Tong L, Winnik MA (2017) Influence of Lu^{3+} doping on the crystal structure of uniform small (5 and 13 Nm) $NaLnF_4$ upconverting nanocrystals. J Phys Chem C 121:18178–18185
28. Shannon R (1976) Revised effective ionic radii and systematic studies of interatomic distances in halides and chalcogenides. Acta Crystallogr Sect A 32:751–767

29. Stouwdam JW, Hebbink GA, Huskens J, van Veggel FCJM (2003) Lanthanide-doped nanoparticles with excellent luminescent properties in organic media. Chem Mater 15:4604
30. Judd B (1966) Hypersensitive transitions in rare-earth ions. J Chem Phys 44:839–840
31. Bunzli J-CG, Piguet C (2005) Taking advantage of luminescent lanthanide ions. Chem Soc Rev 34:1048–1077
32. Singh S, Tripathi A, Rastogi CK, Sivakumar S (2012) White Light from Dispersible Lanthanide-Doped $LaVO_4$ Core–Shell nanoparticles. RSC Adv 2:12231–12236
33. Rastogi CK, Sharma SK, Patel A, Parthasarathy G, Pala RGS, Kumar J, Sivakumar S (2017) Dopant induced stabilization of metastable zircon-type tetragonal $LaVO_4$. J Phys Chem C 121:16501–16512
34. Stouwdam JW, van Veggel FCJM (2002) Near-infrared emission of redispersible Er^{3+}, Nd^{3+}, and Ho^{3+} -Doped LaF_3 nanoparticles. Nano Lett 2:733–737
35. Quici S, Cavazzini M, Marzanni G, Accorsi G, Armaroli N, Ventura B, Barigelletti F (2005) Visible and near-infrared intense luminescence from water-soluble lanthanide [Tb (III), Eu (III), Sm (III), Dy (III), Pr (III), Ho (III), Yb (III), Nd (III), Er (III)] complexes,.Inorg Chem 44:529–537
36. Auzel F (2004) Upconversion and anti-stokes processes with f and d Ions in solids. Chem Rev 104:139–174
37. Boyer JC, Cuccia LA, Capobianco JA (2007) Synthesis of colloidal upconverting $NaYF_4$: Er^{3+}/Yb^{3+} and Tm^{3+}/Yb^{3+} monodisperse nanocrystals. Nano Lett 7:847–852
38. Giri NK, Singh AK, Rai SB (2007) Eficient blue upconversion emission in Tm^{3+} via energy transfer from Yb^{3+} doped in lithium modified tellurite glass. J Appl Phys 101:033102
39. Sarakovskis A, Grube J, Doke G, Springis M (2010) Excited state absorption and energy-transfer mechanisms of up-conversion luminescence in Er^{3+}-doped oxyfluoride glass ceramics at different temperatures. J Lumin 130:805–811
40. Wang X, Xiao S, Yang X, Ding J (2008) Highly efficient cooperative up-conversion of Yb^{3+} in $NaYF_4$, J Mater Chem 43:1354–1356
41. Sivakumar S, van Veggel FCM, May PS (2007) Near-infrared (NIR) to red and green up-conversion emission from silica sol−gel thin films made with $La_{0.45}Yb_{0.50}Er_{0.05}F_3$ nanoparticles, hetero-looping-enhanced energy transfer (hetero-leet): a new up-conversion process. J Am Chem Soc 129:620–625
42. Prorok K, Pawlyta M, Stręk W, Bednarkiewicz A (2016) Energy migration up-conversion of Tb^{3+} in Yb^{3+} and Nd^{3+} codoped active-core/active-shell colloidal nanoparticles. Chem Mater 28:2295–2300
43. Lakowicz JR (2006) Principle of fluorescence spectroscopy
44. Wang X, Zhang X, Wang Y, Li H, Xie J, Wei T, Huang Q, Xie X, Huang L, Huang W (2017) Comprehensive studies of the Li^+ effect on $NaYF_4$:Yb/Er nanocrystals: morphology, structure, and upconversion luminescence. Dalton Trans 46:8968–8974
45. Fischer S, Fröhlich B, Steinkemper H, Krämer K, Goldschmidt J (2014) Absolute upconversion quantum yield of β-$NaYF_4$ doped with Er^{3+} and external quantum efficiency of upconverter solar cell devices under broad-band excitation considering spectral mismatch corrections. Sol Energy Mater Sol Cells 122:197–207
46. Faulkner DO, Petrov S, Perovic DD, Kherani NP, Ozin GA (2012) Absolute quantum yields in $NaYF_4$: Er, Yb upconverters–synthesis temperature and power dependence. J Mater Chem 22:24330–24334
47. MacDougall SK, Ivaturi A, Marques-Hueso J, Krämer KW, Richards BS (2012) Ultra-high photoluminescent quantum yield of β-$NaYF_4$: 10% Er^{3+} via broadband excitation of upconversion for photovoltaic devices. Opt Express 20:A879–A887
48. Boyer J-C, van Veggel FCJM (2010) Absolute quantum yield measurements of colloidal $NaYF_4$: Er^{3+}, Yb^{3+} upconverting nanoparticles. Nanoscale 2:1417–1419
49. Liu Q, Sun Y, Yang T, Feng W, Li C, Li F (2011) Sub-10 nm hexagonal lanthanide-doped $NaLuF_4$ upconversion nanocrystals for sensitive bioimaging in vivo. J Am Chem Soc 133:17122–17125

50. Li X, Shen D, Yang J, Yao C, Che R, Zhang F, Zhao D (2013) Successive layer-by-layer strategy for multi-shell epitaxial growth: shell thickness and doping position dependence in upconverting optical properties. Chem Mater 25:106–112
51. Chen G, Shen J, Ohulchanskyy TY, Patel NJ, Kutikov A, Li Z, Song J, Pandey RK, Ågren H, Prasad PN, Han G (2012) (α-$NaYbF_4$:Tm^{3+})/CaF_2 core/shell nanoparticles with efficient near-infrared to near-infrared upconversion for high-contrast deep tissue bioimaging. ACS Nano 6:8280–8287
52. Kumar GA, Chen CW, Ballato J, Riman RE (2007) Optical characterization of infrared emitting rare-earth-doped fluoride nanocrystals and their transparent nanocomposites. Chem Mater 19:1523–1528
53. Ehlert O, Thomann R, Darbandi M, Nann T (2008) A four-color colloidal multiplexing nanoparticle system. ACS Nano 2:120–124
54. GS Yi GC (2006) Synthesis of hexagonal phase $NaYF_4$: Yb, Er and $NaYF_4$: Yb, Tm nanocrystals with efficient up-conversion fluorescence. Adv Funct Mater 16:2324
55. Zhu Y, Zhao S, Zhou B, Zhu H, Wang Y (2017) Enhancing upconversion luminescence of $LiYF_4$:Yb,Er nanocrystals by Cd^{2+} doping and core–shell structure. J Phys Chem C 121:18909–18916
56. Wang G, Peng Q, Li Y (2009) Upconversion luminescence of monodisperse CaF_2:Yb^{3+}/Er^{3+} nanocrystals. J Am Chem Soc 131:14200–14201
57. Yi G-S, Chow G-M (2005) Colloidal LaF_3:Yb,Er, LaF_3:Yb,Ho and LaF_3:Yb,Tm nanocrystals with multicolor upconversion fluorescence. J Mater Chem 15:4460–4464
58. Silver J, Martinez Rubio M, Ireland T, Fern G, Withnall R (2001) The effect of particle morphology and crystallite size on the upconversion luminescence properties of erbium and ytterbium co-doped yttrium oxide phosphors. J Phys Chem B 105:948–953
59. Mialon G, Türkcan S, Dantelle G, Collins DP, Hadjipanayi M, Taylor RA, Gacoin T, Alexandrou A, Boilot J-P (2010) High up-conversion efficiency of YVO_4:Yb,Er nanoparticles in water down to the single-particle level. J Phys Chem C 114:22449–22454
60. Wu JL, Cao BS, Lin F, Chen BJ, Sun JS, Dong B (2016) A new molybdate host material: synthesis, upconversion, temperature quenching and sensing properties. Ceram Int 42:18666–18673
61. Yin M, Liu Y, Mei L, Molokeev MS, Huang Z, Fang M (2015) Preparation, crystal structure and up-conversion luminescence of Er^{3+}, Yb^{3+} Co-Doped $Gd_2(WO_4)_3$, RSC Adv 5:73077–73082
62. Du YP, Zhang YW, Sun LD, Yan CH (2008) Luminescent monodisperse nanocrystals of lanthanide oxyfluorides synthesized from trifluoroacetate precursors in high-boiling solvents. J Phys Chem C 112:405–415
63. Lu L, Zhang X (2013) Optimization of synthesis of upconversion luminescence material $NaYF_4$:Er^{3+},Yb^{3+} nanometer-phosphor by low-temperature combustion synthesis method. J Rare Earths 31:8–12
64. Zhengquan L, Yong Z (2008) An efficient and user-friendly method for the synthesis of hexagonal-phase $NaYF_4$:Yb, Er/Tm nanocrystals with controllable shape and upconversion fluorescence. Nanotechnol 19:345606
65. Yajuan S, Yue C, Lijin T, Yi Y, Xianggui K, Junwei Z, Hong Z (2007) Controlled synthesis and morphology dependent upconversion luminescence of $NaYF_4$:Yb, Er nanocrystals nanotechnology 18:275609
66. Qin X, Yokomori T, Ju Y (2007) Flame synthesis and characterization of rare-earth (Er^{3+}, Ho^{3+}, and Tm^{3+}) doped upconversion nanophosphors. Appl Phy Lett 90:073104
67. Dong H, Du SR, Zheng XY, Lyu GM, Sun LD, Li LD, Zhang PZ, Zhang C, Yan CH (2015) Lanthanide Nanoparticles: From Design toward Bioimaging and Therapy, Chem Rev 115:10725–10815
68. Na H, Woo K, Lim K, Jang HS (2013) Rational Morphology Control of β-$NaYF_4$:Yb,Er/Tm Upconversion Nanophosphors Using a Ligand, an Additive, and Lanthanide Doping, Nanoscale 5:4242–4251
69. Ullah S, Hazra C, Ferreira-Neto EP, Silva TC, Rodrigues-Filho UP, Ribeiro SJL (2017) Microwave-Assisted Synthesis of $NaYF_4$:Yb^{3+}/Tm^{3+} Upconversion Particles with Tailored

Morphology and Phase for the Design of UV/NIR-Active $NaYF_4:Yb^{3+}/Tm^{3+}@TiO_2$ Core@Shell Photocatalysts, Cryst Eng Comm 19:3465–3475
70. Chen X, Jin L, Kong W, Sun T, Zhang W, Liu X, Fan J, Yu SF, Wang F (2016) Confining energy migration in upconversion nanoparticles towards deep ultraviolet lasing. Nat Commun 7:10304
71. Yi G-S, Chow G-M (2007) Water-soluble $NaYF_4$:Yb,Er(Tm)/$NaYF_4$/polymer core/shell/shell nanoparticles with significant enhancement of upconversion fluorescence chem mater 19:341–343
72. Naccache R, Vetrone F, Mahalingam V, Cuccia LA, Capobianco JA (2009) Controlled synthesis and water dispersibility of hexagonal phase $NaGdF_4:Ho^{3+}/Yb^{3+}$ nanoparticles. Chem Mater 21:717–723
73. Wang F, Deng R, Wang J, Wang Q, Han Y, Zhu H, Chen X, Liu X (2011) Tuning upconversion through energy migration in core–shell nanoparticles. Nat Mater 10:968
74. Prorok K, Bednarkiewicz A, Cichy B, Gnach A, Misiak M, Sobczyk M, Strek W (2014) The impact of shell host ($NaYF_4/CaF_2$) and shell deposition methods on the up-conversion enhancement in Tb^{3+}, Yb^{3+} codoped colloidal α-$NaYF_4$ core-shell nanoparticles. Nanoscale 6:1855–1864
75. Li X, Wang R, Zhang F, Zhou L, Shen D, Yao C, Zhao D (2013) Nd^{3+} sensitized up/down converting dual-mode nanomaterials for efficient in-vitro and in-vivo bioimaging excited at 800 nm. Sci Rep 3:3536
76. Krämer KW, Biner D, Frei G, Güdel HU, Hehlen MP, Lüthi SR (2004) Hexagonal sodium yttrium fluoride based green and blue emitting upconversion phosphors. Chem Mater 16:1244–1251
77. Wen T, Ding R, Zhou Y, Si Y, Yang B, Wang Y (2017) Polymorphism of erbium oxyfluoride: selective synthesis, crystal structure, and phase-dependent upconversion luminescence. Eur J Inorg Chem 2017:3849–3854
78. Yi G, Lu H, Zhao S, Ge Y, Yang W, Chen D, Guo L-H (2004) Synthesis, characterization, and biological application of size-controlled nanocrystalline $NaYF_4$:Yb,Er infrared-tovisible up-conversion phosphors. Nano Lett 4:2191–2196
79. Hou Z, Li C, Ma PA, Cheng Z, Li X, Zhang X, Dai Y, Yang D, Lian H, Lin J, Adv funct mater, up-conversion luminescent and porous $NaYF_4:Yb^{3+}$, $Er^{3+}@SiO_2$ nanocomposite fibers for anti-cancer drug delivery and cell imaging 22:2713–2722
80. Bazylińska U, Wawrzyńczyk D (2017) Encapsulation of topo stabilized $NaYF_4$: Er^{3+},Yb^{3+} nanoparticles in biocompatible nanocarriers: synthesis, optical properties and colloidal stability colloids. Surf A 532:556–563
81. Li S, Ye S, Chen X, Liu T, Guo Z, Wang D (2017) OH^- ions-controlled synthesis and upconversion luminescence properties of $NaYF_4:Yb^{3+}$,Er^{3+} nanocrystals via oleic acid-assisted. J Rare Earth 35:753–760
82. Chang J, Waclawik ER (2014) Colloidal semiconductor nanocrystals: controlled synthesis and surface chemistry in organic media. RSC Adv 4:23505–23527
83. Polte J (2015) Fundamental growth principles of colloidal metal nanoparticles - a new perspective. Cryst Eng Comm 17:6809–6830
84. Mai HX, Zhang YW, Si R, Yan ZG, Sun L, You LP, Yan CH (2006) High-quality sodium rare-earth fluoride nanocrystals: controlled synthesis and optical properties. J Am Chem Soc 128:6426–6436
85. Sun X, Zhang YW, Du YP, Yan ZG, Si R, You LP, Yan CH (2007) From trifluoroacetate complex precursors to monodisperse rare-earth fluoride and oxyfluoride nanocrystals with diverse shapes through controlled fluorination in solution phase. Chem Eur J 13:2320–2332
86. Zhang Y-W, Sun X, Si R, You L-P, Yan C-H (2005) Single-crystalline and monodisperse LaF_3 triangular nanoplates from a single-source precursor. J Am Chem Soc 127:3260–3261
87. Du YP, Zhang YW, Yan ZG, Sun LD, Yan CH (2009) Highly luminescent self-organized sub-2nm EuOF nanowires. J Am Chem Soc 131:16364–16365
88. Du YP, Zhang YW, Sun LD, Yan CH (2009) Atomically efficient synthesis of self-assembled monodisperse and ultrathin lanthanide oxychloride nanoplates. J Am Chem Soc 131:3162–3163

89. Du YP, Zhang YW, Sun LD, Yan CH (2009) Optically active uniform potassium and lithium rare earth fluoride nanocrystals derived from metal trifluroacetate precursors. Dalton Trans 8574–8581
90. Shan J, Ju Y (2009) A single-step synthesis and the kinetic mechanism for monodisperse and hexagonal-phase $NaYF_4$: Yb, Er upconversion nanophosphors. Nanotechnol 20:275603
91. Ren J, Jia G, Guo Y, Wang A, Xu S (2016) Unraveling morphology and phase control of $NaLnF_4$ upconverting nanocrystals. J Phys Chem C 120:1342–1351
92. Hu H, Chen Z, Cao T, Zhang Q, Yu M, Li F, Yi T, Huang C (2008) Hydrothermal synthesis of hexagonal lanthanide-doped LaF_3 nanoplates with bright upconversion luminescence. Nanotechnology 19:375702
93. Wang ZL, Hao J, Chan HLW, Wong W-T, Wong K-L (2012) A strategy for simultaneously realizing the cubic-to-hexagonal phase transition and controlling the small size of $NaYF_4$:Yb^{3+},Er^{3+} nanocrystals for in vitro Ccll imaging. Small 8:1863–1868
94. Lu E, Pichaandi J, Rastogi CK, Arnett LP, Winnik MA (2019) Influence of cubic-to-hexagonal-phase transformation on the uniformity of $NaLnF_4$ (Ho, Tb, Eu, Sm) nanoparticles. Chem Mater 31:9742–9749
95. Znaidi L (2010) Sol–gel deposited ZnO thin films mater. Sci Eng B 174:18–30
96. Georgescu S, Voiculescu AM, Matei C, Secu CE, Negrea RF, Secu M (2013) Ultraviolet and visible up-conversion luminescence of Er^{3+}/Yb^{3+} co-doped CaF_2 nanocrystals in sol–gel derived glass-ceramics. J Lumin 143:150–156
97. Gunaseelan M, Yamini S, Kumar GA, Senthilselvan J (2018) Highly efficient upconversion luminescence in hexagonal $NaYF_4$:Yb^{3+}, Er^{3+} nanocrystals synthesized by a novel reverse microemulsion method. Opt Mater 75:174–186
98. Quintanilla M, Zhang Y, Liz-Marzán LM (2018) Subtissue plasmonic heating monitored with CaF_2:Nd^{3+},Y^{3+} nanothermometers in the second biological window. Chem Mater 30:2819–2828
99. Zhai X, Lei P, Zhang P, Wang Z, Song S, Xu X, Liu X, Feng J, Zhang H (2015) Growth of lanthanide-doped $LiGdF_4$ nanoparticles induced by $LiLuF_4$ core as tri-modal imaging bioprobes. Biomaterials 65:115–123
100. Gai S, Yang P, Li X, Li C, Wang D, Dai Y, Lin J (2011) Monodisperse CeF_3, CeF_3:Tb^{3+}, and CeF_3:Tb^{3+}@LaF_3 core/shell nanocrystals: synthesis and luminescent properties. J Mater Chem 21:14610–14615
101. Dong N-N, Pedroni M, Piccinelli F, Conti G, Sbarbati A, Ramírez-Hernández JE, Maestro LM, Iglesias-de la Cruz MC, Sanz-Rodriguez F, Juarranz A, Chen F, Vetrone F, Capobianco JA, Solé JG, Bettinelli M, Jaque D, Speghini A (2011) NIR-to-NIR two-photon excited CaF_2:Tm^{3+},Yb^{3+} nanoparticles: multifunctional nanoprobes for highly penetrating fluorescence Bio-imaging. ACS Nano 5:8665–8671
102. Gao X, Wang N, Shi T, Wang S, Zhang M, Zhang W, Zhong J, Tong H, Zhang X (2016) Sol-gel synthesis of β-$NaYF_4$:Yb^{3+}/Nd^{3+}/Tm^{3+}/Mn^{2+} nanophosphors and color-tunable upconversion luminescence. J Fluorine Chem 188:23–27
103. Gunaseelan M, Senthilselvan J (2016) Synthesis and characterization of α-$NaYF_4$: Yb, Er nanoparticles by reverse microemulsion method. AIP Conf Proc 1728:020574
104. Naduviledathu Raj A, Rinkel T, Haase M (2014) Ostwald ripening, particle size focusing, and decomposition of sub-10 nm $NaREF_4$ (Re= La, Ce, Pr, Nd) nanocrystals. Chem Mater 26:5689–5694
105. Liu C, Wang H, Zhang X, Chen D (2009) Morphology- and phase-controlled synthesis of monodisperse lanthanide-doped $NaGdF_4$ nanocrystals with multicolor photoluminescence J Mater Chem 19:489–496
106. Shan J, Ju Y (2007) Controlled Synthesis of Lanthanide-Doped $NaYF_4$ Upconversion nanocrystals Via ligand induced crystal phase transition and silica coating, Appl Phy Lett 91:123103
107. Bealing CR, Baumgardner WJ, Choi JJ, Hanrath T, Hennig RG (2012) Predicting nanocrystal shape through consideration of surface-ligand interactions. ACS Nano 6:2118–2127

108. Shang Y, Hao S, Liu J, Tan M, Wang N, Yang C, Chen G (2015) Synthesis of upconversion β-$NaYF_4$:Nd^{3+}/Yb^{3+}/Er^{3+} particles with enhanced luminescent intensity through control of morphology and phase. Nanomaterials 5:218
109. Wang J, Wang F, Wang C, Liu Z, Liu X (2011) Single-band upconversion emission in lanthanide-doped $KMnF_3$ nanocrystals. Angew Chem Int Ed 50:10369–10372
110. Dong C, Raudsepp M, van Veggel FCJM (2009) Kinetically determined crystal structures of undoped and La^{3+}dDoped LnF_3. J Phys Chem C 113:472–478
111. Yu M, Li F, Chen Z, Hu H, Zhan C, Yang H, Huang C (2009) Laser scanning up-conversion luminescence microscopy for imaging cells labeled with rare-earth nanophosphors. Anal Chem 81:930–935
112. Naczynski DJ, Andelman T, Pal D, Chen S, Riman RE, Roth CM, Moghe PV (2010) Albumin nanoshell encapsulation of near-infrared-excitable rare-earth nanoparticles enhances biocompatibility and enables targeted cell imaging. Small 6:1631–1640
113. Pan L, He M, Ma J, Tang W, Gao G, He R, Su H, Cui D (2013) Phase and size controllable synthesis of $NaYbF_4$ nanocrystals in oleic acid/ionic liquid two-phase system for targeted fluorescent imaging of gastric cancer. Theranostics 3:210
114. Li F, Gu W, Wang H, Qi Y, Deng Y, Xiao N, Liu Y, Xu Q, Ye L (2013) Effect of surface functionalities on relaxometric properties of Mr contrast agents based on $NaGdF_4$ nanoparticles. RSC Adv 3:5386–5392
115. Gayathri S, Ghosh OSN, Sudhakara P, Viswanath AK (2015) Chitosan conjugation: a facile approach to enhance the cell viability of LaF_3:Yb,Er upconverting nanotransducers in human breast cancer cells. Carbohyd Polym 121:302–308
116. Wu S, Han G, Milliron DJ, Aloni S, Altoe V, Talapin DV, Cohen BE, Schuck PJ (2009) Proc Natl Acad Sci 106:10917–10921
117. Zhou J, Liu Q, Feng W, Sun Y, Li F (2015) Non-blinking and photostable upconverted luminescence from single lanthanide-doped nanocrystals. Chem Rev 115:395–465
118. Jeyaraman J, Malecka A, Billimoria P, Shukla A, Marandi B, Patel PM, Jackson AM, Sivakumar S (2017) Immuno-silent Polymer capsules encapsulating nanoparticles for bioimaging applications. J Mater Chem B 5:5251–5258
119. Cao T, Yang Y, Gao Y, Zhou J, Li Z, Li F (2011) High-quality water-soluble and surface-functionalized upconversion nanocrystals as luminescent probes for bioimaging. Biomaterials 32:2959–2968
120. Liu Y, Tu D, Zhu H, Chen X (2013) Lanthanide-doped luminescent nanoprobes: controlled synthesis, optical spectroscopy, and bioapplications. Chem Soc Rev 42:6924–6958
121. Xiong L-Q, Chen Z-G, Yu M-X, Li F-Y, Liu C, Huang C-H (2009) Synthesis, characterization, and in vivo targeted imaging of amine-functionalized rare-earth up-converting nanophosphors. Biomaterials 30:5592–5600
122. Yu X-F, Sun Z, Li M, Xiang Y, Wang Q-Q, Tang F, Wu Y, Cao Z, Li W (2010) Neurotoxin-conjugated upconversion nanoprobes for direct visualization of tumors under near-infrared irradiation. Biomaterials 31:8724–8731
123. Roh J, Yu H, Jang J, Appl ACS (2016) Hexagonal β-$NaYF_4$:Yb^{3+}, Er^{3+} nanoprism-incorporated upconverting layer in perovskite solar cells for near-infrared sunlight harvesting. Mater Interfaces 8:19847–19852
124. Chen D, Lei L, Yang A, Wang Z, Wang Y (2012) Ultra-broadband near-infrared excitable upconversion core/shell nanocrystals. Chem Comm 48:5898–5900
125. Wang J, Wei T, Li X, Zhang B, Wang J, Huang C, Yuan Q (2014) Near-infrared-light-mediated imaging of latent fingerprints based on molecular recognition. Angew Chem Int Ed 53:1709–1709
126. Won Jin K, Marcin N, Paras NP (2009) Color-coded multilayer photopatterned microstructures using lanthanide (III) ion co-doped $NaYF_4$ nanoparticles with upconversion luminescence for possible applications in security. Nanotechnology 20:185301

Chapter 7
Synthesis and Characterization of Quantum Cutting Phosphor Materials

Ram Sagar Yadav and Raghumani S. Ningthoujam

Abstract The rare earth ions produce photoluminescence in the entire range of the electromagnetic spectrum particularly in the UV, vis and NIR regions. The present chapter describes the synthesis of quantum cutting phosphor materials using different methods, such as solid-state reaction, combustion, sol–gel, hot-injection, hydrothermal, along with a melting-quenching method for the glass materials and studies the photoluminescence of the rare earth doped quantum cutting phosphor materials. Quantum cutting (QC) is a downconversion (DC) process in which the conversion of a high-energy photon into the two or more low-energy photons takes place. This process not only takes place in the singly rare earth doped materials but also in the doubly and/or triply rare earth doped materials. The difference is only in the energy transfer route between activator and sensitizer ions. This occurs due to cooperative energy transfer (CET) process. In energy transfer process, the photoluminescence intensity of sensitizer ion decreases whereas the photoluminescence intensity of activator ion increases accordingly. The change in photoluminescence intensity of these ions is highly concentration dependent. The photoluminescence intensity versus pump power measurements shows that the photoluminescence intensity of the visible region is a linear process while that of the NIR region occurs due to nonlinear process. The change in photoluminescence intensity of the sensitizer ions can be established from the lifetime measurements. The preparation and characterization of different rare earth-based quantum cutting materials and their applications in large numbers of the emerging fields have been also included.

Keywords Synthesis · Dopant ions · Energy transfer · Quantum cutting · Phosphors · Solar cells

R. S. Yadav (✉)
Department of Zoology, Institute of Science, Banaras Hindu University, Varanasi 221005, India
e-mail: yadavrs@bhu.ac.in

R. S. Ningthoujam (✉)
Chemistry Division, Bhabha Atomic Research Centre, Mumbai 400085, India
e-mail: rsn@barc.gov.in

Homi Bhabha National Institute, Mumbai 400094, India

A. K. Tyagi and R. S. Ningthoujam (eds.), *Handbook on Synthesis Strategies for Advanced Materials*, Indian Institute of Metals Series,
https://doi.org/10.1007/978-981-16-1892-5_7

Acronyms

BG	Band gap
CET	Cooperative energy transfer
CTS	Charge transfer state
DC	Downconversion
DS	Downshifting
ET	Energy transfer
ETE	Energy transfer efficiency
FPD	Flat panel devices
Hg	Mercury
LEDs	Light-emitting diodes
LT	Lifetime
NIR	Near infrared
μm	Micro-meter
nm	Nano-meter
PL	Photoluminescence
PLE	Photoluminescence excitation
PPD	Plasma panel devices
QC	Quantum cutting
QDs	Quantum dots
QE	Quantum efficiency
QY	Quantum yield
SEM	Scanning electron microscopy
TEM	Transmission electron microscopy
UC	Upconversion
UV	Ultraviolet
Vis	Visible
wLEDs	White light-emitting diodes
XRD	X-ray diffraction

7.1 Introduction

The energy is an essential part of our life and it can be neither created nor destroyed. One form of energy is being converted to another form by means of some processes for different technological applications. The conversion of light from high energy to the low energy is termed as downconversion (DC). This process is most likely used in different display devices, optical devices, flat panel devices (FPD), plasma panel devices (PPD), solid-state lighting, white light-emitting diodes (wLEDs), etc. [1–6]. These applications have been developed by the use of different activators and donors in various types of host matrices. The activators are those ions which accept the energy while the donor ions are the energy providers to the activator ions and termed

as the sensitizers. The process of energy transfer from donor ions to acceptor ions improves the photoluminescence (PL) intensity of the activator ions [7–14]. Energy transfer is most efficient if there is maximum overlapping of absorption spectrum of activator ions with emission spectrum of sensitizer ions [15]. Otherwise, there is a loss of energy of sensitizer ions, and this loss is used in multiphonon excitation of surrounding; and only, some energy is transferred to the activator ion. Most commonly, the transition metal ions, rare earth metal ions and even host (VO_4^{3-}, WO_4^{2-}, MoO_4^{2-}) have been selected as activators and sensitizers in the glass, phosphor and composite materials [6, 15–27]. Figure 7.1 shows a typical absorption and emission spectra of activator and sensitizer ions in a host material and energy transfer process [15, 28–31]. Let us suppose that the sensitizer absorbs light at 300 nm and produces a broad emission in the 320–500 nm region. The activator ion has absorption peak at 395 nm whereas the emission peaks appear at 595 and 615 nm. Absorption peak of activator falls in the emission range of sensitizer. Upon excitation through sensitizer in the sensitizer-activator combination, the luminescence intensity of the sensitizer is found to be decreased, but luminescence intensity of the activator gets enhanced. The rare earth ions have a low absorption cross section due to forbidden

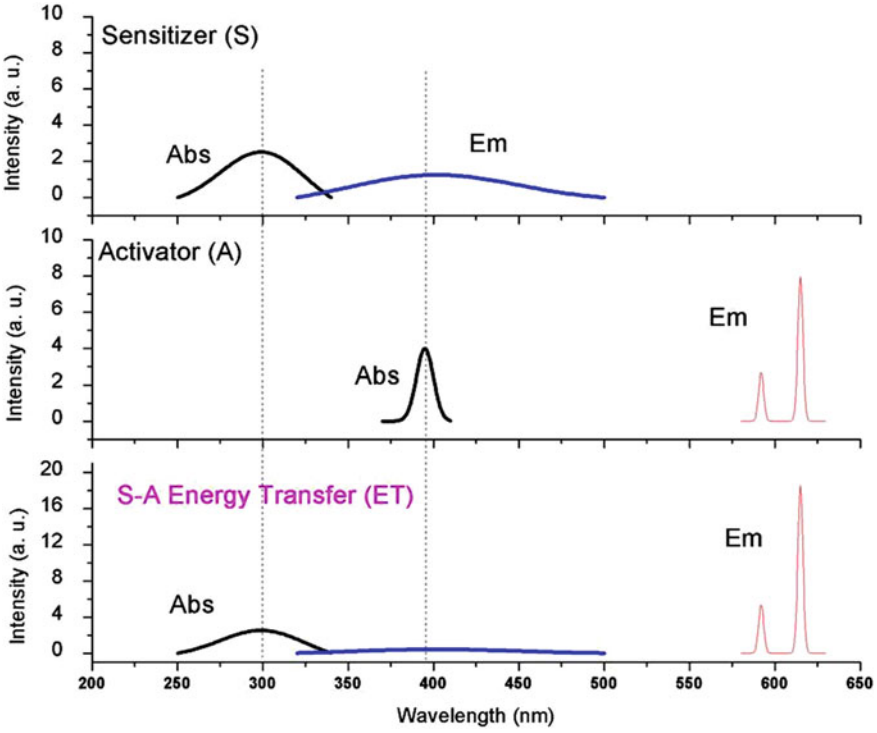

Fig. 7.1 Typical absorption and emission spectra of activator and sensitizer ions in a host material and energy transfer process

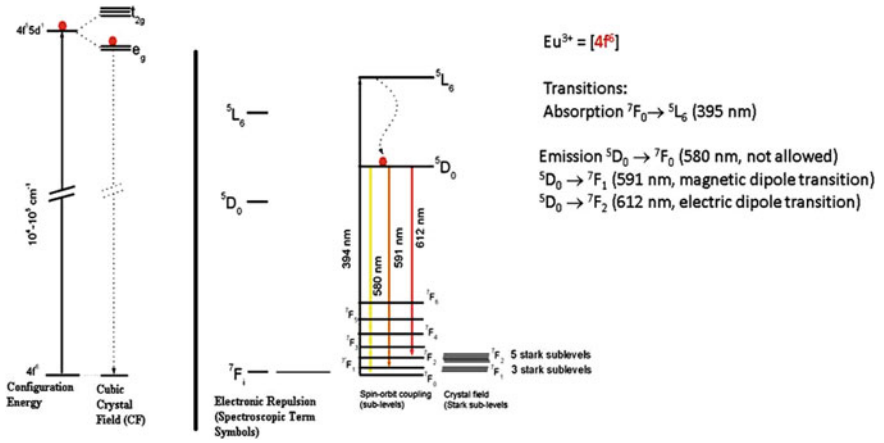

Fig. 7.2 Energy level diagram of Eu^{2+}/Eu^{3+} doped host lattice

nature in f-f transitions. However, the *d–f* transitions are allowed. Figure 7.2 shows an energy level diagram of Eu^{2+}/Eu^{3+} doped host lattice: Eu^{2+} can undergo *f–d* transition, but the emission peak is broad, and this transition wavelength depends on crystal field environment [15]. Eu^{3+} can provide many energy levels due to repulsion among spins of 4*f* electrons, and then Stark splitting occurs due to crystallinity or electric field interactions [15]. The electronic transitions are very sharp and almost unchanged at different crystal field environment. The effect on 4*f* electrons of metal ions by ligands is negligible and 4*f* electrons are protected by outermost orbitals ($5s^2 5p^6$). The *f–f* transitions are weak due to forbidden nature, but very sharp. Sometimes, this is slightly relaxed due to jj mixing [15]. In the case of 3d electrons (say Mn^{2+}), the *d*– transition is broad since there are no outermost orbitals and weak due to forbidden nature. These are demonstrated schematically in Figs. 7.3 and 7.4.

Tb^{3+} ions show absorption peaks at 352, 378, 390 nm and the emission peaks at 480 and 544 nm owing to *f–f* transitions. However, their absorption or emission intensities are very weak. In the case of Ce^{3+} ions, the absorption peaks at 258 and 278 nm owing to allowed *f–d* transitions and the broad emission peak at 350 nm occur, but their absorption or emission intensity is strong. There is an overlapping of absorption peak of Tb^{3+} and the emission peak of Ce^{3+}. If the excitation through Ce^{3+} is performed in the host matrix, there is an increase in emission intensity of Tb^{3+} ion due resonance energy transfer (Fig. 7.5) [32]. By fixing high concentration of Ce^{3+}, luminescence intensity of the Tb^{3+} can also be improved by increase of concentration of Tb^{3+}. Similarly, there is energy transfer from the Ce^{3+} to Dy^{3+} ions in the host matrix or MoO_4^{2-}/WO_4^{2-} to Dy^{3+}/Sm^{3+} through resonance energy transfer [15, 33–35]. In A_2O_3: Eu^{3+} (A = Y, Gd, La), Eu–O peak (oxygen to metal charge transfer band (CTB)) occurs in a range of 240–270 nm and this is allowed transition [15, 36, 37]. Interestingly, the exceptional strong emission transitions have been observed due to ${}^5D_j (j = 1 - 3)$ to ${}^7F_j$ $(j = 1 - 3)$ transitions in the Eu^{3+} doped

Block	Element	Atomic Number	Electronic Configuration
s	Li	3	$1s^2\,2s^1$
	Be	4	$1s^2\,2s^2$
p	B	5	$1s^2 2s^2\,2p^1$
d	Mn	25	$1s^2 2s^2 2p^6 3s^2 3p^6\,(3d^5)\,4s^2$
	Mn^{2+}	(23 es)	$1s^2 2s^2 2p^6 3s^2 3p^6\,(3d^5)$
f	Eu	63	$1s^2 2s^2 2p^6 3s^2 3p^6 3d^{10} 4s^2 4p^6 4d^{10}\,(4f^7)\,5s^2 5p^6 5d^0 6s^2$
	Eu^{3+}	(60 es)	$1s^2 2s^2 2p^6 3s^2 3p^6 3d^{10} 4s^2 4p^6 4d^{10}\,(4f^6)\,5s^2 5p^6$

d-block M^{n+} ions
No-outer-orbitals

The d-d transition is broad
Crystal Field (CF) affects wavelength of transitions
Transition is weak due to forbidden nature

f-block M^{n+} ions
Outer-orbitals: $5s^2 5p^6$

The f-f transition is sharp
CF does not affect transitions
Transition is weak due to forbidden nature

Fig. 7.3 Ground state electronic configurations of a few examples of *s*, *p*, *d* and f block elements/ions

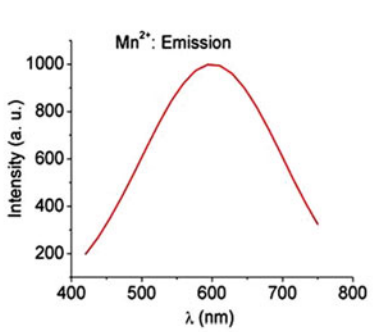

d-d transition

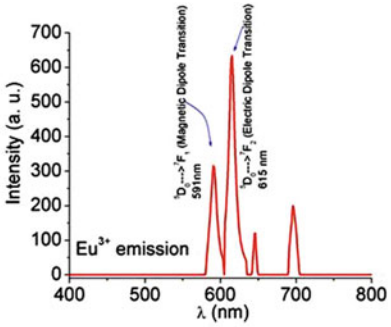

f-f transition

Possible Transitions
1) f-f transition
2) f-d transition
3) Metal-Ligand charge transfer

f-block:
For electric dipole: $\Delta S = 0, \Delta L \leq 6, \Delta J = 2, 4, 6$, opposite parity.
For magnetic dipole: $\Delta S = 0, \Delta L = 0, \Delta J = 0, \pm 1$, same parity.
For electric quadrupole: $\Delta S = 0, \Delta L = 0, \pm 1, \pm 2, \Delta J = 0, \pm 1, \pm 2$, same parity
jj-mixing gives possibility of other transitions

Fig. 7.4 Typical emission spectra of *d*-block ion (Mn^{2+}) and *f*-block ion (Eu^{3+})

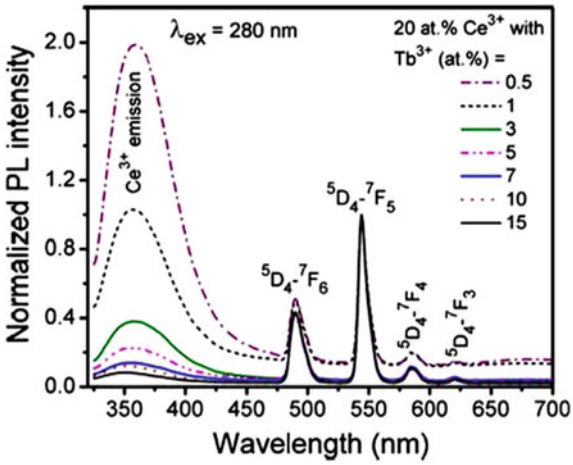

Fig. 7.5 Emission spectra of $GdPO_4$: Ce-Tb by fixing amount of Ce and varying amount of Tb. Reproduced with copyright permission from ACS Publisher [32]

La_2O_3 nanoparticles. The V–O and Eu–O CTBs shift within 30–40 nm according to type of lattice [37].

By excitation of the CaF_2: Eu through Eu–O CTB, the luminescence intensity of Eu^{3+} ion is enriched as compared to direct excitation at 394 nm (Fig. 7.6) [38]. The electric as well as magnetic dipole transitions of Eu^{3+} ion are observed at 592 and 615 nm, respectively. The ratio of the electric to the magnetic dipole transitions of Eu^{3+} ion can be used to predict the symmetry or asymmetry environment around the Eu^{3+}. This should be done upon direct excitation at 394 nm. If the ratio is more than

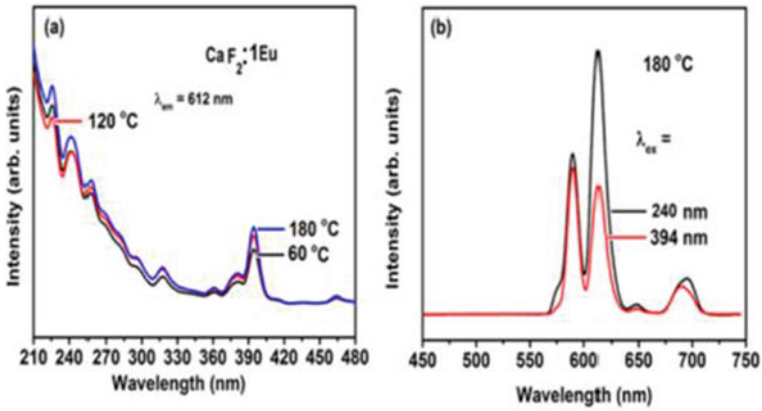

Fig. 7.6 **a** Excitation and **b** emission spectra of CaF_2: Eu. Excitation at 240 nm (Eu–O) gives higher emission intensity as compared to that at 394 nm (direct). Reproduced with copyright permission from ACS Publisher [39]

1, Eu^{3+} ions occupy more asymmetry environment. On excitation through charge transfer band of Eu–O (CTB), no resonance energy transfer takes place to Eu^{3+} ions and thus, there is a loss of excited energy. In comparison with the other rare earth ions, the Eu^{3+} ions in lattice give the information about local environment because it can exhibit the electric and magnetic dipole transitions distinctly [15, 40–51]. In the case of AVO_4: RE (A = Y, Gd, La; RE = Eu, Dy, Sm, Tm), V–O CTB occurs with broad absorption while the emission spectra appeared in 250–350 nm and 340–500 nm ranges, respectively owing to the allowed transitions [15, 24, 25]. Absorption peaks for Eu^{3+} at 395, 460 nm, Dy^{3+} at 352, 390 nm, Sm^{3+} at 410 nm and Tm^{3+} at 365 nm were observed and these peaks are overlapping with emission peak of V–O CTB (Fig. 7.7) [15, 40]. Luminescence intensity of Eu^{3+} in YVO_4: Eu follows the different excitation wavelengths 320 nm (V–O CTB) > 270 nm (Eu–O CTB) > 395 nm (direct). Thus, the emission intensity of RE can be improved. Luminescence intensity of RE ions can be improved by energy transfer from the host, co-doping (say Bi, Li, Sr), Eu–O CTB, V–O CTB, Mo–O CTB, W–O CTB, etc. (Fig. 7.8) [15, 52]. Luminescence intensity of RE can be changed by non-radiative process through imperfect in the lattice of host, nature of host, presence of moisture, concentration quenching and energy transfer to the other ions. There is another process known as

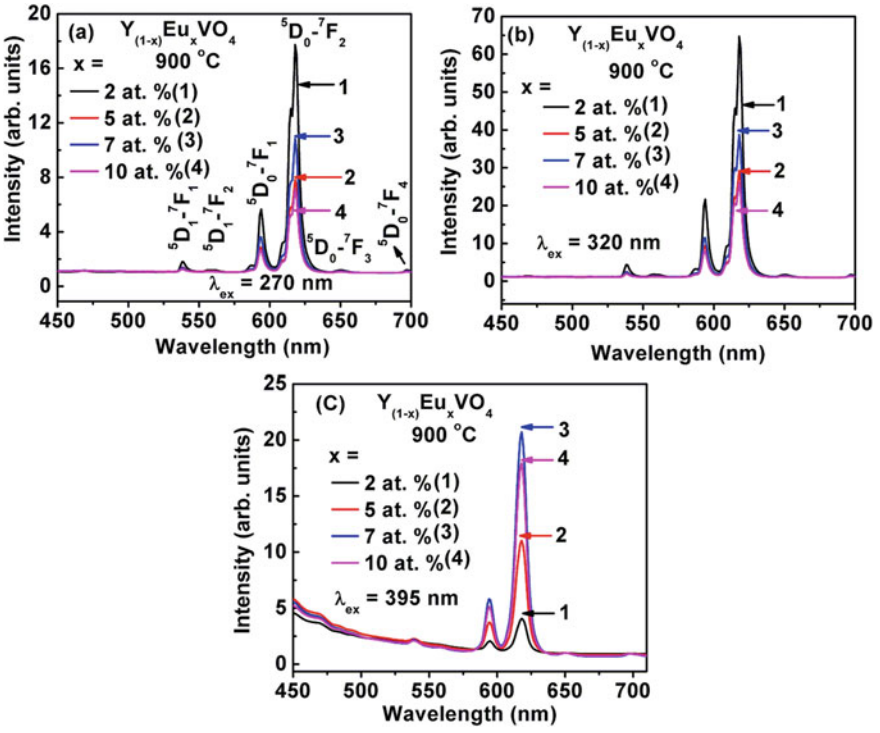

Fig. 7.7 Emission spectra of YVO_4: Eu upon excitation at **a** 270 nm (Eu–O), **b** 320 nm (V–O) and **c** 395 nm (direct). Reproduced with copyright permission from RSC Publisher [40]

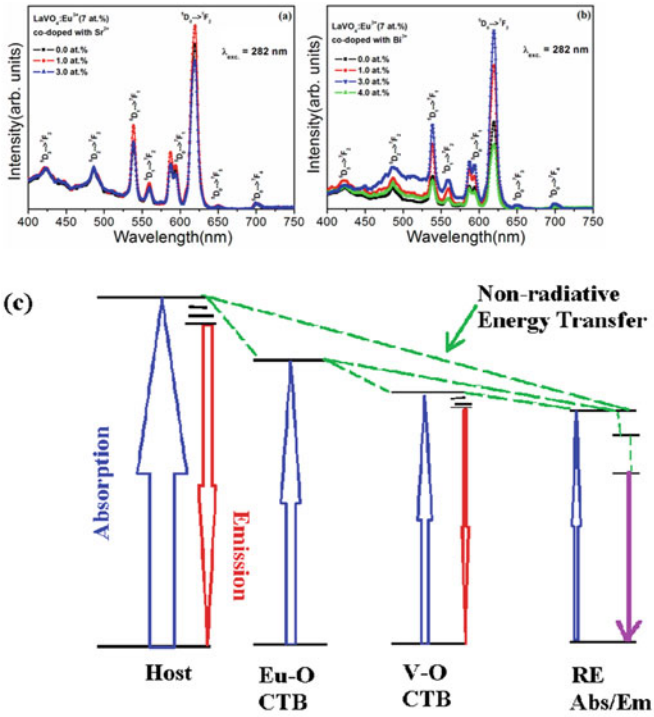

Luminescence enhancement in rare-earth ions (RE) by energy transfer from host (through band gap, Bi (S-P transition)), Eu-O charge transfer band (CTB), V-O CTB or improved crystalinity by annealing or addition of co-dopant

Fig. 7.8 Luminescence spectra of $LaVO_4$: Eu co-doped with **a** Sr and **b** Bi. **c** Possible energy transfer process through host, Bi, Eu–O, V–O, direct. Reproduced with copyright permission from ACS Publisher [52]

upconversion, which converts the lower energy into the higher energy. Examples of upconversion materials are RE doped compounds (Er, Yb–Er or Yb–RE containing compounds, such as $NaYF_4$, LaF_3, CaF_2, APO_4, A_2O_4, AVO_4). When Er^{3+} or Yb^{3+} ions absorb the light at 980 nm, the emission light can be seen in the visible region. Emission intensity of RE is improved by absorption through Yb^{3+} as compared to that through Er^{3+}. Laser power dependent emission intensity study of RE suggests the nonlinear property ($I \propto P^n$) (Fig. 7.9) [53, 54]. Heat can be generated by fluorescence resonance energy transfer (FRET) in $NaYF_4$: Er-Yb@Au composite. Here, 980 nm light is absorbed by Yb^{3+} ions and transferred its excited photons to Er^{3+} ions. Er^{3+} ions produce visible light, which is absorbed by Au nanoparticles. There are two types of process in luminescence: Downshifting (DS) or downconversion (DC) and upconversion (UC) (see Fig. 7.10).

The conversion of light is not limited to the DC process but a new process is also included, which is recognized as a quantum cutting. The quantum cutting (QC) is

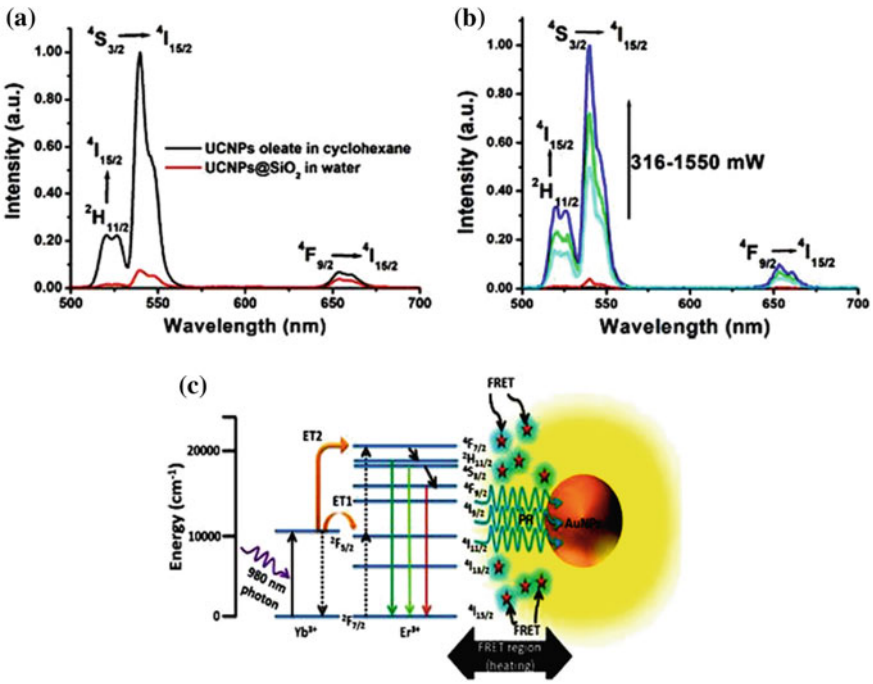

Fig. 7.9 Upconversion emission spectra of **a** $NaYF_4$: Er-Yb (UCNPs), silica coated UCNPs, **b** silica coated UCNPs under different laser powers at 980 nm. **c** Energy level diagram of Yb–Er energy transfer process and fluorescence energy transfer from UCNPs to Au nanoparticles. Reproduced with copyright permission from ACS Publisher [53]

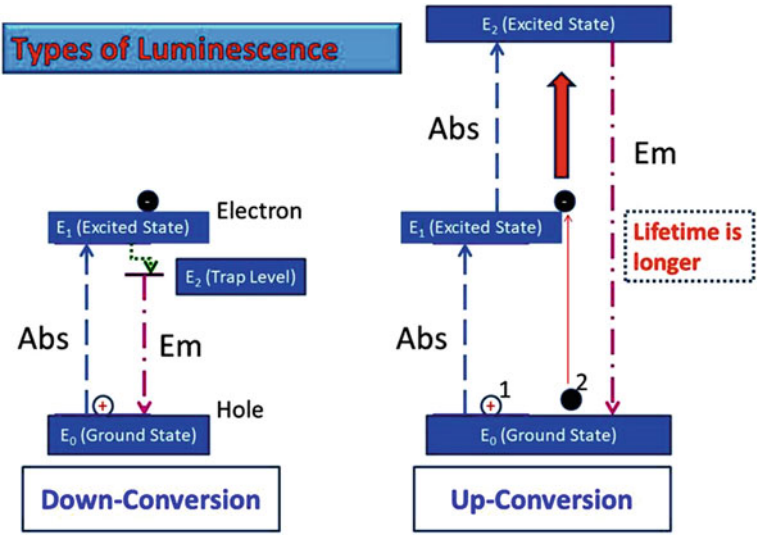

Fig. 7.10 Types of luminescence: downconversion and upconversion

generally a DC process in which a high-energy photon is being converted in the low-energy near infrared (NIR) photons [7, 18, 19]. This process has also been observed in both cases, i.e., the transition metal and the rare earth metal ions [6, 7, 18, 55, 56]. The QC process in various materials has been summarized by Huang et al. and discussed its use in augmenting spectral efficiency of solar cell and the materials involved in this process behave as spectral converters [57]. The QC process is not observed only in the doubly combination of the donor and the acceptor ions but also found significantly in the singly doped materials. This process enables us to realize the visible as well as NIR photons; however, their emission intensity ratio was found to vary [58–64].

The QC process was initially started with the singly rare earth doped fluoride phosphor materials. The Pr^{3+} ion was doped in the fluoride phosphor materials and the phosphor materials were excited with 185 nm resonance radiation of mercury (Hg) source [64]. In the case of YF_3 and LaF_3 phosphor materials, the phosphors emit two visible photons through a simple cascade process. The emission of two visible photons leads is an experimental proof of the QC process. Upon exciting the $LiYF_4$ phosphor with 185 nm, the emission occurs due to $4f$–$5d$ levels and gives four principal bands in the UV region. These emissions mixed together produce another type of the host material. The QC process was also noticed in the Pr^{3+} doped YF_3 and α-$NaYF_4$ phosphor materials and the materials give two photons luminescence on excitation with 210 nm UV photon. The QC emission has been detected in visible region [65]. The singly Eu^{3+} doped $LiGdF_4$ material also gives visible QC emission through downconversion process [58]. The QC process was also studied by Creutz et al. in colloidal Yb^{3+}-doped chalcogenide nanocrystals and perceived long-lived NIR emission band upon excitation with visible photons [59].

In an interesting work, Yu et al. have developed Gd_2O_2S: Tm^{3+} powder samples and studied the QC process in detail [66]. They have observed multi-photon QC emission in Tm^{3+} ions that occurs due to involvement of cross-relaxation among the Tm^{3+} ions. The emission intensity of Tm^{3+} ion increases on increasing its concentrations and decreases on further increase in the concentrations. At low concentration, the cross-relaxation does not take part in the emission process. Sometimes, the higher concentration also augments the emission intensity of activator ions due to cross-relaxation process. Generally, the cross-relaxation takes place at higher concentrations of the dopant ions and also matching of the two consecutive energy levels of a donor to the acceptor ion [67]. The QC emissions of two, three and four photons were reported in the Gd_2O_2S: Tm^{3+} powder samples, and they are found to increase the efficacy of solar cells.

On the other hand, the energy transfer between the donor and acceptor combinations leads to the generation of QC emission using the transition metal and/or the rare earth metal ions in different doped materials [18, 21, 22, 63]. Zhang et al. have observed UV–vis-NIR luminescence properties in the doubly Ce^{3+}, Pr^{3+} co-doped $CaLaGa_3S_6O$ phosphor material and discussed the solar spectral converting mechanism. The phosphor material behaves as dual-mode solar spectral converter [68]. They have excited the phosphor materials with 445, 480, 492 and 605 nm photons and they give NIR emissions at 948, 988 and 1034 nm, respectively. The Ce^{3+}, Pr^{3+}

co-doped $CaLaGa_3S_6O$ phosphor gives two types of spectral conversions in which the first one is the QC emission through $^3P_{J=0,1,2} \rightarrow {}^1G_4 \rightarrow {}^3H_4$ transitions and the second one indicates the downshifting emission (DS) through ($^1D_2 \rightarrow {}^3F_{J=3,4}$) transitions using different excited energy levels of Pr^{3+} and Ce^{3+} ions. The NIR emission band of the phosphor is broad and is found in the range of 930–1060 nm, which is close to spectral range of the Si-solar cells. In the combination of Pr^{3+} and Ce^{3+} ions, there is an efficient energy transfer from the Ce^{3+} to Pr^{3+} ions. Ce^{3+} ion acts as sensitizer while the Pr^{3+} ion acts an activator. The $4f$–$5d$ transition of Ce^{3+} ion is very broad and it transfers its energy to Pr^{3+} ions, which enhances the efficiency of NIR emission bands up to 7.78 times. The dual nature of this phosphor has been found useful candidate for the preparation of UV–vis-NIR phosphors and Si-solar cells.

The perovskite-based metal halide phosphor materials have also contributed widely in the field of photovoltaic devices and solar cells. The perovskite materials are chemically and physically stable. In the quantum cutting process, Yb^{3+} ion is an efficient NIR emitter and has been extensively doped in different metal halide perovskite materials. The Yb^{3+} ion emits a pair of NIR photons that is equivalent to the quantum efficiency to 200% [69–79]. Zhou et al. have studied the influence of host composition and doping on QC emission of Yb^{3+} doped halide perovskite quantum dots (QDs) and discussed its applications in solar cells [72]. Zeng et al. have reported the 1.5 μm photoluminescence of Er^{3+} ion in the $CsPbCl_3$ perovskite nanocrystal and suggested its use in photonic devices operating at telecommunication wavelengths [79]. Recently, Roh et al. have studied quantum cutting in Yb^{3+} doped $CsPbX_3$, X = Cl, Br inorganic metal halide perovskites [80]. They have prepared the nanocrystals and single crystals and monitored the time-resolved photoluminescence dynamics. It has been found that the quantum cutting in both the cases is similar due to similar photoluminescence properties. The prepared materials can be utilized in photonic and solar cell technologies.

The QC process was also studied in the nitride-based phosphor materials. Many Eu^{2+} activated nitride-based phosphor materials have been developed [81–83]. It has been noticed that these phosphor materials produce emissions from blue, yellow to red. The nitride-based compounds are suitable for white LED applications. The oxide-based phosphors were also applied in the field of white LEDs [84]. Liu et al. have also prepared the Eu^{2+} activated $SrSi_2O_2N_2$ phosphors in presence of Ce^{3+}, Dy^{3+}, and Mn^{2+} ions through solid-state reaction method [21]. They studied the influence of Ce^{3+}, Dy^{3+}, and Mn^{2+} ions on PL properties of Eu^{2+} activated $SrSi_2O_2N_2$ phosphor. The Eu^{2+} activated $SrSi_2O_2N_2$ phosphor gives the green emission centered at 540 nm owing to $4f$–$5d$ transition of Eu^{2+} ion. However, the Ce^{3+} activated $SrSi_2O_2N_2$ phosphor gives blue emission at 470 nm. When the Ce^{3+} ion is incapacitated in Eu^{2+} activated $SrSi_2O_2N_2$ phosphor, the emission band at 540 nm remains the same but the emission intensity increases up to 0.04 concentrations of Ce^{3+} ion and above this concentration, its intensity decreases. The increase of PL intensity is because of energy transfer from the Ce^{3+} to Eu^{2+} ions. The emission intensity is enhanced to 144% for the 0.04 concentration of Ce^{3+} ion. The influence of Mn^{2+} and Dy^{3+} ions on the PL properties of Eu^{2+} activated $SrSi_2O_2N_2$ phosphor has also been

studied. The PL intensity of phosphor is enhanced up to 168%. Thus, the emission intensity is relatively more for doping of Mn^{2+} ion in the Eu^{2+} activated $SrSi_2O_2N_2$ phosphor. These prepared phosphors can be suitable materials for white LEDs.

7.2 Quantum Cutting Mechanism

As mentioned above, the quantum cutting is widely investigated in different types of dopant ions and host materials. It occurs in the singly as well as doubly ions activated materials. Basically, it is a conversion of light from a high-energy to the low-energy photons. The mechanism of QC in both the cases can be explained by using energy level diagrams. Figure 7.11 shows the energy level diagrams of quantum cutting mechanisms for the single and double ions.

In the figure, the mechanisms of quantum cutting in both the cases are provided. Figure 7.11a reveals the QC process occurring in the single ion. In case of singly doped materials, the ions are excited with $h\nu$ energy and the electrons are promoted from level 1 to level 3. On returning to level 1, they emit two photons of equal energy. It means that a high-energy photon is converted back into the two low-energy photons, i.e., $2h\nu' = h\nu$. This type of process has been observed in the singly Pr^{3+}, Eu^{3+} and Tm^{3+} doped different host materials [58, 64–66]. The cross-relaxation between the same ions in the Gd_2O_2S: Tm^{3+} power samples have been observed that leads to the generation of QC emissions of the two, three and four NIR photons [66]. It is justified that the QC process takes place in the single ion doped materials.

On the other hand, the donor–acceptor ions are also responsible for QC in the co-doped materials. Figure 7.11b shows a dynamics of energy transfer for the QC process. In this case, the two ions are required and they can be excited either with the same source or using different sources. When the donor ions in level 1 are excited with $h\nu$ energy, the electrons are promoted to their level 3. They relax to the level 2

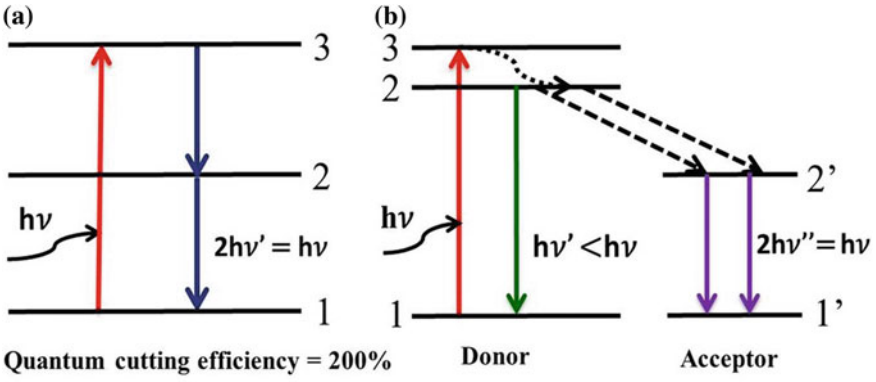

Fig. 7.11 Energy level diagrams of quantum cutting mechanisms for **a** single and **b** double ions

non-radiatively from where they emit a radiative transition of energy lower than the excitation energy, i.e., $h\nu' < h\nu$. Some of donor ions in level 2 transfer its energy to the acceptor ions in the level 1' through dipole–dipole interaction. As a result, the emission of low-energy photons takes place. It confirms the conversion of a high-energy photon to two low-energy photons. Since one photon is converted to the two photons, i.e., $h\nu = 2h\nu'$, therefore, the QC efficiency is 200%. The quantum cutting mechanism has been studied by Yadav and his coworkers in the doubly Eu^{3+}, Yb^{3+} co-activated $Ca_{12}Al_{14}O_{33}$ phosphor and reported a quantum cutting efficiency of 199% upon excitation at 394 nm wavelength [85]. In this case, the Eu^{3+} and Yb^{3+} ions are donor and acceptor ions, respectively. The effective energy transfer takes place from Eu^{3+} to Yb^{3+} ions. However, Bahadur et al. have reported the quantum cutting efficiency of 137% in the Tb^{3+}, Yb^{3+} co-doped LB glasses upon 355 nm excitations.[17] Roh et al. reported the QC efficiency of 200% in Yb^{3+} doped $CsPbX_3$, X = Cl, Br inorganic metal halide perovskites [80]. Moreover, Kroupa et al. have studied QC process in the Yb^{3+} activated $CsPb(Cl_{1-x}Br_x)_3$ perovskite films and they have reported quantum cutting efficiency over to 190% [73].

7.3 Synthesis Methods

In the past decades, the quantum cutting phosphor materials were synthesized by a series of synthesis methods. Actually, there are very crucial role of synthesis methods for preparing the phosphors. The particles size of phosphor materials varies with synthesis method. Generally, the solution-based synthesis methods yield the particles of nano-meter (nm) size. However, the solid-state reaction method and annealing process in different synthesis methods produce micro-meter (μm) sized materials. In this chapter, various synthesis methods, such as combustion method, sol–gel method, hot-injection method, hydrothermal method, solid-state reaction method, and melting-quenching method have been mentioned. The flowchart presentation has been selected to describe every involved step of the synthesis methods by using appropriate examples of the phosphor materials.

7.3.1 Combustion Method

Combustion synthesis is a method that can be used to prepare compounds in a short time. In this, the reaction between a fuel and metal ions oxidant at temperature 300–500 °C can produce a huge amount of exothermic reaction along with large evolution of gases, such as CO, CO_2, N_2, NO_x [86–89]. Metal ions are in the form of nitrates or oxy-nitrates. A fuel is usually the organic compound, such as citric acid, ascorbic acid, glycine, urea, hydrazine, hexa methylene tetra amine (HMTA), other-α-amino acids, dimethyl urea, EDTA that can form a complex with metal ions. Depending on the ratio (ϕ) of net oxidizing valency of oxidants to net reducing valency of fuel

(O/F), different compounds such as alloys, N/C doped compounds, oxides can be prepared. Usually, the compounds obtained by this route provide small size particles (nanoparticles) with a large surface area. Characteristics of oxidants and fuels are important parameters to obtain a high quality of powder material.

The combustion method requires beaker, glass rod, hot plate, magnetic stirrer, and furnace. The nitrate forms of starting materials are dissolved in distilled water. If they are in the oxide form, the nitric acid (conc.) has been used to dissolve them followed by dilution with distilled water. The fuel is added according to $\phi = 1{:}1$ ratio. Yadav et al. prepared the Ho^{3+}, Yb^{3+} co-doped Y_2O_3 quantum cutting phosphor material using solution combustion route [90]. The upconversion (UC), downshifting (DS) and quantum cutting (QC) processes have been explored in the phosphor material. They have used the nitric acid, yttrium oxide (Y_2O_3), holmium oxide (Ho_2O_3) and ytterbium oxide (Yb_2O_3) as starting materials. These oxide precursors were dissolved in nitric acid and urea was now added to this solution as the organic fuel. The obtained solution was stirred to get the homogeneous and transparent one. It was heated at 60 °C until a transparent gel compound is formed. This gel was placed in closed furnace at 600 °C and auto-ignition takes place within few minutes. The gel compound was converted into the foam like structure that was grinded to form a fine powder. This powder was annealed at the higher temperature to enhance the crystalline nature of as-synthesized phosphor. The whole process was represented in Fig. 7.12.

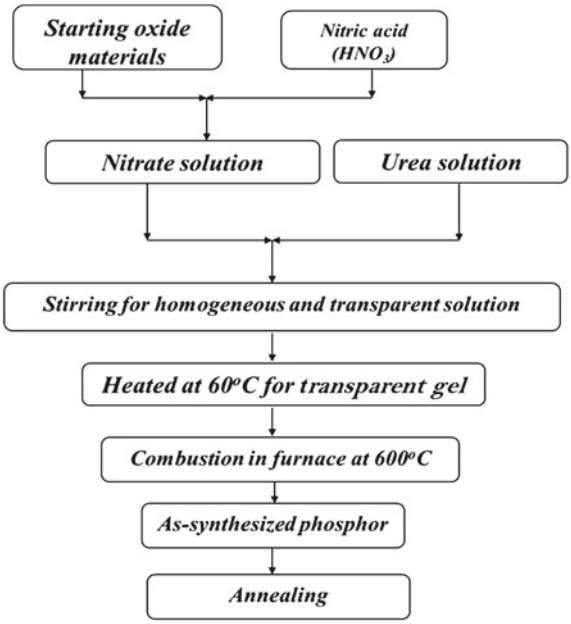

Fig. 7.12 The steps involved in the synthesis of QC phosphor using solution combustion method

In another work, the Pr^{3+}/Yb^{3+} co-doped $CaGdAlO_4$ quantum cutting phosphor materials were synthesized by Zhang et al. using combustion method [91]. They have reported the QC due to energy transfer (ET) from the Pr^{3+} to Yb^{3+} ions and quantum cutting efficacy of this phosphor is 166%. This phosphor acts as protective layer for silicon solar cells. The near infrared QC has been observed in the Ce^{3+}, Er^{3+} and Yb^{3+} co-doped yttrium silicate samples and the phosphor was prepared by combustion method [92]. NIR quantum cutting was found due to ET from Ce^{3+} and Er^{3+} ions to the Yb^{3+} ions in the yttrium silicate powders. Many QC materials such as Eu^{3+}, Yb^{3+} co-doped $Ca_{12}Al_{14}O_{33}$ [85], Er^{3+}/Yb^{3+} co-doped La_2O_2S [93] and Tb^{3+}/Yb^{3+} co-doped $GdBO_3$ [94] have been synthesized by using combustion method. The solution combustion method was also utilized to synthesize the upconversion (UC) and downconversion (DC) based phosphor materials for various potential applications [95–99]. Varma et al. have also summarized a series of nano-scale materials synthesized by using combustion method [100]. The nano- and micro-meter sized photoluminescent materials have also been synthesized by using combustion method [100–103].

7.3.2 Sol–gel Method

In general, the sol–gel method can prepare the fine particles having uniform particles size in nanosized range of the metal oxides [104]. This can give the higher density after compaction of powder than that of any other methods. This method involves the following steps: hydrolysis, polycondensation, gelation, aging, drying, slow heating in 400–600 °C to get the fine powder of metal oxide and finally, annealing of compacted powder can be done to get densification (>95%). Metal alcoxides are generally used as the starting precursor by mixing metal salt with isopropanol alcohol. This is followed by gelation by slow evaporation of water from mixture, and dried material is heated in 400–600 °C to get fine powder. Nowadays, many modifications in the sol–gel-based synthesis have been done by adding other complexing agents, such as citric acid, ethylene glycol, polyethylene glycol, and glycerol. Metal nitrate is sometime used as starting material instead of metal alcoxide. In some cases, ammonia is used to get sol formulation in reaction medium. Starting with metal nitrates gives the better uniform sized particles than that with metal chlorides, bromides and sulfates. The removal of chloride, bromide and sulfate needs a higher temperature (even more than 900 °C).

Yang et al. have prepared the Dy^{3+}/Yb^{3+} co-doped $BaGd_2ZnO_5$ NIR quantum cutting phosphor material using this method [105]. They have used the oxide forms of the starting materials, i.e., the gadolinium oxide (Gd_2O_3), dysprosium oxide (Ho_2O_3), ytterbium oxide (Yb_2O_3) and nitric acid (HNO_3). These oxide materials were dissolved in nitric acid and stirred thoroughly in presence of de-ionized water. The stirring was done until the solution is settled down. After this, the ethylene glycol as well as citric acid were added to this solution and the molar ratios of metal to citric acid to ethylene glycol were kept as 1:1:2. The mixture was stirred for 1.5 h at 70 °C.

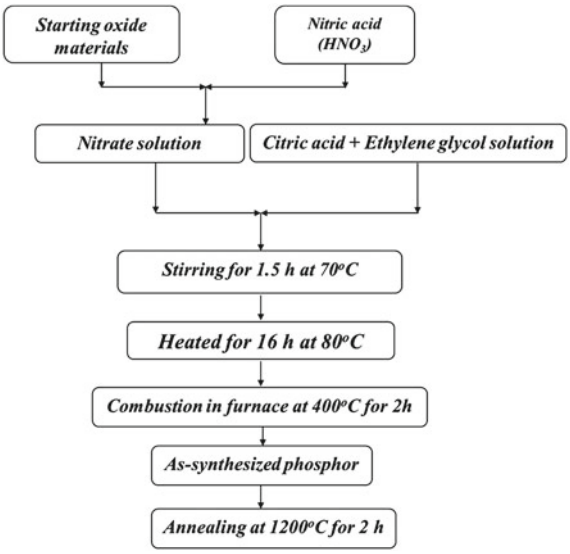

Fig. 7.13 The steps involved in synthesis of QC phosphor using sol–gel method

The final solution was heated in an oven for 16 h at 80 °C. The polymeric type of foam was obtained that was now heated at 400 °C/2 h in furnace to remove the organic residues. The obtained phosphor was annealed at 1200 °C for 2 h and ground properly for the structural as well as optical measurements. The whole process has been described in Fig. 7.13.

The authors have studied the UC photoluminescence and NIR QC in Dy^{3+}/Yb^{3+} co-doped $BaGd_2ZnO_5$ material. The upconversion photoluminescence has been observed in phosphor material due to the ET from the Yb^{3+} to Dy^{3+} ions. The phosphor gives blue, green and NIR emissions at 484, 540 and (800 & 880) nm, respectively under 971 nm excitations. On the other hand, the ET from Dy^{3+} to Yb^{3+} ion tends to the generation of the two NIR emissions in the range of 970–1010 nm upon excitation with 354 nm. They have found a quantum cutting efficiency of 158% in the phosphor and suggested its use in Si-based solar cells.

The combinations of p-block metal as well as rare earth metal ions have been used to prepare QC phosphor materials. Wei et al. have prepared the Yb^{3+} and Bi^{3+} co-doped Y_2O_3 phosphor materials by Pechini sol–gel route and observed intense NIR emission near to 980 nm due to $^2F_{5/2} \rightarrow {}^2F_{7/2}$ transition of Yb^{3+} ions [106]. The QC phosphor materials were excited with 325 and 355 nm excitation wavelengths. Some other phosphor materials were also prepared by this method. Gao et al. have prepared Yb^{3+}, Ho^{3+} as well as Tm^{3+} co-activated β-$NaYF_4$ nanoparticles and observed multi-color UC photoluminescence upon 980 nm excitation [107]. This method produces the particles size from some nano-meter (nm) to sub-micro-meter (μm) [107–110].

7.3.3 Hydrothermal Method

Hydrothermal method is also a solution-based method. It also provides the particles size in the range of sub-micro-meter (μm) to nano-meter (nm). This method does not require any annealing process in normal furnace. Wang et al. have prepared Eu^{3+} doped $NaYbF_4$ nanotubes by using this method [111]. The rare earth metal oxides (Eu_2O_3 and Yb_2O_3) were dissolved in hydrochloric acid (HCl) in the molar ratio of 1:3 and the chloride solution of the rare earth metal oxides (0.2 mol L^{-1}) is formed. The 3 ml aqueous solution of rare earth metal chloride was mixed with 15 ml of ethanol, 15 ml of oleic acid and 0.6 g of NaOH under constant stirring. The 0.3889 g of NH_4F was dissolved in 2 ml solution and then added drop wise to the obtained solution. This solution was stirred for 30 min. It was shifted into a Teflon-lined autoclave and it was sealed followed by heating. The obtained products were collected and it was washed with ethanol many times followed by centrifugation. These steps were summarized in a flowchart and it is shown in Fig. 7.14.

They have monitored the excitation and emission spectra of Eu^{3+} doped $NaYbF_4$ nanotubes. The intensity of excitation peak is maximum at 393 nm due to $^7F_0 \rightarrow$

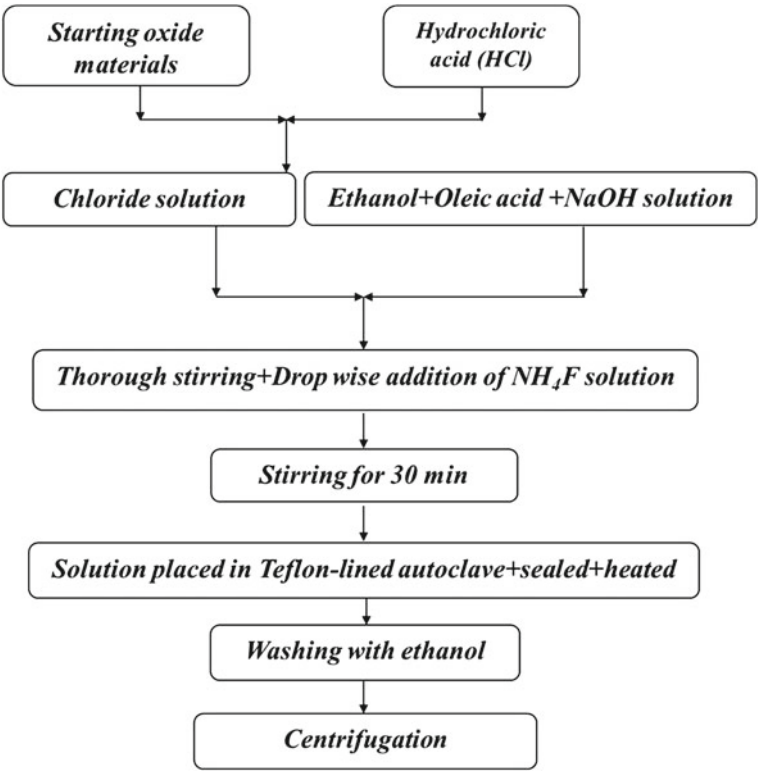

Fig. 7.14 The steps involved in the synthesis of QC phosphor using hydrothermal method

$^5L_6$ transition of Eu^{3+} ion that has been used to monitor the emission spectra. They have observed the visible photoluminescence along with the NIR quantum cutting in the sample. The concentration dependent emission spectra reveal that the emission intensity of samples increases up to 3 mol% and then found to reduce with further increase of dopant due to the concentration quenching [112–114]. The emission intensity of visible and NIR regions is optimum for 3 mol% concentrations of Eu^{3+} ion. However, the emission intensity of the NIR emission band is more owing to ET from Eu^{3+} to Yb^{3+} ions. The broad NIR emission band was observed in the 977–1015 nm, which is at 997 nm corresponding to $^2F_{5/2} \rightarrow {}^2F_{7/2}$ transition of the Yb^{3+} ions. Yu et al. have also prepared β-$NaYF_4$: Tm^{3+} phosphor material using this method and observed a sequential three-step three-photon near infrared quantum cutting [63]. The β-$NaYF_4$: Ho^{3+} phosphor materials were also synthesized by using this method and a three-photon near infrared QC is observed at 850, 1015 and 1180 nm [115]. This method is also selected to prepare the other types of phosphor materials [116–119].

7.3.4 Hot-Injection Method

This is a new method based on injecting one material onto the other material/solvent that was kept at hot condition. Solvents having high boiling points such as 1-octadecence, diphenyl ether are used [120]. In this way, the nucleation and growth of particles can be separated. Mostly, the metal halide perovskite quantum cutting materials are prepared by using this method [121–123]. Zhou et al. have prepared the rare earth Yb^{3+}- doped, Yb^{3+}, Er^{3+}, and Yb^{3+}, Ce^{3+} co-doped $CsPbCl_xBr_{3-x}$ QDs through this method [124]. They used the rare earth and Pb halides (Cl, Br) and mixed with solutions of octadecene, oleylamine, and oleic acid in presence of nitrogen atmosphere at 120 °C. After this, the cesium oleate solution was quickly injected into the obtained solution at 200 °C for 10 s to set the formation of quantum dots (QDs). Different compositions of rare earth doped QDs were prepared to advance the spectral conversion efficiency of the Yb^{3+}- doped, Yb^{3+}, Er^{3+}, and Yb^{3+}, Ce^{3+} co-doped $CsPbCl_xBr_{3-x}$ QDs. The doping concentrations of rare earth ions have been confirmed by inductively coupled plasma optical emission spectroscopy techniques [124]. This method was also used by Parobek et al. to prepare the Mn-doped $CsPbBr_3$ nanocrystals [125]. Cai et al. have prepared the Mn^{2+}/Yb^{3+} co-doped $CsPbCl_3$ perovskite nanocrystals by using this method and observed three emission lines for luminescent solar concentrators [126]. They have observed the quantum cutting emissions through $^2F_{5/2} \rightarrow {}^2F_{7/2}$ transition of the Yb^{3+} ion. This is owing to the ET from Mn^{2+} to Yb^{3+} ions. The PL quantum yield of this sample has been observed to 125.3%. The hot-injection method includes various steps, which are shown in Fig. 7.15.

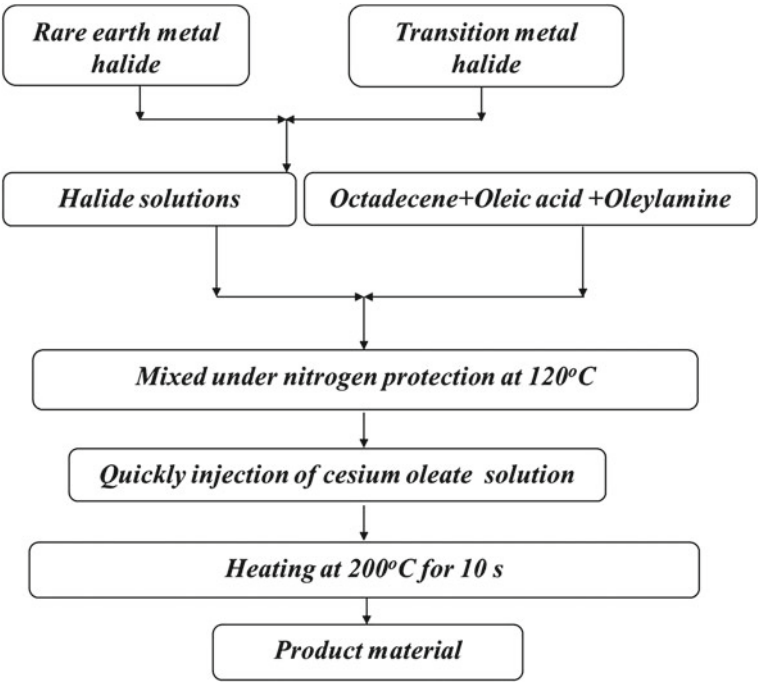

Fig. 7.15 The steps involved in the hot-injection method to prepare the quantum cutting QDs

7.3.5 Solid-State Reaction Method

The solid-state reaction method is the most widely used method among the synthesis methods. It does not require any type of intermediate instrument. This method produces large amount of bulk materials and the particles size falls under micrometer (μm) range. In this method, all the ingredients are mixed together in agate mortar. Acetone has been used as mixing solution. The ingredients are mixed properly for at least 1 h and after this; the final mixture was kept in a platinum/alumina crucible. Crucible was heated in a high temperature furnace (600–900 °C) for many hours (4–30 h). It was then cooled to room temperature normally. The powder was ground and compacted using suitable die in the form of pellets. Pellets were then heated at higher temperature (>1000 °C) to get desired phase with stoichiometry and crystallinity. Palletization helps in enhancement of solid-state reaction through diffusion of ions. Intermediate grinding and palletization help in getting pure stoichiometry [127, 128]. The phosphor material is crushed properly for the structural and optical measurements. Zou et al. have prepared Pr^{3+}, Yb^{3+} co-doped $Ca_2Ga_2GeO_7$ phosphor material through solid-state reaction method and observed long persistence near infrared quantum cutting luminescence [129]. They have used starting materials as $CaCO_3$, Ga_2O_3, GeO_2, Pr_6O_{11}, and Yb_2O_3 and these materials were mixed

homogeneously with anhydrous alcohol. The final product was sintered at 1573 K temperature for 2 h in air and it was cooled down to room temperature.

Dong et al. prepared the Tm^{3+}, Ce^{3+} co-activated $Ca_3(PO_4)_2$ quantum cutting phosphor by using this method [130]. They have used the two-step heating processes, i.e., pre-heated at 400 °C for 2 h and heated at 1100 °C for 8 h to get a pure phase material. The QC was achieved due to ET from Ce^{3+} to Tm^{3+} ions. The Nd^{3+}, Yb^{3+} co-doped $CaWO_4$ quantum cutting phosphor was also prepared by solid-state reaction method and the QC occurs due to ET from Nd^{3+} to Yb^{3+} ions [131]. They have also followed the two-step heating processes, i.e., pre-heated at 200 °C for 2 h and finally heated at 900 °C for 3 h. Yadav and his group have also prepared Bi^{3+}, Yb^{3+} co-activated gadolinium tungstate quantum cutting phosphor by this technique. The acetone solution was used to mix the starting materials homogeneously and the final mixture was heated at 1300 °C/4 h [132]. The other phosphor materials were also prepared by using this method [133–138]. The steps involved in this method are shown in Fig. 7.16a.

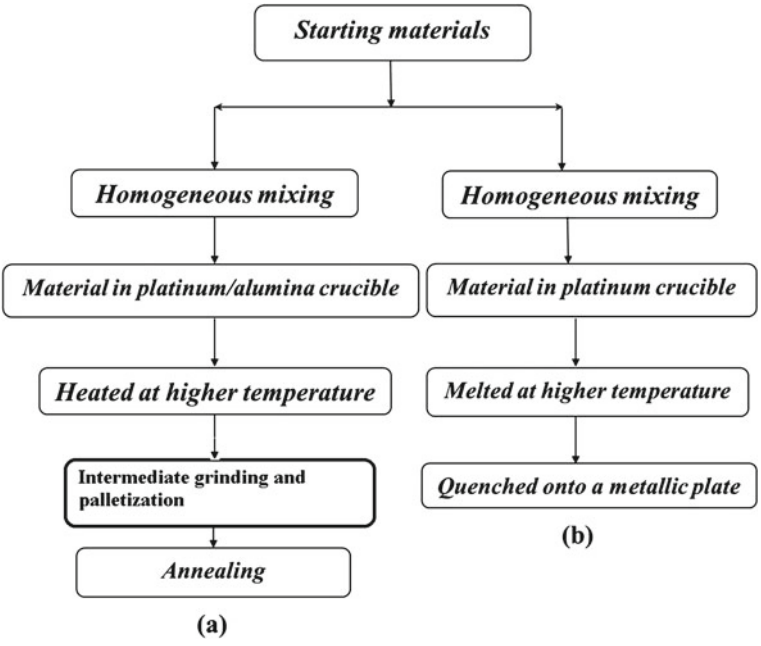

Fig. 7.16 The steps involved in **a** solid-state reaction method and **b** melting-quenching method

7.3.6 *Melting-Quenching Method*

The glass materials were also contributed significantly as QC materials. The melting-quenching method has been used to prepare the glass materials. In this method, all the ingredients are mixed properly and then kept in the platinum crucible. The final material is melted in a furnace and then quenched at room temperature. The advantage of taking a platinum crucible is that the glass sample does not stick in the crucible and also gets cleaned easily. Liu et al. have prepared the Tb^{3+}, Yb^{3+} co-activated quantum cutting lanthanum borogermanate glasses by using this method [139]. They have used La_2O_3, Yb_2O_3, Tb_4O_7, H_3BO_3 and GeO_2 as the starting ingredients. These materials were mixed homogeneously and melted in the platinum crucible at 1300 °C/20 min. It was quenched onto the iron plate and pressed it with another iron plate. They have obtained the glass samples of 2 mm thickness. The photoluminescence with NIR quantum cutting has been observed due to ET from the Tb^{3+} to Yb^{3+} ions. The QC efficiency was stated to be 146%.

Similarly, Yadav and his group have also synthesized Tb^{3+}, Yb^{3+} co-activated lithium borate glasses using this method. H_3BO_3, Li_2CO_3, Yb_2O_3 and Tb_4O_7 were used as the starting materials. In this case, the QC efficiency was obtained as 146% [18]. The steps involved in this method are shown in Fig. 7.16b. In this, the QC occurs due to ET from the Tb^{3+} to Yb^{3+} ions. The Ho^{3+}/Yb^{3+} co-activated tellurite glass ceramics have also been prepared using this method and the quantum cutting has been observed due to ET from Ho^{3+} to Yb^{3+} ions [140]. The NIR quantum cutting efficiency has been reported to be higher as 167%. These glass ceramics can be useful to increase the spectral conversion efficiency of solar cells.

7.4 Characterization of Quantum Cutting Phosphors

The QC phosphor materials are synthesized by different synthesis routes. The nature of phase and crystallinity are investigated by X-ray diffraction (XRD) techniques. The morphology of the phosphor materials is studied using scanning electron microscopy (SEM) and transmission electron microscopy (TEM) techniques. They are common for all the types of synthesized materials. The photoluminescence excitation and photoluminescence emission are essential methods to see the variation in the emission intensity, which describes the origin of QC process. The QC also occurs due to ET between these ions, which can be confirmed by lifetime measurements. There is also another method to prove the QC process that is the emission intensity dependent pump power plot. It shows the nature of emitted photons whether they are linear or nonlinear process [132]. Therefore, the photoluminescence excitation, photoluminescence emission, emission intensity versus pump power plot and lifetime measurements are the main characterization tools to understand the dynamics of energy transfer for the QC process.

7.4.1 Photoluminescence (Excitation and Emission)

When the phosphor materials co-doped with the rare earth ions or transition metal ions are excited, they give the characteristic emission lines/bands of the activator ion. The wavelength selected for exciting a material is decided with the help of photoluminescence excitation (PLE) spectrum. It gives all possible wavelengths through which the material can be excited. The PLE spectrum is generally monitored for the emission peak of highest intensity. The characteristic emission lines of the quantum cutting phosphor materials have been widely investigated by using the photoluminescence excitation and photoluminescence emission (i.e., PLE and PL) measurements. As discussed earlier, the quantum cutting is a downconversion process, which converts a high-energy photon into the two low-energy photons [18, 69–75]. The visible quantum cutting is also a downconversion process [141].

The PLE and PL spectra are related to each other. Huang et al. have monitored the PLE and PL spectra of the Bi^{3+}/Yb^{3+} co-doped Gd_2O_3 phosphors prepared by combustion method [142]. They have prepared phosphor samples with various concentrations of the Yb^{3+} ion with constant concentration of Bi^{3+} ion (1 mol%). The PLE and PL spectra of Bi^{3+}/xYb^{3+} doped and co-doped Gd_2O_3 phosphors are shown in Fig. 7.17a and b. The PLE spectra contain a broad band in 300–400 nm range and that is centered at 347 nm due to $^1S_0 \rightarrow {}^3P_1$ transition of Bi^{3+} ion. The intensity of excitation band is found to decrease significantly upon doping of Yb^{3+} ion. The PL spectrum of the Bi^{3+} doped Gd_2O_3 phosphor contains emissions in the visible region (380–600 nm); however, no emission line lies in NIR region (900–1100 nm). When the Yb^{3+} ion is doped in the Gd_2O_3: Bi^{3+} phosphor the emission in the NIR

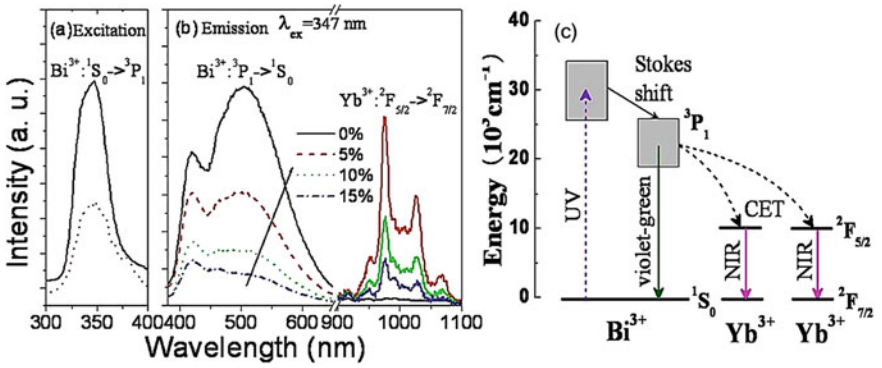

Fig. 7.17 **a** PLE spectra of the Bi^{3+} ion at 506 nm emission monitored in the Bi^{3+} single doped $(Gd_{0.99}Bi_{0.01})_2O_3$ (represented by solid line) and that of Yb^{3+} ion at 977 nm emission monitored in the Bi^{3+}–Yb^{3+} co-doped $(Gd_{0.94}Yb_{0.05}Bi_{0.01})_2O_3$ sample (represented by dashed line). **b** Visible-NIR PL spectra of the $(Gd_{0.99-x}Yb_xBi_{0.01})_2O_3$ samples after the excitation of Bi^{3+} at 347 nm. The different fractions x of Yb^{3+} in the samples are mentioned in the figure. **c** Schematic energy level diagram of the Bi^{3+} and Yb^{3+} in the Gd_2O_3 phosphor is shown and the CET mechanism for the NIR QC luminescence under UV excitation is provided. Reproduced with copyright permission from AIP Publishers [142]

region (900–1100 nm) is now appeared. This is due to ET from the Bi^{3+} to Yb^{3+} ions after excitation through Bi^{3+} ions (347 nm). The bluish-green color of the phosphor is ascribed to $^3P_1 \rightarrow {}^1S_0$ transition of the Bi^{3+} ion while NIR emissions at 977 and 1027 nm are due to transitions from $^2F_{5/2}$ to $^2F_{7/2}$ multiplets of the Yb^{3+} ion. The emission intensity of both the bands decreases with the concentrations of Yb^{3+} ion. However, the emission intensity of NIR range is optimum at 5 mol% concentrations of Yb^{3+} ion and after this, it is found to decrease.

The ET from Bi^{3+} to Yb^{3+} ions can be understood by energy level diagram of these ions, which has been shown in Fig. 7.17c. When the Bi^{3+} ions are excited with 347 nm, they are promoted from $^1S_0$ to $^3P_1$ levels of Bi^{3+} ion. Due to Stokes shift, these ions relax non-radiatively to $^3P_1$ level of the Bi^{3+} ion and a bluish-green emission takes place due to $^3P_1 \rightarrow {}^1S_0$ transition of Bi^{3+} ion. The ions present in $^3P_1$ level of Bi^{3+} ion also transfer its energy to Yb^{3+} ions due to cooperative downconversion ET process. As a result, the emission of the two NIR photons occurs due to the $^2F_{5/2} \rightarrow {}^2F_{7/2}$ transition of the Yb^{3+} ion [143]. These authors have observed the quantum cutting efficiency of 173.92% in the phosphor that can be used in the solar cell application.

Cai et al. have studied quantum cutting in the combinations of transition metal and the rare earth metal ions. They have monitored the absorption, PLE, PL and PL lifetime curves of the Mn^{2+}/Yb^{3+} doped and co-doped $CsPbCl_3$ perovskite nanocrystals [125] and these are shown in Fig. 7.18. The Mn^{2+}/Yb^{3+} co-doped $CsPbCl_3$ perovskite nanocrystals were synthesized by different concentrations of Yb^{3+} ions. The absorption spectra of the pure $CsPbCl_3$ and Mn^{2+}/Yb^{3+} co-doped $CsPbCl_3$ perovskite nanocrystals are similar to each other (see Fig. 7.18a). It shows an absorption band in UV region due to charge transfer state (CTS) of $CsPbCl_3$ host lattice. The $CsPbCl_3$ nanocrystal emits a band gap photoluminescence (BG-PL) of blue color at 404 nm of the $CsPbCl_3$ host lattice. When Mn^{2+} and Yb^{3+} ions were co-doped in $CsPbCl_3$ perovskite the sample emits two distinct emission bands at 618 and 985 nm, which are assigned to $^4T_{1g} \rightarrow {}^6A_{1g}$ and $^2F_{5/2} \rightarrow {}^2F_{7/2}$ transitions of Mn^{2+} and Yb^{3+} ions, respectively. It is clear from Fig. 7.18b that the pure $CsPbCl_3$ perovskite gives only the blue BG-PL at 404 nm; however, the Mn^{2+} doped $CsPbCl_3$ perovskite nanocrystals emit the blue and the red emissions in which the red emission at 618 nm is due to $^4T_{1g} \rightarrow {}^6A_{1g}$ transition (*d–d* transition) of Mn^{2+} ion. Moreover, the Mn^{2+}/Yb^{3+} co-doped $CsPbCl_3$ perovskite nanocrystals produce three emission bands at 404, 618 and 985 nm owing to host lattice, Mn^{2+} and Yb^{3+} ions, respectively. The description of samples from Sample 1 to Sample 6 has also been properly given in Fig. 7.18b.

This occurs due to three types of energy transfer (ET) processes (see Fig. 7.18h). The CTS of $CsPbCl_3$ perovskite transfers its energy to Mn^{2+} ions initially. The CTS of $CsPbCl_3$ perovskite also transfers its energy to the defect states of Yb^{3+} ions. The ET from Mn^{2+} to the Yb^{3+} ions took place. ET between the CTS of host and the Mn^{2+} and Yb^{3+} ions can be verified by photoluminescence lifetime (PL–LT) measurements (see Fig. 7.8d–f). Due to ET, the PL–LTs of band gap photoluminescence (BG–PL) and the Mn^{2+} photoluminescence (Mn–PL) decreases regularly with the doping concentration. However, the PL–LT of Yb^{3+} photoluminescence (Yb–PL) is found to be increased with the doping concentration. This suggests that the increase in PL–LT is due to ET from the host and Mn^{2+} ions to Yb^{3+} ions. The quantum yield of these

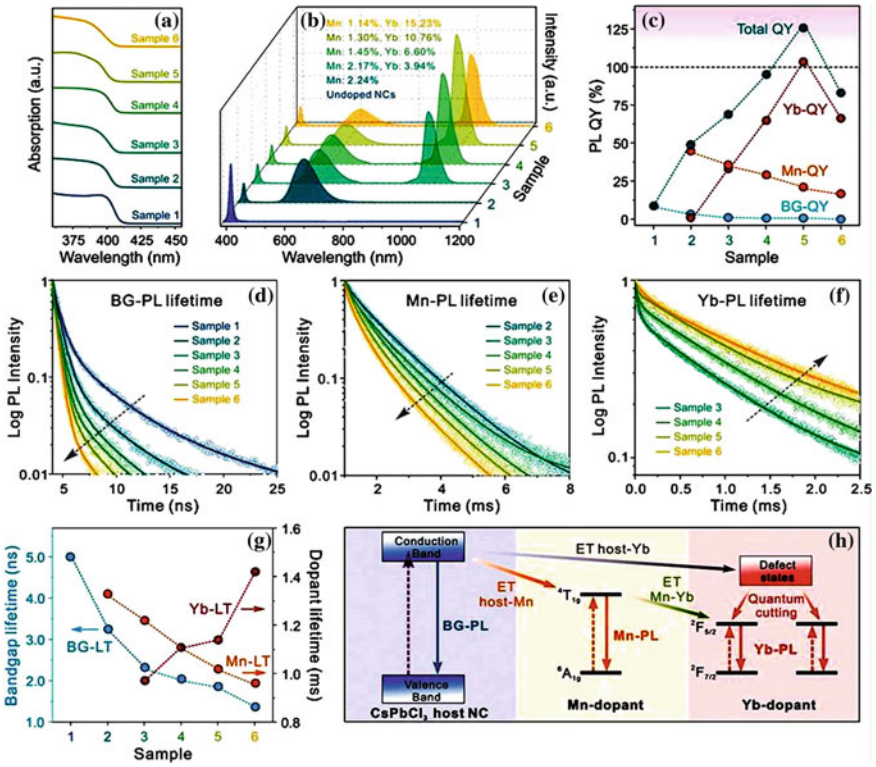

Fig. 7.18 **a** Absorption spectra, **b** PL spectra, and **c** PL QYs of undoped and Mn^{2+}/Yb^{3+} co-doped $CsPbCl_3$ NCs with the various doping concentrations. **d–f** Lifetime (LT) decay curves for the samples upon monitoring BG-PL (**d**), **e** Mn-PL (**d**), and Yb–PL (**f**). **g** The summary of the average LTs for the BG (blue), Mn (orange), and Yb (red) PLs is provided. **h** Schematic of the proposed ET processes in Mn^{2+}/Yb^{3+} co-doped $CsPbCl_3$ perovskite NCs. Reproduced with copyright permission from John Wiley and Sons Publisher [125]

emissions also follows the same trends (see Fig. 7.18c and g) and the maximum quantum yield was observed to be 125.3%. They have also studied the current–voltage relation and found that this material is suitable for Si-based solar cell along with the other applications.

7.4.2 Laser Power Dependent Photoluminescence Intensity

This is another experimental proof to understand the nature of photoluminescence (PL). It also signifies whether the PL of a phosphor material is linear or nonlinear type. The PL intensity of phosphor material increases with increase in pump power of excitation source and after a certain value, it saturates/decreases with the pump

power. This becomes possible due to change in population density of the ions in the excited energy states with the pump power as well as heat generation on the sample due to use of high-power laser. Teng et al. have prepared the $CaAl_2O_4$: Yb^{2+}, Yb^{3+} phosphor through solid-state reaction method [144]. The PLE spectra show the two excitation bands at 275 and 310 nm. The QC emission was observed in this phosphor material under the excitation with 275 and 310 nm wavelengths. It is due to ET from Yb^{2+} to Yb^{3+} ions. Actually, the $4f$–$5d$ state of Yb^{2+} ions are excited with these wavelengths and the excited ions transfer their energy to the Yb^{3+} ions through three-photon cutting. The energy is also transferred to the Yb^{3+} ions through the coupling of phonons and it is phonon-assisted two photon cutting. As a result, an intense NIR emission was obtained at 978 nm along with the weak shoulder peaks. The PL intensity versus pump power behavior was plotted, which gives the slope value (n) of 0.43 under 325 nm excitations. This indicates that one high-energy photon was converted back into the two and three photons due to QC process. The $CaAl_2O_4$: Yb^{2+}, Yb^{3+} phosphor can be also used to increase the efficiency of the solar cells.

Yadav and his group have also studied the quantum cutting in Bi^{3+}, Yb^{3+} co-activated gadolinium tungstate in the presence of Li^+ ion [132]. They have observed the visible and NIR emissions upon excitation with 355 nm. The Bi^{3+} added phosphor sample gives a broad emission band in the 450–750 nm due to $^3P_1 \rightarrow {}^1S_0$ transition of the Bi^{3+} ion upon 355 nm excitation. It does not give any luminescence in NIR region. The PL intensity of Bi^{3+} doped phosphor decreases on increasing the contents of Yb^{3+} ions. It is due to ET from Bi^{3+} to the Yb^{3+} ions, which leads to QC emissions in 900–1030 nm range. The NIR emission is at 976 nm that is due to the $^2F_{5/2} \rightarrow {}^2F_{7/2}$ transition of the Yb^{3+} ions. The PL intensity of Bi^{3+}, Yb^{3+} co-activated phosphor is also monitored in the presence of Li^+ ion. The photoluminescence intensity of visible region is found to decrease while that of NIR region increases up to 3 times. This has been discussed due to growth in the local crystal field around dopant ions.

The PL intensity of Bi^{3+}, Yb^{3+} co-activated phosphor has also been monitored at various pump powers of 355 nm laser. The plots between PL intensity and pump power in absence and presence of Li^+ ion is shown in Fig. 7.19a and b. Figure 7.19a shows that the emission intensity of 611 nm band rises with pump power for both the cases. The slope values have been calculated in both the cases and found to be 1.08 and 1.15. It means that the origin of visible emission shows a linear process. Similarly, the emission intensity of 976 nm band also increases with the pump power for both the cases (see Fig. 7.19b). The slope values are obtained as 0.53 and 0.59 for Bi^{3+}, Yb^{3+} and Bi^{3+}, Yb^{3+}, Li^+ co-doped phosphor materials. The slope value confirms that the NIR emission is a type of nonlinear process.

Duan et al. were also studied the QC mechanism in Tb^{3+}, Yb^{3+} co-doped $NaYF_4$ powder samples. They plotted the graph between emission intensity versus pump power [145]. They have observed that the slope values of the visible region (543 nm) are found to be 0.98, 1.02 and 1.00 for 0, 5 and 10 mol% contents of Yb^{3+} ions, which is suggested that the visible emission shows a linear nature. On the other hand, the slope values of NIR region (1030 nm) are 0.71 and 0.83 for the 5 and 10 mol% Yb^{3+} ion concentrations, respectively. It means that QC emission is a nonlinear type.

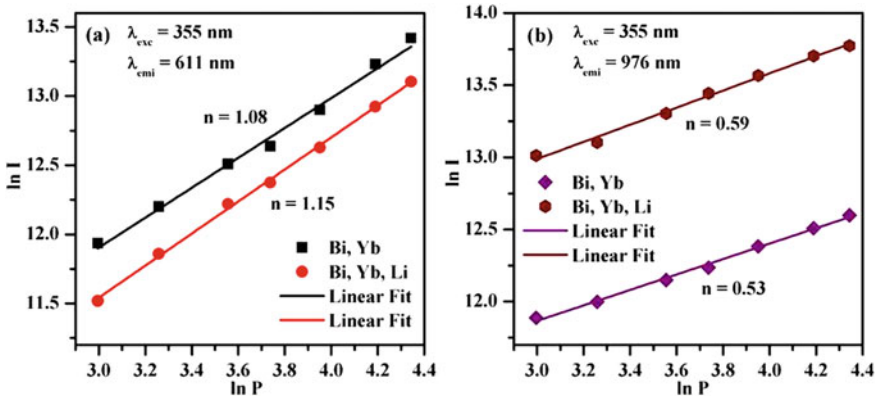

Fig. 7.19 Dual logarithmic plots of integrated emission intensity ~ pump power for **a** 611 nm ($^3P_1 \rightarrow {}^1S_0$), and **b** 976 nm ($^2F_{5/2} \rightarrow {}^2F_{7/2}$) transitions in the Bi^{3+}, Yb^{3+} co-doped gadolinium tungstate phosphor on excitation with 355 nm laser in absence and presence of Li^+ ion. Reproduced with copyright permission from ACS Publisher [132]

Similarly, Shestakov et al. have also found the slope values as ~1.0 and ~0.5 for the visible and the NIR emission bands, respectively in Li^+, Yb^{3+} co-doped ZnO samples [146]. The Tb^{3+}, Yb^{3+} co-activated ZrO_2 phosphor was prepared by Terra et al. by sol–gel method [147]. They have studied the PLE, PL, PL intensity versus pump power and lifetime properties. The QC occurred due to ET from Tb^{3+} to the Yb^{3+} ions. The NIR spectra and the PL intensity versus pump power plot for a NIR emission upon excitation at 488 nm are shown in Fig. 7.20. Figure 7.20a shows the NIR emissions at 981, 1012 and 1044 nm owing to $^2F_{5/2} \rightarrow {}^2F_{7/2}$ transition of the Yb^{3+} ion and the PL intensity is larger for 10 mol% concentrations of the Yb^{3+} ion, which has been confirmed by the inset figure. After this, it reduces because of concentration quenching effect [96, 148]. The PL intensity versus pump power plot of the NIR emission gives the slope values as 0.71 and 0.78 for 1 and 20 mol% concentrations of Yb^{3+} ions, respectively (see Fig. 7.20b). This designates an increase in slope values with increase of concentrations of the Yb^{3+} ions that also shows a nonlinear nature of NIR emission.

7.4.3 Lifetime Characteristics

The lifetime of a level highly depends on the concentrations of dopants ions. It also supports to explain the ET mechanisms between the donor–acceptor ions. Cai et al. discussed the effect of concentrations and ET in Mn^{2+}/Yb^{3+} doped and co-doped $CsPbCl_3$ perovskite nanocrystals [125] and these are shown in Fig. 7.18d–f. They have found that the lifetime of BG–PL decreases on increasing concentrations of Mn^{2+} ions. In case of ET from Mn^{2+} to Yb^{3+} ions, the lifetime of Mn–PL decreases

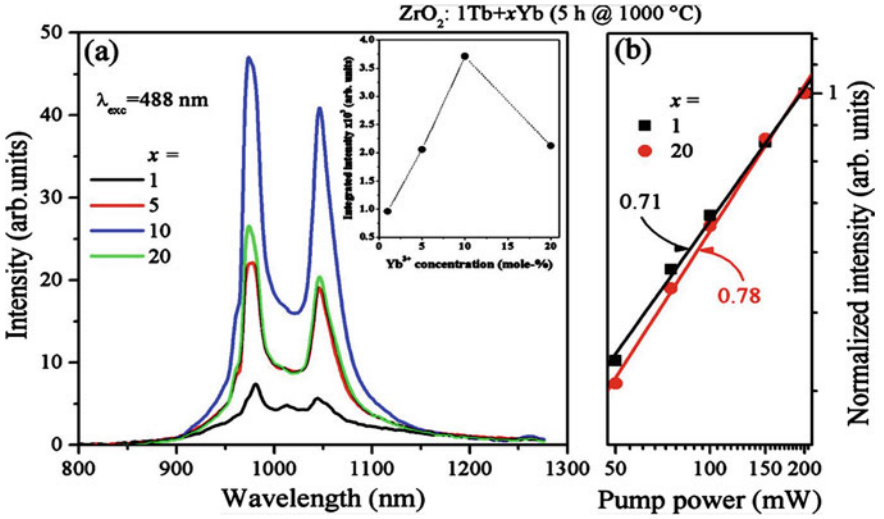

Fig. 7.20 **a** NIR emission spectra of ZrO_2:1 Tb^{3+}, xYb^{3+} annealed samples ($x = 1$, 5, 10, and 20 mol-%) on excitation with 488 nm. The inset shows a dependence of Yb^{3+} emission intensity on the excitation power for $^5D_4$ level of the Tb^{3+} ion, monitored at $\lambda_m = 980$ nm. **b** The plots of the emission intensity versus pump power for 1 and 20 mol% concentrations of Yb^{3+} ions. Reproduced with copyright permission from AIP Publisher [147]

with Yb^{3+} ion concentrations while the lifetime of Yb–PL increases first and then found to decrease (see Fig. 7.18e and f).

The decay curves of the $(Gd_{0.99-x}Yb_xBi_{0.01})_2O_3$ phosphors as a function of the Yb^{3+} doping concentration for $^3P_1 \rightarrow {}^1S_0$ transition of the Bi^{3+} ion upon 347 nm excitations have been studied by Huang et al. and they are shown in Fig. 7.21 [142]. They have recorded lifetime of the $^3P_1$ level of Bi^{3+} ion and found that decay curve of

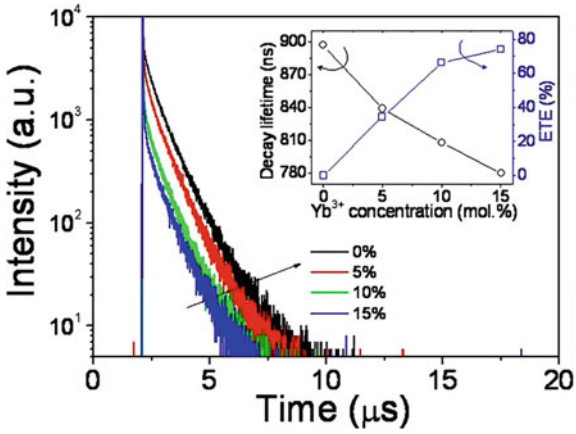

Fig. 7.21 Decay lifetimes of the $(Gd_{0.99-x}Yb_xBi_{0.01})_2O_3$ samples for Bi^{3+}: $^3P_1 \rightarrow {}^1S_0$ luminescence on excitation with 347 nm. The different fractions x of Yb^{3+} ions in the samples are provided in the figure. Inset is the decay lifetime and ETE values with Yb^{3+} doping concentration. Reproduced with copyright permission from AIP Publishers [142]

the $(Gd_{0.99}Bi_{0.01})_2O_3$ sample fits mono-exponentially. When the Yb^{3+} is doped in the $(Gd_{0.99}Bi_{0.01})_2O_3$ sample the decay curve is found to fit with non-exponential nature. The lifetime of $(Gd_{0.99}Bi_{0.01})_2O_3$ sample is 897 ns, which decreases significantly on doping of Yb^{3+} ions from 897 to 780 ns. It is due to ET from Bi^{3+} to the Yb^{3+} ions (see Fig. 7.17c). The non-exponential nature of decay curves fitting occurs due to different ET rates between the Bi^{3+} and Yb^{3+} ions. The inset figure shows the dependency of decay lifetime and ET efficiency (ETE) on the Yb^{3+} doping concentration. It was observed that the decay lifetime decreases regularly with increase of concentrations of Yb^{3+} doping while the ETE of the sample increases with Yb^{3+} doping concentration. The maximum quantum efficiency is 173.92% at 15 mol% doping of Yb^{3+} ions.

They have calculated ET efficiency (ETE, η_{ETE}) and quantum efficiency (QE, η_{QE}) using following relations:

$$\eta_{ETE} = \eta_{x\%Yb} = 1 - \frac{\int I_{x\%Yb} dt}{\int I_{0\%Yb} dt} \tag{7.1}$$

and

$$\eta_{QE} = \eta_{Bi}(1 - \eta_{ETE}) + 2\eta_{Yb}\eta_{ETE} \tag{7.2}$$

where the I is the emission intensity, x%Yb is the Yb^{3+} ion concentrations, the η_{Bi} as well as η_{Yb} are the luminescence *QEs* of the Bi^{3+} and Yb^{3+} ions, respectively. The *ETE* of phosphor is found to be 34.37%, 66.21% and 73.92% for the 5 mol%, 10 mol% and 15 mol% doping concentrations of Yb^{3+} ions, respectively. Assuming the radiative transitions of Bi^{3+} and the Yb^{3+} ions, the values of $\eta_{Bi} = \eta_{Yb} = 1$. The values of η_{QE} are calculated to be 134.37%, 166.21% and 173.92% for the 5 mol%, 10 mol% and 15 mol% concentrations of Yb^{3+} doping, respectively. This indicates that the QE of the phosphor is found optimum for 15 mol% Yb^{3+} doping concentrations.

The PLE, PL, ET and PL decay analyses were carried out by Xie et al. in Tm^{3+}, Yb^{3+} co-activated YPO_4 phosphors [149]. They have observed the NIR QC through CET from Tm^{3+} to the Yb^{3+} ions. The Tm^{3+}, Yb^{3+} co-activated YPO_4 phosphors were excited with 474 nm and give the red and NIR emissions owing to Tm^{3+} to Yb^{3+} ions, respectively. The intensity of red emission decreases regularly while that of NIR region initially increases then decreased because of CET from Tm^{3+} to Yb^{3+} ions. They have also monitored lifetime of the Tm^{3+}, Yb^{3+} co-activated YPO_4 phosphors for different concentrations of Yb^{3+} ions, i.e., 0, 5, 25 and 50 mol%. The decay curves of $^1G_4 \rightarrow {}^3H_4$ transition of Tm^{3+} ion at 647 nm emission for different concentrations of the Yb^{3+} ions are shown in Fig. 7.22a. The decay curves were fitted by using Yokota–Tanimoto model. The figure shows that lifetime of $^1G_4 \rightarrow {}^3H_4$ transition of the Tm^{3+} ion continuously decreases with the increase in concentrations of Yb^{3+} ions and their values are given in the figure. The lifetime of phosphor is longer for

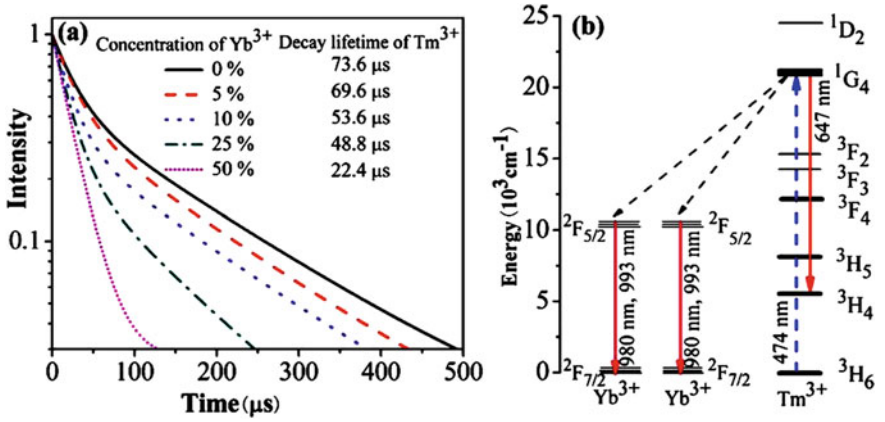

Fig. 7.22 **a** Decay lifetime curves of $^1G_4 \rightarrow {}^3H_4$ transition of Tm^{3+} ion at 647 nm emission fitted by the generalization of Yokota–Tanimoto model; **b** schematic diagram for energy levels of Tm^{3+} and Yb^{3+} ions to show the concept of NIR QC. Reproduced with copyright permission from AIP Publishers [149]

the pure Tm^{3+} doped YPO_4 phosphor whereas it is shorter for 50 mol% Yb^{3+} ion concentrations in the Tm^{3+}, Yb^{3+} co-activated YPO_4 phosphor.

Figure 7.22b shows the schematic diagram of Tm^{3+} and Yb^{3+} ions. The energy of $^1G_4 \rightarrow {}^3H_6$ transition of Tm^{3+} ion is double to that of the $^2F_{5/2} \rightarrow {}^2F_{7/2}$ transition of the Yb^{3+} ion. When the $^1G_4$ level of Tm^{3+} ion is excited with 474 nm, the energy is moved to Yb^{3+} ions through CET. This leads to generation of one red and two NIR emission bands in the phosphors. The NIR emission bands were observed at 980 and 993 nm because of $^2F_{5/2} \rightarrow {}^2F_{7/2}$ transitions of Yb^{3+} ion. They have also calculated ETE and QE of phosphor using relations (i) and (ii), respectively. The ETE and QE of phosphor were found to be 72.8% and 172.8%, respectively for 50 mol% concentrations of Yb^{3+} ions. This phosphor can also be used to improve the quantum efficiency of Si-solar cells.

7.5 Conclusions

In this chapter, the basics of quantum cutting (QC) process are presented. Different synthesis methods used to prepare the QC phosphor materials are included along with a melting-quenching method for the preparation of glass materials. These methods produce the particles size of phosphor materials from μm to nm range. The QC in different rare earth doped and co-doped phosphor materials have been discussed in detail. This process occurs in singly, doubly and triply rare earth added materials. We have explained the origin of QC emissions on the basis of PLE, PL, energy level diagrams, PL intensity versus pump power plot and lifetime measurements. The PL intensity of QC materials highly depends on concentration of the dopant ions. QC

process was justified by the photoluminescence intensity versus pump power plot. The lifetime measurements played a crucial role to estimate a change in the PL intensity of sensitizer ions. This chapter also summarizes different transition metal and rare earth metal-based QC materials for their use in display devises, solid-state lighting, solar cells, photovoltaics, etc.

7.6 Future Scope

This chapter provides a basic learning for QC process. Different types of transition metal and rare earth metal doped QC phosphors have been brought under a single roof. This study will provide a platform for researchers to understand the mechanisms of QC process in the QC materials. This study will also attract researchers to prepare the new class of QC materials using a particular synthesis method. The newly prepared phosphor materials may be a suitable candidate for improving the solar spectral efficiency of various photovoltaic devices. They can fulfill the energy-related needs of our society.

References

1. Han B, Liang H, Huang Y, Tao Y, Su Q (2010) Vacuum ultraviolet-visible spectroscopic properties of Tb^{3+} in Li(Y, Gd)$(PO_3)_4$: tunable emission, quantum cutting, and energy transfer. J Phys Chem C 114:6770
2. Xia Z, Meijerink A (2017) Ce^{3+}-doped garnet phosphors: composition modification, luminescence properties and applications. Chem Soc Rev 46:275–299
3. Xia Z, Liu Q (2016) Progress in discovery and structural design of color conversion phosphors for LEDs. Prog Mater Sci 84:59–117
4. Hou D, Liang H, Xie M, Ding X, Zhong J, Su Q, Tao Y, Huang Y, Gao Z (2011) Bright green-emitting, energy transfer and quantum cutting of $Ba_3Ln(PO_4)_3$:Tb^{3+} (Ln = La, Gd) under VUV-UV excitation. Opt Express 19:11071–11083
5. Swarnkar A, Mir WJ, Nag A (2018) Can B-Site doping or alloying improve thermal- and phase-stability of all-inorganic $CsPbX_3$ (X=Cl, Br, I) perovskites? ACS Energy Lett 3:286–289
6. Das AS, Guria AK, Pradhan N (2019) Insights of doping and the photoluminescence properties of Mn-doped perovskite nanocrystals. J Phys Chem Lett 10:2250–2257
7. Yadav RS, Monika, Rai SB, Dhoble SJ (2020) Recent advances on morphological changes in chemically engineered rare earth doped phosphor materials. Prog Solid State Chem 57:100267
8. Singh P, Yadav RS, Singh P, Rai SB (2021) Upconversion and downshifting emissions of Ho^{3+}-Yb^{3+} co-doped $ATiO_3$ perovskite phosphors with temperature sensing properties in Ho^{3+}-Yb^{3+} co-doped $BaTiO_3$ phosphor. J Alloys Compds 855:157452.
9. Yadav RS, Monika, Dhoble SJ, Rai SB (2020) Optical properties of lanthanide-based pyrophosphate phosphor materials. Nova Science Publishers Inc., USA, pp 47–69
10. Rai E, Yadav RS, Kumar D, Singh AK, Fullari V, Rai SB (2020) Influence of Bi^{3+} ion on structural, optical, dielectric and magnetic properties of Eu^{3+} doped $LaVO_4$ phosphor. Spectrochim Acta Part A 243:118787

11. Yadav RS, Monika, Rai E, Purohit LP, Rai SB (2020) Realizing enhanced downconversion photoluminescence and high color purity in Dy^{3+} doped $MgTiO_3$ phosphor in presence of Li^+ ion. J Lumin 217:116810
12. Baig N, Yadav RS, Dhoble NS, Barai VL, Dhoble SJ (2019) Near UV excited multi-color photoluminescence in RE^{3+} (RE = Tb, Sm, Dy and Eu) doped $Ca_2Pb_3(PO_4)_3Cl$ phosphors. J Lumin 215:116645
13. Yadav RS, Rai SB (2017) Structural analysis and enhanced photoluminescence via host sensitization from a lanthanide doped $BiVO_4$ nano-phosphor. J Phys Chem Solids 110:211–217
14. Monika, Yadav RS, Bahadur A, Rai SB (2020) Near-infrared light excited highly pure green upconversion photoluminescence and intrinsic optical bistability sensing in a Ho^{3+}-Yb^{3+} co-doped $ZnGa_2O_4$ phosphor through Li^+ doping. J Phys Chem C 124:10117–10128
15. Ningthoujam RS (2012)Enhancement of luminescence by rare earth ions doping in semiconductor host. In: Rai SB, Dwivedi Y (eds) Publisher: Nova Science Publisher Inc, USA, Chapter 7, pp 145–182
16. Yadav RS, Rai SB (2017) Surface analysis and enhanced photoluminescence via Bi^{3+} doping in a Tb^{3+} doped Y_2O_3 nano-phosphor under UV excitation. J Alloys Compds 700:228–237
17. Mir WJ, Swarnkar A, Nag A (2019) Postsynthesis Mn-doping in $CsPbI_3$ nanocrystals to stabilize the black perovskite phase. Nanoscale 11:4278–4286
18. Bahadur A, Yadav RS, Yadav RV, Rai SB (2017) Multimodal emissions from Tb^{3+}-Yb^{3+} co-doped lithium borate glass: Upconversion, downshifting and quantum cutting. J Solid State Chem 246:81–86
19. Yuan R, Liu J, Zhang H, Zhang Z, Shao G, Liang X, Xiang W (eds) Eu^{3+}-doped $CsPbBr_{1.5}I_{1.5}$ quantum dots glasses: a strong competitor among red fluorescence solid materials. J Am Ceram Soc 101:4927–4932
20. Zhou Y, Chen J, Bakr OM, Sun H-T (2018) Metal-doped lead halide perovskites: synthesis, properties, and optoelectronic applications. Chem Mater 30:6589–6613
21. Liu RS, Liu YH, Bagkar NC, Hu SF (2007) Enhanced luminescence of $SrSi_2O_2N_2$:Eu^{2+} phosphors by codoping with Ce^{3+}, Mn^{2+}, and Dy^{3+} ions. Appl Phys Lett 91:061119
22. Parchur AK, Ansari AA, Singh BP, Hasan TN, Syed NA, Rai SB, Ningthoujam RS (2014) Enhanced luminescence of $CaMoO_4$: Eu by core@shell formation and its hyperthermia study after hybrid formation with F_e3_O4: Cytotoxicity assessing on human liver cancer cells and mesanchymal stem cells. Integr Biol 6:53–64
23. Phaomei G, Ningthoujam RS, Singh WR, Loitongbam RS, Singh NS, Rath A, Juluri RR, Vatsa RK (2011) Luminescence switching behavior through redox reaction in Ce^{3+} co-doped $LaPO_4$:Tb^{3+} nanorods: Re-dispersible and polymer film. Dalton Trans 40:11571
24. Singh NS, Ningthoujam RS, Singh SD, Viswanadh B, Manoj N, Vatsa RK (2010) Preparation of highly crystalline blue emitting MVO_4:Tm^{3+} (M = Gd, Y) spherical nanoparticles: effects of activator concentration and annealing temperature on luminescence, lifetime and quantum yield. J Lumin 130:2452
25. Singh LR, Ningthoujam RS, Singh NS, Singh SD (2009) Probing Dy^{3+} ions on the surface of nanocrystalline YVO_4: luminescence study. Opt Mater 32:286
26. Rao CM, Sudarsan V, Ningthoujam RS, Gautam UK, Vatsa RK, Vinu A, Tyagi AK (2008) Luminescence studies on low temperature synthesized $ZnGa_2O_4$:Ln^{3+} (Ln = Tb and Eu) nanoparticles. J Nanosci Nanotech 8:5776
27. Ningombam GS, Singh NR, Ningthoujam RS (2017) Controlled synthesis of $CaWO_4$: Sm^{3+} microsphere particles by a reverse-micelle method and their energy transfer rate in luminescence. Colloids Surf A 518:249–262
28. Ningthoujam RS, Sharma A, Sharma KS, Barick KC, Hassan PA, Vatsa RK (2015) Roles of solvent, annealing and Bi^{3+}co-doping on the crystal structure and luminescence properties of YPO_4:Eu^{3+} nanoparticles. RSC Adv 5:68234–68242
29. Wangkhem R, Yaba T, Singh NS, Ningthoujam RS (2018) Red emission enhancement from $CaMoO_4$:Eu^{3+} by co-doping of Bi^{3+} for near UV/blue LED pumped white pcLEDs: Energy transfer studies. J Appl Phys 123:124303

30. Soni AK, Joshi R, Jangid K, Tewari R, Ningthoujam RS (2018) Low temperature synthesized $SrMoO_4:Eu^{3+}$ nanophosphors functionalized with ethylene glycol: a comparative study of synthesize route, morphology, luminescence and annealing. Mater Res Bull 103:1–12
31. Parchur AK, Ningthoujam RS (2012) Preparation, microstructure and crystal structure studies of Li^+ co-doped $YPO_4:Eu^{3+}$. RSC Adv 2:10854–10858
32. Sahu NK, Singh NS, Ningthoujam RS, Bahadur D (2014) Ce^{3+} sensitized $GdPO_4:Tb^{3+}$ nanorods: An investigation on energy transfer, luminescence switching and quantum yield. ACS Photonics 1:337–346
33. Phaomei G, Singh WR, Singh NS, Ningthoujam RS (2013) Luminescence properties of Ce^{3+} co-activated $LaPO_4:Dy^{3+}$ nanorods prepared in different solvents and tunable blue to white light emission from Eu^{3+} co-activated $LaPO_4:Dy^{3+}$, Ce^{3+}. J Lumin 134:649–656
34. Ningombam GS, Khundrakpam NS, Thiyam DS, Ningthoujam RS, Singh NR (2020) Salt assisted size-controlled synthesis and luminescence studies of single phase $CaWO_4:Dy^{3+}$: an insight into morphological evolution, energy transfer and colour evaluation. New J Chem 44:4217–4228
35. Dutta DP, NingthoujamRS, Tyagi AK (2012) Luminescence properties of Sm^{3+} doped YPO_4: effect of solvent, heat-treatment, Ca^{2+}/W^{6+}-co-doping and its hyperthermia application. AIP-Advances 2:042184
36. Singh LR, Ningthoujam RS (2011) Critical view on luminescence properties of $Y_2O_3:Eu^{3+}$ after dispersion in SiO_2. Chem Phys Lett 510:120
37. PrasadAI, Singh LR, Joshi R, Ningthoujam RS (2018) Luminescence study on crystalline phase of $Y_2Si_2O_7$ from mesoporous silica and Y_2O_3: Ln^{3+} at 900 °C. AIP Adv 8:105310
38. Loitongbam RS, Singh NS, Singh WR, Ningthoujam RS (2013) Observation of exceptional strong emission transitions 5Dj (j = 1–3) to 7Fj (j = 1–3): Multicolor from single Eu3+ ion doped La_2O_3 nanoparticles. J Lumin 134:14–23
39. Singh LP, Srivastava SK, Mishra R, Ningthoujam RS (2014) Multifunctional hybrid nanomaterials from water dispersible $CaF_2:Eu^{3+}$, Mn^{2+} and Fe_3O_4 for luminescence and hyperthermia application. J Phys Chem C 118:18087–18096
40. Singh LP, Jadhav NV, Sharma S, Pandey BN, Srivastava SK, Ningthoujam RS (2015) Hybrid nanomaterials YVO_4: Eu/Fe_3O_4 for optical imaging and hyperthermia in cancer cells. J Mater Chem C 3:1965–1975
41. Yaiphaba N, Ningthoujam RS, Singh NS, Vatsa RK, Singh NR (2010) Probing of inversion symmetry site in Eu^{3+} doped $GdPO_4$ by luminescence study: concentration and annealing effect. J Lumin 130:174
42. Sahu NK, Ningthoujam RS, Bahadur D (2012) Disappearance and recovery of luminescence in $GdPO_4:Eu^{3+}$ nanorods: Propose to water/$OH^{\cdot}$ release under near infrared and gamma irradiations. J Appl Phys 112:014306
43. Yaiphaba N, Ningthoujam RS, Singh NR, Vatsa RK (2010) Luminescence properties of redispersible Tb^{3+}-Doped $GdPO_4$ nanoparticles prepared by an ethylene glycol route. Eur J Inorg Chem 2682
44. Meetei SD, Singh SD, Singh NS, Sudarsan V, Ningthoujam RS, Tyagi M, Gadkari SC, Tewari R, Vatsa RK (2012) Crystal structure and photoluminescence correlations in white emitting nanocrystalline $ZrO_2:Eu^{3+}$ phosphor: effect of doping and annealing. S. D. Meetei, S. D. Singh, N. S. Singh, V. Sudarsan, R. S. Ningthoujam, M. Tyagi, S. C. Gadkari, R. Tewari and R. K. Vatsa. J. Lumin. 132:537–544
45. Singh LR, Ningthoujam RS, Sudarsan V, Singh SD, Kulshreshtha SK (2008) Probing of surface Eu^{3+} ions present in ZnO:Eu nanoparticles by covering ZnO: Eu core with Y_2O_3 shell: Luminescence study. J Lumin 128:1544
46. Ningthoujam RS, Gajbhiye NS, Ahmed A, Umre SS, Sharma SJ (2008) Re-dispersible Li^+ and Eu^{3+} co-doped nanocrystalline ZnO: Luminescence and EPR studies. J Nanosci Nanotech 8:3059
47. Gajbhiye NS, Ningthoujam RS, Ahmed A, Panda DK, Umre SS, Sharma SJ (2008) Re-dispersible Li^+ and Eu^{3+} co-doped CdS nanoparticles: luminescence studies. Pramana J Phys 70:313

48. Singh LR, Ningthoujam RS (2010)Critical view on energy transfer, site symmetry, improvement in luminescence of Eu^{3+}, Dy^{3+} doped YVO_4 by core-shell formation. J Appl Phys 107:104304
49. Ningthoujam RS, Singh LR, Sudarsan V, Singh SD (2009) Energy transfer process and optimum emission studies in luminescence of core-shell nanoparticles: YVO_4: Eu-YVO_4 and surface state analysis. J Alloys Comp 484:782
50. Ningthoujam RS, Sudarsan V, Vatsa RK, Kadam RM, Jagannath, Gupta A (2009) Photoluminescence studies on Eu doped TiO_2 nanoparticles. J Alloys Comp 486:864
51. Ningthoujam RS, Vatsa RK, Vinu A, Ariga K, Tyagi AK (2009) Room temperature exciton formation in SnO_2 nanocrystals in SiO_2: Eu matrix: Quantum dot system, heat-treatment effect. J Nanosci Nanotech 9:2634
52. Okram R, Yaiphaba N, Ningthoujam RS, Singh NR (2014) Is higher ratio of monoclinic to tetragonal in $LaVO_4$ a better luminescence host? Redispersion and polymer film formation. Inorg Chem 53:7204–7213
53. Soni AK, Joshi R, Singh BP, Naveen Kumar N, Ningthoujam RS, Near-infrared- and magnetic-field-responsive $NaYF_4$:Er^{3+}/Yb^{3+}@ SiO_2@ AuNP@Fe_3O_4 nanocomposites for hyperthermia applications induced by fluorescence resonance energy transfer and surface plasmon absorption. ACS Appl Nano Mater 2:7350−7361
54. Soni AK, Ningthoujam RS (2018) Observation of energy transfer phenomenon via up and down conversion in Eu^{3+} ions for $BaMoO_4$:Er^{3+}-Eu^{3+} nanophosphor. AIP Conf Proc 1942 (1):140004
55. Yu D, Yu T, van Bunningen AJ, Zhang Q, Meijerink A, Rabouw FT (2020) Understanding and tuning blue-to-near-infrared photon cutting by the Tm^{3+}/Yb^{3+} couple. Light Sci Appl 9:107
56. van der Ende BM, Aarts L, Meijerink A (2009) Near-infrared quantum cutting for photovoltaics. Adv Mater 21:3073–3077
57. Huang XY, Han S, Huang W, Liu XG (2013) Enhancing solar cell efficiency: the search for luminescent materials as spectral converters. Chem Soc Rev 42:173–201
58. Wegh RT, Donker H, Oskam KD, Meijerink A (1999) Visible quantum cutting in $LiGdF_4$:Eu^{3+} through downconversion. Sci 283:663–666
59. Creutz SE, Fainblat R, Kim Y, Siena, De MC, Gamelin DR (2017) A selective cation exchange strategy for the synthesis of colloidal Yb^{3+}-doped chalcogenide nanocrystals with strong broadband visible absorption and long-lived near-infrared emission. J Am Chem Soc 139:11814–11824
60. Timmerman D, Izeddin I, Stallinga P, Yassievich IN, Gregorkiewicz T (2008) Space-separated quantum cutting with silicon nanocrystals for photovoltaic applications. Nat Photonics 2:105–109
61. Strumpel C, McCann M, Beaucarne G, Arkhipov V, Slaouic A, Svrcek V, del Canizo C, Tobias I (2007) Modifying the solar spectrum to enhance silicon solar cell efficiency- an overview of available materials. Solar Energy Solar Cells. 91:238–249
62. Yu DC, Ye S, Peng MY, Zhang QY, Wondraczek L (2012) Sequential three-step three-photon near-infrared quantum splitting in β-$NaYF_4$:Tm^{3+}. Appl Phys Lett 100:191911
63. Chen XB, Li S, Salamo GJ, Li YL, He LZ, Yang GJ, Gao Y, Liu QL (2015) Sensitized intense near-infrared downconversion quantum cutting three-photon luminescence phenomena of the Tm^{3+} ion activator in $Tm^{3+}Bi^{3+}$:$YNbO_4$ powder phosphor. Opt Express 23:A51–A61
64. Piper WW, DeLuca JA, Ham FS (1974) Cascade fluorescent decay in Pr^{3+}-doped fluorides: achievement of a quantum yield greater than unity for emission of visible light. J Lumin 8:344–348
65. Sommerdijk JL, Bril A, de Jager AW (1974) Two photon luminescence with ultraviolet excitation of trivalent praseodymium. J Lumin 8:341–343
66. Yu DC, Martın-Rodrıguez R, Zhang QY, Meijerink A, Rabouw FT (2015) Multi-photon quantum cutting in Gd_2O_2S: Tm^{3+} to enhance the photo-response of solar cells. Light: Sci Appl 4:e344

67. Yadav RS, Verma RK, Bahadur A, Rai SB (2015) Structural characterizations and intense green upconversion emission in Yb^{3+}, Pr^{3+} co-doped Y_2O_3 nano-phosphor. Spectrochim Acta Part A 137:357–362
68. Zhang GG, Liu CM, Wang J, Kuang XJ, Su Q (2012) A dual-mode solar spectral converter $CaLaGa_3S_6O:Ce^{3+}$, $P^{r3}+$: UV-Vis-NIR luminescence properties and solar spectral converting mechanism. J Mater Chem 22:2226–2232
69. Pan G, Bai X, Yang D, Chen X, Jing P, Qu S, Zhang L, Zhou D, Zhu J, Xu W, Dong B, Song H (2017) Doping lanthanide into perovskite nanocrystals: highly improved and expanded optical properties. Nano Lett 17:8005–8011
70. Milstein TJ, Kroupa DM, Gamelin DR (2018) Picosecond quantum cutting generates photoluminescence quantum yields over 100% in ytterbium-doped $CsPbCl_3$ nanocrystals. Nano Lett 18:3792–3799
71. Ishii A, Miyasaka T (2020) Sensitized Yb^{3+} luminescence in $CsPbCl_3$ film for highly efficient near-infrared light-emitting diodes. Adv Sci 7:1903142
72. Zhou D, Sun R, Xu W, Ding N, Li D, Chen X, Pan G, Bai X, Song H (2019) Impact of host composition, codoping, or tridoping on quantum-cutting emission of ytterbium in halide perovskite quantum dots and solar cell applications. Nano Lett 19:6904–6913
73. Kroupa DM, Roh JY, Milstein TJ, Creutz SE, Gamelin DR (2018) Quantum-cutting ytterbium-doped $CsPb(Cl_{1-x}Br_x)_3$ perovskite thin films with photoluminescence quantum yields over 190%. ACS Energy Lett 3:2390–2395
74. Cohen TA, Milstein TJ, Kroupa DM, MacKenzie JD, Luscombe C, Gamelin DR (2019) Quantum-cutting Yb^{3+}-doped perovskite nanocrystals for monolithic bilayer luminescent solar concentrators. J Mat Chem A 7:9279–9288
75. Crane MJ, Kroupa DM, Roh JYD, Anderson RT, Smith MD, Gamelin DR (2019) Single-source vapor deposition of quantum-cutting Yb^{3+}:$CsPb(Cl_{1-X}Br_x)_3$ and other complex metal-halide perovskites. ACS Appl Energy Mater 2:4560–4565
76. Crane MJ, Kroupa DM, Gamelin DR (2019) Detailed-balance analysis of Yb^{3+}:$CsPb(Cl_{1-x}Br_x)_3$ quantum-cutting layers for high-efficiency photovoltaics under real-world conditions. Energy Environ Sci 12:2486–2495
77. Milstein TJ, Kluherz TK, Kroupa DM, Erickson CS, De Yoreo JJ, Gamelin DR (2019) Anion exchange and the quantum-cutting energy threshold in ytterbium-doped $CsPb(Cl_{1-x}Br_x)_3$ perovskite nanocrystals. Nano Lett 19:1931–1937
78. Luo X, Ding T, Liu X, Liu Y, Wu K (2019) Quantum-cutting luminescent solar concentrators using ytterbium-doped perovskite nanocrystals. Nano Lett 19:338–341
79. Zeng M, Artizzu F, Liu J, Singh S, Locardi F, Mara D, Hens Z, Deun RV (2020) Boosting the Er^{3+} 1.5 μm luminescence in $CsPbCl_3$ perovskite nanocrystals for photonic devices operating at telecommunication wavelengths. ACS Appl Nano Mater 3:4699–4707
80. Yeon J, Roh D, Smith MD, Crane MJ, Biner D, Milstein TJ, Krämer KW, Gamelin DR (2020) Yb^{3+} speciation and energy-transfer dynamics in quantum-cutting Yb^{3+}-doped $CsPbCl_3$ perovskite nanocrystals and single crystals. Phys Rev Mater 4:105405
81. Li YQ, de With G, Hintzen HT (2005) Luminescence of a new class of UV-blue-emitting phosphors $MSi_2O_{2-\delta}N_{2+2/3\delta}:Ce^{3+}$ (M = Ca, Sr, Ba). J Mater Chem 15:4492–4496
82. Li YQ, Delsing ACA, De With G, Hintzen HT (2005) Luminescence properties of Eu^{2+}-activated alkaline-earth silicon-oxynitride $MSi_2O_{2-\delta}N_{2+2/3\delta}$ (M = Ca, Sr, Ba): a promising class of novel LED conversion phosphors. Chem Mater 17:3242–3248
83. Hoppe HA, Lutz H, Morys P, Schnick W, Seilmeier A (2000) Luminescence in Eu^{2+}-doped $Ba_2Si_5N_8$: fluorescence, thermoluminescence, and upconversion. J Phys Chem Solids 61:2001–2006
84. Wei XT, Wen J, Li S, Huang S, Cheng J, Chen YH, Duan CK, Yin M (2014) Red-shift of vanadate band-gap by cation substitution for application in phosphor-converted white light-emitting diodes. Appl Phys Lett 104:181904
85. Yadav RV, Yadav RS, Bahadur A, Rai SB (2016) Down shifting and quantum cutting from Eu^{3+}, Yb^{3+} co-doped $Ca_{12}Al_{14}O_{33}$ phosphor: a dual mode emitting material. RSC Adv 6:9049–9056

86. Shukla R, Ningthoujam RS, Tyagi AK, Vatsa RK (2010) Luminescence properties of Dy^{3+} doped Gd_2O_3 nanoparticles prepared by glycine route: annealing effect. Int J Nanotechnol 7:843
87. Ningthoujam RS, Kulshreshtha SK (2009) Nanocrystalline SnO_2 from thermal decomposition of tin citrate crystal: luminescence and Raman studies. Mater Res Bull 44:57
88. Ningthoujam RS, Shukla R, Vatsa RK, Duppel V, Kienle L, Tyagi AK (2009) Gd_2O_3:Eu^{3+} particles prepared by glycine-nitrate combustion: Phase, concentration, annealing, and luminescence studies. J Appl Phys 105:084304
89. Ningthoujam RS, Mishra R, Das D, Dey GK, Kulshreshtha SK (2008) Excess enthalpy and luminescence studies of SnO_2 nanoparticles. J Nanosci Nanotech 8:4176
90. Yadav RV, Singh SK, Rai SB (2015) Effect of the Li^+ ion on the multimodal emission of a lanthanide doped phosphor. RSC Adv 5:26321–26327
91. Zhang X, Liu Y, Zhang M, Yang J, Zhu H, Yan D, Liu CG, Xu CS, Wang XJ (2018) Efficient deep ultraviolet to near infrared quantum cutting in Pr^{3+}/Yb^{3+} codoped $CaGdAlO_4$ phosphors. J Alloys Compd 740:595–602
92. Rakov N, Maciel GS (2011) Near-infrared quantum cutting in Ce^{3+}, Er^{3+}, and Yb^{3+} doped yttrium silicate powders prepared by combustion synthesis. J Appl Phys 110:083519
93. Fan B, Chlique C, Merdrignac-Conanec O, Zhang X, Fan X (2012) Near-infrared quantum cutting material Er^{3+}/Yb^{3+} doped La_2O_2S with an external quantum yield higher than 100%. J Phys Chem C 116:11652–11657
94. Huang XY, Yu DC, Zhang QY (2009) Enhanced near-infrared quantum cutting in $GdBO_3$:Tb^{3+}, Yb^{3+} phosphors by Ce^{3+} cooping. J Appl Phys 106:113521
95. Yadav RS, Dwivedi Y, Rai SB (2012) Structural and optical characterization of nano-sized $La(OH)_3$:Sm^{3+} phosphor. Spectrochim Acta Part A 96:148–153
96. Yadav RS, Verma RK, Rai SB (2013) Intense white light emission in Tm^{3+}/Er^{3+}/Yb^{3+} co-doped Y_2O_3-ZnO nano-composite. J Phys D Appl Phys 46:275101
97. Yadav RS, Dwivedi Y, Rai SB (2014) Structural and optical properties of Eu^{3+}, Sm^{3+} co-doped $La(OH)_3$ nano-crystalline red emitting phosphor. Spectrochim Acta Part A 132:599–603
98. Yadav RS, Dwivedi Y, Rai SB (2015) Structural and optical properties of Eu^{3+} doped red emitting $BiVO_4$ nano-phosphor. Appl Mech Mater 752–753:272–276
99. Yadav RS, Kumar D, Singh AK, Rai E, Rai SB (2018) Effect of Bi^{3+} ion on upconversion-based induced optical heating and temperature sensing characteristics in the Er^{3+}/Yb^{3+} co-doped La_2O_3 nano-phosphor. RSC Adv 8:34699–34711
100. Varma A, Mukasyan AS, Rogachev AS, Manukyan KV (2016) Solution combustion synthesis of nanoscale materials. Chem Rev 116:14493–14586
101. Papadas IT, Ioakeimidis A, Armatas GS, Choulis SA (2018) Low-temperature combustion pynthesis of a spinel $NiCo_2O_4$ hole transport layer for perovskite photovoltaics. Adv Sci 5:1701029
102. Jayasimhadri M, Ratnam BV, Jang K, Lee HS, Chen B, Yi S-S, Jeong J-H, Moorthy LR (2011) Combustion synthesis and luminescent properties of nano and submicrometer-size Gd_2O_3:Dy^{3+} phosphors for white LEDs. Int J Appl Ceram Technol 8:709–717
103. Yadav RS, Rai SB (2019) Effect of annealing and excitation wavelength on the downconversion photoluminescence of Sm^{3+} doped Y_2O_3 nano-crystalline phosphor. Opt Laser Technol 111:169–175
104. Sikka S (2005) Handbook of sol-gel science and technology: Processing, characterization and applications. Kluwar Academic Publishers
105. Yang Y, Liu L, Cai S, Jiao F, Mi C, Su XY, Zhang J, Yu F, Li XD, Li Z (2014) Up-conversion luminescence and near-infrared quantum cutting in Dy^{3+}, Yb^{3+} co-doped $BaGd_2ZnO_5$ nanocrystal. J Lumin 146:284–287
106. Wei X-T, Zhao J-B, Chen Y-H, Yin M, Li Y (2010) Quantum cutting downconversion by cooperative energy transfer from Bi^{3+} to Yb^{3+} in Y_2O_3 phosphor. Chin Phys B 19:077804
107. Gao X, Li T, He J, Ye K, Song X, Wang N, Su JG, Hui CL, Zhang X (2017) Synthesis of Yb^{3+}, Ho^{3+} and Tm^{3+} co-doped β-$NaYF_4$ nanoparticles by sol-gel method and the multi-color upconversion luminescence properties. J Mater Sci Mater Electron 28:11644–11653

108. Mirzaei A, Janghorban K, Hashemi B, Bonyani M, Leonardi SG, Neri G (2016) Highly stable and selective ethanol sensor based on α-Fe_2O_3 nanoparticles prepared by pechini sol-gel method. Ceram Int 42:6136–6144
109. Islam S, Bidin N, Riaz S, Naseem S, Marsin FM (2016) Correlation between structural and optical properties of surfactant assisted sol-gel based mesoporous SiO_2-TiO_2 hybrid nanoparticles for pH sensing/optochemical sensor. Sens Actuators B Chem 225:66–73
110. Ciciliati MA, Silva MF, Fernandes DM, de Melo MAC, Hechenleitner AAW, Pineda EAG (2015) Fe-doped ZnO nanoparticles: synthesis by a modified sol-gel method and characterization. Mater Lett 159:84–86
111. Wang X, Liu C-S, Yu T, Yan XH (2014) Controlled synthesis, photoluminescence, and the quantum cutting mechanism of Eu3+ doped NaYbF4 nanotubes. Phys Chem Chem Phys 16:13440–13446
112. Kadam AR, Yadav RS, Mishra GC, Dhoble SJ (2020) Effect of singly, doubly and triply ionized ions on downconversion photoluminescence in Eu^{3+} doped $Na_2Sr_2Al_2PO_4Cl_9$ phosphor: a comparative study. Ceram Int 46:3264–3274
113. Parauha YR, Yadav RS, Dhoble SJ (2020) Enhanced photoluminescence via doping of phosphate, sulphate and vanadate ions in Eu^{3+} doped $La_2(MoO_4)_3$ downconversion phosphors for white LEDs. Opt Laser Technol 124:105974
114. Yadav RS, Monika, Rai SB (2020) Upconversion photoluminescence in the rare earth doped Y_2O_3 phosphor materials, vol. 12. CRC Press, Taylor & Francis Group, UK
115. Yu DC, Huang XY, Ye S, Peng MY, Zhang QY, Wondraczek L (2011) Three-photon near-infrared quantum splitting in β-$NaYF_4$:Ho^{3+}. Appl Phys Lett 99:161904
116. Dubey A, Soni AK, Kumari A, Dey R, Rai VK (2017) Enhanced green upconversion emission in $NaYF_4$:Er^{3+}/Yb^{3+}/Li^{+} phosphors for optical thermometry. J Alloys Compds 693:194–200
117. Li X, Zhu J, Man Z, Ao Y, Chen H (2014) Investigation on the structure and upconversion fluorescence of Yb^{3+}/Ho^{3+} co-doped fluorapatite crystals for potential biomedical applications. Sci Rep 4:446
118. Guo L, Wang Y, Zhang J, Wang Y, Dong P (2012) Near-infrared quantum cutting in Ho^{3+}, Yb^{3+}-codoped $BaGdF_5$ nanoparticles via first and second-order energy transfers. Nanoscale Res Lett 7:636
119. Zhang L, Zhao S, Liang Z, Zhang J, Zhu W, Liu P, Sun H (2017) The colour tuning of upconversion emission from green to red in $NaScF_4$:Yb^{3+}/Er^{3+} nanocrystals by adjusting the reaction time. J Alloys Compd 699:1–6
120. Ningthoujam RS, Gautam A, Padma N (2017) Oleylamine as reducing agent in syntheses of magic-size clusters and monodisperse quantum dots: optical and photoconductivity studies. Phys Chem Chem Phys 19:2294–2303
121. Tong J, Wu J, Shen W, Zhang Y, Liu Y, Zhang T, Nie S, Deng Z (2019) Direct hot-injection synthesis of lead halide perovskite nanocubes in acrylic monomers for ultrastable and bright nanocrystal-polymer composite films. ACS Appl Mater Interfaces 11:9317–9325
122. Imran M, Caligiuri V, Wang M, Goldoni L, Prato M, Krahne R, De Trizio L, Manna L (2018) Benzoyl halides as alternative precursors for the colloidal synthesis of lead-based halide perovskite nanocrystals. J Am Chem Soc 140:2656–2664
123. Creutz SE, Crites EN, De Siena MC, Gamelin DR (2018) Anion exchange in cesium lead halide perovskite nanocrystals and thin films using trimethylsilyl halide reagents. Chem Mater 30:4887–4891
124. Zhou D, Liu D, Pan G, Chen X, Li D, Xu W, Bai X, Song H (2017) Cerium and ytterbium codoped halide perovskite quantum dots: a novel and efficient downconverter for improving the performance of silicon solar cells. Adv Mater 29:1704149
125. Cai T, Wang J, Li W, Hills-Kimball K, Yang H, Nagaoka Y, Yuan Y, Zia R, Chen O (2020) Mn^{2+}/Yb^{3+} codoped $CsPbCl_3$ perovskite nanocrystals with triple-wavelength emission for luminescent solar concentrators. Adv Sci 7:2001317
126. Parobek D, Dong Y, Qiao T, Son DH (2018) Direct hot-injection synthesis of Mn-doped CsPbBr 3 nanocrystals. Chem Mater 30:2939–2944

127. Sudhakar N, Ningthoujam RS, Gajbhiye NS, Rajeev KP (2007) Structural, magnetic and electron transport studies on nanocrystalline layered manganite $La_{1.2}Ba_{1.8}Mn_2O_7$ system. J Nanosci Nanotech 7:965
128. Mishra R, Ninghthoujam RS (2017) High temperature ceramics. In: Banerjee S, Tyagi AK (eds) 2017 in Materials under extreme conditions: recent trends and future prospects. Elsevier Inc., USA, Chapter 11, pp 377–410
129. Zou Z, Feng L, Cao C, Zhang J, Wang Y (2016) Near-infrared quantum cutting long persistent luminescence. Sci Rep 6:24884
130. Dong SL, Lin HH, Yu T, Zhang QY (2014) Near-infrared quantum-cutting luminescence and energy transfer properties of $Ca_3(PO_4)_2$: Tm^{3+},Ce^{3+} phosphors. J Appl Phys 116:023517
131. Sun J, Sun Y, Cao C, Xia Z, Du H (2013) Near-infrared luminescence and quantum cutting mechanism in $CaWO_4$:Nd^{3+}, Yb^{3+}. Appl Phys B 111:367–371
132. Yadav RV, Yadav RS, Bahadur A, Singh AK, Rai SB (2016) Enhanced quantum cutting emission through Li^+ doping from Bi^{3+}, Y^{b3}+ co-doped gadolinium tungstate phosphor. Inorg Chem 55:10928–10935
133. Yadav RS, Dhoble SJ, Rai SB (2018) Improved photon upconversion photoluminescence and intrinsic optical bistability from a rare earth co-doped lanthanum oxide phosphor *via* Bi^{3+} doping. New J Chem 42:7272–7282
134. Yadav RS, Dhoble SJ, Rai SB (2018) Enhanced photoluminescence in Tm^{3+}, Yb^{3+}, Mg^{2+} tri-doped $ZnWO_4$ phosphor: Three photon upconversion, laser induced optical heating and temperature sensing. Sens Actua B Chem 273:1425–1434
135. Kim D, Park SW, Park SH, Choi BC, Kim JH, Jeong JH (2018) Wide range yellow emission $Sr_8MgLa(PO_4)_7$: Eu^{2+}, Mn^{2+}, Tb^{3+} phosphors for near ultraviolet white LEDs. Mater Res Bull 107:280–285
136. Li L, Chang W, He J, Yan Y, Cui M, Jiang S, Xiang G, Zhou X (2018) Molybdenum substitution simultaneously induced band structure modulation and luminescence enhancement in LiLaMg(W, Mo)$_O$6:E^{u3}+ red-emitting phosphor for near ultraviolet excited white light diodes. J Alloys Compd 763:278–288
137. Vijayakumar R, Devakumar B, Annadurai G, Guo H, Huang XY (2018) Novel high color purity and thermally stable Eu^{3+} ions activated $Ba_2Gd_5B_5O_{17}$ red emitting phosphor for near-UV based WLEDs. Opt Mater 84:312–317
138. Tadge P, Yadav RS, Vishwakarma PK, Rai SB, Chen TM, Sapra S, Ray S (2020) Enhanced photovoltaic performance of Y_2O_3:Ho^{3+}/Yb^{3+} upconversion nanophosphor based DSSC and investigation of color tunability in Ho^{3+}/Tm^{3+}/Yb^{3+} tridoped Y_2O_3. J Alloys Compds 821:153230
139. Liu X, Ye S, Qiao Y, Dong G, Zhu B, Chen D, Lakshminarayana G, Qiu J (2009) Cooperative downconversion and near-infrared luminescence of Tb^{3+}-Yb^{3+} codoped lanthanum borogermanate glasses. Appl Phys B 96:51–55
140. Zhou X, Wang Y, Zhao X, Li L, Wang ZQ, Li Q (2014) Near-infrared quantum cutting via downconversion energy transfers in Ho^{3+}/Yb^{3+} codoped tellurite glass ceramics. J Am Ceram Soc 97:179–184
141. Zhang J, Wang Y, Chen G, Huang Y (2014) Investigation on visible quantum cutting of Tb^{3+} in oxide hosts. J Appl Phys 115:093108
142. Huang XY, Zhang QY (2010) Near-infrared quantum cutting via cooperative energy transfer in Gd_2O_3: Bi^{3+}, Yb^{3+} phosphors. J Appl Phys 107:063505
143. Mir WJ, Sheikh T, Arfin H, Xia Z, Nag A (2020) Lanthanide doping in metal halide perovskite nanocrystals: spectral shifting, quantum cutting and optoelectronic applications. NPG Asia Mater 12:9
144. Teng Y, Zhou J, Liu X, Ye S, Qiu J (2010) Efficient broadband near-infrared quantum cutting for solar cells. Opt Express 18:9671–9676
145. Duan Q, Qin F, Zhang Z, Cao W (2012) Quantum cutting mechanism in $NaYF_4$:Tb^{3+}, Yb^{3+}. Opt Lett 27:521–523
146. Shestakov MV, Tikhomirov VK, Kirilenko D, Kuznetsov AS, Chibotaru LF, Baranov AN, Van Tendeloo G, Moshchalkov VV (2011) Quantum cutting in Li (770 nm) and Yb (1000

nm) co-dopant emission bands by energy transfer from the ZnO nano-crystalline host. Opt Express 19:15955–15964
147. Terra IAA, Borrero-Gonzalez LJ, Carvalho JM, Terrile MC, Felinto MCFC, Brito HF, Nunes LAO (2013) Spectroscopic properties and quantum cutting in Tb^{3+}-Yb^{3+} co-doped ZrO_2 nanocrystals. J Appl Phys 113:073105
148. Yadav RS, Rai SB (2018) Concentration and wavelength dependent frequency downshifting photoluminescence from a Tb^{3+} doped yttria nano-phosphor: a photochromic phosphor. J Phys Chem Solids 114:179–186
149. Xie L, Wang Y, Zhang H (2009) Near-infrared quantum cutting in YPO_4:Yb^{3+}, Tm^{3+} via cooperative energy transfer. Appl Phys Lett 94:061905

Chapter 8
Synthesis, Characterization, Physical Properties and Applications of Metal Borides

Rashmi Joshi and Raghumani S. Ningthoujam

Abstract There is a need to understand boron and boron chemistry of metals and non-metals. Boron is an electron-deficient atom in bonding and can react with other elements (except noble gases) to form stable compounds, namely B_2H_6, MgB_2, AlB_2, B_4C, SiB_3, BN, Cr_2B, Fe_3B, ZrB_2, LaB_6, etc. It forms tetrahedral, cage-type, trigonal and layered structures, etc. B–B bond can be of single (B–B), double (B = B) or triple (B≡B) types. In metal-rich borides, metal–metal interaction occurs. They are used as catalysts, imparting materials for mechanical, thermal and chemical stability, magnetic, superconducting and coating materials, etc. In this article, several ways of synthesis of metal borides and characterization techniques have been discussed. Also, the synthesis methods for nanostructured metal borides are elaborated. The properties (magnetism, electronic structure, electrical resistivity, optics) of some selected compounds of metal borides in addition to BN, CN are described. Lastly, the applications of selected borides are provided.

Keywords Borides · Electron deficient · Synthesis and characterization · Nanostructures

8.1 Introduction

Chemistry of boron is wonderful! Boron can form chemical bonds with most of the elements (except noble gases). The chemical bonds are of covalent, metallic or ionic nature [1–6]. The chemical bonds of boron with other elements are generally electron deficient. The structure of boron compounds can be of tetrahedral, octahedral, cage-type, linear, planar or layered types, etc. The possible bonds will be B–B in boron-rich compounds and M–M (metal–metal) in boron-deficient compounds, in addition to M–B. Most metal borides are good electrical conductors. Because of this, these are not

R. Joshi · R. S. Ningthoujam (✉)
Chemistry Division, Bhabha Atomic Research Centre, Mumbai 400085, India
e-mail: rsn@barc.gov.in

Homi Bhabha National Institute, Mumbai 400094, India

A. K. Tyagi and R. S. Ningthoujam (eds.), *Handbook on Synthesis Strategies for Advanced Materials*, Indian Institute of Metals Series,
https://doi.org/10.1007/978-981-16-1892-5_8

good for photoluminescence properties. They can show different magnetic properties from paramagnetic, antiferromagnetic to ferromagnetic nature depending on type of compound. In terms of electrical resistivity, borides can have good conductivity, insulating or even superconductivity behaviors. Transition metal borides (TMBs) are interesting because they can show ultra-high hard, high thermal and chemical stability, magnetism, etc. TMBs of Ti, Ta, Hf and W are examples of ultra-high hard materials. They are used as coating materials to increase chemical stability and wear resistance of tools. With p-block elements, they can form stable compounds with ultra-high hardness. BN and CN are examples of such ultra-hard compounds, and their hardness is almost comparable with diamond. BN is also used as sample holder in high-temperature magnetic measurement due to diamagnetic property, whereas CN is used as carbon-based super capacitors. With f-block elements, it forms stable compounds such as LaB_6, CeB_6. These are important materials in scanning electron microscopy and synchrotron. With s-block elements, it forms stable phases such as MgB_2.

In case of metal borides, B atoms occupy either interstitial sites of metal lattice or form BM_n (n = 1–12), whereas in cases of transition metal nitrides and carbides, N or C atoms occupy only interstitial sites [1, 7–21]. Most metal nitrides or carbides exhibit high hardness, chemical and thermal stabilities in harsh environment and metallic to superconducting/semiconducting behavior. These properties are similar to metal borides. However, most nitrides with p-block elements such as AlN, GaN, InN and their hybrids are used as UV (ultraviolet), visible light emitters, but most borides are not good as light emitters since they show metallic nature. In some cases, metal borides are near-infrared (NIR) light emitters. Usually, luminescent materials emitting UV–visible-NIR have band gap between valence and conduction bands so that they can absorb light (quantum of light = $h\nu$, which is equal to or slightly more than band gap (h = Plank's constant and ν = frequency of light) and then emit light [22–26]. However, there are a few examples where metal ions in solution or crystal lattice show emission due to d-d or f-f or d-f or charge transfer (M–L, metal–ligand, metal–metal) transitions or defects or agglomeration/clusters of molecules or particles [27–44]. CN and BN are good light emitters since they have appropriate band gap. In terms of hardness, both are comparable to diamond.

Metal borides with compositions from metal rich to boron rich have been reported [1–6]. A few examples are mentioned here. Nb_3B_2, NbB, Nb_5B_6, Nb_3B_4, NbB_2, Cr_2B, Cr_5B_3, CrB, Cr_3B_4, CrB_2, CrB_4, CrB_6, MgB_2, MgB_4, MgB_6, MgB_7, MgB_{12}, LiB, Li_5B_4, Li_3B_{14}, $LiB_{12.93}$, $Li_{1.8}B_{14}$ and LiB_2. Metal borides can have various phases at different synthesis temperatures. For example, Cr–B can have various phases at different temperatures [43, 44]. With p-block elements, boron forms compounds of AlB_2, AlB_{12}, B_4C, SiB_3, SiB_4, SiB_6, BN. With rare-earth elements, boron forms compounds of LaB_6, YB_6, CeB_6, EuB_6, ThB_6. Also, a large number of the substituted compounds (e.g., $Al_{0.5}Mg_{0.5}B_2$) and ternary compounds of boron, e.g., $MgAlB_{14}$, $LiAlB_{14}$, AlB_3C have been reported.

In this chapter, ten different synthesis routes including synthesis of nanostructures are described. The magnetic, electronic, electrical, optical and mechanical properties of some borides are mentioned. Finally, applications of borides are included.

8.2 Synthesis and Characterization

Metal borides are compounds of metal and boron; and their compositions vary from metal rich to boron rich. They exhibit either in amorphous or crystalline forms. The formation of metal borides is highly exothermic. Thus, this should be carried out carefully. Different synthesis methods to prepare metal borides are available in literature [1, 3, 4]. In this chapter, several ways to prepare metal borides are mentioned.

(i) High-temperature synthesis (above 1000 °C) using pure metal powder and boron powder in an inert atmosphere or vacuum (known as solid-state reaction)
(ii) Electrolysis process in molten salts
(iii) Reduction process of metal oxides/halides with boric acid or boron in presence of carbon/aluminum/magnesium
(iv) Reduction process of metal oxides with boron carbide
(v) Self-propagating high-temperature synthesis (SHS)
(vi) Mechano-chemically assisted preparation
(vii) Reduction process of metal salts with borohydrides ($LiBH_4$, $NaBH_4$, KBH_4)
(viii) Deposition from a reactive vapor phase (thin films or single crystals or polycrystals)
(ix) Single-source precursor route
(x) Nanostructure formation in 0D, 1D, 2D and 3D ways.

8.2.1 High-Temperature Synthesis (Above 1000 °C) Using Pure Metal Powder and Boron Powder in Inert Atmosphere or Vacuum by Solid-State Reaction

In this method, stoichiometric amounts of metal (M) powder and amorphous boron (B) powder are mixed and heated at 500–600 °C to remove absorbed water, oxygen in vacuum or Ar–H_2. Then, mixture is pelletized to increase contact between M and B atoms. These pellets are heated at 1000 °C or above in Ar atmosphere to get different phases of metal borides. For example, pure phase of NbB or NbB_2 can be prepared by taking suitable stoichiometric amounts of Nb and B at 1000 °C [40]. The particle sizes of 5–10 μm are observed. At lower temperatures (say 700–800 °C), it gives a mixture of Nb and Nb_xB_y. At high temperature (1800 °C), the formation of pure phase of Nb_3B_4 occurs. This method is also known as solid-state reaction. Sintering of NbB_2 at high pressure of 4 GPa and high temperature of 1600 °C improves density of material (6.85 g/cm^3, which is 98% of theoretical value). Microhardness of 2.6 kKg/mm^2 is obtained.

Similarly, MgB_2 can be prepared by heating a mixture of Mg and B powder at 700 °C for 10 h under inert atmosphere [41]. Here, Mg and B power is mixed in 1:2 mol ratio and pressed into pellets. The pellets are heated at 700 °C under Ar atmosphere and hot isostatic pressure. Figure 8.1a shows the XRD pattern of MgB_2

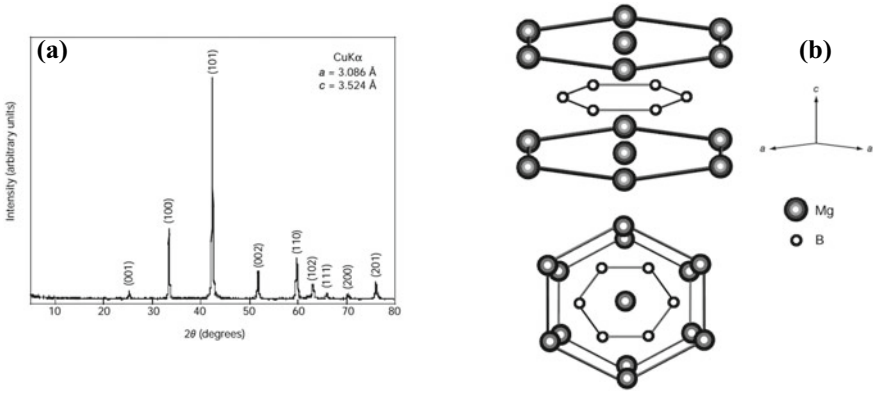

Fig. 8.1 **a** X-ray diffraction pattern of MgB_2 at room temperature and **b** its schematic crystal structure. Reproduced with permission from Nature Publishing Group [41]

and it crystallizes in hexagonal phase with unit cell parameters $a = 3.086$ Å and $c = 3.524$ Å and space group of $P_{6/mmm}$. Figure 8.1b shows the crystal structure of hexagonal structure of MgB_2 in which layers of B atoms are arranged and layer of Mg atoms is between B-layers along c-axis. The layers of B atoms are same as graphite structure. Interestingly, MgB_2 has the superconducting transition at 39 K. This value is the highest transition temperature among all borides, nitrides and carbides till date.

8.2.2 Electrolysis Process in Molten Salts

Metal borides are prepared by electrolysis process at high temperature using molten salts or electrolyte. There are three ways to prepare metal borides through electrolysis [42].

(1) Deposition of boron from a boron-containing electrode to metallic substrates through molten salts having boron ions. For example, the formation of MB_2 (M = Ti, Zr, Nb, Ta) occurs from M and B powders in LiCl/Li melt electrolyte at 900 °C. The chemical reactions are summarized here:

$$\mathrm{B(powder) + yLi(melt) \rightarrow Li_yB}$$
$$\mathrm{Li_yB + m.e^-(cathode) \rightarrow yLi^+ + B^{m-}}$$
$$\mathrm{2B^{m-} + M(substrate) \rightarrow MB_2 + 2.m.e^-}$$

(2) Deposition of boron on metallic cathode from the molten salt containing B^{3+}. The energy for the formation of M_xB_y can be represented by the following:

$$\mathrm{E(M_xB_y) = E(B) - \triangle G^0(M_xB_y)/(3yF)}$$

where

E (B)	Equilibrium deposition potential of boron on the inert cathode without metal boride formation.
$\Delta G^0(M_xB_y)$	Standard free energy of the formation of the given boride.
F	Faraday constant.

Example of B (3+) containing electrolyte is KBF_4. Reduction of B (3+) to B (0) needs 3 e^-. To form metallic borides such as FeB_2, HfB_2, TaB_2, high cathodic current needs to be provided.

(3) Deposition of boron and metal from molten salt containing B^{3+} and M^{n+}. For example, TiB and TiB_2 phases can be deposited on the tungsten cathode (W) using molten salt electrolyte (NaCl–KCl–NaF–K_2TiF_6–KBF_4 system).

In this way, many metal borides in the form of the film or polycrystalline or single crystals powder can be prepared. Synthesis of metal borides with general formula AB_6(A = s, f-block elements) such as CaB_6, LaB_6, ThB_6 and AB_4 (A = d, f-block elements) such as CrB_4, MnB_4, UB_4 and AB, AB_2, A_2B, A_3B and A_xB_y (A = d-block elements) such as VB, TaB, CrB, MoB, WB, NiB, TiB_2, ZrB_2, HfB_2, NbB_2, TaB_2, Fe_2B, Ni_3B, MnB_{12}, Mo_2B_5, Cr_3B_4, Cr_3B_2 have been reported. The different compositions of molten salt electrolytes are used during the synthesis. This electrolysis process can be performed at the different current densities, voltages and temperatures (500–1000 °C) to prepare the different phases of metal borides. The electrolysis process has the following advantages: (a) Uniform coating even at surfaces of complicated geometry. (b) Formation of different phases of metal borides (M_xB_y). (c) Different thickness of coating as per requirement. (d) Formation of single or polycrystalline metal borides.

8.2.3 Reduction of Metal Oxides/Halides with Boron in Presence of Carbon/Aluminum/Magnesium

Most transition metal borides are prepared by reduction of metal oxides/halides with boron. The temperature required for formation of metal borides is reduced in the presence of carbon (C) or aluminum (Al) or magnesium (Mg) [43].

$$M_xO_y + B \rightarrow M_aB_b + B_2O_3$$
$$M_xO_y + B + Al \rightarrow M_aB_b + Al_2O_3$$

However, extra product such as aluminum oxide (Al_2O_3) is associated during the formation of metal borides if Al is used. Sometimes, the presence of Al_2O_3 improves chemical stability and mechanical properties. The different phases of metal borides can be prepared by varying parameters of synthesis procedure (temperature, additive, precursors, pressure, etc.).

8.2.4 Reduction of Metal Oxides with Boron Carbide

Transition metal borides can be prepared by reduction of metal oxides with boron carbide in absence or presence of carbon. The reduction reaction is given below:

$$M_xO_y + B_4C + C \rightarrow M_aB_b + CO$$

or

$$M_xO_y + B_4C \rightarrow M_aB_b + B_2O_3 + C$$

In this way, a large number of metal borides can be prepared. Even CrB_2 has been used as coating materials due to its stability under extreme conditions and a high melting point (2200 °C). This compound can be prepared by this route [45]. 93% density of CrB_2 product is obtained by pressure less sintering at 1850 °C for 6 h. 99% density of CrB_2 product is achieved by hot pressing at 1600 °C and 35 MPa pressure for 2 h. Its hardness and fracture toughness are observed to be 22 GPa and 3.5 MPa $m^{0.5}$, respectively.

8.2.5 Self-propagating High-Temperature Synthesis (SHS)

The self-propagating high-temperature synthesis (SHS) employs the closed vessel (e.g., a stainless-steel windowed chamber) in which highly reactive precursors needed for the formation of compound are added [43]. The vessel is kept in inert environment. Ignition temperature is provided to start reaction. After that, reaction propagates automatically with time. Temperature as high as 1500 °C can be achieved. In this way, metal borides with different compositions can be prepared by taking different ratios of metal or metal oxides and boron powder. The reaction is known as borothermic reduction of metal oxide (such as Cr_2O_3, WO_3). To achieve lower ignition temperature of reaction, reducing agents like metals (Al, Mg) are added; and this helps in achieving higher temperature as compared to borothermic reaction. This is known as metallothermic reduction of metal oxide.

Cr–B phases are prepared by SHS method from Cr_2O_3 and B or Cr_2O_3, B and Al mixture [43]. To get self-sustaining combustion, external temperatures from heater are provided at 300 and 200 °C in Cr_2O_3 and B and Cr_2O_3, B and Al, respectively. The entire sample is burned in both cases in 5.2 s. The combustion wave frame velocity is more in case of Cr_2O_3, B and Al mixture than that in Cr_2O_3 and B mixture. This observation is supported by the brighter burning glow in case of Cr_2O_3, B and Al than that in Cr_2O_3 and B. Figure 8.2a shows the combustion wave frame velocity with different compositions of B/Cr_2O_3. At x = 6 (mole ratio of B/Cr_2O_3), the values corresponding to maximum velocity are 2.66 and 18.5 mm/s, respectively. Figure 8.2b, c shows variation in the combustion temperature of samples having xB/Cr_2O_3 and xB/Cr_2O_3-2Al. At x = 6, the values corresponding to combustion

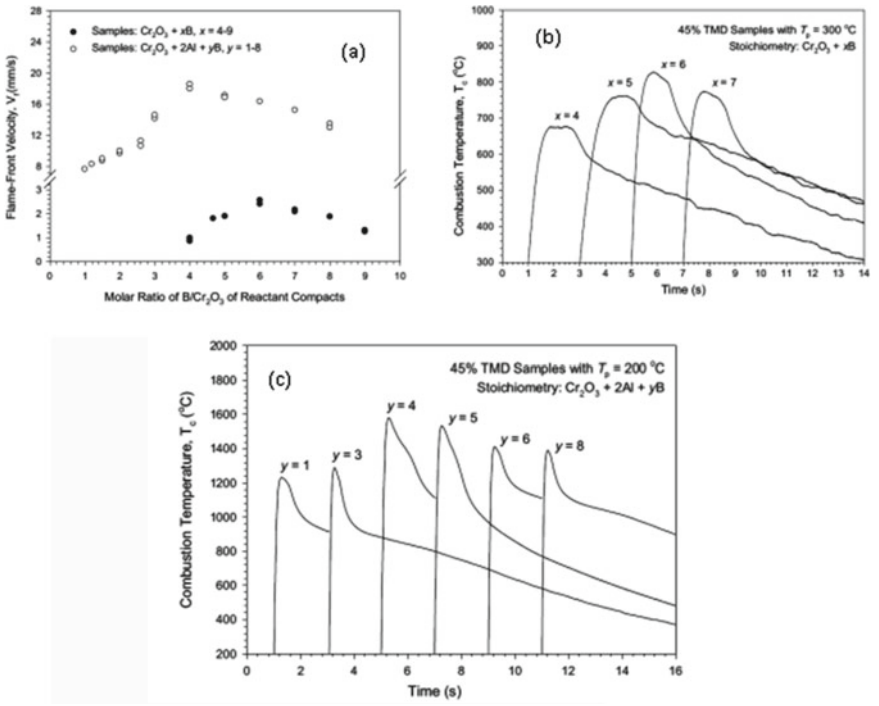

Fig. 8.2 **a** Change of flame-front propagation velocity of Cr_2O_3–B and Cr_2O_3–Al–B powder compacts with molar ratio of B/Cr_2O_3. **b** Variation in combustion temperature of powder compacts with stoichiometry of Cr_2O_3 + xB. **c** Variation in combustion temperature of powder compacts with stoichiometry of Cr_2O_3 + 2Al + yB. Reproduced with permission from Elsevier Publishers [43]

temperature are 830 and 1420 °C, respectively. In most cases, higher amount of boron power is added because some of B atoms got loss during high-temperature reaction (it vaporizes as B_2O_3).

8.2.6 Mechano-Chemically Assisted Preparation

By mixing metal and boron amorphous power in ball-milling apparatus, metal borides can be prepared even at room temperature [46]. This method is known as mechano-chemically assisted preparation of compounds. In presence of air/oxygen, the reaction is exothermic. To avoid oxidation, the reaction is carried out in a glove box filled with argon gas. For example, NbB_2 has been prepared by mixing molar ratio of Nb and B at 1:2. Evolution of phases is determined by X-ray diffraction pattern (Fig. 8.3). Initially, Nb peaks are observed, and no B peaks could be observed due to amorphous nature. After ball-milling for 5 h, a slight shift in position of peaks at lower 2θ is

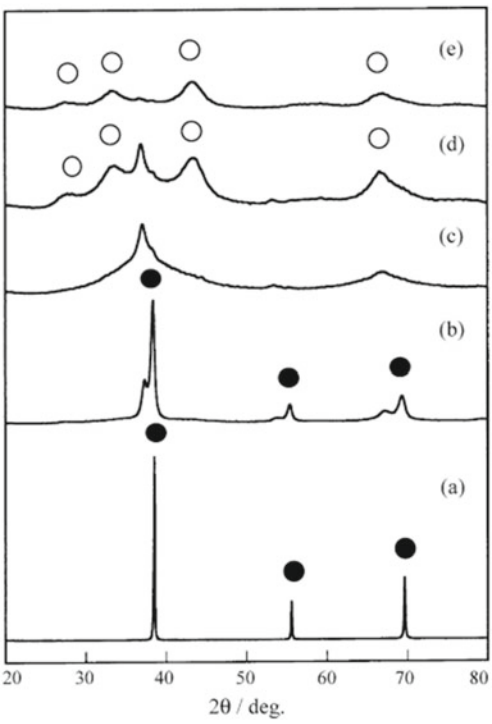

Fig. 8.3 Effect of milling time for Nb–B (1:2) mixture and their X-ray diffraction patterns with milling time of **a** 0 h, **b** 5 h, **c** 10 h, **d** 20 h and **e** 50 h. Here, diameter of ball is 5 mm. Symbols (•) and (o) represent evolution of the phases of Nb and NbB_2, respectively. Reproduced with permission from Elsevier Publishers [46]

observed. This is due to expansion of Nb lattice after incorporation of small amount of B into interstitial sites of lattice. At 10 h, broadening of peaks is observed with no formation of Nb–B phase. At 20 h, the formation of NbB_2 started, but peaks are broad. At 50 h, the highly crystalline phase of NbB_2 is observed.

8.2.7 Reduction Process of Metal Salts with Borohydrides ($LiBH_4$, $NaBH_4$, KBH_4)

When most transition metal salts are reacted with borohydrides, metal borides can be formed in inert environment (say Ar/N_2) [47]. Since the reaction is exothermic, it is preferred to perform in cold environment (say ice bath). Usually, as-prepared compound is amorphous. Upon heating at higher temperature (400–600 °C), it becomes crystalline. Depending on oxygen content or in normal air, association or formation of metal nanoparticles is observed. In water medium, Co_2B and Ni_2B can be formed under Ar atmosphere in case of Co^{2+} and Ni^{2+} salts with borohydride; and Fe nanoparticles are formed in case of Fe^{2+}/Fe^{3+} with borohydride. In dimethyl ether medium (commonly known as diglyme), FeB, Fe_2B can be formed, whereas Co nanoparticles or mixture of Ni, Ni_2B, Ni_3B are formed in inert environment.

However, Cu^{2+}/Cu^{+} salts do not form borides. Instead, it forms Cu nanoparticles. These are due the variation in reduction potentials (E^{o} values of Fe^{3+}, Fe^{2+}, Co^{2+}, Ni^{2+}, Cu^{2+} are -0.04, -0.44, -0.28, -0.23 and $+$ 0.34 V, respectively). In air, chance of formation of metal oxides is high (particularly for Fe/Fe_xO_y, Co/Co_xO_y).

In aqueous medium, Cu^{2+}undergoes the following reaction:

$$2Cu^{2+}(aq) + 4BH_4^-(aq) + 12H_2O \rightarrow 2Cu(s) + 14H_2 + 4B(OH)_3$$

In non-aqueous medium (say dimethyl ether = diglyme), Cu^{2+} undergoes the following possible reaction:

$$2Cu^{2+}(\text{diglyme}) + 4BH_4^-(\text{diglyme}) \rightarrow 2Cu(BH_4)_2(\text{diglyme})_n$$
$$2Cu(BH_4)_2(\text{diglyme})_n \xrightarrow{\Delta,90\,^{\circ}C} 2Cu(s) + 2H_2 + 2B_2H_6$$

Whereas Ni^{2+}undergoes the following reaction in aqueous medium:

$$2Ni^{2+}(aq) + 4BH_4^-(aq) + 9H_2O \rightarrow Ni_2B(s) + 12.5H_2 + 3B(OH)_3$$
$$4Ni_2B(s) + 3O_2 \rightarrow 8Ni + 2B_2O_3$$

Ni^{2+}undergoes the following possible reaction in non-aqueous medium (diglyme):

$$2Ni^{2+}(\text{diglyme})_n + 4BH_4^-(\text{diglyme})_n \rightarrow 2Ni(BH_4)_2(\text{diglyme})_n$$
$$2Ni(BH_4)_2(\text{diglyme})_n \xrightarrow{\Delta,90\,^{\circ}C} 0.5Ni_2B(s) + Ni(s) + 3.5H_2 + 1.5B_2H_6$$
$$Ni_2B(s) + Ni(s) + O_2 \rightarrow Ni(s) + NiO(s) + B_2O_3$$

8.2.8 Deposition from a Reactive Vapor Phase (Thin Films or Single Crystals or Polycrystals)

A reactive vapor phase indicates the vapor phase of molecules or atoms or clusters, which are precursors for the formation of compound/product in the form of thin films or single crystals or polycrystalline. This makes compound from gas states of components/precursors. In case of metal borides, either metal or boron or both are brought to gaseous state. In case of boron or boron precursors in gaseous state, substrate will be metal. If both are gaseous state, the substrate of same metal or other materials (e.g., steel, silicon, indium tin oxide) is used. The deposition of gaseous state requires a particular temperature (known as deposition temperature) so that precursor can decompose to form uniform, crystalline compounds of metal borides. Sometimes, after deposition, appropriate heat treatment is given to get higher crystallinity. Depending on deposition temperature or substrate orientation or nature of precursors or environment of reactor (type of gas, ultrasonic vibration, etc.), the

different compositions of metal/boron with preferred orientation of crystals (i.e., film or single crystals or polycrystals) or amorphous state can be prepared. Besides, there is another method of deposition where vaporization of metal borides (powder or film) is done using physical means, and they are condensed on substrate to get different phases of metal borides with ultra-thin (or the required thickness) of film, coating. The different methods on basis of vapor phase are named as chemical vapor deposition (CVD), ultrasound-assisted chemical vapor deposition (UCVD), noble metal-catalyzed CVD known as vapor–liquid to liquid–solid (VLS), pulsed laser deposition (PLD), molecular beam epitaxy (MBE), single-source CVD, electron beam-induced deposition (EBID), arc plasma in liquid phase, physical vapor deposition (PVD), etc. [4].

Deposition of metal borides (TiB_2) on substrate improves anti-corrosion property and hardness of substrate. Using chemical vapor deposition (CVD), TiB_2 can be prepared using $TiCl_4$, BCl_3, H_2 and Ar sources. Here H_2 and Ar are used as carrier for $TiCl_4$ and BCl_3 precursors [4, 48]. In order to reduce deposition temperature or to change microstructure and particle size of deposited material, ultrasound of different frequency and power can be applied. Since ultrasound is used, the method is known as UCVD. Generally, the three different frequencies (9.5, 22.5 and 55 kHz) with power (0–300 W/cm^2) are used. Figure 8.4 shows the schematic view of UCVD apparatus in which the ultrasound frequencies at 9.5, 22.5 and 55 kHz vibrations are employed and reactor (substrate region where chemical deposition will occur) is also shown. Vapor of $TiCl_4$ maintained at 70 °C is carried by H_2 gas, whereas vapor of BCl_3 is produced by passing Cl_2-Ar gas over B_4C at 700 °C. Vapor of $TiCl_4$ and BCl_3 is coming to substrate (carbon steel), and deposition starts over substrate. The preferred orientation of TiB_2 film (crystals) depends on molar ratio (r) of $TiCl_4/BCl_3$ and deposition temperature (T_d). The (110) plane preferred orientation exists at $T_d > 1000$ °C and $r \leq 15$. At $r = 8.0$, the (100) plane preferred orientation exists at $T < 1000$ °C. The crystallite size decreases with decrease of deposition temperature up to 750 °C. Figure 8.5a, b show the XRD patterns of TiB_2 films prepared at $r = 8.0$ and $T_d = 1100$–700 °C and standard TiB_2 (ASTM, American Society for Testing and Materials). The uniform films of TiB_2 are formed for $r = 4$–8 and $T_d = 850$–1050 °C. The particle size of 10–40 μm can be prepared. Due to ultrasound effect (cavitation effect), a dense and tight film of columnar structure can be prepared. With increase of power or decrease of frequency, the particle size tends to decrease. A film of 100 μm thickness can be grown on carbon steel substrate. Adherence strength of ≥ 60 kg/cm^2 is found in films. The room-temperature Vickers hardness in the range 3600–4000 is observed.

In order to grow materials in one direction (1D, single crystals), it is necessary to add catalyst like noble metal nanoparticles. The noble metal nanoparticles (M_{noble} = Pd, Pt, Au, Ag) are dispersed over substrate (Si or MgO). Vapor of components of compound (M_aB_b) to be formed is passed to substrate using carrier gases (Ar, H_2). At initial stage, a eutectic phase of M_a–M_{noble}–B will be formed and this is liquid state. Then after cooling, it becomes solid. The process continues from vapor–liquid to liquid–solid. This process can prepare spherical or 1D particles depending on

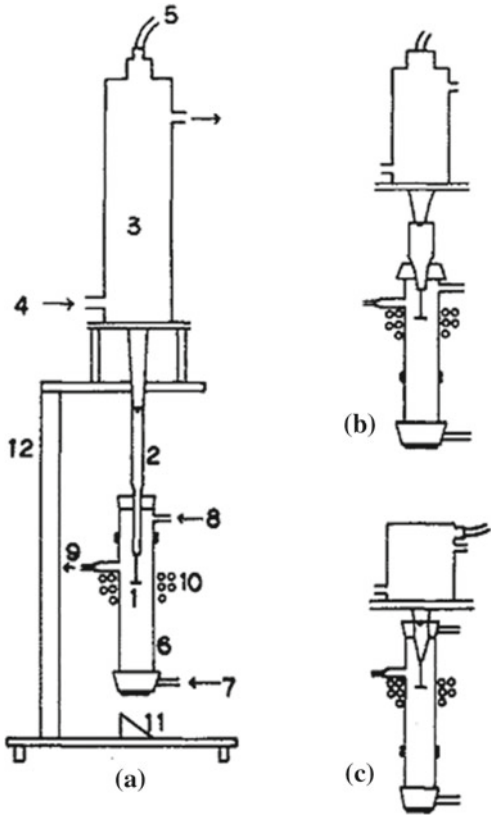

Fig. 8.4 Schematic diagram of UCVD apparatus (three different kHz frequencies are employed): **a** whole view of 9.5 kHz ultrasonic CVD apparatus: (1) substrate, (2) horn, (3) vibrator, (4) cooling water, (5) to oscillator, (6) quartz reactor, (7) $TiCl_4$ + BC_{l3} + H_2 + Ar, (8) H_2, (9) outlet, (10) rf induction coil, (11) mirror, (12) stand. **b** 22.5 kHz and **c** 55 kHz ultrasound vibrator and reactor. Reproduced with permission from Elsevier Publishers [48]

deposition temperature, type of catalyst and precursors used. This is known as metal-catalyzed CVD (known as VLS) [4, 49, 50]. Here, boron source (dodecaborane) is passed through rare-earth metal chloride ($RECl_3$), which is kept at 700–850 °C using Ar/H_2 gases (carrier). Vapor of $RECl_3$ and dodecaborane interacts with noble metal nanoparticles, which is kept at slightly higher temperature 1000 °C. Here, the melting point of eutectic phase of Pd–B, Pt–B or RE–B has a lower temperature than individual melting point of RE, Pd or B. The schematic diagram of the formation of REB_6 (RE = Y, La, Ce, Pr, Nd, Sm, Gd, Tb, Dy, Ho) is shown in Fig. 8.6 [4]. It is to be noted that these REB_6 compounds are an important class of materials due to their high melting points and interesting physical properties such as superconductivity, semiconductivity, variation in valence electrons, metal to insulator transition and low work function. For example, LaB_6 has melting point of 2200 °C and low work function of 2.68 eV. This compound is insoluble in water and hydrochloric acid and stable in vacuum [51]. Because of low work function, this is used for electron emitter as cathode in transmission electron microscope.

As compared to Au or Pt catalyst, Pd is used for the synthesis of hexaborides (REB_6) at lower deposition temperature since B or RE can interact with Pd easily

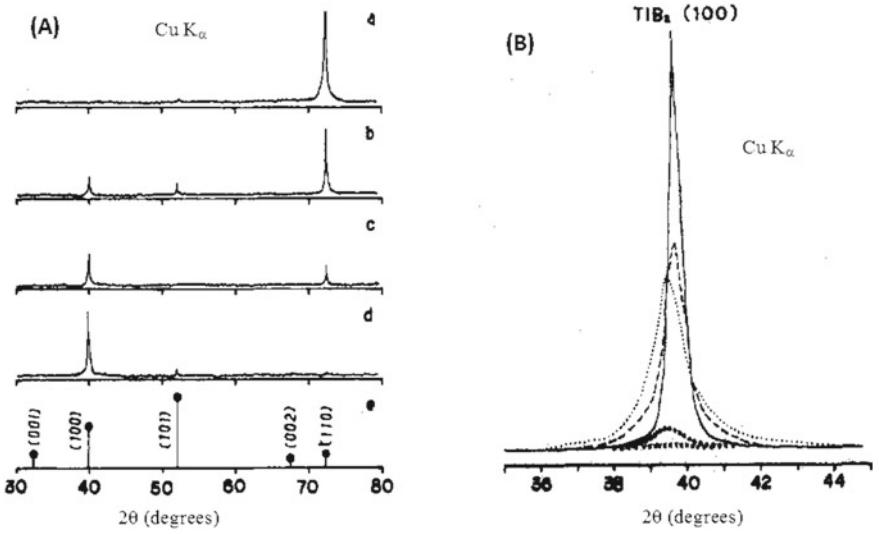

Fig. 8.5 **A** X-ray diffraction patterns of vapor-deposited films. Mole ratio, $r = 8.0$; deposition temperature (in °C): **a** 1100, **b** 1050, **c** 1000, **d** 950, **e** ASTM TiB_2. **B** Variation of (100) diffraction line of TiB_2 film obtained at different deposition temperatures (in °C): (—) 900, (— — —) 850, (•••) 800, (ooo) 750, (xxx) 700. Cu K_α was used as source. Reproduced with permission from Elsevier Publishers [48]

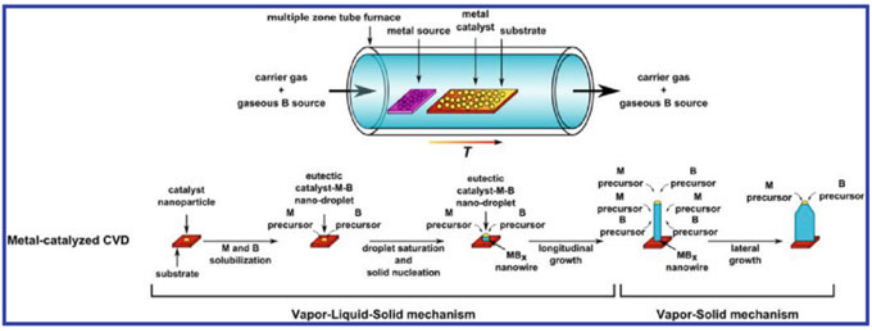

Fig. 8.6 Schematic diagram of a metal-catalyzed CVD process for the synthesis of metal hexaborides (MB_6) nanostructures. Reproduced with permission from ACS Publishers [4]

compared to Au or Pt (Au–B or Au–RE or Pt–B or Pt–RE). The possible phase diagram of depicting eutectic melting points of (a) Au–B, (b) Pt–B, (c) Pd–B, (d) Pd–Y and (e) Pt–Y is provided [50].

Without catalyst, metal borides can be prepared by passing B precursor (BCl_3/H_2) over metal substrate. However, in this case, deposition temperature is more than that with noble metal catalyst [4]. Molecular beam epitaxy (MBE) or pulsed laser deposition (PLD) methods can be used to make the films of metal borides [4]. High-energy

beam or pulse laser produces metal vapor; and the metal vapor reacts B precursor and then it forms metal borides. In this way, MgB_2 films can be prepared on appropriate substrate. Metal borides (even amorphous) can be evaporated and deposited on different substrates to form the thin film of different thicknesses, orientations and microstructures. This is commonly known as physical vapor deposition (PVD). Sometimes, combined CVD and PVD are performed to get the desired shape, sizes, orientation and thickness of particles.

Single-source precursors are used to prepare metal borides (MB_2 = Ti, Zr, Hf) on different substrates (glass, silicon) even at 200–250 °C [52, 53]. Some of single-source precursors are $Ti(BH_4)_3$, $Zr(BH_4)_4$ and $Hf(BH_4)_4$ compounds. The synthesis temperature is less than that of solid-state route (above 1200 °C). However, crystallinity is poor up to deposition temperature 500 °C, but improves significantly upon heated above that. The possible reaction is below:

$$Hf(BH_4)_4(s) \rightarrow HfB_2(s) + B_2H_6(g) + 5H_2(g).$$

The preferred orientation of hexagonal crystal structure of HfB_2 on n-type Si (100) is (0001) for deposition temperature T_d = 700 °C and (1010) for T_d = 800 °C (Fig. 8.7) [53]. HfB_2 has characteristic properties such as high melting point (3250 °C), high hardness (29 GPa) and metallic nature (~15 μ-ohm-cm).

Another way to deposit metal borides on substrate without heating is use of high-energetic electron beam. This method is known as electron beam-induced deposition (EBID). In this technique, the vapor of molecules of precursor is used. The tip of ultra-high vacuum scanning tunneling electron microscopy (UHV STM) is used to record image as well as interact with vapor of molecules of precursor. This tip can be moved, transported and fixed. There is a gap between tip and substrate. During exposure of electron beam, molecules start decomposition. Heavy metal/compound is deposited on a substrate. Using this method, nanosized letters or figures or diagram

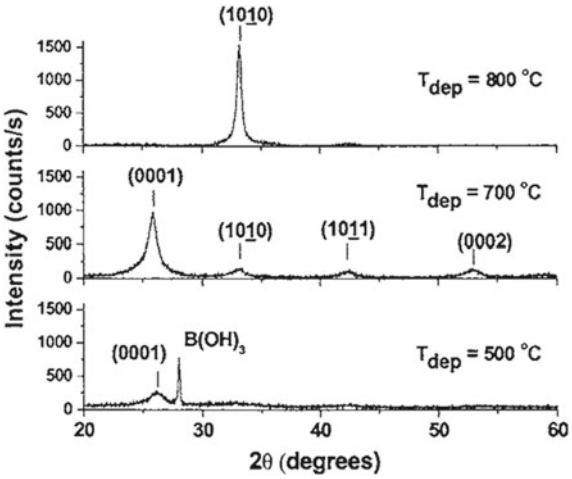

Fig. 8.7 XRD patterns of HfB_2 at different deposition temperatures. Boric acid $B(OH)_3$ crystals are formed when surface boron oxide adsorbs moisture. Reproduced with permission from AIP Publishers [53]

can be written on substrate. Nanodots or wires of HfB_2 have been written on B-doped p-type Si(100): 2 × 1: H using $Hf(BH_4)_4$ precursor [54]. Figure 8.8a shows STM images of HfB_2 nanowires. Here, due to movement of tip, there is an evolution of nanowires as a function of exposure time. Figure 8.8b shows the topographic line contour from (a). Figure 8.8c–f shows the I–V curves of (a 1–4). At initial stage of less exposure time ($t = 80$ s), connection between particles in line (about 5 nm) is not there. This gives semiconducting property in I–V curve. With increase in exposure time ($t = 160$ s), the connection between particles in line is observed and thus it gives the metallic nature in I–V curve. It has aspect ratio of 30/5 (5 nm is diameter at the end of cross section and 30 nm in length). The metallic nature is a characteristic of HfB_2 and this material is considered as a metallic ceramics. When position of tip is fixed, nanodots are formed. With increase of exposure time from 5 to 25 s, there is an increase of nanodots from 5 to 10 nmin size (Fig. 8.9).From I–V curves, it is suggested that nanodots are metallic in nature.

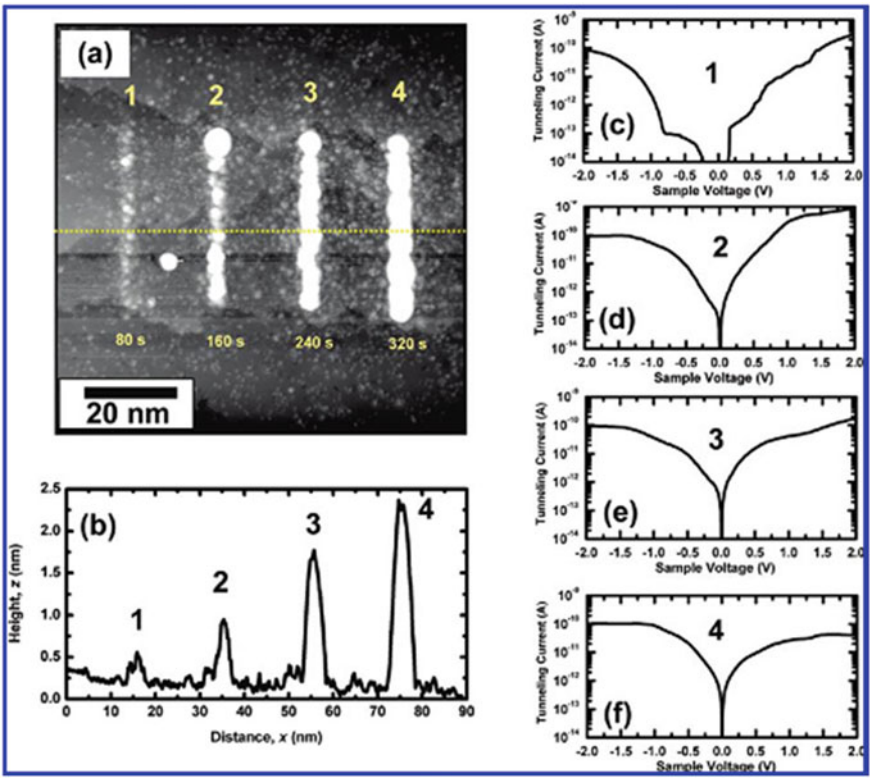

Fig. 8.8 **a** Four HfB_2 nanowires are deposited on the H–Si(100) surface by STM-EBID. Deposition conditions are fixed: sample bias 5 V, I = 1 nA, $Hf(BH_4)_4$ background pressure = 2×10^{-9} Torr; **b** STM topographic line contour is from (**a**) and (**c**–**f**) average I–V tunneling spectra for wires 1–4 shown in (**a**). Reproduced with permission from ACS Publishers [54]

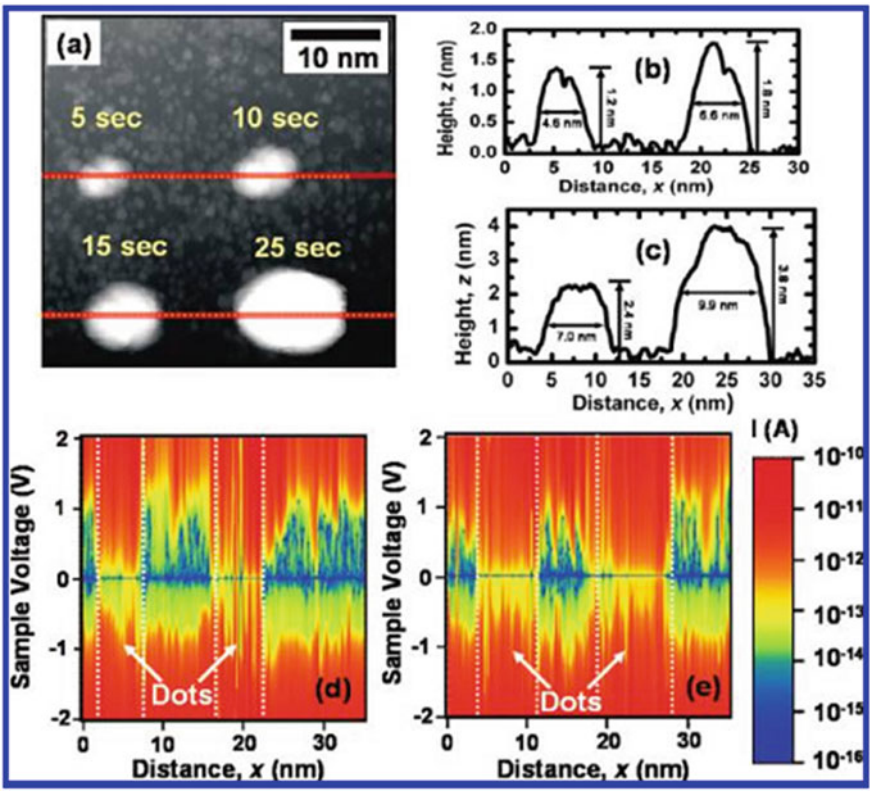

Fig. 8.9 **a** STM topograph of four HfB_2 dots is deposited by STM-EBID. Deposition conditions are fixed: sample bias = 5 V, I = 1 nA, $Hf(BH_4)_4$ pressure = 4×10^{-6} Torr. The writing time for each dot is 5, 10, 20 and 25 s, respectively. The STM line contours are plotted for (**b**) the top two dots and for (**c**) the bottom two dots. Log I–V spectra are plotted as a function of position for (**d**) the top two dots and (**e**) the bottom two dots. Dotted red lines in (**a**) denote where the I–V maps were obtained. Reproduced with permission from ACS Publishers [54]

Vapor deposition of MgB_2 on substrate using arc plasma in inert liquid (Ar or N_2) can form nanotubes of MgB_2 (single and multiwall) [55]. This is similar to PVD. The schematic diagram of experimental set up is shown in Fig. 8.10. Initially, MgB_2 powders are packed into hollow Mo rod (outer diameter = 6 mm, inner diameter = 3 mm, depth of the hole = 3 mm), which is submerged in liquid Ar, and this hollow Mo rod acts as an anode. A thicker Mo rod (diameter = 10 mm) is used as cathode. When two electrodes are connected to a direct-current welding power supply, it generates arc plasma. Due to high thermal heat, crystals of MgB_2 in the anode hole are evaporated and deposited over surface of cathode (Fig. 8.11). Under electron microscopy, single wall and multiwall nanotubes are observed (diameter = 6.0 nm, length = 45.7 nm and diameter = 11.2 nm, length = 63.0 nm) (Fig. 8.12). Possible reason to explain the formation of nanotube is self-curling mechanism.

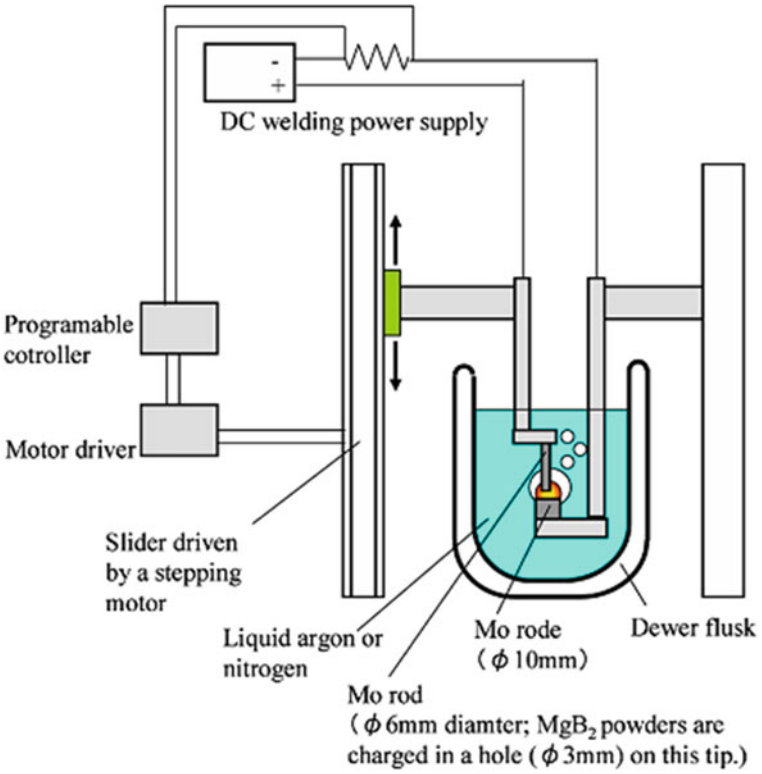

Fig. 8.10 Apparatus using arc plasma in liquid is to synthesize MgB_2 nanotubes. The anode motion is controlled by a slider driven with a stepping motor. DC welding power supply was used to generate the arc plasma between molybdenum electrodes at discharge current of 120 A. The arc plasma duration time is controlled by lifting the anode to break the arc discharge at a target time. Reproduced with permission from AIP Publications [55]

Also, powder of nanotubes of MgB_2 (5 nm in diameter and 20–25 nm in length) is prepared by hydrothermal method [56]. Here, NaOH is mixed with MgB_2 powder, and the mixture is added to autoclave. At temperature 170–200 °C, it is kept for 24–200 h to get homogenous nanotubes of MgB_2. The product is neutralized by adding HCl and finally is washed with water.

8.2.9 Single-Source Precursor Route

In the single-source precursor route, a single compound or complex is used to prepare metal particles or metal borides/nitrides/carbides/phosphides/sulfides/oxides as main products. First time, $Th_{1.0}B_{3.83}$ (metal boride) was prepared by thermal decomposition of single-source precursor $Th(BH_4)_4$ at 300 °C in the year 1949 by Haekstra and

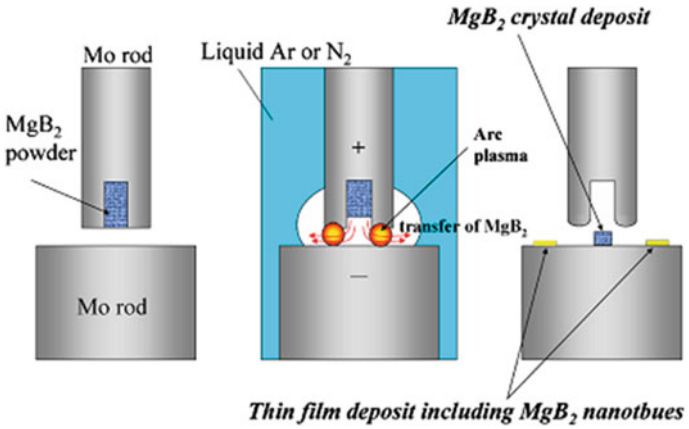

Fig. 8.11 Schematic representation of arrangement and shapes of molybdenum electrodes, and locations of the arc plasma and thin-film products. Left: Before arc discharge. Middle: Location of arc plasma between electrodes. Right: Location of products. Reproduced with permission from AIP Publishers [55]

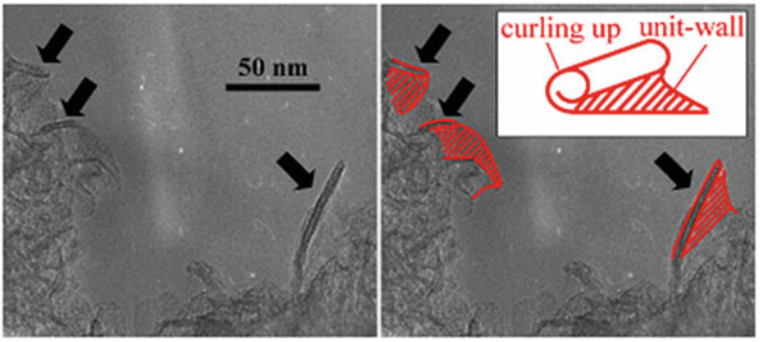

Fig. 8.12 TEM image of the curled edges of MgB_2 particles and schematic image of the curling. Reproduced with permission from AIP Publishers [55]

Katz [57]. Authors also prepared borohydrides of Th, U, Ti, Hf, Zr and studied their thermal properties such as melting point, boiling point, heat of vaporization, heat of sublimation and heat of fusion. In 1988, the films of pure metal diborides (TiB_2, ZrB_2, HfB_2) were prepared from the respective single-source precursor [52, 58, 59]. A large number of metal borides (MgB_2, CrB_2, AlB, Fe_3B, Fe_2B, FeB) prepared by single-source precursor route have been reported by many authors [60–64].

Sometimes, oxygen or carbon impurities are associated along with metal borides if precursor molecule contains C or O atoms. Low-temperature preparation (<500 °C) usually forms amorphous nature, whereas high-temperature preparation forms crystalline phase. Some of examples of precursor molecules are $Ti(BH_4)_3(dme)$ (where dme = 1,2–dimethoxyethane = $CH_3–O–CH_2–CH_2–O–CH_3$) (Fig. 8.13,

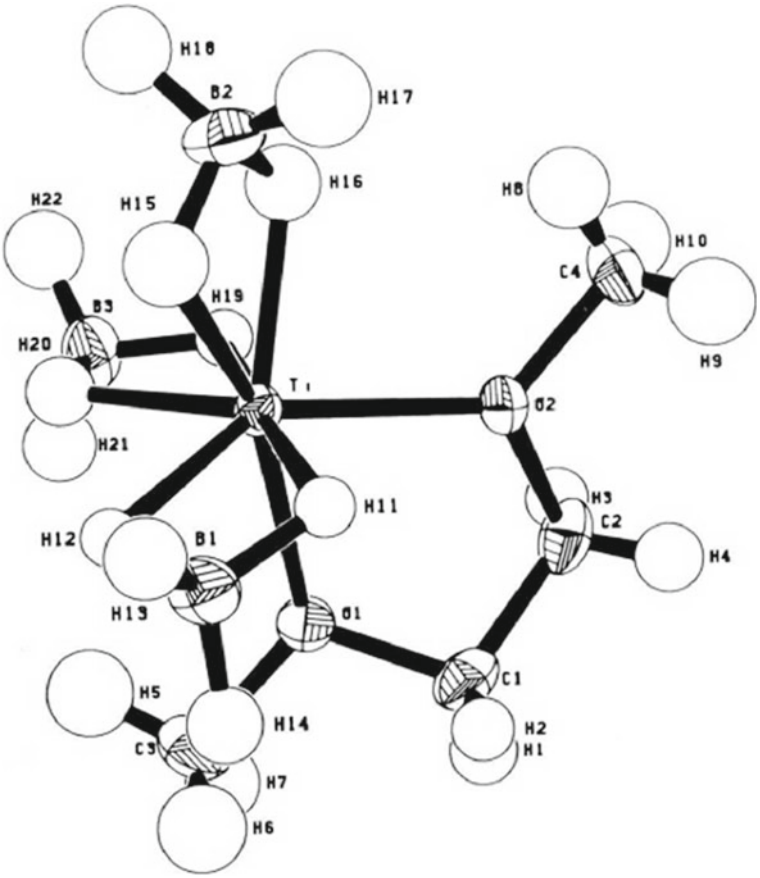

Fig. 8.13 Molecular structure of $Ti(BH_4)_3(dme)$ where dme = 1,2-dimethoxyethane = CH_3–O–CH_2–CH_2–O–CH_3. Reproduced with permission from ACS Publishers [52]

[52]), $Zr(BH_4)_4$ [65], $Hf(BH_4)_4$ [59, 66], $Cr(B_3H_8)_2$ and related octahydrotriborate complexes (Fig. 8.14a–d, [64]), $Mg(B_3H_8)_2$ and its etherates (Fig. 8.15a, b, [60]), $Al(BH_4)_3$, $HfFe_3(CO)_9BH_4$ (Fig. 8.16 [63]), etc.

8.2.10 Nanostructure Formation in 0D, 1D, 2D and 3D Ways

If the particles are spherical with size of a few nanometer, it is considered as 0D (i.e., electrons are confined in all *x*-, *y*-, *z*-axes). Here, symbol "D" refers dimension. If the particles are rod-, wire- and tube-type structure (diameter = nanometer (less than 50 nm); length = nanometer to micrometer), it is considered as 1D (electrons are confined in two of axes). If the particles are planner-type structure, it is considered

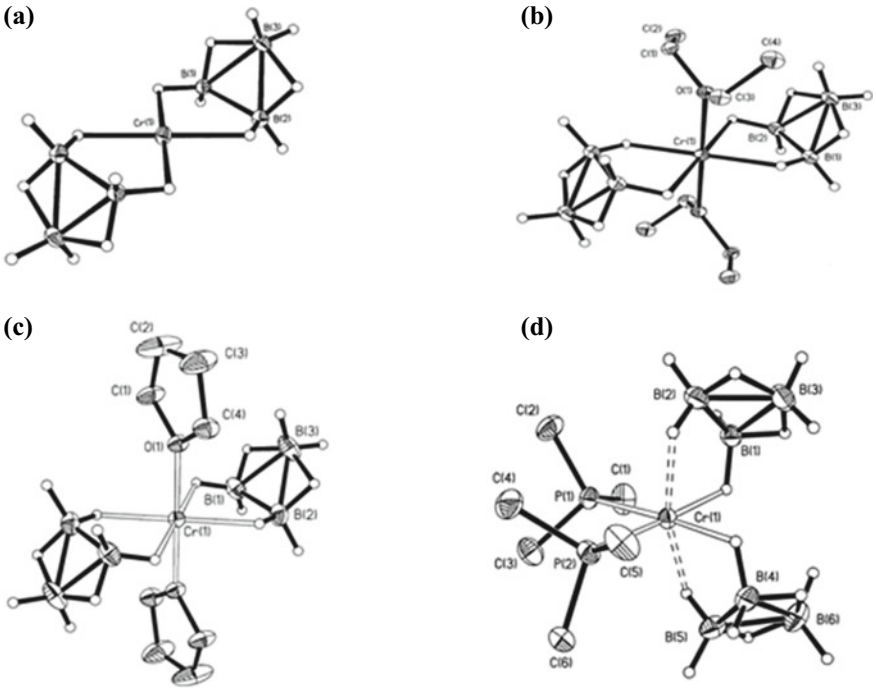

Fig. 8.14 **a** Molecular structure of $Cr(B_3H_8)_2$ (2). The ellipsoids are drawn at 30% probability level, except for hydrogen atoms, which are represented as arbitrary-sized spheres. **b** The molecular structure of $Cr(B_3H_8)_2(Et_2O)_2$ (3). The ellipsoids are drawn at 30% probability level, except for hydrogen atoms, which are represented as arbitrary-sized spheres. **c** The molecular structure of $Cr(B_3H_8)_2(thf)_2$. The ellipsoids are drawn at 30% probability level, except for hydrogen atoms, which are represented as arbitrary-sized spheres. **d** The molecular structure of $Cr(B_3H_8)_2(PMe_3)_2$. The ellipsoids are drawn at 30% probability level, except for hydrogen atoms, which are represented as arbitrary-sized spheres. Reproduced with permission from ACS Publishers [64]

as 2D (electrons are confined in one of axes). If size of particle is so large (a few microns) with any shape, it is considered as 3D (electrons are confined in none of axes).

Metal borides prepared by above-mentioned routes (2.1–2.9) can have particle size varying from micron to nanometer. The particle size depends on the kinetics of nucleation process and the growth process during the course of reaction. Syntheses of nanosized particles of metal borides by borohydride reduction method [47, 67, 68], micelle method [69, 70], surfactant/ligand stabilized route [68, 71], molten salt route [72, 73], direct solid-state route [74], ball-milling method or mechano-chemical route [61, 73, 75], core–shell formation route (say silica coating) [76, 77], RF thermal plasma route [78–80] have been reported. Also, thin films of metal borides in nano-sized particles have been prepared by electron beam-induced deposition (EBID) [54], arc plasma in inert liquid [55], reactive vapor phase reaction [4, 48], etc.

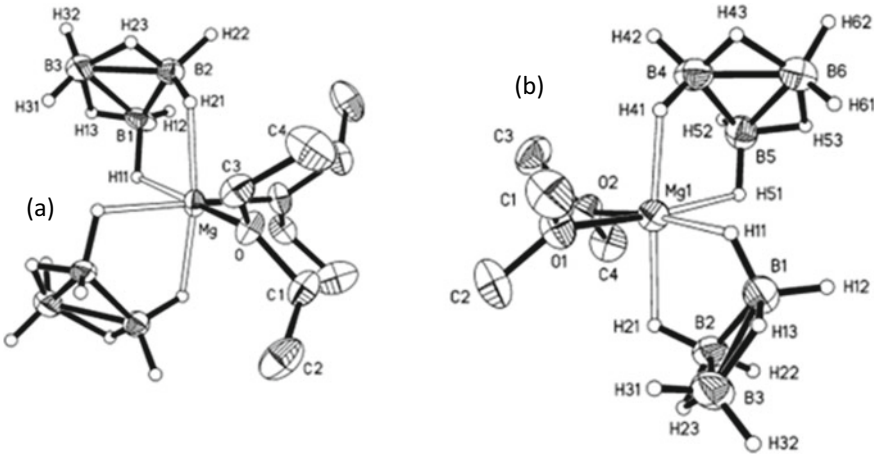

Fig. 8.15 **a** Molecular structure of (2). The ellipsoids are drawn at 35% probability level, except for hydrogen atoms, which are represented as arbitrary-sized spheres. Methyl and methylene hydrogen atoms have been deleted for clarity. **b** The molecular structure of $Mg(B_3H_8)_2(Me_2O)_2$ (3). The ellipsoids are drawn at 35% probability level, except for hydrogen atoms, which are represented as arbitrary-sized spheres. Methyl and methylene hydrogen atoms are deleted for clarity. Reproduced with permission from ACS Publishers [60]

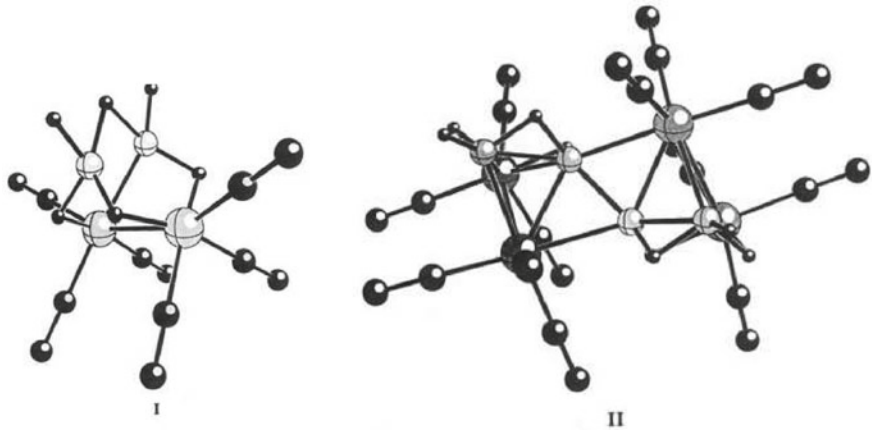

Fig. 8.16 Molecular structure of (I) $B_2H_6Fe_2(CO)_6$, (II) $[B_2H_4Fe_2(CO)_6]_2$ using ball and stick models. Reproduced with permission from ACS Publishers [63]

The Fe–Co–B amorphous phase having particle size of 30 nm has been synthesized by reduction of Fe^{2+}, Co^{2+} by $NaBH_4$ at Ar atmosphere at room temperature [68]. Using reversed micelle route (AOT-water- isooctane = surfactant-water–oil), highly uniform-sized Ni_2B nanoparticles (5–6 nm) are prepared from $NiCl_2$, sodium bis(2-ethyl-hexyl)-sulfosuccinate (AOT) and sodium borohydride ($NaBH_4$)

[70]. The reaction is carried out in inert N_2/Ar atmosphere. Finally, another surfactant (trioctylphosphine = TOP) is added to micelle medium to coat Ni_2B nanoparticles. AOT is removed by washing with ethanol. Black precipitate Ni_2B coated with TOP is collected by centrifugation. If the experiment is performed in open air, it forms Ni nanoparticles along with Ni_2B nanoparticles. Figure 8.17 shows TEM images of nanoparticles prepared in open air (A, C) and in N_2 atmosphere (B, D) [70]. In molten salt route, eutectic mixture is used to make reaction medium for the formation of compound. Mixture of LiCl–KCl (45:55 wt%) has a melting point at 335 °C (eutectic point) [72]. Different ratio of metal chloride and $NaBH_4$ is mixed with LiCl–KCl and ground and heated at 700–900 °C in inert Ar atmosphere [81]. The residue is washed with deionized water to remove unwanted LiCl, KCl, NaCl. Then, the remaining sample is dried under vacuum. In this way, nanosized particles of NbB_2 (5–10 nm), CaB_6 (10 nm), CeB_6 (8 nm), MoB_2 (4 nm) are prepared. NbB_2 and CaB_6 are prepared by heat treatment during 4 h under argon flow of (a) $NbCl_5$:$NaBH_4$ and (b) $CaCl_2$:$NaBH_4$ mixtures in the eutectic salt LiCl/KCl at respective temperatures of 900 and 800 °C [81]. The Co–M–B (M = Fe, Ni) nanoparticles are prepared at 650 °C using molten salt route [82]. The core–shell formation is one of routes to prepare non-agglomerated particles. Metal borides in nanosized form (Fe_2B with size of 90 nm) are coated with SiO_2 layer (4 nm) by reduction of $FeCl_3$ or $FeSO_4$ in

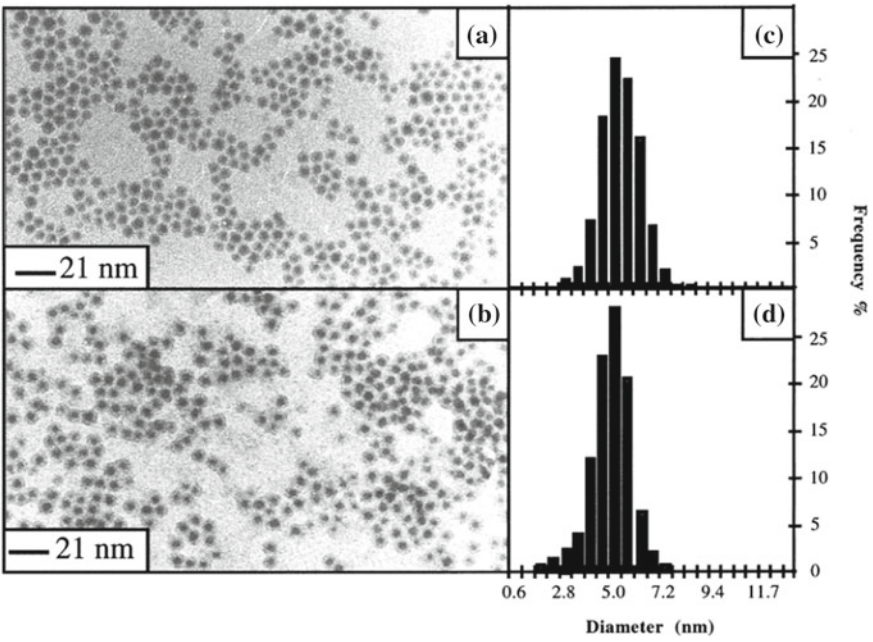

Fig. 8.17 Size distribution and TEM patterns of Ni_2B nanoparticles are obtained in open air (**a** and **c**) and under nitrogen (**b** and **d**). Spontaneous self-assembly is obtained by depositing a drop of solution on a TEM grid coated with amorphous carbon. Reproduced with permission from ACS Publishers [70]

$NaBH_4$ in inert N_2 followed by addition of ethanol-TEOS (tetra ethyl orthosilicate) solution [77]. Nanoparticles of metal borides are prepared by injecting metal–boron mixture powder into thermal plasma flame [78, 79], and the schematic diagram for the formation of metal borides using thermal plasma flame is provided [80].

8.3 Physical Properties

8.3.1 Magnetism

Metal borides (M_xB_y, M = Mn, Fe, Co, Ni) exhibit the magnetic properties from paramagnetic, antiferromagnetic to ferromagnetic behavior [4]. For example, orthorhombic phase FeB with lattice parameters $a = 4.061$ Å, $b = 5.506$ Å and $c = 2.952$ Å out of many phases of Fe–B system is ferromagnetic at room temperature with the Curie temperature T_C ~ 325 °C [83]. The magnetocrystalline anisotropy (MCA) energy (E_A) for orthorhombic crystal in Cartesian coordinates is given by relation:

$$E_A = K_1\cos^2\alpha + K_2\cos^2\beta + K_3\cos^2\gamma$$

where K_1, K_2 and K_3 are the magnetocrystalline anisotropy constants. The α, β and γ are the angles between the direction of vector I_s (saturation magnetization) and OX, OY and OZ axes of the Cartesian coordinate system. There are three crystallographic directions [84], [010] and [001] of orthorhombic structure. To determine the hard and easy magnetic axes, it needs single crystal material (FeB). The vector of I_s is perpendicular to the poles of the electromagnet. Along axis [010], it shows easy magnetization (AEM) and magnetization becomes saturation in a field of about 160 kAm. This is denoted by curve 1 in Fig. 8.18a [83]. Then crystal specimen is oriented in the external magnetic field so that the vector of I_s is parallel to the planes of the poles of the electromagnet. Two maxima at $\theta = 0$ and 180° and two minima at $\theta = 90$ and 270° of the measured signal are over the crystallographic axes [001] and [84], respectively (Fig. 8.18b) [83]. Magnetization-field curves 3 and 2 represent $\theta = 0$ and 90°, respectively. The axis [84] shows the hard magnetization (AHM i.e., curve 2). It becomes saturated in the field of 1440 kAm. The axis [001] becomes intermediate magnetization (AIM, i.e., curve 3). The specific saturation magnetization (σ_s) for the single crystal of FeB is found to be 77 $A.m^2/Kg$ (= 77 emu/g since 1 emu/g = 1 $A.m^2/Kg$). The saturation magnetization ($I_s = d\sigma_s$, where d = density of FeB = 6300 kg/m^3) is found to be 485 kA/m. The effective MCA constants for FeB are ${K_1}^* = K_1 - K_2 = 4.0 \times 10^5$ J/m^3 and ${K_2}^* = K_3 - K_2 = 7.0 \times 10^4$ J/m^3.

When size of particles decreases to a few nanometer ranges, it changes magnetic properties. Sometimes, ferromagnetic particles become paramagnetic or vice versa depending on compensation of net spin moments arising from surface, core, grain boundaries and defects. Bulk FeB is prepared by arc melting of mixture of Fe and

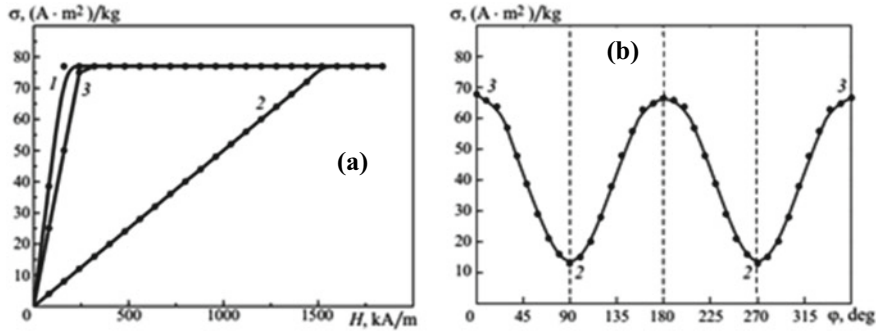

Fig. 8.18 **a** Magnetization curves (σ is the specific magnetization and H is the magnetic field) of a FeB single crystal over the crystallographic directions: (1) [010], (2) [84], (3) [001]. **b** Angular dependence of the specific magnetization (σ) of a FeB single crystal is performed in a field of 40 kA/m in plane (010) perpendicular to the axis of easy magnetization: (2) [84], (3) [001]. Reproduced with permission from Springer Nature Publishers [83]

B powder followed by heating at 1273 K for 24–48 h [73]. Then using ball-milling process as well as capping agent like oleic acid, the different crystallite sizes are prepared at different ball-milling time. The crystallite size decreases with increase of ball-milling time (Fig. 8.19). This is supported by increase of line width in XRD pattern with increase of ball-milling time (t). At $t = 0$ min, the crystallite size is about 77 nm and at $t = 800$ min, the crystallite size is about 18 nm. The field-dependent magnetization (M–H) loops of FeB nanoparticles having different crystallite sizes are shown in Fig. 8.20a. Their coercivity (H_c) and the saturation magnetization (M_s) values are provided in Fig. 8.20b. It is observed that there is a decrease of magnetization value (say about 63 emu/g) with decrease of crystallite size up to 30 nm, whereas H_c increases to 400 Oe. With further decrease to 25 nm, H_c decreases to 200 Oe, whereas Ms increases to 75 emu/g. With further decrease of crystallite size to 17 nm, there is an increase in $H_c = 365$ Oe and decrease in $M_s = 74$ emu/g. It is expected to have $H_c = 0$ Oe (super paramagnetic region) for smallest sized particles, but it does not happen. It is because of exchange bias arising from smallest size particles (ferromagnetic core and surface spin canting as shell). For crystallite size of 17 nm, exchange bias (difference between + ve H_c and –ve H_c) is calculated to be 270 Oe. The crystallite size of 30 nm is considered as single domain limit of FeB. The effective anisotropic constant (K) is calculated from the relation between M_s and coercivity (H_c): $K = 1.56 \times M_s \times H_c$ and this value is found to be 2.4×10^4 J/m^3, which is slightly lower than single crystal, FeB (4×105 J/m^3).

On other hand, bulk Co_2B has ferromagnetic property with saturation magnetization ($\sigma_s = 73$ emu/g) and Curie temperature ($T_c = 435$ K) [85]. Magnetization versus magnetic field (σ–H) at different pressures up to 6 kbar at 4.2 K shows that saturation magnetization is independent of pressure (Fig. 8.21). The magnetic permeability versus temperature curves shows the Curie temperature (T_c), and T_c decreases from

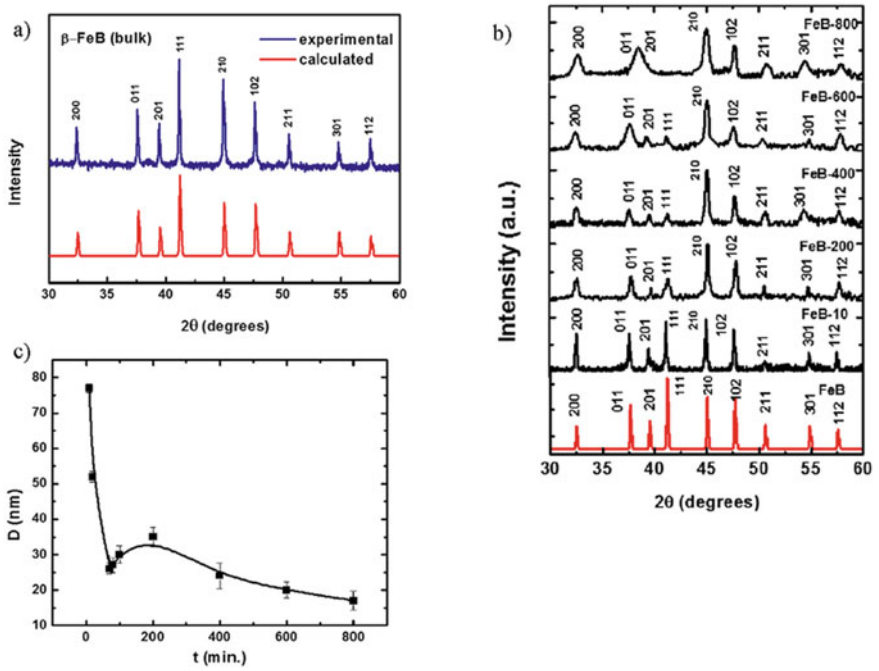

Fig. 8.19 **a** A representative powder X-ray diffraction pattern of an arc-melted β-FeB sample (blue) and the calculated PXRD pattern of β-FeB (red). **b** PXRD patterns of FeB samples ball-milled in n-hexane are recorded at a speed of 500 rpm. The number attached to the sample name indicates the milling time in minutes. **c** Crystallite size (D) is obtained using the Scherrer formula as a function of milling time (t). Reproduced with permission from Elsevier Publishers [73]

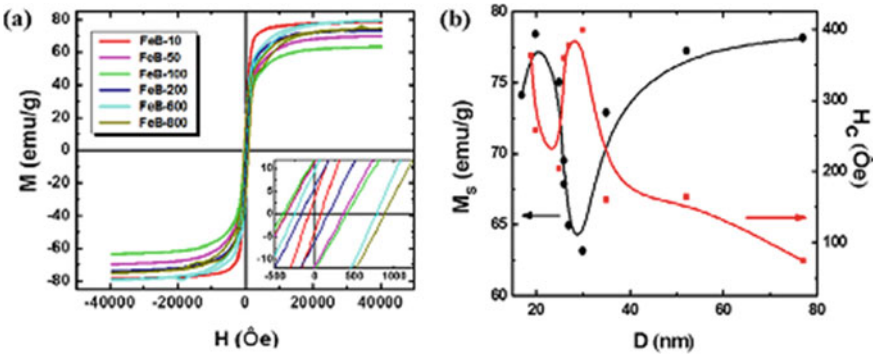

Fig. 8.20 **a** Room-temperature magnetization hysteresis loops of ball-milled FeB samples are obtained at different times (minutes). Inset: the enlarged low-field portion of M–H loops. **b** Saturation magnetization (M_s) and coercivity (H_c) values are extracted from M–H loops for all samples. Reproduced with permission from Elsevier Publishers [73]

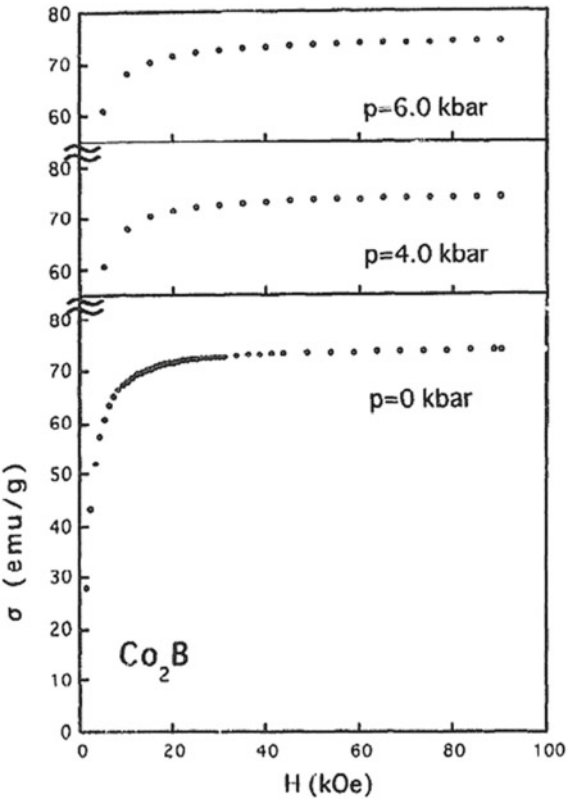

Fig. 8.21 Magnetization curves of Co_2B at 4.2 K are obtained under various pressures. Reproduced with permission from Elsevier Publishers [85]

435 to 430 °C with pressure up to 5.4 kbar (Fig. 8.22). The $\delta T_c/\delta P$ is found to be—1.02 K/kbar. Co_2B has tetragonal structure with lattice parameters ($a = 5.02$ Å, $c = 4.225$ Å). There is a linear thermal expansion in lattice parameter (a), whereas there is a slight increase in lattice parameter (c) than that from the linear extrapolation of the thermal expansion curve at higher temperature (Fig. 8.23a). This happens below the T_c. This is related to the spontaneous magnetostriction. This is reflected in unit cell volume (V) and c/a ratio (Fig. 8.23b).

Co_2B nanoparticles (7–10 nm crystallite sizes) prepared by ball-milling method show the ferromagnetic properties with coercivity ($H_c = 223$–337 Oe) and saturation magnetization ($M_s = 43$–49 emu/g) [75]. The saturation magnetization value is less than that of bulk value (73 emu/g).

In amorphous system of Fe–Co–B, there is a magnetic dipolar interaction among particles. If there is a separation between particles, its magnetization value decreases. This can be proved by dispersion of Fe–Co–B particles in conducting noble metals. Silver (Ag) is highly conducting as well as diamagnetic. When Fe–Co–B ferromagnetic particles are dispersed in Ag nanoparticles, its ferromagnetic behavior becomes different. This was first time shown by Ningthoujam et al. in 2010 [67]. The magnetic

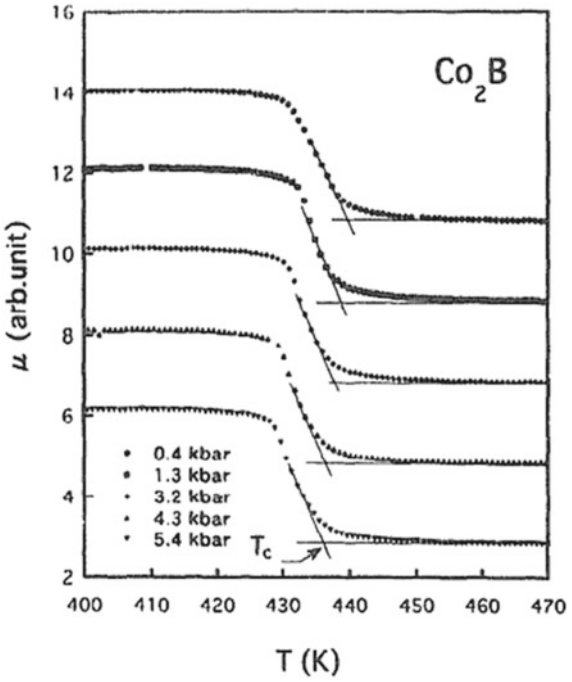

Fig. 8.22 Permeability (μ in arbitrary unit) versus temperature curves are obtained under various pressures for Co_2B. Reproduced with permission from Elsevier Publishers [85]

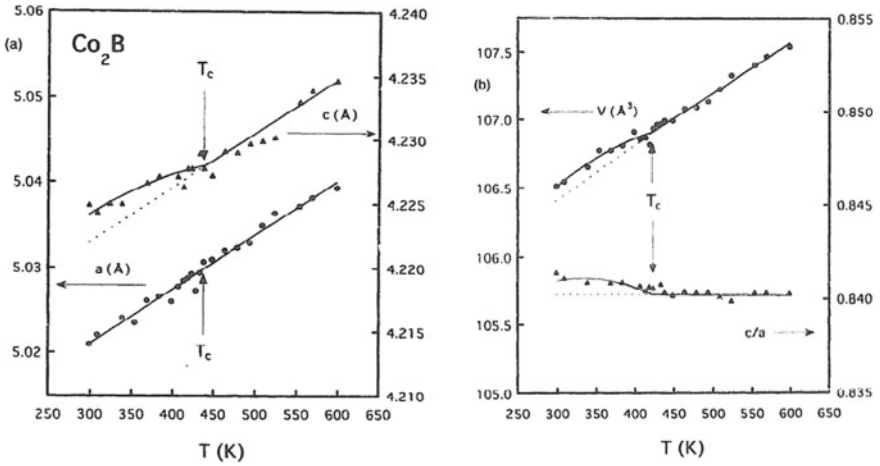

Fig. 8.23 **a** Lattice parameters (*a* and c) against temperature curves for Co_2B. **b** Unit cell volume (V) and lattice parameter ratio (c/a) against temperature curves for Co_2B. Reproduced with permission from Elsevier Publishers [85]

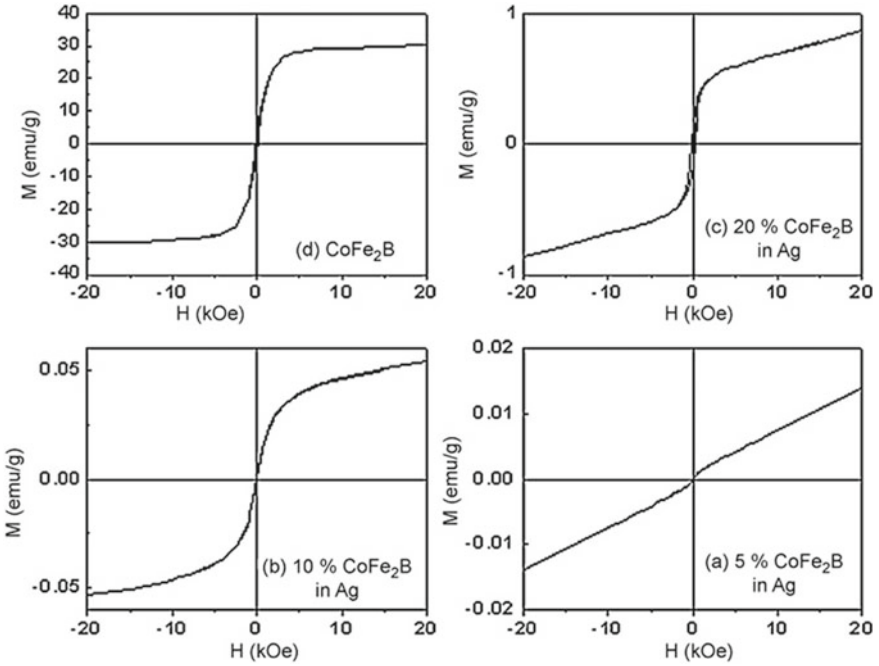

Fig. 8.24 Magnetization against applied field (M–H) for pure Co–Fe–B and Co–Fe–B (wt% 5, 10, 20) in Ag. Reproduced with permission from Elsevier Publishers [67]

dipolar interaction among ferromagnetic particles increases with increase in concentration of ferromagnetic particles in Ag matrix. There is an enhanced increase in magnetization value with a slight increase in concentration of ferromagnetic particles in magnetization-field loops (Fig. 8.24). It does not follow linearity. Similarly, coercivity (H_c) increases with increase of concentration of ferromagnetic particles in Ag matrix (Fig. 8.25). At low concentration of ferromagnetic particles, zero-field cooled (ZFC) and field cooled (FC) magnetizations show that both increase with decrease of temperature (Fig. 8.26). This is similar to paramagnetic behavior, but at high concentration of ferromagnetic particles, ZFC and FC show the ferromagnetic behavior.

8.3.2 Electronic Structure

Boron (B) atom has the ground-state electronic configuration $1s^2$, $2s^2 2p^1$. In the outermost shell, B has three electrons and can form three covalent bonds with other atoms for formation of compounds (e.g., BH_3, BF_3). Still, B in compound has six bonding electrons and thus has deficiency in valence electrons to complete octet of electrons (8 es). In this way, compounds of BA_x (A = other element say H or F) are

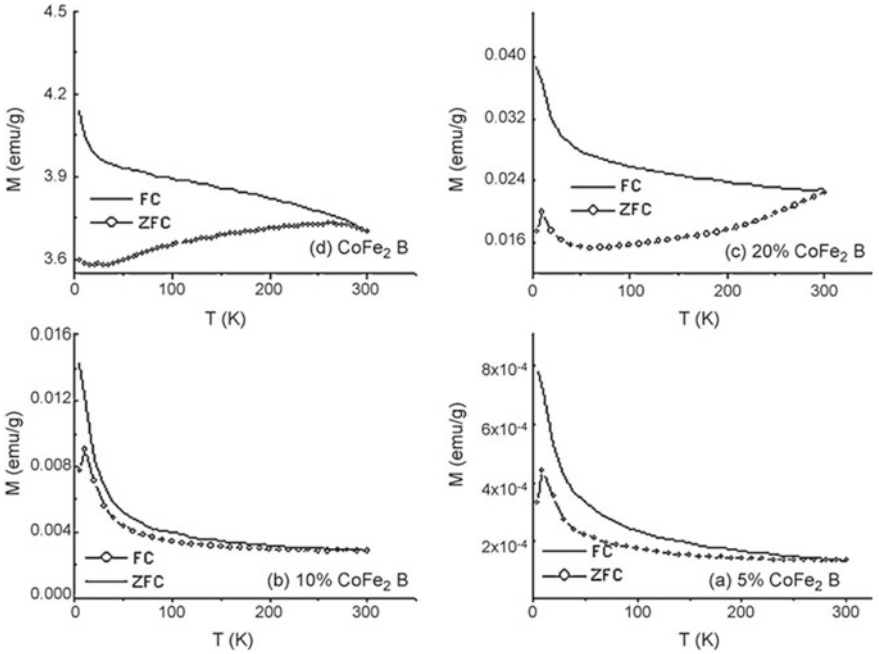

Fig. 8.25 Field cooled (FC, line) and zero-field cooled (ZFC, open circles) magnetization (M–T) curves are obtained at applied field of 25 Oe for pure Co–Fe–B and Co–Fe–B (wt%: 5, 10, 15, 20) in Ag. Reproduced with permission from Elsevier Publishers [67]

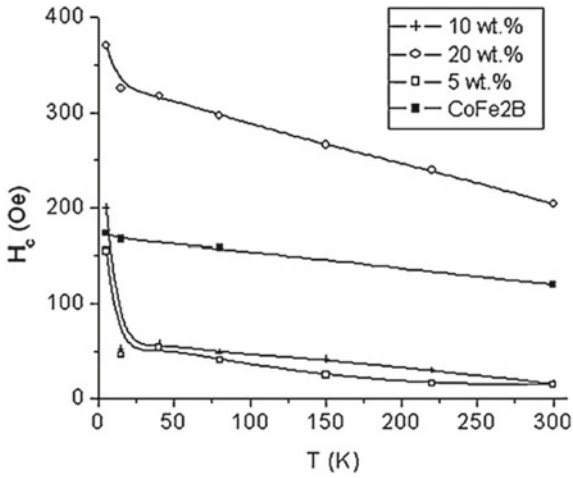

Fig. 8.26 Coercivity (H_c) against temperature (T) for pure Co–Fe–B and Co–Fe–B (wt%: 5, 10, 15, 20) in Ag. Reproduced with permission from Elsevier Publishers [67]

unstable. To make stable, it forms bridging bond with other group of atoms (same or different). For example, B_2H_6 ($H_3B–BH_3$ through 2H bridges) and three atoms B–H–B have 2 es. Another example is $NH_3:BF_3$ ($H_3N: \rightarrow BF_3$ and lone pair of electrons of N is donated to B) [3, 4, 86]. B–B bonds can be of B–B single (one σ type), B = B double (one σ type, one π type) and B≡B triple (one σ type, two π type). The formation of B = B is not preferable since B atom is itself deficient in electrons. B = B double bond can be stabilized by linking with Lewis base ligands ($L \rightarrow HB = BH \leftarrow L$). Similarly, B≡B triple bond can be stabilized by linking with Lewis base ligands ($L \rightarrow B{\equiv}B \leftarrow L$). Examples of L are: NH_3,: C (carbene) containing molecule or ion,: CO, etc. Bond orders of B = B and B≡B are less than 2 and 3, respectively. It is suggested that there are π-back transfer or donation. $L \rightarrow B{\equiv}B \leftarrow L$ can be written as ($L - \overset{\frown}{B{\equiv}B}\overset{\frown}{} - L$ or $L = B = B = L$). In this way, electron rich at B atom by transfer of electrons from L is relieved by π-back transfer or donation from B to L (electron transfer from 2p orbital of B to empty antibonding p orbital of L). Typical B–B bond lengths of the single, double and triple bonds are 1.58–1.93, 1.56 and 1.44 Å, respectively [87–90]. Typical examples of different molecules containing B–B single bond or B–H–B bridge are shown in Fig. 8.27 [87]. The carbenes (:C) are good stabilizing ligands in B-, Al- or Ga-containing compounds. When $RBBr_3$ ($R = :C\{N(Pri)C(CH_3)\}_2$) reacts with KC_8 in

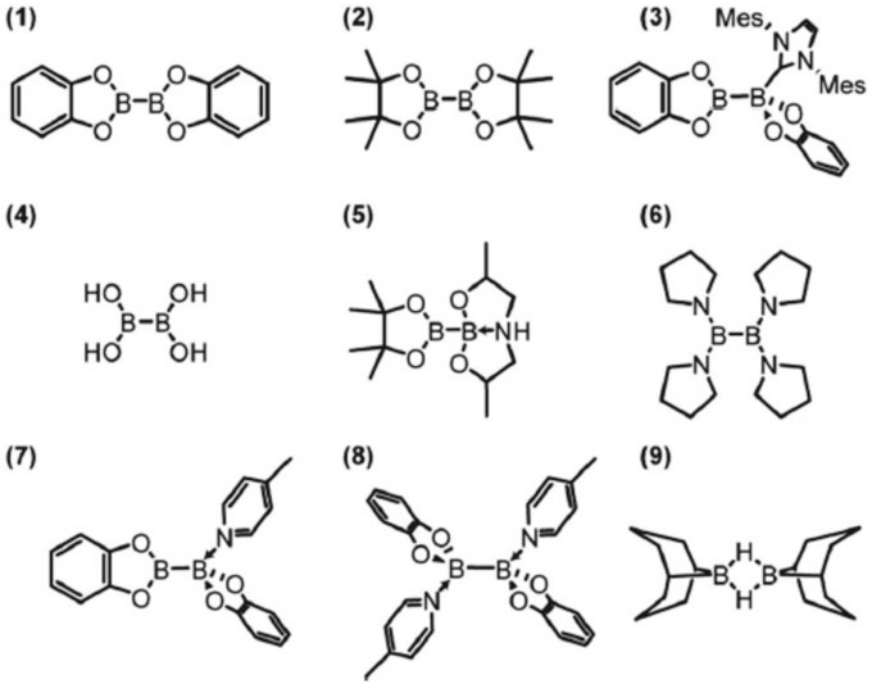

Fig. 8.27 Molecular structures of the different compounds containing the B–B single bond (**1**–**7**) and B–H–B bridge (**8**). Reproduced with permission from RSC Publishers [87]

diethyl ether, two compounds are formed. The first compound is $R(H)_2B–B(H)_2R$ (Fig. 8.28), which is air-stable, colorless block crystals; and the second compound is R(H)B–B(H)R (Fig. 8.29) which is air-sensitive, orange-red sheet-like crystals [88].

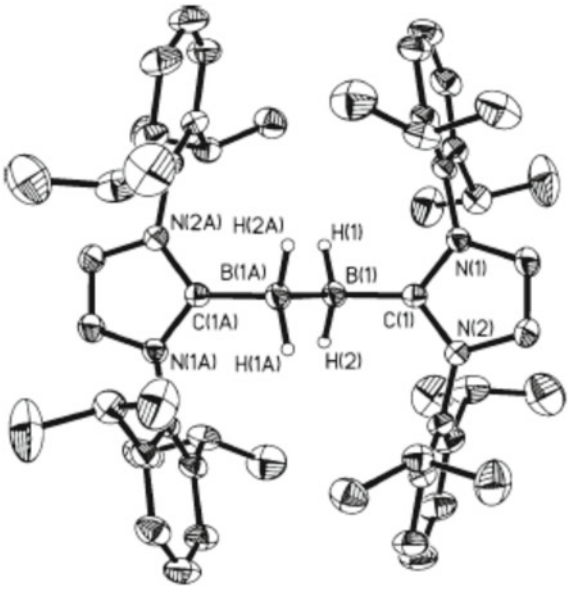

Fig. 8.28 Molecular structure of $R(H)_2B–B(H)_2R$ (thermal ellipsoids represent 30% probability; hydrogen atoms on carbon omitted for clarity). The selected bond distances (Å) and angles (deg): B(1)–B(1A) 1.828(4), B(1)–C(1) 1.577(2), B(1)–H(1) 1.155(18), B(1)–H(2) 1.147(19); B(1A)–B(1)–C(1) 107.45(16), B(1A)–B(1)–H(1) 110.7(9), B(1A)–B(1)–H(2) 110.3(9), C(1)–B(1)–H(1) 108.9(9), C(1)–B(1)–H(2) 108.1(10), H(1)–B(1)–H(2) 111.3(13). Reproduced with permission from ACS Publishers [88]

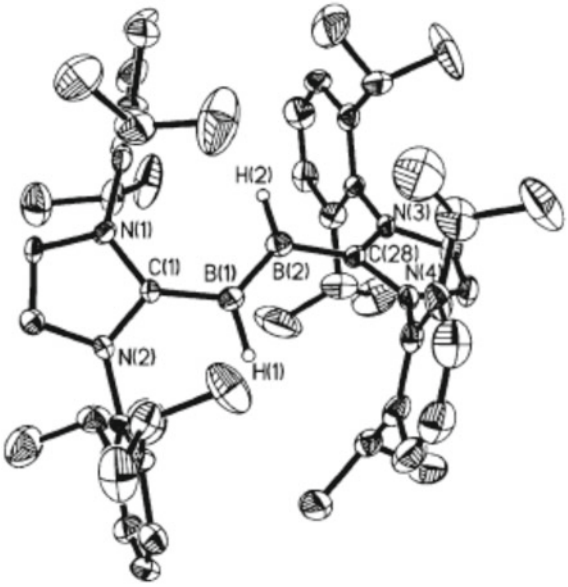

Fig. 8.29 Molecular structure of R(H)B–B(H)R (thermal ellipsoids represent 30% probability; hydrogen atoms on carbon omitted for clarity). The selected bond distances (Å) and angles (deg): B(1)–B(2) 1.561(18), B(1)–C(1) 1.543(15), B(1)–H(1) 1.14(2), B(2)–C(28) 1.532(15), B(2)–H(2) 1.13(2); B(2)–B(1)–C(1) 128.3(12), B(2)–B(1)–H(1) 124(4), C(1)–B(1)–H(1) 107(4), B(1)–B(2)–C(28) 126.1(12), B(1)–B(2)–H(2) 128(4), C(28)–B(2)–H(2)105(4). Reproduced with permission from ACS Publishers [88]

The former and latter ones have B–B single and B = B double bonds, respectively. B≡B triple-bond-containing molecule is RB_2R (Fig. 8.30, [89]).

B reacts with atoms of other elements in the periodic table except noble gases and solid boron belongs to metalloids. In metal borides, *s*, *p*, *d* or *f* orbitals of outermost shell of metal (M) react with 2*p* orbitals of B to form *s*–*p*, *p*–*p*, *d*–*p* or *f*–*p* bonds. Compounds having *s*–*p* bonds are LiB, Li_5B_4, Li_3B_{14} (alkali metal borides), MgB_2, MgB_4, MgB_6, MgB_7, MgB_{12} (alkali earth metal borides). Compounds having *d*–*p* bonding are Cr_2B, Cr_5B_3, CrB, Cr_3B_4, CrB_2, CrB_4 and CrB_6 (transition metal borides). Compounds having *f*–*p* bonding are LaB_6, YB_6, EuB_6, ThB_6 (lanthanide or actinide metal borides). Other compounds of post transition metals and B are AlB_2, AlB_{12}. Here, the bonding will be *p*–*p*. Even it forms compounds with non-metals through p–p bonding such as BN, CN, etc. Besides, there is a chance of other bonding types of metal–metal or B–B present in the compound since the formation of

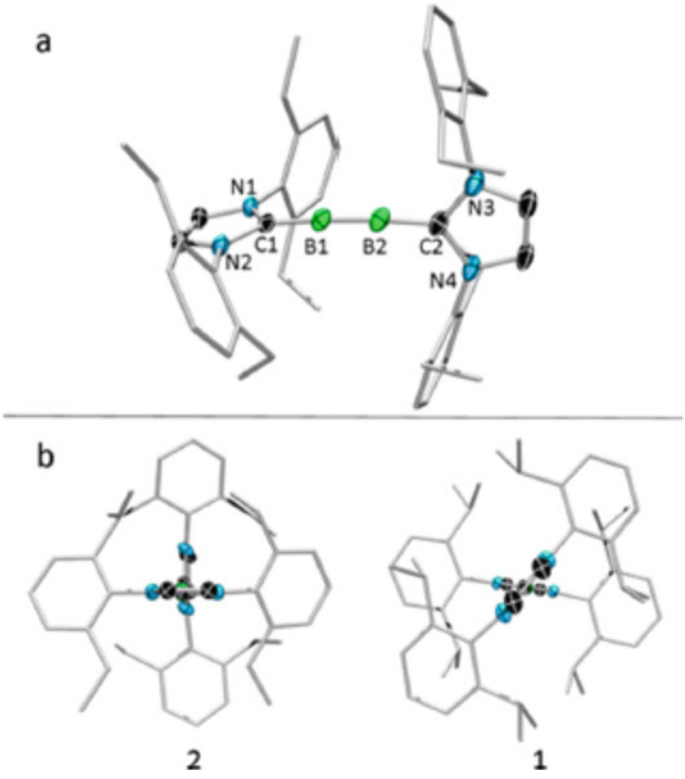

Fig. 8.30 **a** Molecular structure of 2. The thermal ellipsoids represent 50% probability. H atoms and ellipsoids on the N substituents of the NHC ligands are omitted for clarity. The selected bond lengths (Å) and angles (deg): B1–B2, 1.446(3); B1–C1, 1.484(3); B2–C2, 1.488(3); C1–N1, 1.388(2); C1–N2, 1.389(2); C2–N3, 1.376(3); C2–N4, 1.387(2); B1–B2–C2, 175.4(2); B2–B1–C1, 172.0(2); N1–C1–N2, 103.6(2); N3–C2–N4, 103.8(2). **b** The comparison of interplane angles formed by the central rings of the NHC ligands in **2** and **1**. Reproduced with permission from ACS Publishers [89]

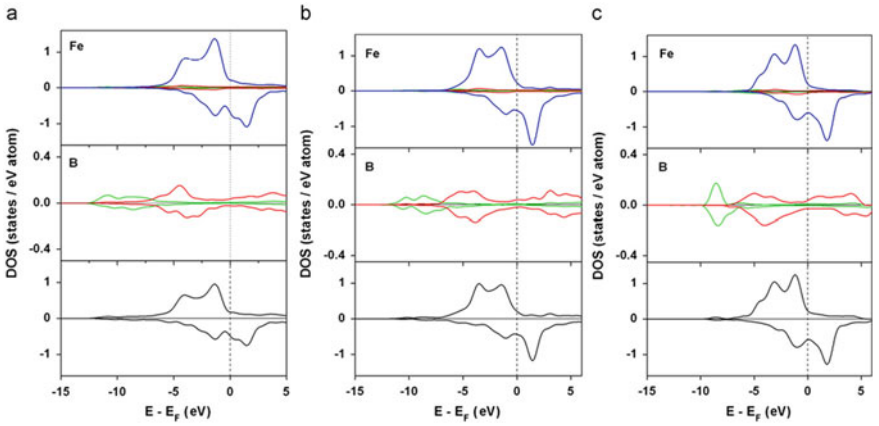

Fig. 8.31 Spin polarized total and the partial electron density of states in amorphous Fe–B alloys: **a** $Fe_{63.7}B_{33.3}$, **b** $Fe_{75}B_{25}$, **c** $Fe_{91}B_9$. Black lines: total DOS; green lines: *s* states; red lines: *p* state; and blue lines: *d* state. Reproduced with permission from Elsevier Publishers [91]

metal-rich or boron-rich compound is possible. In some cases, transfer of electrons from boron to metal occurs. Detailed discussion on electronic structure is given in a book [86].

Electronic density of states of transition metal borides (MB) will be discussed here. B rich and M rich in M_xB_y can arrange polyhedron types of B_nM, BM_n or mixture of both. Maximum coordination number (CN) of B atom in these compounds can be 9 with M atoms, whereas maximum CN of M can be 14 with B atoms [91]. Let us discuss electronic density of states (DOS) of amorphous system of $Fe_{100-x}B_x$. It means that there is no long range order of atoms.

The outermost electronic configurations of B and Fe are $2s^22p^1$ and $3d^64s^2$, respectively. The DOS (partial electron density of states) of B and Fe in amorphous $Fe_{100-x}B_x$ is shown in Fig. 8.31 [91]. It is observed that Fe–d states form a spin-split two-peaked band in DOS. This spin band of majority side of DOS (spin up ↑) is just below the Fermi level, whereas Fermi level is close to the spin band of minority side of DOS (spin down ↓). The Fe–s and Fe–p orbital contributions in DOS are very less as compared to that of Fe–d orbital. In case of B, s electron contribution at Fermi level is negligible and far from it by about 10 eV since s-orbital is fully occupied, non-bonding and below 2*p* orbital in energy level. The *p* electron contribution in Fermi level is still less, but near to it by 4–5 eV. The total DOS of few compounds of $Fe_{100-x}B_x$ is provided in Fig. 8.31. Here, contribution of Fe–*d* and B–*p* orbitals is high in DOS. There is a hybridization of Fe 3*d* and B 2*p* orbitals to form covalent bond in Fe–B.

Figure 8.32 shows the partial and total DOS of the crystalline solids of Fe_2B and Fe_3B. The crystalline compounds show the similar DOS of amorphous phase having a particular Fe/B ratio [91]. This will be related to similar local structure. There is a contribution of minority spin states at the Fermi level, which arises from B-2*p*.

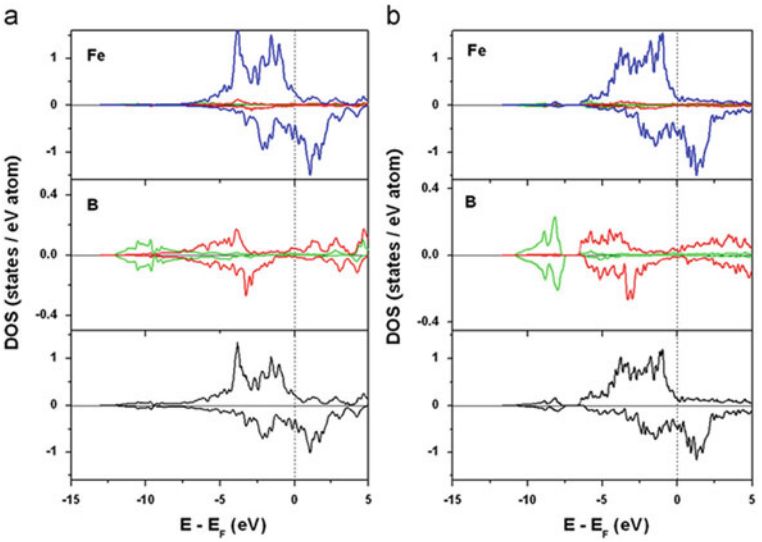

Fig. 8.32 Spin polarized total and the partial electron density of states in the Fe–B crystalline solids: **a** Fe_2B and **b** Fe_3B. Black lines: total DOS; green lines: *s* states; red lines: *p* state; and blue lines: *d* state. Reproduced with permission from Elsevier Publishers [91]

With increase of B concentration, there is a chance of B–B covalent bonds, whereas with decrease of B concentration, there is a chance of M–M metallic bonds. In case of planar or graphite like arrangement of B atoms, interaction among B and metal atoms is different from other cubic phase [92].

In terms of magnetic properties of amorphous $Fe_{100-x}B_x$, Fe atom possesses the positive moment of ~1.9–2.1 μ_B, whereas B atom possesses the negative moment of ~0.07–0.12 μ_B [91]. The distribution of the local magnetic moments on the sites of B and Fe is provided, and average magnetic moment is also shown in Fig. 8.33 [91].

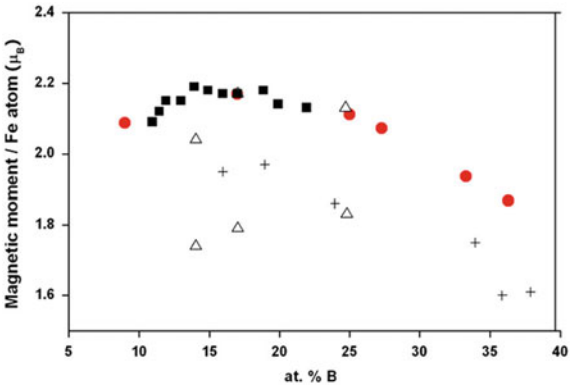

Fig. 8.33 Average magnetic moment per Fe atom in amorphous of $Fe_{100-x}B_x$ alloys is provided as function of composition. Red-filled dots represent theoretical values. Experimental data include open triangles, filled squares, crosses. Reproduced with permission from Elsevier Publishers [91]

This is based on (1) the competition between ferromagnetic and antiferromagnetic exchange interaction at very low concentration of B and (2) the dilution effect from B atoms on Fe sites at higher concentration of B in the $Fe_{100-x}B_x$. Experimental data of crystalline phases of Fe_aB (a = 2–10) are included in Fig. 8.33.

Theoretical dissociation energy of the 3d transition metal borides (MB) is calculated through all electron ab initio calculations and values are represented in Fig. 8.34 [93]. Dissociation energy is highest in case of ScB and lowest in case of MnB. The finite field (μ_{FF}) and the expectation value (μ) dipole moments of 3*d* transition metal borides (ground state) are provided in Fig. 8.35 [93].

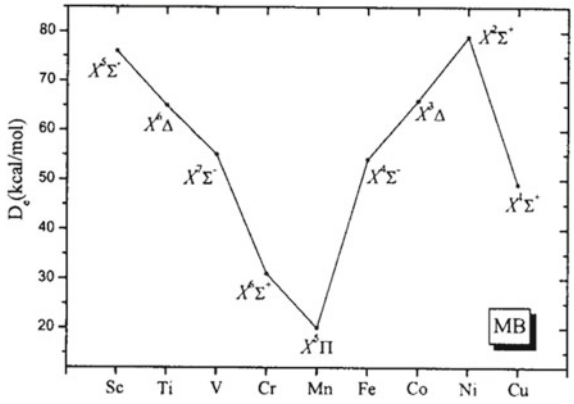

Fig. 8.34 MRCI + Q/Z dissociation energies of the ground states of metal boride MB, M = Sc to Cu. Reproduced with permission from AIP Publishers [93]

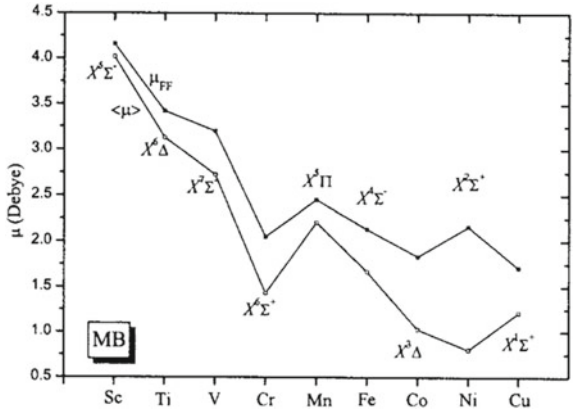

Fig. 8.35 Finite field (μ_{eff}) and expectation value (<μ>) dipole moments of ground-state MBs at the MRCI/5Z level. Reproduced with permission from AIP Publishers [93]

8.3.3 Electrical Resistivity

Most transition metal borides exhibit the metallic behavior (i.e., electrical resistivity increases with temperature) [93]. Some of alkaline earth metal borides (AB_6, A = Ca, Sr, Ba) show the semiconducting property, e.g., CaB_6 has $E_g = 0.4 - 1.0$ eV; while other can exhibit the superconducting property, e.g., MgB_2 has $T_c \sim 39$ K [41], ZrB_2 (5.5 K [94]), TaB_2 (9.5 K [95]) and NbB_2 (5.2 K [95]). Temperature-dependent resistivity of MgB_2 under absence of magnetic field is shown in Fig. 8.36 [41]. It shows T_c at 39 K, which is the highest value among superconducting metal borides, carbides and nitrides.

Interestingly, CaB_6 shows a weak ferromagnetic property and Curie temperature at ~600 K [96, 97]. There are many reports on magnetic and electrical properties of CaB_6, $Ca_{1-x}La_xB_6$, $Sr_{1-x}Ce_xB_6$, $Sr_{1-x}La_xB_6$ [96, 97]. In temperature-dependent resistivity of single crystals of $Ca_{1-x}La_xB_6$, it varies from the semiconductivity behavior at x = 0.0 to metallic at x = 0.0025; and at high x, resistivity drops significantly (Fig. 8.37, [97]). $Ca_{1-x}La_xB_6$ shows ferromagnetic properties. Magnetic moment increases with substitution of La up to x = 0.005 and decreases with further increase of x (Fig. 8.38, [97]). Inset shows the magnetization versus the applied field at 5 K for $Ca_{0.997}Th_{0.0025}B_6$ and $Ca_{0.995}Th_{0.005}B_6$.

Weak ferromagnetic and semiconducting properties of CaF_6 are reported by other group (Fig. 8.39 [96]). Here there are no magnetic ions impurities. Origin of weak ferromagnetism is debated today. It may come from defect related, exciton formation at Fermi level and low-density electron gas probability. Inset shows the expansion of the magnetization curve near-zero field (lower right) and the electrical resistivity as a function of temperature (upper left).

The compounds of B with p-block elements such as boron nitride (BN) and boron carbide (BC) show the wide band semiconducting properties (e.g., BN can have E_g

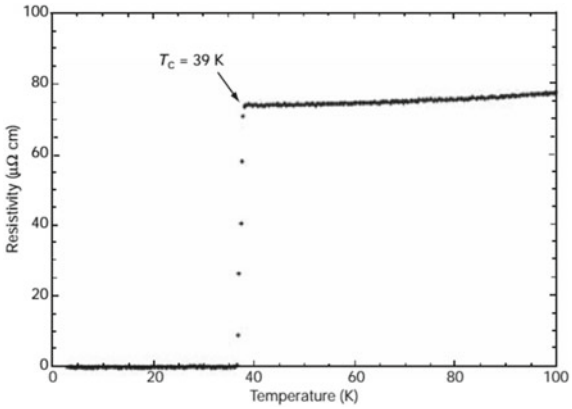

Fig. 8.36 Temperature-dependent resistivity of MgB_2 is obtained in absence of magnetic field. Reproduced with permission from Nature Publishers [41]

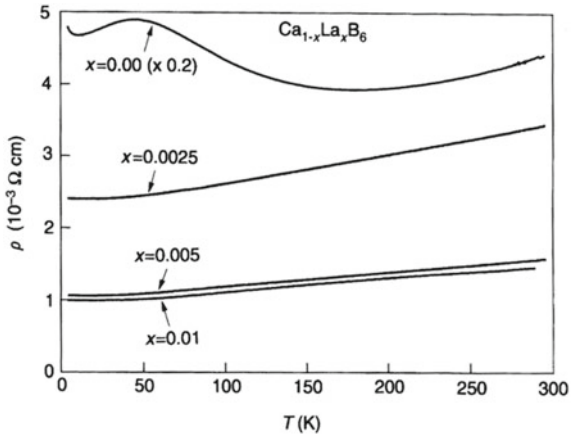

Fig. 8.37 Temperature-dependent electrical resistivities are obtained from of La-doped CaB_6. The resistivity for pure CaB_6 is multiplied by 0.2 to get clarity. Reproduced with permission from Nature Publishers [97]

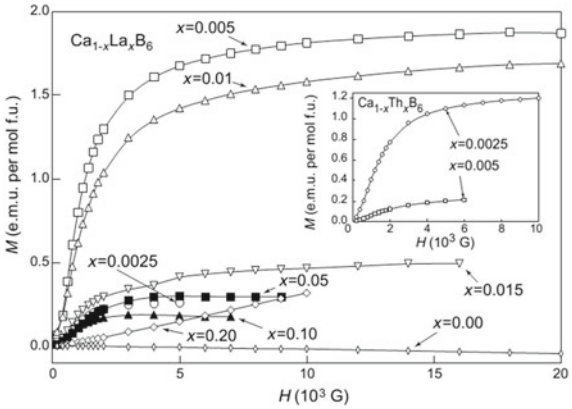

Fig. 8.38 Magnetization per mole of compound against applied field for La-doped CaB_6, measured at 5 K (f.u., formula unit). The data for x = 0 is taken at 10 K. Inset shows the magnetization versus the applied field at 5 K for $Ca_{0.997}Th_{0.0025}B_6$ and $Ca_{0.995}Th_{0.005}B_6$. Magnetizations are measured after cooling in zero field, using a quantum design SQUID magnetometer. Reproduced with permission from Nature Publishers [97]

= 3.8–6 eV) [93]. In some cases, metal borides show the resistivity minimum below 20 K due to possible Kondo or RKKY or antiferromagnetic interaction (Figs. 8.40 and 8.41 [98]) and another resistivity minimum near the Curie temperature due to magnetic ordering (ferromagnetic to paramagnetic or some kind of magnetic atomic ordering). This can be explained by taking crystalline and amorphous phases of $(Co_{1-x}Mn_x)_2B$ (x = 0.0–0.35). Figure 8.40 shows the electrical resistivity as a function of temperature for crystalline phase of $(Co_{1-x}Mn_x)_2B$, where resistivity value

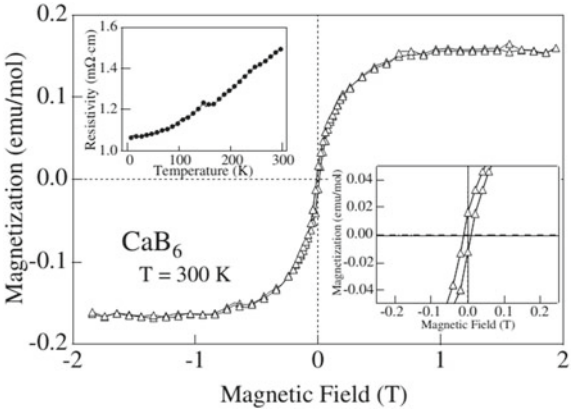

Fig. 8.39 Magnetization curve of CaB_6 single crystal is used in the present study. Inset: expansion of magnetization curve near-zero field (lower right) and electrical resistivity as a function of temperature (upper left). Reproduced with permission from APS Publishers [96]

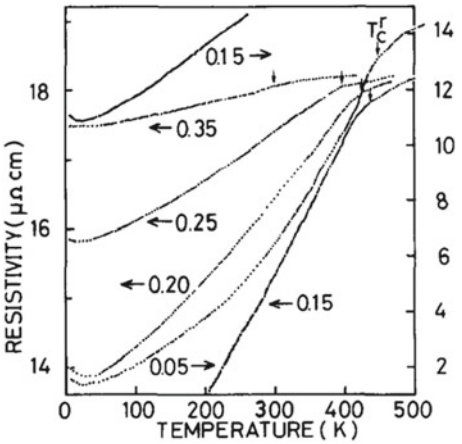

Fig. 8.40 Temperature-dependent electrical resistivity is obtained from crystalline $(Co_{1-x}Mn_x)_2B$ compounds. Reproduced with permission from Elsevier Publishers [98]

increases with increase of Mn content. The behavior is similar to magnetic alloys such as $Co_{1-x}Mn_x$. In 250–400 K, there is a slight decrease in resistivity with temperature. This is related to its respective Curie temperature (ferromagnetic to paramagnetic transition). At higher x (say $x = 0.35$), this anomaly in resistivity temperature is smeared out. At low concentration of Mn, there is a minimum at resistivity below 20 K (i.e., there is a slight rise in resistivity with decrease of temperature below 20 K). This is related to possible Kondo or RKKY or antiferromagnetic interaction among neighboring Co, Mn atoms.

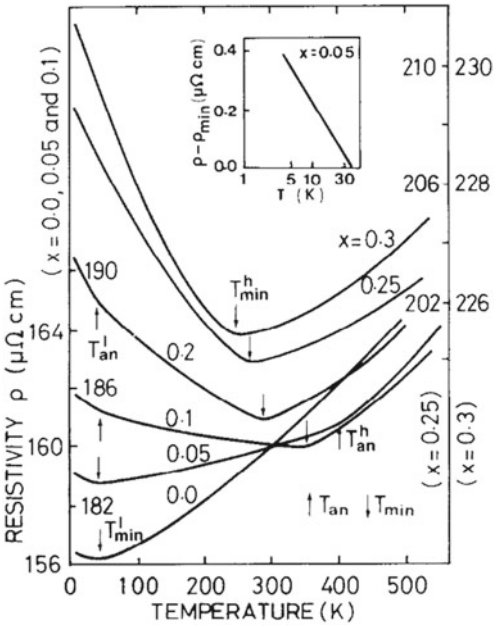

Fig. 8.41 Temperature-dependent electrical resistivity is obtained from amorphous $(Co_{1-x}Mn_x)_2B$ alloys. Reproduced with permission from Elsevier Publishers [98]

In order to compare electrical resistivity (ρ) properties of crystalline $(Co_{1-x}Mn_x)_2B$ (x = 0.0–0.35), the electrical resistivity as a function of temperature is performed for amorphous phase (Fig. 8.41). At x = 0, there is a rise in resistivity with temperature indicating metallic nature. However, there is a resistivity minimum below 20 K (i.e., there is a rise in resistivity below 20 K). This is labeled by symbol ($T_{min}{}^{l}$). With increase of x up to 0.1, there is a minimum in resistivity due to Kondo effect below 20 K, but there is a minimum in resistivity represented by symbol $T_{min}{}^{h}$. At x > 0.1, $T_{min}{}^{l}$ seems to be disappeared, but $T_{min}{}^{h}$ still remains and become more distinct with increase of x. This $T_{min}{}^{h}$ is related to magnetic ordering to disorder transition or Curie temperature. The Kondo effect below 20 K is confirmed by the plotting ln ρ versus T gives a straight line (inset of Fig. 8.41).

8.3.4 Optics

Generally, metal borides are metallic in nature. Because of this, their optical properties are not much studied. Some of borides are semiconducting and thus, they have band gap (between valence and conduction bands), which can absorb light. The value of the dispersity in the Γ-A direction (ΔE^{σ}(Γ-A) of the Brillouin zone (BZ), determined by the degree of interaction between metal–boron layers in metal diborides

(hexagonal phase) such as MgB_2, ZrB_2, VB_2, NbB_2, TaB_2, suggests that band gap is very less in MgB_2 (0.72 eV) as compared to ZrB_2 (1.73 eV), VB_2 (2.69 eV), NbB_2 (2.49 eV), TaB_2 (2.62 eV) [95]. It is therefore expected that the latter diborides will absorb light.

ZrB_2 and HfB_2 samples show the room-temperature hemispherical reflectance spectra in visible—near-infrared (NIR)—infrared region (Fig. 8.42) [84]. It has the reflectance 40–50% in 500–900 nm, where solar spectrum has the highest absorption. In this range, SiC (standard) has 20% reflectance. While ZrB_2 and HfB_2 samples shows total hemispherical emittance of 0.35–0.45, whereas SiC has the total hemispherical emittance of 0.6–0.8 in the temperature range 1100–1600 °C (Fig. 8.43). It is suggested that ZrB_2 and HfB_2 samples are better materials for ultra-high-temperature ceramics for solar thermal absorbers as compared to SiC. The temperature-dependent hemispherical emittance of ZrB_2 and HfB_2 samples in different wavelength ranges (0.6–2.8 μm, 8–14 μm) suggests that emittance values are almost 0.6 in the temperature range 1100–1600 °C in 0.6–2.8 μm wavelength and 0.2–0.3 in 8–14 μm wavelength in the same temperature range. Still search for new materials, new composition

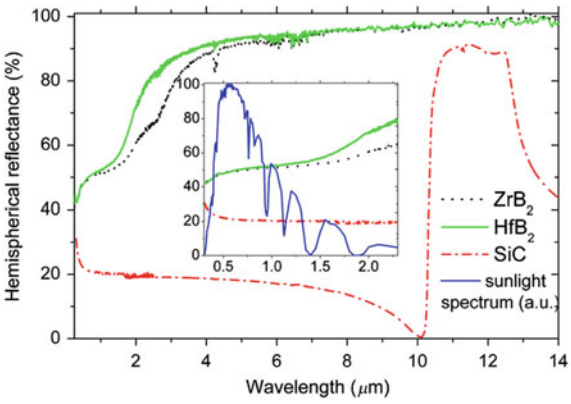

Fig. 8.42 Reflectance curves are obtained from almost fully dense ZrB_2, HfB_2 and SiC samples. Reproduced with permission from SPIE Publishers [84]

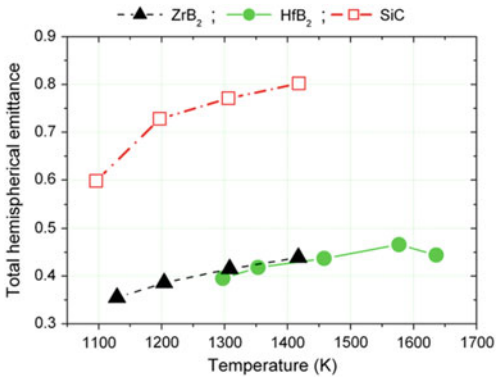

Fig. 8.43 Total hemispherical emittance is obtained from dense ZrB_2, HfB_2 and SiC samples as a function of temperature. Reproduced with permission from SPIE Publishers [84]

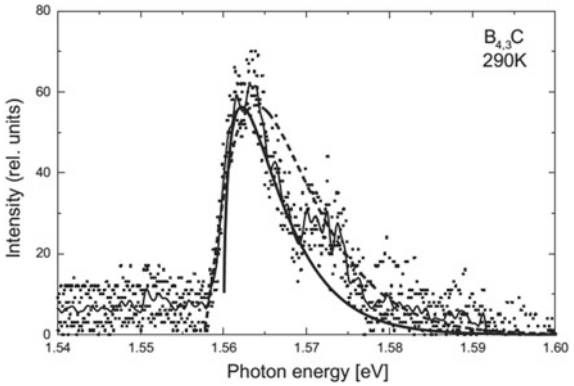

Fig. 8.44 Photoluminescence spectrum is obtained from $B_{4.23}C$ at 290 K. This is obtained after excitation with the 514.5 nm (2.4 eV) line of an Ar laser; and intensity 280mW/mm^2. Squares—experimental results, thin solid line—averaged experimental results, bold solid line—recombination model of free excitons, bold dashed line—model for the transition of electrons between energy band and defect level. Reproduced with permission from Elsevier Publishers [101]

and new synthesis method is going on for ultra-high-temperature boride ceramics, which can show promising properties for novel solar receivers. Another material for novel solar receivers is TaB_2 [99]. It is to be noted that sintering process (hot pressing, cold isostatic pressing), amount of additives used during sintering, porosity and microstructure are also important to get the desired materials for high-temperature ceramics solar receiver applications [99, 100].

Boron nitride (BN) and boron carbide (BC) show the wideband semiconducting behavior (e.g., BN can have $E_g = 3.8$–6 eV) [93]. $B_{4.3}C$ shows the broad luminescence in 1.56–1.59 eV with strong peak at 1.563 eV along with a weak peak at 1.572 eV (Fig. 8.44, [101]). Here, Ar laser ($E = 2.4$ eV) is used as source of excitation. This emission is related to the indirect-allowed recombination of free excitons. This material has indirect interband absorption transition at 2.1 eV.

On other hand, hexagonal phase of boron nitride (BN) has been used as UV light emitter because of large band gap of 6 eV. Depending on the amount of defects present in system and temperature of measurement, it can show indirect band emission (intra-band transitions at about 4 eV) along with band edge emission at 5.5 eV. Figure 8.45 shows the photoluminescence (PL) and cathode luminescence (CL) spectra recorded at room temperature and low temperature. PL is recorded by excitation at 5.82 eV [102]. Both PL and CL show similar behaviors. A broad blue band with a maximum at 4 eV is observed, and a weak continuum near 5 eV is observed at room temperature. At low temperature 77 or 120 K, extra peak in PL spectrum at ~5.5 eV is observed. Figure 8.46 shows the CL spectra at various cathode intensities or applied currents. The broad peak (~3.8 eV) is not much affected, while 5.5 eV peak increases with increase of cathode current from 10 to 60 nA.

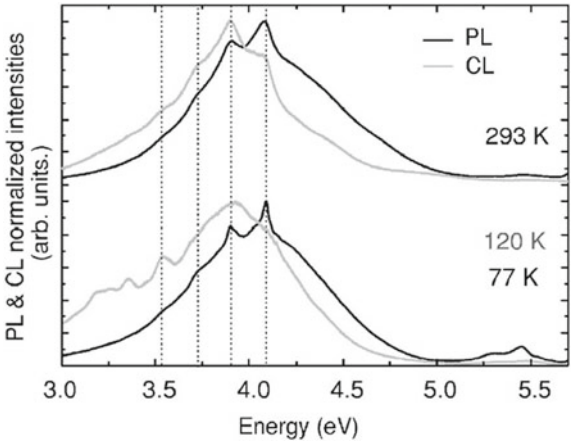

Fig. 8.45 Photoluminescence (PL) and cathode-luminescence (CL) spectra are obtained from h-BN at room and low temperatures. They are not corrected for the system response. The photoluminescence spectra are excited at 5.82 eV. Reproduced with permission from APS Publishers [102]

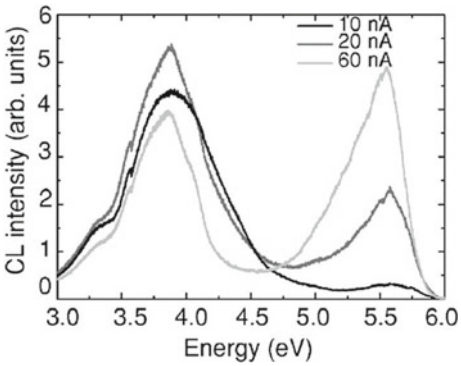

Fig. 8.46 Spatially resolved cathode-luminescence (CL) spectra at 298 K are obtained from h-BN crystallites at various applied currents. Reproduced with permission from APS Publishers [102]

8.4 Applications

8.4.1 Catalyst

Many metal borides are used in catalytic applications. Reduction of aromatic nitro group to amine at room temperature using nickel borides (NiB_2) as catalyst has been reported [103]. As compared to precious metals (Au, Pd, Pt) and abundant metals (Ni, Co, Fe), NiB_2 (obtained by in situ formation from $NiCl_2$ and $NaBH_4$) showed the enhanced reduction properties of aromatic nitro to amine in water medium. However, there is oxidation of NiB_2 catalyst in water, which contains dissolved oxygen molecules. In order to increase yield of product per gram of catalyst and

number of turnover and to protect oxidation of NiB_2, the surface-modified cellulose has been added to reaction medium. The reduction processes using classical reduction with Fe/Pd (1) and nickel borides (using $NaBH_4$) in cellulose (2) are provided below.

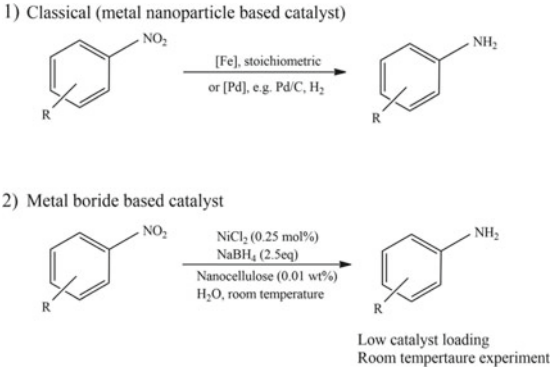

Ultra-thin nanosheets of bimetallic iron-nickel boride (Fe–Ni–B) on Ni foam show better oxygen-evolving activity compared to the precious metal catalyst RuO_2 in electrolysis of water [104]. This requires an over potential of 237 mV to reach a current density of 10 mA cm^{-2} with a small Tafel slope of 38 mV dec^{-1} in 1.0 M KOH electrolyte. The material shows long-term electrochemical stability. At a similar current density, RuO_2 catalyst requires an over potential of 292 mV.

8.4.2 Superconducting Materials

Many metal borides are used as superconducting materials having transition (T_c) up to 39 K [105–107]. Some of superconducting metal borides are: MgB_2 has $T_c \sim 39$ K [103], ZrB_2 (5.5 K [104]), TaB_2 (9.5 K [105]), NbB_2 (5.2 K [105]), Ru_7B_3 (3.3 K [105]), RuB_2 (1.6 K [105]), Mo_2IrB_2 (3.6 K [105]), NbRuB (3.1 K [106]), $WB_{4.2}$ (2.0 K [107]). Figure 8.47 shows the electrical resistivity vs. temperature of NbRuB in which superconducting transition is observed at 3.1 K, which is consistent with zero-field cooled (ZFC) and field cooled (FC) magnetic susceptibility measurement (upper inset of Fig. 8.47) and susceptibility becomes negative below 3.2 K. Its crystal structure is shown in lower inset of Fig. 8.47. Figure 8.48 shows thermodynamic properties of NbRuB: (a) the heat capacity (C_p) versus temperature at 0 and 5 T magnetic field. At 0 field, there is a rise of C_p with temperature up to 2.7 K and then decreases up to 3.7 K, and above this there is a rise of C_p with temperature. At 5 T, there is a rise of C_p with temperature. (b) The C_p/T versus temperature shows the change in entropy at the superconducting transition for 0 field measurement. (c) C_p/T versus T^2 shows the straight line indicating suppression of superconductivity in the presence of magnetic field (5 T).

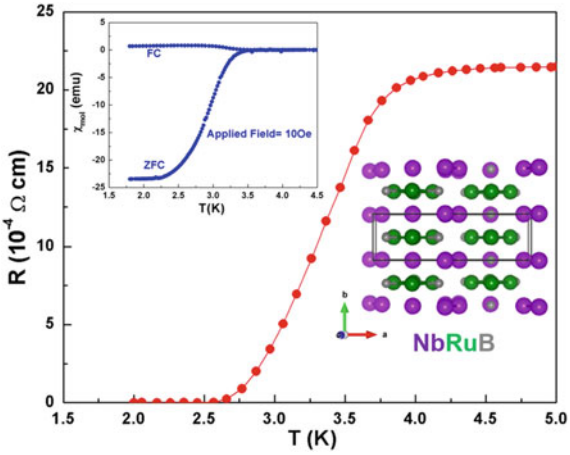

Fig. 8.47 Electrical and magnetic data of the NbRuB superconductor. Main panel: The temperature dependence of electrical resistivity of NbRuB without an applied magnetic field showing a close-up of superconducting transition to zero resistance. Lower Inset: the crystal structure of NbRuB. Upper insert: the temperature dependence of magnetic susceptibility of NbRuB in a 10 Oe applied field from 1.8 K to 4.5 K with zero-field cooling and field cooling, demonstrating expulsion of magnetic flux by the superconductor. Reproduced with permission from ACS Publishers [106]

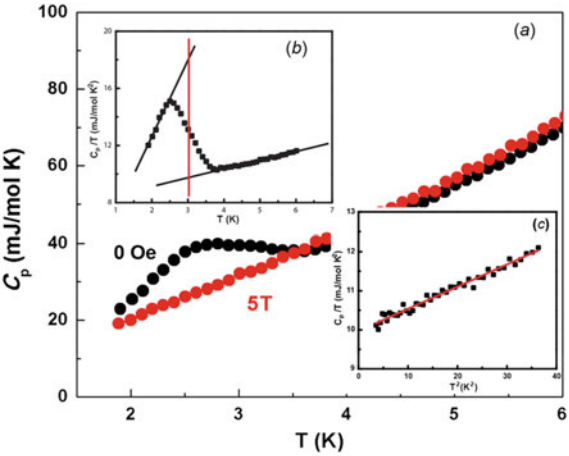

Fig. 8.48 **a** Temperature dependence of the heat capacity C_p is obtained from superconducting NbRuB measured with (5 T) and without an applied magnetic field (0 Oe). **b** Enlarged view of the low-temperature region ($1.9 - 6$ K) of C_p/T (T) for NbRuB showing "the equal area construction" method for determining the change in entropy at the superconducting transition. **c** The fitting of the low temperature C_p/T data versus T^2 in the temperature range $1.9 - 6$ K is under the applied field (5 T), which is sufficient for the suppression of superconductivity, and this is employed to determine the electronic contribution to C_p. Reproduced with permission from ACS Publishers [106]

8.4.3 *Coating Materials to Improve Mechanical Properties (Hardness, Corrosion Resistance, Wear Resistance)*

To improve mechanical properties like hardness, wear resistance, corrosion resistance and stability of metal or alloys in high temperature and harsh environment, coating over products is necessary. Usually, metal/non-metal borides, carbides and nitrides are used as coating materials. Here, coating over product using boron source will be discussed. Boron interacts with upper surface of material to form single or multilayer metal borides. Examples are provided here.

1. Formation of FeB and Fe_2B over surface of steels improves hardness, wear resistance, temperature resistance and corrosion resistance. Figure 8.49 shows the cross-sectional scanning electron microscopy images of formation of Fe–B over surface of steel [108]. 50 μm thickness of coating is formed, and no crack is formed. Energy-dispersive analysis of X-ray (EDAX) spectrum shows the composition of coating that has Fe, B. Since B is a low atomic number element, it is difficult to observe its peak, but there is a small peak below Fe peak. This may be related to boron. The hardness increases with annealing temperature of sample (Fe–B formation over steel), and its hardness is more than that of substrate steel [Fig. 8.50]. The hardness of sample annealed at 900 °C for 8 h has the value of 1100 HV. The corrosion resistance studies of coated sample have been carried out using polarization techniques (Tafel) and electrochemical impedance spectroscopy (EIS) with an electrochemical station. It was performed in 3.5 wt% NaCl solution with a conventional three-electrode cell. The Cl^- ions diffuse into coating, and further interact with iron steel substrate to form the rust ($Fe(OH)_2$, $Fe_2O_3.xH_2O$. The possible electrochemical reactions are given below:

$$\text{Fe (solid/substrate)} + 2Cl^- + 4H2O \rightarrow FeCl_2 \cdot 4H2O + 2e^-$$

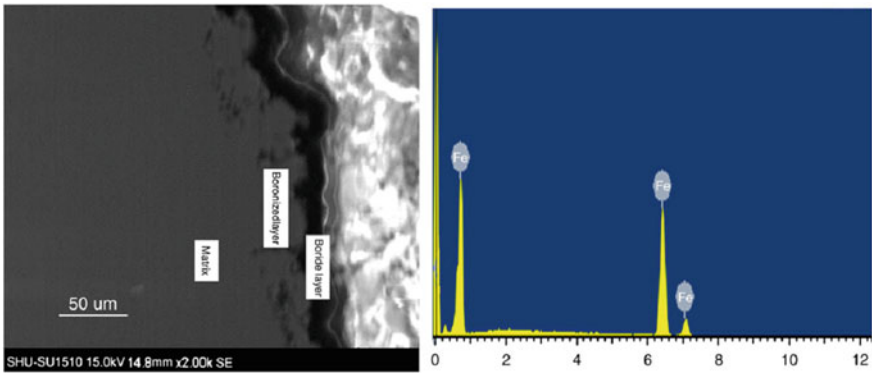

Fig. 8.49 Cross-sectional morphology (Left) and EDAX spectrum (Right) data of the boride layer at 900 °C for 8 h. Reproduced with permission from Elsevier Publishers [108]

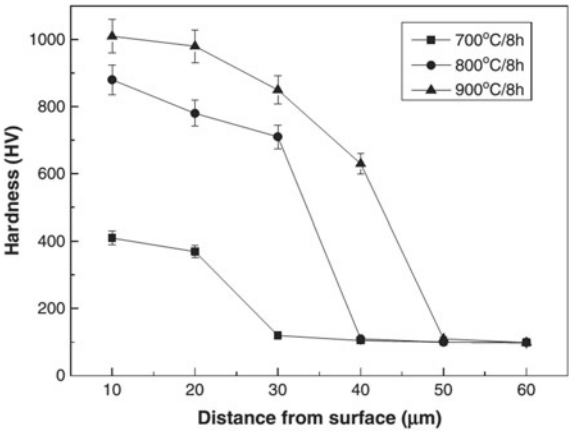

Fig. 8.50 Variation in microhardness is obtained from the surface to the interior of borided low-carbon steel. Reproduced with permission from Elsevier Publishers [108]

$$O_2 + 2H_2O + 4e^- \rightarrow 4OH^-$$
$$FeCl_2 \cdot 4H_2O + 2OH^- \rightarrow Fe(OH)_2 + 2Cl^- + 4H_2O$$
$$4Fe(OH)_2 + 2H_2O + O_2 \rightarrow 4Fe(OH)_3 \text{ or } Fe_2O_3.xH_2O(\text{rust})$$

The corrosion resistance of low-carbon steel is evaluated by polarization curve at ambient temperature (Fig. 8.51). The corrosion inhibiting efficiency ($E_{\text{resistance}}$) is calculated using the following formula.

$$E_{\text{resistance}} = \left[\left(i^0_{\text{corr}} - i_{\text{corr}}\right)/i^0_{\text{corr}}\right] \times 100\%$$

where $i^0{}_{\text{corr}}$ = the corrosion current of the steel and i_{corr} = the corrosion current of the boride-coated steel. The cathodic reaction corresponds to the evolution of H_2, whereas anodic reaction corresponds to the corrosion resistance of the boride coating.

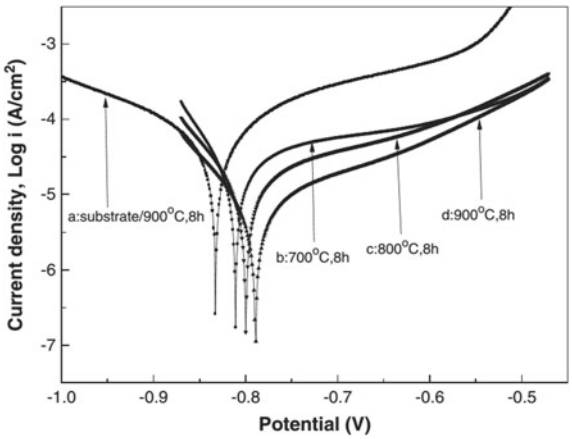

Fig. 8.51 Potentiodynamic curves are obtained from the substrate and borided low-carbon steel in 3.5 wt% NaCl solution. Reproduced with permission from Elsevier Publishers [108]

The corrosion current density (I_{corr}) and corrosion potential (E_{corr}) are obtained from the polarization curves by Tafel extrapolation method. I_{corr} values for substrate (steel), Fe–B-coated steels annealed at 700, 800 and 900 °C are 59.38, 29.76, 16.85 and 8.78 μA/cm^2, respectively. E_{corr} values for substrate (steel), Fe–B-coated steels annealed at 700, 800 and 900 °C are −832.6, −811.4, −797.5 and −788.4 mV, respectively. $E_{resistance}$ values of Fe–B-coated steels annealed at 700, 800 and 900 °C are 49.8, 71.6 and 85.2, respectively. It is suggested that boride coating over substrate protects the surface of samples from the effect of Cl^- ions.

Boron nitride (BN) has same structure of carbon and can exist in cubic or hexagonal phases [109]. The cubic phase has similar hardness property with diamond. BN is therefore coated over the cutting tips of high-speed steel. The film thickness of 15 μm BN over steel shows the hardness of 3000–5000 kg/mm^2. Wear resistance increases by making silicon nitride interface between BN film and steel.

WB_2 and WB_4 have been considered as superhard material (~45 GPa) [110]. This was used as coating material over surface of steel in order to improve mechanical properties (hardness, wear resistance), chemical inertness and electronic conductivity. The hardness of WB_2 coated over surface of steel was measured with the help of a nanoindenter (Nano Indenter G200, Agilent Technologies, USA) with a Berkovich indenter tip. Figure 8.52 shows the hardness–displacement curve of the coated sample. There is a rise of hardness up to about 53 GPa for indentation depth of 60 nm, and then hardness decreases slightly up to 45 GPa for indentation depth of 200 nm and further decreases to 40 GPa for indentation depth of 400 nm. Inset of Fig. 8.52 shows the loading and unloading curves of ten indentations. All indentations are almost overlapping each other indicating the reliable indentation results.

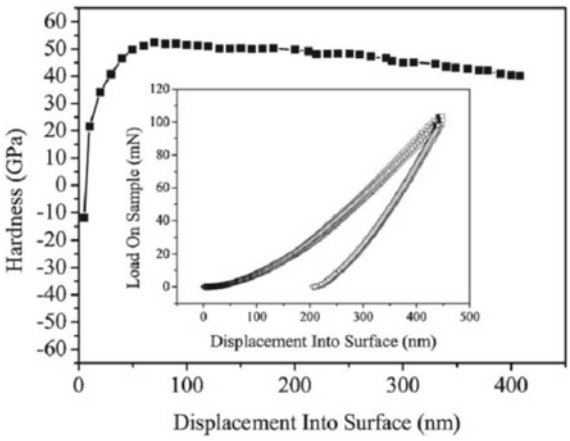

Fig. 8.52 Hardness of the as-deposited WB_2 coatings is plotted as a function of indentation depth. Inset: The load displacement curves of ten indentations. Reproduced with permission from Wiley Publishers [110]

8.4.4 Metallic Ceramics Materials

Since some of borides are having a high melting point (>2000 °C) such as TiB_2, WB_2, ZrB_2, HfB_2, NbB_2, TaB_2, high chemical stability and good electrical conductivity, these are used as interconnector, cutting tools, grinding tools, thermal barriers, diffusion-resistant thin films, etc. [111–115]. They are usually poor in thermal conductivity because of vacancies of boron or defects.

8.4.5 Magnetic Materials

Usually, NiB_x, CoB_x and FeB_x compounds are magnetic materials [116]. There are other boron-based magnetic materials, which include the following: $Nd_2Fe_{14}B$ (permanent magnet), $Nb_6Fe_{1-x}Ir_{6+x}B_8$, $Sc_2FeRu_5B_2$, $Ti_9Fe_2Rh_{18}B_8$, $TiCrIr_2B_2$, $Ti_2FeRh_5B_2$, $Ti_2FeRu_5B_2$, $Sc_2FeRu_{5-x}Rh_xB_2$ and $FeRh_{6-x}Ru_xB_3$, $Ti_3Co_5B_2$, $Zn_{11}Rh_{18}B_8$, etc. [117, 118]. The behavior of magnetic materials depends on their crystal structure, B–B, metal–metal, B-metal bonding, itinerant electrons, Fermi energy, exchange interaction, antiferromagnetic, ferro-/ferri-magnetic interactions, etc. Thus, they are used as magnetic ribbons and magnetocaloric materials for efficient refrigerators.

8.4.6 Brightness in Electron Microscopy and Monochromator for Synchrotron Radiation

Many boron-rich rare-earth borides such as LnB_6 (Ln = f-block elements, Ce, La) have low work functions of 2.3–3.2 eV [119–121]. Upon heating, they can emit electrons. Such materials are used as thermoionic electron emitters. In scanning electron microscope, cathode electron emitters are usually tungsten filament. However, it has high work function of 4.5 eV. Because of this, a high temperature is required to emit electrons. To decrease temperature required for electron emission, single crystals of LaB_6 and CeB_6 are used. It increases brightness of image because they exhibit lower electron spread as well as longer lifetime compared to those of tungsten (W) filament when same current is applied on both W and LaB_6. To determine energy of a synchrotron beam in the range 7–12 keV with uncertainties of 0.1 eV, powder XRD diffraction patterns of LaB_6 is used as standard [122].

8.4.7 Other Hybrids/Composites of Borides for Applications

The production of H_2 by splitting of water is one of the best ways for the storage of renewable electricity. However, it is limited by the slow anodic oxygen evolution reaction (OER). There are reports on improvement of OER using metal and metal oxide catalysts [123]. Hybrid of nickel boride and graphene oxide is better for OER as compared to that of pure graphene oxide or commercial RuO_2 catalyst [124]. The electrolyte used in this work is potassium hydroxide (KOH) pellets and ultra-pure H_2O (18.2 MΩ, Millipore). Interestingly, hybrid of iron-doped nickel boride and graphene oxide is better for OER as compared to that of hybrid of nickel boride and graphene oxide. Hybrid of iron-doped nickel boride and graphene oxide (GO) required a very low overpotential of 230 mV to achieve the current density of 15 mA cm^{-2} with a small Tafel slope of 50 mV $dec^{-1}$and this value was better than those of Ni–B/GO and commercial RuO_2 catalyst at the same mass loading.

The hybrid of Ni_2B and reduce graphene oxide (RGO) has been used as novel electrode material for supercapacitors [125]. This has an excellent specific capacitance of 1073.4 F g^{-1} at a current density of 1 A g^{-1} in 6 M KOH solution. A high energy density of 22.1 Wh kg^{-1} at a power density of 724.9 W kg^{-1} is delivered using this hybrid. About 72% of its initial performance is achieved after 2500 charge–discharge cycles at a current density of 6 A g^{-1}.

8.5 Conclusions

Different ways of synthesis of metal borides are provided. Examples of metal borides of *s*-, *d*- and *f*-block elements are Nb_3B_2, NbB, Nb_5B_6, Nb_3B_4, NbB_2, Cr_2B, Cr_5B_3, CrB, Cr_3B_4, CrB_2, CrB_4, CrB_6, MgB_2, MgB_4, MgB_6, MgB_7, MgB_{12}, LiB, Li_5B_4, Li_3B_{14}, $LiB_{12.93}$, $Li_{1.8}B_{14}$ and LiB_2. With p-block elements, boron forms compounds such as AlB_2, AlB_{12}, B_4C, SiB_3, SiB_4, SiB_6, BN, and these borides are usually nonmetallic in nature. With rare-earth elements, boron forms compounds such as LaB_6, YB_6, CeB_6, EuB_6, ThB_6. The composition of metal borides varies from B rich to metal rich. In some cases, exothermic reaction occurs when metal ions interact with borohydride. Therefore, it is preferred to perform this under ice bath. The particle size and shape of metal borides can be changed depending on synthesis route. Also, the ways to prepare metal borides in nanostructured form (0D, 1D, 2D and 3D ways) are mentioned. Boron can form single, double and triple bonds with another B atom to form compounds. Since B is itself electron deficient, it needs to gain electrons from Lewis base (L) such as: C (carbenes): NH_3: CO. Typical examples are $L: \rightarrow H_2B-BH_2 \leftarrow :L, L: \rightarrow H_1B=BH \leftarrow :L, L: \rightarrow B\equiv B \leftarrow :L$ for formation of stable compounds. Most of metal borides are metallic and because of this, they are not good for optical materials. Some compounds (WB_2, WB_4,TiB_2, ZrB_2, HfB_2, NbB_2, TaB_2) including BN and CN are very hard as well as have high melting points. They are used as coating materials to increase corrosion resistance as well as wear resistance. Metal

borides of Fe–B, Ni–B and Co–B are used as soft magnetic materials. $Nd_2Fe_{14}B$ is used as permanent magnet. Most borides are used as catalysts. LaB_6 and CeB_6 are used as cathode electron sources in electron microscopy. MgB_2, TaB_2 and NbB_2 are used as superconducting materials.

References

1. Ningthoujam RS (2017) Synthesis, characterization of borides, carbides, nitrides and their applications. In: Banerjee S, Tyagi AK (eds) 2017 in Materials under extreme conditions: Recent trends and future prospects. Elsevier Inc., USA, Chapter 10, pp 337–376
2. Ningthoujam RS, Vatsa RK, Prajapat CL, Yashwant G, Ravikumar G (2010) Interaction between amorphous ferromagnetic Co–Fe–B particles in conducting silver matrix prepared by chemical reduction route. J Alloys Comp (Lett) 492:L40
3. Peshev P, Leyarovska L, Bliznakov G (1968) On the borothermic preparation of some vanadium, niobium and tantalum borides. J Less-Common Metals 15:259–267
4. Carenco S, Portehault D, Boissière C, Mézailles N, Sanchez C (2013) Nanoscaled metal borides and phosphides: recent developments and perspectives. Chem Rev 113:7981–8065
5. Pan L-M (1992) Phase equilibrium and elastic moduli of rapidly solidified Fe-Cr-Mo-B and Fe-Cr-Ni-B alloys, Ph.D. Thesis, University of Surrey
6. Franke P, Neuschutz D (2004) Binary systems Part 2. Elements and binary systems from B-C to Cr-Zr. Landolt-Bornstein-Group IV Phys Chem 19B2:1–4
7. Ningthoujam RS, Gajbhiye NS (2015) Synthesis, electron transport properties of transition metal nitrides and applications. Prog Mater Sci 50:50–154
8. Ningthoujam RS, Sudhakar N, Rajeev KP, Gajbhiye NS (2002) Electrical resistivity study of La, B doped nanocrystalline superconducting vanadium Nitride. J Appl Phys 91:6051
9. Gajbhiye NS, Ningthoujam RS, Weissmuller J (2002) Synthesis and magnetic studies of nanocrystalline nickel nitride material. Phys Stat Sol (a) 189:691
10. Ningthoujam RS, Gajbhiye NS (2004) Magnetic and current density studies on nanostructured vanadium nitride material. Ind J Phys 78A(1):89
11. Ningthoujam RS, Gajbhiye NS (2004) Thermal decomposition study of nanocrystalline Ni_3N. Ind J Phys 78A(2):265
12. Sudhakar N, Ningthgoujam RS, Rajeev KP, Nigam AK, Weissmuller J, Gajbhiye NS (2004) Effect of La, B doping on the electrical resistivity and magnetic susceptibility of nanocrystalline vanadium nitride. J Appl Phys 96:688
13. Gajbhiye NS, Ningthoujam RS, Weissmuller J (2004) Mössbauer study of nanocrystalline ε-$Fe_{3-x}Co_xN$ system. Hyperfine Interact 156:51
14. Gajbhiye NS, Panda RN, Ningthoujam RS, Bhattacharyya S (2004) Magnetism of nanostructured iron nitride (Fe-N) systems. Phys Stat Sol (c) 1:3252
15. Gajbhiye NS, Ningthoujam RS (2004) Structural, electrical and magnetic studies of nanocrystalline δ-MoN and γ-Mo_2N. Phys Stat Sol (c) 1:3449
16. Gajbhiye NS, Ningthoujam RS (2006) Low temperature synthesis, crystal structure and thermal stability studies of nanocrystalline VN particles. Mat Res Bull 41:1612
17. Gajbhiye NS, Ningthoujam RS, Bhattacharyya S (2005) Magnetic properties of Co and Ni substituted ε-Fe_3N nanoparticles. Hyperfine Interact 164:17
18. Ningthoujam RS, Gajbhiye NS (2008) Magnetic study of single domain ε-Fe_3N nanoparticles synthesized by precursor techniques. Mater Res Bull 43:1079
19. Dewangan KC, Ningthoujam RS, Kurian S, Gajbhiye NS (2008) Magnetic and Mössbauer properties of Fe doped VN nanoparticles. Hyperfine Interact 183:185
20. Ningthoujam RS, Gajbhiye NS (2010) Magnetization studies on ε- $Fe_{2.4}Co_{0.6}N$ nanoparticles. Mater Res Bull 45:499

21. Ningthoujam RS, Panda RN, Gajbhiye NS (2012) Variation of intrinsic magnetic parameters of single domain Co-N interstitial nitrides synthesized via hexa-ammine cobalt nitrate route. Mater Chem Phys 134:377–381
22. Ningthoujam RS (2012) Enhancement of luminescence by rare earth ions doping in semiconductor host. In Rai SB, Dwivedi Y (eds) Nova Science Publishers Inc, USA, Chapter 7, pp 145–182
23. Ningthoujam RS, Mishra R, Das D, Dey GK, Kulshreshtha SK (2008) Excess enthalpy and luminescence studies of SnO_2 nanoparticles. J Nanosci Nanotech 8:4176
24. Ningthoujam RS, Vatsa RK, Vinu A, Ariga K, Tyagi AK (2009) Room temperature exciton formation in SnO_2 nanocrystals in SiO_2: Eu matrix: Quantum dot system, heat-treatment effect. J Nanosci Nanotech 9:2634
25. Singh LR, Ningthoujam RS, Singh SD (2009) Tuning of ultra-violet to green emission by choosing suitable excitation wavelength in ZnO: quantum dot, nanocrystals and bulk. J Alloys Comp 487:466
26. Ningthoujam RS, Gautam A, Padma N (2017) Oleylamine as reducing agent in syntheses of magic-size clusters and monodisperse quantum dots: optical and photoconductivity studies. Phys Chem Chem Phys 19:2294–2303
27. Soni AK, Joshi R, Jangid K, Tewari R, Ningthoujam RS (2018) Low temperature synthesized $SrMoO_4$:Eu^{3+} nanophosphors functionalized with ethylene glycol: a comparative study of synthesize route, morphology, luminescence and annealing. Mater Res Bull 103:1–12
28. Wangkhem R, Yaba T, Singh NS, Ningthoujam RS (2018) Red emission enhancement from $CaMoO_4$:Eu^{3+} by co-doping of Bi^{3+} for near UV/blue LED pumped white pcLEDs: Energy transfer studies. J Appl Phys 123:124303
29. Ningombam GS, Ningthoujam RS, Kalkura SN, Singh NR (2018) Induction heating efficiency of water dispersible $Mn_{0.5}Fe_{2.5}O_4$@YVO_4:Eu^{3+} magnetic-luminescent nanocomposites in acceptable AC magnetic Field: Haemocompatibility and cytotoxicity studies. J Phys Chem B 122:6862–6871
30. Prasad AI, Singh LR, Joshi R, Ningthoujam RS (2018) Luminescence study on crystalline phase of $Y_2Si_2O_7$ from mesoporous silica and Y_2O_3: Ln^{3+} at 900 °C. AIP Adv 8:105310
31. Yaiphaba N, Ningthoujam RS, Singh NR, Vatsa RK (2010) Luminescence properties of redispersible Tb^{3+}-Doped $GdPO_4$ nanoparticles prepared by an ethylene glycol route. Eur J Inorg Chem 2682
32. Gajbhiye NS, Ningthoujam RS, Ahmed A, Panda DK, Umre SS, Sharma SJ (2008) Redispersible Li^+ and Eu^{3+} co-doped CdS nanoparticles: Luminescence studies. Pramana J Phys 70:313
33. Meetei SD, Singh SD, Singh NS, Sudarsan V, Ningthoujam RS, Tyagi M, Gadkari SC, Tewari R, Vatsa RK (2012) Crystal structure and photoluminescence correlations in white emitting nanocrystalline ZrO_2:Eu^{3+} phosphor: effect of doping and annealing. J Lumin 132:537–544
34. Ningthoujam RS, Shukla R, Vatsa RK, Duppel V, Kienle L, Tyagi AK (2009) Gd_2O_3:Eu^{3+} particles prepared by glycine-nitrate combustion: phase, concentration, annealing, and luminescence studies. J Appl Phys 105:084304
35. Singh BP, Parchur AK, Ningthoujam RS, Ansari AA, Singh P, Rai SB (2014) Influence of Gd^{3+} co-doping on structural property of $CaMoO_4$:Eu. Dalton Trans 43:4770–4778
36. Parchur AK, Ansari AA, Singh BP, Hasan TN, Syed NA, Rai SB, Ningthoujam RS (2014) Enhanced luminescence of $CaMoO_4$: Eu by core@shell formation and its hyperthermia study after hybrid formation with Fe_3O_4: cytotoxicity assessing on human liver cancer cells and mesanchymal stem cells. Integr Biol 6:53–64
37. Okram R, Yaiphaba N, Ningthoujam RS, Singh NR (2014) Is higher ratio of monoclinic to tetragonal in $LaVO_4$ a better luminescence host? Redispersion and polymer film formation. Inorg Chem 53:7204–7213
38. Singh LP, Srivastava SK, Mishra R, Ningthoujam RS (2014) Multifunctional hybrid nanomaterials from water dispersible CaF_2:Eu^{3+}, Mn^{2+} and Fe_3O_4 for luminescence and hyperthermia application. J Phys Chem C 118:18087–18096

39. Sahu NK, Singh NS, Ningthoujam RS, Bahadur D (2014) Ce^{3+} sensitized $GdPO_4$:Tb^{3+} nanorods: an investigation on energy transfer, luminescence switching and quantum yield. ACS Photonics 1:337–346
40. Matsudaria T, Itoh H, Naka S, Hamamoto H (1989) Synthesis of niobium boride powder by solid state reaction between niobium and amorphous boron. J Less-Common Met 155:207–214
41. Nagamatsu J, Nakagawa N, Muranaka T, Zenitani Y, Akimitsu J (2001) Superconductivity at 39 K in magnesium diboride. Nature 410:63–64
42. Kaptay G, Kuznetsov SA (1999) Electrochemical synthesis of refractory borides from molten salts. Plasmas Ions 2:45–56
43. Yeh CL, Lin JZ, Wang HJ (2012) Formation of chromium borides by combustion synthesis involving borothermic and aluminothermic reduction of Cr_2O_3. Ceram Int 38:5691–5697
44. Massalski TB, Okamoto H, Subramanian PR, Kacprzak L (eds) (1996) Binary alloy phase diagrams. ASM International, Materials Park, OH, USA
45. Sonber JK, Murthy TSRC, Subramanian C, Kumar S, Fotedar RK, Suri AK (2009) Investigation on synthesis, pressureless sintering and hot pressing of chromium diboride. Int J Refract Met Hard Mater 27:912–918
46. Iizumi K, Sekiya C, Okada S, Kudou K, Shishido T (2006) Mechanochemically assisted preparation of NbB_2 powder. J Eur Ceram Soc 26:635–638
47. Glavee GN, Klabunde KJ, Sorensen CM, Hadjipanayis GC (1994) Borohydride reduction of nickel and copper ions in aqueous and nonaqueous media. Controllable chemistry leading to nanoscale metal and metal boride particles. Langmuir 10:4726—4730
48. Takahashi T, Itoh H (1980) Ultrasonic chemical vapor deposition of TiB_2 thick films. J Crystal Growth 49:445–450
49. Wagner RS, Ellis WC (1964) Vapor-liquid-solid mechanism of single crystal growth. Appl Phys Lett 4:89
50. Brewer JR, Jacobberger RM, Diercks DR, Cheung CL (2011) Rare earth hexaboride nanowires: General synthetic design and analysis using atom probe tomography. Chem Mater 23:2606–2610
51. Kuznetsov GI, Sokolovsky EA (1997) Dependence of effective work function for LaB_6 on surface conditions. Phys Scr T 71:130–133
52. Jensen JA, Gozum JE, Pollina DM, Girolami GS (1988) Titanium, zirconium and hafnium tetrahydroborates as "Tailored" CVD precursors for metal diboride thin films. J Am Chem Soc 110:1643
53. Jayaraman S, Yang Y, Kim DY, Girolami GS, Abelson JR (2005) Hafnium diboride thin films by chemical vapor deposition from a single source precursor. J Vac Sci Technol A 23:1619
54. Ye W, Martin PAP, Kumar N, Daly SR, Rockett AA, Abelson JR, Girolami GS, Lyding JW (2010) Direct writing of sub-5 nm hafnium diboride metallic nanostructures. ACS Nano 4:6818
55. Sano N, Kawanami O, Tamon H (2011) Synthesis of single and multi unit-wall nanotubes by arc plasma in inert liquid via self-curling mechanism. J Appl Phys 109:034302
56. Sano N, Ikeyama Y, Tamon H (2012) Hydrothermal synthesis of magnesium boride nanotubes. Mater Lett 85:106–108
57. Hoerkstra HR, Katz JJ (1949) The preparation and properties of the group IV-B metal borides. J Am Chem Soc 71:2488–2492
58. Wayda AL, Schneemeyer LF, Opila RL (1988) Low-temperature deposition of zirconium and hafnium boride films by thermal decomposition of the metal borohydrides ($M[BH_4]_4$). Appl Phys Lett 53:361
59. Yang Y, Jayaraman S, Kim DY, Girolami GS, Abelson JR (2006) CVD growth kinetics of HfB_2 thin films from the single-source precursor $Hf(BH_4)_4$. Chem Mater 18:5088–5096
60. Kim DY, Yang Y, Abelson JR, Girolami GS (2007) Volatile magnesium octahydrotriborate complexes as potential CVD precursors to MgB_2. synthesis and characterization of $Mg(B_3H_8)_2$ and its Etherates. Inorg Chem 46:9060−9066

61. Glass JA Jr, Kher SS, Spencer JT (1992) Chemical vapor deposition precursor chemistry. 2. Formation of pure aluminum, alumina, and aluminum boride thin films from boron-containing precursor compounds by chemical vapor deposition. Chem Mater 4:530–538
62. Amini MM, Fehlner TP (1990) Metallaboranes as molecular precursors to thin metal-boride films. Conversion of $HFe_3(CO)_9BH_4$ to amorphous $Fe_{75}B_{25}$. Chem Mater 2:432–438
63. Jun C-S, Fehlner TP (1992) Binary thin films from molecular precursors. Role of precursor structure in the formation of amorphous and crystalline FeB. Chem Mater 4:440–446
64. Goedde DM, Girolami GS (2004) A new class of CVD precursors to metal borides: $Cr(B_3H_8)_2$ and related octahydrotriborate complexes. J Am Chem Soc 126:12230–12231
65. Sung J, Goedde DM, Girolami GS, Abelson JR (2002) Remote-plasma chemical vapor deposition of conformal films at low temperature: a promising diffusion barrier for ultralarge scale integrated electronics. J Appl Phys 91:3904
66. Yang Y, Jayaraman S, Kim DY, Girolami GS, Abelson JR (2006) Crystalline texture in hafnium diboride thin films grown by chemical vapor deposition. J Cryst Growth 294:389–395
67. Ningthoujam RS, Vatsa RK, Prajapat CL, Yashwant G, Ravikumar G, Nataraju V (2010) Interaction between amorphous ferromagnetic Co–Fe–B particles in conducting silver matrix prepared by chemical reduction route. J Alloys Compd 492:L40–L43
68. Ababei G, Gaburici M, Budeanu L-C, Grigoras M, Porcescu M, Lupuand N, Chiriac H (2018) Influence of the chemically synthesis conditions on the microstructure and magnetic properties of the Co-Fe-B nanoparticles. J Magn Magn Mater 451:565–571
69. Nagy JB, Gourgue A, Derouane EG (1983) Preparation of monodispersed nickel boride catalysts using revised micellar systems. In: Poncelet G, Grange P, Jacob PA (eds) Preparation of catalyst III © 1983 Elsevier Science Publishers B.V., Amsterdam—Printed in The Netherlands
70. Legrand J, Taleb A, Gota S, Guittet M-J, Petit C (2002) Synthesis and XPS characterization of nickel boride nanoparticles. Langmuir 18:4131–4137
71. Schmid G, Schops E, Malm J-O, Bovin J-O (1994) Ligand-stabilized nickel and palladium boride colloids. Z Anorg Allg Chem 620:1170–1174
72. Gouget G, Beaunier P, Portehault D, Sanchez C (2016) New route toward nanosized crystalline metal borides with tuneable stoichiometry and variable morphologies. Faraday Discuss 191:511
73. Hamayun MA, Abramchuk M, Alnasir H, Khan M, Pak C, Lenhert S, Ghazanfari L, Shatruk M, Manzoor S (2018) Magnetic and magnetothermal studies of iron boride (FeB) nanoparticles. J Magn Magn Mater 451:407–413
74. Ali AO, Al-Masoudi, Soliyman R (2017) Nano-metal borides of cobalt, nickel and copper. J Nanomed Nanotechnol 8:1000477
75. Baris M, Simesek T, Akkurt A (2016) Mechanochemical synthesis and characterization of pure Co_2B nanocrystals. Bull Mater Sci 39:1119–1126
76. Rinaldi A, Correa-Duarte MA, Salgueirino-Maceira V, Licoccia S, Traversa E, Dávila-Ibáñez AB, Peralta P, Sieradzki K (2010) Elastic properties of hard cobalt boride composite nanoparticles. Acta Mater 58:6474–6486
77. Saiyasombat C, Petchsang N, Tangand IM, Hodak JH (2008) Preparation of iron boride–silicacore–shell nanoparticles with soft ferromagnetic properties. Nanotechnology 19:085705 (7pp)
78. Cheng Y, Tanaka M, Watanabe T, Choi SY, Shin MS, Lee KH (2014) Synthesis of Ni_2B nanoparticles by RF thermal plasma for fuel cell catalyst. J Phys Conf Ser 518:012026
79. Choi S, Matsuo J, Cheng Y, Watanabe T (2013) Preparation of boron-rich aluminum boride nanoparticles by RF thermal plasma. J Nanopart Res 15:1820
80 Ibe TWT, Abe Y, Ishii Y, Adachi K (2004) Nucleation mechanism of boride nanoparticles in induction thermal plasmas. Trans Mater Res Soc Jpn 29:3407
81. Portehault D, Devi S, Beaunier P, Gervais C, Giordano C, Sanchez C, Antonietti M (2011) A general solution route toward metal boride nanocrystals. Angew Chem Int Ed 50:3262–3265
82. Khoshsima S, Altıntaş Z, Somer M, Balcı Ö (2018) Novel synthesis of cobalt based binary boride nanoparticles by using metal chloride powder blends. In: 19th international metallurgy & materials congress (IMMC 2018). pp 563–566

83. Zhdanova OV, Lyakhova MB, Pastushenkov YG (2013) Magnetic properties and domain structure of FeB single crystals. Met Sci Heat Treat 55:68–72
84. Sani E, Meucci M, Mercatelli L, Jafrancesco D, Sans J-L, Silvestroni L, Sciti D (2014) Optical properties of boride ultrahigh-temperature ceramics for solar thermal absorbers. J Photonics Energy 4:045599
85. Kanomata T, Ise Y, Kumagai N, Haga A, Kamishimis K, Goto T, Kimura HM, Yoshida H, Kaneko T, Inoue A (1997) Magnetovolume effect of Co_2B. J Alloys Compd 259:L1–L4
86. Samsonov GV, Kovenskaya BA (1977) The electronic structure of boron compounds in boron and refractory borides. In: Matkovich VI. Springer, Berlin
87. Perras FA, Bryce DL (2014) Boron–boron J coupling constants are unique probes of electronic structure: a solid-state NMR and molecular orbital study. Chem Sci 5:2428
88. Wang Y, Quillian B, Wei P, Wannere CS, Xie Y, King RB, Schaefer HF, III, Schleyer PVR, Robinson GH (2007) A stable neutral diborene containing a B=B double bond. J Am Chem Soc 129:12412–12413
89. Bohnke J, Braunschweig H, Constantinidis P, Dellermann T, Ewing WC, Fischer I, Hammond K, Hupp F, Mies J, Schmitt H-C, Vargas A (2015) Experimental assessment of the strengths of B−B triple bonds. J Am Chem Soc 137:1766–1769
90. Joseph J, Gimarc BM, Zhao M (1993) Correlations between bond order and bond length in the electron-deficient closo-boranes. Polyhedron 12:2841–2848
91. Tian H, Zhang C, Zhao J, Dong C, Wen B, Wang Q (2012) First-principle study of the structural, electronic, and magnetic properties of amorphous Fe–B alloys. Phys B 407:250–257
92. Burdett JM, Canadell E, Miller GD (1986) Electronic structure of transition metal borides with the $A1B_2$ structure. J Am Chem Soc 108:6561–6568
93. Tzelia D, Mavridis A (2008) Electronic structure and bonding of the 3*d* transition metal borides, MB, M = Sc, Ti, V, Cr, Mn, Fe, Co, Ni, and Cu through all electron *ab initio* calculations. J Chem Phys 128:034309
94. Gasparov VA, Kulakov MP, Sidorov NS, Zverkova II, Filipov VB, Lyashenko AB, Paderno YB (2004) On electron transport in ZrB_{12}, ZrB_2, and MgB_2 in normal state. JETP Lett 80:376–380
95. Shein IR, Ivanovskii AL (2001) The band structure of hexagonal diborides ZrB_2, VB_2, NbB_2 and TaB_2 in comparison with the superconducting MgB_2. arXiv:cond-mat/0109445v2 [cond-mat.supr-con] 26 Sep 2001
96. Souma S, Komatsu H, Takahashi T, Kaji R, Sasaki T, Yokoo Y, Akimitsu J (2003) Electronic band structure and fermi surface of CaB_6 studied by angle-resolved photoemission spectroscopy. Phys Rev Lett 90:027202
97. Young DP, Hall D, Torelli ME, Fisk Z, Sarrao JL, Thompson JD, Ott H-R, Oseroff SB, Goodrichk RG, Zysler R (1999) High-temperature weak ferromagnetism in a low-density free-electron gas. Nature 397:412
98. Shirakawa K, Kaneko T, Yoshida H, Masumoto T (1986) Electrical resistivity of amorphous and crystalline $(Co_{1-x}Mn_x)_2B$ alloys. J Magn Magn Mater 54–57:267–268
99. Sani E, Mercatelli L, Meucci M, Silvestroni L, Balbo A, Sciti D (2016) Process and composition dependence of optical properties of zirconium, hafnium and tantalum borides for solar receiver applications. Sol Energy Mater Sol Cells 155:368–377
100. Licheri R, Musa C, Locci AM, Montinaro S, Orrù R, Cao G, Silvestroni L, Sciti D, Azzali N, Mercatelli L, Sani E (2019) Ultra-high temperature porous graded ceramics for solar energy applications. J Eur Ceram Soc 39:72–78
101. Schmechel R, Werheit H, Kampen TU, Mönch W (2004) Photoluminescence of boroncarbide. J Solid State Chem 177:566–568
102. Silly MG, Jaffrennou P, Barjon J, Lauret J-S, Ducastelle F, Loiseau A, Obraztsova E, Attal-Tretout B, Rosencher E (2007) Luminescence properties of hexagonal boron nitride: cathode luminescence and photoluminescence spectroscopy measurements. Phys Rev B 75**:**085205
103. Prathap KJ, Wu Q, Olsson RT, Diner P (2017) Catalytic reductions and tandem reactions of nitro compounds using in situ prepared nickel boride catalyst in nanocellulose solution. Org Lett 19:4746–4749

104. Nsanzimana JMV, Reddu V, Peng Y, Huang Z, Wang C, Wang X (2018) Ultrathin amorphous iron-nickel boride nanosheets for highly efficient electrocatalytic oxygen production. Chem Eur J 24:18502–18511
105. Vandenberg JH, Matthias BT, Corenzwit E, Barz H (1975) Superconductivity of some binary and ternary transition-metal borides. Mat Res Bull 10:889–894
106. Xie W, Luo H, Baroudi K, Krizan JW, Phelan BF, Cava RJ (2015) Fragment-based design of NbRuB as a new metal-rich boride superconductor. Chem Mater 27:1149–1152
107. Carnicom EM, Strychalska-Nowak J, Wiśniewski J, Kaczorowski D, Xie W, Klimczuk T, Cava RJ (2018) Superconductivity in the superhard borideWB$_{4.2}$. Supercond. Sci Technol 31:115005
108. Jiang J, Wang Y, Zhong Q, Zhou Q, Zhang L (2011) Preparation of Fe_2B boride coating on low-carbon steel surfaces and its evaluation of hardness and corrosion resistance. Surf Coat Technol 206:473–478
109. Andoh Y, Nishiyama S, Sakai S, Ogata K (1993) Wear resistance of boron nitride coated metal. Nucl Inst Methods Phys Res B 80(81):225–228
110. Jiang C, Pei Z, Liu Y, Xiao J, Gong J, Sun C (2013) Preparation and characterization of superhard AlB_2-type WB_2 nanocomposite coatings. Phys Status Solidi A 210:1221–1227
111. Williams WS (1998) The thermal conductivity of metallic ceramics. J Miner Met Mater Soc 50:62–66
112. Bellosi A, Monteverde F (2006) Ultra high temperature ceramics: Microstructure control and properties improvement related to materials design and processing procedures, thermal protection systems and hot structures. In: Fletcher K (ed) Proceedings of the 5th European workshop held 17–19 May, 2006 at ESTEC, ESA SP-631. European Space Agency, 2006. Published on CDROM, id.46, Noordwijk, The Netherlands
113. Lozynskyy OZ, Herrmann M, Ragulya A, Andrzejxzuk M, Polotal A (2012) Structure and mechanical properties of spark plasma sintered TiN-based nanocomposites. Arch Metall Mater 57:853
114. Grigor'ev ON, Prilutskii ÉV, Trunova EG (2002) Structure and properties of ceramics based on tungsten and titanium borides and boron carbide. Powder Metall Met Ceram 41:142–146
115. Zoli L, Galizia P, Silvestroni L, Sciti D (2018) Synthesis of group IV and V metal diboride nanocrystals via borothermal reduction with sodium borohydride. J Am Ceram Soc 101:2627–2637
116. Li Y, Tevaarwerk E, Chang RPH (2006) Ferromagnetic iron boride (Fe_3B) nanowires. Chem Mater 18:2552–2557
117. Scheifers JP, Zhang Y, Fokwa BPT (2017) Boron: enabling exciting metal-rich structures and magnetic properties. Acc Chem Res 50:2317–2325
118. Fokwa BPT (2010) Transition-metal-rich borides—Fascinating crystal structures and magnetic properties. Eur J Inorg Chem 3075–3092
119. Williams MD, Jackson T, Kippenhan DO, Leung KN, West MK, Crawford CK Lanthanum hexaboride (LaB_6) resistivity measurement. Appl Phys Lett 50:1844
120. Kerley EL, Hanson CD, Russell DH (1990) Lanthanum hexaboride electron emitter for electron impact and electron-induced dissociation Fourier transform ion cyclotron resonance spectrometry. Anal Chem 62:409–411
121. Yamauchi H, Takagi K, Yuito I, Kawabe U (1976) Work function of LaB_6. Appl Phys Lett 29:638
122. Tantau LJ, Islam MT, Payne AT, Tran CQ, Cheah MH, Best SP, Chantler CT (2014) High accuracy energy determination and calibration of synchrotron radiation by powder diffract ion. Radiat Phys Chem 95:73–77
123. Kim JS, Kim B, Kim H, Kang K (2018) Recent progress on multimetal oxide catalysts for the oxygen evolution reaction. Adv Energy Mater 8:1702774
124. Nsanzimana JMV, Dangol R, Reddu V, Duo S, Peng Y, Dinh KN, Huang Z, Yan Q, Wang X (2019) Facile synthesis of amorphous ternary metal borides—reduced graphene oxide hybrid with superior oxygen evolution activity. ACS Appl Mater Interfaces 11:846–855

125. Cao X, Wang X, Cui L, Jiang D, Zheng Y, Liu J (2017) Strongly coupled nickel boride/graphene hybrid as a novel electrode material for supercapacitors. Chem Eng J 327:1085–1092

Chapter 9
Synthesis and Applications of Borides, Carbides, Phosphides, and Nitrides

Raghumani S. Ningthoujam and Rashmi Joshi

Abstract The borides, carbides, phosphides, and nitrides of metals or non-metals can be prepared by various methods. This chapter covers the preparation, properties, and applications of polycrystalline samples (powder, thin film in micron to nanometer sized particles) and single crystals of borides, carbides, phosphides, and nitrides. Nature of chemical bonding of transition metal or rare-earth metal nitrides is similar to that of respective carbides (i.e., metallic and ionic bonding in nature). When a few percentages of N/C are present in transition metals, the metal lattice expansion occurs (i.e., the interstitial sites of the metal lattice are occupied by N/C atoms) and then new phases of compounds are formed by further addition of N/C in metal lattice. The s-block elements form nitrides or carbides and chemical bond is usually ionic in nature. The p-block elements form nitrides or carbides and chemical bond is usually covalent in nature. The borides of transition metal or rare-earth metal can have metal rich to boron rich phases (M_2B, MB, M_3B_4, MB_2 to MB_{12}) with M–M, M–B, B–B bonding (metallic, ionic, and covalent bonding in nature). The phosphides of transition metal or rare-earth metal can have metallic and ionic bonding. When the shape of particle changes from 0D, 1D, 2D to 3D in nanosize range, their properties vary. They exhibit interesting electrical, mechanical, magnetic, and optical properties. They are used in many applications such as catalysts, permanent magnetic materials, sensors, LEDs, lasers, super-hard materials, high temperature materials, cutting tools, permanent coloring materials (i.e., jewelry), absorbing medium for microwave to radio-wave ranges, insulating materials, high thermal conducting materials, etc.

Keywords Synthesis · Applications · Borides · Carbides · Phosphides · Nitrides

R. S. Ningthoujam (✉) · R. Joshi
Chemistry Division, Bhabha Atomic Research Centre, Mumbai 400085, India
e-mail: rsn@barc.gov.in

Homi Bhabha National Institute, Anushaktinagar, Mumbai 400094, India

A. K. Tyagi and R. S. Ningthoujam (eds.), *Handbook on Synthesis Strategies for Advanced Materials*, Indian Institute of Metals Series,
https://doi.org/10.1007/978-981-16-1892-5_9

9.1 Introduction

Borides, carbides, nitrides, and phosphides of metals or non-metals are interesting in terms of their chemical bonding, crystal structures, properties, and applications [1–3]. Chemical bonding includes metallic, ionic, and covalent types. The compounds can have composition of X_aY_b (X = metal or non-metal, Y = B, C, N or P) and a/b ratio varies from less than 1.0 to more than 1.0. It implies that X_aY_b can be from X-rich to Y-rich.

Borides, carbides, nitrides, and phosphides of s-block elements are very sensitive to air and required to be stored properly [1–10]. The chemical bonding between metal (X = M) and Y = B, C, N, or P is highly ionic in nature. It forms sp-bonding. Examples are Li_3B_{14}, NaB_6, MgB_2, Li_3N, Mg_3N_2, Mg_2C, Li_2C_2, Li_4C, Li_3P, Ca_3P_2. MgB_2 shows superconducting transition at 39 K, which is comparable to several high T_c oxide superconductors and more than that of other intermetallic compounds [2, 7].

Borides, carbides, nitrides, and phosphides of d-block elements are mostly discussed in literature because they have unusual properties in terms of optical, electronic, magnetic and mechanical properties [1–6, 11–30]. They are mostly stable in air and some are stable even under extreme conditions also. The chemical bonding between X = M and Y = B, C, N, or P is slightly ionic and metallic in nature except in B-rich system, in which covalent bonding in B-B is possible. The bond is of dp-type. The electron density of states at the Fermi-level is generally high as compared to the respective transition metal (d-block metal). Examples are VN, VC, WC, Fe_3C, FeB, FeP, Ni_2P. Among them, NbN has the highest superconducting transition at 17 K. Some of the transition metal nitrides have higher superconducting transitions as compared to those of respective metals. Most transition metal borides, carbides, nitrides and phosphides have been used as catalysts due to high surface area, suitable electronic structure and harness, chemical and thermal stabilities (less corrosion). Generally, transition metal nitrides have higher surface area than those of respective metals. However, transition metal phosphides are better catalysts than others (borides, carbides, and nitrides) for water splitting, energy storage (battery) in terms of efficiency. Some of the transition metal nitrides, carbides, and phosphides show ferromagnetic, antiferromagnetic, and paramagnetic behavior. In same system, magnetic behavior varies with change of metal (X) to non-metal (Y) ratio. Example, Fe_aN system (a = 4, 3, 2, 1) can show ferromagnetic, antiferromagnetic, and paramagnetic behavior with increase in nitrogen concentration. CrN has been used as coating material because of its high stability in slightly acidic or alkaline conditions. WC, TiN, TaC, TaN have been used as cutting tools. Borides of transition metals can have metal rich to poor (i.e., M_2B, MB, M_3B_4, MB_2 to MB_{12} with M–M, M–B, B–B bonding). In metal rich system, it can have M–M bonding (metallic type) apart from M–B bonding, whereas, in B-rich system, it can have B–B bonding (covalent type).

Borides, carbides, nitrides, and phosphides of f-block elements are stable in air and their properties are interesting [1–6, 31–40]. The chemical bonding between metal and non-metal (B, C, N, or P) is ionic in nature except B-rich system, in which

covalent bonding in B–B is possible. The bond is of fp-type in X–Y. Examples are LaN, UC, Lu_2C, Gd_3C, NdB_4, LaP_2, CeP_5, LaB_6. CeB_6 and LaB_6 are good material for thermo-emission due to low work function and this can have B–B bonding (covalent type) in addition to La–B bonding. They are good thermal conducting materials. A few of B containing rare-earth compounds have been used as permanent magnets. Some rare-earth carbides have been used as nuclear materials. Some nitrides and carbides and their ternary and quaternary nitrides and carbides (layered systems) exhibit the superconducting property.

Borides, carbides, nitrides, and phosphides of p-block elements are stable in air and their properties are interesting in terms of mechanical and thermal, and optical properties [1–6, 41–50]. The chemical bonding between p-block element and B, C, N, or P is usually covalent. The bond is of pp-type. Nitrides, carbides, and phosphides of p-block elements (e.g., BN, AlN, C_3N_4, Si_3N_4, SiC, GaN, InN, $Ga_{1-x}In_xN$, GaP, AsP, InP) are important phosphor materials for light emitting in UV to visible to IR region. Along with these phosphors, visible NIR light can be produced from rare-earth doped luminescence materials [51–60]. Some carbides such as SiC have been used in high temperature stable phosphor as well as heating elements in furnace. BN, C_3N_4 and AlN are a few examples of hardest materials comparable with diamond. Si_3N_4 has been used in many applications as atomic force microscopy (AFM) scanning tip and sample holder for nuclear magnetic resonance (NMR) experiment. BN has been used as sample holder for magnetic measurement at room temperature and high temperature.

Interestingly, carbides or nitrides of transition metals and rare-earth metals have metal lattices in which C or N occupy the interstitial positions (octahedral) [1]. With occupancy of C or N at initial stage, volume expansion occurs and with increase of occupancy of C or N, it starts formation of other phases such as X_4N, X_3N, X_2N, XN, and XN_2 or X_4C, X_3C, X_2C, XC, and XC_2 to minimize energy. While, borides or phosphides of transition metals and rare-earth metals can have chemical bonding of metal-metal, B–B or M–B or P–P or M–P types [2–6]. Usually, the interstitial positions of the metal lattice are not occupied by B or P atoms.

Some compounds with composition X_2Y or XY_2 can have the layered structures which have sandwich structure (i.e., X is in between Y layers or vice versa). Those are sometimes considered as the layered structured compounds (2D materials) [1–6].

There are reports on preparation of borides, carbides, nitrides, and phosphides in nanosize regions (0, 1, 2, or 3D) [1–6, 12–27, 61–65]. Some show quantum confinement effects. The quantum confinement effects occur when particle size of semiconductor is less than Bohr's radius of its exciton or particles dispersed in another dielectric medium or formed by heterostructure configuration (core-shell, composite, multilayers). Size and shape of these compounds or particles can be controlled by designing synthesis routes. Magnetic nanoparticles of borides, carbides, and nitrides have been used for hyperthermia application very recently and their specific absorption rates (SAR) are comparable with magnetic nanoparticles based on oxides.

In this chapter, the various synthesis routes for borides, carbides, nitrides, and phosphides will be discussed. Synthesis methods of nanosized particles and layered

structure materials are also mentioned. Since one of the chapters is focused on borides in this book, detailed synthesis methods for borides will not be given. This is briefly included here because its properties are similar to nitrides, carbides, and phosphides. Finally, their applications will also be discussed.

9.2 Synthesis Methods of Nitrides

Binary, ternary, and quaternary nitrides were prepared by the following methods:

9.2.1 Interaction of N_2 Gas with the Metal Powder or Film at Elevated Temperature

Metal nitrides are prepared by direct interaction between metal (powder or film) and N_2 gas at elevated temperature [1, 2, 64]. Nitrogen molecule is highly stable since it has three bonds between two N atoms (N≡N, 2 π–bonds, 1 σ–bond). It is difficult to dissociate even at high temperatures. Thermal equilibrium between N_2 and dissociated nitrogen atoms is represented by:

$$N_2 \rightleftarrows 2N \tag{9.1}$$

The fractional dissociation (f) of N_2 gas in the thermal equilibrium at a temperature (T) can be calculated from the equilibrium constant (K(T)). Here, no reaction between nitrogen gas and foreign body in an ideal box takes place (no change in dimension).

$$K(T) = \left[p(N)\right]^2 / \left[p(N_2)\right] \tag{9.2}$$

Total pressure (P) at a particular temperature is defined here,

$$P = p(N) + p(N_2) \tag{9.3}$$

$$f = p(N)/P \tag{9.4}$$

The equilibrium constant (K(T)) can be calculated from the following relation [64]:

$$R\ln(K) = -\Delta\left(F^0 - E_0^0\right)/T - \Delta E_0^0/T \tag{9.5}$$

where R is gas constant, $\left(F^0 - E_0^0\right)$ is the free energy of the components of reaction. ΔE_0^0 is dissociation energy of gas molecules. The dissociation energy of N_2 is calculated to be 8.80 eV.

However, if there is a reaction between N_2 and foreign body (say Fe, Ru, Al), dissociation energy decreases. Here temperature (T) and pressure (P) are important parameters in a container (volume). The physisorption and chemisorption of gases over metal surface occurs. Suppose there is a flow of gas from the left (ingoing) to the right (outgoing) over iron metal surface (alumina crucible) which was inserted into a transparent quartz tube at the elevated temperature. There will be equilibrium between N_2 gas and N atoms dissociated over metal surface [65].

$$N_2 \rightleftarrows 2N(\text{Metal surface}) \tag{9.6}$$

The rate of N_2 dissociation (v, mol/cm^2.s) can be considered of the first order and it is given by,

$$v = kp(N_2) \tag{9.7}$$

The k is the rate constant of N_2 dissociation.

To calculate the rate constant (k), a few precautions are adapted. Initially, iron metal chamber is passed with Ar-H_2 mixture at the temperature of 1873 K. The content of oxygen is reduced (10–11 ppm). Then ingoing gas is changed to Ar-N_2-H_2 mixture. It has about 1 at.% nitrogen isotope ($^{30}N_2$). Total gas flow rate is 1000 cm^2/min at standard temperature and pressure (volume of argon, V(Ar) = 750 cm^3/min, V(N_2) = 50 cm^2/min, V(H_2) = 200 cm^3/min). A quadrupole mass spectrometer is attached to this reaction chamber, which can measure the fraction of the isotope nitrogen in the ingoing and outgoing gases, $^{30}F_i$ and $^{30}F_f$ through a quartz capillary tube. When a fraction of $^{30}N_2$ for total nitrogen ($^{28}N_2$ + $^{29}N_2$ + $^{30}N_2$) in the ongoing gas becomes constant for 10 min, the measurement is finished. This suggests that there is equilibrium between gas and metal phases.

Under this consideration, the fraction of $^{30}N_2$ in the total absorbed nitrogen is given by that in the ingoing nitrogen. $^{30}F_i$ and $^{30}F_f$ can have the following relationship with partial pressure of N_2 gas ($p(N_2)$, atmosphere), volume of gas flow (V, cm^3/s) and the rate of nitrogen dissociation (v, mol/cm^2.s) at the experimental temperature (T).

$$\left[p(N_2)V/RT\right] \times \left[^{30}F_i - ^{30}F_f\right] = [Av] \times \left[^{30}F_i - ^{30}F_{eq}\right] \tag{9.8}$$

The A is the surface area of solid metal (cm^2). $^{30}F_{eq}$ is the equilibrium fraction of $^{30}N_2$. R is the gas constant (82.1 cm^{3}atm/K mol). By substituting Eq. (9.7) in to Eq. (9.8), the rate constant (k) can be calculated:

$$k = [V/ART] \times \left[^{30}F_i - ^{30}F_f\right] / \left[^{30}F_i - ^{30}F_{eq}\right] \tag{9.9}$$

The rate constant of nitrogen dissociation at the surface of iron at 1773 K measurement temperature is about 1.97×10^{-5} mol/(cm^2.s.atm.). The dissociation constant increases with increase of measurement temperature since amount of dissolution of nitrogen at Fe increases with increase of temperature from 1000 to 2000 K. Iron

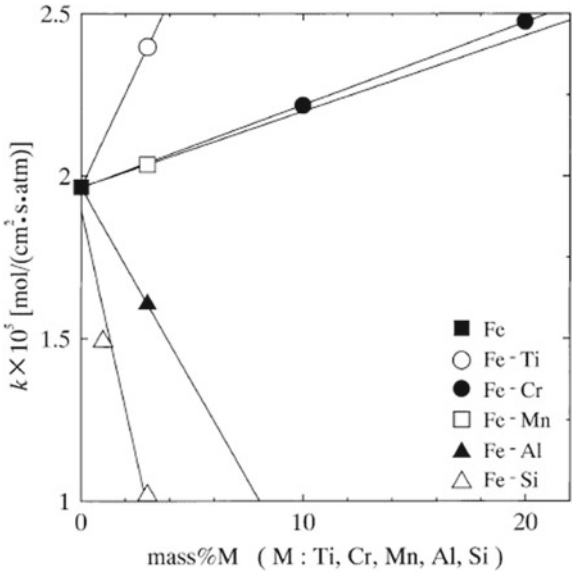

Fig. 9.1 Dependence of the rate constant of N_2 dissociation on the additive element content of iron at 1773 K. Reproduced with permission from ISIJ publishers [65]

can exit as α (bcc phase), γ (fcc phase), δ, and liquid state in different temperatures T < 1200 K, < 1600 K, < 1800 K and < 1800 K, respectively. The presence of additive elements changes dissociation constant at the surface Fe at a particular measurement temperature. The presence of Ti, Cr, Mn in Fe enhances the dissociation constant, whereas the presence of Al, Si reduces the dissociation constant at particular temperature of 1773 K (Fig. 9.1) [65].

The density functional theory (DFT) can explain the chemical reactions of gases (say N_2) on the metal surfaces [66, 67]. During dissociation of N_2 on Ru (0001) undergoes minimum energy path (Fig. 9.2) [66]. At initial stage (I), N_2 molecule comes to surface perpendicular with distance apart (z) and bond length (N–N = b = 1.11 Å). At the final state (F), completion of dissociation of N_2 occurs. When z is short, b becomes longer. In between, it undergoes minimum energy path and this was represented by the solid line. The initial and final stages are connected by the dashed line. Energy coordinated diagram shows that initial and final stages have minima (Fig. 9.3) [66]. At initial stage, N_2 is perpendicular to Ru surface. The N_2 starts bending towards Ru surface to form metastable state (M). N_2 becomes the highest stretch at the transition state (TS) where dissociation starts. At the final state (F), N atoms diffuse into the HCP sites of Ru. The presence of Na or Cs on Ru (0001) decreases the barrier for N_2 dissociation.

Thus many nitrides such as (MN = s, p, d, and f-block elements) can be prepared by passing N_2 over elemental powder or elemental oxides or metal-ligand precursors. Here, nitrides are formed at high temperature (900 °C or above) [1, 2, 9–11, 33–35, 39–44]

$$M + N_2 \xrightarrow{\text{Heat}} MN$$

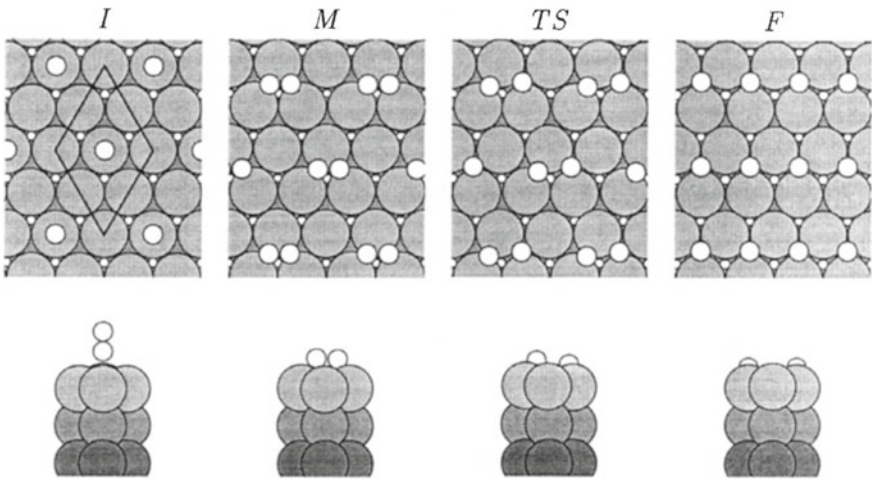

Fig. 9.2 Design of the unit cell used in the calculation and the configurations along the reaction path for N_2 dissociating over Ru(0001): (I) the initial, N_2 molecularly adsorbed state; (M) the metastable molecularly adsorbed state; (TS) the transition state; and (F) the final, dissociated state. Reproduced with permission from Elsevier Publishers [66]

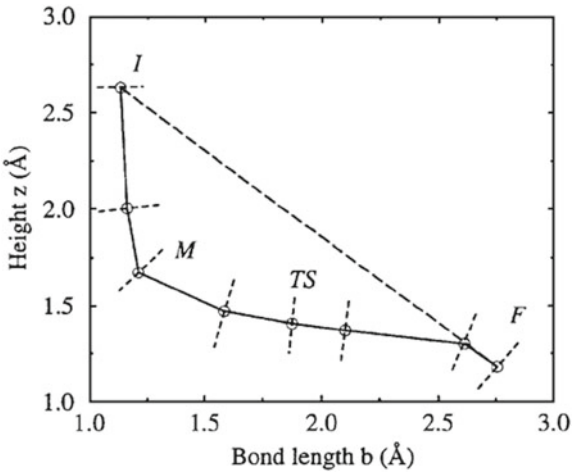

Fig. 9.3 Design of the hyperplane adaptive constraint (HAC) method for finding the minimum energy reaction path. The figure shows the initial guess and the final path for N_2 dissociation on Ru(0001) in the (z, b) plane spanned by the height z of the center of mass of the molecule over the Ru surface plane and the N–N bond length b. The initial guess is just the dashed line connecting the initial (I) and final (F) states. After minimizing the energy perpendicular to the local path the minimum energy path, shown as a solid line, develops. The constraint is defined along the way as the hyperplane perpendicular to the line connecting the two neighboring points on the path. The hyperplanes for the final path are sketched at the images used. Reproduced with permission from Elsevier Publishers [66]

e.g., TiN is prepared at 1200 °C from titanium metal and N_2 gas and its color is golden [68].

9.2.2 *Interaction of NH_3 Gas with the Metal Powder or Film or Oxides or Sulphides or Halides at Elevated Temperature*

At room temperature, ammonia (NH_3) exits in gaseous state and the heat is required to dissociate it into N_2 and H_2 gases [1, 2, 69].

$$2NH_3 \rightarrow N_2 + 3H_2; \quad \Delta H = 11 \text{ kcal/mol}$$

Ammonia can be stored at room temperature under 8 atm pressure.

Thus many nitrides such as (MN = s, p, d, and f-block elements) can be prepared by passing NH_3 over elemental powder or elemental oxides or metal-ligand precursors. Here, metal nitrides are generally formed from metal and NH_3 gas at temperature, which is relatively lower than that prepared from metal and N_2 gas.

(a) $M + NH_3 \xrightarrow{\text{heat}} MN + H_2$

(b) $M_xO_y + NH_3 \xrightarrow{\text{heat}} MN + H_2O$

(c) $MCl_x + NH_3 \xrightarrow{\text{heat}} MN + HCl$

(d) $MS_x + NH_3 \xrightarrow{\text{heat}} MN + H_2S.$

e.g., TiN is prepared at 900–1200 °C from Ti in NH_3 [70]. TiN is prepared at 850 °C from TiO_2 in NH_3 [71]. Nanocrystalline TiN powders can be prepared in 400–1000 °C range from $TiCl_4$ in NH_3 [72]. Initially, $TiCl_4$ is dissolved in $CHCl_3$ in glove box filled with Ar gas (free from water). Anhydrous NH_3 gas is passed over solution. Solvent is evaporated at 100 °C and dry powder is heated at 400–1000 °C by passing ultra-high-purity (UHP)-Ar, N_2, and anhydrous NH_3 atmosphere. Formation of nanocrystalline TiN starts at 400 °C. Low temperature formation is due to the formation of metal-amide compound between $TiCl_4$ and NH_3 in anhydrous medium.

9.2.3 *Decomposition of Single Source Precursor Containing Metal–Nitrogen Link*

Complexes having M–N (metal–nitrogen) linkage can produce metal nitrides. It can be performed with or without reducing atmosphere [1, 2].

(a) $M - N \text{ complex} \xrightarrow{\text{heat}} MN + H_2/H_2O + CO_2/CO$

(b) $M - N \text{ complex} + NH_3 \xrightarrow{\text{heat}} MN + H_2/H_2O + CO_2/CO.$

For example, VN, GaN, Ni_3N, TiN, and CoN_x can be prepared from $[VO(NH_2O)_2Gly]$. H_2O,$Ga(NH_2CONH_2)_6Cl_3$ or Ga-EDTA complex, $[Ni(NH_3)_6](NO_3)_2$, $TiCl_4(NH_3)_4$ and $[Co(NH_3)_6](NO_3)_3$, in the presence of NH_3 atmosphere [12, 13, 21, 27, 73–75].

9.2.4 Use of Urea/Azide and Reductant Precursor

Organic or inorganic compounds such as urea ($OC(NH_3)_2$) and metal azides (e.g., NaN_3) can be source of nitrogen [1, 2, 76]. Carbon nitride (C_3N_4) can be prepared from urea at 400–550 °C by very slow heating (1–2 °C/min). Here, urea powder is transferred to alumina boat, which is covered with another same size boat crucible. This reduces loss of gases coming out from urea powder. Slow heating is needed because the formation of C_3N_4 should be in equilibrium with evaporation of CO_2/CO/N_2 from urea molecules. Otherwise, the yield of carbon nitride product will be less. Metal nitrides can be prepared by the followings:

$$M + OC(NH_3)_2 \xrightarrow{\text{heat}} MN + CO + H_2$$

$$M + NaN_3 \xrightarrow{\text{heat}} MN + Na$$

$$MO + Mg + NaN_3 \xrightarrow{\text{heat}} MN + MgO + Na$$

$$OC(NH_3)_2 \xrightarrow{\text{heat}} C_3N_4.$$

9.2.5 Use of Hard Template Having Nitrogen Source

Here, the hard template means the particle of a host having nitrogen as a component of compound with porous nature, in which metal ions will occupy [1, 2, 77]. At elevated temperatures, nitrogen atoms will be released and then interact with metal ions. In this way, metal nitrides are formed. Usually, mesoporous carbon nitrides are used; and metal chlorides dissolved in ethanol/methanol are used as source of metal ions. Powder of mesoporous carbon nitride is added into metal chloride solution and it is kept for a few hours. Subsequently, powder is removed and dried. In this way, metal chloride is coated over mesoporous particles. It is heated slowly to ensure the formation of metal nitride. For example, AlN, GaN, TiN, VN and Al–Ga–N and Ti–V–N are formed inside pores of mesoporous C_3N_4.

9.2.6 Epitaxial Growth of Nanowires or Nanorods on Substrate

Epitaxial growth of metal nitrides in the form of nanowires or nanorods on appropriate substrates can be obtained [1, 2]. W_2N nanowires can be grown on tungsten oxide nanowires, which are already prepared on the substrates such as quartz, tungsten substrates, and fluorinated tin oxide (FTO) [78]. Here NH_3 gas at 750 °C and 250 mTorr is applied for about 1 h for nitridation. Heterostructured nanowires of GaAsN/GaAs are grown on Si (111) substrate [79]. Here plasma-assisted molecular beam epitaxy is used. AlGaN nanowires are grown on SiO_2/Si substrate by metal-organic vapor phase epitaxy (MOVPE) method. Here graphene is used as a buffer. The self-assembled grown of GaN nanorods are prepared on Si (111) substrate using plasma-assisted molecular beam epitaxy [80]. Nitrogen free radicals are used as source of nitrogen.

9.2.7 In the Form of Thin Film Formation and Coating

Thin films or coating of metal nitrides can be obtained on substrates for protection of corrosion, increase of mechanical properties and coloring, etc. using chemical or physical vapor deposition or magnetron sputtering technique, etc. [1, 2]. TiN coating is done to appear materials as golden color. AlCrN and WN coatings are performed to improve mechanical properties of components and tools. To make insulation between gap of nano-devices and nano-electronics, nitrides of silicon are used as layers [81].

9.2.8 In the Form of Single Crystals

Preparation of single crystals using normal melting of nitrides is difficult due to decomposition of nitride before melting point. A few works on preparation of single crystal of GaN up to a few microns have been reported [1, 2, 82]. One way is use of supercritical ammonia at pressure of 1–5 kbars and 550 °C is used. In another method, Ga in sodium melt is used starting material for formation of GaN at 600–800 °C with nitrogen pressure, which comes from thermal decomposition of sodium azide (Na_3N).

Recently, materials having yellow, as well as red emitter, are demanding for producing warm white color under blue light excitation since Nobel Prize in Physics was awarded jointly to Isamu Akasaki, Hiroshi Amano, and Shuji Nakamura “for the invention of efficient blue light emitting diodes which enabled bright and energy-saving white light sources” in 2014 [1, 83–87]. Single crystals of efficient and stable orange as well as red emitter materials such as $CaAl_2Si_4N_8$:Eu^{2+} have been grown by the vapor phase synthesis method [88].

9.2.9 Mesoporous Metal Nitrides

When NH_3 gas is passed through metal oxides such as $Cd_2V_2O_7$, $CdTiO_3$, Cd_2TaO_7 or $Cd_2Nb_2O_6$ powder at 450–800 °C, VN, TiN, Ta_3N_5 or NbN can be synthesized from respective oxides. In this synthesis, Cd or Zn gets sublimed and remaining transition metal such as V, Ti, Nb, or Ta reacts with NH_3. The transition metal nitrides are prepared by this route to be mesoporous with 10–15 nm pores [1, 2, 89] and this method is template free. However, many transition metal nitrides with ordered mesoporous are prepared from the respective mesoporous metal oxides, which are already prepared using hard template (mesoporous silica SBA-15. Here NH_3 gas is source of nitrogen as well as reducing agent for metal oxides at 300–800 °C. In this way, CoN, WN, CrN, and Ni_3FeN (mesoporous nitrides) can be prepared [90]. Hard template SiO_2 SBA-15 is removed from respective metal oxides by treatment with 2 mol L^{-1} NaOH solution, which is followed by washing with deionized water and methanol. Finally, powder is dried in vacuum.

9.2.10 Metathesis Reaction

When cations and anions exchange takes place between two ionic salt partners in solvent (say water), the reaction is called metathesis. This is similar to a double replacement reaction.

$$A^+X^- + B^+Y^- \rightarrow BX + AY$$

$[A(H_2O)_n]^+$ from A^+X^- and $[Y(H_2O)_n]^-$ from B^+Y^- form AY. Similarly, $[B(H_2O)_n]^+$ from $B^+Y^-$and $[X(H_2O)_n]^-$ from A^+X^- form BX.

In the same way, metal nitrides can be prepared using solid state metathesis (SSM) route without conventional solvent [91]. Metal salt such as $MeCl_n$ is treated with ionic alkali or alkaline-earth nitrides (Li_3N or Ca_3N_2 which are the source of nitrogen) at elevated temperature in the presence of inert atmosphere. Excess NaCl is added to reduce exothermic reaction. Different phases of the metal nitrides can also be produced by applying pressure. The final product has extra mixture of NaCl and LiCl, which can be removed by washing with hot water.

$$MeCl_n + xLi_3N + yNaCl \rightarrow MeN_x + nLiCl + yNaCl$$

Using high pressure and temperature, many nitrides including layered nitrides can be prepared by mixing ternary alkali or alkaline-earth metal oxides with BN (source of nitrogen). The method is known as high pressure solid state metathesis (HPSSM) route [92]. GaN is prepared from $LiGaO_2$ and BN at 5.0 GPa pressure and 1200 °C temperature using HPSSM route.

9.2.11 Layered Nitrides

Layered nitrides have the layers of same species separated by another group or pores or interstitials. Sometimes, they are considered 2D materials if thickness is a few nm. Examples of 2D materials are $La_3Ni_2B_2N_3$, LaNiBN, Sr_2N, Ba_2N, Li_3N, $Li_{3-x-y}\square_yM_xN$ (M = Co, Ni, Cu, $\square$ = Li vacancy) and AMN_2 (A = alkaline-earth metal, M = Ti, Zr, Hf). $La_3Ni_2B_2N_3$ and LaNiBN are produced by arc-melting of respective precursors in N_2 atmosphere for 3 days at temperature above 1000 °C [1, 2] and they crystallize in the tetragonal phase. The structure of $La_3Ni_2B_2N_3$ has a series of three square LaN layers in a rock salt configuration, stacked with single tetrahedral Ni_2B_2 layer. In case of the structure of LaNiBN, a series of two LaN layers in a rock salt configuration is stacked with single tetrahedral Ni_2B_2 layer. Binary materials, Li_3N, Sr_2N and Ba_2N are prepared by reaction of the molten alkali (Li) or alkaline-earth (Sr, Ba) metal in Na in a glove box filled with high purity nitrogen at temperature of 520 to 650 °C [93].

9.2.12 Mechanical Transfer of Metal Nitrides Grown on a Substrate to Another Substrate

In optical and electronic devices of nitrides, it needs to transfer epitaxial grown thin films (2D materials) to another substrate depending on the requirement [1, 2]. It requires the easy way of releasing material from the previous substrate and adhesive nature of material to another substrate. One of the easy ways of releasing material from the previous substrate is use of buffer or transfer layer (e.g., a hexagonal single crystal (0001) h-BN, which has van der Waals forces among BN layers). Indium can be used as an adhesive layer.

Firstly, the (0001) h-BN is grown on (0001) h-sapphire (Al_2O_3) [94]. Nitride layer (GaN or multiple-quantum-well structure AlGaN/GaN/InGaN/GaN) is grown on h-BN. It is upside down and then put on another foreign substrate (Si, glass, metal, plastic), which is already covered with indium layer. The nitride layer of Ga is released or separated from the host sapphire substrate by applying mechanical force. Similarly, high-quality GaN films grown on large-size graphene films are transferred on amorphous SiO_2 [95]. Here, ZnO nano walls are used as intermediate layer between GaN and graphene.

9.2.13 Formation of Heterostructure Types

Heterostructure means a hybrid obtained from two or more dissimilar materials such as metal-semiconductors, semiconductor (lower band gap)—another semiconductor (higher band gap), semiconductor (lower band gap)—another semiconductor (higher

band gap)—semiconductor (lower band gap), etc. and thereby its properties will be different from individual materials [96–98]. This can change electrical and optical polarities in terms of band-gap engineering, electrical polarizability (spontaneous, stress), piezoelectricity, Schottky barrier, etc. Examples are GaN/AlN/Sapphire (developed by Nobel Prize Winners Akasaki and Amano in 1981–1989), GaN/H-BN, p-GaN/n-InGaN/n-GaN (the first blue LED developed in 1993 by Nobel Prize winner Nakamura), InN/GaN, InGaN/Si, AlGaN/GaN, InGaN/GaN/AlGaN, MQW, Graphene-h-BN, free-standing and graphene-like nitrides XN (X = B, Al, and Ga)-MoS_2.

9.2.14 *Formation of Advanced Ceramic Materials of Borides, Carbides, and Nitrides at Low Temperature*

Apart from high temperature ceramic oxides, boron nitrides, boron carbides, carbon nitrides, silicon carbides, and silicon nitrides have been considered as important materials in different areas [1, 2, 99]. BN is used as sample holder in magnetic measurement due to its diamagnetic property as well as high temperature stability. Carbon nitrides are used as hard materials and coating materials. Silicon carbides are used as furnace parts due to high melting point and high thermal conductivity, in semiconducting electronic devices that operate at high temperature or high voltage, as bearing, cutting tools and abrasive, etc. Silicon nitrides are used as cantilever in AFM (atomic force microscopy), as cutting tools, insulators in electronic circuits, and as bearing material. They are prepared from elemental powders with or without N or C under high pressure and high temperature (more than 1000 °C). However, low temperature synthesis methods are adapted from molecular precursors. Si_3N_4 is prepared from polysilazane at 350 °C, followed by heating at 1000–1400 °C in Ar/NH_3 atmosphere. Polycrystalline C_3N_4 is prepared from urea at 500 °C at slow heating rate.

9.2.15 *Formation of Different Phases of Nitrides, Carbides, Oxy-Carbides/Nitrides, and Borides Under High Pressure and Temperature*

New phases of nitrides, carbides, oxy-carbides/nitrides and borides, and the metastable compounds can be prepared under high pressure and temperature [1, 2, 100–102]. The formation of different phases of nitrides (Hf_3N_4, Zr_3N_4, Re_3N, TiN, TaN_x, Hf_3N_4, OsN_2, PtN_2, IrN_2, Si_3N_4, Zn_3N_2, Mo_2N, MoN, W_2N, P_3N_5), oxynitrides (Si_2N_2O, $Si_{3-x}Al_xO_xN_{4-x}$, Al_3O_3N), nitride-diazenides (e.g., SrN_2) and nitride-imides (e.g., Si_2CN_4) are reported under different pressures (even P > 500 GPa) and temperatures (T up to 7000 K) in different atmospheres of N_2, H_2, Ar or N_2–O_2

(mixture). Similarly, different phases of carbides and borides under pressures and temperatures are reported [101]. The following methods are used to provide pressure: autoclave (1–6000 bar), the multi-anvil device (1–20 GPa), the diamond anvil cells (DAC, 1 few hundred GPa), and shock-wave device. The formation of such phases at different pressures and temperatures is characterized by in-situ Raman and XRD studies.

9.2.16 Formation of Different Phases of Nitrides Under Sudden Cooling and Tempering

Some nitrides with different concentrations of nitrogen are usually produced by heating precursor at high temperature and followed by sudden cooling (quenching) to room temperature (or liquid nitrogen temperature). This is followed by tempering process at low temperature (100–150 °C) which was maintained for long duration up to 10 days at different atmospheres [1, 2, 103]. For example, the precursors are α–Fe, γ–Fe, γ–Fe_2O_3 and doped ones for formation of iron nitride phases. Surrounding atmosphere such asN_2, Ar, NH_3 or mixture of H_2 and Ar is used. Fe–N system in phase diagram can have the followings: (1) α (Fe-bcc, ferromagnetic), (2) γ–(Fe-fcc, non-magnetic), (3) ζ–(Fe_2N-orthorhombic, paramagnetic), (4) ε-(Fe_3N-hexagonal, ferromagnetic), (5) γ′–(Fe_4N-fcc, ferromagnetic) and (6) α″–(Fe_8N or $Fe_{16}N_2$-body centered tetragonal, ferromagnetic (bct)). γ′–Fe_4N and α″–Fe_8N or $Fe_{16}N_2$ nitrides are prepared by quenching from high temperature to room temperature, followed by tempering process.

Graphitic carbon nitrides (g-C_3N_4) nanostructures are prepared by heating urea in sealed tube at very slow heating (1–2 °C/min) at 450–500 °C [104]. Then it is suddenly cooled down to room temperature, ice, and liquid nitrogen temperature. The prepared nanostructures have different structural distortions and their photocatalytic properties towards degradation of dyes of reactive red 120 (RR120), rhodamine B, bromophenol, and methylene blue (MB) are different.

The CrN and Cr_2N are precipitated during the process of plate material of super duplex stainless steel grade 2507 in helium gas atmosphere. Initially, material is heated in 1125–1250 °C for 10 s–1 min and quenching at room temperature and sometimes followed by short heat treatments at 900 °C [105].

9.2.17 Formation of Nanotubes

There are a few reports on preparation of nitride nanotubes. First, the preparation of carbon nanotubes was reported in 1991by Iijima [106]. Then many attempts had been made for formation of nanotubes of other compounds or single elements. In 1995, boron nitride nanotubes were prepared by arc discharging of hexagonal BN

inserted into a hollow tungsten electrode as anode and pure copper as cathode [106]. The BN nanotubes prepared by this route have inner diameters (1 to 3 nm), outer diameters (6 to 8 nm), and lengths (>200 nm).

GaN nanotubes can be prepared using ZnO nanowires as a template [1, 107]. The first step is preparation of nanowires of ZnO (diameter of 30–200 nm and length 1–5 μm) grown on (110) sapphire wafers. GaN is deposited over ZnO nanowire using precursor of trimethylgallium in NH_3 atmosphere at 600–700 °C. Decomposition temperatures of Zn_3N_2 and GaN are 600–700 and 2500 °C respectively in inert atmosphere. Decomposition temperature of metal nitride decreases in H_2 atmosphere. In 10% H_2 in Ar at 600 °C, Zn_3N_2 (if formed from ZnO nanowires) and Zn (reduction of ZnO nanowires) are removed due to decomposition of Zn_3N_2 and vaporization of Zn. Finally, GaN nanotubes remain.

9.2.18 Formation of Different Sizes and Shapes

There are a few reports on the preparation of different sizes or shapes of particles in nitride materials [1, 2]. However, one needs to understand the content of nitrogen in nitrides as a function of particle size or shape. With decrease in particle size, there is a chance of surface oxidation. Fe_3N hexagonal phase with crystallite sizes of 16 and 20 nm has been prepared from iron particles in NH_3 gas at 500 and 550 °C, respectively [108]. With decrease in particle size, there is a decrease in magnetization and Curie temperature. Surface oxidation of particles occurs if powder of nitride is kept open in atmosphere.

Also, there are reports on preparation of different sizes of CoN_x by passing NH_3 gas over Cobalt(III) hexa-ammine nitrate complex, $[Co(NH_3)_6](NO_3)_3$ [27]. Their magnetic properties are studied. The preparation of crystallite sizes 8–32 nm of VN by the simultaneous thermal decomposition and nitridation of complex $[VO(NH_2O)_2Gly]H_2O$ in NH_3 atmosphere at 500–700 °C have been reported [21]. The h-BN is grown on Cu substrate by the chemical vapor deposition of borazine ($B_3N_3H_6$) in N_2 gas at 1050 °C. Domain size varies from less than 1 μm to more than 100 μm under different H_2 flows [109]. Different shapes of triangular, trapezoidal, hexagonal, and complex shapes are prepared by annealing under Ar atmosphere. Preparations of different shapes of particles of BN say nanocages, nanotubes, nanosheets, and nanoporous frameworks have been reported [110]. The preparation of hollow TiN particles has been reported [111].

9.2.19 Electrochemical Route

In a three electrode cell, auxiliary electrode (counter electrode), reference electrode, and working electrode are provided, which has advantages over a two electrode cell [1]. In a working electrode, chemical reaction occurs. The reference electrode is

a standard half-cell (aqueous or nonaqueous or quasi types), which can measure potential of the other half. The auxiliary electrode has been used to balance the reaction occurring at the working electrode and allows the potential of the working electrode to be measured with respect to a reference electrode. The common working electrodes are materials including inert metals (Pt, Au, Ag) to inert carbon (glassy carbon, boron doped diamond) and film electrodes of interest.

There are two different ways of deposition of metal nitrides on substrate by electrolysis. The first one is deposition of metal oxide, followed by nitridation at different temperatures in different sources of nitrogen such as N_2, NH_3 or H_2–NH_3. The second one is direct nitridation.

Examples of the first one are below:

1. In 3-electrode cell, the Ni foam (NF) is used as working electrode, a piece of platinum plate as the counter electrode, and Ag/AgCl electrode as the reference electrode [112]. 50 ml of 0.1 M [$Ni(NO_3)_2{\cdot}6H_2O$ or $Co(NO_3)_2{\cdot}6H_2O$ or their combination is taken as electrolyte for preparation of metal hydroxides or oxides on Ni foam support. The deposition of metal hydroxide/oxide on Ni foam is carried out by applying potentiotatic technique at −1.0 V for 10 min. Deposited metal hydroxide/oxide on Ni foam is rinsed with deionized water and dried at 50 °C for 12 h. Then nitridation is performed at 380 °C in NH_3 gas atmosphere. In this way, CoN/NF and $NiCo_2N$/NF are prepared.
2. The h-GaN on Si substrate is prepared by nitridation of Ga_2O_3 deposited on Si [113]. Here, 2-electrode cell is used. Si substrate is used as cathode and Pt as anode. The electrolyte is a mixture of Ga_2O_3 (99.99%), NH_4OH (25%), HCl (36%), and DI water. Ga_2O_3 nanostructures (nanorods) on Si are prepared from 1.0 M electrolyte at pH = 6 at a current density 0.15 A/cm^2. Nitridation process is started by passing N_2 gas at 800–900 °C. After reaching temperature, N_2 gas replaced by NH_3 gas for 15 min. The furnace is stopped and NH_3 is replaced by N_2 gas. In this way, NH_3 decomposed to $N_2 + H_2$. H_2 helps in reduction of Ga_2O_3 to form Ga_2O, which interacts with atomic nitrogen atoms or N_2. This results in the formation of h-GaN nanowires.
3. Ta_3N_5 film is formed from nitridation of TaO_xH_y in NH_3 gas at 850 °C [114]. TaO_xH_y is deposited on substrate Ti, Pt, or Ta (acts as working or cathodic electrode) by electrochemical route from 50 mM solution of $TaCl_5$ in isopropyl alcohol, 1 M KCl, and 0.5 M KNO_3. Deposition is performed at −1 V versus. Ag/AgCl as reference electrode. Pt mesh is used as counter or anodic electrode.

The second one (direct nitridation) requires the molten salt (e.g., LiCl–KCl) as electrolyte and salt of metal (e.g., $CrCl_2$, $TiCl_3$, $NiCl_2$) and NH_4Cl (source of ammonia) [1, 115]. Usually, it avoids the water content. Experiment has been performed in glove box with Ar atmosphere. Initially, all precursors are kept at 100 °C under Ar atmosphere to remove water content and brought back to room temperature. For preparation of CrN, dry NH_4Cl and $CrCl_2$ are mixed with molten salt in glove box. Nickel plate is used as the working electrode. A glassy carbon rod is used as the counter electrode. Ag/AgCl is used as the reference electrode. All

potentials are measured with respect to Li^+/Li electrode potential. At 2.4 V, CrN film is formed.

9.2.20 Deposition of Prepared Nitrides on Substrate

Already prepared nitrides and its composites can be deposited on suitable substrates. A few examples are below:

1. Ni–Si_3N_4 nano-composites are deposited over mild steel using pulse electroplating. This coating enhances hardness and corrosion potential of steel [116].
2. Using electrophoretic technique, deposition of AlN on Al cathode can be performed by dispersing AlN in nonaqueous medium (acetylacetone in I_2) [117].

9.2.21 Supercritical Fluid Ammonia or Solvothermal or Ammono-Thermal Route

At supercriticals condition, gas, and liquid of any substance co-exit. This can be achieved by increasing pressure and temperature [118–122]. Supercritical temperatures (T_c) of NH_3, H_2 and N_2 are 405.37, 33.14, and 126.19 °C, respectively. Supercritical pressures (P_c) of NH_3, H_2 and N_2 are 11.34, 1.29, and 3.39 MPa, respectively. Supercritical density (ρ_c) of NH_3, H_2 and N_2 are 13.75, 15.51, and 11.18 mol/L, respectively. Many chemical reactions can be occurred, which could not be done at room temperature or lower critical conditions. These have been used in many applications including synthesis of metals, alloys, oxides, sulphides, and nitrides. In case of preparation of nitrides of metal or non-metal, ammonia can be used as reducing as well as nitriding substance simultaneously. It is experienced that some materials that could not be dissolved in liquid at room temperature can be dissolved in supercritical fluid. By adding compounds of Li, K (sometimes considered as mineralizers), their nitridation duration and temperature can be varied. When T and P are more than their respective supercritical T_c and P_c, NH_3 decomposes to N_2 and H_2. Experimental setup requires a specific reaction chamber that can hold (1) stability (no leakage of gas), (2) no chemical reaction with surrounding inner walls of reaction reactor, (3) sensors for monitoring temperature and pressure, and (4) proper cooling process facility, etc. This method of preparation of nitride is known as supercritical fluid ammonia or solvothermal or ammono-thermal based route. Nitrides including GaN, Cr_2N, Co_2N, Fe_4N, Cu_3N, Ni_3N and their oxides have been prepared by this method [119]. Using ammonia-hexane mixture as solvent, quantum confined GaN nanoparticles (3.1 nm) has been prepared from $[Ga(NMe_2)_3]_2$ under supercritical condition [123].

9.2.22 Self-propagating High Temperature Synthesis

Self-propagating high temperature synthesis (SHTS) is one type of synthesis of materials (oxides, alloys, metals, nitrides, carbides, borides) in which ignition temperature is provided in a close reaction chamber and reaction propagates automatically with time [124–131]. Temperature as high as 1500 °C can be achieved and there is a propagation of combustion wave of heat. The compounds obtained from SRTS are found to be porous in nature with high surface area. Generally, temperature is supplied by tungsten filament with Ti powders. The precursors are provided in reaction chamber. Sometimes, to start the ignition at lower temperature (500–800 °C), some additional precursors are added. To provide pressure, some gases such as Ar, N_2 are provided. The flame of heat is checked using laser (say gas laser, CuBr). The common precursors for formation of boron nitride (BN) are diborane (B_2H_6), borazine ($B_3N_3H_6$), trimethyl borate ($C_3H_9BO_3$), boric acid (H_3BO_3) and elemental boron. The common sources of nitrogen are NH_3, NH_4Cl, aizide, N_2 and amide, etc. Sometimes, if impurity is present in nitride products, it is removed by dissolving in solvents such as warm DI water or dilute HCl. Usually, nitrides are chemically stable in such solvents. Using SHTS route, the formations of nitrides such as boron nitride nanotubes (from precursors Mg, B_2O_3, and CaB_6), CrN@Cr_2N (from Cr powder), Si_3N_4 (from ferrosilicon), TiN (from Ti powder), AlN (from Al powder), NbN (from Nb powder), and TiN (from sodium azide, $(NH_4)_2TiF_6$) are reported.

The binary, ternary or higher system or doping of others in nitrides can be prepared by above methods mentioned here. It needs to take appropriate amounts of precursors.

9.3 Synthesis Methods of Carbides

Metal and non-metal carbides can be prepared by the following routes:

9.3.1 Carbo-Thermal Route

Carbides can be prepared through direct heating of metal or non-metal powder or wire or metal hydride with carbon source (e.g., graphite) [2, 132–134]. Usually, reaction is performed in inert atmosphere. This is sometimes referred to as carbo-thermal reaction.

$$\mathrm{M} + \mathrm{C} \xrightarrow{\text{heat}} \mathrm{MC}$$

$$\mathrm{MH}_x + \mathrm{C} \xrightarrow{\text{heat}} \mathrm{MC} + \mathrm{H}_2.$$

9.3.2 Carbo-Thermic Reduction Route

The oxides or hydroxides or carbonyl or chloride of metal or non-metal are reacted with carbon or CO with or without H_2/Ar atmosphere at elevated temperature [2, 135–139]. This is referred as carbon-thermal reduction route.

$$\mathrm{MO} + \mathrm{C} \xrightarrow{\text{heat}} \mathrm{MC} + \mathrm{CO}$$

$$\mathrm{M} + \mathrm{CO} \xrightarrow{\text{heat}} \mathrm{MC} + \mathrm{O_2}$$

$$\mathrm{M-carbonyl} + \mathrm{H_2} \xrightarrow{\text{heat}} \mathrm{MC} + \mathrm{CO} + \mathrm{CO_2} + \mathrm{H_2} + \mathrm{H_2O}$$

$$\text{Boric acid } (\mathrm{H_3BO_3}) + \text{black C} \xrightarrow{\text{heat}} \mathrm{BC} + \mathrm{H_2O}.$$

9.3.3 Carburisation Route

The oxides or halides of metal or non-metal are treated with light alkane gases such as CH_4 or C_2H_6 with or without H_2 gas at elevated temperature and carbides can be prepared by this route [2, 140, 141]. This is referred to as carburization route. The possible reaction mechanisms are provided below:

$$\mathrm{M} + \mathrm{C}_x\mathrm{H}_y \xrightarrow{\text{heat}} \mathrm{MC} + \mathrm{H_2}$$

$$\mathrm{MCl}_a + \mathrm{C}_x\mathrm{H}_y + \mathrm{H_2} \xrightarrow{\text{heat}} \mathrm{MC} + \mathrm{HCl}$$

$$\mathrm{MO} + \mathrm{C}_x\mathrm{H}_y \xrightarrow{\text{heat}} \mathrm{MC} + \mathrm{H_2O}.$$

9.3.4 Microwave Route

Carbon sources such as carbon black have high absorption in microwave [132, 142, 143]. Some carbides in different morphologies such as spherical, nanotubes, nanowires, and layered forms can be prepared from precursors and carbon sources.

9.3.5 Hydrothermal or Solvothermal Route

Using water or other organic liquid as solvent, various morphologies of carbides can be prepared from the precursors dissolved or dispersed in solvent under pressure and temperature in closed chamber [143–145].

9.3.6 Self-propagating High Temperature Synthesis Route

Using self-sustaining heating after ignition, many types of carbides can be prepared from their precursors at different high temperatures and pressures. Usually, the formation of carbides is mesoporous [146–149].

9.3.7 Thin Film

Using chemical vapor deposition (CVD) technique, thin film of metal carbides can be prepared. In this, metal halide, light methane or ethane, and H_2 are passed through the substrate [150, 151]. Using physical vapor deposition (PVD) technique, thin film of metal carbides can also be prepared on suitable substrate [152, 153]. In this, metal carbide is vaporized in inert atmosphere (Ar gas).

9.3.8 Single Crystals

Single crystals of metal carbides can be prepared by either growing crystals from liquid or melt or growing over appropriate substrate [154–156]. This has many advantages over polycrystalline samples in many applications such as reproducible results for gas sensing and standardization of systems, etc.

9.3.9 Preparation of Nanostructured Carbides (0D, 1D, 2D, and 3D)

Different preparation routes for various morphologies of carbide particles with different dimensions have been reported [30, 157–159]. 0D nanostructures refer to spherical shapes with a few nanometers. 1D nanostructures refer to nanowires, nanotubes, nanorods, nanofibers, and nanowhiskers. 2D nanostructures include nanosheets, layers structures of a few nanometers, and nanolayers. 3D nanostructures refer to octahedrons, truncated-octahedrons, cubes, hexagonal structures, dendrites,

and terraces. These synthesis routes used many surfactants (oleic acid, oleylamine) to prepare monodispersed particles of carbides in high boiling point solvents (1-octadecence) and such similar synthesis methods are already used in the preparation of monodispered metals, alloys (Co, Ni, FePd, FePdPt, CoNi) or semiconductors/insulators (PbSe, $NaYF_4$:Er, Yb, Fe_3O_4) [63, 160–165].

9.3.10 Sol-gel Approach

Using sol-gel method, some of the carbides are prepared at lower temperatures [166–168]. Initially, metal alkoxides are prepared in aqueous medium; and solution/mixture of precursors is considered as sol and is heated slowly at 100 °C to get gel and gel is heated at 400–500 °C for 2–4 h and in this way, fine oxide powders with narrow size particles are obtained. Oxide powders are treated with carbon (say graphite) and heated in inert atmosphere. Metal carbides are obtained. Also, silicon carbide can be prepared from Si source (tetraethoxysilane, TEOS, $Si(OC_2H_5)_4$) and C source (bakelite varnish $(C_6H_6O{\cdot}CH_2O)_n$) through sol-gel approach. Initially, SiO_2 fine powder is formed from TEOS and then reacts with C source to form SiC powder.

9.3.11 Preparation of Carbides Under Pressure

Most carbides undergo phase transition or decomposition under high pressure and temperature [133, 169–171]. Sometimes, metastable phases of carbide can be prepared. Some carbides show interesting physical properties under pressure. These can be characterized by in-situ experiments (Raman and XRD techniques).

9.4 Synthesis Methods of Phosphides

Metal or non-metal phosphides are prepared in various ways:

9.4.1 Direction Reaction Between Metal or Non-metal and Phosphorus

In inert atmosphere or vacuum, metal or non-metal phosphide can be prepared by reaction between metal or non-metal and phosphorus at higher temperature [3, 4, 31, 36–38, 48].

$$x\mathrm{M} + y\mathrm{P} \xrightarrow{\text{heat}} \mathrm{M}_x\mathrm{P}_y$$

(M = s-block elements such as Li, Na, K, Ca, Ba; M = p-block elements such as B, Al, In, Ga, Si; M = d-block elements such as Fe, Co, Ni, Cu, Zn, Au, Ag, Pd, Pt; M = f-block elements such as La, Ce, Pr, Nd, Sm).

9.4.2 Reaction Between Metal Salt or Complex and PH_3/H_2 Mixture

Reaction of metal precursors such as carbonyls of Fe, Co, Ni, Mo, W, Ru or chlorides of Rh, Pt, Pd with phosphine gas (PH_3) with or without H_2 gas at lower temperature 250–350 °C can provide metal phosphide [3, 4].

$$x\mathrm{ML}_n + y\mathrm{PH}_3 + \mathrm{H}_2 \xrightarrow{\text{heat}} \mathrm{M}_x\mathrm{P}_y + \mathrm{nL}$$

$$\mathrm{L} = \mathrm{CO, X, O.}$$

9.4.3 Reaction Between Metal Salt and Hypophosphite

Reaction of metal salt with hypophosphite produces metal phosphine at elevated temperature [3, 4].

$$x\mathrm{ML}_n + y\mathrm{NaH_2PO_2} \xrightarrow{\text{heat}} \mathrm{M}_x\mathrm{P}_y + \mathrm{NaL} + \text{othr products}$$

Possible other products of P are HPO_4^{2-}, HPO_4^{2-}, $H_3PO_3 + PH_3$ depending on chemical environment. Sometimes, addition of sodium borohydride helps in formation of metal phosphide because it reduces metal ions to metal neutral.

9.4.4 Reaction Between Metal Salt and Phosphorous Acid (H_3PO_3)

Reaction of metal salt with phosphorous acid (H_3PO_3) can provide metal phosphine at elevated temperature [3, 4].

$$x\mathrm{ML}_n + y\mathrm{H_3PO_3} \xrightarrow{\text{heat}} \mathrm{M}_x\mathrm{P}_y + \mathrm{nL} + \mathrm{H_2O.}$$

9.4.5 H_2 Plasma Reduction

In the presence of H_2 plasma, the formation of metal phosphide is easy from metal salt and any phosphorus or phosphate [3, 4]. Here, H_2 plasma can produce very reactive H atoms, which can reduce metal ions to metal neutral.

9.4.6 Reaction of Metal Salts with Organic Compounds of Phosphorous

A few examples of organic compounds of P are trioctylphosphine (TOP), trioctylphosphine oxide (TOPO), $P(SiMe_3)_3$ and $(CH_3CH_2O)_3Si(CH_2CH_2)PPh_2$, etc. [3, 4]. When metal salt interacts with organic compound of P, metal phosphide can be produced. In the presence of oleic acid or oleylamine as capping agent and 1-octadecene or diphenyl ether as solvent, monodispersed nanoparticles of metal phosphides can be prepared.

9.4.7 Metathesis Reactions

In metathesis reaction, there is an exchange of ions between precursors. Metal halide can interact with Na_3P in inert atmosphere to provide metal phosphide [3, 4].

$$MX + Na_3P \rightarrow MP + NaX.$$

9.4.8 Solvothermal Reaction

Many reactions mentioned above can be performed in autoclave that can sustain experiment in high pressure and slightly higher temperature (150–400 °C) using solvents such as water, ammonia, ethylene glycol, glycerin, etc. [3, 4]. Usually, temperature is maintained above boiling point of solvent. Sometimes, capping ligands and/or other nucleation sites are added to prepare the different sizes and shapes of particles (0, 1, 2, and 3D nanostructures) and different phases of crystal structures. Many compounds can be dissolved in above boiling point. In supercritical conditions (high pressure and high temperature), gas-liquid could not be distinguished. This can be achieved by solvothermal reaction and this can provide different morphologies of particles and crystal structures, which could not be achieved by normal reaction or even normal hydrothermal reaction.

9.4.9 Different Sizes and Shapes of Nanoparticles (0D, 1D, 2D, 3D)

Different sizes and shapes of phosphide nanoparticles can be prepared by different techniques [3, 4, 31, 172–174]. Shapes include quantum dots (0D), rodes (1D), wires (1D), tubes, sheets (2D), cages, porous, rice-shaped, sea-urchin-like, core-shell, cubes (3D), flowers, belts, hollow, platelets, flakes, octahedrons, etc. Some phosphides are prepared by thermolysis and hot-injection methods. Oleic acid and oleylamine are used as capping agents; 1-octadecence is used as solvent; and TOP or TOPO is used as source of P. In this method, highly monodispersed particles can be prepared. The synthesis method is similar to preparation of monodispersed nanoparticles, metals, alloys, intermetallic compounds, and semiconductors [160–165].

9.4.10 Thin Film Technique

Thin films of phosphides are prepared by CVD or PVD techniques [3, 4, 31, 172–174]. Some phosphides are prepared by electrodeposition techniques. These films are useful for many applications including catalysis.

The preparation of binary, ternary or higher systems or doping of others in phosphides can be done by taking the respective elements or elements containing precursors in appropriate amounts [3, 4, 31, 172–174].

9.5 Synthesis Methods of Borides

Borides of metals or non-metals are prepared by reaction between elementals B and Ca, C, N, Ni, Fe, La, or Ce in inert atmosphere at higher temperatures [2, 4–9, 175]. In case of other precursors such as metal salts or oxides or complexes, carbo-thermic reduction reaction, boron carbide reduction reaction, aluminothermic, silicothermic, magnesiothermic reduction reaction, borothermic reduction reaction, thermal decomposition, electrochemical reaction, mechanochemical, CVD, PVD techniques, etc. can be used. Borides in nanosizes have been reported and details are provided in one of the chapters of this book.

9.6 Applications

9.6.1 Electronics

The transition metal nitrides, carbides, borides, and phosphides (MN, MC, MB) have metallic to semiconducting/insulating properties [1–6]. Depending on contents of nitrogen in a particular MN_x, it can show metallic to semiconductor/insulators (e.g., TaN_x). Some of them show superconducting behavior. MgB_2 shows superconducting transition at 39 K [7], which is comparable with high T_c cuprates compounds. Due to their chemical and thermal stabilities, they are used in high temperature stable electronic devices. Non-metal nitrides or carbides such as C_3N_4, Si_3N_4, BN or BC are used as insulator in electronic devices and microwave absorbers. Si_3N_4 is used as scanning tip for AFM. LaB_6 has been a source of thermoionic emission due to low threshold energy or work function (2.6 eV) [99]. Figure 9.4 shows the use of LaB_6 as electron emitter [176]. Such metal hexaborides have been used as cathodic materials and high temperature insulating and nuclear materials. Some metal hexaborides are particularly used as detectors for UV, visible, and NIR light. Metal phosphides such as Zn_3P_2 has been used in the field effect transistors and Schottky devices [4]. InP

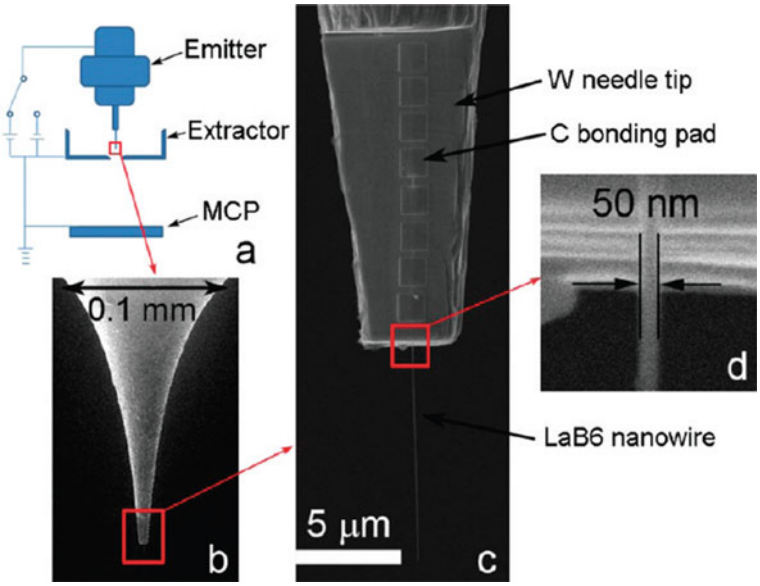

Fig. 9.4 Experimental setup and structure of LaB_6 single nanowire CFE. **a** Schematic of FIM/FEM setup and the location of LaB_6 nanowire in the emitter is indicated. **b** A magnified view of the W needle tip where the LaB6 nanowire is bonded to a flat fabricated at the tip of the W needle by FIB. **c** Top view of the emitter tip showing its constituting parts ofW flat, C bonding pads, and LaB_6 nanowire. **d** Magnified view of the section of the LaB_6 nanowire near the edge of the W flat. Reproduced with permission from ACS publishers [176]

has been used as electronic sensor for hydrogen [4]. Single crystals of AlN have been used for terahertz application [177].

9.6.2 Catalysts

Most transition metal nitrides, carbides, borides, phosphides, and their composites are important materials for heterogeneous catalysis [178–194]. This is due to the following: high surface area, suitable electronic properties, suitable chemical bonding with gases/liquid molecules to be converted over surface of catalyst, and chemical and thermal stabilities. Because of this, these materials can substitute expensive noble metals (Au, Pd, Pt) and their composites, which are important materials for catalysis and electrodes in electrolysis. Most catalysts need specific activity, selectivity, good durability, etc. The nitrides, carbides, borides, phosphides, and their composites have been used as catalysts in various chemical reactions: dehydrogenation, hydrogenation, hydrogenolysis, isomerization, oxidation, oxygen reduction, hydrogen evolution, methanol electrooxidation reactions, ammoxidation, propane to acrylnitrile, nitrogen to ammonia, alkane to alkene, CO_2 to CO or CH_4 to CH_3OH, water splitting, aldehyde to ketone, hydrodenitrogenation (HDN) and hydrodesulfurisation (HDS), (hydrogen evolution reaction (HER), hydrogen oxidation reaction (HOR), oxygen reduction reaction (ORR) and oxygen evolution reaction (OER)), etc. When particle size changes or shape of particle changes from 0D, 1D, 2D, or 3D forms in nanosize, their catalysis properties are different [185, 188].

For the oxygen reduction reaction (ORR), ZrN nanoparticles and commercial Pt/C have been used as a working electrode [180]. Ag|AgCl/KCl (saturated) electrode is used as a reference electrode. Pt wire is used as a counter electrode. The measured potentials are related to the reversible hydrogen electrode (RHE) potential calculated from the equation $E_{RHE} = E_{Ag/AgCl} + (0.197 + 0.059pH)V$. The Cyclic voltammetry (CV) curves of both materials with a scan rate of 10 mVs^{-1} in 0.1 M KOH solution are provided [180]. Their linear sweep voltammetry (LSV) curves are observed. It is found that both have the same half-wave potential ($E_{1/2} = 0.80$ V) in Cyclic voltammetry (CV) measurements. The number of electrons (n) to each O_2 molecule to produce OH^- is 4.0, whereas to produce H_2O_2 is 2. It is observed that both samples show "n" value close to 4. However, value 4 is more closed for ZnN as compared to that of Pt/C. After 1,000 ORR cycles in 0.1 M KOH alkaline solution, ZrN show higher stability ($\Delta E_{1/2} = -3$ mV) than that of the Pt/C catalyst ($\Delta E_{1/2} = -39$ mV). Also, both samples are tested for Zinc-air battery. It is found that ZrN (132 mW/cm^2) exhibits a greater power density than that of Pt/C (122 mW/cm^2) [180]. It is operated at a current density of 10 mA/cm^2 for 100 h to check stability of the air cathode. ZrN battery has a smaller voltage decrease (21 mV) than that of Pt/C (46 mV).

CO_2 is a greenhouse gas, which is released into the atmosphere from various activities such as burning of fossil fuels, trees in hills, ocean acidification, etc. It can be reduced by converting to CO, CH_4 and CH_3OH products, which are useful to us.

(a) $CO_2 + H_2 \rightarrow CO + H_2O\left(\Delta H^{\circ}(298) = 41 \text{ kJ mol}^{-1}\right)$
(b) $CO + 2H_2O \rightarrow CH_3OH$
(c) $CO_2 + 4H_2 \rightarrow CH_4 + 2H_2O$.

CO_2 is slightly acidic in nature. In order to convert using catalyst, it needs to have alkaline medium over surface of particles of catalyst [184]. Metal carbides are one of the ways to use as catalyst. Mo_2C as an example can be used as catalyst to convert CO_2 (gas) to CO or CH_4. Catalytic reaction is carried out at atmospheric pressure and in between 473 and 723 K) with different ratios of CO_2:H_2. At a gas hourly space velocity (GHSV) of 20,000 h^{-1}, the catalytic activity increases with increase in temperature (Fig. 9.5) [184]. In the case of 3:1 (H_2:CO_2) ratio, CO_2 to CO conversion increases from 34% at 473 K to 57% at 723 K. Selectivity of CO reaches 61% at 723 K. In the case of 7:1 (H_2:CO_2) ratio, CO_2 to CO conversion increases from 25% at 473 K to 64% at 723 K. With increase of H_2 amount, the formation of CH_4 gas increases.

Metal borides are capable to catalyze for both oxygen evolution reaction (OER) and hydrogen evolution reaction (HER) from splitting of water (H_2O) at different temperatures in electrochemical setup. In three electrodes setup, catalyst acts as working electrode. The cobalt boride (Co_3B) can act as catalyst for OER using a Hg/HgO (1 M NaOH) reference electrode in 1 M KOH [187]. A glassy carbon is used as the substrate material. The cyclic voltammetry (CV) measurements between 1 and 1.8 V with a scan rate of 10 mV/s for OER and HER between −0.5 and 1.8 V

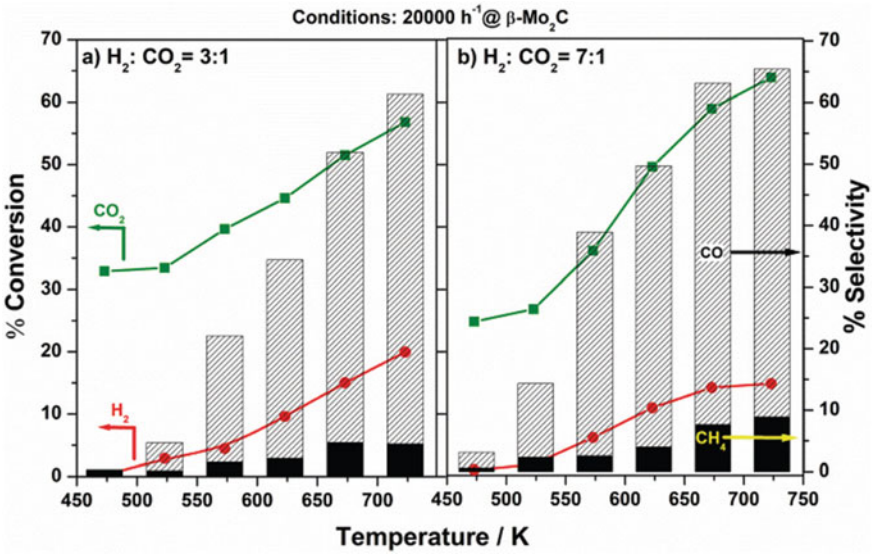

Fig. 9.5 Reactants conversion (CO_2 (green line) and H_2 (red line)) on the β-Mo_2C catalyst with products selectivity (CO (grey bar) and CH4 (black bar)) as a function of temperature with different ratios of reactants—**a** H_2: CO_2 = 3:1, and **b** H_2: CO_2 = 7:1. Reproduced with permission from RSC publishers [184]

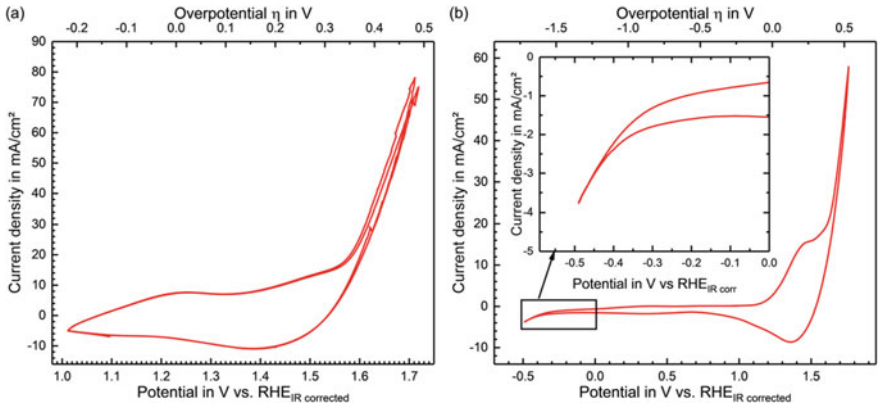

Fig. 9.6 Electrochemical measurements in 1 M KOH. CV curves of Co_3B during the oxygen evolution reaction **a** with a scan rate of 10 mV s^{-1} and **b** over the whole water splitting range with a scan rate of 50 mV s^{-1} (inset gives a more detailed view on the HER). The potential is plotted versus the reversible hydrogen electrode (RHE) and is iR compensated. Reproduced with permission from ACS publishers [187]

with a scan rate of 50 mV/s are performed (Fig. 9.6a) [187]. Voltages presented are calibrated with respect to the reversible hydrogen electrode (RHE). For iR compensation, electrochemical impedance spectroscopy (EIS: 100 kHz to 1 Hz) is used. In Fig. 9.6a, there is a broad hysteresis loop between 1.0 and 1.55 V, which are related to oxidation and reduction over catalysts. This shows onset potential around 1.55 V versus RHE. The over potential is $\eta = 350$ mV at 20 mA/cm^2. Figure 9.6b shows no significance for HER.

In particular, many catalysts such as Ru, Ir, Au and Pd, and the toxic acids have been used to prepare 2,5-diketons, which are useful as intermediate compounds for the formation of surfactants, polymers, and solvents. Nowadays, many metal phosphides have been tested to substitute precious and noble metals in catalysis. The nickel phosphide nanoparticles (Ni_2P NPs) show the selective transformation of biofuranic aldehydes into diketones as compared to other metal phosphides and Ni, NiO nanoparticles (Fig. 9.7) [189].

9.6.3 Optical Materials

Semiconducting materials show luminescence properties because they can absorb suitable energy through valence to conduction bands [195–199]. Some nitrides, carbides, phosphides, and borides of non-metals (in particular) are having semiconducting properties. AlN, GaN, InGaN, InN, C_3N_4, SiN, BN, SiC, AsN, AsP, InP, hybrids of these, multilayers system, heterostructures, and ternary/ quaternary

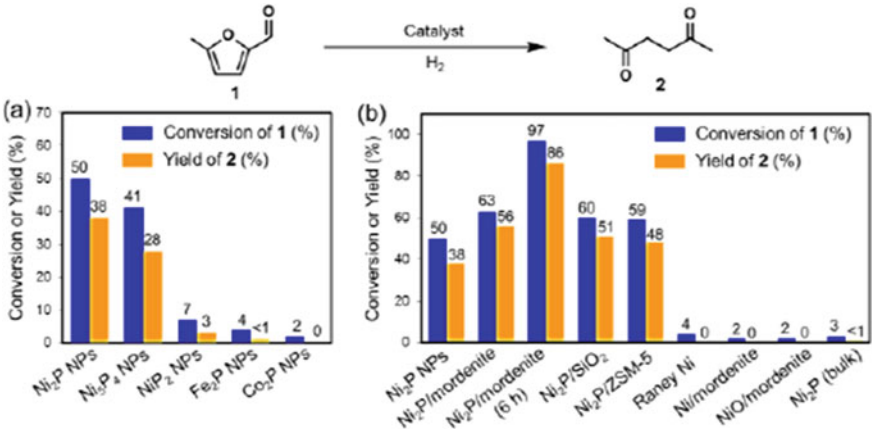

Fig. 9.7 **a** catalytic performance of various metal phosphide NPs in the hydrogenation of **1**. **b** Catalytic performance of Ni_2P NPs supported on different supports, Raney Ni, mordenite-supported Ni(0) NPs, mordenite-supported NiO NPs, and bulk Ni_2P. Reaction conditions: catalyst (metal: 6 mol%), **1** (0.25 mmol), H_2O (10 mL), H_2 (20 atm), 130 °C, 2 h. Reproduced with permission from ACS publishers [189]

system are examples. AIN, GaN, and InN have band gaps of 6.2, 3.4, and 1.9 eV, respectively [200].

Figure 9.8a, b show the absorption and emission spectra of h-BN as-grown and post annealed samples [40]. From absorption spectra, band gap of post annealed sample is found to be 5.8 eV, which is slightly more than that of as-grown sample. As-grown sample did not show emission at 226 nm, but it is observed in case of post

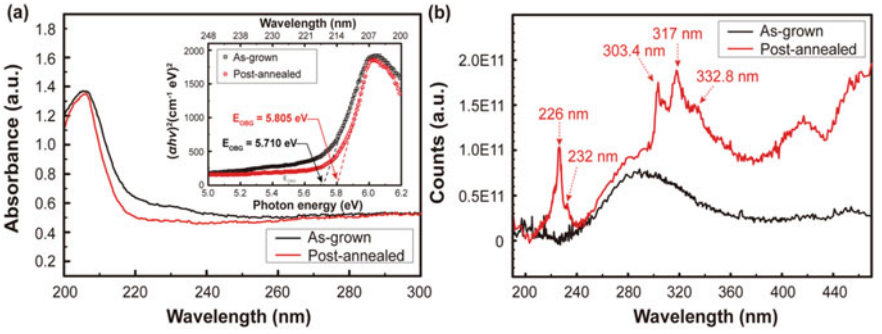

Fig. 9.8 **a** UV–visible absorbance spectra measure at 10 K and corresponding Tauc's plot for optical band gap of direct transition estimation for the as-grown and the post annealed h-BN films is shown in inset. **b** Comparison of PL spectra of the h-BN films measured at 10 K as well on the sapphire substrate before and after the post-annealing. Reproduced with permission from springer nature publishers [40]

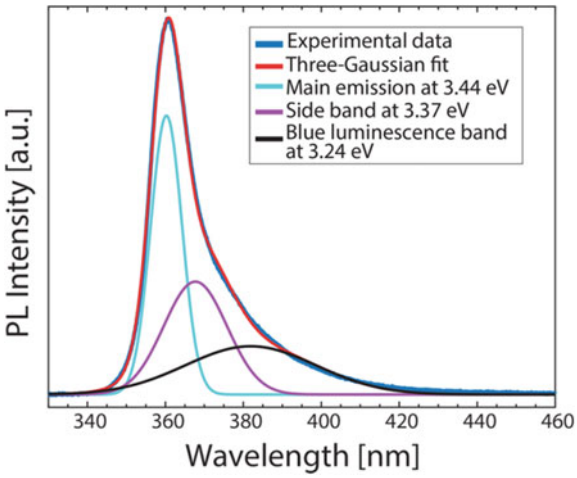

Fig. 9.9 Photoluminescence spectrum of the LED deviceat10 K. The main PL emission is at 360 nm (3.44 eV) with two side bands at 368 nm (3.37 eV) and 382 nm (3.24 eV). Reproduced with permission from ACS publishers [201]

annealed sample. This is related to the band edge excitonic transition. The peaks appeared at longer wavelengths are related to defects or structural imperfection.

GaN/AlGaN nanocolumns grown on graphene show electroluminescence at 365 nm (UV light), which is shown in Fig. 9.9 [201]. The internal quantum efficiency (IQE) is found to be 46%.

Some nitrides, carbides, and phosphides are prepared in the form of films and powders depending on the requirement. They can absorb light from UV to visible to NIR range. There are reports on doping of rare-earth ions (Eu^{3+}, Eu^{2+}, Dy^{3+}, Tm^{3+}, Tb^{3+}, Sm^{3+}, Er^{3+}, Nd^{3+}, Gd, Pm^{3+}) in such compounds to get the required emission in UV, visible, and/or NIR regions [202–208]. Al doped $Sr_2Si_5N_8$:Eu^{2+} single crystal shows the red emission under 450 nm excitation [203]). Tb^{3+} doped AlN show luminescence in visible range (Fig. 9.10) with high thermal conductivity (Fig. 9.11) [205]. This material is highly transparent in visible light. The behavior of their emissions can be comparable with oxides, phosphates, vanadates, molydates, and tungstates of metals [209–221].

AlN is used in many optical applications because of its photoluminescence, cathode- luminescence, and thermo- luminescence properties and this has a wide band gap of 6 eV [42]. Particularly, this is useful in vacuum ultraviolet region (5–9 eV) [41].

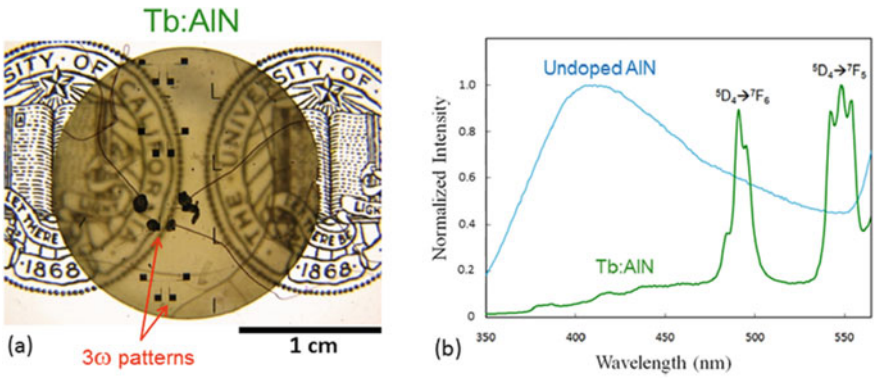

Fig. 9.10 Photograph and PL measurements of the 0.5 at. %Tb:AlN. **a** A photograph of the sample on top of backlit text, demonstrating translucency. **b** Comparison of the PL measurements of an undoped AlN sample and the 0.5 at. % Tb:AlN sample when excited with a 300 nm light source. The undoped sample shows a very broad peak from about 350 nm to 550 nm, with a maximum at 420 nm. The Tb:AlN PL displays two much sharper peaks that are characteristic of Tb transitions at 491 nm and 550 nm. Reproduced with permission from AIP publishers [205]

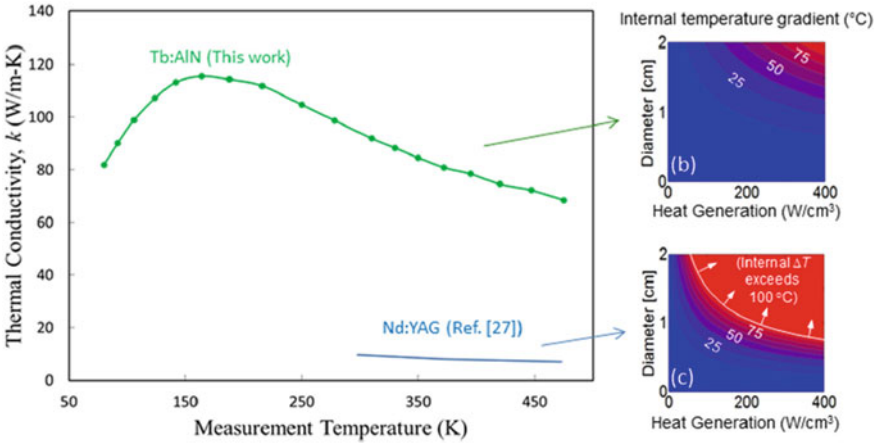

Fig. 9.11 **a** Thermal conductivity, k, measurements of the 0.5 at. % Tb:AlN ceramic along with reported Nd:YAG. **b** and **c** are simulations comparing the internal temperature gradients within a rod of Tb:AlN (k = 94 W/(m K)) and Nd:YAG (k = 14 W/(m K)), as functions of the rod diameter and volumetric heat generation rate. The higher k of Tb:AlN results in much smaller temperature non-uniformities than the state of the art Nd:YAG gain material. Reproduced with permission from AIP publishers [205]

9.6.4 Materials on Basis of Mechanical Properties

The term mechanical properties refer to the physical properties of a material, which reflects in the modulus of elasticity, tensile strength, fatigue limit, and hardness

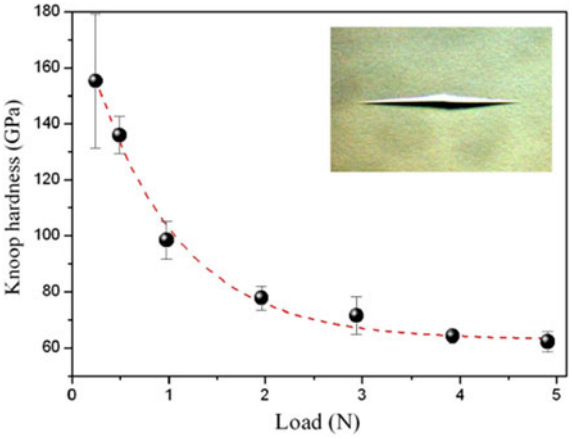

Fig. 9.12 Knoop hardness of bulk nanocrystalline cubic boron nitride versus load. Inset: optical microscope image of the imprint at 5 N load. Reproduced with permission from AIP publishers [222]

upon application of forces. Some transition metals and non-metals can form nitrides, carbides, borides, and phosphides (e.g., BN, C_3N_4, BCN, Si_3N_4, SiC, WN, WC, TaN, TaC, MoC, MoN, MoB, BP), which have ultra-hard properties. Some are comparable with diamond in terms of hardness. Generally, compounds with shorter bond length, covalent nature, and higher cohesive energy have high harness properties. Compounds of lighter elements such as B, C, and N belong to super-hard materials, which are comparable with that of diamond. The Vickers hardness (H_v) values of nano-c-BN, c-BN, c-BC_5, B_4C, c-BC_2N, ReB_2 and diamond are 85, 62, 71, 38, 48, and 115 GPa, respectively [222–226]. Those compounds having more than 40 GPa (H_v) are considered as super-hard or ultra-hard materials. $B_{12}P_2$ (boron phosphides) is considered refractory materials because it has high melting temperature of 2840 K and low compressibility of 174 GPa [226]. From the experiments of Vickers hardness (H_v) and Knoop hardness (H_k) for BP and $B_{12}P_2$ with loading, H_v and H_k decrease [226]. H_v and H_k are 34 and 20 GPa for BF, and 35 and 26 GPa, respectively.

Figure 9.12 shows the measured Knoop hardness of material (bulk nanocrystalline cubic boron nitride) and hardness decreases with the load [222]. At 5 N, it reaches the asymptotic value of $H_K = 63(2)$ GPa.

The cBC_5 has a low compressibility (bulk modulus of 335 GPa), conductive, and Vickers hardness of 71 GPa, fracture toughness (9.5 MPa $m^{0.5}$), and high thermal stability up to 1900 K. This material will be useful for super-abrasive and high temperature electronics [224]. Other materials for super-abrasive purposes (high hardens, high good fracture toughness, and wear resistance) are WC, Co-doped WC, c-BN, and CrAlN, etc. [227–229]. The corrosion oxidation behavior of $Cr_{1-x}Al_xN$ coating over planar steel substrate or cc-insert is carried out (Fig. 9.13) [229]. Each sample is exposed to 800–1100 °C in ambient atmosphere for 30 min at 50 °C and 100 °C intervals. At each temperature setting, cc-inserts are broken and thickness of oxidation is measured. Pure CrN starts oxidation at 800 °C. Thickness of the oxide layer increases with rise in temperature, but with addition of Al, oxidation start at higher temperature. The lifespan of cutting tool is tested using $Cr_{1-x}Al_xN$ coating over

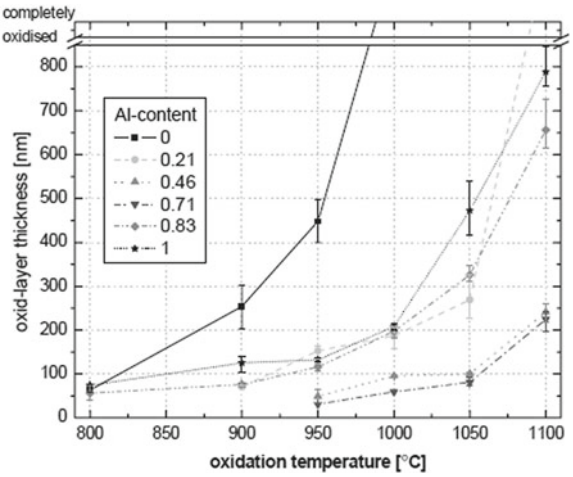

Fig. 9.13 Thickness of oxide layer of various $Al_{1-x}Cr_xN$ ($0 < x < 1$) coatings after annealing at different temperatures in air-atmosphere. Reproduced with permission from Elsevier publishers [229]

planar steel substrate. A drilling test on HSS 6 mm diameters tools is executed in wet conditions. Figure 9.14 shows the lifetime of various $Cr_{1-x}Al_xN$ coatings performed in an HSS-drilling test [229]. It is observed that lifetime is longer with content of Al as compared to pure CrN.

They are used for cutting tools, drilling machines, polishing powder, aerospace and offshore oil exploitation engineering, etc. Most nitrides, carbides, and borides

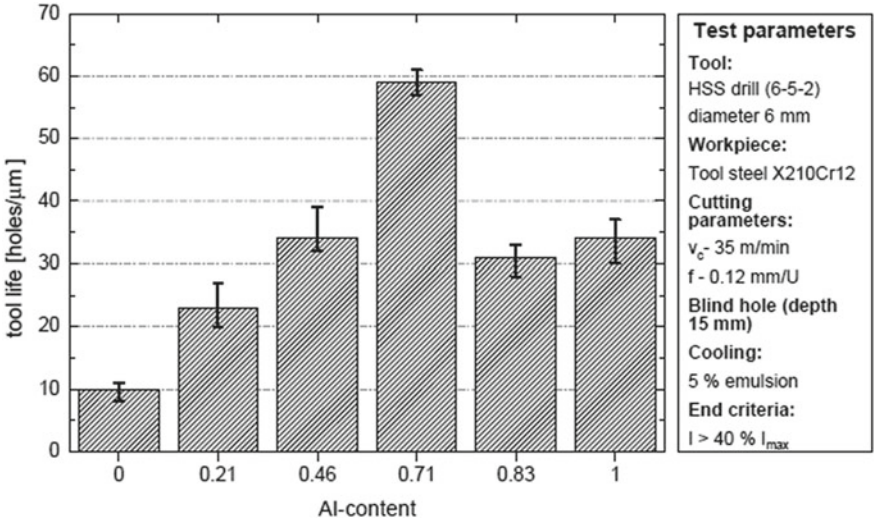

Fig. 9.14 Lifetime of various $Al_{1-x}Cr_xN$ ($0 < x < 1$) coatings performed in a HSS-drilling test. Reproduced with permission from Elsevier publishers [229]

have been used as coating materials over others to improve corrosion properties of other [1, 2, 4–6, 99, 228, 229].

9.6.5 Biomaterials

Some nitrides, carbides, borides, and phosphides can be used as biomaterials. This is due to their biocompatible, chemically stable, and internes to microenvironment of biology.

Hyperthermia based therapy for cancer can be done by various routes. However, localized based heating or hyperthermia can be brought by using nanoparticles (magnetic as well as non-magnetic materials). Magnetic nanoparticles absorb radio-frequency at a particular magnetic field of 100–300 Oe to produce heat up to 42–45 °C. In case of non-magnetic nanoparticles, materials absorb a particular frequency or wavelength of light to produce heat. Recently, it is reported that some ferromagnetic nitrides, carbides, and borides can also absorb radio-frequency (AC frequency) to produce heat [230–234]. Interestingly, their room temperature saturation magnetization is high (50–150 emu/g); and their Curie temperature is much lower than that of Fe_3O_4 (560 °C); and they belong to soft magnetic materials (i.e., low coercivity). Examples of magnetic as well as biocompatible nitrides are Fe_3N and Fe_4N. Saturation magnetization (M_s) and Curie temperature (T_c) of Fe_4N are 180 emu/g and 400 °C, respectively [231, 234]. Examples of magnetic as well as biocompatible carbides are Fe_3C, $Fe_{2.2}C$ and Fe_5C_2. The M_s and T_c values for Fe_3C are obtained to be 140 emu/g and 210 °C, respectively [232]. Examples of magnetic as well as biocompatible borides are FeB_x based compounds [233]. Oxide counter part of Fe has been used as biomaterials and example is the iron oxide magnetic nanoparticles (Fe_3O_4 or γ-Fe_2O_3) have $M_s \sim 60$ emu/g and $H_c = 0$ Oe at room temperature, which are lower than bulk counterpart ($M_s = 90$ emu/g, $T_c = 585$ °C, $H_c = 323$ Oe) [235]. This is due to decrease in particle size as well as superparamagnetic nature at room temperature. Binary nitrides, carbides, and borides belong to the soft magnetic materials (i.e., low coercivity). Heat up to 40–45 °C can be produced using these compounds under AC magnetic field. At this temperature, cancer cells can be killed, but normal cells can survive. Some are monodispersed particles capped with long chain surfactants such as oleic acids, oleylamine. Because of this, they are dispersible in hexane or hydrocarbon solvents. Now, it is developed as water dispersible nanoparticles through ligand exchange or modification of capping ligands.

Oleic acid coated Fe_3C ferrofluids (agglomerated particles) with particle sizes of 22 nm show the heating behavior under AC magnetic field [232]. The saturation magnetization (M_s) at room temperature is found to be 88 emu/g with a coercivity (H_c) of 173 Oe and remanence (M_r) of 6 emu/g. They calculated specific absorption rate (SAR) and the intrinsic loss power (ILP) according to the following formulae:where $\Delta T/\Delta t$ is obtained from the slope of the rise in temperature with time at the initial time. C is the specific heat capacity of combined Fe_3C and water. The value of m_{magn} is considered as amount of Fe_3C per total amount of Fe_3C and water. The frequency

and field independent absorption rate can be calculated from SAR. This is sometimes referred to as intrinsic loss power (ILP).

$$\mathrm{ILP} = \mathrm{SAR}/\mathrm{H}^2\mathrm{f}$$

where H and f are the amplitude and frequency of fields, respectively.

Figure 9.15 shows Temperature vs. Time plots for the ferrofluids having different concentrations (e. g. 2.5, 5, 10 and 20 mg/mL) at (a) 23 mT and 261 kHz, (b) 25 mT and 117 kHz, and their (c) SAR values and (d) ILP values [232]. It can be seen that high rate of heating or SAR is more in high frequency used, i.e., f = 261 kHz has more SAR value than that of f = 117 kHz for same concentration. In case of f = 261 kHz, times required to reach hyperthermia (42 °C) for concentrations of 20, 10, 5, and 2.5 mg/mL are 142, 328, 330, and 351 s, respectively. In case of f = 117 kHz, concentration 2.5 mg/mL could not reach hyperthermia up to 30 min. The concentrations of 20, 10, and 5 mg/mL reach temperatures in 304, 384, and 466 s, respectively. Maximum SAR value of 85 W/g is obtained from f = 261 kHz for 2.5 mg/mL. In case of f = 261 kHz, SAR value decreases with increase of magnetic

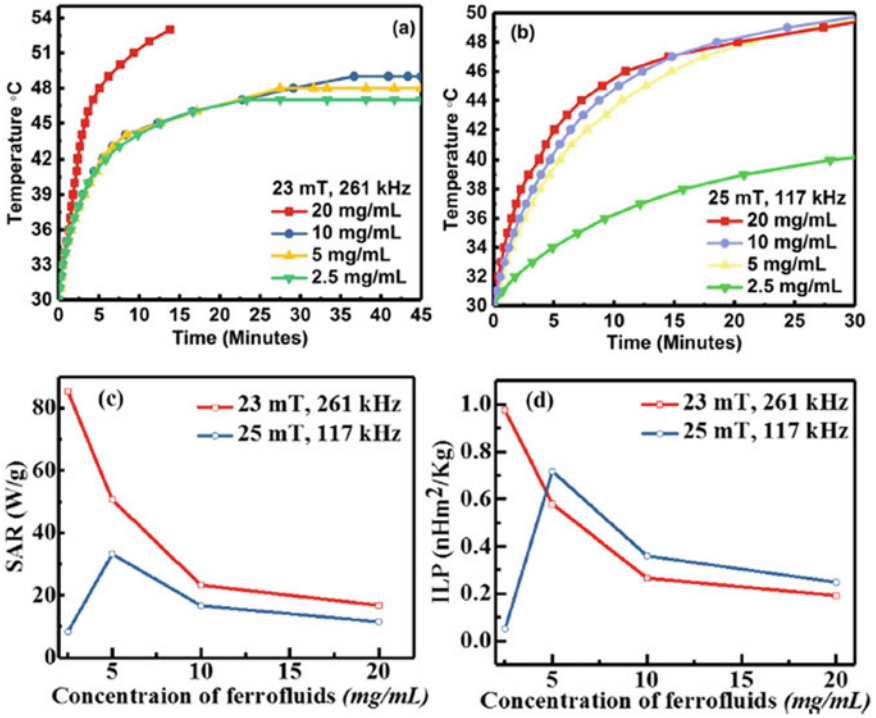

Fig. 9.15 Temperature versus Time curves at **a** 23 mT and 261 kHz, **b** 25 mT and 117 kHz, **c** SAR values for ferrofluids and **d** ILP values for the ferrofluids having various concentrations (e.g., 2.5, 5, 10 and 20 mg/mL) at different fields. Reproduced with permission from Elsevier publishers [232]

nanoparticles, whereas, in case of f = 117 kHz, SAR increases with increase of magnetic nanoparticles from 2.5 to 5 mg/mL and decreases with further increase of magnetic nanoparticles. The trend of ILP values is similar to that of SAR.

Figure 9.16a shows SAR of 2 different particles (pure iron carbide MM1 and core-shell MM2) [30]. The composition of MM1 is $Fe_{2.2}C$–Fe_5C_2 and that of MM2 is Fe(0) surrounded by $Fe_{2.2}C$–Fe_5C_2. The monodispered particles are obtained. The saturation magnetization (M_s) values of MM1, MM2, and pure Fe(0) are obtained to be 132, 195, and 198 emu/g, respectively at room temperature. The rise in SAR is more in case of MM2 as compared to MM1 or Fe(0). Figure 9.16b shows the room temperature normalized hysteresis loops measured at f = 54 kHz. MM2 shows the square loop behavior. Because of this, rapid rise in SAR occurs. They produce SAR (specific absorption rate) up to 350 W/g, which are higher than reported values of cubic ferrites and perovskite compounds [165, 209, 235–245]. Figure 9.16c shows dependence of the coercive fields calculated from the hyperthermia measurements with the iron content determined from XRD data. Figure 9.16d shows theoretical calculation of the SAR for aligned monodispersed nanocrystals.

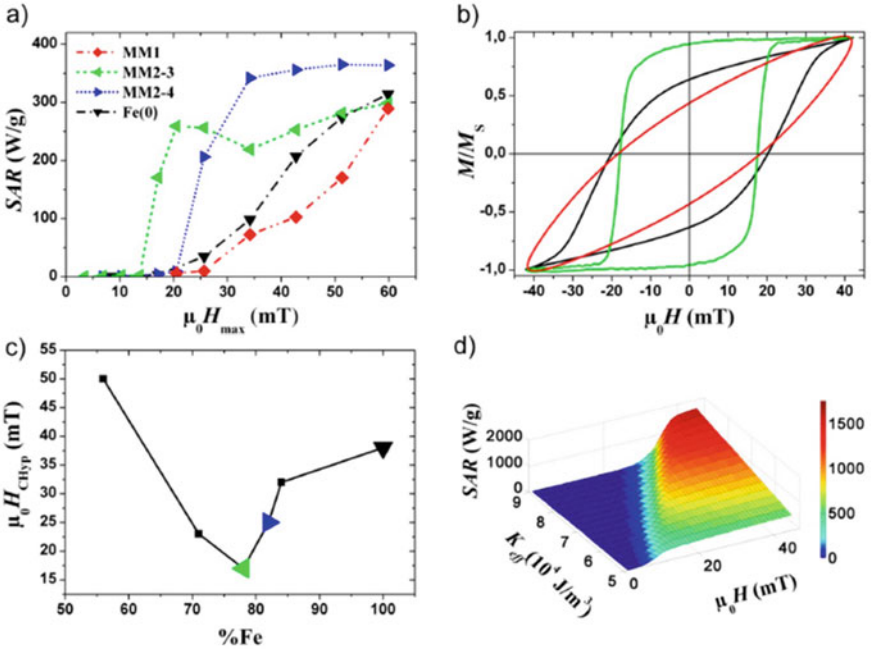

Fig. 9.16 Hyperthermia properties of samples of iron carbide and iron/iron carbide nanocrystals. **a** SAR measurements at f = 54 kHz. **b** Normalized hysteresis loops measured at f = 54 kHz and room temperature on the same samples. **c** Dependence of the coercive fields deduced from the hyperthermia measurements versus the iron content determined from XRD data. **d** Theoretical calculation of the SAR for aligned monodisperse nanocrystals. Reproduced with permission from ACS publishers [30]

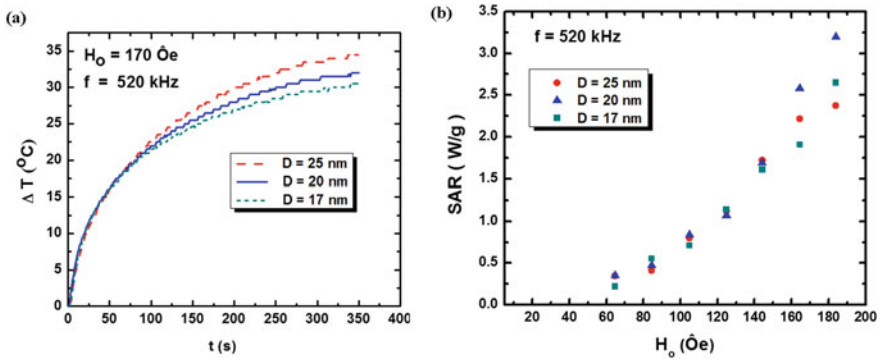

Fig. 9.17 **a** Heating curves of 100 mg FeB nanoparticles measured in an ac magnetic field: frequency 520 kHz and amplitude 170 Oe, **b** Specific absorption rate (SAR) measured at a frequency 520 kHz as a function of ac field amplitude H_o. Reproduced with permission from Elsevier publishers [233]

Figure 9.17 shows the heat rise vs. time for FeB nanoparticles (17 to 30 nm). It does not reach hyperthermia temperature up to 6 min [233]. Their SAR values are very low (3 W/g). Sample incorporated in liposome shows good biocompatibility (>80%) up to 0.01 mg/mL.

Non-magnetic nanoparticles are Au nanoparticles, Ag nanoparticles, graphene and CuS, etc. which shows the Surface Plasmon Resonance (SPR) in visible as well as NIR region. By bringing down dimensions from 3 to 2D, 1D or 0D, their intrinsic properties can be changed in terms of electrical conductivity, thermal conductivity, and optical properties, etc. A few reports on carbides (2D) have shown heating behavior by light absorption. If light absorption occurs in biological windows, i.e., I (650–950 nm), II (1000–1350 nm), and III (1550–1850 nm), it reduces effect from water solvents, and penetration depth of light is more in living body or tissue [246]. 2D materials of carbides such as MXenes including Ti_3C_2, Nb_2C, Ta_3C_4 and Mo_2C have been reported for photothermal-heating based hyperthermia [247]. They can absorb light in biological windows. Figure 9.18 shows the absorption spectra of Mo_2C-PVA nanoflakes in 400–1200 nm [247]. There is a normalized absorbance value divided by a length of quartz cuvette after excitation at two laser wavelengths 808 (top) and 1064 nm (down). The concentrations of Mo_2C are at 0, 7.5, 15, 30, 60, 80, and 120 μg/mL. Behavior of photothermal-heating curves with time (T-t) at 808 and 1064 nm laser is shown in various power densities of 0.5, 0.75, 1.0, and 1.25 W cm^{-2}. There are changes in temperature with laser on/off cycles after exposure to 808 and 1064 nm laser at 1.0 W cm^{-2}. Figure 9.19 shows relative viabilities of 4T1 and L929 cells after treatment with Mo_2C-PVA with various concentrations (12.5, 25, 50, 100, 200, and 400 μg/m for 24 and 48 h [247]. It exhibits biocompatibility of 100%. Under laser excitation at 808 or 1064 nm at 1.0 W/cm^2, cell viability is also shown. Up to 50 mg/mL, cell viability of 4T1 cells is found to be 100%. In 100–200 μg/mL, cell viability is below 20%. Power dependent cell viability of 4T1 cells (200 μg/mL) shows that viability values are about 40, 30, 10 and 5% at 0.5,

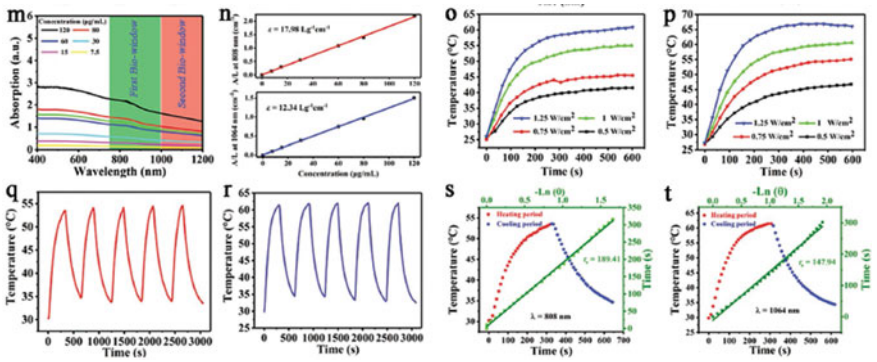

Fig. 9.18 **m** absorption spectra of Mo_2C-PVA nanoflakes dispersion with various concentrations (Mo_2C at 7.5, 15, 30, 60, 80, 120 μg mL^{-1}). **n** Normalized absorbance value divided by the length of the quartz cuvette (A L^{-1}) containing various Mo_2C-PVA nanoflakes concentrations (Mo_2C at 0, 7.5, 15, 30, 60, 80, and 120 μg mL^{-1}) for 808 (top) and 1064 nm (down). The mass extinction coefficient of Mo_2C nanoflakes at 808 and 1064 nm. Photothermal-heating curves of Mo_2C-PVA dispersions under the illumination of **o** 808 and **p** 1064 nm laser for 600 s with a series of power densities (0.5, 0.75, 1.0, and 1.25 W cm^{-2}). Temperature elevation of the Mo_2C-PVA nanoflakes dispersion for five laser on/off cycles after exposure to **q** an 808 and **r** 1064 nm laser at 1.0 W cm^{-2}. Calculation of the light induced-heat efficiency under **s** 808 and **t** 1064 nm laser irradiation. Reproduced with permission from Wiley publishers [247]

0.75, 1.0 and 1.25 W/cm^2, respectively. 2D materials of transition metal carbides and nitrides (MXenes) have been used in cancer therapeutics and diagnostics [248]. 1D and 2D materials such as nanowires, layers of carbon nitrides, and boron nitrides have been used for carrier for drug, imaging, and anti-bacterial purposes [249].

Bulk InP shows bandgap of 1.35 eV (918 nm) and bandgap increases with decrease of particles size if size is less than Bohr's radius [250]. Absorption wavelength values of particle sizes of 4.3, 3.5, 2.9, and 2.6 nm are 650, 625, 600, and 520 nm, respectively [251]. InP QDs (3.5 nm) can emit red light at 650 nm, which lies in biological window [251]. Using InP and InP-ZnS QDs, red emission is observed through cell imaging [250]. This has more biocompatibility than other QDs such PbSe, CdSe because Pb and Cd are toxic. InP-ZnS show the better luminescence intensity than that of InP [250]. InP-ZnS QDs can be used for imaging in cell lines. Folic acid coated InP-ZnS shows more accumulation in case of KB cells than that in A549 cells [252]. Confocal microscopy images are shown in Figs. 9.20 and 9.21 [252]. Figure 9.22 shows two-photon image of KB cells treated with QD-FA for 6 h [252]. This provides better imaging with less photo damage. Confocal and two-photon imaging are performed using MRC-1024, Bio-Rad, Richmond, CA. Ti: sapphire laser at 800 nm (100 fs pulse at 82 MHz) is used as source. For single-photon imaging, Ti: sapphire laser at 840 nm is doubled by the second harmonic generation (SHG) to obtain 420 nm light, which is used.

Nitrides, carbides, and borides have been coated over biomaterials to make them chemically stable for replacement of broken bone, teeth, (implantation) [253–256].

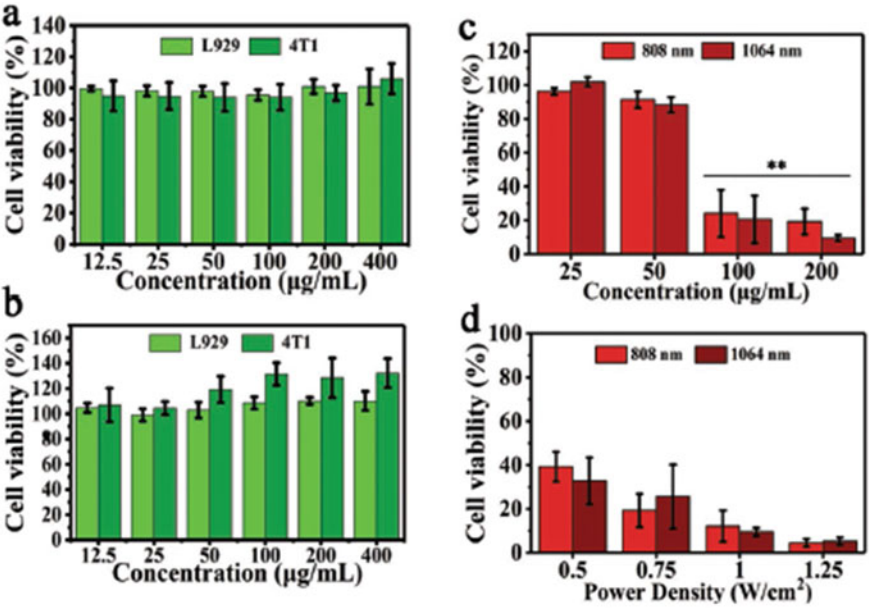

Fig. 9.19 Relative viabilities of 4T1 and L929 cells after treatment with Mo_2C-PVA dispersion at a series of concentrations (Mo_2C at 12.5, 25, 50, 100, 200, and 400 μg mL^{-1}) for **a** 24 and **b** 48 h ($n = 5$, mean ± SD). **c** Relative viabilities of 4T1 cells treated with Mo2C-PVA dispersion at elevated concentrations (Mo_2C at 25, 50, 100, and 200 μg mL^{-1}) under 808 or 1064 nm laser illumination at 1.0 W cm^{-2} for 15 min ($n = 5$, mean ± SD). Statistically significant difference, $^{**}P < 0.01$. **d** Relative viabilities of 4T1 cells treated with Mo_2C-PVA nanoflakes dispersion (Mo_2C at 200 μg mL^{-1}) exposure to 808 or 1064 nm laser illumination with various power densities (0.5, 0.75, 1.0, and 1.25 W cm^{-2}) for 15 min ($n = 5$, mean ± SD). Reproduced with permission from Wiley publishers [247]

Si_3N_4 (bioactive) has been tested in cell lines for stability in osteoarthropathy condition and this will be useful for the medicinal therapies, the effective remedies for various bone or joint maladies and the diseases, etc. [253]. Si_3N_4 will be important biomaterial for hip implants because its coefficient of friction in water decreases. This decrease is due to the formation of SiO_2 or $Si(OH)_4$ over surface [254]. Titanium metal is used as implant due to light weight. However, it suffers from surface oxidation to form $Ti(OH)_3$ and a decrease in its bone integrative properties with surrounding physiological environment. Such can be prevented by coating with TiC over Ti metal and TiC has higher hardness, more corrosion property and biocompatible with biological systems as compared to Ti metal [255]. It is tested through in-vitro and in-vivo experiments. In rabbits and sheep, one TiC-coated dental implant is done into their left femurs, whereas into the right femur, an uncoated implant is done, which acts as a contralateral control. After weeks, it is found that the bone density around the TiC-coated implant is more than that around the uncoated implant. Figure 9.23 shows X-ray analysis of implants in rabbits with time [255]. TiB_x-Ti composites are

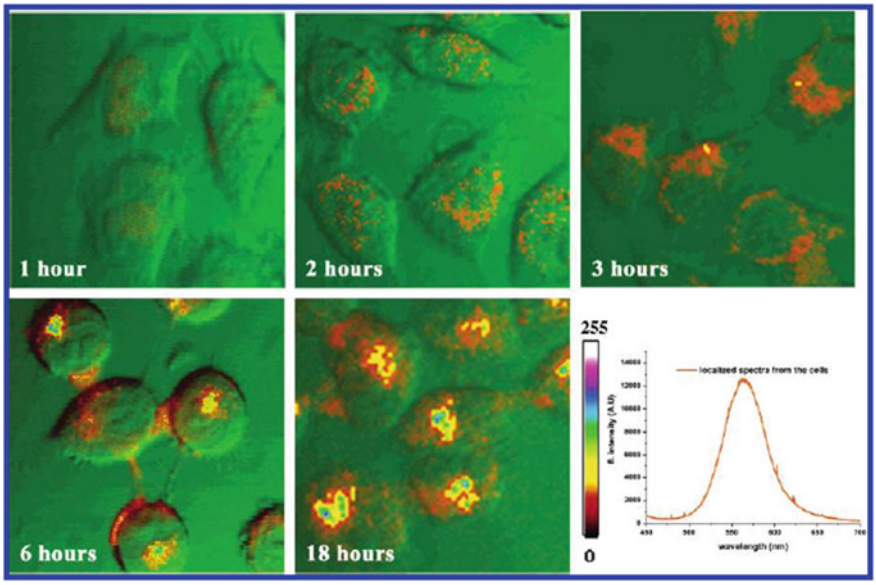

Fig. 9.20 Confocal images are showing fluorescence of QD-FA in KB cells and a localized PL emission spectrum. The green channel shows the transmission images, while the intensity-coded (red to white) channel shows the fluorescence. Reproduced with permission from ACS publishers [252]

better than Ti for implantation [256]. TiB_x-Ti is biocompatible in fibroblast cells and does not cause red blood cell destruction.

9.6.6 Ultra-High Temperature Ceramic Materials

Ultra-high temperature ceramic nitride, carbide, and boride materials are materials having their melting points (mp) and decomposition temperatures (dt) are more than 2000 °C and these include the following: BN (mp = 2800 °C), HfN (mp = 3385 °C), TiN (mp = 2950 °C), NbN (mp = 2573 °C), ZrN (mp = 2950 °C), TaN (mp = 2700 °C), BC (mp = 2763 °C), SiC (mp = 2820 °C), TiC (mp = 3100 °C), NbC (mp = 3490 °C), WC (mp = 2800 °C, TaC (mp = 3768 °C), HfC (mp = 3958 °C), ZrC (mp = 3400 °C), ZrB_2 (mp = 3245 °C), NbB_2 (mp = 3050 °C), HfB_2 (mp = 3380 °C), TiB_2 (mp = 3225 °C). TaB2 (mp = 3040 °C) [257–274]. Here, some of the melting points are considered decomposition temperatures because some decompose to constituent elements or another phase. In addition, they have low thermal expansion coefficient, high hardness, excellent corrosion resistance, and high thermal sock resistance properties. Most are stable in inert environments. In inert environment, they have better stability compared to other oxides at high temperatures. Some of them are used in extreme environments such as acidic or

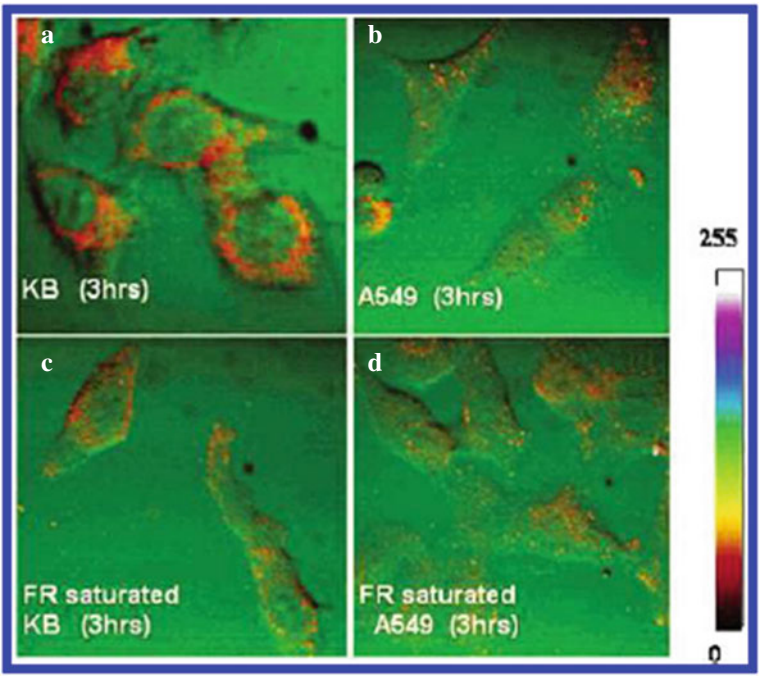

Fig. 9.21 Confocal images are showing fluorescence of QD-FA after 3 h of incubation in **a** KB cells, **b** A549 cells, **c** KB cells with excess folic acid treatment for FR saturation, and **d** A549 cells with excess folic acid treatment. The green channel shows the transmission images, while the intensity-coded (red to white) channel shows the fluorescence. Reproduced with permission from ACS publishers [252]

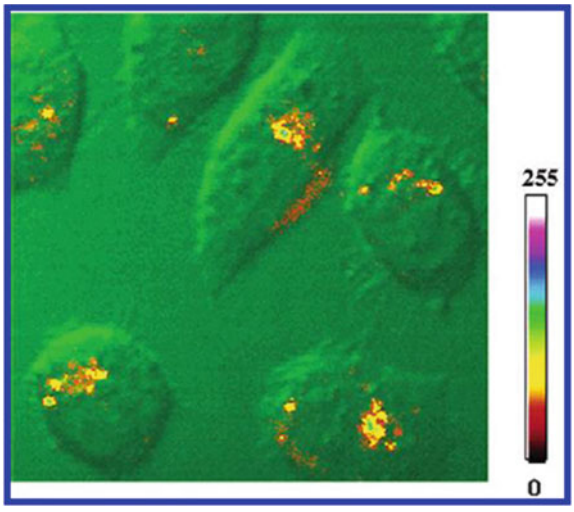

Fig. 9.22 Two-photon images of KB cells are treated with QD-FA for 6 h. Reproduced with permission from ACS publishers [252]

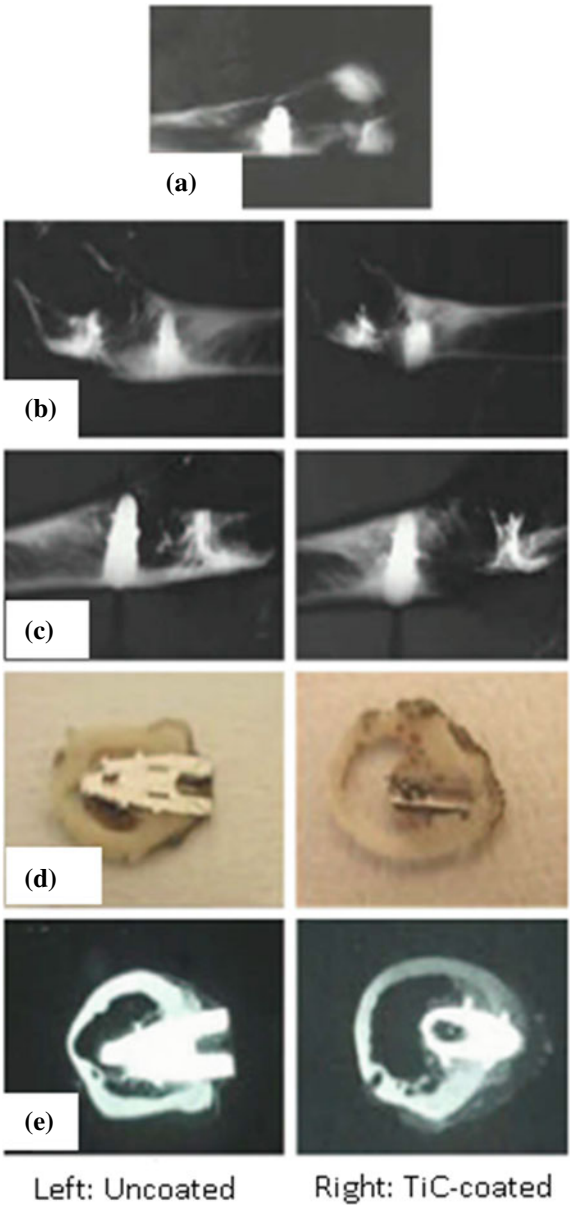

Fig. 9.23 X-ray analysis of implants in rabbits. At zero time **a**, after four **b** and eight **c** weeks, the implantation animals were sacrificed. The bone density around the implants was evaluated by X-ray mammography. Radiographs and pictures at the left are related to uncoated implants, those at the right to the TiC-coated implants which show a major bone density around the implants. The 8-week bones containing the implants were excised and then cut into slices of approx. 60 mm. Images of slices **d** were taken and then exposed overnight to a low intensity X-ray microradiograph **e**. Bone density around the TiC-coated implant was higher than in uncoated Ti implant. Reproduced with permission from Elsevier publishers [255]

alkaline conditions. These ultra-high temperature materials and their composites have been used in many applications such as aerospace, furnace, high resistance electronic devices, high temperature sensors, nuclear and energy, etc. BN material has been used as sample holder in high temperature magnetic studies. This is because BN is diamagnetic material as well as thermally and chemically stable [1, 275]. SiC

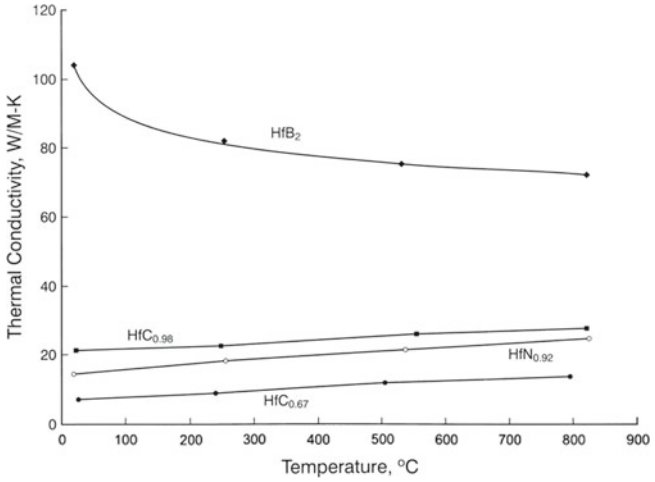

Fig. 9.24 The thermal conductivity of HfB_2, $HfN_{0.92}$, $HfC_{0.98}$ and $HfC_{0.67}$. Reproduced with permission from Elsevier publishers [262]

material has been used as crucible and heating rods/elements for furnace. TaC coated graphite material has been used as crucible. Most metal borides have high thermal conductivity. Because of this, they are used as cooling connectors in electronics. LaB_6 has high melting point of 2210 °C and high thermal conductivity of 110 W/mK [276]. Compared to respective nitrides and carbides, HfB_2 has the higher thermal conductivity in 30–800 °C and they have almost similar thermal expansion in 30–2250 °C (Fig. 9.24) [262].

9.6.7 Coloring Materials

Some nitrides show golden color (e.g., TiN) and they are used to make golden color over any material by coating [1, 2, 277]. WC based materials are used as coloring materials and also are used in the bridal jewelry industry as ring, etc. [278]. It is harder than gold and has high resistance to scratching. They are used as special tools and decorative items, etc.

9.6.8 Materials for Battery, Fuel Cells, Capacitor, Sensors

Some nitrides, carbides, borides, and phosphides are used as components of batteries, fuel cells, capacitors, and sensors [1, 2, 188–204, 279–288]. When dimensions of particles are brought to nanosizes, their properties vary. Also, when it changes from

3D to 2D, 1D or 0D in nanosized range, their properties are different. TiN 1D nanorods/nanowires are very sensitive in H_2O_2 gas. Some are used in bio-sensing applications such as detection of gases, ions, proteins, and DNAs due to stability, less corrosion property, biocompatible, easy processing, and inertness, etc.

9.6.9 Magnetic Materials

Some of Fe, Co, Ni based nitrides, carbides, borides, phosphides, and their combination with rare-earth elements show ferromagnetic properties [1, 2, 31, 33, 93, 99, 289, 290]. Fe_3N, Fe_4N, $Fe_{16}N_{12}$, Co_3N, Ni_3N, Fe_3C, Co_3C, Ni_3C, Fe_xB, Co_xB, Ni_xB, Fe_xP, Co_xP and Ni_xB are examples. Generally, these MY (binary) compounds have low coercivity ($H_c < 500$ Oe) and they are considered as soft magnetic materials. By changing shape of particle, some of them can show high coercivity ($H_c > 1000$ Oe). The acicular particle shape (Co_3C-Co_2N) can provide an enhancement to the coercivity of 3400 Oe [289]. Those with high $H_c > 1000$ Oe are considered as the hard magnetic materials and these are used in data storage applications. Examples are $Sm_2Fe_{17}C$, $Sm_2Fe_{17}N_2$ $Sm_{13}Fe_{87}N$, $Nd_2Fe_{14}B$, $Ti_2FeRu_{5-n}Rh_nB_2$, $(Fe_{1-x}Co_x)_2P$ ($x < 0.28$). They are known as permanent magnets. Wei and his group reported Sm-Fe–N phase which shows a very high coercivity ($H_c = 44$ kOe), high remanent magnetization ($B_r = 8.0$ kG) and high area of loop (BH = 14.3 MGOe). The variation of H_c and $B_r$for $Sm_{13}Fe_{87}N$ with increase of annealing temperature is shown in Fig. 9.25 [290].

9.6.10 Miscellaneous Applications

Many borides, nitrides, carbides, and phosphides have been used in various applications such as removal of dyes, electrides, high thermal conductivity materials, radio-frequency filters or surface acoustic wave devices, lasers, transistors, and superconducting devices. Due to limitation of pages in this chapter, more details are provided in many papers and review articles [1, 4–6, 11, 93, 99, 291–295].

9.7 Conclusions

Synthesis routes from low to high temperatures for borides, carbides, nitrides, and phosphides are dependent on precursors used and types of phases required. Sometimes, high pressure is required to prepare a particular phase. The various synthesis routes for nitrides (about 22 numbers) are mentioned. Similarly, different synthesis routes of carbides and phosphides are provided. For synthesis of borides, brief notes are provided because one chapter in this book is devoted to this area. However,

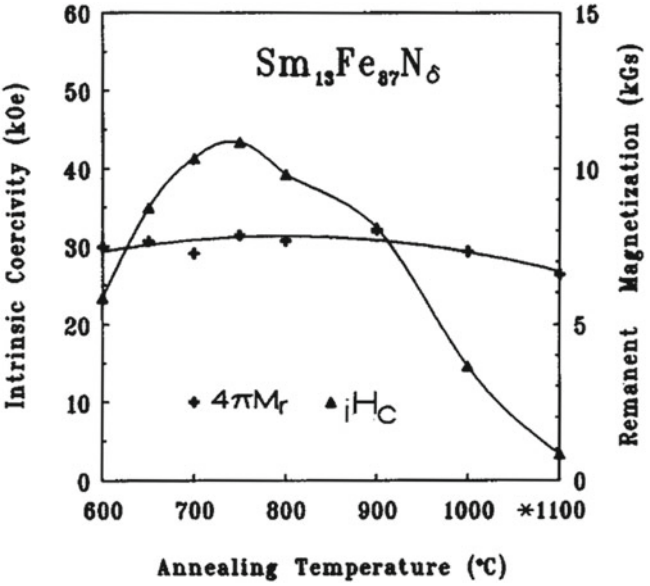

Fig. 9.25 Coercivity (H_c) and remanent magnetization of $Sm_{13}Fe_{87}N$ annealed at different temperatures. Points at 1100 °C are for as-melted ingot. Reproduced with permission from Elsevier publishers [290]

this portion is included in this chapter because its properties are almost similar to nitrides, carbides, and phosphides. All B, C, N, and P are the light p-block elements in the periodic table. Their bonds are short and cohesive energies of compounds are high. Thus, BC, BN, C_3N_4 and their composites are extremely hard and comparable with diamond. Their bonding in B–C, B–N, and C–N is covalent in nature. The borides, carbides, nitrides, phosphides, and their composites are used in many applications such as sensors, catalysts, permanent magnets, hard materials, coating materials, cutting tools, sample holders, tip, insulating materials, components of high temperature furnaces, high temperature conducting and LEDs, etc.

References

1. Ningthoujam RS, Gajbhiye NS (2015) Synthesis, electron transport properties of transition metal nitrides and applications. Prog Mater Sci 50:50–154
2. Ningthoujam RS (2017) Synthesis, characterization of borides, carbides, nitrides and their applications In: Banerjee S, Tyagi AK (eds) Materials under extreme conditions: recent trends and future prospects. Publisher: Elsevier Inc., USA, Chapter 10, pp 337–376
3. Prins R, Bussell ME (2012) Metal phosphides: Preparation, characterization and catalytic reactivity. Catal Lett 142:1413–1436
4. Carenco S, Portehault D, Boissiere C, Mezailles N, Sanchez C (2013)Nanoscaled metal borides and phosphides: Recent developments and perspectives. Chem Rev 113:7981–8065

5. Akopov G, Yeung MT, Kaner RB (2017) Rediscovering the crystal chemistry of borides. Adv Mater 2017:1604506–1604506
6. Golla BR, Mukhopadhyay A, Basu B, Thimmappa SK (2020) Review on ultra-high temperature boride ceramics. Prog Mater Sci 111:100651
7. Nagamatsu J, Nakagawa N, Muranaka T, Zenitani Y, Akimitsu J (2001) Superconductivity at 39 K in magnesium diboride. Nature 410:63–64
8. Benson D, Li Y, Luo W, Ahuja R, Svensson G, Haussermann U (2013) Lithium and calcium carbides with polymeric carbon structures. Inorg Chem 52:6402–6406
9. Bredig MA (1943) The crystal structure of magnesium carbide. J Am Chem Soc 65:1482–1483
10. Reckeweg O, DiSalvo FJ (2002) Alkaline earth metal nitride compounds with the composition M_2NX (M = Ca, Sr, Ba; X = 0, H, Cl or Br). Solid State Sci 4:575–584
11. Gregory DH (2001) Nitride chemistry of the s-block elements. Coord Chem Rev 215:301–345
12. Ningthoujam RS, Sudhakar N, Rajeev KP, Gajbhiye NS (2002) Electrical resistivity study of La, B doped nanocrystalline superconducting vanadium nitride. J Appl Phys 91:6051
13. Gajbhiye NS, Ningthoujam RS, Weissmuller J (2002) Synthesis and magnetic studies of nanocrystalline nickel nitride material. Phys Stat Sol (a) 189:691
14. Ningthoujam RS, Gajbhiye NS (2004) Magnetic and current density studies on nanostructured vanadium nitride material. Ind J Phys 78A(1):89
15. Ningthoujam RS, Gajbhiye NS (2004) Thermal decomposition study of nanocrystalline Ni_3N. Ind J Phys 78A(2):265
16. Sudhakar N, Ningthgoujam RS, Rajeev KP, Nigam AK, Weissmuller J, Gajbhiye NS (2004) Effect of La, B doping on the electrical resistivity and magnetic susceptibility of nanocrystalline vanadium nitride. J Appl Phys 96:688
17. Gajbhiye NS, Ningthoujam RS, Weissmuller J (2004) 17Mössbauer study of nanocrystalline ε-$Fe_{3-x}Co_xN$ system Hyperfine Interact 156:51
18. Gajbhiye NS, Ningthoujam RS (2004) Structural, electrical and magnetic studies of nanocrystalline δ-MoN and γ-Mo_2N. Phys Stat Sol (c) 1:3449
19. Gajbhiye NS, Panda RN, Ningthoujam RS, Bhattacharyya S (2004) Magnetism of nanostructured iron nitride (Fe–N) systems. Phys Stat Sol (c) 1:3252
20. Gajbhiye NS, Ningthoujam RS, Bhattacharyya S (2005) Magnetic properties of Co and Ni substituted ε-Fe_3N nanoparticles. Hyperfine Interact 164:17
21. Gajbhiye NS, Ningthoujam RS (2006) Low temperature synthesis, crystal structure and thermal stability studies of nanocrystalline VN particles. Mat Res Bull 41:1612
22. Ningthoujam RS, Gajbhiye NS (2008) Magnetic study of single domain ε-Fe_3N nanoparticles synthesized by precursor technique. Mater Res Bull 43:1079
23. Dewangan KC, Ningthoujam RS, Kurian S, Gajbhiye NS (2008) Magnetic and Mössbauer properties of Fe doped VN nanoparticles. Hyperfine Interact 183:185
24. Ningthoujam RS, Gajbhiye NS (2010) Magnetization studies on ε-$Fe_{2.4}Co_{0.6}N$ nanoparticles. Mater Res Bull 45:499
25. Ningthoujam RS, Gajbhiye NS (2010) Electron-electron interaction effect and resistivity maximum in nanocrystalline and ordered superconducting γ-Mo_2N. Int J Nanotechnol 7:932
26. Ningthoujam RS, Vatsa RK, Prajapat CL, Yashwant G, Ravikumar G (2010) Interaction between amorphous ferromagnetic Co–Fe–B particles in conducting silver matrix prepared by chemical reduction route. J Alloys Comp (Lett) 492:L40
27. Ningthoujam RS, Panda RN, Gajbhiye NS (2012) Variation of intrinsic magnetic parameters of single domain CoN interstitial nitrides synthesized via hexa-ammine cobalt nitrate route. Mater Chem Phys 134:377–381
28. Takagi Y, Isami K, Yamamoto I, Nakagawa T, Yokoyama T (2010) Structure and magnetic properties of iron nitride thin films on Cu(001). Phys Rev B 81:035422
29. Bourourou Y, Beldi L, Bentria B, Gueddouh A, Bouhafs B (2014) Structure and magnetic properties of the 3*d* transition-metal mono-borides TM–B (TM = Mn, Fe, Co) under pressures. J Magn Magn Mater 365:23–30
30. Meffre A, Mehdaoui B, Kelsen V, Fazzini PF, Carrey J, Lachaize S, Respaud M, Chaudret B (2012) A simple chemical route toward monodisperse iron carbide nanoparticles displaying tunable magnetic and unprecedented hyperthermia properties. Nano Lett 12:4722–4728

31. Yang W, Wu X, Yu Y, Yang C, Xu S, Li H (2016) Controlled synthesis and magnetic properties of iron–cobalt–phosphide nanorods. Nanoscale 8:16187–16191
32. Post B, Moskowitz D, Glaser FW (1955) Borides of rare earth metals. Am Electrometal Corporation 78:1800–1802
33. Flores-Livas JA, Sarmiento-Pérez R, Botti S, Goedecker S, Marques MAL (2019) Rare-earth magnetic nitride perovskites. J Phys: Mater 2:025003
34. Hadjipanayis GC, Wang YZ, Singleton EW, Yelon WB (1992) Rare-earth nitrides and carbides: A new class of permanent magnet materials. J Mater Eng Perform 1:193–203
35. Hirayama Y, Suzuki K, Fujita A, Takagi K (2019) Experimental investigation of nitrogenation process for heavy rare earth nitrides from their hydrides. AIP advances 9:045221
36. Ono S, Nomura K, Hayakawa H (1974) Synthesis of new rare-earth phosphides. J Less-Comnwn Metais 38:119–130
37. Stoyko SS, Blanchard PER, Ramachandran KK, Mar A (2019) Quaternary rare-earth transition-metal phosphides $REMnCuP_2$ (RE = Y, La-Nd, Sm, Gd-Tm, Lu) with $CaAl_2Si_2$-type structure and a polymorph of $LaMnCuP_2$ with $BaCu_2S_2$-type structure. J Solid State Chem 269:100–106
38. Jian M, Yufang R (1991) Studies on the Electrical Properties of Rare Earth Monophosphides. J Solid State Chem 95:346–351
39. Mori T, Rare earth borides, carbides and nitrides, encyclopedia of inorganic and bioinorganic chemistry, Online © 2011–2012, Wiley Ltd
40. Lee SH, Jeong H, Okello OFN, Xiao S, Moon S, Kim DY, Kim G-Y, Lo J-I, Peng Y-C, Cheng B-M, Miyake H, Choi S-Y, Kim JK (2019) Improvements in structural and optical properties of wafer-scale hexagonal boron nitride film by post-growth annealing. Sci Rep 9:10590
41. Yamashita H, Fukui K, Misawa S, Yoshida S (1979) Optical properties of AIN epitaxial thin films in the vacuum ultraviolet region. J Appl Phys 50:896
42. Shi S-C, Chen CF, Chattopadhyay S, Chen K-H, Ke B-W, Chen L-C, Trinkler L, Berzina B (2006) Luminescence properties of wurtzite AlN nanotips. Appl Phys Lett 89:163127
43. Stagi L, Chiriu D, Carbonaro CM, Corpino R, Ricci PC (2016) Structural and optical properties of carbon nitride polymorphs. Diam Relat Mater 68:84–92
44. Zhang L, Jin H, Yang W, Xie Z, Miao H, An L (2005) Optical properties of single-crystalline a-Si_3N_4 nanobelts. Appl Phys Lett 86:061908
45. Feiler D, Williams RS, Talin AA, Yoon H, Goorsky MS (1997) Pulsed laser deposition of epitaxial A1N, GaN, and InN thin films on sapphire (0001). J Cryst Growth 171:12–20
46. Hou HQ, Tu CW (1994) Optical property of InAsP/InP strained quantum wells grown on InP (111) B and (100) substrates. J Appl Phys 75:4673
47. Li LL, Bacaksiz C, Nakhaee M, Pentcheva R, Peeters FM, Yagmurcukardes M (2020) Single-layer Janus black arsenic-phosphorus (b-AsP): Optical dichroism, anisotropic vibrational, thermal, and elastic properties. Phys Rev B 101:134102
48. Václavík J, Vápenka D (2013) Gallium phosphide as a material for visible and infrared optics. EPJ Web Conf 48:00028
49. Shena Z, Chena J, Lia B, Lia G, Zhenga H, Mena J, Hou X (2020) Tunable fabrication and photoluminescence property of SiC nanowires with different microstructures. Appl Surf Sci 506:144979
50. Satake M, Iqbal SA (1995) Chemistry of p-block elements. Discovery Publishing House, New Delhi, India
51. Yaiphaba N, Ningthoujam RS, Singh NS, Vatsa RK, Singh NR (2010) Probing of inversion symmetry site in Eu^{3+}-doped $GdPO_4$ by luminescence study: Concentration and annealing effect. J Lumin 130:174
52. Singh BP, Parchur AK, Ningthoujam RS, Ansari AA, Singh P, Rai SB (2014) Influence of Gd^{3+} co-doping on structural property of $CaMoO_4$:Eu nanoparticles. Dalton Trans 43:4770–4778
53. Sahu NK, Ningthoujam RS, Bahadur D (2012) Disappearance and recovery of luminescence in $GdPO_4$:Eu^{3+} nanorods: Propose to water/OH• release under near infrared and gamma irradiations. J Appl Phys 112:014306

54. Yaiphaba N, Ningthoujam RS, Singh NR, Vatsa RK (2010) Luminescence properties of redispersible Tb^{3+}-Doped $GdPO_4$ nanoparticles prepared by an ethylene glycol route. Eur J Inorg Chem 2682
55. Ningthoujam RS, Shukla R, Vatsa RK, Duppel V, Kienle L, Tyagi AK (2009) Gd_2O_3:Eu^{3+} particles prepared by glycine-nitrate combustion: Phase, concentration, annealing, and luminescence studies. J Appl Phys 105:084304
56. Park JK, Lim MA, Kim CH, Park HD (2003) White light-emitting diodes of GaN-based Sr_2SiO_4:EuSr_2SiO_4:Eu and the luminescent properties. Appl Phys Lett 82:683
57. Kim JS, Kang JY, Jeon PE, Choi JC, Park HL, Kim TW (2004) GaN-based white-light-emitting diodes fabricated with a mixture of $Ba_3MgSi_2O_8$:Eu^{2+} and Sr_2SiO_4:Eu^{2+} Phosphors. Jpn J Appl Phys 43:989
58. Song KM, Kim DH, Kim JM, Cho CY, Choi J, Kim K, Park J, Kim H (2017) White light emission of monolithic InGaN/GaN grown on morphology-controlled, nanostructured GaN templates. Nanotechnology 28:225703
59. Meetei SD, Singh SD, Singh NS, Sudarsan V, Ningthoujam RS, Tyagi M, Gadkari SC, Tewari R, Vatsa RK (2012) Crystal structure and photoluminescence correlations in white emitting nanocrystalline ZrO_2: Eu^{3+} phosphor: Effect of doping and annealing. J Lumin 132:537–544
60. Singh LR, Ningthoujam RS, Sudarsan V, Singh SD, Kulshreshtha SK (2008) Probing of surface Eu^{3+} ions present in ZnO: Eu nanoparticles by covering ZnO: Eu core with Y_2O_3 shell: Luminescence study. J Lumin 128:1544
61. Gajbhiye NS, Ningthoujam RS, Ahmed A, Panda DK, Umre SS, Sharma SJ (2008) Redispersible Li^+ and Eu^{3+} co-doped CdS nanoparticles: luminescence studies. Pramana J Phys 70:313
62. Phaomei G, Ningthoujam RS, Singh WR, Loitongbam RS, Singh NS, Rath A, Juluri RR, Vatsa RK (2011) Luminescence switching behavior through redox reaction in Ce^{3+} co-doped $LaPO_4$: Tb^{3+} nanorods: Re-dispersible and polymer film. Dalton Trans 40:11571
63. Soni AK, Joshi R, Singh BP, Naveen Kumar N, Ningthoujam RS (2019) Near-infrared-and magnetic-field-responsive $NaYF_4$: Er^{3+}/Yb^{3+}@ SiO_2@ AuNP@ Fe_3O_4 nanocomposites for hyperthermia applications induced by fluorescence resonance energy transfer and surface plasmon absorption. ACS Appl Nano Mater 2:7350−7361
64. Hendrie JM (1954) Dissociation energy of N_2. J Chem Phys 22:1503
65. Ono-Nakazato H, Matsui A, Usui T (2002) Nitrogen dissociation rate at solid surface of ferrous alloys. ISIJ Int 42:229–234
66. Mortensen JJ, Morikawa Y, Hammer B, Nørskov JK (1997) Density functional calculations of N_2 adsorption and dissociation on a Ru (0001) surface. J Cat 169:85–92
67. Mavrikakis M, Hansen LB, Mortensen JJ, Hammer B, Nørskov JK (1999) "Dissociation of N_2, NO, and CO on transition metal surfaces". In: D Truhlar (et al) Transition state modeling for catalysis; ACS symposium series; American Chemical Society: Washington, DC, (Chapter 19)
68. McDonald NR, Wallwork GR (1970) The reaction of nitrogen with titanium between 800 and 1200 °C. Oxid Met 2:263–283
69. Choudhary TV, Sivadinarayana C, Goodman DW (2001) Catalytic ammonia decomposition: CO_x-free hydrogen production for fuel cell applications. Catal Lett 72:197
70. Marin-Ayral RM, Pascal C, Martinez F, Tedenac JC (2000) Simultaneous synthesis and densification of titanium nitride by high pressure combustion synthesis. J Eur Ceram Soc 20:2679–2684
71. Chen H, Nambu A, Wen W, Graciani J, Zhong Z, Hanson JC, Fujita E, Rodriguez JA (2007) Reaction of NH_3 with Titania: N-doping of the oxide and TiN formation. J Phys Chem C 111:1366–1372
72. Choi D, Kumta PTN (2005) Synthesis of nanostructured TiN using a two-step transition metal halide approach. J Am Ceram Soc 88:2030–2035
73. Kaskel S, Schlichte K, Chaplais G, Khanna M (2003) Synthesis and characterisation of titanium nitride based nanoparticles. J Mater Chem 13:1496–1499
74. Qiu Y, Gao L (2003) Novel synthesis of nanocrystalline gallium nitride powder from gallium(III)-urea complex. Chem Lett 32:774–775

75. Ganesh V, Suresh S, Balaji M, Baskar K (2010) Synthesis and characterization of nanocrystalline gallium nitride by nitridation of Ga-EDTA complex. J Alloy Compd 498:52–56
76. Fang H-B, Luo Y, Zheng Y-Z, Ma W, Tao X (2016) Facile large-scale synthesis of urea-derived porous graphitic carbon nitride with extraordinary visible-light spectrum photodegradation. Ind Eng Chem Res 55:4506–4514
77. Fischer A, Antonietti M, Thomas A (2007) Growth confined by the nitrogen source: Synthesis of pure metal nitride nanoparticles in mesoporous graphitic carbon nitride. Adv Mater 19:264–267
78. Thangala J, Chen Z, Chin A, Ning CZ, Sunkara MK (2009) Phase transformation studies of metal oxide nanowires. Cryst Growth Des 9:3177–3182
79. Wang Y, Dheeraj D, Liu Z, Liang M, Li Y, Yi X, Wang J, Li J, Weman H (2019) AlGaN nanowires grown on SiO_2/Si (100) using graphene as a buffer layer. Cryst Growth Des 19:5516–5522
80. Furtmayr F, Vielemeyer M, Stutzmann M, Arbiol J, Estradé S, Peirò F, Morante JR, Eickhoff M (2008) Nucleation and growth of GaN nanorods on Si (111) surfaces by plasma-assisted molecular beam epitaxy-The influence of Si- and Mg-doping. J Appl Phys 104:034309
81. Bartzsch H, Glöß D, Frach P, Gittner M, Schultheiß E, Brode W, Hartung J (2009) Electrical insulation properties of sputter-deposited SiO_2, Si_3N_4 and Al_2O_3 films at room temperature and 400 °C. Phys Status Solidi A 206:514–519
82. Niewa R, DiSalvo FJ (1998) Recent developments in nitride chemistry. Chem Mater 10:2733–2752
83. Hashimoto M, Amano H, Sawaki N, Akasaki I (1984) Effects of hydrogen in an ambient on the crystal growth of GaN using $Ga(CH_3)_3$ and NH_3. J Cryst Growth 68:163–168
84. Amano H, Sawaki S, Akasaki I, Toyoda Y (1986) Metalorganic vapour phase epitaxial growth of a high quality GaN films using an AlN buffer layer. Appl Phys Lett 48:353–355
85. Madar R, Jacob G, Hallais J, Fruchart R (1975) High pressure solution growth of GaN. J Cryst Growth 31:197–203
86. Amano H, Kito M, Hiramatsu K, Akasaki I (1989) p-type conduction in Mg-doped GaN treated with low-energy beam irradiation (LEEBI). Jpn J Appl Phys 28:L2112–L2114
87. Nakamula S, Iwasa N, Senoh M, Mukai T (1992) Hole compensation mechanism of p-type GaN films. Jpn J Appl Phys 31:1258–1266
88. Hasegawa S, Hasegawa T, Kim SW, Yamanashi R, Uematsu K, Toda K, Sato M (2019) Single crystal growth and crystal structure analysis of novel orange-red emission pure nitride $CaAl_2Si_4N_8$:Eu^{2+} phosphor. ACS Omega 4:9939–9945
89. Yang M, DiSalvo FJ (2012) Template-free synthesis of mesoporous transition metal nitride materials from ternary cadmium transition metal oxides. Chem Mater 24:4406–4409
90. Cheng Z, Saad A, Guo H, Wang C, Liu S, Thomas T, Yang M (2020) Ordered mesoporous transition metal nitrides prepared through hard template nanocasting and rapid nitridation process. J Alloys Comp 838:155375
91. Kawamura F, Yusa H, Taniguchi T (2012) Synthesis of rhenium nitride crystals with MoS_2 structure. Appl Phys Lett 100:251910–251913
92. Lei L, Yin W, Jiang X, Lin S, He D (2013) Synthetic route to metal nitrides: High-pressure solid-state metathesis reaction. Inorg Chem 52:13356–13362
93. Gregory DH, O'Meara PM, Gordon AG, Siddons DJ, Blake AJ, Barker MG, Hamor TA, Edwards PP (2001) Layered ternary transition metal nitrides; synthesis, structure and physical properties. J Alloys Comp 317–318:237–244
94. Kobayashi Y, Kumakura K, Akasaka T, Makimoto T (2012) Layered boron nitride as a release layer for mechanical transfer of GaN-based devices. Nature 484:223–227
95. Chung K, Park SI, Baek H, Chung J-S, Yi G-C (2012) High-quality GaN films grown on chemical vapor-deposited graphene films. NPG Asia Mater 4:e24
96. Roul B, Chandan G, Mukundan S, Krupanidhi SB (2018) Heterostructures of III-nitride semiconductors for optical and electronic applications. Chapter 8. License Intech, pp 171–201. https://doi.org/10.5772/intechopen.70219.

97. Wang J, Ma F, Sun M (2017) Graphene, hexagonal boron nitride, and their heterostructures: properties and applications. RSC Adv 7:16801
98. Zhang H, Zhang Y-N, Liu H, Liu L-M (2014) Novel heterostructures by stacking layered molybdenum disulfides and nitrides for solar energy conversion. J Mater Chem A 2:15389
99. Xu L, Li S, Zhang Y, Zhai Y (2012) Synthesis, properties and applications of nanoscale nitrides, borides and carbides. Nanoscale 4:4900
100. Bordon EH, Riedel R, Zerr A, McMillan PF, Auffermann G, Prots Y, Bronger W, Kniep R, Kroll P (2006) High-pressure chemistry of nitride-based materials. Chem Soc Rev 35:987–1014
101. Friedrich A, Winkler B, Juarez-Arellano EA, Bayarjargal L (2011) Synthesis of binary transition metal nitrides, carbides and borides from the elements in the laser-heated diamond anvil cell and their structure-property relations. Materials 4:1648–1692
102. Yamamoto Y, Yokota H, Kojima N, Hayashi S, Kobayashi T, Sekine T, Sugarara Y (2013)Effects of structural differences in starting materials on the formation behavior of cubic silicon nitride by shock compression. J Ceramic Soc Jpn 121:741–744
103. Inokuti Y, Nishida N, Ōhashi N (1975)Formation of Fe_3N, Fe_4N and $Fe_{16}N_2$ on the surface of iron. Metall Trans A 6:773
104. Durairaj A, Sakthivel T, Ramanathan S, Vasanthkumar S (2019) Quenching-induced structural distortion of graphitic carbon nitride nanostructures: Enhanced photocatalytic activity and electrochemical hydrogen production. ACS Omega 4:6476–6485
105. Holländer Pettersson N, Lindell D, Lindberg F, Borgenstam A (2019)Formation of chromium nitride and intragranular austenite in a super duplex stainless steel. Metall Mater Trans A50:5594–5601
106. Chopra NG, Luyken RJ, Cherrey K, Crespi VH, Cohen ML, Louie SG, Zettl A (1995) Boron nitride nanotubes. Science 269:966–267
107. Goldberger J, He R, Zhang Y, Lee S, Yan H, Choi HJ, Yang P (2003) Single-crystal gallium nitride nanotubes. Nature 422:599–602
108. Panda RN, Gajbhiye NS (1997) Magnetic properties of single domain -Fe_3N synthesized by borohydride reduction route. J Appl Phys 81:335
109. Wu Q, Park J-H, Park S, Jung SJ, Suh H, Park N, Wongwiriyapan W, Lee S, Lee YH, Song YJ (2015) Single crystalline film of hexagonal boron nitride atomic monolayer by controlling nucleation seeds and domains. Sci Rep 5:16159
110. Li R, Wang Y (2019) Modification of boron nitride nanocages by titanium doping results unexpectedly in exohedral complexes. Nat Commun 10:4908
111. Bang JH, Suslick KS (2009) Dual templating synthesis of mesoporous titanium nitride microspheres. Adv Mater 21:3186–3190
112. Wang Y, Zhang B, Pan W, Ma H, Zhang J (2017) 3D porous nickel–cobalt nitrides supported on nickel foam as efficient electrocatalysts for overall water splitting. Chemsuschem 10:4170–4177
113. Ghazali NM, Yasui K, Hashim AM (2014) Synthesis of gallium nitride nanostructures by nitridation of electrochemically deposited gallium oxide on silicon substrate. Nanoscale Res Lett 9:685
114. Hajibabaei H, Hamann TW (2017) Selective electrodeposition of tantalum (V) oxide electrodes. Langmuir 33:10800–10806
115. Goto T, Niki A, Tsujimura H, Ito Y (2006) Electrochemical deposition of metal nitrides films in molten chloride system. In: Molten salts. XIV: proceedings of the international symposium, electrochemical society, Inc., New Jersey, USA edited by Mantz RA, Trulove PC, De Long HC, Stafford GR, Hagiwara M, Costa DA
116. Kasturibai S, Kalaignan GP (2014) Pulse electrodeposition and corrosion properties of Ni–Si_3N_4 nanocomposite coatings. Bull Mater Sci 37:721–728
117. Workie B, McCandless BE, Gebeyehu Z (2013) Electrophoretic deposition of aluminum nitride from its suspension in acetylacetone using iodine as an additive. J Chem 489734
118. Pimputkar S, Nakamura S (2016) Decomposition of supercritical ammonia and modeling of supercritical ammonia–nitrogen–hydrogen solutions with applicability toward ammonothermal conditions. J Supercrit Fluids 107:17–30

119. Desmoulins-Krawiec S, Aymonier C, Loppinet-Serani A, Weill F, Gorsse S, Etourneau J, Cansell F (2004) Synthesis of nanostructured materials in supercritical ammonia: nitrides, metals and oxides. J Mater Chem 14:228–232
120. Dwilinski R, Baranowski JM, Kaminska M (1996) On GaN crystallization by ammonothermal method. Acta Phys Polonica 90:763–766
121. Lan YC, Chen XL, Xu YP, Cao YG, Huang F (2000) Syntheses and structure of nanocrystalline gallium nitride obtained from ammonothermal method using lithium metal as mineralizator. Mater Res Bull 35:2325–2330
122. Jegier JA, Mckernan S, Mckernan WL, Gladeferter WL (1998) Poly(imidogallane): Synthesis of a crystalline 2-D network solid and its pyrolysis to form nanocrystalline gallium nitride in supercritical ammonia. Chem Mater 10:2041–2043
123. Giroire B, Marre S, Garcia A, Cardinal T, Aymonier C (2016) Continuous supercritical route for quantum confined GaN nanoparticles. React Chem Eng 1:151
124. Wang J, Gu Y, Zhang L, Zhao G, Zhang Z (2010) Synthesis of boron nitride nanotubes by self-propagation high-temperature synthesis and annealing method. J Nanomater 540456
125. Braverman BS, Lepakova OK, Maksimov YM (2008) Features of the growth of nitride layers in the self-propagating high-temperature synthesis of chromium nitrides. Russian J Non-Ferrous Metals 49:126–129
126. Chukhlomina LN, Ivanov YF, Maksimov YM, Akhunova ZS, Krivosheeva EN (2005) Preparation of submicron silicon nitride powders via self-propagating high-temperature synthesis. Inorganic Mater 41:1294–1299
127. Deevi S, Munir ZA (1990) The mechanism of synthesis of titanium nitride by self-sustaining reactions. J Mater Res 5:2177
128. Li L, Ilyin AP, Gubareva FA, Mostovshchikov AV, Klenovskii MS (2018) Study of self-propagating high-temperature synthesis of aluminum nitride using a laser monitor. Ceram Int 44:19800–19808
129. Linde AV, Grachev VV, Marin-Ayral RM (2009) Self-propagating high-temperature synthesis of cubic niobium nitride under high pressures of nitrogen. Chem Eng J 155:542–547
130. Shiganova LA, Bichurov GV, Amosov AP, Titova YV, Ermoshkin AA, Bichurova PG (2011) The self-propagating high temperature synthesis of a nanostructured titanium nitride powder with the use of sodium azide and haloid titanium containing salt. Russian J Non-Ferrous Metals 52:91–95
131. Shin J, Ahn D-H, Shin M-S, Kim Y-S (2000) Self-propagating high-temperature synthesis of aluminum nitride under lower nitrogen pressures. J Am Ceram Soc 83:1021–1028
132. Gunnewiek RFK, Souto PM, Kiminami RHGA (2017) Synthesis of nanocrystalline boron carbide by direct microwave carbothermal reduction of boric acid. J Nanomater 3983468
133. Strobel TA, Kurakevych OO, Kim DY, Godec YL, Crichton W, Guignard J, Guignot N, Cody GD, Oganov AR (2014) Synthesis of β Mg_2C_3: A monoclinic high-pressure polymorph of magnesium sesquicarbide. Inorg Chem 53:7020–7027
134. Long GJ, Leighly HP Jr (1982) The iron-iron carbide phase diagram: A practical guide to some descriptive solid state chemistry. J Chem Educ 59:948–953
135. Sohor MAHM, Mustapha M, Kurnia JC (2017) Silicon carbide- from synthesis to application: a review. MATEC Web Conf 131:04003
136. Shena Z, Chena J, Lia B, Lia G, Zhenga H, Mena J, Hou X (2020) Tunable fabrication and photoluminescence property of SiC nanowires with different microstructures. Appl Surf Sci 506:144979
137. Sugahara Y, Sugimoto K-I, Kuroda K, Kato C (1988) Preparation of silicon carbide and aluminum silicon carbide from a montmorillonite-po1yacrylonitrile intercalation compound by carbotherma1 reduction. J Am Ceram Soc 71:C-325–C-327
138. Namba T, Koyama T, Imada G, Kanno M, Yamawaki M (1987) Kinetics of the carbothermic reduction of a $ThO_2 + UO_2 + C$ mixture to prepare (Th, U)C. J Nuclear Mater 150:226–232
139. Blaha H, Komarek KL (1982) The reduction of thoria with graphite. Monatsh für Chemie—Chem Mon 113:3–14

140. Xiao T, Wang H, York APE, Williams VC, Green MLH (2002) Preparation of nickel–tungsten bimetallic carbide catalysts. J Catalysis 209:318–330
141. Kwitniewski CEF, Tentardini EK, Totten GE (2013) Carburizing and carbonitriding, encyclopedia of tribology. In: Wang QJ, Chung Y-W (eds) Springer, Boston, MA
142. Mnatsakanyan R, Zhurnachyan AR, Matyshak VA, Manukyan KV, Mukasyan AS (2016) Microwave-assisted synthesis of carbon-supported carbides catalysts for hydrous hydrazine decomposition. J Phys Chem Solids 96–97:115–120
143. Jin K, Jia Y, Zhao Z, Song W, Wang S, Guan C (2019) Synthesis of chromium carbide nanopowders by microwave heating and their composition and microstructure change under gamma ray irradiation. Molecules 24:16
144. Pei LZ, Tang YH, Chen YW, Guo C, Li XX, Yuan Y, Zhang Y (2006) Preparation of silicon carbide nanotubes by hydrothermal method. J Appl Phys 99:114306
145. Sagadevan S, Das I, Singh P, Podder J (2017) Synthesis of tungsten carbide nanoparticles by hydrothermal method and its characterization. J Mater Sci: Mater Electron 28:1136–1141
146. Borovinskaya I, Ignatieva T, Vershinnikov V (19 Dec 2012) Self-propagating high-temperature synthesis of ultrafine tungsten carbide powders, tungsten carbide—processing and applications. Kui Liu, IntechOpen
147. Zhang L, Gu Y, Wang W, Wang J, Zhao G, Qian Q, Zhang Z, Zhang F (2011) A fast-pyrolysis self-propagating high temperature synthesis route to single phase of boron carbide ultrafine powders. J Ceramic Soc Jpn 119:631–634
148. Łopaciński M, Puszynski J, Lis J (2001) Synthesis of ternary titanium aluminum carbides using self-propagating high-temperature synthesis technique. J Am Ceram Soc 84:3051–3053
149. Kobashi M, Ichioka D, Kanetake N (2010) Combustion synthesis of porous TiC/Ti composite by a self-propagating mode. Mater (Basel) 3:3939–3947
150. Tabata A, Komura Y, Kanaya M, Narita T, Kondo A, Misutani T (2006) Preparation of nanocrystalline silicon carbide thin films by hot-wire chemical vapor deposition at various filament temperature. IEEE 4th world conference on photovoltaic energy conference, vol 2
151. Pedersen H, Leone S, Kordina O, Henry A, Nishizawa S, Koshka Y, Janzen E (2012) Chloride-based CVD growth of silicon carbide for electronic applications. Chem Rev 112:2434–2453
152. Denkena B, Köhler J, Breidenstein B, Abrão AM, Ventura CEH (2014) Influence of the cutting edge preparation method on characteristics and performance of PVD coated carbide inserts in hard turning. Surf Coat Technol 254:447–454
153. Venkatesh VC, Ye CT, Quinto DT, Hoy DEP (1991) Performance studies of uncoated, CVD-coated and PVD-coated carbides in turning and milling. CIRP Ann 40:545–550
154. Givargizov EI, Grinberg SA (1993) Growth of Crystals, vol 19. Published by Springer, US
155. Engqvist H, Ederyd S, Axen N, Hogmark S (1999) Grooving wear of single-crystal tungsten carbide. Wear 230:165–174
156. Wang S-C, Nayak PK, Chen Y-L, Sung JC, Huang J-L (2012) Growth of single crystal silicon carbide by liquid phase epitaxy using samarium/cobalt as unique solvent. Proc IMechE Part N: J Nanoeng Nanosyst 226:75–79
157. Dong B-X, Qiu F, Li Q, Shu S-L, Yang H-Y, Jiang Q-C (2019) The synthesis, structure, morphology characterizations and evolution mechanisms of nanosized titanium carbides and their further applications. Nanomaterials 9:1152
158. Baddour FG, Roberts EJ, To AT, Wang L, Habas SE, Ruddy DA, Bedford NM, Wright J, Nash CP, Schaidle JA, Brutchey RL, Malmstadt N (2020) An exceptionally mild and scalable solution-phase synthesis of molybdenum carbide nanoparticles for thermocatalytic CO2 hydrogenation. J Am Chem Soc 142:1010–1019
159. Bordet A, Landis RF, Lee Y, Tonga GY, Asensio JM, Li C-H, Fazzini P-F, Soulantica K, Rotello VM, Chaudret B (2019) Water-dispersible and biocompatible iron carbide nanoparticles with high specific absorption rate. ACS Nano 13:2870–2878
160. Ningthoujam RS, Gautam A, Padma N (2017) Oleylamine as reducing agent in syntheses of magic-size clusters and monodisperse quantum dots: optical and photoconductivity studies. Phys Chem Chem Phys 19:2294–2303

161. Gajbhiye NS, Sharma S, Nigam AK, Ningthoujam RS (2008) Tuning of single to multidomain behavior for monodispersed ferromagnetic cobalt nanoparticles. Chem Phys Lett 466:181
162. Sharma S, Gajbhiye NS, Ningthoujam RS (2010) Synthesis and self-assembly of monodisperse Co_xNi_{100-x} (x = 50, 80) colloidal nanoparticles by homogenous nucleation. J. Colloids Interface Sci 351:323
163. Sharma S, Gajbhiye NS, Ningthoujam RS (2010) Effect of annealing on magnetic properties of FePd and FePdPt nanoparticles. AIP Conf Proc 1313:125
164. Gajbhiye NS, Sharma S, Ningthoujam RS (2008) Synthesis of self-assembled monodisperse 3 nm FePd nanoparticles: phase transition, magnetic study and surface effect. J Appl Phys 104:123906
165. Sharma KS, Ningthoujam RS, Dubey AK, Chattopadhyay A, Phapale S, Juluri RR, Mukherjee S, Tewari R, Shetake NG, Pandey BN, Vatsa RK (2018) Synthesis and characterization of monodispersed water dispersible Fe_3O_4 nanoparticles and in vitro studies on human breast carcinoma cell line under hyperthermia condition. Sci Rep 8:14766
166. Biedunkiewicz A, Figiel P, Krawczyk M, Gabriel-Polrolniczak U (2013) Simultaneous synthesis of molybdenum carbides and titanium carbides by sol–gel method. J Therm Anal Calorim 113:253–258
167. Giordano C, Antonietti M (2011) Synthesis of crystalline metal nitride and metal carbide nanostructures by sol—gel chemistry. Nano Today 6:366–380
168. Simonenko EP, Simonenko NP, Derbenev AV, Nikolaev VA, Grashchenkov DV, Sevastyanov VG, Kablov EN, Kuznetsov NT (2013) Synthesis of nanocrystalline silicon carbide using the sol–gel technique. Russ J Inorg Chem 58:1143–1151
169. Limandri S, Garbarino G, Sifre D, Mezouar M, Josa VG (2019) Pressure dependence of the silicon carbide synthesis temperature. J Appl Phys 125:165902
170. Awasthi AP, Subhash G (2019) High-pressure deformation and amorphization in boron carbide. J Appl Phys 125:215901
171. Zhang L, Wang Y, Lv J, Ma Y (2017) Materials discovery at high pressures. Nat Rev Mater 2:17005
172. Wang Y, Kong B, Zhao D, Wang H, Selomulya C (2017) Strategies for developing transition metal phosphides as heterogeneous electrocatalysts for water splitting. Nano Today 15:26–55
173. Pei Y, Cheng Y, Chen J, Smith W, Dong P, Ajayan PM, Ye M, Shen J (2018) Recent developments of transition metal phosphides as catalysts in the energy conversion field. J Mater Chem A 6:23220
174. Kolny-Olesiak J (2019) Recent advances in the colloidal synthesis of ternary transition metal phosphides. Z Naturforsch 74:709–719
175. Haa T, Lee Y-S, Lee J, Shim J-H (2019) Mechanochemical synthesis of CeB_6 nanopowder. Ceram Int 45:19442–19446
176. Zhang H, Tang J, Yuan J, Ma J, Shinya N, Nakajima K, Murakami H, Ohkubo T, Qin L-C (2010) Nanostructured LaB_6 field emitter with lowest apical work function. Nano Lett 10:3539–3544
177. Majkić A, Puc U, Franke A, Kirste R, Collazo R, Sitar Z, Zgonik M (2015) Optical properties of aluminum nitride single crystals in the THz region. Opt Mater Res 5:246709
178. Abghoui Y, Skúlasson E (2015) Transition metal nitride catalysts for electrochemical reduction of nitrogen to ammonia at ambient conditions. Procedia Comput Sci 51:1897–1906
179. Kreider ME, Gallo A, Back S, Liu Y, Siahrostami S, Nordlund D, Sinclair R, Nørskov JK, King LA, Jaramillo TF (2019) Precious metal-free nickel nitride catalyst for the oxygen reduction reaction. ACS Appl Mater Interfaces 11:26863–26871
180. Yuan Y, Wang J, Adimi S, Shen H, Thomas T, Ma R, Attfield JP, Yang M (2020) Zirconium nitride catalysts surpass platinum for oxygen reduction. Nat Mater 19:282–286
181. Zhang H, Zhao Z, Xu C, Duan A (2006) New class of catalysts for the ammoxidation of propane to acrylonitrile over nickel–molybdenum mixed nitrides. Chem Lett 35:36–37
182. Grant JT, Carrero CA, Goeltl F, Venegas J, Mueller P, Burt SP, Specht SE, McDermott WP, Chieregato A, Hermans I (2016) Selective oxidative dehydrogenation of propane to propene using boron nitride catalysts. Science 354:1570–1573

183. Hunt ST, Nimmanwudipong T, Romn-Leshkov Y (2014) Engineering non-sintered, metal-terminated tungsten carbide nanoparticles for catalysis. Angiew Chem Int Ed 53:5131–5136
184. Reddy KP, Dama S, Mhamane NB, Ghosalya MK, Raja T, Satyanarayana CV, Gopinath CS (2019) Molybdenum carbide catalyst for the reduction of CO_2 to CO: surface science aspects by NAPPES and catalysis studies. Dalton Trans 48:12199–12209
185. Lee JS, Oyama ST, Boudart M (1987) Molybdenum carbide catalysts. Molybdenum carbide catalysts: I. Synthesis of unsupported powders. J Catalysis 106:125–133
186. Li Z, Yu L, Milligan C, Ma T, Zhou L, Cui Y, Qi Z, Libretto N, Xu B, Luo J, Shi E, Wu Z, Xin H, Delgass WN, Miller JT, Wu Y (2018) Two-dimensional transition metal carbides as supports for tuning the chemistry of catalytic nanoparticles. Nature Commun 9:5258
187. Zieschang A-M, Bocarsly JD, Schuch J, Reichel CV, Kaiser B, Jaegermann W, Seshadri R, Albert B (2019) Magnetic and electrocatalytic properties of nanoscale cobalt boride, Co_3B. Inorg Chem 58:16609–16617
188. Gupta S, Patel MK, Miotello A, Patel N (2020) Metal boride-based catalysts for electrochemical water-splitting: A review. Adv Funct Mater 30:1906481
189. Fujita S, Nakajima K, Yamasaki J, Mizugaki T, Jitsukawa K, Mitsudome T (2020) Unique catalysis of nickel phosphide nanoparticles to promote the selective transformation of biofuranic aldehydes into diketones in water. ACS Catal 10:4261–4267
190. Geng F, Bonita Y, Jain V, Magiera M, Rai N, Hicks JC (2020) Bimetallic Ru–Mo phosphide catalysts for the hydrogenation of CO_2 to methanol. Ind Eng Chem Res 59:6931–6943
191. Parra-Puerto A, Ng KL, Fahy K, Goode AE, Ryan MP, Kucernak A (2019) Supported transition metal phosphides: Activity survey for HER, ORR, OER and corrosion resistance in acid and alkaline electrolytes. ACS Catal 9:11515–11529
192. Callejas JF, Read CG, Roske CW, Lewis NS, Schaak RE (2016) Synthesis, characterization, and properties of metal phosphide catalysts for the hydrogen-evolution reaction. Chem Mater 28:6017–6044
193. Lv H, Xu D, Sun L, Henzie J, Suib SL, Yamauchi Y, Liu B (2019) Ternary palladium−boron−phosphorus alloy mesoporous nanospheres for highly efficient electrocatalysis. ACS Nano 13:12052–12061
194. Yu F, Zhou H, Huang Y, Sun J, Qin F, Bao J, GoddardIII WA, Chen S, Ren Z (2018) High-performance bifunctional porous non-noble metal phosphide catalyst for overall water splitting. Nat Commun 9:2551
195. Lanje AS, Ningthoujam RS, Sharma SJ, Pode RB (2011) Luminescence and electrical resistivity properties of cadmium oxide nanoparticles. Indian J Pure Appl Phys 49:234–238
196. Ghosh M, Ningthoujam RS, Vatsa RK, Das D, Nataraju V, Gadkari SC, Gupta SK, Bahadur D (2011) Role of ambient air on photoluminescence and electrical conductivity of assembly of ZnO nanoparticles. J Appl Phys 110:054309
197. Umare SS, Ningthoujam RS, Sharma SJ, Shrivastava S, Kurian S, Gajbhiye NS (2008) Mössbauer and magnetic studies on nanocrystalline $NiFe_2O_4$ particles prepared by ethylene glycol route. Hyperfine Interact 184:235
198. Ningthoujam RS, Kulshreshtha SK (2009) Nanocrystalline SnO_2 from thermal decomposition of tin citrate crystal: Luminescence and Raman studies. Mater Res Bull 44:57
199. Ningthoujam RS, Lahiri D, Sudarsan V, Poswal HK, Kulshreshtha SK, Sharma SM, Bhushan B, Sastry MD (2007) Nature of V^{n+} ions in SnO_2: EPR and photoluminescence studies. Mater Res Bull 42:1293
200. Feiler D, Williams RS, Talin AA, Yoon H, Goorsky MS (1997) Pulsed laser deposition of epitaxial A1N, GaN, and InN thin films on sapphire (0001). J Crystal Growth 171:12–20
201. Høiaas IM, Mulyo AL, Vullum PE, Kim D-C, Ahtapodov L, Fimland B-O, Kishino K, Weman H (2019) GaN/AlGaN nanocolumn ultraviolet light-emitting diode using double-layer graphene as substrate and transparent electrode. Nano Lett 19:1649–1658
202. O'Donnell K, Dierolf V (2010) Rare earth doped III-nitrides for optoelectronic and spintronic applications. Springer, Dordrecht
203. Higuchi Y, Iwaki M, Koizumi A, Yamanashi R, Uematsu K, Toda K, Sato M (2019) Single crystal growth of nitride and oxynitride phosphors using a gas–solid phase hybrid synthesis method. Jpn J Appl Phys 58:SFFD01

204. Lorenz K, Nogales E, Miranda SMC, Franco N, Méndez B, Alves E, Tourbot G, Daudin B (2013) Enhanced red emission from praseodymium-doped GaN nanowires by defect engineering. Acta Mater 61:3278–3284
205. Wieg AT, Kodera Y, Wang Z, Imai T, Dames C, Garay JE (2012) Visible photoluminescence in polycrystalline terbium doped aluminum nitride (Tb:AlN) ceramics with high thermal conductivity. Appl Phys Lett 101:111903
206. Schmitt H, Müller R, Maier M, Winnacker A, Wellmann P (2005) Photoluminescence study of in-situ rare earth doped PVT-grown SiC single crystals. Mater Sci Forum 483–485:445–448
207. Kenyon AJ (2002) Recent developments in rare-earth doped materials for optoelectronics. Prog Quantum Electron 26:225–284
208. Pyshkin SL, Anedda A (1993) Preparation and properties of gallium phosphide doped by rare-earth elements. Mat Res Soc Symp Proc 301:207–212
209. Singh LP, Srivastava SK, Mishra R, Ningthoujam RS (2014) Multifunctional hybrid nanomaterials from water dispersible CaF_2:Eu^{3+}, Mn^{2+} and Fe_3O_4 for luminescence and hyperthermia application. J Phys Chem C 118:18087–18096
210. Sahu NK, Singh NS, Ningthoujam RS, Bahadur D (2014) Ce^{3+}-sensitized $GdPO_4$:Tb^{3+} nanorods: An investigation on energy transfer, luminescence switching, and quantum Yield. ACS Photonics 1:337–346
211. Singh LR, Ningthoujam RS (2010) Critical view on energy transfer, site symmetry, improvement in luminescence of Eu^{3+}, Dy^{3+} doped by core-shell formation. J Appl Phys 107:104304
212. Parchur AK, Ningthoujam RS (2012) Preparation, microstructure and crystal structure studies of Li^+ co-doped YPO_4: Eu^{3+}. RSC Adv 2:10854–10858
213. Ningthoujam RS (2012) Enhancement of luminescence by rare earth ions doping in semiconductor host. In: Rai SB, Dwivedi Y (eds) Nova Science Publishers Inc, USA, Chapter 7, pp 145–182
214. Singh NS, Ningthoujam RS, Singh SD, Viswanadh B, Manoj N, Vatsa RK (2010) Preparation of highly crystalline blue emitting MVO_4: Tm^{3+} (M = Gd, Y) spherical nanoparticles: Effects of activator concentration and annealing temperature on luminescence, lifetime and quantum yield. J Lumin 130:2452
215. Ningthoujam RS (2010) Generation of exciton in two semiconductors interface: SnO_2: Eu–Y_2O_3. Chem Phys Lett 497:208
216. Prasad AI, Singh LR, Joshi R, Ningthoujam RS (2018) Luminescence study on crystalline phase of Y2Si2O7 from mesoporous silica and Y_2O_3: Ln^{3+} at C. AIP Adv 8:105310
217. Soni AK, Joshi R, Jangid K, Tewari R, Ningthoujam RS (2018) Low temperature synthesized $SrMoO_4$: Eu^{3+} nanophosphors functionalized with ethylene glycol: A comparative study of synthesize route, morphology, luminescence and annealing. Mater Res Bull 103:1–12
218. Wangkhem R, Yaba T, Singh NS, Ningthoujam RS (2018) Red emission enhancement from $CaMoO_4$:Eu^{3+} by co-doping of Bi^{3+} for near UV/blue LED pumped white pcLEDs: Energy transfer studies. J Appl Phys 123:124303
219. Ningombam GS, Singh NR, Ningthoujam RS (2017) Controlled synthesis of $CaWO_4$: Sm^{3+} microsphere particles by a reverse-micelle method and their energy transfer rate in luminescence. Colloids Surf A 518:249–262
220. Ningthoujam RS, Sharma A, Sharma KS, Barick KC, Hassan PA, Vatsa RK (2015) Roles of solvent, annealing and Bi^{3+} co-doping on the crystal structure and luminescence properties of YPO_4: Eu^{3+} nanoparticles. RSC Adv 5:68234–68242
221. Okram R, Yaiphaba N, Ningthoujam RS, Singh NR (2014) Is higher ratio of monoclinic to tetragonal in $LaVO_4$ a better luminescence host? Redispersion and polymer film formation. Inorg Chem 53:7204–7213
222. Solozhenko VL, Bushlya V, Zhou J (2019) Mechanical properties of ultra-hard nanocrystalline cubic boron nitride. Appl Phys 126:075107
223. Solozhenko VL, Gregoryan E (2005) Synthesis of superhard materials. ISSN:1369 7021 ©Elsevier Ltd 2005 p 44

224. Solozhenko VL, Kurakevych OO, Andrault D, Godec YL, Mezouar M (2009) Ultimate metastable solubility of boron in diamond: Synthesis of superhard diamond like BC_5. Phys Rev Lett 102:015506
225. Qin J, He D, Wang J, Fang L, Lei L, Li Y, Hu J, Kou Z, Bi Y (2008) Is rhenium diboride a superhard material?. Adv Mater 20:4780–4783
226. Solozhenkoa VL, Bushlya V (2019) Mechanical properties of boron phosphides. Mechanical properties of boron phosphides. J Superhard Mater 41:84–89
227. Ma R, Ju S, Chen H, Shu C (2017) Effect of cobalt content on microstructures and wear resistance of tungsten carbide–cobalt-cemented carbides fabricated by spark plasma sintering. IOP Conf Ser: Mater Sci Eng 207:012019
228. Haubner R, Wilhelm M, Weissenbacher R, Lux B (2002) Boron nitrides—properties, synthesis and applications, structure and bonding, vol 102. ©Springer Berlin Heidelberg
229. Reitera AE, Derflingera VH, Hanselmanna B, Bachmanna T, Sartory B (2005) Investigation of the properties of $Al_{1-x}Cr_xN$ coatings prepared by cathodic arc evaporation. Surf Coat Technol 200:2114–2122
230. Shibata M, Ogawa T, Kawashita M (2019) Synthesis of iron nitride nanoparticles from magnetite nanoparticles of different sizes for application to magnetic hyperthermia. Ceram Int 45:23707–23714
231. Wu K, Liu J, Saha R, Ma B, Su D, Peng C, Sun J, Wang J-P (2020) Irregularly shaped iron nitride nanoparticles as a potential candidate for biomedical applications: From synthesis to characterization. ACS Omega 5:11756–11767
232. Gangwar A, Varghese SS, Meena SS, Prajapat CL, Gupta N, Prasad NK (2019) Fe_3C nanoparticles for magnetic hyperthermia application. J Magn Magn Mater 481:251–256
233. Hamayun MA, Abramchuk M, Alnasir H, Khan M, Pak C, Lenhert S, Ghazanfari L, Shatruk M, Manzoor S (2018) Magnetic and magnetothermal studies of iron boride (FeB) nanoparticles. J Magn Magn Mater 451:407–413
234. Meinert M (2016) Exchange interactions and Curie temperatures of the tetrametal nitrides Cr_4N, Mn_4N, Fe_4N, Co_4N, and Ni_4N. J Phys: Condens Matter 28:056006
235. Ghosh R, Pradhan L, Devi YP, Meena SS, Tewari R, Kumar A, Sharma S, Gajbhiye NS, Vatsa RK, Pandey BN, Ningthoujam RS (2011) Induction heating studies of Fe_3O_4 magnetic nanoparticles capped with oleic acid and polyethylene glycol for hyperthermia. J Mater Chem 21:13388
236. Patil RM, Shete PB, Thorat ND, Otari SV, Prasad AI, Ningthoujam RS, Tiwale B, Pawar SH (2014) Non-aqueous to aqueous phase transfer of oleic acid coated iron oxide nanoparticles for hyperthermia application. RSC Adv 4:4515–4522
237. Parchur AK, Ansari AA, Singh BP, Hasan TN, Syed NA, Rai SB, Ningthoujam RS (2014) Enhanced luminescence of $CaMoO_4$: Eu by core@ shell formation and its hyperthermia study after hybrid formation with Fe_3O_4: cytotoxicity assessment on human liver cancer cells and mesenchymal stem cells. Integr Biol 6:53–64
238. Thorat ND, Khot VM, Salunkhe AB, Prasad AI, Ningthoujam RS, Pawar SH (2013) Surface functionalized LSMO nanoparticles with improved colloidal stability for hyperthermia applications. J Phys D 46:105003
239. Majeed J, Pradhan L, Ningthoujam RS, Vatsa RK, Bahadur D, Tyagi AK (2014) Enhanced specific absorption rate in silanol functionalized Fe_3O_4 core–shell nanoparticles: Study of Fe leaching in Fe_3O_4 and hyperthermia in L929 and HeLa cells. Colloids Surf, B 122:396–403
240. Thorat ND, Khot VM, Salunkhe AB, Ningthoujam RS, Pawar SH (2013) Functionalization of $La0.7Sr0.3MnO_3$ nanoparticles with polymer: studies on enhanced hyperthermia and biocompatibility properties for biomedical applications. Colloids Surf B: Biointerfaces 104:40–47
241. Thorat ND, Patil RM, Khot VM, Salunkhe AB, Prasad AI, Barick KC, Ningthoujam RS, Pawar SH (2013) Highly water-dispersible surface-functionalized LSMO nanoparticles for magnetic fluid hyperthermia application. New J Chem 37:2733
242. Shete PK, Patil RM, Ningthoujam RS, Ghosh S, Pawar SH (2013) Magnetic core–shell structures for magnetic fluid hyperthermia therapy application. New J Chem 37:3784–3792

243. Thorat ND, Otari SV, Bohara RA, Yadav HM, Khot VM, Salunkhe AB, Phdatre MR, Prasad AI, Ningthoujam RS, Pawar SH (2014) Structured superparamagnetic nanoparticles for high performance mediator of magnetic fluid hyperthermia: synthesis, colloidal stability and biocompatibility evaluation. Mater Sci Eng, C 42:637–646
244. Nikam DS, Jadhav SV, Khot VM, Ningthoujam RS, Hong CK, Mali SS, Pawar SH (2014) Colloidal stability of polyethylene glycol functionalized $Co0.5Zn0.5Fe_2O_4$ nanoparticles: effect of pH, sample and salt concentration for hyperthermia application. RSC Adv 4:12662
245. Singh LP, Jadhav NV, Sharma S, Pandey BN, Srivastava SK, Ningthoujam RS (2015) Hybrid nanomaterials YVO_4: Eu/Fe_3O_4 for optical imaging and hyperthermia in cancer cells. J Mater Chem C 3:1965–1975
246. Hemmer E, Benayas A, Légaré F, Vetrone F (2016) Exploiting the biological windows: current perspectives on fluorescent bioprobes emitting above 1000 nm. Nanoscale Horiz 1:168–184
247. Feng W, Wang R, Zhou Y, Li D, Gao X, Zhou B, Hu P, Chen Y (2019) Ultrathin molybdenum carbide MXene with fast biodegradability for highly efficient theory-oriented photonic tumor hyperthermia. Adv Funct Mater 29:1901942
248. Sundaram A, Ponraj JS, Wang C, Peng WK, Manavalan RK, Dhanabalan SC, Zhang H, Gaspar J (2020) Engineering of 2D transition metal carbides and nitrides MXenes for cancer therapeutics and diagnostics. J Mater Chem B 8:4990–5013
249. Merlo A, Mokkapati VRSS, Pandit S, Mijakovic I (2018) Boron nitride nanomaterials: biocompatibility and bio-applications. Biomater Sci 6:2298
250. Mushonga P, Onani MO, Madiehe AM, Meyer M (2012) Indium phosphide-based semiconductor nanocrystals and their applications. J Nanomater 869284
251. Mićić OI, Nozik AJ (1996) Synthesis and characterization of binary and ternary III–V quantum dots. J. Luminescence 70:95–107
252. Bharali DJ, Lucey DW, Jayakumar H, Pudavar HE, Prasad PN (2005) Folate-receptor-mediated delivery of InP quantum dots for bioimaging using confocal and two-photon microscopy. J Am Chem Soc 127:11364–11371
253. Pezzotti G, Marin E, Adachi T, Rondinella A, Boschetto F, Zhu W, Sugano N, Bock RM, McEntire B, Bal SB (2017) Bioactive silicon nitride: A new therapeutic material for osteoarthropathy. Sci Rep 7:44848
254. Özmen Y (2016) Si_3N_4 as a biomaterial and its tribo-characterization under water lubrication. Lubr Sci 28:243–254
255. Brama M, Rhodes N, Hunt J, Ricci A, Teghil R, Migliaccio S, Rocca CD, Leccisotti S, Lioi A, Scandurra M, Maria GD, Ferro D, Pu F, Panzini G, Politi L, Scandurra R (2007) Effect of titanium carbide coating on the osseointegration response in vitro and in vivo. Biomaterials 28:595–608
256. Makau FM, Morsi K, Gude N, Alvarez R, Sussman M, May-Newman K (2013) Viability of titanium-titanium boride composite as a biomaterial. ISRN Biomaterials 970535
257. Justin JF, Jankowiak A (2011) Ultra-high temperature ceramics: Densification, properties and thermal stability. J Aerospace Lab 3:1–11
258. Wuchina E, Opila E, Opeka M, Fahrenholtz W, Talmy I (2007) UHTCs: Ultra-high temperature ceramic materials for extreme environment applications. Electrochem Soc 30–36
259. Barraud E, Begin-Colin S, Le Caer G, Barres O, Villieras F (2008) Mechanically activated solid-state synthesis of hafnium carbide and hafnium nitride nanoparticles. J Alloys Compound 456:224–233
260. Fahrenholtz WG, Hilmas GE, Chamberlain AL, Zimmermann JW (2004) Processing and characterization of ZrB_2-based ultra-high temperature monolithic and fibrous monolithic ceramics. J Mater Sci 39:5951–5957
261. Rupa PKP, Sharma P, Mohanty RM, Balasubramanian K (2010) Microstructure and phase composition of composite coatings formed by plasma spraying of ZrO_2 and B_4C powders. J Thermal Spray Technol 19:816–823
262. Opeka MM, Talmy IG, Wuchina EJ, Zaykoski JA, Causey SJ (1999) Mechanical, thermal, and oxidation properties of refractory hafnium and zirconium compounds. J Eur Ceram Soc 19:2405–2414

263. Paul A, Binner J, Vaidhyanathan B (2014) UHTC composites for hypersonic applications. In: Fahrenholtz WG, Wuchina EJ, Lee WE, Zhou Y (eds) © 2014 The American ceramic society, 1st edn. Published Wiley Inc
264. Meshev P, Briznakov G (1968) On the brorothermic preparation of titanium, zirconium and hafnium diborides. J Less Common Metals 14:23–32
265. Zhang G-J, Guo W-M, Ni D-W, Kan Y-M (2009) Ultrahigh temperature ceramics (UHTCs) based on ZrB_2 and HfB_2 systems: powder synthesis, densification and mechanical properties. J Phys: Conf Ser 176:012041
266. Monteverde F, Bellosi A (2004) Efficacy of HfN as sintering aid in the manufacture of ultrahigh-temperature metal diborides-matrix ceramics. J Mater Res 19:3576–3585
267. Thompson R, Production, fabrication and uses of borides. In: Freer R (ed) The physics and chemistry o/carbides; nitrides and borides. © 1990 Kluwer Academic Publishers, pp 113–120
268. Levine SR, Opila EJ, Halbig MC, Kiser JD, Singh M, Salem JA (2002) Evaluation of ultra-high temperature ceramics for aeropropulsion use. J Eur Ceram Soc 22:2757–2767
269. Sannikova SN, Safronova TA, Lukin ES (2006) The effect of a sintering method on the properties of high-temperature ceramics. Refract Ind Ceram 47:299–301
270. Munro RG (1997) Material properties of a sintered α-SiC. J Phys Chem Ref Data 26:1195–1203
271. Cedillos-Barraza O, Manara D, Boboridis K, Watkins T, Grasso S, Jayaseelan DD, Konings RJM, Reece MJ, Lee WE (2016) Investigating the highest melting temperature materials: A laser melting study of the TaC-HfC system. Sci Rep 6:37962
272. https://en.wikipedia.org/wiki/Ultra-high-temperature_ceramics
273. https://en.wikipedia.org/wiki/Boron_nitride
274. https://en.wikipedia.org/wiki/Boron_carbide
275. Zupan J, Komac M, Kolar D (1970) Magnetic susceptibility of boron nitride. J Appl Phys 41:5337
276. Popov PA, Novikov VV, Sidorov AA, Maksimenko EV (2007) Thermal conductivity of LaB_6 and SmB_6 in the range 6–300 K. Inorg Mater 43:1187–1191
277. Mumtaz A, Class WH (1982) Color of titanium nitride prepared by reactive dc magnetron sputtering. J Vac Sci Techn 20:345–348
278. Moser A, Exadaktylos A, Radke A (2016) Removal of a tungsten carbide ring from the finger of a pregnant patient: A case report involving 2 emergency departments and the internet. Case Rep Emer Med 8164524
279. Zhang J, Hu H, Liu X, Li D-S (2019) Development of the applications of titanium nitride in fuel cells. Mater Todays Chem 11:42–59
280. Lia X, Liu X (2017) Group III nitride nanomaterials for biosensing. Nanoscale 9:7320–7341
281. Connolly EJ, O'Halloran GM, Pham HTP, Sarro PM, French PJ (2002) Comparison of porous silicon, porous polysilicon and porous silicon carbide as materials for humidity sensing applications. Sens Actuators, A 99:25–30
282. Stewart DM, Bernhardt GP, Lad RJ (2017) Zirconium diboride thin films for use in high temperature sensors and MEMS devices. Smart sensors, actuators, and MEMS VIII. In: Fonseca L, Prunnila M, Peiner E (eds) Proceeding of SPIE, vol 10246. 102460Q © 2017 SPIE
283. Lei X, Ge S, Tan Y, Wang Z, Li J, Li X, Hu G, Zhu X, Huang M, Zhu Y, Xiang B (2020) High capacity and energy density of Zn–Ni–Co–P nanowire arrays as an advanced electrode for aqueous asymmetric supercapacitor. ACS Appl Mater Interfaces 12:9158–9168
284. Singh D, Shukla V, Panda PK, Mishra YK, Rubahn H-G, Ahuja R (2020) Carbon-phosphide monolayer with high carrier mobility and perceptible I-V response for superior gas sensing. New J Chem 44:3777–3785
285. Hussain S, Chatha SAS, Hussain AI, Hussain R, Mehboob MY, Muhammad S, Ahmad Z, Ayub K (2020) Zinc-doped boron phosphide nanocluster as efficient sensor for SO_2. J Chem 2629596
286. Pradhan B, Kumar GS, Dalui A, Khan AH, Satpati B, Ji Q, Shrestha LK, Arigac K, Acharya S (2016) Shape-controlled cobalt phosphide nanoparticles as volatile organic solvent sensor. J Mater Chem C 4:4967

287. Balogun M-S, Qiu W, Wang W, Fang P, Lu X, Tong Y (2015) Recent advances in metal nitrides as high-performance electrode materials for energy storage devices. J Mater Chem A3:1364–1387
288. Naguib M, Come J, Dyatkin B, Presser V, Taberna P-L, Simon P, Barsoum MW, Gogotsi Y (2012) MXene: a promising transition metal carbide anode for lithium-ion batteries. Electrochem Commun 16:61–64
289. Harris VG, Chen Y, Yang A, Yoon S, Chen Z, Geiler AL, Gao J, Chinnasamy CN, Lewis LH, Vittoria C, Carpenter EE, Carroll KJ, Goswami R, Willard MA, Kurihara L, Gjoka M, Kalogirou O (2010) High coercivity cobalt carbide nanoparticles processed via polyol reaction: a new permanent magnet material. J Phys D: Appl Phys 43:165003
290. Wei L, Qun W, Sun XK, Xin-Guo Z, Tong Z, Zhi-Dong Z, Chuang YC (1994) Metastable Sm-Fe-N magnets prepared by mechanical alloying. J Magn Magn Mater 131:413–416
291. Fokwa BPT (2010) Transition-metal-rich borides – Fascinating crystal structures and magnetic properties. Eur J InorgChem 3075–3092
292. Abdullah Iqbal M, Irfan Ali S, Amin F, Tariq A, Iqbal MZ, Rizwan S (2019) La- and Mn-codoped bismuth ferrite/Ti_3C_2 MXene composites for efficient photocatalytic degradation of Congo red dye. ACS Omega 4:8661−8668
293. Liu X, Zhu T, Gong Y (2019) Efficient removal of azo-dyes in aqueous solution by CeB_6 nanocrystals. ACS Appl Nano Mater 2:5704–5712
294. Li J, Huang Y, Liu Z, Zhang J, Liu X, Luo H, Ma Y, Xu X, Lu Y, Lin J, Zou J, Tang C (2015) Chemical activation of boron nitride fibers for improved cationic dye removal performance. J Mater Chem A 3:8185–8193
295. Ningthoujam RS (2004) Synthesis, solid state reactivity, superconducting, electrical transport and magnetic properties of nanostructured metal nitrides: VN, MoN, Mo_2N, Ni_3N and ε-$Fe_{3-x}Co_xN$ ($0.0 \leq x \leq 0.8$). Ph.D. Thesis, IIT Kanpur, India

Chapter 10
Synthesis Methods for Carbon-Based Materials

Pradip Kumar

Abstract Carbon is a most versatile element and its bonding and special nature have long been noted largely due to the variety and quantity of structures. Carbon can make different allotropes like graphite, diamond and fullerene due to its sp^1, sp^2 and sp^3 possible hybridization nature. The development and understanding of carbon-based materials are topics of major interest in science and technology due to their excellent electrical, thermal, mechanical and optical properties. On the other hand, carbon is hardly considered to be toxic material, which makes it easily biocompatible. Carbon-based materials are synthesized using various top-down and bottom-up synthesis approaches. In this chapter, various conventional and more practical synthesis strategies, as well as their mechanism for diamond, fullerene, carbon nanotubes, carbon nanofibers, graphene and graphene oxide with the extracts from published investigations by numerous researchers, will be discussed.

Keywords Diamond · Fullerene · Carbon nanotubes · Carbon fiber · Graphene · Arc discharge · Chemical vapor deposition · Exfoliation

10.1 Introduction

Carbon-based materials like graphite, fullerene, diamond, carbon fiber, carbon nanotube, graphene, activated carbon and soot particles have been well employed for various applications due to their variety of structure and properties. For example, graphite is well-known electrode material and moderator in nuclear reactors. Graphite is mostly used in composites including in pencil, wind turbine generators, pouring nozzles, thermocouples, crucibles, etc. [1]. In addition to graphite applications, it is being used as a precursor for the synthesis of most emerging carbon materials;

P. Kumar (✉)
Integrated Approach for Design and Product Development Division, CSIR-Advanced Materials and Processes Research Institute, Hoshangabad Road, Bhopal, Madhya Pradesh 462026, India
e-mail: pradip.kg@ampri.res.in

Formely at Chemistry Division Bhabha Atomic Research Centre, Mumbai, Maharashtra 400085, India

A. K. Tyagi and R. S. Ningthoujam (eds.), *Handbook on Synthesis Strategies for Advanced Materials*, Indian Institute of Metals Series,
https://doi.org/10.1007/978-981-16-1892-5_10

graphene. Next to graphite, diamond is one of the well-known carbon materials for its hardness, high thermal conductivity, insulating and transparent properties [2]. Natural as well as synthetic, both types of diamonds are available in the market. Diamond is used in many potential applications including, optics, electronics, medical, and radiation detectors [3]. Due to their hardness, diamonds have been used for cutting, making wedding rings and other jewelry for a long time. Thus, the large-scale synthesis of diamonds with the desired size and shape is important. Another exciting form of carbon, fullerene, was discovered in 1985 at Rice University [4]. Fullerene invention won the Chemistry Novel prize in 1996. Now fullerenes have been greatly considered well-known carbon allotropes, which had previously been limited to graphite, diamond and amorphous carbon.

After the fullerene discovery, carbon nanotubes (CNTs) were first time identified in 1991 by Iijima et al. [5]. They found this new form of carbon materials during the synthesis of fullerene by an arc evaporation method. CNT is rolled from of single-layer carbon atoms. This new form of carbon-based materials has opened many opportunities for materials scientists in many fields. CNTs diameter may vary up to a few nm, while the length may be achieved in tens of micometers [6]. The most important properties of CNTs, which make them ultimate materials, are high electron mobility, thermal conductivity and mechanical strength. CNTs conducting properties highly depend on the way it constructs like armchair (metallic), zigzag or chiral (semiconductor). The ultimate properties of CNTs have been employed in many potential applications including supercapacitors, fuel cells, hydrogen energy storage, electromagnetic interference, sensors, etc. [7]. Along with, CNTs research, carbon nanofibers were also explored [8].

The major breakthrough in carbon-based materials was achieved by the identification of sp^2 hybridized single layer of carbon atoms; graphene in 2004 by Andrew Geim and Novoselov at Manchester University UK [9]. For this wonder material, they have been awarded a Physics Nobel Prize in 2010. Graphene was identified by a simple Scotch-tape method. This method produced very high-quality graphene. Graphene's unique properties like ultrahigh electron mobility, high surface area (~2600 m^2g^{-1}), large aspect ratios, the extreme thermal conductivity of ~5000 W/mK, excellent mechanical stiffness (Young's modulus of 1 TPa) and optical properties make it emerging materials for high-speed electronics, optical devices, energy storage, chemical sensors, thermal management and electromagnetic interference shielding applications [10–13]. Since graphene discovery, it has been considered a wonder material among the scientific community. Thus, the synthesis of graphene and its large-scale production is important. Many top-down including exfoliation and bottom-up including chemical vapor deposition (CVD) approaches are being used for the synthesis of graphene and other carbon materials [14–16]. In this chapter, various synthesis mechanisms for graphite, diamond, CNTs, CNFs and graphene are discussed.

10.2 Synthesis of Graphite

Graphite is one of the most stable and natural crystalline forms of carbon. It is composed of stacked layers of sp^2-hybridized carbon atoms. These stacked layers in graphite are weakly attached by weak Van der Waals force and $\pi-\pi^*$ interaction which gives its low hardness and perfect cleavage. Natural graphite can be formed by the reaction of carbon compounds in the rock during hydrothermal metamorphism. A small amount of graphite can be found in metamorphic and igneous rocks. Most of the graphite seen at earth's surface was formed at convergent plate boundaries where organic-rich limestones and shales were subjected to the pressure and heat of regional metamorphism. This process produced tiny crystals and flakes of graphite. However, synthetic graphite is required for industrial applications.

The first synthetic graphite was manufactured in the late 1800s by Edward Goodrich Acheson. He discovered it accidentally while attempting the manufacture of silicon carbide in an electric furnace. He used a combination of silica and amorphous carbon and found that silicon vaporized at about 4150 °C leaving the carbon behind in graphitic carbon. This discovery of graphite was extremely valuable and used for many potential applications. The commercial production of graphite was started in 1897 when Acheson formed a company in 1899. The synthesized graphite was found to have a purity of over 99% carbon and it is being used in manufacturing products where extremely pure material is required. Currently, many precursor materials are being used for synthetic graphite production. For example, in the USA, high-quality graphite is prepared by using petroleum coke as the primary material. Generally, the process of synthetic graphite manufacturing consists of powder preparation, shape-forming, baking and graphitization [17]. Graphite is also synthesized by the reaction of calcite with hydrogen at different temperatures, pressure and time. The synthetic graphite can be formed in various shapes and size, powders and granular materials.

Since its discovery, graphite has been employed in many industrial applications. The well-known application of graphite is in making pencils, which consist of a mixture of clay and microcrystalline graphite [1]. High purity graphite is being used for manufacturing carbon brushes for electrical motors. Composites of graphite (e.g., silver-graphite and copper-graphite) are used in wind turbine generators, railway technology and tacho generators. Composites of alumina-carbon are used in ladles for pouring nozzles, liquid steel and sliding gates. Thermocouples, heater tubes and crucible for heating are made of composites of clay-graphite and silicon carbide-graphite. Graphite is also used as electrode materials, e.g., in electric arc furnaces. Sliding bearings are made from bronze-graphite composites. Graphite powder is also used for making graphite foil which is used for manufacturing high temperature gaskets and packages. Lithium-ion and zinc-carbon batteries used high purity graphite powder as cathodic material. Graphite is also used in nuclear reactors as a moderator [18]. Not only industrial applications, now graphite is the main source for the top-down synthesis of other carbon materials like CNTs, graphene, graphene

oxide and graphene nanoribbons, which will be discussed later in this chapter [19, 20].

10.3 Synthesis of Diamond

Diamond is a second naturally occurring allotrope of carbon. The name "Diamond" is derived from the ancient Greek–adámas meaning "unbreakable". In diamond, each carbon atom is sp^3-hybridized, arranged in a variation of the face-centered cubic crystal structure. This arrangement of carbon atoms makes the diamond very hard material. Diamond has been considered one of the best materials in the scientific community as well as commercial level due to its remarkable properties including electrically insulation, high thermal conductivity, lowest thermal expansion coefficient, chemical inertness and optical transparency. Most of the natural diamond's formation occurred at high pressure and temperature in the Earth's mantle at depths of 140–190 km Natural diamond is colorless but the color in a diamond can be originated by a small number of defects or impurities such as boron and nitrogen.

Synthetic diamond has been much attracted since its establishment as a crystalline form of carbon. Initially, the diamond was synthesized using a high pressure approach due to its highest density. The first synthesis of a diamond at high pressure was developed by "General Electrics" in 1955 [21]. The Bulk amount of diamonds can be synthesized in a thermodynamic stable region at high pressure and high temperature (HPHT). In contrast, metastable thermodynamic regions at low pressure and low-temperature methods can produce thin diamond coatings and powders. To date, various methods have been successfully developed for diamond synthesis including HPHT, chemical vapor deposition (CVD), thermal activation of graphite, hydrothermal synthesis and the reduction of carbides (HSRC) [22, 23]. However, CVD is the most studied method for diamond fabrication [24]. This section summarizes diamonds synthesis by using various synthetic routes.

10.3.1 High Pressure and High Temperature (HPHT)

By using this technique, gem-purity large diamond crystals can be grown up to several millimeters. This is a conventional and effective method used for diamond synthesis for research as well as commercial applications. The HPHT method can produce high-quality sheets shape large cubic diamonds, which are mostly used for the development of cutting and grinding tools. Nevertheless, these diamonds have disadvantages such as higher cost and size limit. Many companies and researchers are using a reaction cell in HPHT conditions for the synthesis of various types of diamond crystals for commercial applications. Although they used different designs for diamond growth, typical pressure and temperatures used in HPHT are 5–7 GPa and 1200–1800 °C, respectively [25]. Generally, in the growth process, diamond morphology changes

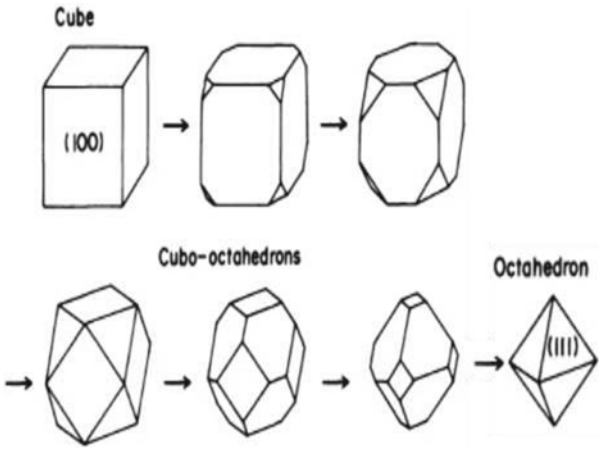

Fig. 10.1 Polyhedral of a diamond (Reproduced with permissions [25]. Copyright 1988, American Physical Society)

from cubic crystal with (100) dominated faces and cuboctahedral crystal with (100) and (111) dominated faces, to octahedral crystals with (111) dominated crystal faces with the increase of reaction temperature (Fig. 10.1).

The obtained results and method proved that they were not good enough to synthesize diamonds in that early experiment. After that many researchers modified the experimental conditions and reported good results using the HPHT method. In the modified HPHT method, Pt-30% Rh/Pt-6% Rh thermocouple was used for temperature monitoring. Room temperature pressure calibration was done by changing the resistance of standard substances. But, high temperature pressure calibration was performed by the graphite-diamond equilibrium. Liu and co-workers used carbonyl iron powder as a catalyst for diamond crystallization in the range of 5–7 GPa pressure and 1200–1800 °C temperatures [26]. A high purity graphite rod was used as source material. In this growth process, the purpose of using carbonyl iron powders was to see the effect of nitrogen and oxygen on diamond growth. The diamond growth process was performed on the mixture of graphite rod and catalyst powders (7:3, weight ratio) for 4 h. After crystallization experiments, sample columns were first cracked. The remaining impurities of graphite and catalysis were removed by dissolving the products in a hot mixture of H_2SO_4 and HNO_3. Diamond growth was first confirmed by XRD measurements as shown in Fig. 10.2. From the XRD pattern, it is evident that the sample has a cubic diamond structure which is composed of {111}, {220} and {311} characteristic lines. In contrast, the SEM image showed an irregularly shaped diamond crystal grown at 1600–1650 °C temperature without a clear {100} or {111} crystal faces (Fig. 10.3a). Further, an increase in reaction time for 15 min, diamond crystals of 0.5–0.9 mm with lamellar and strip shapes were formed (Fig. 10.3b, c). With the further increase in temperature, it was found that {111} faces played a key role in the crystallization of diamond. Diamond crystals obtained at 1700–1750 °C

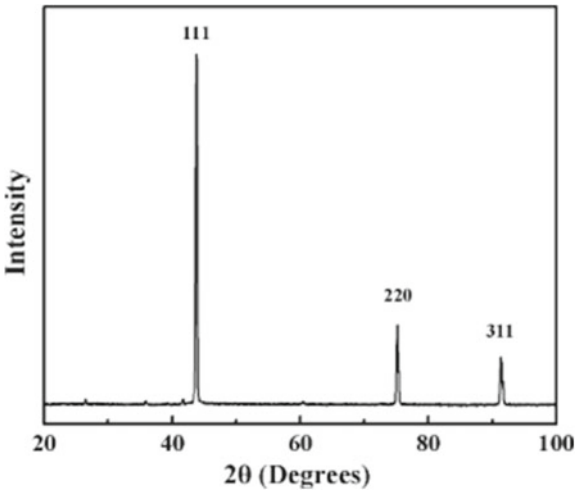

Fig. 10.2 XRD pattern of diamond crystal grown at 6.5 GPa and 1600 °C (Reproduced with permissions [26]. Copyright 2011, American Chemical Society)

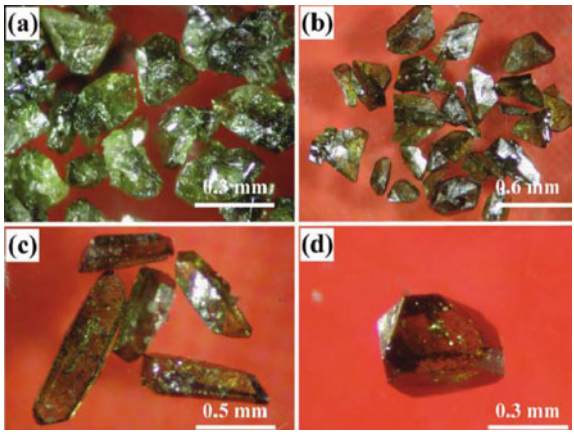

Fig. 10.3 Representative optical images of diamond crystals grown at 6.5 GPa pressure and three different temperatures: **a** 1600 °C, **b**, **c** 1700 °C and **d** 1800 °C in the presence of carbonyl iron powders catalyst (Reproduced with permissions [26]. Copyright 2011, American Chemical Society)

temperature showed {111} dominant faces and minor {100} faces (Fig. 10.3d). The above experimental outcomes revealed that high temperature conditions are more suitable for the stable growth of octahedron diamond crystals.

Diamond crystals were further synthesized from the sulfur-carbon (S–C) mixture at high temperatures (1550–2000 °C) and pressures (6.3–7.5 GPa) [27]. Graphite rod (99.99% pure), sulfur powder and cuboctahedral synthetic diamond crystals of 500 μm size as seed particles were taken as starting materials. For the nucleation of diamond crystals, first, the graphite rod was placed into a capsule of 7.2 mm diameter and 7 mm high. Then, diamond seed crystals and sulfur powder together were placed into a cylindrical sample and then placed into the graphite capsule. Then, diamond crystal growth was investigated at different temperatures and pressures for the time of 3–40 h. Growth of diamond crystals in the above system exhibited

significant dependency on temperature, pressure and nucleation time. For example, there was no diamond growth on seed crystal was found at 6.3 GPa pressure and 1550 °C temperature. In contrast, metastable graphite and slight diamond growth on the {100} and {111} faces of the seed crystals were obtained on higher temperatures (1650 °C). Even at this temperature, there was no spontaneous diamond nucleation was established. Spontaneous nucleated diamond crystals were formed at a high temperature of 1750 °C (Fig. 10.4). The size of nucleated diamond crystals was found to be ~50 μm with {111} dominant and {100} minor faces. The different surface morphology of diamond crystals was depending on the surface indices of seed crystals. For example, the flat growth of layers was found on {111} faces, while {100} and {110} faces result in pyramidal relief and striation structure, respectively. The above findings conclude that the seed crystals can form a stable octahedron diamond crystal at high temperatures. Also, metastable graphite of ~100 μm size was grown in the upper part of the capsule. Further experiment showed the regrown metastable graphite and diamond growth layers at relatively low temperatures (1550 and 1600 °C) and higher pressure (7.0 GPa). There was no sign of spontaneous nucleation of the diamond up to 40 h run. In contrast, intense diamond crystallization

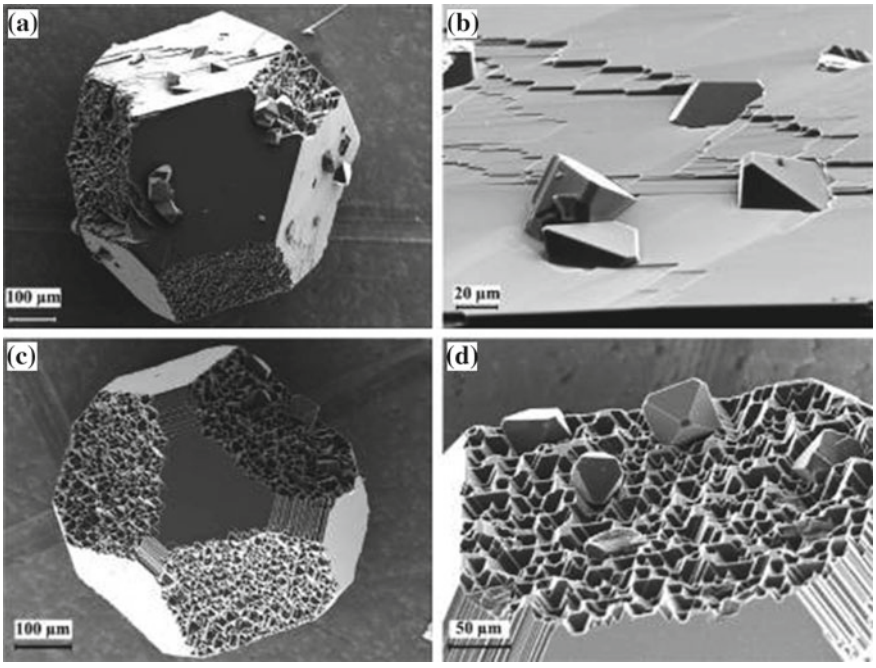

Fig. 10.4 SEM image of an overall view of diamond seed crystals, **a** spontaneous crystals and growth layers on the (111), **b** diamond seed crystal, **c** grown diamond layers on the (100) and (110) surfaces, **d** crystalline diamond obtained from 6.3 GPa pressure and 1750 °C temperature for a reaction time of 9 h (Reproduced with permissions [27]. Copyright 2009, American Chemical Society)

with more than 50% graphite to diamond conversion was found at the temperature of 1700 °C. Obtained diamond crystals show size up to 500–700 μm which can be further grown up to ~1 mm. Spontaneous nucleation of seed crystals and growth of diamond crystals were established at higher temperatures (1750, 1800 and 1900 °C) without any metastable graphite. Further, a rise in temperature up to 2000 °C gives diamond crystals of 400 μm along with metastable graphite crystals.

In recent work, Ge doped single-crystal diamond was synthesized from an Mg-Ge-C system at high pressure of 7.0 GPa and a high temperature of 1500–1900 °C [28]. The mixed powders of $Mg_{0.9}Ge_{0.1}$ and several seed crystals were used. This HPHT system produced relatively large size diamond crystals of 2–3 mm at 1900 °C. Further, they also synthesized diamond crystals using a phosphorous-carbon system at 6.3–7.5 GPa pressure and 1400–1850 °C temperature [29]. Hu et al. also developed high-quality cubic diamond crystals for commercial purposes by using a multiseed method [30]. The diamond crystals were synthesized using Fe–Ni alloy-carbon system under HPHT conditions by a temperature gradient method. Graphite powder as a carbon source and Fe–Ni alloy (64:36 by wt%) as catalyst/solvent were used, respectively. The growth temperature and pressure were set to 1250–1350 °C and 5.5–5.7 GPa, respectively. Pure and large size diamond crystals were successfully synthesized using this HPHT. But this method is extremely expensive for bulk production.

10.3.2 Chemical Vapor Deposition

The chemical vapor deposition (CVD) method is one of the most common synthesis techniques for all types of carbon-based materials. This method involves the decomposition of hydrocarbon gases and then deposition onto a substrate. In this process, a process gas, excitation source and a substrate on which sample will be deposited are required. Various gases including hydrogen, oxygen, methane, carbon dioxide, argon and nitrogen were used as process gas. To activate the chemical process, various energy sources including microwave, radiofrequency, direct current, hot filament, laser-induced and chemical activation have been used. In most of the cases, hydrogen and methane gas mixture were used for carbon-based materials. Methane or other hydrocarbons act as a carbon source, while the role of atomic hydrogen or oxygen is the most critical. The key role of hydrogen or oxygen in the CVD method is to terminate the dangling carbon bonds on the surface of the developed crystalline carbon materials. It is also reported that hydrogen atoms can cleave neutral hydrocarbons and create reactive radicals such as CH_2. The cleaved hydrocarbon can bond with exposed carbon atoms to form tetrahedral sp^3 (ta-C) or trigonal sp^2 (a-C) bonded carbon [31]. Another benefit of using hydrogen in diamond synthesis is to avoid the growth of graphite because atomic hydrogen can etch sp^2 bonded graphite much faster than an sp^3 bonded diamond.

For the first time, Eversole reported the gas-phase synthesis of diamond in 1958 [32]. This method uses a carbon-containing gas, which is passed to diamond seed crystals at a pressure of a few torr and temperature of ~1000 °C. Interestingly, it

was observed that the diamond was grown when source gas has a methyl group (CH_3–) like methane, ethane, methyl mercaptane, propane, methyl chloride and acetone. However, the low growth rate of diamond crystals of ~1 Å/h was the major issue for applications of diamond in real life. In contrast, hydrocarbon gases like benzene, which do not have methyl groups, could not grow diamonds by this method. The systematic procedure of diamond synthesis from the CVD method is illustrated in Fig. 10.5. A few years later, Angus et al. [33] also reported diamond synthesis using the CVD method on diamond seeds crystals by using mixtures of hydrocarbons and hydrocarbon–hydrogen gases. So far, the diamond has been synthesized using various modified CVD methods (Fig. 10.5b). It has been noted that diamond growth in CVD depends on various parameters such as pre-treatment of the sample, range of temperature, type of activation source and substrate selection, which play an important role. Generally, molybdenum, tungsten carbide and silicon nitride are being used as a substrate in CVD growth. In the CVD method, the temperature distribution, internal energy and solubility clearly depend on the excitation source. Based on the excitation sources, CVD processes can be divided into heated gas and ionization plasma CVD techniques which can be further sub-divided into chemical, electrical, or electromagnetically and thermal activation processes.

In the thermal activation CVD process, the gas phase is activated by hot filaments or hot surfaces as shown in Fig. 10.6 [24]. In this approach, the first process gas flows into the chamber and then hot filament was used for heating. The distance between substrate and filament can vary from 5 to 20 mm and substrate temperature can be achieved around 1000 K [24, 34]. Eiichi and co-workers reported the diamond growth by an advanced hot filament CVD method. In this method, the substrate temperature is independently controlled [35]. A mixture of CH_4/H_2 gas was used as a source precursor and silicon as a substrate. The distance between substrate and filament was maintained to 6–10 mm. Filament temperature was measured to be ~2050 ± 10 °C by an optical pyrometer. The controlled pressure of 30 torr was applied by the MKS pressure control system. The gas flow rate was maintained to ~600 sccm and the ratio of methane to hydrogen gas was 1%. It was found that diamond growth mainly

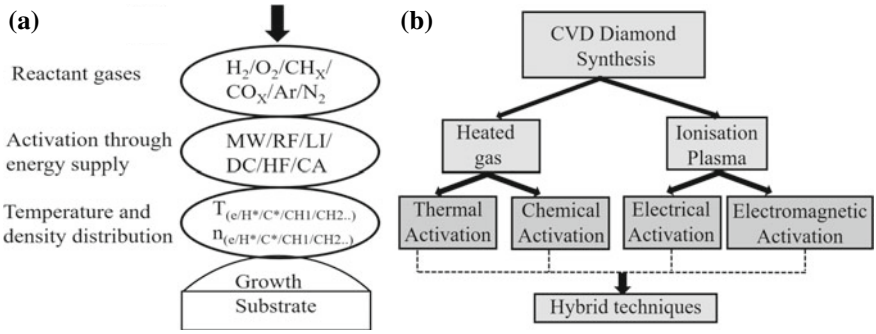

Fig. 10.5 **a** Proposed mechanism of diamond growth processes by a CVD method, **b** diamond CVD techniques (Reproduced with permissions [24]. Copyright 2011, Elsevier)

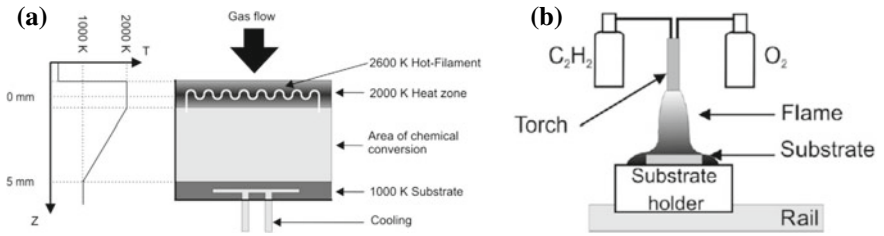

Fig. 10.6 Schematic representation of a hot filament **a** and chemical activated **b** CVD process (Reproduced with permissions [24]. Copyright 2011, Elsevier)

depends on substrate distance and its temperature. Maximum diamond growth was observed in the range of 900–1000 °C temperature. However, with the increase of substrate temperature, the growth rate was reduced. In the same year, Park et al. produced a synthetic diamond film using a hot filament CVD method [36]. They deposited diamond films on a polycrystalline titanium substrate. Direct radiation from filament was used to heat the substrate. The flow of reactant gases (CH_4 and H_2) into the reactor was controlled through a mass flowmeter. Their experimental findings revealed that surface morphology played a significant role in the nucleation and therefore in diamond film growth. The surface roughness increased the nucleation density of diamond and reduced the incubation time required for nucleation. As a result, the growth rate of individual diamond particles decreased. Further, Kobayashi and co-workers established a relationship between growth rate and flow time of source gases in the hot filament method [37]. They set the temperature of filament and substrate to 850 °C and 2100 °C, respectively. The pressure was varied from 5 to 106 kPa. In the pressure range of 5–50 kPa, all growth rates increased very fast and get maximum at a residence time of 1.1 ms. After that growth rate was abruptly deceased and saturated with residence time. Simultaneously, diamond and nanostructured graphite thin films were grown by hot filament CVD [38]. By changing the distance between substrate and filament, diamond and graphite growth can be established. At a distance of 5 mm, the diamond was obtained, while graphite deposition was observed at a distance of 15 mm.

Chemically activated growth of diamond using CVD on combustion flame was the first time described by Hirose et al. [39]. The temperature of the combusting flame can be reached in the range of 2000 to 3550 K. In chemically activated CVD processes, the heating was done by an exothermic conversion of the source gases. In general, acetylene and oxygen gases were applied for the combustion process. Generally, the substrate temperature was used from 770 to 1470 K. Figure 10.6b shows the typical setup for the combustion flame-based CVD method. The flame was generated by a commercially available oxyacetylene torch, which is vertically placed to the substrate. The whole process was controlled by changing the ratio of C_2H_2/O_2 with continuous monitoring of the substrate temperature by thermocouples and finally, diamond crystals were successfully deposited on the substrate. To increase

the deposition area, multiple torches can be used. However, chemically induced diamond deposition is not a significant method for industrial applications.

Similar to the thermally and chemically activated CVD process, diamond growth also has been demonstrated by using mixed-gas plasma [40, 41]. The common growth process in microwave plasma CVD involves placing a substrate in a quartz tube which is perpendicular to the waveguide. Microwave plasma can be generated by a magnetron. The substrate can be fully exposed to the plasma by adjusting through a plunger. Typical gas pressure was adjusted to ~40 torr and the gas flow rate was set to 10–100 sccm. The successful synthesis of high-quality diamonds using plasma CVD was developed by Setaka and co-workers. However, this method has some limitations like large-area deposition because the plasma was limited to the quartz tube size. In this context, Hiroshi et al. developed a new type of microwave plasma deposition system in which they used a high magnetic field with improved plasma density [42]. In another work, a high-quality diamond was grown from microwave plasma CVD by using graphite as the carbon source [43]. In this work, carbon is etched from graphite and placed inside the plasma. They used a conventional bell jar system for plasma generation. The hydrogen flow was fixed around 300 sccm, growth time of 24 h and microwave power was around 940 W. Silicon was used as a substrate. Diamond was grown on four different hydrogen gas pressure of 80, 100, 120 and 140 torr. At low pressure, the growth was not uniform. However, the best quality diamond was obtained at 140 torr pressure. Further, it has also been reported that diamond can be grown using a pre-treated mixed-gas-system of carbon dioxide and hydrogen [44]. However, diamond synthesized in the above methods is not feasible for industrial applications in which large-area diamond films are required.

Scalable fabrication of large-area diamonds was considered as a key step for industrial applications. Tiwari et al. reported that enhanced nucleation and diamond growth by using a microwave plasma CVD method [45]. They have grown diamond film on $Pt/SiO_2/Si$ substrate. In the deposition process, first, the substrate was cleaned by ultrasonication in acetone and alcohol for 10 min. After that, adamantine was seeded on the cleaned substrate by using ultrasonication. Diamond was grown using 1% CH_4 in H_2. The obtained thickness of the diamond film was about 900 nm for the deposition time of 120 min. However, further, the improvement was required for industrial production. Qi and co-workers reported a large area of single-crystal diamond using the microwave plasma CVD method [46]. The bulk production of diamond was achieved using 75 kW and 915 MHz microwave plasma-assisted CVD system. A mixture of $H_2/CH_4/N_2$ gases and pressures from 90 and 180 torr was used with recorded growth rates from 10 to 30 μm/h. A single-crystal diamond of 2.5 mm thickness was obtained in a single deposition run (Fig. 10.7). By using this technique, single-crystal diamonds production was achieved to 100 g/day and out of the 25% of the diamond, crystals were observed to be colorless.

Fig. 10.7 Single-crystal diamond obtained by the 915 MHz microwave plasma CVD. The diamond crystal's weights were ranged from 0.2 to 1.15 carats (Reproduced with permissions [46]. Copyright 2014, American Chemical Society)

10.3.3 Other Methods

Thermally activated graphite also can be used for diamond growth at low pressures. Palnichenko et al. reported diamond nucleation and growth using a short and intense heat pulse [47]. The diamond growth was obtained on different substrates including nickel, copper, aluminum, silicon and quartz. All the substrates were in the form of 10 cm^2 area plates and placed at a distance of 5 ± 1 mm from the electrode tip. The substrate temperature was maintained up to 10 K. As a result, well-shaped colorless diamond particles of 10 μm size were observed on the substrate as shown in Fig. 10.8. The maximum size of diamond particles can be reached up to 100 μm. The average density of diamond particles obtained by a single pulse was measured to be 10 ± 5 microparticles cm^2 with homogenously distributed irrespective of the nature of the substrate. The diamond formation was characterized using XRD, Raman and IR spectroscopic techniques.

Another alternative route for diamond fabrication is hydrothermal synthesis. Syzmanski and co-workers reported diamond synthesis by a hydrothermal process at different supercritical-fluid systems [48]. Gogotsi et al. reported diamond crystals synthesis using hydrothermal synthesis [22]. The sp^3 bonded carbon was obtained in the temperature range of 300–800 °C and pressure within 500 MPa under hydrothermal conditions by selective leaching of silicon carbide (SiC). The formation of diamond upon hydrothermal treatment of SiC has been reported elsewhere [49]. Following the above work, few researchers successfully diamond synthesis without diamond seeds by hydrothermal process. Lou et al. synthesized diamond crystal up

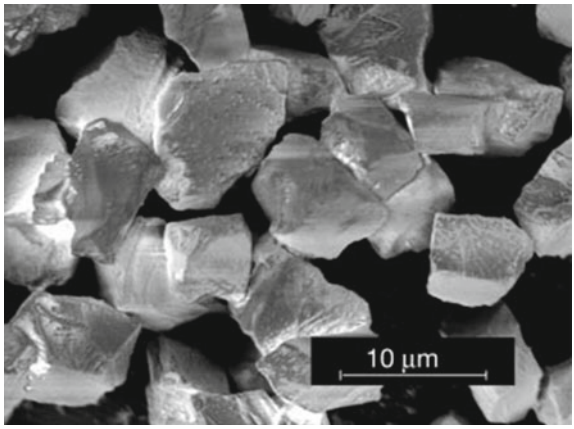

Fig. 10.8 SEM micrograph of diamond microparticles obtained by a dense carbon-phase process (Reproduced with permissions [47]. Copyright 1999, Nature Publishing Group)

to a size of 250 µm by reduction of CO_2 and magnesium carbonate with metallic supercritical- fluid sodium at a temperature of 440 °C [50].

For a long time, diamond has been popular for a variety of applications including, medicals, optics, electronics and radiation detectors. Before the graphene research, the diamond was known for the best thermal conductivity and chemical inertness [2]. Single-crystal diamonds have applications in optical science [3]. It has been well noted that pure diamond revealed the widest spectral transmission range among all solid materials. Diamond windows have been used in the chemical industry for spectroscopic quality control of molten plastics, caustic alkalies and so on. In recent years, diamond coatings have been applied to many medical devices such as temporomandibular joint prostheses, microelectromechanical systems and heart valves [51]. Functionalized nanosized diamonds have been used for the immobilization of chemotherapeutic agents. Many researchers have demonstrated imaging of cell and tissues with nanodiamond particles. Another important application of diamond is in the making of the radiation detectors. Due to its hardness, diamonds have been used for cutting, making wedding rings and other jewelry for a long time.

10.4 Synthesis of Fullerene

The first fullerene molecule was discovered by Richard Smalley, Robert Curl, James Heath, Sean O'Brien and Harold Kroto at Rice University in 1985 [4]. For this new invention, they won the Chemistry Novel prize in 1996. This new form of carbon was found to have truncated icosahedron structure and called fullerene, named Buckminsterfullerene, on the name of architect Buckminster Fuller who designed geodesic domes in the 1960s. A fullerene molecule is made from sp^2 hybridized carbon atoms. Typically, a C_{60} fullerene molecule has icosahedral symmetry closed cage structure with 20 hexagonal and 12 pentagonal rings. To date, fullerenes have

been greatly considered a well-known carbon allotrope. Since its discovery, fullerenes have been significantly considered for fundamental research as well as for potential technological applications, especially in materials science and electronics. In this section, various synthetic routes for fullerene synthesis will be discussed.

Fullerenes can be found in nature like in flames but its first experimental identification was observed in carbon vapor as shown in Fig. 10.9a. This unusual fullerene molecule was detected from laser pulse vaporized carbon species obtained from the surface of graphite, toward high-density helium flow [4]. After that vaporized carbon species traveled toward the ionization region and C_{60} can be formed at particular clustering conditions, which is about 40 times larger than the neighboring clusters. Time of flight mass spectra confirmed the most of the fullerene molecules consist of C_{60} with few C_{70} molecules (Fig. 10.9b). Figure 10.9c confirms the truncated icosahedral structure of featured C_{60} fullerene molecules. This flame technique can produce good quality fullerene molecules. However, this method produced microscopic amounts of fullerenes, which limits its commercialization.

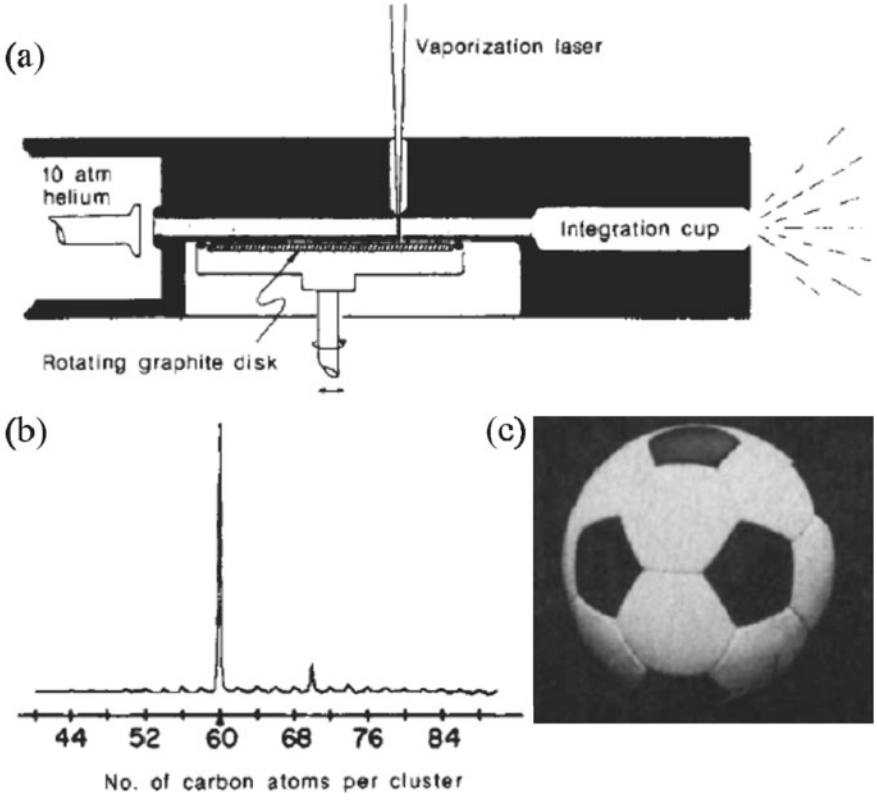

Fig. 10.9 Carbon vapor irradiation setup for fullerene synthesis, **b** time of flight mass spectra and **c** designed structure of C_{60} fullerene molecule (Reproduced with permissions [4]. Copyright 1985, Nature Publishing Group)

Since the first identification of fullerene by Kroto et al., W. Krätschmer and D. R. Huffman (K–H) synthesized C_{60} fullerene using arc method. The arc was created between graphite rods and burned under the helium atmosphere [52]. The carbon radicals were produced by slow evaporation burned graphite rod. However, the rate of clustering is slow in comparison with pulsed laser vaporization. Also, in this K-H method, the cooling rate of condensing carbon vapor is much slower. But, C_{60} clusters were successfully grown by adjusting the pressure of helium buffer gas around the evaporating graphite rods. Later, it was investigated that a simple AC or DC arc can produce C_{60} and the other fullerene molecules in sufficient quantity for commercial applications [53]. The formation of carbon clusters in the size of the range of C_{60} was easily achieved by adjusting the pressure of helium buffer gas around graphite rods. Following the above pioneering work, fullerene was synthesized using various methods like soot, vapor-phase, arc discharge, etc.

10.4.1 Soot Method

After microscopic production by Kroto et al., C_{60} fullerenes growth was identified in flames. Howard et al. reported the fullerene growth in premixed laminar flames of benzene and oxygen with Ar diluent [54]. The flame was stabilized over a copper burner of 70 mm diameter, which was used for delivering the feeding mixture. The flames were produced under various conditions. Soot was deposited for 53–170 min on quartz probe for each flame. Figure 10.10 shows the electron-mass spectrum of the as-deposited soot materials. Based on the reported data, it is confirmed that the soot

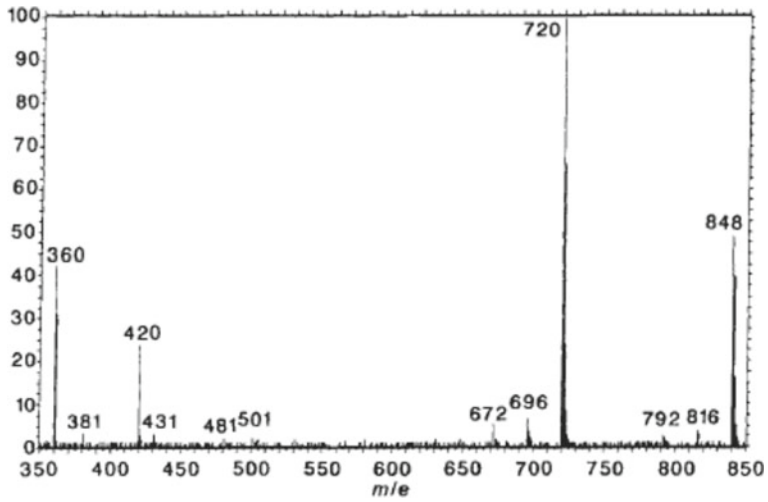

Fig. 10.10 Electron-mass spectrum of a flame-generated soot particles (Reproduced with permissions [54]. Copyright 1991, Nature Publishing Group)

sample contained both C_{70} and C_{60} fullerene molecules, which was further confirmed by FTIR.

In most of the soot method, fullerene was extracted from bulk soot [55]. The first time, Reilly and co-workers demonstrated the direct observation of fullerene growth in flame-generated soot [56]. They used a real-time measurement experimental setup for fullerene detection. They used a burner consisting of four 1.1 mm inner diameter and 1.5 mm outer diameter. A brass tube of 65 mm long was used for creating a torch-like flame. The flow rate of pure acetylene without any oxygen or air was about to be 2.4 cm^3/s through the burner tubes. Soot particles were collected onto exhaust snorkel of 4-inch diameter, which was placed over the flame. The sample tube was allowed to cool down automatically. Based on their experimental findings, it was concluded that the carbonization process of polycyclic aromatic hydrocarbons (PAHs) produced fullerene in the particle phase. This method also produced individual soot particles in low quantities. In summary, by this technique, we can track the composition of fullerene molecules.

10.4.2 Chemical Vapor Deposition

Similar to diamond growth, fullerene formation was demonstrated by CVD using gaseous species such as CH_4 or C_2H_2. Lee et al. reported the fullerene formation during the synthesis of diamond film using the CVD method [57]. The experiment was performed in a conventional hot filament CVD chamber having an 8 cm tungsten filament of 0.75 mm diameter. The current and filament temperature was maintained about 50–55 A and ~2200 °C, respectively. The pressure of the chamber was maintained from 30–35 torr. Methane (99.8% pure) and H_2 (99.99% pure) were used as precursor gases with a controlled flow rate. Silicon wafer placed on flat stainless-steel was used as a substrate and maintained at a temperature from 850 and 900 °C. Fullerene deposition was obtained between 5 to 24 h. In each run, 10–75 mg soot was collected soot. Mass spectrum measurements confirmed the fullerene growth in the hot filament CVD method. Further, it was found that changing the composition of precursor gases (2–5% CH_4, 95–98% H_2), substrate temperature (400–750 °C) and moving the substrate away from filament enhanced the growth of fullerene formation to 10–20 mg/h. There was a strong correlation between the diamond and the fullerene growth process. Figure 10.11 shows the diamond and fullerene formation by using the above process (solid arrow) and by other researchers with other routes (thin arrow).

Some other researchers have also developed other CVD methods for fullerene formation [58]. Fullerene was formed by low-temperature plasma CVD under atmospheric pressure [59]. Low-temperature plasma was generated by applying rf voltage under a constant flow of atmospheric pressure Ar or He gas. Benzene or naphthalene gases were used as a source for deposition. At He (70 sccm) and 70–100 rf powers, the gas plasma produced a tary deposit upon the flow of naphthalene or benzene (0.01–1 sccm). The products from naphthalene (0.3–0.6 sccm) formed soot when Ar

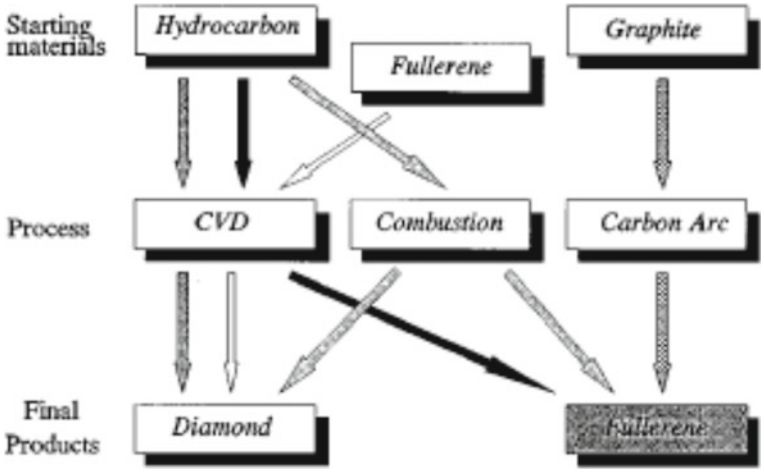

Fig. 10.11 Formation of diamond and fullerene by several processes using different starting materials (Reproduced with permissions [57]. Copyright 1995, American Institute of Physics)

(13 sccm) was introduced into He (47 sccm) plasma. It was found that product appearance depends on the plasma conditions. Fullerene formation was confirmed by UV–visible spectra. Further, Wang et al. produced the Fe-included onion-like fullerenes at a temperature of 1100 °C [60]. The diameter of the as-synthesized fullerenes was in the range of 15–40 nm which was confirmed through microscopic techniques. In this method, fullerene growth mainly depends on the substrate temperature and carbon source.

10.4.3 Arc Discharge

Since its development in the 1990s, the arc discharge method has been considered an effective and popular method for large-scale synthesis of fullerene [61, 62]. In this method, graphite electrodes are vaporized in a low pressure helium atmosphere. Arc is generated by passing the current through electrodes and fullerene containing soot was formed. Kratschmer's group in 1990 developed the first arc discharge system which is the most popular technique for fullerene synthesis till now [52]. After that several authors demonstrated fullerene formation using the arc discharge method. It was found that fullerene formation strongly depends on the operation parameters of carbon plasma-like very high temperature and inert atmosphere at reduced pressure. The typical setup of the arc discharge method is mainly composed of a stainless-steel double-walled cylindrical chamber [63]. Both graphitic electrodes were mounted horizontally near the bottom of the reaction chamber. But anode is mounted in a controlled guiding mechanical system for maintaining a constant distance between both electrodes during arc discharge. For soot formation, the chamber is evacuated

until a pressure of 10^{-3} to 10^{-4} torr. The chamber was filled with an Ar or He gases at the pressure 50–200 torr at 30 ± 2 °C during the process. From the obtained soot, C_{60} fullerene was extracted with toluene and by vacuum evaporation. Fullerene formation was confirmed by XRD measurements. The yield of fullerene synthesis was up to 6–8% which was higher than previous reports. The best yield of fullerene synthesis (~8%) was achieved at an arc current of 150 A and 100 torr of chamber pressure.

It has been noted that synthesis yield depends on the thermal and photochemical stability of C_{60}; however, both have not been defined well. The experimentally low decomposition temperature of 1000 K was determined for C_{60} in a vacuum [64]. Theoretical results showed the fullerene stability up to a temperature of 1800 K [65]. In general, C_{60} has been considered a relatively stable molecule. However, it can degrade under a variety of conditions [66]. It was demonstrated that fullerene decomposition significantly depends on the intensity of emitted light energy [67, 68]. The arc gap also influenced fullerene yields. The maximum yield was reported for large electrode gaps (2–4 mm) [69, 70]. However, in contrast, in some studies maximum yield was reported at a smaller electrode gap [71]. This contrast in experimental findings is considered due to large experimental errors [72].

The first experimentally investigation of the arc gap on the fullerene formation is reported by Andrzej et al. [53]. They optimized the experimental parameters such as input power, pressure, buffer gas and AC or DC feeding mode. The electrode gap was set to 0.5 mm with 4 mm for DC arcing. The whole system is controlled by an optoelectronic system of 0.2 mm accuracy. Initially, the electrodes were positioned close together. In contrast to the conventional method of striking anode against cathode, high-voltage glow discharge was used for arc discharge intimation. A helium pressure of 13.3 kPa was used for tests. The quantity of fullerene resulting from soot obtained from electrode arcing was tested by conventional spectrophotometric techniques. Based on their experimental observation, a significant distinction was found at a smaller electrode gap, while larger gap distance gave a significant difference in the fullerene formation. The fullerene content decreases with the increase of the electrode gap. Further, they also found that not only the electrode gap but also complex vaporization and mass transport phenomena greatly influenced the fullerene yield. Further, fullerene synthesis was also demonstrated from DC discharge between carbon electrodes in the mixture of Ar and ferrocene gas [73]. Another alternative, the solar energy-based approach was also developed for fullerene synthesis [74].

Fullerene has received much attention for a wide range of applications due to its interesting features including nonlinear optical properties and superconductivity [75]. Fullerenes have potential applications in 2D/3D metal–organic frameworks, solar energy conversion, liquid crystals materials, thermoresponsive materials and C_{60}-polymer hybrid materials, etc. [76–80]. Fullerene's unique shape and hydrophobic nature make it very effective for medical applications including sensitizers for photodynamic therapy and as photoactive molecular devices [81, 82].

10.5 Synthesis of Carbon Nanotubes

Carbon nanotubes (CNTs) have received first recognition in 1991, but their history goes long back. Radushkevich and Lukyanovich [83] first observed and described CNTs in 1952, which was later confirmed by Oberlin et al. in 1976 [84]. However, CNTs received significant research interest after its discovery in 1991 by Iijima et al. [5]. MWCNTs were obtained, while they were developing a new arc evaporation method for the synthesis of C_{60} fullerene. After two years later, Iijima et al. [85] described the growth mechanism of SWCNTs. CNTs have a tubular structure with a diameter as small as 1 nm and length can be varied from few nm to microns. The construction principle of SWNTs using a graphene sheet along the chiral vector C is shown in Fig. 10.12 [6]. CNT's structure can be zigzag, armchair, or chiral, totally depending on the chiral vector during construction, which determines its most of the properties. For example, Dresselhaus et al. investigated the electrical properties of CNTs constructed from different chiral vectors [86]. Thus, CNTs properties depend on its structure like chiral angle, length, diameter, etc., which can give them unique properties. Due to the exceptional properties of CNTs, they have been considered novel nanomaterials for a wide range of applications.

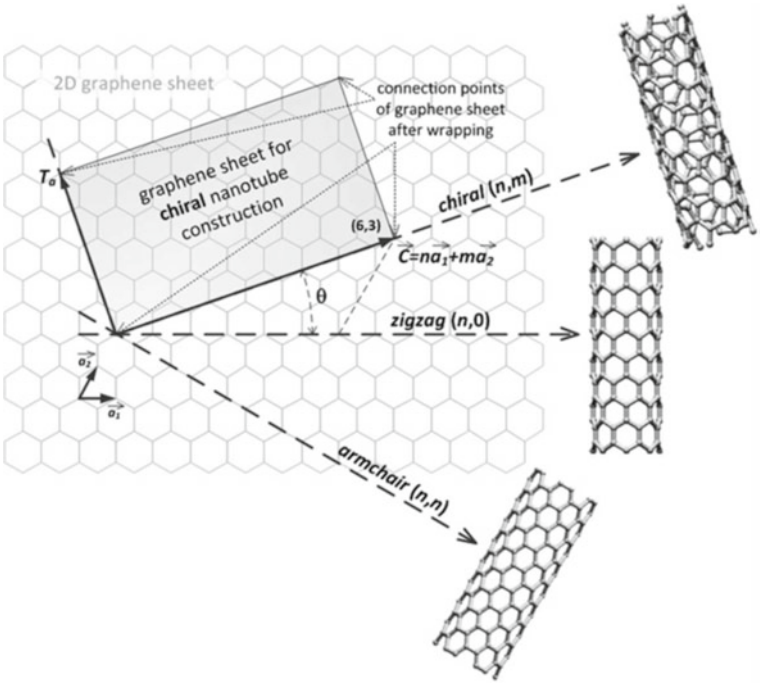

Fig. 10.12 The principle of CNTs construction using a graphene sheet (Reproduced with permissions [6]. Copyright 2011, The Royal Society of Chemistry)

For fundamental study and commercialization of CNTs in the field of material science, various synthesis methods such as CVD, laser ablation and arc discharge have been developed. CNTs were first prepared using arc discharge techniques and then followed by a low-temperature CVD technique (<800 °C). Later, other non-standard methods including liquid pyrolysis and organic approach were also developed. Irrespective of techniques, CNTs can be synthesized in the form of single-wall carbon nanotubes (SWNTs), double-wall carbon nanotubes or multi-wall carbon nanotubes depending on the experimental parameters.

10.5.1 Arc Discharge

Since its first identification by Iijima et al., CNTs growth have been developed by many other groups. The arc discharge technique produced CNTs at higher temperatures (>1700 °C). Arc discharge technique produced CNTs have shown some structural defects. Figure 10.13 showed a typical experimental setup of the arc discharge technique [87]. The arc chamber is composed of two electrodes (anode and cathode) which are mounted vertically or horizontally. The cathode is filled with a pure graphite rod and the anode is filled with powdered carbon precursor along with the catalyst. High temperature is achieved from created arc discharge. SWNTs can be produced by using graphite rods doped with metal catalysts like Fe and Co as the anode and pure graphite as a cathode [5].

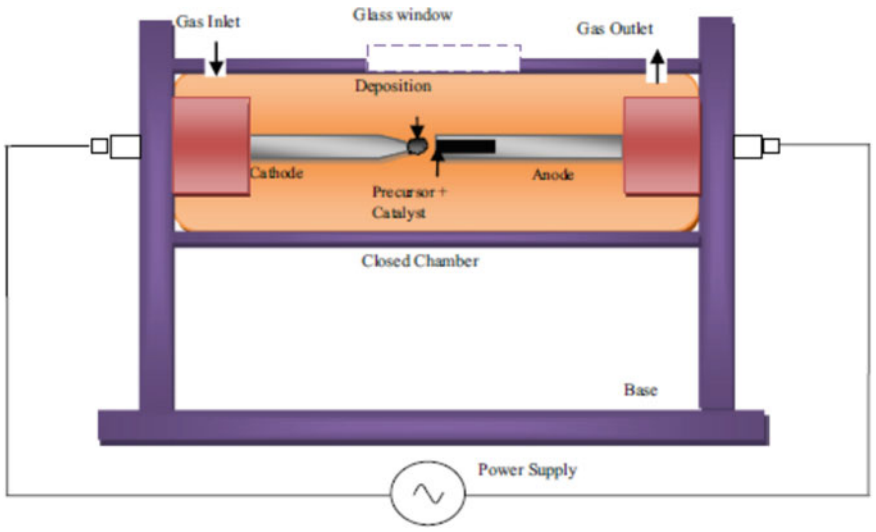

Fig. 10.13 Schematic of an arc discharge for CNTs (Reproduced with permissions [87]. Copyright 2014, Elsevier)

The synthesis of SWNTs was further reported by carbon evaporation with cobalt [6]. Nickel has been considered the most widely used catalyst for SWNTs synthesis. The catalytic role of the growth of carbon nanoclusters was investigated using dc arc discharge. Nickel-filled anode improves the growth of SWNTs [88]. SWNT's growth was further investigated with platinum-group metals (Ru, Rh, Pd, Ir, Pt) and it was found that only Rh, Pd and Pt were found to have catalytic activity for growing SWNTs of 1.3–1.7 nm diameters [89]. In another study, it was found that Mo improved the yield of soot [90]. However, the purity of SWNTs in collected soot was not changed significantly. The mass production of SWNTs can be achieved by using a bimetallic Ni-Y catalyst under He ambient gas [91].

Similar to SWNTs, double-walled nanotubes (DWNTs) were synthesized by the arc discharge method. However, DWNTs synthesis from the arc discharge method is much more complicated in comparison with SWNTs production. Many research groups reported DWNTs synthesis using the arc discharge method [92–94]. Hutchison et al. reported the production of DWNTs from the arc discharge technique by using a mixture of argon and hydrogen [94]. The obtained materials were confirmed as bundles of DWNTs along with SWNTs as a by-product. Further, high-quality DWNTs was synthesized from high temperature pulsed arc discharge method [95]. Later, Huang et al. reported the synthesis of super bundles of DWNTs in a hydrogen-free atmosphere [96]. Liu et al. synthesized selective DWNTs by hydrogen arc discharge technique with nickel formate dihydrate catalyst [97]. Graphite powders or MWNTs/carbon nanofibers were used as a carbon source (Fig. 10.14). The HRTEM results confirmed around 80% DWNTs and the rest of were SWNTs and ends of DWNTs were uncapped. In this work, it was also found that the growth of DWNTs mainly depended on the cobalt catalyst [98].

Arc discharge methods were also used for the production of MWNTs. The morphology of MWNTs depends on the synthesis conditions. Some groups have reported the use of methane or hydrogen atmosphere for MWNTs growth. Wang et al. reported MWNTs synthesis using DC arc discharge under the helium and methane atmosphere [99]. Thin and long MWNTs were obtained by using methane

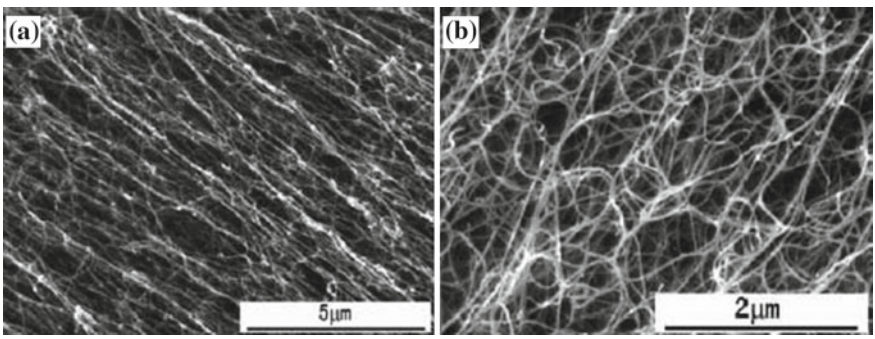

Fig. 10.14 SEM images of the as-synthesized DWNTs (Reproduced with permissions [97]. Copyright 2007, American Chemical Society)

gas pressure of 50 torr and an arc current of 20 A for the anode. Further, long and fine MWNTs can be prepared under a hydrogen gas atmosphere. But a big difference was found with the use of He and methane gas atmosphere. It was found that methane and helium gases atmosphere give more carbon smoke in comparison with the hydrogen gas atmosphere [23]. In another work, it was found that DC arc discharge in the hydrogen gas atmosphere can produce long MWNTs and graphene sheets as a by-product [24]. MWNTs were also synthesized at various pressures ranged from 150 to 500 torr under acetone, ethanol and hexane atmosphere. It was demonstrated that the production of MWNTs was at least two times higher in ethanol, acetone and hexane atmospheres than that of MWNTs produced in the He atmosphere.

Further, the growth of MWNTs was also reported from the arc discharge deposition process with the use of a pulsed laser. Parkansky and co-workers used a single-pulse arc for the synthesis of MWNTs in ambient air [100]. MWNTs were deposited vertically oriented on Ni/glass substrate with a length of up to 3 mm and a diameter of about 10 nm with a single 0.2 ms pulse. Tsai et al. also demonstrated MWNTs with an inner and outer diameter of 5 and 17 mm, respectively by using single-pulse discharge in the air [101]. Moreover, there are several reports on MWNTs deposition by using a gas atmosphere with arc discharge in liquid solutions. Sornsuwit et al. reported the synthesis of high-quality SWNTs and MWNTs in H3VO4 aqueous solution from pure graphite electrodes through arc-discharge [102]. HRTEM analysis revealed the high-quality well-ordered MWNTs without any defects. The outer diameter of MWNTs was 10–20 nm and interlayer distance of ~ 0.35 nm between graphene layers [103]. Similarly, the synthesis of MWNTs in high yield can be obtained by arc discharge in liquid nitrogen [104]. Arc discharge in water can also produce high yield MWNTs production [105].

10.5.2 Laser Ablation

Laser ablation methods have been successfully developed for the production of SWNTs and MWNTs. For the first time, the Smalley group demonstrated the principles and mechanisms of CNTs growth by laser ablation technique [106]. Generally, Nd: YAG and CO_2 lasers are being used in the laser ablation method. In this method, the graphite target is vaporized by a laser beam at high temperatures under an inert atmosphere. The laser generates carbon species, which are swept by the flowing inert gas from the high temperature zone to a conical water-cooled copper collector. The reaction temperature is an important parameter in CNTs production quality and yield. It was reported that the size and average diameter of CNTs can be tuned by tuning the laser power, growth temperature, catalyst composition, type of gases and its pressure [107–109]. Maser and co-workers demonstrated the high-density SWNTs obtained from a simple CO_2 laser system [110]. Also, it was found that laser power, the wavelength of laser and pulse duration can play a key role in the properties of the final product [111]. For example, the average diameter of SWNTs increased with

the increase of CO_2 laser power from 500 to 800 W. However, the excitation wavelength growth mechanism of CNTs has not been clearly understood. Chen et al. [112] reported that SWNTs diameter can be controlled by varying the furnace temperature, catalytic metals and flow rate. Higher furnace temperature produced SWNTs with larger diameters. It was found that the use of a Ni–Y alloy catalyst increases the SWNT diameter, whereas an Rh-Pd catalyst reduces it [113].

For commercial purposes, polystyrene-MWNTs thin films deposited on alumina substrates by PLD techniques with Nd: YAG laser ablation [114]. High-quality DWNTs and SWNTs were produced from a combined method of steady arc discharge and the laser-furnace methods [115, 116]. Impurities such as catalytic metals and amorphous carbon present in CNTs can be removed by purification processes based on chemicals such as H_2O_2 or oxidation by hot air (400–500 °C) [117]. Both arc discharge and laser ablation techniques can give high-quality growth of CNTs, but these are expensive techniques due to high power equipment. Also, the CNTs production yield is low in both methods.

10.5.3 Chemical Vapor Deposition

To date, the CVD technique has been established as one of the best methods for CNTs production. In this method, CNTs are formed by the decomposition of the carbon precursor on the catalytic substrate surface. Thermal or plasma CVD is considered as the standard method for CNTs synthesis. Also, other CVD techniques such as hot filament (HFCVD), water-assisted CVD, oxygen assisted CVD, radiofrequency CVD (RF-CVD) or microwave plasma (MPECVD) have been developed [118–121]. CVD techniques are very economical for industrial production of quite pure CNTs in comparison with laser ablation. In this technique, first, a catalyst is prepared and then the actual synthesis of nanotube was performed. The catalyst role in the CVD method is to improve the decomposition of the carbon precursor. When the catalytic substrate is heated up in a carbon-rich gaseous environment, CNTs were produced at 500 to 1000 °C. The advantage of CVD techniques over arc discharge or laser ablation is that it can produce CNTs in many forms like straight or coiled, films and vertically aligned structures.

The systematic of catalytic CVD reactor system for CNTs synthesis is shown in Fig. 10.15a [122]. A mixture of xylene-ferrocene was used as a carbon source into an inert gas medium. The reaction starts with the decomposition of the ferrocene-xylene mixtures at atmospheric pressure and temperatures of 625–775 °C. As obtained nanotubes were highly pure (Fig. 10.15b, c) with a maximum length of ~50 μm. Many substrates including Ni, Si, Cu, Cu/Ti/Si, SiO_2, etc. were used CNTs growth [123]. CNTs growth was also investigated on the mesoporous silica substrate as it can play as a template for the initial nanotube growth [124, 125].

In the CVD technique, the selection of catalysts is a very important parameter for CNTs growth. The effect of catalytic nanoparticle composition and morphology on CNTs growth in the CVD method has been demonstrated [126]. Also, CNTs

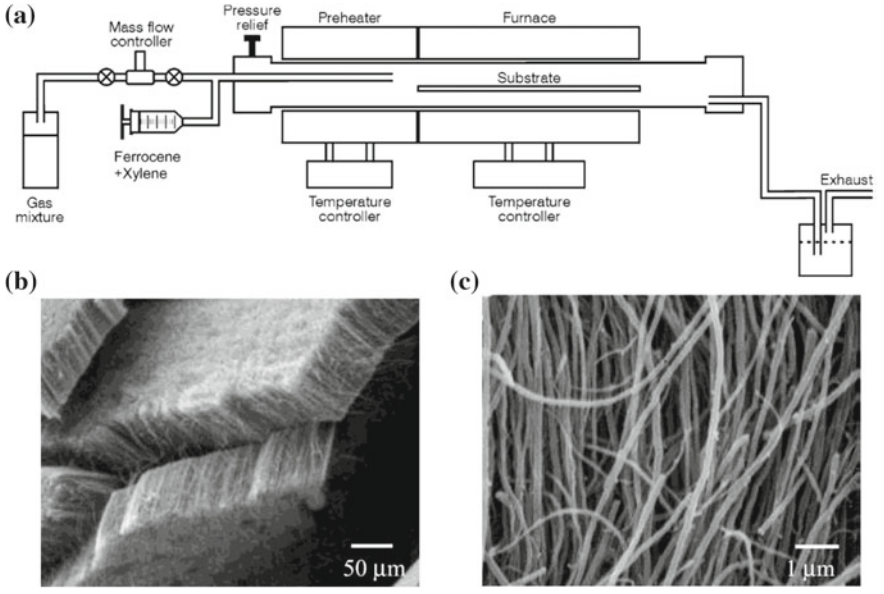

Fig. 10.15 **a** A representative scheme for the production of MWNTs using catalytic CVD reactor. **b** as grown SEM image of well-aligned MWNTs arrays and **c** higher magnified SEM image obtained from catalytic CVD method (Reproduced with permissions [122]. Copyright 2002, American Chemical Society)

growth was reported from catalysts derived from Co/Fe/Al layered double hydroxides (LDHs) [127]. It was found that Co content in precursors showed a significant effect on CNTs growth. CNTs with a smaller diameter and fewer defects were formed at higher Co content. In another work, Flahaut et al. investigated the catalytic effect on the preparation of CNTs [128]. The results showed a significant effect of catalyst composition on CNTs growth. Jiang et al. reported the in situ growth of CNTs on the pre-treated graphite electrode in the presence of $Ni(NO_3)_2$ catalyst via CCVD method. For a shorter growing time, MWNTs revealed the length of 200–1000 nm with the inner and outer diameter of 20 and 80 nm, respectively [129].

Not only catalysis, but carbon source also is a key parameter for CNTs growth. High-quality DWNTs can be obtained by decomposition of benzene at 900 °C in the presence of Fe-Mo/Al_2O_3 catalyst [130]. As-prepared DWNTs bundles were found without any amorphous carbon on the surface, with fewer structural defects. Further, the well-aligned MWNTs were obtained via pyrolysis of C_2H_2 on a large area of Ni deposited Si/SiO_2 substrate using the thermal CVD technique at 900 °C [131]. The studies showed the crucial effect of NH_3 pre-treatment on the surface morphology metal catalyst and therefore to get the vertical aligned CNTs. Highly aligned CNTs can be obtained at a higher density of Ni particles due to the effect of steric hindrance between neighboring CNTs. It was found that the degree of CNTs crystallization increased with the increase of NH_3 pre-treatment time. The

detail of the direct growth of aligned CNTs, substrate effect, growth mechanism and advantages and shortcomings of CVD have been reviewed [132]. Some researchers used Nickel oxide-silica binary aerogels as the catalyst for the growth of MWNTs by decomposition of methane at 680 °C for 120 min. The diameters of DWNTs were observed to be 40–60 nm [133]. Also, CNTs can be grown using two carbon sources of ethanol/Co and benzene/Fe systems [134].

CNTs were further grown by plasma-enhanced CVD (PECVD). The use of the PECVD method for SWCNTs has been well summarized by Lim et al. [135]. PECVD method gives high-quality CNTs. Forest like MWNTs deposited on a solid substrate is shown in Fig. 10.16. PECVD methods can be used in many different modes: direct current (DC-PECVD), radio frequency (RF-PECVD), diffusion (DPECVD) or microwave (MWPECVD). Like thermal CVD, CNTs synthesis using DPECVD has been demonstrated on the various substrate (i.e., Ag, Pt, W, Ta, Ir and NiV) at low-temperature (480–612 °C) [136]. Vollebregt et al. [137] reported self-aligned vertically grown CNTs and CNFs by using Pd as catalyst material. Samples were fabricated using a different catalyst (Pd, Ni, Fe, Co) and at different temperatures such as 450–640 °C for atmospheric pressure chemical vapor deposition (APCVD) and 450–500 °C for PECVD. APCVD produced highly dense self-aligned CNTs when Pd acts as the catalyst, while the random growth of CNTs was found in the Co and Fe catalyst. Further, they also concluded that CNTs grown by PECVD in the presence of Pd catalyst, produced large bundles of tubes, while large-diameter CNFs were formed in the presence of Ni catalyst. Biocompatible supported CNTs electrodes also have been developed using the CVD method by using ferritin as the catalyst. This type of CNTs electrodes might be useful in neuro-implants [138].

Since its discovery in 1991, CNTs have stimulated intensive research in the area of nanotechnology due to their outstanding electronic, thermal and mechanical, properties. Their implementation in various potential applications forms a great research effort and is now in progress. CNTs application has been demonstrated in scanning

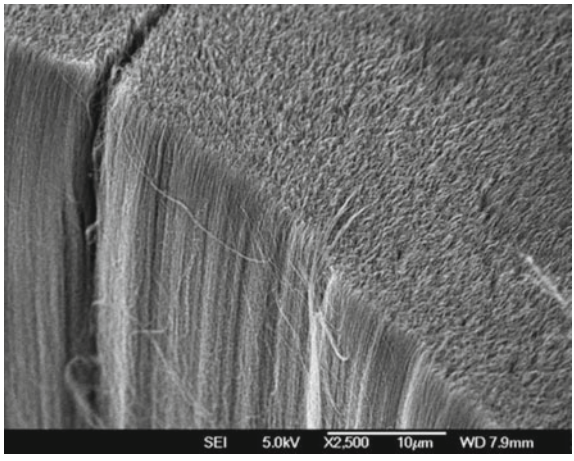

Fig. 10.16 SEM image of forest type MWNTs produced from PECVD at atmospheric pressure (Reproduced with permissions [135]. Copyright 2010, Springer)

tunneling microscopy tips. CNTs have also been demonstrated for solar cells, fuel cells, biosensor, hydrogen storage media and carbon–metal composites for strong and lightweight structures applications. In summary, low cost, rapid and readily scalable route for carbon nanotubes fabrication have been developed for all future applications.

10.6 Synthesis of Carbon Nanofibers

The first synthesis of carbon filaments was reported in the 1970s, but the significant research was carried along with the discovery of CNTs in 1991. These carbon filaments with the cylindrical structure are known to be as carbon fibers (CFs). They can be nanofibers or microfibers, depends on their diameter. Carbon nanofibers may have different microstructural configurations like platelet CNFs as shown in Fig. 10.17 [139]. Herringbone CNFs are formed when graphite sheets are inclined from the fiber axis with some angle. The next structure is tubular CNFs, wherein graphite sheets and fiber axis are parallel to each other. Based on their morphology, CFs can be produced in various shapes including planar, twisted, branched, coiled, spiral, helical and so on. Mainly chemical vapor deposition and electrospinning method have been adapted for significant synthesis of carbon fibers. However, other methods including template-assisted, hot-filament assisted sputtering and microwave-based synthesis have also been reported. In this section, the synthesis and mechanism of carbon fibers using the CVD and electrospinning method will be discussed.

10.6.1 Chemical Vapor Deposition

Again, the CVD technique has been considered as one of the most versatile approaches for carbon nanofibers synthesis. CVD techniques have been developed for scalable and reproducible synthesis of CNFs, in which gaseous precursors such as C_2H_2 and CH_4 are used on a metal catalyst support at elevated temperature. Typically,

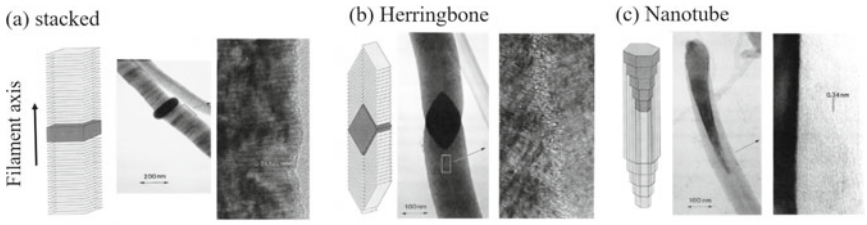

Fig. 10.17 Schematic representations of platelet (**a**), herringbone (**b**) and tubular (**c**) CNFs to the filament axis (Reproduced with permissions [139]. Copyright 1995, American Chemical Society)

the use of catalysts, the chemical composition of precursor and reaction parameters define the final structure of the product. In this method, hydrocarbon decomposition of carbon precursor provides a continuous supply of carbon to produced well-organized tubular filaments of sp^2-carbon in hexagonal form. However, this technique is expensive and also produces short fibers [140].

Catalytic thermal CVD (CTCVD) was mostly used for the fast growth of helical carbon fibers. In the early 1990s, Motojima et al. [141] first time used the CTCVD method for the synthesis of regular coiled shape carbon filaments. The CFs were synthesized by pyrolysis of acetylene on Ni-catalyzed substrate at a temperature of 350–750 °C. The obtained CFs were found to be composed of pair-coiled fibers. These fibers are elastic and can extend up to three times the original length of the coil. Figure 10.18 showed the perpendicular grown carbon coils on the graphitic substrate [142]. Catalyst Ni grain material was found on the tip of all carbon coils, which is shown by arrows. The diameter of the regular carbon coils was ~3 to 6 μm with the coil pitch of 0.5–0.7 μm without any gap. For the reaction time of 2-h, coil length was increased up to 5–8 mm with a growth rate of 7 μm/s. The high yield of carbon nanocoils was obtained by using acetylene as a carbon source and iron-coated indium tin oxide as catalytic material [143]. Similar to CNTs synthesis, CF synthesis has been developed by the decomposition of acetylene, methane, ethylene, etc. over various transition metals catalysts including Fe, Co, Ni, etc. in the temperature range of 500–1000 °C [144, 145].

Further, carbon nanocoils (CNC) were produced by the low-temperature decomposition of acetylene [131]. The obtained CNCs exhibited a yield of 11 g in each run and formed a nanospring. Minea et al. [146] prepared carbon nanofibers at room temperature by plasma-enhanced CVD. They used low pressure, high-density plasma technique and grown the fibers on a thick Ni film deposited upon a silicon substrate. The CNFs were scratched from the substrate by a diamond tip. The obtained CNFs

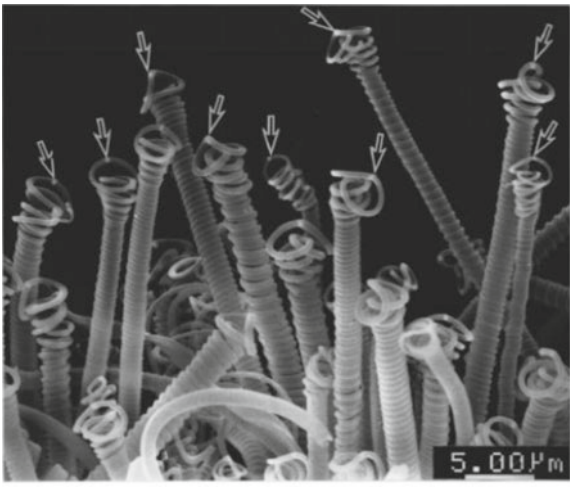

Fig. 10.18 SEM image of vertically grown carbon coils on the substrate (Reproduced with permissions [142]. Copyright 1999, American Institute of Physics)

were amorphous and have a short length of ~50 nm at a deposition rate of 2 nm/min. Carbon nanofibers are also synthesized without any catalyst by microwave pyrolysis CVD using N_2 as a carrier gas and CH_4 as a source at a temperature of 1050–1150 °C [147]. Carbon fibers are radially grown on the porous Al_2O_3 substrate. The prepared CFs were uniform in diameter in the same region. Simultaneously, it was also noted that the ends of fiber were hemispheroidal and some cauliflower-like fiber ends can also be observed in the as-prepared samples.

10.6.2 Electrospinning

Commercial synthesis of carbon fibers was obtained from the electrospinning method. The first patent on electrospinning was published by Cooley in 1902. After that, researchers produced carbon fibers through electrospinning [148]. However, this method got much attention in the last two decades and is optimized for carbon fibers fabrication. This technique is based on the processing of polymeric solutions or melts by using an electrically force fluid system [149]. In the electrospinning process, there are many controlling parameters such as solution properties and processing parameters as well as on surrounding temperature and humidity conditions [150]. The structure of CNFs strongly depends on the nature of the polymeric precursor. The CNFs fabrication has been reported using various polymeric precursor including polyacrylonitrile (PAN), pitch, cellulose, poly (amic acid) (PAA), polybenzimidazole (PBI), polyimide (PI), poly (p-xylenetetrahydrothiophenium chloride) (PXTC) and poly (vinyl alcohol) (PVA) [151, 152]. High-quality CNFs production can be obtained by selecting the right organic polymers, followed by thermal annealing under inert conditions.

Kong et al. [153] successfully synthesized CNFs by electrospinning of PAN/DMF polymer solution and then stabilization and carbonization. The stabilization was carried out in the air between temperature 200 to 300°C. The carbonization process was performed at 2800°C under an inert atmosphere (Fig. 10.19) [154–157]. CNFs

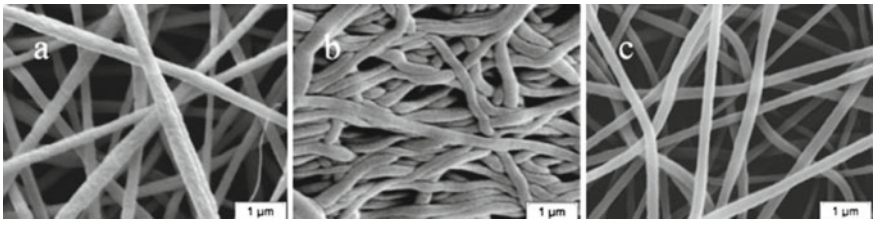

Fig. 10.19 **a** Typical SEM micrograph of electrospun PAN nanofibers obtained from 8% PAN solution in DMF, **b** CNFs produced from a two-step heating: 200 °C for 30 min and 750 °C for 1 h and **c** CNFs produced from a multi-step progressive heating: 5 °C/min from 30 to 230 °C, 1 °C/min from 230 to 270 °C, then 5 °C/min from 270 to 800 °C (Reproduced with permissions [154]. Copyright 2009, Elsevier)

can be also prepared with the addition of inorganic species including MWNTs, Ag, TiO2 and etc. Ra and co-workers first time demonstrated the CNFs preparation by embedding MWNTs in the PAN matrix. Further, electrospun Ag/PAN nanofibers were obtained at the Ag content of 0-5 wt% [158]. Recently, Inagaki et al. reviewed the systematic process for CNF fabrication [151]. Preparation and applications of CNFs prepared by electrospinning have also been reviewed elsewhere [152].

Indeed, carbon nanofibers are currently available on a large scale for a large number of potential applications like field emission sources, catalyst substrate, hydrogen storage, chemical sensors, electrode material, scanning probe tip, nano-electronics and mechanical reinforcements.

10.7 Synthesis of Graphene

Since its discovery in 2004, graphene is being considered as a wonder material for a wide range of potential applications. The unique properties of graphene make it emerging materials for high-speed electronics, optical devices, energy storage, chemical sensors, thermal management and electromagnetic interference shielding applications [11, 12, 159–166]. Optimization of graphene synthesis using various top-down and bottom approach has led to an extraordinary amount of interest in both industry and academics. To date, graphene and graphene oxide has been synthesized from various top-down and bottom-up approaches. In this section, different methods will be discussed for the synthesis of graphene, including the recent developments.

10.7.1 Top-Down Approach

In this approach, graphite is being used as starting materials. Graphite is constructed from sp^2 hybridized carbon atoms arranged in honeycomb lattice structure with an interlayer distance of 3.35 Å along the c-axis. In graphite, all carbon layers bonded together with a weak Van der Waals force. Therefore, graphite can easily exfoliate by either chemical or mechanical exfoliation methods.

10.7.1.1 Mechanical Exfoliation of Graphite

The first single layer of graphene was identified using micromechanical cleavage of highly oriented pyrolytic graphite (HOPG) in 2004 [159]. This method involved an adhesive tape to peel off the graphene layers from HOPG. The peel-off process was repeated many times to achieve a single layer of graphene on tape, followed by transfer on a cleaned substrate [167]. Figure 10.20a showed the optical images of graphene and few-layer graphene deposited on a 300 nm SiO_2 substrate. The thick layer graphene appeared yellow. Upon reduction of the graphene layer thickness, it

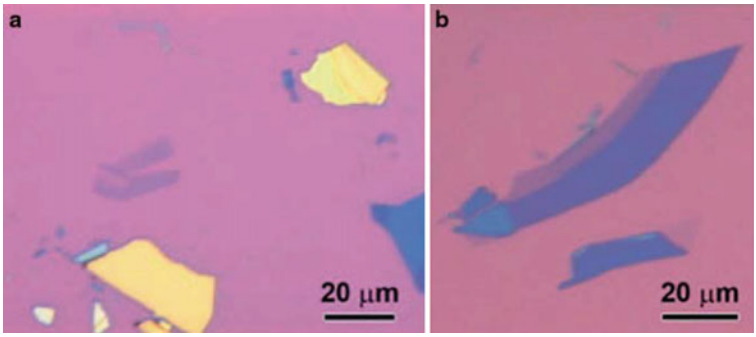

Fig. 10.20 Optical image of exfoliated graphene obtained from the Scotch-tape method. (Reproduced with permissions [168]. Copyright 2010, Elsevier)

showed bluishly. The darker side showed a few layers graphene, while lighter shades showing the single-layer graphene [168]. This micromechanical cleavage process is known as the "Scotch-tape method", which facilitated the initial experimental measurements on the exceptional electronic, thermal conductivity, mechanical and optical properties of graphene. These unique properties generated a huge interest in graphene in almost all branches of science. This Scotch-tape can produce single-layer graphene up to 1 mm with a minimal defect. The produced graphene is good in quality but bulk production is not possible. Therefore, for real-life applications, other synthesis methods are required which can have produced graphene on large scale.

10.7.1.2 Solution-Based Exfoliation of Graphite

Solution exfoliation of graphite has emerged with great interest because it can give producible results on a scalable large scale. Similar to the direct dispersion of carbon nanotubes, many authors directly dispersed the graphite into various organic solvents and then sonicated for exfoliation into a single-layer or multilayer graphene sheets. Coleman et al. obtained good quality graphene sheets by dispersion and sonication of graphite into the NMP solvent [169]. Graphene dispersion was further achieved by 3 h ultrasonication of HOPG in DMF [170]. Various polar and no-polar solvents were explored for graphene synthesis [171]. Bulk production can be achieved by this solution exfoliation method but the production yield is very low. A further attempt was made to ultrasonication-free exfoliation by intercalating graphite with alkaline metals [172]. A high yield of graphene up to 2 mg/mL was obtained by spontaneous exfoliation of HOPG in chlorosulfonic acid [173]. Graphene synthesis in aqueous was also explored by using various surfactants [174, 175]. The analysis confirmed the synthesis of single or few-layer graphene up to a size of a few mm. However, exfoliated graphene sheets are less stable in water in comparison with organic solvents. Graphene synthesis using the solvent exfoliation method depends on many factors

like the size of graphite flakes, sonication time and centrifugation conditions and the solvents. From an industrial point of view, this method is appealing but this solution-based exfoliation approach has several drawbacks. Most of the exfoliated flakes possess a multilayer structure, which gives low yield and large size and thickness heterogeneity among the exfoliated flakes. Moreover, long-time sonication reduces the size of the graphene sheets, resulted in small size graphene sheets, which can significantly affect the properties of graphene sheets. Also, surfactant exfoliated graphene sheets can alter the resulting electronic properties of graphene.

10.7.1.3 Electrochemical Exfoliation of Graphite

After the development of the solution-based exfoliation method, there is a continuous demand for new approaches for the bulk production of high-quality graphene. Then, the researchers developed an electrochemical method for graphene synthesis. The purpose of electrochemical methods is to intercalate the ions within graphite and improve the yield of graphene production [176]. The use of intercalating agents provides an attractive way to exfoliate graphite while retaining the basic properties of graphene. This method involves the application of anodic (oxidation) or cathodic (reduction) potentials in an electrolytes solution, graphitic material as working electrode, reference electrode (SCE, Ag/AgCl, etc.) and a counter (usually Pt) electrodes. The most common and widely studied intercalated ions are Li^+, Ni^{2+}, F^-, $SO_4{}^{2-}$, NO^{3-}, Cl^-, etc. [177]. Several electrolytes and electrochemical conditions were applied to achieve the bulk exfoliation of graphene [178, 179]. It was found that applied potential and electrolytes strongly affected the quality of graphene. Few studies showed that the use of high voltages promotes the formation of oxygen groups on graphene sheets surface and also damages the structure. Graphite intercalation in aqueous SDS surfactant solution explored to drive the exfoliation process. The resulted graphene sheets were found to have a size of 500 and 1 nm thickness was successfully obtained [180]. To avoid the formation of oxygen functionalities on the graphene surface, the cathodic reduction/intercalation method was also attempted [181]. Recently, Adriano and co-workers prepared graphene sheets from commercially available graphite foil as shown in Fig. 10.21a [182]. Three different electrolytes; H_2SO_4, $LiClO_4$ and Na_2SO_4 were tested with a common exfoliation procedure. Optical images of graphite foil before exfoliation and after applying the +10 V potential for prolonged time are shown in Fig. 10.21b, c, respectively. As obtained graphene dispersion in NMP is shown in Fig. 10.21d. Figures 10.21e, f show the exfoliation process at the time of zero, 5 min and 20 min, respectively. As obtained exfoliated graphene was easily dispersible and formed stable dispersion in DMF at the concentration of 1 mg/mL. It was noticed that out of three different electrolytes used in the exfoliation process, either H_2SO_4 or Na_2SO_4 have shown more vigorous and efficient exfoliation.

In comparison with micromechanical cleavage and solvent exfoliation, graphene synthesis using electrochemical exfoliation is more environmentally friendly and generally fast. However, this method also not providing homogenous graphene

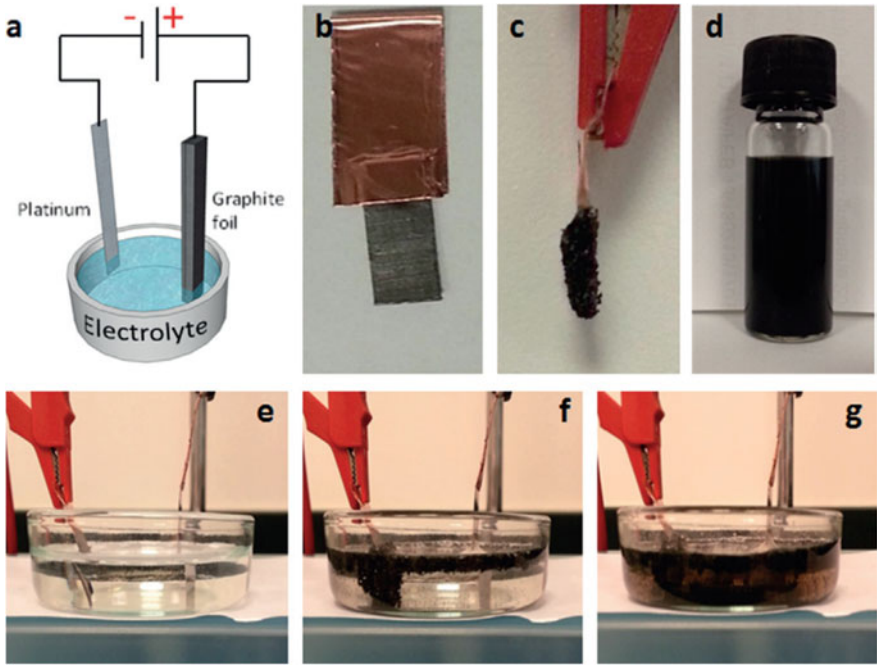

Fig. 10.21 **a** Two electrode electrochemical exfoliation set up, **b** photo of graphite foil before exfoliation, **c** graphite foil after exfoliation process, **d** graphene dispersion in DMF solution (1 mg/ml). **e**, **f** illustrating the exfoliation process at a time (e) zero, (f) after 5 min and (g) after 20 min (Reproduced with permissions [182]. Copyright 2015, Wiley–VCH)

sheets. Also, the use of anodic conditions for ions intercalation causes unwanted oxygen-containing functional groups, which disrupt the sp^2-hybridized carbon structure.

10.7.1.4 Chemical Exfoliation and Reduction

In the chemical exfoliation method, chemical species intercalated within graphitic layers and oxidized the graphitic layers. A little energy in the form of sonication or shaking results as single-layer graphene oxide. Brodie (1859) reported the first successful oxidation of graphite by using potassium chlorate as an oxidizing agent in the presence of nitric acid (HNO_3) [183]. He attempted to establish an exact formula of graphite by producing highly oxidized graphite. He found that the overall mass of graphite flakes was increased upon oxidization due to the presence of hydrogen and oxygen on graphene sheets. This method was further improved by adding chlorate into fuming during the reaction [184]. Further, concentrated sulphuric acid was also added into the mixture to increase oxidization.

Later on, Hummers and Offeman developed another effective oxidation method in which graphite flakes react with the mixture of potassium permanganate ($KMnO_4$) and sodium nitrate in concentrated sulfuric acid (H_2SO_4) with improved experimental safety [19]. This method is considered the primary route for GO preparation and became more popular for the synthesis of graphene. Some researchers have developed slightly modified versions of Hummer's method to avoid the poisonous nitrous gas, which evolves during the reaction in the presence of sodium nitrate in the mixture. After complete oxidation, the interlayer distance between graphitic layers increased to 6 Å or more which is due to the presence of oxygen-containing functional groups on its surface and edges. This increased interlayer distance in graphite oxide weakens the force between layers, can produce a separate layer upon sonication [185]. The separated layers are called graphene oxide (GO). By using this method, a bulk amount of GO can be produced, which is required for commercial applications [186]. Graphene oxide can be dispersed easily in aqueous as well as in organic solvents. But, the main problem with GO is its electrical insulator nature, which is due to the presence of oxygen-containing functional groups on its surface and edges. A lot of research has been performed on GO and its composite materials [187–192]. FESEM images of large size GO prepared by modified Hummer's method is shown in Fig. 10.22a. Figure 10.22b showed its size distribution [188]. More than 50 μm graphene sheets can be synthesized. Size selections of GO sheets strongly depend on the lateral size of graphite flakes and separation conditions. The thickness of as-prepared GO sheets was measured to be ~1 nm (Fig. 10.22c) [189]. The increased thickness of GO sheets is because of oxygen functional groups on the graphene basal plane and edges.

The first serious mechanism of GO synthesis was investigated by Tour and coworkers [193]. In this study, they explained the step-by-step synthesis of graphite into GO as shown in Fig. 10.23. The first step is showing the intercalation of sulphuric acid into graphite, the second step is to covert the intercalated graphite into oxidized graphite and the last step is to exfoliate the graphite oxide into graphene oxide (GO). The study also showed the single-layer GO yield is depending on the oxidation degree of GO sheets. For example, Kim et al. obtained the three different sizes of GO sheets by using different sizes of graphite flakes with variable oxidation time and studied their size-dependent liquid crystalline properties [194]. Production of single-layer GO can be improved by using pre-oxidized graphite flakes. Single-layer GO yield also improved by exfoliation of graphite in presence of tetrabutylammonium ions. However, the process is very time taking [195]. A low-temperature approach was also established for the large production of single-layer GO [196]. Most of the established chemical exfoliation methods used hazardous chemicals, which release poisonous gases. By using the K_2FeO_4 oxidation agent, a 100% yield of GO synthesis was achieved within a short reaction time of 1 h [197]. Similar to other chemical exfoliation methods, this method also releases harmful gases.

The chemically exfoliated graphene oxide has oxygen-containing functional groups on its surfaces. The present functional groups can help for the dispersion of other inorganic nanomaterials and further functionalization of GO for composites and other potential applications. However, graphene oxide sheets are insulating in

nature due to oxygen-containing functional groups. To make it conductive, which is required for most of the graphene applications, we need to remove or reduce these oxygens containing functional groups from the GO surface. There are mainly three common approaches that are being used for such reduction of GO, namely, thermal, chemical and electrochemical reduction methods.

In a thermally reduced approach, GO is annealed at high temperature (1000–2000 °C) under inert conditions. In this method, gaseous species are generated within the interlayers of the GO structures, thin-film/powder and consequently removal of oxygen functional groups and simultaneous graphitization at elevated temperatures, resulting in highly conducting products [198, 199]. Many researchers reported that thermally reduced graphene can improve its electrical and thermal conductivity, but reduced graphene oxide sheets have shown some defects. For example, Xin et al. produced free-standing graphene paper via thermal reduction and graphitization at a very high temperature ~2200 °C [200]. As prepared free-standing graphene paper showed high thermal conductivity of 1238 W/mK. This high temperature thermal annealing approach is straight forward. Thermally reduced graphene oxide has a great potential be used for composite materials, EMI shielding, electrochemical devices

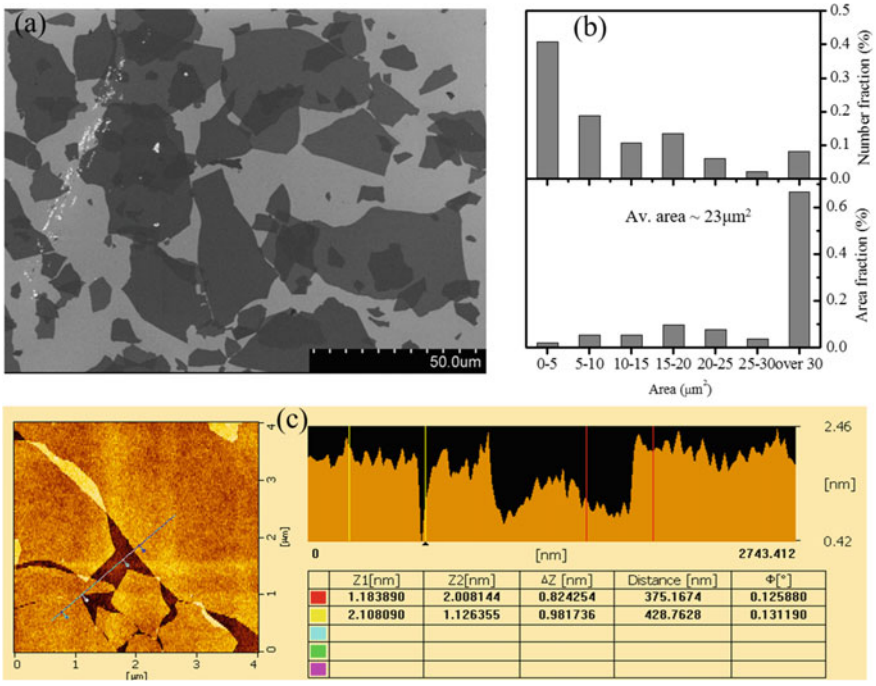

Fig. 10.22 **a** Representative SEM micrograph of large-area GO, **b** size distribution of GO sheets and **c** AFM image of GO sheet (Reproduced with permissions [188, 189]. Copyright 2014, 2015, Elsevier)

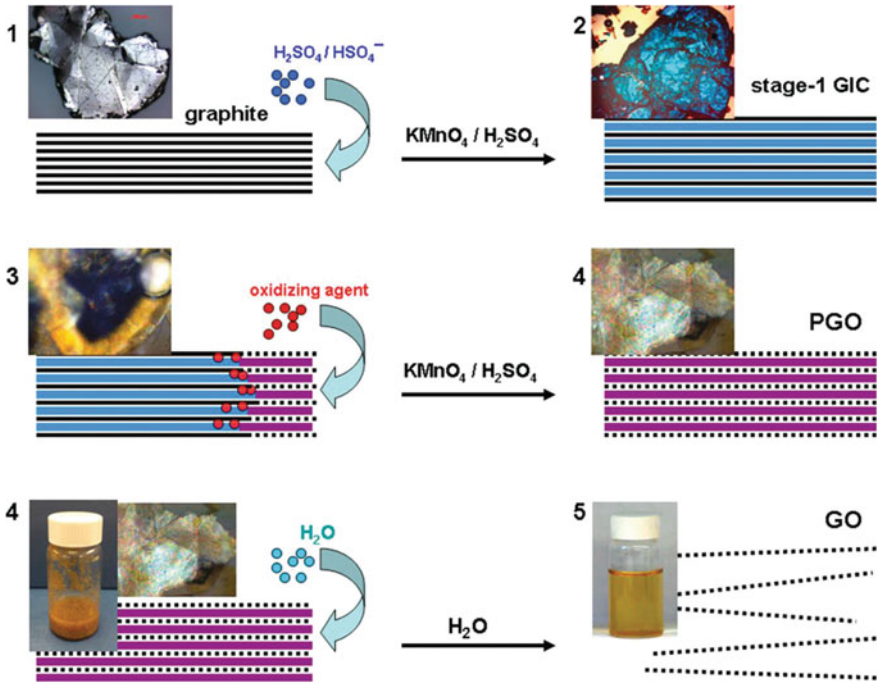

Fig. 10.23 Mechanism of graphite exfoliation into single-layer GO (Reproduced with permissions [193]. Copyright 2014, American Chemical Society)

and conductive ink and paint. But this method has some drawbacks of long-time heating and annealing at high temperature.

Electrochemical reduction of GO is another approach, which can be performed at ambient conditions. Many authors have obtained the pristine graphene-like properties from electrochemically reduced GO [201–203]. Recently, Ambrosi et al. studied the reduction of GO using the electrochemical method, which gives precise control of C/O ratio between 3 to 10 [204]. Thermal and electrochemical reduction methods can reduce GO significantly, however, a chemical reduction is the most widely used method for GO reduction. A chemical reaction/reduction is performed on aqueous GO solution, powder and thin films to remove most of the functional groups. The most studied chemical reducing agent is hydrazine, which was already tested in past in 1937 by Hofmann and König [205]. Beceril et al. investigated GO film reduction by immersing it into a hot aqueous hydrazine solution. In other studies, hydrazine vapor is used for GO reduction even at room temperature. Another reducing agent, $NaBH_4$ was also explored, but all these methods give rigid and fragile rGO films with low electrical conductivity [208]. Experimental findings revealed that both hydrazine and $NaBH_4$ are not effective in reducing agents for GO powder or films. Also, the hydrazine reduction mechanism is not clearly understood.

Further, a more significant route was developed by using halogen hydrohalic acids, which can give highly conductive rGO films [209]. The reduced GO film maintains its flexibility and mechanical strength. Recently, many other reducing agents such as lithium aluminum hydride, hydroxylamine, eco-friendly L-ascorbic acid, saccharides, have been developed for GO reduction [210–213]. Other ways of reducing like a camera flash, UV light and laser scribes were also used for the reduction of GO films [214–216]. It was noticed that chemical reduction procedures can give sufficient electrical, thermal and mechanical properties, however, overall performance is poor compare to pristine graphene. This poor performance of chemically reduced GO is due to incomplete removal of functional groups and the creation of defects on the graphene sheet during the reduction reaction. However, with this poor performance of reduced GO, the chemical reduction method is most widely used for bulk synthesis of reduced GO, which has shown good results in energy storage, sensor and composite applications. For example, Kumar et al. reported the much-improved electrical conductivity of ~3000 S/m and ultrahigh in-plane thermal conductivity of ~19.5 W/mK from low-temperature HI reduced composite film [162].

10.7.1.5 Unzipping Carbon Nanotubes

Unzipping of CNTs can produce graphene. This approach mainly produced different kinds of graphene, called graphene nanoribbons (GNRs) [217, 218]. The typical width of the GNRs is $\leq$50 nm with an aspect ratio of more than 10. Dai et al. reported the GNRs synthesis using partially embedded multiwalled CNTs (MWCNTs) in a PMMA film under an Ar plasma treatment for the various duration [217]. As-prepared GNRs exhibit smooth edges with a narrow width of 10–20 nm (Fig. 10.24). The yield of GNRs is nearly 100% in this method. The resulting graphene nanoribbons contained oxygen functional groups, which can be removed either chemically or thermal annealing method. In contrast to the above work, Tour and co-workers proposed a more scalable approach to open the MWCNTs longitudinally by oxidizing them in presence of sulphuric acid and potassium permanganate [219]. The resulted GNRs exhibited functional groups on their surface. To reduce the defects and vacancies on the GNRs surface, H_3PO_4 was introduced in the oxidation process [218]. Heating of MWNTs in presence of potassium resulted in lower defects on GNRs surface.

Various other methods have been proposed for GNRs synthesis including metal catalyst assisted cutting, thermal exfoliation step, lithium insertion and mechanical sonication in organic solvents [221–225]. Li et al. demonstrated effective intercalation of MWCNTs for the scalable synthesis of GNRs [225]. GNRs have also synthesized the intercalation of Li-NH_3 into MWCNTs and thermal exfoliation [226]. Another interesting approach for GNRs synthesis is catalytic nano-cutting of CNTs [224]. This nano-cutting approach can produce partial or complete unzipping of carbon nanotubes. This technique has some advantages like smooth and sharp edges GNRs with specific orientations can be obtained on large scale. However, the major problem of this technique is that it does not ensure complete cutting in all MWCNTs,

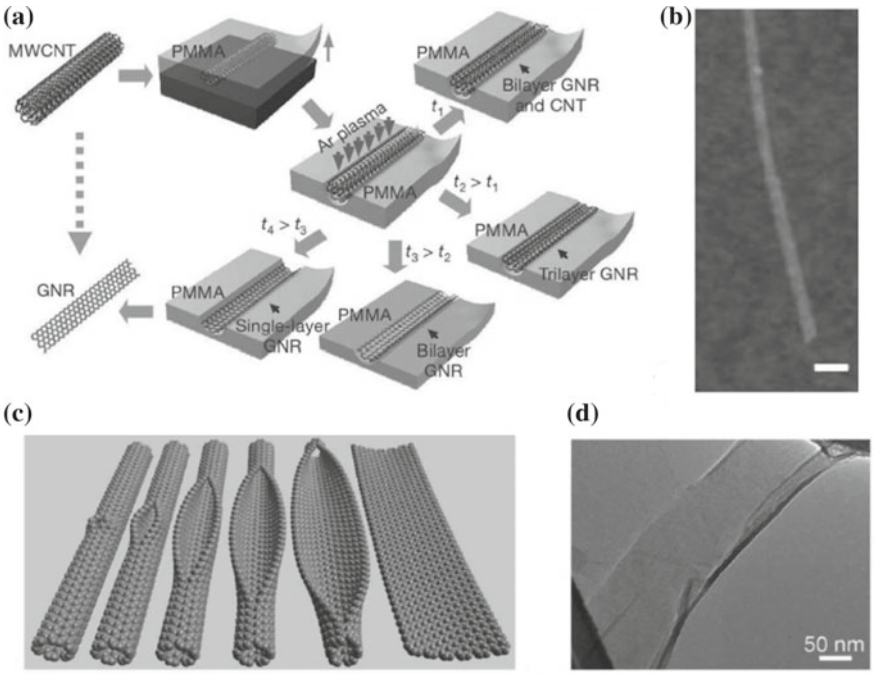

Fig. 10.24 Schematic for GNRs synthesis from unzipping of CNTs with representative TEM images (Reproduced with permissions [221]. Copyright 2010, Wiley–VCH)

which limits its applicability. Synthesis of GNRs without any chemical or catalyst contamination was reported using high DC pulses by using MWCNTs as starting materials [227].

10.7.2 Bottom-Up Methods

This method is mainly based on small molecules to combine by a catalytic process to produce a high-quality graphene sheet [228]. In the first half of the twentieth century, Scholl and Clar pioneered the synthesis of polycyclic aromatic hydrocarbons. Clar et al. (in 1958) firstly synthesized a small graphene sheet with 42 carbon atoms [229]. After that, a series of polycyclic aromatic hydrocarbons with a much larger sp^2 system was proposed [230]. In this route, first branched oligophenylenes were prepared by Diels–Alder reactions and then subjected to oxidative cyclo-dehydrogenation to give planar graphene disks. Under specific conditions, carbon-containing molecules combined into an sp^2-hybridized carbon network. Further, an attempt of graphene synthesis was made using chemical vapor deposition (CVD) and epitaxial growth [231]. These early efforts on the synthesis of monolayer graphene were followed by

a large number of scientists [232]. In this section, synthesis aspects of the bottom-up methods for graphene, specifically, CVD and epitaxial growth approach will discuss.

10.7.2.1 Chemical Vapor Deposition

CVD is a well-established technique for controlled synthesis of various carbon nanomaterials including CNTs, fibers, fullerenes. This method involves the decomposition of carbon sources on transition metal catalyst deposited wafer at high temperature. The decomposed carbon atoms are deposited and then assembled at high temperatures. Large-area epitaxial graphene films (up to a size of few mm) can be obtained. CVD grown graphene was first reported in 2008 and 2009, using Ni and Cu substrates, which was followed by grown over several metal substrates such as iridium, ruthenium, platinum [233–237]. This technique demonstrated the synthesis of single-crystal graphene domains currently up to dimensions of the size in centimeters [238]. The graphene quality was comparable to the Scotch off method produced graphene.

Graphene grown on nickel and copper metal substrates is more popular in comparison with other metal substrates [231, 239, 240]. For graphene growth on a nickel substrate, first polycrystalline Ni films were annealed in Ar/H_2 atmosphere at 900–1000 °C to increase grain size and then the H_2/CH_4 gas mixture was exposed to the substrate. This step involves the decomposition precursor gas and then decomposed carbon atoms dissolve into the Ni film to form a solid solution. Finally, the samples were allowed to cool down in Ar gas. Figure 10.25a illustrates the growth process of graphene on the Ni surface [241]. Ni surface would be an excellent lattice-matched substrate for graphene growth because Ni (111) has a lattice similar to the densely packed hexagonal lattice of graphene (Fig. 10.25b) and they also have similar lattice constants [242]. As-prepared graphene on Ni substrate can be transferred to the required substrate for further study and applications. A low-magnified TEM image of graphene with step-shaped edges is shown in Fig. 10.25c. The inset figure showed the SAED pattern of graphene along the [001] direction. Graphene can main its original structure after transfer on another substrate as shown in Fig. 10.25d. Lewis et al. have also grown graphene on patterned Ni films for desired geometries at specific positions [243]. Wafer-scale graphene synthesis on evaporated Ni films was also demonstrated [239]. It was also demonstrated that the feasibility of transferring graphene on a flexible and transparent substrate has been employed for large-scale flexible transparent electronics applications (Fig. 10.25f) [244]. Tuning of experimental conditions such as deposition temperature, pressure, type and quality of metal substrates and cooling time can improve the graphene growth up to mm scale [245, 246].

Despite good progress in the growth of CVD graphene, there are still many challenges to be overcome for their practical applications. For example, removal of metal catalyst and transfer onto a different arbitrary surface. Thus, the research has been focused on the transfer process of CVD grown graphene on different surfaces. The

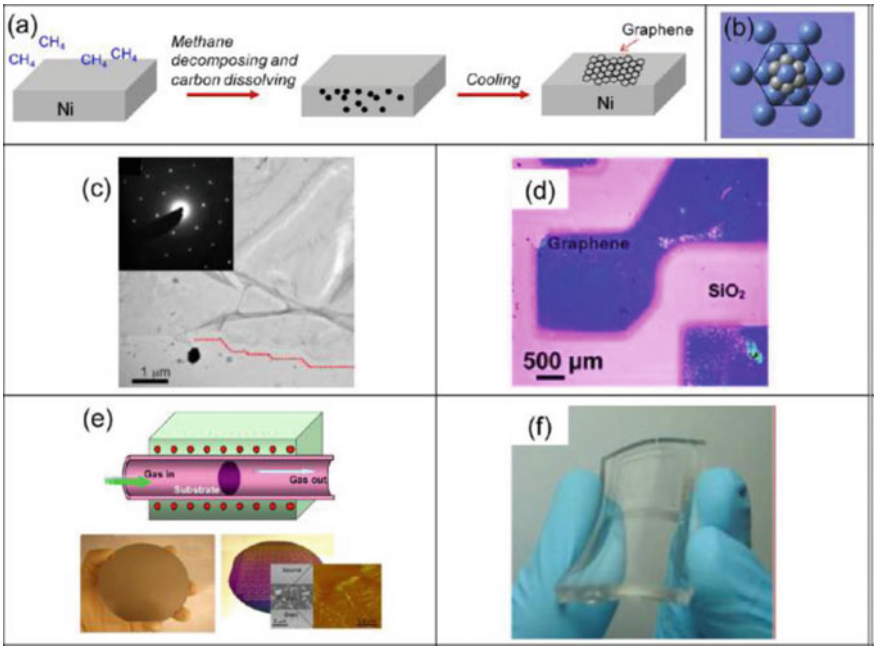

Fig. 10.25 **a** Schematic of graphene formation on Ni substrate, **b** Schematic diagram of graphene atoms (smaller atoms) on Ni (111) lattice (larger atoms), **c** Low magnification TEM image of graphene edges, **d** Optical image of graphene transferred from the Ni surface to SiO_2/Si substrate, **e** Full-wafer-scale deposition of graphene layers on polycrystalline Ni and **f** Flexible and transparent graphene films on the PDMS substrates (Reproduced with permissions [247]. Copyright 2013, American Chemical Society)

transfer of CVD graphene onto arbitrary substrate was obtained using polymer-supported metal etching/transfer or mechanical exfoliation with special functionalized polymers [248]. However, the transfer process usually causes some wrinkles or structural damages, which degrade the quality of graphene [249]. One of the most common transfer methods is the etching of metal substrate while the graphene is supported by an inert polymer such as PMMA or PDMS [247, 250]. So far, several other substrates like PVC, PTFE, PC, CN/CA, PET, paper and cotton cloth have been investigated and applied via a hot/cold lamination process [251]. After complete etching of the metal substrate, the graphene is transferred to the desired substrate followed by the removal of the supporting inert polymer. However, this procedure is very sensitive because it can induce mechanical stress to cause structural damages and alterations. This process also gives some contamination by metallic impurities, which can dramatically alter the electronic properties of the transferred graphene [252, 253]. For example, nickel and copper metal substrates dissolved by etching agents such as $FeCl_3$, $Fe(NO_3)_3$ contaminate the transferred graphene with a significant amount of Fe impurities [254, 255]. Moreover, the incomplete etching process

also can contaminate CVD graphene with an extremely large number of redox-active residuals, such as Cu or Ni metals. Recently, PMMA-graphene was separated from the growth substrates without etching by inducing O_2 bubble generation with a mixture of NH_4OH, H_2O_2 and H_2O [256]. Further, Gao et al. developed a face-to-face transfer of wafer-scale graphene films [257]. This novel approach was based on nascent gas bubbles and capillary bridges that provide high-quality graphene with fewer defects. Several improved techniques were developed such as plasma-enhanced chemical vapor deposition (PECVD) and microwave-assisted CVD for the high-quality fabrication of graphene [258]. Therefore, CVD has been considered as the most versatile and commercially viable technique for the manufacturing of continuous graphene films to meet the industrial demand for electronic-grade materials.

10.7.2.2 Epitaxial Growth

Similar to CVD, the epitaxial technique is also a substrate-based technique in which single-layer graphene is used to grow on a single-crystal carbide (SiC) by vacuum graphitization. The thermal treatment of SiC under vacuum results in the sublimation of the silicon atoms while the carbon-enriched surface rearranges to form graphitic layers (epitaxial graphene). Precise control of the sublimation may lead to the formation of very thin graphitic layers over the entire surface of SiC wafers, with an occasional monolayer of graphene. Recently, a wafer-scale coating of monolayer graphene was achieved by annealing at a higher temperature (1650 °C) under the Ar atmosphere rather than 1150 °C under UHV conditions [259]. The obtained wafer-scale monolayered graphene exhibited carrier mobility of 2000 cm^2/Vs at room temperature for a carrier density of ~10^{13} cm^2. This value is only five times lesser than the mechanically exfoliated graphene. Some other researchers have also reported the mechanisms and kinetics of epitaxial graphene growth on SiC [260, 261]. A schematic of the synthesis process is shown in Fig. 10.26 [262]. Epitaxial growth on SiC can be achieved by an additional supply of carbon without subliming

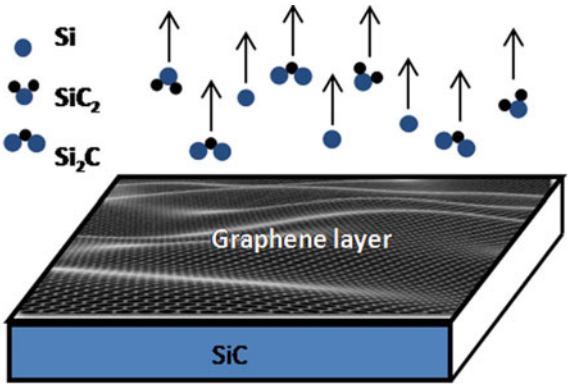

Fig. 10.26 Epitaxial graphene growth on silicon carbide wafer via sublimation of silicon atoms (Reproduced with permissions [262]. Copyright 2016, Wiley–VCH)

Si. This additional supply of carbon may be given by hydrocarbon gas decomposition or by sublimation of solid carbon source in molecular beam epitaxy [263]. Apart from SiC, other carbides have been exploited early on to fabricate supported graphene. Successful preparation of graphene monolayers has been achieved on the (100), (111) and (410) surfaces of titanium and the (111) faces of tantalum by decomposition of ethylene gas [264]. Interestingly the morphology of the TiC faces determines the graphene structure. In particular, monolayer graphene nanoribbons were obtained on the 0.886 nm-wide terraces of TiC(410), while large monolayer crystallites were formed on terrace-free TiC (111). It should be noted that SiC is a wide bandgap semiconductor and no transfer of graphene is required on other substrates, which allows very easy fabrication of the devices. Therefore, epitaxially grown graphene is very promising for the mainstream electronics industry. However, this technique has some limitations for large-scale fabrication due to the high cost of single-crystal SiC wafers. Another challenge in this technique is the uniform growth of large-area single-layer graphene.

Graphene has been considered as one of the most promising materials for a wide range of applications not only because of its excellent electronic, optical, thermal and mechanical properties but also due to its easy synthesis and handling for technology transfer. The unique properties of graphene make it useful in most areas including environment, sensors, solar cells, supercapacitor, batteries, fuel cell and catalysis [265–267]. Chemical exfoliation and reduction procedure can produce a single layer on a large scale which is mainly required for most industrial applications. Nevertheless, CVD produced graphene has shown promising results for electronic/device applications.

Conclusion

This chapter gives clear indications on the synthesis of various carbon materials Several synthesis methods like soot, arc discharge, chemical vapor deposition, mechanical and chemical exfoliation, electrospinning and epitaxial growth have been highlighted. The growth mechanism for all carbon materials has been discussed. Among carbon-based materials, graphene is a newly invented material with ultimate properties. Therefore, high-quality graphene synthesis by various routes in important for different kinds of applications.

References

1. Andresen JM (2001) Graphite and precursors, world of carbon. In: Delhaès P (ed) vol 1. Gordon and Breach Publishers, Amsterdam, p 297. ISBN 90-5699-228-7. $85, Energy & Fuels 16(1):218-218
2. Vavilov VS (1997) Diamond in solid state electronics. Phys Usp 40:15–20
3. Wild C, Müller-Sebert W, Eckermann T, Koidl P (1991) Polycrystalline diamond films for optical applications. In: Tzeng Y, Yoshikawa M, Murakawa M, Feldman A (eds) Materials science monographs. Elsevier, pp 197–205
4. Kroto HW, Heath JR, O'Brien SC, Curl RF, Smalley RE (1985) C60: Buckminsterfullerene. Nature 318(6042):162–163

5. Iijima S (1991) Helical microtubules of graphitic carbon. Nature 354(6348):56–58
6. Prasek J, Drbohlavova J, Chomoucka J, Hubalek J, Jasek O, Adam V, Kizek R (2011) Methods for carbon nanotubes synthesis—review. J Mater Chem 21(40):15872–15884
7. De Volder MFL, Tawfick SH, Baughman RH, Hart AJ (2013) Carbon nanotubes: present and future commercial applications. Science 339(6119):535–539
8. Yadav D, Amini F, Ehrmann A (2020) Recent advances in carbon nanofibers and their applications – a review. Euro Polymer J 138:109963
9. Novoselov KS, Geim AK, Morozov SV, Jiang D, Zhang Y, Dubonos SV, Grigorieva IV, Firsov AA (2004) Electric field effect in atomically thin carbon films. Science 306(5696):666–669
10. Allen MJ, Tung VC, Kaner RB (2010) Honeycomb carbon: a review of graphene. Chem Rev 110(1):132–145
11. Kumar P (2019) Ultrathin 2D nanomaterials for electromagnetic interference shielding. Adv Mater Interfaces 6(24):1901454
12. Yadav MK, Panwar N, Singh S, Kumar P (2020) Preheated self-aligned graphene oxide for enhanced room temperature hydrogen storage. Int J Hydrogen Energy 45(38):19561–19566
13. Vikas, Yadav MK, Kumar P, Verma RK (2020) Detection of adulteration in pure honey utilizing Ag-graphene oxide coated fiber optic SPR probes. Food Chem 332:127346
14. Avouris P, Dimitrakopoulos C (2012) Graphene: synthesis and applications. Mater Today 15(3):86–97
15. Edwards RS, Coleman KS (2013) Graphene synthesis: relationship to applications. Nanoscale 5(1):38–51
16. Baddour CE, Fadlallah F, Nasuhoglu D, Mitra R, Vandsburger L, Meunier J-L (2009) A simple thermal CVD method for carbon nanotube synthesis on stainless steel 304 without the addition of an external catalyst. Carbon 47(1):313–318
17. Ritter S (2001) PENCILS & PENCIL LEAD. Chem Eng News Arch 79(42):35
18. Arregui-Mena JD, Bodel W, Worth RN, Margetts L, Mummery PM (2016) Spatial variability in the mechanical properties of Gilsocarbon. Carbon 110:497–517
19. Hummers WS, Offeman RE (1958) Preparation of graphitic oxide. J Am Chem Soc 80(6):1339–1339
20. Kawamoto M, He P, Ito Y (2017) Green processing of carbon nanomaterials. Adv Mater 29(25):1602423
21. Strong HM (1989) Strong, early diamond making at general electric. Am J Phys 57:794
22. Gogotsi YG, Kofstad P, Yoshimura M, Nickel KG (1996) Formation of sp3-bonded carbon upon hydrothermal treatment of SiC. Diam Relat Mater 5(2):151–162
23. Shenderova OA, Shames AI, Nunn NA, Torelli MD, Vlasov I, Zaitsev A (2019) Review article: synthesis, properties, and applications of fluorescent diamond particles. J Vacuum Sci Technol B 37(3):030802
24. Schwander M, Partes K (2011) A review of diamond synthesis by CVD processes. Diam Relat Mater 20(9):1287–1301
25. Kobashi K, Nishimura K, Kawate Y, Horiuchi T (1988) Synthesis of diamonds by use of microwave plasma chemical-vapor deposition: morphology and growth of diamond films. Phys Rev B 38(6):4067–4084
26. Liu X, Jia X, Zhang Z, Li Y, Hu M, Zhou Z, Ma H-A (2011) Crystal growth and characterization of diamond from carbonyl iron catalyst under high pressure and high temperature conditions. Cryst Growth Des 11(9):3844–3849
27. Palyanov YN, Kupriyanov IN, Borzdov YM, Sokol AG, Khokhryakov AF (2009) Diamond crystallization from a sulfur−carbon system at HPHT conditions. Cryst Growth Des 9(6):2922–2926
28. Palyanov YN, Kupriyanov IN, Borzdov YM, Khokhryakov AF, Surovtsev NV (2016) High-pressure synthesis and characterization of Ge-doped single crystal diamond. Cryst Growth Des 16(6):3510–3518
29. Palyanov YN, Kupriyanov IN, Sokol AG, Khokhryakov AF, Borzdov YM (2011) Diamond growth from a phosphorus–carbon system at high pressure high temperature conditions. Cryst Growth Des 11(6):2599–2605

30. Hu M, Ma H-A, Yan B, Li Y, Li Z, Zhou Z, Jia X (2012) Multiseed method for high quality sheet cubic diamonds synthesis: an effective solution for scientific research and commercial production. Cryst Growth Des 12(1):518–521
31. Ashfold MNR, May PW, Rego CA, Everitt NM (1994) Thin film diamond by chemical vapour deposition methods. Chem Soc Rev 23(1):21–30
32. Holland L, Ojha SM (1979) The growth of carbon films with random atomic structure from ion impact damage in a hydrocarbon plasma. Thin Solid Films 58(1):107–116
33. Angus JC, Will HA, Stanko WS (1968) Growth of diamond seed crystals by vapor deposition. J Appl Phys 39(6):2915–2922
34. Rakha SA, Xintai Z, Zhu D, Guojun Y (2010) Effects of N2 addition on nanocrystalline diamond films by HFCVD in Ar/CH4 gas mixture. Curr Appl Phys 10(1):171–175
35. Kondoh E, Ohta T, Mitomo T, Ohtsuka K (1991) Determination of activation energies for diamond growth by an advanced hot filament chemical vapor deposition method. Appl Phys Lett 59(4):488–490
36. Park SS, Lee JY (1991) Synthesis of diamond films on titanium substrates by hot-filament chemical vapor deposition. J Appl Phys 69(4):2618–2622
37. Kobayashi T, Hirakuri KK, Mutsukura N, Machi Y (1999) Synthesis of CVD diamond at atmospheric pressure using the hot-filament CVD method. Diam Relat Mater 8(6):1057–1060
38. Ali M, Ürgen M (2012) Simultaneous growth of diamond and nanostructured graphite thin films by hot-filament chemical vapor deposition. Solid State Sci 14(1):150–154
39. Hirose Y, Amanuma S, Komaki K (1990) The synthesis of high-quality diamond in combustion flames. J Appl Phys 68(12):6401–6405
40. Kamo M, Sato Y, Matsumoto S, Setaka N (1983) Diamond synthesis from gas phase in microwave plasma. J Cryst Growth 62(3):642–644
41. Matsumoto S (1985) Chemical vapour deposition of diamond in RF glow discharge. J Mater Sci Lett 4(5):600–602
42. Kawarada H, Mar KS, Hiraki A (1987) Large area chemical vapour deposition of diamond particles and films using magneto-microwave plasma. Jpn J Appl Phys 26(Part 2, No. 6):L1032–L1034
43. Salvadori MC, Ager JW III, Brown IG, Krishnan KM (1991) Diamond synthesis by microwave plasma chemical vapor deposition using graphite as the carbon source. Appl Phys Lett 59(19):2386–2388
44. Katsumata S (1992) Diamond synthesis by the microwave plasma chemical vapor deposition method using the pretreated carbon dioxide and hydrogen mixed-gas system. Jpn J Appl Phys 31(Part 1, No. 3):868–871
45. Tiwari RN, Tiwari JN, Chang L, Yoshimura M (2011) Enhanced nucleation and growth of diamond film on Si by CVD using a chemical precursor. J Phys Chem C 115(32):16063–16073
46. Liang Q, Yan C-S, Lai J, Meng Y-F, Krasnicki S, Shu H, Mao H-K, Hemley RJ (2014) Large area single-crystal diamond synthesis by 915 MHz microwave plasma-assisted chemical vapor deposition. Cryst Growth Des 14(7):3234–3238
47. Palnichenko AV, Jonas AM, Charlier JC, Aronin AS, Issi JP (1999) Diamond formation by thermal activation of graphite. Nature 402(6758):162–165
48. Szymanski A, Abgarowicz E, Bakon A, Niedbalska A, Salacinski R, Sentek J (1995) Diamond formed at low pressures and temperatures through liquid-phase hydrothermal synthesis. Diam Relat Mater 4(3):234–235
49. Gogotsi YG, Yoshimura M (1994) Formation of carbon films on carbides under hydrothermal conditions. Nature 367(6464):628–630
50. Lou Z, Chen Q, Zhang Y, Wang W, Qian Y (2003) Diamond formation by reduction of carbon dioxide at low temperatures. J Am Chem Soc 125(31):9302–9303
51. Narayan RJ, Boehm RD, Sumant AV (2011) Medical applications of diamond particles & surfaces. Mater Today 14(4):154–163
52. Krätschmer W, Lamb LD, Fostiropoulos K, Huffman DR (1990) Solid C60: a new form of carbon. Nature 347(6291):354–358

53. Huczko A, Lange H, Byszewski P, Poplawska M, Starski A (1997) Fullerene formation in carbon arc: electrode gap dependence and plasma spectroscopy. J Phys Chem A 101(7):1267–1269
54. Howard JB, McKinnon JT, Makarovsky Y, Lafleur AL, Johnson ME (1991) Fullerenes C60 and C70 in flames. Nature 352(6331):139–141
55. McKinnon JT, Bell WL, Barkley RM (1992) Combustion synthesis of fullerenes. Combust Flame 88(1):102–112
56. Reilly PTA, Gieray RA, Whitten WB, Ramsey JM (2000) Fullerene evolution in flame-generated soot. J Am Chem Soc 122(47):11596–11601
57. Chow L, Wang H, Kleckley S, Daly TK, Buseck PR (1995) Fullerene formation during production of chemical vapor deposited diamond. Appl Phys Lett 66(4):430–432
58. Kleckley S, Wang H, Oladeji I, Chow L, Daly TK, Buseck PR, Solouki T, Marshall A (1997) Fullerenes and polymers produced by the chemical vapor deposition method, synthesis and characterization of advanced materials. American Chemical Society, pp 51–60
59. Inomata K, Aoki N, Koinuma H (1994) Production of fullerenes by low temperature plasma chemical vaper deposition under atmospheric pressure. Jpn J Appl Phys 33(Part 2, No. 2A):L197–L199
60. Wang X, Xu B, Liu X, Guo J, Ichinose H (2006) Synthesis of Fe-included onion-like fullerenes by chemical vapor deposition. Diam Relat Mater 15(1):147–150
61. Churilov GN (2008) Synthesis of fullerenes and other nanomaterials in arc discharge, Fullerenes. Nanotubes Carbon Nanostruct 16(5–6):395–403
62. Lieber CM, Chen CC (1994) Preparation of fullerenes and fullerene-based materials. Solid State Phys Adv Res Appl 109–148
63. Caraman M, Lazar JB, Stamate M, La (2008) ARC DISCHARGE INSTALATION FOR FULLERENE PRODUCTION
64. Sundar CS, Bharathi A, Hariharan Y, Janaki J, Sankara Sastry V, Radhakrishnan TS (1992) Thermal decomposition of C60. Solid State Commun 84(8):823–826
65. Wang CZ, Xu CH, Chan CT, Ho KM (1992) Disintegration and formation of fullerene (C60). J Phys Chem 96(9):3563–3565
66. Taylor R, Parsons JP, Avent AG, Rannard SP, Dennis TJ, Hare JP, Kroto HW, Walton DRM (1991) Degradation of C60 by light. Nature 351(6324):277–277
67. Carbon arc solar simulator. Appl Opt 30(10):1290–1293
68. Meubus P (1986) Effects of UV light irradiation on propane in an argon plasma. Plasma Chem Plasma Process 6(2):143–157
69. Parker DH, Chatterjee K, Wurz P, Lykke KR, Pellin MJ, Stock LM, Hemminger JC (1992) Fullerenes and giant fullerenes: synthesis, separation, and mass spectrometric characterization. Carbon 30(8):1167–1182
70. Scrivens WA, Tour JM (1992) Synthesis of gram quantities of C60 by plasma discharge in a modified round-bottomed flask. Key parameters for yield optimization and purification. J Org Chem 57(25):6932–6936
71. Lamb LD, Huffman DR (1993) Fullerene production. J Phys Chem Solids 54(12):1635–1643
72. Yu T, Li J-C, Cai F-X, Fan X-J (1994) Chen M-SYR, Wu W, Xiao N, Tian D-C, Zhao W-K, Fang Y-L, Kuang A-Y. Fullerene Sci Technol 2(3):223–231
73. Koprinarov N, Marinov M, Konstantinova M, Ranguelov B (2000) Fullerene structure synthesis by DC arc discharge in ferrocene vapours. Vacuum 58(2):208–214
74. Chibante LPF, Thess A, Alford JM, Diener MD, Smalley RE (1993) Solar generation of the fullerenes. J Phys Chem 97(34):8696–8700
75. Brusatin G, Signorini R (2002) Linear and nonlinear optical properties of fullerenes in solid state materials. J Mater Chem 12(7):1964–1977
76. He YJ, Chen H-Y, Hou JH, Li YF (2010) Indene−C60 bisadduct: a new acceptor for high-performance polymer solar cells. J Am Chem Soc 132(4):1377–1382
77. Peng P, Li F-F, Neti VSPK, Metta-Magana AJ, Echegoyen L (2014) Design, synthesis, and X-ray crystal structure of a fullerene-linked metal–organic framework. Angew Chem Int Ed 53(1):160–163

78. Figueira-Duarte TM, Clifford J, Amendola V, Gegout A, Olivier J, Cardinal F, Meneghetti M, Armaroli N, Nierengarten J-F (2006) Synthesis and excited state properties of a fullerene derivative bearing a star-shaped multi-photon absorption chromophore. Chem Commun 19:2054–2056
79. Garg V, Kodis G, Chachisvilis M, Hambourger M, Moore AL, Moore TA, Gust D (2011) Conformationally constrained macrocyclic diporphyrin−fullerene artificial photosynthetic reaction center. J Am Chem Soc 133(9):2944–2954
80. Sawamura M, Kawai K, Matsuo Y, Kanie K, Kato T, Nakamura E (2002) Stacking of conical molecules with a fullerene apex into polar columns in crystals and liquid crystals. Nature 419(6908):702–705
81. Inglis AJ, Pierrat P, Muller T, Bräse S, Barner-Kowollik C (2010) Well-defined star shaped polymer-fullerene hybrids via click chemistry. Soft Matter 6(1):82–84
82. Nava MG, Setayesh S, Rameau A, Masson P, Nierengarten J-F (2002) Fullerene-functionalized polyesters: synthesis, characterization and incorporation in photovoltaic cells. New J Chem 26(11):1584–1589
83. Radushkevich LV, Lukyanovich VM (1952) The structure of carbon forming in thermal decomposition of carbon monoxide on an iron catalyst. Russ J Phys Chem 26:88–95
84. Oberlin A, Endo M, Koyama T (1976) Filamentous growth of carbon through benzene decomposition. J Cryst Growth 32(3):335–349
85. Iijima S, Ichihashi T (1993) Single-shell carbon nanotubes of 1-nm diameter. Nature 363(6430):603–605
86. Dresselhaus MS, Dresselhaus G, Saito R (1995) Physics of carbon nanotubes. Carbon 33(7):883–891
87. Arora N, Sharma NN (2014) Arc discharge synthesis of carbon nanotubes: comprehensive review. Diam Relat Mater 50:135–150
88. Seraphin S, Zhou D, Jiao J, Minke MA, Wang S, Yadav T, Withers JC (1994) Catalytic role of nickel, palladium, and platinum in the formation of carbon nanoclusters. Chem Phys Let 217(3):191–195
89. Saito Y, Nishikubo K, Kawabata K, Matsumoto T (1996) Carbon nanocapsules and single-layered nanotubes produced with platinum-group metals (Ru, Rh, Pd, Os, Ir, Pt) by arc discharge. J Appl Phys 80(5):3062–3067
90. Wang H, Li Z, Inoue S, Ando Y (2010) Influence of mo on the growth of single-walled carbon nanotubes in arc discharge. J Nanosci Nanotechnol 10(6):3988–3993
91. Xing G, Jia S, Xing J, Shi Z (2007) Analysis of the carbon nano-structures formation in liquid arcing. Plasma Sci Technol 9:770
92. Shi Z, Lian Y, Liao F, Zhou X, Gu Z, Zhang Y, Iijima S (1999) Purification of single-wall carbon nanotubes. Solid State Commun 112(1):35–37
93. Maschmann MR, Franklin AD, Amama PB, Zakharov DN, Stach EA, Sands TD, Fisher TS (2006) Vertical single- and double-walled carbon nanotubes grown from modified porous anodic alumina templates. Nanotechnology 17(15):3925–3929
94. Hutchison JL, Kiselev NA, Krinichnaya EP, Krestinin AV, Loutfy RO, Morawsky AP, Muradyan VE, Obraztsova ED, Sloan J, Terekhov SV, Zakharov DN (2001) Double-walled carbon nanotubes fabricated by a hydrogen arc discharge method. Carbon 39(5):761–770
95. Sugai T, Yoshida H, Shimada T, Okazaki T, Shinohara H, Bandow S (2003) New synthesis of high-quality double-walled carbon nanotubes by high-temperature pulsed arc discharge. Nano Letter 3(6):769–773
96. Huang HJ, Kajiura H, Tsutsui S, Murakami Y, Ata M (2003) High-quality double-walled carbon nanotube super bundles grown in a hydrogen-free atmosphere. J Phys Chem B 107(34):8794–8798
97. Liu Q, Ren W, Li F, Cong H, Cheng H-M (2007) Synthesis and high thermal stability of double-walled carbon nanotubes using nickel formate dihydrate as catalyst precursor. J Phys Chem C 111(13):5006–5013
98. Li L, Li F, Liu C, Cheng H-M (2005) Synthesis and characterization of double-walled carbon nanotubes from multi-walled carbon nanotubes by hydrogen-arc discharge. Carbon 43(3):623–629

99. Wang M, Zhao XL, Ohkohchi M, Ando Y (1996) Carbon nanotubes grown on the surface of cathode deposit by arc discharge. Fullerene Sci Technol 4(5):1027–1039
100. Parkansky N, Boxman RL, Alterkop B, Zontag I, Lereah Y, Barkay Z (2004) Single-pulse arc production of carbon nanotubes in ambient air. J Phys D Appl Phys 37(19):2715–2719
101. Tsai YY, Su JS, Su CY, He WH (2009) Production of carbon nanotubes by single-pulse discharge in air. J Mater Process Technol 209(9):4413–4416
102. Sornsuwit N, Maaithong W (2008) Study of multi-walled carbon nanotube synthesis using liquid nitrogen and post-process filtration. Int J Precis Eng Manuf 9(3):18–21
103. Montoro LA, Lofrano RCZ, Rosolen JM (2005) Synthesis of single-walled and multi-walled carbon nanotubes by arc-water method. Carbon 43(1):200–303
104. Jung SH, Kim MR, Jeong SH, Kim SU, Lee OJ, Lee KH, Suh JH, Park CK (2003) High-yield synthesis of multi-walled carbon nanotubes by arc discharge in liquid nitrogen. Appl Phys A Mater Sci Process 76(2):285–286
105. Guo J, Wang X, Yao Y, Yang X, Liu X, Xu B (2007) Structure of nanocarbons prepared by arc discharge in water. Mater Chem Phys 105(2):175–178
106. Guo T, Nikolaev P, Thess A, Colbert DT, Smalley RE (1995) Catalytic growth of single-walled manotubes by laser vaporization. Chem Phys Lett 243(1):49–54
107. Yudasaka M, Yamada R, Sensui N, Wilkins T, Ichihashi T, Iijima S (1999) Mechanism of the effect of NiCo, Ni and Co catalysts on the yield of single-wall carbon nanotubes formed by pulsed Nd:YAG laser ablation. J Phys Chem 103(30):6224–6229
108. Thess A, Lee R, Nikolaev P, Dai H, Petit P, Robert J, Xu C, Lee YH, Kim SG, Linzler AG, Colbert DT, Scuseria GE, Tomanek D, Fischer JE, Smalley RE (1996) Crystalline ropes of metallic carbon nanotubes. Science 273(5274):483
109. Bandow S, Asaka S, Saito Y, Rao AM, Grigorian L, Richter E, Eklund PC (1998) Effect of the growth temperature on the diameter distribution and chirality of single-wall carbon nanotubes. Phys Rev Lett 80(17):3779–3782
110. Maser WK, Muñoz E, Benito AM, Martínez MT, de la Fuente GF, Maniette Y, Anglaret E, Sauvajol JL (1998) Production of high-density single-walled nanotube material by a simple laser-ablation method. Chem Phys Lett 292(4):587–593
111. Braidy N, El Khakani MA, Botton GA (2002) Single-wall carbon nanotubes synthesis by means of UV laser vaporization. Chem Phys Lett 354(1):88–92
112. Chen M, Chen C-M, Koo H-S, Chen C-F (2003) Catalyzed growth model of carbon nanotubes by microwave plasma chemical vapor deposition using CH4 and CO2 gas mixtures. Diam Relat Mater 12(10):1829–1835
113. Purohit R, Purohit K, Rana S, Rana RS, Patel V (2014) Carbon nanotubes and their growth methods. Proc Mater Sci 6:716–728
114. Bonaccorso F, Bongiorno C, Fazio B, Gucciardi PG, Maragò OM, Morone A, Spinella C (2007) Pulsed laser deposition of multiwalled carbon nanotubes thin films. Appl Surf Sci 254(4):1260–1263
115. Muñoz E, Maser WK, Benito AM, de la Fuente GF, Martínez MT (1999) Single-walled carbon nanotubes produced by laser ablation under different inert atmospheres. Synth Met 103(1):2490–2491
116. Muñoz E, Maser WK, Benito AM, Martínez MT, de la Fuente GF, Maniette Y, Righi A, Anglaret E, Sauvajol JL (2000) Gas and pressure effects on the production of single-walled carbon nanotubes by laser ablation. Carbon 38(10):1445–1451
117. Hiura H, Ebbesen TW, Tanigaki K (1995) Opening and purification of carbon nanotubes in high yields, Adv Mater 7(3):275–276
118. Varshney D, Weiner BR, Morell G (2010) Growth and field emission study of a monolithic carbon nanotube/diamond composite. Carbon 48(12):3353–3358
119. Tempel H, Joshi R, Schneider JJ (2010) Ink jet printing of ferritin as method for selective catalyst patterning and growth of multiwalled carbon nanotubes. Mater Chem Phys 121(1):178–183
120. Patole SP, Alegaonkar PS, Lee H-C, Yoo J-B (2008) Optimization of water assisted chemical vapor deposition parameters for super growth of carbon nanotubes. Carbon 46(14):1987–1993

121. Brown B, Parker CB, Stoner BR, Glass JT (2011) Growth of vertically aligned bamboo-like carbon nanotubes from ammonia/methane precursors using a platinum catalyst. Carbon 49(1):266–274
122. Andrews R, Jacques D, Qian D, Rantell T (2002) Multiwall carbon nanotubes: synthesis and application. Acc Chem Res 35(12):1008–1017
123. Dumpala S, Jasinski JB, Sumanasekera GU, Sunkara MK (2011) Large area synthesis of conical carbon nanotube arrays on graphite and tungsten foil substrates. Carbon 49(8):2725–2734
124. Ramesh P, Okazaki T, Taniguchi R, Kimura J, Sugai T, Sato K, Ozeki Y, Shinohara H (2005) Selective chemical vapor deposition synthesis of double-wall carbon nanotubes on mesoporous silica. J Phys Chem B 109(3):1141–1147
125. Zhu J, Yudasaka M, Iijima S (2003) A catalytic chemical vapor deposition synthesis of double-walled carbon nanotubes over metal catalysts supported on a mesoporous material. Chem Phys Lett 380(5):496–502
126. Szabó A, Perri C, Csató A, Giordano G, Vuono D, Nagy JB (2010) Synthesis methods of carbon nanotubes and related materials. Materials 3(5):3092–3140
127. Xiang X, Zhang L, Hima HI, Li F, Evans DG (2009) Co-based catalysts from Co/Fe/Al layered double hydroxides for preparation of carbon nanotubes. Appl Clay Sci 42(3):405–409
128. Flahaut E, Laurent C, Peigney A (2005) Catalytic CVD synthesis of double and triple-walled carbon nanotubes by the control of the catalyst preparation. Carbon 43(2):375–383
129. Jiang Q, Song LJ, Yang H, He ZW, Zhao Y (2008) Preparation and characterization on the carbon nanotube chemically modified electrode grown in situ. Electrochem Commun 10(3):424–427
130. Lyu SC, Liu BC, Lee CJ, Kang HK, Yang C-W, Park CY (2003) High-quality double-walled carbon nanotubes produced by catalytic decomposition of benzene. Chem Mater 15(20):3951–3954
131. Tang N, Kuo W, Jeng C, Wang L, Lin K, Du Y (2010) Coil-in-coil carbon nanocoils: 11 gram-scale synthesis, single nanocoil electrical properties, and electrical contact improvement. ACS Nano 4(2):781–788
132. Liu Z, Jiao L, Yao Y, Xian X, Zhang J (2010) Aligned, ultralong single-walled carbon nanotubes: from synthesis, sorting, to electronic devices. Adv Mater 22(21):2285–2310
133. Zhang D, Yan T, Pan C, Shi L, Zhang J (2009) Carbon nanotube-assisted synthesis and high catalytic activity of CeO2 hollow nanobeads. Mater Chem Phys 113(2):527–530
134. Sano N, Ishimaru S, Tamaon H (2010) Synthesis of carbon nanotubes in graphite microchannels in gas-flow and submerged-in-liquid reactors. Mater Chem Phys 122(2):474–479
135. Lim S, Luo Z, Shen Z, Lin J (2010) Plasma-assisted synthesis of carbon nanotubes. Nanoscale Res Lett 5(9):1377
136. Kim SM, Gangloff L (2009) Growth of carbon nanotubes (CNTs) on metallic underlayers by diffusion plasma-enhanced chemical vapour deposition (DPECVD). Phys E 41(10):1763–1766
137. Vollebregt S, Derakhshandeh J, Ishihara R, Wu MY, Beenakker CIM (2010) Growth of high-density self-aligned carbon nanotubes and nanofibers using palladium catalyst. J Electron Mater 39(4):371–375
138. Häffner M, Schneider K, Schuster BE, Stamm B, Latteyer F, Fleischer M, Burkhardt C, Chassé T, Stett A, Kern DP (2010) Plasma enhanced chemical vapor deposition grown carbon nanotubes from ferritin catalyst for neural stimulation microelectrodes. Microelectron Eng 87(5):734–737
139. Rodriguez NM, Chambers A, Baker RTK (1995) Catalytic engineering of carbon nanostructures. Langmuir 11(10):3862–3866
140. Zhou Z, Lai C, Zhang L, Qian Y, Hou H, Reneker DH, Fong H (2009) Development of carbon nanofibers from aligned electrospun polyacrylonitrile nanofiber bundles and characterization of their microstructural, electrical, and mechanical properties. Polymer 50(13):2999–3006
141. Motojima S, Kawaguchi M, Nozaki K, Iwanaga H (1990) Growth of regularly coiled carbon filaments by Ni catalyzed pyrolysis of acetylene, and their morphology and extension characteristics. Appl Phys Lett 56(4):321–323

142. Motojima S, Chen Q (1999) Three-dimensional growth mechanism of cosmo-mimetic carbon microcoils obtained by chemical vapor deposition. J Appl Phys 85(7):3919–3921
143. Zhang M, Nakayama Y, Pan L (2000) Synthesis of carbon tubule nanocoils in high yield using iron-coated indium tin oxide as catalyst. Jpn J Appl Phys 39(Part 2, No. 12A):L1242–L1244
144. Raghubanshi H, Dikio ED (2015) Synthesis of helical carbon fibers and related materials: a review on the past and recent developments. Nanomaterials (Basel, Switzerland) 5(2):937–968
145. Song H, Shen W (2014) Carbon nanofibers: synthesis and applications. J Nanosci Nanotechnol 14(2):1799–1810
146. Minea TM, Point S, Granier A, Touzeau M (2004) Room temperature synthesis of carbon nanofibers containing nitrogen by plasma-enhanced chemical vapor deposition. Appl Phys Lett 85(7):1244–1246
147. Zou J-z, Zeng X-r, Xiong X-b, Tang H-l, Li L, Liu Q, Li Z-q (2007) Preparation of vapor grown carbon fibers by microwave pyrolysis chemical vapor deposition. Carbon 45(4):828–832
148. Wen Y, Kok MDR, Tafoya JPV, Sobrido ABJ, Bell E, Gostick JT, Herou S, Schlee P, Titirici M-M, Brett DJL, Shearing PR, Jervis R (2021) Electrospinning as a route to advanced carbon fibre materials for selected low-temperature electrochemical devices: a review. J Energ Che 59:492–529
149. Huang C, Soenen SJ, Rejman J, Lucas B, Braeckmans K, Demeester J, De Smedt SC (2011) Stimuli-responsive electrospun fibers and their applications. Chem Soc Rev 40(5):2417–2434
150. Ding B, Wang M, Wang X, Yu J, Sun G (2010) Electrospun nanomaterials for ultrasensitive sensors. Mater Today 13(11):16–27
151. Inagaki M, Yang Y, Kang F (2012) Carbon nanofibers prepared via electrospinning. Adv Mater 24(19):2547–2566
152. Zhang L, Aboagye A, Kelkar A, Lai C, Fong H (2014) A review: carbon nanofibers from electrospun polyacrylonitrile and their applications. J Mater Sci 9(2):463–480
153. Qing-qiang K, Mang-guo Y, Cheng-meng C, Yong-gang Y (2012) Preparation and characterization of graphene-reinforced polyacrylonitrile-based carbon nanofibers. New Carbon Mater 27(3):188
154. Zhang L, Hsieh Y-L (2009) Carbon nanofibers with nanoporosity and hollow channels from binary polyacrylonitrile systems. Eur Polym J 45(1):47–56
155. Kim C, Yang KS, Kojima M, Yoshida K, Kim YJ, Kim YA, Endo M (2006) Fabrication of electrospinning-derived carbon nanofiber webs for the anode material of lithium-ion secondary batteries. Adv Func Mater 16(18):2393–2397
156. Zussman E, Chen X, Ding W, Calabri L, Dikin DA, Quintana JP, Ruoff RS (2005) Mechanical and structural characterization of electrospun PAN-derived carbon nanofibers. Carbon 43(10):2175–2185
157. Hou H, Ge JJ, Zeng J, Li Q, Reneker DH, Greiner A, Cheng SZD (2005) Electrospun polyacrylonitrile nanofibers containing a high concentration of well-aligned multiwall carbon nanotubes. Chem Mater 17(5):967–973
158. Ko F, Gogotsi Y, Ali A, Naguib N, Ye H, Yang GL, Li C, Willis P (2003) Electrospinning of continuous carbon nanotube-filled nanofiber yarns. Adv Mater 15(14):1161–1165
159. Geim AK, Novoselov KS (2007) The rise of graphene. Nat Mater 6(3):183–191
160. Morozov SV, Novoselov KS, Katsnelson MI, Schedin F, Elias DC, Jaszczak JA, Geim AK (2008) Giant intrinsic carrier mobilities in graphene and its bilayer. Phys Rev Lett 100(1):016602
161. Ferrari AC, Bonaccorso F, Fal'ko V, Novoselov KS, Roche S, Bøggild P, Borini S, Koppens FHL, Palermo V, Pugno N, Garrido JA, Sordan R, Bianco A, Ballerini L, Prato M, Lidorikis E, Kivioja J, Marinelli C, Ryhänen T, Morpurgo A, Coleman JN, Nicolosi V, Colombo L, Fert A, Garcia-Hernandez M, Bachtold A, Schneider GF, Guinea F, Dekker C, Barbone M, Sun Z, Galiotis C, Grigorenko AN, Konstantatos G, Kis A, Katsnelson M, Vandersypen L, Loiseau A, Morandi V, Neumaier D, Treossi E, Pellegrini V, Polini M, Tredicucci A, Williams GM, Hee Hong B, Ahn J-H, Min Kim J, Zirath H, van Wees BJ, van der Zant H, Occhipinti L,

Di Matteo A, Kinloch IA, Seyller T, Quesnel E, Feng X, Teo K, Rupesinghe N, Hakonen P, Neil SRT, Tannock Q, Löfwander T, Kinaret J (2015) Science and technology roadmap for graphene, related two-dimensional crystals, and hybrid systems. Nanoscale 7(11):4598–4810
162. Kumar P, Yu S, Shahzad F, Hong SM, Kim Y-H, Koo CM (2016) Ultrahigh electrically and thermally conductive self-aligned graphene/polymer composites using large-area reduced graphene oxides. Carbon 101:120–128
163. Kumar P, Narayan Maiti U, Sikdar A, Kumar Das T, Kumar A, Sudarsan V (2019) Recent advances in polymer and polymer composites for electromagnetic interference shielding: review and future prospects. Polym Rev 59(4):687–738
164. Kumar P, Shahzad F, Hong SM, Koo CM (2016) A flexible sandwich graphene/silver nanowires/graphene thin film for high-performance electromagnetic interference shielding. RSC Advances 6(103):101283–101287
165. Kumar P, Kumar A, Cho KY, Das TK, Sudarsan V (2017) An asymmetric electrically conducting self-aligned graphene/polymer composite thin film for efficient electromagnetic interference shielding. AIP Advances 7(1):015103
166. Kumar P, Yadav MK, Panwar N, Kumar A, Singhal R (2019) Temperature dependent thermal conductivity of free-standing reduced graphene oxide/poly (vinylidene fluoride-co-hexafluoropropylene) composite thin film. Mater Res Express 6(11):115604
167. Bolotin KI, Sikes KJ, Jiang Z, Klima M, Fudenberg G, Hone J, Kim P, Stormer HL (2008) Ultrahigh electron mobility in suspended graphene. Solid State Commun 146(9):351–355
168. Soldano C, Mahmood A, Dujardin E (2010) Production, properties and potential of graphene. Carbon 48(8):2127–2150
169. Hernandez Y, Nicolosi V, Lotya M, Blighe FM, Sun ZY, De S, McGovern IT, Holland B, Byrne M, Gun'ko YK, Boland JJ, Niraj P, Duesberg G, Krishnamurthy S, Goodhue R, Hutchison J, Scardaci V, Ferrari AC, Coleman JN (2008) High-yield production of graphene by liquid-phase exfoliation of graphite. Nat Nanotechnol 3(9):563–568
170. Blake P, Brimicombe PD, Nair RR, Booth TJ, Jiang D, Schedin F, Ponomarenko LA, Morozov SV, Gleeson HF, Hill EW, Geim AK, Novoselov KS (2008) Graphene-based liquid crystal device. Nano Lett 8:1704–1708
171. Hernandez Y, Lotya M, Rickard D, Bergin SD, Coleman JN (2010) Measurement of multicomponent solubility parameters for graphene facilitates solvent discovery. Langmuir 26(5):3208–3213
172. Vallés C, Drummond C, Saadaoui H, Furtado CA, He M, Roubeau O, Ortolani L, Monthioux M, Pénicaud A (2008) Solutions of negatively charged graphene sheets and ribbons. J Am Chem Soc 130(47):15802–15804
173. Behabtu N, Lomeda JR, Green MJ, Higginbotham AL, Sinitskii A, Kosynkin DV, Tsentalovich D, Parra-Vasquez ANG, Schmidt J, Kesselman E, Cohen Y, Talmon Y, Tour JM, Pasquali M (2010) Spontaneous high-concentration dispersions and liquid crystals of graphene. Nat Nanotechnol 5(6):406–411
174. Lotya M, Hernandez Y, King PJ, Smith RJ, Nicolosi V, Karlsson LS, Blighe FM, De S, Wang ZM, McGovern IT, Duesberg GS, Coleman JN (2009) Liquid phase production of graphene by exfoliation of graphite in surfactant/water solutions. J Am Chem Soc 131(10):3611–3620
175. Lotya M, King P, Khan U, De S, Coleman JN (2010) Coleman, high-concentration, surfactant-stabilized graphene dispersions. ACS Nano 4(6):3155–3162
176. Parvez K, Wu Z-S, Li R, Liu X, Graf R, Feng X, Mìllen K (2014) Exfoliation of graphite into graphene in aqueous solutions of inorganic salts. J Am Chem Soc 136(16):6083–6091
177. Huang X, Qi X, Boey F, Zhang H (2012) Graphene-based composites. Chem Soc Rev 41(2):666–686
178. Low CTJ, Walsh FC, Chakrabarti MH, Hashim MA, Hussain MA (2013) Electrochemical approaches to the production of graphene flakes and their potential applications. Carbon 54:1–21
179. Su C-Y, Lu A-Y, Xu Y, Chen F-R, Khlobystov AN, Li L-J (2011) High-quality thin graphene films from fast electrochemical exfoliation. ACS Nano 5(3):2332–2339

180. Alanyalıoğlu M, Segura JJ, Oró-Solè J, Casañ-Pastor N (2012) The synthesis of graphene sheets with controlled thickness and order using surfactant-assisted electrochemical processes. Carbon 50(1):142–152
181. Wang J, Manga KK, Bao Q, Loh KP (2011) High-yield synthesis of few-layer graphene flakes through electrochemical expansion of graphite in propylene carbonate electrolyte. J Am Chem Soc 133(23):8888–8891
182. Ambrosi A, Pumera M (2015) Electrochemically exfoliated graphene and graphene oxide for energy storage and electrochemistry applications. Chem: Euro J 22(1):153–159
183. Brodie BC (2009) On the atomic weight of graphite. https://nbn-resolving.org/urn:nbn:de:hebis:30-1133136
184. Staudenmaier L (1898) Verfahren zur Darstellung der Graphitsäure. Ber Dtsch Chem Ges 31(2):1481–1487
185. Dreyer DR, Ruoff RS, Bielawski CW (2010) From conception to realization: an historial account of graphene and some perspectives for its future. Angew Chem Int Ed 49(49):9336–9344
186. Zhu Y, Murali S, Cai W, Li X, Suk JW, Potts JR, Ruoff RS (2010) Graphene and graphene oxide: synthesis, properties, and applications. Adv Mater 22(35):3906–3924
187. Stankovich S, Dikin DA, Dommett GHB, Kolhaas KM, Zimney EJ, Stach EA, Piner RD, Nguyen ST, Ruoff RS (2006) Graphene-based composite materials. Nature 442(7100):282–286
188. Kumar P, Shahzad F, Yu S, Hong SM, Kim Y-H, Koo CM (2015) Large-area reduced graphene oxide thin film with excellent thermal conductivity and electromagnetic interference shielding effectiveness. Carbon 94:494–500
189. Kumar P, Maiti UN, Lee KE, Kim SO (2014) Rheological properties of graphene oxide liquid crystal. Carbon 80:453–461
190. Cho KY, Yeom YS, Seo HY, Kumar P, Lee AS, Baek K-Y, Yoon HG (2017) Molybdenum-doped PdPt@Pt core–shell octahedra supported by ionic block copolymer-functionalized graphene as a highly active and durable oxygen reduction electrocatalyst. ACS Appl Mater Interfaces 9(2):1524–1535
191. Cho KY, Yeom YS, Seo HY, Kumar P, Lee AS, Baek K-Y, Yoon HG (2015) Ionic block copolymer doped reduced graphene oxide supports with ultra-fine Pd nanoparticles: strategic realization of ultra-accelerated nanocatalysis. J Mater Chem A 3(41):20471–20476
192. Cho KY, Seo HY, Yeom YS, Kumar P, Lee AS, Baek K-Y, Yoon HG (2016) Stable 2D-structured supports incorporating ionic block copolymer-wrapped carbon nanotubes with graphene oxide toward compact decoration of metal nanoparticles and high-performance nano-catalysis. Carbon 105:340–352
193. Dimiev AM, Tour JM (2014) Mechanism of graphene oxide formation. ACS Nano 8(3):3060–3068
194. Kim JE, Han TH, Lee SH, Kim JY, Ahn CW, Yun JM, Kim SO (2011) Graphene oxide liquid crystals. Angew Chem Int Ed 50(13):3043–3047
195. Ang PK, Wang S, Bao Q, Thong JTL, Loh KP (2009) High-throughput synthesis of graphene by intercalation−exfoliation of graphite oxide and study of ionic screening in graphene transistor. ACS Nano 3(11):3587–3594
196. Eigler S, Enzelberger-Heim M, Grimm S, Hofmann P, Kroener W, Geworski A, Dotzer C, Röckert M, Xiao J, Papp C, Lytken O, Steinrück H-P, Müller P, Hirsch A (2013) Wet chemical synthesis of graphene. Adv Mater 25(26):3583–3587
197. Peng L, Xu Z, Liu Z, Wei Y, Sun H, Li Z, Zhao X, Gao C (2015) An iron-based green approach to 1-h production of single-layer graphene oxide. Nat Commun 6:5716
198. Schniepp HC, Li J-L, McAllister MJ, Sai H, Herrera-Alonso M, Adamson DH, Prud'homme RK, Car R, Saville DA, Aksay IA (2006) Functionalized single graphene sheets derived from splitting graphite oxide. J Phys Chem B 110(17):8535–8539
199. McAllister MJ, Li JL, Adamson DH, Schniepp HC, Abdala AA, Liu J, Herrera-Alonso M, Milius DL, Car R, Prud'homme RK, Aksay IA (2007) Single sheet functionalized graphene by oxidation and thermal expansion of graphite. Chem Mater 19(18):4396–4404

200. Xin G, Sun H, Hu T, Fard HR, Sun X, Koratkar N, Borca-Tasciuc T, Lian J (2014) Large-area freestanding graphene paper for superior thermal management. Adv Mater 26(26):4521–4526
201. Kotov NA, Dékány I, Fendler JH (1996) Ultrathin graphite oxide–polyelectrolyte composites prepared by self-assembly: transition between conductive and non-conductive states. Adv Mater 8(8):637–641
202. Ambrosi A, Bonanni A, Sofer Z, Cross JS, Pumera M (2011) Electrochemistry at chemically modified graphenes. Chem: Euro J 17(38):10763–10770
203. Jin AS, Yanwu Z, Hwa LS, Meryl DS, Tryggvi E, Sungjin P, Aruna V, Jinho A, Rodney RS (2010) J Phys Chem Lett 1:1259
204. Ambrosi A, Pumera M (2013) Precise tuning of surface composition and electron-transfer properties of graphene oxide films through electroreduction. Chem Euro J 19(15):4748–4753
205. Hofmann U, König E (1937) Untersuchungen über Graphitoxyd. Zeitschrift für anorganische und allgemeine Chemie 234(4):311–336
206. Becerril HA, Mao J, Liu Z, Stoltenberg RM, Bao Z, Chen Y (2008) Evaluation of solution-processed reduced graphene oxide films as transparent conductors. ACS Nano 2(3):463–470
207. Park S, An J, Potts JR, Velamakanni A, Murali S, Ruoff RS (2011) Hydrazine-reduction of graphite- and graphene oxide. Carbon 49(9):3019–3023
208. Shin H-J, Sim KK, Benayad A, Yoon S-M, Park HK, Jung I-S, Jin MH, Jeong H-K, Kim JM, Choi J-Y, Lee YH (2009) Efficient reduction of graphite oxide by sodium borohydride and its effect on electrical conductance. Adv Func Mater 19(12):1987–1992
209. Pei S, Zhao J, Du J, Ren W, Cheng H-M (2010) Direct reduction of graphene oxide films into highly conductive and flexible graphene films by hydrohalic acids. Carbon 48(15):4466–4474
210. Gao W, Alemany LB, Ci LJ, Ajayan PM (2009) New insights into the structure and reduction of graphite oxide. Nat Chem 1(5):403–408
211. Wang G, Yang J, Park J, Gou X, Wang B, Liu H, Yao J (2008) Facile synthesis and characterization of graphene nanosheets. J Phys Chem C 112(22):8192–8195
212. Thakur S, Karak N (2012) Green reduction of graphene oxide by aqueous phytoextracts. Carbon 50(14):5331–5339
213. Akhavan O, Ghaderi E (2012) Escherichia coli bacteria reduce graphene oxide to bactericidal graphene in a self-limiting manner. Carbon 50(5):1853–1860
214. Cote LJ, Cruz-Silva R, Huang JX (2009) Flash reduction and patterning of graphite oxide and its polymer composite. J Am Chem Soc 131(31):11027–11032
215. Ji T, Hua Y, Sun M, Ma N (2013) The mechanism of the reaction of graphite oxide to reduced graphene oxide under ultraviolet irradiation. Carbon 54:412–418
216. Strong V, Dubin S, El-Kady MF, Lech A, Wang Y, Weiller BH, Kaner RB (2012) Patterning and electronic tuning of laser scribed graphene for flexible all-carbon devices. ACS Nano 6(2):1395–1403
217. Jiao L, Zhang L, Wang X, Diankov G, Dai H (2009) Narrow graphene nanoribbons from carbon nanotubes. Nature 458(7240):877–880
218. Higginbotham A, Kosynkin D, Sinitskii A, Sun Z, Tour JM (2010) Lower-defect graphene oxide nanoribbons from multiwalled carbon nanotubes. ACS Nano 4(4):2059–2069
219. Kosynkin DV, Higginbotham AL, Sinitskii A, Lomeda JR, Dimiev A, Price BK, Tour JM (2009) Longitudinal unzipping of carbon nanotubes to form graphene nanoribbons. Nature 458(7240):872–876
220. Wei D, Liu Y (2010) Controllable synthesis of graphene and its applications. Adv Mater 22:3225–3241
221. J. Li, S. Ye, T. Li, X. Li, X. Yang, S. Ding, Preparation of Graphene Nanoribbons (GNRs) as an Electronic Component with the Multi-walled Carbon Nanotubes (MWCNTs), Procedia Engineering 102 (2015):492–498
222. Xiao B, Li X, Li X, Wang B, Langford C, Li R, Sun X (2014) Graphene nanoribbons derived from the unzipping of carbon nanotubes: controlled synthesis and superior lithium storage performance. J Phys Chem C 118(2):881–890
223. Lim J, Maiti UN, Kim N-Y, Narayan R, Lee WJ, Choi DS, Oh Y, Lee JM, Lee GY, Kang SH, Kim H, Kim Y-H, Kim SO (2016) Dopant-specific unzipping of carbon nanotubes for intact crystalline graphene nanostructures. Nat Commun 7(1):10364

224. Elías AL, Botello-Méndez AR, Meneses-Rodríguez D, Jehová González V, Ramírez-González D, Ci L, Muñoz-Sandoval E, Ajayan PM, Terrones H, Terrones M (2009) Longitudinal cutting of pure and doped carbon nanotubes to form graphitic nanoribbons using metal clusters as nanoscalpels. Nano Lett 10(2):366–372
225. Li Y-S, Liao J-L, Wang S-Y, Chiang W-H (2016) Intercalation-assisted longitudinal unzipping of carbon nanotubes for green and scalable synthesis of graphene nanoribbons. Sci Rep 6(1):22755
226. Cano-Márquez A, Rodríguez-Macías F, Campos-Delgado J, Espinosa-González C, Tristán-López F, Ramírez-González D, Cullen D, Smith D, Terrones M, Vega-Cantú Y (2009) Ex-Mwnts: graphene sheets and ribbons produced by lithium intercalation and exfoliation of carbon nanotubes. Nano Letter 9:1527–1533
227. Kim WS, Moon SY, Bang SY, Choi BG, Ham H, Sekino T, Shim KB (2009) Fabrication of graphene layers from multiwalled carbon nanotubes using high dc pulse. Appl Phys Lett 95(8):083103
228. Wu JS, Pisula W, Mullen K (2007) Graphenes as potential material for electronics. Chem Rev 107:718–747
229. Proceedings of the Chemical Society (May) (1958) 125–156
230. Simpson CD, Brand JD, Berresheim AJ, Przybilla L, Rader HJ, Mullen K (2002) Synthesis of a giant 222 carbon graphite sheet. Chem Eur J 8(6):1424–1429
231. Eizenberg M, Blakely JM (1979) Carbon monolayer phase condensation on Ni(111). Surf Sci 82(1):228–236
232. Aizawa T, Souda R, Otani S, Ishizawa Y, Oshima C (1990) Anomalous bond of monolayer graphite on transition-metal carbide surfaces. Phys Rev Lett 64(7):768–771
233. Cui Y, Fu Q, Bao X (2010) Dynamic observation of layer-by-layer growth and removal of graphene on Ru(0001). Phys Chem Chem Phys 12(19):5053–5057
234. Liu M, Zhang Y, Chen Y, Gao Y, Gao T, Ma D, Ji Q, Zhang Y, Li C, Liu Z (2012) Thinning segregated graphene layers on high carbon solubility substrates of rhodium foils by tuning the quenching process. ACS Nano 6(12):10581–10589
235. Sutter P, Sadowski JT, Sutter E (2009) Graphene on Pt(111): growth and substrate interaction. Phys Rev B 80(24):245411
236. Nie S, Walter AL, Bartelt NC, Starodub E, Bostwick A, Rotenberg E, McCarty KF (2011) Growth from below: graphene bilayers on Ir(111). ACS Nano 5(3):2298–2306
237. Li X, Cai W, Colombo L, Ruoff RS (2009) Evolution of graphene growth on Ni and Cu by carbon isotope labeling. Nano Lett 9(12):4268–4272
238. Kim R-H, Bae M-H, Kim DG, Cheng H, Kim BH, Kim D-H, Li M, Wu J, Du F, Kim H-S, Kim S, Estrada D, Hong SW, Huang Y, Pop E, Rogers JA (2011) Stretchable, transparent graphene interconnects for arrays of microscale inorganic light emitting diodes on rubber substrates. Nano Lett 11(9):3881–3886
239. Reina A, Jia X, Ho J, Nezich D, Son H, Bulovic V, Dresselhaus MS, Kong J (2009) Large area, few-layer graphene films on arbitrary substrates by chemical vapor deposition. Nano Lett 9(1):30–35
240. Sun Z, Yan Z, Yao J, Beitler E, Zhu Y, Tour JM (2010) Growth of graphene from solid carbon sources. Nature 468(7323):549–552
241. Yu Q, Lian J, Siriponglert S, Li H, Chen YP, Pei S-S (2008) Graphene segregated on Ni surfaces and transferred to insulators. Appl Phys Lett 93(11):113103
242. Li X, Cai W, An J, Kim S, Nah J, Yang D, Piner R, Velamakanni A, Jung I, Tutuc E, Banerjee SK, Colombo L, Ruoff RS (2009) Large-area synthesis of high-quality and uniform graphene films on copper foils. Science 324(5932):1312–1314
243. Arco LGD, Zhang Y, Kumar A, Zhou C (2009) Synthesis, transfer, and devices of single- and few-layer graphene by chemical vapor deposition. IEEE Trans Nanotechnol 8(2):135–138
244. Kim KS, Zhao Y, Jang H, Lee SY, Kim JM, Kim KS, Ahn J-H, Kim P, Choi J-Y, Hong BH (2009) Large-scale pattern growth of graphene films for stretchable transparent electrodes. Nature 457(7230):706–710

245. Li X, Magnuson CW, Venugopal A, Tromp RM, Hannon JB, Vogel EM, Colombo L, Ruoff RS (2011) Large-area graphene single crystals grown by low-pressure chemical vapor deposition of methane on copper. J Am Chem Soc 133(9):2816–2819
246. Gong Y, Zhang X, Liu G, Wu L, Geng X, Long M, Cao X, Guo Y, Li W, Xu J, Sun M, Lu L, Liu L (2012) Layer-controlled and wafer-scale synthesis of uniform and high-quality graphene films on a polycrystalline nickel catalyst. Adv Func Mater 22(15):3153–3159
247. Zhang Y, Zhang L, Zhou C (2013) Review of chemical vapor deposition of graphene and related applications. Accounts Chem Res 46(10):2329–2339
248. Kang J, Shin D, Bae S, Hong B (2012) Graphene transfer: key for applications. Nanoscale 4(18):5527–5537
249. Liang X, Sperling BA, Calizo I, Cheng G, Hacker CA, Zhang Q, Obeng Y, Yan K, Peng H, Li Q, Zhu X, Yuan H, Walker ARH, Liu Z, Peng L-M, Richter CA (2011) Toward clean and crackless transfer of graphene. ACS Nano 5(11):9144–9153
250. Li X, Zhu Y, Cai W, Borysiak M, Han B, Chen D, Piner R, Colombo L, Ruoff RS (2009) Transfer of large-area graphene films for high-performance transparent conductive electrodes. Nano Lett 9(12):4359–4363
251. Martins LG, Song Y, Zeng T, Dresselhaus MS, Kong J, Araujo PT (2013) Direct transfer of graphene onto flexible substrates. Proc Natl Acad Sci 110(44):17762–7
252. Hu FM, Ma TX, Lin HQ, Gubernatis JE (2011) Magnetic impurities in graphene. Phys Rev B 84(7):075414
253. Krasheninnikov AV, Nieminen RM (2011) Attractive interaction between transition-metal atom impurities and vacancies in graphene: a first-principles study. Theoret Chem Acc 129(3):625–630
254. Alemán B, Regan W, Aloni S, Altoe V, Alem N, Girit C, Geng BS, Maserati L, Crommie M, Wang F, Zettl A (2010) Transfer-free batch fabrication of large-area suspended graphene membranes. ACS Nano 4(8):4762–4768
255. Ambrosi A, Pumera M (2014) The CVD graphene transfer procedure introduces metallic impurities which alter the graphene electrochemical properties. Nanoscale 6(1):472–476
256. Gorantla S, Bachmatiuk A, Hwang J, Alsalman HA, Kwak JY, Seyller T, Eckert J, Spencer MG, Rummeli MH (2014) A universal transfer route for graphene. Nanoscale 6(2):889–896
257. Gao L, Ni G-X, Liu Y, Liu B, Castro Neto AH, Loh KP (2014) Face-to-face transfer of wafer-scale graphene films. Nature 505(7482):190–194
258. Jacob MV, Rawat RS, Ouyang B, Bazaka K, Kumar DS, Taguchi D, Iwamoto M, Neupane R, Varghese OK (2015) Catalyst-free plasma enhanced growth of graphene from sustainable sources. Nano Lett 15(9):5702–5708
259. Kar R, Patel NN, Chand N, Shilpa RK, Dusane RO, Patil DS, Sinha S (2016) Detailed investigation on the mechanism of co-deposition of different carbon nanostructures by microwave plasma CVD. Carbon 106:233–242
260. Emtsev KV, Bostwick A, Horn K, Jobst J, Kellogg GL, Ley L, McChesney JL, Ohta T, Reshanov SA, Roehrl J, Rotenberg E, Schmid AK, Waldmann D, Weber HB, Seyller T (2009) Towards wafer-size graphene layers by atmospheric pressure graphitization of silicon carbide. Nat Mater 8(3):203–7
261. Tromp RM, Hannon JB (2009) Thermodynamics and kinetics of graphene growth on SiC(0001). Phys Rev Lett 102(10):106104
262. Mishra N, Boeck J, Motta N, Iacopi F (2016) Graphene growth on silicon carbide: A review. Phys Status Solidi A 213(9):2277–2289
263. Hupalo M, Conrad EH, Tringides MC (2009) Growth mechanism for epitaxial graphene on vicinal $6H\text{-SiC}(0001)$ surfaces: A scanning tunneling microscopy study. Phys Rev B 80(4):041401
264. Moreau E, Ferrer FJ, Vignaud D, Godey S, Wallart X (2010) Graphene growth by molecular beam epitaxy using a solid carbon source. Phys Status Solidi A 207(2):300–303
265. Hu M, Yao Z, Wang X (2017) Graphene-based nanomaterials for catalysis. Ind Eng Chem Res 56(13):3477–3502

266. Ambrosi A, Chua CK, Bonanni A, Pumera M (2014) Electrochemistry of graphene and related materials. Chem Rev 114(14):7150–7188
267. Syama S, Mohanan PV (2019) Comprehensive application of graphene: emphasis on biomedical concerns. Nano-Micro Lett 11(1):6

Chapter 11
Synthesis, Properties and Applications of Luminescent Carbon Dots

Sharmistha Dutta Choudhury

Abstract Carbon dots (CDs) are the newest addition to the family of carbon nanomaterials that have generated enormous excitement because of their unique photoluminescence (PL) property. The superior optical properties, biocompatibility, low toxicity and aqueous solubility of CDs have projected these materials as potent alternatives to conventional fluorophores and semiconductor quantum dots. The promising characteristics of CDs, together with their facile synthesis, have led to a rapid pace of research in these nanomaterials. This chapter outlines the various synthesis procedures that are used to obtain CDs from a variety of carbon sources and precursor molecules, their general properties and characterization techniques and the proposed PL mechanisms of CDs. The applications of CDs in diverse areas, like sensing, photocatalysis, bio-imaging, therapeutics and optoelectronics, are also discussed.

Keywords Carbon dot · Photoluminescence · Quenching · Biocompatibility · Sensing · Photocatalysis · Imaging

11.1 Introduction

Carbon dots (CDs) are quasi-spherical carbon nanomaterials that are generally less than 10 nm in size and exhibit photoluminescence (PL) as one of their most distinctive properties [1–4]. The PL of CDs is in contrast to the common perception of carbon as a black non-emissive material. Structurally, the CDs are comprised of sp^2/sp^3-hybridized carbonaceous core that is appended with multiple oxygen or nitrogen-containing functional groups, such as, aldehyde, carboxyl and hydroxyl or amino moieties (Fig. 11.1). Based on their intrinsic chemical structures and surface functional groups, the luminescent CDs are further classified as graphene

S. Dutta Choudhury (✉)
Radiation & Photochemistry Division, Bhabha Atomic Research Centre, Mumbai 400085, India
e-mail: sharmidc@barc.gov.in

Homi Bhabha National Institute, Mumbai 400094, India

A. K. Tyagi and R. S. Ningthoujam (eds.), *Handbook on Synthesis Strategies for Advanced Materials*, Indian Institute of Metals Series,
https://doi.org/10.1007/978-981-16-1892-5_11

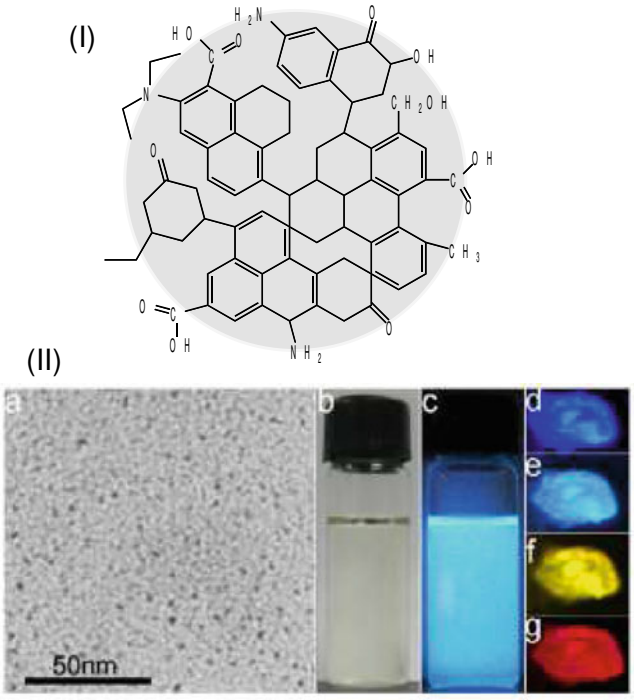

Fig. 11.1 (I) Schematic representation of carbon dot (CD) structure. (II) TEM images of CDs prepared from glucose by ultrasonic treatment (**a**), photographs of the aqueous dispersions of CDs under ordinary light (**b**) and UV light (**c**), fluorescence microscope images of the CDs with different excitation wavelengths: 360 nm, 390 nm, 470 nm, 540 nm (**d**–**e**, respectively). Reprinted with permission from [10]. Copyright 2011 Elsevier

quantum dots (GQDs), carbon nanodots (CNDs) and polymer dots (PDs) [5–7]. The GQDs comprise a few graphene layers with edge-connected functional groups. They have anisotropic disc-like shapes with lateral dimensions greater than the height. The CNDs are mostly spherical in shape and can be either crystalline or amorphous in nature. Recent evidences suggest that fluorophores and polyaromatic structures are generated and associated with the CNDs during their synthesis. The PDs are also largely spherical nanoparticles, consisting of aggregated or cross-linked polymers. The diversity of the CDs has made them amenable for many different synthetic approaches, including top-down nano-fabrication procedures and bottom-up chemical synthesis procedures [4, 8, 9].

Luminescent CDs were discovered serendipitously by Xu et al. in 2004, during the purification of single-walled carbon nanotubes from arc-discharge soot [11]. The potential of these luminescent species as interesting nanomaterials was rightly identified and soon triggered an explosion of research on these novel materials. The PL of CDs captured the interests of researchers for many fundamental experimental and theoretical studies, as well as for various possible applications [1, 12–15]. Both

excitation wavelength-dependent and excitation wavelength-independent emissions have been observed from CDs that have intrigued the practitioners of fluorescence spectroscopy [16–19]. The sensitivity of CD emission to temperature, pH conditions of the solution and polarity of the solvent medium have also been explored [20–24]. This has resulted in enhanced prospects of CDs as excellent optical probes for chemical and biological sensing. Attempts are being made to improve the PL quantum yields of CDs and expand the colour palette of their emission through doping and surface passivation [25–27]. Although the mechanism and origin of the PL from CDs are still open topics of research, the consensus so far is that the emission arises from the participation of many optically active centres, including the core, molecular state and the surface states associated with the CD structures [5, 7, 22, 28].

In addition to their PL property, the CDs have several other merits like convenient and cost-effective synthesis, aqueous solubility, biocompatibility, photostability and low toxicity [1]. These attributes of CDs offer significant advantages over classical organic fluorescent dyes or metal-based semiconductor quantum dots and make the CDs promising candidates for many useful applications [29]. Some of the areas where CDs have made their mark are as follows: optoelectronics, catalysis, energy conversion/storage, sensing, bio-imaging and nanomedicine [6–9, 12, 30]. The CDs are indeed emerging to be truly "shining" stars in the family of carbon nanomaterials.

This chapter attempts to provide a comprehensive overview of the major synthesis protocols for CD preparation; information regarding the variety of starting materials that can be used for making CDs, from small chemical precursors to biomass or bio-waste; the recent research forays into CD composite materials; the characterization and general physicochemical properties of CDs; insights on the PL mechanisms of CDs and their applications across a wide range of disciplines.

11.2 Synthesis

The CDs can be readily prepared using top-down or bottom-up methods. Moreover, they can be generated from a variety of precursors including naturally and abundantly available biomaterials [31–37]. Considering the huge application potential of these materials, attempts have also been made to scale up the synthesis protocols in order to obtain large quantities of CDs [38]. Some of the important and commonly employed protocols for CD synthesis are described in the following sections and depicted in Fig. 11.2. Interestingly, though CDs may be fabricated using diverse methods or from different precursors, they are found to have recurrent physicochemical and optical properties that can be further optimized for targeted applications.

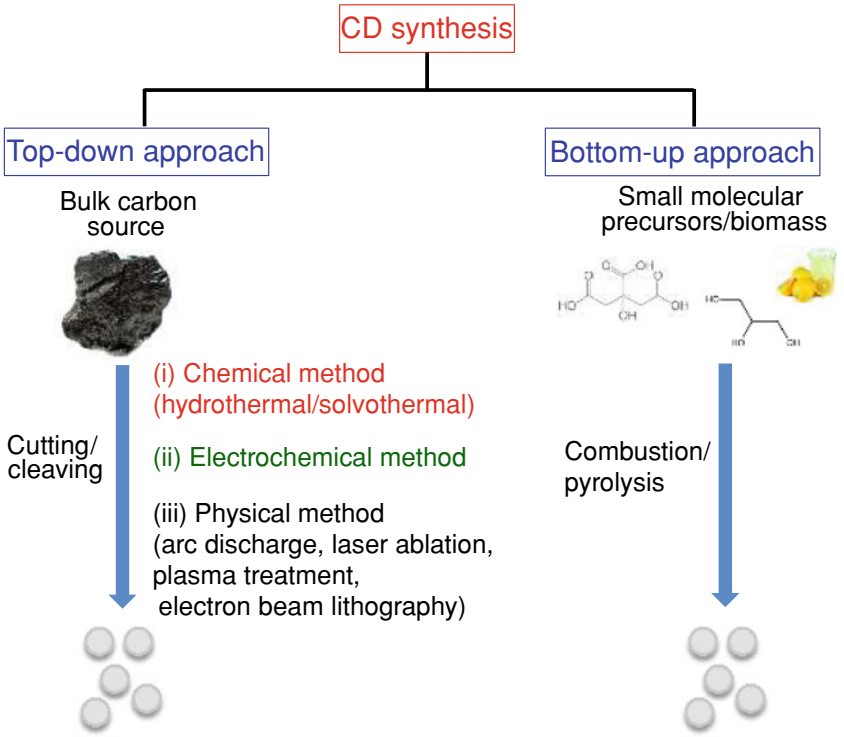

Fig. 11.2 Different approaches for CD synthesis

11.2.1 Top-Down Synthesis

The top-down methods of CD synthesis are based on breaking or cleavage of the large carbon materials like graphite, carbon soot, graphene oxide, carbon nanotubes, coal, carbon black or activated carbon [31, 39–47]. This is accomplished through (i) chemical routes including hydrothermal or solvothermal treatments, (ii) electrochemical methods or (iii) physical approaches [1, 31].

The chemical methods usually involve multiple steps of decomposition/exfoliation of carbon materials. These usually require harsh conditions, like strong oxidants or concentrated acids and high temperatures. For example, Pan et al. prepared blue luminescent CDs with a PL quantum yield of 6.9% and an average diameter of 9.6 nm from graphene oxide sheets by first cutting the sheets by subjecting them to oxidation with a mixture of sulphuric and nitric acids under ultrasonication. This was followed by hydrothermal reduction in Teflon-lined autoclave at high temperature to obtain GQDs [31]. In another study, the synthesis of CDs having crystalline lattice and average diameter of about 4.8 nm was reported by Tian et al. from the combustion soot of natural gas, by refluxing the soot in nitric acid [40]. The PL yield of the material was, however, quite low (<1%). The facile preparation of

GQDs with a PL yield of about 7.4% has been shown by Shen et al., by the reduction of graphene oxide with hydrazine hydrate [48]. Briefly, graphene oxide was first oxidized with nitric acid for cutting into small sheets. These were then treated with an oligomeric polyethylene glycol diamine for surface passivation and finally reduced by hydrazine hydrate. Blue PL could be observed from the prepared CDs under UV excitation, while green up conversion luminescence was observed on excitation with a 980 nm laser. CDs with variable PL property have also been prepared from coal pitch powder by reaction with a mixture of formic acid and hydrogen peroxide. The formation of the CDs was found to depend on the reaction time and the ratio of the reagents, formic acid and hydrogen peroxide [41].

The electrochemical synthesis of CDs from bulk carbon material has been found to be a relatively simple route to obtain CDs under normal temperature and pressure conditions and has been carried out by several research groups [43, 44, 49–51]. In this method, a voltage difference is applied between carbon-based electrodes in an electrochemical cell to initiate the electrochemical reaction that leads to the corrosion and exfoliation of the electrode material to eventually generate the CDs (Fig. 11.3). The procedure was demonstrated for the first time by Zhou et al. [43]. In their study, first carbon nanotubes were fabricated on a carbon paper as the source material. The carbon paper was subsequently introduced as the working electrode in an electrochemical cell with acetonitrile as the electrolyte and 0.1 M tetrabutyl ammonium perchlorate as the supporting electrolyte, to generate the CDs [43]. The electrochemical step was followed by evaporation of acetonitrile, dissolution of the solid material in water and dialysis to obtain the purified CDs. Wang and co-workers demonstrated the preparation of CDs with interesting electro-chemiluminescence property directly from graphite rod. In this case, the electrochemical set-up consisted of the graphite

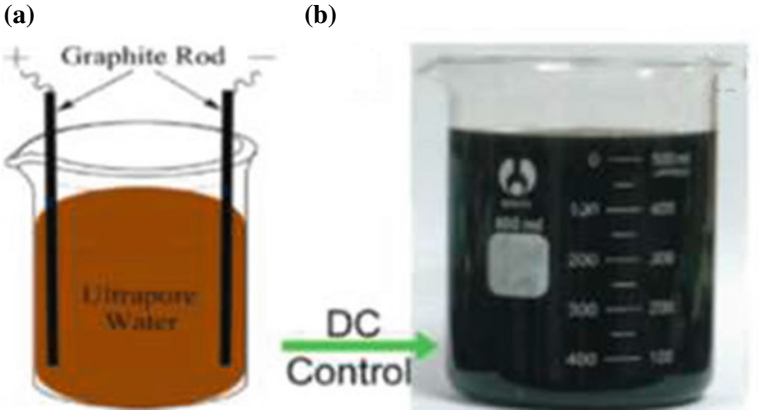

Fig. 11.3 Experimental set-up (**a**) and photograph of the CD solution (**b**) obtained by electrochemical synthesis from graphite rod. Reprinted with permission from [50]. Copyright 2012 The Royal Society of Chemistry

rod as working electrode, Pt mesh as counter-electrode and Ag/AgCl as the reference electrode, all of which were dipped in phosphate buffer (pH 7) [44]. Li and co-workers have prepared CDs with controlled sizes and size-dependent PL properties in an electrochemical cell having graphite rods as the anode as well as cathode and NaOH/EtOH as the electrolyte [49]. In another variation, CDs with high purity were prepared by applying a static potential of 15–60 V between two graphite rods dipped in ultrapure water under continuous stirring. After 120 h, the anode graphite rod was observed to corrode yielding a dark-coloured solution containing the CDs that were further purified [50]. Ionic liquid-assisted CD synthesis by electrochemical oxidation of graphite has also been demonstrated with water-soluble imidazolium-based ionic liquids as the electrolyte [51]. Interestingly, when the water content in the ionic liquid was greater than 10%, the generated CDs were found to be oxidized and water soluble, whereas when the water content in the ionic liquid was less than 10%, the generated carbon nanomaterials were found to be functionalized by the ionic liquid.

The physical approaches for CD synthesis include a variety of processes like arc discharge, laser ablation, plasma treatment, electron beam lithography and reactive ion etching [11, 52–55]. The initial discovery of CDs by Xu et al. was based on the arc-discharge method [11]. However, due to the simultaneous formation of different kinds of carbon nanoparticles in the arc-discharge method, rigorous separation and purification steps were required to isolate the CDs. Su et al. have demonstrated the synthesis of CDs with narrow size distribution by combining the arc synthesis of carbon by-products with centrifugal separation and chemical oxidation procedures [56]. The arc-discharge method has also been used recently by Rao and co-workers to prepare doped GQDs with strong blue emission. In their procedure, the arc discharge of graphite electrodes was accompanied with chemical shearing in ($H_2 + He + B_2H_6$) or ($H_2 + He + NH_3$) atmospheres to produce B, N-doped GQDs, respectively [57].

The preparation of CDs by the laser ablation of a carbon target prepared from graphite powder and cement was first carried out by Sun's group [53]. The initially obtained carbon nanomaterial was non-emissive and required further surface passivation steps to obtain high PL yield. CDs have also been prepared by laser irradiation of a suspension of carbon-based materials in organic solvents. It was observed that tunable light emission could be obtained by using different solvents, due to modification of the surface states of the generated CDs [58]. In another procedure, reported by Morell and co-workers, a mixture of nickel (II) oxide powder and benzene was irradiated for 30 min with pulsed Nd:YAG laser at 1064 nm, having energy of 30 mJ/pulse [59]. The experimental set-up is shown in Fig. 11.4. A mixture of GQDs and NiO was generated which was centrifuged. The supernatant was evaporated, and the resulting material was dispersed in water and further filtered to obtain the GQDs in aqueous medium. In addition to single-pulsed laser, double-pulsed laser technology has also been used to take advantage of the shock wave generated by the second pulse for obtaining smaller particles sizes [60].

Oxygen plasma treatment has been reported to increase the PL yield of single-layered graphene [54]. Submerged arc plasma reactor has also been used by Jiang et al. for single-step synthesis as well as functionalization of CDs [61]. In another

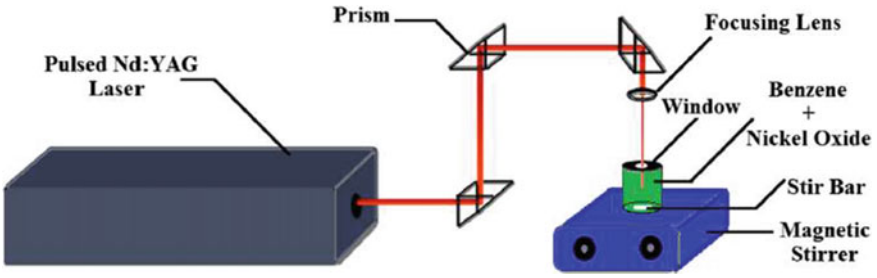

Fig. 11.4 Experimental set-up for the synthesis of CDs by laser ablation method. Reprinted with permission from [59]. Copyright 2013 Elsevier

top-down approach, Lee et al. have fabricated uniform sized CDs by using block copolymer nanospheres as etch mask on graphene films that were grown by chemical vapour deposition. The CDs consisted of one or two layers of graphene and had diameters corresponding to that of the block copolymer nanospheres [55].

In general, the top-down processes are energy intensive, and it is often difficult to control the size distribution and morphology of the produced particles. However, the CDs produced by these methods usually have good sp^2 conjugation that is believed to facilitate their PL property.

11.2.2 Bottom-Up Synthesis

The bottom-up approach for CD synthesis is based on the reactions of small molecular or polymeric precursors to generate nanometre-sized particles by the polycondensation and carbonization of the precursors. The processes involved include combustion, pyrolyzation and hydrothermal-, solvothermal-, microwave- or ultrasonication-assisted pyrolysis [1, 8, 9]. A wide variety of starting materials have been used for the synthesis of CDs. Some of the commonly employed chemicals are as follows: citric acid, ethylenediamine, glycerol, glycol, cellulose, urea, glucose, sucrose, amino acids, acetic acid and folic acid [7, 31–35, 62–65]. Apart from this, various naturally available biomaterials and even bio-waste have been converted to CDs through the bottom-up approach. Some examples in this category include the following: orange juice, lemon juice, leaves, fruit peels, egg shells, seeds and paper waste [7, 21, 36–38, 66]. Due to the wide availability of cheap raw materials, simple and scalable synthesis procedures, less reaction times and tunable reaction conditions, the bottom-up approach has rapidly grown as the preferred route for CD synthesis, compared to the top-down approach. Some representative bottom-up synthesis procedures are discussed in the following paragraphs.

The pyrolysis of citric acid has been one of the most commonly used methods for CD synthesis. The direct pyrolysis of citric acid was pioneered by Dong et al. in 2012 [62]. In their study, citric acid (2 g) was heated to 200 °C using a heating mantle.

After 5 min, the citric acid turned into a colourless liquid that gradually developed a pale-yellow colour followed by orange colouration after 30 min, suggesting the formation of CDs. The orange-coloured liquid was neutralized with NaOH to obtain the final CD solution with a PL quantum yield of 9%. When heating of the orange-coloured liquid was continued, it eventually turned into a black solid. This study revealed that increasing the reaction time increased the degree of carbonization and finally led to the formation of graphene oxide. Wang et al. further extended this procedure by carefully varying the reaction temperature and duration [67]. They concluded that higher temperatures and longer heating times led to the formation of large particles that depicted excitation wavelength-dependent emission. A similar observation has also been made in our studies using lemon juice (instead of citric acid) for CD synthesis [22]. Recently, Bagheri et al. have carried out a systematic study on the pyrolysis conditions of citric acid and concluded that CDs fabricated at 160 °C with 50 min reaction time attain the highest PL yield of 29% (Fig. 11.5) [68].

It is worth mentioning at this juncture that many recent studies have confirmed that certain fluorescent pyridine derivatives are formed during CD synthesis from citric acid and nitrogenous molecules, like ethylenediamine or cysteine (Fig. 11.6), that also contribute significantly to the PL yield of the CDs [69–72]. In the CDs prepared from citric acid and 1,2-ethylenediamine under hydrothermal synthesis conditions (discussed later), the formation of the fluorescent molecular species (imidazo[1,2-a]pyridine-7-carboxylicacid, 1,2,3,5-tetrahydro-5-oxo-, IPCA) was clearly identified by Yang's group [71]. This species was considered to be responsible for the high PL yield (~80%) of the CDs. Formation of molecular fluorophores was noted in a previous study as well, by Krysmann et al., for CDs prepared by the pyrolytic decomposition of citric with ethanolamine, although no fluorescent species was clearly

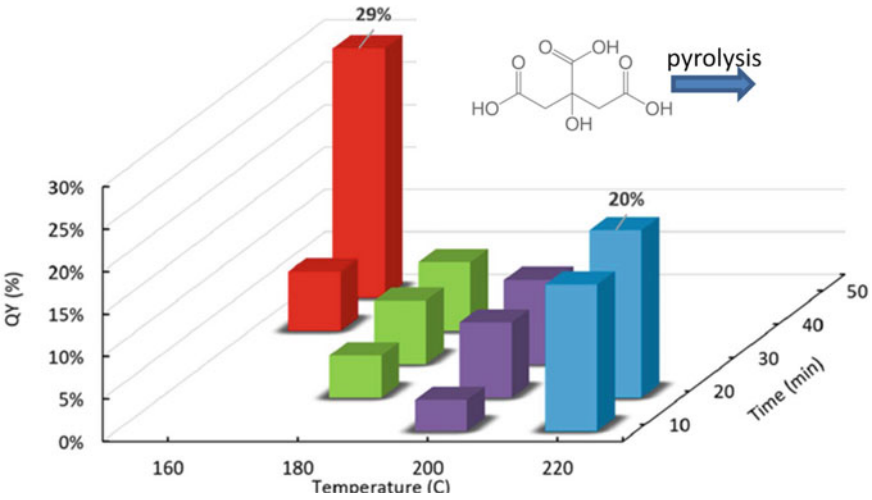

Fig. 11.5 PL quantum yield (QY) of CDs obtained by the pyrolysis of citric acid at different heating temperatures and duration. Adapted from [68], under Creative Commons Licence

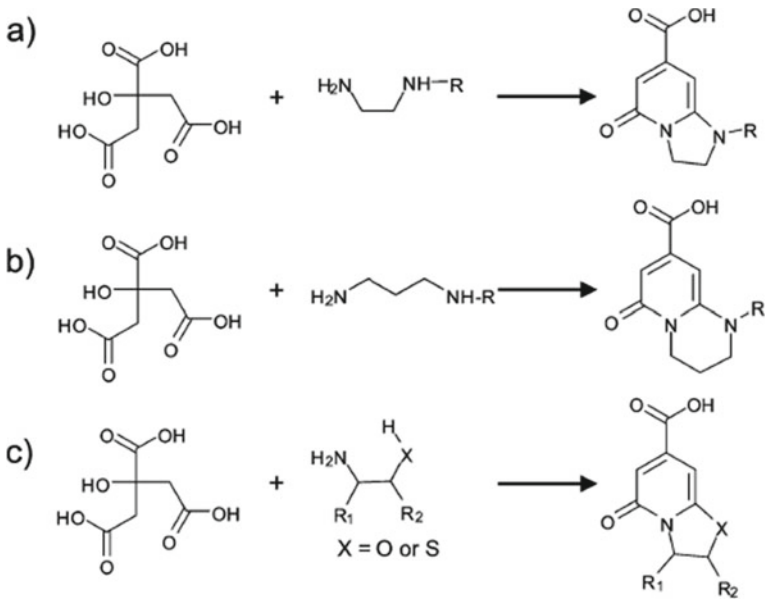

Fig. 11.6 Potential molecular fluorophores produced during the synthesis of CDs from citric acid and various nitrogen-containing precursors. Reprinted with permission from [71]. Copyright 2015 The Royal Society of Chemistry

identified [73]. The authors reported that molecular fluorophores are predominantly formed at low pyrolysis temperatures while the carbogenic core starts forming at higher temperatures [73].

In the hydrothermal/solvothermal-assisted synthesis of CDs, the reaction between the precursor molecules dissolved in water or a suitable solvent is carried out under high-pressure and high-temperature conditions in an autoclave (Fig. 11.7). The first bottom-up hydrothermal synthesis of CDs was demonstrated by Zhang et al. in 2010 using ascorbic acid as the precursor [63]. The PL quantum yield of the synthesized CDs was found to be dependent on the reaction time, solvent conditions and consequently the size of the CDs. In the previously discussed highly luminescent CDs (80% PL yield) that were prepared from citric acid, the hydrothermal synthesis procedure involved dissolution of citric acid and 1,2-ethylenediamine (both 1 mM) in 10 ml ultrapure water as the first step. The reaction was subsequently carried out in a Teflon-lined autoclave for 10 h at 140 °C [71]. Liu et al. have prepared monodisperse nitrogen-doped CDs having PL quantum yield of about 46% by the hydrothermal reaction of ammonium citrate and betaine hydrochloride for 5 h at 200 °C [74]. Based on the hydrothermal method, Chen et al. have prepared multiple fluorescent CDs with PL quantum yield up to 41.8% by varying the concentration of a single precursor, arginine [64]. Although the hydrothermal synthesis process is relatively simple, it requires high temperatures and long reaction times. These limitations are largely circumvented in the microwave-assisted synthesis of CDs.

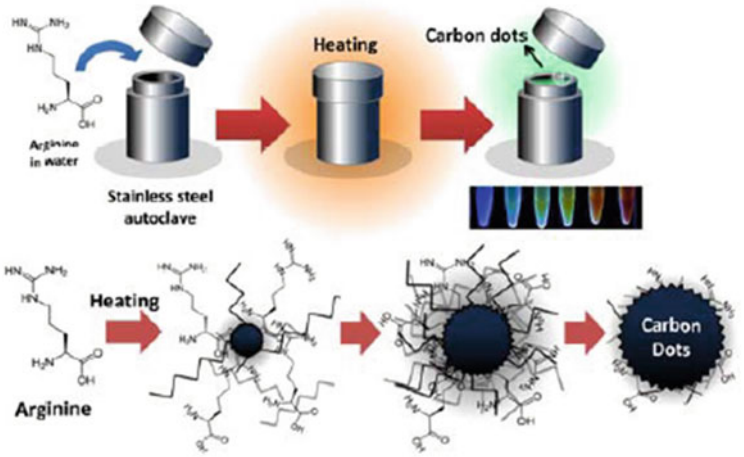

Fig. 11.7 Schematic representation of the hydrothermal synthesis of CDs from a single precursor, arginine. Reprinted with permission from [64]. Copyright 2016 The Royal Society of Chemistry

A facile and economical approach to prepare CDs through microwave pyrolysis was first reported by Zhu et al. [65]. A transparent aqueous solution of polyethylene glycol 200 and saccharide (glucose or fructose) was heated in a microwave oven at 500 W for 2–10 min. The solution colour gradually changed from colourless to yellow and finally became dark brown in colour, signifying the formation of CDs. In an alternate procedure demonstrated by Wang et al. [75], 70% (v/v) glycerol was mixed with 7.1 mM phosphate solution (pH 7.4) and heated in a microwave oven (750 W) for 14 min to obtain CDs having height around 2 nm and PL quantum yield around 3%. The formation rate and quantum yield of CDs was found to depend on the concentration of the phosphate ions and also increased with the increasing valence of other added cations or anions. More recently, Choi et al. have carried out microwave pyrolysis of the AB_2-type branched amino acid, lysine, to obtain CDs with PL quantum yield of 23.3% with a short reaction time of 5 min [76]. CDs with a quantum yield of 5.1% have been produced within 3 min from chitin fibres by the microwave-assisted method [77]. These CDs have been further used for the sensitive and selective fluorescence sensing of the drug D-penicillamine. The microwave-assisted pyrolysis is currently one of the most preferred methods for CD synthesis due to the easy operation and rapid reaction times and generally yields CDs with small sizes.

The ultrasound-assisted synthesis offers a facile method to prepare CDs with small size by using the energy of ultrasound waves to break the carbon materials into nanoparticles [10, 78–80]. The procedure was first demonstrated by Li et al. by the synthesis of CDs by ultrasonic treatment of a solution of glucose in acidic or basic condition for 4 h [10]. The particles obtained were less than 5 nm in size and depicted excitation wavelength-dependent emission. Lu et al. have recently demonstrated the synthesis CDs by ultrasonic treatment of dopamine in dimethyl formamide solvent for

8 h [79]. These CDs were water dispersible and could be used to sense temperature as well as Fe^{2+} ions [79]. Functionalized CDs with thiol terminated polyethylene glycol coating have also been synthesized by ultrasonic treatment [80].

11.2.3 Large-Scale Synthesis of CDs

In order to promote the application prospects of CDs, several researchers have carried out large-scale synthesis of these materials. In this regard, "green" synthesis from biomass has been preferred, so as to minimize the concern of environmental pollution by the use of harsh chemicals and strong acids. Apart from the synthetic method and carbon source used, some of the challenges that are being addressed are as follows: uniformity in size, reproducibility, carbon aggregation, exact chemical identity and surface functionality [38, 81, 82]. Yang et al. have reported the production of 120 g of CDs by one pot hydrothermal synthesis from Chinese ink [83]. Using chicken eggs as the raw material and plasma-induced pyrolysis method, Chen et al. have achieved large-scale synthesis of luminescent CDs up to 10 g, for multicolour printing applications [84]. Choi et al. have prepared 6.56 g of CDs in a single batch of microwave pyrolysis within 5 min, using citric acid and 4,7,10-trioxa-1,13-tridecanediamine (TTDA) as the precursors. In this case, TTDA served as both monomer and surface passivation agent, leading to high PL yield (29%) and better solubility of the CDs [85]. Park et al. have used the ultrasound technology to prepare large quantities of CDs from food wastes (120 g CDs per 100 kg of food waste). These CDs had good photostability and were suitable for bio-imaging applications [86]. The reproducibility of CD synthesis in large scale was examined by Zhang et al. [87]. Using the hydrothermal method, they could prepare about 3 g of CDs from 10 g of bee pollen. The synthesis was repeated five times with a feeding mass of 1 g, and the yield was found to be quite consistent with an average of about 30.8%.

11.2.4 Surface Passivation, Functionalization and Doping of CDs

Surface passivation, functionalization and doping of CDs are some of the commonly employed strategies to improve the PL quantum yields, solubility or functionality of the CDs. Surface passivation is usually accomplished by forming a thin coating layer of a polymeric substance on the CD surface. That surface passivation can largely improve the PL yield of CDs which was first demonstrated by Sun and co-workers [53], by the conversion of non-emissive CDs prepared by laser ablation into bright luminescent species on surface passivation by diamine-terminated oligomeric poly(ethylene glycol) $H_2NCH_2(CH_2CH_2O)_nCH_2CH_2CH_2NH_2$ (average $n \sim 35$, PEG_{1500N}). Zheng et al. demonstrated that the CD surface could be modified

by reduction with $NaBH_4$, which not only enhanced the PL yield from 2 to 24% but also changed the emission of the CDs from green (520 nm) to blue (450 nm) [88]. It may be noted that some of the one-step CD synthesis methods described earlier allow direct incorporation of the surface functionality without post-processing steps [51, 58]. Introduction of functional groups, like amino or carboxylate, is reported to impose defects on the surface of the CDs that leads to variations in the luminescence properties [34, 84, 89]. Often the passivation agent can also act as the functionalizing agent as reported by Dong et al. in the one-step synthesis of CDs by the pyrolysis of citric acid with branched polyethylenimine (BPEI). In this case, the CDs are capped by abundant BPEI, whose free amine groups allow further functionalization of the CDs by chemical conjugation methods [90]. Capping and functionalization of CDs are important modifications that are carried out for many applications. As an example, in one of the studies, CDs derived from sorbitol by microwave-assisted pyrolysis were capped first by bovine serum albumin (BSA), followed by conjugation with folic acid and further loaded with doxorubicin for drug delivery and biological imaging (Fig. 11.8) [91]. In another interesting variation, CDs have been functionalized with macrocyclic host molecules such as cyclodextrins. The attached macrocycle imparts the CDs with the ability to trap drugs or analytes through specific binding interactions with the host cavity. This is useful for drug delivery or sensing applications [92, 93].

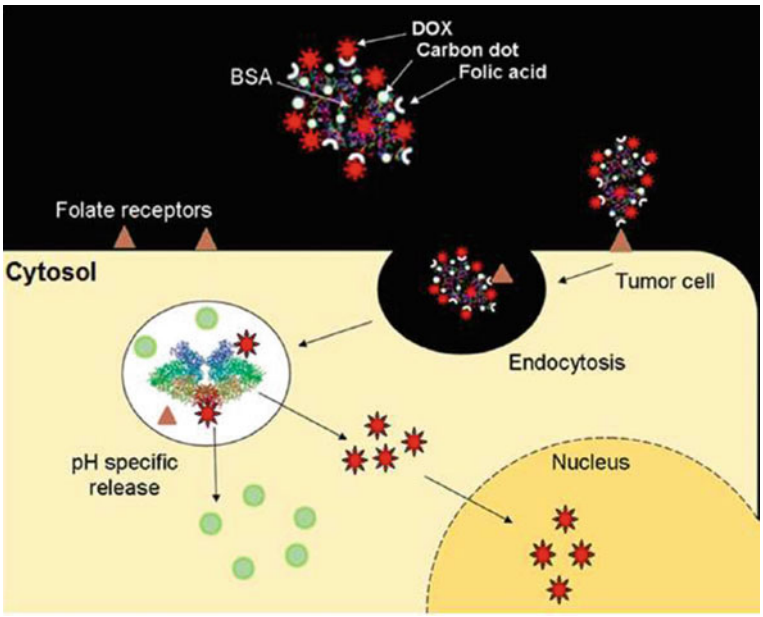

Fig. 11.8 Schematic representation of BSA functionalized CDs that are further conjugated with folic acid and doxorubicin (DOX) for tumour targeting and pH specific release of components. Reprinted with permission from [91]. Copyright 2014 The Royal Society of Chemistry

Doping helps in regulating the properties of CDs by modifying their chemical and electronic structures. The various doping elements that have been used in CD synthesis include nitrogen, phosphorus, sulphur, boron and some metal ions like Gd [57, 71, 94–99]. Among these, nitrogen is the most widely employed heteroatom for doping, as its atomic size is comparable to that of carbon. In addition to single heteroatom doping, recent approaches have also been made for co-doping of CDs, to benefit from the synergistic coupling between heteroatoms [97, 98]. Doping is usually carried out by introducing suitable chemicals, containing the desired elements, during the synthesis of the CDs. For example, a mixture of sodium citrate and sodium thiosulphate has been used in the hydrothermal synthesis of S-doped CDs [95]; a mixture of citric acid and 1,2-ethlenediamine has been used to obtain N-doped CDs [71], while a mixture of citric acid, boric acid and ethylenediamine has been used in the microwave-assisted synthesis of N-B-co-doped CDs [97]. Gd-doped CDs have been synthesized by Chen et al. from $Gd(NO_3)_3$ and *m*-phenylenediamine as precursors in ethanol-based solvothermal synthesis. These CDs were demonstrated to be useful for magnetic resonance imaging (MRI) and photodynamic therapy [96]. Sarkar et al. have observed that the blue luminescence observed from the CDs produced from a mixture of citric acid and amino acid can be converted to green luminescence by phosphorus doping, on introduction of K_2HPO_4 during the synthesis [99]. Rogach and co-workers have carried out extensive studies on the solvatochromic behaviour of N-doped and N-S-co-doped CDs and concluded that the doping atom has a significant effect on the solvent-dependent emission bands of the CDs [98].

11.2.5 CD Nanocomposites

The rich chemical functionality and facile modification of CDs has been exploited to generate different kinds of CD composites that further expand the application potential of this interesting carbon nanomaterial. Nanocomposites of CDs have been prepared with various nanostructures such as TiO_2, ZnS nanospheres, CdSe, Ag, Cu and Pd [40, 49, 100–103]. Tian et al. demonstrated the formation of CD metal nanoparticle composites by the reduction of metal salts by ascorbic acid in the presence of CDs derived from soot [66]. The PL quantum yield was found to increase from 0.43% for the bare CDs to 60.1%, 33.4% and 36.7% for the CD nanocomposites of Cu, Pd and Ag, respectively. Li et al. have demonstrated the CD-TiO_2 nanocomposites as excellent photocatalytic systems for the degradation of dyes like methylene blue [49]. The nanocomposites were prepared by adding TiO_2 nanoparticles to a solution of with electrochemically synthesized CDs, stirring the mixture for 10 min, followed by heating in a vacuum oven at 80 °C for 12 h. By heating a mixture of ammonia-treated CDs and urea powder, Liu et al. have synthesized, a metal-free CD-C_3N_4 composite that was found to be an excellent photocatalyst for water splitting [104]. In another study, a facile “dots-in-zeolites” strategy was developed for the in situ fabrication of CDs confined in zeolite matrices through

hydrothermal/solvothermal procedure [105]. The synthesized CDs@zeolite composites had high PL yields (52.14%) and exceptionally long lifetimes of 350 ms that was suitable for thermally activated delayed fluorescence. Very recently, Rathore et al. have prepared heterostructures of $CsPbBr_3$perovskite nanocrystals with N-doped CDs and examined the charge transfer properties across the interface [106].

The very rapid pace of research in the field of CDs and the easy bottom-up synthesis procedures from a variety of resources has also been accompanied by a number of critical issues, especially with regard to the nomenclature of the generated carbon nanomaterials and their purification [48, 107]. It has been highlighted by Baker and co-workers that rigorous and consistent purification steps need to be uniformly followed by all researchers after CD synthesis, to remove any undesired impurities and fluorescent by-products that may be generated during the synthesis [107]. Among the different separation and purification methods that are currently employed (like centrifugation, filtration, dialysis and chromatographic separation), chromatography is suggested to be the best analytical technique for fractionating the complex mixtures of products that are generated during the bottom-up synthesis procedures and obtained the desired pure CD samples.

11.3 Characterization

Although the exact chemical composition and structures of the CDs obtained by various synthesis methods are not the same, they all possess a common sp^2/sp^3-hybridized core and are connected with oxygen or nitrogen functional groups, depending on the carbon source used for the preparation. A large number of techniques are used to determine the composition, size, morphology, lattice parameters and PL properties of CDs. The common characterization methods of CDs are described below with representative examples.

Elemental analysis provides a good idea about the chemical composition of CDs, while ^{13}C NMR is useful to determine the chemical environment of the carbon atoms present in the sample. In an early study on CDs obtained from candle soot by Liu et al., it was observed that the chemical composition of the purified CD was quite different (C 36.79%, H 5.91%, N 9.59%, O (calculated) 44.66%) from that of the raw soot (C 91.69%, H 1.75%, N 0.12%, O (calculated) 4.36%) [60]. Specifically, the CDs had significantly higher oxygen content than the precursor material. Solid-state ^{13}C NMR for the synthesized CDs (Fig. 11.9) provided further details about the nature of the C atoms. Notably, no signals were observed below 120 ppm, which suggested the absence of any aliphatic sp^3 carbon in the CDs. Amidst the series of peaks that were observed within the range of 120 to 150 ppm, the broad peak centred at 138 ppm was assigned to internal C = C sp^2 carbons, and those between 120 and 130 ppm were assigned to polycyclic aromatic carbons. The third batch of peaks between 170 and 180 ppm was assigned to carboxylic/carbonyl carbons.

Fourier transform infrared spectroscopy (FTIR) and X-ray photoelectron spectroscopy (XPS) are also used to determine the elemental composition, functional

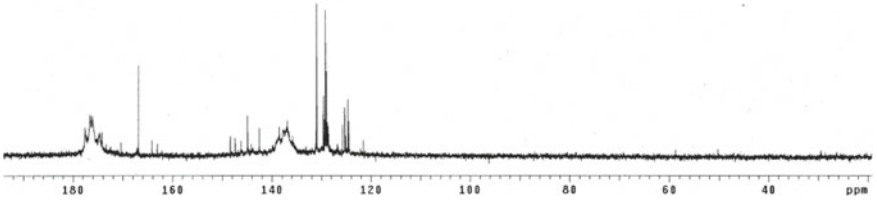

Fig. 11.9 ^{13}C NMR of CDs prepared from candle soot. Reprinted with permission from [40]. Copyright 2009 American Chemical Society

groups and covalent bonding patterns within CD structures. Representative FTIR and XPS spectra of GQDs obtained from carbon fibres (CF) by acidic oxidation are shown in Fig. 11.10 [42]. The XPS spectra show graphitic C_{1s} peak at 284.8 eV and O_{1s} peak at 532 eV for both GQDs and the precursor CF. However, the C:O ratio is much lower for GQDs (3.22) compared to CF (6.52). The high-resolution spectra of C_{1s}further reveal that the chemical environment of C in the GQDs is quite different from that in CF. The FTIR spectra of the GQD sample suggest the presence of many oxygen-containing functional groups (carbonyl, carboxyl, hydroxyl and epoxy) on the prepared nanoparticles, in accordance with the XPS results.

The size, morphology and microstructure of CDs are mainly determined by transmission electron microscopy (TEM)/high-resolution TEM (HRTEM) and atomic force microscopy (AFM). Figure 11.11 shows typical TEM and HRTEM images of CDs prepared by the pyrolysis of *p*-phenylenediamine in diphenyl ether [108]. The CDs appear as spherical particles with an average diameter of 2.6 nm. Well-resolved lattice fringes with an interplanar spacing of 0.21 nm are observed in the HRTEM

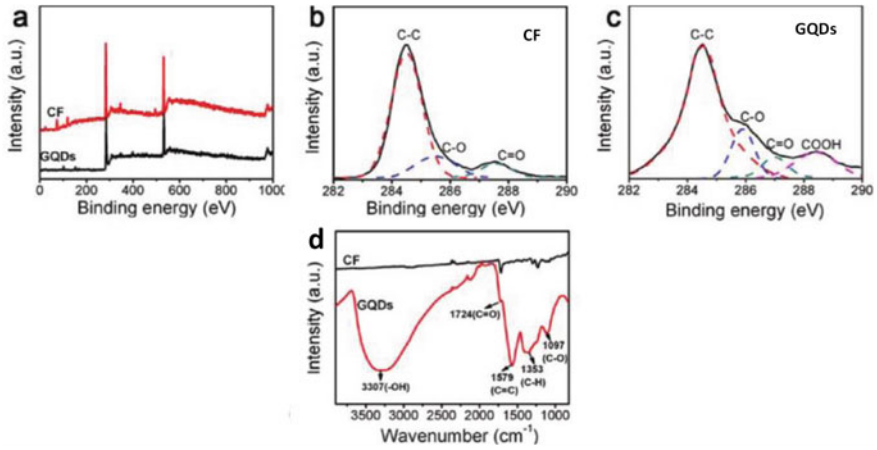

Fig. 11.10 XPS spectra of GQDs prepared from carbon fibre (CF) (**a**); high-resolution XPS C_{1s} spectra of GQDs and CF (**b**, **c**); FTIR spectra of GQDs and CF (**d**). Adapted with permission from [42]. Copyright 2012 American Chemical Society

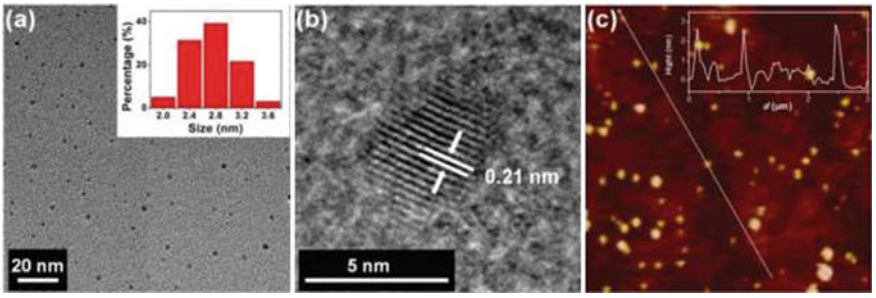

Fig. 11.11 **a** TEM, **b** HRTEM and **c** AFM images of CDs prepared by the pyrolysis of *p*-phenylenediamine in diphenyl ether. Reprinted with permission from [108]. Copyright 2017 The Royal Society of Chemistry

image. This is attributed to the diffraction from the (100) plane of graphitic carbon and indicates that the prepared CDs have a crystalline nature. The AFM image of the CDs corresponds with the TEM image and also reveals that the particles are nearly spherical with a height of 2.7 nm.

The crystalline or amorphous nature of CDs is ascertained through X-ray diffraction (XRD) studies. A broad peak around 23° suggests amorphous carbon while peaks around 25° and 44° suggest graphitic carbon structure corresponding to the (002) and (100) diffraction [109]. Raman spectroscopy is another useful and non-destructive technique for characterizing the crystalline and amorphous carbon content in the CDs. Raman peaks near 1360 cm^{-1} (D band) and 1560 cm^{-1} (G band) correspond to the E_{2g} vibrational modes of the aromatic domains and the breathing modes of the graphitic domains, respectively. The intensity ratio (I_D/I_G) provides an indication of the ratio of sp^3 to sp^2 carbon hybridization in the CDs [110, 111]. Representative XRD and Raman spectra of CDs prepared by the top-down electrochemical method from graphite electrode are shown in Fig. 11.12 [50]. The spectra of pure graphite are also shown for a direct comparison.

The optical properties of CDs are characterized by UV–vis spectroscopy, steady-state fluorescence spectroscopy and time-resolved fluorescence spectroscopy. The PL

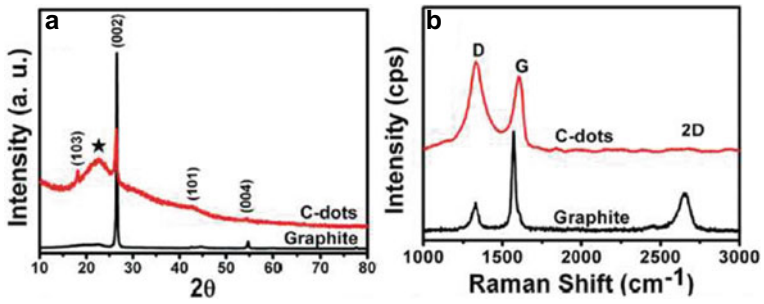

Fig. 11.12 **a** XRD and **b** Raman spectra of CDs prepared by electrochemical method from graphite. Adapted with permission from [50]. Copyright 2012 The Royal Society of Chemistry

quantum yields of CDs are measured by comparative method using quinine sulphate as the reference fluorophore. The optical absorption of CDs is quite strong in the UV region and extends into the visible region [1–4]. Most CDs exhibit blue emission on excitation with UV light; however, as mentioned previously, the emission wavelength of CDs can be tuned by doping and surface modifications. Figure 11.13 shows the typical absorption and excitation wavelength-dependent emission spectra and PL decay trace of CDs [112]. The characteristic absorption bands attributed to electronic transitions in the carbogenic core, the n-π* and π-π* transitions of the molecular state and the long absorption tail attributed to the surface state transitions in the CDs are indicated in the figure [22, 28, 97, 113]. The red-shifted emission of CDs with increasing excitation wavelengths, as depicted in Fig. 11.13, is a phenomenon that is observed for many CD samples [1–4, 114]. The PL decay traces are generally multi-exponential in nature, with average lifetimes in the range of 3–14 ns [18, 112, 115].

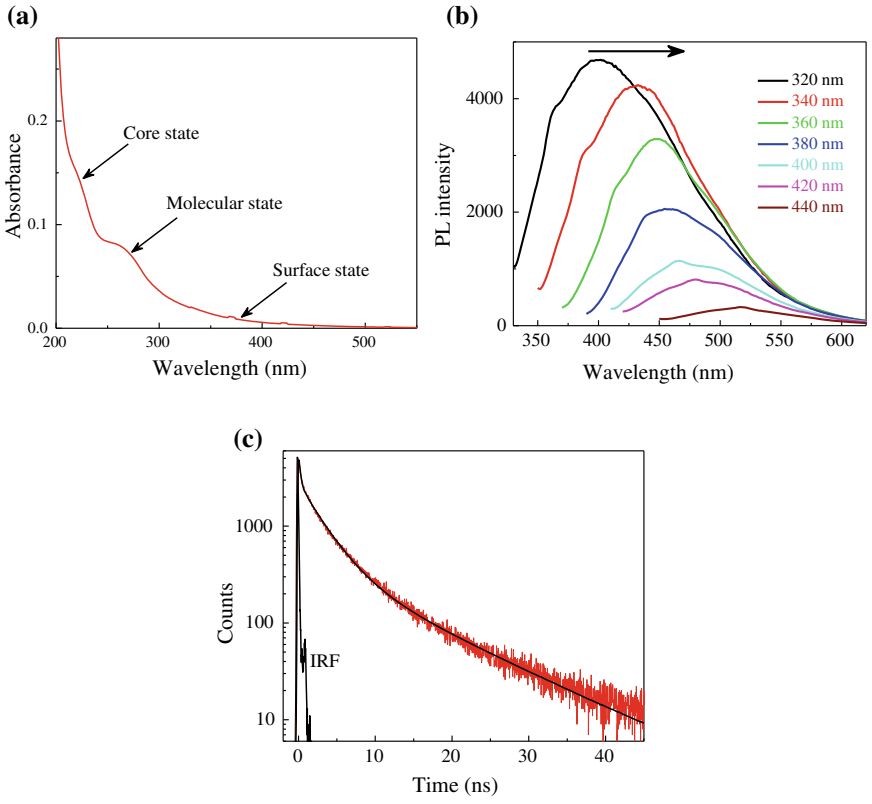

Fig. 11.13 Absorption spectrum (**a**); emission spectra (for excitation at different wavelengths from 320 to 440 nm) (**b**); and PL decay trace (**c**) of CDs prepared from glycerol by microwave synthesis. Adapted with permission from [112]. Copyright 2019 Elsevier

11.4 Properties

The most distinctive feature of CDs that sets them apart from other kinds of carbon nanomaterials is their PL property. The non-blinking emission and superior photostability of CDs is a key advantage over conventional fluorophores and semiconductor quantum dots (SQDs). Most of the applications of CDs are based on their PL property. However, despite numerous studies, a clear explanation for the PL mechanism of CDs is still not achieved. The unusually large Stokes' shifts (difference in energy between absorption and emission band maxima) of CDs and the excitation wavelength-dependent spectral shift that seems to violate the Kasha–Vavilov rule are some peculiarities that remain challenging to resolve. One of the major difficulties for arriving at a unified theory for CD luminescence is the wide variety of ingredients and approaches used to prepare CDs, which leads to variable and complex components in the generated particles. The general PL characteristics of CDs in comparison with SQDs [6] and the diversity of structures, interactions and excited-state processes that can occur in these nanoparticles [70] are depicted in Fig. 11.14.

From the vast available literature, the primary contributors that have been recognized to be involved in the emission of CDs are as follows: (i) the conjugated π-domains in the carbogenic core or the quantum confinement effect, (ii) the functional groups connected with the carbon backbone or the surface state, (iii) the molecular fluorophores or quasi-molecular structures on the surface or interior of the CDs, known as the molecular state and (iii) the cross-link-enhanced (CEE) effect [5, 16, 22, 28, 71, 98, 116–120]. The intriguing PL characteristics, like the excitation wavelength-dependent emission and large Stokes' shift, are interpreted to arise from multiple electronic states and heterogeneity of CDs [17, 28]. Recently, Demchenko et al. have proposed that many of the properties of CD luminescence can be addressed by considering CDs as collective H-aggregate excitonic systems comprised of stacked fluorescent molecular precursors [114].

The PL of CDs can be influenced by pH and polarity of the solvent medium [20, 23, 121, 122]. The emission peak positions of CDs have been found to be red-shifted with increase in the solvent polarity parameters (solvatochromic effect). Reckmeier et al. have observed opposite solvatochromic shifts of the different emission bands of CDs, depending on the doping heteroatoms [98]. In one of our studies, we have examined the effect of excitation wavelength on the solvatochromic behaviour of CDs derived from lemon juice [22]. A unique solvent-mediated transformation in the PL characteristics of CDs was observed, from excitation wavelength-independent emission in aqueous medium to excitation wavelength-dependent emission in organic solvents of lower polarity. This was attributed to different extents of solvatochromism exhibited by the molecular state and the surface state of CDs, thus leading to a useful method of discrimination between the emissions arising from these states (Fig. 11.15).

The lemon juice-derived CDs also presented interesting pH-dependent modulations in their absorption and emission characteristics [21]. FTIR studies revealed that the pH-induced changes in the optical properties are correlated with the prototropic

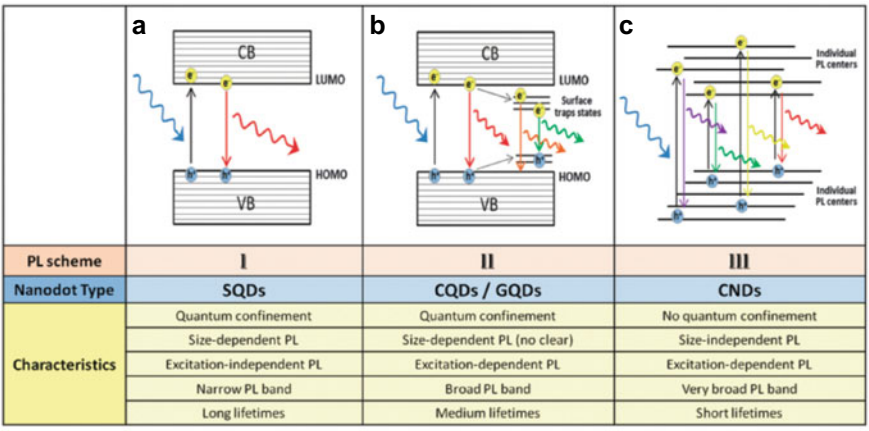

PL scheme	I	II	III
Nanodot Type	SQDs	CQDs / GQDs	CNDs
Characteristics	Quantum confinement	Quantum confinement	No quantum confinement
	Size-dependent PL	Size-dependent PL (no clear)	Size-independent PL
	Excitation-independent PL	Excitation-dependent PL	Excitation-dependent PL
	Narrow PL band	Broad PL band	Very broad PL band
	Long lifetimes	Medium lifetimes	Short lifetimes

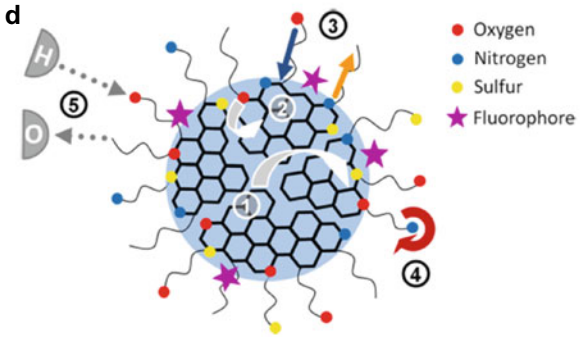

Fig. 11.14 PL characteristics of CDs in comparison with semiconductor quantum dots (SQDs) (**a**, **b**, **c**). Reprinted with permission from [6]. Copyright 2016 The Royal Society of Chemistry. **d** Summary of various interactions and excited state processes in CDs; (1) $\pi - \pi^*$ charge transfer, (2) $n - \pi^*$ transitions from the edge/surface groups, (3) charge transfer to surface states, (4) intrinsic transitions of surface state and (5) H-bonding interactions. Reprinted with permission from [98]. Copyright 2016 American Chemical Society

transformations of the surface functional groups of the CDs. Moreover, among the two prototropic equilibria, phenol ↔ phenolate and carboxylic ↔ carboxylate, only the former was suggested to be coupled with the emissive moiety of the CDs and involved in determining its electronic energy levels and optical transitions. As a result, a single pK_a corresponding to the phenol ↔ phenolate equilibrium was detected from the optical measurements (Fig. 11.16).

In addition to their PL, CDs also possess important photo-induced electron transfer and redox properties that is useful for photocatalytic applications [18, 49, 123]. Depending on the redox properties of the counterpart, CDs can act either as electron donors or as electron acceptors [18]. The photo-induced electron transfer process is manifested as a quenching in the PL of the CDs and has been widely applied as a tool for the fluorescence sensing of metal ions and various biomolecules [124–126]. We have elucidated the quenching mechanism of CDs with a representative heavy

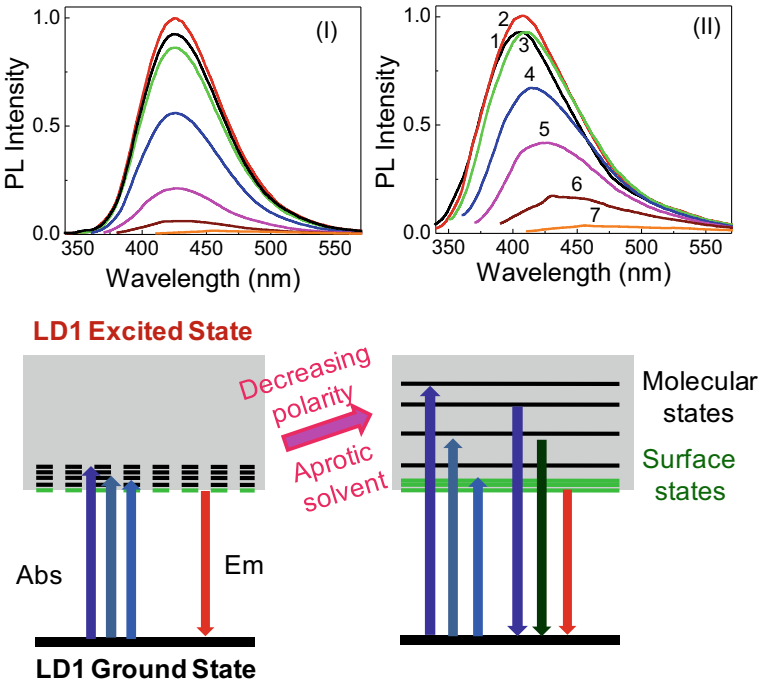

Fig. 11.15 Emission spectra of CDs derived from lemon juice (designated as LD1) in methanol (I) and ethyl acetate (II) for excitation at 300, 320, 340, 360, 380, 400 and 430 nm (1–7). The solvent stabilizations of the molecular state and surface state energy levels are schematically depicted. Reprinted with permission from [22]. Copyright 2019 The Royal Society of Chemistry

metal ion, Hg^{2+} and a nitroaromatic compound, nitrobenzene (NBz) [112]. While the reduction in the emission intensity of CDs in the presence of NBz occurred due to transient quenching and dynamic quenching interactions, in the presence of Hg^{2+}, the static quenching due to electrostatic interactions was found to play a major role in addition to the dynamic quenching (Fig. 11.17).

Some CD samples are also known to exhibit electro-chemiluminescence (ECL) property [44, 65, 127–130]. It has been suggested that the ECL arises due to the presence of surface trap states and depends on the surface functional groups present in the CDs. The mechanism involves the formation of excited-state CD (R*) due to electron transfer annihilation of the negatively charged ($R^{\bullet -}$) and positively charged ($R^{\bullet +}$) species that are electrochemically generated at the electrodes. The ECL luminescence property of CDs also serves as a valuable approach towards sensing applications [128].

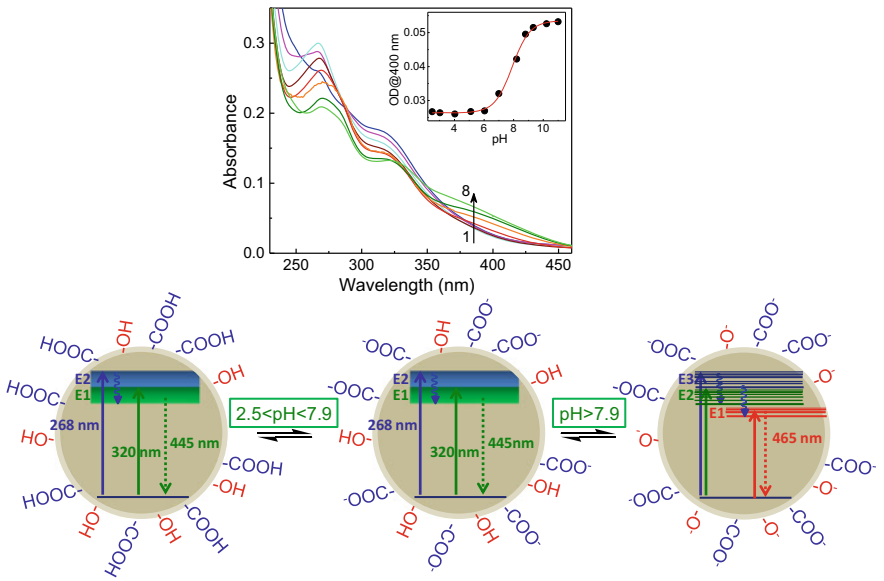

Fig. 11.16 Absorption spectra of lemon juice-derived CDs at different pH [2.5, 4.0, 5.1, 6.0, 7.0, 8.8, 9.3 and 10.2 (1–8)] of the solution. Inset shows the change in the absorbance at 400 nm with pH. The prototropic transformations of the surface functional groups and their effect on the electronic transitions are depicted schematically. Adapted with permission from [21]. Copyright 2017 American Chemical Society

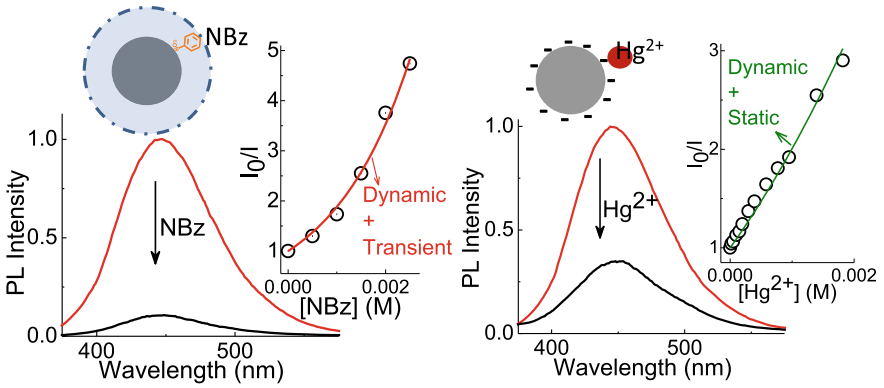

Fig. 11.17 Different PL quenching mechanisms of CDs for interaction with nitrobenzene (NBz) and Hg^{2+}. Reprinted with permission from [112]. Copyright 2019 Elsevier

11.5 Applications

CDs have developed to be valuable nanomaterials with huge impact in the fields of sensing, environment, health and energy. Some of the main application areas of CDs are summarized in Fig. 11.18 [2].

The luminescence property of CDs has been widely used for the sensing of metal ions, like Hg^{2+}, Pb^{2+}, Cu^{2+}, Fe^{3+}, Cr^{6+} and Zn^{2+} [131–136]. The basic principle involved in these cases is the quenching of CD luminescence by the metal ions. A representative example for the detection of Hg^{2+} by CDs synthesized by hydrothermal method from citric acid and ethylenediamine (PL yield 65.5%) is shown in Fig. 11.19 [131]. The detection limit of Hg^{2+} was estimated to be 226 nM in this study. The outstanding selectivity and sensitivity for PL quenching by Hg^{2+} ions were attributed to the presence of abundant carboxylate functionality on the surface of the CDs, which leads to the specific interaction with these metal ions. Interestingly, the PL intensity of the CDs was reversible and could be recovered by the addition of EDTA (cf. Fig. 11.19) due to competitive binding and displacement of the metal ion by the chelating ligand.

This luminescence "off to on" strategy opens up new possibilities for sensor design with CDs. Notably, in addition to metal ion assays that leverage on the quenching effect, CDs have been used to detect several anions like $C_2O_4^{2-}$, PO_4^{3-}, CN^-, F^-, S^{2-}, ClO^-, and I^-, based on the luminescence recovery of the already quenched CD metal ion system [136–141]. A similar strategy has been demonstrated by Zhou et al. for the sequential detection of Hg^{2+} and glutathione (GSH), by the fluorescence switching of CDs from "off" to "on" state by addition of GSH to the quenched CD-Hg^{2+} system [132]. Variations in the PL intensity of CDs in the presence of analytes have also been used for sensing of other molecular species like ascorbic acid, 4-nitrophenol, dopamine, amoxicillin, penicillamine and so on [77, 142–145].

To further improve on the sensing opportunities offered by CDs, ratiometric fluorescence sensing methods have been developed by coupling CDs with another emissive species that provides a second emission band at a different wavelength [146–148]. In this case, instead of monitoring the absolute intensity of the sole emission

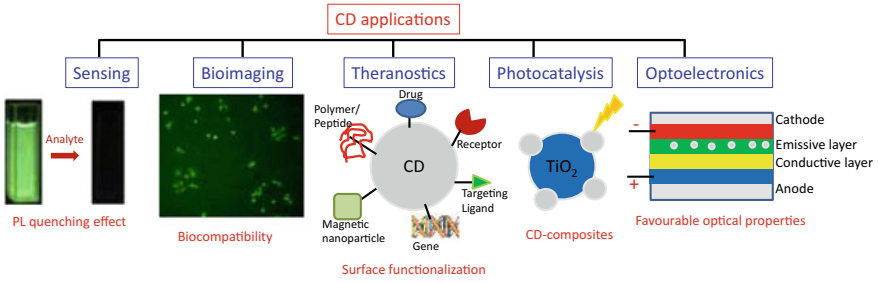

Fig. 11.18 Application range of CDs

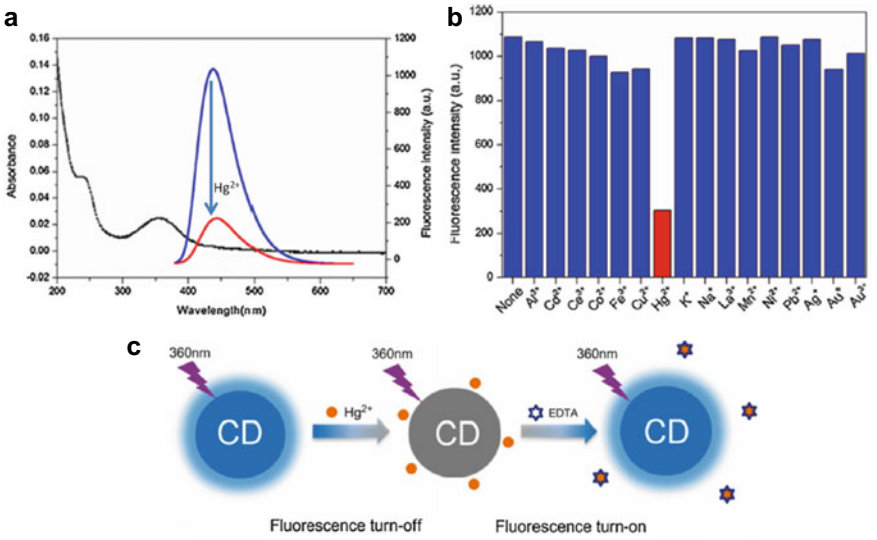

Fig. 11.19 Selective PL quenching of CDs by Hg^{2+} ions (**a**, **b**) and schematic representation of the fluorescence "off to on" mechanism by sequential addition of Hg^{2+} and EDTA (**c**). Adapted with permission from [131]. Copyright 2014 Elsevier

band of the CDs, it becomes possible to measure the intensity ratio of two emission bands. This leads to improved detection accuracy by eliminating any errors that may arise due to intensity variations arising from changes in probe concentration or excitation source intensity. In one such study, Lu and co-workers coupled CDs with a fluorescent dye, Rhodamine B and observed two distinct emission bands corresponding to the two species. In the presence of Hg^{2+}, the emission from CD was quenched while the emission intensity from Rhodamine B remained unchanged. On further addition of GSH, the CD emission intensity was recovered, but the Rhodamine B emission band remained unaffected. With the ratiometric approach, the limit of detection for Hg^{2+} was reported to be 20 nM [146]. In another variation, CDs were coupled with semiconductor quantum dots for NO_2 sensing (Fig. 11.20). In this case, the red emission from the quantum dots was quenched by NO_2, while the blue emission of CDs remained unchanged, leading to a change in the fluorescence colour from red to blue in the presence of NO_2 [147]. Another type of ratiometric sensing is based on fluorescence resonance energy transfer (FRET) from CDs to a conjugated fluorescent dye. In the presence of the analyte, the FRET process is either enhanced or hindered, thus leading to a change in the ratio of emission intensities of the CD and the conjugated dye [148].

The excellent luminescence property of CDs has also been used for their application as fluorescent labels in immunoassays, for immunosensing of antigens, for detection of base mismatch or single nucleotide polymorphism in DNA, aptamer-based sensing of thrombin, detection of α-fetoprotein and in the field of food analysis [30, 149–153].

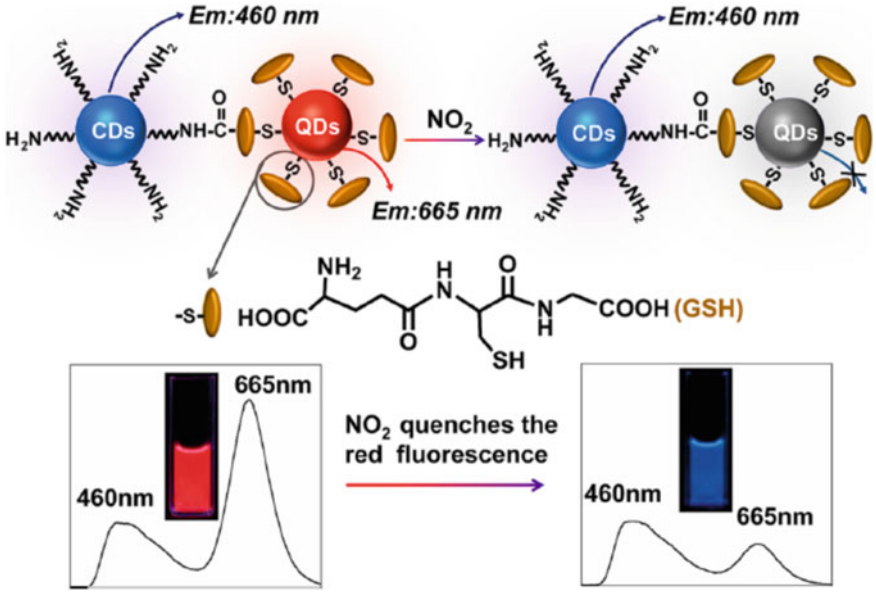

Fig. 11.20 Ratiometric fluorescence sensing of NO_2 by CDs conjugated with quantum dots (QDs). The red emission (665 nm) of QDs is quenched by NO_2 while blue emission from CDs (460 nm) remains unaffected. Reprinted with permission from [147]. Copyright 2015 American Chemical Society

Apart from the PL-based assays, CDs have also proven useful for electrochemiluminescence assays of many species like Cu^{2+}, pentachlorophenol and peroxydisulphate ions [127, 154, 155].

Bio-imaging and cellular targeting is another important area where CDs have found niche applications. The easy surface functionalizations of CDs, low cytotoxicity, resistance to photo bleaching and excitation-dependent emission are advantages over other available fluorescent materials. The excitation wavelength-dependent emission of CDs allows excitation and emission at longer wavelengths, where tissue autofluorescence is significantly reduced, thereby improving the signal-to-noise ratio [156]. Since the emission intensity of CDs in the red region is generally weak, intense efforts are ongoing to develop red and NIR emissive CDs by doping or through surface modifications, especially to boost their bio-imaging and theranostic applications [157].

Figure 11.21 shows representative confocal fluorescence microscope images of L929 mouse fibroblast cells at different excitation wavelengths, after being incubated with CDs synthesized from citric acid and ethylenediamine by microwave pyrolysis [158]. As observed in this case, the CDs are generally found to localize in the cell membrane and cytoplasmic area. The uptake of CDs by the cell nucleus was demonstrated for the first time by Datta et al., by using CDs synthesized from the quaternary ammonium (betaine) precursor [159]. The affinity towards the cell

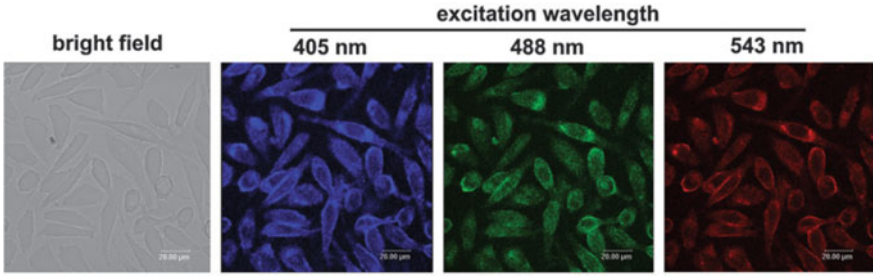

Fig. 11.21 Confocal fluorescence microscope images of L929 cells incubated with CDs at different excitation wavelengths. Reprinted with permission from [158]. Copyright 2012 The Royal Society of Chemistry

nucleus was attributed to the positive charge of the synthesized particles. The low cytotoxicity of CDs has been especially useful for imaging of stem cells. It was observed by Zhang et al. that CDs could penetrate stem cells without causing any genetic disruptions and had good photostability [160]. As compared to single-photon excitation, two-photon excitation imaging has the advantages of deeper tissue penetration, lower autofluorescence and less photo damage. The potential of CDs for cell imaging with two-photon excitation at 800 nm was first demonstrated by Cao et al. using femtosecond-pulsed laser excitation at 800 nm [161]. This was followed by other reports using doped CDs that showed significant enhancement in the depth for tissue imaging [162, 163].

As compared to unmodified CDs, specially functionalized CDs can be used for specific cell targeting and labelling. For example, considering that folate receptors are overexpressed in cancer cells, folic acid-capped CDs have been used to distinguish between cancerous and normal cells for selective imaging or drug delivery (cf. Fig. 11.8) [91, 164]. In vivo optical imaging using CDs has also been carried out [165–168]. In the study by Zheng et al., it was observed that CDs prepared by pyrolysis of D-glucose and L-aspartic acid could self-target the C6 glioma cells. The in vivo images of glioma-bearing mice were of high contrast and showed that the CDs could cross the blood–brain barrier to specifically accumulate at the glioma site (Fig. 11.22) [165].

The CDs have also been integrated with paramagnetic species like gadolinium (a well-known MRI contrast agent) and iodine (used for contrast in X-ray computer tomography, CT) to go beyond their applications as simple fluorescent labels and confer them with multimodal imaging options. Gd-doped CDs prepared by Chen et al. by direct calcination of Gd-pentetic acid (Gd-DTPA) had excellent PL yield (19.7%) as well as higher longitudinal relaxation rate than the commercially available MRI contrast agent [169]. Their study highlighted the applicability of Gd-CDs as efficient dual-mode (fluorescence and MRI) imaging agents. The I-doped CDs were also found to have good PL yields, X-ray attenuation property and biocompatibility for use as CT/fluorescence imaging agents [170, 171]. Recently, Zhao et al. have prepared gadolinium and ytterbium co-doped CDs for their use as multimodal (CT, MRI,

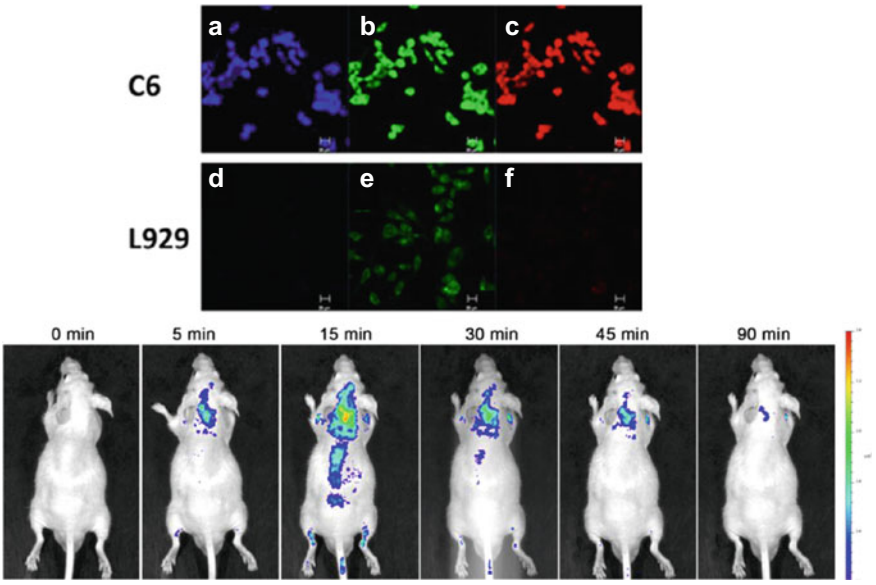

Fig. 11.22 Confocal fluorescence microscope images on excitation at 405, 488 and 555 nm, showing the selective affinity of CDs for C6 cells (**a**–**c**) over the L929 cells (**d**–**f**). The lower panel shows in vivo images of glioma-bearing mice at different time intervals after intravenous tail injection of CDs. Adapted with permission from [165]. Copyright 2015 American Chemical Society

fluorescence) nanoprobes that can provide comprehensive diagnosis information [172].

The therapeutic applications of CDs are based on their abilities as a carrier for drug delivery and enhanced photodynamic/photothermal effects [173]. As already mentioned, folic acid-capped CDs are readily internalized into cancerous cells and are thus useful for the targeted delivery of medicines (cf. Fig. 11.8) [91]. CDs have been loaded with a range of drugs used for cancer treatments like doxorubicin, cisplatin, oxiplatin, niclosamide, chlorin e6 and porphyrin [174–179]. The integration of the imaging capability of CDs with therapeutic agents allows effective monitoring of the concentration and localization of the drugs, which is of help in developing improved treatment protocols. Chlorin e6 and porphyrin are typical photosensitizers widely used for photodynamic therapy (PDT) that is based on the principle of using suitable photosensitizer dyes for generating reactive oxygen species to destroy cancer cells by the action of light. Conjugation with CDs has been established to improve the stability, solubility and tumour targeting capability of the PDT agents [178, 179]. Photothermal therapy (PTT),which is based on the activation of photosensitizer agents by light, to generate heat for the thermal killing of tumour cells, has also been investigated by using suitable CD conjugates [180, 181]. The combination of CDs with SiO_2 capped gold nanorods has been demonstrated by Jia et al. as multimodal photo-theranostic agents that can be used to guide PDT/PTT treatment through fluorescence imaging

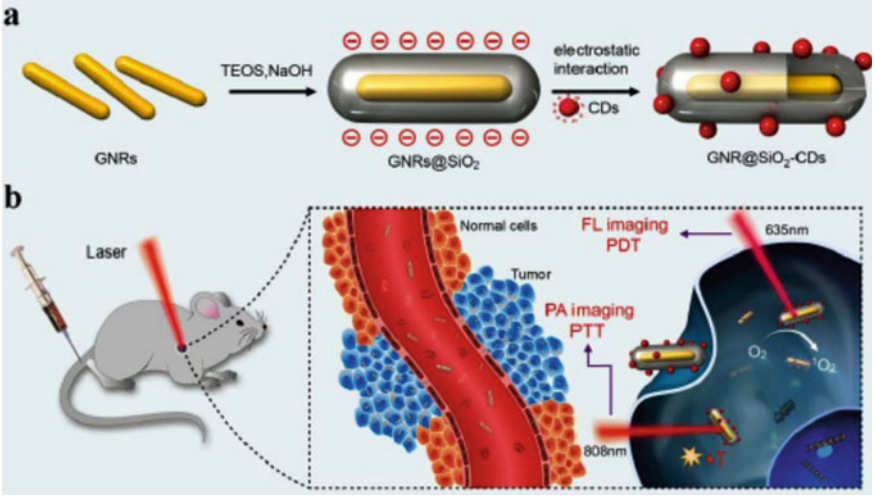

Fig. 11.23 Conjugation of CDs with gold nanorods (GNR) for multimodal theranostic application. Reprinted with permission from [180]. Copyright 2016 The Royal Society of Chemistry

(FI) or photoacoustic (PA) imaging (Fig. 11.23) [180]. This nanomedicine approach proved effective for killing the cancerous cells by using relatively low dose of laser irradiation (<0.5 Wcm^{-2}).

In the field of photocatalysis, CDs have made a major contribution by offering useful properties like ability to utilize light in the visible or near UV range, resistance towards photocorrosion and eco-friendliness [49, 104, 182–188]. The CD-TiO_2 conjugates are a notable example of improved photocatalytic performance [49, 182–184]. Although TiO_2 is one of the most popular photocatalytic materials, it is limited by its ineffectiveness to absorb visible light, since its band gap lies in the UV region (3.0–3.2 eV). The CD-TiO_2 conjugates have been shown not only to harness visible light for creating electron hole pairs in TiO_2 but also provide a conducting path for the transport of electrons, thereby leading to better charge separation and creation of long-lived holes on the surface of TiO_2 [182–184]. This leads to improved catalytic performance of the nanomaterials in the photodegradation of dyes or H_2 generation by water splitting. Based on similar principles, other CD composites, like CD-ZnO, CD-Fe_2O_3, CD-Cu_2O, CD-Ag_3PO_4, have been prepared for photocatalytic applications [185–188]. The processes involved in the improved catalytic activity of CD-Ag_3PO_4 system are depicted in Fig. 11.24 [186]. In this study, Kang et al. observed that the CDs enhanced visible light absorption, helped to improve the stability of the nanocatalyst by preventing the dissolution of Ag_3PO_4 in the aqueous medium and acted as electron reservoir to hinder electron–hole recombination. They also demonstrated that the catalyst could be reused multiple times for photodegradation of the dye, methyl orange.

In recent years, tremendous progress has been made in the optoelectronic applications of CDs, especially with regard to their potential for improving the efficiencies

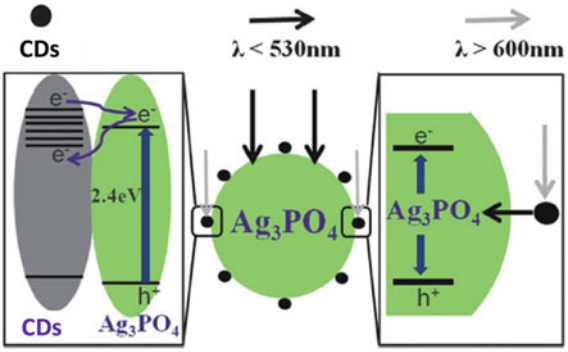

Fig. 11.24 Processes involved in the photocatalytic activity of CD-Ag_3PO_4 conjugates. Adapted with permission from [186]. Copyright 2012 The Royal Society of Chemistry

of photovoltaic devices, light-emitting diodes (LEDs), supercapacitors and batteries [7, 9].

The tunable emission and large PL bandwidth of CDs makes them promising alternatives to expensive rare-earth-based phosphors and semiconductor quantum dots that are presently used for LED design. The application of CDs in LEDs is based either on their optical excitation, in which case, the CDs participate as colour-converting phosphors, or based on the direct electrical excitation of the CDs using their electroluminescence property, where CDs participate as the light-emitting source. The application of CDs as colour-converting phosphors was first demonstrated by Tang et al., by coating a layer of GQDs on commercially available blue LEDs. The blue emission of the LEDs at 410 nm excited the CDs, to further generate a new broad emission band with maximum around 510 nm. The subsequent mixing of the two emission components, from the blue LED and the CDs, resulted in the eventual creation of white light. The Commission International d'Eclairage (CIE) chromaticity coordinates of the LED was found to shift from the initial values of (0.242, 0.156)–(0.282, 0.373) [189]. Extensive studies are being carried out to bring out further improvements in the CD-based LED designs by reducing the aggregation-induced quenching effect of the CDs, improving the PL yields of the CDs and development of solid-state fluorescent CDs [190–193]. In the electroluminescence-based approach, the CDs are used as the active emissive layer in the LED structure [194–196]. A representative LED design that is based on the electroluminescence property of CDs is depicted in Fig. 11.25 [196]. In this study by Wang et al., the CDs (synthesized from citric acid and passivated with 1-hexadecylamine) were placed as the emissive layer. Poly (ethylenedioxythiophene):polystyrenesulfonate (PEDOT:PSS) was used as the hole injection layer, and 1,3,5-tris (*N*-phenylbenzimidazol-2-yl) benzene (TPBI) was used as electron transport layer. LiF and Al were deposited as the electrode material. The quantum efficiency of the device was found to be 0.083% with a current density of 5 mA cm^{-2}, having colour rendering index (CRI) of 82.

CDs have been successfully used for energy harvesting, energy conversion and energy storage applications [197, 198]. Wei et al. have coupled electrochemically synthesized CDs with $Ni(OH)_2$ supercapacitor electrodes for improving their electrical conductivity [199]. With this modification, the specific capacitance was found

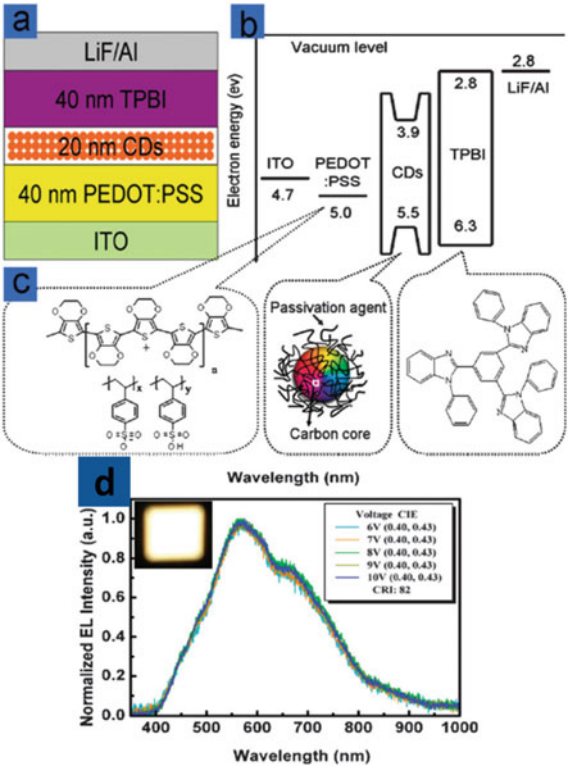

Fig. 11.25 **a** Structure of the LED device fabricated using CDs as the emissive layer. **b** Energy band diagram of the LED. **c** Molecular structures and schematic of PEDOT:PSS, TPBI and CDs. **d** Electroluminescence spectra of the device at different applied voltages. Inset shows a photograph of the observed white emission. Adapted with permission from [196]. Copyright 2011 The Royal Society of Chemistry

to be 2900 F/g at 1 A/g. In general, CDs have been found to provide a good interface between the electrolyte and electrode in supercapacitors, which helps to improve their cycling stability and specific capacitance. The performance of electrodes in lithium and sodium ion batteries has also been found to increase on modification with CDs [200–202]. The wide optical absorption range of CDs has been exploited for their use as sensitizers in light-harvesting solar cells. In a study by Ma et al., it was found that compared to the Rhodamine B (RhB)-TiO_2 dye sensitized solar cell system, the photoelectric conversion increased seven times in the CD-RhB-TiO_2 photovoltaic system [203]. It was shown that the CDs effectively bridged the RhB molecules and the TiO_2 substrate by acting as an electron transfer intermediary. Apart from their role as photosensitizers, CDs have been explored for use as electron acceptors with respect to the active layer of poly(3-hexylthiophene) (P3HT), in organic solar cells [204, 205]. In these studies, it was expected that CDs could be promising alternatives to the more expensive fullerenes that are currently employed as the electron acceptors. CDs have also been investigated as electron blocking layer in CD/Si nanowire arrays core–shell heterojunction solar cells to prevent charge recombination and thus improve the carrier transfer and collection capability [206, 207]. Although the photoelectric conversion efficiency of CD-based solar cells is at

present low, the findings are encouraging and more advances in the applications of CDs for photovoltaic devices may be expected in the future.

11.6 Conclusions and Future Prospects

In the past sixteen years since their discovery, the luminescent CDs have evolved to be valuable members in the family of carbon nanomaterials with vast and far-reaching applications. The extensive research on CDs is undoubtedly driven by their convenient synthesis procedures, their intriguing PL property and their outstanding biocompatibility. Despite the rapid growth in the research and applications of CDs, their rational design and controlled synthesis to obtain desired functionalities are still challenging. Advanced synthesis and purification procedures for efficient control of the emission colour and quantum yields of CDs, on a large scale, will surely boost the potential of these materials. In this regard, the development of red/NIR emissive CDs is particularly important, for their biomedical applications. Uniform synthesis procedures will also help in arriving at an unequivocal and coherent understanding about the intriguing optical properties and PL mechanism of the CDs. Although still in the midst of development, CDs have already made a profound influence in the fields of nanomedicine, phototherapy, sensing and photocatalysis. The diversion into newer areas, like clean and green energy, is a welcome development. Progress in CD research is expected to reveal many more exciting opportunities with this interesting material.

Acknowledgements The author gratefully acknowledges all collaborators and co-authors of the published work cited in this chapter; the support from the host institute, Bhabha Atomic Research Centre (BARC), Mumbai; the many insightful discussions on carbon nanomaterials with Dr. A. K. Tyagi, Director, Chemistry Group, BARC; the support and encouragement from Dr. A. Kumar, Head, Radiation and Photochemistry Division, BARC, and Dr. A. C. Bhasikuttan, Head, Molecular Photochemistry Section, BARC.

References

1. Baker SN, Baker GA (2010) Luminescent carbon nanodots: Emergent nanolights. Angew Chem Int Ed 49:6726–6744
2. Demchenko A, Dekaliuk M (2013) Novel fluorescent carbonic nanomaterials for sensing and imaging. Methods Appl Fluoresc 1:042001 (1–17)
3. Kozák O, Sudolská M, Pramanik G, Cígler P, Otyepka M, Zbořil R (2016) Photoluminescent carbon nanostructures. Chem Mater 28:4085–4128
4. Wang Y, Hu A (2014) Carbon quantum dots: Synthesis, properties and applications. J Mater Chem C 2:6921–6939
5. Zhu S, Song Y, Zhao X, Shao J, Zhang J, Yang B (2015) The photoluminescence mechanism in carbon dots (graphene quantum dots, carbon nanodots, and polymer dots): Current state and future perspective. Nano Res 8:355–381

6. Cayuela A, Soriano ML, Carrillo-Carrion C, Valcarcel M (2016) Semiconductor and carbon-based fluorescent nanodots: The need for consistency. Chem Commun 52:1311–1326
7. Semeniuk M, Yi Z, Poursorkhabi V, Tjong J, Jaffer S, Lu Z-H, Sain M (2019) Future perspectives and review on organic carbon dots in electronic applications. ACS Nano 13:6224–6255
8. Atabaev TS (2018) Doped carbon dots for sensing and bioimaging applications: A minireview. Nanomaterials 8:342
9. Yuan F, Li S, Fan Z, Meng X, Fan L, Yang S (2016) Shining carbon dots: Synthesis and biomedical and optoelectronic applications. Nano Today 11:565–586
10. Li HT, He XD, Liu Y, Huang H, Lian SY, Lee ST, Kang ZH (2011) One-step ultrasonic synthesis of water-soluble carbon nanoparticles with excellent photoluminescent properties. Carbon 49:605–609
11. Xu X, Ray R, Gu Y, Ploehn HJ, Gearheart L, Raker K, Scrivens WA (2004) Electrophoretic analysis and purification of fluorescent single-walled carbon nanotube fragments. J Am Chem Soc 126:12736–12737
12. Lim SY, Shen W, Gao Z (2015) Carbon quantum dots and their applications. Chem Soc Rev 44:362–381
13. Eda G, Lin Y-Y, Mattevi C, Yamaguchi H, Chen H-A, Chen I-S, Chen C-W, Chhowalla M (2010) Blue photoluminescence from chemically derived graphene oxide. Adv Mater 22:505–509
14. Sk MA, Ananthanarayanan A, Huang L, Lim KH, Chen P (2014) Revealing the tunable photoluminescence properties of graphene quantum dots. J Mater Chem 2:6954–6960
15. Sudolská M, Dubecký M, Sarkar S, Reckmeier CJ, Zbořil R, Rogach AL, Otyepka M (2015) Nature of absorption bands in oxygen-functionalized graphitic carbon dots. J Phys Chem C 119:13369–13373
16. Gan Z, Xu H, Hao Y (2016) Mechanism for excitation-dependent photoluminescence from graphene quantum dots and other graphene oxide derivates: consensus, debates and challenges. Nanoscale 8:7794–7807
17. Sharma A, Gadly T, Gupta A, Ballal A, Ghosh SK, Kumbhakar M (2016) Origin of excitation dependent fluorescence in carbon nanodots. J Phys Chem Lett 6:3695–3702
18. Strauss V, Margraf JT, Dolle C, Butz B, Nacken TJ, Walter J, Bauer W, Peukert W, Spiecker E, Clark T, Guldi DM (2014) Carbon nanodots: Toward a comprehensive understanding of their photoluminescence. J Am Chem Soc 136:17308–17316
19. Wang L, Zhu S-J, Wang H-Y, Qu S-N, Zhang Y-L, Zhang J-H, Chen Q-D, Xu H-L, Han W, Yang B, Sun H-B (2014) Common origin of green luminescence in carbon nanodots and graphene quantum dots. ACS Nano 8:2541–2547
20. Pan D, Zhang J, Li Z, Wu C, Yana X, Wu M (2010) Observation of pH-, solvent-, spin-, and excitation-dependent blue photoluminescence from carbon nanoparticles. Chem Commun 46:3681–3683
21. Dutta Choudhury S, Chethodil JM, Gharat PM, Praseetha PK, Pal H (2017) pH-elicited luminescence functionalities of carbon dots: mechanistic insights. J Phys Chem Lett 8:1389–1395
22. Gharat PM, Chethodil JM, Srivastava AP, Praseetha PK, Pal H, Dutta Choudhury S (2019) An insight into the molecular and surface state photoluminescence of carbon dots revealed through solvent-induced modulations in their excitation wavelength dependent emission properties. Photochem Photobiol Sci 18:110–119
23. Sciortino A, Marino E, van Dam B, Schall P, Cannas M, Messina F (2016) Solvatochromism unravels the emission mechanism of carbon nanodots. J Phys Chem Lett 7:3419–3423
24. Yuan F, Ding L, Li Y, Li X, Fan L, Zhou S, Fang D, Yang S (2015) Multicolor fluorescent graphene quantum dots colorimetrically responsive to all-pH and a wide temperature range. Nanoscale 7:11727–11733
25. Zhang Y, Yuan R, He M, Hu G, Jiang J, Xu T, Zhou L, Chen W, Xiang W, Liang X (2017) Multi-colour nitrogen-doped carbon dots: tunable photoluminescence and sandwich fluorescent glass-based light-emitting diodes. Nanoscale 9:17849–17858

26. Miao X, Qu D, Yang D, Nie B, Zhao Y, Fan H, Sun Z (2018) Synthesis of carbon dots with multiple color emission by controlled graphitization and surface functionalization. Adv Mater 30:1704740
27. Jiang K, Sun S, Zhang L, Lu Y, Wu A, Cai C, Lin H (2015) Red, green, and blue luminescence by carbon dots: Full-color emission tuning and multicolor cellular imaging. Angew Chem Int Ed 54:5360–5363
28. Sharma A, Gadly T, Neogy S, Ghosh SK, Kumbhakar M (2017) Molecular origin and self-assembly of fluorescent carbon nanodots in polar solvents. J Phys Chem Lett 8:1044–1052
29. Wolfbeis OS (2015) An overview of nanoparticles commonly used in fluorescent bioimaging. Chem Soc Rev 44:4743–4768
30. Pan M, Xie X, Liu K, Yang J, Hong L, Wang S (2020) Fluorescent carbon quantum dots—synthesis, functionalization and sensing application in food analysis. Nanomaterials 10:930
31. Pan D, Zhang J, Li Z, Wu M (2010) Hydrothermal route for cutting graphene sheets into blue-luminescent graphene quantum dots. Adv Mater 22:734–738
32. Gao F, Ma S, Li J, Dai K, Xiao X, Zhao D, Gong W (2017) Rational design of high quality citric acid-derived carbon dots by selecting efficient chemical structure motifs. Carbon 112:131–141
33. Choi Y, Ryu GH, Min SH, Lee BR, Song MH, Lee Z, Kim B-S (2014) Interface-controlled synthesis of heterodimeric silver–carbon nanoparticles derived from polysaccharides. ACS Nano 8:11377–11385
34. Yang Y, Cui J, Zheng M, Hu C, Tan S, Xiao Y, Yang Q, Liu Y (2012) One-step synthesis of amino-functionalized fluorescent carbon nanoparticles by hydrothermal carbonization of chitosan. Chem Commun 48:380–382
35. Bourlinos AB, Stassinopoulos A, Anglos D, Zboril R, Georgakilas V, Giannelis EP (2008) Photoluminescent carbogenic dots. Chem Mater 20:4539–4541
36. Krysmann MJ, Kelarakis A, Giannelis EP (2012) Photoluminescent carbogenic nanoparticles directly derived from crude biomass. Green Chem 14:3141–3145
37. Briscoe J, Marinovic A, Sevilla M, Dunn S, Titirici M (2015) Biomass-derived carbon quantum dot sensitizers for solid-state nanostructured solar cells. Angew Chem Int Ed 54:4463–4468
38. Zhang J, Yu S-H (2016) Carbon dots: Large-scale synthesis, sensing and bioimaging. Mater Today 19:382–393
39. Shen J, Zhu Y, Yang X, Li C (2012) Graphene quantum dots: Emergent nanolights for bioimaging, sensors, catalysis and photovoltaic devices. Chem Commun 48:3686–3699
40. Tian L, Ghosh D, Chen W, Pradhan S, Chang X, Chen S (2009) Nanosized carbon particles from natural gas soot. Chem Mater 21:2803–2809
41. Meng X, Chang Q, Xue CR, Yang JL, Hu SL (2017) Full-colour carbon dots: from energy-efficient synthesis to concentration-dependent photoluminescence properties. Chem Commun 53:3074–3077
42. Peng J, Gao W, Gupta BK, Liu Z, Romero-Aburto R, Ge L, Song L, Alemany LB, Zhan X, Gao G, Vithayathil SA, Kaipparettu BA, Marti AA, Hayashi T, Zhu J-J, Ajayan PM (2012) Graphene quantum dots derived from carbon fibers. Nano Lett 12:844–849
43. Zhou JG, Booker C, Li RY, Zhou XT, Sham T-K, Sun XL, Ding ZF (2007) An electrochemical avenue to blue luminescent nanocrystals from multiwalled carbon nanotubes (MWCNTs). J Am Chem Soc 129:744–745
44. Zheng L, Chi Y, Dong Y, Lin J, Wang B (2009) Electrochemiluminescence of water-soluble carbon nanocrystals released electrochemically from graphite. J Am Chem Soc 131:4564–4565
45. Qiao Z, Wang Y, Gao Y, Li H, Dai T, Liu Y, Huo Q (2009) Commercially activated carbon as the source for producing multicolor photoluminescent carbon dots by chemical oxidation. Chem Commun 46:8812–8814
46. Ye R, Xiang C, Lin J, Peng Z, Huang K, Yan Z, Cook NP, Samuel EL, Hwang C-C, Ruan G, Ceriotti G, Raji ARO, Martí AA, Tour JM (2013) Coal as an abundant source of graphene quantum dots. Nat Commun 4:2943
47. Dong Y, Chen C, Zheng X, Gao L, Cui Z, Yang H, Guo C, Chi Y, Li CM (2012) One-step and high yield simultaneous preparation of single- and multi-layer graphene quantum dots from CX-72 carbon black. J Mater Chem 22:8764–8766

48. Shen J, Zhu Y, Chen C, Yang X, Li C (2011) Facile preparation and upconversion luminescence of graphene quantum dots. Chem Commun 47:2580–2582
49. Li HT, He XD, Kang ZH, Huang H, Liu Y, Liu JL, Lian SY, Tsang CHA, Yang XB, Lee ST (2010) Water-soluble fluorescent carbon quantum dots and photocatalyst design. Angew Chem Int Ed 49:4430–4434
50. Ming H, Ma Z, Liu Y, Pan KM, Yu H, Wang F, Kang ZH (2012) Large scale electrochemical synthesis of high quality carbon nanodots and their photocatalytic property. Dalton Trans 41:9526–9531
51. Lu J, Yang JX, Wang J, Lim A, Wang S, Loh KP (2009) One-pot synthesis of fluorescent carbon nanoribbons, nanoparticles, and graphene by the exfoliation of graphite in ionic liquids. ACS Nano 3:2367–2375
52. Ponomarenko L, Schedin F, Katsnelson M, Yang R, Hill E, Novoselov K, Geim A (2008) Chaotic Dirac billiard in graphene quantum dots. Science 320:356–358
53. Sun YP, Zhou B, Lin Y, Wang W, Fernando KAS, Pathak P, Meziani MJ, Harruff BA, Wang X, Wang H, Luo PG, Yang H, Kose ME, Chen B, Veca LM, Xie SY (2006) Quantum-sized carbon dots for bright and colorful photoluminescence. J Am Chem Soc 128:7756–7757
54. Gokus T, Nalr RR, Bonettl A, Bohmler M, Lombardo A, Novoselov KS, Gelm AK, Ferrarl AC, Hartschuh A (2009) Making graphene luminescent by oxygen plasma treatment. ACS Nano 3:3963–3968
55. Lee J, Kim K, Park WI, Kim B, Park JH, Kim T, Bong S, Kim C, Chae G, Jun M, Hwang Y, Jung YS, Jeon S (2012) Uniform graphene quantum dots patterned from self-assembled silica nanodots. Nano Lett 12:6078–6083
56. Su Y, Xie M, Lu X, Wei H, Geng H, Yang Z, Zhang Y (2014) Facile synthesis and photoelectric properties of carbon dots with upconversion fluorescence using arc-synthesized carbon by-products. RSC Adv 4:4839–4842
57. Dey S, Govindaraj A, Biswas K, Rao CNR (2014) Luminescence properties of boron and nitrogen doped graphene quantum dots prepared from arc-discharge-generated doped graphene samples. Chem Phys Lett 595:203–208
58. Hu SL, Niu KY, Sun J, Yang J, Zhao NQ, Du XW (2009) One-step synthesis of fluorescent carbon nanoparticles by laser irradiation. J Mater Chem 19:484–488
59. Habiba K, Makarov VI, Avalos J, Guinel MJF, Weiner BR, Morell G (2013) Luminescent graphene quantum dots fabricated by pulsed laser synthesis. Carbon 64:341–350
60. Nguyen V, Zhao N, Yan LH, Zhong P, Nguyen VC, Le PH (2020) Double-pulse femtosecond laser ablation for synthesis of ultrasmall carbon nanodots. Mater Res Express 7:015606
61. Jiang HQ, Chen F, Lagally MG, Denes FS (2010) New strategy for synthesis and functionalization of carbon nanoparticles. Langmuir 26:1991–1995
62. Dong Y, Shao J, Chen C, Li H, Wang R, Chi Y, Lin X, Chen G (2012) Blue luminescent graphene quantum dots and graphene oxide prepared by tuning the carbonization degree of citric acid. Carbon 50:4738–4743
63. Zhang B, Liu CY, Liu Y (2010) A novel one-step approach to synthesize fluorescent carbon nanoparticles. Eur J Inorg Chem 28:4411–4414
64. Chen Y-C, Nien C-Y, Albert K, Wen C-C, Hsieha Y-Z, Hsu HY (2016) Pseudo-multicolor carbon dots emission and the dilution-induced reversible fluorescence shift. RSC Adv 6:44024–44028
65. Zhu H, Wang XL, Li YL, Wang ZJ, Yang F, Yang XR (2009) Microwave synthesis of fluorescent carbon nanoparticles with electrochemiluminescence properties. Chem Commun 1:5118–5120
66. Sahu S, Behera S, Maiti TK, Mohapatra S (2012) Simple one-step synthesis of highly luminescent carbon dots from orange juice: Application as excellent bio-imaging agents. Chem Commun 48:8835–8837
67. Wang S, Chen ZG, Cole I, Li Q (2015) Structural evolution of graphene quantum dots during thermal decomposition of citric acid and the corresponding photoluminescence. Carbon 82:304–313

68. Bagheri Z, Ehtesabi H, Rahmandoust M, Ahadian MM, Hallaji Z, Eskandari F, Jokar E (2017) New insight into the concept of carbonization degree in synthesis of carbon dots to achieve facile smartphone based sensing platform. Sci Rep 7:11013
69. Zhu S, Zhao X, Song Y, Lu S, Yang B (2016) Beyond bottom-up carbon nanodots: Citric-acid derived organic molecules. Nano Today 11:128–132
70. Schneider J, Reckmeier CJ, Xiong Y, Seckendorff M, Susha AS, Kasák P, Rogach AL (2017) Molecular fluorescence in citric acid-based carbon dots. J Phys Chem C 121:2014–2022
71. Song Y, Zhu S, Zhang S, Fu Y, Wang L, Zhao X, Yang B (2015) Investigation from chemical structure to photoluminescent mechanism: A type of carbon dots from the pyrolysis of citric acid and an amine. J Mater Chem C 3:5976–5984
72. Shi L, Yang JH, Zeng HB, Chen YM, Yang SC, Wu C, Zeng H, Yoshihito O, Zhang Q (2016) Carbon dots with high fluorescence quantum yield: the fluorescence originates from organic fluorophores. Nanoscale 8:14374–14378
73. Krysmann MJ, Kelarakis A, Dallas P, Giannelis EP (2012) Formation mechanism of carbogenic nanoparticles with dual photoluminescence emission. J Am Chem Soc 134:747–750
74. Wen L, Cui Y, Li T, Diao H, Wei S, Li L, Chang H, Zhang B, Wei W (2018) Green and facile synthesis of highly photoluminescent nitrogen-doped carbon dots for sensors and cell imaging. Chem Lett 47:421–424
75. Wang XH, Qu KG, Xu BL, Ren JS, Qu XG (2011) Microwave assisted one-step green synthesis of cell-permeable multicolor photoluminescent carbon dots without surface passivation reagents. J Mater Chem 21:2445–2450
76. Choi Y, Thongsai N, Chae A, Jo S, Kang EB, Paoprasert P, Park SY, In I (2017) Microwave-assisted synthesis of luminescent and biocompatible lysine-based carbon quantum dots. J Ind Eng Chem 47:329–335
77. Naghdi T, Atashi M, Golmohammadi H, Saeedi I, Alanezhad M (2017) Carbon quantum dots originated from chitin nanofibers as a fluorescent chemoprobe for drug sensing. J Ind Eng Chem 52:162–167
78. Qiang RB, Yang SR, Hou KM, Wang JQ (2019) Synthesis of carbon quantum dots with green luminescence from potato starch. New J Chem 43:10826–10833
79. Lu M, Zhou L (2019) One-step sonochemical synthesis of versatile nitrogen-doped carbon quantum dots for sensitive detection of Fe^{2+} ions and temperature in vitro. Mater Sci Eng, C 101:352–359
80. Huang HY, Cui Y, Liu MY, Chen JY, Wan Q, Wen YQ, Deng FJ, Zhou NG, Zhang XY, Wei Y (2018) A one-step ultrasonic irradiation assisted strategy for the preparation of polymer-functionalized carbon quantum dots and their biological imaging. J Colloid Interface Sci 532:767–773
81. So RC, Sanggo JE, Jin L, Diaz JMA, Guerrero RA, He J (2017) Gram-Scale Synthesis and kinetic study of bright carbon dots from citric acid and Citrus japonica via a microwave-assisted method. ACS Omega 2:5196–5208
82. Du X-Y, Wang C-F, Wu G, Chen S (2021) The rapid and large-scale production of carbon quantum dots and their integration with polymers. Angew Chem Int Ed 60:8585–8595
83. Yang S, Sun J, Li X, Zhou W, Wang Z, He P, Ding G, Xie X, Kang Z, Jiang M (2014) Large-scale fabrication of heavy doped carbon quantum dots with tunable-photoluminescence and sensitive fluorescence detection. J Mater Chem A 2:8660–8667
84. Wang J, Wang CF, Chen S (2012) Amphiphilic egg-derived carbon dots: rapid plasma fabrication, pyrolysis process, and multicolor printing patterns. Angew Chem Int Ed 51:9297–9301
85. Choi Y, Jo S, Chae A, Kim YK, Park JE, Lim D, Park SY, In I, Appl ACS (2017) Simple microwave-assisted synthesis of amphiphilic carbon quantum dots from A_3/B_2 polyamidation monomer set. Mater Interfaces 9:27883–27893
86. Park SY, Lee HU, Park ES, Lee SC, Lee JW, Jeong SW, Kim CH, Lee YC, Huh YS, Lee J, Appl ACS (2014) Photoluminescent green carbon nanodots from food-waste-derived sources: large-scale synthesis, properties, and biomedical applications. Mater Interfaces 6:3365–3370

87. Zhang J, Yuan Y, Liang G, Yu S-H (2015) Scale-up synthesis of fragrant nitrogen-doped carbon dots from bee pollens for bioimaging and catalysis. Adv Sci 2:1500002
88. Zheng H, Wang Q, Long Y, Zhang H, Huang X, Zhu R (2011) Enhancing the luminescence of carbon dots with a reduction pathway. Chem Commun 47:10650–10652
89. Ding H, Li X-H, Chen X-B, Wei J-S, Li X-B, Xiong H-M (2020) Surface states of carbon dots and their influences on luminescence. J Appl Phys 127:231101
90. Dong YQ, Wang RX, Li H, Shao JW, Chi YW, Lin XM, Chen GN (2012) Polyamine-functionalized carbon quantum dots for chemical sensing. Carbon 50:2810–2815
91. Mewada A, Pandey S, Thakur M, Jadhav D, Sharon M (2014) Swarming carbon dots for folic acid mediated delivery of doxorubicin and biological imaging. J Mater Chem B 2:698–705
92. Yang T, Huang J-L, Wang YT, Zheng AQ, Shu Y, Wang J-H (2019) β-Cyclodextrin-decorated carbon dots serve as nanocarriers for targeted drug delivery and controlled release. Chem Nano Mat 5:479–487
93. Cayuela A, Sorianoa ML, Valcárcel M (2016) β-Cyclodextrin functionalized carbon quantum dots as sensors for determination of water-soluble C60 fullerenes in water. Analyst 141:2682–2687
94. Zhou J, Shan X, Ma J, Gu Y, Qian Z, Chen J, Feng H (2014) Facile synthesis of P-doped carbon quantum dots with highly efficient photoluminescence. RSC Adv 4:5465–5468
95. Xu Q, Pu P, Zhao J, Dong C, Gao C, Chen Y, Chen J, Liu Y, Zhou H (2015) Preparation of highly photoluminescent sulfur-doped carbon dots for Fe(III) detection. J Mater Chem A 3:542–546
96. Chen H, Qiu Y, Ding D, Lin H, Sun W, Wang GD, Huang W, Zhang W, Lee D, Liu G, Xie J, Chen X (2018) Gadolinium-encapsulated graphene carbon nanotheranostics for imaging-guided photodynamic therapy. Adv Mater 30:1802748
97. Choi Y, Kang B, Lee J, Kim S, Kim GT, Kang H, Lee BR, Kim H, Shim SH, Lee G, Kwon OH (2016) Integrative approach toward uncovering the origin of photoluminescence in dual heteroatom-doped carbon nanodots. Chem Mater 28:6840–6847
98. Reckmeier CJ, Wang Y, Zboril R, Rogach AL (2016) Influence of doping and temperature on solvatochromic shifts in optical spectra of carbon dots. J Phys Chem C 120:10591–10604
99. Sarkar S, Das K, Ghosh M, Das PK (2015) Amino acid functionalized blue and phosphorous-doped green fluorescent carbon dots as bioimaging probe. RSC Adv 5:65913–65921
100. Xie S, Su H, Wei W, Li M, Tong Y, Mao Z (2014) Remarkable photoelectrochemical performance of carbon dots sensitized TiO_2 under visible light irradiation. J Mater Chem A 2:16365–16368
101. Wang J, Lim Y-F, Hoa GW (2014) Carbon-ensemble-manipulated ZnS heterostructures for enhanced photocatalytic H_2 evolution. Nanoscale 6:9673–9680
102. Qi Y-X, Zhang M, Fu Q-Q, Liu R, Shi G-Y (2013) Highly sensitive and selective fluorescent detection of cerebral lead(II) based on graphene quantum dot conjugates. Chem Commun 49:10599–10601
103. Liu J, Zhang H, Tang D, Zhang X, Yan L, Han Y, Huang H, Liu Y, Kang Z (2014) Carbon quantum dot/silver nanoparticle/polyoxometalate composites as photocatalysts for overall water splitting in visible light. ChemCatChem 6:2634–2641
104. Liu J, Liu Y, Liu N, Han Y, Zhang X, Huang H, Lifshitz Y, Lee S-T, Zhong J, Kang Z (2015) Metal-free efficient photocatalyst for stable visible water splitting via a two-electron pathway. Science 347:970–974
105. Liu J, Wang N, Yu Y, Yan Y, Zhang H, Li J, Yu J (2017) Carbon dots in zeolites: A new class of thermally activated delayed fluorescence materials with ultralong lifetimes. Sci Adv 3:e1603171
106. Rathore E, Maji K, Rao D, Saha B, Biswas K (2020) Charge transfer in the heterostructure of $CsPbBr_3$ nanocrystals with nitrogen-doped carbon dots. J Phys Chem Lett 11:8002–8007
107. Essner JB, Kist JA, Polo-Parada L, Baker GA (2018) Artifacts and errors associated with the ubiquitous presence of fluorescent impurities in carbon nanodots. Chem Mater 30:1878–1887
108. Wang H, Sun C, Chen X, Zhang Y, Colvin VL, Rice Q, Seo J, Feng S, Wang S, Yu WW (2017) Excitation wavelength independent visible color emission of carbon dots. Nanoscale 9:1909–1915

109. Hou H, Banks CE, Jing M, Zhang Y, Ji X (2015) Carbon quantum dots and their derivative 3d porous carbon frameworks for sodium-ion batteries with ultralong cycle life. Adv Mater 27:7861–7866
110. Ferrari AC (2007) Raman spectroscopy of graphene and graphite: Disorder, electron–phonon coupling, doping and nonadiabatic effects. Solid State Commun 143:47–57
111. Zhang X, Wang J, Liu J, Wu J, Chen H, Bi H (2017) Design and preparation of a ternary composite of graphene oxide/carbon dots/polypyrrole for supercapacitor application: Importance and unique role of carbon dots. Carbon 115:134–146
112. Gharat PM, Pal H, Dutta Choudhury S (2019) Photophysics and luminescence quenching of carbon dots derived from lemon juice and glycerol. Spectrochim Acta A Chem 209:14–21
113. Zhu S, Meng Q, Wang L, Zhang J, Song Y, Jin H, Zhang K, Sun H, Wang H, Yang B (2013) Highly photoluminescent carbon dots for multicolor patterning, sensors, and bioimaging. Angew Chem Int Ed 52:3953–3957
114. Demchenko AP (2019) Excitons in carbonic nanostructures. C-J Carbon Res 5:71
115. Ge L, Pan N, Jin J, Wang P, LeCroy GE, Liang W, Yang L, Teisl LR, Tang Y, Sun Y-P (2018) Systematic comparison of carbon dots from different preparations—consistent optical properties and photoinduced redox characteristics in visible spectrum and structural and mechanistic implications. J Phys Chem C 122:21667–21676
116. Zhu S, Song Y, Wang J, Wan H, Zhang Y, Ning Y, Yang B (2017) Photoluminescence mechanism in graphene quantum dots: Quantum confinement effect and surface/edge state. Nano Today 13:10–14
117. Wang Y, Kalytchuk S, Zhang Y, Shi H, Kershaw SV, Rogach AL (2014) Thickness-dependent full-color emission tunability in a flexible carbon dot ionogel. J Phys Chem Lett 5:1412–1420
118. Dong Y, Pang H, Yang HB, Guo C, Shao J, Chi Y, Li CM, Yu T (2013) Carbon-Based dots co-doped with nitrogen and sulfur for high quantum yield and excitation-independent emission. Angew Chem Int Ed 52:7800–7804
119. Galande C, Mohite AD, Naumov AV, Gao W, Ci L, Ajayan A, Gao H, Srivastava A, Weisman RB, Ajayan PM (2011) Quasi-molecular fluorescence from graphene oxide. Sci Rep 1:1–5
120. Shang J, Ma L, Li J, Ai W, Yu T, Gurzadyan GG (2012) The origin of fluorescence from graphene oxide. Sci Rep 2:1–8
121. Kong W, Wu H, Ye Z, Li R, Xu T, Zhang B (2014) Optical properties of pH-sensitive carbon-dots with different modifications. J Lumin 148:238–242
122. Konkena B, Vasudevan S (2014) Spectral migration of fluorescence in graphene oxide aqueous dispersions: evidence for excited-state proton transfer. J Phys Chem Lett 5:1–7
123. Wang X, Cao L, Lu FS, Meziani MJ, Li H, Qi G, Zhou B, Harruff BA, Kermarrec F, Sun YP (2009) Photoinduced electron transfers with carbon dots. Chem Commun, 3774–3776
124. Gao G, Jiang Y, Jia H, Yang J, Wu F (2018) On-off-on fluorescent nanosensor for Fe^{3+} detection and cancer/normal cell differentiation via silicon-doped carbon quantum dots. Carbon 134:232–243
125. Lan M, Zhang J, Chui Y-S, Wang P, Chen X, Lee C-S, Kwong H-L, Zhang W, Appl ACS (2014) Carbon nanoparticle-based ratiometric fluorescent sensor for detecting mercury ions in aqueous media and living cells. ACS Appl Mater Interfaces 6:21270–21278
126. Liu R, Li H, Kong W, Liu J, Liu Y, Tong C, Zhang X, Kang Z (2013) Ultra-sensitive and selective Hg^{2+} detection based on fluorescent carbon dots. Mat Res Bull 48:2529–2534
127. Dong Y, Chen C, Lin J, Zhou N, Chi Y, Chen G (2013) Electrochemiluminescence emission from carbon quantum dot-sulfite coreactant system. Carbon 56:12–17
128. Chen Y, Cao Y, Zhu J-J (2020) Carbon-based dots for electrochemiluminescence sensing. Mater Chem Front 4:369–385
129. Han T, Yan T, Li Y, Cao W, Pang X, Huang Q, Wei Q (2015) Eco-friendly synthesis of electrochemiluminescent nitrogen-doped carbon quantum dots from diethylene triamine pentacetate and their application for protein detection. Carbon 91:144–152
130. Li L-L, Ji J, Fei R, Wang C-Z, Lu Q, Zhang J-R, Jiang L-P, Zhu J-J (2012) A Facile microwave avenue to electrochemiluminescent two-color graphene quantum dots. Adv Func Mat 22:2971–2979

131. Yan FY, Zou Y, Wang M, Mu XL, Yang N, Chen L (2014) Highly photoluminescent carbon dots-based fluorescent chemosensors for sensitive and selective detection of mercury ions and application of imaging in living cells. Sens Actuators B 192:488–495
132. Zhou L, Lin YH, Huang ZZ, Ren JS, Qu XG (2012) Carbon nanodots as fluorescence probes for rapid, sensitive, and label-free detection of Hg^{2+} and biothiols in complex matrices. Chem Commun 42:1147–1149
133. Zhang SR, Wang Q, Tian GH, Ge HG (2014) A fluorescent turn-off/on method for detection of Cu^{2+} and oxalate using carbon dots as fluorescent probes in aqueous solution. Mater Lett 115:233–236
134. Qu KG, Wang JS, Ren JS, Qu XG (2013) Carbon dots prepared by hydrothermal treatment of dopamine as an effective fluorescent sensing platform for the label-free detection of iron(iii) ions and dopamine. Chem Eur J 19:7243–7249
135. Zhang Y-L, Wang L, Zhang H-C, Liu Y, Wang H-Y, Kang Z-H, Lee S-T (2013) Graphitic carbon quantum dots as a fluorescent sensing platform for highly efficient detection of Fe^{3+} ions. RSC Adv 3:3733–3738
136. Wee SS, Ng YH, Ng SM (2013) Synthesis of fluorescent carbon dots via simple acid hydrolysis of bovine serum albumin and its potential as sensitive sensing probe for lead (II) ions. Talanta 116:71–76
137. Zhao HX, Liu LQ, Liu ZD, Wang Y, Zhao XJ, Huang CZ (2011) Highly selective detection of phosphate in very complicated matrixes with an off–on fluorescent probe of europium-adjusted carbon dots. Chem Commun 47:2604–2606
138. Dong YQ, Wang RX, Tian WR, Chi YW, Chen GN (2014) "Turn-on" fluorescent detection of cyanide based on polyamine-functionalized carbon quantum dots. RSC Adv 4:3701–3705
139. Liu JM, Lin LP, Wang XX, Jiao L, Cui ML, Jiang SL, Cai WL, Zhang LH, Zheng ZY (2013) $Zr(H_2O)_2$EDTA modulated luminescent carbon dots as fluorescent probes for fluoride detection. Analyst 138:278–283
140. Hou XF, Zeng F, Du FK, Wu SZ (2013) Carbon-dot-based fluorescent turn-on sensor for selectively detecting sulfide anions in totally aqueous media and imaging inside live cells. Nanotechnology 24:335502–335510
141. Du FK, Zeng F, Ming YH, Wu SZ (2013) Carbon dots-based fluorescent probes for sensitive and selective detection of iodide. Microchim Acta 180:453–460
142. Zheng M, Xie ZG, Qu D, Li D, Du P, Jing XB, Sun ZC (2013) On–off–on fluorescent carbon dot nanosensor for recognition of chromium(VI) and ascorbic acid based on the inner filter effect. ACS Appl Mater Interfaces 5:13242–13247
143. Zhou Y, Qu ZB, Zeng YB, Zhou TS, Shi GY (2014) A novel composite of graphene quantum dots and molecularly imprinted polymer for fluorescent detection of paranitrophenol. Biosens Bioelectron 52:317–323
144. Jiang Y, Wang B, Meng F, Cheng Y, Zhu C (2015) Microwave-assisted preparation of N-doped carbon dots as a biosensor for electrochemical dopamine detection. J Colloid Interface Sci 452:199–202
145. Niu J, Gao H (2014) Synthesis and drug detection performance of nitrogen-doped carbon dots. J Lumin 149:159–162
146. Lu S, Wu D, Li G, Lv Z, Chen Z, Chen L, Chen G, Xia L, You J, Wu Y (2016) Carbon dots-based ratiometric nanosensor for highly sensitive and selective detection of mercury(II) ions and glutathione. RSC Adv 6:103169–103177
147. Yan Y, Sun J, Zhang K, Zhu H, Yu H, Sun M, Huang D, Wang S (2015) Visualizing gaseous nitrogen dioxide by ratiometric fluorescence of carbon nanodots-quantum dots hybrid. Anal Chem 87:2087–2093
148. Yu C, Li X, Zeng F, Zheng F, Wu S (2013) Carbon-dot-based ratiometric fluorescent sensor for detecting hydrogen sulfide in aqueous media and inside live cells. Chem Commun 49:403–405
149. Gordon J, Michel G (2008) Analytical sensitivity limits for lateral flow immunoassays. Clin Chem 54:1250–1251
150. Bu D, Zhuang HS, Yang GX, Ping XX (2014) An immunosensor designed for polybrominated biphenyl detection based on fluorescence resonance energy transfer (FRET) between carbon dots and gold nanoparticles. Sens Actuators B 195:540–548

151. Li HL, Zhang YW, Wang L, Tian JQ, Sun XP (2011) Nucleic acid detection using carbon nanoparticles as a fluorescent sensing platform. Chem Commun 47:961–963
152. Xu L, Zhao CQ, Wei WL, Ren JS, Miyoshi D, Sugimoto N, Qu XG (2012) Aptamer carbon nanodot sandwich used for fluorescent detection of protein. Analyst 137:5483–5486
153. Dai H, Yang CP, Tong YJ, Xu GF, Ma XL, Lin YY, Chen GN (2012) Label-free electrochemiluminescent immunosensor for α-fetoprotein: performance of Nafion–carbon nanodots nanocomposite films as antibody carriers. Chem Commun 48:3055–3057
154. Li JZ, Wang NY, Thanh TTT, Huang CA, Chen L, Yuan LJ, Zhou LP, Shen R, Cai QY (2013) Electrogenerated chemiluminescence detection of trace level pentachlorophenol using carbon quantum dots. Analyst 138:2038–2043
155. Xu Y, Wu M, Feng X-Z, Yin X-B, He X-W, Zhang Y-K (2013) Reduced carbon dots versus oxidized carbon dots: Photo- and electrochemiluminescence investigations for selected applications. Chem Eur J 19:6282–6288
156. Tao HQ, Yang K, Ma Z, Wan JM, Zhang YJ, Kang ZH, Liu Z (2012) In vivo NIR fluorescence imaging, biodistribution, and toxicology of photoluminescent carbon dots produced from carbon nanotubes and graphite. Small 8:281–290
157. Zhou B, Guo Z, Lin Z, Zhang L, Jiang B-P, Shen X-C (2019) Recent insights into near-infrared light-responsive carbon dots for bioimaging and cancer phototherapy. Inorg Chem Front 6:1116–1128
158. Zhai X, Zhang P, Liu C, Bai T, Li W, Dai L, Liu W (2012) Highly luminescent carbon nanodots by microwave-assisted pyrolysis. Chem Commun 48:7955–7957
159. Datta KKR, Kozak O, Ranc V, Havrdova M, Bourlinos AB, Safarova K, Hola K, Tomankova K, Zoppellaro G, Otyepka M, Zboril R (2014) Quaternized carbon dot-modified graphene oxide for selective cell labelling–controlled nucleus and cytoplasm imaging. Chem Commun 50:10782–10785
160. Zhang M, Bai L, Shang W, Xie W, Ma H, Fu Y, Fang D, Sun H, Fan L, Han M, Liu C, Yang S (2012) Facile synthesis of water-soluble, highly fluorescent grapheme quantum dots as a robust biological label for stem cells. J Mater Chem 22:7461–7467
161. Cao L, Wang X, Meziani MJ, Lu F, Wang H, Luo PG, Lin Y, Harruff BA, Veca LM, Murray D, Xie S-Y, Sun Y-P (2007) Carbon dots for multiphoton bioimaging. J Am Chem Soc 129:11318–11319
162. Liu Q, Guo B, Rao Z, Zhang B, Gong JR (2013) Strong two-photon-induced fluorescence from photostable, biocompatible nitrogen-doped graphene quantum dots for cellular and deep-tissue imaging. Nano Lett 13:2436–2441
163. Hu Y, Yang J, Tian J, Jia L, Yu J-S (2015) Oxygen-driven, high-efficiency production of nitrogen-doped carbon dots from alkanolamines and their application for two-photon cellular imaging. RSC Adv 5:15366–15373
164. Song Y, Shi W, Chen W, Li X, Ma H (2012) Fluorescent carbon nanodots conjugated with folic acid for distinguishing folate-receptor-positive cancer cells from normal cells. J Mater Chem 22:12568–12573
165. Zheng M, Ruan S, Liu S, Sun T, Qu D, Zhao H, Xie Z, Gao H, Jing X, Sun Z (2015) Self-targeting fluorescent carbon dots for diagnosis of brain cancer cells. ACS Nano 9:11455–11461
166. Ruan S, Quan J, Shen S, Chen J, Zhu J, Jiang X, He Q, Yang W, Gao H (2014) Fluorescent carbonaceous nanodots for noninvasive glioma imaging after angiopep-2 decoration. Bioconjug Chem 25:2252–2259
167. Yang S-T, Cao L, Luo PG, Lu F, Wang X, Wang H, Meziani MJ, Liu Y, Qi Q, Sun Y-P (2009) Carbon dots for optical imaging in vivo. J Am Chem Soc 131:11308–11309
168. Ko HY, Chang YW, Paramasivam G, Jeong MS, Cho S, Kim S (2013) In vivo imaging of tumour bearing near-infrared fluorescence-emitting carbon nanodots derived from tire soot. Chem Commun 49:10290–10292
169. Chen H, Wang GD, Tang W, Todd T, Zhen Z, Tsang C, Hekmatyar K, Cowger T, Hubbard RB, Zhang W, Stickney J, Shen B, Xie J (2014) Gd-encapsulated carbonaceous dots with efficient renal clearance for magnetic resonance imaging. Adv Mater 26:6761–6766

170. Du F, Ju M, Zhang H, Zhang L, Sun M, Zhou Z, Dai Z, Zhang L, Gong A, Wu C (2015) Engineering iodine-doped carbon dots as dual-modal probes for fluorescence and X-ray CT imaging. Int J Nanomed 10:6943–6953
171. Su H, Liao Y, Wu F, Sun X, Liu H, Wang K, Zhu X (2018) Cetuximab-conjugated iodine doped carbon dots as a dual fluorescent/CT probe for targeted imaging of lung cancer cells. Colloids Surf B 170:194–200
172. Zhao Y, Hao X, LuW,Wang R, Shan X, Chen Q, Sun G, Liu J (2018) Facile preparation of double rare earth-doped carbon dots for MRI/CT/FI multimodal imaging. ACS Appl NanoMater 1:2544–2551
173. Qu D, Wang X, Bao Y, Sun Z (2020) Recent advance of carbon dots in bio-related applications. J Phys Mater 3:022003
174. Zheng M, Liu S, Li J, Qu D, Zhao H, Guan X, Hu X, Xie Z, Jing X, Sun Z (2014) Integrating oxaliplatin with highly luminescent carbon dots: an unprecedented theranostic agent for personalized medicine. Adv Mater 26:3554–3560
175. Feng T, Ai X, An G, Yang P, Zhao Y (2016) Charge-convertible carbon dots for imaging-guided drug delivery with enhanced in vivo cancer therapeutic efficiency. ACS Nano 10:4410–4420
176. Wang H, Di J, Sun Y, Fu J, Wei Z, Matsui H, Alonso ADC, Zhou S (2015) Biocompatible PEG-chitosan@carbon dots hybrid nanogels for two-photon fluorescence imaging, near-infrared light/ph dual-responsive drug carrier, and synergistic therapy. Adv Funct Mater 25:5537–5547
177. Pei M, Pai J-Y, Du P, Liu P (2018) Facile synthesis of fluorescent hyper-cross-linked β-cyclodextrin-carbon quantum dot hybrid nanosponges for tumor theranostic application with enhanced antitumor efficacy. Mol Pharm 15:4084–4091
178. Du D, Wang K, Wen Y, Li Y, Li YY (2016) Photodynamic graphene quantum dot: reduction condition regulated photoactivity and size dependent efficacy. ACS Appl Mater Interfaces 8:3287–2394
179. Wang J, Zhang Z, Zha S, Zhu Y, Wu P, Ehrenberg B, Chen JY (2014) Carbon nanodots featuring efficient FRET for two-photon photodynamic cancer therapy with a low fs laser power density. Biomaterials 35:9372–9381
180. Jia Q, Ge J, Liu W, Liu S, Niu G, Guo L, Zhang H, Wang P (2016) Gold nanorod@silica-carbon dots as multifunctional phototheranostics for fluorescence and photoacoustic imaging-guided synergistic photodynamic/photothermal therapy. Nanoscale 8:13067–13077
181. Nandi S, Bhunia SK, Zeiri L, Pour M, Nachman I, Raichman D, Lellouche JM, Jelinek R (2017) Bifunctional carbon-dot-WS_2 nanorods for photothermal therapy and cell imaging. Chem Eur J 23:963–969
182. Kang ZH, Tsang CHA, Wong N-B, Zhang ZD, Lee S-T (2007) Silicon quantum dots: A general photocatalyst for reduction, decomposition, and selective oxidation reactions. J Am Chem Soc 129:12090–12091
183. Yao Y, Li GH, Ciston S, Lueptow RM, Gray KA (2008) Photoreactive TiO_2/carbon nanotube composites: Synthesis and reactivity. Environ Sci Technol 42:4952–4957
184. Yu XJ, Liu JJ, Yu YC, Zuo SL, Li BS (2014) Preparation and visible light photocatalytic activity of carbon quantum dots/TiO_2 nanosheet composites. Carbon 68:718–724
185. Li HT, Liu RH, Liu Y, Huang H, Yu H, Ming H, Lian SY, Lee S-T, Kang ZH (2012) Carbon quantum dots/Cu_2O composites with protruding nanostructures and their highly efficient (near) infrared photocatalytic behavior. J Mater Chem 22:17470–17475
186. Zhang HC, Huang H, Ming H, Li HT, Zhang LL, Liu Y, Kang ZH (2012) Carbon quantum dots/Ag_3PO_4 complex photocatalysts with enhanced photocatalytic activity and stability under visible light. J Mater Chem 22:10501–10506
187. Zhang HC, Ming H, Lian S, Huang H, Li H, Zhang L, Liu Y, Kang Z, Lee ST (2011) Fe_2O_3/carbon quantum dots complex photocatalysts and their enhanced photocatalytic activity under visible light. Dalton Trans 40:10822–10825
188. Yu H, Zhang HC, Li HT, Huang H, Liu Y, Ming H, Kang ZH (2012) ZnO/carbon quantum dots nanocomposites: one-step fabrication and superior photocatalytic ability for toxic gas degradation under visible light at room temperature. New J Chem 36:1031–1035

189. Tang L, Ji R, Cao X, Lin J, Jiang H, Li X, Teng KS, Luk CM, Zeng S, Hao J, Lau SP (2012) Deep ultraviolet photoluminescence of water-soluble self-passivated graphene quantum dots. ACS Nano 6:5102–5110
190. Feng XT, Zhang F, Wang YL, Zhang Y, Yang YZ, Liu XG (2015) Luminescent carbon quantum dots with high quantum yield as a single white converter for white light emitting diodes. Appl Phys Lett 107:213102
191. Zhang W, Yu SF, Fei L, Jin L, Pan S, Lin P (2015) Large-area color controllable remote carbon white-light light-emitting diodes. Carbon 85:344–350
192. Guo X, Wang C-F, Yu Z-Y, Chen L, Chen S (2012) Facile access to versatile fluorescent carbon dots toward light-emitting diodes. Chem Commun 48:2692–2694
193. Chen Y, Zheng M, Xiao Y, Dong H, Zhang H, Zhuang J, Hu H, Lei B, Liu Y (2016) A self-quenching-resistant carbon-dot powder with tunable solid-state fluorescence and construction of dual-fluorescence morphologies for white light-emission. Adv Mater 28:312–318
194. Zhang X, Zhang Y, Wang Y, Kalytchuk S, Kershaw SV, Wang Y, Wang P, Zhang T, Zhao Y, Zhang H, Cui T, Wang Y, Zhao J, Yu WW, Rogach AL (2013) Color-switchable electroluminescence of carbon dot light-emitting diodes. ACS Nano 7:11234–11241
195. Kwon W, Kim Y-H, Lee C-L, Lee M, Choi HC, Lee T-W, Lee S-W (2014) Electroluminescence from graphene quantum dots prepared by amidative cutting of tattered graphite. Nano Lett 14:1306–1311
196. Wang F, Chen Y-H, Liu C-Y, Ma D-G (2011) White light-emitting devices based on carbon dots' electroluminescence. Chem Commun 47:3502–3504
197. Essner JB, Baker GA (2017) The emerging roles of carbon dots in solar photovoltaics: A critical review. Environ Sci NANO 4:1216–1263
198. Fernando KAS, Sahu S, Liu Y, Lewis WK, Guliants EA, Jafariyan A, Wang P, Bunker CE, Sun Y (2015) Carbon quantum dots and applications in photocatalytic energy conversion. ACS Appl Mater Interfaces 7:8363–8376
199. Wei G, Xu X, Liu J, Du K, Du J, Zhang S, An C, Zhang J, Wang Z (2017) Carbon quantum dots decorated hierarchical $Ni(OH)_2$ with lamellar structure for outstanding supercapacitor. Mater Lett 186:131–134
200. Zhang Y, Foster CW, Banks CE, Shao L, Hou H, Zou G, Chen J, Huang Z, Ji X (2016) Graphene-rich wrapped petal-like rutile TiO_2 tuned by carbon dots for high-performance sodium storage. Adv Mater 28:9391–9399
201. Yang Y, Ji X, Jing M, Hou H, Zhu Y, Fang L, Yang X, Chen Q, Banks CE (2015) Carbon dots supported upon N-doped TiO_2 nanorods applied into sodium and lithium ion batteries. J Mater Chem A 3:5648–5655
202. Jing M, Wang J, Hou H, Yang Y, Zhang Y, Pan C, Chen J, Zhu Y, Ji X (2015) Carbon quantum dot coated Mn_3O_4 with enhanced performances for lithium-ion batteries. J Mater Chem A 3:16824–16830
203. Ma Z, Zhang Y-L, Wang L, Ming H, Li HT, Zhang X, Wang F, Liu Y, Kang ZH, Lee S-T (2013) Bioinspired photoelectric conversion system based on carbon-quantum-dot-doped dye–semiconductor complex. ACS Appl Mater Interfaces 5:5080–5084
204. Li Y, Hu Y, Zhao Y, Shi G, Deng L, Hou Y, Qu L (2011) An electrochemical avenue to green-luminescent graphene quantum dots as potential electron-acceptors for photovoltaics. Adv Mater 23:776–780
205. Gupta V, Chaudhary N, Srivastava R, Sharma GD, Bhardwaj R, Chand S (2011) Luminscent graphene quantum dots for organic photovoltaic devices. J Am Chem Soc 133:9960–9963
206. Xie C, Nie B, Zeng L, Liang F-X, Wang M-Z, Luo L, Feng M, Yu Y, Wu C-Y, Wu Y, Yu S-H (2014) Core–shell heterojunction of silicon nanowire arrays and carbon quantum dots for photovoltaic devices and self-driven photodetectors. ACS Nano 8:4015–4022
207. Gao P, Ding K, Wang Y, Ruan K, Diao S, Zhang Q, Sun B, Jie J (2014) Crystalline Si/graphene quantum dots heterojunction solar cells. J Phys Chem C 118:5164–5171

Chapter 12
Synthesis and Applications of Colloidal Nanomaterials of Main Group- and Transition- Metal Phosphides

G. Kedarnath

Abstract Technological advances based on miniaturization of devices have always been pivoted around the synthesis of high-quality advanced inorganic nanomaterials with respect to size and shape and the understanding of the corresponding exotic properties developed. Among them, colloidal metal phosphide nanomaterials have an edge over other colloidal nanomaterials owing to their exceptional properties due to structural and compositional diversity. Furthermore, the presence of earth abundant and environmentally friendly phosphorus makes them cheaper and benign materials. This chapter will give a brief introduction followed by introductory background of metal phosphides including history and properties of metal phosphides. Subsequently, a discussion on synthesis of colloidal metal phosphide nanomaterials is included which deals with methods for the synthesis of colloidal metal phosphide nanomaterials and common phosphorus sources for the metal phosphide synthesis. In the following sections, literature on synthesis of colloidal main group metal- and transition metal phosphide nanomaterials and their applications are incorporated. In the end, the chapter will be concluded with a brief note on future prospective of colloidal metal phosphide nanomaterials.

Keywords Metal phosphide · Colloidal · Main group metal phosphide · Transition metal phosphide · Properties

12.1 Introduction

The effective utilization of nano-science in advanced technologies is centered around the control of size, shape and composition on the nanoscale level and the knowledge of the physiochemical properties developed due to their tailoring and surface modifications. Based on this approach, the quest for miniaturization or scaling down the size

G. Kedarnath (✉)
Chemistry Division, Bhabha Atomic Research Centre, Mumbai 400085, India
e-mail: kedar@barc.gov.in

Homi Bhabha National Institute, Anushaktinagar, Mumbai 400094, India

A. K. Tyagi and R. S. Ningthoujam (eds.), *Handbook on Synthesis Strategies for Advanced Materials*, Indian Institute of Metals Series,
https://doi.org/10.1007/978-981-16-1892-5_12

of materials has moved beyond traditional metals, metal oxides in the last few decades as evident from the development made in the synthetic approaches and applications of metal chalcogenide quantum dots [1–3] and also the investigations carried on catalytic properties of nanoscaled nitrides and carbides [4]. In contrast, metal phosphide nanomaterials were explored very little and have only picked up momentum in the last few years despite their well-known bulk properties and existing industrial applications in semiconductors [5, 6] and catalysts [7]. Scaling down the size of phosphides to few nanometers lead to emergence of unique properties and performance, especially in the field of optoelectronics, catalysis and energy harvesting, etc. These new properties accompanied by the need to develop earth-abundant and environment-friendly alternatives to toxic and heavy metal chalcogenides are the key driving forces for exploring new synthetic ways to prepare metal phosphide nanomaterials.

Among the nanomaterials, colloidal nanomaterials or nanocrystals have emerged as promising candidates for many applications due to their tailorable properties through size, shape and composition along with their convenient processability. Furthermore, colloidal nanocrystals can be produced in large quantities making them affordable for thin films devices or catalysts by appropriate coating and printing techniques. In addition, employment of colloidal nanocrystals benefits the development of high-performance devices and efficient catalysts due to the size-, shape and composition-dependent properties. Therefore, a combination of colloidal nanomaterials and metal phosphide, i.e., colloidal metal phosphide nanomaterials would further result in many potential applications in optoelectronics [8, 9], photovoltaics [10], catalysis [11, 12], lithium ion batteries (LIBs) [13] and biomedicine [14], etc. leading to advanced technologies.

Although metal phosphide nanomaterials have been reviewed recently by several authors [11–13, 15–20], most of them were focused on metal phosphides for specific applications like catalysis, lithium ion batteries and photovoltaics, etc. but they are limited to transition metal phosphides. Therefore, the objective of the present review is to give over view of the colloidal synthesis of metal phosphide nanomaterials and their applications which have been investigated to date.

In this article, an introductory background of metal phosphides including brief history and properties of metal phosphides will be discussed. Subsequently, a discussion on the synthetic approaches for the colloidal metal phosphide nanocrystals and their applications will be described. Finally, a short conclusion will be included.

12.2 Introductory Back Ground of Metal Phosphides

12.2.1 History

In eighteenth century, German scientist Andreas Marggraf synthesized zinc phosphide, after isolating zinc. During the same period, Bertrand Pelletier prepared a

series of metal phosphides including Ag_2P and Ni_2P by heating white phosphorus with silver and nickel and characterized them on quantitative basis. Based on these reactions, several methods have been proposed to prepare bulk metal phosphides. However, due to the lack of finding their utility, it remained confined to books only until the 1960s when other metal phosphides have been isolated, structurally characterized and utilized them in metallurgy and pesticides. Initially, most of the syntheses of bulk metal phosphides adopted heat and beat method where the metal and phosphorus sources were heated under harsh conditions to yield crystalline bulk materials. Only countable syntheses were solvent mediated reactions.

12.2.2 Properties of Metal Phosphides

During early years of research, metal phosphides were defined as any compound that contains phosphorus and one or more metals with a general formula of M_xP_y, but without oxygen. Currently, phosphide is considered as a compound of phosphorus with one or several less electronegative elements. Accordingly, metal phosphides are defined as metal-phosphorus compounds where the metal is less electronegative than phosphorus with formula of M_xP_y. Phosphorus forms at least one stable compound with all the main group-, transition- metals and most of the rare-earth metals. Many metal phosphides exhibit several stoichiometries providing various crystal structures for binary and ternary metal phosphides. Most of them have M–P bonds with a strong covalent character [21]. These M–P bonds are often combined with highly covalent P–P bonds under harsher reaction conditions (highly active precursors or high reaction temperature). These bonding abilities accompanied by a wide range of compositions, crystal structures and electronic states, offer distinctive properties to metal phosphides and also facilitate many potential applications.

Stable binary metal phosphides are formed by most of the elements. Metal phosphides exist in wide range of compositions such as M_2P, M_3P_2, M_4P_3, M_6P_5, MP, MP_2, MP_5, etc. Metal phosphides can be broadly classified as metal-rich phosphides (M_nP_m, $m < n$; e.g., M_2P, M_3P_2, MP_2, M_4P_3, M_6P_5, etc.), monophosphides (MP), phosphorus-rich phosphides (M_nP_m, $m > n$; e.g., MP_2, MP_5, etc.) and phosphides with ionic-covalent bonding (e.g., phosphides of Li, Be and lanthanides, etc.).

A comprehensive account of metal phosphide structures was given by Schnering and Hönle in late nineteen eighties [22]. Recently, a structural survey of binary transition metal phosphides has been consummated by Chen and Whitemire [23]. Metal phosphides are categorized as dumbbells, cages, chains, tubes, etc. depending on the nature of the phosphorous units in the lattice. The explanation of P framework according to the nature of P units is due to the ionic nature of MP which in turn is a result of the higher electronegativity of phosphorus [22]. The structural description of phosphorus-rich metal phosphide families is difficult due to more diversity for a given stoichiometry which might be due to the more diffusive nature of the phosphorus orbitals and the hyper valence tendency of phosphorus. Therefore, P frameworks display high flexibility with P–P–P angles ranging from 60° to 120° and varying P–P

distances depending on the coordination around the metal center and on the M/P ratio.

The lower transition metal phosphides M_3P, M_2P and MP exhibit electron delocalization in the metal sub-lattice of phosphides as revealed by XPS [24–26] and XAENS [26] measurements. However, the degree of delocalization swiftly decreases with the increase in phosphorus content. This may be due to the ionic character of metal phosphides owing to the electronegative nature of P and also due to the substantial back-donation of electrons from metal to phosphorus.

The oxidation state of the metal in a metal phosphide lattice is neither easy to define nor to relate with the experimental properties. XPS [24–26] and XANES [26] studies indicated that phosphorus in M_3P, M_2P and MP exists in P^- oxidation state. However, the ionic character increases with the increasing content of phosphorus. Even then valence electrons are localized in phosphorus-rich metal phosphides and considered as valence compounds so that MPs can be approximately described in Zintl–Klemm framework. Accordingly, the P can be attributed with a formal charge and can adopt oxidation states ranging from 0 to −3.

Metal phosphides in general are semiconductors or insulators, due to localization of their electrons around phosphorus atoms. However, many of the metal-rich phosphides exhibit metallic properties. The electronic properties of the metal phosphides depend on the electronegativity difference between M and P, the M/P ratio and the crystal structure. Some of the bulk metal phosphides like LiFeP are superconducting in nature [27].

Metal phosphides exhibit wide range of compositional diversity which in turn gives rise to different physiochemical properties. This can be demonstrated by comparing the properties of the materials containing the same elements but with different phases. Likewise, magnetic properties are also dependent on the crystal- and band structure of that specific composition. Hence, metal phosphides exhibit different magnetic properties with varying compositions and structures. For instance, orthorhombic Co_2P is Pauli paramagnetic [28] whereas hexagonal Co_2P is ferromagnetic [29] in nature.

True and profound knowledge of the magnetic properties of metal phosphide is difficult to realize because the M:P stoichiometry is ambiguous and possible contamination by impurities in the materials. However, many studies have been dedicated to understanding the magnetic properties of metal phosphides. The magnetic studies of metal phosphides are mainly focused on bulk- and nano-transition metal phosphides, however, few investigations with doped main group metal phosphides have also been reported.

Among metal phosphides, investigations on magnetic properties in transition metal phosphide nanomaterials are mostly limited to 3d series transition metal phosphides, in particular, iron- and manganese-phosphide phases [30]. A list of structural and magnetic data for a few transition metal phosphide phases is given in Table 12.1. Most of 3d metal phosphides are either Pauli paramagnetic or antiferromagnetic or diamagnetic and very few like MnP, Fe_2P, Fe_3P and Co_2P are ferromagnetic.

Among bulk manganese phosphides, only MnP is ferromagnetic [31] with a T_C of 292 K while Mn_2P [32], Mn_3P [33] are antiferromagnetic and MnP_4 [34] is

Table 12.1 A list of structural and magnetic data of a few transition metal phosphide phases

S. No.	Phase	Magnetic property/structure	References
1	VP	Weakly paramagnetic	[36]
2	CrP	Weakly paramagnetic	[36]
3	Cr_3P	Pauli paramagnetic	[33]
4	MnP	Ferromagnetic, $T_c = 292$ K/Orthorhombic	[31]
5	Mn_2P	Antiferromagnetic, $T_N = 103$ K/Hexagonal Fe_2P	[32]
6	Mn_3P	Antiferromagnetic, $T_N = 115$ K/Tetragonal Fe_3P	[33]
7	MnP_4	Diamagnetic/Triclinic	[34]
8	FeP	Antiferromagnetic, $T_N = 115$ K/Orthorhombic	[38, 39]
9	Fe_2P	Ferromagnetic, $T_C = 217$ K/Hexagonal	[40]
10	Fe_3P	Ferromagnetic, $T_C = 692$ K/Tetragonal	[42]
11	CoP	Weakly paramagnetic	[36]
12	Co_2P	Pauli paramagnetic/Orthorhombic	[28]
		Feromagnetic, $T_C = 580$ K/Hexagonal	[29]
13	NiP	Pauli paramagnetic	[43]
14	Ni_2P	Pauli paramagnetic	[44]
15	Ni_3P	Pauli paramagnetic	[33]
16	NiP_2	Diamagnetic	[45]
17	CuP_2	Diamagnetic	[45]
18	NbP	Pauli paramagnetic	[47]
19	Mo_3P	Superconductor, diamagnetic	[48]
20	Mo_8P_5	Superconductor	[48]
21	Mo_4P_3	Superconductor	[48]
22	Ru_2P	Paramagnetic	[50]
23	Rh_2P	Superconductor	[51]
24	RhP_2	Diamagnetic	[52]
25	RhP_3	Diamagnetic	[45]
26	AgP_2	Diamagnetic	[52]
27	AgP_3	Diamagnetic	[52]
28	Ag_3P_{11}	Diamagnetic	[52]
29	Re_3P_4	Diamagnetic	[53, 54]
30	Re_2P_5	Diamagnetic	[53, 54]
31	ReP_4	Diamagnetic	[53, 54]
32	Ir_2P	Antiferromagnetic	[55]
33	IrP	Antiferromagnetic	[52]
34	IrP_2	Diamagnetic	[52]
35	IrP_3	Diamagnetic	[52]

diamagnetic. Huber et al. were the first to report the magnetic measurements of an MnP single crystal [35]. The same group later measured temperature dependent magnetic measurements on a spherical single crystal of high-purity stoichiometric MnP in the range 4 to 500 K and found that the ferromagnetic Curie temperature was 291.5 ± 0.2 K. Furthermore, it was observed MnP is metamagnetic below 50 K and shows an antiferromagnetic-ferromagnetic transition which is a function of applied field and temperature (also referred as helimagnetic ordering) [31]. Later Stein and Walmsley confirmed this transition and also demonstrated that monophosphides of V, Cr and Co do not exhibit a magnetic transition [36]. The distinct magnetism in MnP is attributed to the intersection of the Fermi level with a localized electron state before exchange splitting occurs [36]. The results were found to be consistent with a band structure proposed by Goodenough [37].

In the case of the iron phosphides, magnetic properties of bulk FeP, Fe_2P and Fe_3P phases are known. The magnetic properties differ considerably according to the composition of the phase in spite of same constituent elements. The orthorhombic FeP phase show antiferromagnetic properties below 120 K [38, 39]. Fe_2P crystallizes in hexagonal and orthorhombic structures and both of them exhibit ferromagnetism. Fe_2P is a ferromagnet with a Curie temperature (T_C) of 209 K with a Weiss constant of 400 K [40]. The former also exhibit defect dependent magnetic properties [41]. Fe_3P adopts tetragonal crystal structure and shows ferromagnetism with a relatively high Curie temperature of 692 K [42].

In cobalt and nickel phosphide series, bulk CoP [36], NiP [43], Ni_2P [44] and Ni_3P [33] are paramagnetic while phosphorus-rich phase of nickel, NiP_2 is diamagnetic [45]. Similar to NiP_2, its copper counterpart CuP_2 is also diamagnetic in nature [45].

As mentioned earlier, Co_2P magnetically behaves differently in its two structural forms. The orthorhombic form of Co_2P [28] exhibit paramagnetism while its hexagonal crystal system show ferromagnetism [29] similar to that of its manganese and iron analogs [29].

Stein and Walmsley demonstrated that the monophosphides of V, Cr, Fe and Co in the range of 4.2 K to room temperature are weakly paramagnetic by measuring magnetic susceptibilities [36].

Other than mono- and di- metal phosphides, the magnetic moments of metal phosphides with the composition M_3P (M=Cr, Mn, Fe, or Ni) have been reported to resemble the Slater-Pauling curve. However, the moments of Fe_3P, Co_3P and Ni_3P are lower than that of the corresponding metals which are attributed to the filling of some of the 3d orbitals by electron transfer from the phosphorus [33]. The temperature dependent magnetic measurements indicated that Ni_3P and Cr_3P show a temperature-independent Pauli-type paramagnetism while Mn_3P exhibit antiferromagnetic properties with T_N of 115 K [33].

The magnetic properties of binary metal phosphides can further be modified by combining two phosphides of 3d transition metals that lie apart. For instance, neither Co_2P nor Mn_2P are ferromagnetic, but intermediate phase MnCoP reach maximum Curie temperature at 576 K and magnetization at 3.03 μ_B/molecule [46].

In addition to the most studied 3d metal phosphides, the magnetic properties of 4d metal phosphides have also been studied. For instance, magnetic susceptibility measurements of randomly oriented NbP single crystals show very weak Pauli paramagnetism ($\sim 10^{-5}$ emu/mol) [47]. Yagi et al. investigated magnetic properties of molybdenum phosphides of different compositions and observed that the Tc of the binary molybdenum phosphides decreases with decreasing density. The T_c of Mo_3P (7 K) with the largest density is highest among the binary molybdenum phosphides and exhibits type II superconductivity. The superconducting transition of orthorhombic Mo_4P_3 is observed at 3 K [48] while MoP does not show the superconducting transition down to 1 K [49]. The magnetic susceptibility measurements by Ohta revealed that Ru_2P is paramagnetic while the presence of Co in ruthenium phosphide (RuCoP) exhibits antiferromagnetism with T_N of 11 ± 1 [50].

Among rhodium phosphides, the metal-rich Rh_2P is superconducting at 1.3 K [51] while the phosphorus-rich RhP_2 and RhP_3 are diamagnetic in nature [45, 52]. Similarly, the phosphorus-rich silver phosphides, AgP_2, AgP_3 and Ag_3P_{11} are diamagnetic semiconductors [52].

In addition to 3d and 4d transition metal phosphides, 5d transition metal phosphides have been studied. For instance, Re_3P_4, Re_2P_5 and ReP_4 are diamagnetic [53, 54]. However, the high metal content of Re_2P is expected to behave paramagnetic.

Among iridium phosphides, IrP is antiferromagnetic with $T_N = 0.35$ K while phosphorus-rich IrP_2 and IrP_3 are diamagnetic [52]. In contrast, Ir_2P shows the temperature dependent susceptibility. Furthermore, the violation of Curie–Weiss law and the negative Curie–Weiss temperature of Ir_2P revealed the spin glass behavior in an antiferromagnetic interaction background [55].

Magnetic properties of main group metal phosphide are rarely studied. Among group 13 metal phosphides, InP and GaP are diamagnetic in nature [56], however, their properties can be altered by doping with suitable dopants. For instance, manganese doped-InP quantum dots and GaP nanowires exhibit ferromagnetism [57, 58]. In group 14 metal phosphides, SiP_3 is nonmagnetic but can be transformed to ferromagnetic by hole doping [59] while Sn_4P_3 show diamagnetic behavior [60]. While the magnetic properties of germanium phosphide have not been studied, the ternary phosphide $MnGeP_2$ is known to exhibit ferromagnetism with different magnetic anisotropy to that of MnP [61].

12.3 Synthesis of Colloidal Metal Phosphide Nanomaterials

A number of methods and phosphorus precursors were accessible for the preparation of bulk metal phosphides in early eighties. In general, metal phosphides are produced by ball milling, solid- and liquid-phase syntheses and phosphorization. Nevertheless, these methods, pose different challenges. For instance, ball milling often requires longer duration for synthesizing the product and also causes agglomeration of the

particles while solid-state synthesis is not useful for large-scale synthesis of contaminant free compounds. Similarly, phosphorization through incipient wetness impregnation of a support with a metal- and a phosphite- or phosphate-salt and subsequent calcination and reduction often requires elevated temperatures and yield polydisperse particles. In few cases, the final catalysts with active material made up of these materials undergo surface oxidation which impacts negatively on the catalytic performance.

However, substantial advances in solution-phase synthesis of nanoparticles, particularly colloidal approaches for the synthesis of nanomaterials facilitated overcoming the problems that arose in the above traditional methods for the preparation of materials. The colloidal routes empower a great control over the size, shape and composition of the nanomaterials and are accompanied by the post surface modifications. Furthermore, post-synthetic dispersion on support reduces the impact of the supporting material on the properties of the final catalyst and the capping agents or surface ligands present on the nanomaterials passivate the surface and avoids the need for oxidative passivation prior to catalytic testing.

Among various colloidal nanomaterials, synthesis of colloidal metal phosphide nanomaterials is quite challenging due to the presence of strong covalent components in M–P bonds of metal phosphides. This requires extra efforts to control the dimensions and morphology of the nanomaterials by restricting the growth of the nanocrystallites through proper choice of surface ligands, suitable precursors with appropriate reactivity, reaction temperature and duration. Synthesis of colloidal metal phosphide nanomaterials needs harsh conditions such as high reaction temperature due to the higher heat of formation of M–P bonds of metal phosphides owing to their strong covalent component and also the need of high energy for the covalent bond formation when some of the M–P bonds combined with covalent P–P bonds [21].

Initially, the search for the development of synthetic protocols for designed metal phosphide nanomaterials is started with the size controlled band gap engineering of III–V semiconductors. However, the quest for other metal phosphide nanomaterials leads to the development of methods that have better control over the morphology of the materials. In addition to this, the possibility of depositing InP in the form of thin films leading to new fields of applications such as photoemitting diodes [62] and microwave oscillators [63] prompted the need to synthesize processable materials which could be deposited as thin films. Such processable materials can be achieved by synthesis of colloidal nanomaterials.

In general, synthesis of colloidal metal phosphide nanomaterials requires a metal- (cationic) and a phosphorus- (anionic) precursor with ligands, coordinating or non-coordinating solvents and heating. Broadly the colloidal routes can be categorized as multiple- and single-source precursor approach. Both these approaches adopt reactions involving thermal activation like solvothermal, hydrothermal, thermal decomposition (heat up and hot injection) and reduction methods to produce the metal phosphide nanocrystals.

12.3.1 Multiple Source Methods

Phosphorus precursors for the synthesis of colloidal metal phosphide nanocrystals

Different types of phosphorus precursors which have been used in the multiple source methods are elemental phosphorus, $[P(SiMe_3)_3]$, amino phosphines, alkali metal phosphorus (Na_3P) and PH_3 gas. One of the important criteria for the synthesis of nanocrystals is selecting appropriate precursors, ligands and reaction conditions like temperature and time.

Trimethylsilyl phosphine ($[P(SiMe_3)_3]$)

Trimethylsilyl phosphine is a highly reactive phosphorus precursor not only due to low dissociation energy (around 363 kJ mol^{-1}) of the P–Si bond but also due to the driving force imparted by highly electropositive Si attached to phosphorus atom to react with metal precursors.

The decomposition of $[P(SiMe_3)_3]$ is dependent on the different protic species present in the medium, pH and the metal precursors, however, its mechanism is still unclear.

However, this precursor has its own drawbacks like its pyrophoric nature, high cost, hazardous nature and secondary products produced during the course of reaction. In addition, high reactivity of $[P(SiMe_3)_3]$ results in the growth of nanocrystals to proceed via the Ostwald ripening mechanism leading to a broader size distribution.

Phosphine (PH_3)

A number of phosphorus precursors have been explored with the main aim of improving the size distribution. Of these, phosphine (PH_3) is a more stable, safer (if generated in situ) and moderately reactive precursor, compared to pyrophoric $[P(SiMe_3)_3]$. PH_3 is a gaseous precursor which is toxic and fatal even at a level of few ppm. However, most of the time, it is generated in situ either from sodium hypophosphite in basic conditions or HCl addition on Ca_3P_2 or Zn_3P_2.

Aminophosphines

Aminophosphines offer a cheaper, stable, safe and easy to handle phosphorus precursor with moderate reactivity. Aminophosphines being a P(III) compound require a reduction of the former to form InP using In(III) precursor.

The first step in the reaction mechanism involves an exchange of amino groups between primary amines and aminophosphine. The second step includes the formation of InP by oxidating three equivalents of $[P(NHR)_3]$ to a phosphonium salt (Scheme 12.1). The substituted aminophosphine acts as both phosphorus source and reducing agent. The proposed mechanism involves a nucleophilic attack by the P of one aminophosphine on an amino group of another aminophosphine [64]. Initially, $InCl_3$ reacts with $[P(NHR)_3]$ to form adducts with different resonance structures (Scheme 12.1). The positive charge delocalize over the P center and the N atoms enabling another $[P(NHR)_3]$ to nucleophilic attack on the N atom of the resonating

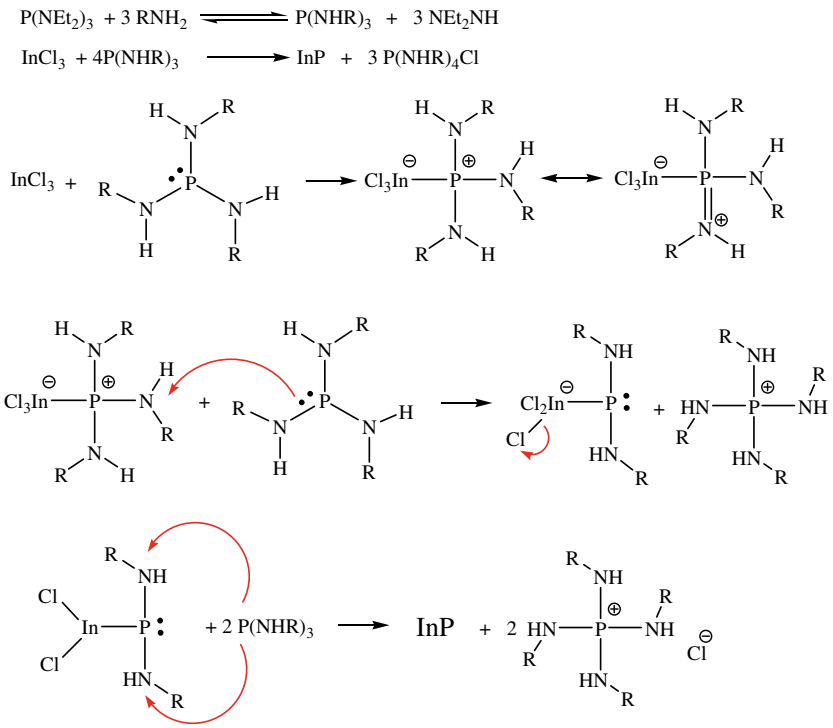

Scheme 12.1 Formation mechanism of InP nanocrystals (Reproduced from ref 64 with the permission of American Chemical Society)

structure (Scheme 12.1). Subsequently, InP is formed as a result of phosphorus nucleophilic substitution.

Tri-n-octyl phosphine (TOP)

In general, TOP is used in a large excess as it also serves both as a solvent for the metal precursors and also a capping agent on the surface of nanocrystals. In general, the decomposition of TOP is incomplete. To date, there is no relation could be found to how much TOP is required for a particular M/P ratio or a nanocrystal architecture in the final product.

Most common approach for the synthesis of metal phosphide nanocrystals is the wet chemical or solution-phase method involving the thermal decomposition of a metal precursor in the presence of TOP or a similar alkyl/aryl phosphine. This results in the formation of a metal-TOP complex at temperatures in the range of 200–250 °C and decomposes to TOP capped metal nanoparticles. The latter, catalyze the decomposition of the organophosphines and transform to metal phosphide nanoparticles via phosphidation at higher temperatures (≥300 °C) [18]. However, such a process often results in hollow particles as a result of the Kirkendall effect. In some cases, either an amorphous- intermediate or -product can be obtained. Further, the amorphous

intermediate can crystallize and undergo phosphidation to form metal phosphide nanoparticles. These materials can adopt a variety of stoichiometric phases due to the variable oxidation states of the metals.

Elemental Phosphorus

Historically, elemental P (white or red) has been the earlier source of phosphorus for the preparation of metal phosphide. Nowadays, this has been extended to the synthesis of metal phosphide nanoparticles using softer reaction conditions using molecular metal precursors.

White Phosphorus (P_4)

In general, white phosphorus is used in solid form and reacts indirectly with the metal precursor. Instead, the former converts to phosphate or phosphine depending on the reaction conditions like pH and solvent (protic or aprotic), etc. However, in few cases, it can also directly react with the metal precursor either in dry form or in the presence of aprotic solvent).

Most commonly, an excess amount of white phosphorus with respect to the metal precursor (typically in M(II) state) is used in hydrothermal or solvothermal processes results in polydispersed metal phosphide nanomaterials. A variety of morphologies were obtained using different solvent combinations in these reactions. With M(II) precursors such as metal chlorides, two approaches have been used for metal phosphide nanomaterials. One of them use an additional reducing agent such as $NaBH_4$ in ethanol to a solution containing metal and excess P_4 for producing metal phosphide nanoparticles. An excess of phosphorus avoids the side products. In this type of reaction, P_4 reacts with $NaBH_4$ to generate a phosphorus species which in turn reacts with the metal. In another approach, a part of P_4 reduces the metal giving PCl_3 as a byproduct while the remaining P_4 acts as phosphorus donor to yield P-rich metal phosphide nanoparticles. This route has been used for the synthesis of CuP_2, CoP_3 and NiP_2 nanoparticles.

To improve the size distribution, M(II) precursor was replaced either by M(0) precursor or metal nanoparticles and treated with P_4. For instance, the phase controlled metal phosphide nanomaterials could be achieved by using metal(0) nanoparticles and phosphorus with corresponding M:P stoichiometries as in the case of palladium (Pd_5P_2 and PdP_2) and copper (Cu_3P and CuP_2). The use of substoichiometric amounts of P_4 in such reactions leads to the formation of core-shell (Ni_2P–Ni) nanoparticles as in the case of Ni. However, reactions with metal(0) precursors delivered mixed phase materials. For example, [$Pd_2(dba)_3$], dba=dibenzylideneacetone] afforded a mixture of Pd_6P and Pd_3P_2 particles [65].

Red Phosphorus

The titled phosphorus has also been used as a phosphorus source in the hydrothermal or solvothermal synthesis of metal phosphide nanoparticles. In many cases, the low reactivity of the former P could be overcome by using higher reaction temperatures.

Alternative Phosphorus Sources

PCl_3 has also been used as a phosphorus source in a reaction of sodium with Ni(II) precursor to produce Ni_2P nanoparticles. The former has also been used for the synthesis of InP nanocrystals with an indium precursor and a strong reducing agent ($LiBEt_3H$).

In addition to the above phosphorus precursors, aryl-phosphines and -phosphites like triphenylphosphine and triphenyl phosphite (TPP), etc. have also been used for the synthesis of metal phosphide nanomaterials.

12.3.2 Single Source Molecular Precursor Method

In addition to multiple source methods, single source molecular precursors have also been adopted for the synthesis of colloidal metal phosphide nanomaterials. However, the number of reports is scanty and will be discussed at the end of each of the following sections immediately after the synthesis of metal phosphides using multiple source methods.

12.4 Syntheses of Colloidal Nanomaterials of Main Group Metal Phosphides

To date, a large number of metal phosphides are known due to their structural and compositional diversity. Among them, a limited number of main group metal phosphides either exist in nature or are synthesized by various methods compared to transition metal phosphides because main group metals can only adopt fewer oxidation states. Despite their restricted number, they have a wide range of applications in optoelectronics [66], solar cells [67], lithium ion batteries [68], thermoelectrics [69] and catalysis [70] owing to their interesting properties.

The main group metals mainly constitute metals of groups 1 and 2 (s-block) and groups 13 to 18 (p-block). Sometimes, metals of groups 3 and 12 are also included in the main group metals. However, the present article mainly focuses on group 12 to group 14 metal phosphides. As mentioned above, only a limited number of main group metal phosphides either known or synthesized over the years which have been listed in Table 12.2.

Table 12.2 A list of main group metal phosphides synthesized over the years

Main group metal phosphides			
Group 12 metal phosphides	Group 13 metal phosphides	Group 14 metal phosphides	Group 15 metal phosphides
Zn_3P_2 [71]	AlP [77]	$Si_{12}P_5$ [82]	AsP_n ($n = 1, 3$) [93, 94]
ZnP_n ($n = 2, 4$) [72, 73]	InP[78]	SiP_n ($n = 1, 2$) [83, 84]	SbP [95]
Cd_6P_7 [74]	GaP [79]	GeP_n ($n = 1$–$3, 5$) [85–88]	BiP [95]
Cd_3P_2 [75]	TlP_n ($n = 3,5$) [80, 81]	Sn_4P_3 [89]	
Hg_3P_n ($n = 1, 2, 4$) [76]		SnP_n ($n = 1, 3$) [89, 90]	
		Sn_3P_4 [90]	
		Pb_2P [91], PbP_7 [92]	

12.4.1 Syntheses of Colloidal Nanomaterials of Group 12 Metal Phosphides

Group 12 metal phosphides (e.g., Zn_3P_2 and Cd_3P_2, etc.) have been the subject of interest owing to their distinct physical properties. For instance, Zn_3P_2 is a potential solar absorber material in photovoltaics owing to its high absorption coefficient (10^{-4} to 10^{-5} cm^{-1}), large carry diffusion length of 5–10 μm [96] and an apt band gap of 1.5 eV [71]. The comparable band gap of Zn_3P_2 to that of CdTe (1.4 eV) and CdSe (1.7 eV) accompanied by nontoxic and earth abundant nature of Zn and P elements, suggests a possible environmentally friendly alternative to these toxic cadmium chalcogenides. Besides this, the synthesis of luminescent Zn_3P_2 quantum dots ensured the replacement of heavier cadmium chalcogenides in optoelectronic applications. Other phosphide the same group, Cd_3P_2 having a bulk band gap of 0.55 eV [97] with high dielectric constant (5.8) [98], large Bohr exciton radius (36 nm) [71] in its quantum dot form can be a potential candidate with emission wavelengths ranging from visible to near-infrared region.

To date, there are limited number of reports on synthesis of Zn_3P_2 and Cd_3P_2 nanocrystals compared to indium-phosphide nanocrystals due to the large reactivity difference between zinc and cadmium precursors with phosphorus precursors [10, 71, 74, 99–108]. All these colloidal syntheses utilized either P_4 or TOP or PH_3 or $[P(SiMe_3)_3]$ as a phosphorus precursor and dimethylzinc ($ZnMe_2$) or diethylzinc ($ZnEt_2$) or zinc stearate as a zinc precursor and $Cd(OAc)_2.2H_2O$, cadmium propionate, as cadmium source.

Synthesis of Zn_3P_2 quantum dots in solution forms is difficult compared with other metal phosphides owing to surface oxidation and hydrolysis of Zn_3P_2 quantum dots. Synthesis of Zn_3P_2 nanocrystals usually require higher temperatures. Therefore, only

few reports on the synthesis of colloidal Zn_3P_2 nanostructures have been documented in the literature [10, 71, 99–103].

Weller and co-workers are the first to report the synthesis of luminescent Zn_3P_2 nanoparticles with quantum yields (QYs) up to 15%. The nanoparticles have been prepared by passing PH_3 into the zinc precursor with hexametaphosphate as complexing agent [99]. The crystal structure of the product however was not corroborated by powder X-ray diffraction or TEM studies. Later, colloidal Zn_3P_2 nanoparticles were synthesized by hot injection of $ZnMe_2$ and HP^tBu_2 in TOP into preheated tri-n-octyl phosphine oxide (TOPO) at 150 or 250 °C. The resulting particles were a mixture of both crystalline and amorphous materials. The nanoparticles displayed quantum confinement effect [71]. Miao et al. reported the synthesis of Zn_3P_2 nanocrystals using either PH_3 or $[P(SiMe_3)_3]$ and $ZnEt_2$ or zinc stearate as P and Zn sources. An emission was observed for nanocrystals prepared using $ZnEt_2$ and PH_3, but attributed it to Zn_3P_2/ZnO core/shell nanocrystals [100]. Buriak et al. prepared tetragonal phase Zn_3P_2 nanocrystallites of different sizes between 3 and 15 nm are using dimethylzinc and TOP and $[P(SiMe_3)_3]$ as phosphorus sources. Reaction of TOP with $ZnMe_2$ occurs at 350 °C and proceeds through in situ formations of Zn(0) and the following reaction with TOP to yield Zn_3P_2 nanoparticles. The size of the particles has been controlled by varying the concentration of TOP concentration in solution. The particle size decreases with increasing TOP concentration. TEM images of different sized nanoparticles obtained by varying the ratio of TOP/1-octadecene (ODE) are depicted in Fig. 12.1. However, the reaction with reactive $[P(SiMe_3)_3]$ takes place at 150 °C with shorter reaction times of 1 h. Here, the reaction mechanism undergoes via phosphido-bridged dimeric Zn(II) intermediates [101]. The same group synthesized crystalline Zn_3P_2 nanoparticles using dimethylzinc and TOP as precursors and fabricated nanoparticle thin films which exhibited excellent rectification behavior and photoconductivity [10]. In contrast to Buriak et al. synthesis of Zn_3P_2 nanocrystallites using $ZnMe_2$ and $[P(SiMe_3)_3]$ without strong passivating ligands, Glassy et al. produced monodisperse colloidal Zn_3P_2 quantum dots of size 2.6–2.9 nm using $ZnEt_2$, $[Zn(O_2CR)_2]$ and $[P(SiMe_3)_3]$ as precursors where carboxylate ligand acts as passivating agent [102]. These quantum dots (QDs) exhibit exciton peaks in the range of 424–535 nm, depending on the growth temperature. The growth mechanism is supported by NMR spectroscopy. The investigation of the size-dependent optical properties of Zn_3P_2 in the quantum confinement regime is a challenging task. Taking the challenge forward, Arachchige et al. synthesized tetragonal phase Zn_3P_2 crystallites with varying sizes (approximately 3–9 nm) through hot injection of $ZnEt_2$ and $[P(SiMe_3)_3]$ in hexadecylamine (HDA) and ODE. The nanocrystals with size-tunable absorption (2.11–2.73 eV) and emission (469–545 nm) (Fig. 12.2) in the visible region of electromagnetic spectrum were synthesized either by changing reaction temperature or the growth duration [103].

The first colloidal synthesis of Cd_3P_2 nanoparticles were reported by Weller and co-workers [99] by the injection of phosphine gas (PH_3) into a solution of cadmium propionate. These nanoparticles exhibited broad absorption and emission indicating

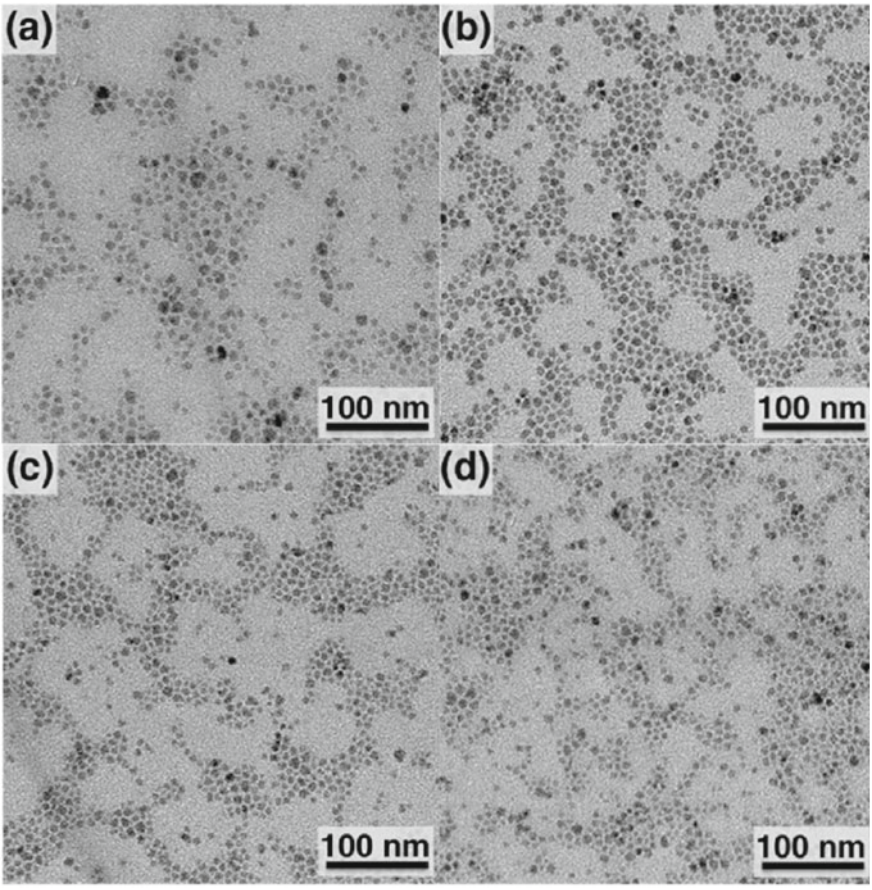

Fig. 12.1 TEM images of Zn_3P_2 nanoparticles of different sizes obtained by varying TOP/ODE ratios: **a** 3:7 (v/v), **b** 2:3 (v/v), **c** 1:1 (v/v), **d** 3:2 (v/v) of TOP and ODE, respectively (Reproduced from Ref. [101] with the permission of American Chemical Society)

a broad size distribution, together with defects, resulting from fast growth after nucleation.

The first single-sized Cd_3P_2 nanoparticles or magic-sized nanoparticles (MSNs) were synthesized via a non-injection or a heat up method by heating $Cd(OAc)_2.2H_2O$ and $[P(SiMe_3)_3]$ together in oleic acid (OA) and ODE, respectively to 240 °C. The Cd_3P_2 nanoparticles exhibited emission at 455 nm with a full width at half-maximum (fwhm) of only 17 nm and narrow band gap absorption peaking at 451 nm [104]. Later, colloidal synthesis of high-quality and emission tunable Cd_3P_2 nanocrystals in the range of 650 to 1200 nm and high quantum yields (38%) reported for the first by Miao and co-workers. The synthesis involves hot injection of $[P(SiMe_3)_3]$ into cadmium oleate at different temperatures and growth times [105]. The same group established that using PH_3 in place of $[P(SiMe_3)_3]$ as a phosphorus precursors results

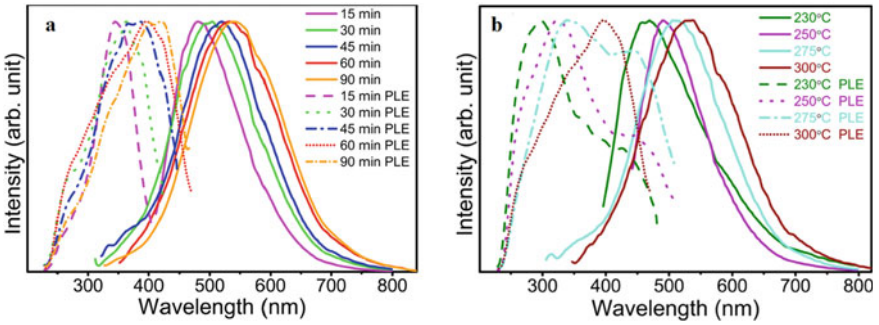

Fig. 12.2 Photoluminescence (PL) and Photoluminescence excitation (PLE) spectra of **a** Zn_3P_2 nanocrystals synthesized in HDA/ODE at 300 °C for 15–90 min along with the **b** Zn_3P_2 nanocrystals prepared at different temperatures for a fixed growth time of 1 h (Reproduced from Ref. [103] with the permission of American Chemical Society)

in the formation of Cd_6P_7 nanocrystals with a better size distribution. TEM images illustrate monodispersed spherical Cd_6P_7 nanocrystals with the average size of 6.5 $\pm$ 0.3 nm. The improved size distribution was attributed to lesser reactivity of PH_3 compared to $[P(SiMe_3)_3]$ which helps in controlling the size due to slower reaction rate. This is one of the potential methods for large-scale synthesis of metal phosphide nanocrystals [74].

Xie et al. demonstrated synthesis of nearly monodispersed Cd_3P_2 nanocrystals in a size range of 1.6 to 12 nm without any size selection methods by injecting reactive $[P(SiMe_3)_3]$ in ODE into a solution containing CdO in ODE and varying amounts of OA at 230 °C and setting a growth temperature of 250 °C under argon flow. The emission of as-prepared Cd_3P_2 nanocrystals are tunable in the range of 450–1500 nm with quantum yield higher than 30% [106].

Cd_3P_2 nanocrystals can easily undergo surface oxidation, which in turn deteriorate the quantum yield of the nanocrystals. To inhibit the surface oxidation, a protecting shell such as ZnS can be coated on Cd_3P_2 nanocrystals to improve the quantum yield. In this direction, Delpech reported a method where ZnS can be coated by using $Zn(OAc)_2.2H_2O$ and ethylene sulfide as the Zn and S precursors, respectively. They obtained Cd_3P_2/ZnS nanocrystals show photoluminescent quantum yield (PLQY) over 50% with modest air stability [107].

In addition to these dual/multiple source precursors, synthesis of Cd_3P_2 nanoparticles using single source precursor was reported by O'Brien and co-workers via thermolysis of cadmium di-organophosphide, $[MeCd(P^tBu_2)]_3$ in TOPO or 4-ethyl pyridine [108]. These Cd_3P_2 nanoparticles exhibited broad absorption peaks ranging from 400 to 500 nm and emission with an FWHM larger than 60 nm. The nanoparticles were polydispersed in size.

12.4.2 Syntheses of Colloidal Nanomaterials of Group 13 Metal Phosphides

Group 13 metal phosphide semiconductors have been attracting great interest because of their fundamental significance owing to the sturdiness of the covalent bond, larger excitonic Bohr radius and potential device applications [10, 109]. The presence of the covalent bond improves the optical stability of their QDs and reduces the toxicity caused due to the nonerosion of the constituent species in biological environment [14, 110]. Being less toxic and suitable band gaps, they have been considered as an alternative to the heavy metal of cadmium or lead chalcogenide QDs. Group 13 metal phosphide QDs exhibit stronger size quantization effects owing to their larger excitonic Bohr. Furthermore, Group 13 metal phosphide semiconductors with their tunable energy band gap and good minority carrier properties are suitable candidates for photovoltaic applications [10].

Bulk GaP is a non-emitting semiconductor with an indirect band gap of 2.24 eV [111]. GaP can be made light emitting by manipulating its indirect band gap structure to direct band gap through quantum confinement effect. Therefore, GaP has applications in optoelectronic devices [112] and solar cells [113]. Especially, GaP-based ternary and quaternary compound semiconductors (e.g., InGaP and AlInGaP) are suitable for multi-junction solar cell applications [114]. Amorphous GaP (a-GaP) has a number of localized states and finds applications in LEDs and high temperature transistors [115].

InP has a direct band gap of 1.35 eV, large component of covalent bonding and a Bohr exciton radius of 9.6 nm making its nanocrystals a suitable candidate for tunable emitting materials in visible and near- IR regions [116].

Investigations on group 13 metal phosphide colloidal semiconductor nanocrystals are limited, despite their technological importance. The main reason is the intricacies involved in producing the quality nanocrystals which in turn is due to difficulty in crystallizing them at low temperature (<400 °C) owing to a greater degree of covalent bonding in these materials and also absence of suitable precursors. These problems lead to the synthesis of polydispersed nanocrystals with larger sizes which are the least required for device applications. Therefore, the development of methodologies for synthesizing quality nanocrystals is inevitable. Accordingly, few researchers focused on producing the colloidal nanocrystals which have been discussed in the following paragraphs.

Synthesis of GaP nanocrystals includes heat up, hot injection of dual source precursor and thermal decomposition of single-molecule precursors. Nozik and coworkers [117] synthesized GaP QDs by heating reaction mixture of $GaCl_3$ and $[P(SiMe_3)_3]$ in TOP/TOPO mixture at 360 °C for 3 days. The average size of these QDs is 3 nm and exhibit exciton peak in their absorption spectrum due to the quantum confinement. Prasad et al. [118] synthesized GaP using TOPO and dodecylamine (DDA) as surfactants. These nanoparticles exhibited transverse optical (bulk) and surface optical phonons as studied by infrared transmission spectroscopy of solid nanoparticles. Recently, Kim et al. [111] reported a simplistic synthesis of GaP

nanocrystals by hot injection of $GaCl_3$ and $[P(SiMe_3)_3]$ as precursors into a mixture of ODE and palmitic acid (PA) at 200 °C. The optical properties of these nanocrystals showed the quantum confinement effect and also exhibited photo conducting properties.

In addition to the multiple source precursor methods, single source precursors have also been used for producing GaP nanocrystals of good quality. For example, monodispersed gallium phosphide nanocrystals were synthesized by thermal decomposition of a single molecular precursor, tris(di-tert-butylphosphino)gallane $[Ga(P^tBu_2)_3]$, in a hot mixture of trioctylamine (TOA) and HDA [119]. Size and shape of the GaP nanocrystals were controlled by the type and amount of surfactants. Wells et al. reported the synthesis of cubic phase GaP by thermal decomposition of $[H_2GaP(SiMe_3)_2]_3$ under vacuum in a range of at 200–600 °C [120]. The average particle sizes of GaP calculated by XRD peaks are 2.3 and 29.4 nm for two different decomposition temperatures.

The first colloidal synthesis of zinc blende InP quantum dots was synthesized by heating acetonitrile solution of chloroindium oxalate complex and $[P(SiMe_3)_3]$ either in TOPO or in a mixture of TOPO and TOP at 270 °C for several days. InP QDs with narrow size distribution and a mean diameter of 25 ± 1.9 Å (2.5 nm) were obtained when an excess of chloroindium oxalate was used in the reaction [121]. Later, this approach was extended to synthesis of GaP and $GaInP_2$ QDs [117]. After this groundbreaking report, $[P(SiMe_3)_3]$ was widely used as a phosphorus precursor in the synthesis of colloidal metal phosphide nanocrystals. Highly efficient band-edge emission was obtained when these nanocrystals were treated with a solution of HF [122, 123]. However, $[P(SiMe_3)_3]$ being a highly reactive precursor, the size distribution widens due to Ostwald ripening and hence, a number of phosphorus precursors have been explored with an aim of improving the size distribution.

To overcome the reactivity, safety and size distribution problems, Li et al. synthesized high-quality InP nanocrystals by passing the in situ generated PH_3 from Ca_3P_2 into a mixture of $[In(OAc)_3]$, MA and ODE maintained in the temperature range of 210–290 °C [124, 125]. The mean diameter size of nanocrystals (by XRD) as calculated by TEM images of two different samples are 3.0 and 6.4 nm with a size distribution of approximately 11 and 9%, respectively. Since the size and its distribution of InP nanocrystals are larger, Reiss et al. [126] synthesized InP nanocrystals by injecting an ethanolic solution of $NaBH_4$ as a reducing agent into a preheated flask containing $InCl_3$ and an elemental P (red P) at 40–70 °C. The reaction yield is approximately 100%. Park et al. [127] has prepared highly luminescent InP/ZnS nanocrystals by the reaction of white phosphorus with indium (In) precursor in the absence of any reducing agent. This offers an important method for the large-scale synthesis of InP nanocrystals. To decrease the reactivity of $[P(SiMe_3)_3]$, Harris and Bawendi [128] substituted Si with Ge or Sn by decreasing the polarity of Si–P bond.

Even with these less reactive precursors, the precursor conversion rates for InP QDs still occurs on a time scale faster than particle growth. Joung et al. replaced methyl with sterically hindered tert-butyl [129] or aryl group [130] in order to reduce the precursor reactivity. However, there is no improvement in the size distribution.

An alternative safe, stable and moderately reactive phosphorus precursor is aminophosphine [131–133]. Accordingly, high-quality InP nanocrystals were synthesized by hot injection of $[P(NMe_2)_3]$ into a solution of $InCl_3$ and $ZnCl_2$ in oleylamine (OLA) at 220 °C [134]. The dependency of growth behavior of InP QD was also studied with respect to the amount of $[P(NMe_2)_3]$, $ZnCl_2$ and the growth temperature. Laufersky et al. [132] reported the synthesis of InP nanocrystals by injecting tris(diethylamino)phosphine $[P(NEt_2)_3]$ into a mixture of $InCl_3$, $ZnCl_2$ and OLA at 180 °C. Using density functional theory calculations, they have also demonstrated that zinc salts in reaction solutions activate the aminophosphine for a disproportionation reaction to release P^{3-}, which is useful to obtain narrow size distribution irrespective of the phosphorus source.

12.4.3 Syntheses of Colloidal Nanomaterials of Group 14 Metal Phosphides

Group 14 phosphides have drawn considerable interest due to their compositional and phase dependent physical properties and applications [69, 70, 135]. For example, Sn-rich rhombohedral Sn_4P_3 is metallic in nature, whereas P-rich SnP_3, SnP and Sn_3P_4 are narrow band gap semiconductors [89]. These properties can be improved further by engineering shape and size of the materials to few nanometers. Tin-rich rhombohedral Sn_4P_3 having a layered structure is a potential anode material for alkali metal ion batteries [135], a photocatalyst for degradation of organic compounds [70] whereas phosphorus-rich trigonal Sn_3P_4 has potential application in thermoelectrics [69].

Synthesis of Sn_4P_3 was first reported in 1967 [136]. Later in 2004, Kim et al. [137] synthesized Sn_4P_3 nanoparticles using a mechanochemical method and tested for Li-ion battery applications. Although this material demonstrated a high reversible capacity, it has a drawback of large irreversible capacity loss due to the inactive Li_3P. To overcome this problem, the same group synthesized tin-rich $Sn_{4+\delta}P_3$ ($0 \leq \delta \leq 1$) which exhibited a high reversible capacity above 530 mA h g^{-1} [138]

Xie et al. [139] reported the first synthesis of Sn_4P_3 nanorods by metathesis reaction between $SnCl_2$ and Na_3P using ethylenediamine as a solvent via solvothermal method. The method however lacks control over the growth of these structures. Later, Liu et al. [140] reported the preparation of Sn_4P_3 nanoparticles with an average size of 15 nm by employing a solvothermal approach at a reaction temperature of 180 °C. However, SEM and TEM images show agglomerated nanoparticles. These nanoparticles show a high reversible capacity of 442 mAh g^{-1} at a current density of 100 mA g^{-1}. However, these methods including solvothermal syntheses resulted in either micrometer-sized or aggregated structures or hollow nanostructures with a large dispersion.

Kim et al. [68] produced uniformly dispersed tetrapod-shaped $SnP_{0.94}$ nanoparticles by the thermal decomposition reaction of tin acetate in TOP/TOPO. These

nanoparticles displayed superior cycling stability which was attributed to structural reversibility. The authors also explored the lithium storage mechanism which revealed that Li^+ intercalated in the intermolecular channel between the $SnP_{0.94}$ slabs.

Recently, Arachchige and co-workers [89] reported colloidal synthesis of monodisperse rhombohedral Sn_4P_3, hexagonal SnP and trigonal Sn_3P_4 nanoparticles with better control over size, morphology and phase by using SnI_4 and $[P(SiMe_3)_3]$ as precursors at 180 °C. The nanoparticles displayed tunable morphologies and size-dependent physical properties. The control over shape and phase was realized by varying the nucleation and growth temperature, the Sn/P molar ratio of precursors and the concentration of coordinating solvents (TBP or TOP). Figure 12.3a–d shows TEM images of the hexagonal SnP nanocrystals synthesized in the OLA/OA/ODE at 250 °C for different durations. A representative HRTEM image and selective area diffraction pattern (SAED) pattern of SnP nanocrystals is shown in Fig. 12.3e HRTEM image display (011) lattice spacing while SAED pattern (Fig. 12.3f) show concentric ring like pattern indicating polycrystalline nature of SnP nanocrystals. The absorption spectra of Sn_3P_4 nanoparticles exhibit size-dependent energy gaps which are consistent with quantum confinement effect.

Colloidal syntheses of group 14 metal phosphides other than tin phosphides are rare. Although mesoporous GeP_x microspheres and GeP_5 nanoflakes have been studied, there is no literature available on the colloidal synthesis of germanium phosphide. However, only a single report by Mézailles et al. [91] is available on colloidal synthesis of nearly spherical Pb_2P nanoparticles. The procedure involves the reaction

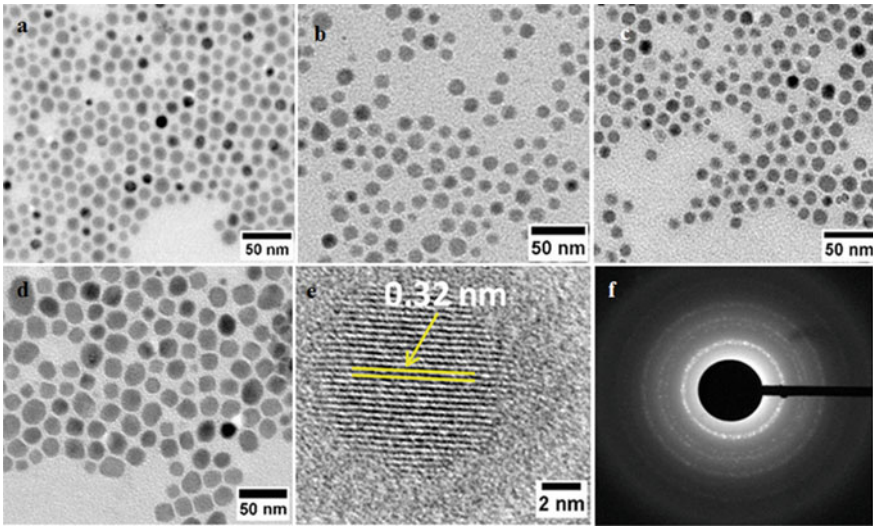

Fig. 12.3 TEM images of the hexagonal SnP nanocrystals synthesized in the OLA/OA/ODE system at 250 °C for **a** 5 s, **b** 30 s, **c** 60 s and **d** 180 s. A representative **e** HRTEM image and **f** a SAED pattern of the hexagonal SnP nanocrystals is shown (Reproduced from Ref. [89] with the permission of American Chemical Society)

of Pb nanoparticles with P_4 dissolved in toluene and oleylamine at 150 °C for 1 h. TEM images revealed polydispersed nanoparticles of size in the range of 5–10 nm.

12.5 Syntheses of Colloidal Nanomaterials of Transition Metal Phosphides

Transition metal phosphide nanocrystals have drawn considerable attention due to their unique electrochemical, magnetic and structural properties accompanied by a wide range of stoichiometry. These properties lead to potential applications in catalysis [12, 30], magnetic recording media [30] and in lithium ion batteries [13, 15]. For instance, transition metal phosphides are known to show high catalytic performance in hydrotreating [141], hydrogenation [142] and hydrogen evolution reactions [11, 17].

Transition metal phosphides exist in a large number of phases with a wide range of compositions, especially, a number of binary transition metal phosphides exists in M:P stoichiometry (Table 12.3). The existence of a wide range of binary metal phosphides is mainly due to the diversified crystal structures for a specific composition of M:P accompanied by variable oxidation states of transition metals. The most studied transition metal phosphides include phosphides of 3d transition elements such as Mn, Fe, Co, Ni, Cu along with some 4d-, 5d- transition elements like Mo, Ru, Rh, Pd, Ag; W, Pt, Au, etc. A number of these transition metal phosphides have been synthesized. These metal phosphides can be categorized into single or mono transition metal phosphides (e.g., Co_2P, Ni_2P, FeP, Fe_2P, etc.) and multiple transition metal phosphides (e.g., $NiCo_2P_x$, etc.).

Synthetic methodologies such as solvothermal, arrested precipitation, transformation of metal particles to phosphides are available for the preparation of transition metal phosphide nanostructures. However, all these methods have disadvantages of polydispersity and aggregation of particles for the investigations of size-dependent physical properties. For this reason, colloidal methods used for the synthesis of monodispersed metal chalcogenide quantum dots have been adopted for the preparation of transition metal phosphide nanomaterials. These colloidal methods involve the reaction of metal and phosphorus precursors at high temperatures in high boiling coordinating solvents such as TOPO. In general, spherical or 3D nanomaterials are obtained either with the use of reactive precursors (e.g., $[P(SiMe_3)_3]$) or upon rapid injection of less reactive precursor (e.g., TOP). Both these factors result in rapid nucleation with higher concentrations of reactants followed by a sudden decrease in reactant concentration favoring 3D growth.

The discussion on transition metal phosphide in the present article will be limited to preparative methods for colloidal nanomaterials of single transition metal phosphides.

Table 12.3 A list of transition metal phosphide

Transition metal phosphides								
3d metal phosphides								
Sc	Ti	V	Cr	Mn	Fe	Co	Ni	Cu
Sc_nP ($n = 3, 1$)	Ti_nP ($n = 3, 2$) Ti_5P_3 TiP_n ($n = 1, 2$)	V_nP ($n = 3$–1) VP_2 ($n = 2, 4$)	Cr_nP ($n = 3$–1) CrP_n ($n = 2, 4$)	Mn_nP ($n = 3$–1) MnP_4	Fe_nP ($n = 3$–1) FeP_2 ($n = 2, 4$)	Co_nP ($n = 2$–1) CoP_2	Ni_nP ($n = 3, 2$) $Ni_{12}P_5$ Ni_5P_4 NiP_n ($n = 1$–3)	Cu_3P CuP_2
[143, 144]	[145]	[146–148]	[33, 46, 149, 150]	[150, 151]	[33, 46, 150, 152]	[46, 148, 153]	[33, 46, 154–156]	[157, 158]
4d metal phosphides								
Y	Zr	Nb	Mo	Tc	Ru	Rh	Pd	Ag
YP_n ($n = 1, 5$)	Zr_nP ($n = 3, 2$) Zr_7P_4 $Zr_{14}P_9$ ZrP_n ($n = 1, 2$)	Nb_3P Nb_7P_4 NbP_n ($n = 1, 2$)	Mo_3P Mo_8P_5 Mo_4P_3 MoP_n ($n = 1, 2, 4$)	Tc_3P TcP_4	Ru_2P RuP_n ($n = 1$–4)	Rh_2P Rh_3P_2 Rh_4P_3 RhP_n ($n = 2, 3$)	$Pd_{12}P$ $Pd_{15}P_2$ Pd_nP ($n = 3, 5$–7) Pd_5P_2 PdP_n ($n = 2, 3$)	AgP_n ($n = 2, 3$) Ag_3P_{11}
[159, 160]	[161]	[47, 162, 163]	[48, 164–166]	[167]	[168–170]	[171]	[172–177]	[171]
5d metal phosphides								
Ln	Hf	Ta	W	Re	Os	Ir	Pt	Au
	HfP Hf_3P_2	Ta_3P Ta_5P_4 TaP_n ($n = 1, 2$)	W_3P WP_n ($n = 1, 2$)	Re_2P ReP_n ($n = 1$–3) Re_3P_4 Re_6P_{13}	OsP_n ($n = 2, 4$)	Ir_2P IrP_n (n = 2, 3)	Pt_5P_2 PtP_2	Au_2P_3
	[178, 179]	[162]	[162]	[53, 180, 181]	[170, 182]	[171, 176]	[183]	[184]

12.5.1 Syntheses of Colloidal Nanomaterials of Group 6 Metal (Cr, Mo, W) Phosphide

Bulk group 6 transition metal phosphides emerged as potential non-noble metal based catalysts in hydrogen evolution reaction (HER) [164], oxygen reduction reaction (ORR) [185] and hydrotreating reactions [141], etc. However, their counterparts in nano-regime have not been investigated extensively. In particular, syntheses of the colloidal nanomaterials of group 6 metal phosphides have been reported rarely, which will be presented in the following discussion.

Chromium Phosphide

As mentioned above, group 6 transition metal phosphides are potentially low cost and stable catalysts in various processes. Especially, chromium phosphide is a prospective ORR catalyst that is a vital component in fuel cells and metal-air batteries. In view of this, recently colloidal CrP nanocrystals were synthesized by reacting $[Cr(CO)_6]$ and triphenyl phosphite (TPP) in OLA at 320 °C for 2 h and evaluated its performance as ORR electrocatalyst. TEM images of the nanocrystals shows spheroidal shaped particles with an average size of 17 ± 3 nm. This CrP nanocrystals based catalyst showed significant catalytic activity comparable to commercial Pt/C, but with better stability and tolerance in alkaline solution. The exceptional ORR activity of CrP nanocrystals was attributed to the support provided by CrP for chemisorption of O_2 enabling the easy reduction of O_2 [186].

Molybdenum Phosphide

Among the extensively studied non-noble heterogeneous hydrogen evolution reaction (HER) electrocatalysts, materials based on molybdenum exhibit a wide range of compositions, structures and activities [187]. Of these, MoP is an active and stable catalyst for both hydrogen evolution and hydrodesulfurization (HDS) reactions. The former also catalyzes hydrodenitrogenation, hydrazine decomposition and hydrogenation reactions. Moreover, it was also established that different degrees of phosphorization going from Mo, Mo_3P to MoP gives rise to distinct catalytic activity and stability.

Joshua et al. [187] synthesized amorphous MoP nanoparticles (with diameters of 4.2 ± 0.5 nm) with good HER properties by heating $[Mo(CO)_6]$ and TOP in squalane at 320 °C. These nanoparticles remained amorphous even after heating at 450 °C in H_2/Ar and are stable in acidic media under operating conditions.

Recently, Shavel and co-workers [188] have synthesized MoP nanoparticles by heating $[Mo(CO)_6]$ with TPP in the presence of HDA and ODE and heated to 280–300 °C and kept at this temperature for a fixed time. These nanoparticles were thermally treated at 800 °C for 2 h to obtain crystalline nanoparticles. It is important to note that $[Mo(CO)_6]$ being a low boiling point compound, must be injected to the reaction flask after the purging step at 150 °C to prevent its loss during purging.

Tungsten Phosphide

Recently, research on catalysts for water splitting to produce hydrogen and hydrodesulfurization (HDS) is mainly focused on transition metal phosphides due to their encouraging electrical conductivity which will boost electron transfer and in turn promote these reactions. Especially, tungsten phosphides (WP_2 and WP) have attracted considerable attention as operating electrocatalysts in the above reactions due to their high electrical conductivity and catalytic properties [189]. Accordingly, substantial efforts have been focused on the composition, morphology and structure of these materials to improve their catalytic performance. However, the size and shape control of tungsten phosphide nanostructures is difficult due to their agglomeration. Hence, it is a great challenge to synthesize quality colloidal tungsten phosphide nanocrystals.

Accordingly, a limited number of synthetic approaches emerged for the synthesis of tungsten phosphide nanostructures. For instance, Li and co-workers [189] employed a facile method to synthesize highly crystalline WP_2 nanorods by heating the as-prepared $(NH_4)_{0.25}WO_3$ nanorods and NaH_2PO_2 at 750 °C and held at this temperature for 2 h in argon atmosphere, followed by a purification process. These nanorods exhibit good catalytic properties with nearly 100% Faradaic efficiency in acidic media and require only overpotentials of 101 and 148 mV to achieve current densities of 2 and 10 mA cm^{-2}, respectively. It preserves its catalytic activity in acidic, neutral and basic media.

Mu's group [190] reported synthesis of ultra-small tungsten phosphide nanoparticles of size less than 5 nm encapsulated within nitrogen doped carbon matrix. The catalyst made up of these nanoparticles exhibits superb catalytic activity in a hydrogen evolution reaction. The catalyst shows an excellent HER activity and stability in all pH conditions.

Recently, Liu et al. [191] prepared WP_2 nanosheets on W foil via an in situ two-step process. In the first step, W foil is oxidized to WO_3 particles which were subsequently converted into WP_2 nanosheets by phosphorization using NaH_2PO_2 at high temperature in a furnace. The electrodes made up of these nanosheets exhibited remarkable catalytic performance and stability in acidic and basic media.

Although there are routes available for the synthesis of tungsten phosphide nanostructures as described above, there is only one report by Schaak et al. [192] discussing the colloidal synthesis of uniform and amorphous WP nanoparticles. The synthesis involves heating of $[W(CO)_6]$ and TOP up to 320 °C for a fixed duration in squalane. TEM image of the product show nearly spherical particles with an average diameter of 3 nm. These amorphous nanoparticles exhibit catalytic properties in acidic HER reactions which are better than that of WS_2, W_2N and WC materials. The WP electrodes are also highly stable in strongly acidic aqueous solutions.

12.5.2 Syntheses of Colloidal Nanomaterials of Group 7 (Mn, Tc, Re) Metal Phosphide

Group 7 metal phosphide nanomaterials have known for understanding interesting magnetic, superconducting properties and also for their potential as catalysts in different reactions of industrial importance. Among them, the most studied system is manganese phosphide while two other colloidal metal phosphide nanomaterials (technetium- and rhenium-phosphides) were seldom studied. Accordingly, the following section will discuss the synthetic protocols available for these colloidal metal phosphides nanomaterials.

Manganese phosphide

Bulk manganese phosphide (MnP) is of great interest due to its magnetic, magneto-optical, magneto-caloric and superconducting properties [31, 193–195]. Especially, their nano counterparts demonstrate different and improved properties. For instance, MnP nanoclusters show characteristic texture [196], larger magnetic anisotropy [197] and superior magneto-optical response compared to bulk MnP [193].

For the first time, Brock et al. reported a new synthetic strategy for the preparation of MnP nanoparticles with low polydispersity by hot injection of zerovalent manganese carbonyl complex, $[Mn_2(CO)_{10}]$ with $[P(SiMe_3)_3]$ in TOPO/myristic acid (MA) at 100 °C and then heated to 220 °C for a fixed duration to have a particle size of approximately 5 nm. The appearance of lattice fringes in HRTEM indicates high degree of crystallinity of the particles. These nanoparticles exhibit super paramagnetic behavior below T_C [198].

The same group prepared MnP nanorods with narrow polydispersities by a quick injection of $[Mn_2(CO)_{10}]$ in ODE into TOP/TOPO at 350 °C and continued the reaction for a duration of 1 h [199]. HRTEM images indicated that growth of these rods occurs along the b-axis of the orthorhombic MnP. The rods were ferromagnetic and revealed only weak inter-particle interactions. However, polydisperse longer rods were obtained with multiple injections. Post-annealing of the rods at temperatures lower than the nucleation temperature results in the formation of cubes due to assembly of rods. Later, Hyeon et al. [200] improved polydispersity of MnP rods by thermal decomposition of continuously delivered Mn-TOP complex with constant injection rates of 10 and 20 mL/h, respectively. The sizes of MnP nanorods are 8 nm $\times$ 16 nm and 6 nm $\times$ 22 nm, respectively.

Rhenium Phosphide

Rhenium is one of the prospective noble metal based catalysts due to its inherent properties. Accordingly, rhenium based catalysts have been explored considerably with the prospect of cutting down the cost of catalyst and also improving the performance of the catalyst. For instance, Wang et al. [201] recently fabricated Re_2P and Re_3P_4 nanoparticles supported in N, P doped vesicular carbon (NPVC) by pyrolyzing ammonium perrhenate (NH_4ReO_4), 1-hydroxyethylidene-1,1-diphosphonic acid (HEDP) and melamine on the surface of SiO_2 spherical

particles and were examined for HER catalytic activity. The Re_3P_4@NPVC heterostructures demonstrated efficient catalytic activity compared to the commercial Pt/C. The enhancement in the catalytic activity was attributed to Re and P coupling drove attainment of optimum ΔG_H value for balancing adsorption and desorption of hydrogen. Furthermore, the synergetic electronic coupling of NPVC layer and nanoparticles improves the proton adsorption and reduction kinetics.

12.5.3 Syntheses of Colloidal Nanomaterials of Group 8 (Fe, Ru, Os) Metal Phosphides

Group 8 metal phosphides have been in focus owing to wide range of magnetic and catalytic properties [12, 26] associated with their structural and compositional diversity. These properties further improved going down to nano-regime which provides impetus for designing synthetic methods to produce quality colloidal nanocrystals. Accordingly, few protocols have been explored for the synthesis of colloidal nanomaterials of group 8 metal phosphides.

Iron Phosphide

Among transition metal phosphides, iron phosphides adopt a wide range of compositions displaying unique physical and electronic properties depending on their structures. For instance, Fe_3P and Fe_2P are ferromagnetic, FeP is super paramagnetic while FeP_2 and FeP_4 are antiferromagnetic semiconductors [26]. These iron phosphides exhibit exotic magnetic properties different from their bulk forms when their crystallite dimensions approach to few nanometers. Therefore, a number of methods have been explored and have also been employed for the preparation of colloidal iron phosphide nanomaterials.

The pioneering work on the colloidal synthesis of round shaped FeP nanocrystals was reported by Perera and co-workers [202]. The synthesis involves the reaction of $[Fe(acac)_3]$ with $[P(SiMe_3)_3]$ at 240–320 °C using TOPO as a solvent and DDA, MA, or hexyl phosphonic acid (HPA) as capping agents. The nanocrystals were highly stable and size distribution is narrow.

In contrast to reactive $[P(SiMe_3)_3]$, reactions with less reactive TOP require higher reaction temperatures (>300 °C) due to higher dissociation energy of the P–C bond compared to P–Si bond [18]. The breaking of P–C bond is a key step for in situ generations of phosphorus from TOP, then the P–Si bond of $[P(SiMe_3)_3]$. The use of TOP favors anisotropic growth in crystals due to high reagent concentrations assisting in the formation of anisotropic nanorods and nanowires.

Nanorods of iron phosphides have been synthesized by using TOP with molecular precursor of iron such as $[Fe(CO)_5]$ and $[(\eta^4\text{-}C_6H_8)Fe(CO)_3]$. Hyeon and co-workers [203] prepared Fe_2P nanorods by the reaction of $[Fe(CO)_5]$ with TOP using OLA and octyl ether as solvents at temperatures of 300 °C. The same reactants with TOPO as solvent and the reaction temperature at 360 °C afforded FeP nanorods [204]. Chi et al.

[205] used pre-reacted [(η^4-C_6H_8)$Fe(CO)_3$] with TOP, to prepare FeP nanorods. The nature of solvent and the reaction temperature may be the deciding factors for the formation of different phases. Hyeon et al. [200] also synthesized FeP nanorods by thermal decomposition of Fe-TOP complex (readily prepared by reacting [$Fe(CO)_5$] and TOP at 50 °C) by adopting the method of continuous injection of reagents. The latter approach is one of the important ways of maintaining a high concentration of precursors in solution, which is an important factor for achieving anisotropic growth. The relative reactivity of the metal-TOP complex is the deciding factor for establishing a correlation between the length of the rods and the injection rate. This in turn depends on the nature of the metal. The TEM images of the different aliquots collected by injecting Fe-TOP complex into TOPO at 330 °C revealed that at the short durations, nanorods of size 4 nm × 15 nm along with small nanospheres were produced. Continuing the injection of the Fe-TOP further, the lengths and diameter thickness of the nanorods grow indicating seed-mediated growth mechanism as depicted in the Scheme 12.2.

In addition to the above phosphorus precursors, Mézailles and co-workers [206] reported the synthesis of hollow FeP nanoparticles by reacting Fe(0) nanoparticles (prepared in situ by injecting [$Fe(CO)_5$] into OLA and ODE at 180 °C) with equivalent amount of white phosphorus (P_4) in solution at 250 for 2 h. TEM images showed a hollow structure with a shell thickness of 4 nm corresponding to FeP. The formation of hollow structure can be explained by simultaneous diffusion of phosphorus atoms and iron atoms in the inward and outward directions, respectively during the reaction. Such type of simultaneous diffusion resulting in hollow structures is also called the nanoscaled Kirkendall effect. It was also observed that the crystalline FeP phase was stable upon limited air exposure.

Although [$P(SiMe_3)_3$] and TOP are the most commonly used phosphorus precursor, they are expensive, toxic and readily oxidize in air and hence required to carry out all the handlings under inert atmosphere. Thus, there is a need for alternative phosphorus sources which are compatible with large-scale synthesis of the

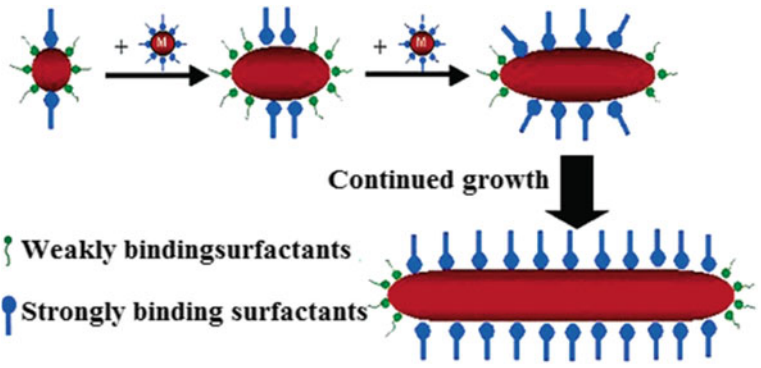

Scheme 12.2 Proposed growth mechanism for nanorod formation (Reproduced from Ref. [200] with the permission of American Chemical Society)

metal phosphides. Of them, TPP is one of the suitable substitutes to TOP. TPP is an inexpensive and stable precursor under ambient conditions. Recently, Liu et al. reported a simple, scalable and cost-effective heating up method to produce Fe_2P rods using cheaper, less toxic and air-stable TPP as a phosphorus source and metal chlorides as metal precursor [188]. Other than metal salts, metal nanocrystals have also been used as the metal precursor for the synthesis of metal phosphide nanocrystals. For instance, Schaak et al. reported the synthesis of FeP nanocrystals by injecting pre-synthesized Fe nanocrystals mixed with TOP into refluxing HDA and heated at 350 °C for 1–2 h [207].

In addition to dual or multiple source methods, single source precursors were also employed for the synthesis of transition metal phosphide nanomaterials. Whitmire and co-workers [208] synthesized Fe_3P nanorods by thermal decomposition of $[H_2Fe_3(CO)_9P^tBu]$ in TOA and OA. The formation of Fe_2P instead of Fe_3P may be explained on the conversion of $[H_2Fe_3(CO)_9P^tBu]$ to $[Fe_4(CO)_{12}(P^tBu)_2]$ at 140 °C before yielding Fe_2P as the final product.

Ruthenium Phosphides

Platinum based materials are the most active HER catalysts [209]. Yet, their industrial applications are limited by their abundance and high cost. Therefore it necessitates the quest for low cost alternatives to these costly materials. Accordingly, catalysts based on non-noble metals were explored for the HER. In spite of affordable costs, inferior activity of non-noble metals compared to platinum in alkaline medium triggered the research on cheaper noble metal based catalysts to continue.

Ruthenium being cheaper and having a hydrogen bond energy similar to that of Pt (65 kcal mol^{-1}) makes it a suitable platinum substitute in the hydrogen evolution reaction [210, 211]. In line with the expectation, ruthenium exhibited exceptional HER activity [212], however, the cost compared to non-noble metal still remain high. Hence, to make ruthenium economically viable it is necessary to enhance catalytic activity which in turn minimizes its usage. The catalytic activity can be boosted by improving increasing the effective surface area by decreasing the size of the particles.

Minimizing the size of the particles also improves the utilization efficiency of a catalyst. Recently, the activity of ruthenium has also been enhanced by alloying with phosphorous yielding ruthenium phosphides [213, 214].

Ruthenium phosphides can crystallize in different phases such as Ru_2P, RuP and RuP_2, etc. The former can be synthesized by reacting ruthenium and phosphorous sources under suitable reaction conditions. The phosphorous sources can be either inorganic or organic compounds. Inorganic phosphorous precursors can discharge sufficient P and can be used to produce bulk ruthenium phosphides in a controlled fashion. In contrast, an organic phosphorous source can deliver both carbon and phosphorous together during annealing. Therefore, the former can be utilized to prepare carbon-coated nano ruthenium phosphides, but in an uncontrolled manner [215].

Accordingly, Mu et al. [215] synthesized RuP_2 nanoparticles encapsulated in an N, P dual doped carbon framework (RuP_2@NPC) through the pyrolysis of self-assembled phytic acid cross-linked ruthenium complexes and melamine. TEM

images of RuP_2@NPCshows that RuP_2 nanoparticles of average size 8 nm are homogeneously distributed on the N, P doped carbon matrix with uniform size distribution. RuP_2@NPC exhibits a Pt-like HER activity and stability in acidic, neutral and basic media.

Recently, Qin et al. [216] adopted novel strategy to produce uniform Ru_2P and RuP nanocrystals in situ on N- and P-codoped graphene by pyrolysis of $[RuCl_2(PPh_3)_3]$ and pyritic acid (PA) with N-doped graphene. Ru_2P and RuP can be prepared in a controlled manner by varying the molar ratio of PA to $[RuCl_2(PPh_3)_3]$. Among both these phosphides, Ru_2P shows better HER activity than RuP in alkaline media, but comparable to that of the commercial Pt/C catalyst.

Recently, Cai et al. [217] synthesized amorphous ruthenium phosphide (RuP_x) with 1 nm diameter by reducing $RuCl_3$ and NaH_2PO_2 with $NaBH_4$ at room temperature. The phosphorus and ruthenium produced during the reduction concurrently deposit on the carbon surface and form Ru–P bonds resulting in minimizing the growth of nanoparticles and hence the particle size of RuP_x. The catalytic activity of RuP_x/C catalyst was compared with benchmark Pt/C for a hydrogen evolution reaction.

Feng and co-workers [218] reported the synthesis of Ru_2P nanoparticles of size 8–10 nm and demonstrated their utility as a highly efficient HER catalyst in different pH electrolytes. The catalytic activity of these particles significantly improved compared to ruthenium nanoparticles due to the change in electronic state originating from Ru–P coordination. The HER activity of Ru_2P nanoparticles in an acidic and basic media are comparable to Pt/C catalyst. In view of the lower price of ruthenium compared to Pt and the catalytic activity and stability of Ru_2P nanoparticles make it a promising HER catalyst.

12.5.4 Syntheses of Colloidal Nanomaterials of Group 9 (Co, Rh, Ir) Metal Phosphides

Group 9 transition metal phosphides have been explored for their versatile applications in magnetic field sensing devices and inductors owing to their magnetic properties [219–221], lithium ion batteries [222], HER catalysts [223], syngas-related catalysis [224] and theranostic applications [225].

Cobalt Phosphide

Among transition metal phosphides, cobalt phosphides have received significant attention due to their potential applications in magnetic field sensing devices and inductors due to low coercivity and high permeability [219–221]. They also can be used as anode materials in lithium ion batteries [222], electrocatalysts for hydrogen evolution reaction (HER) [223] and tumor theranostic applications [225].

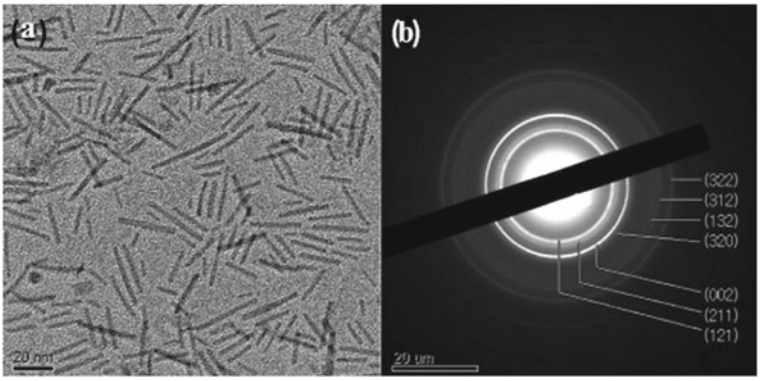

Fig. 12.4 **a** TEM image and **b** SAED patterns of Co_2P nanorods synthesize during [$Co(acac)_2$] and HDA (Reproduced from Ref. [200] with the permission of American Chemical Society)

Adopting the highly reactive traditional [$P(SiMe_3)_3$] as phosphorus precursor, Brock and co-workers [198] have synthesized CoP nanocrystals by the treatment of zerovalent cobalt metal carbonyl complex with [$P(SiMe_3)_3$] in TOPO/MA at 320 °C.

Hyeon et al. [200] reported synthesis of uniform sized (2.5 nm × 20 nm) Co_2P nanorods by thermal decomposition of continuously delivered Co-TOP complex (prepared by reacting [$Co(acac)_2$] and TOP at 70 °C) into a mixture containing octyl ether and HDA at 300 °C and kept at this temperature for 1 h. TEM image and SAED pattern of the same is shown in Fig. 12.4. These nanorods demonstrated interesting magnetic properties, which are considerably different from those of their bulk counterparts.

Schaak et al. [207] adopted a modified Hyeon method for the synthesis of CoP nanoparticles by injecting TOP into a preheated solution containing [$Co(acac)_2$] in OLA and HDA at 330 °C and then heated to 370 °C and held at this temperature for 1 h. This method involves the solution-mediated reaction of pre-formed Co nanoparticles with TOP at temperatures below 370 °C. O'Brien et al. prepared orthorhombic phase CoP nanowires by thermal decomposition of [$Co(acac)_2$] and tetradecylphosphonic acid (TDPA) as cobalt and phosphorus precursors in a mixture of TOPO and HDA at 370 °C for 3 h [226]. They have also observed that a mixed solvent system (HDA and TOPO) is vital for the growth of CoP nanowires. The dimensions of nanowires (the diameter and length) can be tuned by changing the ratio of HDA to TOPO. For instance, with a 1:2 and 1:1 weight ratios of HDA to TOPO the dimensions were 10 nm in diameter, 100 ± 10 nm in length and 7 nm in diameter and 400 ± 20 nm in length, respectively. Longer nanowires were formed with increased concentration of HDA.

Liu et al. [223] have synthesized CoP nanorods and Co_2P microspheres by injecting TOP or triphenylphosphine, respectively into a mixture containing [$Co(acac)_2$] in ODE and OLA at 120 °C and then heated to 330 °C and stirred for 1–2 h. Their investigations show that the HER catalytic efficiency of CoP is

better than Co_2P and it can be improved further by adjusting active phase and carbon species structures.

A cheaper and conveniently handled aminophosphine with moderate reactivity offers an alternate phosphorus precursor to air sensitive phosphorus precursors like TOP.

Cossairt group has synthesized Co_2P and CoP nanocrystals by hot injection of tris-diethylamino phosphine [$P(NEt_2)_3$] into a solution of $CoCl_2$ in OLA at 200 and 250 °C, respectively for a definite time.TEM images show CoP and Co_2P of various morphologies with widths/diameters of 7.8 ± 0.7 nm and 6.5 ± 0.6 nm, respectively. It was also observed that phase purity of the nanocrystals at a given temperature is determined by the halide precursor. For instance, the use of CoI_2 gives a mixture of Co_2P and CoP whereas phase pure CoP was obtained from $CoCl_2$ under similar reaction conditions. However, Co_2P in the mixture can be converted to CoP by increasing the reaction duration. These nanocrystals were examined as electrocatalysts for the hydrogen evolution reaction. Among Co_2P and CoP nanocrystals, Co_2P is the most active material [133].

Other than the expensive, toxic and difficult to handle phosphorus under ambient atmosphere, in expensive, less toxic and scalable source of phosphorus like TPP is very useful in the preparation of metal phosphides. In view of this, Shavel et al. prepared Co_2P nanorods or quasi-spherical nanoparticles by the reaction of $CoCl_2$ with TPOP in the presence of HDA and ODE and heated to 280–300 °C. The formation of Co_2P nanorods or quasi-spherical nanoparticles depend on the occurrence or absence of HDA·HCl during the reaction, which in turn is governed by the ability of argon flow to purge this compound. The dimensions of nanorods are 6.9 ± 0.8 nm $\times$ 33 ± 9 nm [188].

Other than these reports, recently Kapri and Bhattacharyya [227] reported polydopamine-capped cobalt phosphide nanorods with aspect ratios ranging from 1.4 to 10 were prepared by single step thermal decomposition method. The nanorods with aspect ratio of 6.4 exhibited good dispersibility in physiological solutions and an exceptional near-infrared (NIR) photothermal performance with a photothermal conversion efficiency (PCE) of 64%. The rods are highly photostable with no cytotoxic effects on normal cells and are useful in controlled drug release to the cancer cells. The photochemothermal property of these rods makes them potential candidates in tumor theranostic applications.

Rhodium Phosphides

The development of alternate noble metal based catalysts is desirable for large-scale applications due to the high cost and scarcity of platinum in spite of its excellent HER catalytic performance.

Rhodium phosphides are the most studied compounds among all the platinum group metal phosphides in the field of catalysis due to their applications in hydroprocessing and syngas-related catalysis [224]. The former exists in different compositions viz. Rh_2P, Rh_3P_2, Rh_4P_3, RhP_2 and RhP_3 [228]. The diversity in the compositions and crystal structures of rhodium phosphide and cheaper prices of rhodium

relative to platinum make it a promising candidate for catalysis. The active material of the catalyst can further make it affordable by enhancing its performance by reducing the particle size of the material to nanoscale which in turn increases the surface area of the catalyst. Furthermore, controlling and tuning the size and shape of the particles to be used as catalyst also helps the catalyst to have flexibility and better performance. However, the control of size and shape depends on synthetic methods.

In general, two important synthetic routes are developed for the preparation of transition metal phosphides, i.e., solution-phase and solid-state reactions which have applications in catalysis. Of these, solution methods have better control over size, shape and crystal structure. Solution methods include reduction of phosphates, solvothermal and thermal decomposition (through hot injection and heat up) using suitable metal and phosphorus precursor. Among these, the last method produces quality colloidal nanoparticles compared with the former methods, though sometimes solvothermal also gives quality nanoparticles. At least for the synthesis of rhodium phosphide nanoparticles, the phosphorus source is always TOP. To the author's knowledge, there is only report by Li and co-workers [229] which employed a solvothermal method for the preparation of monodispersed Rh_2P nanocubes with an average edge length of 4.7 nm. The synthetic protocol involves heating a mixture containing [$Rh(acac)_3$], TOP and OLA in an autoclave at 180 °C followed by the purification procedure. Rh_2P nanocubes supported on carbon (Rh_2P/C) shows extraordinary performance for hydrogen evolution reaction and oxygen evolution reactions compared to Rh/C and Pt/C catalysts.

Other than the above method, all other studies involving synthesis of colloidal nanoparticles of rhodium phosphide are via thermal decomposition of suitable rhodium precursor and TOP as phosphorus source, except one report dealing with the thermal decomposition of single source precursor. Schaak et al. [230] synthesized Rh_2P nanocrystals of an average size <10 nm by converting rhodium metal nanoparticles into corresponding phosphides by solution-mediated reaction with TOP at 300–360 °C.

Chen et al. [231] reported colloidal synthesis of monodisperse spherical Rh_2P nanocrystals with an average size of 2.8 nm by injecting TOP into a solution containing [$Rh(acac)_3$], OLA and ODE at 240 °C and kept at a growth temperature of 320 °C for 60 min. The catalyst made up of these monodispersed Rh_2P nanocrystals display better HER activities than commercial Pt/C over a wide range of pH.

Guo's group [232] designed wrinkled ultrathin 2D nanosheets of Rh_2P for enhancing HER catalysis at all pHs. Rh_2P nanosheets were synthesized by phosphorization of Rh nanosheets (prepared by reducing [$Rh(acac)_3$] using ascorbic acid, OLA as solvent and surfactant and carbon monoxide as a surface confining agent) through the decomposition of TOP at 300 °C. The thickness of nanosheets is about 3.3 nm as determined by atomic force microscopy. The nanosheets exhibited excellent HER activity and durability than the commercial Pt/C catalyst. Rh_2P nanosheets are efficient and stable HER catalysts in both acid and neutral electrolytes.

In addition to the above methods, single source precursor approach provides an alternate pathway for the synthesis of phase pure nanocrystals. This method has been

adopted for the synthesis of cubic shape Rh_2P nanocrystals with an average side of 10.3 ± 2.8 nm. The synthesis involves thermal decomposition of $[Rh(PPh_3)_2(CO)Cl]$ in OLA and ODE through heat up approach by heating the mixture to 300 °C and held at this temperature for 1 h [233].

Iridium Phosphides

Iridium is a metal belonging to group 9 and occupies the same group as iron and rhodium in the periodic table. The former has been hardly explored as an HER catalyst. Furthermore, iridium phosphide being metallic in nature is expected to have high HER activity. However, synthesis of iridium phosphide requires harsh conditions.

Accordingly, for the first time Mu et al. [234] reported synthesis of N-doped carbon (NC) encapsulated IrP_2 (IrP_2@NC) nanoparticles at ambient conditions. The synthesis involves a solid-state reaction using $IrCl_4 \times H_2O$, phytic acid and melamine as Ir, P and C sources, respectively. Electrochemical measurements show that IrP_2@NC exhibits better HER activity and durability than both Pt/C and Ir/NC catalysts under acidic and basic conditions.

12.5.5 Syntheses of Colloidal Nanomaterials of Group 10 (Ni, Pd, Pt) Metal Phosphides

Group 10 metal comprise both noble (Pd, Pt) and non-noble (e.g., Ni, etc.) metals. While noble metals have already been established as catalysts in various reactions, their higher cost and scarcity gave thrust to explore cheaper alternatives with improved catalytic performance. Among the alternatives, non-noble metal based Ni_2P on silica support proved as an efficient catalyst in hydrodesulfurization (HDS) and hydrodenitrogenation (HDN) [235] while Pd_xP materials exhibited comparable catalytic activity to that of Ni_2P [236, 237]. In the latter case, the addition of phosphorus to Pd helps in cutting down the costs to some extent with improved performance with respect Pd metal. The efficiency of these phosphides can be enhanced further by scaling down the crystallite dimensions to few nanometers. Therefore, the development of synthetic methods to produce size and shape controlled colloidal nanomaterials of these phosphides is highly desirable and has been discussed below.

Nickel Phosphide

A number of transition metal phosphides (e. g. WP, MoP and Ni_2P, etc.) act as HDS and HDN catalysts. Especially, silica-supported Ni_2P [235] exhibited the highest HDS (98%) and HDN (90%) activities compared to other transition metal phosphides and are also better than commercially available catalysts like sulfided $Co–Mo/Al_2O_3$ [238]. Furthermore, nickel phosphides are brilliant corrosion-, oxidation- and water-resistant materials. Particularly, nanoscale phosphides have unique mechanical and

thermal properties. Binary phase diagram of Ni–P show that Ni_3P, $Ni_{12}P_5$, Ni_5P_4 and Ni_2P are the possible nickel phosphide phases.

Synthetic routes such as solvothermal [239], high temperature reduction of supported phosphates [240] and reaction of supported Ni and NiO particles with PH_3 [241] and microwave synthesis [242] have been utilized for the preparation of nickel phosphide nanocrystals in the literature. Among these, solution based methods involving reaction of metal salts or organometallic precursors together with phosphines or conversion of metal or metal oxide nanoparticles with phosphines offers great control over the size, shape and phase of the nanocrystals.

Hyeon and co-workers [200] have employed a continuous injection method to produce Ni_2P nanorods by thermal decomposition of a Ni-TOP complex solution into TOPO at 330 °C through continuous injection. Henkes et al. applied a new approach for the synthesis of Ni_2P nanocrystals via the reaction between nickel nanoparticles and TOP below 370 °C [207]. Similarly, Chiang and co-workers [243] utilized Kirkendall effect to synthesize hollow Ni_2P nanospheres through the reaction between Ni nanocrystals and TOP. The former adopts heat up approach where a reaction mixture containing nickel acetate, ODE, OLA and TOP were heated to 320 °C and held at this temperature for 1 h. It is observed that the concentration of TOP and the reaction temperature are crucial for obtaining hollow Ni_2P nanospheres. They also found that the reactivity of intermediate Ni nanoparticles can be changed by the nature of the ligands or surfactants at the interface. Accordingly, hollow nanorods to nanospheres were obtained by using different surfactants such as alkylamines (OLA and HDA), oleic acid and TOPO.

Brock et al. [244] reported synthesis of monodispersed spherical Ni_2P nanoparticles by a hot injection method involving rapid injection of TOP solution of bis(1,5-cyclooctadiene)nickel(0) ($[Ni(COD)_2]$) into TOPO at 340 °C and continued the reaction for 24 h. An average crystallite size of Ni_2P nanoparticles are 10.2 ± 0.7 nm. The surface modifications of the Ni_2P nanoparticles were performed either by washing with $CHCl_3$ or by replacing TOP/TOPO groups with mercaptoundecanoic acid (MUA). Both the surface modified nanoparticles act as better HDS catalysts than Ni_2P nanoparticles or the bulk Ni_2P prepared by thermal reduction of a phosphate precursor.

Although the synthesis of Ni_2P nanoparticles have been studied by few groups as mentioned above, literature on the preparation of nickel phosphide nanocrystals with different phases ($Ni_{12}P_5$, Ni_2P and Ni_5P_4) and shapes are scanty and the underlying mechanism of nickel phosphide nanocrystals formation has not been discussed.

Accordingly, Tracy and co-workers [245] prepared mixed phase $Ni_2P/Ni_{12}P_5(Ni_xP_y)$ nanoparticles by the thermolysis of $[Ni(acac)_2]$ using TOP as a ligand and phosphorus source. It was also demonstrated that the size and morphology (hollow and solid structures) depend on the molar ratio of P:Ni. For molar ratios of 1–3, Ni nanoparticles were formed below 240 °C which consequently yield crystalline-hollow Ni_xP_y nanoparticles at 300 °C while higher P:Ni ratios drive the direct formation of Ni_xP_y rather than nickel. The reason for the latter is due to the requirement of higher temperatures for nanoparticle growth due to the formation of a Ni-TOP complex. However, the issue of phase impurity remains unresolved.

To overcome this problem, Brock et al. [246] carried out a number of reactions to evaluate the influence of temperature, reaction duration, Ni:P precursor ratio and amount of reactants on the phase of the ultimate product. Accordingly, the group has reported the synthesis of phase, size and shape controlled nickel phosphides by adopting one-pot approach where [$Ni(acac)_2$] and TOP were used in the synthesis of precursor nanoparticles at 230 °C followed by their conversion to crystalline phosphide at higher temperatures. In another approach, the precursor nanoparticles were separated and then redispersed in octyl ether and OLA and reacted with TOP as the phosphorus source, at 350 °C. Hollow and solid nanoparticles of $Ni_{12}P_5$ and Ni_2P were prepared in a range of sizes (10–32 nm) by modifying the reaction parameters (P:Ni precursor ratio, temperature, time, OLA quantity). It was observed that large and hollow particles were formed at low P:Ni while small and solid particles were produced at high P:Ni ratio. The P:Ni ratio also influences the type of phase formed at the crystallization temperature. For instance, $Ni_{12}P_5$ is formed at low P:Ni whereas Ni_2P at high P:Ni [246].

Similarly, Liu et al. [247] reported the preparation of monodispersed nickel phosphide nanocrystals with different phases ($Ni_{12}P_5$, Ni_2P and Ni_5P_4) by the thermal decomposition route using [$Ni(acac)_2$] and TOP as the metal and the phosphorus source and OLA in ODE as the reducing agent. The phases of the nickel phosphide nanocrystals were controlled by varying the P:Ni precursor ratio. They have also studied phase dependent electrocatalytic properties of nickel phosphide nanocrystals for hydrogen evolution reaction. Among all the phases, solid Ni_5P_4 nanocrystals show higher catalytic activity which has been attributed to the higher positive charge of Ni and a stronger ensemble effect of P in Ni_5P_4 nanocrystals. The investigations also revealed that the crystalline phase is one of the key factors which affect the electrocatalytic properties.

As mentioned above, a number of synthetic protocols used TOP as phosphorus source due to its coordination behavior and the donor nature of P atom via thermal decomposition at around 330 °C to produce metal phosphides. However, this method uses excess amount of TOP than that is required stoichiometrically for the final production an uncontrolled practice making it a costlier method.

Furthermore, TOP is toxic and readily oxidizes in air and hence all the manipulations involving have to be carried out under inert atmosphere. So, there is a need for cheaper alternative phosphorus sources. Accordingly, Mézailles and his group [248] reported a new, simple, cheaper and controlled method for stoichiometric Ni_2P nanocrystals at low temperature based on the high reactivity of P_4 toward reactive Ni(0) complexes. They have also established that the reaction between Ni(0) and P_4 result in the insertion of in P–P bonds leading to the required stoichiometric nickel phosphide. Synthesis of Ni_2P nanocrystals involve heating of a mixture of Ni nanoparticles [prepared by heating a mixture of [$Ni(COD)_2$] and TOPO or OLA at 100 °C for 2 h] and TOPO or OLA and a solution of P_4 in toluene at 100 °C under inert atmosphere. Ni_2P nanoparticles of size 4.8 nm were obtained by this method. The same group has studied the relation between crystallization and phosphorus diffusion in the synthesis of metal phosphide nanoparticles from metal nanoparticles using reactive white phosphorus (P_4) as P(0) source. These studies lead to thorough

understanding of metal phosphide synthesis in the context of obtaining specific M_xP_y phases and the basis for the reaction temperature required for crystallization [206].

In addition to the multiple source precursor methods mentioned above, single source molecular precursors have also been used for the preparation of nickel phosphide nanocrystals. Single source precursor method offers an alternative technique for the preparation of size and phase controlled metal phosphide nanoparticles without the formation of metal nanoparticle intermediates which leads to hollow particles.

Obrien and co-workers prepared nickel phosphide (Ni_2P and $Ni_{12}P_5$) nanoparticles by thermolysis of dialkyldiselenophosphinatonickel(II), $[Ni(Se_2PR_2)_2]$ (R=^{i}Pr, ^{t}Bu and Ph) in TOPO or HDA. Depending on the alkyl group of the precursor, reaction temperature and capping agent, nanoparticles of either nickel selenide or nickel phosphide or both were formed. To evaluate the role of capping agents, HDA and TOPO were used as optional capping agents under the same experimental conditions. It was observed that thermolysis of $[Ni(Se_2P^iPr_2)_2]$ in HDA and TOPO gave different phases of nickel phosphide nanoparticles while $[Ni(Se_2P^tBu_2)_2]$ gave hexagonal phase Ni_2P at 330 °C and mixed phase nickel selenide nanoparticles at 280 °C. The latter indicated that higher temperatures favor the formation of nickel phosphide nanoparticles because of either higher phosphorous availability or via TOP decomposition. Thermolysis of the precursor, $[Ni(Se_2PPh_2)_2]$ offered only mixed phase nickel selenide nanoparticles in HDA whereas in TOPO gave only phosphide [249]. It was also found that the phosphorous rich phase Ni_2P (P:Ni = 0.5) was always produced in TOPO as the capping agent whereas the phase $Ni_{12}P_5$ (P:Ni = 0.42) was formed in HDA.

Recently, Liu et al. [250] developed a single source precursor method for the preparation of nickel phosphide nanocrystals by thermal decomposition of $[NiCl_2(PPh_3)_2]$ in the presence of OLA. They found that size of nanocrystals can be altered by the reaction temperature and the amount of OLA while the phase can be controlled by changing the reaction duration. The shorter and longer reaction times were favorable for the formation of $Ni_{12}P_5$ and Ni_2P nanocrystals, respectively which have been explained on the required time for the completion of phosphorization at a particular temperature. A possible growth mechanism of nickel phosphide nanocrystals based on nucleation, diffusion, aggregation growth process was also proposed.

Recently, Habas and co-workers utilized $[Ni(PPh_3)_2(CO)_2]$ as a single source precursors for the preparation of Ni_2P nanoparticles. The synthesis includes the rapid heating of the mixture containing $[Ni(PPh_3)_2(CO)_2]$ and triphenylphosphine in OLA and ODE to 320 °C (ca. 10 °C/min) and continued the reaction at this temperature for 2 h [233].

Palladium Phosphides

Palladium phosphide is an interesting phosphide because of its existence in a number of crystalline phases with different compositions of metal and phosphorus ranging from $Pd_{15}P_2$ to PdP_3 [251]. The catalytic activity of Pd_xP ($Pd_{4.8}P$, Pd_3P and Pd_5P_2) nanoparticles in heterogeneous hydrogenation reactions are comparable with that of Ni_2P catalysts [236, 237]. The presence of phosphorus even in small amounts in the palladium lattice enables it to pick up substantial amount of hydrogen.

For instance, both stoichiometric Pd_6P and non-stoichiometric $Pd_3P_{0.80}$ forms the interstitial solutions with H_2 [252, 253].

Among the several methods available for the synthesis of palladium phosphides, the most commonly adopted methods for the preparation of platinum group metal phosphides are the incipient wetness impregnation method combined with calcination and reduction, the reaction of metals or metal oxides with a phosphorus precursor under reducing conditions and the deposition of metal phosphide nanoparticles prepared through colloidal synthesis on a support material. Of these methods, the impregnation method often requires high reaction temperatures and the catalyst needs to be passivated by surface oxidation in few cases. This surface oxide layer needs to be reduced completely before its evaluation as a catalyst which otherwise, can impact its catalytic activity. Furthermore, the former two methods in general produce polydisperse particles of the active material due to the nature of the support. However developments in the colloidal method enable a great control over the size shape and phase of the nanoparticles and post synthetic dispersion of these nanoparticles on the support eliminates the influence of the support on the size, shape and distribution of the nanoparticles.

Colloidal synthesis of palladium phosphide nanoparticles in general produced by reacting palladium precursors such as $[Pd(acac)_2]$, $[Pd_2(dba)_3]$ (dba = dibenzylideneacetone] with phosphorus sources like PH_3, white phosphorus, trioctyl-, triphenylphosphine. Shmidt and co-workers [65] used PH_3 and $[Pd(acac)_2]$ as precursors to synthesize a mixture of palladium phosphide (Pd_6P, $Pd_{4.8}P$ and Pd_5P_2) nanoparticles along with Pd(0) clusters. The catalyst made up of this mixture was used for the hydrogenation of styrene and phenylacetylene, nitrobenzene and benzaldehyde. The same group reacted $[Pd(acac)_2]$ with an excess of P_4 to obtain a mixture of crystalline PdP_2 and Pd_5P_2 [254].

To improve the phase purity and size distribution, reactions of metal precursors either in M(0) state or in metal nanoparticles form were carried out with white phosphorus. For instance, Sanchez et al. [255] synthesized phase pure Pd_5P_2 and PdP_2 nanoparticles by reacting Pd(0) nanoparticles in OLA and ODE with required amount of P_4 in toluene at 310 °C [206]. However, synthesis involving the use of Pd(0) precursor $[Pd_2(dba)_3]$, dba = dibenzylideneacetone] with an excess of P4 in solution yielded a mixture of polydispersed Pd_6P and Pd_3P_2 particles with average particle sizes of 140 and 65 nm, respectively.

The same group carried out a number of reactions of Pd(0) nanoparticles with phosphorus (P_4) in various stoichiometric amounts to study the mechanism of the formation of crystalline palladium phosphide nanoparticles. They proposed that the formation of crystalline palladium phosphide nanoparticles takes place through an intermediate step involving the formation of amorphous palladium phosphide nanoparticles and the crystallization temperature depends on Pd/P ratio [256].

The quality palladium phosphide nanoparticles were obtained by replacing P_4 with TOP as the phosphorus source. Schaak et al. synthesized monodispersed spherical nanocrystals of Pd_5P_2 and PdP_2 nanorods by injecting $[Pd(acac)_2]$ into a hot TOP/TOPO or octyl ether at 300–360 °C. The stoichiometry control is achieved by adjusting the reaction conditions [230].

Similarly, Brock et al. [257] prepared monodispersed Pd_5P_2nanoparticles of size 5–10 nm by encapsulation in a mesoporous silica network. Precursor palladium phosphide amorphous nanoparticles were prepared by reacting [$Pd(acac)_2$] with TOP at 300 °C. Crystallization of these amorphous particles by maintaining their size was carried out by encapsulating these particles in a mesoporous silica shell and subsequent treatment of these particles at 500 °C under a reducing atmosphere. This crystalline Pd_5P_2@$mSiO_2$ shows high BET surface areas (>1000 m^2/g) and average pore size of 3.7 nm.

Although quality phosphide nanocrystals were obtained by using TOP as phosphorus precursor, TOP is air sensitive and readily oxidizes in air. So, an inexpensive and stable alternative like triphenylphosphine (PPh_3) can be a better phosphorous source. Accordingly, Zhao has synthesized phase pure and monodispersed $Pd_3P_{0.95}$ nanoparticles of size 3.9 nm. The synthesis involves the heating of [$Pd(acac)_2$] with triphenylphosphine in a mixture containing TOPO as a surfactant, borane tert-butylamine complex as a reducing agent and OLA as a co-reducing agent as well as a stabilizer at 270 °C for 15 min. These nanoparticles were annealed at 300 and 400 °C, to grow to a size of 4.0 and 4.8 nm, respectively. Palladium phosphide nanocrystals of 4.8 nm exhibited high catalytic selectivity in semi- and stereoselective hydrogenation of alkynes [258].

Other than dual or multiple source methods, single source precursor method is one of the versatile routes for the synthesis of metal phosphide nanocrystals. Recently, Habas et al. [233] synthesized spherical Pd_3P nanocrystals of size 4.0 ± 0.8 nm by thermal decomposition of single source precursor [$Pd(PPh_3)_4$] in OLA and ODE by heating the mixture to 300 °C and held at this temperature for 1 h.

Platinum Phosphide

Platinum metal is a known commercial catalyst in many industrial applications. However, scarcity and cost per unit mass make the industrial processes expensive. Therefore, cheaper alternatives in the form of its phosphide derivatives are a viable option to reduce the cost of large-scale processes. Furthermore, platinum phosphides such as PtP_2 pertain to a fascinating category of phosphorus-rich polyphopsides which are difficult to produce in bulk form. Hence, colloidal synthesis provides a way to access these phosphide phases. The only report for synthesizing colloidal platinum phosphide nanoparticles involves the injection of metal salt solution in TOP into a hot TOP at 300–360 °C. The formation of PtP_2 nanoparticles take place through a metal nanoparticle intermediate step [230].

12.5.6 Syntheses of Colloidal Nanomaterials of Group 11 (Cu, Ag, Au) Phosphides

The growing energy demands accompanied by increasing carbon emissions have motivated us to harvest and store more renewable energy through solar cells and

lithium ion batteries, etc. and converting CO_2 into useful chemicals by utilizing renewable energy to reduce carbon emissions. In the above process, group 11 metal phosphides have contributed significantly through their utilization as anode in lithium batteries [158] and as a catalyst to convert CO_2 to CO [259]. Therefore, the development of synthesis of colloidal nanomaterials of group 11 metal phosphides with different shapes and size in a controlled matter further enhance the efficiencies of their bulk counterparts. Accordingly, fewer synthetic protocols which have been explored are accounted for in the following section.

Copper Phosphides

Copper phosphides are air-stable and environmentally friendly materials. Copper phosphide is a promising candidate for applications in lithium ion batteries [158], field effective transistors (FET) [158] and electrocatalysis [260]. Especially, phosphorus-rich copper phosphides have higher theoretical weight- and volumetric capacitances than that of graphite. Therefore, CuP_2 can be an alternative anode material for graphite due to high energy density and power density requirements in lithium ion batteries [261].

The first colloidal synthesis of hexagonal shaped Cu_3P nanocrystals were performed by the hot injection of Cu nanocrystals and TOP into TOPO at high temperature. Schaak et al. in this report found that metals can dissociate the P–C bond leading to diffusion of phosphorus into the metal [207]. Later, the size distribution of hexagonal plates like Cu_3P nanocrystals were improved by using CuCl to react with TOP instead of Cu nanocrystals. The sizes of these nanocrystals can be tuned in the range of 5–50 nm depending on the duration of the reaction. The mechanism of the formation of Cu_3P can be either by direct nucleation of Cu_3P or via the formation of Cu nanocrystals which is dependent on the ratio of TOP and CuCl. The direct nucleation of Cu_3P gives rise to reproducible and size controllable pure Cu_3P, while the Cu nanocrystals mediated mechanism results in the formation of Cu–Cu_3P Janus-like nanocrystals [262]. The latter type of nanocrystals is not apt for battery applications.

Manna et al. [263] reported the synthesis of single-crystalline hexagonal shape Cu_3P nanoplatelets by using PH_3 and CuCl as the phosphorus and copper sources in a mixture of alkylamine and TOPO as solvent and TOP as the nucleation controlling agent at moderate temperatures (200–230 °C). The width of these platelets can be tunable in the range of 10 to 1000 nm by controlling the number of nucleations followed by rapid growth along two feasible directions. In the entire size range, the platelets are single crystalline, have narrow size distribution and hexagonal shape. These Cu_3P nanoplatelets have semiconducting, plasmonic and rectification properties. Recently, Liu et al. prepared size controlled $Cu_{3-x}P$ nanocrystals using $[P(SiMe_3)_3]$ as the P precursor by pulsed laser at low reaction temperature). These nanocrystals showed the localized Surface Plasmon Resonance and nonlinear optical absorption. They also demonstrated that plasmonic $Cu_{3-x}P$ nanocrystals can act as simple, effective and solution-processed nonlinear absorbers for fiber laser [264].

In addition to the above costly phosphorus precursors, Mézailles et al. [206] synthesized Cu_3P and CuP_2 nanoparticles by reacting Cu(0) nanoparticles (prepared

by heating [$Cu(acac)_2$] in a mixture of OLA and ODE at 250 °C for 2 h) were reacted with stoichiometric amounts of white phosphorus (P_4) in solution at 250 and 320 °C, respectively. The formation of phase pure Cu_3P_2 occurs via Cu–Cu_3P_2 core-shell intermediate step. It was observed that CuP_2 nanoparticles are prone to aggregation compared to Cu_3P_2 nanoparticles. This could be explained by the dominance of diffusion kinetics below 250 °C which is taken over by aggregation phenomena at reaction temperatures >250 °C.

In addition to the methods using [$P(SiMe_3)_3$], PH_3, TOP, P_4 as phosphorus precursors, inexpensive and less toxic phosphorus precursor like TPP is an alternative for the preparation of metal phosphides and their large-scale production. Shavel et al. [188] synthesized disc or hexagonal shaped Cu_3P_2 nanocrystals with dimensions of 4.5 ± 1 nm $\times$ 17 ± 1 nm by heating of $CuCl_2$ with TPP in the presence of HDA and ODE and heated to 280–300 °C.

Silver- and Gold Phosphides

The conversion of CO_2 into useful chemicals by employing renewable energy is an ideal method to reduce carbon emissions. Therefore, the development of an effective and selective catalyst is crucial for the above process. Gold and silver were realized as highly selective electrocatalysts for conversion of CO_2 to CO. Accordingly, various approaches using silver based catalysts have been adopted to decrease the required overpotential for highly selective reduction of CO_2 to CO, but in vain. Furthermore, the integration with the current chemical infrastructure is hindered due to the limited range of the ratio of $CO:H_2$. Therefore, alloying phosphorus with silver is an effective way to modify the electronic structure and surface properties of silver for electrocatalytic applications. Thus, AgP_2 can be a potential electrocatalyst for the reduction of CO_2 to CO and studying the influence of phosphorus insertion in the lattice of Ag on the catalytic performance, durability and selectivity for CO_2 reduction applications is necessary. However, the reports on synthesis of AgP_2 nanostructures are rare due to the difficulty in controlling the size, shape and purity [207, 259]. Especially, colloidal synthesis which is known to afford quality monodispersed nanostructures with effective control over the shape is still a more challenging task in case of silver phosphide.

Schaak and co-workers [207] are the first to report the synthesis of colloidal AgP_2 nanocrystals by injecting Ag nanocrystals in TOP solution into hot TOP at 370 °C and maintained at that temperature for 2 h. AgP_2 nanocrystals were always accompanied by Ag impurity and the size of AgP_2 nanocrystals are approximately 500 nm.

Although the above method yields AgP_2 nanocrystals, the nanocrystals were larger in size and were not employed for CO_2 reduction. Therefore, Geyer et al. [259] synthesized monodispersed spherical AgP_2 nanocrystals of an average size of 3.5 ± 0.5 nm by injecting [$P(Me_3Si)_3$] in ODE into a solution containing silver acetate, OLA, OA and ODE at 180 °C and continued heating for 10 min and demonstrated their use as a catalyst for the reduction of CO_2 to CO. AgP_2 nanocrystals exhibited a threefold reduction in overpotential for electrochemical reduction of CO_2 to CO compared to the benchmark Ag catalyst.

Gold is one of the most studied metals for synthesis of nanoparticles. In contrast, only a limited number of methods are available for the synthesis of gold phosphide nanoparticles [265]. Only few methods for colloidal gold phosphide nanomaterials have been reported [184, 230, 266, 267]. Early works of Oberkampf [266] and Baker and Usher [267] for the synthesis of gold phosphide involves the reaction of PH_3 with Au(III) or Au(I) in solution, however, their size could not be estimated. In 2007, Henkes et al. reported the synthesis of Au_2P_3 nanoparticles by the reaction of Au nanoparticles with TOP as phosphorus source at 360 °C. The phase of the nanoparticles was determined by XRD, but the size was not estimated [230]. Recently, Sanchez and co-workers synthesized Au_2P_3 nanocrystals by reacting gold nanoparticles with soluble white phosphorus (P_4) donor at 250 and 320 °C. At 250 °C, the reaction limited to the surface of the nanoparticles with the unreacted P_4 in the solution. Later, the surface is modified by reducing the stoichiometry of P_4 to Au: P to 10:1 and decreasing the temperature to 110 °C. The reaction when carried out at 320 °C for 3 h produced crystalline Au_2P_3 and the nanoparticles aggregated to form nanowires. Furthermore, composite Au_2P_3-Au nanostructures were also formed wherever the gold phosphide domains are larger than the unreacted gold nanoparticles. These results reveal that gold is hesitant to form gold phosphide due to its metastable nature of this phase [184].

12.6 Application of Colloidal Metal Phosphide Nanomaterials

Traditional methods for manufacturing electronic devices include expensive physically manufacturing processes such as wafer fabrication from single crystals and thin film deposition from bulk materials. Likewise, catalysts are fabricated by impregnation technique. All these processes involve lot of costs due to higher materials costs and material losses during the manufacturing leading to more cost burden on the final product. However, these products can be made cost effective either by adopting modern technologies which can cut down the material wastage or improvising the performance of the device or catalyst. In view of this, usage of active materials in the form of colloidal nanocrystals makes the fabrication of the devices and catalysts inexpensive. This is due to the easy processability and scalability of colloidal nanocrystals which enables the manufacturing of cheaper thin films devices or catalysts by suitable coating and printing techniques. Furthermore, usage of colloidal nanocrystals helps in the development of high performance devices and catalysts due to the size- and shape-dependent properties.

Among colloidal nanocrystals, metal phosphide nanocrystals provide a benign and environmentally friendly alternative to toxic and heavy metal chalcogenides (e.g., CdE and PbE (E=Se or Te)) for solution-processable optoelectronic devices, including photodetectors [268], photovoltaic cells [269] and LEDs [270] due to their photo-physical properties.

In addition, colloidal metal phosphide nanocrystals can also replace costly noble metal catalysts in the field of catalysis due to their abundance, high activity and excellent stability. Especially, transition metal phosphides exhibit better performance in catalytic applications of hydrogenation, hydrodesulfurization, hydrodenitrogeneration [12, 141, 271] and water splitting [273, Chem Mater, 28 (2016) 6017–6044] compared to sulfides and nitrides. Furthermore, metal phosphides can also be used as resourceful anode materials for Li-ion batteries (LIBs) [13, 15] and biological applications [14, 110].

12.6.1 Optoelectronic and Photovoltaic Applications

Of the metal phosphide nanocrystals, Zn_3P_2 and InP nanocrystal/quantum dots are noteworthy in light absorption and emission-based applications due to their suitable band gap which can be tuned in visible region. The main attraction of these semiconductors is due to the presence of covalent bonds compared to the ionic bond in group 12 chalcogenides (e.g., ZnE or CdE (E=Se, Te)). The covalent bond improves the optical stability of these metal phosphide QDs and also reduce their toxic nature due to the nonerosion of the constituent species in biological ambiance [14, 110]. In spite of excellent properties, metal phosphide nanocrystals exhibit broad size distributions, low photoluminescent quantum yields and poor thermal- and photostability. Accordingly, considerable attention has been given to overcome these problems through chemistry, structure engineering at the interface and exciton dynamics leading to high performance optoelectronic- and photovoltaic- devices.

Among group 13 metal phosphides, InP has a bulk bandgap of 1.35 eV and exciton Bohr radius of 10 nm providing it considerable bandgap tunability. For instance, synthesis of high-quality InP QDs have been used in white LEDs and electroluminescence (EL) devices [66]. Lim et al. [8] demonstrated efficient InP QD based light emitting diodes (QLEDs) by creating exciton within QD through suitable carrier injection into QDs and the subsequent radiative exciton recombination within QDs. The QLEDs show 3.46% of external quantum efficiency and 3900 cd m^{-2} of maximum brightness, which are manifold better than their predecessors. The brightness was further enhanced in an inverted QLED device with InP/ZnSeS/ZnS quantum dot as an active material and ZnMgO as the electron transporting layer through an improved electron injection [9].

In contrast to metal chalcogenide nanocrystals, metal phosphide nanocrystals exhibit low photoluminescent quantum yields (PLQYs) and poor thermal- and photostability. In view of this, considerable attention has been given to optimize their photo-physical properties through interfacial engineering and managing the exciton dynamics. Recently, advances in the synthesis of core–shell-type InP QDs has been made with reference to both PL and EL [9, 66, 273] (Fig. 12.5). In spite of this, problems such as smaller size of InP@ZnS QDs as a result of lattice mismatch between the core and shell leads to more interface defects which in turn causes low PLQY and poor stability. Furthermore, the negative effects of Auger recombination

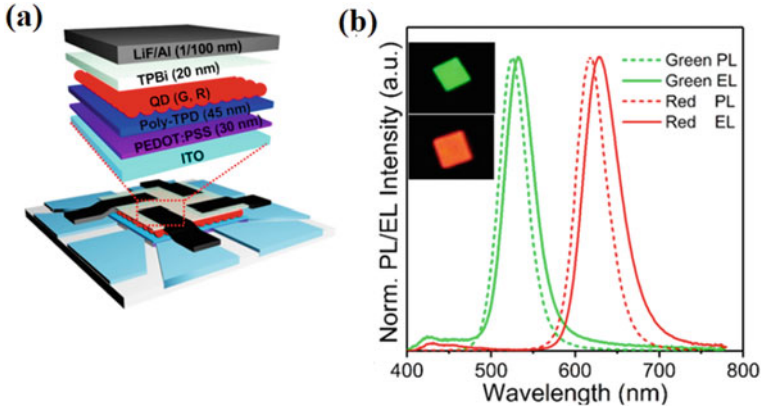

Fig. 12.5 **a** Schematic illustration of InP/ZnSe/ZnS based QLEDs structure. **b** photoluminescence (PL) spectra of QDs in solution, electroluminescence (EL) spectra and photographs of the QLEDs at 0.1 mA (Reproduced from Ref. [66] with the permission of American Chemical Society)

and non-radiative Förster resonant energy transfer (FRET) among closely packed QDs severely affect the performance of QLEDs due to thinner shells of QDs [274]. The above problems have been overcome by the synthesis of InP/ZnSe/ZnS QDs (size of 15 nm) with a thick ZnS shell by layer-by-layer shell growth strategy. The thickness of ZnS shell was sufficient to suppress the negative effects resulting in a record external quantum efficiency of 6.6% in environmentally friendly red QLEDs. The highly stable QDs exhibit the highest PLQY of 73% with narrow emission line width.

In addition, the use of narrow band green, red InP/ZnSeS/ZnS QD films by blue QD-emissive liquid–crystal displays (LCDs) in place of conventional red, green, blue (RGB) color filters improves the relative luminance levels and EQE values significantly [275].

Semiconductor nanowires (NWs) lasers have drawn significant attention in nanophotonics due to their use as a potential for nanoscale photonic sources. At present, their prospects for on-chip light sources are limited due to poor directionality and high threshold gain. Recently, Ren et al. [276] overcome these problems by designing a laser with InP NW integrated in a cat's eye (CE) antenna. This laser exhibits a higher degree of polarization, narrower emission angle, enhanced internal quantum efficiency and reduced lasing threshold. This system offers excellent prospects in future integrated nanophotonics systems.

Main group metal phosphides nanocrystals have also been utilized as potential absorbing materials for photovoltaic applications. For instance, Zn_3P_2 is a potential solar absorber in photovoltaics [277], due to its high absorption coefficient (10^{-4} to 10^{-5} cm^{-1}), large carries diffusion length of 5–10 μm and suitable band gap of 1.5 eV [71]. These physiochemical properties can be improved further by producing these metal phosphides in nanoscale.

Luber and co-workers [10] fabricated a heterojunction device consisting of ITO/ZnO/Zn_3P_2/MoO_3/Ag and evaluated its photovoltaic performance. The device shows exceptional rectification behavior and strong photosensitivity under 100 mW cm^{-2}AM 1.5G illumination.

Another important group 12 metal phosphide is Cd_3P_2 which has a direct band gap of 0.55 eV and exciton Bohr radius of 18 nm providing it tunability in visible to near-IR range within the quantum confined size regime [278]. Thus, making Cd_3P_2 colloidal quantum dots a promising material for light harvesting in a wide range.

Cao et al. fabricated PbS CQDs/Cd_3P_2 CQDs the quantum heterojunction colloidal quantum dot (CQD) solar cell where both p- and n-layers were tunable light absorbers. The optimized device exhibited an efficiency of 1.5% [279].

Group 13 metal phosphide materials because of their direct, tunable energy band gap and good minority carrier properties are potential candidates for photovoltaic applications. For instance, InP has a bulk band gap of 1.35 eV and exciton Bohr radius of 10 nm offers it band gap tunability over a wide range which enables it to absorb solar energy from visible to near-IR. In fact, for a single junction solar cell, InP has an energy band gap very close to the ideal band gap value of 1.1 eV for a maximum theoretical power conversion efficiency of 30% [280].

Chang-Hasnain and co-workers [67] fabricated a single-crystalline indium-phosphide (InP) nanopillar solar cell grown on a silicon substrate with an an open circuit voltage (V_{oc}) of 0.534 V under Air Mass 1.5 Global (AM 1.5 G) illumination at room temperature and a power conversion efficiency of 19.6%. The high V_{oc} for the solar cell is attributed to a novel regrowth technique that reduces the dark current to sub-fA/μm.

InP and InZnP CQDs are less toxic and have suitable band gaps, high absorption coefficient and high charge carrier mobilities. The charge carrier mobilities and life times of InP and InZnP QDs can be improved with appropriate ligand-exchange treatments. QD thin films made up of such materials can be used in solar cells which have power conversion efficiencies of 0.65 and 1.2% (Fig. 12.6) [281].

Recently, the problem of both quantity and mobility of photocarriers has been overcome by a hybrid system comprising of graphene and self-doped colloidal copper phosphide ($Cu_{3-x}P$) QDs and have been used for broadband photodetection. Here, $Cu_{3-x}P$ nanocrystals cause strong doping in graphene, which assists the formation of a p–n junction by partially covering graphene with $Cu_{3-x}P$ NCs. The three-terminal photodetector based on graphene-$Cu_{3-x}P$ exhibit broadband photoresponse from

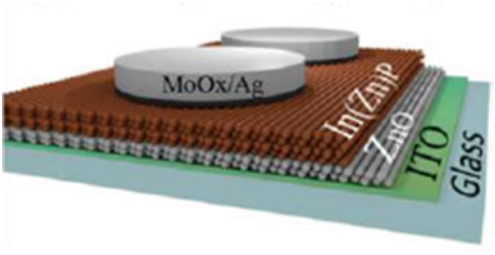

Fig. 12.6 Device structure of solar cell made up of InP and InZnP QDs (Reproduced from Ref. [281] with the permission of American Chemical Society)

400 to 1550 nm with an ultrahigh responsivity and high photoconductive gain at 405 nm and a good responsivity at 1550 nm. Such type of flexible graphene- $Cu_{3-x}P$ photodetectors operated at near-IR wavelengths may find potential applications in optical sensing, biological imaging and wearable devices [282].

12.6.2 Catalytic Applications

The increasing interest for hydrogenation and hydrotreating processes with metal phosphides as alternate to traditional catalysts (e.g., noble metals, metal sulfides, carbides and nitrides, etc.) accompanied by the advances made in the synthesis of metal phosphide nanostructures provided thrust to the catalytic applications of metal phosphide nanostructures. In particular supported or unsupported colloidal metal phosphide nanomaterials have assisted in boosting the catalytic performances.

The improvement in catalytic properties is mainly due to the change in the internal electronic structure of transition metals due to incorporation of phosphorus in metal lattice. In addition, phosphorus anion can distort the electron cloud around the metals and modify the surface charge state of transition metal phosphides to ease the intermediate process of catalysis [283].

The potential of metal phosphide nanostructures in catalysis was realized after a groundbreaking work of nitrobenzene hydrogenation over bulk Ni_2P [284] followed by the strict environmental regulations to limit the sulfur content in fuels, upgradation of bio oils as an energy alternative and growing demand for large-scale utilization and storage of electrical energy derived from renewable energy in the form of hydrogen further generated tremendous momentum for investigating metal phosphide nanostructures as potential catalysts in hydrotreating, hydrogenation and water splitting processes.

Hydrotreating

Hydrotreating is a process to eliminate impurities such as sulfur, oxygen and nitrogen from different feed stocks or substrates using molecular hydrogen. The strict regulations on the usage of fuels due to environmental issues gave thrust to research on materials for catalysts in hydrotreating petroleum feeds and refined products, particularly for sulfur removal. Hydrodesulfurization (HDS) and hydrodeoxygenation (HDO) are the two important hydrotreatment processes that are employed to remove sulfur from petroleum-related fuels and to remove oxygen from biomass for upgraded bio oils. Reduction of oxygen content in biomass is necessary to control the damaging characteristics such as high viscosity, immiscibility with hydrocarbon fuels, poor heating value and low thermal stability, etc.

At present, catalysts employed in hydrotreating are mainly metal sulfides. However, the stringent regulations to reduce the sulfur content in fuels and deactivation of the sulfide catalyst in HDO process due to the replacement of sulfur by oxygen necessitates the search for new catalysts with higher HDS activity and sulfur

free catalysts. Therefore, nanoscaled metal phosphides could play an important role in hydrodesulfurization and hydrodeoxygenation.

Hydrodesulfurization (HDS)

Hydrodesulfuriztion is the process of the removal of organosulfur compounds such as thiophene, dibenzothiophene and substituted dibenzothiophenes from crude oils. The direct reaction between these organosulfur compounds and H_2 is difficult even at high temperature and pressure, due to the high activation energy for the reaction. Therefore, a suitable catalyst is required to facilitate the HDS reaction by lowering the activation energy and resulting in high rates of conversion. Although catalysts such as metal sulfides, noble metals are available for HDS, the demerits associated with these catalysts drive the search for new catalysts. For instance, metal sulfide catalysts are avoided due to stringent regulations to have low sulfur content in fuel while noble metals are vulnerable to sulfur poisoning leading to decreased activity over time [285]. These problems can be dealt with by replacing the noble metals with noble metal phosphides as phosphides are more resistant to sulfur poisoning and do not add any sulfur to the products while sustaining good HDS activity. For instance, Rh_2P catalysts exhibit better sulfur tolerance and higher dibenzothiophene HDS activity compared to commercial Ni-Mo/Al_2O_3 and Rh/SiO_2 catalysts [286].

In general, transition metal phosphides adopting isotropic structures exhibit appreciable capacity for HDS [238, 240]. Among metal phosphides, silica-supported Ni_2P shows the highest HDS (98%) and HDN (90%) activity compared to other nickel phosphides (Ni_5P_4 and NiP_2) and transition metal phosphides [235]. However, these nickel phosphide samples are polydispersed in size. Therefore, examining the role of the particle size on catalytic activity would be useful for improvising the performance of catalyst. Accordingly, Brock and co-workers [287] studied the size-dependent catalytic activity of Ni_2P nanoparticle of size in the range $5 - 20$ nm probed against dibenzothiophene (DBT) for HDS by loading them on silica support via incipient wetness. Contrary to the expectation, materials prepared by temperature programmed reduction (TPR) are more active than the above Ni_2P nanoparticles. In fact, the smallest particles were the least active which is attributed to sintering of the particles under HDS conditions. However, HDS activity of the Ni_2P nanoparticles is doubled by minimizing sintering by encapsulating them in a mesoporous silica shell.

Similar to the size-dependent studies, catalytic activities of unsupported nanoscale Ni_2P materials are rarely investigated [288] compared to the HDS activities of supported Ni_2P materials. In view of this, exploring the catalytic activities of unsupported Ni_2P nanoparticles and studying the influence of surface ligand on the thermal stability and activity of catalysts at high temperatures and reducing atmospheres would be interesting. Therefore, the same group investigated the surface dependent thermal stability and thiophene HDS activity of monodisperse, unsupported Ni_2P nanoparticles [244]. They have shown that the surface modified Ni_2P nanoparticles influence the catalytic activity and phase stability under high temperature reducing and/or HDS conditions and are more active than bulk materials.

Other than the non-noble metal phosphide like nickel phosphides, noble metal phosphide like palladium phosphide nanoparticles were also employed as HDS

catalysts. For instance, Brock et al. [257] produced monodisperse Pd_5P_2 of size 5–10 nm and encapsulated in a mesoporous silica network and employed them for HDS. Encapsulation maintains the particle size during the sintering. The resultant Pd_5P_2@mSiO_2 shows an increase in HDS activity as a function of temperature, with dibenzodithiophene (DBT) conversion of 60% at 402 °C.

Hydrodeoxygenation (HDO)

Hydrodeoxygenation is the process of the removal of oxygen from oxygen-containing compounds. The former process has significant importance in the upgradation of bio oils to possible biofuels by converting oxygenated groups present in bio oils. The upgradation is required to improve the properties of biofuels by improving their thermal and chemical durability, heating value and volatility. The HDO reaction is commonly carried out under harsh conditions in the presence of a catalyst to improve efficiency. In general, industrial hydrotreating process uses metal sulfides as catalysts due to their high selectivity and activity in HDO of bio oils. However, the loss of sulfur during the process leads to both deactivations of these catalysts as well as contamination of the cleaned products [285]. Although noble metal catalysts overcome these problems, the scarcity and the cost of these metals limit their industrial applications. In view of this, research is focused on non-noble-and noble metal phosphide based catalysts for HDO due to their satisfactory catalytic activity and cost effectiveness.

Among noble metal phosphides, nickel- and cobalt phosphides have drawn significant attention due to their remarkable catalytic activity. Most of these reports deal with the catalyst prepared by using either supported- or unsupported metal phosphide or doped metal phosphide on support where metal phosphide is being prepared by incipient wetness impregnation method combined with reduction and the conversion of supported metals or metal oxides with a phosphorus source combined with under reducing conditions. Although there are various reports discussing the metal phosphide applications in HDO [289–292], investigations dealing with HDO applications using colloidal nanoparticles are very rare. Habas and co-workers synthesized phase pure metal phosphide nanoparticles of Ni_2P, Rh_2P and Pd_3P by single source molecular precursor route and supported on SiO_2 to evaluate them as a catalyst for hydrodeoxygenation of acetic acid. The catalytic performance of these supported nanoparticles was compared to the corresponding metal and metal phosphide catalysts prepared by incipient wetness (IW) over the range of 200–500 °C. The catalysts prepared by colloidal Ni_2P and Rh_2P nanoparticles were stable and comparable to the IW metal phosphides. Interestingly, Ni_2P nanoparticle catalyst shows H_2 activation and incorporation, in difference with IW-Ni, suggesting that both the metal phosphide and the parent metal behave differently from each other [233].

Using the above single source molecular precursor route, Schaidle et al. [293] synthesized Ni_2P and Rh_2P nanoparticles along with ligand-capped Ni, Pt, Rh nanoparticles and utilized as catalysts for studying the hydrodeoxygenation of guaiacol under fast pyrolysis conditions. The catalyst comprised of Rh_2P nanoparticles supported on SiO_2 (NP-Rh_2P/SiO_2) is less active for guaiacol conversion than

NP-Ni/SiO_2. However, the former catalyst produce completely deoxygenated products and has the highest selectivity to anisole, benzene and cyclohexane, indicating that it is a favorable catalyst for deoxygenation of aryl-OH bonds. The commercial Pt/SiO_2 catalyst and the catalyst prepared by incipient wetness impregnation method, i.e., IW-Pt/SiO_2 demonstrated the highest normalized rate of guaiacol conversion per m^2 and per gram of active phase, respectively, but only produce incompletely deoxygenated products.

Hydrogenation

Hydrogenation is a reaction between molecular hydrogen (H_2) and another compound or element, in the presence of a suitable catalyst such as palladium, etc. Hydrogenation reaction is commonly employed to reduce or saturate a molecule by adding pairs of hydrogen atoms [294]. In general, hydrogenation involves the transfer of hydrogen atoms to unsaturated compounds from gaseous hydrogenation or other hydrogenation sources (e.g., hydrazine, formic acid, dihydronaphthalene isopropyl alcohol).

The potential of bulk metal phosphides such as Ni_2P recognized with the pioneering work of Brown and co-workers dealing with nitrobenzene hydrogenation [284] which subsequently received thrust from the application of metal phosphide nanoparticles in hydrogenation catalysis [295, 296]. In general, hydrogenation reactions were either performed using unsupported or supported nanoparticles (amorphous or crystalline).

Ni_2P nanoparticles selectively hydrogenate a range of functional alkynes into alkenes in milder conditions. Carenco et al. [297] employed Ni_2P nanoparticles of size 25 nm as a catalyst for the selective hydrogenation of terminal and internal alkynes. Cis-alkenes were obtained under mild conditions with good conversion and selectivity. For instance, phenylacetylene was selectively hydrogenated to styrene in solution. The phosphorus inserted in the Ni–P nanoparticles is critical for the selectivity of the catalyst. Mechanistic studies were probed using isotope labeling for understanding the interactions of the reactants with the nanoparticle's surface.

Pd_xP nanophosphides hydrogenated selectively olefins and polyolefins. For instance, Belykh et al. [298] employed palladium phosphide nanoparticles formed by the interaction of [$Pd(dba)_2$] with N, N-dimethylformamide and white phosphorus as catalyst for hydrogenation. An inhibiting effect was observed on the catalytic process when elemental phosphorus is added to Pd(0) due to the formation of palladium phosphide- nanoclusters and nanoparticles. The same group has studied the effect of the ligands in the palladium precursor on the varying action of elemental phosphorus on Pd catalysts for hydrogenation of styrene. In the case of oxygen-containing ligands in the palladium precursors, at small P/Pd ratios phosphorus shows an encouraging effect leading to an increase in the TON and TOF values by a factor of about 9. On the contrary, with $PdCl_2$ as the precursor, phosphorus wields a hindering effect while improving the durability of the catalyst and elevating the TON value at P/Pd = 0.3 [299].

Zhao [258] has demonstrated the utility of crystalline and single phase $Pd_3P_{0.95}$ nanocrystals as highly active catalysts in semi- and stereoselective hydrogenation

of alkynes. In this investigation, monodisperse palladium phosphide nanoparticles of size 3.9 nm were produced by using triphenylphosphine as phosphorous source. These nanoparticles were deposited and calcined at 300 and 400 °C, respectively. The resulting single phase of $Pd_3P_{0.95}$ nanocrystals acted as the catalyst for the hydrogenation of alkynes.

Synthesis of aromatic alcohols by selective hydrogenation of aromatic ketones is challenging. For instance, when noble metal catalysts like Pt, Rh and Ru are employed, they show similar reactivity towards the hydrogenation of the C=O group and the aromatic ring [300–302]. To enhance the selectivity of C=O hydrogenation towards C–OH, Pd supported catalysts were used. However, Pd further catalyzes the hydrogenolysis of C–OH to give ethylbenzene as a final product [303–305]. To overcome these problems, Vetere et al. [306] supported $Ni_2P/Ni_{12}P_5$ nanoparticles (obtained by thermal decomposition of $[Ni(acac)_2]$ together with tripheynl phosphine) on mesoporous silica and utilized the same for the hydrogenation of the acetophenone carbonyl group to 1-phenylethanol. The nanoparticles exhibited activity and high selectivity for the mentioned hydrogenation reaction which is attributed to the specific geometry of the Ni–P locations on the surface of the nanoparticles. The findings are interesting as nickel phosphides exist in different crystallographic structures which could be active and selective to hydrogenate multi functional molecules.

Analyzing the results based on the above reports, Vetere et al. [307] explored the possible promoter effect due to the presence of phosphorus in nickel phosphides during chemoselective hydrogenation of an aromatic ketone. Accordingly, catalysts were prepared with monodisperse Ni and Ni_2P nanoparticles of the same average diameter (16.0 ± 0.2 nm vs. 15.1 ± 0.6 nm, respectively) so that the exact effect of the electronic and structural differences between the nickel and the nickel phosphides on the catalytic activity and selectivity in hydrogenation of acetophenone can be found without any misleading effects that can be produced due to different sizes of nanoparticles. The nanoparticles were supported on mesoporous silica nanospheres for their use as catalysts in the hydrogenation of acetophenone in liquid phase. Surprisingly, both the catalysts produced the same product with similar final conversion of 30% and selectivity to 1-phenylethanol of about 95%. The only difference is that nickel phosphides show a lower reaction velocity than Ni.

Other than the above hydrogenation reactions, substrates such as cinnamaldehyde and acetonitrile were selectively hydrogenated with Ni_2P on SiO_2 [308] and Mo_xP, respectively [309]. For instance, the selective hydrogenation of α,β-unsaturated aldehydes using nickel phosphides as a non-noble metal catalyst has been explored as the reaction is of great importance in industrial production. In view of this, Liu and co-workers employed an amorphous nickel phosphide for the selective hydrogenation of cinnamaldehyde. Amorphous nickel phosphide exhibited better activity and selectivity compared to crystalline nickel phosphide and commercial Pd/C catalyst. Furthermore, initial P/Ni ratio affects the activity of amorphous nickel phosphide. In addition, amorphous nickel phosphide show better catalytic performance in the selective hydrogenation of different α,β-unsaturated aldehydes and ketones[310].

However, in the case of hydrogenation using Mo_xP, the reaction is dependent on the M/P ratio. High M/P ratio of 1.1 produced ethylamine as the major product while low ratio of 0.9 yielded diethylamine and triethylamine as the product [309].

Hydrogen production through water splitting

The rapid consumption of traditional energy sources such as petroleum and coal worsened both the global energy and the environmental pollution problems. In addition, the large-scale storage requirement of renewable energy sources like wind or solar energy to allay these problems is not solved yet. Converting the electricity derived from these renewable energies to hydrogen fuel via water electrolysis opens an interesting path to realize both energy conversion as well as scalable storage technology. Hydrogen is considered an ideal fuel for storage and supply due to its clean and high energy density.

Among various methods available for the production of hydrogen, water splitting is one of the most encouraging technologies. Water splitting can be achieved either electro- or photo catalytically. Electrocatalytic water splitting is the main approach to produce H_2 through HER of the electrolysis of water. The electrolysis of water involves hydrogen evolution reaction (HER) and oxygen evolution reaction (OER) [272] as mentioned below.

Cathodic reaction:

$$2H^+(aq) + 2e^- \rightarrow H_2(g)$$

Anodic reaction:

$$2H_2O(l) \rightarrow 4e^- + 4H^+(aq) + O_2(g)$$

In general, HER in acidic medium involves the absorption of $H^+(aq)$ and the desorption of H_2 from the surface of the catalyst [311]. The absorption step also known as Volmer reaction is a discharge process that involves an electron transfer to the cathode surface to capture a proton of the electrolyte forming an intermediate state of an adsorbed hydrogen atom on the active site of the catalyst.

$$H^+(aq) + e^- + \text{Catalyst} \leftrightarrow H_{ads} \quad \text{(Volmer reaction)}$$

The desorption step follows two different paths to produce H_2 depending on the coverage of adsorbed hydrogen atom on the catalyst which in turn depends on the absorption of the catalyst towards H^+ [311]. Under lower coverage condition of the adsorbed hydrogen atom (H_{ads}), the electrochemical desorption step is known as Heyrovsky reaction where as the chemical desorption involving high H_{ads} coverage is called Tafel reaction.

$$H_{ads} + H^+(aq) + e^- \leftrightarrow H_2(g) \quad \text{(Heyrovsky reaction)}$$

$$H_{ads} + H_{ads} \leftrightarrow H_2(g) \quad \text{(Tafel reaction)}$$

Overall, the above reactions could be described as thermodynamic adsorption and desorption processes of H_{ads} from the active sites of a catalyst.

Theoretically, water splitting requires a minimum Gibbs free energy (ΔG_o) of 237.13 kJ mol^{-1} to overcome an energy barrier for dissociating each mole of water [12]. This is equivalent to a potential difference of 1.23 V in electrochemical process and equal to photon energy of 1.23 eV in photochemical process. However, the required voltage in the actual electrochemical reaction is much larger than 1.23 V due to the various energy barriers in electrochemical process. Absolute value of the difference between the experimental potential and the thermodynamically calculated potential is called overpotential. The latter is caused by polarization of the electrode which always demands more energy for electrolysis than that is predicted by theory. Overpotential is one of the important parameters for evaluating an electrocatalyst and should be low for an excellent electrocatalyst.

Therefore, the use of catalysts in these energy conversion reactions is crucial to reduce the energy requirement by lowering the activation energy and increase the efficiency of energy conversion. In view of this, exploration of a suitable catalyst is crucial for water splitting. Accordingly, noble metals like Pt and its composites have been studied as possible catalysts for many energy conversion reactions such as electrolytic and photocatalytic water splitting and found to be excellent catalysts. However, their high cost and scarcity restrict their industrial/ large-scale applications. Therefore, efforts towards the development of low cost and earth abundant metals and their alloys and other derivatives with better catalytic performance gained momentum. Accordingly, a number of metal selenides [312], chalcogenides [313], borides [314], nitrides [315], carbides [316] and phosphides [164] were studied as the potential HER catalysts. Among them, metal phosphides have benefits such as the most earth abundant and cheaper non-metallic elements, phosphorus as its constituent and the moderate P–H bond strength which has an important role in producing hydrogen and reducing the H-poisoning effect [317].

Accordingly, the investigations on transition metal phosphides for electrochemical hydrogen evolution were performed by a number of groups including Shi et al. [272], Popczun et al. [318] and Jiang et al. [319]. These reports have encouraged the research of transition metal phosphides as efficient HER electrocatalyst.

Liu and Rodriguez [320] were the first to predict $Ni_2P(001)$ as a potential HER catalyst using density functional theory (DFT) calculations. $Ni_2P(001)$ exhibits structural and electronic similarities to the active biological HER catalyst namely [NiFe] hydrogenase. Inspired by these theoretical predictions, Schaak et al. [318] experimentally demonstrated that nanostructured Ni_2P is an active HER electrocatalyst with improved performance and stability compared to other earth abundant electrocatalysts. Here, hollow Ni_2P nanoparticles were prepared by heating $[Ni(acac)_2]$ in ODE, OLA and TOP to 320 °C for 2 h.

However, shape-dependent effect of the nickel phosphide nanoparticles on HER activity remains unexplored, due to the difficulty in the synthesis of nanomaterials

with different morphologies. Therefore, Joo et al. studied the morphology-dependent HER catalytic activity of nickel phosphide nanoparticles using spherical and rod shaped Ni_2P nanoparticles. The investigations revealed that spherical Ni_2P nanoparticles with (001) surface exhibited better HER activity than Ni_2P nanorods with the (210) surface. This is attributed to better interactions of $Ni_2P(001)$ surface with the adsorbent and lower activation energy requirement for hydrogen adsorption. The outcome of the study emphasizes the significance of shape of the nanoparticles in electrocatalysts for improving catalytic activities [321].

Recently, Zhang and co-workers [322] demonstrated that nickel phosphide nanoparticles of composition $Ni_{12}P_5$ loaded on silicon nanowires also show efficient HER catalytic activity and stability and are at par with other nonexpensive catalysts. The best possible overpotential required for 20 mA/cm^2 current density using these nanoparticles as HER electrocatalyst is 143 mV in acidic solution. The HER activity of $Ni_{12}P_5$ nanoparticles were linked to the charged natures of Ni and P.

Iron phosphide nanomaterials have also been studied for their use as HER catalyst as early as nickel phosphide nanomaterials have been investigated for the same purpose. Zhang and co-workers [323] high HER catalytic performance of transition metal nanomaterials using FeP nanosheets. The FeP nanosheets with porous nature were synthesized through an anion exchange reaction of $Fe_{18}S_{25}$–TETAH (TETAH = protonated triethylenetetramine) nanosheets with phosphorus ions. The FeP nanosheets show high HER catalytic activity with a low overpotential (~0.1 V) and small Tafel slope (~67 mV per decade).

However, highly active HER catalysts made up of high-quality iron phosphide nanoparticles are still desirable. Accordingly, Schaak et al. [324] reported FeP nanoparticles of remarkable electrocatalytic activity for H_2 generation in both acidic and neutral-pH aqueous solutions. At a current density of 10 mA cm^{-2}, these nanoparticles show overpotentials of 50 and 102 mV in acidic and neutral solutions, respectively. The performance of FeP nanoparticles is comparable to their non-noble metal nanoparticle predecessor as HER electrocatalysts in both acidic and neutral-pH aqueous solutions.

Other than nickel phosphides, cobalt phosphides have also been known as good HER catalysts with different morphologies [319], particle sizes, support materials [325–327] and synthetic procedures [327–330]. The common methods used to synthesize these CoP nanomaterials include colloidal synthesis involving the reaction of readily prepared cobalt nanoparticles with TOP [325] or phosphidation of nanostructured templates of cobalt oxide and related compounds [327].

Of these, only colloidal cobalt phosphide nanomaterials which have potential HER catalytic activity will be the part of this discussion. For example, Schaak et al. [325] reported uniform multifaceted hollow CoP nanoparticles on Ti foil showing reasonably comparable HER electrocatalytic activity under strongly acidic conditions. The CoP nanoparticles were synthesized by reacting Co nanoparticles with TOP at 320 °C. Electrodes made up of these CoP nanoparticles on a Ti support generated a cathodic current density of 20 $mAcm^{-2}$ at an over potential of –85 mV.

Although it is known that CoP nanostructures exhibit high HER activity of CoP nanostructures, understanding the origin of the activity is important which requires

synthesis of high-quality and morphologically discrete samples. Accordingly, Schaak et al. [325] synthesized CoP nanostructures which have the most of its (111) crystal facets exposed. These nanostructures were assessed for HER electrocatalysts and compared with that of multifaceted CoP nanocrystals. The activity is better for multifaceted CoP nanocrystals. The comparison indicated that the high HER activity is intrinsic to the CoP system and also elucidated that morphology has no significant influence on the activity and stability of nanostructured HER electrocatalysts [321].

Cobalt phosphide nanostructures other than CoP, which is known for efficient HER catalytic activity and has a compositionally and structurally distinct phase is Co_2P. For instance, Chen and co-workers [322] synthesized Co_2P nanorods and evaluated their HER activities by depositing on glassy carbon and Ti electrodes. The nanorods were prepared by injecting a hot oleic acid and OLA solution of $[Co(acac)_2]$ into a mixture containing OLA and TOP at 330 °C with the injection rate of 0.125 mL/min and heated at the same temperature for 10 min. The former shows better activity, stability and reversibility than Ni_2P counterparts. The Co_2P nanorods on glassy carbon have the lowest Tafel slope while their exchange current density on Ti electrode is comparable to that of Pt electrode.

Similarly, Huang et al. [333] also reported efficient HER catalytic activity for Co_2P nanorods with the overpotentials required as low as 167 and 171 mV in acidic and basic solutions, respectively for a current density of 20 mA/cm^2.

Recently, Robinson and co-workers [334] prepared morphologically alike Co_2P and CoP nanoparticles using premade Co nanoparticles. Motivated by such synthetic capabilities, Schaak et al. [335] synthesized morphologically equivalent, uniform, hollow Co_2P and CoP nanoparticles and evaluated their HER activities in 0.50 M H_2SO_4. Both nanoparticles are highly crystalline with identical shapes, sizes and distributions. Such identical nanostructures help in correlating similarities and differences in HER activity directly with composition and structure while curtailing contributions from morphology, size, size distribution and facets. Co_2P exhibit high HER electrocatalytic activity with high acid durability. Although catalytic performance of Co_2P is comparable to that of CoP, the higher overpotentials required for Co_2P compared to CoP when correlated with the relative Co/P ratios indicates that CoP may offer a higher density of possible active sites due to the proximity of cobalt and phosphorus atoms on the surface [335].

Other than iron-, cobalt- and nickel phosphide nanostructures, amorphous MoP nanoparticles are among the best molybdenum-based HER catalysts and also one of the active, acid-durable, non-noble-metal HER catalysts. Schaak et al. [187] synthesized amorphous MoP nanoparticles of diameter 4.2 ± 0.5 nm and loaded the nanoparticles on Ti to evaluate as electrocatalysts for the HER at pH 0.3 conditions. Amorphous MoP nanoparticles were obtained by heating $[Mo(CO)_6]$ and TOP in squalane at 320 °C which stayed amorphous after heating at 450 °C in H_2(5%)/Ar(95%) to take out the surface ligands. MoP/Ti electrodes showed overpotentials of −90 and −105 mV at current densities of −10 and −20 mA cm^{-2}, respectively and remained stable over 500 cycles in acidic media under operating conditions.

Similarly, another amorphous system of colloidal WP nanoparticles with an average diameter of 3 nm was produced and demonstrated as a novel HER electrocatalyst in acidic aqueous solutions. WP/Ti electrodes showed overpotentials of only −120 mV and −140 mV at current densities of −10 mA cm^{-2} and −20 mA cm^{-2}, respectively in acidic medium [192].

12.6.3 Lithium Ion Battery Applications

The expansion of renewable and long lasting energy sources is very much needed to decrease the dependence on fossil fuels. For storing and transporting, the renewable energy generated by different sources electrochemical energy storage devices such as rechargeable batteries and supercapacitors are required which can be further used in portable electronics and electric vehicles [336]. Among them, lithium ion batteries (LIBs) are source of power for handy electronic devices owing to their high energy density, durability and environmental friendly nature [337–339]. However, for their affordable applications in electric- and hybrid electric vehicles, important requirements such as safety, affordability, longer shelf time, power- and energy–density have to be met. The efficiency of LIBs mostly depends on the electrode material. Hence, the development of cheaper and efficient electrodes is the need of the hour. Moreover, nanostructurization of electrodes enhances the electrode/electrolyte contact area facilitating higher lithium ion flux across the interfaces for LIBs improving rate capability. The former also enhances diffusion rate due to the short ion and electron transport path and helps in managing volume expansion of the electrode with Li-ion incorporation.

Accordingly, a number of nanostructures have been synthesized for fabricating electrode materials for LIBs with an intention to improve electrochemical performance [13]. Metal phosphides are interesting materials and exhibit better chemical properties due to the existence of multi-electron orbitals. Hence, metal phosphides have been used as HDS catalysts [271] and HER [11, 17], etc. Metal phosphides are considered as potential anode materials for LIBs owing to their lower intercalation potentials and remarkably high volumetric and gravimetric capacities compared to carbonaceous materials available in the market.

The pioneering work of Nazar and co-workers [340] on CoP_3 as an electrode material demonstrated promising Li-storage performance which has garnered huge interest due to low cost, low intercalation potentials and high theoretical capacity. Ever since a number of binary metal phosphides such as Co_2P [153], Zn_3P_2 [341], GaP [342] and FeP_2 [343], etc. have emerged as potential anode materials for LIBs. Furthermore, the size and shape tuning of nanostructures added new dimensions to the research on metal phosphides for LIB applications.

To date, a number of colloidal metal phosphide nanostructures, including nanoparticles [344], nanosheets [345], nanorods [222], nanowires [346], hollow spheres [153] and hierarchical nanospheres [347] have been reported.

The following section will discuss the colloidal metal phosphide nanostructures based on anodes for LIBs including nickel-, iron-, cobalt—and tin-phosphide nanostructures.

Among the metal phosphides, nickel phosphides (e.g., Ni_3P [348], Ni_2P [345], $Ni_{12}P_5$ [349], Ni_5P_4 [350], NiP_2 [351] and NiP_3 [352]) are the most studied materials for LIB applications. Of these, phosphorus-rich phases have higher capacities. However, both phosphorus- and metal-rich nickel phosphides degrade on continuous cycling due to volume change and separation from the copper foil. Therefore, many researchers focused on improving the cycling performance of these phosphides and trimming down the irreversible capacity loss. To date, a number of nickel phosphides with distinct morphologies have been documented.

One of the ways to improve electrochemical performance is nanostructurization of nickel phosphides, especially synthesis of porous nanostructures efficiently contain the large volume changes and directed a short diffusion length for Li^+ ions during cycling [345]. For instance, thin porous Ni_2P nanosheets (thickness of 3 nm) synthesized by organometallic precursors used as potential anode materials for LIBs. The nanosheets exhibit a reversible discharge capacity of 379.8 mAh g^{-1} after 50 cycles. The enhanced performances of nanosheet electrodes are ascribed to the porous thin sheet structure, creating an improved contact between the active material and electrolyte and also result in a short diffusion length of Li^+ ions [345].

Although nanostructurization of electrodes improves the performance of lithium ion batteries, fabrication of electrodes using nanoparticles is not simple. Their cohesive structure has to be attained both mechanically and electronically for long-term cyclic performance and effective electronic percolation. The former has been accomplished by carbon coating of the nanoparticles either by the deposition or growth of nanoparticles on nanostructured carbonaceous materials (e.g., graphite layers [353] and carbon nanotubes [354], etc.) or by the use of molecular sources of carbon (e.g., glucose [355], etc.). These nanoparticles coated nanostructured electrodes are generally less sensitive to oxidation or carbide formation than anode materials which have been simply carbon coated using molecular sources of carbon. So, there is still scope for novel carbon coating methods that would be well-suited for highly oxidation sensitive nanoparticles and would guarantee a coating with better electronic percolation through the electrode, without sintering of nanoparticles. Therefore, Sanchez et al. [344] designed a simple in situ generated carbon coating method, using Ni_2P nanoparticles of size 25 nm where a soft thermal treatment (400 °C, 30 min) decomposed the surface ligands of the nanoparticles to form a thin carbon layer without sintering of the nanoparticles. The thickness of carbon coating can be tailored by changing the surface ligands. Electrochemical properties of the anode comprised of Ni_2P/C composite vs Li compared with the electrode made up of bulk Ni_2P. The capacity of the electrode fabricated by Ni_2P/C nanoparticles were much better than that of bulk material even after few cycles. The self-generated carbon coating offers an electron-conductive penetrating network for Li permeability which enhances the uptake of Li and also ameliorates the mechanical integrity of the electrode.

Furthermore, coating nickel phosphides with carbonaceous materials (e.g., graphene, or carbon nanotubes) or making composites of nickel phosphides with

carbon materials alleviates the volume changes caused due to lithium ion insertion and also avoid the accumulation of the nickel phosphide. These factors enhance their lithium storage performance. For instance, Tu and co-workers synthesized hierarchical nickel phosphide (h-Ni_2P) nanospheres comprising of nanoparticles with 5–10 nm sizes and filled by amorphous carbon. The structure enhances the contact between Ni_2P and electrolyte providing space for lithium ion accommodation shortens the diffusion length of Li^+ and improves the reactivity of the electrode reaction. The amorphous carbon filled hierarchical Ni_2P nanostructures provide cushion to buffer volume expansion and hence improves the electrode durability. The h-Ni_2P electrode displays high-capacity and Coulombic efficiency [347].

Among various carbonaceous materials, one dimensional tubular structures namely carbon nanotubes (CNTs) have several advantages of high stability, -electronic conductivity, -Young's modulus and excellent surface properties for perfect supporting material. Furthermore, CNTs also act as a conductive medium benefiting good contact between the nanoparticles and ease volume changes and prevent the aggregation of nanoparticles during the charge/discharge processes. CNTs also offer shorter paths for electron transport and Li^+ diffusion due to their large surface-to-volume ratio resulting in short charge/discharge times. Accordingly, Yang et al. [349] synthesized unique hybrid nanostructures of $Ni_{12}P_5$/CNT by direct in situ deposition of $Ni_{12}P_5$ nanocrystals onto oxidized multiwall CNTs. The conductivity of the hybrids is enhanced and the aggregation of $Ni_{12}P_5$ nanoparticles are avoided with the help of CNTs. The $Ni_{12}P_5$/CNT nanohybrid anode exhibit improved electrochemical performance for LIBs and display a high capacity and remarkable stability. The improved properties are a result of a synergetic effect between $Ni_{12}P_5$ and CNTs.

The 1-D nanowires are useful for realizing high performance of LIBs as they assist in improved lithium ion and electron transportation than the electrodes comprised of small particles where transportation is limited by the inter-particle connections and continuities. In view of this, Tu et al. [346] produced single-crystalline Ni_2P nanowires with a uniform diameter of about 8 nm and lengths of few hundred nanometers demonstrated that the nanowires deliver much higher reversible capacity with good rate performance compared with the hexangular structured Ni_2P nanoparticles. The better electrochemical performance is ascribed to the small size and stable cylindrical structure of the nanowires which increase the interfacial contact area with the electrolyte improve the efficiency of lithium ion transportation. Electrochemical impedance spectra endorse that Ni_2P nanowires have superior electrical conductivity facilitating better movement of the lithium ion and electron in the electrode.

Among carbon-coated transition metal phosphide (TMP) nanomaterials and composites of nanostructured TMPs, mono-phosphorus TMPs are less compared to metal-rich phosphides due to lack of appropriate synthetic methods. Moreover, the high carbon content in carbon-coated transition metal phosphide nanomaterials and their composites make it difficult to maintain high energy density. Therefore, Yang et al. [350] choosing PPh_3 and [$Ni(acac)_2$] as phosphorus and nickel precursor, successfully prepared Ni_5P_4@C nanoparticles with reduced the carbon content and demonstrated that the composite show high lithium storage capacity, cyclic stability and exceptional rate capability.

Iron phosphides have drawn considerable due to their earth abundance, affordability and high theoretical capacities [356]. Similar to nickel phosphides, the phosphorus-rich iron phosphides as anode materials show higher reactivity versus Li. The factors affecting their performance as anode materials are Fe/P ratio, structure and electronic properties of the active material [356]. Until now, countable reports of colloidal iron phosphides for lithium battery applications are available.

Hall et al. [343] produced amorphous FeP_2 nanoparticles by treating $[Fe(N(SiMe_3)_2)_3]$ with PH_3 in THF at 100 °C and demonstrated their brilliant performance in electrochemical lithiation/de-lithiation by utilizing as the anode material in LIBs. The gravimetric charging and discharging capacities are 766 and 1258 mA h g^{-1}, respectively. Moreover, a reversible capacity of 906 mA h g^{-1} after ten cycles was achieved which corresponds to 66% of the theoretical capacity of amorphous FeP_2 nanostructures.

Cobalt phosphides (Co_2P [153], CoP [153] and CoP_3 [340, 357]) have been explored as anode materials in LIBs. Depending on the physiochemical structure of cobalt phosphides, their theoretical capacities can go beyond 500 mA h g^{-1}. However, their poor electrical conductivity and substantial volume changes during cycling make their applications as anode materials in LIBs very challenging. Use of nanostructured cobalt phosphides such as Co_2P nanorods [222] and CoP hollow nanoparticles [153] as active materials of anodes in LIBs is one of the ways to overcome the above problems. For instance, Co_2P nanorods and CoP hollow nanoparticles synthesized by thermal decomposition method when examined as anode materials for LIBs, it was observed that the effective Li^+ insertion/extraction was improved and the volume strain was alleviated. The hollow CoP particles show the best reversible capacity of 630 mA h g^{-1}after 100 cycles and excellent rate capability [153].

Another approach is to employ cobalt phosphide/carbon-based composites as anode materials as carbon increases the conductivity of the electrode and also accommodates the volume variations during cycling. For instance, Lu et al. [222] reported Co_2P nanorod/graphene nanocomposite with graphene sheets supporting Co_2P nanorods. The composite exhibits a relative reversible capacity of 888 mA h g^{-1}after 250 cycles at 100 mA g^{-1} and remarkable cycle stability. This capacity is greater than the individual theoretical capacity of Co_2P and grapheme. The performance of composite was better than its bulk counterpart. The improved performance has been attributed to microspores in Co_2P/graphene nanocomposites. Recently, Jiang et al. synthesized CoP@C nanorods that displayed lithium ion reversible capacity of around 530 mA h g^{-1}after 200 cycles at 900 mA g^{-1} with good cyclic stability [350].

In addition to transition metal phosphide nanostructures, main group metal phosphide nanostructures have also been for LIB application. For instance, Sn_4P_3 has a layered structure with alternating P and Sn layers. Utilizing this layered structure Sn_4P_3, Liu et al. [140] synthesized Sn_4P_3 nanoparticles with an average size of 15 nm and demonstrated their use as anodes in LIBs. The nanoparticles evidenced a high reversible capacity of 442 mA h g^{-1} after 320 cycles at 100 mA $g^{-1}$and admirable cycling performance, which has been ascribed to their small size. Kim et al. [68] established the application of teardrop like ultrafine $SnP_{0.94}$ nanoparticles as anode materials for LIBs. The nanoparticles show a reversible capacity of

681 mA h g^{-1} after 40 cycles at 120 mA g^{-1}. The greater stability exhibited during a large number of cycles was attributed to flexible structural reversibility based on the intercalation/deintercalation mechanism by molecular channels.

12.6.4 Biology, Medicine, Toxicology and Environmental Applications

Some of the most important applications of QDs are in the field of biology, medicine and environment. The crucial requirements for biomedical applications are cheaper, less toxic- and biocompatible-luminescent QDs [358]. Colloidal metal phosphide QDs based on InP based QDs are one of these QDs which have applications in biology and medicine [359]. For instance, Prasad et al. produced highly monodispersed hydrophillic InP–ZnS core-shell nanocrystals and utilized them as luminescent probes for cell imaging. Here, the surface of the mercaptoacetic acid-capped InP/ZnS core/shell nanocrystals was conjugated with folic acid for biofunctionalization and demonstrated their delivery into folate-receptor-positive cell lines by using confocal microscopy. The folate-receptors are overexpressed in human cancerous cells [110]. Mercaptosuccinic acid-capped InP/ZnS QDs surface functionalized with antibodies and utilized for imaging of human pancreatic cancer cells [14]. The surface modification and bioconjugation of QDs for targeting and imaging cells has been shown in Scheme 12.3. Recently, InP/ZnS QDs in combination with rare-earth emitters and peptide functionalization on QD surface were used for cell labeling [360].

In addition to cell imaging, the toxicity of InP/ZnS nanoparticles has also been studied and compared with that of CdSe/ZnS [361]. Recently while examining the toxicity of InP QDs, Nadeau, et al. [362] observed that it is the phototoxicity that contributes to cytotoxicity of these QDs though the constituent elements are less toxic.

Apart from the biological applications, metal phosphide nanostructures have also been used in environmental applications for the removal of heavy metal ions [363, 364] and as a photocatalyst for treating environment [365].

12.7 Conclusion and Future Perspective

In conclusion, a number of strategies have been developed for the synthesis of colloidal nanomaterials of main group- and transition- metal phosphides over the years and have been employed in various applications. In spite of interesting properties, colloidal synthesis of metal phosphides has encountered problems such as broad size distributions, poor stability and lower quantum yields compared to other conventional nanocrystals. Although considerable progress has been made in the

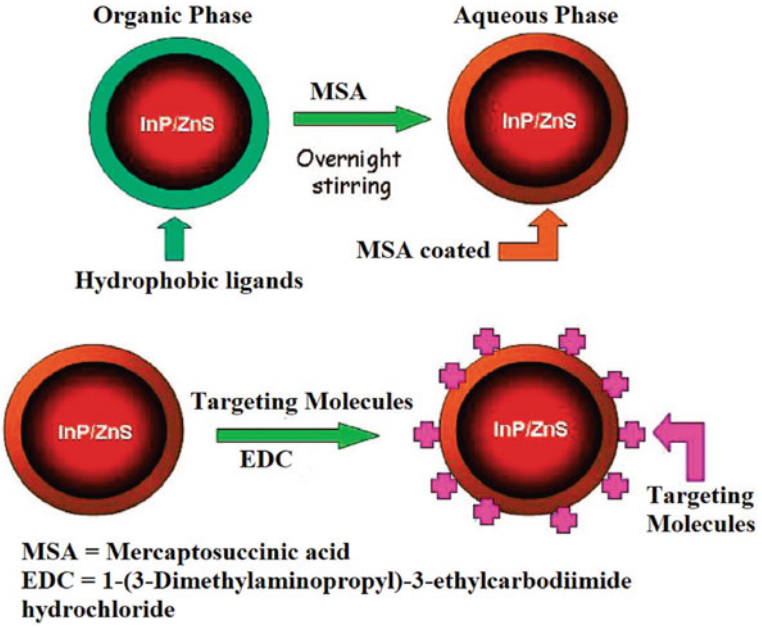

Scheme 12.3 An illustration of the formation of the water-dispersible InP/ZnS QD bioconjugates (Reproduced from Ref. [14] with the permission of American Chemical Society)

synthesis of quality colloidal metal phosphides by addressing many of these issues, a thorough understanding of the underlying mechanisms is much awaited. More systematic investigations and comprehensive understanding of the various synthetic mechanisms could be helpful to have better control over shape, structure and stoichiometry. This in turn can be useful in tailoring the physiochemical properties and hence in the device applications. Therefore, future prospects of colloidal metal phosphide nanomaterials to replace conventional nanocrystals in various applications lie in understanding the synthetic mechanisms and tackling the stoichiometry issues by using single source molecular precursors.

References

1. Yin Y, Alivisatos AP (2005) Colloidal nanocrystal synthesis and the organic–inorganic interface. Nature 437:664; Hughes B, Luther J, Beard M (2012) The subtle chemistry of colloidal, quantum-confined semiconductor nanostructures. ACS Nano 6:4573
2. Rosenthal SJ, Chang JC, Kovtun O, McBride JR, Tomlinson ID (2011) Biocompatible quantum dots for biological applications. Chem Biol 18:10
3. Mattoussi H, Palui G, Na HB (2012) Luminescent quantum dots as platforms for probing in vitro and in vivo biological processes. Adv Drug Deliv Rev 64
4. Giordano C, Antonietti M (2011) Synthesis of crystalline metal nitride and metal carbide nanostructures by sol–gel chemistry. Nano Today 6:366

5. Sharon M, Tamizhmani GJ (1986) Transition metal phosphide semiconductors for their possible use in photoelectrochemical cells and solar chargeable battery. Mater Sci 21:2193
6. Trindade T, O'Brien P, Pickett NL (2001) Nanocrystalline semiconductors: synthesis, properties, and perspectives. Chem Mater 13:3843
7. Landau MV, Herskowitz M, Hoffman T, Fuks D, Liverts E, Vingurt D, Froumin N (2009) Ultradeep hydrodesulfurization and adsorptive desulfurization of diesel fuel on metal-rich nickel phosphides. Ind Eng Chem Res 48:5239
8. Lim J, Park M, Bae WK, Lee D, Lee S, Lee C, Char K (2013) Highly efficient cadmium-free quantum dot light-emitting diodes enabled by the direct formation of excitons within InP@ ZnSeS quantum dots. ACS Nano 7:9019–9026
9. Wang HC, Zhang H, Chen HY, Yeh HC, Tseng MR, Chung RJ, Chen S, Liu RS (2017) Cadmium-free InP/ZnSeS/ZnS heterostructure-based quantum dot light-emitting diodes with a ZnMgO electron transport layer and a brightness of over 10 000 cd m^{-2}. Small 13:1603962
10. Luber EJ, Mobarok Md H, Buriak JM (2013) Solution-processed zinc phosphide (α-Zn_3P_2) colloidal semiconducting nanocrystals for thin film photovoltaic applications. ACS Nano 7:8136–8146
11. Shi Y, Zhang B (2016) Recent advances in transition metal phosphide nanomaterials: synthesis and applications in hydrogen evolution reaction. Chem Soc Rev 45:1529–1541
12. Pei Y, Cheng Y, Chen J, Smith W, Dong P, Ajayan PM, Ye M, Shen J (2018) Recent developments of transition metal phosphides as catalysts in the energy conversion field. J Mater Chem A 6:23220–23243
13. Lu Y, Wang T, Li X, Zhang G, Xue H, Pang H (2016) Synthetic methods and electrochemical applications for transition metal phosphide nanomaterials. RSC Adv 6:87188–87212
14. Yong K-T, Ding H, Roy I, Law W-C, Bergey EJ, Maitra A, Prasad PN (2009) Imaging pancreatic cancer using bioconjugated InP quantum dots. ACS Nano 3:502–510
15. Wang X, Kim H-M, Xiao Y, Sun Y-K (2016) Nanostructured metal phosphide-based materials for electrochemical energy storage. J Mater Chem A 4:14915–14931
16. Xiao P, Chen W, Wang X (2015) A review of phosphide-based materials for electrocatalytic hydrogen evolution. Adv Energy Mater 5:1500985
17. Callejas JF, Read CG, Roske CW, Lewis NS, Schaak RE (2016) Synthesis, characterization, and properties of metal phosphide catalysts for the hydrogen-evolution reaction. Chem Mater 28:6017–6044
18. Carenco S, Portehault D, Boissière C, Mézailles N, Sanchez C (2013) Nanoscaled metal borides and phosphides: recent developments and perspectives. Chem Rev 113:7981–8065
19. Li H, Jia C, Meng X, Li H (2019) Chemical synthesis and applications of colloidal metal phosphide nanocrystals. Front Chem 6:652
20. Mushonga P, Onani MO, Madiehe AM, Meyer M (2012) Indium phosphide-based semiconductor nanocrystals and their applications. J Nanomater 869284
21. Greenwood NN, Parish RV, Thornton P (1966) Metal borides. Q Rev 20:441–464
22. Von Schnering HG, Hoenle W (1988) Chemistry and structural chemistry of phosphides and polyphosphides. 48. Bridging chasms with polyphosphides. Chem Rev 88:243
23. Chen J-H, Whitmire KH (2018) A structural survey of the binary transition metal phosphides and arsenides of the d-block elements. Coord Chem Rev 355:271–327
24. Grosvenor AP, Wik SD, Cavell RG, Mar A (2005) Examination of the bonding in binary transition-metal monophosphides MP (M = Cr, Mn, Fe, Co) by X-ray photoelectron spectroscopy. Inorg Chem 44:8988
25. Diplas S, Løvvik OM (2009) Electronic structure studies of Ni–X (X: B, S, P) alloys using x-ray photoelectron spectroscopy, x-ray induced Auger electron spectroscopy and density functional theory calculations. J Phys Condens Matter 21:245503
26. Blanchard PER, Grosvenor AP, Cavell RG, Mar A (2008) X-ray photoelectron and absorption spectroscopy of metal-rich phosphides M_2P and M_3P (M = Cr−Ni). Chem Mater 20:7081–7088
27. Ganguli AK, Prakash J, Thakur GS (2013) The iron-age of superconductivity: structural correlations and commonalities among the various families having–Fe–Pn–slabs (Pn = P, As and Sb). Chem Soc Rev 42:569

28. Hbkabe T (1978) J Sri Hiroshimu Univ Ser A 42:1
29. Fujii S, Ishida S, Asano S (1988) Electronic structures and magnetic properties of Fe_2P, Co_2P and CoMnP. J Phys F: Met Phys 18:971–980
30. Brock SL, Senevirathne K (2008) Recent developments in synthetic approaches to transition metal phosphide nanoparticles for magnetic and catalytic applications. J Solid State Chem 181:1552–1559
31. Huber EE Jr, Ridgely DH (1964) Magnetic properties of a single crystal of manganese phosphide. Phys Rev 135:A1033–A1040
32. Yessik M (1968) The magnetic structure of Mn_2P. Phil Mag 17:623
33. Gambino RJ, McGuire TR, Nakamura Y (1967) Magnetic properties of the iron-group metal phosphides. J Appl Phys 38:1253–1255
34. Ruhl R, Jeitschko W (1981) Acta Cryst, B 97:39–44
35. Huber EE Jr, Ridgley DH (1963) Magnetic properties of a single crystal of manganese phosphide. J Appl Phys 34:1099
36. Stein BF, Walmsley RH (1966) Magnetic susceptibility and nuclear magnetic resonance in transition-metal monophosphides. Phys Rev 148:933
37. Goodenough JB (1960) Direct cation–cation interactions in several oxides. Phys Rev 117:1442
38. Felcher GP, Smith FA, Bellavance D, Wold A (1971) Magnetic structure of iron monophosphide. Phys Rev B 3:3046–3052
39. Häggström L, Narayanasamy A (1982) Mössbauer study of the magnetic structure of FeP. J Magn Magn Mater 30:249–256
40. Fujii H, Hökabe T, Kamigaichi T, Okamoto T (1977) Magnetic properties of Fe_2P single crystal. J Phys Soc Jpn 43:41–46
41. Chiba S (1960) Magnetic properties of iron phosphide Fe_2P. J Phys Soc Jpn 15:581–585
42. Liu H, James P, Broddefalk A, Andersson Y, Granberg P, Eriksson O (1998) Structural and magnetic properties of $(Fe_{1-x}Co_x)_3P$ compounds: experiment and theory. J Magn Magn Mater 189:69–82
43. Alleg S, Boussaha A, Tebib W, Zergoug M, Suňol JJ (2016) Microstructure and magnetic properties of NiP alloys. J Superconduct Novel Magnet 29:1001–1011
44. Zeppenfeld K, Jeitschko W (1993) Magnetic behaviour of Ni_3P Ni_2P, NiP_3 and the series $Ln_2Ni_{12}P_7$ (Ln = Pr, Nd, Sm, Gd-Lu). J Phys Chem Solids 54:1527–1531
45. Odile JP, Soled S, Casro CA, Wold A (1978) Crystal growth and characterization of the transition-metal phosphides copper diphosphide, nickel diphosphide, and rhodium triphosphide. Inorg Chem 17:283–286
46. Fruchart R, Roger A, Senateur JP (1969) Crystallographic and magnetic properties of solid solutions of the phosphides M_2P, M = Cr, Mn, Fe, Co, and Ni. J Appl Phys 40:1250–1257
47. Xu J, Greenblatt M, Emge T, Höhn P, Hughbanks T, Tian Y (1996) Crystal structure, electrical transport, and magnetic properties of niobium monophosphide. Inorg Chem 35:845–849
48. Shirotani I, Kaneko I, Takaya M, Sekine C, Yagi T (2000) Superconductivity of molybdenum phosphides prepared at high pressure. Phys B 281–282:1024–1025
49. Blaugher RD, Hulm JK (1965) Superconducting phosphides of the transition metals. J Phys Chem Solids 26:2037–2039
50. Ohta S (1996) Magnetic properties of 4d metal phosphides containing Co and Ni. J Phys Soc Jpn 65:4090–4091
51. Raub ChJ, Zachariasen WH, Geballe TH, Matthias BT (1963) Superconductivity of some new Pt-metal compounds. J Phys Chem Solids 24:1093–1100
52. Sweeney CM, Stamm KL, Brock SL (2008) On the feasibility of phosphide generation from phosphate reduction: the case of Rh, Ir, and Ag. J Alloys Compd 448:122–127
53. Rühl R, Flörke U, Jeitschko W (1984) Crystal growth, properties, and structure refinements of some rhenium phosphides and arsenophosphides. J Solid State Chem 53:55–63
54. Rühl R, Jeitschko W (1982) Preparation and crystal structure of dirhenium pentaphosphide, Re_2P_5, a diamagnetic semiconducting polyphosphide with rhomboidal Re_4 clusters. Inorg Chem 21:1886–1891

55. Wang P, Wang Y, Wang L, Zhang X, Yu X, Zhu J, Wang S, Qin J, Leinenweber K, Chen H, He D, Zhao Y (2016) Elastic, magnetic and electronic properties of iridium phosphide Ir_2P. Sci Rep 6:21787
56. Sahu T (1991) Magnetic susceptibility of InP, InAs, and InSb. Phys Rev B 43:2415–2418
57. Sahoo Y, Poddar P, Srikanth H, Lucey DW, Prasad PN (2005) Chemically fabricated magnetic quantum dots of InP: Mn. J Phys Chem B 109:15221–15225
58. Han DS, Bae SY, Seo HW, Kang YJ, Park J, Lee G, Ahn J-P, Kim S, Chang J (2005) Synthesis and magnetic properties of manganese-doped GaP nanowires. J Phys Chem B 109:9311–9316
59. Huang B, Zhuang H, Yoon M, Sumpter BG, Wei S–H (2015) Highly stable two-dimensional silicon phosphides: different stoichiometries and exotic electronic properties. Phys Rev B 91:121401 (R)
60. Kovnir KA, Kolen'ko YV, Ray S, Li J, Watanabe T, Itoh M, Yoshimura M, Shevelkov AV (2006) A facile high-yield solvothermal route to tin phosphide Sn_4P_3. J Solid State Chem 179:3756–3762
61. Minami K, Jogo J, Mori M, Ishibashi T, Sato K (2005) 2005 IEEE international magnetics conference (INTERMAG), Nagoya, pp 271–272
62. Williams R, McGovern I (1975) Surface characterisation of indium phosphide. Surf Sci 51:14–28
63. Tycko R (1998) Optical pumping in indium phosphide: 31P NMR measurements and potential for signal enhancement in biological solid state NMR. Solid State Nucl Magn Reson 11:1
64. Tessier MD, Nolf KD, Dupont D, Sinnaeve D, Roo JD, Hens Z (2016) Aminophosphines: a double role in the synthesis of colloidal indium phosphide quantum dots. J Am Chem Soc 138:5923–5929
65. Shmidt FK, Belykh LB, Skripov NI, Belonogova LN, Umanets VA, Rokhin AV (2007) Nano-sized hydrogenation catalyst based on palladium bisacetylacetonate and phosphine: formation, the origin of activity, and properties. Kinet Catal 48:640–648
66. Ramasamy P, Ko KJ, Kang JW, Lee JS (2018) Two-step "seed-mediated" synthetic approach to colloidal indium phosphide quantum dots with high-purity photo-and electroluminescence. Chem Mater 30:3643–3647
67. Ko WS, Tran T-TD, Bhattacharya I, Ng KW, Sun H, Chang-Hasnain C (2015) Illumination angle insensitive single indium phosphide tapered nanopillar solar cell. Nano Lett 15:4961–4967
68. Kim YS, Hwang HS, Yoon CS, Kim MG, Cho JP (2007) Reversible lithium intercalation in teardrop-shaped ultrafine $SnP_{0.94}$ particles: an anode material for lithium-ion batteries. Adv Mater 19:92–96
69. Zaikina JV, Kovnir KA, Sobolev AN, Presniakov IA, Kytin VG, Kulbachinskii VA, Olenev AV, Lebedev OI, Van Tendeloo G, Dikarev EV, Shevelkov AV (2008) Highly disordered crystal structure and thermoelectric properties of Sn_3P_4. Chem Mater 20:2476–2483
70. Liu S, Li S, Li M, Yan L, Li H (2013) Synthesis of tin phosphides (Sn_4P_3) and their high photocatalytic activities. New J Chem 37:827–833
71. Green M, O'Brien P (2001) A novel metalorganic route to nanocrystallites of zinc phosphide. Chem Mater 13:4500–4505
72. Fleet ME, Mowles TA (1984) Structure of monoclinic black zinc diphosphide, ZnP_2. Acta Cryst, C 40:1778–1779
73. Li X, Peng F, Zhou X, Wang P (2013) The synthesis of ZnP_4 based on liquid–solid reaction under high pressure and temperature. Solid State Sci 21:51–53
74. Miao SD, Hickey SG, Waurisch C, Lesnyak V, Otto T, Rellinghaus B, Eychmüller A (2012) Synthesis of monodisperse cadmium phosphide nanoparticles using ex-situ produced phosphine. ACS Nano 6:7059–7065
75. Zanin IE, Aleinikova KB, Antipin M Yu, Afanasiev MM (2006) The structure of the compound Cd_3P_2. J Struct Chem 47:78–81
76. Mellor JW (1947) The metal phosphides. In: A comprehensive treatise on inorganic and theoretical chemistry, phosphorus. Longmans, London, pp 844, 849, 851

77. White WE, Bushey AH (1944) Aluminum phosphide—preparation and composition. J Am Chem Soc 66:1666–1672
78. Kuisl M (1967) Synthesis of indium phosphide from indium and phosphorus pentoxide. Angew Chem 6:177–177
79. Ringel CM (1971) Synthesis of gallium phosphide. J Electrochem Soc 118:609–613
80. Karimov S, Mavlonov S (1976) Izvestiya Akademii Nauk SSSR. Neorg Mater 12:1290–1292
81. Olofsson O, Gullman J (1971) The crystal structure of TlP_5. Acta Chem Scand 25:1327–1337
82. Carlsson JRA, Madsen LD, Johansson MP, Hultman L, Li X-H, Hentzell HTG (1997) A new silicon phosphide, $Si_{12}P_5$: formation conditions, structure, and properties. J Vacuum Sci Technol A 15:394
83. Reinhold R, Mikhailova D, Gemming T, Missyul AB, Nowka C, Kaskel S, Giebeler L (2018) Silicon monophosphide as a possible lithium battery anode material. J Mater Chem A 6:19974–19978
84. Kwon H-T, Kyoung Lee C, Jeon K–J, Park C-M (2016) Silicon diphosphide: a Si-based three-dimensional crystalline framework as a high-performance Li-ion battery anode. ACS Nano 10:5701–5709
85. Li L, Wang W, Gong P, Zhu X, Deng B, Shi X, Gao G, Li H, Zhai T (2018) 2D GeP: an unexploited low-symmetry semiconductor with strong in-plane anisotropy. Adv Mater 30:1706771
86. Osugi J, Namikawa R, Tanaka Y (1967) Chemical reaction at high temperature and high pressure IV: high pressure phases in the Ge-P system. Rev Phys Chem Jpn 37:81–93
87. Nam K-H, Jeon K-J, Park C-M (2019) Layered germanium phosphide-based anodes for high-performance lithium-and sodium-ion batteries. Energy Storage Mater 17:78–87
88. Yang B, Nie A, Chang Y, Cheng Y, Wen F, Xiang J, Li L, Liu Z, Tian Y (2018) Metallic layered germanium phosphide GeP_5 for high rate flexible all-solid-state supercapacitors. J Mater Chem A 6:19409–19416
89. Tallapally V, Alan Esteves RJ, Nahar L, Arachchige IU (2016) Multivariate synthesis of tin phosphide nanoparticles: temperature, time, and ligand control of size, shape, and crystal structure. Chem Mater 28:5406–5414
90. Gullman J, Olofsson O (1972) The crystal structure of SnP_3 and a note on the crystal structure of GeP_3. J Solid State Chem 5:441
91. Carenco S, Demange M, Shi J, Boissiere C, Sanchez C, Le Flochz P, Mézailles N (2010) White phosphorus and metal nanoparticles: a versatile route to metal phosphide nanoparticles. Chem Commun 46:5578–5580
92. Schäfer K, Benndorf C, Eckert H, Pöttgen R (2014) PbP_7–a polyphosphide with a three-dimensional $[P_7]^{2-}$ network of condensed and P-bridged P_6 hexagons. Dalton Trans 43:12706–12710
93. Liu B, Köpf M, Abbas AN, Wang X, Guo Q, Jia Y, Xia F, Weihrich R, Bachhuber F, Pielnhofer F, Wang H, Dhall R, Cronin SB, Ge M, Fang X, Nilges T, Zhou C (2015) Black arsenic–phosphorus: layered anisotropic infrared semiconductors with highly tunable compositions and properties. Adv Mater 27:4423–4429
94. Hsu C–W, Tsai Y-C, Cossairt B, Camp C, Arnold J, Cummins C (2018) Synthetic route to white phosphorus (P_4) and arsenic triphopshide (AsP_3). Inorgan Syntheses 123–134
95. Allen GC, Carmalt CJ, Cowley AH, Hector AL, Kamepalli S, Lawson YG, Norman NC, Parkin IP, Pickard LK (1997) Preparation and characterization of a material of composition BiP (Bismuth Phosphide) and other intergroup 15 element phases. Chem Mater 9:1385–1392
96. Kimball GM, Mueller AM, Lewis NS, Atwater HA (2009) Photoluminescence-based measurements of the energy gap and diffusion length of Zn_3P_2. Appl Phys Lett 95:112103
97. Nayak A, Rao DR (1993) Photoluminescence spectra of Zn_3P_2-Cd_3P_2 thin films. Appl Phys Lett 63:592
98. Sharma SB, Paliwal P, Kumar M (1990) Electronic dielectric constant, energy gap and fractional ionic character of polyatomic binary compounds. J Phys Chem Solids 51:35
99. Weller H, Fojtik A, Henglein A (1985) Photochemistry of semiconductor colloids: properties of extremely small particles of Cd_3P_2 and Zn_3P_2. Chem Phys Lett 117:485–488

100. Miao S, Yang T, Hickey SG, Lesnyak V, Rellinghaus B, Xu J, Eychmüller A (2013) Emissive ZnO@Zn_3P_2 nanocrystals: synthesis, optical, and optoelectrochemical properties. Small 9:3415–3422
101. Mobarok MH, Luber EJ, Bernard GM, Peng L, Wasylishen RE, Buriak JM (2014) Phase-pure crystalline zinc phosphide nanoparticles: synthetic approaches and characterization. Chem Mater 26:1925–1935
102. Glassy BA, Cossairt BM (2015) Ternary synthesis of colloidal Zn_3P_2 quantum dots. Chem Commun 51:5283
103. Ho MQ, Esteves RJA, Kedarnath G, Arachchige IU (2015) Size-dependent optical properties of luminescent Zn_3P_2 quantum dots. J Phys Chem C 119:10576–10584
104. Wang R, Ratcliffe CI, Wu X, Voznyy O, Tao Y, Yu K (2009) Magic-sized Cd_3P_2 II−V nanoparticles exhibiting bandgap photoemission. J Phys Chem C 113:17979–17982
105. Miao SD, Hickey SG, Rellinghaus B, Waurisch C, Eychmuller A (2010) Synthesis and characterization of cadmium phosphide quantum dots emitting in the visible red to near-infrared. J Am Chem Soc 132:5613–5615
106. Xie RG, Zhang JX, Zhao F, Yang WS, Peng XG (2010) Synthesis of monodisperse, highly emissive, and size-tunable Cd_3P_2 nanocrystals. Chem Mater 22:3820–3822
107. Ojo WS, Xu S, Delpech F, Nayral C, Chaudret B (2012) Room-temperature synthesis of air-stable and size-tunable luminescent ZnS-coated Cd_3P_2 nanocrystals with high quantum yields. Angew Chem Int Edn 51:738–741
108. Green M, O'Brien P (1998) A novel synthesis of cadmium phosphide nanoparticles using the single-source precursor $[MeCdP^tBu_2]_3$. Adv Mater 10:527
109. Yang X, Zhao D, Leck KS, Tan ST, Tang YX, Zhao J, Demir HV, Sun XW (2012) Full visible range covering InP/ZnS nanocrystals with high photometric performance and their application to white quantum dot light-emitting Diodes. Adv Mater 24:4180–4185
110. Bharali DJ, Lucey DW, Jayakumar H, Pudavar HE, Prasad PN (2005) Folate-receptor-mediated delivery of InP quantum dots for bioimaging using confocal and two-photon microscopy. J Am Chem Soc 127:11364–11371
111. Kim S, Lee K, Kim S, Kwon O-P, Heo JH, Im SH, Jeong S, Lee DC, Kim S-W (2015) Origin of photoluminescence from colloidal gallium phosphide nanocrystals synthesized via a hot-injection method. RSC Adv 5:2466–2469
112. Muskens OL, Diedenhofen SL, Kaas BC, Algra RE, Bakkers E, Rivas JG, Lagendijk A (2009) Large photonic strength of highly tunable resonant nanowire materials. Nano Lett 9:930–934
113. Allen CR, Jeon J-H, Woodall JM (2010) Simulation assisted design of a gallium phosphide n–p photovoltaic junction. Sol Energy Mater Sol Cell 94:865–868
114. Yamaguchi M, Takamoto T, Khan A, Imaizumi M, Matsuda S, Ekins-Daukes NJ (2005) Super-high-efficiency multi-junction solar cells. Prog Photovolt: Res Appl 13:125–132
115. Elgun N, Davis EA (1994) Transport and optical properties of a-GaP prepared at different substrate temperatures. J Phys: Condens Matter 6:779
116. Toufanian R, Piryatinski A, Mahler AH, Iyer R, Hollingsworth JA, Dennis AM (2018) Bandgap engineering of indium phosphide-based core/shell heterostructures through shell composition and thickness. Front Chem 6:567
117. Mićić OI, Sprague JR, Curtis CJ, Jones KM, Machol JL, Nozik AJ (1995) Synthesis and characterization of InP, GaP, and $GaInP_2$ quantum dots. J Phys Chem 99:7754–7759
118. Manciu FS, Sahoo Y, MacRae DJ, Furis M, McCombe BD, Prasad PN (2003) Optical phonon spectra of GaP nanoparticles prepared by nanochemistry. Appl Phys Lett 82:4059–4061
119. Kim Y–H, Jun Y–w, Jun B-H, Lee S–M, Cheon J (2002) Sterically induced shape and crystalline phase control of GaP nanocrystals. J Am Chem Soc 124:13656–13657
120. Janik JF, Wells RL, Young VG Jr, Rheingold AL, Guzei IA (1998) New pnictinogallanes $[H_2GaE(SiMe_3)_2]_3$ (E = P, As) formation, structural characterization, and thermal decomposition to afford nanocrystalline GaP and GaAs. J Am Chem Soc 120:532–537
121. Mićić OI, Curtis CJ, Jones KM, Sprague JR, Nozik AJ (1994) Synthesis and characterization of InP quantum dots. J Phys Chem 98:4966–4969

122. Mićić OI, Sprague J, Lu ZH, Nozik AJ (1996) Highly efficient band-edge emission from InP quantum dots. Appl Phys Lett 68:3150–3152
123. Mićić OI, Cheong HM, Fu H, Zunger A, Sprague JR, Mascarenhas A, Nozik AJ (1997) Size-dependent spectroscopy of InP quantum dots. J Phys Chem B 101:4904–4912
124. Li L, Protiere M, Reiss P (2008) Economic synthesis of high quality InP nanocrystals using calcium phosphide as the phosphorus precursor. Chem Mater 20:2621–2623
125. Zan F, Ren JC (2012) Gas-liquid phase synthesis of highly luminescent InP/ZnS core/shell quantum dots using zinc phosphide as a new phosphorus source. J Mater Chem 22:1794–1799
126. Ung TDT, Tran TTH, Nguyen QL, Reiss P (2008) Low temperature synthesis of InP nanocrystals. Mater Chem Phys 112:1120–1123
127. Bang E, Choi Y, Cho J, Suh Y-H, Ban HW, Son JS, Park J (2017) Large-scale synthesis of highly luminescent InP@ZnS quantum dots using elemental phosphorus precursor. Chem Mater 29:4236–4243
128. Harris DK, Bawendi MG (2012) Improved precursor chemistry for the synthesis of III–V quantum dots. J Am Chem Soc 134:20211–20213
129. Joung S, Yoon S, Han CS, Kim Y, Jeong S (2012) Facile synthesis of uniform large-sized InP nanocrystal quantum dots using tris (tert-butyldimethylsilyl) phosphine. Nanoscale Res Lett 7:93
130. Gary DC, Glassy BA, Cossairt (2014) Investigation of indium phosphide quantum dot nucleation and growth utilizing triarylsilylphosphine precursors. Chem Mater 26:1734–1744
131. Xie R, Battaglia D, Peng XG (2007) Colloidal InP nanocrystals as efficient emitters covering blue to near-infrared. J Am Chem Soc 129:15432–15433
132. Laufersky G, Bradley S, Frecaut E, Lein M, Nann T (2018) Unraveling aminophosphine redox mechanisms for glovebox-free InP quantum dot syntheses. Nanoscale 10:8752–8762
133. Mundy ME, Ung D, Lai NL, Jahrman EP, Seidler GT, Cossairt BM (2018) Aminophosphines as versatile precursors for the synthesis of metal phosphide nanocrystals. Chem Mater 30:5373–5379
134. Song W-S, Lee H-S, Lee JC, Jang DS, Choi YY, Choi M, Yang H (2013) Amine-derived synthetic approach to color-tunable InP/ZnS quantum dots with high fluorescent qualities. J Nanoparticle Res 15:1750
135. Ueda A, Nagao M, Inoue A, Hayashi A, Seino Y, Ota T, Tatsumisago M (2013) Electrochemical performance of all-solid-state lithium batteries with Sn_4P_3 negative electrode. J Power Sources 244:597–600
136. Olofsson O (1967) X-ray investigation of the tin-phosphorus system. Acta Chem Scand 21:1659–1660
137. Kim YU, Lee CK, Sohn HJ, Kang T (2004) Reaction mechanism of tin phosphide anode by mechanochemical method for lithium secondary batteries. J Electrochem Soc 151:A933–A937
138. Kim YU, Lee SI, Lee CK, Sohn HJ (2005) Enhancement of capacity and cycle-life of $Sn_4 + {}_\delta P_3$ ($0 \leq \delta \leq 1$) anode for lithium secondary batteries. J Power Sources 141:163–166
139. Xie Y, Su H, Li B, Qian Y (2000) Solvothermal preparation of tin phosphide nanorods. Mater Res Bull 35:675–680
140. Liu S, Zhang H, Xu L, Ma L, Chen X (2016) Solvothermal preparation of tin phosphide as a long-life anode for advanced lithium and sodium ion batteries. J Power Sources 304:346–353
141. Wang Y, Li X, Sun Z, Wang A (2015) Metal phosphides as high-performance hydrotreating catalysts. J Jpn Petroleum Institute 58:197–204
142. Hydrogenation with low-cost transition metals (2016). In: Sa J, Srebowata A (eds) Taylor & Francis Group
143. Berger R (1981) Acta Chern Scand Ser A A 35:635–636
144. Parthe E (1963) Note on the structure of ScP and YP. Acta Crystallogr 16:71
145. Lundstrom T, Snell PO (1967) Studies of crystal structures and phase relationships in the Ti-P system. Acta Chern Scand 21:1343–1352
146. Blackman CS, Carmalt CJ, O'Neill SA, Parkin IP, Molloy KC, Apostolico L (2004) Atmospheric-pressure CVD of vanadium phosphide thin films from reaction of tetrakisdimethyl-amidovanadium and cyclohexylphosphine. Chem Vap Depos 10:253–255

147. Goelin M, Carlsson B, Rundqvist J (1975) Refinement of the crystal structure of VP_2. Acta Chem Scand A 29:706–708
148. Jeitschko W, Floerke U, Scholz D (1984) Ambient pressure synthesis, properties, and structure refinements of VP_4 and CoP_2. J Solid State Chem 52:320–326
149. Artigas M, Bacmann M, Fruchart D, Fruchart R (1996) La structure cristalline de Cr_2P: distorsion orthorhombique de la structure hexagonale de type Fe_2P. J Solid State Chem 123:306–312
150. Gong N, Deng C, Wu L, Wan B, Wang Z, Li Z, Gou H, Gao F (2018) Structural diversity and electronic properties of 3d transition metal tetraphosphides, TMP_4 (TM = V, Cr, Mn, and Fe). Inorg Chem 57:9385–9392
151. Rundqvist S (1962) X-ray investigations of Mn_3P, Mn_2P and Ni_2P. Acta Chem Scand 16:992–998
152. Son CY, Kwak IH, Lim YR, Park J (2016) FeP and FeP_2 nanowires for efficient electrocatalytic hydrogen evolution reaction. Chem Commun 52:2819–2822
153. Yang D, Zhu J, Rui X, Tan H, Cai R, Hoster HE, Yu DYW, Hng HH, Yan Q, Appl ACS (2013) Synthesis of cobalt phosphides and their application as anodes for lithium ion batteries. Mater Interfaces 5:1093–1099
154. Kucernak ARJ, Sundaram VNN (2014) Nickel phosphide: the effect of phosphorus content on hydrogen evolution activity and corrosion resistance in acidic medium. J Mater Chem A 2:17435–17445
155. Li D, Senevirathne K, Aquilina L, Brock SL (2015) Effect of synthetic levers on nickel phosphide nanoparticle formation: Ni_5P_4 and NiP_2. Inorg Chem 54:7968–7975
156. Shirotani I, Takahashi E, Mukai N, Nozawa K, Kinoshita M, Yagi T, Suzuki K, Enoki T, Hino S (1993) Japanese J Appl Phys 32:32–33
157. Olofsson O (1972) The crystal structure of Cu_3P. Acta Chem Scand 26:2777–2787
158. Li G-A, Wang C-Y, Chang W-C, Tuan H-Y (2016) Phosphorus-rich copper phosphide nanowires for field-effect transistors and lithium-ion batteries. ACS Nano 10:8632–8644
159. Jian M, Yufang R (1991) Studies on the electrical properties of rare earth monophosphides. J Solid State Chem 95:346–351
160. von Schnering HG, Vu D, Peters K (1998) Crystal structure of yttrium pentaphosphide, YP_5. Z Kristallogr - New Cryst Struct 213:459–459
161. Perrone J (2005) (volume ed) In: Mompean FJ (ed) Chemical thermodynamics of zirconium, vol 8. Elsevier, p 201
162. Rundqvist S (1966) New metal-rich phosphides of niobium, tantalum and tungsten. Nature 211:847–848
163. Rundqvist S (1966) The crystal structure of Nb_7P_4. Acta Chem Scand 20:2427
164. Xiao P, Alam Sk M, Thia L, Ge X, Lim RJ, Wang J–Y, Lim KH, Wang X (2014) Molybdenum phosphide as an efficient electrocatalyst for the hydrogen evolution reaction. Energy Environ Sci 7:2624–2629
165. Leclaire A, Borel M-M, Grandin A, Raveau B (1989) Redetermination of the crystal structure of Mo_4P_3. Acta Crystallogr Sect C: Struct Chem C 45:540–542
166. Faller FE, Biltz W (1941) Beiträge zur systematischen Verwandtschaftslehre. 99. Über Phosphide von Wolfram, Molybdän und Chrom. Z Anorg Allg Chem 248:209–312
167. Rühl R, Jeitschko W, Schwochau K (1982) Preparation and crystal structures of technetium phosphides. J Solid State Chem 44:134–140
168. Chernogorenko VB, Lynchak KA, Kulik LY, Shkaravskij YuF, Klochkov LA (1977) Synthesis of ruthenium phosphides. Zh Neorg Khim 22:1170–1173
169. Hönle W, Kremer R, von Schnering HG, Krist Z (1987) Ruthenium(III)triphosphide RuP_3: preparation, crystal structure and properties. Z Krist Cryst Mater 179:443–454
170. Flörke U, Jeitschko W (1982) Preparation and properties of new modifications of RuP_4 and OsP_4 with CdP_4-type structure. J Common Met 86:247–253
171. Hulliger F (1968) Struct Bond 4:83–229
172. Andersson Y (1977) Chem Inform 31:355–358

173. Andersson Y, Rundqvist S, Tellgren R, Thomas JO, Flanagan TB (1981) Neutron powder diffraction investigation of pure and deuterated palladium phosphide Pd_6P. Acta Crystallogr B 37:1965–1972
174. Wiehage G, Weibke F, Blitz W, Meisel K, Wiechmann FZ (1936) Anorg Allg Chem 228:357–371
175. Gullman L-O (1966) X-ray diffraction and thermo-analytical investigation of the palladium-phosphorus system. J Common Met 11:157–167
176. Zachariasen WH (1963) The crystal structure of palladium diphosphide. Acta Crystallogr 16:1253–1255
177. Rundqvist S (1960) Phosphides of the platinum metals. Nature 185:31
178. Meganathan MD, Huang T, Fang H, Mao J, Sun G (2019) Electrochemical impacts of sheet-like hafnium phosphide and hafnium disulfide catalysts bonded with reduced graphene oxide sheets for bifunctional oxygen reactions in alkaline electrolytes. RSC Adv 9:2599–2607
179. Kleinke H, Franzen HF (1996) The binary hafnium phosphide Hf_3P_2. Acta Crystallogr Sect C Crystal Struct Commun 52:2127–2129
180. Savitskii EM, Tylkina MA, Povarova KB (1970) In: "Rhenium Alloys". IPST Press, Jerusalem
181. Orishchin SV, Babizhetskyy V, Kuz'ma YB (1998) Inorg Mater 34:1227–1230
182. Chakrabartty S, Barman BK, Raj CR (2019) Nitrogen and phosphorous co-doped graphitic carbon encapsulated ultrafine OsP_2 nanoparticles: a pH universal highly durable catalyst for hydrogen evolution reaction. Chem Commun 55:4399–4402
183. Takada K, Sato T (2009) Bunseki Kagaku 58:1–5
184. Carenco S, Florea I, Ersen O, Boissière C, Mézaillesz N, Sanchez C (2013) Towards nanoscaled gold phosphides: surface passivation and growth of composite nanostructures. New J Chem 37:1231–1237
185. Parra-Puerto A, Ng KL, Fahy K, Goode AE, Ryan MP, Kucernak A (2019) Supported transition metal phosphides: activity survey for HER, ORR, OER, and corrosion resistance in acid and alkaline electrolytes. ACS Catal 9:11515–11529
186. Liu J, Yu X, Du R, Zhang C, Zhang T, Llorca J, Arbiol J, Wang Y, Meyns M, Cabot A (2019) Chromium phosphide CrP as highly active and stable electrocatalysts for oxygen electroreduction in alkaline media. Appl Catal, B 256:117846
187. McEnaney JM, Crompton JC, Callejas JF, Popczun EJ, Biacchi AJ, Lewis NS, Schaak RE (2014) Amorphous molybdenum phosphide nanoparticles for electrocatalytic hydrogen evolution. Chem Mater 26:4826–4831
188. Liu J, Meyns M, Zhang T, Arbiol J, Cabot A, Shavel A (2018) Triphenyl phosphite as the phosphorus source for the scalable and cost-effective production of transition metal phosphides. Chem Mater 30:1799–1807
189. Du H, Gu S, Liu R, Li CM (2015) Tungsten diphosphide nanorods as an efficient catalyst for electrochemical hydrogen evolution. J Power Sources 278:540–545
190. Pu Z, Ya X, Amiinu IS, Tu Z, Liu X, Li W, Mu S (2016) Ultrasmall tungsten phosphide nanoparticles embedded in nitrogen-doped carbon as a highly active and stable hydrogen-evolution electrocatalyst. J Mater Chem A 4:15327–15332
191. Qin Q, Li J, Guo Z, Jian C, Liu W (2019) Tungsten phosphide nanosheets seamlessly grown on tungsten foils toward efficient hydrogen evolution reaction in basic and acidic media. Int J Hydrogen energy 44:27483–27491
192. McEnaney JM, Crompton JC, Callejas JF, Popczun EJ, Read CG, Lewis NS, Schaak RE (2014) Electrocatalytic hydrogen evolution using amorphous tungsten phosphide nanoparticles. Chem Commun 50:11026–11028
193. Monette G, Nateghi N, Masut RA, Francoeur S, Ménard D (2012) Plasmonic enhancement of the magneto-optical response of MnP nanoclusters embedded in GaP epilayers. Phys Rev B 86:45312
194. Booth RA, Majetich SA (2009) Crystallographic orientation and the magnetocaloric effect in MnP. J Appl Phys 105:07A926
195. Cheng JG, Matsubayashi K, Wu W, Sun JP, Lin FK, Luo JL, Uwatoko Y (2015) Pressure induced superconductivity on the border of magnetic order in MnP. Phys Rev Lett 114:117001

196. Lambert-Milot S, Lacroix C, Ménard D, Masut RA, Desjardins P, Garcia-Hernandez M, de Andrés A (2008) Metal-organic vapor phase epitaxy of crystallographically oriented MnP magnetic nanoclusters embedded in GaP (001). J Appl Phys 104:083501
197. Lacroix C, Lambert-Milot S, Masut RA, Desjardins P, Ménard D (2013) Ferromagnetic resonance measurements of GaP epilayers with embedded MnP nanoclusters grown on GaP (001). Phys Rev B 87:024412
198. Perera SC, Tsoi G, Wenger LE, Brock SL (2003) Synthesis of MnP nanocrystals by treatment of metal carbonyl complexes with phosphines: a new, versatile route to nanoscale transition metal phosphides. J Am Chem Soc 125:13960–13961
199. Gregg KA, Perera SC, Lawes G, Shinozaki S, Brock SL (2006) Controlled synthesis of MnP nanorods: effect of shape anisotropy on magnetization. Chem Mater 18:879–886
200. Park J, Koo B, Yoon KY, Hwang Y, Kang M, Park J-G, Hyeon T (2005) Generalized synthesis of metal phosphide nanorods via thermal decomposition of continuously delivered metal−phosphine complexes using a syringe pump. J Am Chem Soc 127:8433–8440
201. Sun F, Wang Y, Fang L, Yang X, Fu W, Tian D, Huang Z, Li J, Zhang H, Wang Y (2019) New vesicular carbon-based rhenium phosphides with all-pH range electrocatalytic hydrogen evolution activity. Appl Catal, B 256:117851
202. Perera SC, Fodor PS, Tsoi GM, Wenger LE, Brock SL (2003) Application of de-silylation strategies to the preparation of transition metal pnictide nanocrystals: the case of FeP. Chem Mater 15:4034–4038
203. Park J, Koo B, Hwang Y, Bae C, An K, Park J-G, Park YM, Hyeon T (2004) Novel synthesis of magnetic Fe_2P nanorods from thermal decomposition of continuously delivered precursors using a syringe pump. Angew Chem Int Ed 43:2282–2285
204. Qian C, Kim F, Ma L, Tsui F, Yang P, Liu J (2004) Solution-phase synthesis of single-crystalline iron phosphide nanorods/nanowires. J Am Chem Soc 126:1195–1198
205. Chen J-H, Tai M-F, Chi K-M (2004) Catalytic synthesis, characterization and magnetic properties of iron phosphide nanowires. J Mater Chem 14:296–298
206. Carenco S, Hu Y, Florea I, Ersen O, Boissière C, Mézailles N, Sanchez C (2012) Metal-dependent interplay between crystallization and phosphorus diffusion during the synthesis of metal phosphide nanoparticles. Chem Mater 24:4134–4145
207. Henkes AE, Schaak RE (2007) Trioctylphosphine: a general phosphorus source for the low-temperature conversion of metals into metal phosphides. Chem Mater 19:4234–4242
208. Kelly AT, Rusakova I, Ould-Ely T, Hofmann C, Luettge A, Whitmire KH (2007) Iron phosphide nanostructures produced from a single-source organometallic precursor: nanorods, bundles, crosses, and spherulites. Nano Lett 7:2920–2925
209. Walter MG, Warren EL, McKone JR, Boettcher SW, Mi Q, Santori EA, Lewis NS (2010) Solar water splitting cells. Chem Rev 110:6446
210. Mahmood J, Li F, Jung SM, Okyay MS, Ahmad I, Kim SJ, Park N, Jeong HY, Baek JB (2017) An efficient and pH-universal ruthenium-based catalyst for the hydrogen evolution reaction. Nat Technol 12:441
211. McCrory CCL, Jung S, Ferrer IM, Chatman SM, Peters JC, Jaramillo TF (2015) Benchmarking hydrogen evolving reaction and oxygen evolving reaction electrocatalysts for solar water splitting devices. J Am Chem Soc 137:4347
212. Zheng Y, Jiao Y, Zhu Y, Li LH, Han Y, Chen Y, Jaroniec M, Qiao S-Z (2016) High electrocatalytic hydrogen evolution activity of an anomalous ruthenium catalyst. J Am Chem Soc 138:16174
213. Yu J, Guo YN, She SX, Miao SS, Ni M, Zhou W, Liu ML, Shao ZP (2018) Bigger is surprisingly better: agglomerates of larger RuP nanoparticles outperform benchmark Pt nanocatalysts for the hydrogen evolution reaction. Adv Mater 39:1800047
214. Zhai TT, Zhu YZ, Li Y, Peng WC, Zhang GL, Zhang FB, Fan XB (2019) Ultra-small RuPx nanoparticles on graphene supported schiff-based networks for all pH hydrogen evolution. Int J Hydrogen Energy 44:5717
215. Pu Z, Amiinu IS, Kou ZK, Li WQ, Mu SC (2017) RuP_2-based catalysts with platinum-like activity and higher durability for the hydrogen evolution reaction at all pH values. Angew Chem, Int Ed 56:11559–11564

216. Li Y, Chu F, Bu Y, Kong Y, Tao Y, Zhou X, Yu H, Yu J, Tang L, Qin Y (2019) Controllable fabrication of uniform ruthenium phosphide nanocrystals for the hydrogen evolution reaction. Chem Commun 55:7828–7831
217. Guo L, Luo F, Guo F, Zhang Q, Qu K, Yang Z, Cai W (2019) Robust hydrogen evolution reaction catalysis by ultrasmall amorphous ruthenium phosphide nanoparticles. Chem Commun 55:7623–7626
218. Wang Y, Liu Z, Liu H, Suen N-T, Yu X, Feng L (2018) Electrochemical hydrogen evolution reaction efficiently catalyzed by Ru_2P nanoparticles. Chemsuschem 11:2724–2729
219. Roger A, Senateur J, Fruchart R (1969) Ann Chim France 4:79
220. Lucas I, Perez L, Aroca C, Sanchez P, Lopez E, Sanchez MC (2005) Magnetic properties of CoP alloys electrodeposited at room temperature. J Magn Magn Mater 290:1513
221. da Silva RC, dos Santos EM, Sartorelli ML, Sinnecker JP, Gundel A, Sommer RL, Pasa AA (2004) Magnetic properties and magnetoimpedance in electrodeposited amorphous CoP layers. J Magn Magn Mater 272:1460
222. Lu A, Zhang X, Chen Y, Xie Q, Qi Q, Ma Y, Peng D-L (2015) Synthesis of Co_2P/graphene nanocomposites and their enhanced properties as anode materials for lithium ion batteries. J Power Sources 295:329–335
223. Pan Y, Lin Y, Chen Y, Liu Y, Liu C (2016) Cobalt phosphide-based electrocatalysts: synthesis and phase catalytic activity comparison for hydrogen evolution. J Mater Chem A 4:4745–4754
224. Rupflin LA, Boscagli C, Schunk SA (2018) Platinum group metal phosphides as efficient catalysts in hydroprocessing and syngas-related catalysis. Catalysts 8:122
225. Li Z, Hu S, Liu J, Hu Y, Chen L, Jiang T, Sun L, Sun Y, Besenbacher F, Chen C, Yu M (2018) Cobalt phosphide nanoparticles applied as a theranostic agent for multimodal imaging and anticancer photothermal therapy. Part Part Syst Charact 35:1800127
226. Li Y, Malik MA, O'Brien P (2005) Synthesis of single-crystalline cop nanowires by a one-pot metal−organic route. J Am Chem Soc 127:16020–16021
227. Kapri S, Bhattacharyya S, Appl ACS (2018) Cobalt phosphide nanorods with controlled aspect ratios as synergistic photothermo-chemotherapeutic agents. Nano Mater 1:5237–5245
228. Okamoto H (1990) Bull Alloy Phase Diagr 11:415–417
229. Duan H, Li D, Tang Y, He Y, Ji S, Wang R, Lv H, Lopes PP, Paulikas AP, Li H, Mao SX, Wang C, Markovic NM, Li J, Stamenkovic VR, Li Y (2017) High-performance Rh_2P electrocatalyst for efficient water splitting. J Am Chem Soc 139:5494–5502
230. Henkes AE, Vasquez Y, Schaak RE (2007) Converting metals into phosphides: a general strategy for the synthesis of metal phosphide nanocrystals. J Am Chem Soc 129:1896–1897
231. Yang F, Zhao Y, Du Y, Chen Y, Cheng G, Chen S, Luo W (2018) A monodisperse Rh_2P-based electrocatalyst for highly efficient and pH-universal hydrogen evolution reaction. Adv Energy Mater 8:1703489
232. Wang K, Huang B, Lin F, Lv F, Luo M, Zhou P, Liu Q, Zhang W, Yang C, Tang Y, Yang Y, Wang W, Wang H, Guo S (2018) Wrinkled Rh_2P nanosheets as superior pH-universal electrocatalysts for hydrogen evolution catalysis. Adv Energy Mater 8:1801891
233. Habas SE, Baddour FG, Ruddy DA, Nash CP, Wang J, Pan M, Hensley JE, Schaidle JA (2015) A facile molecular precursor route to metal phosphide nanoparticles and their evaluation as hydrodeoxygenation catalysts. Chem Mater 27:7580–7592
234. Pu Z, Zhao J, Amiinu IS, Li W, Wang M, He D, Mu S (2019) A universal synthesis strategy for P-rich noble metal diphosphide-based electrocatalysts for the hydrogen evolution reaction. Energy Environ Sci 12:952–957
235. Korányi TI (2003) Phosphorus promotion of Ni (Co)-containing Mo-free catalysts in thiophene hydrodesulfurization. Appl Catal A 239:253–267
236. Kanda Y, Temma C, Nakata K, Kobayashi T, Sugioka M, Uemichi Y (2010) Preparation and performance of noble metal phosphides supported on silica as new hydrodesulfurization catalysts. Appl Catal, A 386:171–178
237. Bowker RH, Smith MC, Carrillo BA, Bussell ME (2012) Synthesis and hydrodesulfurization properties of noble metal phosphides: ruthenium and palladium. Top Catal 55:999–1009

238. Oyama ST (2003) Novel catalysts for advanced hydroprocessing: transition metal phosphides. J Catal 216:343–352
239. Liu S, Liu X, Xu L, Qian Y, Ma X (2007) Controlled synthesis and characterization of nickel phosphide nanocrystal. J Cryst Growth 304:430–434
240. Sawhill SJ, Phillips DC, Bussell ME (2003) Thiophene hydrodesulfurization over supported nickel phosphide catalysts. J Catal 215:208–219
241. Yang S, Prins R (2005) New synthesis method for nickel phosphide hydrotreating catalysts. Chem Commun 4178–4180
242. Hu X, Yu JC (2008) High-yield synthesis of nickel and nickel phosphide nanowires via microwave-assisted processes. Chem Mater 20:6743–6749
243. Chiang R-K, Chiang R-T (2007) Formation of hollow Ni_2P nanoparticles based on the nanoscale Kirkendall effect. Inorg Chem 46:369–371
244. Senevirathne K, Burns AW, Bussell ME, Brock SL (2007) Synthesis and characterization of discrete nickel phosphide nanoparticles: effect of surface ligation chemistry on catalytic hydrodesulfurization of thiophene. Adv Funct Mater 17:3933–3939
245. Wang J, Johnston-Peck AC, Tracy JB (2009) Nickel phosphide nanoparticles with hollow, solid, and amorphous structures. Chem Mater 21:4462–4467
246. Muthuswamy E, Savithra GHL, Brock SL (2011) Synthetic levers enabling independent control of phase, size, and morphology in nickel phosphide nanoparticles. ACS Nano 5:2402–2411
247. Pan Y, Liu Y, Zhao J, Yang K, Liang J, Liu D, Hu W, Liu D, Liu Y, Liu C (2015) Monodispersed nickel phosphide nanocrystals with different phases: synthesis, characterization and electrocatalytic properties for hydrogen evolution. J Mater Chem A 3:1656–1665
248. Carenco S, Resa I, Goff XL, Floch PL, Mézailles N (2008) White phosphorus as single source of "P" in the synthesis of nickel phosphide. Chem Commun 2568–2570
249. Maneeprakorn W, Nguyen CQ, Malik MA, O'Brien P, Raftery J (2009) Synthesis of the nickel selenophosphinates $[Ni(Se_2PR_2)_2]$ ($R = {}^{i}Pr, {}^{t}Bu$ and Ph) and their use as single source precursors for the deposition of nickel phosphide or nickel selenide nanoparticles. Dalton Trans 2103–2108
250. Pan Y, Liu Y, Liu C (1959) An efficient method for the synthesis of nickel phosphide nanocrystals via thermal decomposition of single-source precursors. RSC Adv 5(2015):11952–11961
251. Okamoto H (1994) The P-Pd (phosphorus-palladium) system. J Phase Equilib 15:58
252. Flanagan TB, Bowerman BS, Rundqvist S, Andersson Y (1983) Solution of hydrogen and deuterium in palladium phosphide, Pd_6P. J Am Chem Soc, Faraday Trans 1, 79:1605–1616
253. Flanagan TB, Biehl GE, Clewley JD, Rundqvist S, Andersson Y (1980) Solution of hydrogen in non-stoichiometric Pd_3P_{1-x} compounds. J Am Chem Soc Faraday Trans 1, 76:196
254. Belykh LB, Skripov NI, Belonogova LN, Rokhin AV, Shmidt FK (2009) Reaction of palladium bisacetylacetonate with elemental phosphorus. Effect of water on the composition of palladium phosphides. Russ J Gen Chem 79:92–97
255. Kagirov RM, Voloshin AV, Kadirov MK, Nizameev IR, Sinyashin OG, Yakhvarov DG (2011) Selective synthesis of nanosized palladium phosphides from white phosphorus. Mendeleev Commun 21:201
256. Carenco S, Hu Y, Florea I, Ersen O, Boissière C, Sanchez C, Mézailles N (2013) Structural transitions at the nanoscale: the example of palladium phosphides synthesized from white phosphorus. Dalton Trans 42:12667–12674
257. Savithra GHL, Bowker RH, Carrillo BA, Bussell ME, Brock SL, Appl ACS (2013) Mesoporous matrix encapsulation for the synthesis of monodisperse Pd_5P_2 nanoparticle hydrodesulfurization catalysts. Mater Interfaces 5:5403–5407
258. Zhao M (2016) Fabrication of ultrafine palladium phosphide nanoparticles as highly active catalyst for chemoselective hydrogenation of alkynes. Chem Asian J 11:461–464
259. Li H, Wen P, Itanze DS, Hood ZD, Ma X, Kim M, Adhikari S, Lu C, Dun C, Chi M, Qiu Y, Geyer SM (2019) Colloidal silver diphosphide (AgP_2) nanocrystals as low overpotential catalysts for CO_2 reduction to tunable syngas. Nat Commun 10:5724

260. Han A, Zhang H, Yuan R, Ji H, Du P, Appl ACS (2017) Crystalline copper phosphide nanosheets as an efficient janus catalyst for overall water splitting. Mater Interfaces 9:2240–2248
261. Bichat MP, Politova T, Pascal JL, Favier F, Monconduit L (2004) Electrochemical reactivity of Cu_3P with lithium. J Electrochem Soc 151:A2074–A2081
262. Trizio LD, Figuerola A, Manna L, Genovese A, George C, Brescia R, Saghi Z, Simonutti R, Huis MV, Falqui A (2011) Size-tunable, hexagonal plate-like Cu_3P and Janus-like Cu–Cu_3P nanocrystals. ACS Nano 6:32–41
263. Manna G, Bose R, Pradhan N (2013) Semiconducting and plasmonic copper phosphide platelets. Angew Chem Int Ed 52:6762–6766
264. Liu Z, Mu H, Xiao S, Wang R, Wang Z, Wang W, Wang Y, Zhu X, Lu K, Zhang H, Lee S-T, Bao Q, Ma W (2016) Pulsed lasers employing solution-processed plasmonic $Cu_{3-x}P$ colloidal nanocrystals. Adv Mater 28:3535–3542
265. Panyala NR, Peña-Méndez EM, Havel J (2012) Laser ablation synthesis of new gold phosphides using red phosphorus and nanogold as precursors. Laser desorption ionisation time-of-flight mass spectrometry. Rapid Commun Mass Spectrom 26:1100–1108
266. Oberkampf M (1811) Ann Chim Phys 80:140
267. Baker A, Usher FL (1940) Nuclear gold sols. II. Mechanism of formation. Trans Faraday Soc 35:385
268. Keuleyan S, Lhuillier E, Brajuskovic V, Guyot-Sionnest P (2011) Mid-infrared HgTe colloidal quantum dot photodetectors. Nat Photo 5:489–493
269. Ayub A, Kamboh AH, Imran M, Rizvi TZ, Khan NA (2017) Cadmium sulphide/cadmium selenide quantum dot solar cells with inexpensive electrodeposited silver/polyaniline composite counter-electrode. J Renew Sustain Energy 9:063703
270. Steckel JS, Coe-Sullivan S, Bulovic V, Bawendi MG (2003) 1.3 μm to 1.55 μm tunable electroluminescence from PbSe quantum dots embedded within an organic device. Adv Mater 15:1862–1866
271. Kanda Y, Kawanishi K, Tsujino T, Al-otaibi AMFM, Uemichi Y (2018) Catalytic activities of noble metal phosphides for hydrogenation and hydrodesulfurization reactions. Catalysts 8:160
272. Shia Y, Zhang B (2016) Recent advances in transition metal phosphide nanomaterials: synthesis and applications in hydrogen evolution reaction. Chem Soc Rev 45:1529–1541
273. Xu S, Ziegler J, Nann T (2008) Rapid synthesis of highly luminescent InP and InP/ZnS nanocrystals. J Mater Chem 18:2653–2656
274. Cao F, Wang S, Wang F, Wu Q, Zhao D, Yang X (2018) A layer-by-layer growth strategy for large-size InP/ZnSe/ZnS core–shell quantum dots enabling high-efficiency light-emitting diodes. Chem Mater 30:8002–8007
275. Kang H, Kim S, Oh JH, Yoon HC, Ho Jo J, Yang H, Do YR (2018) Color-by-blue QD-emissive LCD enabled by replacing RGB color filters with narrow-band GR InP/ZnSeS/ZnS QD films. Adv Optic Mater 6:1701239
276. Xu W-Z, Ren F-F, Jevtics D, Hurtado A, Li L, Gao Q, Ye J, Wang F, Guilhabert B, Fu L, Lu H, Zhang R, Tan HH, Dawson MD, Jagadish C (2018) Vertically emitting indium phosphide nanowire lasers. Nano Lett 18:3414–3420
277. Bhushan M, Catalano A (1981) Polycrystalline Zn_3P_2 Schottky barrier solar cells. Appl Phys Lett 38:39–41
278. Wu KF, Liu Z, Zhu HM, Lian TQ (2013) Exciton annihilation and dissociation dynamics in group II–V Cd_3P_2 quantum dots. J Phys Chem A 117:6362–6372
279. Cao H, Liu Z, Zhu X, Peng J, Hu L, Xu S, Luo M, Ma W, Tang J, Liu H (2015) PbS/Cd_3P_2 quantum heterojunction colloidal quantum dot solar cells. Nanotechnology 26:035401
280. Shockley W, Queisser HJ (1961) Detailed balance limit of efficiency of p-n junction solar cells. J Appl Phys 32:510–519
281. Crisp RW, Kirkwood N, Grimaldi G, Kinge S, Siebbeles LDA, Houtepen AJ, Appl ACS (2018) Highly photoconductive InP quantum dots films and solar cells. Energy Mater 1:6569–6576

282. Sun T, Wang Y, Yu W, Wang Y, Dai Z, Liu Z, Shivananju BN, Zhang Y, Fu K, Shabbir B, Ma W, Li S, Bao Q (2017) Flexible broadband graphene photodetectors enhanced by plasmonic $Cu_{3-x}P$ colloidal nanocrystals. Small 1701881
283. Fang L, Wang Y, Yang X, Zhang H, Wang Y (2019) Uniform OsP_2 nanoparticles anchored on N, P-doped carbon: a new electrocatalyst with enhanced activity for hydrogen generation at all pH values. J Catal 370:404–411
284. Sweeny N, Rohrer C, Brown O (1958) Dinickel phosphide as a heterogeneous catalyst for the vapor phase reduction of nitrobenzene with hydrogen to aniline and water. J Am Chem Soc 80:799–800
285. Viljava TR, Komulainen RS, Krause AOI (2000) Effect of H_2S on the stability of $CoMo/Al_2O_3$ catalysts during hydrodeoxygenation. Catal Today 60:83–92
286. Hayes JR, Bowker RH, Gaudette AF, Smith MC, Moak CE, Nam CY, Pratum TK, Bussell ME (2010) Hydrodesulfurization properties of rhodium phosphide: comparison with rhodium metal and sulfide catalysts. J Catal 276:249–258
287. Savithra GHL, Muthuswamy E, Bowker RH, Carrillo BA, Bussell ME, Brock SL (2013) Rational design of nickel phosphide hydrodesulfurization catalysts: controlling particle size and preventing sintering. Chem Mater 25:825–833
288. Yang S, Liang C, Prins R (2006) J Catal 241:465
289. Guo C, Rao KTV, Yuan Z, He S, Rohan S, Xu C (2018) Hydrodeoxygenation of fast pyrolysis oil with novel activated carbon-supported NiP and CoP catalysts. Chem Eng Sci 178(178):248–259
290. Song H, Gong J, Song H-L, Li F, Zhang J, Chen Y-G (2016) Preparation of core-shell structured Ni_2P/Al_2O_3@TiO_2 and its hydrodeoxygenation performance for benzofuran. Catal Commun 85:1–4
291. Yu Z, Wang Y, Sun Z, Li X, Wang A, Camaioni DM, Lercher JA (2018) Ni_3P as a high-performance catalytic phase for the hydrodeoxygenation of phenolic compounds. Green Chem 20:609–619
292. Zhu T, Song H, Dai X, Song H (2017) Preparation of Ni_2P/Al-SBA-15 catalyst and its performance for benzofuran hydrodeoxygenation. Chin J Chem Eng 25:1784–1790
293. Griffin MB, Baddour FG, Habas SE, Ruddy DA, Schaidle JA (2016) Evaluation of silica-supported metal and metal phosphide nanoparticle catalysts for the hydrodeoxygenation of guaiacol under ex situ catalytic fast pyrolysis conditions. Top Catal 59:124–137
294. Su J, Chen J-S (2017) Synthetic porous materials applied in hydrogenation reactions. Microporous Mesoporous Mater 237:246–259
295. Deng J, Zhang X (1989) Amorphous alloy deposited on support and its hydrogenation activity. Solid State Ionics 32–33:1006–1011
296. Deng J, Chen H, H. (1993) A novel amorphous Ni-WP alloy powder and its hydrogenation activity. J Mater Sci Lett 12:1508
297. Carenco S, Concepción P, Boissière C, Mézailles N, Corma A (2012) Nickel phosphide nanocatalysts for the chemoselective hydrogenation of alkynes. Nano Today 7:21–28
298. Belykh LB, Skripov NI, Belonogova LN, Umanets VA, Stepanova TP, Schmidt FK (2011) Nature of the modifying action of white phosphorus on the properties of nano-sized hydrogenation catalysts based on bis(dibenzylideneacetone) palladium(0). Kinet Catal 52:702–710
299. Skripov NI, Belykh LB, Belonogova LN, Umanets VA, Ryzhkovich EN, Schmidt FK (2010) Effect of the nature of the acido ligand in the precursor on the properties of nanosized palladium-based hydrogenation catalysts modified with elemental phosphorus. Kinet Catal 51:714–723
300. Chen CS, Chen HW, Cheng WH (2003) Study of selective hydrogenation of acetophenone on Pt/SiO_2. Appl Catal A 248:117–128
301. Bergault I, Fouilloux P, Joly-Vuillemin C, Delmas H (1998) Kinetics and intraparticle diffusion modelling of a complex multistep reaction: hydrogenation of acetophenone over a rhodium catalyst. J Catal 175:328–337

302. Kluson P, Cerveny L (1996) Hydrogenation of substituted aromatic compounds over a ruthenium catalyst. J Mol Catal A 108:107–112
303. Drelinkiewicz A, Waksmundzka A, Makowski W, Sobczak JW, Król A, Zięba A (2004) Acetophenone hydrogenation on polymer–palladium catalysts. The effect of polymer matrix. Catal Lett 94:143–156
304. Aramendia MA, Borau V, Jimenez C, Marinas JM, Sempere ME, Urbano P (1988) Reduction of acetophenone with palladium catalysts by hydrogen transfer and with molecular hydrogen. Appl Catal 43:41–45
305. Tundo P, Zinovyev S, Perosa A (2000) Multiphase catalytic hydrogenation of p-chloroacetophenone and acetophenone. A kinetic study of the reaction selectivity toward the reduction of different functional groups. J Catal 196:330–338
306. Costa DC, Soldati AL, Pecchi G, Bengoa JF, Marchetti SG, Vetere V (2018) Preparation and characterization of a supported system of $Ni_2P/Ni_{12}P_5$ nanoparticles and their use as the active phase in chemoselective hydrogenation of acetophenone. Nanotechnology 29:215702
307. Costa DC, Soldati AL, Bengoa JF, Marchetti SG, Vetere V (2019) Phosphorus as a promoter of a nickel catalyst to obtain 1-phenylethanol from chemoselective hydrogenation of acetophenone. Heliyon 5:e01859
308. Wang H, Shu Y, Zheng M, Zhang T (2008) Selective hydrogenation of cinnamaldehyde to hydrocinnamaldehyde over SiO_2 supported nickel phosphide catalysts. Catal Lett 124:219
309. Yang P, Jiang Z, Ying P, Li C (2008) Effect of surface composition on the catalytic performance of molybdenum phosphide catalysts in the hydrogenation of acetonitrile. J Catal 253:66–73
310. Liu P, Zhu Y-L, Zhou L, Zhang W-H, Li Y-X (2020). Amorphous nickel phosphide nanoparticles for selective hydrogenation of cinnamaldehyde. Catal Lett. https://doi.org/10.1007/s10562-019-03022-z
311. Zou X, Zhang Y (2015) Noble metal-free hydrogen evolution catalysts for water splitting. Chem Soc Rev 44:5148–5180
312. Wu H, Lu X, Zheng G, Ho GW (2018) Electrocatalysis: topotactic engineering of ultrathin 2D nonlayered nickel selenides for full water electrolysis. Adv Energy Mater 8:1702704
313. Zhu Z, Yin H, He C, Al-Mamun M, Liu P, Jiang L, Zhao Y, Wang Y, Yang H, Tang Z, Wang D, Chen X, Zhao H (2018) Ultrathin transition metal dichalcogenide/3d metal hydroxide hybridized nanosheets to enhance hydrogen evolution activity. Adv Mater 30:1801171
314. Vrubel H, Hu X (2012) Molybdenum boride and carbide catalyze hydrogen evolution in both acidic and basic solutions. Angew Chem, Int Ed 51:12703
315. Chen W, Sasaki K, Ma C, Frenkel AI, Marinkovic N, Muckerman JT, Zhu Y, Adzic RR (2012) Hydrogen-evolution catalysts based on non-noble metal nickel–molybdenum nitride nanosheets. Angew Chem, Int Ed, 51:6131–6135
316. Wu HB, Xia BY, Yu L, Yu X-Y, Wen X (2015) Porous molybdenum carbide nano-octahedrons synthesized via confined carburization in metal-organic frameworks for efficient hydrogen production. Nat Commun 6:6512
317. Hansen MH, Stern LA, Feng L, Rossmeisl J, Hu X (2015) Widely available active sites on Ni_2P for electrochemical hydrogen evolution–insights from first principles calculations. Phys Chem Chem Phys 17:10823
318. Popczun EJ, McKone JR, Read CG, Biacchi AJ, Wiltrout AM, Lewis NS, Schaak RE (2013) Nanostructured nickel phosphide as an electrocatalyst for the hydrogen evolution reaction. J Am Chem Soc 135:9267–9270
319. Jiang P, Liu Q, Ge C, Cui W, Pu Z, Asiri AM, Sun X (2014) CoP nanostructures with different morphologies: synthesis, characterization and a study of their electrocatalytic performance toward the hydrogen evolution reaction. J Mater Chem A 2:14634–14640
320. Liu P, Rodriguez JA (2005) Catalysts for hydrogen evolution from the [NiFe] hydrogenase to the $Ni_2P(001)$ surface: the importance of ensemble effect. J Am Chem Soc 127:14871–14878
321. Seo B, Baek DS, Sa YJ, Joo SH (2016) Shape effects of nickel phosphide nanocrystals on hydrogen evolution reaction. Cryst Eng Comm 18:6083–6089
322. Huang Z, Chen Z, Chen Z, Lv C, Meng H, Zhang C (2014) $Ni_{12}P_5$ nanoparticles as an efficient catalyst for hydrogen generation via electrolysis and photoelectrolysis. ACS Nano 8:8121–8129

323. Xu Y, Wu R, Zhang J, Shi Y, Zhang B (2013) Anion-exchange synthesis of nanoporous FeP nanosheets as electrocatalysts for hydrogen evolution reaction. Chem Commun 49:6656–6658
324. Callejas JF, McEnaney JM, Read CG, Crompton JC, Biacchi AJ, Popczun EJ, Gordon TR, Lewis NS, Schaak RE (2014) Electrocatalytic and photocatalytic hydrogen production from acidic and neutral-pH aqueous solutions using iron phosphide nanoparticles. ACS Nano 8:11101–11107
325. Popczun EJ, Read CG, Roske CW, Lewis NS, Schaak RE (2014) Highly active electrocatalysis of the hydrogen evolution reaction by cobalt phosphide nanoparticles. Angew Chem Int Ed 53:5427–5430
326. Li Q, Xing Z, Asiri AM, Jiang P, Sun X (2014) Cobalt phosphide nanoparticles film growth on carbon cloth: a high-performance cathode for electrochemical hydrogen evolution. Int J Hydrogen Energy 39:16806
327. Tian J, Liu Q, Asiri AM, Sun X (2014) Self-supported nanoporous cobalt phosphide nanowire arrays: an efficient 3D hydrogen-evolving cathode over the wide range of pH 0–14. J Am Chem Soc 136:7587–7590
328. Liu Q, Tian J, Cui W, Jiang P, Cheng N, Asiri AM, Sun X (2014) Carbon nanotubes decorated with CoP nanocrystals: a highly active non-noble-metal nanohybrid electrocatalyst for hydrogen evolution. Angew Chem, Int Ed, 53:6710
329. Pu Z, Liu Q, Jiang P, Asiri AM, Obaid AY, Sun X (2014) CoP nanosheet arrays supported on a Ti plate: an efficient cathode for electrochemical hydrogen evolution. Chem Mater 26:4326
330. Du H, Liu Q, Cheng N, Asiri AM, Sun X, Li CM (2014) Template-assisted synthesis of CoP nanotubes to efficiently catalyze hydrogen-evolving reaction. J Mater Chem A 2:14812
331. Popczun EJ, Roske CW, Read CG, Crompton JC, McEnaney JM, Callejas JF, Lewis NS, Schaak RE (2015) Highly branched cobalt phosphide nanostructures for hydrogen-evolution electrocatalysis. J Mater Chem A 3:5420–5425
332. Lu A, Chen Y, Li H, Dowd A, Cortie MB, Xie Q, Guo H, Qi Q, Peng D-L (2014) Magnetic metal phosphide nanorods as effective hydrogen-evolution electrocatalysts. Int J Hydrogen energy 39:18919–18928
333. Huang Z, Chen Z, Chen Z, Lv C, Humphrey MG, Zhang C (2014) Cobalt phosphide nanorods as an efficient electrocatalyst for the hydrogen evolution reaction. Nano Energy 9:373–382
334. Ha DH, Moreau LM, Bealing CR, Zhang H, Hennig RG, Robinson RD (2011) The structural evolution and diffusion during the chemical transformation from cobalt to cobalt phosphide nanoparticles. J Mater Chem 21:11498–11510
335. Callejas JF, Read CG, Popczun EJ, McEnaney JM, Schaak RE (2015) Nanostructured Co_2P electrocatalyst for the hydrogen evolution reaction and direct comparison with morphologically equivalent CoP. Chem Mater 27:3769–3774
336. Armand M, Tarascon JM (2008) Building better batteries. Nature 451:652–657; Bruce PG, Freunberger SA, Hardwick LJ, Tarascon JM (2012) Li–O_2 and Li–S batteries with high energy storage. Nat Mater 11:19–29
337. Dunn B, Kamath H, Tarascon JM (2011) Electrical energy storage for the grid: a battery of choices. Science 334:928–935
338. Scrosati B, Hassoun J, Sun YK (2011) Lithium-ion batteries. A look into the future. Energy Environ Sci 4:3287–3295
339. Wang ZY, Wang ZC, Liu WT, Xiao W, Lou XW (2013) Amorphous $CoSnO_3$@C nanoboxes with superior lithium storage capability. Energy Environ Sci 6:87–91
340. Pralong V, Souza DCS, Leung KT, Nazar LF (2002) Reversible lithium uptake by CoP_3 at low potential: role of the anion. Electrochem Commun 4:516–520
341. Bichat M, Pascal J, Gillot F, Favier FJ (2006) Electrochemical lithium insertion in Zn_3P_2 zinc phosphide. J Phys Chem Solids 67:1233–1237
342. Hwang H, Kim MG, Cho J (2007) Li reaction behavior of GaP nanoparticles prepared by a sodium naphthalenide reduction method. J Phys Chem C 3:1186–1193
343. Hall JW, Membreno N, Wu J, Celio H, Jones RA, Stevenson KJ (2012) Low-temperature synthesis of amorphous FeP_2 and its use as anodes for li ion batteries. J Am Chem Soc 134:5532–5535

344. Carenco S, Surcin C, Morcrette M, Larcher D, Mézailles N, Boissière C, Sanchez C (2012) Improving the li-electrochemical properties of monodisperse Ni_2P nanoparticles by self-generated carbon coating. Chem Mater 24:688–697
345. Lu Y, Tu JP, Xiong QQ, Zhang H, Gu CD, Wang XL, Mao SX (2012) Large-scale synthesis of porous Ni_2P nanosheets for lithium secondary batteries. Cryst EngComm. 14:8633–8641
346. Lu Y, Tu J-P, Xiong Q-Q, Qiao Y-Q, Wang X-L, Gu C-D, Mao SX (2012) Synthesis of dinickel phosphide (Ni_2P) for fast lithium-ion transportation: a new class of nanowires with exceptionally improved electrochemical performance as a negative electrode. RSC Adv 2:3430–3436
347. Lu Y, Tu JP, Xiang JY, Wang XL, Zhang J, Mai YJ, Mao SX (2011) Improved electrochemical performance of self-assembled hierarchical nanostructured nickel phosphide as a negative electrode for lithium ion batteries. J Phys Chem C 115:23760–23767
348. Xiang JY, Tu JP, Wang XL, Huang XH, Yuan YF, Xia XH, Zeng ZY (2008) Electrochemical performances of nanostructured Ni_3P–Ni films electrodeposited on nickel foam substrate. J Power Sources 185:519–525
349. Wang C, Ding T, Sun Y, Zhou X, Liu Y, Yang Q (2015) $Ni_{12}P_5$ nanoparticles decorated on carbon nanotubes with enhanced electrocatalytic and lithium storage properties. Nanoscale 7:19241–19249
350. Jiang J, Wang C, Li W, Yang Q (2015) One-pot synthesis of carbon-coated Ni_5P_4 nanoparticles and CoP nanorods for high-rate and high-stability lithium-ion batteries. J Mater Chem A 3:23345–23351
351. Aso K, Hayashi A, Tatsumisago M (2011) Phase-selective synthesis of nickel phosphide in high-boiling solvent for all-solid-state lithium secondary batteries. Inorg Chem 50:10820–10824
352. Boyanov S, Gillot F, Monconduit L (2008) The electrochemical reactivity of the NiP_3 skutterudite-type phase with lithium. Ionics 14:125–130
353. Zhou G, Wang D-W, Li F, Zhang L, Li N, Wu Z-S, Wen L, (M.). Lu GQ, Cheng H-M (2010) Graphene-wrapped Fe_3O_4 anode material with improved reversible capacity and cyclic stability for lithium ion batteries. Chem Mater 22:5306–5313
354. Kim S-W, Seo D-H, Gwon H, Kim J, Kang K (2010) Fabrication of FeF_3 nanoflowers on CNT branches and their application to high power lithium rechargeable batteries. Adv Mater 22:5260–5264
355. Yang S, Zhou X, Zhang J, Liu Z (2010) Morphology-controlled solvothermal synthesis of $LiFePO_4$ as a cathode material for lithium-ion batteries. J Mater Chem 20:8086–8091
356. Boyanov S, Zitoun D, Menetrier M, Jumas JC, Womes M, Monconduit L (2009) Comparison of the electrochemical lithiation/delitiation mechanisms of FeP_x ($x = 1, 2, 4$) based electrodes in li-ion batteries. J Phys Chem C 113:21441–21452
357. Liu Q, Luo Y, Chen W, Yan Y, Xue L, Zhang W (2018) CoP_3 @ PPy microcubes as anode for lithium-ion batteries with improved cycling and rate performance. Chem Eng J 347:455–461
358. Chan WCW, Nie S (1998) Quantum dot bioconjugates for ultrasensitive nonisotopic detection. Science 281:2016–2018
359. Mushonga P, Onani MO, Madiehe AM, Meyer M (2012) Indium phosphide-based semiconductor nanocrystals and their applications. J Nanomater 2012:869284
360. Stasiuk GJ, Tamang S, Imbert D, Poillot C, Giardiello M, Tisseyre C, Barbider EL, Fries PH, Waard MD, Reiss P, Mazzanti M (2011) Cell-permeable Ln (III) chelate-functionalized InP quantum dots as multimodal imaging agents. ACS Nano 5:8193–8201
361. Brunetti V, Chibli H, Fiammengo R, Galeone A, Malvindi MA, Vecchio G, Cingolani R, Nadeau JL, Pompa PP (2013) InP/ZnS as a safer alternative to CdSe/ZnS core/shell quantum dots: in vitro and in vivo toxicity assessment. Nanoscale 5:307–317
362. Chibli H, Carlini L, Park S, Dimitrijevic NM, Nadeau JL (2011) Cytotoxicity of InP/ZnS quantum dots related to reactive oxygen species generation. Nanoscale 3:2552–2559
363. Ni Y, Li J, Jin L, Xia J, Hong J, Liao K (2009) Co_2P nanostructures constructed by nanorods: hydrothermal synthesis and applications in the removal of heavy metal ions. New J Chem 33:2055–2059

364. Ni Y, Mi K, Cheng C, Xia J, Ma X, Hong J (2011) Urchin-like Ni–P microstructures: facile synthesis, properties and application in the fast removal of heavy-metal ions. Chem Commun 47:5891–5893
365. Ni Y, Liao K, Li J (2010) In situ template route for synthesis of porous $Ni_{12}P_5$ superstructures and their applications in environmental treatments. CrystEngComm 12:1568–1575

Chapter 13
Synthesis Strategies for Organoselenium Compounds and Their Potential Applications in Human Life

Prasad P. Phadnis

Abstract This article describes the prime role of selenium (Se) and its compounds in mammalian biochemical systems, performing diverse functions like maintenance of health through various selenoenzymes, diagnostic, therapeutic functions and as targeted drug delivery system. The role of inorganic selenium compounds in food chain and in nourishing human health is also briefed. The deficiency, as well as excess selenium, leads to detrimental effects on health. Hence, the essential dose required and its food sources or supplements have been described. Its role in materials science serving for facilitating human life through various electronic devices, solar cells, H_2 evolution catalysts, etc. has also been described briefly. To harness the full potential of such a useful element, what we need is a real compound, material or its formulation in hand with utmost purity. As the properties of compounds are governed by their structures, the literature knowledge helps us to design the selenium compounds appropriately for desired applications. The present article underlines the importance of design, synthesis, purification and characterization of the selenium compounds. In view of this, various classes of selenium compounds and their classical and newly reported synthesis strategies have been described. In the later part of the chapter, the prominent characterization and estimation methods for selenium species have also been described briefly.

Keywords Selenium · Synthesis · Characterization · Estimation · Biomedical · Materials

P. P. Phadnis (✉)
Chemistry Division, Bhabha Atomic Research Centre, Mumbai 400085, India
e-mail: phadnisp@barc.gov.in

Homi Bhabha National Institute, Anushaktinagar, Mumbai 400094, India

A. K. Tyagi and R. S. Ningthoujam (eds.), *Handbook on Synthesis Strategies for Advanced Materials*, Indian Institute of Metals Series,
https://doi.org/10.1007/978-981-16-1892-5_13

13.1 Introduction

The research in area of design and synthesis of selenium (Se) compounds has achieved the paramount position due to the extraordinary properties of Se compounds making their impact in various aspects of human life. Currently, the Se compounds are making strides in biochemistry, chemical biology, human health related applications, material science, in developing organic synthesis strategies—catalysts or reagents, as ligands in coordination chemistry for exploring fundamental chemistry, diverse industrial and agricultural applications. It finds direct relevance for human life—as a constituent of bio-system, pharmacological or therapeutic applications to treat various disease states including current COVID-19 and other respiratory viral infections, antioxidant, anticancer, radioprotectors, neuroprotective agent, in treating bipolar disorders and hearing loss, inhibitory effect on HIV as well as diagnostic and therapeutic ^{75}Se labelled radiopharmaceuticals. In case of pharmacology, the new concept of their thiol modifier ability responsible for pharmacological action has also been proposed. Besides the pharmacological actions, its forms as biomaterials have exhibited utility for targeted drug delivery to a diseased site. Recently, Se compounds and its nano-form have been explored as fertilizer for crops and plants. The inorganic form of selenium compounds mainly selenites and selenates have prime importance in food chain since they are absorbed through roots of plants and enter in food chain [1]. In materials science, the binary or ternary metal selenides have been utilized for applications like supercapacitors, photovoltaic, optoelectronic, H_2 evolution by water splitting, solar cells, energy harvesting, sodium ion batteries (SIBs), etc., [2]. In this perspective, the researchers have developed novel synthetic strategies for the synthesis of appropriate organoselenium compounds and novel structural features were proposed in their design in order to achieve appropriate properties as well as stability for certain unstable derivatives [3]. Subsequently, the account of selenium chemistry, pharmacology has also been reported in some reviews [4].

In this chapter, the approach is to give a brief account of importance of selenium compounds, mainly for human health and materials and principally summarize the design strategies, various synthetic approaches of different classes of organoselenium compounds, their characterization and estimation. The difficulties and risks associated during synthesis, hence, the required precautions and the waste disposal after reactions are also summarized. It is expected that it will be helpful for beginner researchers in this field. Hence at this moment, it will be worthy to comprehend the historical milestones from discovery of selenium element, its general properties and subsequent progress in understanding its crucial role in biological systems and other material applications which was a directive for today's research.

13.2 Background and General Properties

The selenium (Se) element was discovered by a Swedish chemist J. J. Berzelius (1817) in the reddish deposits appeared in the lead chambers in a sulphuric acid plant [5]. It was named as selenium in honour of Greek Goddess '*Selene*' meaning The Moon. Initially, it was thought to be tellurium; but subsequently, it was observed that even though it exhibited very similar properties to tellurium, it was actually a new element. Hence, Berzelius termed it selenium, which originated from a Greek word *Selene*, meaning the Moon with the purpose to match the name tellurium, which was derived from the Latin word *Tellus* which means the Earth. Selenium is a trace element occurring nearly 0.09 ppm in the crust of earth and 0.2 ppm in aquatic system. It is metalloid in nature. The natural selenium exists as a mixture of 6 isotopes viz., ^{74}Se (0.87%), ^{76}Se (9.02%), ^{77}Se (7.58%), ^{78}Se (23.52%), ^{80}Se (49.82%) and ^{82}Se (9.19%). The Se exists in three stable allotropic forms. The amorphous form is either red (powder form) or black (vitreous form) while a monoclinic selenium in crystalline form is deep red and the most stable variety, a crystalline hexagonal form, is a metallic grey. Selenium belongs to *p*-block, *Chalcogen* (group 16) elements having electronic configuration [Ar] $3d^{10}$ $4s^2$ $4p^4$. It exists with −2, −1, +2, +4 and +6 oxidation states in its compound forms. These vulnerable oxidation states confer high reactivity to the selenium compounds which have evidenced in vast chemistry of selenium compounds. In case of organoselenium chemistry, the Se^{2+} state is the dominant form while in case of inorganic chemistry +4 and +6 states are dominant forms.

13.3 Strides in Biological Sciences and Medicine

To begin with, the glimpses of role of selenium chemistry in biological and medical fields are given. In case of biological sciences, since 1930s selenium has been regarded as a potentially toxic substance due to high toxicity of livestock (selenosis) in areas of soil with high selenium content known as seleniferous soil. This event attracted the attention for study of biochemical properties of selenium compounds [6]. Subsequently, in 1957, Schwarz and Foltz find Se as a micronutrient for mammals, birds and bacteria as well as Se was identified as an essential component of a nutritional factor which protected rats from severe necrotic degeneration of liver [7]. Since then it is treated as an essential micronutrient. Further in vivo experimental studies on selenium deficiency syndromes in animals resulted in finding of two selenium containing bacterial enzymes viz., formate dehydrogenase and glycine reductase [8]. These findings lead to a beginning of a new research domain of selenium biochemistry. Concurrently the biochemical role of selenium in mammals was actually established by the identification of Se as a part of the active site of the antioxidant enzyme glutathione peroxidase (GPx) [9]. This encouraged further work in this domain and consequently, the number of selenoproteins authenticated has increased

significantly in recent years [10]. They contain the selenium at their active sites in form of selenocysteine (Sec) which is regarded as 21st proteinogenic amino acid that imparts catalytic activity to the selenoezymes [11]. The reason for its activity can be explained on the basis of its physicochemical properties. At physiological pH (7.4) the selenocysteine exists mainly in anionic selenohydryl (RSe^-) form which is a good nucleophile as well as a good leaving group as compared to cysteine which is its sulphur analogue [12]. Although all the selenoenzymes have the same selenocysteine moiety at their active sites, their specificities for substrate are strikingly different which enables them to perform diverse functions for maintaining health of mammals. The unique redox properties of Se influence the catalytic activities of organoselenium compounds. The most significant selenoenzymes are viz., glutathione peroxidise (GPx), thioredoxin reductase (TrxR) (enzymes responsible for detoxification) and iodothionine deiodinase (IDs), etc.[13].

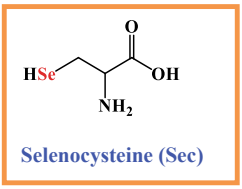

Selenocysteine (Sec)

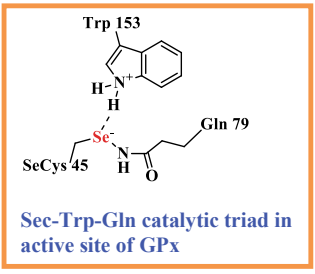

Sec-Trp-Gln catalytic triad in active site of GPx

These findings encouraged to evaluate selenium compounds for their pharmacological actions in various disease states and study further selenium biochemistry. As a result, the selenium compounds were evaluated for treatment of various disease states which exhibited their potent activities. Their potency has been clearly proved in vitro as well as in vivo. At present the selenium compounds have clearly exhibited the antioxidant, GPx mimicking, radioprotection, anticancer, antiviral agents and in healing of indomethacin-induced stomach ulceration, neuroprotective action as well as their inhibitory role in case of AIDS. In case of GPx mimetic actions, new thoughts in this area are also coming up. Accordingly, thiol modifier effects (oxidation of thiol groups of proteins) of the organoselenium compounds to save the selenoproteins from the inactivation caused due to soft electrophiles like Hg^{2+}, CH_3Hg^+, Cd^{2+}, etc. may be more appropriate for explaining their pharmacological properties than their GPx like catalytic activity. Hence the utilization of the thiol modifier property [thiol oxidase (TOx) potential] of selenium compounds can be utilized more thoughtfully than use of low molecular weight compounds to mimic the activity of selenoenzymes. Very recently ebselen was evaluated mainly to treat the current Covid-19 pandemic disease and other viral infections. The main M^{pro} (a cysteine protease) activity is crucial for virus replication in the host cells. Hence, inhibition of M^{pro} activity will obviously lead to cure the diseased state. The studies of Sies et al., clearly revealed that M^{pro} of the corona virus SARS-CoV-2 was the potential target during evaluations of potential drugs. Among the ten thousand compounds evaluated, the researchers have identified

ebselen as a promising inhibitor of M^{pro} activity. In this application, it is proposed that the ebselen reacts with a multitude of protein thiols, forming a selenosulphide bond resulting in pleiotropic effects of antibacterial, antiviral and anti-inflammatory actions required especially in lung inflammation. Additionally, it is hypothesized that selenium may prevent cardiovascular and related chronic diseases [1]. Some of them like ebselen [14], ethaselen [15] have been undergone clinical trials in phases III and II respectively. Especially the ebselen is an important compound which exhibited radio-protecting, hydroperoxide- and peroxynitrite-reducing activity and exhibited a glutathione peroxidase and peroxiredoxin enzyme mimicking activities also. Additionally, it has exhibited potency during clinical trials performed for treating the bipolar disorder.

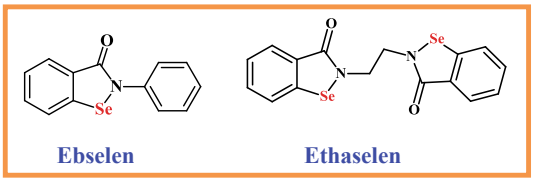

These established results of selenium compounds lead their further studies for applications of its nanoparticle form as biomaterials for pharmacology [16] as well as site specific targeted drug delivery [17]. Further the ^{75}Se labelled compounds have been explored for physiological and pharmacological studies [18] as well as diagnostic probes in disease states [19]. All the facts have clearly established that selenium is essential for mammalian health. Hence let's discuss about its requirement for various functions, its dietary sources and amounts required for maintaining good health. In case of Se deficiency, its implication in diverse disease states, as well as its excessive dose leading to detrimental effects on health shall also be discussed.

13.4 Food Sources of Se for Health and Recommended Dietary Allowance

Till this point, there is a clear view about biological and pharmacological role of selenium which is an essential micronutrient (trace element) required for many important biochemical functions in mammals. These functions are part of the maintenance of normal metabolic status, immune regulation and to reduce inflammation. Hence identifying the food sources and have them in our usual diet, which will provide us Se is of prime importance to maintain health and keep away from diseases. We obtain selenium from food sources in the form of amino acid based organoselenium compounds especially L-selenomethionine present mainly in cereal grains (wheat, maize and rice, etc.), soybeans and enriched yeast, selenoneine present in tuna fish, Se-methylselenocysteine present in broccoli vegetable, selenocysteine present mainly in foods of animal origin (meats). Additionally, Se-methyl-selenomethionine

and Se-methyl-selenocysteine are obtained from food sources like onion, garlic, etc. Selenium yeast (Na-selenide source) is also a better food supplement [20].

The minimum requirement of selenium for an adult human is 50–70 μg/day. Recommended dietary allowance (RDA) allows daily an adequate intake for adults of 200 μg/day only [21].

13.5 Deficiency of Selenium Leading to Disease States

Selenium deficiency is associated with various disease states. It negatively affects the activity of several selenoenzymes including glutathione peroxidases (GPx1 and GPx3), thioredoxin reductase (TrxR), iodothyronine deiodinases (IDs), selenoprotein W and methionine-R-sulfoxide reductase B1 (MsrB1). It results in weak immune system, leading to current COVID-19 infections as well as other viral infections like AIDS, fatigue, mental fog, degeneration of muscles from oxidative damage and infertility. Additionally, prolonged selenium deficiency is linked with skeletal myopathy as well as cardiovascular diseases like cardiomyopathy and congestive heart failure (inflammation and damage to the heart muscle—Keshan disease), liver necrosis, disfiguring form of arthritis resulting from cartilage atrophy breakdown (Kashin-Beck disease) and finally death. The risk of selenium deficiency may be increased after bariatric surgery (weight loss surgery) or in severe gastrointestinal diseases like Crohn's disease (an inflammatory bowel disease—inflammation of digestive tract). Generally, the selenium deficient individuals are more susceptible to physiological stress, leading to various disease states [22].

13.6 Scope for Designing New Bioactive Selenium Compounds

In case of regions with selenium deficient soil the selenium contained in food chain is less. Hence the Se supplements can be externally provided to individuals in the form of synthetic selenium compounds. Further, the Se compounds can be utilized for therapeutic applications as antioxidant, radioprotector, anticancer drugs for treatment in disease states resulted due to its deficiency. Hence, it provides a lot of scope for scientists to design the novel selenium compounds with appropriate structural features for their desired therapeutic applications.

13.7 Selenium Toxicity—Selenium is Double Edged Sword

As the deficiency is linked with various disease states, the excess of selenium intake (acute or chronic) by either food (from seleniferous soils) or external supplementation is also hazardous to health which is called as selenosis [23, 24]. The symptoms of selenosis are garlic odour in the breath (foul breath), gastrointestinal disorders, sloughing of nails, hair loss, irritability, fatigue as well as neurological damages. In case of extreme selenosis, patients can develop cirrhosis of liver, pulmonary edema, or even death. According to RDA, the intake of 400 μg/day for adults is critical and 800 μg/day leads to coma and even death in 24 h [25]. In view of this, it is inferred that the selenium is double edged sword. Hence, precise intake of required selenium is an essential thing for maintaining good health.

13.8 Strides in Materials Science

After having glimpses about the role of selenium in biological sciences let's have a tour through its domain of material science. The Se compounds have established their applications in many demanding aspects in commercial areas as the materials useful for facilitating the living of human life. Additionally, they have exhibited applications as biomaterials for body appendages, diagnostics and therapeutics as well as in targeted drug delivery systems. Majority of commercial applications of selenium materials are based on an extraordinary susceptibility of electrons of selenium which get excited by incident light, generating an electric current. This phenomenon has enabled selenium to be used as metal chalcogenides (ZnSe, CdSe, HgCdSe, CuInSe) in electronic industry like photoelectric cells, light meters, rectifiers and xerographic copying machines, etc. The thin films of $Cu_2Sn(S_xSe_{1-x})_3$ and $Cu_2ZnSn(S_xSe_{1-x})_4$ ($0 \leq x \leq 1$) materials were deposited for fabrication of solar cells which exhibited ~7% efficiencies under AM1.5 illumination. Furthermore, the transition metal chalcogenides (TMCs) have attracted a great deal of attention due to their optoelectronic properties that make them potential candidates essentially for energy conversion applications. Additionally, the metal selenides like zinc selenide in combination with copper gallium selenide (ZnSe:CGSe), as their solid solutions have been employed as photocatalysts for hydrogen (H_2) evolution by splitting of pure water, giving the opportunities for metal-selenide materials based photocatalytic systems for producing the solar fuel. The iron-nickel selenide, iron-cobalt selenide and nickel-cobalt selenide have exhibited potential applications as electrode materials in the development of sodium ion batteries (SIBs). Selenium is also used for decolorization of a greenish tint of glass resulted because of iron impurities or in excess to generate the ruby red color seen in warning signals and tail lights of automobile. Additionally, the selenium sulphide (2.5%) containing shampoos for dermatological care have been used in daily life [2, 26].

13.9 Importance of Design and Synthesis Strategies of Selenium Compounds

The above account of applications of selenium compounds gives us a clear view of its importance in life. Its versatile utility is dependent on its reactivity which can be modulated by designing the appropriate structure of a selenium compound having suitable functional groups. The literature regarding structure activity relationship (SAR) directs for further design of molecules which are to be explored for an anticipated application. Hence using the fundamental knowledge of synthetic chemistry, one has to design the selenium compounds for specific purposes then synthesize them precisely and evaluate their anticipated activities. All the applications are possible only when a pure selenium compound, its material formulation for pharmacology or nano-materials for material applications are available in hand with high purity. This prominently underlines the importance of synthesis, purification and characterization of selenium compounds which is a difficult task due to the inherent toxicity and instability associated with them. Hence it gives a golden opportunity to the synthetic chemists for designing molecules with appropriate functional groups which will confer the stability as well as reduce the toxicity. It can be achieved through analysis of toxicological data from literature reports as well as theoretical studies through bio- and chemo-informatics using techniques like computer aided drug design (CADD) and molecular modelling or combinatorial chemistry techniques. The computational methods are used to envisage, how a particular compound interacts with a given biological target. These techniques are valuable in conceptualizing the hypotheses about desirable chemical properties while designing the selenium containing pharmacological molecules and additionally, these approaches can be employed to refine and formulate drug candidates as per desired applications [27].

13.10 Milestones in Development of Synthetic Strategies of Selenium Compounds

Since in this chapter, the predominant focus will be on synthesis aspects of organoselenium compounds, it is worthwhile to go through the landmarking developmental steps of their synthesis strategies which will be helpful in further research related to this domain.

As one goes through literature, it is realized that although the first organoselenium compound ever isolated was diethyl selenide by Löwig in 1836 but it was isolated in the pure form in 1869 [28]. Later the ethylselenol was reported by F. Wöhler and C. Siemens in 1847 [29]. The initial growth for synthetic selenium chemistry was hampered because of (i) instability (ii) malodorous nature and (iii) toxicity associated with selenium compounds. But knowledge acquisition regarding the reduction in toxicity and more biocompatibility of organoselenium compounds over the inorganic based selenium compounds as well as further developments in synthetic

strategies by 1970s, have marched ahead of the synthetic organoselenium chemistry more efficiently. It has resulted in today's wealth of various useful selenium compounds. But since the aim of scientists is to discover further or innovatively use these compounds for more efficient applications; the research goes on. The research is a continuous process that takes both practice and time. Hence in this chapter, the attempt is to provide a brief account of synthetic strategies for various classes of selenium compounds, their purification and characterization methods with the hope that it will be beneficial for a beginner researcher in this field.

13.11 Synthesis Strategies for Organoselenium Compounds

In this section, the synthetic strategies for various types of selenium compounds are discussed along with the account of difficulties and risks involved and precautionary measures to be implemented while synthesizing the selenium compounds. Later the treatment for selenium waste after extraction of desired reaction products will be discussed briefly.

13.11.1 Difficulties and Risks Involved in Synthesis of Selenium Compounds

Before discussing the synthesis strategies for different classes, it is worthwhile to consider few characteristic properties of selenium compounds which negatively influence the successful synthesis. Hence, one must overcome these difficulties by precautionary measures. At the outset, it must be noted that the vulnerable oxidation states of selenium compounds impart them a high redox activity [30] rendering them air and moisture sensitive species. It necessitates the use of dried solvents and performing reactions in an inert atmosphere, preferentially argon. The Se compounds are unstable due to low bond energies of C–Se and Se–Se bonds (C–Se, 244 kJ mol^{-1} and Se–Se, 172 kJ mol^{-1}) [31] while Se–O and Se–S (233 kJ mol^{-1} and 203 kJ mol^{-1}, respectively) [32], which makes them easy to be oxidized or reduced and lead to decomposition giving side products during synthesis process. Hence the reactions can be made more product specific using lower temperatures during synthesis. Their malodorous nature is attributable to the emissions of volatile compounds of selenium formed during synthesis procedures especially selenium compounds having small aliphatic chains. Since Se is toxic, acute selenium poisoning leads to accidental death [33]. Hence the reactions must be performed in well ventilated fume hoods or in the glove boxes.

13.11.2 Physiological Properties and Health Hazards of Selenium Compounds

Hydrogen selenide irritates the eyes, nose, lung, tissues, etc. and implicates in detrimental effects on the digestive and nervous systems. The solutions of selenium compounds can cause burning of skin and severe pain by skin absorption. Selenium dioxide (SeO_2) dust irritates the skin, eyes and respiratory tract system. SeO_2 is particularly harmful in case of its skin absorption. Its swallowing causes severe irritation as well as poisoning. The prolonged exposure to selenium dust may cause fatigue, digestive upset, dermatitis and bronchitis. Hence, one must avoid breathing the Se dust, contact with skin and eyes. The Threshold limit value-time weighted average (TLV-TWA) for selenium is 0.2 mg/m^3 [34]. The TLV-TWA value represents a time weighted average concentration of any toxic substance over a normal workday (8 h) and workweek (40 h), to which almost all workers may be repeatedly exposed, every day, without any adverse health effects. Such a small value of TLV-TWA clearly indicates the extent of toxicity of selenium compounds.

13.11.3 Preparations and Precautions Before Starting Synthesis of Selenium Compounds

In this section, the precautionary measures and preparations are discussed which is essential before starting the synthesis of selenium compounds. As a scientist, one must follow synthetic strategies very meticulously and in a planned way taking care of health of all the individuals working in laboratory. Performing any reaction must start with the knowledge of physical properties of chemicals to be used, their toxicity limits and handling of any accident associated with them. It can be easily leant from material safety data sheets (MSDS). Additionally, the general fire extinguishers and multi-gas detectors to protect from toxic and combustible gases, fire alarm system in laboratory must be functional. Let's come back to our topic of interest of synthesis of selenium compounds. In view of the toxicity associated with selenium compounds, the first and foremost thing is that the researcher must wear gloves and mask/respirator, safety glasses while performing any activity while handling selenium compounds. If inhalation or ingestion of any sort like gases produced during synthesis like H_2Se (highly poisonous and offensive smell) or selenium salts in form of selenites and selenates [35], the researcher must seek medical help. All the reactions must be performed in well ventilated fume hoods. The processing of reactions like testing the reaction completion with thin layer chromatography, iodine chamber or other identifying reagents followed by purification, either by column chromatography, recrystallizations must be performed in fume hoods. After processing, the selenium compounds must be stored in fume cupboards or desiccators in view of their toxicity and volatile nature.

The synthesis of organoselenium compounds involves highly inflammable, pyrophoric, air and moisture sensitive reagents like *n*-butyllithium, *t*-butyllithium, superhydride ($LiBEt_3H$), sodium hydride, sodium borohydride, most dangerous elemental sodium and potassium for reducing elemental selenium in situ in liquid NH_3 and further substitution reactions. These reactions are performed most of the times in organic solvents like tetrahydrofuran, diethyl ether, ethyl alcohol, acetonitrile and hexane, etc. with exception of reduction of selenium with sodium borohydride in aqueous medium, however, it is an exothermic reaction, care must be taken by slow addition of reagent and performing reactions at low temperature (0–5 °C). Rest of the reactions involving especially *n*-butyl lithium and *t*-butyl lithium must be performed at a very low temperature (−84 °C) by using cooling bath consisting of freezing the ethyl acetate by liq. N_2 or dry ice-acetone mixture (−78 °C). Hence the use of moisture free solvents freshly dried over sodium (Na) and benzophenone are mandatory during synthesis in order to avoid highly exothermic reactions which may cause severe accidents. The solvents and precursors used for synthesis must be purified by standard practices in order to avoid the undesired side products from reaction. Additionally, the solvents must be oxygen free which can be achieved by purging them with inert gases preferentially argon (Ar) in round bottom flask with septum and small exit by piercing a syringe needle through septum to dissipate the pressure generated during purging. The transfers of reagent solutions must be performed using the cannula techniques. Most selenium compounds are purified by column chromatography which involves lot of organic solvents as eluents in combinations of their mixtures like ethylacetate-petroleum ether/hexane, chloroform-methanol, etc. These organic solvents are highly inflammable; hence in general care must be taken to inhibit their ignition by direct flames, hot plates or even by electric sparks. In case of purification by recrystallization, the excessively long duration for standing the solutions of organoselenium compounds should be avoided in order to protect them from decomposition [36], disproportionation reactions [37] and photochemical reactions leading to side products or decomposition. E.g. dibenzyldiselenide under photolytic as well as thermolytic conditions leading to liberation of selenium from compound, i.e. decomposition [38].

13.11.4 Treatment and Disposal of Selenium Waste After Extraction of Desired Reaction Products

It is the obvious responsibility of the researchers to ensure the safe and correct disposal of all wastes produced in the process of handling selenium compounds. Improper and irresponsible disposal of chemical wastes down drains, into the environment or refuse to the local authority for collection, leads to various hazards to environment and ultimately cause various health hazards to living organisms. Hence after extracting the reaction products from the reaction mixtures it is mandatory to

treat properly the remaining solutions or solids before discharge or stored conveniently in a separate labelled bottle or jar for disposal. In any case, different types of waste should never be mixed. Additionally, advice should be sought from the safety co-ordinator of organization before beginning any work [39].

Selenium waste disposal

Recycle the selenium materials whichever possible. Avoid release to the environment. The manufacturer should be consulted for getting information about any option for recycling or regional or local waste management authority should be consulted before disposal in case of no disposal facility or suitable treatment is found. The treatments and neutralization of the selenium wastes should be done at the authorized treatment plants. The selenium waste should include, the neutralization using soda ash (Na_2CO_3) or soda lime (mixture of $Ca(OH)_2$ and NaOH) followed by buried in dumping ground, specifically registered to accept pharmaceutical or chemical wastes. They can also be incinerated in a licensed device after preparing their admixture with appropriate combustible substances. Later the empty containers should be decontaminated using 5% aq. NaOH or Na_2CO_3 and then cleaned by water. All label safeguards must be observed until containers are thoroughly cleaned and destroyed.

Large quantities of Se waste: Store it in a labelled and covered container for recycling or disposal at authorized dumping area.

Small quantities of Se waste: The trained personnel equipped with personal protective equipment (PPE) like laboratory coat, eye protection, nitrile rubber gloves, respirator and working in well ventilated fume hoods should perform the disposal of selenium waste. The Se salt should be dissolved in water and followed by its neutralization by aq. NaOH (1 M) or sulphuric acid (1 M). An aqueous solution of sodium sulphide (1 M) should be added to the selenium salt solution followed by pH adjustment to neutralize (pH 7) by addition of sulphuric acid (1 M) solution. The precipitate should be separated by decantation or preferably filtration. Then precipitate should be washed, dried and recycled or sent for disposal process at a safe landfill [40].

Additionally, all the glassware after waste disposal organoselenium reactions is mandatory to be treated with dil. HNO_3 (strong oxidizing agent) solution which lead to water soluble selenius acid (H_2SeO_3). Subsequently, the glassware shall be cleaned further with chromic acid solution (H_2CrO_4) conveniently prepared by adding concentrated sulphuric acid to a potassium dichromate ($K_2Cr_2O_7$) which is a strong oxidizing agent (Cr^{6+} state) which will decompose any traces of compounds remained in glassware. Alternatively, the aq. NaOH-ethanol mixture may be used for the same cause. These oxidizing agents and base NaOH lead to formation of selenite salts (Na_2SeO_3 or K_2SeO_3). Due to toxicity associated with selenium compounds, it is categorized in 'red list' hence it should never be washed down a drain. It should be recycled or disposed in a secure landfill.

In general, the guidelines for laboratory waste treatment must be followed. These guidelines are outlined by various universities as well as governing bodies or chemical companies [41]. At all instances, the disposal to drainage may be performed according to rules and regulations of local governing bodies which should be considered with

priority. Whenever one is in doubt, consult with responsible authority. From the waste, try to recycle whichever possible for economic purpose or seek guidance from the manufacturer for any options for recycling. Consult the state land waste management authorities for disposal. Bury the residue only in an authorized landfill. Even the containers can also be recycled as long as they are in good condition otherwise dispose them at an approved dumping area.

After this account, let's march to actual processes of synthesis of organoselenium compounds.

13.12 Synthesis of Various Classes of Oganoselenium Compounds

As discussed earlier due to vulnerable oxidation states, rendering high reactivity, the selenium compounds exist in various classes. Now typical and newly developed synthesis strategies will be discussed for the prominent classes which are contributing in biomedical as well as material applications in facilitating human life.

13.12.1 Diorgano Diselenides (R_2Se_2)

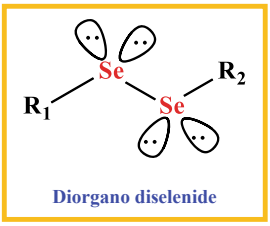

The diorgano diselenides contribute to majority of applications of selenium compounds because of their versatile structures modulating their activities and stability achieved by structural features like weak inter- and intra-molecular interactions like Se–N or Se–O non-bonding interactions [42]. Such interactions are contributing to enhancing their biomimetic activities like selenoenzymes. These interactions result in stability of their intermediates species (formed during biomimetic activities) like selenols, selenenic acids which also functions as antioxidants making them more potent [43]. Additionally, such interactions give better shelf life to diorgano diselenides than other selenide species. Using polar functional group moieties (COOH, OH, NH_2) or heterocyclic organic frames (pyrodinol, nicotinamide, nicotinic acid) the compounds achieve water solubility, e.g. di-nicotinamide diselenide, diselenodipropioniic acid [$(SeCH_2CH_2COOH)_2$], dipyridinol diselenide

[44]. It makes them convenient for exploring therapeutic applications [45]. Additionally, the GSeSeG, a diselenide analogue of oxidized glutathione (GSSG) has exhibited potential applications for effective oxidative protein folding [46].

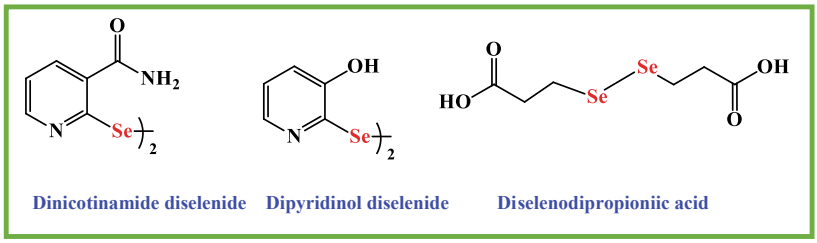

Dinicotinamide diselenide Dipyridinol diselenide Diselenodipropioniic acid

Furthermore, they exhibit important role as precursors as well as reagents in synthetic chemistry, e.g. diphenyl diselenide (Ph_2Se_2) is primely used as a reagent [47]. Additionally, diorgano diselenides exhibit remarkable redox behaviour. The diselenides can be oxidized to electrophilic species (e.g. RSeX or $RSeX_3$) and reduced to nucleophilic selenolate ions (RSe^-) by the cleavage of a Se–Se bond. Hence, both electrophilic and nucleophilic reagents can be conveniently synthesized from the diselenides. Many diselenides have been used to obtain metal chalcogenides utilized for materials applications in electronic devices [2, 26, 48].

General methods for synthesis of diorgano diselenides

There are some synthetic approaches in practice for preparation of diorgano diselenides and still, there is a lot of scope for developing new strategies which may avoid the strong bases or exothermic reagents as classical methods are employing.

The diorgano diselenides are conveniently prepared by treatment of their alkali metal diselenide frames prepared in situ with appropriate halofunctionalized organic moieties (aliphatic and some heterocyclic) in appropriate polar solvents like THF, DMF, diethyl ether, water, ethanol, etc. The choice of solvents depends on compatibility with reagents which are involved in performing the synthesis. Initially, the elemental selenium is treated with strong reducing agents like superhydride ($LiBEt_3H$), Na or K in liquid NH_3, $NaBH_4$, NaH, NaOH or NH_2NH_2, etc. in compatible solvents, in order to achieve reduced Se^{2-} species (diselenide frames) like Na_2Se_2 or Li_2Se_2 in situ which further react with halofunctionalized moieties to afford the diorgano diselenides (Scheme 13.1) [49]. Instead of halofunctionalized species, the diazonium salts prepared in situ from amine based moieties (by diazotization reactions of amines using aq. $NaNO_2$ and HCl at 0–5 °C) can also be reacted with alkali metal diselenides (M_2Se_2) for obtaining diaryl diselenides [50]. Even the diseleno dipeptides can also be prepared by this method [51]. It should be noted here that the molar ratios of elemental Se and a reducing agent matter in formation of diselenide salts. Even the solvent of reaction also matters, e.g. Se reactions with $NaBH_4$ in ethanol and water rendering NaSeH or Na_2Se_2, as clearly given by Klayman and Griffin [52]. Additionally, sodium hydrogen selenide (NaSeH) generated in situ either by $NaBH_4$ reduction of selenium or by treatment of H_2Se with NaOEt, NaOH,

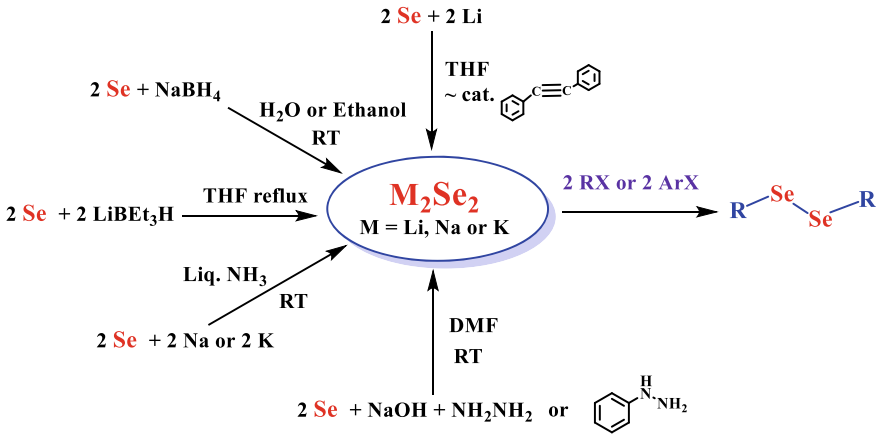

Scheme 13.1 Synthesis of diorgano diselenides from alkali metal diselenide frames

or Na_2CO_3 in ethanol; can be used for the synthesis of diselenides [53]. In some cases, the formation of selenol (RSeH) is observed. It can be converted easily to its diselenide form by oxidizing agents like H_2O_2 or even by aerial oxidation through bubbler for few hours [54].

In case of diorgano diselenides consisting of aromatic or heterocyclic aryl organic moieties, their heteroatom directed lithiation with *n*-, *t*- or *sec*-butyl lithium (*n*-BuLi/*t*-BuLi or *sec*-BuLi) in appropriate solvents at −78 to −90 °C followed by insertion of elemental selenium and aerial oxidation results in formation of corresponding diselenides (Scheme 13.2) [55].

Another route of lithiation strategies, using lithium diisopropylamide (LDA) also yields the diorgano diselenides [56]. In addition to this, the aromatic diselenides can also be prepared from the reduction of selenocyanates (RSeCN) by $LiAlH_4$, $NaBH_4$ or by treatment with base like KOH, NaOMe followed by aerial oxidation (Scheme 13.3) [57].

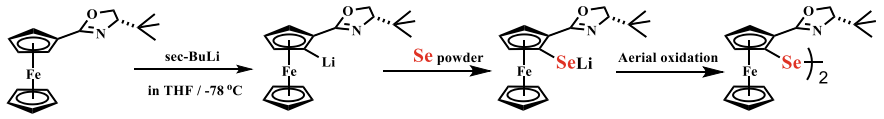

Scheme 13.2 Lithiation based strategies for synthesis of diselenides

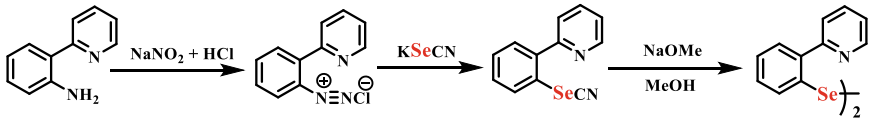

Scheme 13.3 Synthesis of diorganodiselenides through diazotization

In some cases, the treatment of Na_2Se_2 with 2-bromo pyridine or 2-bromo pyridinol with refluxing in aqueous solutions yields the desired py_2Se_2 or $(SepyOH)_2$ due to high lability of Br leaving group on heterocycle as compared to Br on simply aryl group (Scheme 13.4). In such reactions, the selenol and selone, the tautomeric forms existing in equilibrium, were also isolated which on slow aerial oxidation finally yielded the corresponding highly stable diselenides (Scheme 13.5) [58].

Additionally, the position of leaving group Br on pyridine as well as substitution on aromatic moieties is also directive for the product formation and yields. It is evident from the failure of reactions of Na_2Se_2 with substituted pyridine or even phenyl bromide or analogues. But nothing is impossible if we search for new methods. The reactions with aryl groups were successful with the Grignard reagent route. Initially, the Grignard product of PhMgBr can be prepared in diethyl ether as a polar solvent. Its further reaction with elemental Se for insertion of Se in frame and subsequent reaction with bromine followed by oxidation leads to easy formation of diphenyl diselenide (Ph_2Se_2) (Scheme 13.6) [59].

New strategies for synthesis of diorgano diselenides

The diorgano dislenides were prepared conveniently from analogous diorgano-disulphides by treatment of disulphides with $Ph_3.I_2$ in 4-dimethylaminopyridine (DMAP) followed by treatment with NaHSe and subsequent oxidation (Scheme 13.7) [60]. Additionally, the chiral aliphatic amino functional diselenides have also been

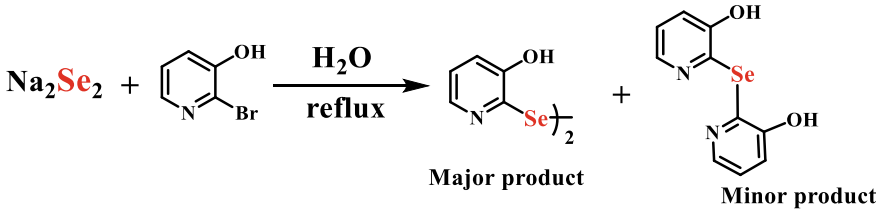

Scheme 13.4 Synthesis of dipyridinol diselenide

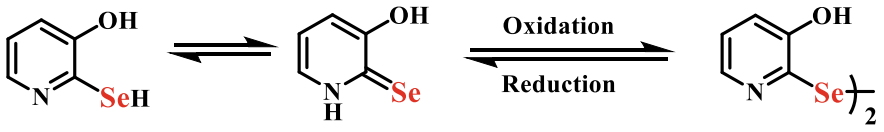

Scheme 13.5 The equilibrium between selenol and selone and their oxidation to dislenide

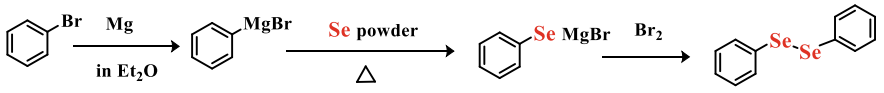

Scheme 13.6 Synthesis of a diselenide (Ph_2Se_2) through Grignard reagent route

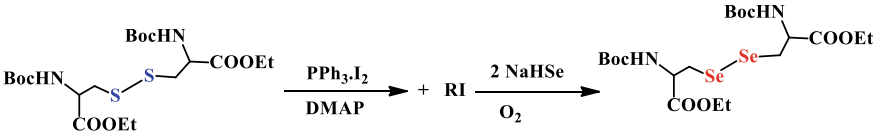

Scheme 13.7 Synthesis of diselenides from disulphides

reported. They were readily synthesized via the ring opening reactions of appropriate Boc-N protected aziridine rings (Scheme 13.8) by treatment with Li_2Se_2 at room temperatures [61].

Furthermore, simple and efficient Cu(II) catalyzed coupling reactions between aryl halides substituted with halo, alkyl or alkoxy groups and elemental selenium have been developed to yield various diselenides in excellent yields (up to 96%) (Scheme 13.9) [62]. Additionally, a cupric oxide (CuO) nanoparticles catalyzed coupling reactions of alkyl, aryl and hetero-aryl halides (Br or I) or with Se element were reported in presence of strong base like KOH at higher temperatures (90 °C) in a polar solvent dimethyl sulfoxide (DMSO). By following this strategy, various symmetrically substituted diselenides were obtained with excellent product yields (Scheme 13.10) [63].

In further efforts, microwave assisted one pot synthesis of symmetrical diselenides from organoyl iodides and elemental selenium catalyzed by cupric oxide nanoparticles has also been reported [64]. Recently, the one pot and efficient synthesis of diorgano diselenides from aryl halides with functional groups like Cl, Br or OTs and elemental selenium in polyethylene glycols (PEGs), using metal organic frameworks (e.g. MOF-199) in basic medium as catalysts have been reported to yield a

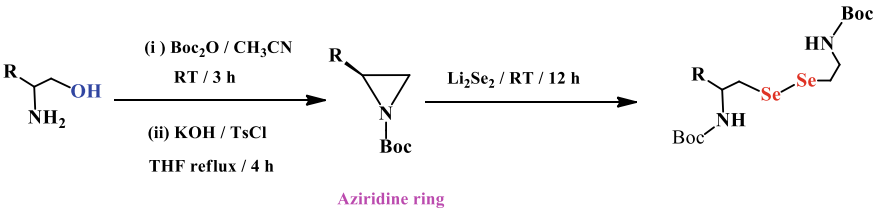

Scheme 13.8 Synthesis of diselenides through aziridine ring opening

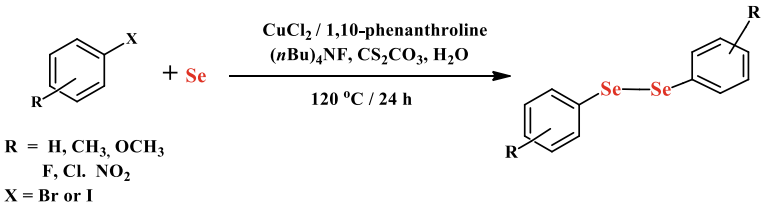

Scheme 13.9 Synthesis of diselenides from aryl halides using Cu(II) catalyst

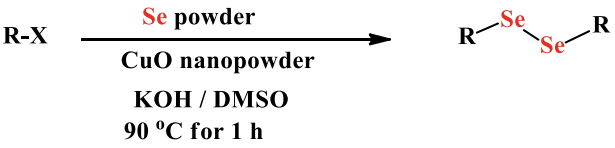

R = alkyl. aryl or heteroaryl
X = Br, I

Scheme 13.10 Synthesis of diselenides from aryl halides using CuO nanoparticles as catalyst

variety of diselenides in excellent (up to 98%) yields in relatively short duration for reaction completion (Scheme 13.11) [65]. Furthermore, by using one pot synthesis strategies, the symmetrical dibenzyl diselenides were obtained from the reactions of corresponding benzyl alcohols with $NaBH_2Se_3$ as a selenium transfer reagent. By using these reaction methods, the structurally diverse substituted benzyl alcohols yielded the corresponding diselenides in excellent yields at easy and mild reaction conditions and in a short reaction time (Scheme 13.12) [66].

Recently, the iodine mediated synthesis of diphenyl diselenides by treatment of aryl-boronic acids with selenium dioxide (SeO_2) as a selenium source in THF solvent under milder conditions (60 °C) has been reported to give about 70–90% yields (Scheme 13.13) [67].

Further, a fast and effective procedure for large-scale synthesis of symmetrical diselenides was developed which involved the oxidative coupling of corresponding selenols using bipyridinium hydrobromide perbromide (BPHP) catalyst at room temperatures (Scheme 13.14) [68]. Additionally, the aromatic and heterocyclic diselenides have been reported to obtain from the reductive selenation of corresponding aldehydes (ArCHO) treated with elemental Se in presence of carbon

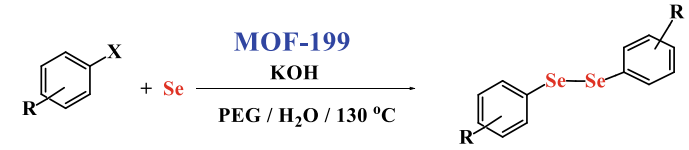

X = Cl, Br, OTs

Scheme 13.11 Synthesis of diselenides using metal organic framework (MOF-199)

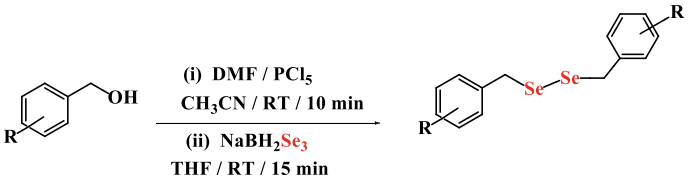

Scheme 13.12 Synthesis of diselenides using $NaBH_2Se_3$ as selenium transfer reagent

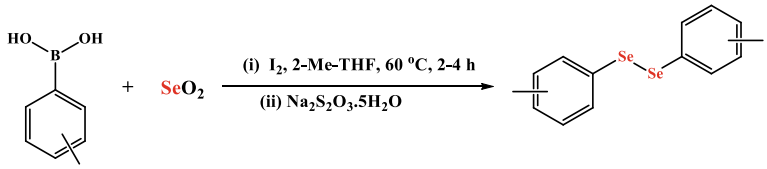

Scheme 13.13 Synthesis of substituted diphenyl diselenides from aryl-boronic acids

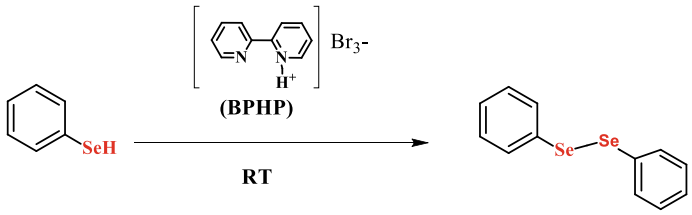

Scheme 14.14 Oxidative coupling of selenols

monoxide (CO) in their aqueous or DMF solutions, afforded the anticipated diselenides, $ArCH_2SeSeCH_2Ar$ where carbonyl group has been reduced to methylene (CH_2). The reaction yields the product in high yields under atmospheric (1 atm) pressure without using any base (Scheme 13.15) [69].

It should be noted here that, the synthesis of diorgano diselenides in majority of classical reactions is usually accompanied by the formation of corresponding monoselenides (R_2Se) in variable amounts, as an impurity. It necessitates requirement of purifications of diorgano diselenides by recrystallization, column purification or vacuum distillation techniques whichever is convenient for individual products depending on their stability, functional groups and physical states.

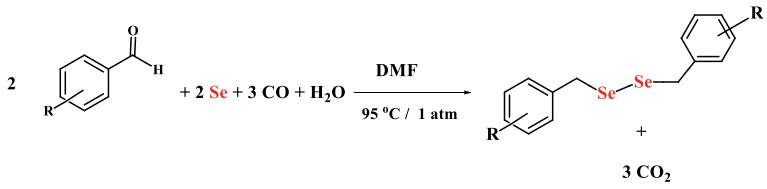

Scheme 13.15 Synthesis of diselenides by Reductive selenation of aldehydes

13.12.2 Diorgano Monoselenides (R_2Se)

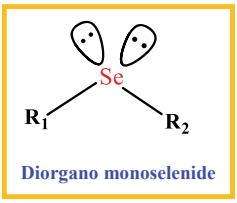

The class of monoselenides is the most prevalent among the organoselenium compounds. Because of structural similarity of monoselenides with ethers (R–O–R), this class is also called—selenoethers. As discussed earlier in historical milestones, the first organoselenium compound, i.e. diethylselenide (Et–Se–Et) belongs to this class. Hence, it is the oldest class among the various classes of organoselenium compounds.

The class of diorgano monoselenides has exhibited biological and pharmacological applications in diverse areas. The monoselenides with aliphatic chains bearing hydroxyl, amine and carboxyl groups have been explored for biological applications like antioxidant and GPx mimicking activities. The monoselenides lead to formation of seleninate esters which are the bioactive species for such antioxidant functions [70]. The significance of the monoselenides in biological functions is realized because of presence of such monoselenide species in food sources like in *Allium* family vegetables like garlic and onion. They contain the monoselenides like allyl methyl selenide, dimethyl selenide, Se-methyl selenocysteine and γ-glutamyl-Se-methyl selenocysteine and some others like bis(allylthio)selenide [71]. Additionally, the selenium based amino acids present in food sources like Se-methionine, Se-methylselenocysteine are also belonging to the same monoselenides class [72]. The most important selenocysteine (Sec) present at active sites of selenoenzymes like GPx, TrxR and IDs also exist as a monoselenide form. The crucial functions of these selenoenzymes in physiology, ultimately in human health is now unambiguously recognized [73].

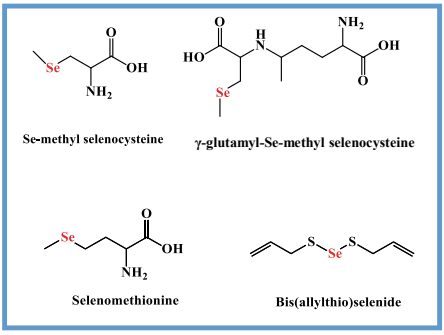

In view of the biological importance of this class, the various symmetrical and unsymmetrical diorgano monoselenides were synthesized along with their mono- and di-cyclic analogues. Their cyclic analogues were initially observed as intermediates during evaluation of antioxidant activities of monoselenides. Their synthesis will also be explained subsequently as a separate class, later in this chapter. During the physicochemical studies, it is observed that diorgano monoselenides undergo a variety of reactions. They get readily oxidized by one- and two-electron oxidants [74]. Their oxidation is considered as the rate determining step for the catalytic activities for reducing the detrimental hydrogen peroxide or hydroperoxides species (formed in mammals during oxygen metabolism) to harmless water or alcohol. Hence, faster the oxidation better is the performance of diorgano monoselenide compounds as a catalyst. Their easy oxidation process as inferred from reports of physicochemical studies renders them a potential for use as antioxidants [75].

Additionally, diorgano monoselenides have been extensively used as ligands in coordination and organometallic chemistry and as nucleophilic reagents in various organic reactions. The organometallic compounds with selenides find extensive applications in material science as molecular precursors for synthesis of metal selenides and related materials for electronic applications [76].

General methods for preparation of monoselenides

At this point, the various synthetic strategies employed for synthesis of monoselenides are discussed. The monoselenides are most conveniently synthesized by some commonly employed methods (Scheme 13.16). They include reduction of elemental selenium with $NaBH_4$, $LiBEt_3H$ (superhydride) or sodium element in ammonia, etc., to obtain alkali metal monoselenides which further react with halofunctionalised moieties yielding various symmetrical as well as functionalized diorgano

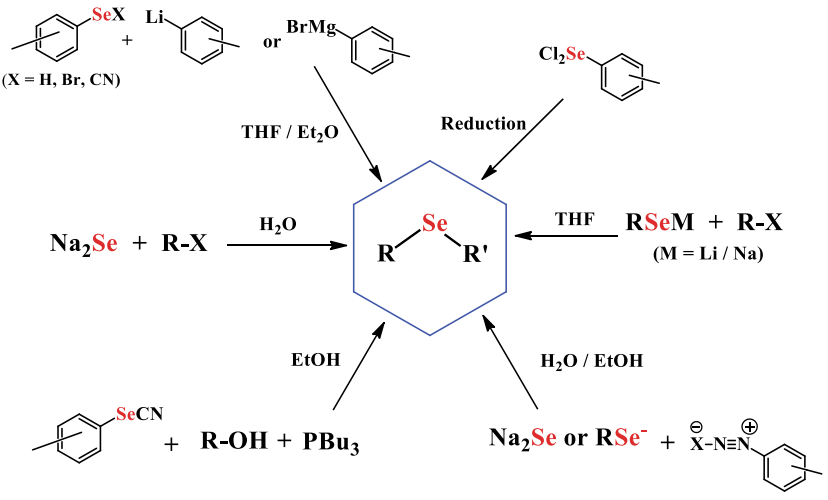

Scheme 13.16 Various routes for synthesis of diorgano monoselenides

monoselenides [77]. Additionally, in situ generation of selenolate species (RSe ion) by reductive cleavage of the Se–Se bond of a diselenide by common reducing agents like $NaBH_4$, $LiBEt_3H$ or hydrazine in the presence of NaOH in DMF followed by their treatment with halo functionalized moieties (aromatic, hetero-aromatic), yields the desired diorgano monoselenides [78]. Similarly, the treatment of selenolates with diazonium salts has also afforded the desired monoselenides [79]. Additionally, an effectual one pot synthesis strategy of symmetrical pyridyl monoselenides by the reaction of bromo- or iodo-pyridine with an appropriate Grignard reagent followed by quenching with selenyl chloride ($SeCl_2$) yielded the diorgano monoselenides [80]. Additionally, using Grignard's reagent route, as reported by Tang et al., the monoselenides were conveniently synthesized [81]. Under an inert atmosphere of nitrogen, a simple and effective method for the preparation of symmetrical monoselenides has been developed by the reaction of alkyl or aryl halides with magnesium and elemental selenium and ligand in THF and toluene under reflux at 86 °C; in the absence of any catalyst. This strategy has been used for the preparation of a variety of symmetrical selenides in excellent yields. In course of this reaction, the PhSeMgBr could be formed by reacting elemental selenium with phenyl Grignard reagent. Then, PhSeMgBr reacts with phenyl bromide to give diphenyl selenide in the absence of catalyst and ligand. There are various synthetic approaches employed for the preparation of selenides using selenocyanates [82].

Additionally, the selenides with functionalized moieties with polar functional groups like NH_2, OH were efficiently synthesized by treatment of epoxides, aziridines or appropriate molecules with selenols, which are ring opening reactions. For example, β-hydroxyaryl selenides or $Se\{(CH_2)_nOH\}_2$ (n = 2–4) were suitably yielded by a regioselective ring opening reactions of appropriate epoxides with a nucleophile like selenophenol ($PhSe^-$) (Scheme 13.17) in a basic medium at lower temperatures [83]. Similar reactions with aziridine rings afforded the selenides with amine functionalities. In such reactions, the aziridine N must be protected by tosyl (Ts) or *tert*-butoxycarbonyl (Boc) (Scheme 13.18) [84].

Furthermore, the unsymmetrical organoselenium monoselenides were prepared by exploiting the high reactivity of selenenamide bond in selenazoles towards nucleophiles. It has been found that benzisoselenazol-3(2H)-ones (ebselen derivatives) having a Se–N moiety when treated with Grignard reagent afforded unsymmetrical aryl–alkyl and aryl-aryl monoselenides in moderate to good yields [85]

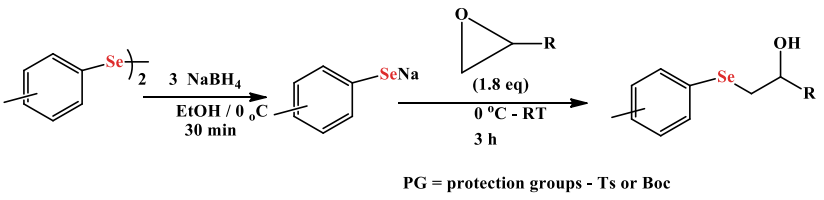

Scheme 13.17 Synthesis of monoselenides from epoxides

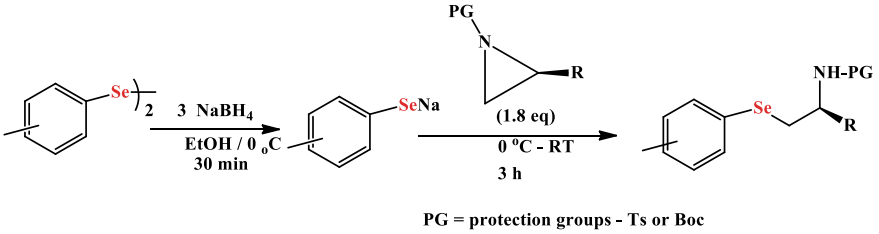

Scheme 13.18 Synthesis of monoselenides from aziridines

(Scheme 13.19). The electrophilic (RSeX; X=Cl or Br) and nucleophilic (RSeH) selenium compounds were reported to add to alkynes, alkenes and carbonyl compounds to afford the functionalized selenides [86]. A redox transmetalation of $Ag(C_5H_4N)$ with red selenium in EtCN at room temperature yielded $(NH_4C_5)_2Se$, but at 50 °C formation of analogous diselenide was reported (Scheme 13.20) [87].

New strategies for synthesis of diorgano monoselenides

The diaryl selenides have been synthesized by treatment of phenyl boronic acid with SeO_2 over PEG-400 and K_2CO_3 as a base at 110 °C (Scheme 13.21) [88].

A copper(II) catalyzed selenation of aryl-boronic acids by Se element in DMSO and pyridine is established, which affords diaryl diselenides or diaryl monoselenides in good yields with excellent selectivities (Scheme 13.22) [89]. Furthermore, an effective one pot strategy for synthesis of unsymmetrical diorgano monoselenides has

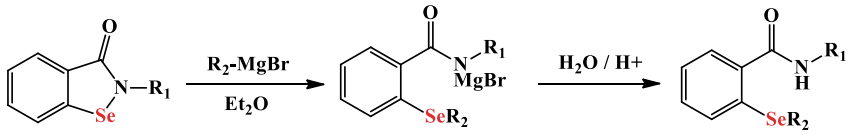

Scheme 13.19 Synthesis of monoselenides from selenamide with Grignard reagent

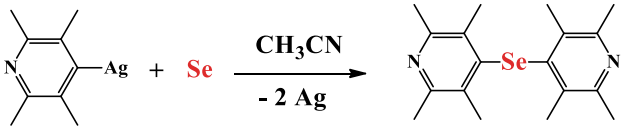

Scheme 13.20 Synthesis of selenides from redox transmetalation

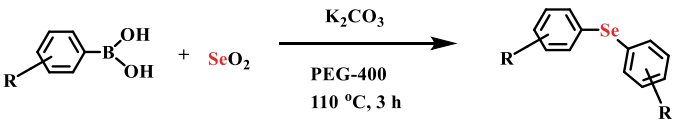

Scheme 13.21 Synthesis of diaryl monoselenides from phenyl boronic acid

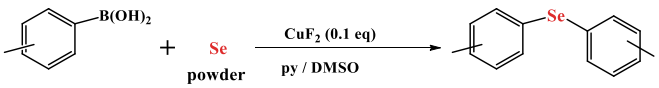

Scheme 13.22 Cu catalyzed synthesis of aryl monoselenides from organo boronic acids

been designed which employ the Ru(III)-chloride catalyzed treatments of diphenyl or dibenzyl diselenides with alkyl halides in presence of zinc. In such reactions, organic bromides, iodides and activated chlorides were observed to undergo the reactions efficiently. The unreactive organic chlorides have also undergone the same reactions of selenation in presence of sodium bromide as the additive (Scheme 13.23) [90]. Additionally, the CuBr catalyzed, direct selenation of C–H bond of aromatic moieties leading to diaryl selenides by using elemental selenium sources under oxidative conditions in polar solvents like DMSO and water at higher temperatures (Scheme 13.24) [91]. The novel strategy by utilizing a CuI-bpy catalyzed synthesis of various diorgano monoselenides from corresponding diselenides using organoboronic acids has also been used. Accordingly, the unsymmetrical diorgano monoselenides can be conveniently synthesized by a coupling of dichalcogenides with alkyl- or aryl-boronic acids in presence of a copper compound as a catalyst followed by aerial oxidation (Scheme 13.25) [92].

Additionally, C–Se coupling of aryl bromides with diaryl diselenides in BMIM-BF_4 solvent and catalyzed by CuO nanoparticles and KOH as a base yielded the corresponding diaryl monoselenides in high yields [93]. The substitution of

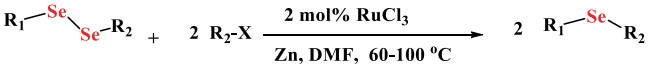

Scheme 13.23 Ru(III) catalyzed synthesis of monoselenides from diselenides

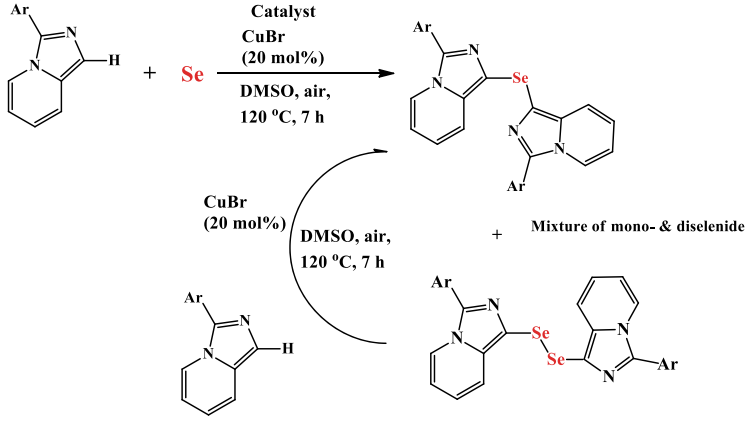

Scheme 13.24 Cu(I) catalyzed C-H bond selenation to synthesize diselenides

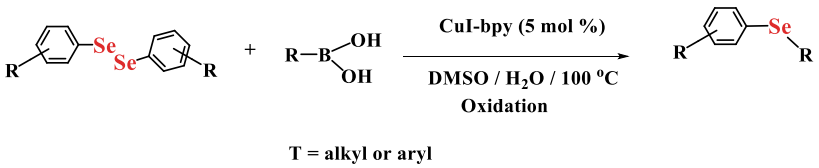

Scheme 13.25 Cu catalyzed synthesis of monoselenides from diaryl diselenides

halogen atom on diverse aryl, pyridyl and thienyl bromides or iodides by sodium benzeneselenolate (PhSeNa) was catalyzed by various nickel(I1)-bromide complexes with nitrogen heterocycles or chelating phosphine moieties. For this reaction, bis(bipyridyl)nickel(II) bromide was found as the most effective catalyst. This reaction is regioselective and gave high yields of the corresponding aryl-phenyl selenides, pyridyl-phenyl selenides and thienyl-phenyl selenides (Scheme 13.26) [94]. Additionally, a suitable and effective procedure was developed for the preparation of alkyl-phenyl selenides and selenoesters in one pot reaction by utilizing indium metal. The reaction exhibited the selectivity for *tert*-alkyl, benzylic and allylic halides over primary and secondary alkyl halides. In case of a reaction of primary and secondary alkyl iodides and bromides, the yields of monoselenide products were improved by an addition of catalytic amounts of iodine (Scheme 13.27) [95]. Similarly, the palladium (Pd) catalyzed reactions also were developed to afford the monoselenides. The palladium complexes, such as $[Pd(PPh_3)_4]$ catalyzed the reaction of phenyl tributylstannyl selenide ($PhSeSnBu_3$) with alkyl and aryl halides, yielding the corresponding diaryl and alkyl-aryl monoselenides in good yields (Scheme 13.28) [96].

Furthermore, the synthesis of diorgano monoselenides has been reported by methodologies which utilize the selenium dioxide (SeO_2) as selenating agent. The SeO_2 is a stable, effective and commercially available oxidizing agent. In this novel and easy protocol, it involves formation of biphenols along with a desired diaryl selenides, which depends on the solvent used for reaction. The oxidative treatment of

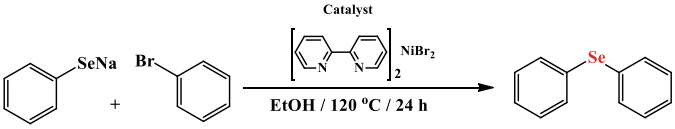

Scheme 13.26 Nickel(I1) bromide catalyzed synthesis of aryl selenides

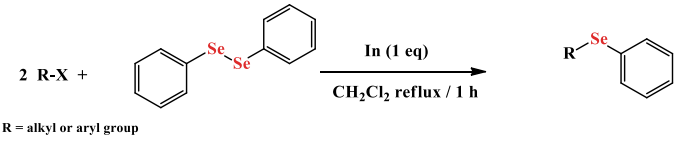

Scheme 13.27 Indium mediated synthesis of unsymmetrical monoselenides from diselenides

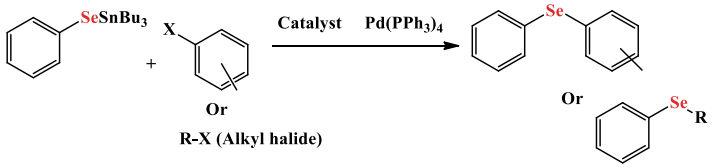

Scheme 13.28 Pd catalyzed synthesis of monoselenides

phenols in acetic acid as solvent affords the corresponding biphenols, whereas reactions in pyridine as a solvent, results in the preferential formation of diaryl selenides. Henceforth, isolation of novel diaryl selenides is possible. These compounds act as pincer-like ligands having further applications in organic synthesis or as ligands in transition metal complexes for catalysis (Scheme 13.29) [97].

A new methodology for preparation of unsymmetrical diaryl selenides from triaryl-bismuthines and diaryl diselenides through a photoinduced pathway has been designed. Usually, arylation reactions with triaryl-bismuthines are reported to be catalyzed by transition metal complexes, this type of arylation reaction of diaryl diselenides with triaryl-bismuthines proceeds through a photoirradiation in absence of transition metal catalysts. A wide range of unsymmetrical diaryl monoselenides were conveniently synthesized by utilizing this arylation strategy (Scheme 13.30) [98].

Further strategies like activation of aliphatic hydroxyl group containing moieties like L-serin have been employed by either tosylation or treatment with phenylmethanesulfonyl fluoride (PMSF) and the resultant sulfonylated product is further treated with excess of selenium nucleophile like hydrogenselenide (NaHSe) yields selenium insertion yielding monoslenols. This process was used for synthesis of semisynthetic enzymes or chemical modifications of L-serin based enzymes to insert Se at the side-chain alcohol of Ser221 of subtilisin to afford the chemically-mutated or

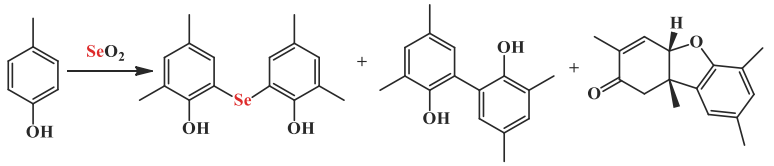

Scheme 13.29 Synthesis of monoselenides by using selenium dioxide as a Se source

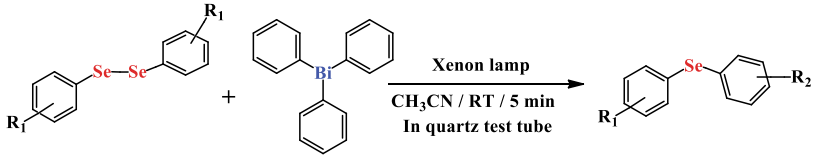

Scheme 13.30 Photoinduced synthesis of unsymmetrical diaryl selenides

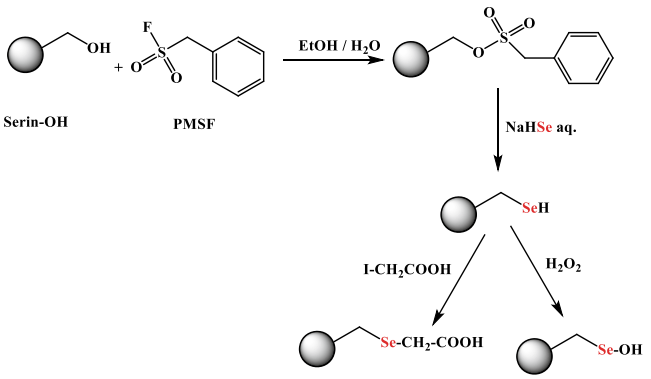

Scheme 13.31 Chemical modifications of serin proteases to form selenides

-modified selenosubtilisin which exhibited outstanding glutathione peroxidase-like catalytic and antioxidant activity (Scheme 13.31) [99]. It indicated the importance of synthetic strategy in chemical biology field.

In view of these reports, it can be concluded that such kinds of novel strategies for synthesis of monoselenides have underlined their utility for synthesizing monoselenides which play a crucial role in biology, biochemistry, pharmacology, physiology, chemical biology as well as materials science. It gives an opportunity for scientists to develop new strategies specifically for novel biologically and pharmacologically important aspects like chemical modifications of enzymes.

13.12.3 Diorganoselenoxides ($R_2Se=O$)

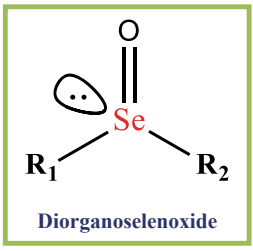

The diorganoselenoxides ($R_2Se=O$; R = alkyl or Ar) class of organoselenium compounds possess the catalytically important compounds as intermediates in biochemical or pharmacological processes as well as catalysts or reagents for industrially important processes and as ligands for synthesis of organometallic compounds. In case of biochemical processes like oxidative metabolism of seleno-L-methionine, the corresponding oxidized species L-methionine selenoxide is formed as well as in

catalytic scavenging of myloperroxidase (MPO) derived oxidants, the L-methionine selenoxide is observed to play a crucial role [100]. In case of pharmacological actions of monoselenides as antioxidants, GPx mimics the corresponding selenoxides are formed which is a rate determining step [101]. Additionally, the selenoxides were evaluated for understanding protein chemistry, as efficient oxidizing reagents for protein disulphide-bond formation. The rationale for such applications is interconversion reactions between thiols and disulphides which are biochemically significant processes involved in antioxidant functions of cells against reactive oxygen species and the oxidative folding of proteins having several disulphide (SS) bonds [102]. In further developments, the organoselenium metabolite Se-adenosylselenohomocysteine selenoxide (SeAHO) was designed and synthesized via hydrogen peroxide oxidation of Se-adenosylselenohomocysteine to evaluate the biochemical pathways [103].

The selenoxides have exhibited diverse applications in chemical synthesis strategies as oxygen transfer agents [104] in organic as well as organometallic synthesis [105]. The property of allyl-selenoxides to undergo fast [2, 3]-sigmatropic rearrangement was utilized for preparing optically pure alcohols and allens [106]. Moreover, the selenoxide syn elimination gives a suitable strategy for introducing olefins into various molecules [107]. In this way, the dissociative cycloelimination, new selenium based pericyclic reactions exhibited catalytic applications. [108]. Further, several procedures for the preparation of α-phenylseleno ketones have been developed. The most useful procedures are direct selenenylation of ketone enolates is performed by using PhSeBr. This transformation of ketones to enones takes place through selenenylation followed by selenoxide elimination [109]. Furthermore, the aryl benzyl selenoxides are used as catalysts for epoxidation of several olefinic substrates and the Baeyer–Villiger oxidation of aldehydes and ketones with H_2O_2 in CH_2Cl_2 at 2.5 mol% catalyst. Benzyl 3,5-bis(trifluoromethyl)phenyl selenoxide was the most effective catalyst and using it and H_2O_2, Mono-, di- and tri-substituted alkenes were epoxidized and adarnantanone, cyclohexanone and 3,4,5-trimethoxybenzaidehyde underwent Baeyer–Villiger oxidation [110]. Some more applications of selenoxides in combination with other reagents have been reported. In case of hydrogen peroxide oxidation, the selenides R_2Se and selenoxides R_2SeO were used as the catalysts, e.g. 2-Carboxyphenyl phenyl selenide was successfully used as a catalyst for oxidation of sulphides into sulfoxides and/or sulfones [111]. The diorganoselenoxides like diphenyl selenoxide, dibenzyl selenoxide and several aryl benzyl selenoxides were used as catalysts for the bromination of organic substrates [112]. The selenoxides also served in coordination chemistry as oxygen donor ligands [113]. The selenoxides of unsymmetrical type can achieve chirality and they exhibit stability towards pyramidal inversion at room temperature, but their racemization is facilitated in acidic media [114]. The selenoxides get reduced easily with biomolecules like thiols (glutathione, GSH) or by triaryl phosphites [115] to regenerate active selenides in redox reactions of selenides which is a prime biological application. All these strategies are used for developing the various biologically or industrially important molecules.

Strategies for synthesis of selenoxides

In view of the importance of diorganoselenoxides, researchers have designed and developed various strategies for their synthesis which will be discussed briefly. The selenoxides were conveniently synthesized by the treatment of diorgano monoselenides with commonly used oxidizing agents like hydrogen peroxide (Scheme 13.32) [116], *tert*-butyl hydrogen peroxide (TBHP) [117], cumene hydroperoxide [118], ozone, sodium hypochlorite (NaOCl) (Scheme 13.33) or *tert*-butyl hypochlorite in methanol or DMF [119], peroxy acids like *meta*-chloroperbenzoic acid (*m*CPBA) or *tert*-butylhypochlorite (Scheme 13.34) [120].

Additionally, selenoxides were obtained by the hydrolysis of diorganoselenium dichlorides by their treatment with alkali metal hydroxides, sodium acetate and silver oxide in aqueous medium. The oxidation of 3,3′-selenodipropionic acid readily afforded a dehydrated cyclized product, whereas the homologous 4,4′-selenodibutyric acid and 5,5′-seleno divaleric acid yielded corresponding selenoxides [121]. In other efforts, the monoselenides were oxidized with 2-nitrobenzenesulfonyl chloride and potassium superoxide in dry acetonitrile at −15 °C, e.g. alkyl-phenyl selenoxides were produced in excellent yields by oxidation of the corresponding selenides by this method [122] (Scheme 13.35).

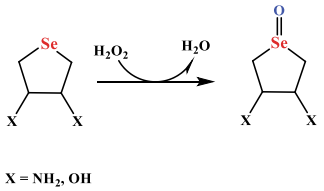

Scheme 13.32 Selenoxide formation by selenide oxidation by hydrogen peroxide

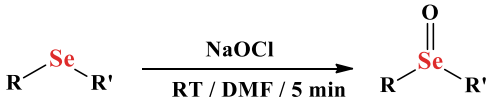

Scheme 13.33 Oxidation of selenide with sodium oxy chloride

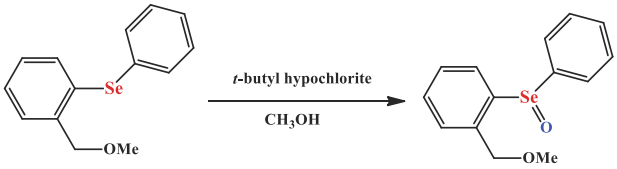

Scheme 13.34 Oxidation of selenide with *tert*-butylhyposhlorite

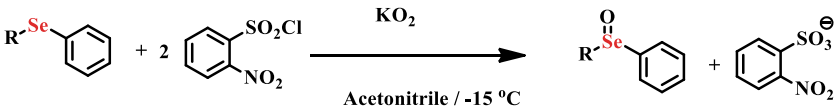

Scheme 13.35 Synthesis of selenoxides using potassium superoxide

13.12.4 Selenuranes

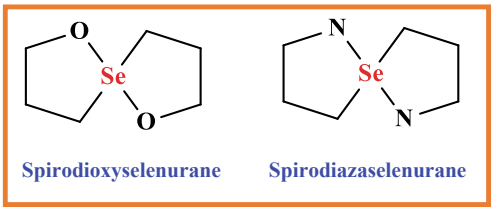

Now let us discuss further about a prominent class of selenium compounds—selenuranes. The compounds from this class were observed during the antioxidant GPx mimetics mechanism of diorgano monoselenides and -selenoxides. It infers that this class consists of the compounds derived by reactions on the selenoxides. In view of its emerging importance as intermediates directing further progress of reaction, as well as individual antioxidant activities of compounds belonging to this class, further studies were performed which revealed that their structure plays a crucial role. Hence, the choice of starting selenoxide also matters for choosing as the catalyst or GPx mimic for their anticipated applications in biological studies which further lead to pharmacology of the potent candidate. Hence this class play a crucial role and hence it is worthwhile to discuss the class.

The class of selenurane consisting mainly the spirodioxyselenurane and spirodiazaselenurane and related compounds; is emerging as a new class of biological antioxidants which mimic glutathione peroxidase (GPx) activity [123]. As mentioned earlier the structures play a crucial role in the biological activities of the compounds of this class [124]. They are intermediates in GPx mimetics of selenoxides as an antioxidant catalyst. The variation in structure of this type of compound leads to another type of selenuranes, i.e. pincer is achieved. They also exhibited the potent GPx like catalytic activities [125]. Although they were found as intermediates, they were fairly stable to isolate and characterize by NMR spectroscopy as well as single crystal XRD analyzes [126]. In this perspective, they are potential candidates for their further investigations till accomplishment of their pharmacological applications.

Let us discuss synthesis of these species. They were conveniently synthesized by oxidation of diorgano monoselenides followed by dehydration leading to a desired species [127]. The rearrangement reactions may take place during oxidation in case of selenoxides which have protic (e.g. OH, COOH) groups on organic moieties boded with selenium atoms. E.g. oxidation of di(3-hydroxypropyl)selenide with *tert*-butyl hydroperoxide results in the formation of corresponding selenoxide which

readily undergoes intra-molecular dehydration to yield a spiro selenurane compound (Scheme 13.36) [128].

Similarly, using hydrogen peroxide as oxidizing agent, the cyclohexene fused selenuranes, as well as bezylic moiety-based analogues, have been prepared [129]. Additionally, the oxidation process of 2,2'-selenobis(benzamide) by using commonly used oxidizing agents like hydrogen peroxide or N-chlorosuccinimide (NCS) in methanolic solutions afforded corresponding stable azaselenonium chloride and hydroxide, respectively (Scheme 13.37) [130]. Similarly, the pincer type azaselenuranes have been synthesized (Scheme 13.38) [125b]. Along with this, oxidation of 3,3′-selenodipropionic acid readily afforded a dehydrated cyclized compound (Scheme 13.39) [131].

Another type of selenurane class, the pincer selenuranes are designed by the variations of spirodioxy-selenuranes and spirodiaza-selenuranes. In this case of pincer compounds, both nucleophilic groups (hydroxyl or amido) originate from ortho positions of the same arylseleno substituent, while the remaining selenium substituent is an independent aryl or alkyl group. The selenium pincer compounds have exhibited

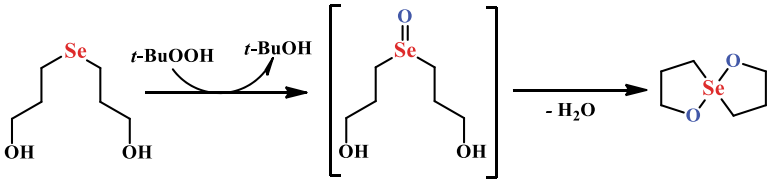

Scheme 13.36 Synthesis of spiro selenurane from a monoselenide

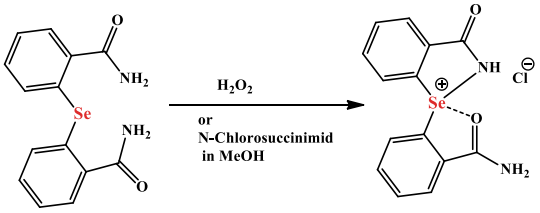

Scheme 13.37 Synthesis of azaselenonium chloride

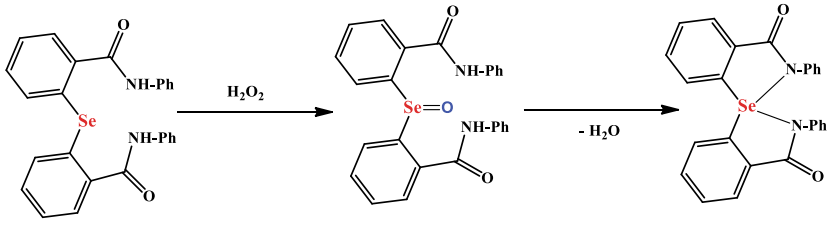

Scheme 13.38 Synthesis of pincer selenuranes

Scheme 13.39 Synthesis of selenurane from 3,3′-selenodipropionic

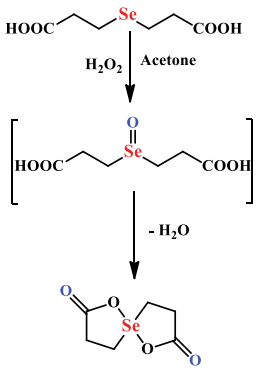

applications in GPx mimetics, as well as their metal complexes, especially Pd(II) complexes have exhibited catalytic applications.

The first example of this class was synthesized by Singh et al., who prepared pincer selenide from treatment of bromo-functionalized aryl moiety with in situ generated selenolate, i.e. sodium benzeneselenolate ($PhSeNa^+$) to achieve dirgano monoselenide. It was further treated with $LiAlH_4$ followed by oxidation by H_2O_2 to obtain the selenoxide species, which on dehydration yielded the desired pincer selenium compound [132]. These compounds also exhibited the antioxidant and GPx mimetic activities (Scheme 13.40).

Additionally, the pincer selenides were synthesized by treatment of bromo-functionalized diaryl amido compounds with Woollin's reagent to yield selenides which were coordinated with metal ions to give the complexes. Although less number of metal complexes with pincer selenium ligands have been reported, they exhibited reasonable utility in catalysis [133]. Additionally, the pincer compounds served as ligands in coordination chemistry [134]. Their versatility has made them

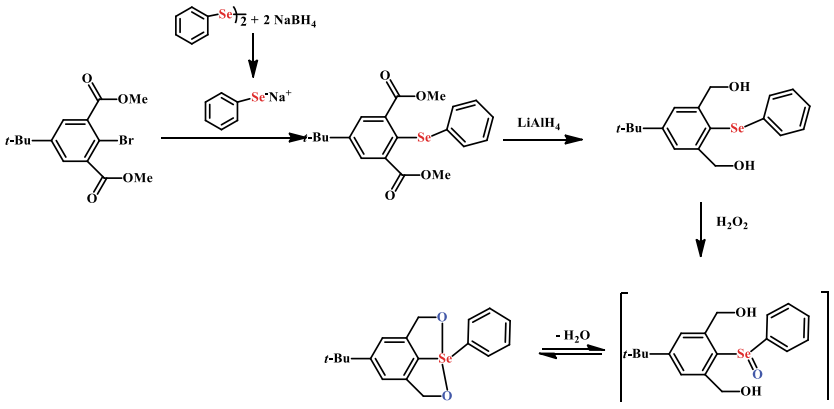

Scheme 13.40 Synthesis of pincer selenurane from diorgano monoselenide

convenient for preparing metal complexes as precursors suitable for making metal selenides, which further transform into active catalysts for Suzuki-Miyara and Heck coupling reactions [135]. Further, the palladium(II) complexes with organoselenium pincer ligands catalyzed Suzuki coupling reactions in aqueous media through in situ generated palladium quantum dots [136]. Additionally, the palladium(II) complexes of the first pincer seleno ligand, 2,6-bis((phenylseleno)methyl)pyridine as well as bis(chalcogenones) has exhibited the catalytic applications for Heck Reaction [137]. One can find from literature more details about catalytic applications of pincer ligands containing a Se site which have been reviewed [138].

This account of selenuranes gives the clear idea that, despite their potential, the literature on SeNSe pincer compounds is limited. This gives us a scope for further development of their synthetic protocols and applications for further research in health related applications as well as exploring their utility in materials and catalytic applications.

13.12.5 Cyclic Seleninate Esters

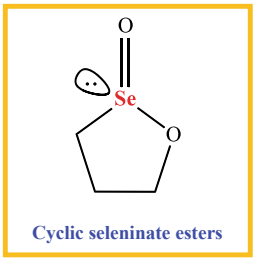

Now let us discuss an important class of selenium compounds which were observed during the antioxidant GPx mimetic reaction mechanism of diorgano monoselenides like allyl 3-hydroxypropyl selenide. The said class consists of the compounds derived by further oxidations reaction on such selenides being evaluated as GPx mimics. In view of their emerging importance as intermediates, which are potentially active species for reduction of hydrogen peroxide or hydroperoxides using sacrificial thiols to form stable and harmless species like water or alcohol, the seleninate esters were synthesized. These compounds are fairly stable and water soluble species, suitable for biological applications. They were characterized for their crystal structures and evaluated for GPx mimetics. The studies performed, reveal that their structure plays a crucial role in conferring them the potential activity.

Synthesis strategies for seleninate esters

The seleninate esters were conveniently synthesized by oxidation of allyl 3-hydroxypropyl selenide with *tert*-butyl hydroperoxide. This reaction afforded the

novel cyclic seleninate ester, rapidly and quantitatively through the oxidation followed by [2, 3]-sigmatropic rearrangement steps. They were obtained similarly by oxidation of or 3-hydroxypropyl-selenol with *tert*-butyl hydroperoxide. Their aromatic congeners were also reported. The seleninate esters exhibited remarkably effective catalytic activity for reduction of peroxides at the expense of thiols. The catalytic activity of seleninate ester was found to be much better than the several other known GPx mimics containing cyclic selenenamide [123, 139, 140] (Scheme 13.41).

Furthermore, starting from bromo-functionalized aryl-benzylic moiety, its treatment with Na_2Se_2 and subsequent oxidation with H_2O_2 the seleninate ester species were obtained [141]. Furthermore, Singh et al., have reported a seven-membered cyclic seleninate ester species which was derived from 2-phenoxyethanol. It was obtained from allyl (2-(2-hydroxyethoxy)phenyl) selenide through a series of oxidation and [2, 3]-sigmatropic rearrangement steps (Scheme 13.42). This seleninate ester exhibited good GPx like activity evaluated coupled reductase assay [142]. Moreover,

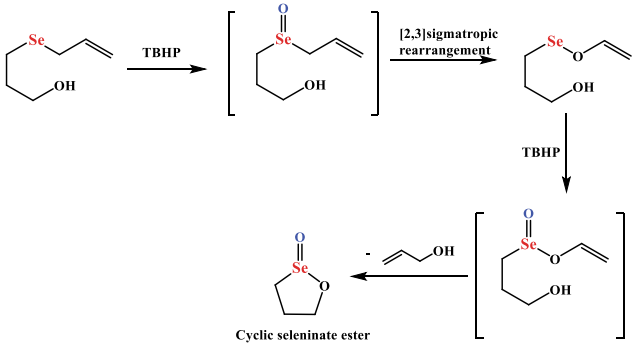

Scheme 13.41 Synthesis of seleninate ester from allyl-based monoselenides

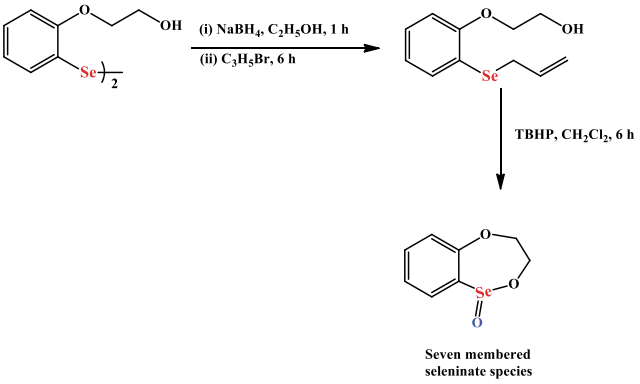

Scheme 13.42 Synthesis of 7 membered seleninate ester

the selena-heterocyclic compounds, aliphatic- and aryl based, cyclic, seleninate esters were also reported which found their potential as the GPx mimics [143].

Due to natural drive of researchers to create new structural modifications in known structures targeting for enhanced activities, methoxy substituents on of an aromatic cyclic seleninate were designed and effect on their activation barriers of the glutathione peroxidase-like mechanism was investigated by density functional theory (DFT) models. It revealed that methoxy substitutions affect the rate of scavenging of reactive oxygen species differently depending upon the position. The activities were found to be enhanced when the methoxy substituent at *para* position, unaffected for *meta*- and decreased for *ortho*-substituted derivatives. The analyzes from DFT calculations showed that the activation barrier for oxidation of selenenyl sulphide (Se-S species) which is an anticipated key intermediate, is higher for the *ortho*- methoxy substituted derivative than for its analogues where substitution of methoxy at other positions. Additionally, it was found to be consistent with the low experimental conversion rate [144].

In addition to GPx mimetic applications, the seleninate esters were evaluated for oxidation of disulphides to thiolsulfinates. The results from this study have revealed the potency of seleninate esters for medicinal applications because of the possibility of catalyzing the undesired oxidation of disulphide-containing spectator proteins and peptides. It is known that the seleninate esters catalyze the reduction of harmful peroxides with thiols, which are converted to disulphides in the process. Hereafter, the possibility that seleninate esters may be able to catalyze further oxidation of disulphides to thiolsulfinates species or other over oxidation products formed in these conditions was evaluated. In this study, the benzo-1,2-oxaselenolane Se-oxide was used as catalysts for further catalytic reactions with disulphide species. The results confirm the possibility that cyclic seleninate esters could catalyze the further undesired oxidation of disulphides in vivo (Scheme 13.43) [145]. This property of seleninate ester added further in its biological applicability and encouraged their further research.

In continued research endeavours, the optically active seleninate esters were obtained through chromatographic resolution on an optically active column and the absolute configuration of some of them was determined by X-ray crystallographic analyzes. The optically active seleninate esters, generally tend to racemize in solution. The racemization process was studied by the oxygen exchange reaction with H(2)(18)O. Additionally, the theoretical studies also cleared that the racemization

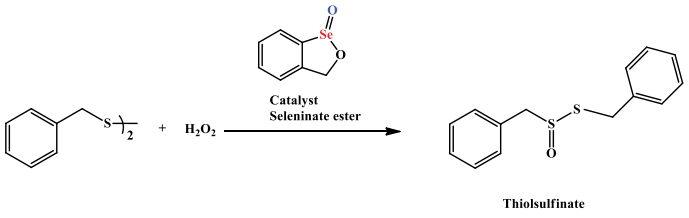

Scheme 13.43 Application of seleninate esters for oxidation of disulphides

of optically active seleninate esters in solution state proceeded through formation of achiral hypervalent selenurane intermediate species due to the addition reaction of water which was present in the solvent. The treatment of optically active seleninate ester having bulky substituents with Grignard reagents was found to undergo by retaining the stereochemistry and yield the optically active selenoxides [146].

This account of cyclic seleninate esters clearly indicates their importance in biomimetics as well as further utility in disulphide oxidation to neutralize the detrimental effects of hydroperoxides and unwanted disulphides for health related applications. It gives a good opportunity for further research for new pharmacological concepts and eventually uses in medicine.

13.12.6 Thioselenuranes [RSSe(=O)OH)]

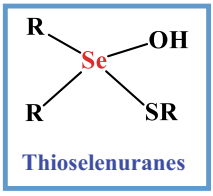

Earlier spiro-, pincer- and seleninate ester species were discussed as the intermediates formed during the GPx mimetic of monoselenides. In subsequent research other short lived, tetra-coordinate species as intermediates were proposed by Chen et al., for catalytic reaction of methylphenyl selenoxide with GSH [147]. Additionally, the efforts were directed for the isolation and authentication of thioselenurane by ^{77}Se NMR spectroscopy, mass spectrometry and stop flow techniques, etc. These intermediates were named thioselenurane species. In this mechanism, the oxidation of diorgano monoselenides to selenoxides, apparently the active oxidant in the GPx catalytic cycle was assigned as a rate determining step [148].

It has been seen earlier, that GPx mimetic catalytic mechanism of selenoxides to reduce the hydroperoxides proceeds to the stable and harmless forms like water or alcohol at the expense of thiol cofactors. The theoretical investigations on this mechanism have been performed by Craig Bayse. The mechanism for ebselen as a catalyst was investigated by SAPE network theoretical calculations which suggested that it proceeds through a short lived, tetra-coordinate intermediate thioselenurane [(RSSe(=O)OH)] species. Hence, there were efforts to calculate their ^{77}Se NMR chemical shifts (δ) theoretically by using the GIAO method which suggests that δ values of selenoxide and intermediate thioselenurane are well separated for detection [149]. However, since intermediate has a very short half-life, in earlier efforts the species could not be detected using ^{77}Se NMR spectroscopy [150]. Henceforth, the researchers focused on isolation and characterization of thioselenurane intermediate species but high reactivity and instability of such tetra-coordinate selenium

species having fast reaction rates of organoselenium compounds with oxidants or with reducing agents, have made it difficult to clearly characterize thioselenurane species like intermediates [128, 147, 150–154]. Even the identification of such species by using ^{77}Se NMR spectroscopy was unsuccessful. Hence, the strategies by employing the bulky organic moieties were thought. In such efforts, the mesityl selenoxide was synthesized and further treated with thols like mesityl thiol and HS-$CH_2CH_2NMe_2$ and investigated for GPx mimetics by using the ^{77}Se NMR spectroscopic analyzes but still the thioselenurane species was not possible to detect. Instead of identifying thioselenurane species, it was observed that the selenoxide acted as a hydrogen bond acceptor to afford $Mes_2Se{=}O{-}HX$ species (HX = thiols) [79]. Additionally, Iwaoka et al., (Scheme 13.44) [101b] also studied the reduced dihydroxy selenonane (DHS^{red}) compound for the study of thiol to disulphide (S–S) formation reactions pertaining to peptide and protein chemistry. It revealed that the reaction mechanism of S–S formation in a polypeptide chain using DHS^{ox} is a two steps process: (i) the attack of cysteinyl SH group to the selenoxide (DHS^{ox}) to form a short lived unstable intermediate species having a selenenyl sulphide (Se–S) linkage and (ii) intra-molecular rearrangement of thioselenurane intermediate species to form an S–S bond with elimination of DHS^{red} and a water molecule. The stochastic behaviour of the S–S formation indicated that the first step (i) is the rate determining step. Hence, as long as, polypeptide chain is in a random-coil state, velocity for S–S formation reaction would depend on probability of molecular contact between DHS^{ox} and SH groups on a polypeptide chain (Scheme 13.45) [155].

Finally, the evidence from stopped-flow kinetics and ESI–MS and ESI–MS/MS experiments revealed that the oxidation-reduction reaction between phenylaminoalkyl selenoxides and glutathione occurs through a two-step process that involves the intermediacy of a tetra-coordinate thioselenurane species (Scheme 13.46) [156] as well as by mass spectral analyzes of aryl selenides as

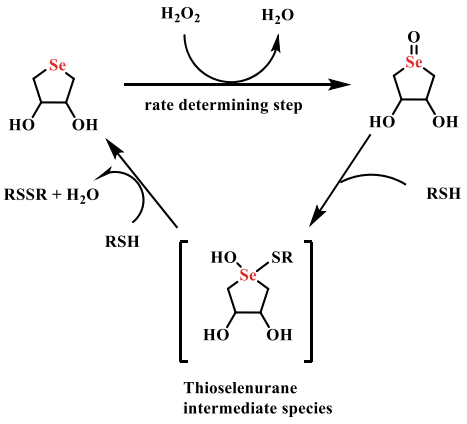

Scheme 13.44 Thioselenurane species as intermediate in GPx cycle of monoselenides

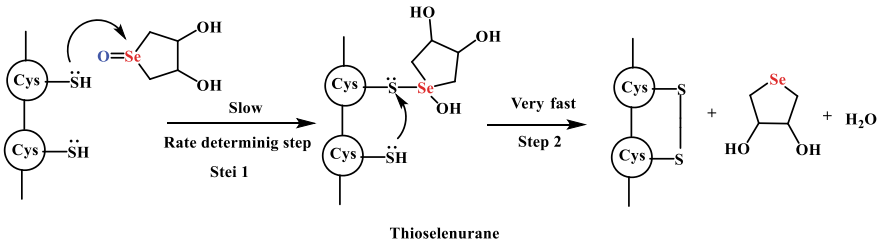

Scheme 13.45 Thioselenurane intermediate during formation of S–S

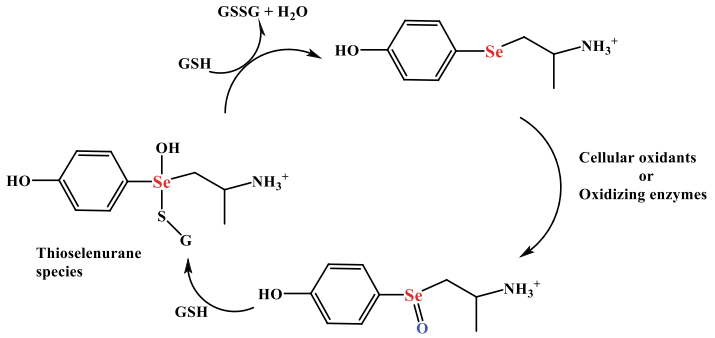

Scheme 13.46 Characterization of phenylaminoalkyl thioslenurane species

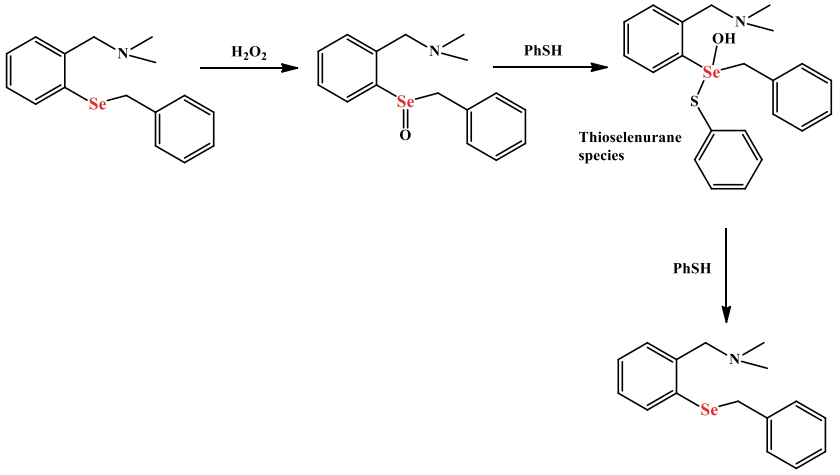

Scheme 13.47 Identification of thioselenurane species by mass spectral analyzes

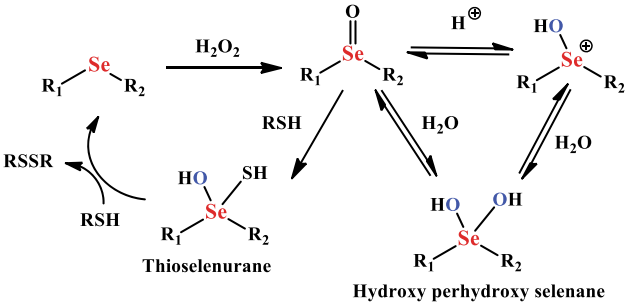

Scheme 13.48 Identification of perhydroxy hydroxy selinenes species along with selenuranes

reported by Singh et al., (Scheme 13.47) [153]. These examples unambiguously prove the formation of thioselenurane species as intermediates.

Later, based on experimental evidence, a more consistent catalytic cycle for the GPx like activity of selenides and selenoxides was proposed by Braga et al., (Scheme 13.48). It suggested the hydroxy perhydroxy selenane species which react with a thiol in two different attacking modes resulting in two different products [157].

This account gives us a clear idea that in the mechanism of seleoxides as catalysts for GPx activities, the tetra-coordinate and short lived species, thioselenurane plays a crucial role. In view of its instability and scarcity of detailed studies, it gives us opportunity to explore it further to get more knowledge of pathway.

13.12.7 Selenenic (RSeOH), Seleninic (RSeOOH) and Selenonic (RSeOOOH) Acids

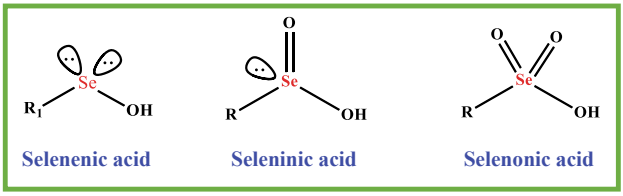

These are important short lived intermediate species generated in the antioxidant GPx catalytic cycle of organoselenium compounds. The GPx active catalysts having selenol group or the diorgano diselenide species react with H_2O_2 or hydroperoxide to produce the Se(II) species known as selenenic acids (RSeOH). Its over oxidation due to high concentration of peroxides leads to formation of Se(III) and Se(IV) species known as seleninic- and seleninic- acids respectively [158]. All these species are highly reactive intermediates which are generated during the oxidation of selenols and diselenides (Scheme 13.49) [159]. They are postulated in various reactions like

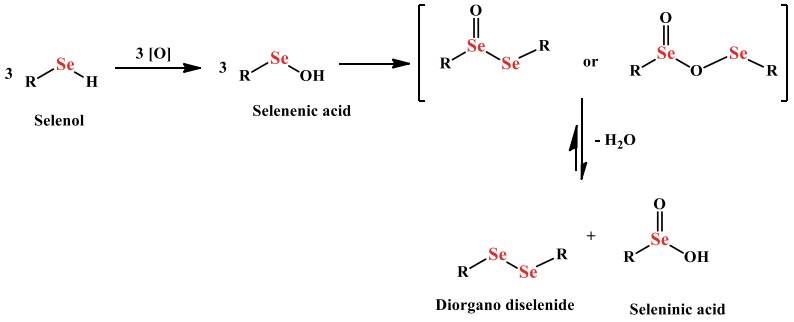

Scheme 13.49 Identification of selenenic and selenininc acid species

selenoxide syn elimination. These species are highly unstable and undergo disproportionation, probably involving intermediates, to the corresponding diselenides and seleninic acids or anhydrides [160].

The studies related to their biochemical roles were hampered because of their instability. Hence, several strategies were designed in order to isolate or synthesize these species by favourable structural features like internal functionalization or steric hindrance. It was anticipated because of their stabilization by coordination of amine, nitro, carbonyl functional groups in solution state [161]; but alkylselenenic acid could not be detected in any case. However, by use of bulky aryl moieties the efforts were successful. Using bulky aryl groups [162] like 2,4,6-$Pr^{i}_{3}C_6H_2$ and triptycyl (trip) [163] the seleninic acid, ArSeOH has obtained and was characterized using NMR spectroscopy. Additionally, the redox behaviour of tripSeOH was also investigated [164]. Furthermore, by using a bulky bowl-shaped organic moiety, a stable seleninic acid, BmtSeOH species (Scheme 13.50), has been isolated by the direct oxidation of selenol with H_2O_2 and it was structurally characterized also. The compound exhibited remarkable stability, both in solid and solution states [165].

There are reports of some other strategies also for synthesis and isolation of these species. Hydrolysis of selenenyl halides or reduction of seleninic anhydrides also afforded selenenic acids. Such reactions have been used for in situ generations of selenenic acids. E.g. 2-Nitrobenzene seleninic acid on reduction with NaH_2PO_2 yielded the corresponding selenenic acid [167a]. the hydrolysis of selenenyl bromide

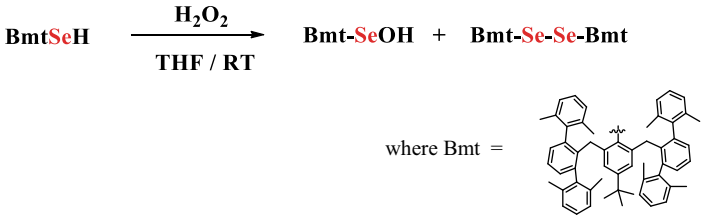

Scheme 13.50 Synthesis of stable selenenic acid species

during crystallization proceeds to a formation of selenenate esters [166]. Oxidation of secondary and tertiary amide based diselenides by hydrogen peroxide has been investigated. It is envisaged that such reactions proceed through involvement of seleninic acid. In the case of the secondary amide group, rapid cyclization takes place to produce seleneyl amides which on oxidation with excess H_2O_2 yield seleninic acids. The seleninic acids of tertiary amides undergo further oxidation with an excess of H_2O_2 to afford selenonic acids (Scheme 13.51). The seleninic acids exhibited intra-molecular Se· · · O interactions [167].

In other efforts Goto et al., have isolated a stable selenenic acid species by using strategies of steric hindrance created by bulky organic moieties like *m*-phenylene dendrimer framework (Scheme 13.52) [168].

Unlike selenenic acids, seleninic and selenonic acids are stable, isolable, colorless and odourless solids. They are used as oxidants in organic synthesis. Both aliphatic

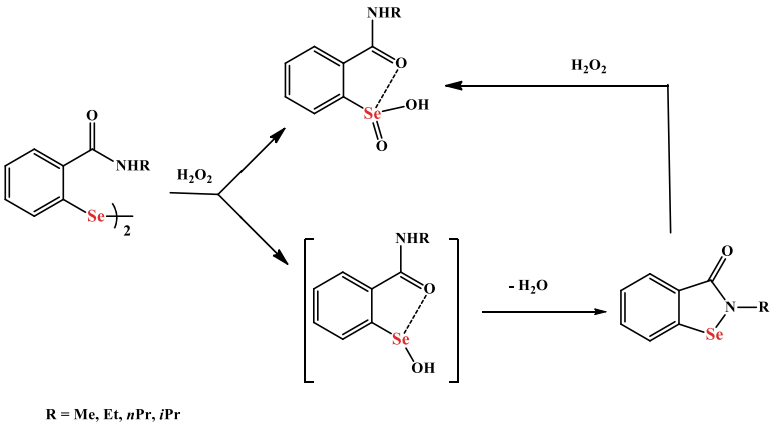

Scheme 13.51 Selenenic acid species with Se–O non-bonded interaction

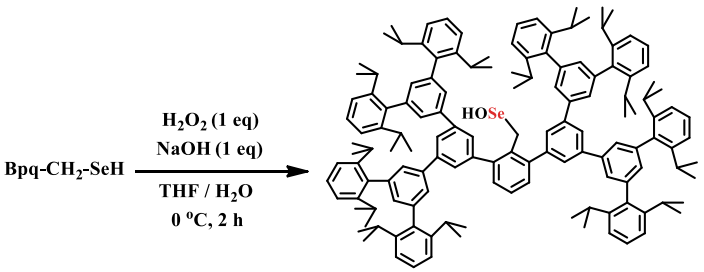

(Bsq = *m*-phenylene dendrimer framework)

Scheme 13.52 Isolation of stable selenenic acid using bulky organic moiety

and aromatic seleninic acids are obtained by oxidation of diselenides or selenocyanates with concentrated HNO_3, H_2O_2, potassium permanganate ($KMNO_4$) in acetic acid or chlorine in aqueous medium (Scheme 13.53).

Nitration of aromatic groups can be observed on oxidation of aromatic selenium compounds with HNO_3 [169]. Hydrolysis of organoselenium trihalides affords seleninic acids. Isolation of trihalides can be circumvented if chlorination or bromination of diselenides is carried out in aqueous media [170]. Other oxidants like dimethyldioxirane (DMD) [163, 171] and ozone [172] were also utilized for conversion of selenium compounds to seleninic acids. Oxidation of selenenic acid species, tripSeOH by DMD afforded the corresponding seleninic acid, tripSe(O)OH in quantitative amounts (Scheme 13.54) [163]. Similarly, polyfunctional seleno esters, such as Se-glucopyranosylphenyl seleno acetate, were oxidized by using DMD to seleninic acid [171]. Further oxidation of seleninic acids like PhSe(O)OH by H_2O_2 resulted in peroxyseleninic acids, PhSe(O)OOH, which find applications in Baeyer–Villiger oxidation of various carbonyl compounds (Scheme 13.55) [173].

Although isolation of optically pure seleninic acid is a tedious process due to their apparent racemization, seleninic acids are optically active molecules. Kamigata et. al., obtained the enantiomeric pure forms of seleninic acids by using either a chiral column in medium pressure liquid chromatography or chiral crystallization (e.g. MeSeOOH) [174, 175].

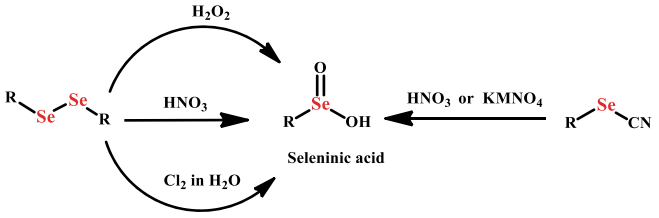

Scheme 13.53 Various synthesis routes of seleninic acid

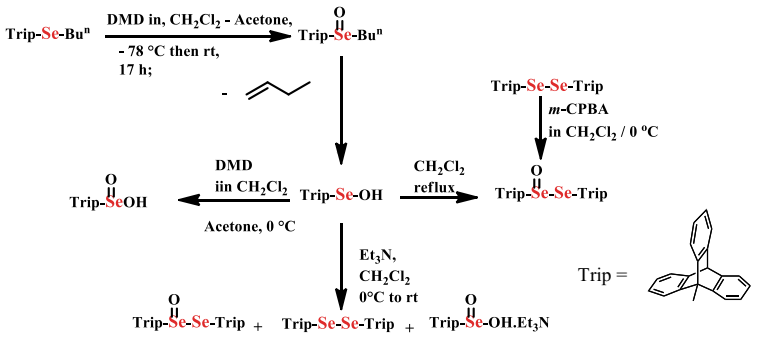

Scheme 13.54 Oxidation of polyfunctional seleno esters

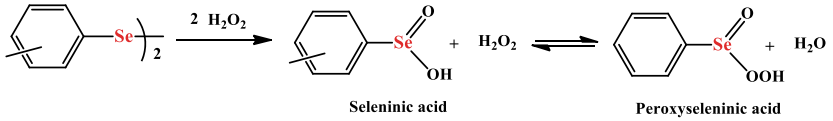

Scheme 13.55 Over oxidation of diaryl diselenides leading to seleninic and peroxyseleninic acids formation

It should be noted that the oxidation of seleninic acids by using strong oxidizing agents, like $KMnO_4$ in aqueous KOH, results in the formation of potassium salts of selenonic acid, RSeOOOK. The selenonic acids are strong oxidizing agents and can be reduced to seleninic acids in conc. HCl.

13.12.8 Selenoesters

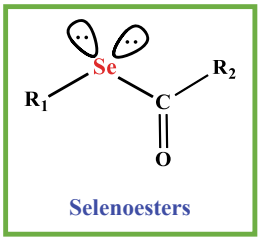

It is one of the important classes of organoselenium compounds exhibiting biological activities with promising biomedical applications. Recently this class has attracted attention due to the lability of Se–CO ester bond. In earlier developments, selenium compounds were employed for prevention of various disease states in humans, mainly through their supplementation. But since the appropriate supplementation depends on species like selenomethionine or sodium selenite, which proved to have limited solubility and bioavailability resulting in limited activity. To overcome this limitation, other selenium species were needed to be explored. Hence the organoselenium compounds which will liberate selenium species easily in situ were thought to be explored. Hence, the class of selenoesters was explored for biomedical applications. Eventually, the selenoethers exhibited potent applicability in treatment of cancer, due to their cytotoxicity and capacity to reverse multidrug resistances (MDR) [176]. The $COSeCH_2COCH_3$ and $COSeCH_2CO(CH_3)_3$ moieties have proved their importance as cytotoxic, apoptosis inducing, chemopreventive, antiproliferative agents and adjuvants in cancer treatments. They exhibited GPx like catalytic activity also [177]. Additionally, the selenoesters were reported to exhibit antiviral, antimicrobial and antibiofilm activities also [178]. Recently, these compounds like imidazole based heterocyclic selenoesters exhibited utility for chemical detoxification of mercuric chloride ($HgCl_2$) [179].

The compounds are useful as reagents in organic synthesis processes [180] even for peptide bond formation and peptide ligation reactions (Schemes 13.56 and 13.57) [181]. The amides based on carbohydrate moieties were conveniently prepared in good yields from various substrates like pyranosyl and furanosyl derivatives. This strategy is dependent on the in situ generations of lithium selenocarboxylates by reactions of elemental Se with a reducing agent superhydride ($LiEt_3BH$) and carboxylic acids or acyl chlorides and their treatment with sugar azides [182]. They have been used in synthesis of organometallic complexes as molecular precursors for deposition

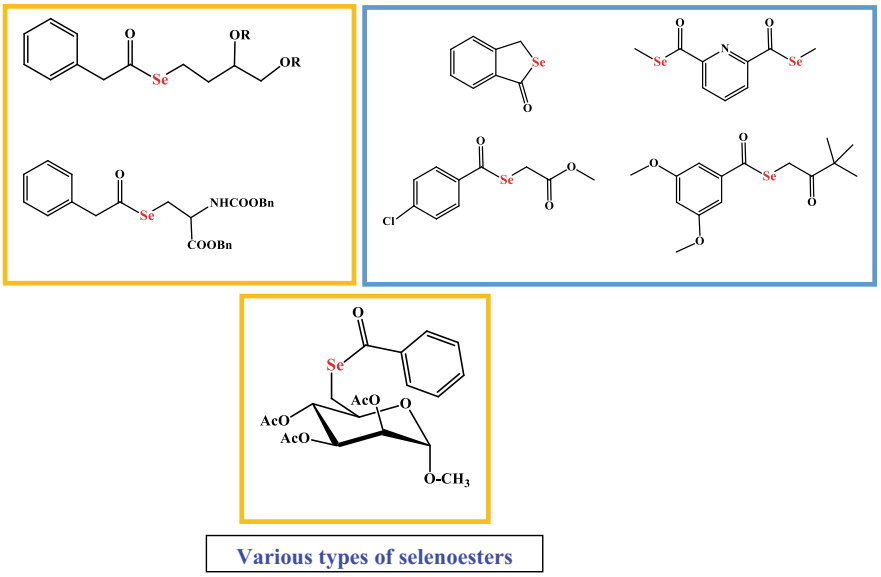

Scheme 13.56 Application of selenoester in glycopeptide ligation through a direct aminolysis

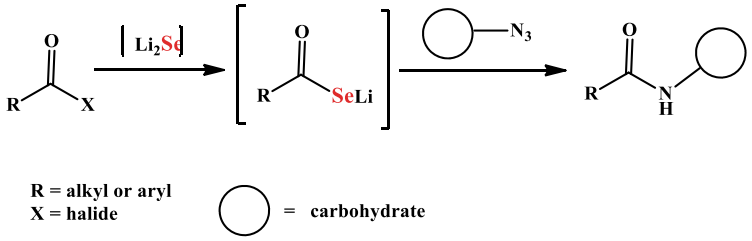

Scheme 13.57 Application of selenoester in peptide bond formation

of metal chalcogenides. Especially the selenocarboxylates have exhibited potential applications for materials preparations [183].

The selenoesters can be conveniently synthesized by treatment of sodium hydrogen selenide (NaHSe) with acyl chlorides followed by treatment with chloroacetamide (Scheme 13.58) [183b]. Additionally, reactions of diaryl and dialkyl diselenides with aldehydes afforded selenoesters. In such reactions, di-*tert*-butyl peroxide (DTBP) is a promoter of C–H selenation of aldehydes by using the diselenides under metal free and solvent free conditions (Scheme 13.59) [184].

Additionally, the synthesis of selenoesters starting from selenoalkynes followed by an acid catalyzed, redox neutral oxyarylation process was also reported. The activation of a selenoalkyne by Brønsted acid resulted in a selenium stabilized vinyl cation, which was captured by an aryl sulfoxide and undergone a sigmatropic rearrangement to afford α-arylated selenoester product (Scheme 13.60) [185].

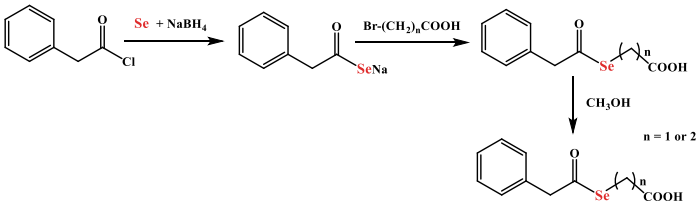

Scheme 13.58 Synthesis of selenoesters

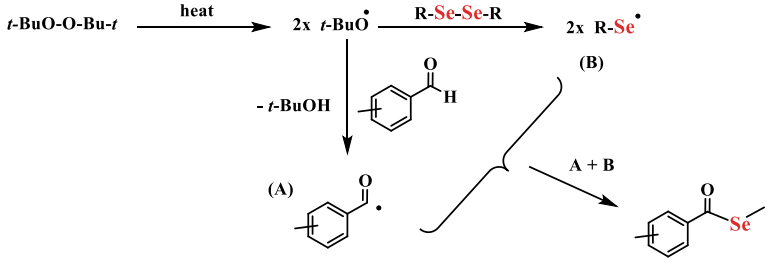

Scheme 13.59 Selenoester synthesis via DTBP promoted the C–H selenation of aldehydes

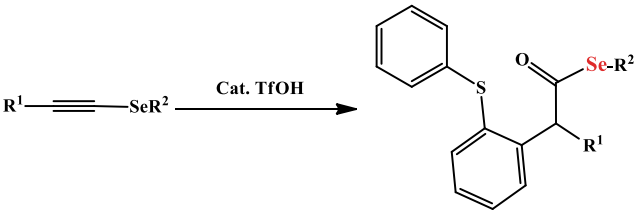

Scheme 13.60 Synthesis of selenoester from selenoalkyne

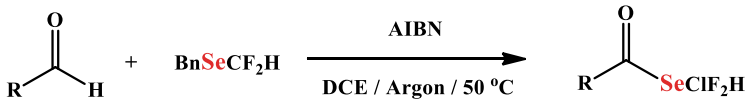

R = alkyl, aryl,
alkenyl or heteroaryl

Scheme 13.61 Synthesis of selenoesters from aldehydes

Recently, difluoromethylselenoesters are efficiently synthesized from aldehydes and $BnSeCF_2H$ through a radical process. The reaction is catalyzed by AIBN (Scheme 13.61) [186].

This brief account of selenoesters clearly depicts the importance of selenoesters in biomedical applications. Since it is not well explored yet, this gives an opportunity for researchers for further pharmacological studies.

13.12.9 Selenoanhydrides

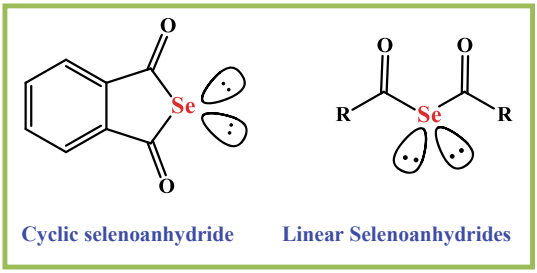

The selenoanhydride class is analogous to earlier discussed selenoethers. This class has also attracted attention recently for biological activities. Due to structural and physicochemical similarity selenoanhydrides also exhibit pharmacological properties similar to selenoethers.

The selenoanhydrides exhibited potent anticancer activities. They were observed to trigger apoptosis in majority (>80%) of MDR mouse cells. Additionally, they possess the ability to reverse the cancer multidrug resistance (MDR) [176]. One of the compounds from this class, phthalic selenanhydrides exhibited diverse biological activities including anticancer, cancer MDR, apoptosis inducer, efflux pump inhibitor as well as antimicrobial activities. They exhibited antioxidant radical scavenging activities also. It was conveniently synthesized by phthalic anhydride by lithiation strategies (Scheme 13.62) [187].

It was also synthesized by treatment of phtholyl chloride (in toluene) with Na_2Se prepared in situ by treatment of elemental selenium and $NaBH_4$ in an aqueous solution. The phase transfer catalyst tetrabutylammonium hydrogen sulphate was utilized as phase transfer catalyst (Scheme 13.63) [188].

The linear selenoaldehydes were also synthesized (Scheme 13.64) by treatment of benzoyl chloride with LiAlHSeH. Further, the obtained selenoanhydrides were used

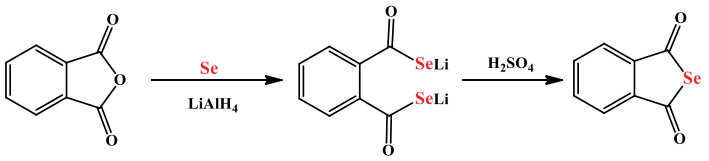

Scheme 13.62 Synthesis of phthallic selenoanhydride from phthallic anhydride

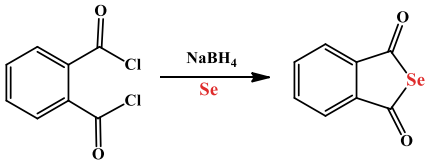

Scheme 13.63 Synthesis of phthallic selenoanhydride from phtholyl chloride

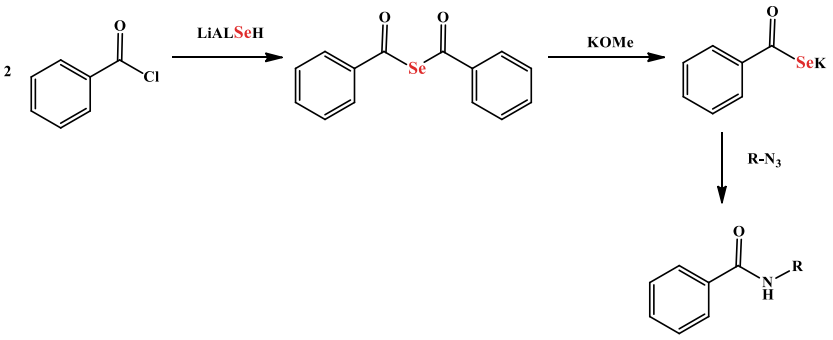

Scheme 13.64 Synthesis of linear selenoaldehyde and its application

for amide bond formation through a reaction of potassium selenocarboxylates with aromatic azides at room temperature. Such strategies have importance in synthesis of bioactive molecules [189].

In view of the recent applications of selenoanhydrides in biomedical domain, we have a lot of scope for their further detailed studies.

13.12.10 Diorganoselenenyl Sulphides (RSe-SR′)

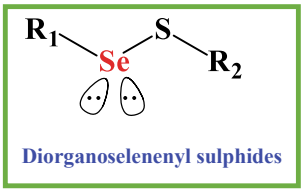

The diorganoselenenyl sulphides are well known important intermediates formed in the catalytic cycle of glutathiome peroxidase (GPx). The high reactivity of diselenides with thiols has been utilized for the synthesis of selenenyl sulphides [190]. This process was employed for the synthesis of selenenyl sulphide glycopeptides [191] and selenenyl sulphide bearing lipids [192] also, which were characterized by using mass spectroscopic analyzes. The reaction of ebselen and its analogues with aromatic thiols yielded selenenyl sulphides (Scheme 13.65), which exhibit strong Se–O intra-molecular interactions [192]. These interactions prevent the regeneration of catalytically active selenol species resulting in low catalytic activity of ebselen analogues in the presence of thiols and hence such species are considered as the dead-end products [193]. Additionally, the hypervalent T-shaped selenenyl sulphides, $\{2\text{-}R_2NCH_2C_6H_4\}Se\text{-}SP(S)R'_2$, exhibiting weak intra-molecular Se–N (~2.67 Å) interactions [194], have been isolated by redistribution reactions between diorganodiselenides and bis(diorganophosphinothioyl)disulfanes, $[R_2P(S)S]_2$. The diorganoselenenyl sulphides have also been prepared by the treatment of RSeX with the sodium salt of a thiol.

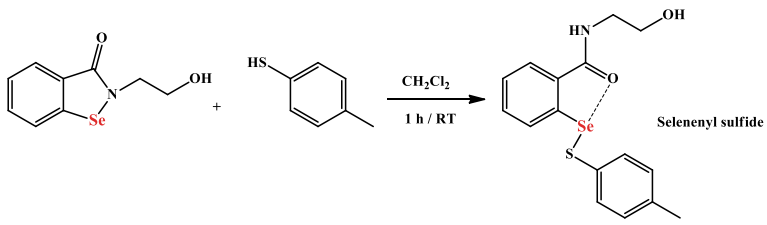

Scheme 13.65 Synthesis of ebselen based selenenyl sulphide

Additionally, the *N*,*N*-dimethyl diselenide react with benzene thiols to yield the selenenyl sulphide species (Scheme 13.66),

In case of GPx mimetic activities, G. Mugesh et al., have proved that selenenyl sulphides play a key role. The attack of thiols at S atom of selenenyl sulphide is more favoured for the forward reaction resulting in formation of harmless products from the hydroperoxides (Scheme 13.67) [195].

Additionally, selenenyl sulphides can be obtained by reactions of selenenic acids with thiol cofactors, as a part of GPx mechanism (Scheme 13.68) [196].

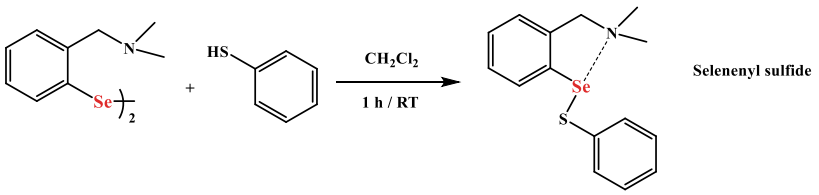

Scheme 13.66 Synthesis of *N, N*-dimethylbenzyl amine based selenenyl sulphide

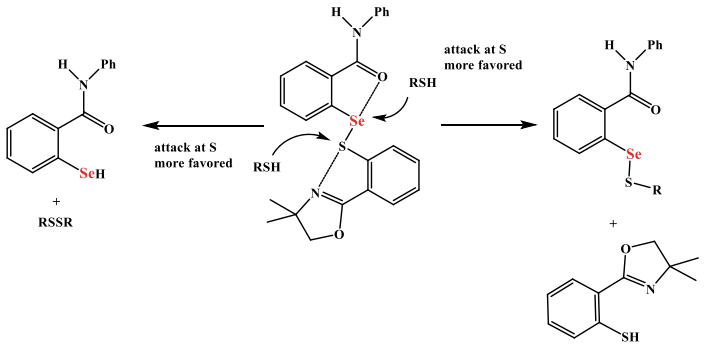

Scheme 13.67 Selenenyl sulphide key intermediate in GPx mechanism

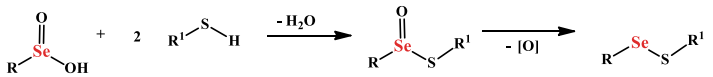

Scheme 13.68 Formation of selenenyl sulphide in GPx mimetics

13.12.11 Selenols (ArSeH) and Selones (Ar=Se)

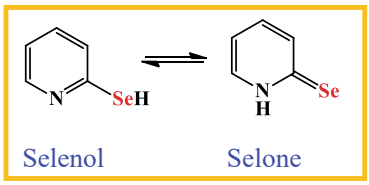

Selenols are biologically important moieties as they constitute the active site of selenoenzymes in the form of selenocysteine (Sec) moiety. The enhanced catalytic activity of selenoenzymes is a result of easy deprotonation or dissociation of Sec group at physiological pH (7.4). This phenomenon is possible because of improved physicochemical properties of selenol as compared to analogous thiol group. Some biologically important molecules like a histdine based amino acid selenoneine (Se analogue of ergothioneine) found in Tuna fish and in skin of Beluga whales, constitute the active centre of Se in the form of selone form. In fact, the selenol and its tautomeric form selone are present in equilibrium in synthetic molecules (as seen earlier). However, in case of enzymes, the selenol is stabilized because of hydrogen bonding with neighbouring amino acids. In view of biological importance of selenol and selone, it is worthwhile to synthesize these compounds and utilize them for their pharmacological applications. Hence, their appropriate design and synthesis are important.

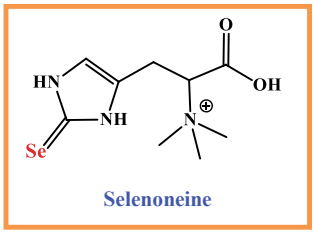

The selenols are selenium analogues of thiols and alcohols. They are stronger acids than the corresponding thiols (pKa of PhSeH 5.9 and pKa of PhSH 6.5). They can be easily oxidized to diselenides by aerial oxidation and hence they must be generated in situ for any kind of reaction. The selenols have been synthesized by various methods (Scheme 13.69) [197–200]. Some common methodologies for their synthesis are discussed now. The treatment of organolithium species or Grignard reagent with elemental selenium followed by hydrolysis by using dilute acids afforded the selenol species. Such reactions were often accompanied by the formation of selenides, diselenides and H_2Se as the by-products. For example, carboraneselenol ($B_{10}H_{11}C_2SeH$) was prepared by lithiation route. Accordingly, the treatment

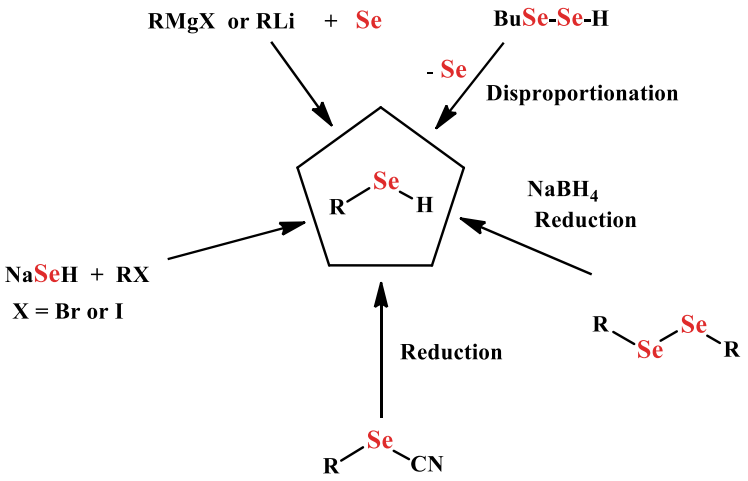

Scheme 13.69 Various routes for synthesis of selenol

of 1,2-dicarba-closo-dodecaborane with *n*-BuLi in DME followed by selenium insertion with elemental Se followed by hydrolysis by aqueous HCl [201]. This reaction was accompanied by formation of diselenide as a by-product. The treatments of organic halides [202] or aromatic diazonium bromides [203] with sodium biselenide (NaHSe) or Na_2Se_2 are other general strategies for preparation of selenols. Generally, organic bromides and iodides are utilized in such reactions. Additionally, the selenols were obtained conveniently after reduction of diselenides by various commonly used reducing agents like sodium borohydride [204] and hypophosphorus acid (H_3PO_2) in hydrochloric acid or in organic solvents [203, 205]. The thiols like PhSH, dithiothreitol (DTT^{red}) [206, 207] and Bu_3SnH [208] were also used for reduction of diselenides, but in such reactions selenenyl sulphides (RSe-SR′) and $Bu_3SnSeAr$, respectively were also observed. Hydrolysis or reductions of selenocyanates in alkaline conditions were also used for synthesis of selenols [198, 209]. Additionally, the aliphatic and aromatic selenocyanates (RSeCN) were reduced by zinc powder in acidic conditions affording the selenols. The treatments of alkylsulfates with potassium selenide and reactions between selenourea and *tert*-butylmalonodialdehyde [202] in ethanolic solutions at refluxing conditions were also employed to obtain the selenols (Scheme 13.70). In addition to this, pyridyl based selenol species were

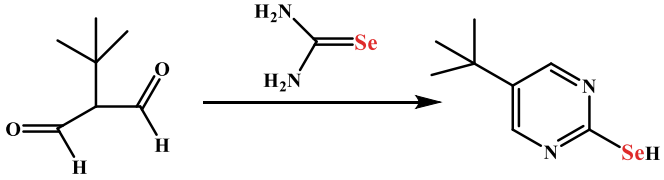

Scheme 13.70 Synthesis of selenol using selenourea

obtained by reactions of bromo-functionalized pyridyl compounds with a sodium selenol (Scheme 13.71).

Although the selenols were easily oxidized to diselenides, natural enzymes stabilize them by hydrogen bonding with neighbouring amino acids. Along with this, inventive human minds have used strategies like stearic hindrance for selenol stabilization. Accordingly, the stable selenol was obtained by using a bulky organic framework (Bmt). The stearic hindrance of bulky organic groups restricts the selenol group from easy oxidation (Scheme 13.72) eventually afforded a stable selenol.

Along with synthesis methodologies, it is worth to discuss about reactivates of selenols. These species get easily deprotonated in basic solutions to give selenolate ions. Selenols consisting of unsaturated N-heterocyclic moieties exhibit tautomerism. Hence selenol and corresponding selone (C=Se linkage) exists in equilibrium [210, 211] which can be isolated easily. For example, in case of pyridyl based selenides (pyridyl, pyridinol, nicotinamide, etc., the selenol and selone were identified as two discrete species, e.g. 2-pridyl selenol and 2-pryridylselone (Scheme 13.73) [210].

Similarly, in case of reduction of di-nicotinamide diselenide by $NaBH_4$ in ethanolic solution, initially, the selenol and selones were observed to coexist, but as time proceeds only the selone form was observed as a stable and dominating species in a solution (Scheme 13.74).

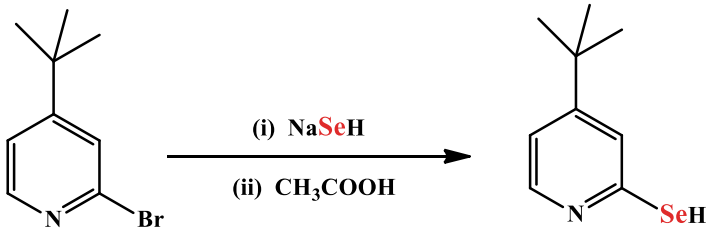

Scheme 13.71 Synthesis of pyridyl based selenol

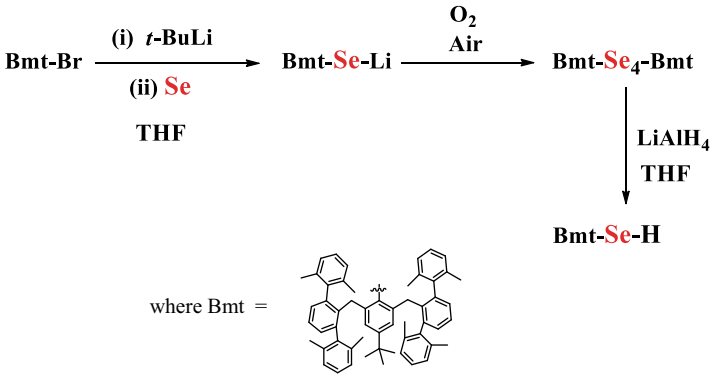

Scheme 13.72 Isolation of selenol with bulky organic moiety

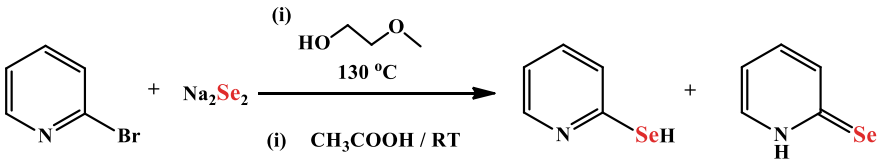

Scheme 13.73 Existence of selenols and selone as a mixture

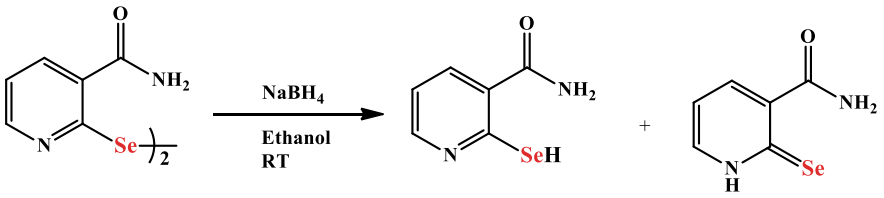

Scheme 13.74 Synthesis of nicotinamide based selenol and selone

The oxidation of both, selenol and selone lead to formation of corresponding diselenides as we have seen earlier.

Their high reactivates of selenols and their conjugate bases, i.e. selenolates (RSe–) attributable to their high energy highest occupied molecular orbitals (HOMO) and are weak bases but potent nucleophiles and react easily with electrophilic organic and inorganic compounds [197, 198]. The selenols are significant reagents for conjugating organoselenium moieties with organic molecules either by reaction with epoxides, organic halides, carboxylic acid chlorides, etc. or addition to carbon-carbon multiple bonds. Selenols were observed to undergo addition of Se–H bond to alkynes to afford α,β-unsaturated organoselenium compounds [212]. Additionally, the non-catalytic (radical or base initiated) or photochemical addition reactions were progressed through non-stereoselectively to afford a mixture of anti-Markovnikov products, whereas palladium catalyzed processes resulted in Markovnikov products (Scheme 13.75) [213].

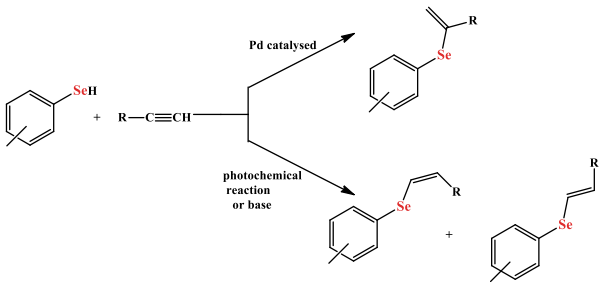

Scheme 13.75 Reactivity of aryl selenol

13.12.12 Organoselenium Halides (RSeX)

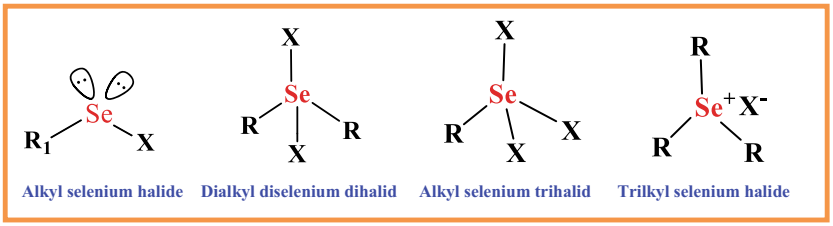

The class of organoselenium halides perform functions as the electrophilic reagents for introducing selenium atoms in organic moieties. These compounds exist in diverse oxidation states viz., +2 (RSeX) and + 4 (R_3SeX, $RSeX_3$ and R_2SeX_2) (X = halides). The stability of an individual organoselenium halide depends on nature of X and the organic moiety attached to selenium atom. The organoselenium halides existing in +4 oxidation state are less stable. For example, the oxidative addition of bromine to diorgano monoselenides (R_2Se) afforded diorganoselenium dibromide (R_2SeBr_2) which are susceptible to decomposition on standing (lose bromine and/or bromoalkanes). Hence, they must be freshly prepared in situ for their use in organic synthesis processes [214]. Additionally, phenyl selenenyl trichloride ($PhSeCl_3$) obtained by reaction of Ph_2Se_2 with SO_2Cl_2 (1:3) in $CHCl_3$, is utilized for inserting a selenium atom at α-position of ketonic substrates [215]. The trihalides ($RSeX_3$) on heat treatment in a vacuum above their melting points were observed to decompose affording relatively stable selenenyl halides and halogens. Further, the selenenyl halides find applications mainly as electrophilic reagents for selenenylation reaction. On way of synthesis, selenenyl halides (RSeX) were also synthesized by treatments of diorgano diselenides with halogens or halogenating agents like sulphuryl chloride (Scheme 13.76). The selenocyanates (RSeCN) were susceptible for cleavage by solutions of chlorine or bromine in chloroform affording selenenyl halides.

The potential reactivity of selenenyl halides is attributable to the low-lying lowest unoccupied molecular orbitals (LUMO) which makes them effective electrophiles. Among them, phenyl selenenyl halides (PhSeX where X=Cl or Br) are commonly used electrophilic reagents, *e.g.*, selenenylation of olefins and carbonyl compounds [216, 217]. On the other hand, nucleophilicity of halide atoms in organo-selenenyl halides usually resulted in diving side reactions during organic synthesis processes. As a result, various non-halide compounds were developed which exhibited similar reactivities with RSeX, e.g. trifilate (RSeOTf) reagent is preferred over RSeX. Other such preferred compounds were obtained by the treatments of RSeX with suitable silver salts (Scheme 13.77) [218–222].

Let's discuss about the reactivity of selenenyl halides with other organic substrates affording the useful products. The treatment of selenium electrophiles with alkenes

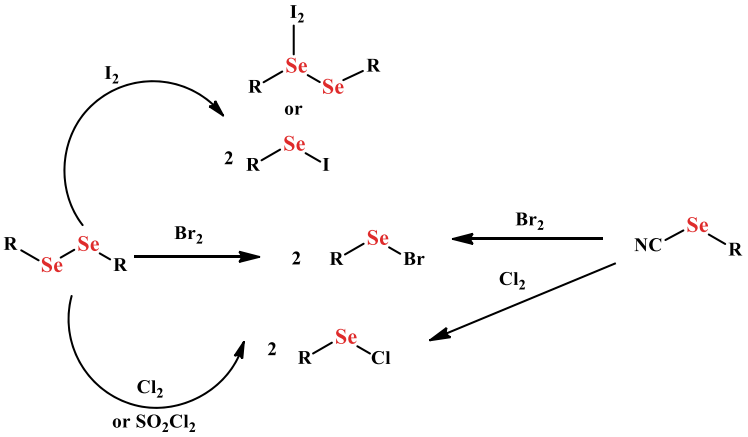

Scheme 13.76 Various routes for synthesis of selenenyl halides

Scheme 13.77 Reactivity of selenenyl halides with Ag salts

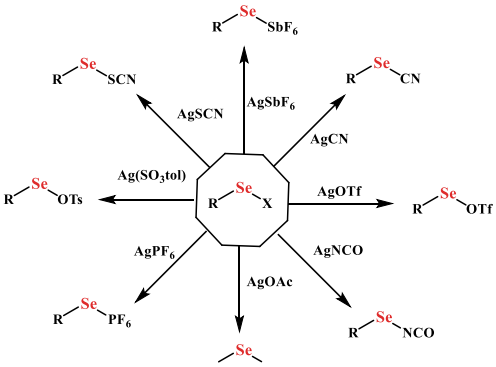

Scheme 13.78 Reactions of aryl selenenyl halides with alkenes

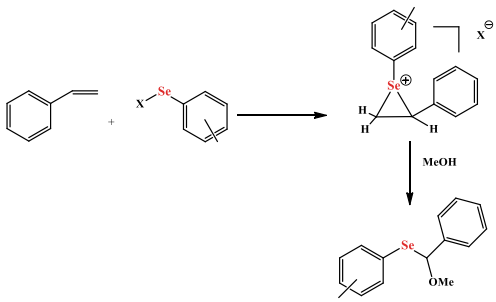

proceeds in a stereospecific manner and progresses through a formation of seleniranium ion as an intermediate. The nucleophilic attack resulted in the opening

of seleniranium ion ring giving addition products (Scheme 13.78) [217]. The α-phenylselenocarbonyl compounds were prominently used to afford olefins through a selenoxide elimination reaction. It should be noted that the 2- and 4-pyridyl seleno groups are preferred leaving group than phenyl seleno moieties in selenoxide elimination reactions (Scheme 13.79) [223–225]. The pyridyl based seleno compounds formed the enone species in excellent yields, even in reactions where reasonable yields were not obtained with α-phenylselenocarbonyl compounds. Additionally, the selenenyl halides were found to react with esters at low temperatures and undergo selenolactonization reactions (Scheme 13.80) forming the cyclic selenide species [226].

The selenenyl chlorides and bromides exist as discrete molecules, but their analogous iodo compounds demonstrate significant structural diversity. The selenenyl halides based on bulky organic moieties [227] or aryl moieties having hetero atoms (O or N) on the pendant arms [228, 229] generally exist as RSeI with a covalent Se–I bond. Most of the selenenyl iodides are charge transfer (CT) species in which Se–Se bond of diselenide species remain intact. The iodide (I_2) molecule interacts either with a selenium atom {e.g. biphenSe_2I_2, $Me_2Se_2{\cdot}I_2$, $(4\text{-}FC_6H_4)_2Se_2{\cdot}I_2$} [230, 231] to afford a three-coordinate spoke structure. In another way, I_2 molecule coordinates with both Se atoms forming a centrosymmetric dimer {e.g. $(Ph_2Se_2{\cdot}I_2)_2$} (Scheme 13.81) [232].

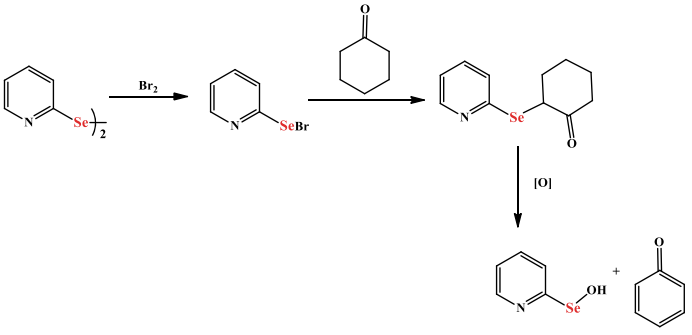

Scheme 13.79 Reaction of pyridyl selenenyl halide to form selenides

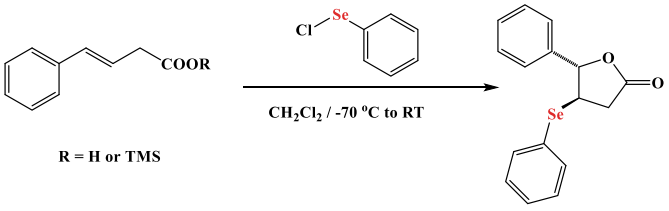

Scheme 13.80 Selenolactonization of selenenyl halides

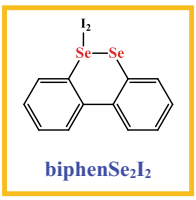

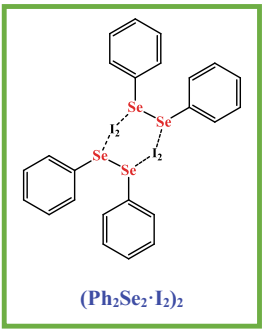

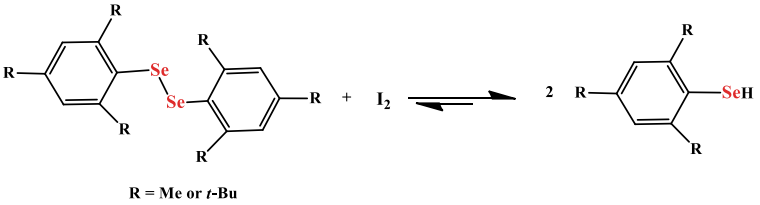

Scheme 13.81 Iodine mediated synthesis of aryl selenol from aryl diselenides

It is known that the electron donating alkyl or aryl groups which increase basicity of selenium atom result in charge transfer selenenyl halide compounds [233]. A charge transfer compound (1:1) containing a covalent Se–I bond, e.g. p-$ClC_6H_4SeI{\cdot}I_2$ was isolated by treatment of $(p\text{-}ClC_6H_4Se)_2$ with three molar equivalents of iodine [231]. The presence of Se···X (X=N, O, S) non-bonding interactions in various organo-selenenyl halides was observed in several compounds which were authenticated by X-ray crystallography and NMR spectroscopic analyzes. Such interactions were supported theoretically also by density functional theory calculations (Scheme 13.82) [234].

Scheme 13.82 Synthesis of selenenyl halide from bulky diselenide

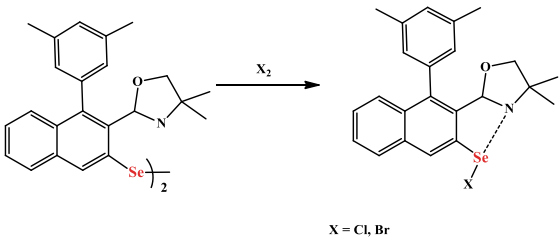

13.12.13 Selenocynates (RSeCN)

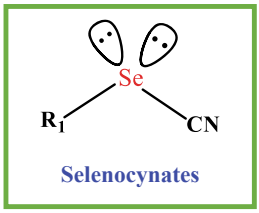

The compounds belonging to selenocynate class also exhibit potential pharmacological applications. They have demonstrated antioxidative, antistress, radioprotecting, anticarcinogen, chemopreventive, antimutagenic and antileishmanial pharmacological properties [235]. Most of the organic selenocyanates have been conveniently synthesized by treatment of appropriate organic moieties with potassium selenocyanate (KSeCN) which is highly toxic and foul-smelling compound. Hence precautions must be taken while synthesis. Generally, diselenocyanates like selenium diselenocyanate or selenium dicyanate have been reported. The selenocynates are conveniently synthesized by the treatment of cyanide ions with selenenyl halides or cyanogen bromide with selenolates. One example of selenocynate synthesis is discussed here. The isoquinoline based selenocynate was conveniently synthesized. The biologically active naphthalimide based compound, 2-(2-selenocyanic acid ethyl ester)-1*H*-benz[*d*]isoquinoline-1,3-(2*H*)-dione is anticipated to exhibit anticancer, antitumour and other potential therapeutic properties of considerable potency with low systematic toxicity [236]. Various organoselenocyanate compounds with 1,8-naphthalimide moiety were synthesized as shown in (Scheme 13.83). In this process, their hydroxyl derivatives were converted to corresponding bromo derivatives by their treatment with phosphorous tribromide in a

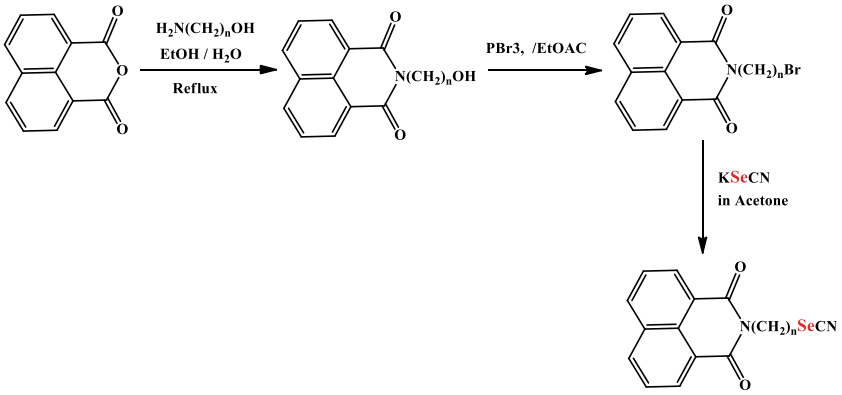

Scheme 13.83 Synthesis of isoquinoline based selenocynate

polar solvent like ethyl acetate (70 °C). The subsequent nucleophilic substitution of a bromide group with anhydrous KSeCN in acetone with refluxing conditions afforded the desired organoselenocyanates.

Furthermore, selenocyanates are often used in preparation of other selenium derivatives.

13.12.14 Cyclic Selenides

The class of cyclic selenides has gained importance since the ebselen—a cyclic selenamide has exhibited potent pharmacological properties and subsequent applications as drug as we have discussed earlier. The cyclic selenide species are found as intermediates or really active pharmacological species as we have discussed earlier. The prominent examples this class are discussed now.

(i) **Selenolanes (tetrahydroselenophene)**

The class of organoselenium, compound consists of the cyclic monoselenide species. These compounds have proved their importance in pharmacological studies due to their potency as an antioxidant, glutathione peroxidase (GPx) mimic, radioprotector, an anti-inflammatory agent and ulcer curative agents. The well known compounds are 3,4-dihydroxy selenolane (DHS^{red}) [237], monoamine selenolane (MAS) [238] and their derivatives with fatty acid conjugates as well as α-seleno tocopherols.

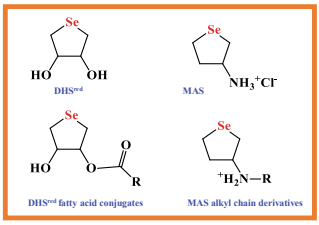

It is necessary to discuss the synthesis of some compounds. The DHS^{red} is conveniently synthesized by reaction of 1,3-butadiene diepoxide by the reaction with sodium hydrogen selenide (NaHSe) in aqueous medium (Scheme 13.84a, b) [239], was treated with various acid chlorides (RCOCl) or strong bases like NaH and further treatment with halo functionalized moieties to obtain various compounds with fatty acids (Scheme 13.85) [240] or bioactive organic and luminescent moieties like indolyl and naphthyl based compounds respectively for biological applications (Scheme 13.86) [241].

Additionally, different kinds of cyclic monoselenide compounds having hydroxylated selenolane rings were synthesized by the treatment of monobenzylated petioles and aldoses dithioacetals with NaHSe (obtained from reaction of elemental Se and $NaBH_4$) in good yields (Scheme 13.87) [242].

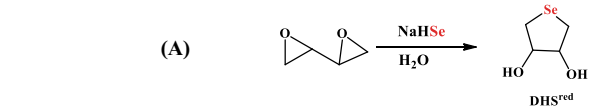

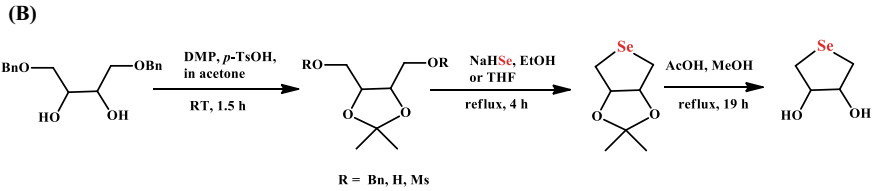

Scheme 13.84 Synthesis of DHS^{red}

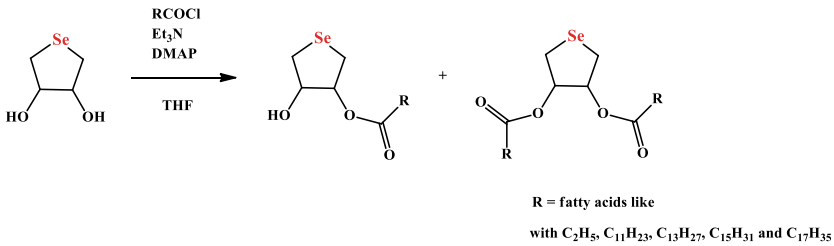

Scheme 13.85 Synthesis of fatty acids substituted derivatives of DHS^{red}

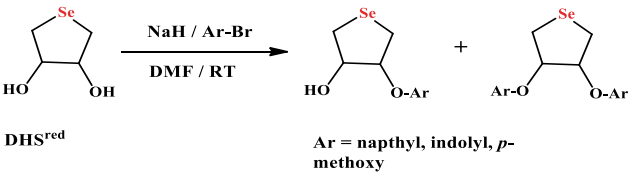

Scheme 13.86 Luminescent and bioactive moieties substituted derivatives of DHS^{red}

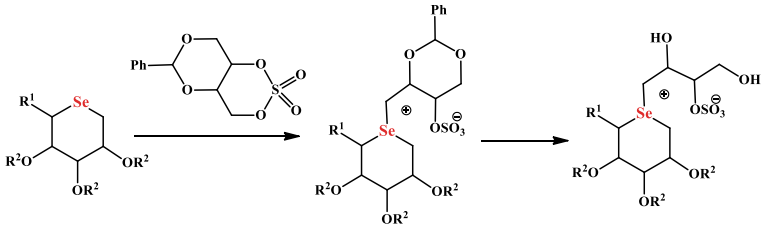

Scheme 13.87 Synthesis of cyclic selenolanes

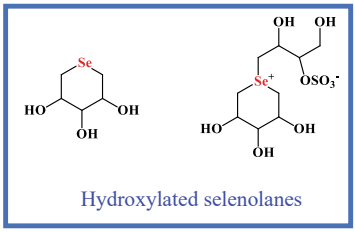

Furthermore, selenolanes were also prepared by the treatments of hydroxylated aliphatic compounds by selective bromination of terminal hydroxyl groups which reacted with selenide ions (Se^{2-}) obtained in situ by reaction of elemental Se with $NaBH_4$) as depicted below (Scheme 13.88) [242].

(ii) **Selenamides**

The cyclic selenamides like ebselen were conveniently prepared by some modifications in the method of lithiation of benzanilide by BuLi followed by Se insertion and subsequent oxidation with hydrogen peroxide (Scheme 13.89) [243].

With slight modification by using $CuBr_2$ induced oxidative cyclization after lithiation and selenium insertion of step L. Engman et al., have reported the efficient synthesis of ebselen [244]. Additionally, the nitro-, azo- and amino derivatives of ebselen were also reported by L. Engman et al., which exhibited the cytoprotective activities (Scheme 13.90) [245].

Recently, Mugesh et al., have reported various derivatives of ebselen which exhibited potent antioxidant activities (Scheme 13.91) [246].

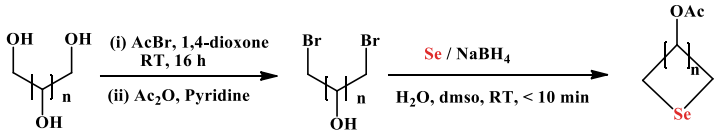

Scheme 13.88 Synthesis of selenolanes

Scheme 13.89 Synthesis of ebselen

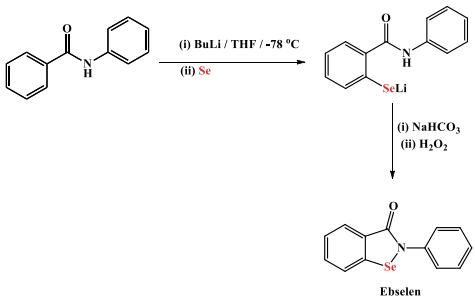

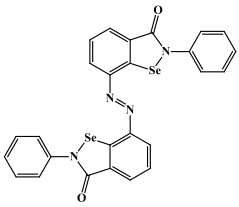

Scheme 13.90 Aazo-derivatives of ebselen

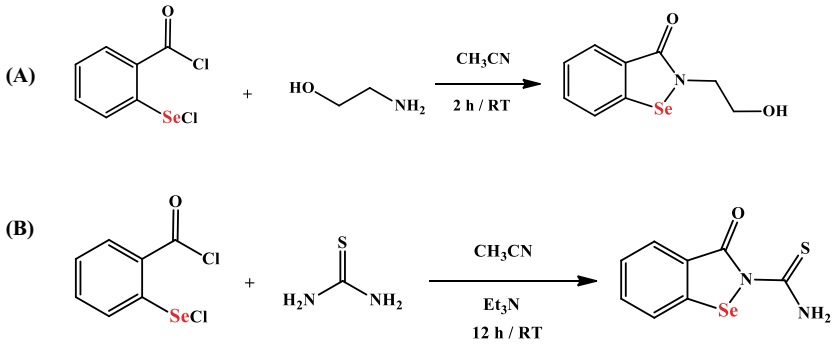

Scheme 13.91 Synthesis of ebselen derivatives

Similarly, the five and six membered selenoheterocyclic compounds viz., 1,2-benzoselenazine and 1,2-benzoselenazols respectively which are the homologues of ebselen have also been reported (Scheme 13.92) [247].

In view of the pharmacological importance of ebselen compounds, they were further developed by fluorescent tags since fluorescence-labelled probes containing

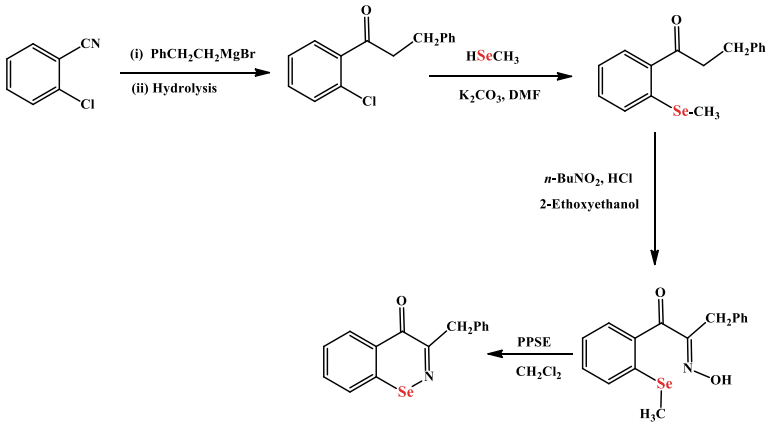

Scheme 13.92 Synthesis of six membered selenoheterocyclic

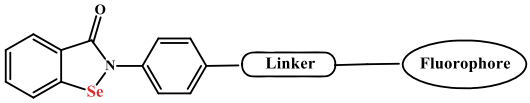

Scheme 13.93 Fluorescence-labelled probes containing ebselen

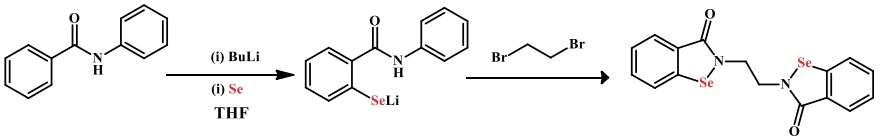

Scheme 13.94 Synthesis of ethaselen

ebselen suitable for mechanistic, biological and medicinal studies. E.g. coumarin-tagged activity-based probes' bearing the ebselen was explored (Scheme 13.93) [248].

The ebselen analogue, ethaselen was synthesized by lithiation of benzanilide in THF at lower temperatures, followed by selenium insertion and treating the selenolate with 1,2-dibromoethane (Scheme 13.94) [249].

In view of the established pharmacological importance of ebselen, ethaselen and related compounds, the researchers have a good scope for further development in synthetic strategies for addition of new features in their structures appropriately for enhancing the activities.

13.12.15 Selenopeptides

The peptides which contain selenocysteine (Sec/U), a 21st proteinogenic amino acid moiety are known as selenopeptides. They are the constituents of selenoproteins which acts as redox enzymes and are essential for living organisms as they participate in diverse biological processes such as the control of cellular redox balance [250]. The Sec moiety is supposed to be the most conservative substitution for cysteine (Cys) residues belonging to proteins or enzymes. The Sec imparts the interesting properties to selenoenzymes due to difference in pKa of Sec (pKa ~5.5) and thiol group (pKa ~ 8.3) of Cysteine residues. In such processes, one or more Sec residues are inserted co-translationally in proteins. Also, the redox properties of disulphides and diselenides differ significantly, since the redox potential of diselenides being significantly lower than corresponding disulphides. Hence, the strategy of replacement of Cys by Sec is increasingly used in protein engineering approaches for modulating the desired properties of constituent peptides in selenoproteins. Hence, this interesting class of selenopeptides has fascinating and characteristic properties which enables them for diverse range of applications such as modulating stability, physicochemical properties structural, functional and mechanistic probes, robust scaffolds,

enzymatic reaction design, peptide conjugations and folding tools. Hence, design and synthesis strategies have significance especially for structure activity relationship (SAR) studies for further design of selenopeptides for appropriate applications [251].

One typical example of designed selenopeptide is as shown below.

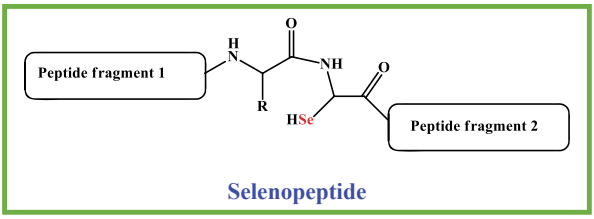

Various synthesis strategies have been adopted for synthesis of selenopeptides. The selenopeptides synthesis started with solution phase or solution method in 1964 as evidenced by reported synthesis for selenoglutathione [252, 253]. Later, the Boc-SPPS (solid state peptide synthesis) stratergies for synthesis of metalloselenoein were started to use in 1991 [254]. Further, the chemical ligation strategies were developed in 2007 for synthesis of Se15P [255]. Additionally, the selenopeptides and proteins have been obtained by recombinant expression methods [256]. Later, various types of selenopeptides have been reported by modified methods of synthesis [257].

In general, by the chemical synthesis strategies, the peptides are synthesized by two major procedures (i) solution method and (ii) a solid phase method carried out on a resin. The peptide synthesis is based on following basic chemical principles (i) selection of protecting groups for amino acids, followed by deprotection and (ii) peptide bond formation. Hence, the strategies for peptide synthesis in solution can be directly applied to solid phase methodology.

Among them, the native chemical ligation (NCL) requires extensive organic synthesis strategies. One example of the NCL strategy is given below [258] (Scheme 13.95).

Similarly, the cyclic selenopeptides can also be prepared by native chemical ligation method (Scheme 13.96) [259].

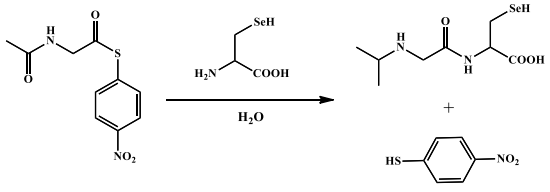

Scheme 13.95 Synthesis of selenopeptide through native chemical ligation

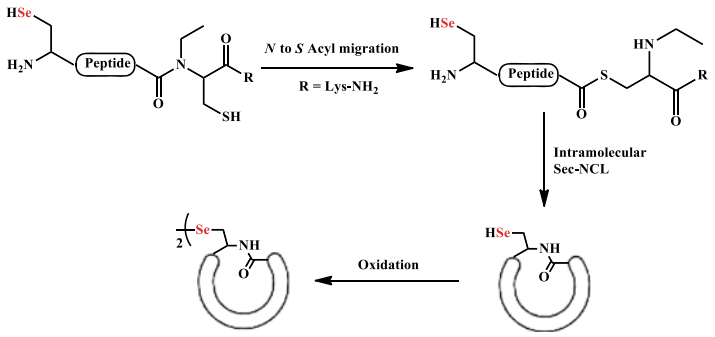

Scheme 13.96 Synthesis of cyclic selenopeptides

13.12.16 Selenium Containing Peptides

This class of compounds consists of the organoselenium compounds bearing the peptide bond. Inspired from the selenoenzymes, the mimics like ebselen developed and they exhibited potential antioxidant, radical scavenging, GPx mimicking, radioprotecting activities. For further development in activities and achieving biocompatibility for bio relevant applications, the peptide frames were utilized for designing the organoselenium molecules.

The appropriate peptide frameworks were initially designed and then Se moieties were couple with them to obtain the desired compounds. In one such approach, the phenylseleno N-acetyl-α-amino acids were designed. The treatment of glycine with chloroacetyl chloride in a basic aqueous medium at lower temperatures (0–5 °C) afforded a chloro functionalized peptide frame which on treatment with $PhSe^{-}Na^{+}$ (phenylselenolate) in ethanol yielded the selenium containing peptides as shown in (Scheme 13.97). Such compounds as evidenced from single crystal XRD analyzes are associated through hydrogen bonding leading to supramolecular assemblies. It

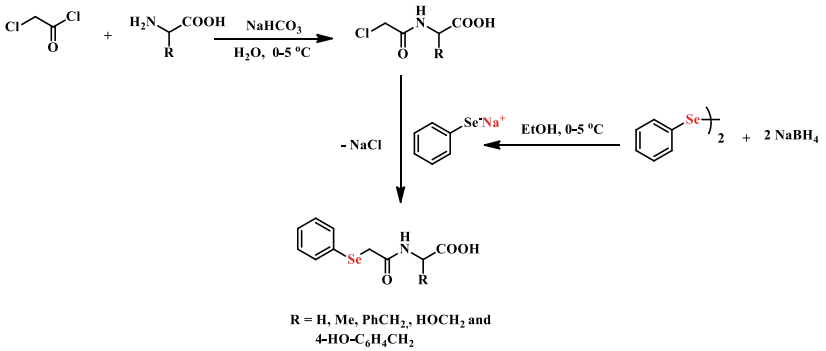

Scheme 13.97 Synthesis of phenylseleno N-acetyl-α-amino acids

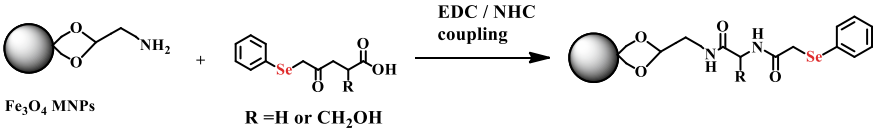

Scheme 13.98 Conjugation of N-acetyl α-amino acid compounds on Fe_3O_4 MNPs

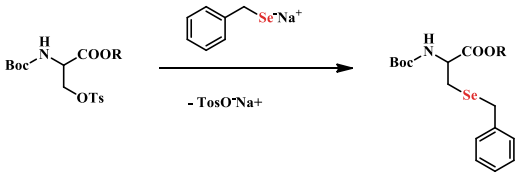

Scheme 13.99 Synthesis of Se-benzyl-L-selenocysteine based peptides

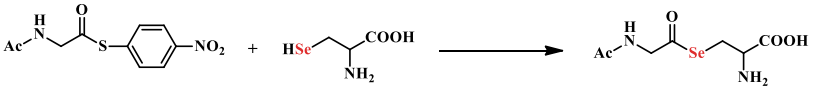

Scheme 13.100 Synthesis of selenium containing peptides

was observed that the variation of amino acid fragments results in stabilizing different motifs of secondary structures. These Se containing peptides exhibited free-radical scavenging activities. The additional feature of their supramolecular assembly may be useful for exploring their biological and medicinal applications [260].

In further developments for their targeted delivery, Fe_3O_4 (MNPs) based formulations of selenoglycine and selenoserine based selenium compounds were prepared for targeted delivery. The EDC-NHS coupling reaction was employed for formation of peptide bond between COOH group of selenium compound and primary amine functionalized over surface of MNPs [261] (Scheme 13.98). The formulations exhibited the DPPH radical scavenging activities.

In earlier reports, the Se-benzyl-L-selenocysteine based peptides have been reported. Their synthesis strategies proceed through nucleophilic displacement of the *O*-tosyl moiety in *O*-tosylated serine derivatives and *O*-tosylated serine residues within peptides by sodium benzyl selenolate (Scheme 13.99) [262].

Similarly, following selenium containing peptides have been synthesized by nucleophilic displacement by selenocysteine selenol group (Scheme 13.100) [263].

13.12.17 Semisynthetic Selenoproteins/Enzymes

It was discussed earlier regarding biochemical importance of a selenoenzyme GPx. It is now established that GPx has potential therapeutic value as an antioxidant,

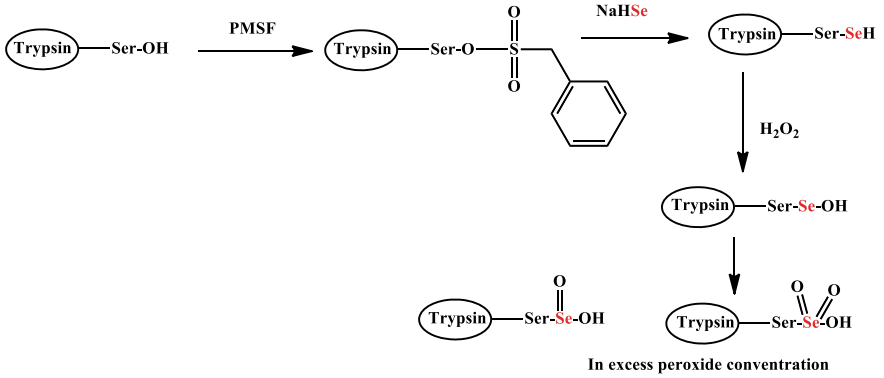

Scheme 13.101 Typical synthesis of serin based selenoenzymes

however, its pharmacological progress was restricted because GPx is known to use a selenocysteine as its catalytic site and it is difficult to generate selenium containing proteins with traditional recombinant DNA technology. Hence, the new strategies were designed in order to obtain the selenoproteins. The naturally occurring proteins like subtilisin or trypsin can be chemically modified to generate the semisynthetic selenoenzyme which exhibited GPx activity. This modification can confer exceptional structural and catalytic properties to proteins and enzymes. The chemical modification strategies were developed to replace the serine residues with selenocysteine. The serin groups can be activated by phenylmethanesulfonyl fluoride (PMSF) to give sulfonated products which on treatment with strong nucleophiles like NaHSe for insertion of Se in the native host proteins. The chemically modified selenoenzymes like selenosubtilisin [264], selenoglutathione transferase [265] and selenotrypsin [266] exhibit high GPx activities due to their high biocompatibility and enhanced physicochemical properties (Scheme 13.101).

In another approach, the semeisynthetic selenoproteins/enzymes can also be prepared by peptide ligation on the target proteins. One example of intein-mediated peptide ligation with peptides containing N-terminal Sec residues is shown below (Scheme 13.102) [263]. This method also utilizes chemical treatment strategies.

13.12.18 Selenium Containing Bio-materials

The class of selenium containing biomaterials constitutes the dendrimeric or polymeric compounds which bear one or more Se atoms at their active centres. Such compounds find promising biomedical applications for controlled drug release or as synthetic enzyme mimics. Earlier, researchers have developed responsive polymeric materials for controlled drug release or diagnosis but therapeutic applications have not achieved till expectations. Hence the design of specific materials which

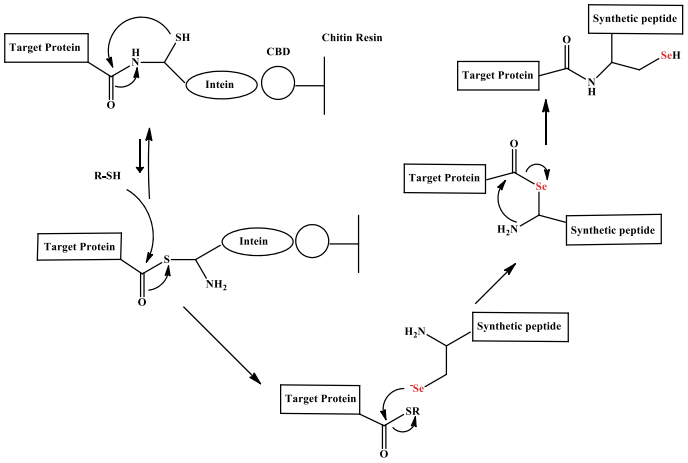

Scheme 13.102 Synthesis of selenoproteins by peptide ligation on the target protein

precisely respond to physiologically relevant concentrations, within the micromolar or nanomolar concentration range is still challenging.

Hence such compounds have been designed to obtain biomaterials with unique properties and that respond to mild biochemical signals or biomarkers related to disease states. In view of this, the selenium containing biomaterials have been developed. The reason for use of selenium compounds is unique bond energy conferring the C–Se or Se–Se covalent bonds a dynamic character and make them responsive to mild stimuli. Therefore, selenium containing copolymers, hyperbranched selenium containing polymers and dendrimeric materials can disassemble in response to changes under physiological relevant conditions. This property of selenium containing biomaterials renders them as promising biomaterial for controlled drug release or their use as synthetic enzyme mimics.

In developing such materials, the main skill is in the synthesis of selenium containing main chain block copolymers. An example is dialkyl diselenide containing polyurethane (PUSeSe) blocks. They were then synthesized via stepwise polymerization of toluene diisocyanate in slight excess with mono- and diselenide containing diols and finally terminated by PEG monomethyl ether. They are denoted as PEG-PUSeSe-PEG and a monoselenide analogue PEG-PUSe-PEG (Scheme 13.103). They have been utilized for doxorubicin drug delivery applications in combination with radiotherapy for anticancer applications [267].

Other selenium containing materials like PEG_{43}-b-PAA_{153}-SeQTA exhibited GPx like enzyme mimetic activities (Scheme 13.104).

Hyperbranched polyselenides (HBPSe)

The HBPSe species were synthesized by using diverse strategies. They exhibited GPx mimicking catalytic activities (Schemes 13.105 and 13.106) [274].

(A)

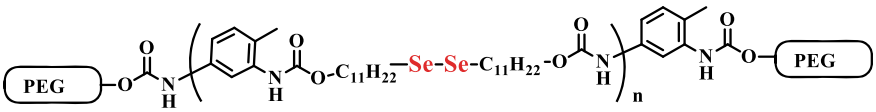

(B)

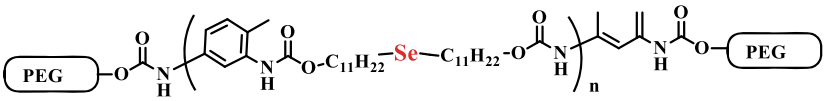

Scheme 13.103 Selenium containing main chain block copolymers **a** PEG-PUSeSe-PEG and **b** PEG-PUSe-PEG for drug delivery applications

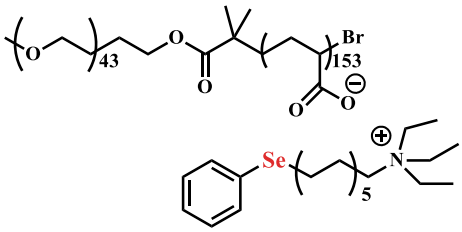

Scheme 13.104 Selenium biomaterial PEG_{43}-b-PAA_{153}-SeQTA exhibiting GPx activity

(A)

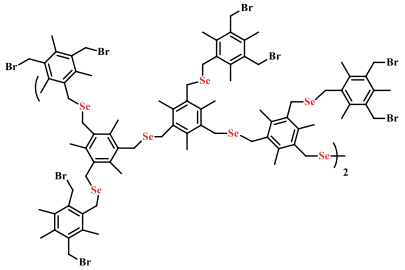

(B)

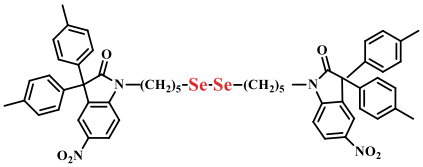

Scheme 13.105 Hyperbranched polyselenides A and B acting as GPx mimics

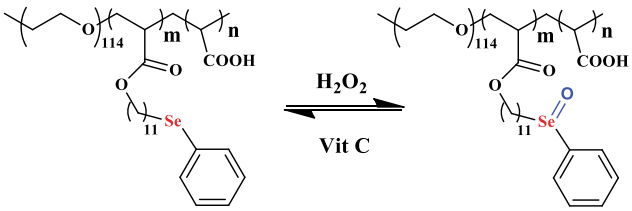

Scheme 13.106 Selenium biomaterials in GPx mimetics

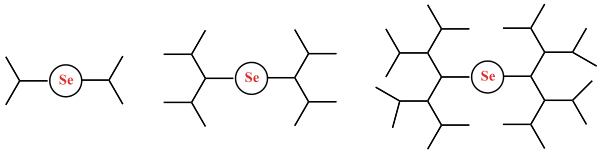

Scheme 13.107 Dendrimeric selenium biomaterials

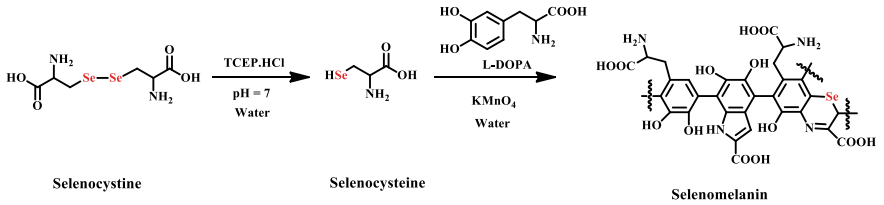

Scheme 13.108 Synthesis of selenomelanin

Dendrimeric compounds containing Selenium

The selenium cantered dendrimeric compounds have also been reported which find applications for a targeted drug delivery (Scheme 13.107).

Furthermore, the selenomelanin NP was synthesized through an oxidative copolymerization reaction of L-DOPA and selenocystine in aqueous solutions at neutral pH (Scheme 13.108) [268].

13.12.19 Organic Polyselenides

This class of organoselenium compounds consists of a limited number of compounds due to inherent instability leading to decomposition. There are very few reports which depict that the triselenide species have superior GPx activity when compared to their diselenide analogues [269]. The example is a diorganoyl triselenide species bearing 2-phenyl-5,6-dihydro-4H -1,3-oxazine moiety. It was synthesized by initial ortho lithiation by *n*-BuLi in Et_2O followed by selenium insertion and subsequent

oxidation leading to a mixture of corresponding diselenide and triselenide. The latter can be converted to diselenide by treatment with Br_2 followed by sodium borohydride (Scheme 13.109). Although the triselenide derivative is interesting and its crystal structure is also reported, a triselenide cannot be a suitable drug candidate due to its relative instability [270].

Further, the organo-triselnide, bis[4-methyl-1,3-dithiol-2-one] triselenide was reported to form unexpectedly in reactions of 4-methyl-5-tri-*n*-butylstannyl-1,3-dithiol-2-one and selenium dioxide. Although the compound is fairly stable since the crystal structure has been determined in the same report, its utility in biological studies is not yet reported (Scheme 13.110) [271].

Further tetra or higher oregano polyselenides are scarcely known unlike the sulphur analogues the polysulphide moieties are present as constituents in vegetables of *Allium* family like garlic [272]. Additionally, the organic polyselenide ions have been obtained; along with material applications their utility for biological applications is also observed [273].

The organic moieties based hyperbranched polyselenide were synthesized and they exhibited GPx like catalytic activities [274]. This has been already discussed

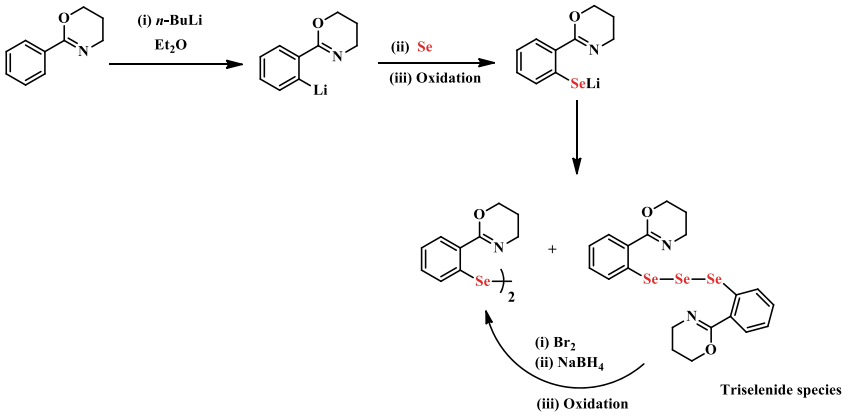

Scheme 13.109 Synthesis of triselenides

Scheme 13.110 Synthesis of triselenide

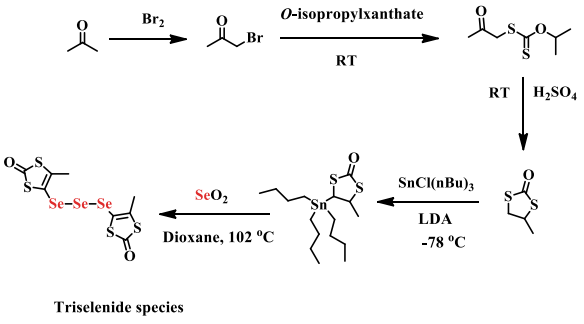

in class of selenium biomaterials. Although such polyselenides were explored for biological applications, still the potential selenium based materials are not used in therapeutics.

In view of the relative instability of organic polyselenides, the utility for biological and therapeutic applications is hampered. It gives the researchers a lot of scope for stabilizing such species by the structural modifications using appropriate organic frames. This will be helpful for further pharmacological applications since the compounds will be analogous to polysulphides present in vegetables, which play vital role in human health.

13.12.20 Inorganic Selenium Compounds—In Biological Applications

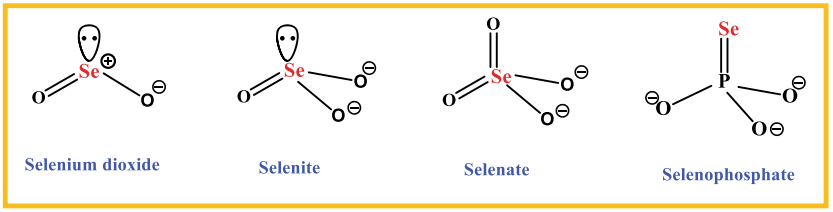

The inorganic selenium species like elemental Se (Se^0), selenium dioxide (SeO_2), its alkali metal salts (Na or K) of selenides (Se^{2-}), selenite (Se^{4+}), selenate (Se^{6+}) are known to exist in nature [275]. These selenium species can be found in air, natural water and soil in a varied concentrations. These species are water soluble (except Se element), hence can easily enter food chain from through root absorption of plants and then further plays its most important role in producing selenoproteins and selenoenzymes through the intermediacy of selenophosphate ($PSeO_3^{3-}$) in mammal. It is now established that the Se plays a crucial role in maintenance of heath of mammals as well as plants [276]. The deficiency of selenium causes diverse disease states, ill immunity and its excess lead to selenium toxicity. The type of selenium species found is a result of its oxidation state. It may change according to ambient conditions, such as pH and microbial activity. The various Se species established in the mammalian selenium metabolism are depicted in Scheme 13.111 [277]. Further, the importance of selenophosphate has been shown in Scheme 13.112 [278].

Particulate Se enters in air because of volcanic eruptions or burning coal or oil. Majority of Se in air is bound to fly ash and to suspended particles. The selenium element available in fossil fuels leads to formation of selenium dioxide during their burning as fuels. The selenium dioxide (SeO_2) observed to form selenious acid (H_2SeO_3) by reacting with moisture or sweat exerting harmful effects on human health. It is also observed that the selenium anhydride was released in the

Scheme 13.111 Selenium species identified in selenium metabolism

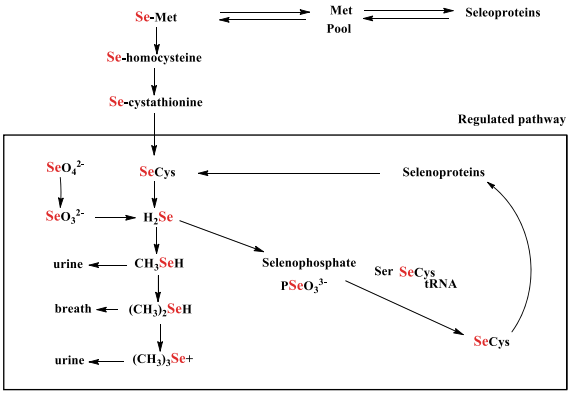

Scheme 13.112 Role of selenophosphate in health

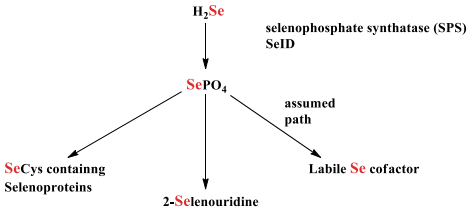

heating processes of lead, zinc and copper and selenium containing ores. Most toxic, hydrogen selenide is also released in environment from industrial processes [279].

The Se released in environment is helpful ultimately for health but its high concentration leads to toxicity as we have already discussed.

Synthesis strategies for selenite and selenate species

The sodium selenite and sodium selenate can be conveniently prepared by the reaction of selenium dioxide with sodium hydroxide in aqueous medium (Eq. 13.1) [280].

$$SeO_2 + 2\ NaOH\ aq. \rightarrow Na_2SeO_3 + H_2O \tag{13.1}$$

The hydrated form of sodium selenite gets converts to an anhydrous salt after heat treatment at 40 °C.

Additionally, the treatment of elemental Se with nitric acid (HNO_3) in aqueous medium leads to formation of selenious (selenous) acid (H_2SeO_3) which on neutralization with sodium carbonate (Na_2CO_3) yields the sodium selenite (Eqs. 13.2 and 13.3).

$$Se\ +\ 2\ HNO_3 \rightarrow\ H_2SeO_3 +\ NO\ +\ NO_2 \tag{13.2}$$

$$H_2SeO_3 +\ Na_2CO_3 \rightarrow Na_2SeO_3 +\ H_2O\ +\ CO_2 \tag{13.3}$$

Further, the sodium selenite is oxidized in a basic medium by hydrogen peroxide to form a sodium selenate (Eq. 13.4) [281].

$$Na_2SeO_3 + H_2O_2 \rightarrow Na_2SeO_4 + H_2O \tag{13.4}$$

13.12.21 Inorganic Selenium Compounds—In Commercial and Material Applications

There are diverse synthetic inorganic selenium species like polysenides or their alkali metal salts, transition metal clusters and transition metal selenides (PdSe, ZnSe, $CuInSe_2$, $CuInSnSe_4$, etc. The synthetic inorganic selenides or metal selenides find applications mainly in optoelectronic, thermo-electric and electroluminescent devices, IR detection and imaging, solar cells, rechargeable batteries and industrial processes for rendering appropriate properties to the products. Selenium compounds are extensively used in paints, dyes, glass, electricals, rubber, insecticides and industries. The selenium in form of nanoparticles has been used in textiles, paints, antimicrobial coatings, keyboards, engineering, electronics, cosmetics, food industry, biosensing, wound dressings and even in biomedical devices [282]. The lithium polyselenides are used in Li-Se batteries [283]. It was observed that the cyclic Se_8 molecules in ordered mesoporous carbon greatly improved the Li–Se battery performance [291a], similarly, sodium polyselenides were also conveniently prepared [291b]. The polyselenides have also been utilized to produce selenium films by electrochemical deposition [284]. The polyselenides exhibited applications for reaction strategies for preparation of metal chalcogenides also [285]. Some DMF soluble metal polyselenide frames are shown below (Scheme 13.113). Their thermolysis afforded the

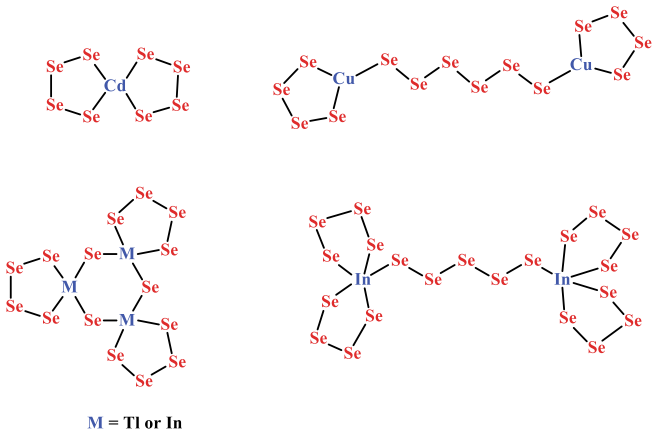

Scheme 13.113 Metal polyselenide frames as precursors for metal selenides by thermolysis

binary metal selenides like CuSe, InSe, TlSe, etc., useful for electronic applications [293b].

The $[SbSe_4Cu(\mu_2\text{-}Se_4)]^{4-}$ cluster containing a five-numbered $\{Cu(\mu_2\text{-}Se_4)\}$ ring have been treated with $Mn(dien)_2$ to obtain the heterobimetallic complexes like a copper-antimony polyselenide, $[Mn(dien)_2]_2[SbSe_4Cu(\mu_2\text{-}Se_4)]$. Their thermolysis leads to formation of ternary materials (Scheme 13.114). This report was the first example of Cu-Sb polyselenide [286].

Further, the reactions of polyselenides (like $K_2Se_3^{2-}$) with the metal carbonyls yielded the selenometalates with formulae viz., $MoSe_4^{2-}$ and WSe_4^{2-} in a DMF, as shown in equation below (Eq. 13.5) [287].

$$2\,Se_3^{2-} + M(CO)_6 \rightarrow MSe_4^{2-} + Se_2^{2-} + 6CO(M = Mo \text{ or } W) \tag{13.5}$$

Further, MSe_4^{2-} reacted with excess of grey selenium (5 equivalents) at room temperature in DMF solvent yielding the MSe_9^{2-} within 2 h in high yield. Further, slow and equimolar addition of tetrahydrofuran (THF) to deep red crystals of $[(C_6H_5)_4P]_2[MoSe_9]$. The anionic frame is shown below (Scheme 13.115).

Similarly, the reactions of metal carbonyls $[Re_2(CO)_{10}]$ with DMF soluble anhydrous polyselenides (K_2Se_4) yielded the rhenium complexes containing a dianion fragment with polyselenides (Eq. 13.6 and Scheme 13.116). Their further thermal treatment yielded the binary metal selenides [288].

$$\left[M_2(CO)_{10}\right] + Se_4^{2-} \rightarrow \left[M_2(Se_4)_2(CO)_6\right]^{2-} \quad (M = Mn, Re) \tag{13.6}$$

Further, the Mo complexes with cyclic selenides were reported (Scheme 13.117) [289].

The treatments of $(\eta^5\text{-}C_5H_5)_2Mo_2(CO)_6$ with elemental selenium and sodium (Na) in DMF afforded the $[(\eta^5\text{-}C_5H_5)_2Mo_(Se_4)_2]$.

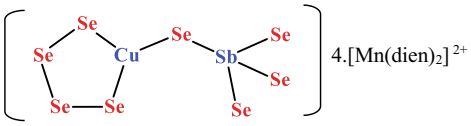

Scheme 13.114 Preparation of heterobimatallic complex

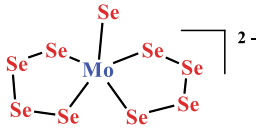

Scheme 13.115 Formation of molybdenum selenide anion $MoSe_9^{2-}$

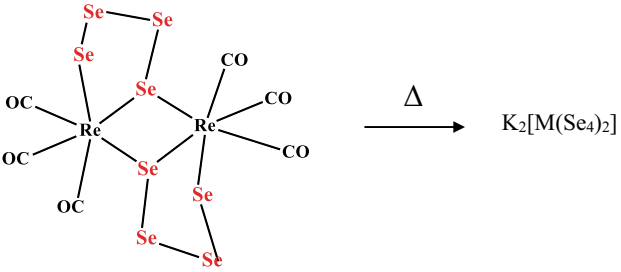

Scheme 13.116 Formation of $K_2[Re_2(Se_4)_2(CO)_6]$ and its thermal treatment leading to formation of $K_2[M(Se_4)_2]$

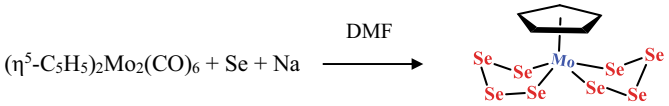

Scheme 13.117 Complexes of molybdenum with polyselenides

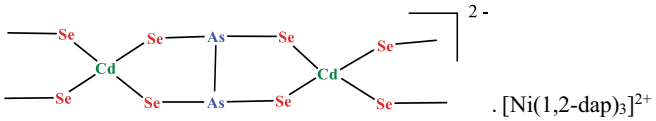

Scheme 13.118 The structure of $[As_2CdSe_4]^{2-}$ chain which forms complex with $[Ni(1,2\text{-dap})_3]^{2+}$

Additionally, the Ni and Zn complexes with cadmium selenidoarsenates like, $[Ni(1,2\text{-dap})_3][As_2CdSe_4]$, $[Zn(1,2\text{-dap})_3][As_2CdSe_4]$ (where 1,2-dap: 1,2-diaminopropane) have been synthesized by solvothermal process (Scheme 13.118) [290]. These complexes exhibited optical properties.

13.13 Characterization of Se and Selenium Compounds

13.13.1 Nuclear Magnetic Resonance (NMR) Spectroscopy

Nuclear magnetic resonance (NMR) technique detects the radiofrequency absorbed by changes in the nuclear spin state. The nucleus with non-zero nuclear spin gives rise to a characteristic spectrum for each nucleus as well as determines the interactions between neighbouring nuclei. This multinuclear characterization property as well as 2D NMR tool has imparted a lot of potential for this technique for elucidating structures mainly for organic, organometallic, inorganic compounds. The variable

temperature NMR is also useful for this cause [291]. The application of NMR spectroscopy for the study of peptides, proteins and nucleic acids provides unique information for structure, the dynamics and chemical kinetics of these biomolecules, over time scales ranging from seconds to pico-seconds [292].

As far as characterization of selenium compounds is concerned, the ^{77}Se isotope possesses spin quantum number ½ and natural abundance of 7.58%. Non-zero spin confers it an NMR active nucleus. Its other useful features are its positive magnetogyric ratio ($\gamma = 5.101$) and relative receptivity (5.26×10^{-4}) with respect to proton [293]. Additionally, in case of ^{77}Se NMR the nuclear Overhauser effects are absent and the longitudinal relaxation times (T_1 ~ 1 to 30 s) is influenced by spin-rotation for analytes consisting of small molecules and chemical shift anisotropy mechanisms for larger molecules [294]. As a result, ^{77}Se NMR spectroscopy has been used prominently as a characterization tool in the area of organoselenium chemistry [295, 296].

While recording the ^{77}Se NMR spectrum the universally accepted reference is Me_2Se ($\delta\ ^{77}Se = 0$ ppm). Due to its volatility and malodorous nature, a fairly stable, odourless solid as secondary reference, i.e. Ph_2Se_2 ($\delta\ ^{77}Se = 463$ ppm) in $CDCl_3$ or C_6D_6 is commonly used.

The chemical shifts for ^{77}Se NMR analyzes are spread over a wide spectral window of about 3300 ppm. The ^{77}Se NMR chemical shifts are highly sensitive to their oxidation states, the stereochemistry of selenium and its local environment [297–300]. The decrease in electron density of selenium (deshielding) is responsible for larger δ values and increase in electron density (shielding) gives smaller δ values in ppm scale. A wide variation in ^{77}Se NMR chemical shifts with respect to the chemical state of selenium can be noted in biologically important compounds [299]. Additionally, the intra-molecular non-bonding Se···X interaction leads to a downfield shift of the ^{77}Se NMR resonance [301]. Approximate linear correlation between the ^{77}Se NMR shifts and the strength of non-bonding Se···X interaction has been found using theoretical calculations [302]. ^{77}Se NMR spectroscopy is now widely used for understanding various processes, like conformational mobility, molecular interactions of selenocysteine (sec) in biological macromolecules, etc., involving selenoproteins in biological samples [303]. Glutathione Peroxidase (GPx) activity of semisynthetic selenoenzymes like selenosubtilisin and designed organoselenium compounds selenonicotinamide has been investigated using ^{77}Se NMR spectroscopy and the presence of selenol (RSeH), selenenic acid (RSeOH), selenenyl sulphide (RSe-SR′) and seleninic acid (RSe(O)OH) species were identified in the catalytic cycle of their GPx like catalytic activities [304, 305].

The presence of other nuclear spins 1/2 nuclei results in spin-spin couplings which appear as satellite peaks and provide invaluable information about the structure and stereochemistry of the molecule. Most of the coupling constants $^{n}J(^{77}Se–X)$ are now reported [306].

13.13.2 Mass Spectrometry

The mass spectrometry is also an appropriate tool for characterization of organoselenium compounds because of a characteristic isotopic pattern exhibited by Se species due to presence of six isotopes viz., ^{74}Se (0.87%), ^{76}Se (9.02%), ^{77}Se (7.58%), ^{78}Se (23.52%), ^{80}Se (49.82%) and ^{82}Se (9.19%) in natural selenium. This has enhanced its utility for systematic characterization of organoselenium compounds. Additionally, mass spectrometry has been largely used for characterization of selenium containing biological species like metabolites in Se-rich yeast. The technique is useful for study of mechanism of pharmacological actions of organoselenium compounds in therapeutics like anticancer treatment [307, 308].

13.13.3 Single Crystal X-Ray Diffraction (XRD) Analyzes

Single crystal XRD is a non-destructive analytical tool that can afford comprehensive data regarding the internal crystal lattice of crystalline matters. It is based on Bragg's law. It correctly identifies the elements depending on electron densities around them which are a characteristic of each nucleus. Hence, it is possible to analyze Se from the crystalline compounds along with its crystal lattice structure.

For employing this technique, we need to grow the crystals of the selenium compounds which diffract the X-rays. There are few general techniques for crystal growth. But the solution methods, at low temperatures or at room temperature with slow evaporation are very commonly used. Other methods include: convection, solvent diffusion, vapour diffusion, reactant diffusion, seeding, sublimation, fluid phase growth. In case of inorganic compounds, the solid state synthesis method can also be used for crystal growth [309].

Hence by obtaining the single crystals we can unambiguously identify the Se from the compound.

13.13.4 Powder X-Ray Diffraction Analyzes (PXRD)

The PXRD analyzes can be performed to authenticate the elemental selenium, its nanoparticle forms as well as inorganic selenium compounds especially metal selenides. The characteristic pattern with appropriate 2θ values is decisive for the crystal lattice systems in which the material exists. The material, as well as biological properties of the selenides, is dependent on the crystal systems. Hence the PXRD is useful for characterization of materials.

13.13.5 X-Ray Spectroscopy Techniques

Energy dispersive X-Ray spectroscopy (EDS/EDX/XEDS/EDXA)

The energy dispersive X-ray (EDX) is a qualitative as well as quantitative X-ray microanalytical technique which offers information pertaining to chemical composition of a test sample except for some lighter elements (atomic number <3). The EDS functions on the principle that high energy electromagnetic radiation (X-rays) incident on sample leads to eject the core electrons of an atom. Since each element has a unique set of energy levels, hence Se from selenium compounds exhibits characteristic X-rays, rendering a qualitative detection of selenium [310].

EDS is used for characterization especially in materials science. It is used effectively in characterization in biomedical research like drug delivery as well as clinical utility.

13.14 Estimation of Selenium

Selenium is an essential micronutrient as well as itvis toxic in higher concentrations. Hence for analyzing safety levels, the estimation of Se from biomedical, food grains, as well as geological, oceanographical and chemical samples is essential. It is present naturally in soil and eventually in water sources and environment. It occurs in the biological materials in a wide range of concentrations which vary from a few parts per billion (ppb) to a few per cent. Hence the various destructive, as well as non-destructive methods, have been employed for analysis or estimation of selenium in the samples from various sources. But currently, the non-destructive techniques for estimation of Se have been preferred [311].

13.14.1 Destructive Analysis Methods

Such methods require the destruction of the organic matter from biological materials is for the analysis of selenium by chemical means. Following this step, there are various methods which can be appropriately used for measuring the Se concentration. Among them, some methods require Se isolation from interfering substances and other methods require heat treatment like ashing or combustion in a closed system and wet digestion.

Inductively coupled plasma-based techniques

This technique is popularly used for estimation of selenium. It has detection limits of approximately the parts per million (1 ppm) levels. Some of the reported techniques for selenium estimation are noted below [312–314].

(i) Inductively coupled plasma mass spectrometry (ICP-MS).
(ii) Inductively coupled plasma—optical emission spectrometry (ICP-OES) or Inductively coupled plasma atomic emission spectroscopy (ICP-AES).
(iii) High performance liquid chromatography/Ion chromatography and inductively coupled plasma mass spectrometry (HPLC-ICP-MS).

13.14.2 Non-destructive Techniques

As the name suggests such techniques don't proceed through the destruction of sample. Hence the sample can be analyzed with multiple appropriate analysis techniques for selenium estimation as well as sample can be re-used for any other studies. There are several reports of such techniques used for analysis of selenium compounds.

Atomic absorption spectroscopy

The various hyphenated techniques were used in AAS. E.g. Electrothermal atomic absorption spectrometry (ETAAS) [315], flow injection hydride generation atomic absorption spectrometry (HGAAS) [316], graphite furnace atomic absorption spectrophotometry (GFAAS), electrothermal atomic absorption spectrometry, (ETAAS) was used for direct determination of selenium in human blood serum, blood plasma. The flame atomic absorption spectrometer (FAAS) was used for detection of selenomethionine (SeMet) and trimethylselenonium ion (TMSe) [312].

Atomic fluorescence spectrometry (AFS)

The AFS is considered an appropriate detection tool for speciation studies. It is a very sensitive and selective method for the determination of environmentally and biomedically important elements. The literature reports its use in detection of diverse selenium species [317]. The AFS has detection limits below the $\mu g\ L^{-1}$ renders it utility for bioanalytical and toxicology related studies.

Neutron activation analysis (NAA)

It is an important non-destructive analytical method used for selenium determination from biological samples [318]. The sample is bombarded with neutrons resulting in the formation radioactive isotopes from target elements. Radioactive emissions, as well as paths of radioactive decay for each individual element, are well established. This information is helpful to study spectra of emissions of radioactive samples and for determination of concentrations of its constituent elements.

Energy dispersive X-Ray fluorescence spectroscopy (EDXRF)

EDXRF is used to determine selenium at 0.1–5.1 $\mu g\ g^{-1}$ levels in biological samples. It is used for analysis of selenium in food grains, vegetables and cereals. It is applied for analysis of geological as well as oceanographical samples also [319].

13.15 Conclusions

In this chapter, various classes of selenium compounds, their applications in biochemical and pharmacological domains have been discussed. Their applications in materials science have been briefly discussed. Hence to perform these functions, it is required to synthesize the desired molecules with specific structural features appropriate for desired application. Hence the strategies to design and synthesis of organoselenium compounds belonging to all these classes have been mentioned. The preparations and precautions needed while syntheses of organoselenium compounds have been briefly mentioned. After synthesis, characterization and purity are most important criteria before any kind of application. Hence the important characterization methods have been discussed. Additionally, the estimation of Se from biological, biomedical samples, environment or chemical sources is an important task. Hence the methods for estimation of Se from biological samples are mentioned. We conclude with hope that this present chapter may be helpful for the beginner researcher in organoselenium chemistry.

References

1. (a) Jin Z, Du X, Xu Y, Deng Y, Liu M, Zhao Y, Zhang B, Li X, Zhang L, Peng C, Duan Y, Yu J, Wang L, Yang K, Liu F, Jiang R, Yang X, You T, Liu X, Yang X, Bai F, Liu H, Liu X, Guddat LW, Xu W, Xiao G, Qin C, Shi Z, Jiang H, Rao Z, Yang H (2020) Structure of Mpro from SARS-CoV-2 and discovery of its inhibitors. Nature 582:289; (b) Sies H, Parnham MJ (2020) Potential therapeutic use of ebselen for COVID-19 and other respiratory viral infections. Free Radic Biol Med 156:107; (c) Yan D, Wang G, Xiong F, Sun W-Y, Shi Z, Lu Y, Li S, Zhao J (2018) A selenium-catalysed para-amination of phenols. Nature Commun 9:4293 (1–9); (d) Mugesh G, du Mont W-W, Sies H (2001) Chemistry of biologically important synthetic organoselenium compounds. Chem Rev 101(7):2125; (e) Nogueira CW, Zeni G, Rocha JBT (2004) Organoselenium and organotellurium compounds: toxicology and pharmacology. Chem Rev 104(12):6255; (f) Freudendahl DM, Santoro S, Shahzad SA, Santi C, Wirth T (2009) Green chemistry with selenium reagents: development of efficient catalytic reactions. Angew Chem Int Ed 48(45):8409; (g) Kanatzidis MG, Huang S-P (1994) Coordination chemistry of heavy polychalcogenide ligands. Coord Chem Rev 130(1–2):509; (h) Bryce MR (1991) Recent progress on conducting organic charge-transfer salts. Chem Soc Rev 20:355; (i) Dutton JL, Ragogna PJ (2011) Recent Developments in the Lewis Acidic Chemistry of Selenium and Tellurium Halides and Pseudo-Halides. In: Woollins JD, Laitinen RS (eds) Selenium and tellurium chemistry. From small molecules to biomolecules and materials. Springer, Heidelberg, p 179; (j) Wirth T (ed) Organoselenium chemistry - modern development in organic synthesis. In: Topics in current chemistry, vol 208. Springer, Berlin; (k) Xu H, Cao W, Zhang X (2013) Selenium-Containing polymers: promising biomaterials for controlled release and enzyme mimics. Acc Chem Res 46(7):1647; (l) Mukherjee AJ, Zade SS, Singh HB, Sunoj RB (2010) Organoselenium chemistry: role of intramolecular interactions. Chem Rev 110(7):4357; (m) Kieliszek M, Lipinski B (2020) Selenium supplementation in the prevention of coronavirus infections (COVID-19). Med Hypotheses 143:109878 (1–2); (n) Stadtman TC (1974) Selenium biochemistry: proteins containing selenium are essential components of certain bacterial and mammalian enzyme systems. Science 183:915; (o) Gudkov SV, Shafeev GA, Glinushkin AP, Shkirin AV, Barmina EV, Rakov II, Simakin AV,

Kislov AV, Astashev ME, Vodeneev VA, Kalinitchenko VP (2020) Production and use of selenium nanoparticles as fertilizers. ACS Omega 5(28):17767; (p) Chen L, Yang F, Xu J, Hu Y, Hu Q, Zhang Y, Pan G (2002) Determination of selenium concentration of rice in China and effect of fertilization of selenite and selenate on selenium content of rice. J Agric Food Chem 50(18):5128; (q) Hassan W, Oliveira CS, Noreen H, Kamdem JP, Nogueira CW, Rocha JBT (2016) Organoselenium compounds as potential neuroprotective therapeutic agents. Curr Org Chem 20(2):218; (r) Stone CA, Kawai K, Kupka R, Fawzi WW (2010) Role of selenium in Hiv infection. Nutrit Rev 68(11):671; (s) Dworkin BM (1994) Selenium deficiency in HIV infection and the acquired immunodeficiency syndrome (AIDS). Chem-Biol Interact 91(2–3):181; (t) Iwaoka M, Arai K (2013) From sulfur to selenium. A new research arena in chemical biology and biological chemistry. Curr Chem Biol 7(1):2; (u) Barbosa NV, Nogueira CW, Nogara PA, de Bem AF, Aschner M, Rocha JBT (2017) Organoselenium compounds as mimics of selenoproteins and thiol modifier agents. Metallomics 9:1703; (v) Occai BK, Hassan W, Rocha JBT (2018) Gender-based behavioral and biochemical effects of diphenyl diselenide in Drosophila melanogaster. Chem-Biol Interact 279:196; (w) Singh N, Halliday AC, Thomas JM, Kuznetsova O, Baldwin R, Woon ECY, Aley PK, Antoniadou I, Sharp T, Vasudevan SR, Churchill GC (2013) A safe lithium mimetic for bipolar disorder. Nat Commun 4:1332 (1–14); (x) Kil J, Pierce C, Tran H, Gu R, Lynch ED (2007) Ebselen treatment reduces noise induced hearing loss via the mimicry and induction of glutathione peroxidase. Hear Res 226(1–2):44; (y) Tieu C, Campbell KC (2013) Current pharmacologic otoprotective agents in or approaching clinical trials: how they elucidate mechanisms of noise-induced hearing loss. Otolaryngology 3(1):130; (z) Hammill TL, Campbell KC (2018) Protection for medication-induced hearing loss: the state of the science. Int J Audiol 57(sup4):S87

2. (a) Cui Y, Zhou Z, Li T, Wang K, Li J, Wei Z (2019) Metal chalcogenides: versatile crystal structures and (opto)electronic applications of the 2D metal nono-, di-, and tri-chalcogenide nanosheets. Adv Funct Mater 29(24):1970161; (b) Zhang T, Zhang L, Yin Y, Jiang C, Li S, Zhu C, Chen T (2019) A thiol-amine mixture for metal oxide towards device quality metal chalcogenides. Sci China Mater 62(6):899; (c) Theerthagiri J, Karuppasamy K, Durai G, Rana AHS, Arunachalam P, Sangeetha K, Kuppusami P, Kim H-S (2018) Recent advances in metal chalcogenides (MX; X = S, Se) nanostructures for electrochemical supercapacitor applications: a brief review. Nanomaterials 8:256 (1–28); (d) Joe J, Yang H, Bae C, Shin H (2019) Metal chalcogenides on silicon photocathodes for efficient water splitting: a mini overview. Catalysts 9:149 (1–37); (e) Freitas JN, Gonçalves AS, Nogueira AF (2014) A comprehensive review of the application of chalcogenide nanoparticles in polymer solar cells. Nanoscale 6:6371
3. (a) Phadnis PP, Mugesh G (2005) Internally stabilized selenocysteine derivatives: syntheses, 77Se NMR and biomimetic studies. Org Biomol Chem 3:2476; (b) Mugesh G, Singh HB (2002) Heteroatom-directed aromatic lithiation: A versatile route to the synthesis of organochalcogen (Se, Te) compounds. Acc Chem Res 35:226
4. (a) Hua G, Woollins JD (2009) Formation and reactivity of phosphorus–selenium rings. Angew Chem Int Ed 48(8):1368; (b) Crich D, Grant D, Krishnamurthy V, Patel M (2007) Catalysis of stannane-mediated radical chain reactions by benzeneselenol. Acc Chem Res 40(6):453; (c) Boyle PD, Godfrey SM (2001) The reactions of sulfur and selenium donor molecules with dihalogens and interhalogens. Coord Chem Rev 223(1):265; (d) Mathur P (1997) Chalcogen-bridged metal-carbonyl complexes. Adv Organomet Chem 41:243; (e) Kanatzidis MG, Huang S-P (1994) Coordination chemistry of heavy polychalcogenide ligands. Coord Chem Rev 130(1–2):509; (f) Rocha JBT, Piccoli BC, Oliveira CS (2017) Biological and chemical interest in selenium: a brief historical account. Arkivoc, part II 457
5. Berzelius JJ (1818) Undersökning af en ny Mineral-kropp, funnen i de orenare sorterna af det vid Fahlun tillverkade svaflet. Afhandl Fys Kemi Mineral 6:42
6. (a) Jones CO (1909) The physiological effects of selenium compounds with relation to their action on glycogen and sugar derivatives in the tissues. Biochem J 4:405; (b) Chabrie C, Lapicque L (1890) Sur l'action physiologique l'acide selenieux. Comp Rend Acad Sci

110:152; (c) Olson OE (1986) Selenium toxicity in animals with emphasis on man. J Am Coll Toxicol 5(1):45

7. (a) Schwarz K, Foltz CM (1957) Selenium as an integral part of factor 3 against dietary necrotic liver degeneration. J Am Chem Soc 79:3292; (b) Muth OH, Oldfield JE, Remmert LF, Schubert JR (1958) Effects of selenium and vitamin E on white muscle disease. Science 128:1090
8. Turner DC, Stadtman TC (1973) Purification of protein components of the clostridial glycine reductase system and characterization of protein A as a selenoprotein. Arch Biochem Biophys 154:366
9. (a) Flohé L, Günzler EA, Schock HH (1973) Glutathione peroxidase: a selenoenzyme. FEBS Lett 32:132; (b) Rotruck JT, Pope AL, Ganther HE, Swanson AB, Hafeman DG, Hoekstra WG (1973) Selenium: biochemical role as a component of glutathione peroxidase. Science 179:588
10. (a) Böck A (1994) Selenium proteins containing selenocysteine. In: King RB (ed) Encyclopedia of inorganic chemistry, vol 8. Wiley, Chichester, p 3700; (b) Flohé L, Andreesen JR, Brigelius-Flohé R, Maiorino M, Ursini F (2000) Selenium, the element of the moon, in life on earth. IUBMB Life 49:411
11. (a) Zinoni F, Birkmann A, Stadtman TC, Bock A (1986) Nucleotide sequence and expression of the selenocysteine-containing polypeptide of formate dehydrogenase (formate-hydrogen-lyase-linked) from Escherichia coli. Proc Natl Acad Sci USA 83(13):4650; (b) Johansson L, Gafvelin G, Arnér ESJ (2005) Selenocysteine in proteins-properties and biotechnological use. BBA-Gen Subjects 1726(1):1; (c) Garcin E, Vernede X, Hatchikian EC, Volbeda A, Frey M, Fontecilla-Camps JC (1999) The crystal structure of a reduced [NiFeSe] hydrogenase provides an image of the activated catalytic center. Structure 7(5):557
12. Roy GP, Sarma BK, Phadnis PP, Mugesh G (2005) Selenium-containing enzymes in mammals: chemical perspectives. J Chem Sci 117(4):287
13. (a) Rotruck JT, Pope AL, Ganther HE, Swanson AB, Hafeman DG, Hoekstra WG (1973) Selenium: biochemical role as a component of glutathione peroxidase. Science 179(4073):588; (b) Biterova EI, Turanov AA, Gladyshev VN, Barycki JJ (2005) Crystal structures of oxidized and reduced mitochondrial thioredoxin reductase provide molecular details of the reaction mechanism. Proc Nat Acad Sci, USA 102(42):15018; (c) Sarma BK, Mugesh G (2008) Thiolcofactors for selenoenzymes and their synthetic mimics. Org Biomol Chem 6(6):965; (d) Benhar M (2018) Roles of mammalian glutathione peroxidase and thioredoxin reductase enzymes in the cellular response to nitrosative stress. Free Radic Biol Med 127:160; (e) St Germain DL, Galton VA (1997) The deiodinase family of selenoproteins. Thyroid 7(4):655; (f) St. Germain DL (2001) Selenium, deiodinases and endocrine function. In: Hatfield DL (eds) Selenium. Springer, Boston, MA (Print ISBN:978-1-4613-5639-4); (g) Mustacich D, Powis G (2000) Thioredoxin reductase. Biochem J 346(Pt 1):1; (h) Jr. Williams H, Arscott LD, Muller S, Lennon BW, Ludwig ML, Wang P-F, Veine DM, Becker K, Schirmer RH (2000) Thioredoxin reductase; Two modes of catalysis have evolved. Eur J Biochem 267(20):6110; (i) Berry MJ, Banu L, Larsen PR (1991) Type I iodothyronine deiodinase is a selenocysteine-containing enzyme. Nature 349(6308):438; (j) Köhrle J (2002) Iodothyronine deiodinases. Methods Enzymol 347:125
14. (a) Müller A, Cadenas E, Graf P, Sies H (1984) A novel biologically active seleno-organic compound--I. Glutathione peroxidase-like activity in vitro and antioxidant capacity of PZ 51 (Ebselen). Biochem Pharmacol 33(20):3235; (b) Sies H (1993) Ebselen, a selenoorganic compound as glutathione peroxidase mimic. Free Radic Biol Med 14(3):313; (c) Sies H (1991) Oxidative stress: from basic research to clinical application. Am J Med 91(3):S31
15. (a) Ye S-f, Yang Y, Wu L, Ma W-w, Zeng H-h (2017) Ethaselen: a novel organoselenium anticancer agent targeting thioredoxin reductase 1 reverses cisplatin resistance in drug-resistant K562 cells by inducing apoptosis. J Zhejiang Univ Sci B 18(5):373; (b) Shi C, Yu L, Yang F, Yan J, Zeng H (2003) A novel organoselenium compound induces cell cycle arrest and apoptosis in prostate cancer cell lines. Biochem Biophys Res Commun 309(3):578; (c) Wang L, Yang Z, Fu J, Yin H, Xiong K, Tan Q, Jin H, Li J, Wang T, Tang W, Yin J, Cai G, Liu M,

Kehr S, Becker K, Zeng H (2012) Ethaselen: a potent mammalian thioredoxin reductase 1 inhibitor and novel organoselenium anticancer agent. Free Radic Biol Med 52(5):898

16. (a) Geoffrion LD, Hesabizadeh T, Medina-Cruz D, Kusper M, Taylor P, Vernet-Crua A, Chen J, Ajo A, Webster TJ, Guisbiers G (2020) Naked Selenium Nanoparticles for Antibacterial and Anticancer Treatments. ACS Omega 5(6):2660; (b) Khurana A, Tekula S, Saifi MA, Venkatesh P, Godugu C (2019) Therapeutic applications of selenium nanoparticles. Biomed Pharmacother 111:802
17. (a) Maiyo F, Singh M (2017) Selenium nanoparticles: potential in cancer gene and drug delivery. Nanomedicine (Lond) 12(9):1075; (b) Hosnedlova B, Kepinska M, Skalickova S, Fernandez C, Ruttkay-Nedecky B, Peng Q, Baron M, Melcova M, Opatrilova R, Zidkova J, Bjørklund G, Sochor J, Kizek R (2018) Nano-selenium and its nanomedicine applications: a critical review. Int J Nanomed 13:2107; (c) Liu W, Li X, Wong YS, Zheng W, Zhang Y, Cao W, Chen T (2012) Selenium nanoparticles as a carrier of 5-fluorouracil to achieve anticancer synergism. ACS Nano 6(8):6578
18. (a) Koizumi M, Endo K, Watanabe Y, Saga T, Sakahara H, Konishi J, Yamamuro T, Toyama S (1989) Pharmacokinetics of internally labeled monoclonal antibodies as a gold standard: comparison of biodistribution of ^{75}Se-, ^{111}In-, and ^{125}I-labeled monoclonal antibodies in osteogenic sarcoma xenografts in nude mice. Cancer Res 49(7):1752; (b) Glass RS, Singh WP, Jung W, Veres Z, Scholz TD, Stadtman T (1993) Monoselenophosphate: synthesis, characterization, and identity with the prokaryotic biological selenium donor, compound SePX. Biochemistry 32(47):12555
19. (a) Blau M, Bender MA (1962) Se^{76}-selenomethionine for visualization of the pancreas by isotope scanning. Radiology 78(6):974; (b) McCarthy DM, Brown P, Melmed RN, Agnew JE, Bouchier IAD (1972) ^{75}Se-selenomethionine scanning in the diagnosis of tumours of the pancreas and adjacent viscera: the use of the test and its impact on survival. Gut 13(2):75; (c) Goto R, Unno K, Takeda A, Okada S, Tamemasa O (1987) Tumor accumulation of D-selenomethionine-Se-75 in tumor-bearing mice. J Pharmacobiodyn 10(9):456
20. (a) Combs Jr F (1988) Selenium in Foods. Adv Food Res 32:85; (b) Cuderman P, Kreft I, Germ M, Kovačevič M, Stibilj V (2008) Selenium species in selenium-enriched and drought-exposed potatoes. J Agric Food Chem 56(19):9114; (c) A nutrition guide for men with prostate cancer, BC Cancer Agency, 2nd Ed (2014) (ISBN-10-1-896624-24-3); (d) Sager M (2006) Selenium in agriculture, food, and nutrition. Pure Appl Chem 78(1):111; (e) Mabeyo PE, Manoko MLK, Gruhonjic A, Fitzpatrick PA, Landberg G, Erdélyi M, Nyandoro SS (2015) Selenium accumulating leafy vegetables are a potential source of functional foods. Int J Food Sci 2015:Article ID 549676 (1–8); (f) Yang R, Liu Y, Zhou Z (2017) Selenium and selenoproteins, from structure, function to food resource and nutrition. Food Sci Technol Res 23(3):363
21. (a) Thomson CD (2004) Assessment of requirements for selenium and adequacy of selenium status: a review. Eur J Clin Nutr 58(3):391; (b) Slencu BG, Ciobanu C, Cuciureanu R (2012) Selenium content in foodstuffs and its nutritional requirement for humans. Clujul Med 85(2):139; (c) Levander OA, Burk RF (2006) Update of human dietary standards for selenium. In: Hatfield DL, Berry MJ, Gladyshev VN (eds) Selenium - its molecular biology and role in human health. Springer, New York, p 399; (d) Nagabhushanam K, Majeed M (2007) Selenium compounds in medicine and nutrition. Chimica Oggi 25(5):36
22. (a) Shor-Posner G, Miguez M-J, Pineda LM, Rodriguez A, Ruiz P, Castillo G, Burbano X, Lecusay R, Baum M (2002) Impact of selenium status on the pathogenesis of mycobacterial disease in HIV-1-infected drug users during the era of highly active antiretroviral therapy. J Acquir Immune Defic Syndr 29(2):169; (b) Fordyce FM (2013) Selenium deficiency and toxicity in the environment. In: Selinus O (ed) Essentials of medical geology. Springer, Dordrecht, p 375; (c) Reich HJ, Hondal RJ (2016) Why nature chose selenium. ACS Chem Biol 11:821
23. (a) Nuttall KL (2006) Evaluating selenium poisoning. Ann Clin Lab Sci 36(4):409; (b) MacFarquhar JK, Broussard DL, Melstrom P, Hutchinson R, Wolkin A, Martin C, Burk RF, Dunn JR, Green AL, Hammond R, Schaffner W, Jones TF (2010) Acute selenium toxicity associated with a dietary supplement. Arch Intern Med 170(3):256

24. (a) Tinggi U (2003) Essentiality and toxicity of selenium and its status in Australia: a review. Toxicol Lett 137(1–2):103; (b) Davis TZ, Stegelmeier BL, Hall JO (2014) Analysis in horse hair as a means of evaluating selenium toxicoses and long-term exposures. J Agric Food Chem 62(30):7393
25. (a) Schellmann B, Raithel HJ, Schaller KH (1986) Acute fatal selenium poisoning. Toxicological and occupational medical aspects. Arch Toxicol 59(1):61; (b)Koppel C, Baudisch H, Beyer KH, Kloppel I, Schneider V (1986) Fatal poisoning with selenium dioxide. J Toxicol Clin Toxicol 24(1):21; (c) MacFarquhar JK, Broussard DL, Melstrom P, Hutchinson R, Wolkin A, Martin C, Burk RF, Dunn JR, Green AL, Hammond R, Schaffner W, Jones TF (2010) Acute selenium toxicity associated with a dietary supplement. Arch Intern Med 170(3):256; (d) Aldosary BM, Sutter ME, Schwartz M, Morgan BW (2011) Case series of selenium toxicity from a nutritional supplement. Clin Toxicol 50(1):57–64; (e) Painter EP (1941) The chemistry and toxicity of selenium compounds, with special reference to the selenium problem. Chem Rev 28(2):179
26. (a) Lin H, Zhu Q, Shu D, Lin D, Xu J, Huang X, Shi W, Xi X, Wang J, Gao L (2019) Growth of environmentally stable transition metal selenide films. Nat Mater 18(6):602; (b) Luo M, Yu H, Hu F, Liu T, Cheng X, Zheng R, Bai Y, Shui M, Shu J (2020) Metal selenides for high performance sodium ion batteries. Chem Eng J 380:122557; (c) Ali Z, Asif M, Zhang T, Huang X, Hou Y (2019) General approach to produce nanostructured binary transition metal selenides as high-performance sodium ion battery anodesl. General Small 15(33):1901995; (d) Hoover GC, Seferos DS (2019) Photoactivity and optical applications of organic materials containing selenium and tellurium. Chem Sci 10(40):9182; (e) Chen S, Ma G, Wang Q, Sun S, Hisatomi T, Higashi T, Wang Z, Nakabayashi M, Shibata N, Pan Z, Hayashi T, Minegishi T, Takata T, Domen K (2019) Metal selenide photocatalysts for visible-light-driven Z-scheme pure water splitting. J Mater Chem A 7:7415; (f) Zhang R, Cho S, Lim DG, Hu X, Stach EA, Handwerker CA, Agrawal R (2016) Metal-metal chalcogenide molecular precursors to binary, ternary, and quaternary metal chalcogenide thin films for electronic devices chem commun 52(28):5007; (g) Kagkoura A, Skaltsas T, Tagmatarchis N (2017) Transition metal chalcogenides/graphene ensembles for light induced energy applications. Chem Eur J 23(53):12967
27. (a) Lipinski B (2019) Redox-active selenium in health and disease: a conceptual review. Mini-Rev Med Chem 19(9):720; (b) Mohammod TGM, Misbahudd M (2018) In silico design of a drug from the compounds that are suggestive in the treatment of arsenicosis using molecular docking. J Comput Methods Mol Des 8(3):10; (c) Mezey PG (2000) Computer aided drug design: some fundamental aspects. J Mol Model 6(2):150–157; (d) Thakur M, Chandan N (2012) Int J Res Pharm Biomed Sci 3:2229; (e) Parikesit AA (2018) Introductory chapter: the contribution of bioinformatics as blueprint lead for drug design. In: Molecular insight of drug design (IntechOpen) (Chap. 1); (f) Liu R, Li X, Lama KS (2017) Combinatorial chemistry in drug discovery. Curr Opin Chem Biol 38:117; (g) Kennedy JP, Williams L, Bridges TM, Daniels RN, Weaver D, Lindsley CW (2008) Application of combinatorial chemistry science on modern drug discovery. J Comb Chem 10(3):345
28. (a) Löwig CJ (1836) "Ueber schwefelwasserstoff - und selenwasserstoffäther" (About hydrogen sulfide and selenium hydrogen ether). Annalen der Physik 37:550; (b) Rathke B (1869) Ann Chem 152:211
29. Wöhler F, Siemens C (1847) Ueber das Selenmercaptan. Ann Chem 61:360
30. (a) Haygarth PM (1994) Global importance and global cycling of selenium. In: Frankenberger Jr WT, Benson S (eds) Selenium in the environment. Marcel Dekker Inc., New York; (b) Jacob C, Giles GI, Giles NM, Sies H (2003) Sulfur and selenium: the role of oxidation state in protein structure and function. Angew Chem Int Ed 42(39):4742; (c) Maroney MJ, Hondal RJ (2018) Selenium versus sulfur: reversibility of chemical reactions and resistance to permanent oxidation in proteins and nucleic acids. Free Radic Biol Med 127:228; (d) Ji S, Xia J, Xu H (2016) Dynamic chemistry of selenium: Se–N and Se–Se dynamic covalent bonds in polymeric systems. ACS Macro Lett 5:78; (e) Martens DA (2003) Selenium. In: Stewart BA, Howell T (Ed) Encyclopedia of Water Science, Marcel Dekker Inc., p 840

31. Plano D, Lizarraga E, Font M, Palop JA, Sanmartín C (2009) Thermal stability and decomposition of sulphur and selenium compounds. J Therm Anal Calorim 98(2):559
32. (a) Kildahl NK (1995) Bond energy data summarized. J Chem Educ 72(5):423; (b) Ji S, Xia J, Xu H (2016) Dynamic chemistry of selenium: Se–N and Se–Se dynamic covalent bonds in polymeric systems. ACS Macro Lett 5(1):78
33. (a) Winkel LHE, Johnson CA, Lenz M, Grundl T, Leupin OX, Amini M, Charlet L (1983) Environmental selenium research: from microscopic processes to global understanding. Environ Sci Technol 46(2):571; (b) Jukes TH (1983) Selenium, an "essential poison". J Appl Biochem 5(4–5):233; (c) Alexander J (2015) Selenium. Handbook on the toxicology of metals 4E (Chap. 52). Elsevier B.V., p 1175
34. Toxicological Profile for Selenium. In: U.S. Department of Health and Human Services, (2003)
35. (a) Acute Exposure Guidelines Levels for selected airborne Chemicals, Volume 16; National Research Council of the National Academies, The National Academies Press, Washington D.C. (2014); (b) Cupp-Sutton KA, Ashby MT (2016) Biological chemistry of hydrogen selenide. Antioxidants 5(4):42 (1–18)
36. Foster DG (1928) Organic selenium compounds: the decomposition of some phenyl selenium halides. J Am Chem Soc 50:1184
37. (a) Shimodaira S, Asano Y, Arai K, Iwaoka M (2017) Selenoglutathione diselenide: unique redox reactions in the GPx-like catalytic cycle and repairing of disulfide bonds in scrambled protein. Biochemistry 56(42):5644; (b) Lamoure M, Milne J (1989) The disproportionation of diselenium dichloride, Se_2CI_2, and diselenium dibromide, Se_2Br_2. Can J Chem 67:1936
38. (a) Chu YC, Marsh DG, Günther WHH (1975) Photochemistry of organochalcogen compounds. I. Photolysis of benzyl diselenide. J Am Chem Soc 97(17):4905; (b) Chen Y-W, Zhou X-L, Tong J, Truong Y, Belzile N (2005) Photochemical behavior of inorganic and organic selenium compounds in various aqueous solutions. Anal Chim Acta 545(2):149; (c) McCulla RD (2005) Photochemistry and internal eliminations of organosulfur and organoselenium compounds. Dissertation of PhD work, Iowa State University, ISA
39. Management of Hazardous Waste, Yale Environmental Health & Safety (2018)
40. Armour M-A (2003) Hazardous laboratory chemicals disposal guide, 3rd ed, ISBN 1-56670-567-3. CRC Press, FL
41. (a) Lenga RE (ed) (1988) The sigma-aldrich library of chemical safety data, 2nd ed (ISBN-10: 0941633160; ISBN-13: 978-0941633161), Aldrich Chemical Company, Milwaukee, WI; (b) Waste disposal Guide, Michigan State University (2009); (c) Disposal of laboratory wastes: requirements for chemical disposal to sinks and drains. Environmental Health and Safety Office Ball State University (2011)
42. (a) Sarma BK, Mugesh G (2009) Theoretical investigation on the effect of different nitrogen donors on intramolecular Se···N interactions. ChemPhysChem 10(17):3013; (b) Shimizu T, Enomoto M, Taka H, Kamigata N (1999) Optical resolution and configurational stability of selenoxides stabilized by intramolecular coordination. J Org Chem 64(22):8242; (c) Singh VP, Singh HB, Butcher RJ (2011) Synthesis of cyclic selenenate/seleninate esters stabilized by ortho-nitro coordination: their glutathione peroxidase-like activities. Synthesis Chem Asian J 6:1431
43. Phadnis PP, Mugesh G (2005) Internally stabilized selenocysteine derivatives: syntheses, ^{77}Se NMR and biomimetic studies. Org Biomol Chem 3:2476–2481
44. (a) Prabhu CP, Phadnis PP, Wadawale AP, Priyadarsini KI, Jain VK (2012) Synthesis, Synthesis, characterization, structures and antioxidant activity of nicotinoyl based organoselenium compounds. J Organomet Chem 713:42; (b) Phadnis PP, Kunwar A, Kumar M, Mishra R, Wadawale A, Priyadarsini KI, Jain VK (2017) Study of polymorphism in 2, 2′-diselenobis(3-pyridinol). J Organomet Chem 852:1; (c) Kunwar A, Patil A, Kumar S, Deshpande R, Gota V, Goda JS, Jain VK, Indira Priyadarsini K (2018) Toxicological safety evaluation of 3,3'-diselenodipropionic acid (DSePA), a pharmacologically important derivative of selenocystine. Regul Toxicol Pharmacol 99:159

45. (a) Azad GK, Tomar RS (2014) Ebselen, a promising antioxidant drug: mechanisms of action and targets of biological pathways. Mol Biol Rep 41(8):4865; (b) Bueno DC, Meinerz DF, Allebrandt J, Waczuk EP, dos Santos DB, Mariano DOC, Rocha JBT (2013) Cytotoxicity and genotoxicity evaluation of organochalcogens in human leucocytes: a comparative study between ebselen, diphenyl diselenide, and diphenyl ditelluride. BioMed Res Internat 2013:Article ID 537279, 1–6; (c) Gota V, Goda JS, Doshi K, Patil A, Sunderajan S, Kumar K, Varne M, Kunwar A, Jain VK, Priyadarshini KI (2016) Biodistribution and pharmacokinetic study of 3,3' diseleno dipropionic acid (DSePA), a synthetic radioprotector, in mice. Eur J Drug Metab Pharmacokinet 41:839; (d) May HC, Yu J-J, Guentzel1 MN, Chambers JP, Cap AP, Arulanandam BP (2018) Repurposing auranofin, ebselen, and PX-12 as antimicrobial agents targeting the thioredoxin system. Front Microbiol 9:Article 336 (1–10)
46. Beld J, Woycechowsky KJ, Hilvert D (2007) Selenoglutathione: efficient oxidative protein folding by a diselenide. Biochemistry 46(18):5382
47. (a) Pfeiffer W-D (2008) 1,3,4-Oxadiazines and 1,3,4-Thiadiazines. In: Comprehensive heterocyclic chemistry III, p 401; (b) Rosa RM, Roesler R, Braga AL, Saffi J, Henriques JAP (2007) Pharmacology and toxicology of diphenyl diselenide in several biological models. Braz J Med Biol Res 40(10):1287; (c) Jain VK (2017) An overview of organoselenium chemistry: from fundamentals to synthesis (Chap. 1). In: Jain VK, Priyadarsini KI (eds) Organoselenium Compounds in biology and medicine: synthesis, biological and therapeutic treatments, Print ISBN 978-1-78801-029-0
48. (a) Bhasin KK, Jain VK, Kumar H, Sharma S, Mehta SK, Singh J (2003) Preparation and characterization of methyl substituted 2,2′-dipyridyl diselenides, 2,2′-dipyridyl-ditellurides, and their derivatives. Synth Commun 33(6):977; (b) Jain VK (2019) Pyridyl and pyrimidyl chalcogenolates of coinage metals and their utility as molecular precursors for the preparation of metal chalcogenides. New J Chem 43:11034
49. (a) Thompson DP, Boudjouk P (1988) A convenient synthesis of alkali metal selenides and diselenides in tetrahydrofuran and the reactivity differences exhibited by these salts toward organic bromides. Effect of ultrasound. J Org Chem 53(9):2109; (b) Gladysz JA, Hornby JL, Garbe JE (1978) Convenient one-flask synthesis of dialkyl selenides and diselenides via lithium triethylborohydride reduction of Sex. J Org Chem 43(6):1204; (c) Krief A, Derock M (2002) Synthesis of diselenides and selenides from elemental selenium. Tetrahedron Lett 43:3083; (d) Krasowska D, Begini F, Santi C, Mangiavacchi F, Drabowicz J, Sancinetoa L (2019) Ultrasound-assisted synthesis of alkali metals diselenides (M2Se2) and their application for the gram-scale preparation of 2,2'-diselenobis(benzoic acid). Arkivoc II, 24; (e) Syper L, Mlochowski J (1988) Lithium diselenide in aprotic medium - a convenient reagent for synthesis of organic diselenides. Tetrahedron, 44(19):6119; (f) Bhasin KK, Singh N, Doomra S, Arora E, Ram G, Singh S, Nagpal Y, Mehta SK, Klapotke TM (2007) Regioselective synthesis of bis(2-halo-3-pyridyl) dichalcogenides (E = S, Se and Te): directed ortho-lithiation of 2-halopyridines. Bioinorg Chem Appl 2007:Article ID 69263 (1–9); (g) Li JQ, Bao WL, Lue P, Zhou X-J (1991) A convenient method for the preparation of dialkylditellurides and dialkyldiselenides. Synth Commun 21:799
50. Vafai M, Renson M (1966) Synthèse du Sélénopheno [2′, 3′: 5, 6] Benzo [B] Thiophène. Bull Soc Chim Belg 75:145
51. Aravindhan S, Singh HB, Zeller M, Butcher RJ (2019) Synthesis of selenopeptides: an alternative way of incorporating selenocystine. Synthesis Amino Acids 51:661
52. Klayman DL, Griffin TS (1973) Reaction of selenium with sodium borohydride in protic solvents. A Facile Method for the introduction of selenium into organic molecules. J Am Chem Soc 95(1):197
53. (a) Młochowski J, Syper L (2001) Sodium hydrogen selenide. In: Encyclopedia of reagents for organic synthesis; (b) Ishihara H, Sato S, Hirabayashi Y (1977) The synthesis and properties of diacyl selenides. Bull Chem Soc Jpn 50(11):3007; (c) Jensen KA, Nielsen PH (1966) Infrared spectra of thioamides and selenoamides. Acta Chem Scand 20:597

54. (a) Landry VK, Minoura M, Pang K, Buccella D, Kelly BV, Parkin G (2006) Synthesis and structural characterization of 1-mesityl-1,3-dihydro-imidazole-2-selone and bis(1-mesitylimidazol-2-yl)diselenide: experimental evidence that the selone is more stable than the selenol tautomer. J Am Chem Soc 128:12490; (b) Roy G, Nethaji M, Mugesh G (2004) Mugesh, Biomimetic studies on anti-thyroid drugs and thyroid hormone synthesis. J Am Chem Soc 126(9):2712; (c) Jayaram PN, Roy G, Mugesh G (2008) Effect of thione-thiol tautomerism on the inhibition of lactoperoxidase by anti-thyroid drugs and their analogues. J Chem Sci 120(1):143; (d) Roy G, Mugesh G (2005) Anti-thyroid drugs and thyroid hormone synthesis: effect of methimazole derivatives on peroxidase-catalyzed reactions. J Am Chem Soc 127(43):15207
55. (a) Bolm C, Kesselgruber M, Grenz A, Hermanns N, Hildebrand JP (2001) A novel ferrocenyl diselenide for the catalytic asymmetric aryl transfer to aldehydes. New J Chem 25:13; (b) Mugesh G, Panda A, Singh HB, Punekar NS, Butcher RJ (2001) Glutathione peroxidase-like antioxidant activity of diaryl diselenides: a mechanistic study. J Am Chem Soc 123(5):839; (c) Mugesh G, Singh HB (2002) Heteroatom-directed aromatic lithiation: a versatile route to the synthesis of organochalcogen (Se, Te) compounds. Acc Chem Res 35:226
56. Zade SS, Singh HB (2012) Synthesis of organoselenium compounds. PATAI'S Chemistry of Functional Groups, Online 2009–2012. Wiley. https://doi.org/10.1002/9780470682531.pat0706
57. (a) Plano D, Baquedano Y, Moreno-Mateos D, Font M, Jiménez-Ruiz A, Antonio Palop J, Sanmartín C (2011) Selenocyanates and diselenides: a new class of potent antileishmanial agents. Eur J Med Chem 46(8):3315; (b) Kumar S, Tripathi SK, Singh HB, Wolmershäuser G (2004) Synthesis, reactivity, electrochemical and crystallographic studies of diferrocenoyl diselenide and ferrocenoyl selenides. J Organomet Chem 689:3046
58. (a) Phadnis PP, Kunwar A, Kumar M, Mishra R, Wadavale A, Priyadarsini KI, Jain VK (2017) Study of polymorphism in 2, 2′-diselenobis(3-pyridinol). J Organomet Chem 852:1; (b) Hodage AS, Prabhu CP, Phadnis PP, Wadawale A, Priyadarsini KI, Jain VK (2012) Synthesis, characterization, structures and GPx mimicking activity of pyridyl and pyrimidyl based organoselenium compounds. J Organomet Chem 720:19
59. Reich HJ, Cohen ML, Clark PS (1979) Reagents for synthesis of organoselenium compounds: diphenyl diselenide and benzeneselenenyl chloride. Org Synth 59:141; Collective 6:533
60. (a) Iwaoka M, Haraki C, Ooka R, Miyamoto M, Sugiyama A, Kohara Y, Isozumi N (2006) Synthesis of selenocystine derivatives from cystine by applying the transformation reaction from disulfides to diselenides. Tetrahedron Lett 47(23):3861; (b)Oae S, Togo H (1981) Facile conversions of aliphatic sulfonic acids, sulfinic acids, thiols, sulfonates, thiolsulfonates, and disulfides to the corresponding alkyl iodides by triphenylphosphine/iodine. Synthesis 371
61. Braga AL, Paixão MW, Lüdtke DS, Silveira CC, Rodrigues OED (2003) Synthesis of new chiral aliphatic amino diselenides and their application as catalysts for the enantioselective addition of diethylzinc to aldehydes. Org Lett 5(15):2635
62. Li Z, Ke F, Deng H, Xu H, Xiang H, Zhou X (2013) Synthesis of disulfides and diselenides by copper-catalyzed coupling reactions in water. Org Biomol Chem 11:2943
63. Singh D, Deobald AM, Camargo LRS, Tabarelli G, Rodrigues OED, Braga AL (2010) An efficient one-pot synthesis of symmetrical diselenides or ditellurides from halides with CuO nanopowder/Se^0 or Te^0/Base. Org Lett 12(15):3288
64. Botteselle GV, Godoi M, Galetto FZ, Bettanin L, Singh D, Rodrigues OED, Braga AL (2012) Microwave-assisted one-pot synthesis of symmetrical diselenides, ditellurides and disulfides from organoyl iodides and elemental chalcogen catalyzed by CuO nanoparticles. J Mol Catal A: Chem 365:186
65. Soleiman-Beigi M, Yavari I, Sadeghizadeh F (2015) The direct synthesis of symmetrical disulfides and diselenides by metal–organic framework MOF-199 as an efficient heterogenous catalyst. RSC Adv 5(106):87564
66. Panduranga V, Prabhu G, Prabhu B, Panguluri NR, Sureshbabu VV (2016) Alternative protocol for the synthesis of symmetrical dibenzyl diselenides and disulfides. Synthesis 48(11):1711

67. Kommula D, Li Q, Ning S, Liu W, Wang Q, Zhao ZK (2020) Iodine mediated synthesis of diaryl diselenides using SeO_2 as a selenium source. Synth Commun 50(7):1026
68. Joshaghani M, Khosropour AR, Jafary H, Mohammadpoor-Baltork I (2005) Mild and highly efficient preparation of symmetrical disulfides and diselenides using bipyridinum hydrobromide perbromide as a new oxidative reagent. Phosphorus Sulfur Silicon 180:117
69. Tian F, Yu Z, Lu S (2004) Efficient reductive selenation of aromatic aldehydes to symmetrical diselenides with Se/CO/H_2O under atmospheric pressure. J Org Chem 69, 13:4520
70. (a) Back TG, Moussa Z (2002) Remarkable activity of a novel cyclic seleninate ester as a glutathione peroxidase mimetic and its facile in situ generation from allyl 3-hydroxypropyl selenide. J Am Chem Soc 124:12104; (b) Back TG, Moussa Z (2003) Diselenides and allyl selenides as glutathione peroxidase mimetics. Remarkable activity of cyclic seleninates produced in situ by the oxidation of allyl omega-hydroxyalkyl selenides. J Am Chem Soc 125(44):13455; (c) Iwaoka M, Kumakura F (2008) Applications of water-soluble selenides and selenoxides to protein chemistry. Phosphorus, Sulfur Silicon 183:1009
71. (a) Arnault I, Auger J (2006) Seleno-compounds in garlic and onion. J Chromatography A, 1112:23; (b) Block E (1997) Organoselenium and organosulfur phytochemicals from genus allium plants (onion, garlic): relevance for cancer protection. In: Ohigashi H, Osawa T, Terao J, Watanabe S, Yoshikawa T (eds) Food factors for cancer prevention. Springer, Tokyo. Print ISBN: 978-4-431-67019-3
72. (a) Lyi SM, Heller LI, Rutzke M, Welch RM, Kochian LV, Li L (2005) Molecular and biochemical characterization of the selenocysteine se-methyltransferase gene and se-methylselenocysteine synthesis in broccoli. Plant Physiol 138(1):409; (b) Schrauzer GN (2000) Selenomethionine: a review of its nutritional significance, metabolism and toxicity. J Nutrit 130(7):1653; (c) Ellis DR, Sors TG, Brunk DG, Albrecht C, Orser C, Lahner B, Wood KV, Harris HH, Pickering IJ, Salt DE (2004) Production of Se-methylselenocysteine in transgenic plants expressing selenocysteine methyltransferase. BMC Plant Biol 4:Article number: 1 (1–11); (d) El-Bayoumy K, Sinha R, Pinto JT, Rivlin RS (2006) Cancer chemoprevention by garlic and garlic-containing sulfur and selenium compounds. J Nutrit 136(3):864S
73. (a) Borchert A, Kalms J, Roth S, Rademacher M, Schmidt A, Holzhutter H-G, Kuhn H, Scheerer P (2018) Crystal structure and functional characterization of selenocysteine-containing glutathione peroxidase 4 suggests an alternative mechanism of peroxide reduction. Biochimica et Biophysica Acta (BBA) – Mol Cell Biol Lipids 1863(9):1095; (b) Schweizer U, Schlicker C, Braun D, Kohrle J, Steegborn C (2014) Crystal structure of mammalian selenocysteine-dependent iodothyronine deiodinase suggests a peroxiredoxin-like catalytic mechanism. Proc Natl Acad Sci U S A 111(29):10526; (c) Hondal RJ, Ruggles EL (2011) Differing views of the role of selenium in thioredoxin reductase. Amino Acids 41:73
74. (a) Kumar PV, Singh BG, Phadnis PP, Jain VK, Priyadarsini KI (2016) Effect of molecular interactions on electron-transfer and antioxidant activity of bis(alkanol)selenides: a radiation chemical study. Chem Eur J 22:1; (b) Singh BG, Kumar P, Phadnis P, Iwaok M, Priyadarsini KI (2019) Free radical induced selenoxide formation in isomeric organoselenium compounds: the effect of chemical structures on antioxidant activity. New J Chem 43:13357
75. (a) Arai K, Tashiro A, Osaka Y, Iwaoka M (2017) Glutathione peroxidase-like activity of amino-substituted water-soluble cyclic selenides: a shift of the major catalytic cycle in methanol. Molecules 22(3):354 (1–13); (b) Hodage AS, Phadnis PP, Wadawale A, Priyadarsini KI, Jain VK (2011) Synthesis, characterization and structures of 2-(3,5-dimethylpyrazol-1-yl)ethylseleno derivatives and their probable glutathione peroxidase (GPx) like activity. Org Biomol Chem 9:2992
76. (a) Khan MD, Revaprasadua N (2020) Metal-organic precursors for ternary and quaternary metal chalcogenide nanoparticles and thin films. Nanoscience 6:1–31. https://doi.org/10.1039/9781788017053-00001; eISBN: 978-1-78801-705-3; (b) Jain VK (2006) Synthesis and characterization of single-source molecular precursors for the preparation of metal chalcogenides. J Chem Sci 118:547; (c) Stuczynski SM, Brennan JG, Steigerwald ML (1989) Formation of metal-chalcogen bonds by the reaction of metal-alkyls with silyl chalcogenides. Inorg Chem 28(25):4431; (d) Kolay S, Wadawale A, Das D, Kisan HK, Sunoj RB, Jain VK (2013)

Cyclopalladation of dimesityl selenide: synthesis, reactivity, structural characterization, isolation of an intermediate complex with C–H· · · Pd intra-molecular interaction and computational studies. Dalton Trans 42:10828

77. (a) Krief A (1995) Selenium, comprehensive organometallic chemistry-II. In: Abel EW, Stone FGA, Wilkinson G (eds) Elsevier, Oxford, p 515; (b) Renson M (1987) The chemistry of organic selenium and tellurium compounds. In: Patai S, Rappoport Z (ed) Wiley, Chicheter; (c) Zade SS, Singh HB (2014) Synthesis of organoselenium compounds, the chemistry of organic selenium and tellurium compunds. In: Rappoport Z (ed) Wiley, p 1; (d) Milton MD, Khan S, Sigh JD, Mishra V, Khandelwal BL (2005) A facile access to chalcogen and dichalcogen bearing dialkylamines and diols. Tetrahedron Lett 46:755; (e) Panda A (2009) Chemistry of selena macrocycles. Coord Chem Rev 253:1056; (f) Levason W, Orchard SD, Reid G (2002) Recent developments in the chemistry of selenoethers and telluroethers. Coord Chem Rev 225(1–2):159
78. (a) Hodage AS, Prabhu CP, Phadnis PP, Wadawale A, Priyadarsini KI, Jain VK (2009) Synthesis, characterization, structures and GPx mimicking activity of pyridyl and pyrimidyl based organoselenium compounds. J Organomet Chem 720:19; (b) Bhalla A, Nagpal Y, Kumar R, Mehta SK, Bhasin KK, Bari SS (2009) Synthesis and characterization of novel pyridyl/naphthyl/(diphenyl)methylseleno substituted alkanoic acids: X-ray structure of 2-pyridylselenoethanoic acid, 2-naphthylselenoethanoic acid and 2-(diphenyl)methylselenoethanoic acid. J Organomet Chem 694:179
79. Ghavale N, Phadnis PP, Wadawale A, Jain VK (2011) Synthesis, structure and reactivity of a selenoxide derived from a bulky selenide: Bis(2,4,6-trimethylphenyl) selenoxide. Ind J Chem Sec A 50(1):22
80. (a) Bhasin KK, Singh RS, Kumar H, Mehta SK (2010) A one-flask synthesis and characterization of novel symmetrical pyridyl monoselenides and X-ray crystal structure of bis(5-bromo-2-pyridyl) selenide and bis(2-bromo-5-pyridyl) selenide. J Organomet Chem 695:648; (b) Zade SS, Panda S, Singh HB, Wolmershäuserb G (2005) Synthesis of diaryl selenides using the in situ reagent $SeCl_s$. Tetrahedron Lett 46:665
81. Lin HM, Tang Y, Li ZH, Liu KD, Yang J, Zhang YM (2012) A novel and efficient synthesis of selenide. ARKIVOC (viii) 146
82. (a) Zhang Y, Wu D, Weng Z (2017) Synthesis of 1,2,2-trifluorovinyl sulphides and selenides from trifluorovinylation of organic thiocyanates and selenocyanates. Org Chem Front 4:2226; (b) Huang Y, Chen R (2000) A novel synthesis of allyl selenides by reaction of an organosamarium reagent with alkyl selenocyanates. Synth Commun 30(2):377; (c) Greenberg B, Gould ES, Burlant Wm (1956) The reaction of aryllithium compounds with aryl selenocyanates. A new synthesis of unsymmetric diaryl selenides. J Am Chem Soc 78(16):4028
83. (a) Berlin S, Ericsson C, Engman L (2002) Construction of tetrahydrofuran-3-ones from readily available organochalcogen precursors via radical carbonylation/reductive cyclization. Org Lett 4:3; (b) Zade SS, Singh HB (2014) Synthesis of organoselenium compounds. In: Rappoport Z (ed) The chemistry of organic selenium and tellurium compounds. Wiley, p 1
84. Angeli A, Tanini D, Capperucci A, Supuran CT, Med ACS (2017) Synthesis of novel selenides bearing benzenesulfonamide moieties as carbonic anhydrase I, II, IV, VII, and IX inhibitors. Chem Lett 8(12):1213
85. Lisiak R, Młochowski J (2009) Selenium-nitrogen bond cleavage in selenazole ring system with grignard reagent: a convenient synthesis of unsymmetrically substituted selenides. Synth Commun 39(17):3141
86. Liotta D (1984) New organoselenium methodology. Acc Chem Res 17:28
87. Aboulkacem S, Naumann D, Tyrra W, Patenburg I (2012) 4-Tetrafluoropyridyl silver(I), AgC5F4N, in redox transmetalations with selenium and tellurium. Organometallics 31(4):1559
88. Kumar RU, Reddy KHV, Satish G, Swapna K, Nageswar YVD (2016) Metal free synthesis of diaryl selenides using SeO_2 as a selenium source. Tetrahedron Lett 57(37):4138

89. Yu J-T, Guo H, Yi Y, Fei H, Jiang Y (2014) The chan–lam reaction of chalcogen elements leading to aryl chalcogenides. Adv Synth Catal 356(4):749
90. Zhao X, Yu Z, Yan S, Wu S, Liu R, He W, Wang L (2005) Ruthenium(III) chloride catalyzed efficient synthesis of unsymmetrical diorganyl selenides via cleavage of dibenzyl and diphenyl diselenides in the presence of zinc. J Org Chem 70(18):7338
91. Shibahara F, Kanai T, Yamaguchi E, Kamei A, Yamauchi T, Murai T (2013) Copper-catalyzed C-H bond direct chalcogenation of aromatic compounds leading to diaryl sulfides, selenides, and diselenides by using elemental sulfur and selenium as chalcogen sources under oxidative conditions. Chem Asian J 9(1):237
92. Taniguchi N (2007) Convenient synthesis of unsymmetrical organochalcogenides using organoboronic acids with dichalcogenides via cleavage of the S-S, Se-Se, or Te-Te bond by a copper catalyst. J Org Chem 72(4):1241
93. Singh D, Alberto EE, Rodrigues OED, Braga AL (2009) Eco-friendly cross-coupling of diaryl diselenides with aryl and alkyl bromides catalyzed by CuO nanopowder in ionic liquid. Green Chem 11:1521
94. Cristau HJ, Chabaud B, Labaudiniere R, Christol H (1985) Synthesis of aryl phenyl and heteroaryl phenyl selenides by nickel(II)-catalyzed arylation of sodium benzeneselenolate. Organometallics 4(4):657
95. Munbunjong W, Lee EH, Ngernmaneerat P, Kim SJ, Singh G, Chavasiri W, Jang DO (2009) Indium-mediated cleavage of diphenyl diselenide and diphenyl disulfide: efficient one-pot synthesis of unsymmetrical diorganyl selenides, sulfides, and selenoesters. Tetrahedron 65:2467
96. Nishiyama Y, Tokunaga K, Sonoda N (1999) New synthetic method of diorganyl selenides: palladium-catalyzed reaction of $PhSeSnBu_3$ with aryl and alkyl halides. Org Lett 1(11):1725
97. Quell T, Mirion M, Schollmeyer D, Dyballa KM, Franke R, Waldvogel SR (2016) Solvent-dependent facile synthesis of diaryl selenides and biphenols employing selenium dioxide. ChemistryOPEN 5(2):115
98. Kobiki Y, Kawaguchi S, Ohe T, Ogawa A (2013) Photoinduced synthesis of unsymmetrical diaryl selenides from triarylbismuthines and diaryl diselenides. Beilst J Org Chem 9:1141
99. (a) Wu Z-P, Hilvert D (1989) Conversion of a protease into an acyl transferase: selenolsubtilisin. J Am Chem Soc 111:4513; (b) Wu Z-P, Hilvert D (1990) Selenosubtilisin as a glutathione peroxidase mimic. J Am Chem Soc 112(14):5647
100. (a) Krause RJ, Glocke SC, Sicuri AR, Ripp SL, Elfarra AA (2006) Oxidative metabolism of seleno-L-methionine to L-methionine selenoxide by flavin-containing monooxygenases. Chem Res Toxicol 19(12):1643; (b) Carroll L, Pattison DI, Fu S, Schiesser CH, Davies MJ, Hawkins CL (2017) Catalytic oxidant scavenging by selenium-containing compounds: Reduction of selenoxides and N-chloramines by thiols and redox enzymes. Selenosubtilisin as a glutathione peroxidase mimic. Redox Biol 12:872
101. (a) Arai K, Tashiro A, Osaka Y, Iwaoka M (2017) Glutathione peroxidase-like activity of amino-substituted water-soluble cyclic selenides: a shift of the major catalytic cycle in methanol. Molecules 22(3):354 (1–13); (b) Kumakura F, Mishra B, Priyadarsini KI, Iwaoka M (2010) A water-soluble cyclic selenide with enhanced glutathione peroxidase-like catalytic activities. Eur J Org Chem 440
102. (a) Iwaoka M, Kumakura F (2008) Applications of water-soluble selenides and selenoxides to protein chemistry. Phosphorus, Sulfur, Silicon 183:1009; (b) Shinozaki R, Iwaoka M (2017) Effects of metal ions, temperature, and a denaturant on the oxidative folding pathways of bovine α-lactalbumin. Int J Mol Sci 18:1996 (1–14); (c) Arai K, Noguchi M, Singh BG, Priyadarsini KI, Fujio K, Kubo Y, Takayama K, Ando S, Iwaoka M (2013) A water-soluble selenoxide reagent as a useful probe for the reactivity and folding of polythiol peptides. FEBS Open Bio 3:55; (d) Arai K, Iwaoka M (2019) Oxidative protein folding using trans-3,4-dihydroxyselenolane oxide. Methods Mol Biol 1967:229; (e) Arai K, Kumakurmy F, Iwaoka M (2012) Kinetic and thermodynamic analysis of the conformational folding process of SS-reduced bovine pancreatic ribonuclease a using a selenoxide reagent with high oxidizing ability. FEBS Open Bio 2:60

103. Duclos RI Jr, Cleary DC, Catcott KC, Zhou ZS (2015) Synthesis and characterization of Se-adenosyl-L-selenohomocysteine selenoxide. J Sulfur Chem 36(2):135
104. (a) Kelly AM, Rosini GP, Goldman AS (1997) Oxygen transfer from organoelement oxides to carbon monoxide catalyzed by transition metal carbonyls. J Am Chem Soc 119(26):6115; (b) Młochowski J, Wójtowicz-Młochowska H (2015) Developments in synthetic application of selenium (IV) oxide and organoselenium compounds as oxygen donors and oxygen-transfer agents. Molecules 20:10205
105. Ariyoshi A, Aso Y, Otsubo T, Ogura F (1984) Application of bis(p-methoxyphenyl) selenoxide as an oxidizing agent of kornblum oxidation. Chem Lett 13(6):891
106. Nishibayashi Y, Uemura S (2000) Selenoxide elimination and [2,3]sigmatropic rearrangement. In: Wirth T (eds) Organoselenium chemistry. Topics in current chemistry, Vol 208. Springer, Berlin
107. (a) Zhou ZS, Jiang N, Hilvert D (1997) An antibody-catalyzed selenoxide elimination. J Am Chem Soc 119:3623; (b) Sharpless KB, Young MW (1975) Olefin synthesis. Rate enhancement of the elimination of alkyl aryl selenoxides by electron-withdrawing substituents. J Org Chem 40:947; (c) Reich HJ, Wollowitz S, Trend JE, Chow F, Wendelborn DF (1978) Syn elimination of alkyl selenoxides. Side reactions involving selenenic acids. Structural and solvent effects of rates. J Org Chem 43:1697; (d) Reich HJ (1979) Functional group manipulation using organoselenium reagents. Acc Chem Res 12(1):22; (e) Sharpless KB, Young MW, Lauer RF (1973) Reactions of selenoxides: thermal syn-elimination and $H_2{}^{18}O$ exchange. Tetrahedron Lett 14(22):1979
108. Henriksen L, Jakobsen S (2001) Dissociative cycloelimination, a new selenium based pericyclic reaction. Chem Commun 2448
109. (a) Reich HJ, Renga JM, Reich LL (1975) Organoselenium chemistry. Conversion of ketones to enones by selenoxide syn elimination. J Am Chem Soc 97(19):5434; (b) Goodman MA, Detty MR (2006) Selenoxides as catalysts for epoxidation and Baeyer-Villiger oxidation with hydrogen peroxide. Synlett 7:1100; (c) Yaremenko IA, Vil VA, Demchuk DV, Terentev AO (2016) Rearrangements of organic peroxides and related processes. Beilstein J Org Chem 12:1647
110. Reich HJ, Renga JM, Reich LL (1975) Organoselenium chemistry. Conversion of ketones to enones by selenoxide syn elimination. J Am Chem Soc 97(19):5434
111. Drabowicz J, Łyżwa P, Łuczak J, Mikołajczyk M, Laur (1997) New procedures for theoxidation of sulphides to sulfoxides and sulfones. Phosphorus Sulfur. Silicon Relat Elem 120–121:425
112. Goodman MA, Detty MR (2004) Selenoxides as catalysts for the activation of hydrogen peroxide. Bromination of organic substrates with sodium bromide and hydrogen peroxide. Organometallics 23(12):3016
113. Dikarev V, Petrukhina MA, Li X, Bock E (2003) Small organoselenium molecules. 1. Dimethyl Selenoxide: structure, complexation, and gas-phase transformation. Inorg Chem 42(6):1966
114. (a) Krasowska D, Sancineto L, Desk M, Drabowicz J (2020) Optically active selenoxides: structural and synthetic aspects. Symmetry 12(3):349 (1–24); (b) Davis FA, Billmers JM, Stringer OD (1983) First synthesis of simple optically active selenoxides. Tetrahedron Lett 24(31):3191
115. Stratakis M, Rabalakos C, Sofikiti N (2003) Selective deoxygenation of aryl selenoxides by triaryl phosphites. Evidence for a concerted transformation. Tetrahedron Lett 44(2):349
116. Arai K, Kumakura F, Takahira M, Sekiyama N, Kuroda N, Suzuki T, Iwaoka M (2015) Effects of ring size and polar functional groups on the glutathione peroxidase-like antioxidant activity of water-soluble cyclic selenides. J Org Chem 80(11):5633
117. Michio K, Hiromi O, Toshio S (1986) Synthesis of selenoxides by oxidation of selenides with t-butyl hypochlorite, and its application for synthesis of optically active selenoxide. Bull Chem Soc Jpn 59(2):503; (b) Mochowski J, Peczyńska-Czoch W, Piętka-Ottlik M, Wójtowicz-Młochowska H (2011) Non-metal and enzymatic catalysts for hydroperoxide oxidation of organic compounds. Open Catal J 4:54

118. (a) Bhabak KP, Mugesh G (2009) Synthesis and structure–activity correlation studies of secondary- and tertiary-amine-based glutathione peroxidase mimics. Chem Eur J 15(38):9846; (b) Cotgreave IA, Moldéus P, Brattsand R, Hallberg A, Andersson CM, Engman L (1992) Alpha-(phenylselenenyl)acetophenone derivatives with glutathione peroxidase-like activity. A comparison with ebselen. Biochem Pharmacol 43(4):793
119. Sama T, Shimizu T, Hirabayashi K, Kamigata N (2007) Stabilizing effect of intramolecular lewis base toward racemization of optically active selenoxides. Heteroat Chem 18:301
120. Khurana JM, Kandpal BM, Chauhan YK (2003) Rapid oxidation of selenides, selenoxides, tellurides, and telluroxides with aqueous sodium hypochlorite. Phosphorus. Sulfur Silicon Relat Elem 178(6):1369
121. Agenäs LB, Lindgren G (1970) The oxidation products of some straight chain selenosubstituted dicarboxylic acids. Acta Chem Scand 24:3301
122. Tiecco M, Testaferri L, Temperini A, Terlizzi R, Bagnoli L, Marini F, Santi C (2005) Synthesis of selenoxides by oxidation of selenides with superoxide radical anions and 2-nitrobenzenesulfonyl chloride. Tetrahedron Lett 46(31):5165
123. Sands KN, Tuck TA, Back TG (2018) Cyclic seleninate esters, spirodioxyselenuranes and related compounds: new classes of biological antioxidants that emulate glutathione peroxidase. Chem Eur J 24(39):9714
124. Press DJ, Mercier EA, Kuzma D, Back TG (2008) Substituent effects upon the catalytic activity of aromatic cyclic seleninate esters and spirodioxyselenuranes that act as glutathione peroxidase mimetics. J Org Chem 73(11):4252
125. (a) McNeil NMR, Matz MC, Back TG (2013) Fluxional cyclic seleninate ester: nmr and computational studies, glutathione peroxidase-like behavior, and unexpected rearrangement. J Org Chem 78(20):10369; (b) Selvakumar K, Singh HB, Goel N, Singh UP, Butcher RJ (2011) Synthesis and structural characterization of pincer type bicyclic diacyloxy- and diazaselenuranes. Dalton Trans 40:9858
126. (a) Sarma BK, Manna D, Minoura M, Mugesh G (2010) Synthesis, structure, spirocyclization mechanism, and glutathione peroxidase-like antioxidant activity of stable spirodiazaselenurane and spirodiazatellurane. J Am Chem Soc 132(15):5364; (b) Day RO, Holmes RR (1981) Crystal structures of a tetraoxy spirocyclic selenurane and tellurane. Lone pair effects. Inorg Chem 20(9):3071
127. Drabowicz J, Mikołajczyk M (2000) Selenium at higher oxidation state. In: Wirth T (ed) Organoselenium chemistry. Topics in current chemistry, Vol 208. Springer, Berlin, Heidelberg, pp 143–176
128. Back TG, Moussa Z, Parvez M (2004) The exceptional glutathione peroxidase-like activity of di(3-hydroxypropyl) selenide and the unexpected role of a novel spirodioxaselenanonane intermediate in the catalytic cycle. Angew Chem Int Ed. 43:1268
129. (a) PrasadPR, Singh HB, Butcher RJ (2015) Synthesis, structure and antioxidant activity of cyclohexene-fused selenuranes and related derivatives. Molecules 20(7):12670; (b) Lamani DS, Bhowmick D, Mugesh G (2015) Substituent effects on the stability and antioxidant activity of spirodiazaselenuranes. Molecules 20(7):12959; (c) Upadhyay A, Batabyal M, Kanika, Kumar S (2020) Organoseleniums: generated and exploited in oxidative reactions. Chem Lett 49(4):395
130. Kuzma D, Parvez M, Back TG (2007) Formation of a spirodiazaselenurane and its corresponding azaselenonium derivatives from the oxidation of 2,2′-selenobis(benzamide). Structure, properties and glutathione peroxidase activity. Org Biomol Chem 5(19):3213
131. (a) Agenäs LB, Lindgren G (1970) The oxidation products of some straight chain selenosubstituted dicarboxylic acids. Acta Chem Scand 24:3301; (b) Iwaoka M, Kumakura F (2008) PApplications of water-soluble selenides and selenoxides to protein chemistry. Phosphorus Sulfur Silicon Relat Elem 183(4):1009
132. Selvakumar K, Singh HB, Goel N, Singh UP, Butcher RJ (2011) Synthesis and structural characterization of pincer type bicyclic diacyloxy- and diazaselenuranes. Dalton Trans 40:9858

133. Lawrence MAW, Green K-A, Nelson PN, Lorraine SC (2018) Review: pincer ligands-Tunable, versatile and applicable. Polyhedron 143:11
134. (a) Charette BJ, Ritch JS (2016) A selenium-containing diarylamido pincer ligand: synthesis and coordination chemistry with group 10 metals. Inorg Chem 55(12):6344; (b) Das D, Singh P, Singh M, Singh AK (2010) Tetradentate selenium ligand as a building block for homodinuclear complexes of Pd(ii) and Ru(ii) having seven membered rings or bis-pincer coordination mode: high catalytic activity of Pd-complexes for Heck reaction. Dalton Trans 39:10876
135. Kumar A, Rao GK, Kumar S, Singh AK (2014) Formation and role of palladium chalcogenide and other species in suzuki–miyaura and heck C–C coupling reactions catalyzed with palladium(II) complexes of organochalcogen ligands: realities and speculations. Organometallics 33(12):2921
136. Kumar S, Rao GK, Kumar A, Singh MP, Singh AK (2013) Palladium(II)-(E,N,E) pincer ligand (E = S/Se/Te) complex catalyzed Suzuki coupling reactions in water via in situ generated palladium quantum dots. Dalton Trans 42:16939
137. (a) Das D, Rao GK, Singh AK (2009) Palladium(II) complexes of the first pincer (Se,N,Se) ligand, 2,6-Bis((phenylseleno)methyl)pyridine (L): solvent-dependent formation of [PdCl(L)]Cl and Na[PdCl(L)][PdCl4] and high catalytic activity for the heck reaction. Organometallics 28(20):6054; (b) Ghavale N, Manjare ST, Singh HB, Butcher RJ (2015) Bis(chalcogenones) as pincer ligands: isolation and Heck activity of the selone-ligated unsymmetrical C,C,Se–Pd pincer complex. Dalton Trans 44:11893
138. Kumar A, Rao GK, Saleem F, Singh AK (2012) Organoselenium ligands in catalysis. Dalton Trans 41(1977):11949
139. Back TG, Moussa Z (2002) Remarkable activity of a novel cyclic seleninate ester as a glutathione peroxidase mimetic and its facile in situ generation from allyl 3-hydroxypropyl selenide. J Am Chem Soc 124(41):12104
140. Back TG, Kuzma D, Parvez M (2005) Aromatic derivatives and tellurium analogues of cyclic seleninate esters and spirodioxyselenuranes that act as glutathione peroxidase mimetics. J Org Chem 70(23):9230
141. Singh VP, Singh HB, Butcher RJ (2011) Synthesis of cyclic selenenate/seleninate esters stabilized by ortho-nitro coordination: their glutathione peroxidase-like activities. Chem Asian J 6:1431
142. Tripathi SK, Sharma S, Singh HB, Butcher RJ (2011) 2-Phenoxyethanol derived diselenide and related compounds; synthesis of a seven-membered seleninate ester. Org Biomol Chem 9(2):581
143. Młochowski J, Kloc K, Lisiak R, Potaczek P, Wójtowicz H (2007) Developments in the chemistry of selenaheterocyclic compounds of practical importance in synthesis and medicinal biology. ARKIVOC, (vi) 14
144. Bayse CA, Shoaf AL (2015) Effect of methoxy substituents on the activation barriers of the glutathione peroxidase-like mechanism of an aromatic cyclic seleninate. Molecules 20(6):10244
145. McNeil NMR, McDonnell C, Hambrook M, Back TG (2015) Oxidation of disulfides to thiolsulfinates with hydrogen peroxide and a cyclic seleninate ester catalyst. Molecules 20(6):10748
146. Nakashima Y, Shimizu T, Hirabayashi K, Iwasaki F, Yamasaki M, Kamigata N (2005) Optically active seleninate esters: isolation, absolute configuration, racemization mechanism, and transformation into chiral selenoxide. J Org Chem 70(13):5020
147. Chen GP, Ziegler DM (1994) Liver microsome and flavin-containing monooxygenase catalyzed oxidation of organic selenium compounds. Arch Biochem Biophys 312(2):566
148. (a) Kumar S, Johansson H, Engman L, Valgimigli L, Amorati R, Fumo MG, Pedulli GF (2007) Regenerable chain-breaking 2,3-dihydrobenzo[b]selenophene-5-ol antioxidants. J Org Chem 72(7):2583; (b) Kumar S, Engman L, Valgimigli L, Amorati R, Fumo MG, Pedulli GF (2007) Antioxidant profile of ethoxyquin and some of its S, Se, and Te analogues. J Org Chem 72(16):6046; (c) Iwaoka M, Kumakura F (2008) Applications of water-soluble selenides and selenoxides to protein chemistry. Phosphorus, Sulfur Silicon Relat Elem 183(4):1009; (d)

Kumakura F, Mishra B, Priyadarsini KI, Iwaoka M (2010) A water-soluble cyclic selenide with enhanced glutathione peroxidase-like catalytic activities. Eur J Org Chem 440; (e) Cowan EA, Oldham CD, May SW (2011) Identification of a thioselenurane intermediate in the reaction between phenylaminoalkyl selenoxides and glutathione. Arch Biochem Biophys 506(2):201; (f) Arai K, Dedachi K, Iwaoka M (2011) Rapid and quantitative disulfide bond formation for a polypeptide chain using a cyclic selenoxide reagent in an aqueous medium. Chem Eur J 17(2):481; (g) Hodage AS, Phadnis PP, Wadawale A, Priyadarsini KI, Jain VK (2011) Synthesis, characterization and structures of 2-(3,5-dimethylpyrazol-1-yl)ethylseleno derivatives and their probable glutathione peroxidase (GPx) like activity. Org Biomol Chem 9:2992

149. (a) Bayse CA (2010) Model mechanisms of sulfhydryl oxidation by methyl- and benzeneseleninicacid, inhibitors of zinc-finger transcription factors. J Inorg Biochem 104(1):1; (b) Antony S, Bayse CA (2011) Modeling the mechanism of the glutathione peroxidase mimic ebselen. Inorg Chem 50(23):12075; (c) Antony S (2011) Computational investigation of the bioactive selenium compounds Ebselen and Selenious Acid; Doctor of Philosophy (PhD), dissertation, Chemistry and Biochemistry, Old Dominion University. https://doi.org/10.25777/z6fr-rn66
150. Fischer H, Dereu N (1987) Mechanism of the catalytic reduction of hydroperoxides by ebselen: a selenium-77 Nmr study. Bull Soc Chim Belg 96:757
151. Reich HJ, Jasperse CP (1987) Organoselenium chemistry.' redox chemistry of selenocysteine model systems. J Am Chem Soc 109(18):5549
152. Kice JL, Lee TW (1978) Oxidation-reduction reactions of organoselenium compounds. 1. Mechanism of the reaction between seleninic acids and thiols. J Am Chem Soc 100(16):5094
153. Kumar S, Singh HB, Wolmershauser G (2006) Protection against peroxynitrite-mediated nitration reaction by intramolecularly coordinated diorganoselenides. Organometallics 25(2):382
154. Kumakura F, Mishra B, Priyadarsini KI, Iwaoka M (2010) A water-soluble cyclic selenide with enhanced glutathione peroxidase-like catalytic activities. Eur J Org Chem 2010(3):440
155. Arai K, Noguchi M, Singh BG, Priyadarsini KI, Fujio K, Kubo Y, Iwaoka M (2013) A water-soluble selenoxide reagent as a useful probe for the reactivity and folding of polythiol peptides. FEBS Open Bio 3(1):55
156. (a) De Silva V, Woznichak MM, Burns KL, Grant KB, May SW (2004) Selenium redox cycling in the protective effects of organoselenides against oxidant-induced dna damage. J Am Chem Soc 126(8):2409; (b) Cowan EA, Oldham CD, May SW (2011) Identification of a thioselenurane intermediate in the reaction between phenylaminoalkyl selenoxides and glutathione. Arch Biochem Biophys 506(2):201
157. Nascimento V, Alberto EE, Tondo DW, Dambrowski D, Detty MR, Nome F, Braga AL (2012) GPx-like activity of selenides and selenoxides: experimental evidence for the involvement of hydroxy perhydroxy selenane as the active species. J Am Chem Soc 134(1):138
158. Li F, Liu J, Rozovsky S (2014) Glutathione peroxidase's reaction intermediate selenenic acid is stabilized by the protein microenvironment. Free Radic Biol Med 0:127
159. (a) Zhao R, Holmgren A (2002) A novel antioxidant mechanism of ebselen involving ebselen diselenide, a substrate of mammalian thioredoxin and thioredoxin reductase. J Biol Chem 277(42):39456; (b) Farina M, Barbosa NB, Nogueira CW, Folmer V, Zeni G, Andrade LH, Braga AL, Rocha JB (2002) Reaction of diphenyl diselenide with hydrogen peroxide and inhibition of delta-aminolevulinate dehydratase from rat liver and cucumber leaves. Brazilian J Med Biol Res 35(6):623
160. Prasad PR, Singh HB, Butcher RJ (2015) Synthesis, structure and antioxidant activity of cyclohexene-fused selenuranes and related derivatives. Molecules 20(7):12670
161. (a) Rheinboldt H, Giesbrecht E (1955) Über Selenensäuren, III. Mitteil.1): Bildung von Selenensäuren durch Reduktion von Seleninsäuren mittels Unterphosphoriger und Phosphoriger Säure. Chem Ber 88:1974; (b) Jenny W (1958) Zur Kenntnis der Sulfen- und Selenensäuren und ihrer Derivate. 5. Mitteilung. Anthrachinon-1,4-disulfen- und Anthrachinon-1,4-diselenensäure. Helv Chim Acta 41(2):317; (c) Reich H, Hoeger CA, Willis WW Jr (1982)

Organoselenium chemistry. characterization of reactive intermediates in the selenoxide syn elimination: selenenic acids and selenolseleninate esters. J Am Chem Soc 104(10):2936
162. Reich HJ, Jasperse CP (1988) Organoselenium chemistry. Preparation and reactions of 2,4,6-tri-tert-butylbenzeneselenenic acid. J Org Chem 53(10):2389
163. Ishii A, Matsubayashi S, Takahashi T, Nakayama J (1999) Preparation of a selenenic acid and isolation of selenoseleninates. J Org Chem 64(4):1084
164. Zielinski Z, Presseau N, Amorati R, Valgimigli L, Pratt DA (2014) Redox chemistry of selenenic acids and the insight it brings on transition state geometry in the reactions of peroxyl radicals. J Am Chem Soc 136(4):1570
165. Goto K, Nagahara M, Mizushima T, Shimada K, Kawashima T, Okazaki R (2001) The first direct oxidative conversion of a selenol to a stable selenenic acid: Experimental demonstration of three processes included in the catalytic cycle of glutathione peroxidase. Org Lett 3(22):3569
166. Selvakumar K, Singh HB, Butcher RJ (2010) Aromatic ring strain in arylselenenyl bromides: role in facile synthesis of selenenate esters via intramolecular cyclization. Chem Eur J 16(34):10576
167. (a) Bhabak KP, Mugesh G (2009) Amide-based glutathione peroxidase mimics: effect of secondary and tertiary amide substituents on antioxidant activity. Chem Asian J 4(6):974; (b) Bhabak KP, Mugesh G (2009) Synthesis and structure–activity correlation studies of secondary- and tertiary-amine-based glutathione peroxidase mimics. Chem Eur J 15(38):9846
168. Sase S, Kimura R, Masuda R, Goto K (2019) Model study on trapping of protein selenenic acids by utilizing a stable synthetic congener. New J Chem 43:6830
169. Kozlov VV, Suvorova SE (1961) Zh Obshch Khim 31:3034
170. Pichat L, Herbert M, Thiers M (1961) Etudes sur les methodes de preparation de la selenocystamine, selenohypotaurine et selenotaurine. Tetrahedron 12(1–2):1
171. Abdo M, Knapp S (2008) Biomimetic seleninates and selenonates. J Am Chem Soc 130(29):9234
172. Shimizu T, Nakashima Y, Watanabe I, Hirabayashi K, Kamigata N (2002) Optical resolution and racemization of areneseleninic acids. J Chem Soc, Perkin Trans 1:2151
173. (a) Brink G, Vis JM, Arends IWCE, Sheldon RA (2001) Selenium-catalyzed oxidations with aqueous hydrogen peroxide. 2. Baeyer−Villiger reactions in homogeneous solution[1]. J Org Chem 66(7):2429; (b) Crich D, Zou Y (2005) J Org Chem 70:3309
174. Kamigata N (2005) Synthesis and stereochemistry of optically active selenium and tellurium compounds. Phosphorus. Sulfur Silicon Relat Elem 180(3–4):667
175. Nakashima Y, Shimizu T, Hirabayashi K, Yasui M, Nakazato M, Iwasaki F, Kamigata N (2005) Optically active seleninic acid: isolation, absolute configuration, stability, and chiral crystallization. Bull Chem Soc Jpn 78(4):710
176. Domínguez-Álvarez E, Gajdács M, Spengler G, Palop JA, Marć MA, Kieć-Kononowicz K, Amaral LM, Jacob CJ, Handzlik J, Sanmartín C (2016) Identification of selenocompounds with promising properties to reverse cancer multidrug resistance. Bioorg Med Chem Lett 26(12):2821
177. (a) Csonka A, Kincses A, Nové M, Vadas Z, Sanmartín C, Domínguez-Álvarez E, Spengler G (2019) Selenoesters and selenoanhydrides as novel agents against resistant breast cancer. Anticancer Res 39(7):3777; (b) Domínguez-Álvarez E, Plano D, Font M, Calvo A, Prior C, Jacob C, Palop JA, Sanmartín C (2014) Synthesis and antiproliferative activity of novel selenoester derivatives. Eur J Med Chem 73:153
178. Spengler G, Kincses A, Mosolygó T, Marć MA, Nové M, Gajdács M, Sanmartín C, McNeil HE, Blair JMA, Domínguez-Álvarez E (2019) Antimicrobial and antibiofilm activity of selenoesters and selenoanhydrides. Molecules 24(23):4264 (1–16)
179. Sharma N, Kumar S, Kumar S, Mehta SK, Bhasin KK (2018) Synthesis and characterization of fused imidazole heterocyclic selenoesters and their application for chemical detoxification of $HgCl_2$. New J Chem 42:2702
180. Sviridov AF, Ermolenko MS, Yashunsky DV, Kochetkov NK (1983) Selenoesters in organic synthesis. 1. A novel synthesis of ketones. Tetrahedron Lett 24(40):4355

181. (a) Du J-J, Xin L-M, Lei Z, Zou S-Y, Xu W-B, Wang C-W, Zhang L, Gao X-F, Guo J (2018) Glycopeptide ligation via direct aminolysis of selenoester. Chin Chem Lett 29(7):1127; (b) Silva L, Affeldt RF, Lüdtke DS (2016) J Org Chem 81(13):5464
182. Raibaut L, Drobecq H, Melnyk O (2015) Selectively activatable latent thiol and selenolesters simplify the access to cyclic or branched peptide scaffolds. Org Lett 17(14):3636
183. Jagadese J (2006) Chemistry of metal thio- and selenocarboxylates: precursors for metal sulfide/selenide materials, thin films, and nanocrystals. Vittal and Meng Tack Ng. Acc Chem Res 39(11):869
184. Liou J-C, Singh Badsara S, Huanga Y-T, Lee C-F (2014) Syntheses of selenoesters through C–H selenation of aldehydes with diselenides under metal-free and solvent-free conditions. RSC Adv 4:41237
185. Baldassari LL, Mantovani AC, Senoner S, Maryasin B, Maulide N, Lüdtke DS (2018) Redox-neutral synthesis of selenoesters by oxyarylation of selenoalkynes under mild conditions. Org Lett 20(18):5881
186. Guo R-L, Zhu X-Q, Zhang X-L, Wang Y-Q (2020) Synthesis of difluoromethylselenoesters from aldehydes via a radical process. Chem Commun 56:8976
187. Kharma A, Misak A, Grman M, Brezova V, Kurakova L, Baráth P, Jacob C, Chovanec M, Ondrias K, Domínguez-Álvarez E (2019) Release of reactive selenium species from phthalic selenoanhydride in the presence of hydrogen sulfide and glutathione with implications for cancer research. New J Chem 43:11771
188. Bergman J, Engman L (1978) Preparation of selena- and tellura phthalic anhydeide. Organ Preparat Procedures Int 10(6):289
189. Wu X, Hu L (2005) Amide bond formation from selenocarboxylates and aromatic azides. Tetrahedron Lett 46(48):8401
190. Wessjohann LA, Schneider A, Abbas M, Brandt W (2007) Selenium in chemistry and biochemistry in comparison to sulfur. Biol Chem 338(10):997
191. (a) Gamblin DP, Garnier P, van Kasteren S, Oldham NJ, Fairbanks AJ, Davis BG (2004) Glyco-SeS: selenenylsulfide-mediated protein glycoconjugation—a new strategy in post-translational modification. Angew Chem Int Ed 43(7):828; (b) Boutureira O, Bernardes GJL, Gonzalez MF, Anthony DC, Davies DG (2012) Selenenylsulfide-linked homogeneous glycopeptides and glycoproteins: synthesis of human "Hepatic Se Metabolite A". Angew Chem Int Ed 51(6):1432
192. Haratake M, Tachibana Y, Emaya Y, Yoshida S, Fuchigami T, Nakayama M (2016) Synthesis of nanovesicular glutathione peroxidase mimics with a selenenylsulfide-bearing lipid. ACS Omega 1(1):58
193. Bhabak KP, Mugesh G (2007) Synthesis, characterization and antioxidant activity of some ebselen analogues. Chem Eur J 13(16):4594
194. Duhamel E, Pöllnitz A, Stegarescu A, Silvestru A, Anorg Z (2011) Hypervalent organoselenium(II) compounds with organophosphorus ligands. crystal and molecular structure of $[2\text{-}(iPr_2NCH_2)C_6H_4]Se[S_2PR'_2]$ ($R' = Ph, O^iPr$). Allg Chem 637(10):1355
195. Sarma BK, Mugesh G (2005) Glutathione peroxidase (GPx)-like antioxidant activity of the organoselenium drug ebselen: unexpected complications with thiol exchange reactions. J Am Chem Soc 127(32):11477
196. Abdo M, Sun Z, Knapp S (2013) Biohybrid -Se-S- coupling reactions of an amino acid derived seleninate. Molecules 18(2):1963
197. Back TG (1994) Selenium: organoselenium chemistry. In: King RB (ed) Encyclopedia of inorganic chemistry. Wiley, p 3690
198. Iwaoka M (2012) Nucleophilic selenium. In: Wirth T (eds) Organoselenium chemistry: synthesis and reactivity. Wiley-VCH Verlag, GmbH, p 53
199. Zade SS, Singh HB (2014) Synthesis of organoselenium compounds. In: Rappoport Z (ed) The chemistry of organic selenium and tellurium compunds. Wiley, p 1
200. Krief A, van Wemmed T, Redon M, Dumont W, Delmotte C (1999) The first synthesis of organic diselenolates: application to the synthesis of diorganyl diselenides. Angew Chem Int Ed 38(15):2245

201. Canales S, Crespo O, Gimeno MC, Jones PG, Laguna A, Romero P (2003) Gold and silver derivatives with the carborane-selenolate ligand $[B_{10}H_{11}C_2Se]^-$. Dalton Trans 4525
202. (a) Donahue CJ, Martin VA, Schoenfelner BA, Kosinski EC (1991) Preparation and spectral and electrochemical characterization of the tetrakis eight-coordinate molybdenum(IV) and tungsten(IV) complexes containing tert-butyl- and 2-hydroxy-, 2-mercapto-, and 2-(hydroseleno)-substituted pyridine and pyrimidine ligands. Inorg Chem 30(7):1588; (b) Kienitz CO, Thöne C, Jones PG (1996) Coordination Chemistry of 2,2′-Dipyridyl Diselenide: X-ray Crystal Structures of PySeSePy, $[Zn(PySeSePy)Cl_2]$, $[(PySeSePy)Hg(C_6F_5)_2]$, $[Mo(SePy)_2(CO)_3]$, $[W(SePy)_2(CO)_3]$, and $[Fe(SePy)_2(CO)_2]$ (PySeSePy) C5H4NSeSeC_5H_4N; SePy) $[C_5H_4N(2\text{-Se})\text{-N,Se}]$). Inorg Chem 35(13):3990
203. (a) Ashaks J, Bankovsky Yu, Zoruma D, Shestakova I, Domracheva I, Nesterova A, Lukevics E (2004) Synthesis of quinoline-8-selenol, its complex compounds with metals and their cytotoxic activity. Chem Heterocycl Compd 40:776; (b) Lukevics E, Zoruma D, Ashaks J, Shestakova I, Domracheva I, Bridane V, Yashchenko E (2009) Synthesis and cytotoxicity of methyl-substituted 8-quinolineselenolates of ruthenium, rhodium, osmium, and iridium. Chem Heterocycl Compd 45:182
204. (a) Sharpless KB, Lauer RF (1973) Mild procedure for the conversion of epoxides to allylic alcohols. First organoselenium reagent. J Am Chem Soc 95(8):2697; (b) Comasseto JV, Ling LW, Petragnani N, Stefani HA (1997) Vinylic selenides and tellurides - preparation, reactivity and synthetic applications. Synthesis 1997(4):373; (c) Manna D, Mugesh G (2010) A chemical model for the inner-ring deiodination of thyroxine by iodothyronine deiodinase. Angew Chem Int Ed 49(48):9246
205. Metanis N, Keinan E, Dawson PE (2006) Synthetic seleno-glutaredoxin 3 analogues are highly reducing oxidoreductases with enhanced catalytic efficiency. J Am Chem Soc 128(51):16684
206. Bhabak KP, Mugesh G (2008) A simple and efficient strategy to enhance the antioxidant activities of amino-substituted glutathione peroxidase mimics. Chem Eur J 14(28):8640
207. Yoshida S, Kumakura F, Komatsu I, Arai K, Onuma Y, Hojo H, Singh BG, Priyadarsini KI, Iwaoka M (2011) Antioxidative glutathione peroxidase activity of selenoglutathione. Angew Chem Int Ed 50(9):2125
208. Crich D, Hwang JT, Gastaldi S, Recupero F, Wink DJ (1999) Diverging effects of steric congestion on the reaction of tributylstannyl radicals with areneselenols and aryl bromides and their mechanistic implications. J Org Chem 64(8):2877
209. Gosselck J (1958) Über einige selenhaltige Heterocyclen. Chem Ber 91(11):2345
210. Laube J, Jäger S, Thöne C (2001) Thöne, synthesis and structural studies of pyridine-2-selenolates - reactions with electrophilic phosphorus (III) compounds and related complex chemistry. Eur J Inorg Chem 2001(8):1983
211. (a) Landry VK, Minoura M, Pang K, Buccella D, Kelly BV, Perkin G (2006) Synthesis and structural characterization of 1-Mesityl-1,3-dihydro-imidazole-2-selone and Bis(1-mesitylimidazol-2-yl)diselenide: experimental evidence that the selone is more stable than the selenol tautomer. J Am Chem Soc 128(38):12490; (b) Guziec LJ, Guziec FS Jr (1994) A directed metalation route to the selenium analog of methimazole. J Org Chem 59(16):4691
212. Perkin G, Lenardo EJ, Jacob RG, Panatieri RB (2009) Synthesis of vinyl selenides. Chem Rev 109(3):1277
213. (a) Beletskaya IP, Ananikov VP (2007) Addition reactions of E-E and E-H bonds to triple bond of alkynes catalyzed by Pd, Pt, and Ni complexes (E=S, Se). Pure Appl Chem 79(6):1041; (b) Ananikov VP, Orlov NV, Zalesskiy SS, Beletskaya IP, Khrustalev VN, Morokuma K, Musaev DG (2012) Catalytic adaptive recognition of thiol (SH) and selenol (SeH) groups toward synthesis of functionalized vinyl monomers. J Am Chem Soc 134(15):6637
214. Kumar S, Helt JCP, Autschbach J, Detty MR (2009) A new reaction for organoselenium compounds: alkyl transfer from diorganoselenium(IV) dibromides to alkenoic acids to give γ- and δ-lactones. Organometallics 28(12):3426
215. Engman L (1985) Phenyl selenium trichloride in synthesis. Reaction with ketones. A new variation of the selenoxide elimination reaction. Tetrahedron Lett 26(51):6385

216. Holzle G, Jenny W (1958) Zur Kenntnis der Sulfen- und Selenensäuren und ihrer Derivate. 9. Mitteilung Additions- und Substitutionsreaktionen organischer Selen- verbindungen mit unpolaren und polaren Äthylenen[2]. Helv Chim Acta 41:593
217. Santi C, Santoro S (2012) Electrophilic selenium. In: Wirth T (ed) Organoselenium chemistry: synthesis and reactivity. Wiley-VCH Verlag, GmbH, pp 1–51
218. Jackson WP, Ley SV, Whittle AJ (1980) Selenium-mediated cyclization reactions of alkenyl-substituted β-ketoesters. J Chem Soc Chem Commun 1173
219. Davis FA, Zhou R, Lal GS (1990) A new synthesis of α-functionalized unsubstituted sulfonamides. Tetrahedron Lett 31(12):1653
220. Back TG, Murlidharan KR (1991) Formation and electrophilic reactions of benzeneselenenyl p-Toluenesulfonate. Preparation and properties of addition products with acetylenes. J Org Chem 56(8):2781
221. Murata S, Suzuki T (1987) Stereoselective formation of tetrahydrofuran and -pyran by benzeneselenenyl triflate. Tetrahedron Lett 28(38):4415
222. Lapkin II, Dedugov AN, Pavlova NN, Org Zh (1985) Organoselenium compounds IV. Methyl Arylselenocarboxylates and their synthesis and properties. Khim 21:345
223. Toshimitsu A, Owada H, Terao K, Uemura S, Okano M (1984) Pyridylseleno group in organic synthesis. Preparation and oxidation of a-(2-Pyridylseleno) carbonyl compounds leading to α,ß-unsaturated ketones and aldehydes. J Org Chem 49(20):3796
224. Boduszek B, Gancarz R (1996) Pyridine-4-selenenyl bromides as new reagents for seleneny-lation of olefins. J Prakt Chem 338(1):186
225. Andreou T, Bures J, Vilarrasa J (2010) Reaction of dess–martin periodinane with 2-(alkylselenyl)pyridines. Dehydration of primary alcohols under extraordinarily mild conditions. Tetrahedron Lett 51(14):1863
226. Denmark SE, Edwards MG (2006) On the mechanism of the selenolactonization reaction with selenenyl halides. J Org Chem 71(19):7293
227. (a) du Mont WW, Kubiniok S, Peters K, von Schnering HG (1987) Synthesis and structure of a stable iodoselenide. Angew Chem Int Ed 26(8):780; (b) du Mont WW, Marlens A, Pohl S, Saak W (1990) Reversible dismutation and coordination of bis(2,4,6-triisopropylphenyl) diselenide with iodine. A model study that relates to iodine intercalation between selenium chains. Inorg Chem 29(24):4847; (c) Goto K, Sonoda D, Simada K, Sare S, Kawashima T (2010) Modeling of the 5′-deiodination of thyroxine by iodothyronine deiodinase: chemical corroboration of a selenenyl iodide intermediate. Angew Chem Int Ed 49(3):545
228. Kandasamy K, Kumar S, Singh HB, Butcher RJ, Holman KT (2004) Synthesis, structural characterization and fluorescence properties of organoselenium compounds bearing a ligand containing both bulky and nonbonding groups − the first observation of both intramolecular Se···N and Se···O interactions in a diselenide structure. Eur J Inorg Chem 2004(4):1014
229. Mugesh G, Singh HB, Butcher RJ (1999) Novel chiral organoselenenyl halides stabilized by Se···N nonbonded interactions: synthesis and structural characterization. Tetrahedron: asymmetry 10(2):237
230. Mueller B, Takaluoma TT, Laitinen RS, Seppelt K (2011) Syntheses and structures of two dimethyl diselenide–diiodine adducts and the first well characterized diorgano disulfide–nitrosonium adduct. Eur J Inorg Chem 2011(52):4970
231. Barnes NA, Godfrey SM, Hughes J, Khan RZ, Mushtaq I, Ollerenshaw RTA, Pritchard RG, Sarwar S (2013) The reactions of para-halo diaryl diselenides with halogens. A structural investigation of the CT compound $(p\text{-}FC_6H_4)_2Se_2I_2$, and the first reported "$RSeI_3$" compound, $(p\text{-}ClC_6H_4)SeI{\cdot}I_2$, which contains a covalent Se–I bond. Dalton Trans 42:2735
232. Kubniok S, du Mont WW, Pohl S, Saak W (1988) The reagent diphenyldiselane/iodine: no phenylselenenyl iodide but a charge transfer complex with cyclic moieties. Angew Chem Int Ed 27:431
233. Kaltsoyannis N (1997) Computational study of the electronic and geometric structures of the dihalogenodimethylselenium compounds, Me2SeX2 (X = F, Cl, Br, I or At). J Chem Soc Dalton Trans 4759

234. Mukherjee AJ, Zade SS, Singh HB, Sunoj RB (2010) Organoselenium chemistry: role of intramolecular interactions. Chem Rev 110:4357
235. (a) Guillemin J-C (2011) Organic selenocyanates: synthesis, characterization and uses in chemistry and biology. Curr Organ Chem 15(11):1670; (b)Ali W, Álvarez-Pérez M, Marć MA, Salardón-Jiménez N, Handzlik J, Domínguez-Álvarez E (2018) The anticancer and chemopreventive activity of selenocyanate-containing compounds. Curr Pharmacol Rep 4:468
236. (a) Ghosh SK, Hossain SU, Bhattacharya S, Bhattacharya SC (2005) 2-(2-Selenocyanic acid ethyl ester)-1H-benz[de] isoquinoline-1,3-(2H)-dione, synthesis photophysics and interaction with bovine serum albumin: A spectroscopic approach. J Photochem Photobiol B: Bio 81(2):121; (b) Hossain SU, Sengupta S, Bhattacharya S (2005) Synthesis and evaluation of antioxidative properties of a series of organoselenium compounds. Bioorg Med Chem 13(20):5750
237. Chakraborty S, Yadav SK, Subramanian M, Priyadarsini KI, Iwaoka M, Chattopadhyay S (2012) DL-*trans*-3,4-Dihydroxy-1-selenolane (DHS_{red}) accelerates healing of indomethacin-induced stomach ulceration in mice. Free Radical Res 46(11):1378
238. Verma P, Kunwar A, Arai K, Iwaoka M, Priyadarsini KI (2016) Alkyl chain modulated cytotoxicity and antioxidant activity of bioinspired amphiphilic selenolanes. Toxicol Res 5(2):434
239. Iwaoka M, Takahashi T, Tomoda S (2001) Syntheses and structural characterization of water-soluble selenium reagents for the redox control of protein disulfide bonds. Heteroat Chem 12(4):293
240. Iwaoka M, Katakura A, Mishima J, Ishihara Y, Kunwar A, Priyadarsini KI (2015) Mimicking the lipid peroxidation inhibitory activity of phospholipid hydroperoxide glutathione peroxidase (GPx4) by using fatty acid conjugates of a water-soluble selenolane. Molecules 20(7):12364
241. Phadnis PP, Wadawale A, Priyadarsini KI, Jain VK, Iwaoka M (2015) Synthesis, characterization, and structure of *trans*-3,4-dihydroxy-1-selenolane $\{DHS(OH)_2\}$ substituted derivatives. Tetrahedron Lett 56(18):2293
242. Danquigny A, Meziane MAA, Demailly G, Benazza M (2005) Short synthesis of hydroxylated thiolane and selenolane rings from mono-benzylated pentitols and aldoses dithioacetals bis-thionocarbonates as bis-electrophilic substrates. Tetrahedron 61(28):6772
243. Mao C-L, Barnish IT, Hauser CR (1969) Synthesis of phthalimidines. Acid-catalyzed cyclodehydration versus cyclodeamination of γ-hydroxyamides obtained from dilithio-N-substituted benzamides and ketones. J Heterocycl Chem 6(4):475
244. Engman L, Hallberg A (1989) Expedient synthesis of ebselen and related compounds. J Org Chem 54(12):2964
245. Singh VP, Poon J-F, Yan J, Lu X, Ott MK, Butcher RJ, Gates PJ, Engman L (2017) Nitro-, Azo-, and Amino derivatives of ebselen: synthesis, structure, and cytoprotective effects. J Org Chem 82(1):313
246. (a) Bhabak KP, Mugesh G (2007) Synthesis, characterization, and antioxidant activity of some ebselen analogues. Chemistry 13(16):4594–601; (b) Bhabak KP, Mugesh G (2007) Synthesis, characterization, and antioxidant activity of some ebselen analogues. Chem Eur J 13(16):4594
247. Messali M, Abboudi M, Aouad MR, Rezki N, Christiaens LE (2011) Synthesis and characterization of a new five and six membered selenoheterocyclic compounds homologues of ebselen. Organ Chem Int 2011 (2011) Article ID 389615 (p 7)
248. Küppers J, Schulz-Fincke AC, Palus J, Giurg M, Skarżewski J, Gütschow M (2016) Convergent synthesis of two fluorescent ebselen-coumarin heterodimers. Pharmaceuticals 9(3):43 (1–11)
249. Shi C, Yu LZ, Yang FG, Yan J, Zeng HH (2003) A novel organoselenium compound induces cell cycle arrest and apoptosis in prostate cancer cell lines. Biochem Biophys Res Commun 309(3):578
250. Ollivier N, Blanpain A, Boll E, Raibaut L, Drobecq H, Melnyk O (2014) Selenopeptide transamidation and metathesis. Org Lett 16(15):4032

251. (a) Muttenthaler M, Andersson A, de Araujo AD, Dekan Z, Lewis RJ, Alewood PFJ (2010) Modulating oxytocin activity and plasma stability by disulfide bond engineering. J Med Chem 53(24):8585; (b) Berry SM, Gieselman MD, Nilges MJ, van der Donk WA, Lu Y (2002) An engineered azurin variant containing a selenocysteine copper ligand. J Am Chem Soc 124(10):2084; (c) Gowd KH, Yarotskyy V, Elmslie KS, Skalicky JJ, Olivera BM, Bulaj G (2010) Site-specific effects of diselenide bridges on the oxidative folding of a cystine knot peptide, omega-selenoconotoxin GVIA. Biochemistry 49(12):2741
252. Muttenthaler M, Alewood PF (2008) Selenopeptide chemistry. J Pept Sci 14(12):1223
253. (a) Frank W, Hoppe-Seyler's Z (1964) [Syntheses of selenium-containing peptides. II. Preparation of Se-analogous oxidated glutathionee (Se-Se-glutathion)]. Physiol Chem 339(1):214; (b) Theodoropoulos D, Schwartz IL, Walter R (1967) Synthesis of selenium-containing peptides. Biochemistry 6(12):3927
254. Oikawa T, Esaki N, Tanaka H, Soda K (1991) Metalloselenonein, the selenium analogue of metallothionein: synthesis and characterization of its complex with copper ions. Proc Natl Acad Sci USA 88(8):3057
255. Casi G, Hilvert D (2007) Reinvestigation of a selenopeptide with purportedly high glutathione peroxidase activity. J Biol Chem 282(42):30518
256. (a) Liu J, Chen Q, Rozovsky S (2018) Selenocysteine-mediated expressed protein ligation of SELENOM. Methods Mol Biol 1661:265, Humana Press, New York, NY; (b) Liu J, Chen Q, Rozovsky S (2017) Utilizing selenocysteine for expressed protein ligation and bioconjugations. J Am Chem Soc 139(9):3430
257. (a) Liu J, Cheng R, Rozovsky S (2018) Synthesis and semisynthesis of selenopeptides and selenoproteins. Curr Opin Chem Biol 46:41; (b) Aravindhan S, Singh HB, Zeller M, Butcher RJ (2019) Synthesis of selenopeptides: an alternative way of incorporating selenocystine. Amino Acids 51(4):661; (c) Shimodaira S, Iwaoka M (2017) Improved synthetic routes to the selenocysteine derivatives useful for Boc-based peptide synthesis with benzylic protection on the selenium atom. Arkivoc, Part II 260
258. Hondal RJ, Nilsson BL, Raines RT (2001) Selenocysteine in native chemical ligation and expressed protein ligation. J Am Chem Soc 123(21):5140
259. Shimodaira S, Takei T, Hojo H, Iwaoka M (2018) Synthesis of selenocysteine-containing cyclic peptides via tandem *N*-to-*S* acyl migration and intramolecular selenocysteine-mediated native chemical ligation. Chem Commun 54:11737
260. Prabhu CP, Phadnis PP, Wadawale A, Priyadarsini KI, Jain VK (2013) One-pot synthesis of phenylseleno N-acetyl α-amino acids: supra-molecular self-assembling in organoselenium compounds. J Organomet Chem 745–746:140
261. Barick KC, Dutta B, Gawali SL, Phadnis PP, Priyadarsini KI, Jain VK, Hassan PA, (2020) Phenylseleno N-acetyl α-amino acids conjugated magnetic nanoparticles: synthesis, characterization and radical scavenging ability. Chem Lett 49(11):1426
262. Theodoropoulos D, Schwartz IL, Walter R (1967) Synthesis of selenium-containing peptides. Biochemistry 6(12):3927
263. Hondal RJ (2005) Incorporation of selenocysteine into proteins using peptide ligation. Protein Pept Lett 12(8):757
264. (a) Wu Z-P, Hilvert D (1991) Redesign of protein function: a semisynthetic selenoenzyme. In: Gebelein CG (ed) Biotechnology and polymers. Springer, Boston; (b) Wu ZP, Hilvert D (1989) Conversion of a protease into an acyl transferase: selenolsubtilisin. J Am Chem Soc 111(12):4513; (c) Bell IM, Fisher ML, Wu ZP, Hilvert D (1993) Kinetic studies on the peroxidase activity of selenosubtilisin. Biochemistry 32(14):3754; (d) Wu ZP, Hilvert D (1990) Selenosubtilisin as a glutathione peroxidase mimic. J Am Chem Soc 112(14):5647; (e) House KL, Dunlap RB, Odom JD, Wu ZP, Hilvert D (1992) Structural characterization of selenosubtilisin by selenium-77 NMR spectroscopy. J Am Chem Soc 114(22):8573
265. Ren X, Jemth P, Board PG, Luo G, Mannervik B, Liu J, Zhang K, Shen J (2002) A semisynthetic glutathione peroxidase with high catalytic efficiency: selenoglutathione transferase. Chem Biol 9(7):789

266. (a) Liu JQ, Jiang MS, Luo GM, Yan GL, Shen JC (1998) Conversion of trypsin into a selenium containing enzyme by using chemical mutation. Biotechnol Lett 20(7):693; (b) Huang Y, Ge D-Y, Zong H, Yin J-X, Qu X-N, Lv S-W (2017) Active site mimicry of glutathione peroxidase by glutathione imprinted selenium-containing trypsin. Catalysts 7(10):282 (1–12)
267. Xu H, Cao W, Zhang X (2013) Selenium-containing polymers: promising biomaterials for controlled release and enzyme mimics. Acc Chem Res 46(7):1647
268. Cao W, McCallum NC, Ni QZ, Li W, Boyce H, Mao H, Zhou X, Sun H, Thompson MP, Battistella C, Wasielewski MR, Dhinojwala A, Shawkey MD, Burkart MD, Wang Z, Gianneschi NC (2020) Selenomelanin: an abiotic selenium analogue of pheomelanin. J Am Chem Soc 142(29):12802
269. Braga AL, Rafique J (2013) Synthesis of biologically relevant small molecules containing selenium. Part A. Antioxidant compounds, in PATAI's Chemistry of Functional Groups. Wiley
270. (a) Kumar S, Kandasamy K, Singh HB, Wolmershuser G, Butcher RJ (2004) Chelate ring size effect on the reactivity of [2-(2-Phenyl-5,6-dihydro-4H-1,3-oxazinyl)]lithium and Se···N interactions in low-valent organoselenium compounds: facile isolation of diorganotriselenide. Organometallics 23(18):4199; (b) Press DJ (2013) The design and properties of organoselenium compounds with glutathione peroxidase-like activity. Thesis for PhD, University of Calgary, Canada; (c) Mukherjee AJ, Zade SS, Singh HB, Sunoj RB (2010) Organoselenium chemistry: role of intramolecular interactions. Chem Rev 110(7):4357
271. Schindler C, Schulzke C (2017) The unexpected formation of a triselenide from 4-methyl-5-tri-n-butylstannyl-1,3-dithiol-2-one and selenium dioxide. Inorg Chem Commun 77:80
272. Münchberg U, Anwar A, Mecklenburg S, Jacob C (2007) Polysulfides as biologically active ingredients of garlic. Org Biomol Chem 5(10):1505
273. Ahrika A, Robert J, Anoutia M, Paris J (2001) Characterization of organic polyselenide ions in *N,N*-dimethylacetamide. New J Chem 25:741
274. Xu H, Gao J, Wang Y, Wang Z, Smet M, Dehaen W, Zhang X (2006) Hyperbranched polyselenides as glutathione peroxidase mimics. Chem Commun 7:796
275. Pyrzynska K (2002) Determination of selenium species in environmental samples. Mikrochim Acta 140:55
276. (a) Glass RS, Singh WP, Jung W, Veres Z, Scholz TD, Stadtman TC (1993) Monoselenophosphate: Synthesis, characterization, and identity with the prokaryotic biological selenium donor, compound SePX. Biochemistry 32(12):12555; (b) Xu X-M, Carlson BA, Irons R, Mix H, Zhong N, Gladyshev VN, Hatfield DL (2007) Selenophosphate synthetase 2 is essential for selenoprotein biosynthesis. Biochem J 404(Pt 1):115
277. Lobinski R, Edmonds JS, Suzuki KT, Uden PC (2000) Species-selective determination of selenium compounds in biological materials. Pure Appl Chem 72(3):447
278. Srivastava M, Mallard C, Barke T, Hancock LE, Self WT (2011) A selenium-dependent xanthine dehydrogenase triggers biofilm proliferation in enterococcus faecalis through oxidant production. J Bacteriol 193(7):1643
279. Gad SC, Pham T (2014) Selenium. In: Encyclopedia of toxicology, 3rd ed, p 232
280. Féher F (1963) Sodium selenite. In: Brauer G (ed) Handbook of preparative inorganic chemistry, 2nd ed. Academic Press, New York, vol 1, p 432
281. Bjornberg A, Martensson US, Paulsson KM, (Boliden Aktiebolag) (1986) Method for producing selenium salts. US Patent 4, 605, 544, August 12
282. Verma P, Maheshwari SK (2018) Preparation of sliver and selenium nanoparticles and its characterization by dynamic light scattering and scanning electron microscopy. J Microsc Ultrastruct 6(4):182
283. (a) Cui Y, Abouimrane A, Sun C-J, Ren Y, Amine K (2014) Li–Se battery: absence of lithium polyselenides in carbonate based electrolyte. Chem Commun 50:5576; (b) Sharp KW, Koehler WH (1977) Synthesis and characterization of sodium polyselenides in liquid ammonia solution. Inorg Chem 16(9):2258
284. Rasche B, Amin HMA, Clarke SJ, Compton RG (2019) Polyselenides on the route to electrodeposited selenium. J Electroanal Chem 835:239

285. (a) Page EM (1998) Reaction with alkali metal selenides, polyselenides, tellurides, and polytellurides. In: Zuckerman JJ, Norman AD (eds) Inorganic reactions and methods. Wiley-VCH Inc.; (b) Dhingra S, Kanatzidis MG (1990) The use of soluble metal-polyselenide complexes as precursors to binary and ternary solid metal selenides. MRS Online Proc Library 180:825
286. Wang Y-L, Feng M-L, Wang K-Y, Li J-R, Huang X-Y (2016) $[Mn(dien)_2]_2[SbSe_4Cu(\mu_2\text{-}Se_4)]$: A heterometallic polyselenide containing a chelating μ_2-Se_4. Inorg Chem Commun 72:141
287. O'Neal SC, Kolis JW (1988) Convenient preparation and structures of selenometalates $MoSe_4^{2-}$, WSe_4^{2-} and $MoSe_9^{2-}$ from polyselenide anions and metal carbonyls. J Am Chem Soc 110(6):1971
288. O'Neal SC, Pennington WT, Kolis JW (1989) Reaction of transition metal carbonyls with soluble polyselenides: synthesis and structure of $[(C_6H_5)_4P]_2[Re_2(Se_4)_2(CO)_6]$. Can J Chem 67(1):1980
289. (a) Herath Banda RM, Cusick J, Scudder ML, Craig DC, Dance IG (1989) Syntheses and structures of anionic metal polyselenide complexes $[(C_5H_5)Mo(Se_4)_2]^-$ and $[Sn(Se4)3]2^-$, crystallized with Ph_4P^+. Polyhedron 8(15):1999; (b) Herath Banda RM, Cusick J, Scudder ML, Craig DC, Dance IG (1989) Syntheses and X-ray structures of molecular metal polyselenide complexes $[M(Se_4)_2]^{2-}$ M = Zn, Cd, Hg, Ni, Pb. Polyhedron 8(15):1995
290. Cuixia DU, Juan C, Menghe B (2019) Solvothermal syntheses and characterization of three one-dimension cadmium selenidoarsenates $[Ni(1,2\text{-dap})_3][As_2CdSe_4]$, $[Zn(1,2\text{-dap})_3][As_2CdSe_4]$ and $[Ni(en)_3][As_2CdSe_4]$. Chem Res Chinese Universities 35(4):560
291. (a) Pretsch E, Buhlmann P, Badertscher M (2009) Structure determination of organic compounds. Springer, Berlin, Heidelberg. ISBN 978-3-540-93809-5; (b) Mann BE (1988) Recent developments in NMR spectroscopy of organometallic compounds. Adv Organomet Chem 28:397; (c) Elyashberg M (2015) Identification and structure elucidation by NMR spectroscopy. Trends Anal Chem 69:88
292. (a) Wüthrich K (2001) The way to NMR structures of proteins. Nat Struct Mol Biol 8(11):923; (b) Cavalli A, Salvatella X, Dobson CM, Vendruscolo M (2007) Protein structure determination from NMR chemical shifts. PNAS 104(23):9615; (c) Driscoll PC (2013) Structure determination by NMR: overview. In: Roberts GCK (eds) Encyclopedia of biophysics. Springer, Berlin, Heidelberg
293. Harris RK, Mann BE (1978) NMR and periodic table. Academic Press, London
294. Odom JD, Dawson WH, Ellis PD (1979) Selenium-77 relaxation time studies on compounds of biological importance: dialkyl selenides, dialkyl diselenides, selenols, selenonium compounds, and seleno oxyacids. J Am Chem Soc 101(19):5815
295. Duddeck H (1995) Selenium-77 nuclear magnetic resonance spectroscopy. Prog Nucl Magn Reson Spectrosc 27(1–3):1
296. (a) Klapötke TM, Broschag M (1996) Compilation of reported ^{77}Se NMR chemical shifts. Wiley, New York; (b) Duddeck H (2004) 77Se NMR spectroscopy and its applications in chemistry. Annu Rep NMR Spectrosc 52(51):105 (c) Demko BA, Wasylishen RE (2009) Solid-state selenium-77 NMR. Prog Nucl Magn Reson Spectrosc 54(3–4):208; (d) Panda A, Singh HB (2014) Chemistry of organic selenium and tellurium compounds. In: Rappoport Z (ed) Wiley, pp 277–445
297. Llabrès G, Baiwir M, Piette JL, Christiaens L (1981) ^{77}Se, ^{13}C and ^{1}H NMR investigations on ortho-carbonyl benzeneselenenyl derivatives. Org Magn Reson 15(2):152
298. Irgolic KJ, Knapp FF Jr., (1983) Tellurium-125 and selenium-77 NMR shifts for symmetric and unsymmetric diorganyl chalcogenides. Organometallics 2(2):305
299. Dowd D, Gettins P (1988) Model compounds for the active site selenocysteine of glutathione peroxidase: A ^{77}Se NMR study. Magn Reson Chem 26:1
300. Tan KS, Arnold AP, Rabenstein DL (1988) Selenium-77 nuclear magnetic resonance studies of selenols, diselenides, and selenenyl sulfides. Can J Chem 66(1):54
301. Iwaoka M, Tomoda S (1994) A model study on the effect of an amino group on the antioxidant activity of glutathione peroxidase. J Am Chem Soc 116(6)(6):2557; (b) Komatsu H, Iwaoka M, Tomoda S (1999) Intramolecular non-bonded interaction between selenium and oxygen

as revealed by ^{17}O and ^{77}Se NMR spectroscopy and natural bond orbital analysis. Chem Commun 205
302. (a) Iwaoka M, Tomoda S (2005) Physical- and bio-organic chemistry of nonbonded selenium· · ·oxygen interactions. Phosphorus, Sulfur, Silicon Relat Elem 180(3–4):755; (b) Hayashi S, Nakanishi W (2013) Hypervalent chalcogen compounds. In: Devillanova FA, Du Mont WW (eds) Handbook of chalcogen chemistry: new perspectives in sulfur, selenium and tellurium. RSC Publishing
303. Liu J, Rozovsky S (2016) ^{77}Se NMR spectroscopy of selenoproteins. In: Hatfield DL, Berry MJ, Gladyshev VN (eds) Selenium in molecular biology & human health. Springer, p 187
304. House KL, Dunlap RB, Odom JD, Wu ZP, Hilvert D (1992) Structural characterization of selenosubtilisin by selenium-77 NMR spectroscopy. J Am Chem Soc 114(22):8573
305. Prabhu P, Singh BG, Noguchi M, Phadnis PP, Jain VK, Iwaoka M, Priyadarsini KI (2014) Stable selones in Glutathione-peroxidase-like catalytic cycle of selenonicotinamide derivative. Org Biomol Chem 12(15):2404
306. Jain VK (2017) An overview of organoselenium chemistry: from fundamentals to synthesis (Chap. 1). In: Organoselenium compounds in biology and medicine: synthesis, biological and therapeutic treatments, pp 1–33. eISBN: 978-1-78801-190-7
307. Gross JH (2004) Mass spectrometry, a textbook. Springer, Berlin, Heidelberg
308. (a) Yamashita Y, Yamashita M (2010) Identification of a novel selenium-containing compound, selenoneine, as the predominant chemical form of organic selenium in the blood of bluefin tuna. J Biol Chem 285:18134; (b) Dernovics M, Far J, Lobinski R (2009) Identification of anionic selenium species in Se-rich yeast by electrospray QTOF MS/MS and hybrid linear ion trap/orbitrapMS. Metallomics. 7(4):317; (c) Schaefer SA, Dong M, Rubenstein RP, Wilkie WA, Bahnson BJ, Thorpe C, Rozovsky S (2012) (77)Se enrichment of proteins expands the biological NMR toolbox. J Mol Biol 425(2):222; (d) Haratake M, Hongoh M, Miyauchi M, Hirakawa R, Ono M, Nakayama M (2008) Albumin-mediated selenium transfer by a selenotrisulfide relay mechanism. Inorg Chem 47(14):6273
309. Clegg W (ed) (2009) Crystal structure analysis: principles and practice, In: Clegg W, Blake AJ, Cole JM, Evans JSO, Main P, Parsons S, Watkin DJ (Eds)2nd ed. Oxford University Press Inc., New York. ISBN 978-0-19-921946-9
310. Scimeca M, Bischetti S, Lamsira HK, Bonfiglio R, Bonanno E (2018) Energy dispersive X-ray (EDX) microanalysis: a powerful tool in biomedical research and diagnosis. Eur J Histochem 62(1):2841
311. Shamberger RJ (1983) Analytical methods of selenium determination. In: Biochemistry of selenium. Biochemistry of the elements, vol 2. Springer, Boston, MA, pp 311–327
312. Li F, Goessler W, Irgolic KJ (1999) Determination of selenium compounds by HPLC with ICP-MS or FAAS as selenium-specific detector. Chin J Chromatogr 17(3):240
313. Soruraddin MH, Heydari R, Puladv M, Zahedi MM (2011) A new spectrophotometric method for determination of selenium in cosmetic and pharmaceutical preparations after preconcentration with cloud point extraction. Int J Anal Chem 2011 Article ID 729651 (1–8)
314. (a) Chatterjee A, Tao H, Shibata Y, Morita M (2003) Determination of selenium compounds in urine by high-performance liquid chromatography–inductively coupled plasma mass spectrometry. J Chromatogr A 997(1–2):249; (b) Chandrasekaran K, Ranjit M, Arunachalam J (2009) Determination of inorganic selenium species [Se(IV) and Se(VI)] in tube well water samples in Punjab, India. Chem Spec Bioavailab 21(1):15–22
315. Viñas P, Pardo-Martínez M, Hernández-Córdoba M (2000) Rapid determination of selenium, lead and cadmium in baby food samples using electrothermal atomic absorption spectrometry and slurry atomization. Analytica Chimica Acta 412(1–2):121
316. Chan CCY, Sadana RS (1992) Determination of arsenic and selenium in environmental samples by flow-injection hydride generation atomic absorption spectrometry. Anal Chim Acta 270(1):231
317. (a) Sanchez-Rodas D, Corns WT, Chen B, Stockwell PB (2010) Atomic fluorescence spectrometry: a suitable detection technique in speciation studies for arsenic, selenium, antimony and mercury. J Anal At Spectrom 25:933; (b) Cai Y (2000) Speciation and analysis of mercury, arsenic, and selenium by atomic fluorescence spectrometry. Trends Anal Chem 19(1):62

318. Lavi N, Mantel M, Alfassi ZB (1988) Determination of selenium in biological materials by neutron activation analysis. Analyst 113(12):1855
319. (a) Paltridge NG, Milham PJ, Ortiz-Monasterio JI, Velu G, Yasmin Z, Palmer LJ, Guild GE, Stangoulis JCR (2012) Energy-dispersive X-ray fluorescence spectrometry as a tool for zinc, iron and selenium analysis in whole grain wheat. Plant Soil 361(1–2):261; (b) Cevik U, Akbulut S, Makarovska Y, Grieken RV (2013) Polarized-beam high-energy EDXRF in geological samples. Spectroscopy Lett 46(1):36; (c) Oyedotun TDT (2018) X-ray fluorescence (XRF) in the investigation of the composition of earth materials: a review and an overview. Geol Ecol Landsc 2(2):148

Chapter 14
Synthesis and Development of Platinum-Based Anticancer Drugs

Prasad P. Phadnis

Abstract This article describes the prime role of anticancer drugs based on platinum in clinical treatment, their limitations and side effects. The efforts to investigate the molecular mechanism of their anticancer action proved by crystal structural and NMR spectrometric analyses and other techniques have been summarized in order to give clear picture of developments in establishing the mechanism. It has given clear evidences of platinum(II) interactions with DNA forming the adducts leading to death of cancer cells. Along with these interactions, the harmful as well as beneficial interactions of platinum with various sulphur containing biomolecules and sulphur containing molecules have been briefly described; which has given a new direction to design the novel platinum-based drugs and the use of sulphur containing molecule as chemoprotective actions. After the understanding the reason, *i.e.* high reactivity of platinum(II) leading to such undesired interactions; the new strategy of kinetically inert Pt(IV) prodrug concept was developed to overcome such limitation. Such Pt(IV) compounds having additional features of axial groups which confer the favourable biocompatible properties have been described. After the understanding of developmental stages, the synthesis of representative examples various types of platinum(II) as well as platinum(IV) compounds have been described. Later the evaluation methods for anticancer properties have mentioned. The drug delivery systems in order to overcome the side effects have been mentioned. It is anticipated that this account of platinum-based anticancer drug development, will help in designing novel compounds which will overcome limitations of existing drugs.

Keywords Anticancer drugs · Cisplatin · Pt–DNA adduct · Pt-sulphur · Pt(IV) prodrug · Novel design, etc.

P. P. Phadnis (✉)
Chemistry Division, Bhabha Atomic Research Centre, Mumbai 400085, India
e-mail: phadnisp@barc.gov.in

Homi Bhabha National Institute, Anushaktinagar, Mumbai 400094, India

A. K. Tyagi and R. S. Ningthoujam (eds.), *Handbook on Synthesis Strategies for Advanced Materials*, Indian Institute of Metals Series,
https://doi.org/10.1007/978-981-16-1892-5_14

14.1 Introduction

The cancer is a 2nd foremost cause for worldwide deaths. It tolled about 9.6 million lives globally in 2018 and about 18.1 million new cases were estimated for a next year. Worldwide, about 1 among 6 deaths is because of cancer [1]. Hence, to treat such a deadly disease, various treatments mainly chemotherapy, radiotherapy and surgery as well as newly developing immunotherapy, hyperthermia, boron neutron capture therapy (BNCT) and photodynamic therapy (PDT), etc. have been employed in the modern era of medicine [2]. Among them in most of the cases, chemotherapy is conveniently used since it is a less invasive mode of treatment. Additionally, the innovations in chemotherapy led to a new era of oral and topical chemotherapy. As the name suggests, the chemotherapy employs chemical compounds to treat cancers. Among them, various classes of compounds like, plant alkaloids, antitumour antibiotics, alkylating agents, topoisomerase inhibitors, antimetabolites, etc. have been employed. In case of alkylating agents, the metallodrugs, based on metals like platinum (Pt), gold (Au), ruthenium (Ru), osmium (Os), iridium (Ir), copper (Cu), etc. have exhibited potency [3]. Among them, the Pt-based drugs have made great strides in the clinical treatment of cancers [4]. Among the approved metallodrugs, majority of candidates are the platinum-based drugs.

The new era of platinum-based antineoplastic drugs started after an unexpected finding of cisplatin cytotoxicity by Rosenberg et al. and subsequent FDA approval in 1978 as an anticancer (antineoplastic) drug for clinical applications [5]. It is widely applied for treating various cancers like ovarian, testicular, bladder cervical, breast, head and neck, esophageal, lung, mesothelioma, neuroblastoma cancers and brain tumours [6]. But it has severe side effects including neurotoxicity, ototoxicity (hearing loss), nephrotoxicity (kidney damage), hair loss as well as nausea [7]. Additionally, limitations like poor water solubility, development of cellular resistance to cisplatin after prolong treatment and undesired side reactions with cellular thiols and sulphur containing biomolecules like L-methionine have been a main clinical impediment [8]. It directed the research for structural modifications of cisplatin to minimize side effects and overcome the limitations. In due course, various compounds were designed and evaluated for anticancer activities. Among them carboplatin (in 1989), oxaliplatin (in 2002), were globally approved for cancer treatment while nedaplatin, lobaplatin and heptaplatin, got approval for clinical applications in Japan, China and South Korea respectively (Scheme 14.1). They exhibited reduced side effects relative to cisplatin. Overall, the Pt(II) based antineoplastic drugs have been used globally for treatment of various malignancies [9]. Additionally, the Pt(IV) prodrug-based compounds where axial positions have acetato, chloro and hydroxo groups viz., satraplatin, tetraplatin and iproplatin respectively, were found less toxic than cisplatin [10] and they were further investigated under clinical trials (Scheme 14.2) [9c, 11]. This significant contribution of Pt-based compounds has initiated a new research area known as ‘medicinal inorganic chemistry’ [12].

This brief account of Pt-based anticancer drugs clearly depicts their pivotal role in clinical treatment. The wealth of Pt-based approved anticancer drugs and Pt

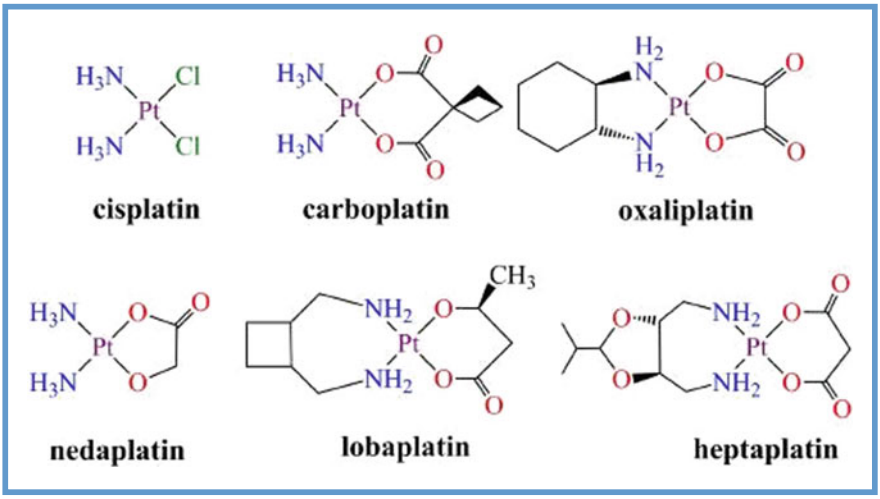

Scheme 14.1 Platinum(II) based compounds: approved drugs for clinical treatment of cancer Reproduced with permission from ACS Publications Ref. [13b]

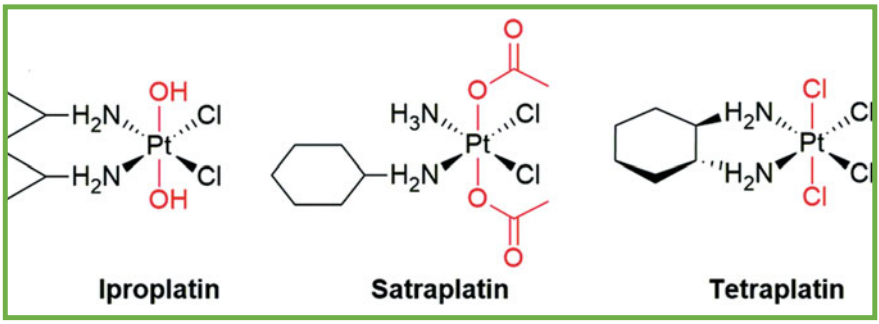

Scheme 14.2 Pt(IV) based prodrugs investigated under clinical trials Reproduced with permission from ACS Publications Ref. [13b]

compounds under clinical trials as well as new Pt compounds under pharmacological studies was achieved through their appropriate structural modifications. The account of these studies has also been reported in some reviews [13]. Hence, at this instance, it will be worthwhile to discuss the molecular mechanism of anticancer action of platinum-based clinical drugs and summarize diverse strategies used to develop various platinum(II) based compounds. The effort of this chapter may be useful for the beginner researchers in this research area for designing the novel platinum compounds for achieving reduced side effects, enhanced biocompatibility and for overcoming the limitations of existing drugs.

14.2 General Properties of Platinum Contributing to Its Anticancer Action

Before starting to molecular mechanism of Pt drugs and their appropriate design strategies, it is worth to discuss general electronic properties of platinum. These properties attribute to its reactivity and structures which performs a key role in molecular mechanism and activity of anticancer action of these compounds.

Platinum belongs to transition (*d*-block) elements with electronic configuration [Xe] $4f^{14}$ $5d^9$ $6s^1$. Platinum compounds exist most commonly in +2 and +4 oxidation states having square planar (d^8 system) and octahedral (d^6 system) respectively. They occur less commonly in +1 and +3 oxidation states and generally achieve stability by metal bonding in bimetallic or polymetallic compounds. [14]. The Pt(II) undergoes dsp^2 hybridization forming highly reactive complexes with square planar geometry where cis- and/or trans-isomers are possible. The bond angles are typically 90° or with slight distortion depending on donor species. The Pt being a soft metal, such Pt(II) compounds have high affinity for soft nucleophiles like sulphur-based compounds present in body. They are labile compounds susceptible for substitution or replacement reactions and their kinetics depend on electronic properties of donor species. While in case of Pt(IV) compounds, platinum ion undergoes d^2sp^3 hybridization affording kinetically inert complexes with octahedral geometry [15]. They are stable or inactive complexes. However, the Pt(IV) species on treatment with reducing agents or by photon activation, can be reduced to Pt(II) species, i.e. active form. After understanding the molecular mechanism of cisplatin, these properties of platinum have been very trickily used in designing novel platinum compounds to be targeted for anticancer applications [16].

14.3 Molecular Mechanism of Anticancer Properties of Platinum(II) Based Drugs

14.3.1 Platinum DNA Binding

14.3.1.1 Platinum Binding with Purine Bases on DNA

Molecular mechanism of anticancer action of cisplatin is now well established. Accordingly, the DNA (deoxyribo nucleic acid) is a primary target of cisplatin and later the mechanism is observed for other platinum-based drugs also. The platination of DNA, i.e. binding of Pt drugs with DNA takes place which consequently interfere with transcription and DNA replication, hence inhibiting cell growth and division, eventually resulting in apoptotic cell death [17].

It is proved that cisplatin after intravenous injection undergoes sequential aquation in cells where chloride groups are replaced by water, forming $[PtCl(NH_3)_2(H_2O)]^+$

and further aquation forms $[Pt(NH_3)_2(H_2O)_2]^{2+}$ as an activated cationic species which interact with DNA in a mono- and bifunctional modes. This aquation is a fast reaction and takes place in cells as soon as cisplatin is injected. The favourable physiological conditions in body facilitate this process. The presence of chloride ions (Cl^-) in blood plasma in high concentration (100 mM) maintains stability of cisplatin towards hydrolysis [18]. While lower intra-cellular concentration of chloride (4 mM) facilitates fast hydrolysis ($t_{1/2}$ ~ 2 h) of chlorides of the drug. This process of cisplatin aquation and its subsequent binding with DNA is experimentally well studied and then reviewed also (Fig. 14.1) [19].

Furthermore, it is interesting to investigate about the binding sites on DNA and overall modes of cisplatin–DNA interactions. In this regard, various computational and theoretical studies have evidenced the binding mechanism [20]. The vast experimental investigations by NMR spectroscopy and single crystal structural analyses have unambiguously established the binding modes. In these investigations, the first crystal structure was reported by Lippard et al. which revealed, *cis*-$[Pt(NH_3)_2]^{2+}$ binding with a dinucleotide [21] and they further confirmed its binding with a double-stranded oligonucleotide [22]. Additionally, Lippard et al. in their further investigations reported the crystal structure of binding of Pt with DNA duplex also [23]. The same findings were established by analysing the structure of the same adducts by NMR spectroscopy in solution state with additional information of structural aspects by Lippard et al. [24]. In the further investigations, Lippard et al. have established

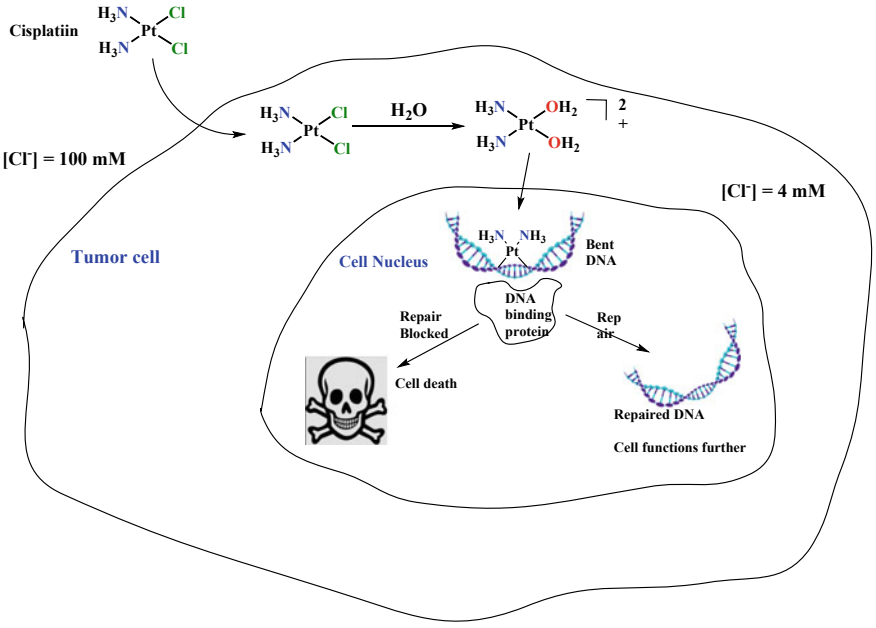

Fig. 14.1 Schematic presentation of cisplatin anticancer mechanism

the role of HMG (high mobility group) and other proteins, in anticancer mechanism of cisplatin. Their studies revealed that the major proportion of adducts viz., intrastrand d(ApG) and d(GpG) cross-links are formed leading to bend and unwind the duplex DNA. This alteration in structure attracts HMG and other proteins resulting in binding between cisplatin binded DNA and proteins of high mobility group (HMG) domain; which is considered to mediate the antitumour activity of cisplatin. There are various HMG-domain proteins which have ability to recognize the altered DNA structures. Hence to understand the molecular basis for such recognition, Lippard et al. have investigated the pathways by crystal structure analysis of an adduct (1:1) between cisplatin modified DNA and HMG [25]. Other extensive investigations by structural and spectral analyses as well as molecular dynamic simulations have also supported the Pt–DNA interactions [26]. Additionally, these interactions have been authenticated by infrared-multiple photon dissociation (IRMPD) and Tandem mass spectrometry (MS/MS) analyses also [27].

Another drug, carboplatin is used for treating especially testis, ovary, head, neck, as well as small-cell lung cancer [28]. In case of carboplatin also, the molecular mechanism of its anticancer property is proposed to follow a binding of Pt–DNA which inhibit the replication and transcription, which further leads to cell death. The investigation for molecular mechanism of carboplatin was performed by Lippard et al. with the help of crystal structural analysis. They established the binding between the $[Pt(ammine)(cyclohexylamine)]^{2+}$ and dodecamer-DNA Duplex [29]. Similarly, Brabec et al. have investigated the same interactions responsible for anticancer properties of carboplatin [30]. Additionally, carboplatin binding with DNA was investigated by using an accelerator mass spectrometry (AMS) as a very much sensitive technique for detection which is quantifying the radiocarbon ^{14}C labelled species. These studies revealed the kinetics of adduct formation between [^{14}C] carboplatin and genomic DNA and drug uptake also [31]. Even the biochemical mechanisms for a developed resistance to carboplatin drug have been proposed [32]. Additionally, the adduct formation between carboplatin and DNA was evaluated in vitro as well as in situ drug reactions with RIF-1 and CHO cell lines and in human buccal cells by using a quantitative immunostaining assay. The rate of Pt–DNA was evaluated by using atomic absorption spectroscopy [33].

Oxaliplatin is utilized especially for the treatment of colorectal cancer [34]. Its molecular mechanism was also investigated which revealed the same type adduct formation between Pt and the same sites (purine bases) on DNA as established in case of cisplatin. In these efforts, Chaney et al. have investigated the structures of binding between oxaliplatin and two guanine residues (oxaliplatin-GG complex) [35]. Additionally, the same group has authenticated the binding of oxaliplatin with a DNA dodecamer duplex in 1,2-d(GG) intrastrand cross-linking fashion [36] as well as adduct of oxaliplatin-GG 12-mer DNA [37] by using NMR spectroscopic analyses.

Along with such finding, some investigations of binding between oxaliplatin and other biomolecules like a protein lysozyme (protein in hen egg white) were performed by using X-ray structure analyses. Their structures were found significantly different than the structures of adducts of Pt drugs and proteins. Hence, it is proposed that their

resultant different reactivates may lead to different biological implications which possibly influence the drug efficiency [38].

14.3.1.2 Platinum Binding with Pyrimidine Bases on DNA

All such studies revealed the various types of possible modes of interaction between cisplatin with DNA. Eventually, it is established theoretically as well as experimentally that the purine bases adenine and guanine of DNA preferentially coordinate covalently with Pt(II) ion through their N atom [39]. However, recently, Wang and Wu et al. have discovered a binding of the cisplatin with pyrimidine bases thymine and cytosine also. They have investigated such binding of cisplatin with a single stranded oligodeoxynucleotide, which was proved by high resolution Fourier transform-ion cyclotron resonance mass spectrometry (FT-ICR MS) [40].

14.3.2 Binding Modes of Platinum with DNA

Let us focus on established modes of interactions of cisplatin with DNA. Accordingly, the cisplatin binds especially with purine bases present on DNA. The nitrogen N7 atoms belonging to purine bases [guanine (G) and adenine(A)] are the best donors since they are having maximum electron density as well as they are at easily approachable sites present on DNA for the electrophilic attack of platinum ions (Pt^{2+}). Additionally, N1 of adenine and N3 of cytosine, can also contribute in binding with platinum (II) centre [41].

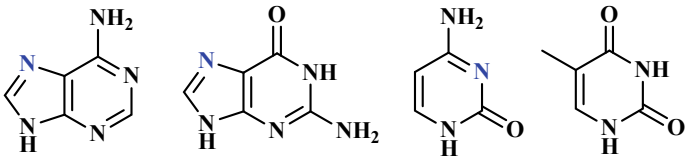

Eventually, the Pt^{2+} binds with them in various modes to form Pt–DNA adducts (Fig. 14.2). Among them, the predominant mode (in ~60% cases) is formation of a bifunctional guanine-guanine (GG) intrastrand cross-links, between Pt^{2+} and nitrogen N7 of neighbouring guanine (G) residues belonging to same DNA strand which is referred as 1,2-intrastrand d(GpG) [39a] (Fig. 14.3). Similarly, the bifunctional adenine and guanine are possible between adenine and adjacent guanine which are referred as 1,2-intrastrand d(ApG) cross-links (in ~25% cases). While bifunctional guanine-guanine intrastrand [1,3-intrastrand d(GpNpG)] cross-links between the purine bases separated by one or more interfering bases as well as inter-strand cross-links forming the monofunctional adducts to guanine residues were present in less than 10%, altogether together [19i, 42].

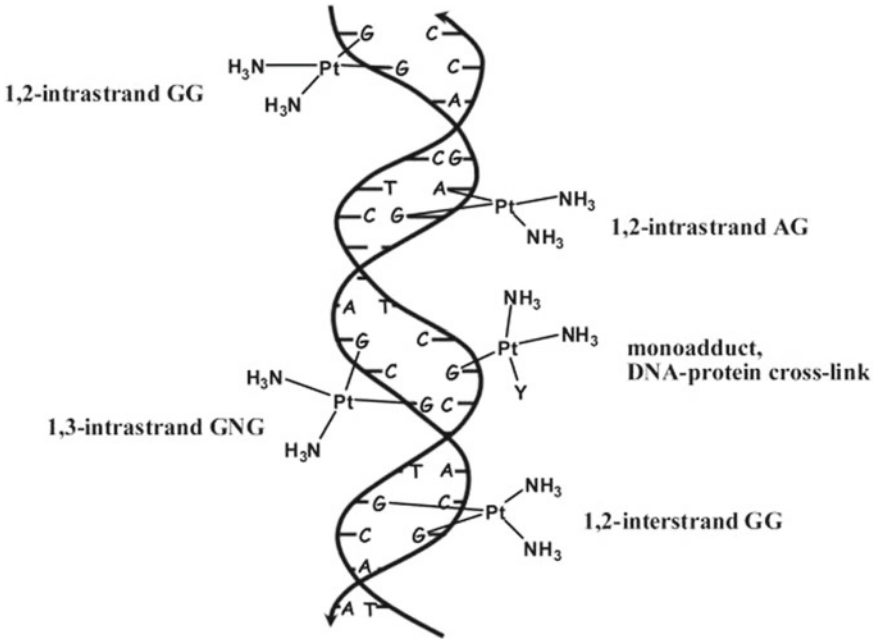

Fig. 14.2 Prominent modes of Pt^{2+} binding with DNA. Reproduced with permission from Elsevier Publications Ref. [19i]

Fig. 14.3 A1,2-intrastrand d(GpG)

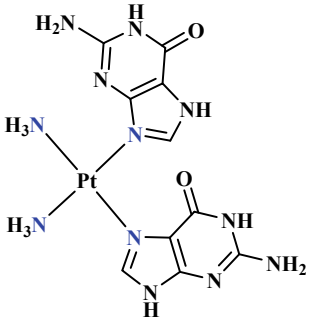

14.3.3 Platinum RNA Binding

There are very few studies reported on cisplatin binding with RNA (ribonucleic acids) contributing to its cytotoxicity. In such efforts, Steitz et al. have investigated the binding of cisplatin with RNA with authentic evidence by the X-ray structure analysis [43]. Some more reports have also depicted the RNA platination [44–46]. But, this interaction is not considered to be effective in imposing cisplatin toxicity because a damaged RNA-molecule can be possibly replaced with a newly synthesized RNA. In

this regard, the investigations have shown that that cisplatin doesn't hamper synthesis of RNA, while it negatively affects DNA synthesis. Additionally, in vitro studies have exhibited very minor damage of RNA molecules (maximum 10%) when treated with cisplatin of concentration range found as lethal dose for cancer cells [47]. Hence, this concept is not yet well established and requires more detailed investigations.

14.3.4 Harmful Interactions of Platinum and S Containing Endogenous Biomolecules

After knowing about all these possibilities, it is worthy to note here that, the Pt^{2+} has a potential to interact competitively with various other sulphur (S) containing endogenous biomolecules like glutathione (GSH, a tripeptide) or S containing amino acids (e.g. methionine or cysteine) and eventually such proteins (e.g., metallothionein and albumin) also. These reactions were observed in many stages of platinum drug treatments like drug uptake, its excretion and even slowly developed cellular resistance to drug also. In context to anticancer properties, such interactions are considered as undesired or non-selective interaction, which hamper the efficiency due to unavailability of activated Pt^{2+} in sufficient concentration to interact with DNA. Additionally, these non-selective interactions are the cause of severe side effects also, since they bind with proteins leading to their structural changes and hence hamper them from performing their desired functions. Although reports revealed, that the Pt^{2+} bindings with guanine bases of DNA prevails over other such interaction, but still complete avoiding for such ubiquitous interactions is difficult. It has been reviewed well by J. Reedijk [48].

14.3.5 Beneficial Interactions of Platinum with Sulphur Containing Exogenous Molecules

In contrast to endogenous Pt-sulphur interactions leading to side effects, the exogenous S containing drug molecules like amifostine (FDA approved radioprotector) and dimesna (uroprotective agent) were observed to alleviate the side effects of platinum(II) based anticancer drugs [49]. Similarly, various S-based natural as well as synthetic compounds like N-acetyl cysteine, methionine, glutathione, sodium thiosulfate, diethyldithiocabamate, etc. have exhibited utility as chemoprotective agents during in vivo (in animal models) studies and in cancer patients also. In one exemplary report, J. Gailer et al. have reported the structural features platinum–sulphur complexes and tried to find best possible chemoprotective agent to overcome severe toxic side effects of cisplatin making it relatively safer and more effectual anticancer drug [50]. Additionally, during earlier investigations of metabolic and mechanistic pathways of cisplatin therapy, the platinum complexes with L-methionine, i.e.

[Pt(Met-*S,N*)$_2$] was extracted from the urine of patients [51] as well as L-methionine complex with carboplatin treated animals was isolated from their urine [52]. As a result, Pt-sulphur interactions have given a thought to look positively into such interactions rather than considering them as a barrier. Hence, it was further investigated and revealed that such complexes play a crucial role as intermediates which were formed prior to Pt^{2+} and DNA binding [53]. Hence, all the reports revealed that such platinum sulphur interactions may prove beneficial in efficient clinical applications of Pt-based anticancer drugs. With their proper understanding, it is anticipated to employ them for a rational designing of novel platinum-based anticancer drugs.

14.3.6 Pt(IV) Prodrugs Concept for to Win Over Limitations of Existing Pt(II) Drugs and Molecular Mechanism of Their Anticancer Activity

From the discussion till this point, it is clear that along with anticancer potential the cisplatin and other platinum-based drugs pose the side effects due to their undesired or non-selective side reactions with various biomolecules rather than a desired target DNA. This is possible in fact due to high reactivity of these drugs which are in their vulnerable 2+ oxidation state. It can possibly be avoided by using an oxidized cisplatin in +4 oxidation state which confers kinetic stability to compound, i.e. reduce its reactivity [13a, 16, 54]. Hence the Pt(IV) inert analogue of cisplatin was supposed to act as prodrug since it was anticipated to get reduced to the active cisplatin in Pt(II) state by the cellular reductants in acidic pH (~6) existing only at cancerous cells or in tumour periphery. In rest of body at physiological pH (7.4), the Pt(IV) prodrug will remain unaffected [55]. Further, the additional modes of reduction of Pt(IV) species to Pt(II), like using photon were also investigated [56]. These research outcomes led to synthesis of Pt(IV) prodrugs of other platinum-based drugs also [57]. This initiated a thought to utilize the axial positions of Pt(IV) species for attaching the appropriate functional groups to enhance water solubility [58] or attaching bio-relevant molecules like vitamin E [59] and many others bioactive groups [60] for making the prodrugs biocompatible or lipophilic or fluorescent moieties [61] attaching known drug molecules to act as adjunct and enhance the potency [62]. In this regard, proper choice of axial ligands which facilitate enhanced cellular accumulation and uptake [63] as well as easy reduction at acidic pH of cancer site is essential [64]. Hence, it is essential for such drugs to reach specifically at tumour site and reduce easily to active form. The reports of mechanistic studies have clearly established that the cytotoxicity of Pt(IV) compounds is mainly depend on their capability of accumulation in the cancerous cells and to enhance the intra-cellular basal ROS (reactive oxygen species) concentrations, causing a loss of the mitochondrial membrane potential and induction of apoptosis [65]. Considering all these facts, one should design and synthesize the new Pt(IV) prodrugs for therapeutic applications.

14.4 Synthesis of Platinum-Based Anticancer Compounds

The understanding of molecular mechanism discussed till this point has given the direction for design of new compounds for their evaluation for anticancer activities. In this effort, a myriad of platinum-based compounds was synthesized and about 3000 compounds were evaluated for anticancer activities. Hence, at this point, it is necessary to look into design and synthesis strategies of representative examples of platinum compounds. It will be helpful for design of new compounds which are anticipated to overcome the limitations of existing drugs.

14.4.1 Design and Synthesis Strategies of Platinum(II) Based Complexes

As discussed earlier in introduction and general properties, the platinum compounds exist in their most common and stable oxidation states +2 and +4. Regarding all the six clinically approved drugs, central platinum ion has d^8 electronic configuration and exist in +2 oxidation state. These complexes exist in square planar geometries. The synthesis of such Pt(II) complexes follows the associative ligand substitution mechanism. Additionally, the stereochemistry of Pt(II) compounds has impact on their anticancer activities. The cisplatin acts as anticancer agent but its geometrical isomer transplatin does not exhibit anticancer activities. Hence, while designing the new anticancer Pt(II) complexes one must aim to achieve complexes with cis-stereochemistry. For achieving this purpose, one must choose the appropriate ligands since their trans-effect plays a decisive role in dictating stereochemistry of a resulting product [11b, 66].

There are some reports, about the trans-compounds exhibiting anticancer activity. In such species, the amine ligands of cisplatin or its derivatives were substituted by imino ligands, branched aliphatic amines or bulky aromatic N-donor heterocycles [67]. Hence while designing the trans-compounds, the N-substituent groups should be suitable to achieve biocompatibility and having appropriate functional groups which facilitate formation of adducts with DNA through their interactions with functional groups on DNA.

New Pt(II) based compounds for anticancer activities, were developed by structural modifications of cisplatin. As we see its structure, there are two cis-chloride leaving groups and two amino non-leaving groups. Hence, the leaving group modifications with acetate or ester groups like easily hydrolysable groups lead to better solubility and reduced side effects. Similarly, the non-leaving group modifications by substituting the H atoms of amine with aliphatic chain rendered enhanced lipophilicity which may facilitate penetration through cancer cell membrane. Such structural modifications have effectual for improving kinetic, lipo- and hydrophilic properties as well as on toxicity and resistance profile of new compounds to be eval-

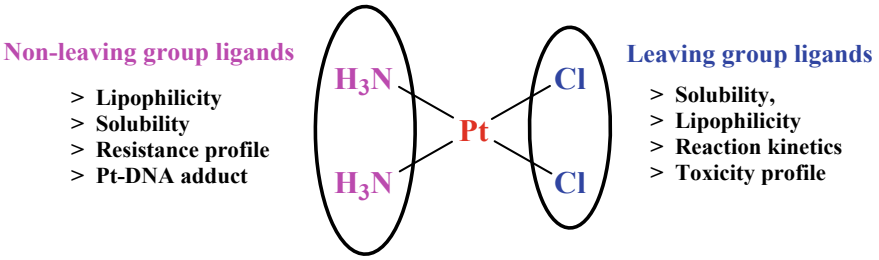

Fig. 14.4 Strategies for structural modifications to achieve improved properties of new drugs

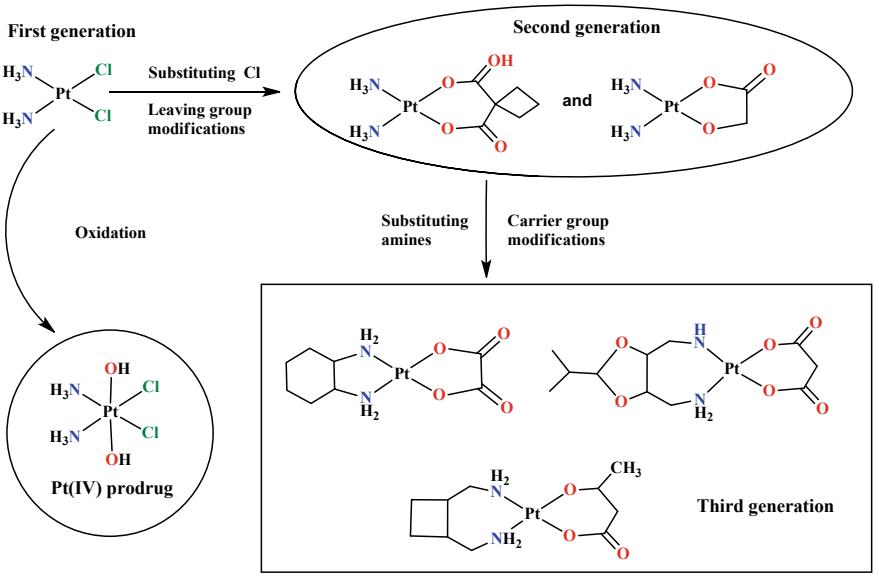

Scheme 14.3 Development of platinum-based anticancer drugs

uated for anticancer properties. The beneficial aspects of further modifications of cisplatin are shown schematically in Fig. 14.4 and structural developments in Pt(II) based drugs have been depicted in Scheme 14.3.

14.5 Synthesis Strategies for Various Classes of Pt(II) Compounds

Since the discovery of cisplatin and its modifications followed by new designs, various compounds (~3000) were evaluated for anticancer applications. They are categorized in different classes according to their chemical composition. Let us discuss the salient features and optimized synthesis routes of these classes.

14.5.1 Synthesis Methods for Cisplatin and Its Characterization

The *trans* Pt(II) compounds can be conveniently synthesized by treatment of Pt(II) precursors like K_2PtCl_4 salt or $[PtCl_2(RCN)_2]$ (R = Me, Ph) dissolved in aqueous-methanolic or polar organic solvents with two molar equivalents of appropriate ligands (L) and stirring of reaction mixtures for ~4–5 h. The resultant compounds of general formula *trans*-$[PtCl_2L_2]$ can be precipitated out with solvent in which the compounds have poor solubility or can be recrystallized by their slow evaporation or by cooling their solutions at 5–10 °C. The *cis* Pt(II) compounds can be prepared, by appropriate use of trans-effect of ligands.

In case of synthesis of *cis* Pt(II) compounds, the concept of trans-effect plays a key role which was proposed by Chernyaev in 1926 [68] to elucidate the experiential observation that, a rate of substitution of any ligand present in a square planar or octahedral metal complex is reliant on a group present at *trans* position to it rather than the groups at *cis* positions. Hence, a knowledge of trans-series helps to design such complexes. The following trans-series of some usual ligands exhibiting the trans-effect intensity which is a measure of rate of substitution of ligand at their trans-position [3b, 69].

$$F^-, H_2O, OH^-, NH_3 < py < C1^- < Br^- < I^-, SCN^-, NO_2{}^-, Ph^- < SO_3{}^{2-} < PR_3, SR_2, H^-, NO, CO, CN^-, C_2H_4$$

The well-known example of trans-effect strategy is a synthesis of cisplatin (Scheme 14.4) described by Dhara [70]. The treatment of aqueous K_2PtCl_4 with excess iodine afforded tetraiodoplatinate $[K_2PtI_4]$. Its treatment with first ammonia

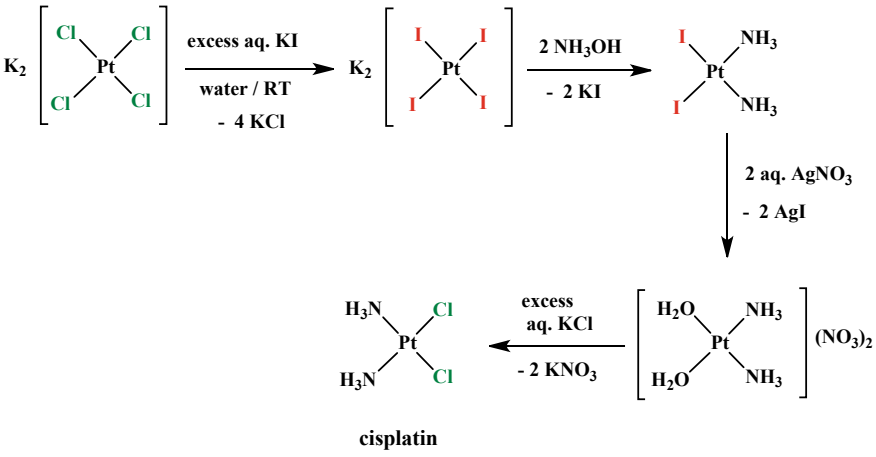

Scheme 14.4 Synthesis of cisplatin by using ammonia solution

molecule forms an intermediate triiodo species, $K[PtI_3(NH_3)]$ which reacts further with second ammonia molecule to form a *cis*-$[PtI_2(NH_3)_2]$. In this process the second step is directed by trans-effect. From the above trans-series, it is understood that the iodo ligand have stronger trans-directing effect as compared to ammonia ligand. As a result of this, the ligand present at trans-position to the iodide is more labile, so that is displaced easily by second NH_3 ligand resulting in the anticipated *cis* configuration forming the *cis*-$[PtI_2(NH_3)_2]$ which is treated further with aq. $AgNO_3$ to give *cis*-$[Pt(OH_2)_2(NH_3)_2]^{2+}$ which on treatment with aq. KCl yields a desired *cis*-$[PtCl_2(NH_3)_2]$, cisplatin. Although initial time preparations of cisplatin by similar procedure did not involve iodination steps; the iodination step was amended by Dhara to ensure the desired cis-geometry formation without any side product formations of $[Pt(NH_3)_4][PtCl_4]$ known as Magnus' Green salt, because of stronger trans-effect of iodo ligands as compared to chloro ligands.

This method by Dhara is most frequently used for synthesis of cisplatin. Additionally, cisplatin can also be synthesized by treatment of aqueous solution of $[K_2PtI_4]$ with ammonium chloride (NH_4Cl) at basic pH yield *cis*-$[PtI_2(NH_3)_2]$ which on further treatment $AgNO_3$ followed by KCl affords the cisplatin (Scheme 14.5).

Confirmation of cis-Geometry of Reaction Product

(i) Kurnakow Test

Since, it is established that only *cis* form, i.e. cisplatin exhibits anticancer action while its stereoisomer tranplatin does not exhibit anticancer potency; it is indispensable to obtain the product in exclusive *cis*-form. It has proved true for the cisplatin derivatives or compounds with general formula $[PtCl_2L_2]$ also. Hence, during synthesis of cisplatin or its derivative for anticancer applications, the exclusive formation of *cis* isomers without any *trans* impurity must be evaluated by Kurnakow test [13b, 71]. In this test, the treatment of an aqueous solution of test compound $[Pt(NH_3)_2Cl_2]$ or its derivatives is treated with an excess of thiourea. Formation of a white, sparingly

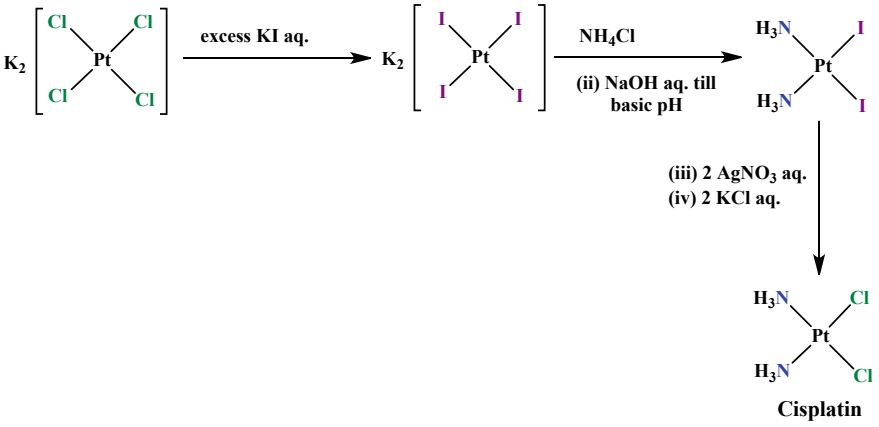

Scheme 14.5 Synthesis of cisplatin

water-soluble precipitate indicates the presence of *trans* isomer because of resulted *trans*-$[Pt(NH_3)_2(thiourea)_2]Cl_2$, while clear yellow solution is seen due to formation of water-soluble complex $[Pt(thiourea)_4)]Cl_2$ (Scheme 14.6). The test products are resulted due high *trans* effect of thiourea ligands.

(ii) **HPLC analyses of Kurnakow test products**

The high performance liquid chromatography (HPLC) analysis is a highly sensitive technique to separate and detect the isomeric impurities owing to different retention times for the thiourea coordinated complexes of cis- and transplatin. Their strong UV–Vis absorption properties allow these species to be detected by easily by UV detector of HPLC [72].

(iii) **NMR spectroscopy**

^{1}H NMR spectroscopic analysis is also a helpful to distinguish between the *cis* and *trans* isomers. Three bond platinum-hydrogen coupling constants ($^3J_{Pt\text{-}H}$) can be determined by using ^{1}H NMR spectral analyses. It has revealed that the values of $^3J_{Pt\text{-}H}$ are higher for cis-isomers than trans-isomers by magnitude of ~8–14 Hz [73]. But, the ^{195}Pt NMR spectral analyses are not helpful for distinguishing

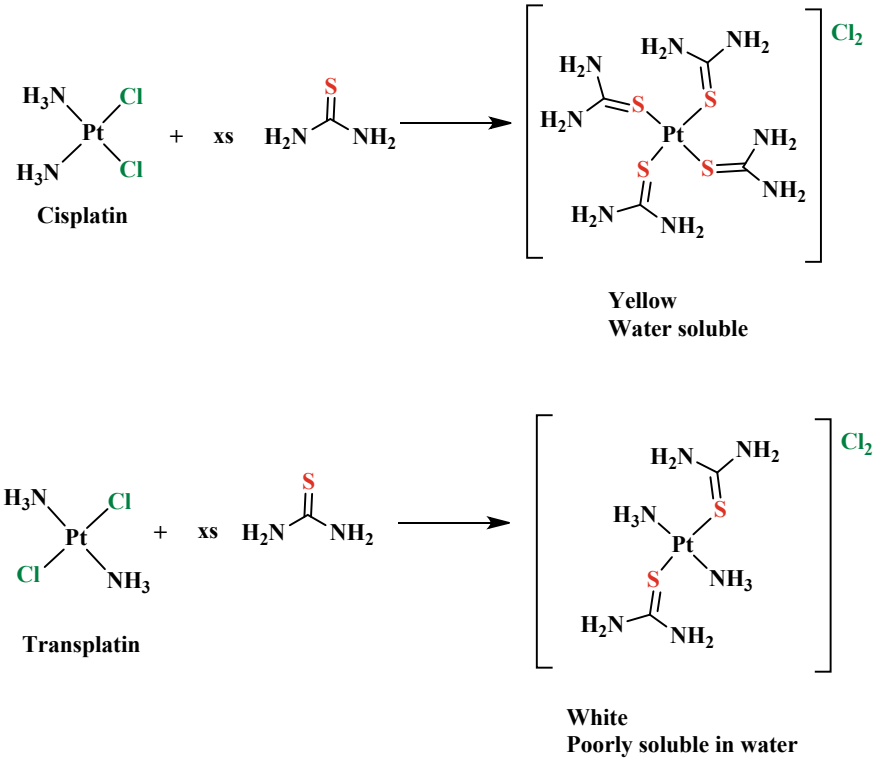

Scheme 14.6 Kurnakow test for distinguishing the *cis* and *trans* products

the cis and trans, because their chemical shifts (δ) do not differ much, e.g. cisplatin (δ = − 2104 ppm) while transplatin (δ = − 2101 ppm) [74].

After distinguishing the products can be thoroughly characterized by using:

(i) Elemental analyses
(ii) ^{1}H, ^{13}C and ^{195}Pt NMR spectroscopy (and other NMR active nuclei if present)
(iii) FT-IR spectroscopy
(iv) Raman Spectroscopy
(v) Single crystal X-ray diffraction analyses
(vi) Mass spectrometry.

Hence, following the synthesis and characterization strategies discussed till this point, various types of compounds were synthesized for their anticancer applications. These compounds exhibited different structures and stereochemistry depending on the ligand systems, their bonding modes like mono- or bidentate or chelating, etc. with central Pt(II) ion. These compounds are categorized based on geometry, ligand system and depending on no. of sites available to interact with DNA. Let us discuss some prominent classes of Pt(II) compounds which were evaluated for anticancer activities.

14.5.2 Classical Pt(II) Compounds Having Cis *Geometry for Anticancer Applications*

After discovery of cisplatin, it was observed that its stereoisomer transplatin is lacks the anticancer activity. Hence, the influence of this fact was existing on designs of platinum(II) based anticancer agents in earlier time. Hence, the efforts were focussed only on Pt(II)-ammine based compounds having *cis* geometry which resembled to cisplatin. Some examples of such classical *cis*-$[Pt(NH_3)_2(L)_2]$ (L = NO_3^-, NO_2^-, H_2O, Br^-, I^-, SCN^-, etc.) type compounds which were prepared by modifying the leaving group, i.e. substituting the chloride group by various ligands (L). Some reports depict their anticancer activities (cytotoxicity) against the sarcoma 180 tumour cell lines in vitro (Scheme 14.7) as well as treatment against test tumour Sarcoma 180 implanted in Swiss mice (female).

Additionally, strategies to substitute the non-leaving amine groups were also employed. In such efforts, the classical complexes with non-leaving group (NH_3) modifications with substituted amines like $[Pt(Amine)Cl_2]$ (Amine = en, pyrrolidine or aziridine rings) were developed which exhibited anticancer activities against ADJ PC6 plasma cell tumour (Scheme 14.8). In both the cases of modifications, the resultant compounds exhibited the superior anticancer activities over their *trans* analogues [75].

Further Developments in Cisplatin Derivatives

This trend of modifications of cisplatin derivatives encouraged the researchers to develop the new cisplatin-based derivatives in recent time also. In such efforts, various

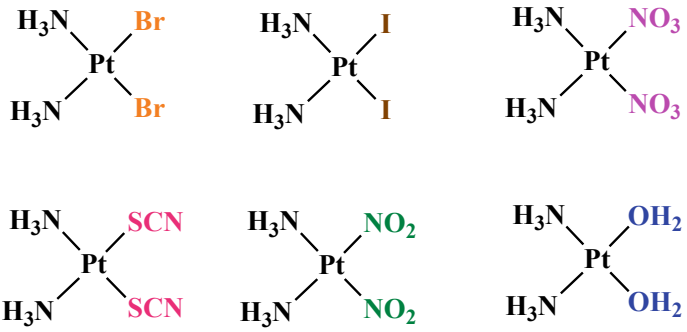

Scheme 14.7 Cisplatin derivatives obtained by leaving group modifications

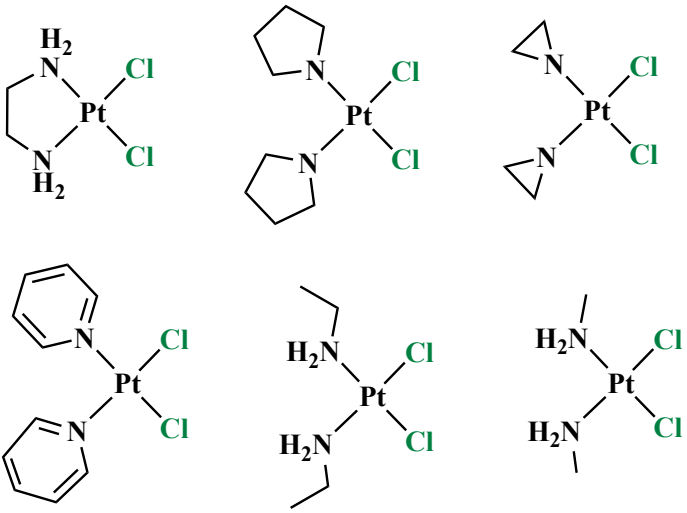

Scheme 14.8 Cisplatin derivatives obtained by non-leaving group modifications

cisplatin derivatives with N-benzyl ethylenediamine, 1,2-phenylenediamine and 2- or 4-picoline were conveniently synthesized offering the reasonable yields by treatment of K_2PtCl_4 with appropriate ligands. Although they exhibited slight less activity than cisplatin, such synthesis strategies help to develop new structural modifications to enhance potency (Scheme 14.9) [76].

Additionally, other cisplatin derivatives like picoplatin and JM-118 were developed which exhibited excellent anticancer activities and were investigated in clinical trials (Scheme 14.10). There structural features offer them potency. For example, in case of picoplatin, a methyl group present on pyridine ring protects it from undesired or non-selective side reactions with biological nucleophiles, such as methionine and cysteine containing proteins or peptides [77] and enables it to attain a higher nuclear

Scheme 14.9 Amine substituted cisplatin derivatives

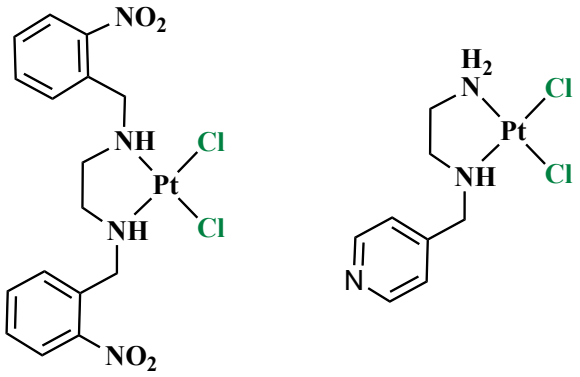

Scheme 14.10 Picoplatin and JM-118: undergone clinical trials

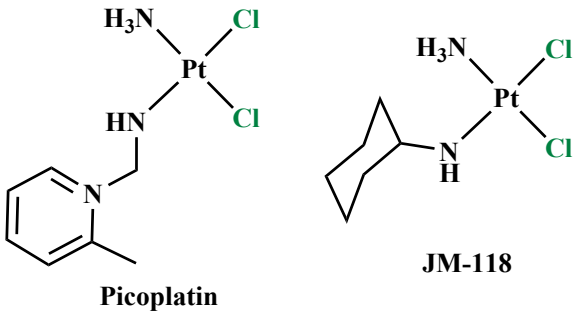

concentration as compared with both BBR3464 and cisplatin [78]. These properties contribute for enhanced efficacy of such derivatives.

The leaving chloride groups were substituted with acetate or oxalato groups. Very recently, Lippard et al. have reported the acetate bridged Pt(II) complexes derived from cisplatin (Scheme 14.11) [79] where leaving group of cisplatin (Cl) was substituted with a bridging acetate group rendering a dinuclear platinum(II) compound. Hence, these observations catalyze the thinking for developing new designs of cisplatin derivatives and research goes with drive to achieve superior anticancer activities.

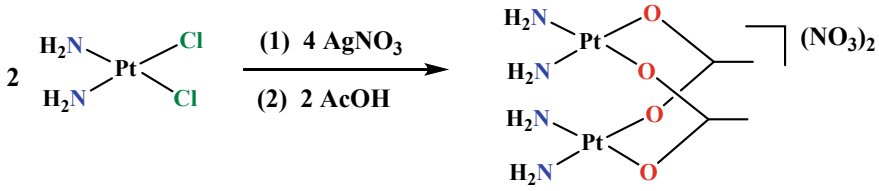

Scheme 14.11 Synthesis of acetate bridged cisplatin derivative

Furthermore, the cycloplatam having modifications at both leaving as well as non-leaving groups was developed which has exhibited potent anticancer activities and has undergone clinical trials (Scheme 14.12) [80]. Its analogue was also reported (Scheme 14.12b) In similar efforts, the indazole derivatives of cisplatin were also designed (Scheme 14.13).

The strategies of structural modification of cisplatin, were applied to other clinically approved platinum-based drugs also. For example, oxaliplatin was modified by substituting its oxalato leaving group by ester chains to enhance lipophilicity (A) [63c] or by emissive organic moieties (B) [81] as given below.

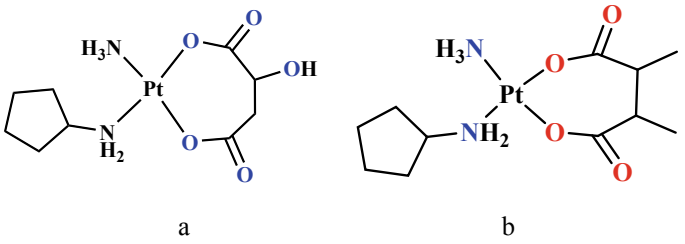

Scheme 14.12 Cycloplatam investigated under clinical trials

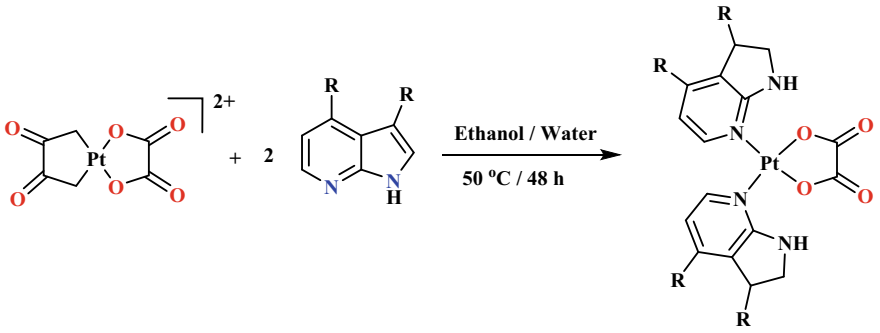

Scheme 14.13 Synthesis of indazole derivatives of cisplatin

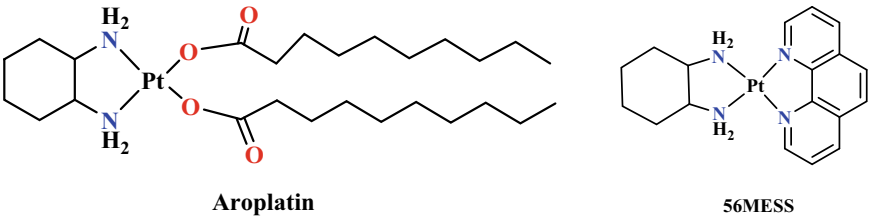

Scheme 14.14 Structural modification of cisplatin

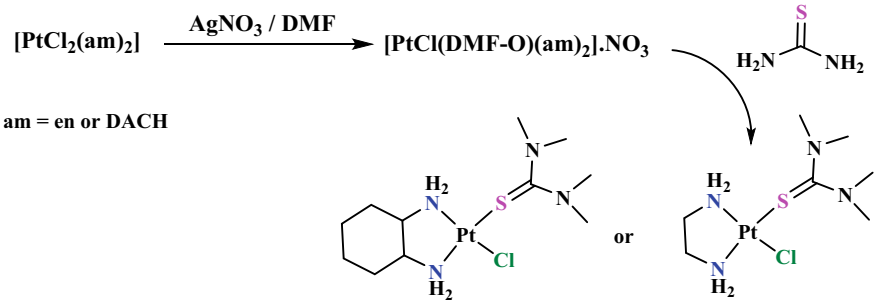

Scheme 14.15 Oxaliplatin derivatives with thiourea

Furthermore, the oxaliplatin derivatives with leaving group modifications by urea have also been synthesized and exhibited potent anticancer activities (Scheme 14.15).

14.5.3 Platinum(II) Complexes with Trans *Geometry*

As discussed earlier, the substitution of NH_3 group of transplatin by bulky and planar N-heterocycles or substituted amines afforded the symmetrical as well as unsymmetrical platinum(II) based *trans* compounds exhibiting the cytotoxicity significantly enhanced as compared to the parent transplatin drug and in most of the cases it was found equivalent to potency of cisplatin [82].

The rationale behind the activity exhibited by such compounds over the native transplatin is property of bifunctional adducts of DNA which is dependent prominently on the nature of amine groups. Additionally, the stability of the monofunctional adducts facilitates the preferential formation of cross-links between DNA and protein. It was clearly observed that the *trans*-platinum type of compounds can confer remarkable potential for designing the selective DNA–protein cross-linking complexes (Scheme 14.16) [83].

Similarly, other reports also have established the potency of *trans* platinum(II) compounds with various symmetrical as well as unsymmetrical planar N-heterocycles like quinoline, thiazole, Me-imidazole derivatives (Scheme 14.17).

The results of their biological studies supported the concept of activating the *trans* geometry by utilizing the planar donor. Their cytotoxicity evaluations against murine leukaemia (LI210) cell lines viz., sensitive as well as rendered resistant to cisplatin, exhibited their cytotoxic efficacy comparable with cisplatin. It is evident that, the anticancer activities of trans-compounds with substituted ammine are of higher magnitude than the *trans*-$[PtCl_2(NH_3)_2]$. The substituted compounds exhibited cytotoxic potency against cisplatin resistant cancer cell lines. Although only cis-geometry compounds were thought to exhibit the anticancer activities, the compounds with

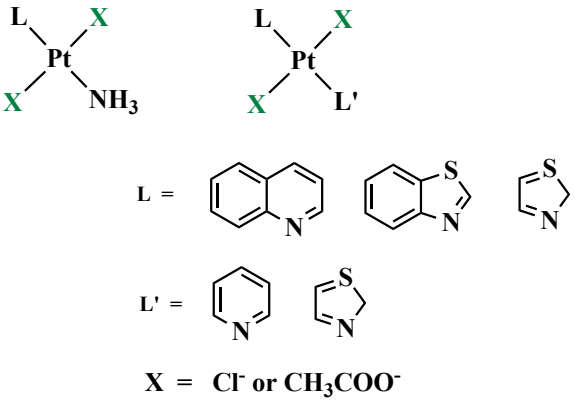

Scheme 14.16 Some platinum(II) complexes with trans-geometry

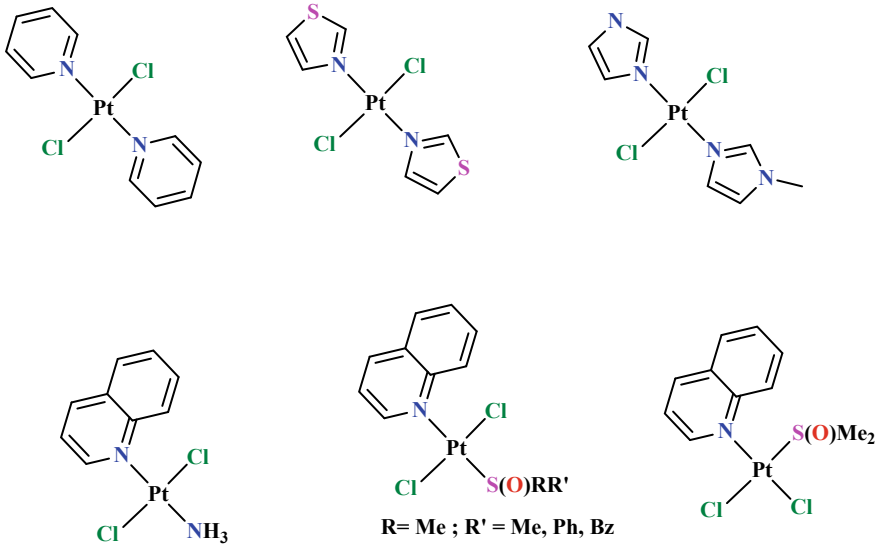

Scheme 14.17 Platinum(II) complexes with N-heterocycles with trans-geometry

trans geometry have also exhibited cytotoxicity equivalent to cytotoxicity of analogous cis-isomer. These observations have pointed to a further cause of platinum-based anticancer complexes acting through the different molecular mechanism than the mechanism cisplatin with the potential for antitumour potency equivalent with the clinically used drug [84].

Additionally, large no of compounds where trans-ammines were substituted variously were also reported (Scheme 14.18).

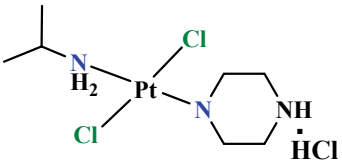

trans-[$PtCl_2$(ipa)(pz)].HCl

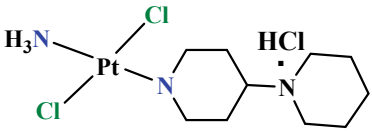

trans-[$PtCl_2(NH_3)$(pip-pip)].HCl

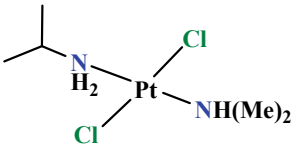

trans-[$PtCl_2$(dma)(ipa)]

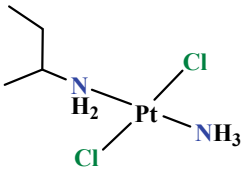

trans-[$PtCl_2$(sba)(NH_3)]

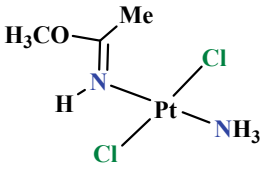

trans-[$PtCl_2$(HN=C(OMe)Me)(NH_3))]

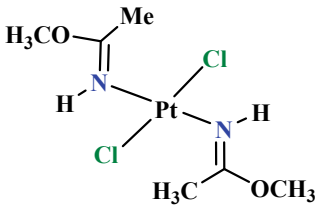

trans-[$PtCl_2$(HN=C(OMe)Me)$_2$)]

Scheme 14.18 Trans-ammine substituted Pt(II) compounds exhibiting anticancer activities

Additionally, using the both, leaving and carrier group modification by aldehyde groups and N-substituted planar ring like picolin, the derivative of transplatin, *trans*-[$Pt(CCHO)_2(NH_3)$(4-pic)] was reported to possess potent anticancer activities (Scheme 14.19).

Scheme 14.19 Picoplatin, i.e. *Trans*-[$Pt(CCHO)_2(NH_3)$(4-pic)]

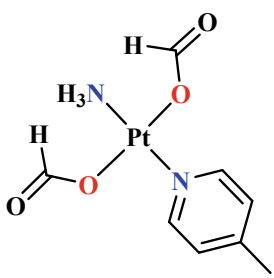

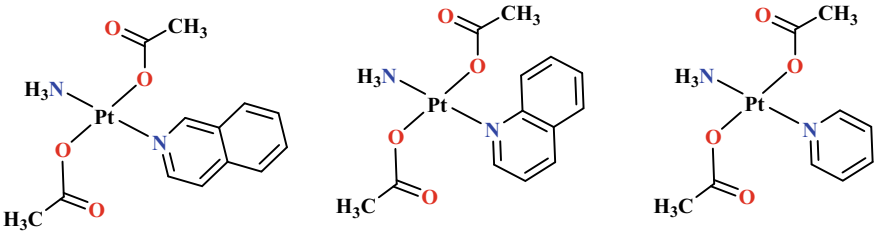

Scheme 14.20 *Trans*-Pt(II) compounds with acetate leaving groups

In similar efforts, the ammines substituted by pyridyl (py) or quinoline while chloride substituted by acetate groups were also reported with better biocompatible features as compared to transplatin (Scheme 14.20).

14.5.4 Synthesis Strategies for Pt(II) Based Trans-Isomers

Synthesis of Transplatin

The transplatin can be synthesized easily by performing the ammonation reaction of K_2PtCl_4 with an excess of ammonia solution (aq. NH_4OH solution) followed by treatment with HCl in aqueous solutions at higher temperatures 70–80 °C (Scheme 14.21) [85].

This reaction of transplatin synthesis also follows a trans-effect principle. After amination forming at cationic species, treatment of HCl leads to coordination of first chloride non-selectively while the second chloride attack selectively substitutes the ammine group at trans to initially coordinated chloride, leading to formation of trans-isomer due to higher trans-effect exhibited by chloride ions than that of ammonia molecules. This typical reaction procedure is also useful for the synthesis of *trans*-Pt(II) compounds having various amine ligands as well as N-heterocycles [86].

Other Synthesis Routes of Pt(II) Based Trans-Isomers

Additionally, the trans-complexes are also obtained from $[PtX_2L_4]$ compounds without using the hydrochloric acid (HCl). Accordingly, the suspension of $[PtX_2L_4]$ in the organic solvents or as a solid were heated *in vacuo* which led to the substitution

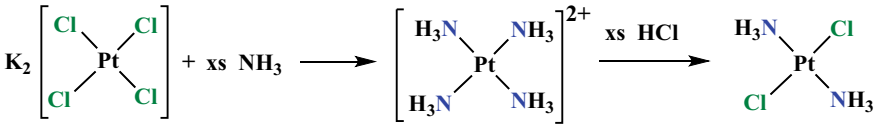

Scheme 14.21 Synthesis of transplatin

inner sphere N-heterocycle or amine by of outer sphere halides exclusively forming the trans-isomer [86, 87]. In other strategies where the treatment of $[PtCl_2L_4]$ with an excess of Et_4NCl in DMF at refluxing conditions also afforded the anticipated trans-geometry complexes [88]. In case of analogous complex, *trans*-$[PtL_2Cl_2]$ (L = pyrazole) can be obtained conveniently from treatment of $[PtCl_2L_4]$ and hydrocholoric acid (HCl) [89].

Let us go through other types of amine modified Pt(II) based compounds.

14.5.5 Platinum(II) Iminoether Compounds

The compound of this class consists of *cis*- as well as *trans*-Pt(II) based compounds, with the iminoether as non-leaving group. Both the symmetrical as well as unsymmetrical iminoether compounds have been synthesized. The typical structure of iminoether is as shown below:

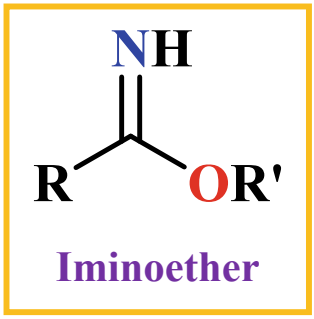

Natile et al. have presented the extensive work on the Pt(II) compounds with iminoethers. The Pt(II)-imonoether compounds are synthesized by base catalyzed treatment of *cis*- as well as *trans*-$[PtCl_2(RCN)_2]$ (R = Me or Ph) with alcohols at 0–20 °C (Scheme 14.22). In this type of compounds, the leaving group is chlorido group similar to cisplatin.

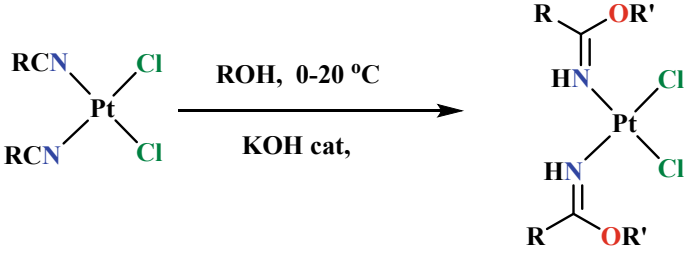

Scheme 14.22 Synthesis of *cis*-$[PtCl_2(iminoether)_2]$

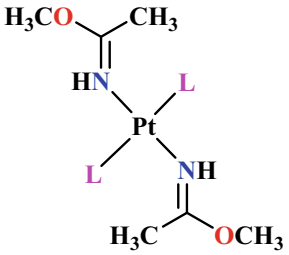

L = PPh_3, $AsPh_3$, Me_2S=O and Thiourea

Scheme 14.23 Pt(II)-iminoether compounds with various ligands

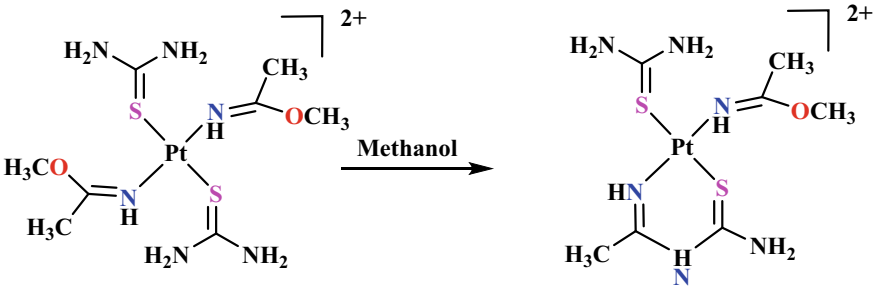

Scheme 14.24 Synthesis of cyclic Pt(II)-iminoether derivative

Additionally, the Pt(II) iminoether compounds where various donor ligands like PPh_3, $AsPh_3$, thiourea or dimethyl sulfoxide have been coordinated instead of chlorido groups (Scheme 14.23).

Additionally, the thiourea complexes of Pt(II)-iminoethers complexes lead to formation of a cyclic species which exhibited a potent anticancer activity (Scheme 14.24) [90].

Additionally, the unsymmetrically substituted iminoethers with general formulae, *trans*-[$PtC1_2$(L)(L′)] (where L and/or L′ = pyridine) or *trans*-[$PtC1_2L_2$] with L = iminoether have been reported (Scheme 14.25) [91].

In other reports, various *cis*-Pt(II)-iminoethers derivatives with various structures were synthesized. Accordingly, the treatment of *cis*-[$PtC1_2(MeNC)_2$], with KOPh or KOH in methanol, ethanol or isopropanol yielded the Pt-iminoether complexes of general formulae [$PtCl_2(NH = C(OR)Me)_2$] [92].

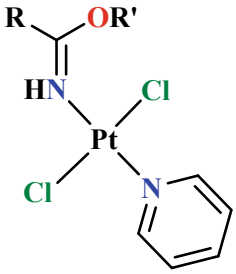

Scheme 14.25 Un-symmetric iminoether Pt(II) compound

14.5.6 Platinum(II)-Thioether Compounds

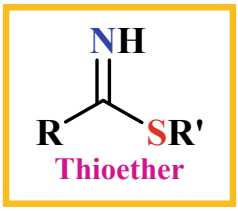

The platinum(II)-thioether compounds which are structurally analogous to iminoether analogues have also been synthesized. The treatment of *trans*-$[PtCl_2(RCN)_2]$ with *n*-butyl lithium followed by thiols (RSH) yields the Pt(II)-thioether compounds (Scheme 14.26) [92].

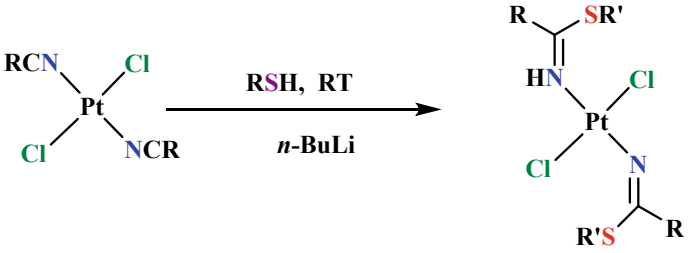

Scheme 14.26 Synthesis of *trans*-$[PtCl_2(thioether)_2]$

14.5.7 Platinum(II)-Amidine Compounds

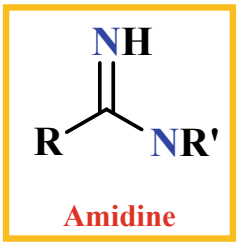

Amidines are possessing the RC(NR)NR′$_2$ functional group (R = R′ or R ≠ R′). They are nothing but the imine derived from corresponding amides (RC(O)NR′$_2$). The amidines can conveniently synthesized by the treatment of the nitrile species with alcohols by addition of acid to afford iminoether which further reacts with ammonia or by treatment of dimethylformamide acetal with primary amines (RNH$_2$) affording the amidine [93]. The various drugs or drug candidates like imidocarb, amitraz, tribendimidine, and xylamidine, consists of amidine moieties in their structures [94]. Most importantly, the amidine derivatives have exhibited the anti-inflammatory and anticancer activities [95]. Hence, the Eventually, the complexes of amidines with platinum(II) were investigated for anticancer activities anticipating the synergistic action of both the species. This has originated the novel anticancer compounds of platinum(II). Let us discuss few examples.

Synthesis of Pt(II)-amidine Complexes

The Pt(II)-amidine type of compounds were synthesized by treatments of [PtCl$_2$(RCN)$_2$] with excess of amines in dichloromethane at lower temperatures (about -10 °C). Accordingly, *trans*-[Pt(amine)$_2$(amidine)$_2$]Cl$_2$, *cis*- and *trans*-[PtCl$_2$(NH$_3$)(amidine)] and *cis*- and *trans*-[PtCl$_2$(amidine)$_2$] have been synthesized and were evaluated, both in vitro and in vivo for their anticancer properties (Schemes 14.27 and 14.28) [96].

14.5.8 Monofunctional Platinum(II) Compounds

The monofunctional platinum-based complexes are able to bind with DNA at only a single site, inducing a smaller alteration in their double helix. In spite of this fact, these compounds have exhibited extraordinary anticancer potency, with a different spectrum of activity as compared to activity exhibited by classical bifunctional cross-linking drugs like cisplatin. Their binding with DNA was investigated well [97]. In the efforts to obtain a most potent monofunctional platinum compound, Lippard et al. have synthesized various derivatives of type cis-[Pt(NH$_3$)$_2$(N-heterocycle)Cl](NO$_3$)

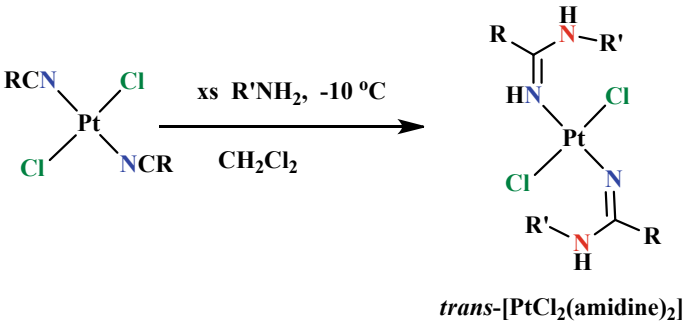

Scheme 14.27 Synthesis of platinum(II)-Amidine compounds

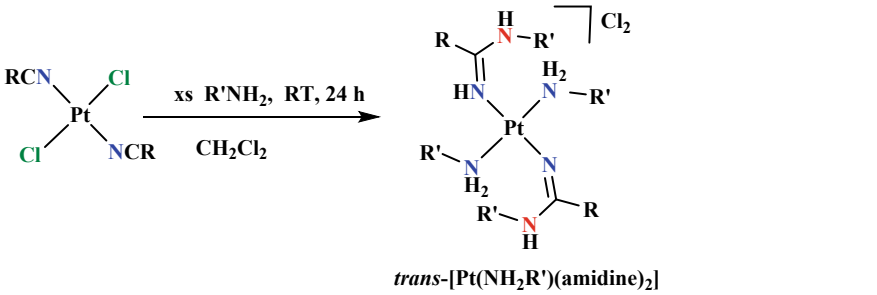

Scheme 14.28 Synthesis of platinum(II)-Amidine cyclic species

where the N-heterocycle was varied from small pyridine, quinoline to phenanthroline derivatives (Scheme 14.29) which are anticipated to modulate a steric protection about the Pt(II) centre. Among them phenathriplatin has exhibited most potent activity against a large number of human cancer cell lines. In general, these monofunctional Pt(II) complexes have been obtained by treatment of cisplatin with equimolar aq. $AgNO_3$ in DMF solution followed by treatment with an appropriate equimolar of N-heterocyclic ligand. The reaction was worked up in the methanolic

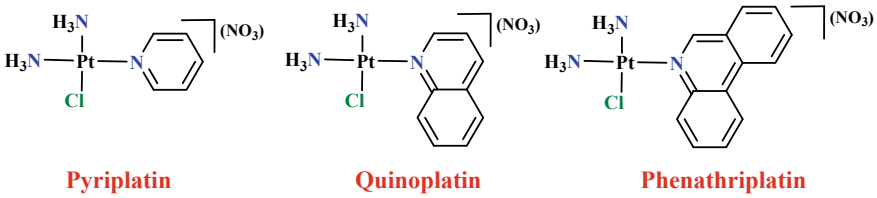

Scheme 14.29 Representative monofunctional *cis*-[$Pt(NH_3)_2$(N-heterocycle)Cl](NO_3) complexes

solution to obtain the desired product. The representative synthesis of phenanthroline is shown in Scheme 14.30 [98].

Additionally, Bierbach et al. have reported the platinum-acridine-based monofunctional complex which exhibited an effective anticancer ability against non-small-cell lung cancer (Scheme 14.31). The notable thing about this complex is that it is the first non-cross-linking platinum agent but by substituting the thiourea with an amidine group, it was observed that the cytotoxicity against H460 non-small-cell lung cancer (NSCLC) was greatly enhanced in vitro as well as in vivo [99].

Furthermore, Bierbach et al. using the similar synthesis strategies (Scheme 14.18) have reported the diverse analogues of Pt-acridine-based monofunctional complexes by incorporating NH_3, ethylenediamine (en) or propane-1,3-diamine (pn) to render better biocompatibility were synthesized. These complexes were further linked to various biologically active molecules bearing the primary and secondary amine functional groups (e.g. rucaparib, E/Z-endoxifen, quinazoline) (Scheme 14.32). Hence these complexes the monofunctional Pt(II) complexes linked with bio-relevant moieties has originated a class of highly potent anticancer compounds by adopting the linker technology [100].

Furthermore, Bierbac and Farrell et al. have reported the platinum(II) based monofunctional complexes with mono- and bifunctional thiourea derivative. The results of their evaluations have suggested that the steric and electronic effects of the peralkylated thiourea derivatives have potential for modulating their affinity for biomolecules (Scheme 14.33). Their synthesis was performed by following the strategies similar to discussed earlier. The treatment of $[Pt(en)Cl_2]$, cis-$[Pt(NH_3)_2Cl_2]$ or $[Pt(DACH)Cl_2]$ with aq. $AgNO_3$ in DMF solvent followed by treatment of urea-based ligands afford the desired products. The reaction work-up was performed on methanolic solution [101].

Additionally, Smith et al. synthesized diethylenediamine ligated Pt(II) based monofunctional complexes viz. $[Pt(dien)Cl]^+$ and $[Pt(Et_2dien)Cl]^+$ (Scheme 14.34) along with pyriplatin and phenanthriplatin. Their binding with 5-GMP s well as their uptake in cancer cells (A549, Caco2, HTB16) was also evaluated. It is inferred from the results that, a greater steric hindrance posed at *cis* positions to one side of Pt^{2+}

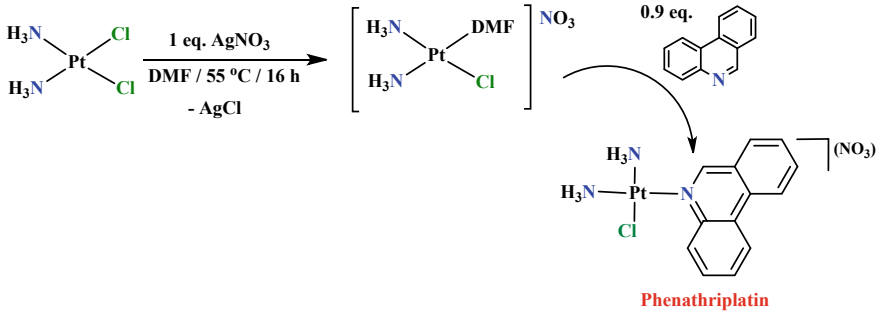

Scheme 14.30 Synthesis of phenathriplatin

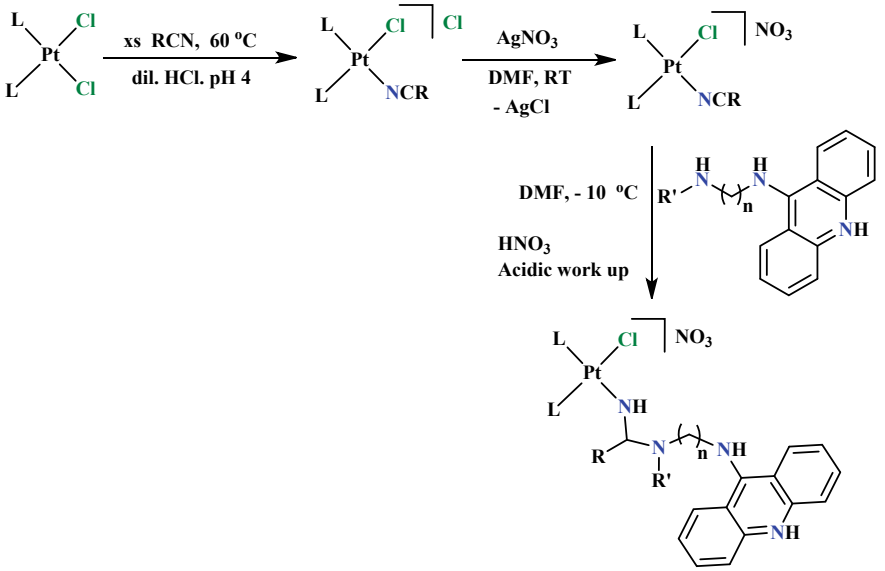

Scheme 14.31 Synthetic route for monofunctional platinum-amidine complexes

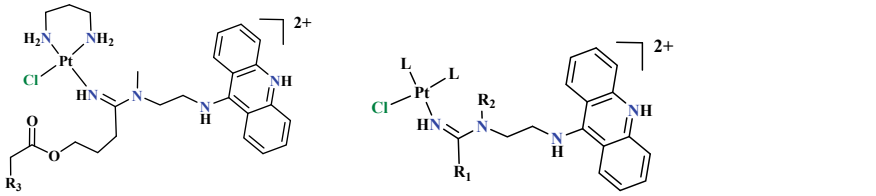

R_3 = butyric- or valproic-ester

L= NH_3 or pn and R_1 = Me, Et

R_2 = $(CH_2)_2OH$, $(CH_2)_2COOH$ or Me

Scheme 14.32 Pt-acridine-based monofunctional complexes

Scheme 14.33 Some platinum(II) based monofunctional complexes

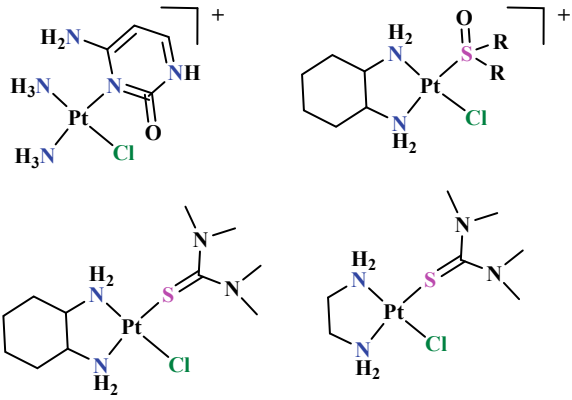

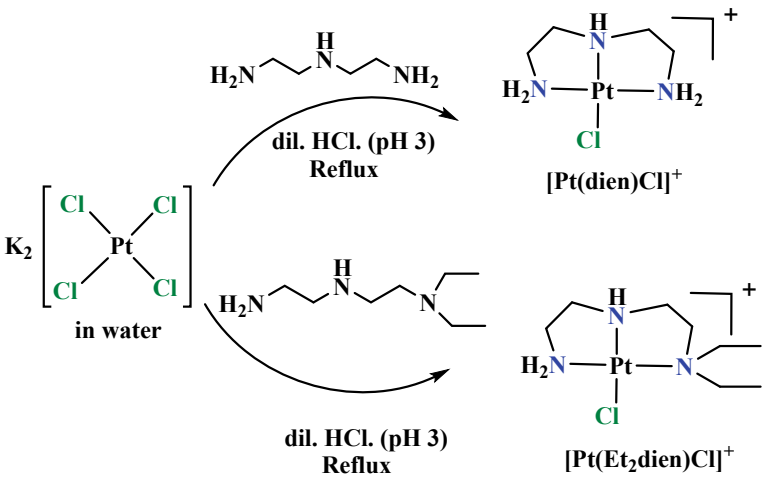

Scheme 14.34 Synthesis of amine-based monofunctional Pt(II) compounds

coordinating centre of the monofunctional platinum(II) complexes promotes an efficient targeting of the nuclear compartment of cancer cells and the guanosine residues which may be responsible for cancer cell deaths. Additionally, the monofunctional platinum(II) compounds caused shifts in hearing threshold with reduced effect on hair cell density. It clearly reveals that the monofunctional Pt(II) complexes may adopt different mechanism than cisplatin for their cytotoxic effects.

The $[Pt(dien)Cl]^+$ and $[Pt(Et_2dien)Cl]^+$ complexes were conveniently synthesized from treatment of aqueous solution of potassium tetrachloroplatinate (K_2PtCl_4) with appropriate amine at acidic lower conditions (pH ~ 3) achieved by addition of dil. HCl, followed by reflux of reaction mixture for 6 h. The yellow precipitate of anticipated platinum(II) based complex was obtained which was recrystallized in hot water [102].

14.5.9 Trifunctional Di- and Tri-Nuclear Platinum(II) Compounds

The clinically approved Pt(II) based anticancer drugs, after their hydrolysis bind with DNA at two sites, hence they act in bifunctional way. But, as discussed earlier, to overcome the drawbacks of existing drugs, the new drugs were designed to enhance potency by creating more favourable modes of Pt–DNA binding, i.e. improving DNA binding profile, leading to enhanced killing of cancer cells.

For this cause, Farrell et al. have designed dinuclear platinum compounds where two cisplatin molecules were linked by an aliphatic carbon chain having terminal amino groups $[\{cis\text{-}PtCl(NH_3)_2\}\mu\text{-}H_2N(CH_2)_6NH_2\text{-}\{cis\text{-}PtCl_2(NH_3)\}]^+$

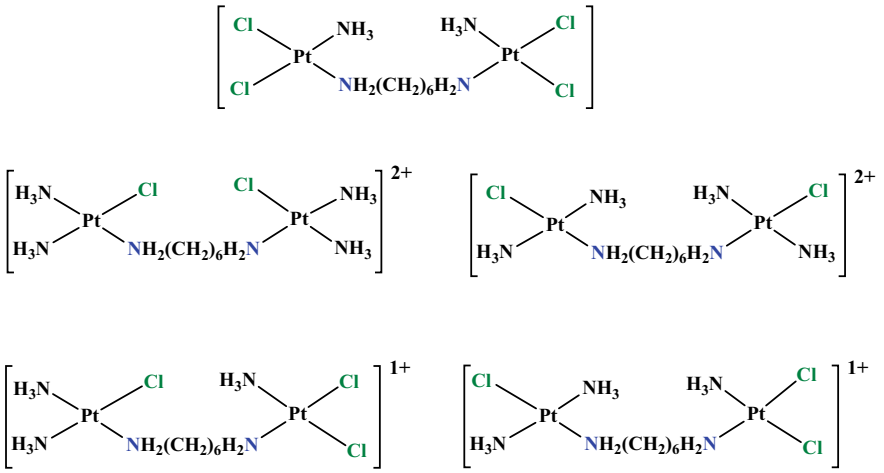

Scheme 14.35 The dinuclear trifunctional Pt(II) based anticancer agents

and another consist of one cis- and one transplatin linked by the same chain $[\{trans\text{-}PtCl(NH_3)_2\}\mu\text{-}H_2N(CH_2)_6NH_2\{cis\text{-}PtCl_2(NH_3)\}]^+$ (Scheme 14.35) [103].

Such complexes were investigated for binding with DNA as well as their capacity to enforce covalent ternary cross-links between DNA and protein. Their cytotoxic activities were compared with some bifunctional dinuclear Pt(II) compounds like $[\{PtCl(NH_3)_2\}_2\mu\text{-}H_2N(CH_2)_nNH_2]^{2+}$. Their interactions studies were performed by various techniques and assays like inhibition of ethidium bromide (EthBr) fluorescence, circular dichroism (CD), inter-strand cross-linking and unwinding assays, etc. All the results have evidenced that the (Pt,Pt) inter-strand cross-links were responsible for predominant lesion of such trifunctional complexes and the best possible structure to form the ternary cross-links between DNA and protein. From the results obtained, it is anticipated that the trifunctional agents have better prospects to be used as drugs that target proteins and as well as investigation tools for studying the conformational effects on interactions between DNA and proteins.

A typical synthesis strategy for a representative complex is shown (Scheme 14.36).

14.5.10 Platinum-Oxalato Compounds

The drive to design and develop novel anticancer drugs, directed the researchers to (i) replace the existing leaving as wells carrier ligands by new groups or (ii) modify the existing groups. This leads to design of derivatives of existing drugs. In this regard, looking into structures of existing platinum(II) based clinical drugs, the leaving carboxylate-based anionic groups are of prime importance. They lead to hydrolysis at physiological conditions forming Pt^{2+} species which bind with DNA followed

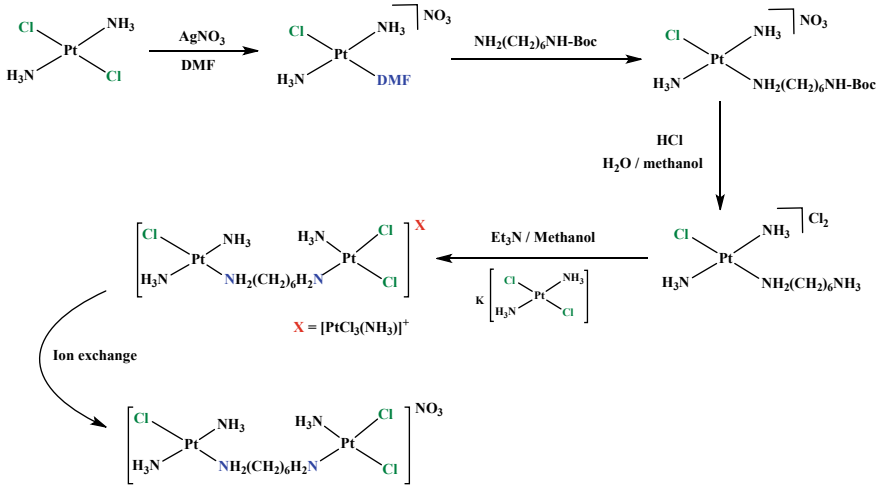

Scheme 14.36 Synthesis strategy to obtain a trifunctional Pt(II) complex

by cancer cell killing. Such drugs include carboplatin, nedaplatin, lobaplatin, heptaplatin, etc. Among the leaving groups of carboxylate-based moieties, the oxalate dianion is important group which is coordinated to Pt^{2+} centre of oxaliplatin, used mainly for treatment of colorectal cancer [104]. Hence, design and development of the complexes of platinum(II) with oxalate species which are anticipated to be biocompatible and worth of studying candidates for design of new compounds.

In view of this, new platinum(II) based compounds with oxalato groups were designed and were evaluated for anticancer activities. Few representative examples are of worth to discuss here.

The platinum(II)-oxalato-based complexes having the *cis* 7-azaindole moieties as the co-ligands were synthesized. The treatment of aqueous solution of bis-oxalato cationic species was treated with 7-azaindole ligand in 1:2 stoichiometry (Scheme 14.37). These compounds exhibited antitumour activities in vitro [105].

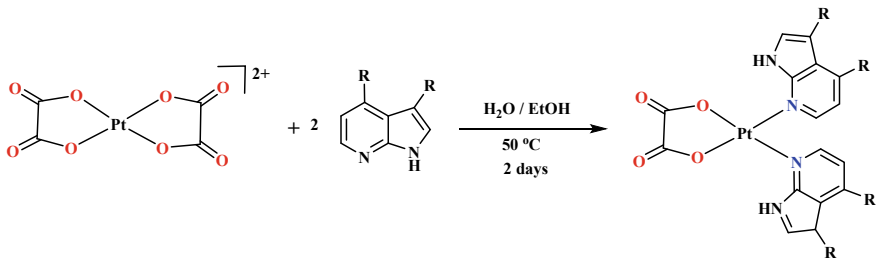

Scheme 14.37 Platinum(II) complexes with diverse cis-7-azaindole compounds

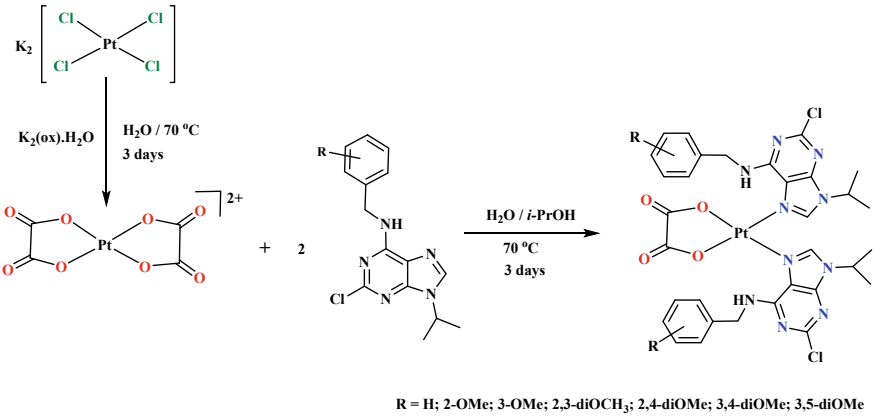

Scheme 14.38 Synthesis of various platinum(II) oxalato complexes

Additionally, various platinum(II) oxalato-based complexes bonded with adenine-derivatives as the carrier ligands have been reported (Scheme 14.38). They exhibited cytotoxic ability against breast adenocarcinoma (MCF7) and osteosarcoma (HOS) human cancer cell lines as evaluated by MTT assay [106].

The potent cytotoxicity exhibited by these compounds, suggested for potential to develop the compounds from this class since they are structurally analogous to a potent clinical drug oxaliplatin.

14.5.11 Platinum(II)-B-Diketonate Compounds

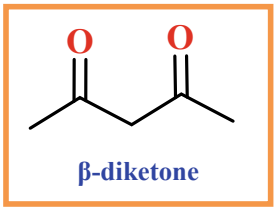

The β-diketonates are useful moieties as ligands for synthesis of various metal complexes which find diverse applications in fundamental chemistry exhibiting various compounds and achieving the mixed-metal coordination networks [107], as highly effective catalysts for fixation of CO_2 into cyclic carbonates [108]. Especially, the lanthanide-based complexes of β-diketonates have exhibited the excellent photophysical [109] or photothermal properties [110] and most notably electroluminescent properties [111]. The Pt(II)-β-diketonates find excellent applications in biological imaging [112].

Regarding biological applications, the β-diketone compounds have exhibited various pharmacological properties like antimicrobial [113], anti-viral [114], anti-inflammatory [115], antioxidant [116], most importantly anticancer [117] and immunomodulatory [118] activities.

In view of the potent biological activities of β-diketonates and prominent photophysical properties exhibited by its metal complexes, it is worthwhile to design the complexes anticipating the synergistic effect of β-diketonates and platinum(II) in a resulting complex which may have potential for anticancer treatment as well as useful in imaging during the treatment. Hence, such compounds were designed and were investigated for anticancer applications.

The first example of such β-diketonate platinum(II) complex along with dimethyl sulfoxide as ligands was synthesized by Fanizzi et al. (Scheme 14.39) [119]. The treatment of *cis*-[$PtCl_2(Me_2S=O)_2$] with β-diketone yielded the Pt(II)-diketonate. Further, various Pt(II)-diketonates incorporating diverse amine, phosphine, halides sulphides or heterocycles were obtained by the same group (Scheme 14.40).

Additionally, the cyclometalated platinum(II)-β-diketonates were efficiently synthesized in high yield in a one-pot synthesis strategy at optimum temperature (Scheme 14.41) [120]. By similar strategies their phosphine-based analogues bearing naphthyl moieties were also synthesized. (Scheme 14.42). These compounds are anticipated to serve as anticancer agents as well as helpful in cellular studies due to their excellent photophysical properties.

Furthermore, Lippard et al. have reported the cisplatin derivatives where the cis-chlorides were replaced by a chelating β-diketone as shown in Scheme 14.43 [121].

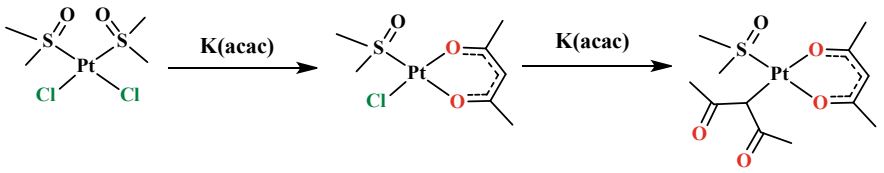

Scheme 14.39 Synthesis of first platinum(II)-β-diketonate

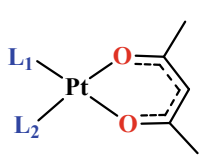

$L_1 = L_2$ = acac, Cl, Et_2NH, PPh_3, PEt_3 ot piperidine

L_1 = Cl and L_2 = PEt_3

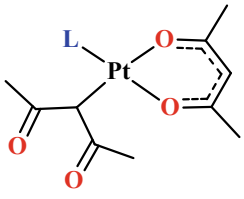

L = Cl, Et_2NH, PPh_3, Et_2S PCy_3 ot Py

Scheme 14.40 Various Pt(II)-diketonates

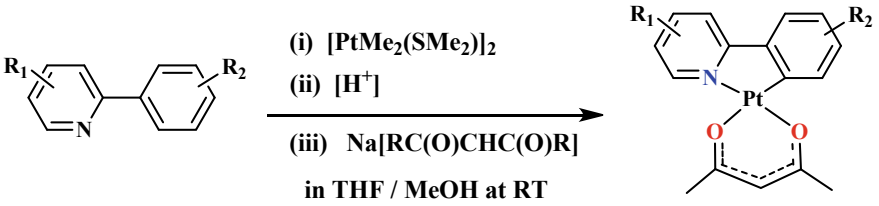

Scheme 14.41 Synthesis of cyclometallated platinum(II)-β-diketonates

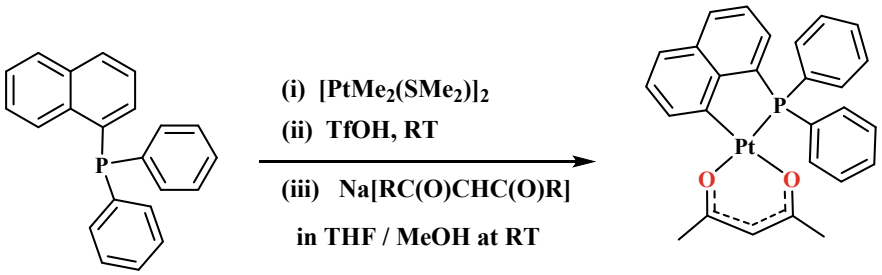

Scheme 14.42 Synthesis of phosphine-based platinum(II)-β-diketonates

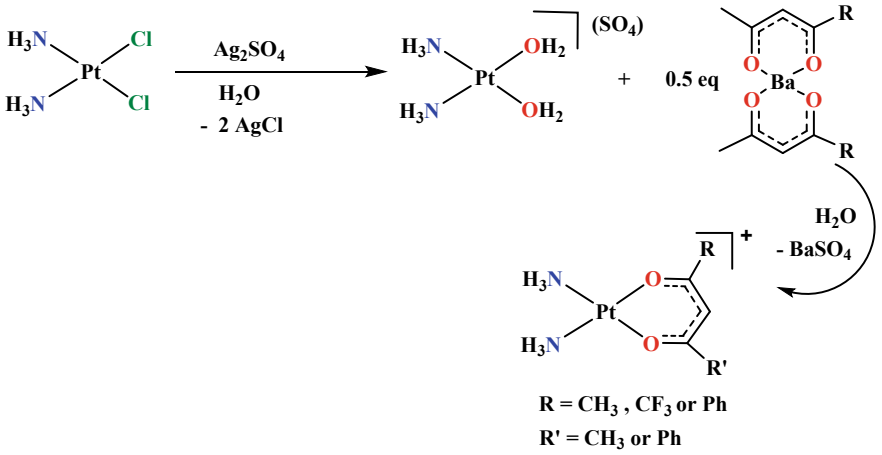

Scheme 14.43 Synthesis of cisplatin-β-diketonates

Additionally, by using the similar strategies using aq. $AgNO_3$ and Na-salt of diketone like Na[PhC(O)CHC(O)R] or Na[PhC(O)CHC(O)Ph], the various derivatives with substituted β-diketone were synthesized (Scheme 14.44).

It was observed that, the induction of Ph rings enhances the lipophilicity and eventually the uptake of drug in the HeLa cells but the CF_3 groups are accountable for the decreasing stability of such complexes in the aqueous solutions. Additionally, the

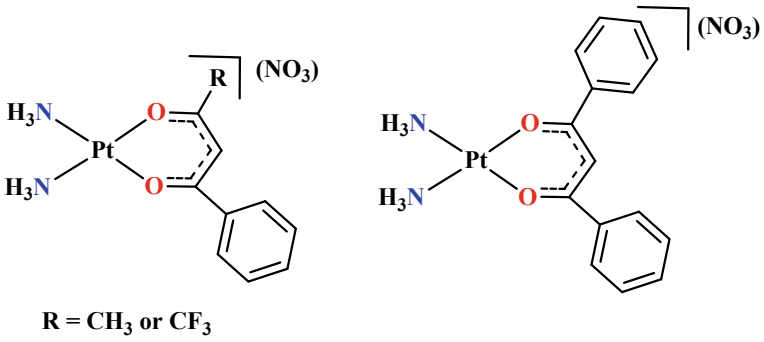

Scheme 14.44 Synthesis of cisplatin derivatives coordinated with substituted β-diketone

cytotoxicity studies revealed that some of these compounds have exhibited potency to kill cancer cells comparable to cisplatin [121].

Recently, Chakravarty et al. have reported the synthesis and phot-cytotoxicity associated with the novel Pt(II)-β-diketone derivatives where the cis-amines of cisplatin were replaced by azo-based bulky aromatic rings like anthracene. The treatment of $[K_2PtCl_4]$ with 3-chloro-2-methyl-1-propene in refluxing ethanolic solution yielded the dimeric allyl-platinum(II) compound which on further treatment with azo-based bulky aryl moieties afforded the chloro-bridged dimeric Pt(II) compounds which on further treatment with appropriate diketone moieties including a bioactive molecule like curcumin (H-cur) or acac (H-acac) or pyridyl substituted analogue (Hpy-acac) in dichloromethane afforded the desired products. (Scheme 14.45) [122].

A typical strategy of synthesis is as shown below (Scheme 14.46).

These compounds exhibited anticancer activities. During the evaluation the diketonate species were released in situ after addition of glutathione (GSH). The resulted platinum(II) species play a role as transcription inhibitor while the β-diketonate base released during reaction exhibited photochemotherapeutic action. The Pt(II)-β-diketonates induced the photo-cleavage in plasmid DNA upon exposure to 457 nm (blue light) leading to formation of major nicked circular DNA (NC-DNA) (~75%) along with hydroxyl radicals ($HO^{\cdot}$) and singlet oxygen ($^1O_2$) as the reactive oxygen

Scheme 14.45 Photo-cytotoxic Pt(II)-β-diketonates

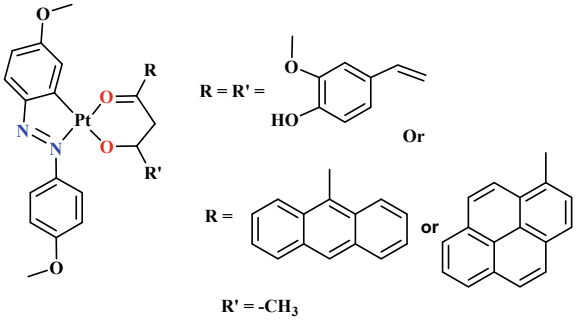

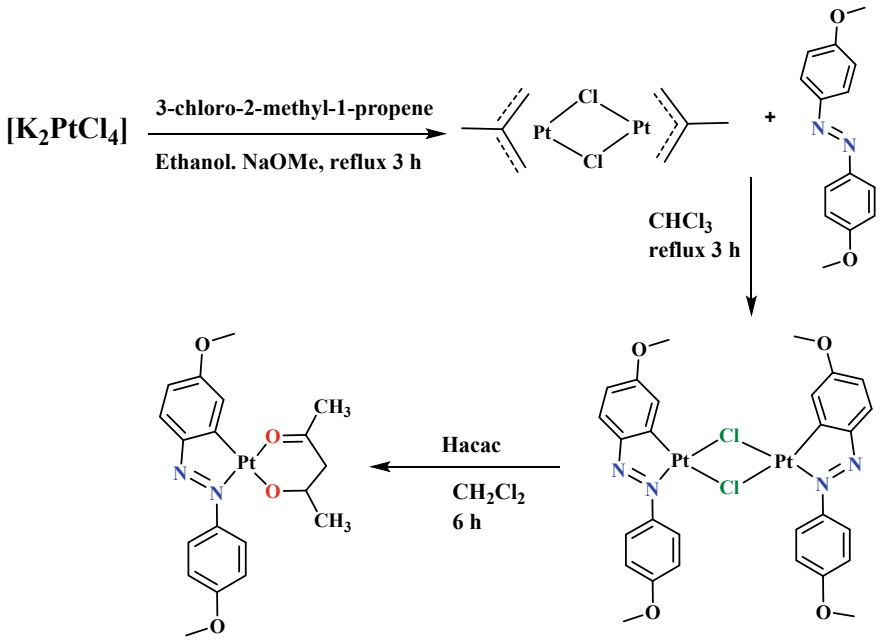

Scheme 14.46 Synthesis strategy of photo-cytotoxic Pt(II)-β-diketonates

species. Some of the Pt(II)-β-diketonate complexes exhibited photocytotoxicity against the skin keratinocyte HaCaT cells upon exposing under visible light but non-toxic in dark conditions. Some complexes were responsible for generating cellular ROS which cause an apoptotic cell death after exposing to the visible light.

This account has clearly indicated the importance of the Pt(II) based complexes with β-diketone moieties, may prove an innovative strategy for delivering therapeutically active platinum(II) species as well as the photo-toxic β-diketones to the cancer site.

14.5.12 Platinum(II)-Schiff Base Compounds

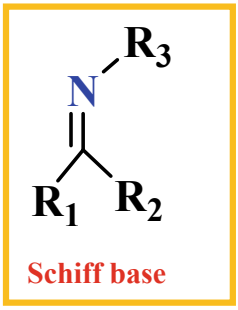

Schiff bases are primary-aldimines or -ketimines with a general formula, $R_1R_2C = NR_3$ which are readily formed by condensation of primary amines with aldehydes or ketones. They have proved to be the versatile pharmacophores for developing various bioactive compounds. Schiff bases have exhibited potent pharmacological like antioxidant, anti-inflammatory, antimicrobial, analgesic, antidepressant, anticonvulsant, antitubercular, anthelmintic, anticonvulsant, antiglycation and most importantly the anticancer potency also [123]. Additionally, the Schiff bases find the industrial applications in as the catalyzing agents, dyes and pigments, stabilizers in polymerization process, active intermediates during organic synthesis and corrosion inhibitors also.

Let us focus on their anticancer properties. The Schiff bases [124] as well as their complexes with transition metal (e.g. Ru, Pt, Pd, Fe, Ni, Cu, Zn) have exhibited the anticancer activities [125]. In view of FDA approved Pt(II) based anticancer drugs for the anticancer treatment, it was worth to synthesize the novel platinum(II) compounds with appropriate Schiff bases anticipating the superior anticancer activities, enhanced biocompatibility and reduced toxicity. Let us discuss the synthesis strategies of representative Schiff base and synthesis of its complexes with platinum(II) centre.

The Schiff base was conveniently synthesized by condensation of pyrrolidine-2-carbaldehyde with benzylamine in methanol for overnight (~10 h). This obtained Schiff base was treated with $[Pt(DMSO)_2Cl_2]$ in CH_2Cl_2 solution and stirred at room temperature which afforded a chloro-bridged dinuclear platinum(II) complex $[Pt_2(\mu\text{-}Cl)_2(DMSO)_2(\text{Schiff base})_2]$ which in slow evaporation recrystallized in a mononuclear platinum(II) complex $[PtCl_2(DMSO)(\text{Schiff base})]$. This compound was evaluated foe biological activities. It exhibited strong affinity for CT-DNA (calf thymus DNA) and it exhibited remarkably high selectivity for cancerous cells leading to reduction in time of their viability and observed to be harmless for noncancerous breast cell lines. (Scheme 14.47). [126]

Using the same reaction strategies, the analogous Schiff bases were also conveniently synthesized (Scheme 14.48) which formed the analogous Pd(II) complexes. Hence, they have the potential to form the Pt(II) complex also.

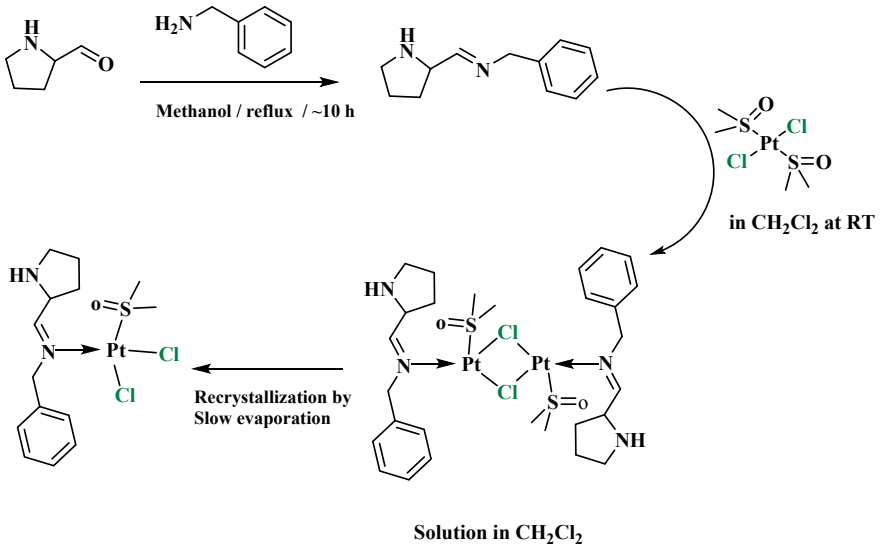

Scheme 14.47 A convenient synthesis of platinum(II) complex with Schiff base

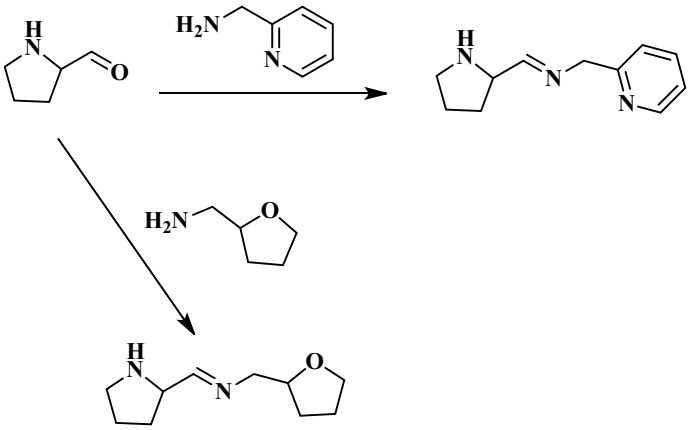

Scheme 14.48 Synthesis strategies for the Schiff bases

The Schiff bases as well as their metal complexes exert their anticancer activities by targeting (i) DNA and (ii) mitochondria which involve the DNA damage and oxidative stress respectively (Scheme 14.49).

This account of Schiff bases clearly depicted the pharmacological role of Schiff bases as well as their platinum(II) complexes. These complexes can be made more potent and biocompatible by a selecting the appropriate biocompatible organic frames, which are found as structural parts of biomolecules like. Usually pyridyl, pyrimidyl, imidazolyl and nicotinoyl moieties with NH_2, OH or COOH functional

Scheme 14.49 Anticancer mechanism of Schiff bases and their metal complexes

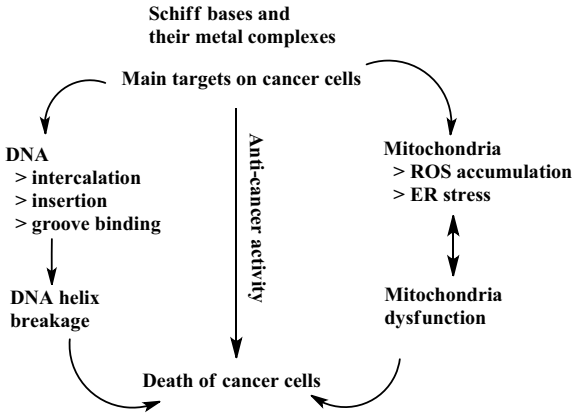

groups have been found to exert various pharmacological properties including anticancer activities. Hence the Schiff bases containing such moieties followed by synthesis of platinum(II) based complexes may afford the highly potent anticancer drugs.

14.5.13 Platinum(II)-Sulphur-Based Compounds

As discussed earlier, the undesired side reaction of hydrolyzed cisplatin with various biomolecules especially proteins containing sulphur-based amino acids like L-Cys or L-Met or peptides like glutathione (GSH) (Scheme 14.50) lead to inactivation of

Scheme 14.50 Sulphur containing biomolecules

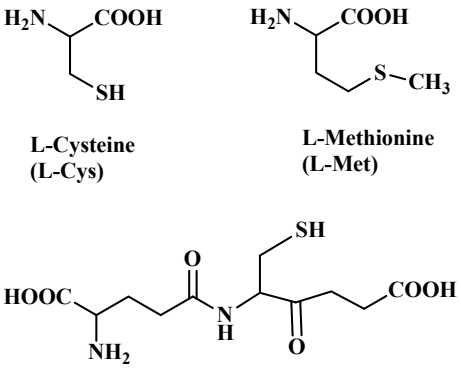

cisplatin due displacement of amine groups as well as a cause of severe side effects [127].

This fact was investigated further to understand the mechanism of Pt binding with DNA. The platinum(II) complexes with thioether or thiols like [Pt(Met-*S,N*)$_2$] and ring opened carboplatin with L-Met were obtained from cisplatin and carboplatin treated patients and animals, respectively. Additionally, the theoretical investigations also revealed that after initial binding of $[Pt(NH_3)_2(H_2O)_2]^{2+}$, an aquated form of cisplatin with thiols or thioethers, the loss of the ammine *trans* to the sulphur ligand is predicted to be more favoured than the substitution of the sulphur ligand itself by any other donors like guanine-N7 [128]. Various experimental investigations also performed in model systems where the sulphur containing biomolecules like urea and thiourea react with an aquated forms of cisplatin, i.e. $[Pt(NH_3)_2(H_2O)_2]^{2+}$ by ligand exchange leading to short lived *cis*-$[PtCl(NH_3)_2(L)]^+$ complexes that have been identified by ESI–MS, IRMPD spectroscopy and as well as supported with computational studies [129]. Similarly, the interactions of glutathione (GSH) with Pt(II) were also investigated by UV–Vis spectroscopy [130]. Such interactions of Pt(II) with sulphur in cells during the anticancer action have been explained in details by Guo et al. [131].

Considering these facts, it was interesting to design the platinum(II) complexes with sulphur containing ligands and investigate their anticancer activities.

In this regard, Williams et al. have designed the complexes of platinum(II) with S containing amino acids and a 5′-GMP as fragment on DNA. The treatment of $[Pt(Me_4en)(D_2O)_2]^{2+}$ with moieties like methionine, N-acetylmethionine and guanine 5′-GMP was monitored by NMR spectral analyses. The results reveal that the guanine residue of 5′-GMP reacted platinum(II) in 2:1 ratio whereas the N-acetylmethionine and methionine reacted with platinum(II) in only a 1:1 stoichiometry. The methionine formed the chelate through a sulphur and nitrogen donors while N-acetylmethionine was observed to form a chelate through the sulphur and oxygen donors. The oxygen atom of the chelate formed with N-acetylmethionine was easily displaced by an addition of 5′-GMP, although the complete displacement of N-acetylmethionine was not observed. It reveals that the Pt(II)-sulphur-based compounds are anticipated to get formed prior to binding with DNA and then act as anticancer agents by damaging DNA. This process has been supported by molecular mechanics and dynamics calculations also [132].

The typical reactions strategies where the $[Pt(en)Cl_2]$ or $[Pt((Me_4en)Cl_2]$ were treated with S containing amino acids forming their chelated compounds are depicted in Schemes 14.52 and 53.

Furthermore, Becker et al. have designed and synthesized variously substituted terpyridine (terpy) based platinum(II) complexes with diverse sulphur-based moieties like 2-hydroxyethanethiol, 2-mercaptopyridine, 2-mercaptopyrimidine, 1-thiolatoglucose, etc., These compounds were investigated for their biological activities. They exhibited the potent thioredoxin reductase (TrxR) inhibitor activities in a dose depended manner. Since in cancerous cells the over expression of TrxR is a characteristic feature, the inhibition of TrxR leads to cancer cell death. Hence the said compounds exhibit the anticancer property (Scheme 14.54) [133]. In

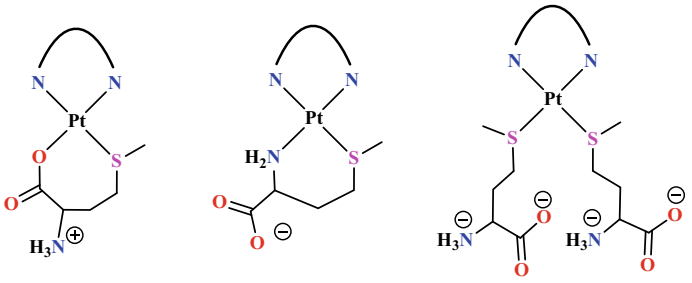

Scheme 14.51 Formation of platinum-diamine and methionine complexes

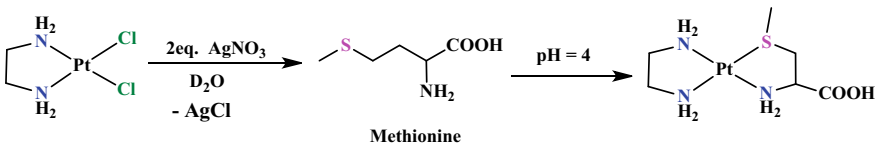

Scheme 14.52 Formation of [Pt(en)(N,S-Met)]

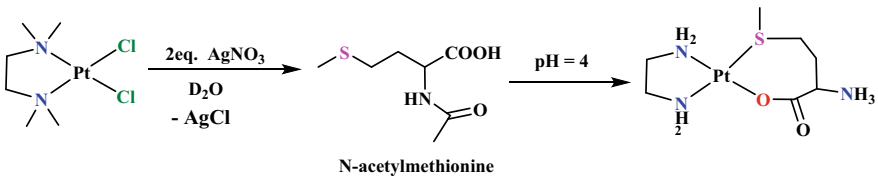

Scheme 14.53 Formation of [Pt(Me4en)(O,S-acetyl-Met)]

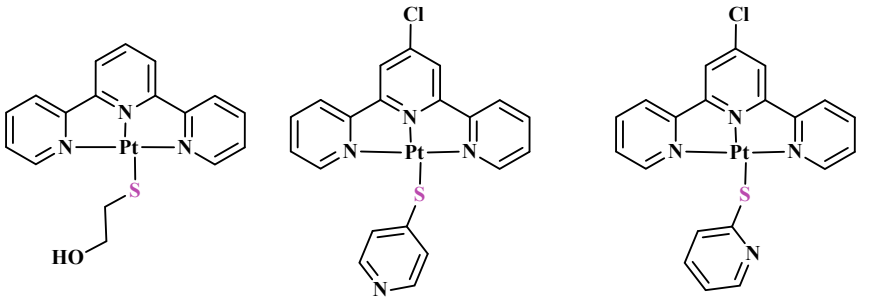

Scheme 14.54 Thioredoxin reductase inhibitor Pt(terpy)-sulphur-based compounds

the further developments, the Pt(II)-terpyridine-based compounds were covalently conjugated with 4-pyridylthiol to form a monocation [Pt(Clterpy)(4-pyridylthiol)]$^{+}$ or with *N,S*-thioacetimine forming a dinuclear and tricationic [{Pt(terpy)}$_2$(μ-*N,S*-thioacetimine)]$^{3+}$ complexes. They were found to exhibit the antiproliferative activities against C6 glioma brain tumour cell lines (Scheme 14.55) [134].

Additionally, terpyridine-based platinum compounds bonded with sulphur moieties have also been reported to exhibit anticancer activities (Scheme) [135].

The competition in binding of platinum(II) based anticancer compounds preferentially with N7 of guanine or adenine from DNA and S containing amino acids like methionine and cysteine belonging to proteins is critical to metabolism as well as for a stability of the cytotoxic lesions of anticancer drugs. Recently, the competitive investigations for compounds of Pt(II) with amines and nucleobases and sulphur-donor ligands have revealed that the easy transfer from a thioether-S ligand takes place exclusively at N7 of guanine site, and not from thiolates or to N7 of adenine (Scheme 14.56) [136].

As per fundamentals of antioxidant, the TrxR (thioredoxin reductase) and Trx (thioredoxin) are playing crucial role to prevent neoplastic progressions. But, during the tumour growth, the Trx system is known to support the proliferation of cells by helping in synthesis of DNA as well as an antioxidant defence. It is evident

Scheme 14.55 Various terpyridine-based compounds exhibiting anticancer activities

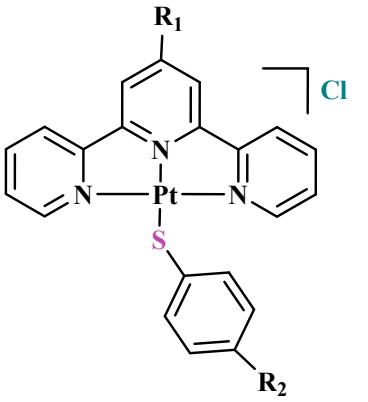

R_1 = H or *p*-tolyl R_2 = OH, NH_2 or $NHCOCH_3$

Scheme 14.56 Terpyridine Pt(II) complexation with glutathione(GSH)—a tripeptide

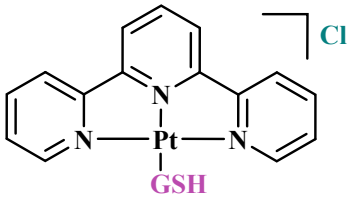

from literature that the increased concentrations of Trx which is directly associated with expression of TrxR and its localization were found in many tumours [137]. Therefore, researchers have focussed for the development of novel TrxR inhibitors (Scheme 14.57) which is a prime interest in the domain of biomedical research [138, 139].

Additionally, they can be synthesized by following methods (Scheme 14.58) [140].

This discussion clearly stated the importance of platinum(II)-sulphur-based compounds for anticancer applications.

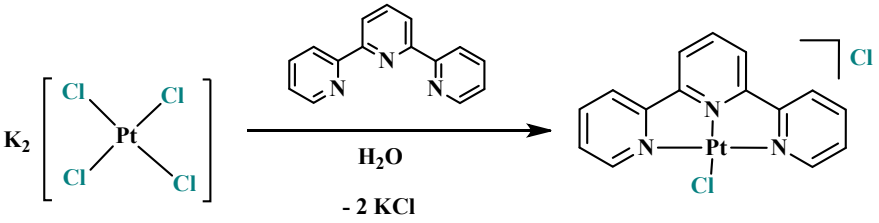

Scheme 14.57 Synthesis of terpyridine Pt(II) complex exhibiting TrxR inhibitor activity

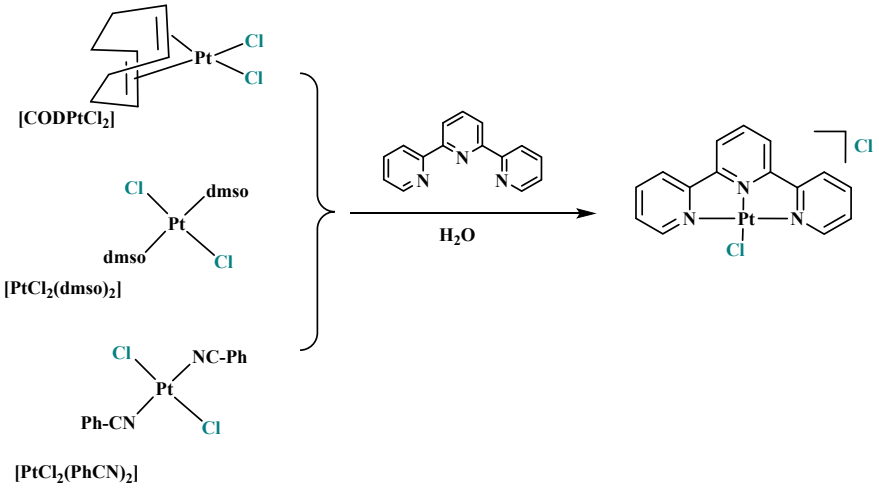

Scheme 14.58 Synthesis of Pt(II)-terpyridine complex by various routs

14.5.14 Platinum-Thiosemicarbazone Compounds

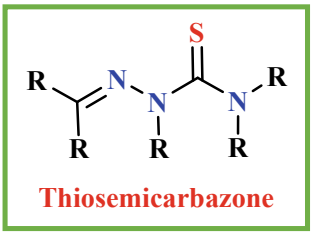

The thiosemicarbazones ($R_2N–C(=S)–NR–N=CR_2$) are the condensation products of thiosemicarbazide [$H_2N(=S)CNHNH_2$] with aldehydes and ketones [141]. Further, appropriate substitutions on either thioamide nitrogen atom, sulphur atom, or hydrazine nitrogen atoms afford their derivatives which have exhibited interesting pharmacological properties. The thiosemicarbazones have reported to exhibit anti-cancer [142], antiproliferative [143], anti-viral (e.g. metisazone) [144], anti-bacterial, antifungal [145] antibiotic (e.g. thioacetazone) [146] and various other biological activities like anti-protozoal and in general antimicrobial [147] activities. One example of the synthesis of thiosemicarbazone derivatives by condensing thiourea derivatives with quinaldehyde is depicted in Scheme 14.59. These compounds exhibited the antiproliferative activities and exhibited interaction with albumin and DNA leading to potential anticancer activities. They inhibited the growth of breast cancer cell also. [148].

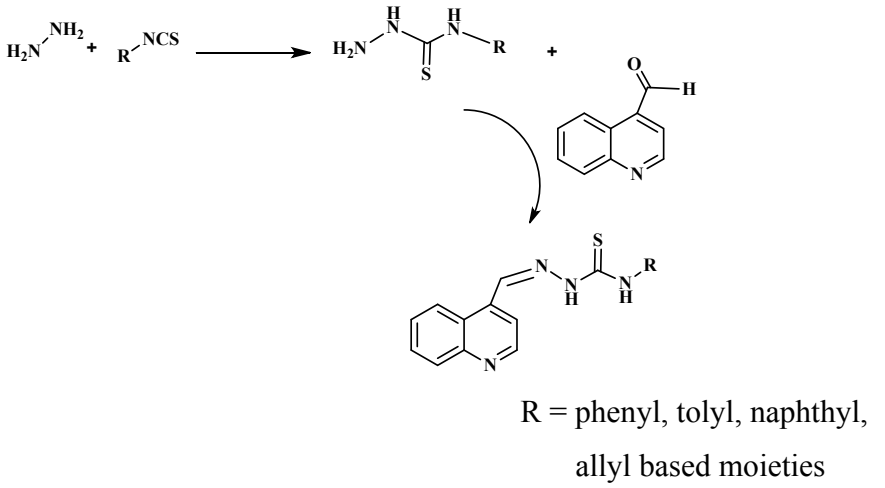

Scheme 14.59 Synthesis of thiosemicarbazone derivatives

Similarly, Mohan et al. have designed and synthesized the 8-nitroquinoline-based thiosemicarbazone derivatives which induced the cancer cell cycle arrest and apoptosis through the ROS (reactive oxygen species) (Scheme 14.60) [149]. Additionally, the diverse synthesis strategies and the pharmacological activities of various thiosemicarbazone derivatives having single hetero atoms (N, O or S) as well as multiple hetero atoms (N,O, N,S or N,O,S) based hybrid thiosemicarbazide derivatives along with their pharmaceutical and medicinal applications on basis of structure activity relationship have been comprehensively reviewed by Patel et al. [150].

Additionally, their transition metal complexes have also exhibited the potent biological activities [151]. Recently, the biological applications of newly reported thiosemicarbazones and their metal complexes have been reviewed well [152]. Most notably, their metal complexes have exhibited potent anticancer applications. In case of treatment of cancer, such compounds have ability for controlling iron accumulation which leads to formation reactive ROS which lead to damage of normal cell also [153].

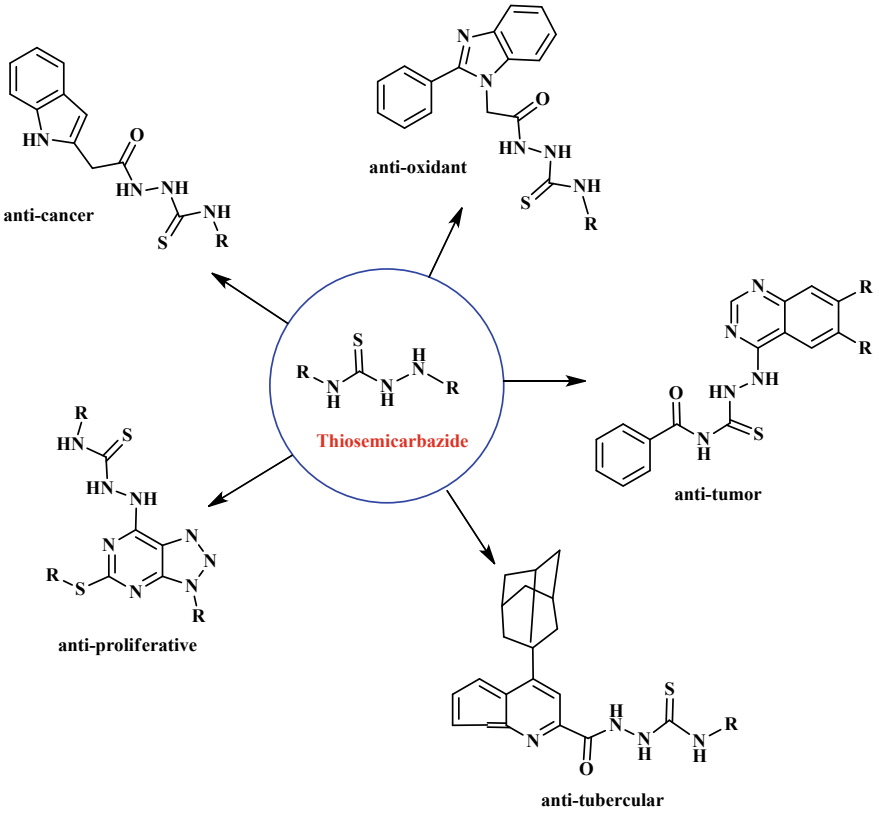

Scheme 14.60 Various thiosemicarbazone derivatives with potent biological activities

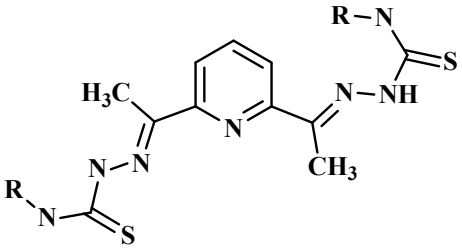

R = *o*-tolyl or *p*-tolyl

Scheme 14.61 Pyridyl-based tetradentate thiosemicarbazone derivatives

In case of fundamental studies, the thiosemicarbazones find extensive applications as ligands in coordination chemistry [154].

In view of this, some Pt(II) complexes with thiosemicarbazones were designed and evaluated for biological applications. Hence, few examples of Pt(II)-thiosemicarbazone derivatives which find pharmacological applications specially, anticancer properties will be discussed. The thiosemicarbazone forms the complexes with Pt(II) through a thionic sulphur and azomethine nitrogen atom of the thiosemicarbazone.

In such efforts, Souza et al. have reported the platinum(II) complexes with bis(thiosemicarbazone) linked with 2,6-diacetylpyridine moiety. These novel complexes exhibited non-toxicity to normal or noncancerous cells (LLC-PK1 cells) while high cytotoxicity against the cisplatin resistant tumour cells (A2780cisR). Additionally, they exhibited antiproliferative properties *in vitro* against MCF-7, HepG2, A2780, A2780cisR and NCI-H460, human cancer cell lines. They proved their potency for circumventing the resistance to cisplatin in case of A2780cisR cell lines. The general structure of pyridyl substituted thiosemicarbazone is as shown in Scheme 14.61 and typical synthesis of their complexes with Pt(II) is shown in Scheme [155].

The platinum(II) complexes were synthesized by coordinating these moieties at basic reaction mixtures using triethylamine at room temperature. The filtrate on standing slowly formed the precipitate of the desired Pt(II)-thiosemicarbazone complex (Scheme 14.62).

Their single crystal XRD analyses revealed that the pyridyl-based thiosemicarbazone derivatives function as a tetradentate donors which coordinate to the platinum(II) centre having square planar geometry via the pyridinic and iminic N atoms and the S atoms belonging thiosemicarbazone fragment, whereas the fourth coordination position is occupied by the hydrazinic N atom of other thiosemicarbazone moiety of a ligand. Such versatile structures initiate thought for new designs also.

Furthermore, Xu et al. have also reported the synthesis and structural characterization of pyridyl-based thiosemicarbazone compounds as well as their platinum(II) complexes. They exhibited bio-relevant activities like their binding with proteins like

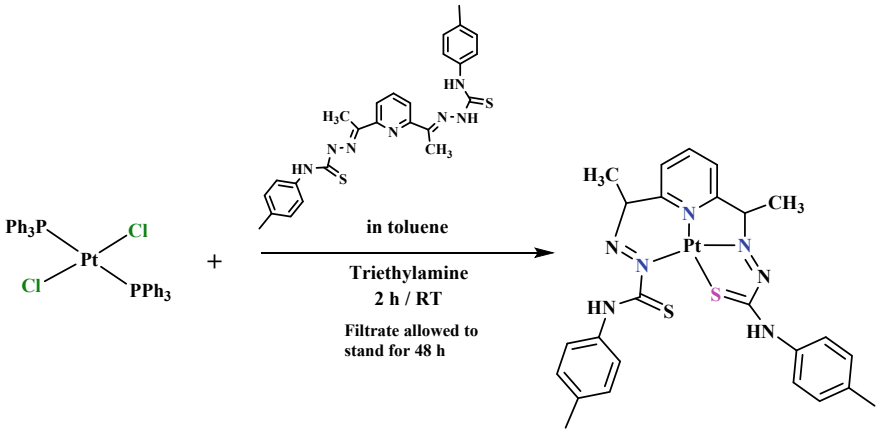

Scheme 14.62 Synthesis of Pt(II)-thiosemicarbazone derivative

human serum albumin (HSA) as evidenced by UV–visible and fluorescence spectral analyses. They exhibited the antiproliferative properties against human breast (MCF-7), human liver hepatocellular (HepG-2), non-small-cell lung (NCI-H460) as well as human epithelial cervical (HeLa) banker cell lines. These complexes acted in a monofunctional way resulting to their cytotoxicity against various cancer cell lines with $IC_{50} = 1.7–9.6\ \mu M$ which is much better than the cisplatin cytotoxicity ($IC_{50} = 5.2–13.5\ \mu M$). Some of them have exhibited much higher and rapid accumulation in cancer cells which is additional feature in designing the new platinum-based drugs. Additionally, the flow cytometric analysis and fluorescence microscopic studies for mechanistic investigations have revealed that some of these complexes have killed the cancer cells by inducing the apoptosis in HeLa cell lines. The representative structures of these Pt(II) based thiosemicarbazones have been shown in Scheme 14.63 while the typical synthesis strategy leading to coordination of pyridyl-based thiosemicarbazones with K_2PtCl_4 in aqueous solution affording the monofunctional complexes has been depicted in Scheme 14.64 [156].

Further efforts in structural modifications of thiosemicarbazone derivatives with their conjugation with biomolecules like steroidal moieties have lead to formation of

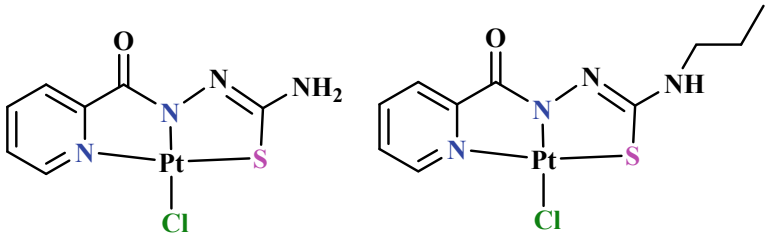

Scheme 14.63 Platinum(II) complexes with pyridyl-based thiosemicarbazones

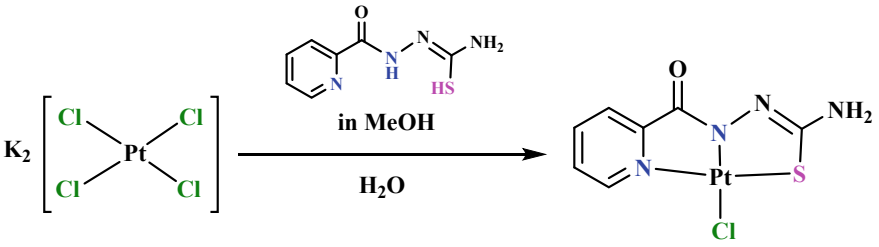

Scheme 14.64 Synthesis of monofunctional platinum(II)-pyridyl-based thiosemicarbazone

new biocompatible compounds with potent biological activities. They were obtained by treatment of appropriate thiosemicarbazides with the steroidal ketones of estrone-17. Such thiosemicarbazone derivatives were coordinated with K_2PtCl_4 affording the platinum(II)-thiosemicarbazone compounds which were the structural derivatives of cisplatin (Scheme 14.65). They exhibited optimum cytotoxicity against HeLa and Bel-7404 cancer cells lines. Some of them exhibited an excellent inhibitory selectivity

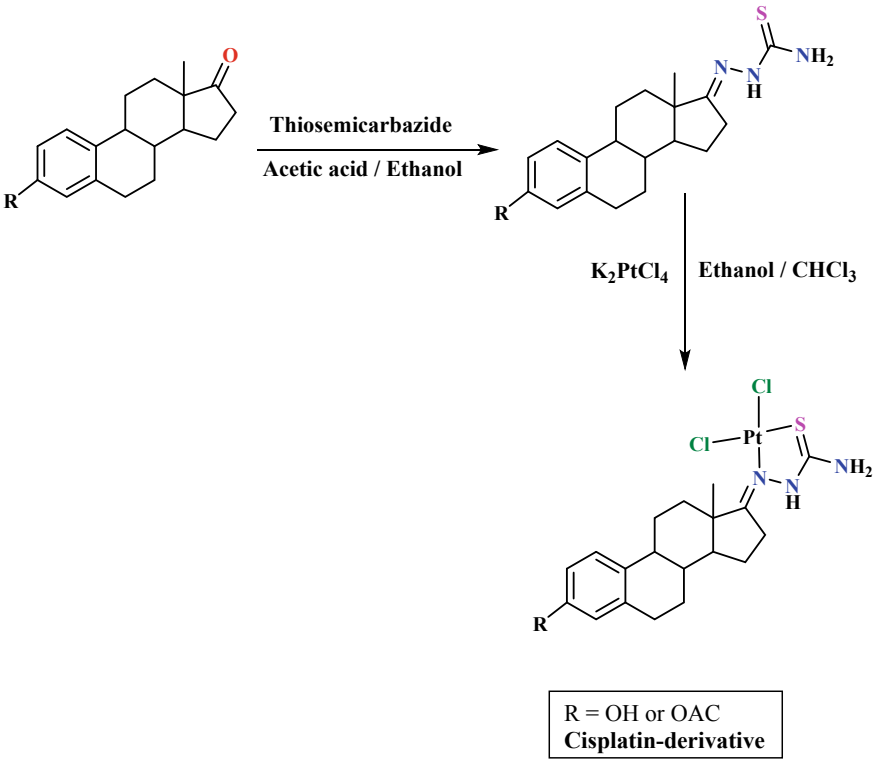

Scheme 14.65 Synthesis of Pt(II)-estrone-17-thiosemicarbazone-based cisplatin derivative

against HeLa cells ($IC_{50} = 9.2\ \mu M$). Most importantly all the compounds were almost non-toxic to normal kidney epithelial cell lines (HEK293T). The insights from such results may be useful for the novel design for new chemotherapeutic drugs [157].

This account gives clear view that the thiosemicarbazones and their metal complexes have a great potential for further design conferring them with potent bio-relevant and pharmacological properties.

14.5.15 Platinum(II)-Selenium-Based Compounds

The era of platinum(II)-selenium-based compounds has been started mainly because of their similarity with their sulphur-based analogues, in their chemical reactivity, structural aspects as well as known anticancer anticancer potency of selenium-based compounds. As discussed earlier, the identification of platinum(II)-sulphur-based short lived species as intermediates before DNA platination were formed. Additionally, similar to organosulphur compounds the organoselenium compounds (e.g. selenomethionine) also are well known for the promising anticancer activities [158]. Additionally, the reactions of L-selenomethionine with cisplatin were studied by using the electrospray-mass spectrometry (ESI–MS) and formation of diverse platinum(II) complexes with selenomethionine (Se-Met) have been observed [159]. Hence, it was anticipated that the conjugation of selenium compounds with platinum affording the analogues of existing Pt(II) based drugs, may achieve the potent anticancer properties due to synergistic effect of both species. Additionally, the superior chemical reactivities of selenium, especially the higher redox properties confer the enhanced potency to selenium compounds. Additional feature of selenium of having the ^{77}Se as the NMR active nucleus which renders it most useful in characterization as well as studying the mechanism of anticancer action of the Pt(II)-selenium-based compounds due to distinct chemical shifts of various species of selenium involved during anticancer function. These facts have led to beginning of new era of research anticipating anticancer applications of platinum(II)-selenium-based compounds.

In continuation to earlier work of identifications of Pt(II)-methionine(*S,N*) derivatives found in cisplatin treated patients, the researchers have thought about the similar reactions of Pt(II) based drugs with selenomethionine (Se-Met) as well as further interactions of Pt(II)-methionine(*S,N*) species with selenium containing amino acids like selenomethionine (Se-Met) in body of Pt(II) drug treated patients. In this regard, S. Robey and K. Williams have performed the exclusive work by studying the various reactions of Pt(II)-methionine species as well as synthesizing the Pt(II) based compounds with slenomethionine (Se-Met) at different pH conditions since the pH at normal cell (7.4 units) and the acidic pH of cancerous cells (3–5 units) differ substantially. [160]. All these studies were performed by using ^{1}H NMR spectroscopic tool.

Treatment of K_2PtCl_4 with selenomthionine (Se-Met) and sodium chloride in D_2O solvent (placed in NMR tube) and warmed on water bath at 80 °C afforded

Scheme 14.66 Cisplatin derivative with selenomethionine

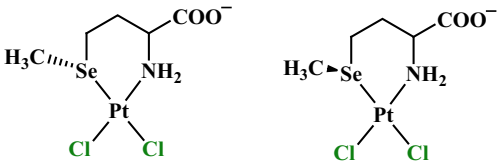

the monochelated complex of composition $[Pt(Se\text{-}Met\text{-}Se,N)Cl_2]^{2+}$ existing as two isomeric forms (Scheme 14.66). It is treated as the cisplatin derivative.

In case of treatments of methionine chelated Pt(II) compound $[Pt(L\text{-}Met\text{-}S,N)Cl_2]^{2+}$ with Se-Met, the monochelated as well as well as bischelated species were formed at lower pH (~ 2.8) and higher pH (~6.5) respectively (Scheme 14.67).

Formation of these products was authenticated by ^1H NMR spectroscopy.

Additionally, the reactions between oxaliplatin derivative $[Pt(en)ox]^{2+}$ and excess of selenomethionine (Se-Met) were evaluated. Their reactions at acidic pH (4 units) afforded the bis chelated $[Pt(Se\text{-}Met\text{-}Se)_2]^{2+}$ intermediate with removal of en group while the same reaction at higher pH (7 units) afforded exclusively the monochelated $[Pt(en)(Se\text{-}Met\text{-}Se)_2]^{2+}$ with retaining the en group (Schemes 14.68 and 14.69).

Additionally, the same reaction using excess of $[Pt(en)ox]^{2+}$ lower pH (4 units) afforded the nonchelated $[Pt(en)(Se,Met\text{-}Se,N)]^{2+}$ species (Scheme 14.70).

All these above efforts suggested the versatile chemistry resulting in various structures of platinum(II)-selenomethionine species which are likely to form in the body of Pt(II) based drug treated patients before they bind with the cellular target DNA which lead to killing of cancer cells. Hence, this triggered the thoughts to design, synthesize the Pt(II)-organoselenium compounds and evaluate them for anticancer potency.

For this cause, highly water-soluble cationic Pt(II)-selenium-based compounds having structural similarity to existing Pt(II) based drugs were designed and synthesized (Scheme 14.71). They were designed as cisplatin analogues by replacing chlorides of cisplatin by Se-O chelate of selenoethers with terminal COOH functional

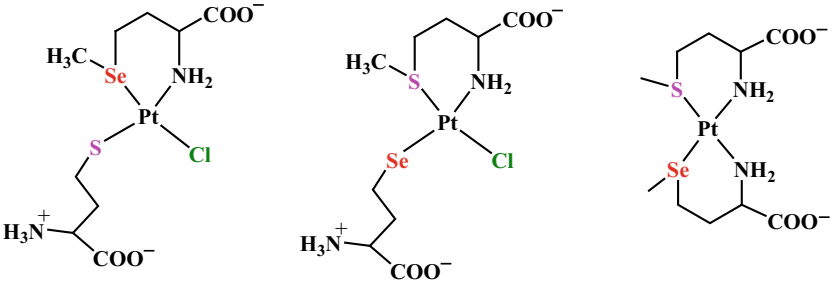

Scheme 14.67 pH dependent product formed after treatment of $Pt(L\text{-}Met\text{-}S,N)Cl_2]^{2+}$ with Se-Met

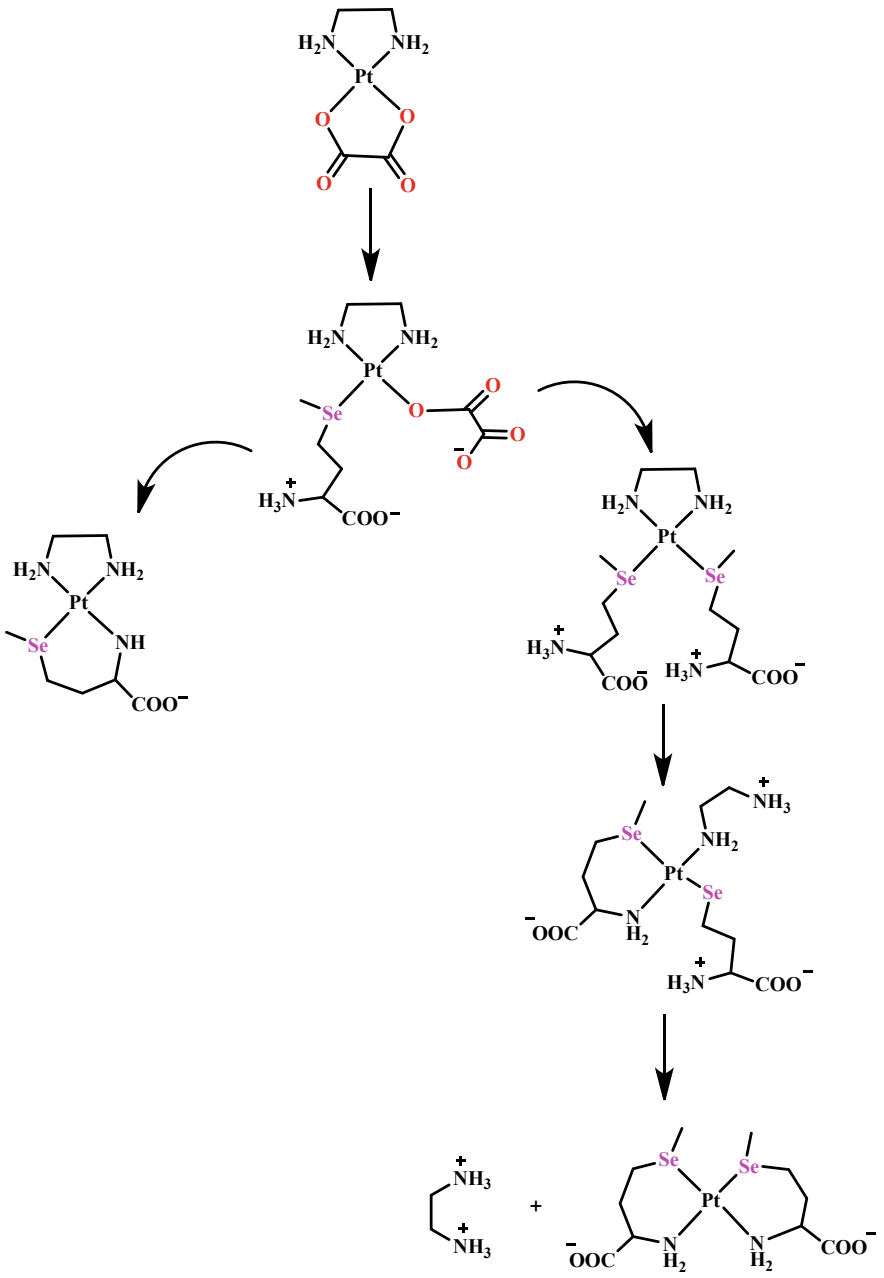

Scheme 14.68 Treatment of oxaliplatin with Se-Met at acidic pH

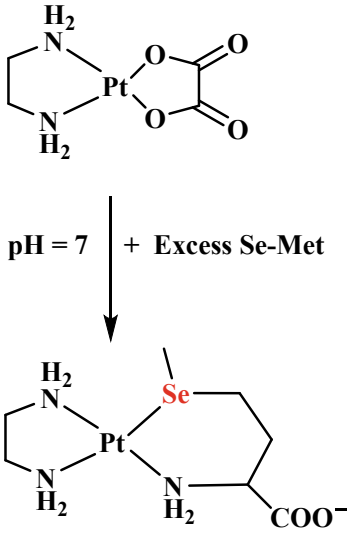

Scheme 14.69 Treatment of oxaliplatin with excess Se-Met at neutral pH

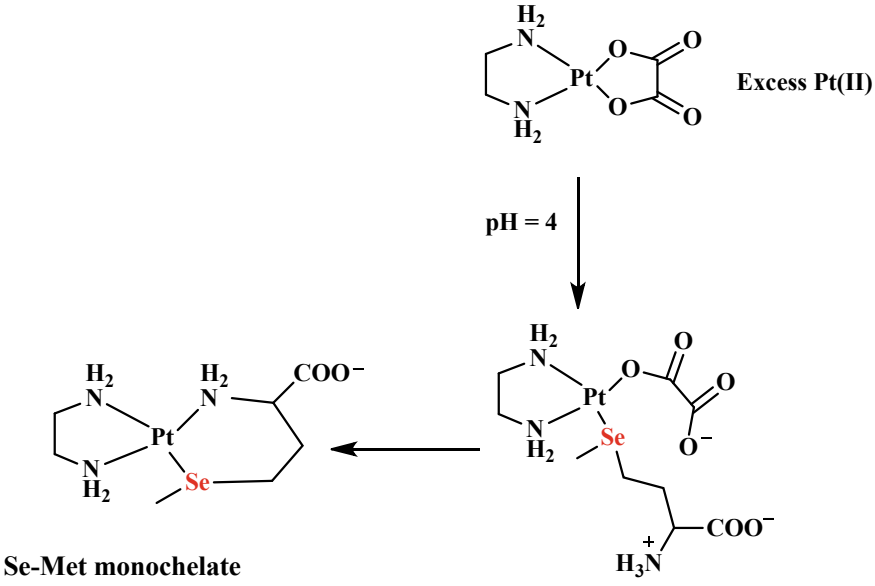

Scheme 14.70 Treatment of oxaliplatin with Se-Met at acidic conditions

Scheme 14.71 Various complexes of Pt(II) with selenoethers

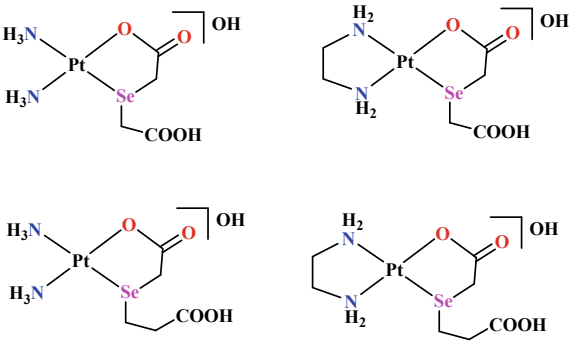

groups. Further, the same selenoethers coordinated with Pt(en) fragment affording the compounds having structural similarity with oxaliplatin [161].

The typical synthesis strategy for achieving these compounds is shown in Scheme 14.72. Accordingly, the aqueous solutions of $[Pt(en)Cl_2]$ or *cis*-$[Pt(NH_3)_2Cl_2]$ were reacted with two molar equivalents of aq. $AgNO_3$ followed by two equivalents of aq. NaOH forming $[Pt(NH_3)_2(OH)_2]$ or $[Pt(en)(OH)_2]$ species in situ which on further treatment with appropriate selenoethers afforded the highly water-soluble Pt(II)-Selenoether complexes having general formula $[Pt(N^{\wedge}N)(OOC(CH_2)_nSe(CH_2)_nCOOH)][OH]$ ($N^{\wedge}N = 2\ NH_3$ or en). They were well characterized especially with NMR spectroscopy (^1H, ^{13}C, ^{77}Se and ^{195}Pt) and single crystal X-ray diffraction analyses.

The binding of these $[Pt(N^{\wedge}N)(OOC(CH_2)_nSe(CH_2)_nCOOH)][OH]$ complexes with 5′-guanosine monophosphate (5′-GMP) which a mononucleotide fragment on

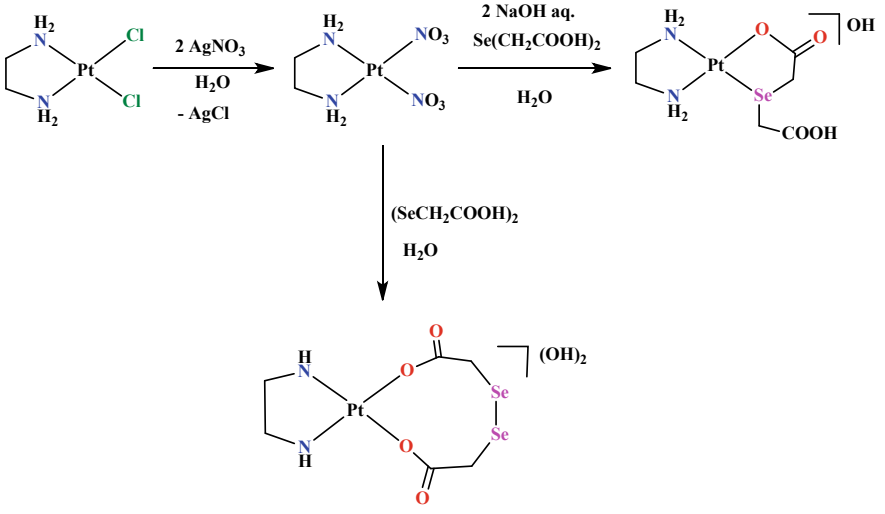

Scheme 14.72 Synthesis of water-soluble complexes of platinum(II) with selenoethers

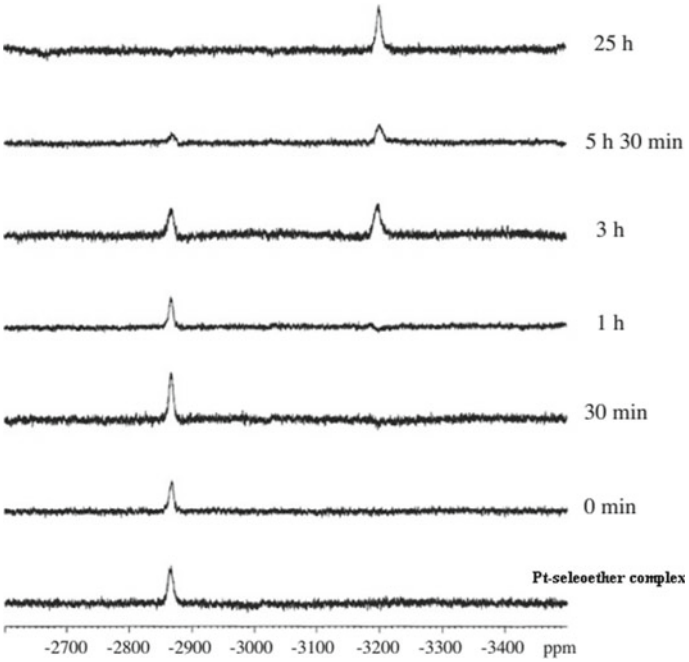

Fig. 14.5 Time-dependent $^{195}Pt\{^{1}H\}$ NMR spectral analyses clearly depicting the binding of a Pt-selenoether complex [Pt(en)($OOCCH_2SeCH_2COOH$)][OH] (δ = - −2865 ppm) with 5′-GMP [Pt-5′-GMP binded product (δ = -−3198 ppm)]

DNA was evaluated by time-dependent $^{195}Pt\{^{1}H\}$ and $^{77}Se\{^{1}H\}$ NMR spectral analyses. It revealed that these, complexes bind with 5′-GMP within 8 h time (Fig. 14.5). The complete binding was unambiguously established from the distinct chemical shifts of $^{195}Pt\{^{1}H\}$ resonances. The test complex exhibited $^{195}Pt\{^{1}H\}$ NMR resonance at δ = – 2865 ppm while its 4′-GMP binded product exhibited resonance at δ = – 3198 ppm. Additionally, the $^{77}Se\{^{1}H\}$ NMR analyses in D_2O also supported the fact. The complex [Pt(en)($OOCCH_2SeCH_2COOH$)][OH] ($^{77}Se\{^{1}H\}$ NMR spectrum in D_2O: δ 148 ppm ($^{1}J_{Pt\text{-}Se}$ = 280 Hz) after complete binding with 5′-GMP formed [Pt(en)($HOOCCH_2SeCH_2COOH$)(5′-GMP)][OH] complex which exhibited a single resonance at $^{77}Se\{^{1}H\}$ NMR spectrum in D_2O: δ 188 ppm ($^{1}J_{Pt\text{-}Se}$ = 438 Hz). The deshielding of Pt-5′-GMP product by 40 ppm as compared to staring complex and a vast difference in their coupling constants (158 Hz) is a clear evidence of two distinct species. The anticipated product is as shown in Scheme 14.73.

Furthermore, by using similar synthesis strategies the highly water-soluble cationic cisplatin derivatives by either substituting the labile chlorides with a chelating dimethyl pyrazolyl-based selenoethers or their analogues with substituted amines [162]. Some of such compounds have been shown in Scheme 14.74.

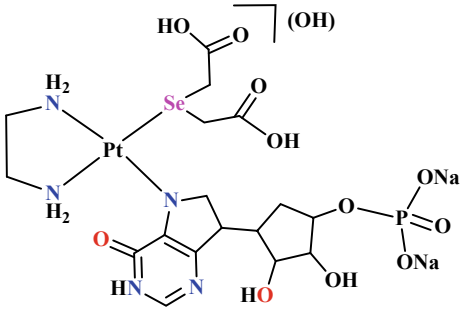

Scheme 14.73 The 5′-GMP binded Pt(II)-selenoether complex

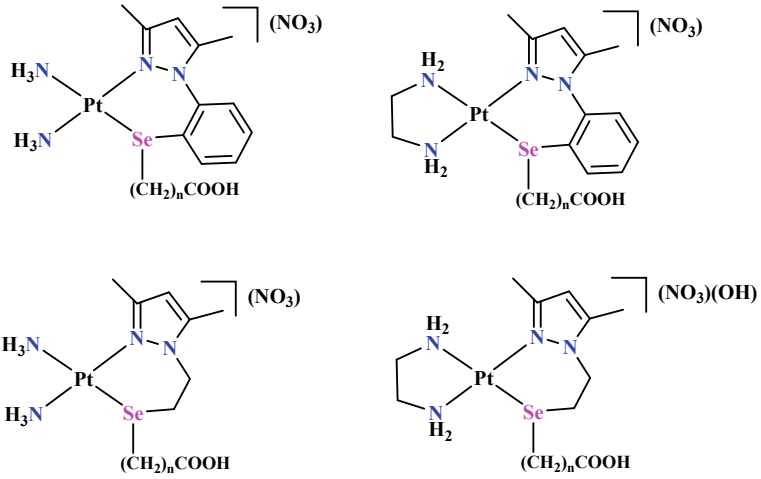

Scheme 14.74 The water-soluble Pt(II) compounds with dimethyl pyrazolyl-based selenoethers

These compounds have also been prepared by using the similar reactions strategies as discussed earlier for platinum(II)-selenium complexes. The synthesis of a representative complex is as depicted below (Scheme 14.75).

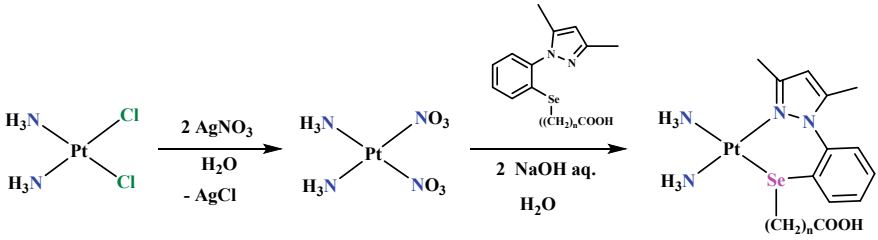

Scheme 14.75 Synthesis of Pt(II)-dimethylpyrazolyl-based selenides

Additionally, the treatment of $[PtCl_2(PhCN)_2]$ with dimethylpyrazolyl-based selenoether (1:1 and 1:2 molar ratio) in CH_2Cl_2 solution has afforded the cationic bis dimethylpyrazolyl platinum(II) complex as a precipitated form. It is worthy to note here that, a bis coordinated Pt(II) complex was formed exclusively irrespective of stoichiometry of Pt(II) and selenoether moieties during synthesis (Scheme 14.76).

All these compounds have been evaluated for cytotoxicity against human ovarian (A2780), colon (Colo205, HT29) and bladder (T24) cancer cell lines and compared with the cytotoxicity of cisplatin and doxorubicin (adriamycin). They exhibited cytotoxicity lower than the doxorubicin but comparable with cisplatin.

Furthermore, the preparation of Se containing Pt(II) based anticancer compound Pt- EG-Se was performed by Sun and Xu et al. (Scheme 14.77) [163]. The coordination of Se containing amphiphile (possessing both hydrophilic and lipophilic properties) molecules like EG-Se with a cisplatin afforded the Pt-(EG-Se) complex which was characterized with MALDI-TOF mass spectrometric analyses as well as by ^{77}Se NMR spectroscopy. This Pt-(EG-Se) complex induced apoptosis in the

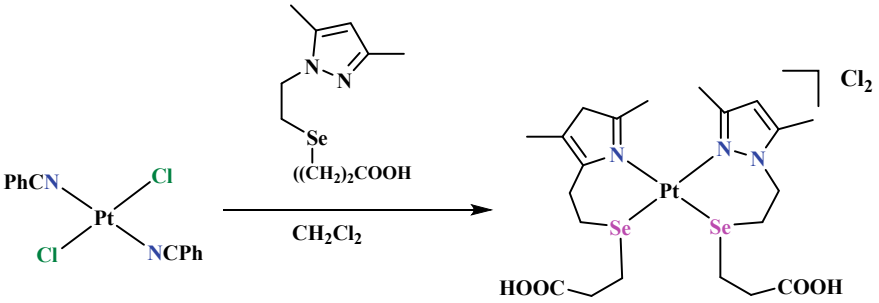

Scheme 14.76 Synthesis of Pt(II)-bis-dimethyl pyrazolyl complex

Scheme 14.77 The amphiphilic Pt-(EG-Se) complex

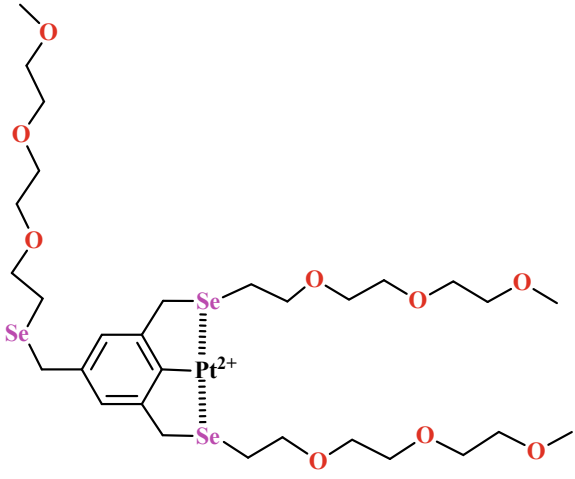

cancer cells (viz., A549, MCF-7 and HT-29 cell lines) and tumour reduction in tumour (HepG2) in the female BALB/C nude mice via the formation of ROS. The ROS lead to high selectivity between cancer cells and normal cells in cytotoxicity assays. It is important to note here that the Pt-(EG-Se) compound has exhibited effective inhibition of the tumour growth in case of tumour inducted mice. It is expected that tuning the ROS concentrations in cells through the assembly of Se containing compounds may be a general strategy to achieve anticancer selectivity. The anticancer mechanism of such compounds is established to follow the ROS mediated pathway leading for apoptosis induced by Pt-(EG-Se) complex. The same Pt-(EG-Se) has exhibited killing of lymphoma and leukaemia cells (T-LBL/ALL) by inducing cell cycle arrest as well as caspase and ROS mediated apoptosis via mitochondrial signalling pathway [164]. The results have revealed that Pt-(EG-Se) compound is anticipated as a potentially therapeutic compound for a treatment of T-cell acute lymphoblastic leukaemia/lymphoma (T-ALL/LBL) cancer. Additionally, the results exhibited that the complex, Pt-(EG-Se) exhibited the inhibition of Jurkat and Molt-4 cell lines viability which was dependent on a dose and time.

Recently, Xu et al. have reported about the selectivity in cytotoxic property of Pt-(EG-Se) towards cancer cells. The basis for the mechanism behind selectivity in toxicity is considered to be associated with defence system of glutathione (GSH) antioxidant. It is known that the elevated ROS level offer higher vulnerability for cells for further elevation of ROS levels. The Pt-(EG-Se) compounds can enforce the abnormal rise in reactive oxygen species, by depletion of glutathione. As a consequence, the mitochondrial membrane potential falls leading to release of cytochrome, which further results in apoptotic death of cell. These findings revealed that the glutathione (GSH)-antioxidant system is an active target for achieving therapeutic selectivity to the Pt(II) based anticancer compounds. The amphiphilic nature of platinum-selenium coordination complexes enables them for assembling into nanoparticles and helps in prolonging the circulation time of a drug in bloodstream, which is an important feature for *in vivo* drug delivery. The *in vivo* anticancer investigations have exhibited that the rate of inhibition of tumour growth for Pt-(EG-Se) compound was reached up to ~70%. The most encouraging thing is that, the Pt-(EG-Se) exhibited minimum side effects as compared to a drug, cisplatin. These results provide new opportunities for design and development of novel therapeutic strategies against cancer [165].

Furthermore, Xu et al. have reported the monodispersed Pt-Se-based coordination dendrimers with a Pt-Se core located deep inside. The structures of these dendrimers were authenticated by various techniques. In this case, the Pt-Se-based coordination dendrimers have shown the controlled anticancer activities, without any loading of additional anticancer drugs. Additionally, their in vivo evaluations demonstrated their potent anticancer activity with a desired low toxicity to the normal tissues [166].

The anticancer activity of these dendrimers was evaluated against liver cancer cell lines (HepG2) by MTT assay. The cytotoxic potency of Pt-Se coordination dendrimers was compared with Se containing dendrimers and cisplatin. The MTT assay results revealed that Pt-Se coordination dendrimers have exhibited the anticancer activity equivalent to cisplatin, while Se containing dendrimer exhibited lower activity. The *in vivo* studies of the same compound were performed against tumour

implanted by injecting 4T1 breast cancer cells in Balb/c mouse model which exhibited the anticancer efficiency and most importantly the low toxicity to normal cells [167].

The dendrimeric selenium compounds were prepared as follows. The L-lysine mono-dendrons up to the third generation were prepared by utilizing *N*-Boc protected, amino surface groups and N-(2-aminoethyl)amide group at the focal side were synthesized according to the method reported by Appelhans et al. (Scheme 14.78) [168]. Accordingly, treatment of a dichloromethane. solution of LG1-NH_2 and 4,4′- (selenobis(methylene))dibenzoic acid with N,N-diisopropylethylamine under argon atmosphere was done yielding a solid which was dissolved followed by addition of (benzotriazol-1-yloxy)tris(dimethylamino)- phosphonium. The reaction mixture on stirring for 48 h, dissolved in dichloromethane and washed with 1 M hydrochloric acid followed by washing with saturated sodium bicarbonate. The obtained product was processed for purification with column chromatography using a mixture of dichloromethane and methanol (8:1 v/v) to obtain a pure LG1Se compound. Other derivatives LG_3Se and LG_2Se were also prepared by following similar procedure. Their structures are depicted in scheme as follows.

The synthesis of their Pt(II) complexes has been described. Accordingly, preparation of Pt-Se coordination dendrimers viz., Pt/DLG1Se, Pt/DLG2Se/ and Pt/DLG3Se. The dichloromethane solution of LG1Se treated with trifluoroacetic under argon atmosphere for 39 min. On concentrating the solution, the product was precipitated in diethyl ether. It was followed by centrifugation to isolate a solid sample DLG1Se which was washed with diethyl ether to obtain a clean product. The obtained product was further reacted with cisplatin in aqueous solutions and stirred to afford DLG1Se/Pt. Other derivatives viz., Pt/DLG2Se and Pt/DLG3Se were synthesized by following similar synthesis strategies.

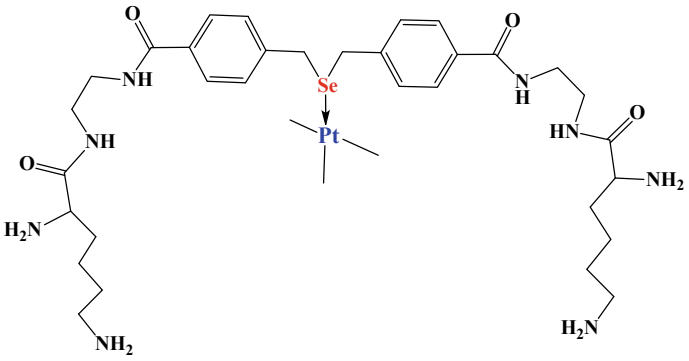

Scheme 14.78 A typical Pt(II) complexe with dendrimeric selenium compounds

14.5.16 Platinum(II)-Phosphine-Based Compounds

The drive for the search of novel anticancer agents having superior potency as well as reduced toxicity over the existing Pt(II) based anticancer drugs has directed the researchers to explore various Pt(II) based with diverse functional groups or moieties which are known for biological potency, biocompatibility with human physiological system, enhanced water solubility as well as better physicochemical properties. In this regard, the phosphine-based moieties like 1,3,5-triaza-7-phosphaadamantane (pta) were also explored. The rationale for use of such moieties was their high catalytic activities [169], stability due to strong Pt-P bond as well as high water solubility [170]. Additionally, the gold(I)- and gold(III)-phosphines have exhibited potent antiproliferative and anticancer activities against H460, K562 and OVCAR8 cell lines with IC_{50} in the range of ~ 0.10–2.53 μM [171]. Along with these, the auranofin, a phosphine containing gold compound is FDA approved antirheumatic agent Additionally, various metal (e.g. Cu, Fe, Ru) complexes with phosphine-based ligands have exhibited anticancer properties [172].

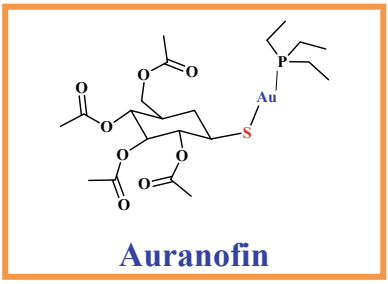

In view of the importance of various metal-based phosphine complexes as pharmacological agents including anticancer potency, the design of platinum(II) compounds with phosphines anticipating their potent anticancer activities was a prime interest of researchers. In these efforts, the monofunctional platinum(II) complexes with 1,3,5-triaza-7-phosphaadamantane (pta) which show potent anticancer activity have been synthesized (Scheme 14.79). These compounds exhibited cytotoxicity against melanoma (A375) and human lung fibroblasts (MRC5) as evaluated by MTT assay [170].

Furthermore, several new Pt(II) based complexes with saccharinate (sac) which contained the phosphine ligands like PPh_3, PPh_2Cy, $PPhCy_2$ and PCy_3 having successive substitution of Ph (phenyl) group by Cy (cyclohexyl) group have been synthesized by using diverse reaction conditions (Schemes 14.80 and 14.81) [173]. Their anticancer activities were evaluated against a panel of cancer cell lines viz., lung (A549), human breast (MCF-7), prostate (DU145) and colon (HCT116) cancer cell lines and against normal bronchial epithelial (BEAS-2B) cell lines also. The lipophilic nature and the accumulation of these complexes in cell are contributing are contributing to their cytotoxic activity. The mechanistic studies of their anticancer

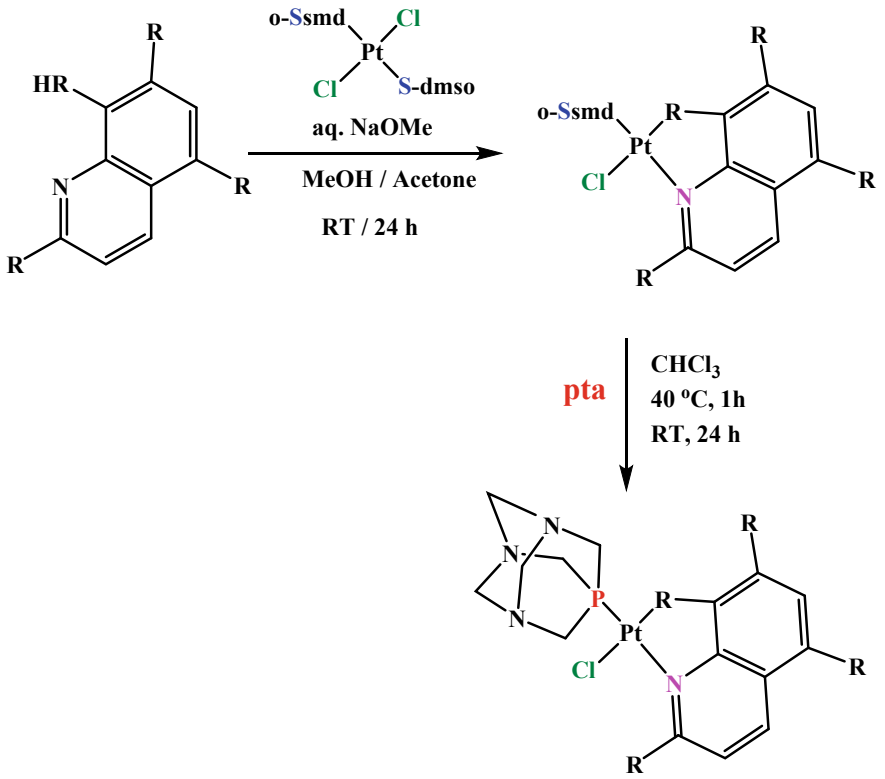

Scheme 14.79 Synthesis of monofunctional Pt(II)-phosphine compound

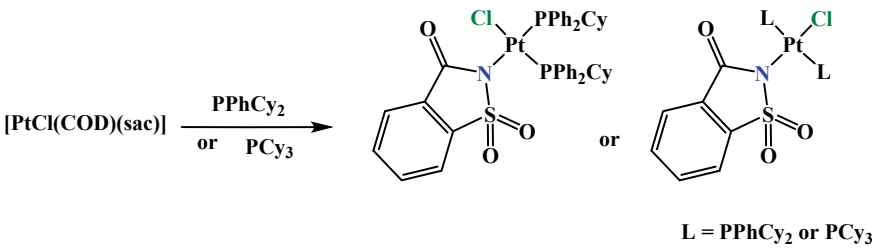

Scheme 14.80 Synthesis of monofunctional Pt(II)-saccharinate-phosphine complexes

properties revealed that these complexes are responsible for disproportionate formation of ROS and exhibit a dual-action, simultaneously targeting both genomic DNA and mitochondria.

This brief account of findings of anticancer properties of Pt(II) complexes with phosphines have clearly established them as a prominent class of Pt(II) based compounds for future applications in medicine.

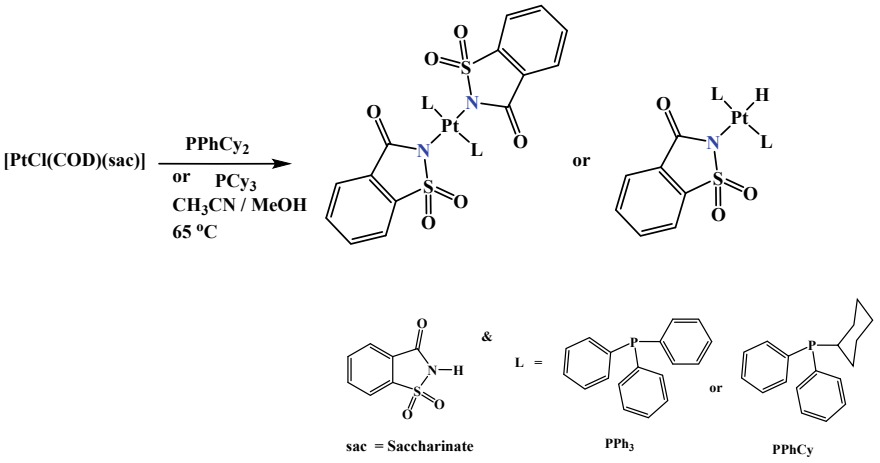

Scheme 14.81 Synthesis strategies for Pt(II)-phosphine complexes with saccharinate

14.5.17 Multinuclear Platinum(II) Based Anticancer Compounds

Although the second and third generation platinum(II) based anticancer drugs have exhibited reduced side effects as well as the acquired resistance as compared to a drug, cisplatin [174], but their toxicity profile does not differ much since the binding mode remain same [175]. Hence, anticipating the possibility to overcome the limitations of earlier Pt(II) based drugs, the multinuclear platinum complexes were designed synthesized and evaluated for anticancer applications. As the name suggests, two or more platinum centres linked through aliphatic carbon chains constitute the multinuclear platinum complexes. Each Pt centre can covalently bind to DNA. Owing to their structures, they are able to form entirely different types of DNA adducts as compared to DNA adducts with cisplatin and its derivatives [176], which facilitates the enhanced killing of cancer cells. From literature, it is clear that, the multinuclear platinum complexes achieve their activity from the distinct adducts which they form with DNA. The design, synthesis and activities of multinuclear platinum complexes has been reviewed well by Collins et al. and Farrell et al. [177]. It should be noted here that along with the excellent anticancer activity, the multinuclear platinum complexes have the associated toxicity for the normal cells also, this fact limits their clinical use. Hence, the search for novel multinuclear platinum complexes without severe side effects is of prime interest.

It will of worth to discuss few examples of multinuclear complexes. In initial efforts, the multinuclear platinum complexes were prepared by the linking of two cisplatin or cisplatin-like centres by an aliphatic diamine chain (Scheme 14.82) [178]. Further efforts were directed with leaving group modification strategies. Hence, the chlorides were replaced by malonate species which afforded the complexes with

Scheme 14.82 Dinuclear platinum complexes containing two linked cisplatin centres, where n = 2–6

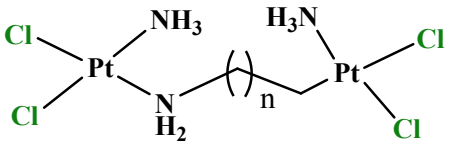

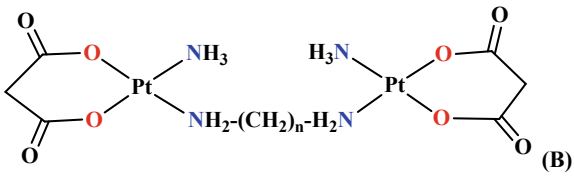

enhanced water solubility. Such complexes exhibited better anticancer activity in cisplatin resistant cancer cell lines [179].

These complexes exhibited their binding DNA similarly to cisplatin through the GpG intrastrand cross-links, Additionally, they formed longer range intra- as well as inter-strand adducts also [24]. The mechanistic studies revealed that these complexes produced a high percentage of inter-strand adducts [179].

By using similar strategies further structural developments were performed by linking two cisplatin molecules through a 4,4′-dipyrazolylmethane (dpzm) linker. Its analogous compounds where one of cis-ammine was replaced with DMSO were reported (Scheme 14.83). Furthermore, the doubly bridged analogous complexes were also developed (Scheme 14.84). Additionally, their Pt(IV) analogues were also synthesized by using the similar synthesis strategies (Scheme 14.85). They were evaluated for anticancer activities both *in vitro* and in vivo [180].

Scheme 14.83 A single bridged dinuclear platinum(II) complexes linked by 4,4′-dipyrazolylmethane

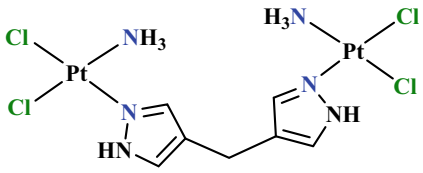

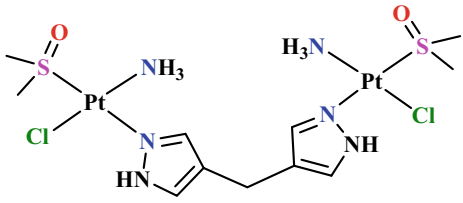

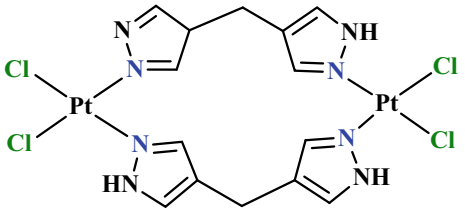

Scheme 14.84 A doubly bridged dinuclear platinum(II) complexes linked by 4,4′-dipyrazolylmethane

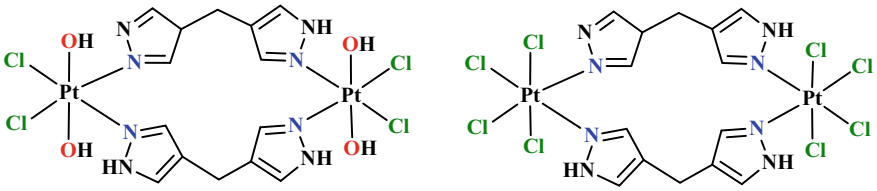

Scheme 14.85 Double bridged dinuclear platinum(IV) complexes linked by 4,4′-dipyrazolylmethane

Furthermore, the platinum(II) complexes where two cisplatin were linked with a sulphur or selenium containing dipyridyl linker have been synthesized by Zhao et al. (Scheme 14.86) [181]. Additionally, the Wheate et al. have reported the di- as well as tri-nuclear Pt(II) complexes linked by the dipyrazolylmethane (dpzm) moieties (Scheme 14.87).

Additionaly, in a different approach, Komeda et al. designed and synthesized a various multinuclear Pt(II) complexes where Pt(II) centres were linked by pyrazole (Scheme 14.88) [182].

Additionally, a tetranuclear complex using a branched aminoalkane linking chain was designed and synthesized by Jensen et al. (Scheme 14.89) [183].

This account clearly depicted that the multinuclear platinum(II) and platinum(IV) complexes were designed to overcome limitations of existing Pt(II) based drugs. The multinuclear complexes have advantage of enhanced killing of cancer cells owing to

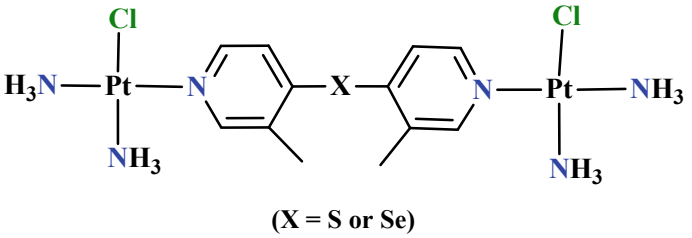

(X = S or Se)

Scheme 14.86 Cisplatin linked through dipyridyl mono-sulphide or mono-selenide

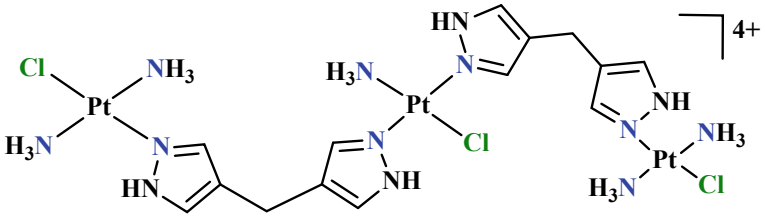

Scheme 14.87 Tri-nuclear platinum—Pt centres linked with 4,4′-dipyrazolylmethane

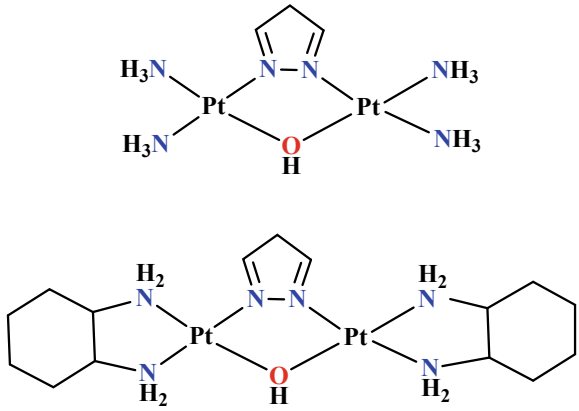

Scheme 14.88 Platinum(II) multinuclear compounds linked by pyrazole

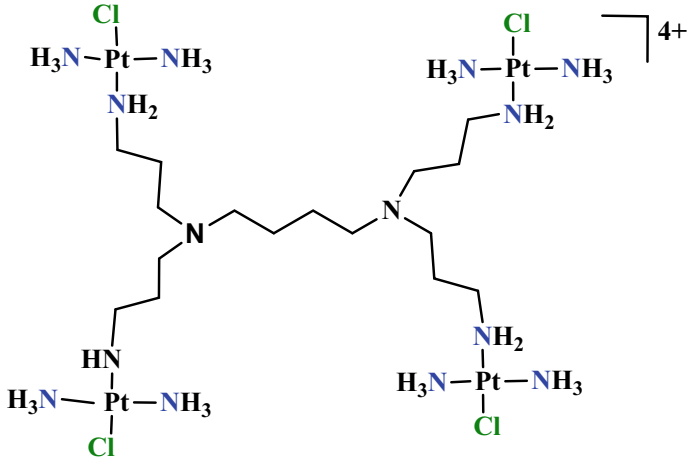

Scheme 14.89 Tetranuclear Pt complex—Pt centres linked through branched aminoalkane

their different modes of Pt–DNA interaction and subsequent binding. But the high toxicity to the normal cell is a limiting its clinical application. Hence, it gives a lot of scope to design and develop these complexes conjugated with biologically compatible groups or better the biomolecules.

14.5.18 Photoactivable Platinum(II)- and Platinum(IV) Based Anticancer Compounds

(a) **Photoactivable platinum(II) compounds**

This class of platinum(II) as well as Pt(IV) based anticancer compounds is also known as class of photochemotherapeutic agents. This class was also explored to overcome the side effects and limitations of conventional platinum(II) based FDA approved anticancer drugs. Hence, the photo-activatable Pt-based antitumour agents are designed in order to increase a selectivity for cancer cells while sparing the undamaged tissues which eventually leads to lowering the toxicity. Such compounds work on principle of photoactivation to form cytotoxic platinum(II) species. In such strategies, it is should to be noted that the photo-therapeutic window is in 620–850 nm range which is relatively narrow, hence any new photo-activatable drug is needed to be excited within this range only. Hence, they must be designed in order to facilitate them to enforce a direct interaction of a metallic centre and DNA after the irradiation in the photo-therapeutic window. In case of Pt(II) based compounds, the leaving groups should be cleaved upon photo-irradiation forming the Pt^{2+} suitable for binding with DNA. While in case of Pt(IV) the photo-irradiation should lead to photo-reduction of axial ligand species liberating the cytotoxic Pt(II) based compounds which are able to interact with DNA to perform their anticancer function. Hence, the both Pt(II) and Pt(IV) complexes were designed. It is revealed from the reports that such compounds have a potential to be applied for treating the localized tumours which are accessible for laser-based fibre-optic devices.

In case of platinum(II) based compounds, the modifications of amines were performed with the variously substituted bulky aryl or heterocyclic moieties (*e.g.* biphenyl, dipyridyl, anthracene) which are susceptible for photoactivation. These compounds are nothing but the photoactivable cisplatin derivatives. Some representative compounds were developed by Jacquemin et al. and they were theoretically studied by molecular dynamics simulations and density functional theory for their time-dependent binding with DNA forming Pt–DNA adduct as well as for the computational studies for their optical properties [184]. Some representative compounds are shown in Scheme 14.90.

Furthermore, the Pt(II)-terpyridine-based monocationic complexes having the photoreleasable azide group [Pt(terpyridine)(N_3)]CF_3SO_3 or [Pt(N^C^N)(N_3)] were synthesized (Scheme 14.91).

They were evaluated for anticancer activities. They exhibited potential as dual photoactivable (photochemotherapeutic) as well as photodynamic therapeutic agents.

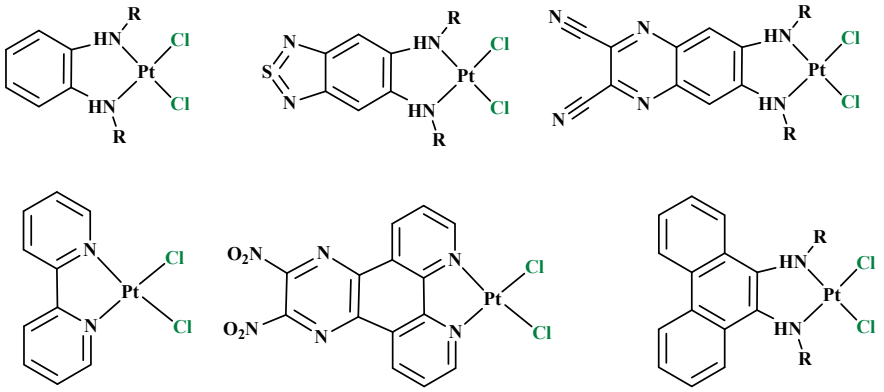

Scheme 14.90 Photoactivable Pt(II) compounds

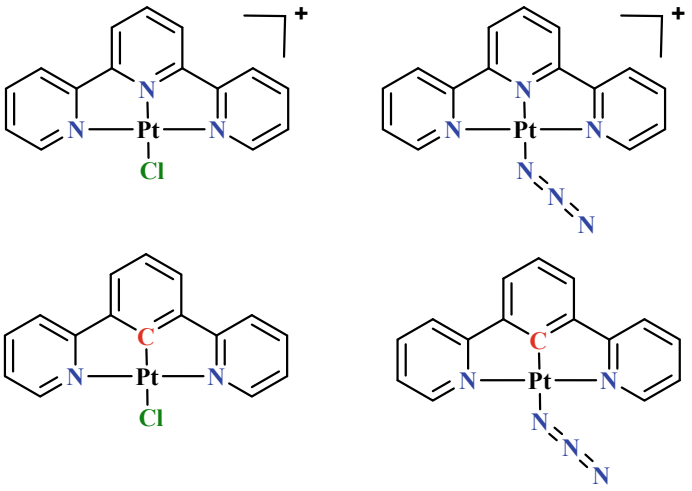

Scheme 14.91 Synthesis of photoactivable compounds

These complexes exhibited intercalation with DNA similarly to their chlorido analogues. Additionally, they generated the singlet oxygen species upon irradiation with a blue light having 420 nm wavelength. The singlet oxygen is known for its potency to kill the cancer cells. The photoactivation of azido-based Pt(II) complexes results in releasing of azide (N_3) ligands with formation of new platinum(II) species which eventually bind with DNA and ultimately exhibit cytoxicity. These crucial properties seem to be responsible for conferring a potential cytotoxicity for dual-action photoactive prodrugs (Fig. 14.6).

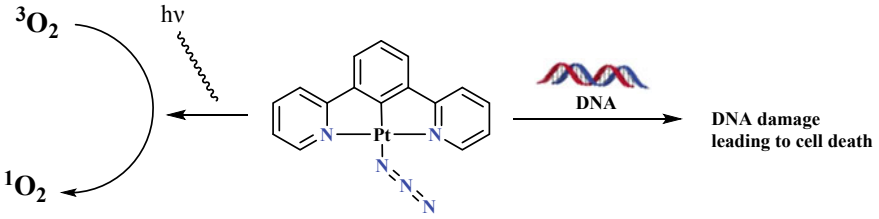

Fig. 14.6 Pt(II) photo-therapeutic and photodynamic therapy applications of Pt(II) compounds

In addition to these two representative examples, few more photoactivable platinum(II) complexes, were reported to possess anticancer activities. They are typically transplatin derivatives. The representative compounds are as depicted in Scheme 14.92 [185].

Similarly, some reports of the photosensitive Pt(II) based compounds have described the excitation of triplet oxygen species enabling the compound for cancer cell killing and the process known as photodynamic therapy (PDT) [186].

(b) **Photoactivable platinum(IV) compounds**

The Pt(IV) prodrug photoactivable compounds usually formed by substituting the leaving chlorido groups of cisplatin or its derivatives by the photocleavable iodo (I) or azido groups (–N=N=N). Two types of photo-activatable platinum diam(m)ine complexes viz., diiodo-platinum(IV) and diazido-platinum(IV) are explored so far. These compounds after irradiation with photon, lead to photochemical reduction forming the cytotoxic Pt(II) species which bind with DNA, ultimately leading to cancer cell death.

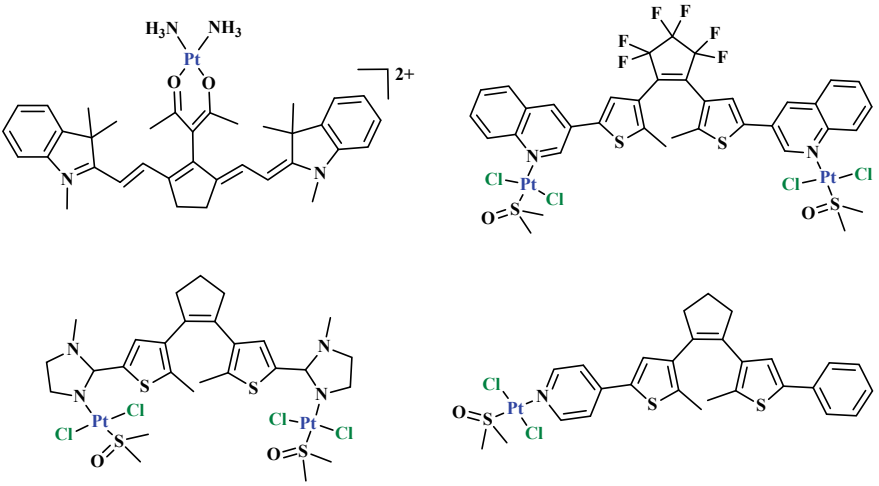

Scheme 14.92 Various photoactivable Pt(II) compounds

The first generation of Pt(IV) photoactivable prodrugs were cisplatin derivatives with iodo ligands as leaving groups while non-leaving groups were either ammine (NH_3) or ethylenediamine. The axial OH groups of primary prodrug were substituted with chloride, ester or sulphur-based ligands (Scheme 14.93).

A representative photo-reduction reaction of iodo-based platinum(IV) compounds forming cytotoxic products after irradiation (hυ) which binds with which bind with the 5′-GMP, a fragment on DNA. It clearly evidenced the photo-reduction of Pt(IV) species to form a hydroxyl-based product which bind with the 5′-GMP (Scheme 14.94) [187].

The first generation, platinum (IV)-I_2 complexes like cis, *trans*-[Pt(en) $I_2(OAc)_2$], react with visible light followed by their irreversible binding with DNA or forming the adducts with 5′-GMP (fragment on DNA) in the same mode as [Pt(en)Cl_2] binds with these species. Additionally, the products formed after photolysis are cytotoxic to human cancer cells in vitro. However, it is evident that such complexes are highly

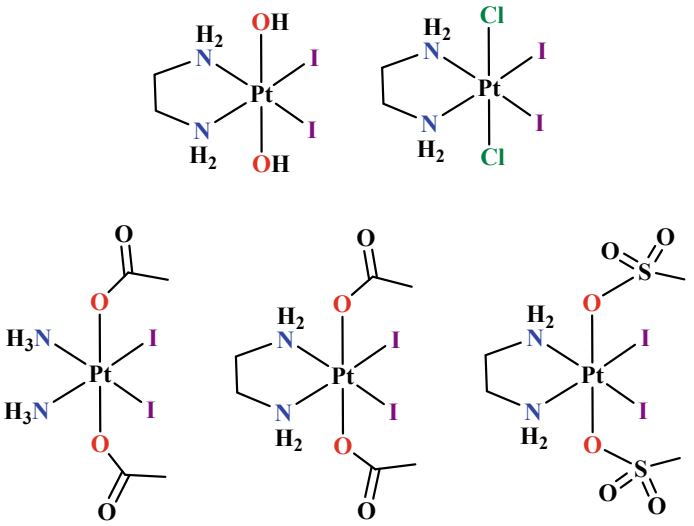

Scheme 14.93 Photoactivable compounds with iodide (I)—first generation compounds

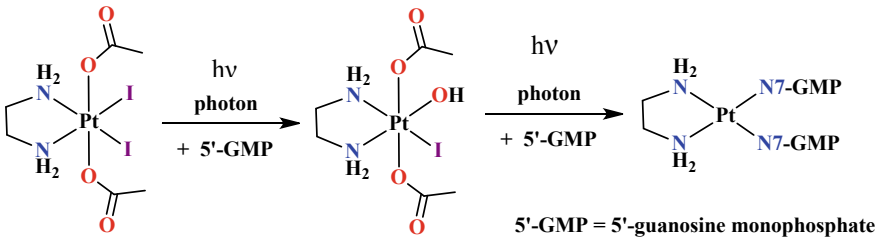

Scheme 14.94 Anticancer mechanism of photoactivable Pt(II) compounds

reactive towards the thiols in biosystem (e.g. glutathione), which quickly reduce them to the cytotoxic Pt(II) species. This makes them unsuitable to use as the drugs.

Further developments have lead to second generation Pt(IV) photoactivable prodrugs. These compounds were having the substituted amines like pyridyl, dipyridyl, anthracene, picolyl or thiazolyl moieties. The photocleavable groups were the azide. They were derivatives of cis- or transplatin (Scheme 14.95) [13a].

These compounds exhibited cytotoxicity. The typical mechanism of *in situ* reduction of Pt(IV) is discussed. The irradiation of azide-based Pt(IV) with photon lead to photo-reduction forming the real cytotoxic Pt(II) species (Scheme 14.96).

The Pt(IV)-diazido complexes belong to the second generation of such photoactivable complexes. They are represented as and *cis, trans*-$[Pt(en)(N_3)_2(OH)_2]$ and *cis, trans, cis*-$[Pt(N_3)_2(OH)_2(NH_3)_2]$. They also exhibit the photosensitivity, their irreversible binding with DNA and formation of similar types of products with DNA or 5′-guanosine monophosphate up on exposure to light similarly to the respective Pt(II) based complexes. But, they are stable and don't react with glutathione (GSH), consequently they exhibit very less cytotoxicity in the dark conditions. Their exposure to light of wavelength 366 nm leads to their activation to cytotoxic species which efficiently kill the cancer cells. Interestingly, the all the *-trans* analogue (e.g. transplatin), *trans, trans, trans*-$[Pt(N_3)_2(OH)_2(NH_3)_2]$ does not exhibit toxicity to HaCaT keratinocytes cells in dark conditions while it exhibits cytotoxicity comparable to cisplatin up on exposure to light. The studies have revealed that the

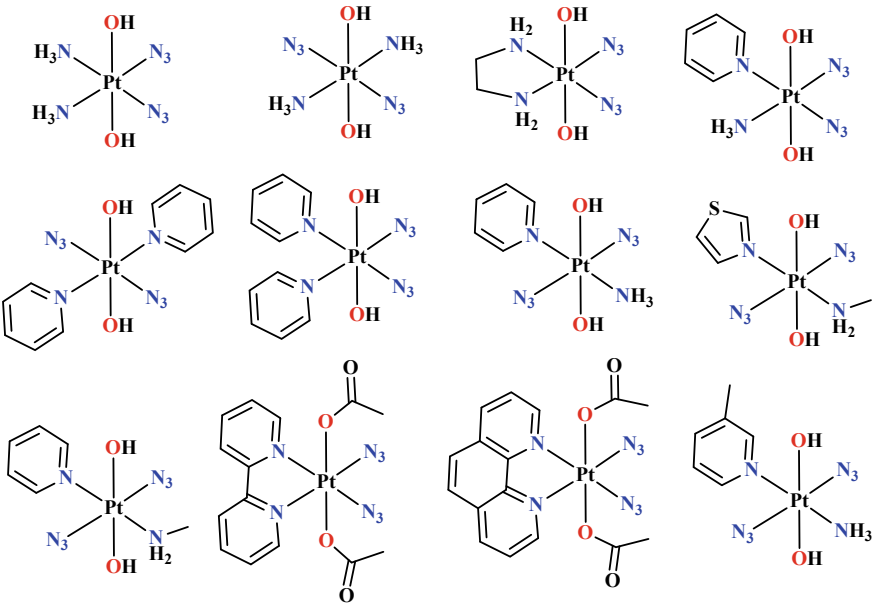

Scheme 14.95 Photoactivable compounds with azide (N_3) groups—second generation

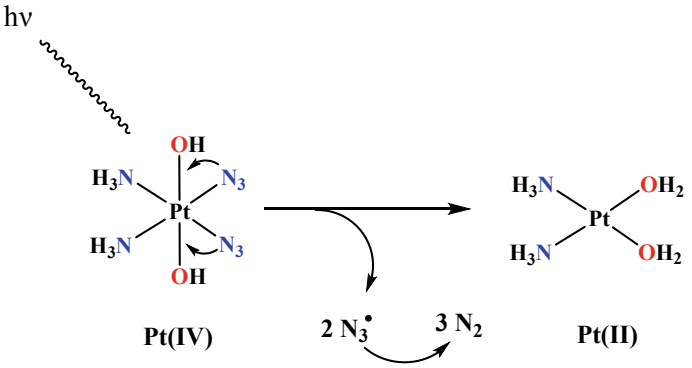

Scheme 14.96 Mechanism of photoactivable Pt(IV) prodrug to form Pt(II) species

photo-activatable and antitumour complexes of Pt(IV)-azido type signify a promising domain of research for new development of novel anticancer drugs.

Additionally, some complexes like Pt(IV)-diazido complex *trans*,*trans*,*trans*-$[Pt(N_3)_2(OH)_2(py)_2]$ were observed to interact with DNA when activated by UVA as well as by visible light. Activation by visible light is beneficial for further developments of modality.

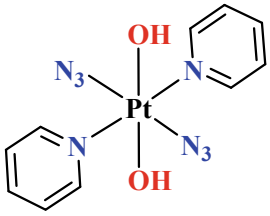

$[Pt(N_3)_2(OH)_2(py)_2]$

The complex $[Pt(N_3)_2(OH)_2(py)_2]$ is not reactive in dark conditions but it exhibited cytotoxicity when it was photoactivated by irradiating with UVA as well as with visible light. Now it is proved that after photoactivation Pt(IV)-diazido complex accumulates in the tumour cells, which facilitate its binding to DNA under the conditions in which it exhibits toxicity to the tumour cells. In such cases, the features of DNA adducts like conformational alterations induced by photoactivated *trans*,*trans*,*trans*-$[Pt(N_3)_2(OH)_2(py)_2]$ are particularly different as compared to those produced usually in DNA by cisplatin or transplatin. The findings help to elucidate the different cytotoxic effects of $[Pt(N_3)_2(OH)_2(py)_2]$ after photoactivation and a cisplatin. Hence, these facts thereby new visions in regard to mechanism associated with the anticancer effects of photoactivable platinum complexes.

Along with the Pt(IV)-iodo and -azido complexes, the new class of photoactive compounds is under investigations. These compounds on irradiation with photon

(365 nm) lead to homolytic Pt–O bond cleavage forming aryl carboxyl radicals via spin-trapping and exhibited that the photoreduced platinum species mirror cisplatin reactivity towards DNA (Scheme 14.97).

Some compounds belonging to this class are as follows (Scheme 14.98).

In addition to the applications of the porphyrin-based compounds to kill cancer cells by using photodynamic therapy (PDT), their complexes with platinum(II) were observed to exhibit light-induced anticancer properties also. These tetra platinated, Pt(II)-porphyrin complexes exhibited minor cytotoxicity in the dark conditions, but after irradiation with light by visible light at 420 nm they exhibited potent cytotoxicity (IC_{50} values <19 nM) against HeLa cells. Hence, such complexes are acting for a dual purpose of PDT as well as cytotoxic agents. Hence such compounds having synergistic effects of two or more properties can lead for further developments in anticancer drugs (Scheme 14.99) [188].

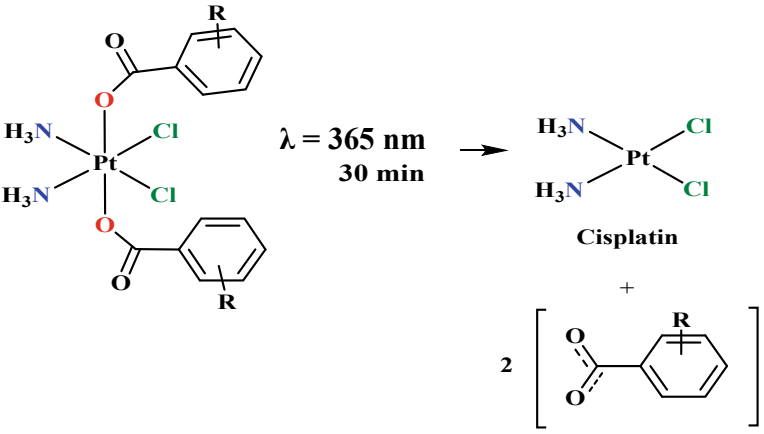

Scheme 14.97 A typical reaction of photolytic reduction P(IV) leading to formation of Pt(II)

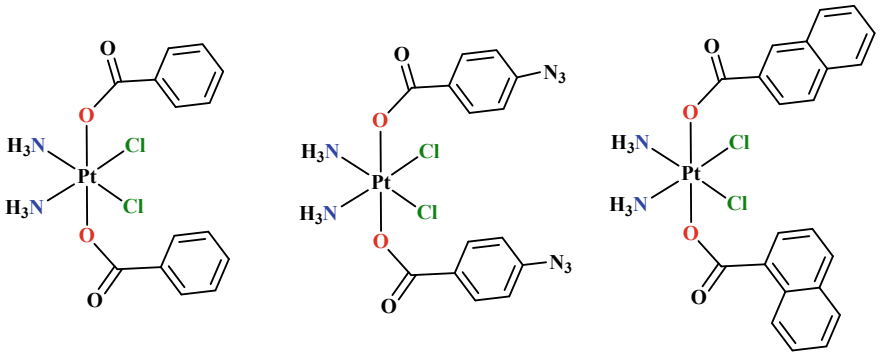

Scheme 14.98 Photoactivable Pt(IV) compounds with aryl moieties—as cisplatin derivatives

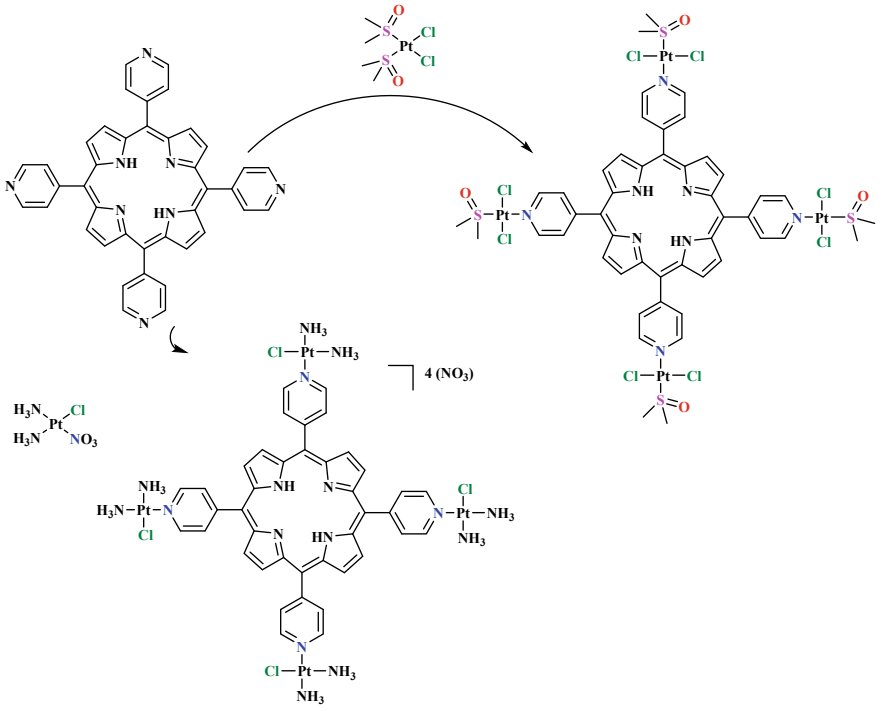

Scheme 14.99 Synthesis of tetra platinated porphyrin-based compounds exhibiting photoinduced cytotoxicity

This account clearly states the utility of photoactivable platinum(II) as well as platinum(IV) complexes for anticancer applications by (i) photo-cleavage of the iodo, azide or organic groups through reduction leading to platinum(II) species which bind with DNA and kill cancer cells (ii) the photosensitive bulky organic moieties (e,g., porphyrin, terpyridine) produce reactive oxygen species like singlet oxygen killing cancer cells—knows as photodynamic therapy. Even the complexes having combination of both aspects have been reported which act synergistically.

Hence, such complexes are useful for treatment of deep sited cancers in body. It gives opportunities for the researchers to develop such compounds which can be photoactivated by their irradiation with an appropriate wavelength of harmless visible light.

14.5.19 *Luminescent Platinum(II) Based Anticancer Compounds*

In developments of anticancer compounds, designing of novel complexes can be performed only after understanding of the mechanism of drug action, its interactions with biological system from entry point till interactions with molecules present in cancer cells. These aspects can be investigated by continuous monitoring of drug molecule after the treatment. Hence the drug molecules should be modified by applying the fundamental knowledge of chemistry. It can be achieved by (i) radiolablling of drug molecules and (ii) conjugating the drugs with luminescent moieties. The latter way of luminescent molecules is more convenient way. Additionally, instead of attaching a luminescent moiety to drug, it is more preferable to design a drug which itself exhibits excellent luminescence after irradiation with light. In this regard, it should be noted that the lanthanide-based organometallic compounds exhibit the luminescent properties due to electronic transitions in lanthanon metal ion itself; the structural features related to ligand system of them can be extended to platinum-based compounds also because the platinum ion has ability of appropriate binding with DNA due to its suitable ionic size. This can also be achieved by using knowledge of chemistry related to chromophoric organic moieties and transitions of electrons among the appropriate energy levels. Hence, one needs to choose the ligand systems which are usually the organic moieties which afford the luminescence properties to a drug molecule. Few complexes have reported for this cause. Let us discuss the representative examples of platinum-based luminescent molecules exhibiting potential anticancer properties.

The luminescent platinum(II) complexes exhibiting the anticancer properties: were developed by Che et al. [189] (Scheme 14.100). Under physiological conditions,

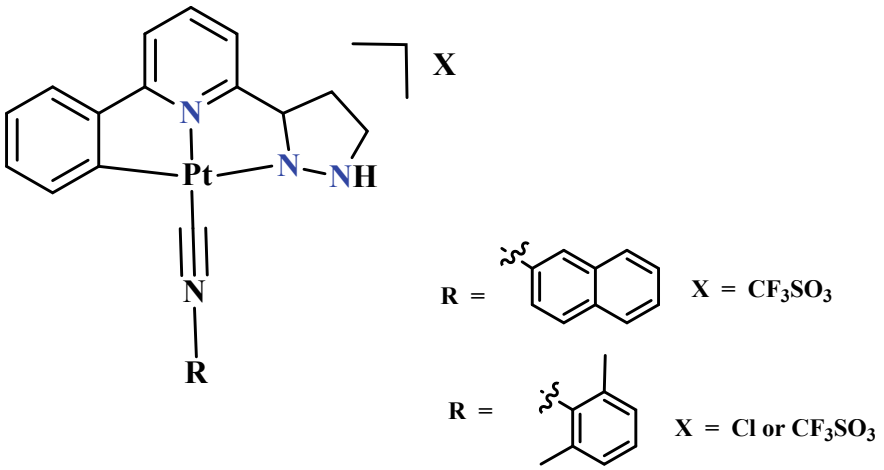

Scheme 14.100 Chemical structures of the platinum(II) complexes

these complexes exhibited colour emission and sustained release properties which rely on pH conditions. The cyclometalated Pt(II) luminescent complexes with various isocyanide groups as ligands were synthesized by treatment of [Pt(CˆNˆNpyr)Cl] with an excess of isocyanide ligand followed by stirring of a reaction mixture for 10–12 h at the room temperature.

Furthermore, Contel et al. designed and synthesizes the platinum(II) complex with a luminescent iminophosphorane ligand obtained from 8-aminoquinoline frame [Ph_3P = N–C_9H_6N]. The obtained platinum(II) coordination compound, after performing the C–H activation of a Ph group of PPh_3 fragment, was evolved to afford a stable cyclometalated *endo* [Pt{κ3–*C,N,N*–C_6H4(PPh_2 = N–8–C_9H_6N)}Cl] complex. Iminophosphorane as well as its Pt(II) complex exhibited luminescence in DMSO or DMSO and H_2O mixture(1: 1 v/v) solutions at room temperature. The compound exhibited antiproliferative properties against human ovarian (A2780S), in human lung (A549) cancer cells and in a non-tumorigenic human embryonic kidney cell line (HEK-293 T). The platinum compound exhibited more toxicity to the cancer cell line than to the non-tumorigenic cell line. Studies of the interactions of the compound with DNA revealed that, they exert their *in vitro* anticancer properties based on diverse mechanisms of action as compared to cisplatin (Scheme 14.101) [190].

Additionally, the same group (Che et al.) have developed the luminescent platinum(II) complexes coordinated with bidentate N-heterocyclic carbine ligands (Scheme 14.102). These compounds exhibited selective localization in the endoplasmic reticulum (ER) domain and induced the ER stress which eventually leads to

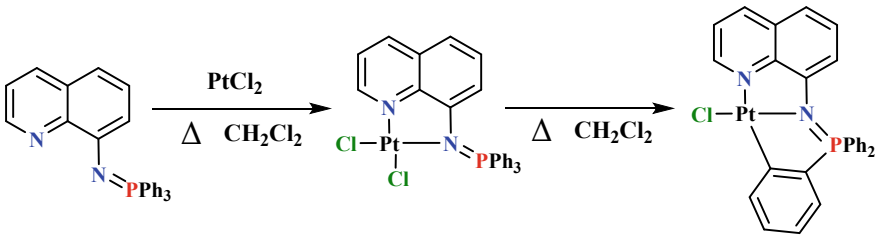

Scheme 14.101 Preparation of the Pt(II) luminescent complex

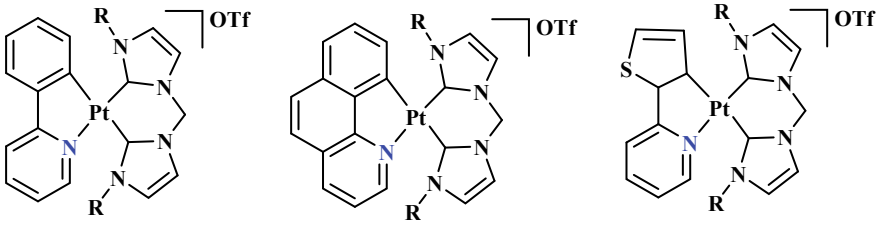

R = -$(CH_2)_nCH_3$ n = 0,3 or 5

Scheme 14.102 Pt(II) luminescent compounds

cell apoptosis. Some of them have exhibited the potent phototoxicity to cancer cell lines [191].

In view of the importance of understanding mechanistic aspects and develop novel platinum-based drugs with multiple functions, there is a lot of scope to design the water-soluble platinum-based luminescent molecules for anticancer applications.

14.5.20 Radio-Labelled Platinum(II)- and Platinum(IV) Based Compounds

The research for the novel platinum(II) or platinum(IV) complexes as anticancer agents is still progressing to overcome the limitations as well detrimental side effects of existing platinum-based drugs in clinical treatments. This process of drug development requires proper understanding of mechanism of their anticancer actions. To achieve this goal, the synergistic use of molecular imaging and targeted drug delivery strategies provide better opportunities new research areas like 'image-guided drug delivery' (IGDD), which holds tremendous potential towards clinical translation of novel cancer drugs [192] which help to track the mechanism, measure the delivery efficiency of drugs, bioavailability, therapeutic efficacy, etc. Although fluorescent probes can be conjugated with the drug, but limitations like non-photostability or auto fluorescence associated on using these fluorescence [193] hamper their application in human body.

But the most promising option for this purpose would be the synthesis of suitable radio-labelled analogues of platinum-based drugs under investigation. This could be achieved by incorporation of the radionuclide ^{195m}Pt during the synthesis of novel platinum-based drugs or existing drugs under study [194]. The radionuclide ^{195m}Pt decays to stable ^{195}Pt by isomeric transition (IT) (half-life ~ 4.02 days) and emits gamma photons of 66.8 keV (39%), 65.1 keV (22.5%), 75.7 keV (16.8%) and 98.9 keV (11.4%) energy [195] which would allow the visualization of the ^{195m}Pt(IV)-prodrug after it is administered into the patient. This can help to achieve multiple goals, real-time assessment of efficiency of targeting of the drug in the diseased site, its accumulation in healthy organ/tissue, modes of excretion and monitoring the progress of drug treatment.

In view of this the ^{195m}Pt labelled existing Pt(II) based drugs as well as novel Pt(IV) prodrugs under investigation have been synthesized and have been investigated for anticancer applications as well as for mechanistic investigations.

In such efforts, the ^{195m}Pt labelled cisplatin was synthesized. It exhibited cytotoxicity against Ehrlich's adenocarcinoma tumour cells. The cytotoxicity was exerted through apoptotic and necrotic pathways [196]. In other efforts, El-Sharkawi et al. have performed the gamma camera scintigraphy of tumours using ^{195m}Pt-labelled cisplatin [197].

Furthermore, the ^{195m}Pt labelled transplatin, *trans*-[$^{195m}PtCl_2(NH_3)_2$] was also synthesized. It exhibited chemotoxicity and radiotoxicity against Chinese hamster

V79 cell lines. The results revealed the efficacy of ^{195m}Pt in causing high-LET radiation type biological effects. The radiotoxicity associated with ^{195m}Pt localized in nucleus of cells, along with ability of platinum-based anticancer compounds to bind with DNA in the cell nucleus, anticipates that the synergistic combination of chemical and Auger electrons effects from the ^{195m}Pt labelled radioplatinum coordination complexes may have a great potential in the treatment of cancer [198].

Additionally, the ^{195m}Pt labelled carboplatin derivative was also synthesized with its chemical purity >99.3%, the radionuclidic purity of nearly 100% and the specific activity was 6.0 MBq, mg^{-1} [199].

Furthemore, to understand the mechanism of newly developed Pt(IV) prodrugs of cisplatin, the strategies of ^{195m}Pt labelled compounds were designed. A typical synthesis methodology was developed by Phadnis et al. (Scheme 14.103). [200]. Accordingly, a highly water-soluble ^{195m}Pt-labelled [$^{195m}PtCl_2(OCOCH_2CH_2COOH)_2(NH_3)_2$] compound which is a Pt(IV) prodrug of cisplatin, was conveniently synthesized. The radio thin layer chromatography as well as gamma ray spectrum of the product has confirmed the ^{195m}Pt labelling (Fig. 14.7).

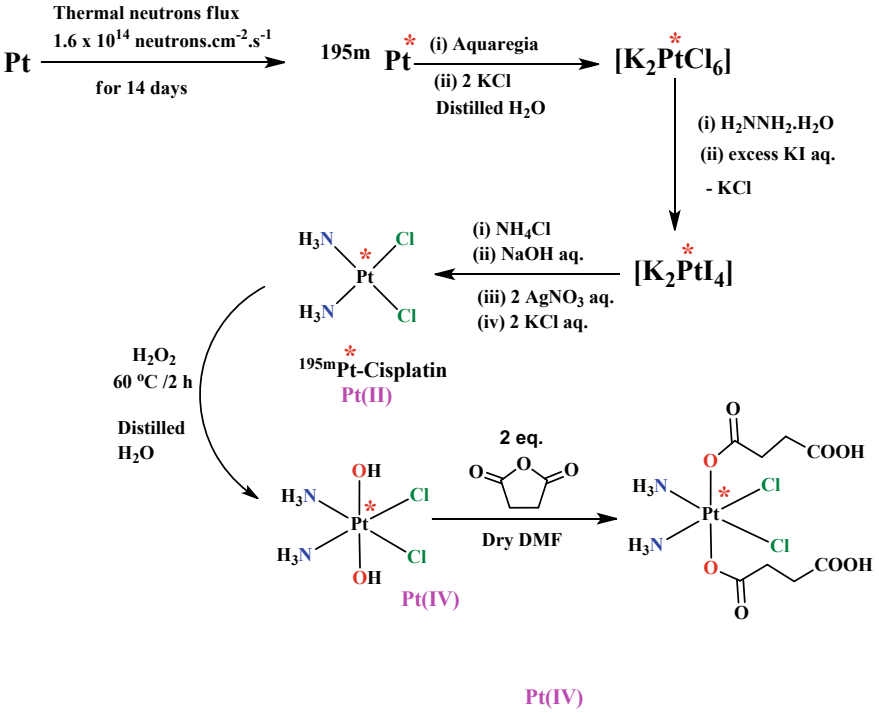

Scheme 14.103 Synthesis of ^{195m}Pt(IV) prodrug of cisplatin (*Pt indicates ^{195m}Pt)

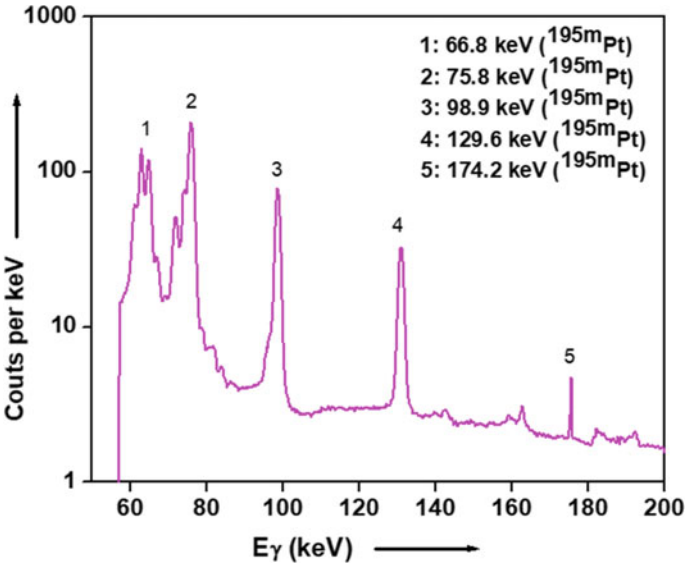

Fig. 14.7 A typical gamma ray spectrum of intrinsically ^{195m}Pt-labelled Pt(IV)-cisplatin prodrug

14.6 Design and Synthesis Strategies Platinum(IV) Prodrug Complexes

The octahedral Pt(IV) prodrug compounds have been proposed for anticancer applications to overcome the limitations of cisplatin. The rationale behind this design and strategies of developing the Pt(IV) prodrugs by conjugating axial groups with polar functional group containing organic frames, biomolecules, clinical drugs or fluorescent tags have been described already in Sect. 3.6. All the strategies are schematically presented in (Fig. 14.8). The Pt(IV) prodrugs after entering in cancerous cell, readily get reduced to corresponding Pt(II) species which are active drugs. After this stage the anticancer action of these compounds follow the same mechanism of clinically

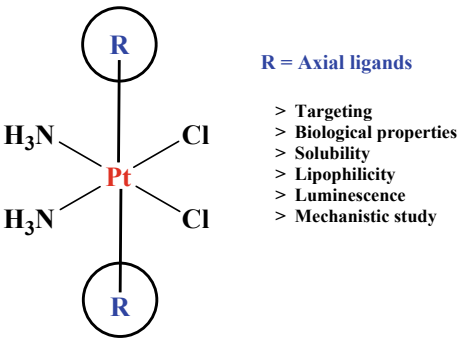

Fig. 14.8 Pt(IV) prodrug approach to overcome limitations of Pt(II) based drugs

approved Pt(II) based drugs like cisplatin. The reduction of axial groups is performed by chemical reductants in cancer cells as well as external photolysis process also help for this cause.

Synthesis Strategies

The platinum(IV) prodrugs are conveniently synthesized by oxidation of Pt(II) based drugs by treatment of H_2O_2 in aqueous solutions at hot conditions (~60 °C) and stirring for 5 h. The oxidized Pt(IV) having two axial hydroxide (OH) geoups gets formed. It's a key molecule. The substitution rections perfomed with OH group help to conjugate various bioactive, biocompatible species as discussed earlier. The typical synthesis strategoes are depicted in Scheme 14.104.

Furthermore, the two derivatives of Pt(IV) prodrugs containing Vit E (α-tocopherol; α-TOS) linked at axial positions are conveniently synthesized (Scheme 14.105) in a single step by treatment of $[Pt(NH_3)_2Cl_2(OH)_2]$ or $[PtCl_2(NH_3)_2(OH)(OEt)]$ with the acid anhydride derivative of α-tocopherol in DMF solutions and warmed at 50 °C for overnight (~10 h) [201].

Recently, the axial groups were linked with chlorambucil which is a chemotherapy drug used to treat chronic lymphocytic leukaemia, Hodgkin lymphoma, and non-Hodgkin lymphoma. As described in earlier processes, oxoplatin $[Pt(NH_3)_2Cl_2(OH)_2]$ was synthesized in aqueous solution. Further, it was treated

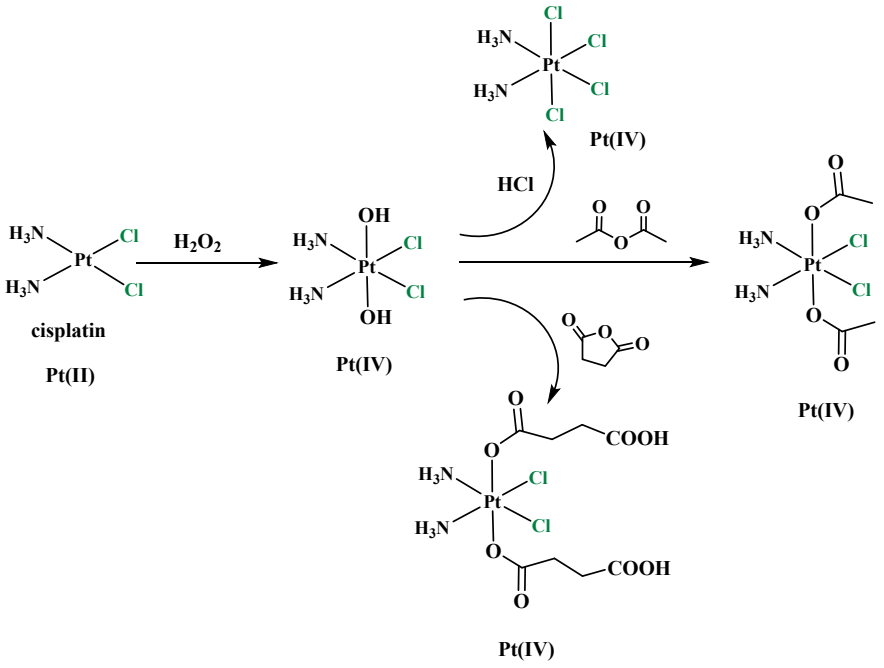

Scheme 14.104 Synthesis strategies of some Pt(IV) prodrugs of cisplatin

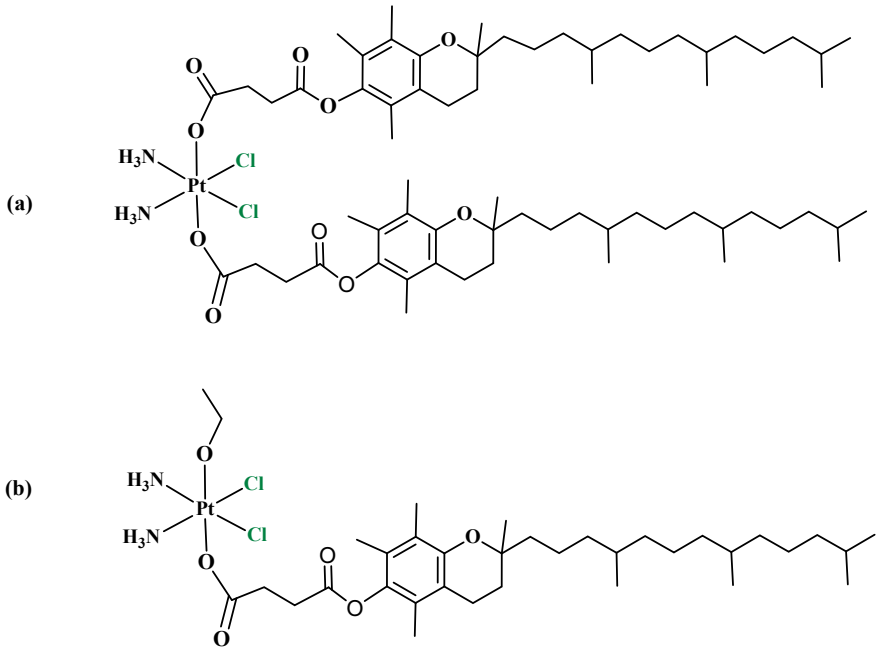

Scheme 14.105 Pt(IV) prodrugs with vit E—**a** Pt(IV)(Vit E)$_2$ and **b** Pt(IV)(Vit E)(OEt)

with an equimolar N-hydroxysuccinimide (NHS) protected chlorambucil in dimethyl sulfoxide (DMSO) solution at room temperature afforded a Pt(IV) prodrug of cisplatin linked with chlorambucil (Scheme 14.106) [202]. It is anticipated that such linking of anticancer drugs will enhance efficiency or treatment since both the drugs will acts in synergistic manner.

Additionally, the Pt(IV) prodrugs linked with fluorescent probes were also developed in order to be helpful for the mechanistic studies as well as understand efficiency of killing of cancer cells, means to ensure the complete killing of cancer cell. Even if few cancer cells remain they lead the further growth of cancer. Hence complete eradication of cancer cells is essential which can be judged precisely with the help of fluorescence probe. In this effort, Lippard et al. have developed the Pt(IV) prodrug of cisplatin conjugated with the fluorescein (Scheme 14.107).

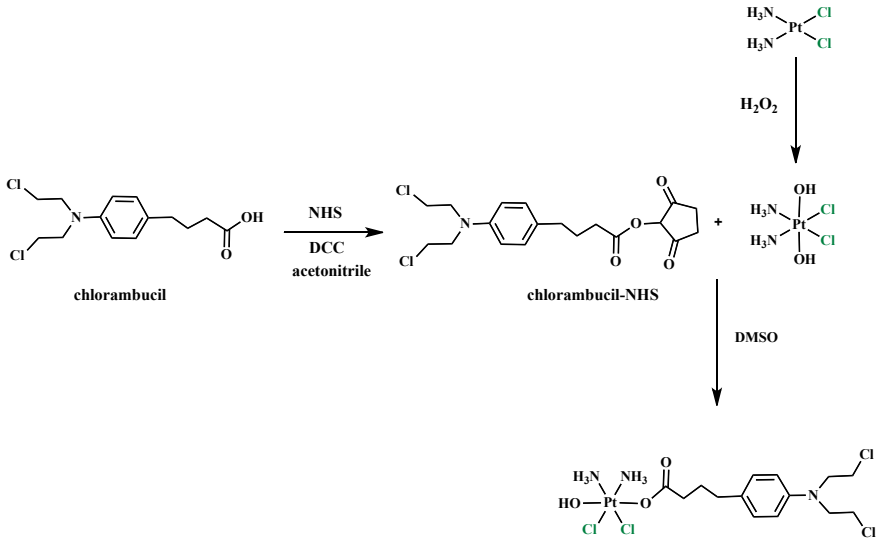

Scheme 14.106 Synthesis strategy for Pt(IV) prodrug of cisplatin coupled with chlorambucil

14.7 Conclusions

In this chapter, initially the anticancer mechanism of platinum(II) based clinical drugs proved crystal structural analyses has been explained. The new insights and results in the research related to the anticancer mechanism are also briefed. Later the account of development of the Pt(II) based drug has been given. It is followed by the new design strategies with objective of overcoming the side effects and drawbacks of clinically approved Pt(II) based drugs. Eventually, various Pt(II) complexes were designed and evaluated which led to various classed depending on their chemical composition (modifications in leaving or carrier groups of clinical drugs) and physical properties (luminescent, photoactivable, radioactive labelled compounds, etc.). Hence, the various classes of platinum(II) based anticancer compounds have been described with representative examples of the complexes evaluated for anticancer activities. Additionally, the prodrug concept which led to develop Pt(IV) compounds with various modifications was also briefly described. From this account, we hope that the present chapter may be helpful for the beginner researcher in the domain of design and developing synthesis strategies of novel platinum-based anticancer agents.

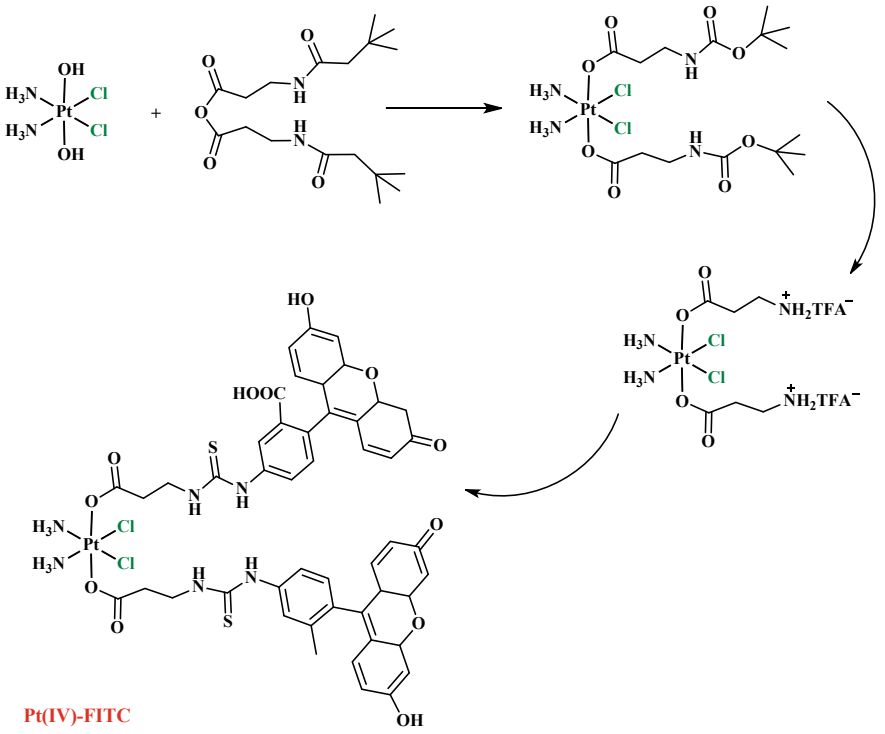

Scheme 14.107 Synthesis strategy for Pt(IV) prodrug conjugated with fluorescein isothiocyanate (FITC)

References

1. WHO report on cancer: setting priorities, investing wisely and providing care for all. Geneva: world Health Organization (2020) Licence: CC BY-NC-SA 3.0 IGO; ISBN 978-92-4-000129-9 (electronic version)
2. (a) Esfahani K, Roudaia L, Buhlaiga N, Rincon SVD, Papneja N, Miller WH, Jr (2020) A review of cancer immunotherapy: from the past, to the present, to the future. Curr Oncol (Suppl 2):S87; (b) Oiseth SJ, Aziz MS (2017) Cancer immunotherapy: a brief review of the history, possibilities, and challenges ahead. J Cancer Metastasis Treat 3:250; (c) dos Santos AF, de Almeida DRQ, Terra LF, Baptista MS, Labriola L (2019) Photodynamic therapy in cancer treatment - an update review. J Cancer Metastasis Treat 5:25; (d) Nedunchezhian K, Aswath N, Thiruppathy M, Thirugnanamurthy S (2016) Boron Neutron Capture Therapy - A Literature Review. J Clin Diagn Res 10(12):ZE01; (e) Miyatake S, Wanibuchi M, Hu N, Ono K (2020) Boron neutron capture therapy for malignant brain tumors. J Neurooncol 149:1; (f) Soares PIP, Ferreira IMM, Igreja RAGBN, Novo CMM, Borges JPMR (2012) Application of hyperthermia for cancer treatment: recent patents review. Recent Pat Anti-Cancer Drug Discovery 7(1):64
3. (a) Barry NPE, Sadler PJ (2014) 100 years of metal coordination chemistry: from Alfred Werner to anticancer metallodrugs. Pure Appl Chem 86(12):1897; (b) Alderden RA, Hall MD, Hambley TW (2006) The discovery and development of cisplatin. J Chem Educ 83(5):728; (c)

Komeda S, Casini A (2012) Next-generation anticancer metallodrugs. Curr Top Med Chem 12(3):219 (p 1–18); (d) Alessio E, Guo Z (2017) Metal anticancer complexes – activity, mechanism of action, future perspectives. Eur J Inorg Chem 2017(12):1539

4. Ghosh S (2019) Cisplatin: the first metal based anticancer drug. Bioorg Chem 88:102925
5. Rosenberg BH, Cavalieri LF (1965) Template deoxyribonucleic acid and the control of replication. Nature 206(988):999; (b) Rosenberg B, VanCamp L, Trosko JE, Mansour VH (1969) Platinum compounds: a new class of potent antitumour agents. Nature 222:385
6. Aldossary SA (2019) Review on pharmacology of cisplatin: clinical use, toxicity and mechanism of resistance of cisplatin. Biomed Pharmacol J 12(1):7
7. Sastry J, Kellie SJ (2005) Severe neurotoxicity, ototoxicity and nephrotoxicity following high-dose cisplatin and amifostine. Pediatr Hematol Oncol 22(5):441
8. (a) Amable L (2016) Cisplatin resistance and opportunities for precision medicine. Pharmacol Res 106:27; (b) Kasherman Y, Sturup S, Gibson D (2009) Is glutathione the major cellular target of cisplatin? A study of the interactions of cisplatin with cancer cell extracts. J Med Chem 52(14):4319
9. (a) Kelland L (2007) The resurgence of platinum-based cancer chemotherapy. Nat Rev Cancer 7:573; (b) Mcwhinney SR, Goldberg RM, Mcleod HL (2009) Platinum neurotoxicity pharmacogenetics. Mol Cancer Ther 8(1):10; (c) Wheate NJ, Walker S, Craig GE, Oun R (2010) The status of platinum anticancer drugs in the clinic and in clinical trials. Dalton Trans 39:8113
10. Rehm T, Rothemund M, Dietel T, Kempe R, Schobert R (2019) Synthesis, structures and cytotoxic effects in vitro of cis- and trans-$[Pt^{IV}Cl_4(NHC)_2]$ complexes and their Pt^{II} precursors. Dalton Trans 48:16358
11. Hall MD, Dolman RC, Hambley TW (2004) Platinum(IV) Anticancer complexes. Met Ions Biol Syst 41:297
12. Metzler-Nolte N, Guo Z (2016) Themed issue on Metallodrugs: activation, targeting, and delivery. Dalton Trans 45:12965
13. (a) Johnstone TC, Suntharalingam K, Lippard SJ (2016) The next generation of platinum drugs: targeted Pt(II) agents, nanoparticle delivery, and Pt(IV) prodrugs. Chem Rev 116(5):3436; (b) Wilson JJ, Lippard SJ (2013) Synthetic methods for the preparation of platinum anticancer complexes. Chem Rev 114(8):4470; (c) Kostova I (2006) Platinum complexes as anticancer agents. Recent Pat Anticancer Drug Discov 1(1):1(1–22)
14. (a) O'Halloran TV, Lippard SJ (1985) The chemistry of platinum in the +3 oxidation state. Isr J Chem 25(2):130; (b) Balch AL (1984) Odd oxidation states of palladium and platinum. Comments Inorg Chem 3(2–3):51
15. (a) Huheey JE, Keiter EA, Keiter RL (1997) Inorg Chem: Principles Struct React; (b) Cotton FA, Wilkinson G, Murillo CA, Bochmann M (1999) Advanced inorganic chemistry, 6th edn; ISBN: 978-0-471-19957-1
16. (a) Johnstone TC, Park GY, Lippard SJ (2014) Understanding and improving platinum anticancer drugs – phenanthriplatin. Anticancer Res 34(1):471; (b) Hall MD, Mellor HR, Callaghan R, Hambley TW (2007) Basis for design and development of platinum(IV) anticancer complexes. J Med Chem 50(15):3403
17. Lippard SJ (1991) Platinum DNA chemistry. In: Howell SB (ed) Platinum and other metal coordination compounds in cancer chemotherapy. Springer, Boston, MA
18. Jennerwein M, Andrews PA (1995) Effect of intracellular chloride on the cellular pharmacodynamics of cis-diamminedichloroplatinum (II). Drug Metab Dispos 23(2):178
19. (a) Wang D, Lippard S (2005) Cellular processing of platinum anticancer drugs. Nat Rev Drug Discov 4:307; (b) Davies MS, Berners-Price SJ, Hambley TW (1998) Rates of platination of AG and GA containing double-stranded oligonucleotides: insights into why cisplatin binds to GG and AG but not GA sequences in DNA. J Am Chem Soc 120(44):11380; (c) Boreham CJ, Broomhead JA, Fairlie DP (1981) A ^{195}Pt and ^{15}N N.M.R. study of the anticancer drug, *cis*-diammine-dichloroplatinum(II), and its hydrolysis and oligomerization products. Aust J Chem 34(3):659; (d) Legendre F, Bas V, Kozelka J, Chottard JC (2000) A complete kinetic study of GG versus AG platination suggests that the doubly aquated derivatives of cisplatin are the actual DNA binding species. Chem Eur J 6(11):2002; (e) Hambley

TW (2001) Platinum binding to DNA: structural controls and consequences. J Chem Soc Dalton Trans 2711; (f) Kozelka J, Legendre F, Reeder F, Chottard J-C (1999) Kinetic aspects of interactions between DNA and platinum complexes. Coord Chem Rev 190–192:61; (g) Davies MS, Berners-Price SJ, Hambley TW (2000) Slowing of cisplatin aquation in the presence of DNA but not in the presence of phosphate: improved understanding of sequence selectivity and the roles of monoaquated and diaquated species in the binding of cisplatin to DNA. Inorg Chem 39(25):5603; (h) Miller SE, House DA (1989) The hydrolysis products of cis-dichlorodiammineplatinum(II) 2. The kinetics of formation and anation of the cis-diamminedi(aqua)platinum(II) cation. Inorg Chim Acta 166(2):189; (i) Pizarro AM, Sadler PJ (2009) Unusual DNA binding modes for metal anticancer complexes. Biochimie 91(10):1198; (j) Berners-Price SJ, Appleton TG (2000) The chemistry of cisplatin in aqueous solution. In: Kelland LR, Farrell NP (eds) Platinum-based drugs in cancer therapy. Humana Press Inc.: Totowa pp 3–35

20. (a) Baik M-H, Friesner RA, Lippard SJ (2003) Theoretical study of cisplatin binding to purine bases: why does cisplatin prefer guanine over adenine? J Am Chem Soc 125(46):14082; (b) Mantri Y, Lippard SJ, Baik M-H (2007) Bifunctional binding of cisplatin to DNA: why does cisplatin form 1,2-Intrastrand cross-links with AG but not with GA? J Am Chem Soc 129(16):5023; (c) Raber J, Zhu C, Eriksson LA (2005) Theoretical study of cisplatin binding to DNA: the importance of initial complex stabilization. J Phys Chem B 109(21):11006
21. Sherman SE, Gibson D, Wang AH, Lippard SJ (1985) X-ray structure of the major adduct of the anticancer drug cisplatin with DNA: cis-[$Pt(NH_3)_2$(d(pGpG))]. Science 230(4724):412
22. Takahara PM, Rosenzweig AC, Frederick CA, Lippard SJ (1995) Crystal structure of double stranded DNA containing the major adduct of the anticancer drug cisplatin. Nature 377(6550):649
23. Takahara PM, Frederick CA, Lippard SJ (1996) Crystal structure of the anticancer drug cisplatin bound to duplex DNA. J Am Chem Soc 118(49):12309
24. Gelasco A, Lippard SJ (1998) NMR solution structure of a DNA dodecamer duplex containing a cis-Diammineplatinum(II) d(GpG) intrastrand cross-link, the major adduct of the anticancer drug cisplatin. Biochemistry 37(26):9230
25. Ohndorf UM, Rould MA, He Q, Pabo CO, Lippard SJ (1999) Basis for recognition of cisplatin-modified DNA by high-mobility-group proteins. Nature 399(6737):708
26. (a) Nakamoto K, Tsuboi M, Strahan GD (2008) Drug-DNA interactions: structures and spectra. Methods Biochem Anal 51:1; (b) Téletchéa S, Skauge T, Sletten E, Kozelka J (2009) Cisplatin adducts on a GGG sequence within a DNA duplex studied by NMR spectroscopy and molecular dynamics simulations. Chemistry 15(45):12320
27. Chiavarino B, Crestoni M-E, Fornarini S, Scuderi D, Salpin J-Y (2013) Interaction of cisplatin with adenine and guanine: a combined IRMPD, MS/MS, and theoretical study. J Am Chem Soc 135(4):1445
28. Fuertes MA, Alonso C, Perez JM (2003) Perez, Biochemical modulation of cisplatin mechanisms of action: enhancement of antitumor activity and circumvention of drug resistance. Chem Rev 103(3):645
29. Silverman AP, Bu W, Cohen SM, Lippard SJ (2002) 2.4-Å Crystal structure of the asymmetric platinum complex {Pt(ammine)(cyclohexylamine)}$^{2+}$ bound to a dodecamer DNA duplex. J Biol Chem 277(51):49743
30. Brabec V, Kasparkova J (2005) Modifications of DNA by platinum complexes: relation to resistance of tumors to platinum antitumor drugs. Drug Resist Updat 8(3):131
31. Hah SS, Stivers KM, de Vere White RW, Henderson PT (2006) Kinetics of carboplatin−DNA binding in genomic DNA and bladder cancer cells as determined by accelerator mass spectrometry. Chem Res Toxicol 19(5):622
32. de Sousa GF, Wlodarczyk SR, Monteiro G (2014) Carboplatin: molecular mechanisms of action associated with chemoresistance. Braz J Pharm Sci 50(4):693
33. Terheggen PMAB, Begg AC, Emondt JY, Dubbelman R, Floot BGJ, den Engelse L (1991) Formation of interaction products of carboplatin with DNA in vitro and in cancer patients. Br J Cancer 63:195

34. (a) Rothenberg ML (2000) Efficacy of oxaliplatin in the treatment of colorectal cancer. Oncology 14(12 Suppl 11):9; (b) Comella P, Casaretti R, Sandomenico C, Avallone A, Franco L (2009) Role of oxaliplatin in the treatment of colorectal cancer. Ther Clin Risk Manag 5:229
35. Chaney SG, Campbell SL, Bassett E, Wu Y (2005) Recognition and processing of cisplatin- and oxaliplatin-DNA adducts. Crit Rev Oncol Hematol 53(1):3
36. Wu Y, Pradhan P, Havener J, Boysen G, Swenberg JA, Campbell SL, Chaney SG (2004) NMR solution structure of an oxaliplatin 1,2-d(GG) intrastrand cross-link in a DNA dodecamer duplex. J Mol Biol 341(5):1251
37. Chaney SG, Campbell SL, Temple B, Bassett E, Wu Y, Faldu M (2004) Protein interactions with platinum–DNA adducts: from structure to function. J Inorg Biochem 98(10):1551
38. Messori L, Marzo T, Merlino A (2014) The X-ray structure of the complex formed in the reaction between oxaliplatin and lysozyme. Chem Commun 50:8360
39. (a) Caradonna JP, Lippard SJ, Gait MJ, Singh M (1982) The antitumor drug cis-$[Pt(NH_3)_2Cl_2]$ forms an intrastrand d(GpG) cross-link upon reaction with $[d(ApGpGpCpCpT)]_2$. J Am Chem Soc 104(21):5793; (b) Sarmah A, Roy RK (2013) Understanding the preferential binding interaction of aqua-cisplatins with nucleobase guanine over adenine: a density functional reactivity theory based approach. RSC Advance 3:2822
40. Zeng W, Zhang Y, Zheng W, Luo Q, Han J, Liu J, Zhao Y, Jia F, Wu K, Wang F (2019) Discovery of cisplatin binding to thymine and cytosine on a single-stranded oligodeoxynucleotide by high resolution FT-ICR mass spectrometry. Molecules 24(10)(1852):1–24
41. (a) Lippard SJ (1987) Chemistry and molecular biology of platinum anticancer drugs. Pure Appl Chem 59(6):731; (b) Barton JK, Lippard SJ (1980) In: Spiro TG (ed) Metal ions in biology, vol 1. Wiley: New York, p 31
42. Pinto AL, Lippard SJ (1985) Binding of the antitumor drug cis-diamminedichloroplatinum(II) (cisplatin) to DNA. Biochim Biophys Acta 780(3):167
43. Melnikov SV, Söll D, Steitz TA, Polikanov YS (2016) Insights into RNA binding by the anticancer drug cisplatin from the crystal structure of cisplatin-modified ribosome. Nucleic Acids Res 44(10):4978
44. Alberti E, Zampakou M, Donghi DJ (2016) Covalent and non-covalent binding of metal complexes to RNA. Inorg Biochem 163:278
45. Chapman EG, Hostetter AA, Osborn MF, Miller AL, DeRose VJ (2011) Binding of kinetically inert metal ions to RNA: the case of platinum(II). Met Ions Life Sci 9:347
46. Zampakou M (2016) Interaction of platinum(II) anticancer drugs with RNA. University of Zurich, Faculty of Science, dissertation. https://doi.org/10.5167/uzh-134915
47. Pil P, Lippard SJ (1997). In: Bertino JR (ed) Encyclopedia of cancer, vol 1. Academic Press, San Diego, CA, pp 392–410
48. Reedijk J (1999) why does cisplatin reach guanine-N7 with competing S-donor ligands available in the cell? Chem Rev 99(9):2499
49. Wang X, Guo Z (2007) The role of sulfur in platinum anticancer chemotherapy. Anti-Cancer Agents Med Chem 7(1):19
50. Sooriyaarachchi M, George GN, Pickering IJ, Narendrane A, Gailer J (2016) Tuning the metabolism of the anticancer drug cisplatin with chemoprotective agents to improve its safety and efficacy. Metallomics 8(11):1170
51. Riley CM, Sternson LA, Repta AJ, Slyter SA (1983) Monitoring the reactions of cisplatin with nucleotides and methionine by reversed-phase high-performance liquid chromatography using cationic and anionic pairing ions. Anal Biochem 130(1):203
52. Barnham KJ, Djuram MI, del Murdoch PS, Ranford JD, Sadler PJ (1996) Ring-opened adducts of the anticancer drug carboplatin with sulfur amino acids. Inorg Chem 35(4):1065
53. (a) Reedjik J (1999) Why does cisplatin reach guanine-N7 with competing S-donor ligands available in the cell? Chem Rev 99(9):2499; (b) Barnham KJ, Djuran MI, Del P, Mudroch S, Sadler PJ (1994) Intermolecular displacement of S-bound L-methionine on platinum(II) by guanosine 5′-monophosphate: implications for the mechanism of action of anticancer drugs. J Chem Soc Chem Commun 721; (c) Van Boom SSGE, Reedjik J (1993) Unprecedented migration of $[Pt(dien)]^{2+}$(dien = 1,5-diamino-3-azapentane) from sulfur to guanosine-N^7 in S-guanosyl-L-homocysteine (sgh). J Chem Soc Chem Commun 1397

54. (a) Hall MD, Hambley TW (2002) Platinum(IV) antitumour compounds: their bioinorganic chemistry. Coord Chem Rev 232(1–2):49; (b) Kenny RG, Chuah SW, Crawford A, Marmion CJ (2017) Platinum(IV) prodrugs – a step closer to Ehrlich's vision. Eur J Inorg Chem 2017(12):1596; (c) Gibson D (2016) Platinum(IV) anticancer prodrugs - hypotheses and facts. Dalton Trans 45:12983; (d) Chin CF, Wong DYQ, Jothibasu R, Ang WH (2011) Anticancer platinum (IV) prodrugs with novel modes of activity. Curr Top Med Chem 11(21):2602; (e) Venkatesh V, Sadler PJ, Pt(IV) prodrugs, in metallo-drugs: development and action of anticancer agents. In: Sigel A, Sigel H, Freisinger E, Sigel RKO (eds) Metal ions in life sciences, 18 series; pp 69–108; (f) Nemirovski A, Kasherman Y, Tzaraf Y, Gibson D (2007) Reduction of cis, trans, cis-[$PtCl_2(OCOCH_3)_2(NH_3)_2$] by aqueous extracts of cancer Cells. J Med Chem 50(23):5554
55. Pathak RK, Wen R, Kolishetti N, Dhar S (2017) A prodrug of two approved drugs, cisplatin and chlorambucil, for chemo war against cancer. Mol Cancer Ther 14(4):625
56. Zhao Y, Woods JA, Farrer NJ, Robinson KS, Pracharova J, Kasparkova J, Novakova O, Li H, Salassa L, Pizarro AM, Clarkson GJ, Song L, Brabec V, Sadler PJ (2013) Diazido mixed-amine platinum(IV) anticancer complexes activatable by visible-light form novel dna adducts. Chemistry 19(29):9578
57. Tian H, Dong J, Chi X, Xu L, Shi H, Shi T (2017) Reduction of cisplatin and carboplatin Pt(IV) prodrugs by homocysteine: kinetic and mechanistic investigations. Int J Chem Kinet 49(9):681
58. Percástegui EG, Ronson TK, Nitschke JR (2020) Design and applications of water-soluble coordination cages. Chem Rev 120(24):13480
59. Suntharalingam K, Song Y, Lippard SJ (2014) Conjugation of vitamin E analog α-TOS to Pt(IV) complexes for dual-targeting anticancer therapy. Chem Commun 50(19):2465
60. Li X, Liu Y, Tian H (2018) Current developments in Pt(IV) prodrugs conjugated with bioactive ligands. Bioinorg Chem Appl 2018:1–18. Article ID 8276139
61. (a) Ravera M, Gabano E, Zanellato I, Bonarrigo I, Alessio M, Arnesano F, Galliani A, Natile G, Osella D (2015) Cellular trafficking, accumulation and DNA platination of a series of cisplatin-based dicarboxylato Pt(IV) prodrugs. J Inorg Biochem 150:1; (b) Song Y, Suntharalingam K, Yeung JS, Royzen M, Lippard SJ (2013) Synthesis and characterization of Pt(IV) fluorescein conjugates to investigate Pt(IV) intracellular transformations. Bioconjug Chem 24(10):1733
62. (a) Gabano E, Ravera M, Osella D (2014) Pros and cons of bifunctional platinum(IV) antitumor prodrugs: two are (not always) better than one. Dalton Trans 43:9813; (b) Gibson D (2016) Platinum(IV) anticancer prodrugs - hypotheses and facts. Dalton Trans 45:12983
63. (a) Novohradsky V, Zanellato I, Marzano C, Pracharova J, Kasparkova J, Gibson D, Gandin V, Osella D, Brabec V (2017) Epigenetic and antitumor effects of platinum(IV)-octanoato conjugates. Sci Rep 7(1):) 3751(1–14); (b) Alessio M, Zanellato I, Bonarrigo I, Gabano E, Ravera M, Osella D (2013) Antiproliferative activity of Pt(IV)-bis(carboxylato) conjugates on malignant pleural mesothelioma cells. J Inorg Biochem 129:52; (c) Ammar AA, Raveendran R, Gibson D, Nassar T, Benita S (2016) A lipophilic Pt(IV) oxaliplatin derivative enhances antitumor activity. J Med Chem 59(19):9035; (d) Zanellato I, Bonarrigo I, Colangelo D, Gabano E, Ravera M, Alessio M, Osella D (2014) Biological activity of a series of cisplatin-based aliphatic bis(carboxylato) Pt(IV) prodrugs: How long the organic chain should be? J Inorg Biochem 140:219
64. (a) Wexselblatt E, Yavin E, Gibson D (2013) Platinum(IV) prodrugs with haloacetato ligands in the axial positions can undergo hydrolysis under biologically relevant conditions. Angew Chem Int Ed 125(23):6175; (b) Choi S, Filotto C, Bisanzo M, Delaney S, Lagasee D, Whitworth JL, Jusko A, Li C, Wood NA, Willingham J, Schwenker A, Spaulding K (1998) Reduction and anticancer activity of platinum(IV) complexes. Inorg Chem 37(10):2500
65. Tolan D, Gandin V, Morrison L, El-Nahas A, Marzano C, Montagner D, Erxleben A (2016) Oxidative stress induced by Pt(IV) pro-drugs based on the cisplatin scaffold and indole carboxylic acids in axial position. Sci Rep 6(29367):1–13
66. (a) Nandi D, Karmakar P, Ray S, Chattopadhyay A, Sarkar (Sain) R, Ghosh AK (2018) Kinetics and mechanism for ligand substitution reactions of some square-planar platinum(II)

complexes: stability and reactivity correlations. Inorg Nano-Met-Chem 48(1):16; (b) Peloso A (1973) Kinetics of nickel, palladium and platinum complexes. Coord Chem Rev 10(1–2):123; (c) Basolo F, Pearson RG (1962) The trans effect in metal complexes. Prog Inorg Chem Vol II (Ed. F. A. Cotton) 4:381; (d) Cattalini L (1970) The intimate mechanism of replacements in d^8 square planar complexes, in inorganic reaction mechanisms, Part 1 (Ed. J. O. Edwards). Prog Inorg Chem 13:263

67. (a) Coluccia M, Natile G (2007) Trans-platinum complexes in cancer therapy. Anti-Cancer Agents Med Chem 7(1):111; (b) Aris SM, Farrell NP (2009) Towards antitumor Active trans-platinum compounds. Eur J Inorg Chem 2009(10):1293
68. (a) Chernyaev II, Ann Inst Platine USSR, 4(1926):261; (b) Basolo F, Pearson RG (eds) (1967) Mechanisms of inorganic reactions: a study of metal complexes in solution. Wiley, Inc.: New York, pp 351–453
69. Nicholls D (1974) Complexes and first-row transition elements. The Macmillan Press Ltd., London
70. Dhara SC (1970) A rapid method for the synthesis of cis-$[Pt(NH_3)_2Cl_2]$. Indian J Chem 8:193
71. Kurnakow NJ (1894) Ueber complexe Metallbasen. Prakt Chem 50:481
72. (a) Arpalahti J, Lippert B (1987) An alternative HPLC method for analysing mixtures of isomeric platinum(II) diamine compounds. Inorg Chim Acta 138(3):171; (b) Woollins JD, Woollins A, Rosenberg B (1983) The detection of trace amounts of trans-$Pt(NH_3)_2Cl_2$ in the presence of cis-$Pt(NH_3)_2Cl_2$. A high performance liquid chromatographic application of kurnakow's test. Polyhedron 2(3):175
73. Ha TBT, Souchard J-P, Wimmer FL, Johnson NP (1990) Determination of cis-trans isomers of amine and pyridine platinum(II) complexes by J(Pt-H) coupling constants. Polyhedron 9(21):2647
74. Priqueler JRL, Butler IS, Rochon FD (2006) An overview of ^{195}Pt nuclear magnetic resonance spectroscopy. Appl Spectrosc Rev 41(3):185
75. (a) Connors TA, Cleare MJ, Harrap KR (1979) Structure-activity relationships of the anti-tumor platinum coordination complexes. Cancer Treat Rep 63:1499; (b) Cleare MJ, Hoeschele JD (1973) Studies on the antitumor activity of group VIII transition metal complexes. Part I. Platinum (II) complexes. Bioinorg Chem 2(3):187; (c) Cleare MJ, Hoeschele JD (1973) Antitumour platinum compounds, relationship between structure and activity. Platinum Met Rev 17(1):2
76. de Almeida MV, Chaves JDS, Fontes APS, CésarI ET, Gielen M (2006) Synthesis and characterization of platinum(II) complexes from trifluoromethyl phenylenediamine, picoline and N-benzyl ethylenediamine derivatives. J Braz Chem Soc 17(7):1266
77. Raynaud FI, Boxall FE, Goddard PM, Valenti M, Jones M, Murrer BA, Abrams M, Kelland LR (1997) cis-Amminedichloro(2-methylpyridine) platinum(II) (AMD473), a novel sterically hindered platinum complex: in vivo activity, toxicology, and pharmacokinetics in mice. Clin Cancer Res 3:2063; (b) Holford J, Raynaud F, Murrer BA, Grimaldi K, Hartley JA, Abrams M, Kelland LR (1998) Chemical, biochemical and pharmacological activity of the novel sterically hindered platinum co-ordination complex, cis-[amminedichloro(2-methylpyridine)] platinum(II) (AMD473). Anti-Cancer Drug Des 13(1):1; (c) Munk VP, Diakos CI, Ellis LT, Fenton RR, Messerle BA, Hambley TW (2003) Investigations into the interactions between DNA and conformationally constrained pyridylamineplatinum(II) analogues of AMD473. Inorg Chem 42(11):3582
78. Smith II JW, McIntyre KJ, Acevedo PV, Encarnacion CA, Tedesco KL, Wang Y, Asmar L, O'Shaughnessy JA (2009) Breast Can Res Treat 118(2):361; (b) Trynda-Lemiesz L, Śliwińska-Hill U (2011) Metal complexes in anticancer therapy. Present and future (Kompleksy metali w terapii nowotworowej. Teraźniejszość i przyszłość o). Nowotory J Oncol 61(5):465
79. Wilson JJ, Lippard SJ (2012) Acetate-bridged platinum(III) complexes derived from cisplatin. Inorg Chem 51:9852
80. (a) Drees M, Dengler WM, Hendriks HR, Kelland LR, Fiebig HH (1995) Cycloplatam: a novel platinum compound exhibiting a different spectrum of anti-tumour activity to cisplatin. Eur J

Cancer 31A(3):356; (b) Nersesyan A, Perrone E, Roggieri P, Bolognesi C (2003) Genotoxic action of cycloplatam, a new platinum antitumor drug, on mammalian cells in vivo and in vitro. Chemotherapy 49(3):132
81. Kemp S, Wheate NJ, Buck DP, Nikac M, Collins JG, Aldrich-Wright JR (2007) The effect of ancillary ligand chirality and phenanthroline functional group substitution on the cytotoxicity of platinum(II)-based metallointercalators. J Inorg Biochem 101(7):1049
82. (a) Farrell N, Ha TTB, Souchard J-P, Wimmer FL, Cros S, Johnson NP (1989) Cytostatic trans-platinum(II) complexes. J Med Chem 32:2240; (b) Farrell N, Kelland LR, Roberts JD, Van Beusichem M (1992) Activation of the trans geometry in platinum antitumor complexes: a survey of the cytotoxicity of trans complexes containing planar ligands in murine L1210 and human tumor panels and studies on their mechanism of action. Cancer Res 52(18):5065; (c) Van Beusichem M, Farrell N (1992) Activation of the trans geometry in platinum antitumor complexes. Synthesis, characterization, and biological activity of complexes with the planar ligands pyridine, N-methylimidazole, thiazole, and quinoline. Crystal and molecular structure of trans-dichlorobis(thiazole)platinum(II). Inorg Chem 31(4):634
83. Aris SM, Farrell NP (2009) Towards Antitumor Active trans-Platinum Compounds. Eur J Inorg Chem 2009(10):1293
84. Beusichem MV, Farrell N (1992) Activation of the trans geometry in platinum antitumor complexes. Synthesis, characterization, and biological activity of complexes with the planar ligands pyridine, N-methylimidazole, thiazole, and quinoline. Crystal and molecular structure of trans-dichlorobis(thiazole)platinum(II). Inorg Chem 31(4):634
85. Kauffman GB, Cowan DO, Slusarczuk G, Kirschner S (1963) cis- and trans-dichlorodiammineplatinum(II). Inorg Synth 7:239
86. Van Beusichem M, Farrell N (1992) Activation of the trans geometry in platinum antitumor complexes. Synthesis, characterization, and biological activity of complexes with the planar ligands pyridine, N-methylimidazole, thiazole, and quinoline. Crystal and molecular structure of trans-dichlorobis(thiazole)platinum(II). Inorg Chem 31(4):634
87. (a) Appleton TG, Bailey AJ, Barnham KJ, Hall JR (1992) Aspects of the solution chemistry of trans-diammineplatinum(II) complexes. Inorg Chem 31(14):3077; (b) Rochon FD, Buculei V (2005) Study of Pt(II)-cyclic amines complexes of the types cis- and trans-Pt(amine)$_2$I$_2$ and cis- and trans-Pt(amine)$_2$(NO$_3$)$_2$ and their aqueous products. Inorg Chim Acta 358(6):2040; (c) Johnstone TC, Lippard SJ (2013) Conformational isomerism of trans-[Pt(NH$_2$C$_6$H$_{11}$)$_2$I$_2$] and the classical Wernerian chemistry of [Pt(NH$_2$C$_6$H$_{11}$)$_4$]X$_2$ (X = Cl, Br, I). Polyhedron 52:565
88. van Kralingen CG, de Ridder JK, Reedijk J (1979) Coordination compounds of Pt(II) and Pd(II) with imidazole as a ligand. New synthetic procedures and characterization. Inorg Chim Acta 36:69
89. van Kralingen CG, de Ridder JK, Reedijk J (1980) Coordination compounds of platinum(II) and palladium(II) with pyrazole as a ligand. New synthetic procedures and characterisation. Transition Met Chem 5:73
90. Natile G, Coluccia M (1999) Trans-platinum compounds in cancer therapy: a largely unexplored strategy for identifying novel antitumor platinum drugs. In: Clarke MJ, Sadler PJ (eds) Metallopharmaceuticals I. Topics in biological inorganic chemistry, vol 1. Springer, Berlin, Heidelberg
91. Giardina-Papa D, Intini FP, Pacifico C, Natile G (2013) Isomerization of platinum-coordinated iminoethers induced by spectator ligands: stabilization of the Z anti configuration. Inorg. Chem 52(22):13058
92. Casas JM, Chisholm MH, Sicilia MV, Streib WE (1991) Imino-ether complexes of platinum: cis-[PtCl$_2$(NH=C(OR)Me)$_2$] and [PtCl$_4$(NH=C(OR)Me)$_2$], where R = Me, Et and Pri. Preparation, characterization and X-ray structure for [PtCl$_4$(NH=C(OPr^i)Me)$_2$]$_2$. Polyhedron 10(13):1573

93. Dox AW (1928) Acetamidine hydrochloride, organic syntheses, Coll. vol 1, p 5 (1941); vol 8, p 1 (1928); (b) Dickman DA, Boes M, Meyers AI (1989) (S')-N,N-Dimethyl-N'-(1-tert-Butoxy-3-Methyl-2-Butyl Formamidine, [Methanimidamide, N'-[1-[(1,1-dimethylethoxy)methyl]-2-methylpropyl]-N,N-dimethyl-, (S)-]. Organic Syntheses, Coll. vol 8, p 204 (1993); vol 67, p 52 (1989)
94. Greenhill JV, Lue P (1993) 5 amidines and guanidines in medicinal chemistry. Prog Med Chem 30:203
95. (a) Arya S, Kumar N, Roy P, Sondhi SM (2013) Synthesis of amidine and bis amidine derivatives and their evaluation for anti-inflammatory and anticancer activity. Eur J Med Chem 59:7; (b) Omar AM, Bajorath J, Ihmaid S, Mohamed HM, El-Agrody AM, Mora A, El-Arabya ME, Ahmed HEA (2020) Novel molecular discovery of promising amidine-based thiazole analogues as potent dual Matrix Metalloproteinase-2 and 9 inhibitors: anticancer activity data with prominent cell cycle arrest and DNA fragmentation analysis effects. Bioorg Chem 101(103992):1–14; (c) Sondhi SM, Rani R, Gupta PP, Agrawal SK, Saxena AK (2009) Synthesis, anticancer, and anti-inflammatory activity evaluation of methanesulfonamide and amidine derivatives of 3,4-diaryl-2-imino-4-thiazolines. Mol Divers 13:357
96. (a) Marzano C, Sbovata SM, Bettio F, Michelin RA, Seraglia R, Kiss T, Venzo A, Bertani R (2007) Solution behaviour and biological activity of bisamidine complexes of platinum(II). J Biol Inorg Chem 12:477; (b) Intini FP, Pellicani RZ, Boccarelli A, Sasanelli R, Coluccia M, Natile G (2008) Synthesis, characterization, and in vitro antitumor activity of new amidine-platinum(II) complexes obtained by addition of ammonia to coordinated acetonitrile. Eur J Inorg Chem 29:4555; (c) Sbovata SM, Bettio F, Marzano C, Mozzon M, Bertani R, Benetollo F, Michelin RA (2008) Benzylamidine complexes of platinum(II) derived by nucleophilic addition of primary and secondary amines. X-ray crystal structure of trans-$[PtCl_2\{Z\text{-}N(H)=C(NHMe)CH_2Ph\}_2]$. Inorg Chim Acta 361(11):3109; (d) Marzano C, Sbovata SM, Gandin V, Michelin RA, Venzo A, Bertani R, Seraglia R (2009) Cytotoxicity of cis-platinum(II) cycloaliphatic amidine complexes: ring size and solvent effects on the biological activity. J Inorg Biochem 103(8):1113; (e) Marzano C, Sbovata SM, Gandin V, Colavito D, Del Giudice E, Michelin RA, Venzo A, Seraglia R, Benetollo F, Schiavon M, Bertani R (2010) A new class of antitumor trans-amine-amidine-Pt(II) cationic complexes: influence of chemical structure and solvent on in vitro and in vivo tumor cell proliferation. J Med Chem 53(16):6210; (f) Michelin RA, Sgarbossa P, Sbovata SM, Gandin V, Marzano C, Bertani R (2011) Chemistry and biological activity of platinum amidine complexes. Chem Med Chem 6(7):1172
97. Hambley TW (2001) Platinum binding to DNA: structural controls and consequences. J Chem Soc, Dalton Trans 2711
98. Park GY, Wilson JJ, Song Y, Lippard SJ (2012) Phenanthriplatin, a monofunctional DNA-binding platinum anticancer drug candidate with unusual potency and cellular activity profile. PNAS 109(30):11987
99. Ma Z, Choudhury JR, Wright MW, Day CS, Saluta G, Kucera GL, Bierbach U (2008) A non-cross-linking platinum−acridine agent with potent activity in non-small-cell lung cancer. J Med Chem 51(23):7574
100. Ding S, Bierbach U (2016) Linker design for the modular assembly of multifunctional and targeted platinum(II)-containing anticancer agents. Dalton Trans 45:13104
101. Bierbach U, Hambley TW, Farrell N (1998) Modification of platinum(II) antitumor complexes with sulfur ligands. 1. Synthesis, structure, and spectroscopic properties of cationic complexes of the types $[PtCl(diamine)(L)]NO_3$ and $[\{PtCl(diamine)\}_2(L\text{-}L)](NO_3)_2$ (L = Monofunctional Thiourea Derivative; L-L = Bifunctional Thiourea Derivative). Inorg Chem 37(4):708
102. Monroe JD, Hruska HL, Ruggles HK, Williams KM, Smith ME (2018) Anti-cancer characteristics and ototoxicity of platinum(II) amine complexes with only one leaving ligand. *PLoS ONE* 13(3):e0192505 (1–21)

103. Kloster M, Kostrhunova H, Zaludova R, Malina J, Kasparkova J, Brabec V, Farrell N (2004) Trifunctional dinuclear platinum complexes as DNA−protein cross-linking agents. Biochemistry 43(24):7776
104. Kidani Y, Inagaki K, Iigo M, Hoshi A, Kuretani K (1978) Antitumor activity of 1,2-diaminocyclohexaneplatinum complexes against Sarcoma-180 ascites form. J Med Chem 21(12):1315
105. Štarha P, Trávníček Z, Popa I, Dvořák Z (2014) Synthesis, characterization and in vitro antitumor activity of platinum(II) oxalato complexes involving 7-azaindole derivatives as coligands. Molecules 19(8):10832
106. Štarha P, Trávníček Z, Popa I (2010) Platinum(II) oxalato complexes with adenine-based carrier ligands showing significant in vitro antitumor activity. J Inorg Biochem 104(6):639
107. (a) Otway DJ, Rees Jr WS (2000) Group 2 element β-diketonate complexes: synthetic and structural investigations. Coord Chem Rev 210(1):279; (b) Burrows AD, Mahon MF, Renouf CL, Richardson C, Warren AJ, Warren JE (2012) Dipyridyl β-diketonate complexes and their use as metalloligands in the formation of mixed-metal coordination networks. Dalton Trans 41:4153; (c) Hori A, Mizutani M (2011) Synthesis and crystal structure differences between fully and partially fluorinated β-diketonate metal (Co^{2+}, Ni^{2+}, and Cu^{2+}) Complexes. Int J Inorg Chem 2011:1–8. Article ID 291567
108. Wang H, Zhang Z, Wang H, Guo L, Li L (2019) Metal β-diketonate complexes as highly efficient catalysts for chemical fixation of CO_2 into cyclic carbonates under mild conditions. Dalton Trans 48:15970
109. (a) Biju S, Ambili Raj DB, Reddy MLP, Kariuki BM (2006) Synthesis, crystal structure, and luminescent properties of novel Eu^{3+} heterocyclic β-diketonate complexes with bidentate nitrogen donors. Inorg Chem 45(26):10651; (b) Lima NBD, Silva AIS, Gerson Jr PC, Gonçalves SMC, Simas AM (2015) Faster synthesis of beta-diketonate ternary europium complexes: elapsed times & reaction yields. PLoS ONE 10(12):e0143998; (c) Andreiadis ES, Gauthier N, Imbert D, Demadrille R, Pécaut J, Mazzanti M (2013) Lanthanide complexes based on β-diketonates and a tetradentate chromophore highly luminescent as powders and in polymers. Inorg Chem 52(24):14382; (d) Hasegawa Y, Kitagawa Y, Nakanishi T (2018) Effective photosensitized, electrosensitized, and mechanosensitized luminescence of lanthanide complexes. NPG Asia Materials 10:52
110. Fu C-Y, Chen L, Wang X, Lin L-R (2019) Synthesis of bis-β-diketonate lanthanide complexes with an azobenzene bridge and studies of their reversible photo/thermal isomerization properties. ACS Omega 4(13):15530
111. (a) Hudson ZM, Sun C, Helander MG, Amarne H, Lu Z, Wang S (2010) Enhancing phosphorescence and electrophosphorescence efficiency of cyclometalated Pt(II) compounds with triarylboron. Adv Funct Mater 20(20):3426; (b) Hudson ZM, Helander MG, Lu Z, Wang S (2011) Highly efficient orange electrophosphorescence from a trifunctional organoboron-Pt(II) complex. Chem Commun 47:755
112. Mou X, Wu Y, Liu S, Shi M, Liu X, Wang C, Sun S, Zhao Q, Zhou X, Huang WJ (2011) Phosphorescent platinum(II) complexes containing different β-diketonate ligands: synthesis, tunable excited-state properties, and their application in bioimaging. J Mater Chem 21:13951
113. Vaidya SR, Shelke VA, Jadhav SM, Shankarwar SG, Chondhekar TK (2012) Synthesis and characterization of β-diketone ligands and their antimicrobial activity. Arch Appl Sci Res 4(4):1839
114. Antony S, Kuttan R, Kuttan G (1999) Immunomodulatory activity of curcumin. Immun Invest 28(5–6):291
115. Srimal RC, Dhawan B (1973) Pharmacology of diferuloyl methane (curcumin), a non-steroidal anti-inflammatory agent. J Pharm Pharmacol 25(6):447
116. Elizabeth K, Rao MNA (1990) Oxygen radical scavenging activity of curcumin. Int J Pharm 58(3):237
117. (a) Kuttan R, Bhanumathy P, Nirmala K, George MC (1985) Potential anticancer activity of turmeric (Curcuma longa). Cancer Lett 29(2):197; (b) Ruby AJ, Kuttan G, Babu KD, Rajasekharan KN, Kuttan R (1995) Anti-tumour and antioxidant activity of natural curcuminoids. Cancer Lett 94(20):74

118. Karvembu R, Jayabalakrishnan C, Natarajan K (2002) Thiobis(β-diketonato)-bridged binuclear ruthenium(III) complexes containing triphenylphosphine or triphenylarsine: synthetic, spectral, catalytic and antimicrobial studies. Trans Met Chem 27:574
119. De Pascali SA, Papadia P, Ciccarese A, Pacifico C, Fanizzi FP (2005) First examples of β-diketonate platinum(II) complexes with sulfoxide ligands. Eur J Inorg Chem 2005(4):788
120. Hudson ZM, Blight BA, Wang S (2012) Efficient and high yield one-pot synthesis of cyclometalated platinum(II) β-diketonates at ambient temperature. Org Lett 14(7):1700
121. Wilson JJ, Lippard SJ (2012) In vitro anticancer activity of cis-diammineplatinum(II) complexes with β-diketonate leaving group ligands. J Med Chem 55(11):5326
122. Raza MK, Mitra K, Shettar A, Basu U, Kondaiah P, Chakravarty AR (2016) Photoactive platinum(II) β-diketonates as dual action anticancer agents. Dalton Trans 45:13234
123. Kajal A, Bala S, Kamboj S, Sharma N, Sain V (2013) Schiff bases: a versatile pharmacophore. J Catal 2013:1–14 Article ID 893512
124. Miri R, Razzaghi-asl N, Mohammadi MK (2013) QM study and conformational analysis of an isatin Schiff base as a potential cytotoxic agent. J Mol Model 19(2):727
125. (a) Tadele KT, Tsega TW (2019) Schiff bases and their metal complexes as potential anticancer candidates: a review of recent works. Anti-Can Agents Med Chem 9(15):1786; (b) Abd El-Halim HF, Mohamed GG, Anwar MN (2018) Antimicrobial and anticancer activities of Schiff base ligand and its transition metal mixed ligand complexes with heterocyclic base. Appl Organomet Chem 32(1):e3899; (c) Ejidike IP, Ajibade PA (2016) Synthesis, characterization, anticancer, and antioxidant studies of Ru(III) complexes of monobasic tridentate Schiff bases. Bioinorg Chem Appl (8)(2016):1–11 Article ID 9672451; (d) Parveen S (2020) Recent advances in anticancer ruthenium Schiff base complexes. Appl Organomet Chem 34(8):e5687
126. Mbugua SN, Sibuyi NRS, Njenga LW, Odhiambo RA, Wandiga SO, Meyer M, Lalancette RA, Onani MO (2020) New palladium(II) and platinum(II) complexes based on pyrrole schiff bases: synthesis, characterization, x-ray structure, and anticancer activity. ACS Omega 5(25):14942
127. (a) Kelley SL, Basu A, Teicher BA, Hacker MP, Hamer DH, Lazo JS (1988) Overexpression of metallothionein confers resistance to anticancer drugs. Science 241(4874):1813; (b) Ishikawa T, Ali-Osman FJ (1993) Glutathione-associated cis-diamminedichloroplatinum(II) metabolism and ATP-dependent efflux from leukemia cells. Molecular characterization of glutathione-platinum complex and its biological significance. Biol Chem 268(27):20116; (c) Marchan V, Moreno V, Pedroso E, Grandas A (2001) Towards a better understanding of the cisplatin mode of action. Chem Eur J 7(4):808
128. Lau JK-C, Deubel DV (2005) J loss of ammine from platinum(II) complexes: implications for cisplatin inactivation, storage, and resistance. Chem Eur J 11(9):2849
129. Corinti D, Coletti C, Re N, Paciotti R, Maître P, Chiavarino B, Crestoni ME, Fornarini S (2019) Short-lived intermediates (encounter complexes) in cisplatin ligand exchange elucidated by infrared ion spectroscopy. Int J Mass Spectrom 435:7
130. (a) Halamikova A, Heringova P, Kasparkova J, Intini FP, Natile G, Nemirovski A, Gibson D, Brabec V (2008) Cytotoxicity, mutagenicity, cellular uptake, DNA and glutathione interactions of lipophilic trans-platinum complexes tethered to 1-adamantylamine. J Inorg Biochem 102(5–6):1077; (b) Hagrman D, Goodisman J, Dabrowiak JC, Souid AK (2003) Kinetic study on the reaction of cisplatin with metallothionein. Drug Metabol Disp 31(7):916; (c) Kasparkova J, Novakova O, Vrana O, Intini F, Natile G, Brabec V (2006) Molecular aspects of antitumor effects of a new platinum(IV) drug. Mol Pharmacol 70(5):1708
131. Wang X, Guo Z (2007) The role of sulfur in platinum anticancer chemotherapy. Anti-can. Agents. Med Chem 7(1):19
132. Williams KM, Rowan C, Mitchell J (2004) Effect of amine ligand bulk on the interaction of methionine with platinum(II) diamine complexes. Inorg Chem 43(3):1190
133. Becker K, Herold-Mende C, Park JJ, Lowe G, Schirmer RH (2001) Human thioredoxin reductase is efficiently inhibited by (2,2′:6′,2′ ′-terpyridine)platinum(iII complexes. Possible implications for a novel antitumor strategy. J Med Chem 44(17):2784; (b) Cummings SD (2009) Platinum complexes of terpyridine: interaction and reactivity with biomolecules. Coord Chem Rev 253(9–10):1495

134. Ahmadi R, Urig S, Hartmann M, Helmke BM, Koncarevic S, Allenberger B, Kienhoefer C, Neher M, Steiner H-H, Unterberg A, Herold-Mende C, Becker K (2006) Antiglioma activity of 2,2′:6′,2″-terpyridineplatinum(II) complexes in a rat model-effects on cellular redox metabolism. Free Radic Biol Med 40(5):763
135. Lo Y-C, Ko T-P, Su W-C, Su T-L, Wang AH-J (2009) Terpyridine–platinum(II) complexes are effective inhibitors of mammalian topoisomerases and human thioredoxin reductase 1. J Inorg Biochem 103(7):1082
136. Reedijk J (1999) Why does cisplatin reach guanine-N7 with competing s-donor ligands available in the cell? Chem Rev 99(9):2499; Bloemink M, Reedijk J (1996) In: Sigel A, Sigel H (eds) Metal ions in biological systems, vol 32. Marcel Dekker, New York, p 641
137. (a) Gladyshev VN, Factor VM, Housseau F, Hatfield DL (1998) Contrasting patterns of regulation of the antioxidant selenoproteins, thioredoxin reductase, and glutathione peroxidase, in cancer cells. Biochem Biophys Res Commun 251(2):488; (b) Lincoln DT, Emadi WMA, Tonisson KF, Clarke FM (2003) The thioredoxin-thioredoxin reductase system: overexpression in human cancer. Anticancer Res 23(3B):2425; (c) Kahlos K, Soini Y, Saily M, Koistinen P, Kakko S, Paakko P, Holmgren A, Kinnula VL (2001) Up-regulation of thioredoxin and thioredoxin reductase in human malignant pleural mesothelioma. Int J Cancer 95(3):198; (d) Sasada T, Ueda H, Nakamura S, Sato N, Kitaoka Y, Gon Y, Takabayashi A, Spyrou G, Holmgren A, Yodoi J (1999) Possible involvement of thioredoxin reductase as well as thioredoxin in cellular sensitivity to cis-diamminedichloroplatinum (II). Free Radic Biol Med 27(5–6):504
138. Gromer S, Urig S, Becker K (2004) The thioredoxin system-from science to clinic. Med Res Rev 24(1):40
139. Morgan GT, Burstall FH (1934) Researches on residual affinity and co-ordination. Part XXXV. 2:2′:2″-Tripyridylplatinum salts. J Chem Soc 1498
140. (a) Annibale G, Brandolisio M, Pitteri B (1995) New routes for the synthesis of chloro(diethylenetriamine) platinum(II) chloride and chloro(2,2′:6′,2″-terpyridine) platinum(II) chloride dehydrate. Polyhedron 14(3):451; (b) Cini R, Donati A, Giannettoni R (2001) Synthesis and structural characterization of chloro(2,2′;6′,2″-terpyridine)platinum(II) trichloro(dimethylsulfoxide)platinate(II). Density functional analysis of model molecules. Inorg Chim Acta 315(1):73; (c) Chakraborty S, Wadas TJ, Hester H, Flaschenreim C, Schmehl R, Eisenberg R (2005) Synthesis, structure, characterization, and photophysical studies of a new platinum terpyridyl-based triad with covalently linked donor and acceptor groups. Inorg Chem 44(18):6284; (d) Cummings SD (2009) Platinum complexes of terpyridine: synthesis, structure and reactivity. Coord Chem Rev 253(3–4):449
141. Casas J, Garcıa-Tasende M, Sordo J (2000) Main group metal complexes of semicarbazones and thiosemicarbazones. A structural review. Coord Chem Rev 209(1):197
142. (a) Mrozek-Wilczkiewicz A, Malarz K, Rejmund M, Polanski J, Musiol R (2019) Anticancer activity of the thiosemicarbazones that are based on di-2-pyridine ketone and quinoline moiety. Eur J Med Chem 171:180; (b) Arora S, Agarwal S, Singhal SB (2014) Anticancer activities of thiosemicarbades/thiosemicarbazones: a review. Int J Pharm Pharmaceutic Sci 6(9):34; (c) Heffeter P, Pape VFS, Enyedy ÉA, Keppler BK, Szakacs G, Kowol CR (2018) Anticancer thiosemicarbazones: chemical properties, interaction with iron metabolism, and resistance development. Antiox Redox Signal 30(8):1–63 https://doi.org/10.1089/ars.2017.7487
143. Malarz K, Mrozek-Wilczkiewicz A, Serda M, Rejmund M, Polanski J, Musiol R (2018) The role of oxidative stress in activity of anticancer thiosemicarbazones. Oncotarget 9(25):17689
144. (a) Shipman Jr C, Smith SH, Drach JC, Klayman DL (1981) Antiviral activity of 2-acetylpyridine thiosemicarbazones against herpes simplex virus. Antimicrob Agents Chemother 19(4):682; (b) Padmanabhan P, Khaleefathullah S, Kaveri K, Palani G, Ramanathan G, Thennarasu S, Sivagnanam UT (2017) Antiviral activity of thiosemicarbazones derived from α-amino acids against dengue virus. J Med Virol 89(3):546
145. Pahontu E, Julea F, Rosu T, Purcarea V, Chumakov Y, Petrenco P, Gulea A (2015) Antibacterial, antifungal and in vitro antileukaemia activity of metal complexes with thiosemicarbazones. J Cell Mol Med 19(4):865

146. Grayson ML, Crowe SM, McCarthy JS, Mills J, Mouton JW, Norrby SR, Paterson DL, Pfaller MA (2010) Kucers' the use of antibiotics sixth edition: a clinical review of antibacterial, antifungal and antiviral drugs. CRC Press. pp 1673. ISBN 978-1-4441-4752-0
147. Moorthy NSHN, Cerqueira NMFSA, Ramos MJ, Fernandes PA (2013) Aryl- and heteroaryl-thiosemicarbazone derivatives and their metal complexes: a pharmacological template. Recent Pat Anticancer Drug Discov 8(2):168
148. Ribeiro AG, de Almeida SMV, de Oliveira JF, de Lima Souza TRC, dos Santos KL, de Barros Albuquerque AP, de Britto Lira Nogueira MC, de Carvalho Jr LB, de Moura RO, da Silva AC, Pereira VRA, de Castro MCAB, De Lima MCA (2019) Novel 4-quinoline-thiosemicarbazone derivatives: Synthesis, antiproliferative activity, in vitro and *in silico* biomacromolecule interaction studies and topoisomerase inhibition. Eur J Med Chem 182(111592):1–16
149. Shyamsivappan S, Vivek R, Saravanan A, Arasakumar T, Suresh T, Athimoolam S, Mohan PS (2020) A novel 8-nitro quinoline-thiosemicarbazone analogues induces G1/S & G2/M phase cell cycle arrest and apoptosis through ROS mediated mitochondrial pathway. Bioorg Chem 97:103709
150. Acharya PT, Bhavsar ZA, Jethava DJ, Patel DB, Patel HD (2021) A review on development of bio-active thiosemicarbazide derivatives: recent advances. J Mol Struct 1226(Part A):129268
151. (a) Beraldo H, Gambinob D (2004) The wide pharmacological versatility of semicarbazones, thiosemicarba-zones and their metal complexes. Mini-Rev Med Chem 4(1):31; (b) Melha KSA (2008) In-vitro antibacterial, antifungal activity of some transition metal complexes of thiosemicarbazone Schiff base (HL) derived from N4-(7′-chloroquinolin-4′-ylamino) thiosemicarbazide. J Enz Inhib Med Chem 23(4):493
152. Prajapati NP, Patel HD (2019) Novel thiosemicarbazone derivatives and their metal complexes: recent development. Synth. Commun Rev 49(21):2767
153. Merlot AM, Kalinowski DS, Richardson DR (2013) Novel chelators for cancer treatment: where are we now? Antiox Redox Signal 18(8):973
154. Campbell MJM (1975) Transition metal complexes of thiosemicarbazide and thiosemicarbazones. Coord Chem Rev 15(2–3):279
155. Matesanz AI, Leitao I, Souza P (2013) Palladium(II) and platinum(II) bis(thiosemicarbazone) complexes of the 2,6-diacetylpyridine series with high cytotoxic activity in cisplatin resistant A2780cisR tumor cells and reduced toxicity. J Inorg Biochem 125:26
156. Lin X-D, Liu Y-H, Xie C-Z, Baoa W-G, Shen J, Xu J-Y (2017) Three Pt(II) complexes based on thiosemicarbazone: synthesis, HSA interaction, cytotoxicity, apoptosis and cell cycle arrest. RSC Adv 7:26478
157. Huang Y, Kong E, Gan C, Liu Z, Lin Q, Cui J (2015) Synthesis and antiproliferative activity of steroidal thiosemicarbazone platinum (Pt(II)) complexes. Bioinorg Chem Appl 2015(742592):1–7
158. (a) Kelloff GJ, Crowell JA, Hawk ET, Steele VE, Lubet RA, Boone CW, Covey JM, Doody LA, Omenn GS, Greenwald P, Hong WK, Parkinson BR, Baghery D, Baxter GT, Blunden M, Doeltz MK, Zisenhamer KM, Johnson K, Knapp GG, Longfellow DG, Malone WF, Nayfield SG, Seifried HZ, Swall LM, Sigman CC (1996) Strategy and planning for chemopreventive drug development: clinical development plans II. J Cell Biochem 63(S26)(Suppl.):54; (b) Mugesh G, du Mont WW, Sies H (2001) chemistry of biologically important synthetic organoselenium compounds. Chem Rev 101(7):2125; (c) Nogueira CW, Zevi G, Rocha JBT (2004) Organoselenium and organotellurium compounds: toxicology and pharmacology. Chem Rev 104(12):6255
159. Liu Q, Zhang J, Ke X, Mei Y, Zhu L, Guo Z (2001) ESMS and NMR investigations on the interaction of the anticancer drug cisplatin and chemopreventive agent selenomethionine. J Chem Soc, Dalton Trans 911
160. Robey S (2013) Reactions of platinum(II) compounds with selenium containing amino acids. Masters Theses & Specialist Projects. Paper 1252
161. Chopade SM, Phadnis PP, Wadawale A, Hodage AS, Jain VK (2012) Synthesis and characterization of (ethylenediamine)/(diammine)platinum(II) coordinated to seleno ligands containing carboxylic acid functionality. Inorg Chim, Acta 385:185.

162. Chopade SM, Phadnis PP, Hodage AS, Wadawale A, Jain VK (2015) Synthesis, characterization, structures and cytotoxicity of platinum(II) complexes containing dimethylpyrazole based selenium ligands. Inorg Chim, Acta 427:72
163. Zeng L, Li Y, Li T, Cao W, Yi Y, Geng W, Sun Z, Xu H (2014) Selenium–platinum coordination compounds as novel anticancer drugs: selectively killing cancer cells via a reactive oxygen species (ROS)-mediated apoptosis route. Chem Asian J 9(8):2295
164. Wu F, Cao W, Xu H, Zhu M, Wang J, Ke X (2017) Treatment with a selenium-platinum compound induced T-cell acute lymphoblastic leukemia/lymphoma cells apoptosis through the mitochondrial signaling pathway. Oncol Lett 13(3):1702
165. Li F, Li T, Han X, Zhuang H, Nie G, Xu H (2018) Nanomedicine assembled by coordinated selenium–platinum complexes can selectively induce cytotoxicity in cancer cells by targeting the glutathione antioxidant defense system. ACS Biomater Sci Eng 4(6):1954
166. Li T, Smet M, Dehaen W, Xu H, Appl ACS (2016) Selenium–platinum coordination dendrimers with controlled anti-cancer activity. Mater Interfaces 8(6):3609
167. Li T, Smet M, Dehaen W, Xu H (2015) Selenium–platinum coordination dendrimers with controlled anti-cancer activity. ACS Appl Mater Interfaces 8(6)(2016):3609
168. Appelhans D, Smet M, Khinmich G, Komber H, Voigt D, Lhotak P, Kuckling D, Voit B (2005) Lysine dendrimers based on thiacalix[4]arene core moieties as molecular scaffolds for supramolecular host systems. New J Chem 29:1386
169. (a) Phillips AD, Gonsalvi L, Romerosa A, Vizza F, Peruzzini M (2004) Coordination chemistry of 1,3,5-triaza-7-phosphaadamantane (PTA): transition metal complexes and related catalytic, medicinal and photoluminescent applications. Coord Chem Rev 248(11–12):955; (b) Murray BS, Babak MV, Hartinger CG, Dyson PJ (2016) The development of RAPTA compounds for the treatment of tumors. Coord Chem Rev 306(Part 1):86
170. Živković MD, Kljun J, Ilic-Tomic T, Pavic A, Veselinović A, Manojlović DD, Nikodinovic-Runic J, Turel I (2018) A new class of platinum(II) complexes with the phosphine ligand pta which show potent anticancer activity. Inorg Chem Front 5:39
171. Kim JH, Reeder E, Parkin S, Awuah SG (2019) Gold(I/III)-phosphine complexes as potent antiproliferative agents. Sci Rep 9(12335):1–18
172. (a) Fourie E, Erasmus E, Swarts JC, Jakob A, Lang H, Joone GK, Van Rensburg CEJ (2011) Cytotoxicity of ferrocenyl–ethynyl phosphine metal complexes of gold and platinum. Anticancer Res 31(3):825; (b) Cini R, Tamasi G, Defazio S, Corsini M, Zanello P, Messori L, Marcon G, Piccioli F, Orioli P (2003) Study of ruthenium(II) complexes with anticancer drugs as ligands. Design of metal-based phototherapeutic agents. Inorg Chem 42(24):8038; (c) Tisato F, Porchia M, Santini C, Gandin V, Marzano C (2019) Phosphine-copper(I) complexes as anticancer agents: design, synthesis, and physicochemical characterization. Part I, copper(I) chemistry of phosphines, functionalized phosphines and phosphorus heterocycles. pp 61–82; (d) Khan RA, Usman M, Dhivya R, Balaji P, Alsalme A, AlLohedan H, Arjmand F, AlFarhan K, Akbarsha MA, Marchetti F, Pettinari C, Tabassum S (2017) Heteroleptic copper(I) complexes of "scorpionate" bis-pyrazolyl carboxylate ligand with auxiliary phosphine as potential anticancer agents: an insight into cytotoxic mode. Sci Rep 7(45229):1–17; (e) Berners-Price SJ, Sadler PJ (1988) Phosphines and metal phosphine complexes: Relationship of chemistry to anticancer and other biological activity. In: Bioinorganic chemistry. Structure and bonding, vol 70. Springer, Berlin, Heidelberg
173. Yilmaz VT, Icsel C, Turgut OR, Aygun M, Erkisa M, Turkdemir MH, Ulukaya E (2018) Synthesis, structures and anticancer potentials of platinum(II) saccharinate complexes of tertiary phosphines with phenyl and cyclohexyl groups targeting mitochondria and DNA. Eur J Med Chem 155:609
174. Lippert B (1999) Cisplatin: Chemistry and biochemistry of a leading anticancer drug. Wiley-VCH, Weinheim
175. Wong E, Giandomenico CM (1999) Current status of platinum-based antitumor drugs. Chem Rev 99(9):2451
176. Farrell N (2000) Platinum-based drugs in cancer therapy. In: Kelland LR, Farrell NP (eds) Humana Press, Totowa, pp 321–338

177. (a) Wheate NJ, Collins JG (2003) Multi-nuclear platinum complexes as anti-cancer drugs. Coord Chem Rev 241(1–2):133; (b) Farrell NP (2015) Multi-platinum anti-cancer agents. Substitution-inert compounds for tumor selectivity and new targets. Chem Soc Rev 44:8773
178. (a) Farrell N, Qu Y (1989) Chemistry of bis(platinum) complexes. Formation of trans derivatives from tetraamine complexes. Inorg Chem 28(18):3416; (b) Farrell N, del Ameida SG, Skov KA (1988) Bis(platinum) complexes containing two platinum cis-diammine units. Synthesis and initial DNA-binding studies. J Am Chem Soc 110(15):5018
179. Farrell N, Qu Y, Feng L, Van Houten B (1990) A comparison of chemical reactivity, cytotoxicity, interstrand crosslinking and DNA sequence specificity of bis(platinum) complexes containing monodentate or bidentate coordination spheres with their monomeric analogs. Biochemistry 29(41):9522
180. (a) Broomhead JA, Rendina LM, Sterns M (1991) Dinuclear complexes of platinum with the 4,4'-dipyrazolylmethane ligand. Synthesis, characterization, and x-ray crystal structure of .gamma.-bis(4,4'-dipyrazolylmethane-N,N')bis[dichloroplatinum(II)]-N,N-dimethylformamide (1/2) and related complexes. Inorg Chem 31(10):1880; (b) Broomhead JA, Rendina LM, Webster LK (1993) Dinuclear complexes of platinum having anticancer properties. DNA-binding studies and biological activity of Bis(4,4′-dipyrazolylmethane-N,N′)-bis[dichloroplatinum(II) and related complexes. J Inorg Biochem 49(3):221; (c) Rendina LM (1991) Ph.D. Thesis, Australian National University
181. Zhao G, Lin H, Zhu S, Sun H, Chen Y (1998) Synthesis and biological activity of binuclear platinum complexes containing two monofunctional cis-$[Pt(NH_3)2Cl]^+$ units bridged by 4,4′-dipyridyl selenides or sulfides. Anti-Cancer Drug Des 13(7):769
182. Komeda S, Lutz M, Spek AL, Chikuma M, Reedijk J (2000) New antitumor-active azole-bridged dinuclear platinum(II) complexes: synthesis, characterization, crystal structures, and cytotoxic studies. Inorg Chem 39(19):4230; (b) Komeda S, Lutz M, Spek AL, Yamanaka Y, Sato T, Chikuma M, Reedijk J (2002) A novel isomerization on interaction of antitumor-active azole-bridged dinuclear platinum(II) complexes with 9-ethylguanine. Platinum(II) Atom Migration from N2 to N3 on 1,2,3-triazole. J Am Chem Soc 124(17):4738
183. Jansen BAJ, van der Zwan J, Reedijk J, den Dulk H, Brouwer J (1999) A tetranuclear platinum compound designed to overcome cisplatin resistance. Eur J Inorg Chem 1999(9):1429
184. Cerón-Carrasco JP, Jacquemin D (2015) Photoactivatable platinum(II) compounds: in search of novel anticancer drugs. Theor Chem Acc 134, Article No. 146:1–8
185. (a) Heringiova P, Woods J, Mackay FM, Kasparkova J, Sadler PJ, Brabec V (2006) Transplatin is cytotoxic when photoactivated: enhanced formation of DNA cross-links. J Med Chem 49(26):7792; (b) Zhao Y, Roberts GM, Greenough SE, Farrer NJ, Paterson MJ, Powell WH, Stavros VG, Sadler PJ (2012) Two-photon-activated ligand exchange in platinum(II) complexes. Angew Chem, Int Ed 51(45):11263; (c) Mitra K, Gautam S, Kondaiah P, Chakravarty AR (2015) The cis-diammineplatinum(II) complex of curcumin: a dual action DNA crosslinking and photochemotherapeutic agent. Angew Chem, Int Ed 54(47):13989; (d) Mitra K, Lyons CE, Hartman MCT (2018) A platinum(II) complex of heptamethine cyanine for photoenhanced cytotoxicity and cellular imaging in near-IR light. Angew Chem, Int Ed 57(32):10263; (e) Shi H, Clarkson GJ, Sadler PJ (2019) Dual action photosensitive platinum(II) anticancer prodrugs with photoreleasable azide ligands. Inorg Chim Acta 489:230; (f) Liu D, Ma J, Zhou W, He W, Guo Z (2012) Synthesis and photoactivity of a Pt(II) complex based on an o-nitrobenzyl-derived ligand. Inorg Chim Acta 393:198; (g) Ciesienski KL, Hyman LM, Yang DT, Haas KL, Dickens MG, Holbrook RJ, Franz KJ (2010) A photo-caged platinum(II) complex that increases cytotoxicity upon light activation. Eur J Inorg Chem 2010(15):2224; (h) Presa A, Vázquez G, Barrios LA, Roubeau O, Korrodi-Gregório L, Pérez-Tomás R, Gamez P (2018) Photoactivation of the cytotoxic properties of platinum(II) complexes through ligand photoswitching. Inorg Chem 57(7):4009; (i) Presa A, Brissos RF, Caballero AB, Borilovic I, Korrodi-Gregório L, Pérez-Tomás R, Roubeau O, Gamez P (2015) Photoswitching the cytotoxic properties of platinum(II) compounds. Angew Chem Int Ed 54(15):4561

186. (a) Zou T, Lok C, Funga YME, Che CM (2013) Luminescent Organoplatinum(II) complexes containing bis(N-heterocyclic carbene) ligands selectively target the endoplasmic reticulum and induce potent photo-toxicity. Chem Commun 49(47):5423; (b) Naik A, Rubbiani R, Gasser G, Spingler B (2014) Visible-light-induced annihilation of tumor cells with platinum-porphyrin conjugates. Angew Chem, Int Ed 53(27):6938
187. Bednarski PJ, Mackay FS, Sadler PJ (2007) Photoactivatable platinum complexes. Anti-Can. Agents. Med Chem 7(1):75
188. Naik A, Rubbiani R, Gasser G, Spingler B (2014) Visible-light-induced annihilation of tumor cells with platinum-porphyrin conjugates. Angew Chem Int Ed Engl 53(27):6938
189. Tsai JL-L, Zou T, Liu J, Chen T, Chan AO-Y, Yang C, Lok C-N, Che C-M (2015) Luminescent platinum(II) complexes with self-assembly and anti-cancer properties: hydrogel, pH dependent emission color and sustained-release properties under physiological conditions. Chem Sci 6(2015):3823
190. Frik M, Jiménez J, Vasilevski V, Carreira M, de Almeida A, Gascón E, Benoit F, Sanaú M, Casini A, Contel M (2014) Luminescent iminophosphorane gold, palladium and platinum complexes as potential anticancer agents. Inorg Chem Front 1:231
191. Zou T, Lok C-N, Fung YME, Che C-M (2013) Luminescent organoplatinum(II) complexes containing bis(N-heterocyclic carbene) ligands selectively target the endoplasmic reticulum and induce potent photo-toxicity. Chem Commun 49(47):5423
192. (a) Chakravarty R, Hong H, Cai W (2014) Positron emission tomography image-guided drug delivery: current status and future perspectives. Mol Pharm 11(11):3777; (b) Chakravarty R, Hong H, Cai W (2015) Image-guided drug delivery with single-photon emission computed tomography: a review of literature. Curr Drug Targets 16(6):592
193. (a) Song Y, Suntharalingam K, Yeung JS, Royzen M, Lippard SJ (2013) Synthesis and characterization of Pt(IV) fluorescein conjugates to investigate Pt(IV) intracellular transformations. Bioconjug Chem 24(10):1733; (b) Montagner D, Yap SQ, Ang WH (2013) A fluorescent probe for investigating the activation of anticancer platinum(IV) prodrugs based on the cisplatin scaffold. Angew Chem Int Ed 52(45):11785; (c) Leblond F, Davis SC, Valdés PA, Pogue BW (2010) Pre-clinical whole-body fluorescence imaging: Review of instruments, methods and applications. J Photochem Photobiol B 98(1):77
194. (a) Sathekge M, Wagener J, Smith SV, Soni N, Painter BM, Zinn C, de Wiele CV, D'Asseler Y, Perkins G, Zeevaart JR (2013) Biodistribution and dosimetry of ^{195m}Pt-cisplatin in normal volunteers. Nuklearmedizin 52(06):222; (b) Buckley SE, Ali PA, Evans CJ, El-Harkawi AM (2006) Gamma camera scintigraphy of tumours using ^{195m}Pt-cisplatin. Phys Med Biol 51(5):1325
195. (a) Firestone RB (1998) Table of isotopes. Wiley Sons Inc; (b) U. Reus, W. Westmeier (1983) Catalog of gamma rays from radioactive decay. Atomic Data Nuclear Data Tables 29:1–192
196. Dykiy MP, Dovbnya AN, Lyashko YV, Medvedeva EP, Medvedev DV, Uvarov VL (2007) Photonuclear production of ^{193m},^{195m}Pt and synthesis of radioactive cisplatin. J Label Comp Radiopharm 50(5–6):480
197. Buckley SE, Ali PA, Evans CJ, El-Sharkawi AM (2006) Gamma camera scintigraphy of tumours using (195m)Pt-cisplatin. Phys Med Biol 51(5):1325
198. Howell RW, Kassis AI, Adelstein SJ, Rao DV, Wright HA, Hamm RN, Turner JE, Sastry KSR (1994) Radiotoxicity of platinum-195m-labeled trans-platinum(II) in mammalian cells. Radiat Res 140(1):55
199. Kawai K, Tanaka Y, Nakano Y, Ehrlich W, Akaboshi M (1995) Synthesis of platinum-195m radiolabelled cis-diammine(1,1-cyclobutanedicarboxylato) platinum(II) of high radionuclidic purity. J Label Compds Radiopharm 36(1):65
200. Sharma KS, Vimalnath KV, Phadnis PP, Chakravarty R, Chakraborty S, Dash A, Vatsa RK (2021) Facile synthesis of a Pt(IV) prodrug of cisplatin and its intrinsically ^{195m}Pt labeled analog: a step closer to cancer theranostic. Ind J Nucl Med 36(2)(2021):140
201. Suntharalingam K, Song Y, Lippard SJ (2014) Conjugation of vitamin E analog α-TOS to Pt(IV) complexes for dual-targeting anticancer therapy. Chem Commun 50:2465

202. Montagner D, Tolan D, Andriollo E, Gandin V, Marzano C (2018) A Pt(IV) prodrug combining chlorambucil and cisplatin: a dual-acting weapon for targeting DNA in cancer cells. Int J Mol Sci 19(12), Article No. 3775:1–11

Chapter 15
Synthesis, Properties and Applications of Intermetallic Phases

Ratikant Mishra and Rimpi Dawar

Abstract Intermetallic phases constitute a unique class of materials composed of two or more metals, sometimes non-metallic elements also, in definite proportions. They have well-defined stoichiometry, crystal structure and can exhibit metallic, covalent or ionic bonding. High mechanical strength, resistance to corrosion and adequate ductility of intermetallic phases make them widely applicable as structural materials for automobiles, aerospace, telecommunication, electronics, transport and heavy industries. There is a huge demand for alloys having high mechanical strength and corrosion resistance at elevated temperatures for energy applications. The physical properties and mechanical strength of alloys are governed by the presence of intermetallic phases in these alloys. The formation of these phases in a given alloy system on other hands is governed by the nature of synthesis of alloys, level of impurity phases present and the heat treatment process. Experimental conditions, like, level of vacuum, annealing temperature, rate of cooling and thermal shock are among the factors that play vital role in tailoring their properties. In the present chapter, types of intermetallic phases, various experimental procedures for their synthesis, processing and their properties will be discussed. Details of synthesis processes including heat treatment in different types of furnaces, mechanical alloying, electrochemical processes, chemical reduction methods will be discussed. Influence of annealing conditions on material properties will also be presented. The knowledge of phase diagram, structure and thermodynamic parameters in fixing the material properties will be brought out. The chapter will also include some of the technologically important intermetallic phases, their method of synthesis, properties and applications.

Keywords Intermetallic phases · Synthesis · Nanoalloys · Heat treatment process · Applications

R. Mishra (✉) · R. Dawar
Chemistry Division, Bhabha Atomic Research Centre, Trombay, Mumbai 400085, India
e-mail: mishrar@barc.gov.in

R. Dawar
e-mail: rimpid@barc.gov.in

A. K. Tyagi and R. S. Ningthoujam (eds.), *Handbook on Synthesis Strategies for Advanced Materials*, Indian Institute of Metals Series,
https://doi.org/10.1007/978-981-16-1892-5_15

15.1 Introduction

Intermetallic phases (IPs) are fascinating group of materials that have attracted attention in recent years [1–3]. These phases contain two or more metallic /semi-metallic elements with a fixed composition and have a distinct crystal lattice compared to their constituent elements [4–6]. They can be considered as ordered phases of two or more metals in fixed atomic ratio [7]. The impact of intermetallic compounds could not be realized for a very long time, mainly due to the problems associated in finding high strength, ductile and tenacious materials that can meet the demands for high-temperature applications [8]. The potential of intermetallic phases for high-temperature applications was realized in the early 1900s. Kurnakov et al. [9] led the foundation of the subject of intermetallic compounds in 1916. The subject of intermetallic phases gained importance after the path making discoveries of Aoki and Izumi [10] in 1980s. Last few decades have witnessed a huge progress in the field of intermetallics on production of high-temperature alloys for power generation, aero engines, automobiles, turbochargers etc. Apart from the above applications, intermetallic phases have been extensively used for chemical, magnetic, optical and semiconducting applications.

Initial attempts to synthesize intermetallic phases with adequate ductility and high-temperature creep strength did not succeed. These attempts have led to the germination of many ideas which have helped in the development of a series of alloys and phases. For example, introduction of additional elements/new phases and modifying the process parameters to change the properties of intermetallic phases have allowed tailor making of the microstructures as per the application demand.

Intermetallic phases generally melt at higher temperature. The properties of intermetallic phases are intermediate between metals and ceramics. While these materials are often resistant to oxidation at high temperature, there is significant reduction in the toughness and processing abilities [11–13] of these materials as compared to constituent elements at high temperature. Due to their high structural stability and improved ductility, many intermetallic phases are extensively used in engineering applications. For example, titanium aluminides have been used as construction material for Boeing [14], whereas nickel aluminides are used as structural material for fabrication of aeroplane turbine engine parts [15].

Intermetallic phases are most commonly defined by system of Pearson symbols [16] which consist of an array of two letters and a number. The small letter (first) refers to the crystal system, whereas capital letter (second) corresponds to the lattice type. The numerical value at the last gives the number of atoms present in the unit cell. Some times Strukturbericht symbol, such as A2 and B2, is used for identifying a crystal structure. In this representation, pure elements are symbolized as A, compounds of type XY are symbolized as B, compounds of type XY_2 type as C, X_mY_n type as D and a compound having three or more elements as E, F, G, etc. Examples of typical intermetallic phases with their respective Strukturbericht and Pearson symbols are given in Table 15.1.

Tabel 15.1 Strukturbericht and Pearson symbols of some intermetallic phases

Phases	Strukturbericht symbol	Pearson symbols	Phases	Strukturbericht symbol	Pearson symbols
FeAl	B2	*hR1*	Cu_2Te	D6	*hP6*
CuPt	B2	*cP2*	Mo_2B_5	D7	*hR7*
ZnS (blende)	B3	*hR2*	Nb_3Al	D8	*cP8*
AuCu	B4	*hP3*	Ni_3Sn	D8	*hP8*
CrB	B8	*tP4*	Ni_3Al	D9	*cP4*
AgZn	B9	*oC8*	Er_3Ru_2	D10	*hP10*
γ-CuTi	B11	*hP9*	Fe_7W_6	D13	*hR13*
β'-AuCd	B19	*hP12*	Fe_3Te_3	D14	*hP14*
PdAl	B26	*hR26*	Mg_2Ni	D18	*hP18*
σ-FeCr	B30	*tP30*	Fe_3Th_4	D20	*hP20*
$CoSi_2$	C2	*cF2*	Cu_3P	D24	*hP24*
$MoSi_2$	C6	*tI6*	Mn_7C_3	D40	*oP40*
$IrGe_4$	C15	*hP15*	Cu_5Zn_8	D52	*cI52*
$MgCu_2$	C24	*cF24*	$ScRh_6P_4$	E4	*hP11*
Li_3N	D4	*hP4*	AlN_3Ti_4	E16	*hP16*
Cu_3Au	D4	*cP4*	$Fe_{12}Zr_2P_7$	E21	*hP21*
Al_3Ni_2	D5	*hP5*	Al_9Mn_3Si	E26	*hP26*
Bi_2Te_3	D5	*hR5*	Co_2Al_5	D28	*hP28*

15.2 Types of Intermetallic Phases

Intermetallic phases may be classified as stoichiometric or non-stoichiometric phases. Stoichiometric intermetallic phases have fixed compositions. They are represented by a vertical line in the phase diagram. Some examples of stoichiometric intermetallic phases are: AlSb in Al–Sb system, Mg_3Ni in Mg–Ni system, Fe_3Te_2 in Fe–Te system, Fe_3C in Fe–C system, etc. Non-stoichiometric compounds, on the other hand, have a range of solubility of their constituent elements in the parent lattice. The ratio of well-defined natural numbers can not represent the elemental composition in these compounds. They may be called as intermediate solid solutions. Based on the crystal structure, nature of bonding and particle size, IPs can be classified into the following categories.

15.2.1 CsCl Type Phases

In CsCl type of phases, one of the atoms occupies the (0, 0, 0) lattice positions in cubic unit cell, while the other atom occupies (½, ½, ½) position. For example, Cl^-

ions form a primitive array of cubic lattice. Coordination number (C.N.) of Cs^+ and Cl^- is 8. Typical examples of such phases are MgSe, PbSe, CaTe, CuZn, CuPd and TiX with X = Fe, Co, Ni.

15.2.2 CaF_2 Type Phases

In calcium fluoride type structure, each of the less electropositive metal is surrounded by four more electropositive metal and each more electropositive is surrounded by eight less electropositive metal. These phases form cubic close packing (CCP) type of arrangement with electropositive metal at all the corners (000) and at the centre of each face of the cube. Electronegative atoms occupy all the tetrahedral sites (¼, ¼, ¼). Some of the coloured intermetallic phases of platinum and gold with alloying elements such as X = Al, In and Ga exhibit CaF_2 structure. The colour effects in such phases are generally achieved by changing content of gold and platinum while keeping ratio (Au, Pt)X_2 constant.

15.2.3 Zinc Blende Structure Type Phases

The elements of group III–V form intermetallic phases with ZnS type crystal structure. Examples are: GaP, GaAs, GaSb, InP, InAs, InSb. Most semiconductors of commercial importance are isomorphous with diamond and zinc blende crystal structure. For example, the structure of GaAs crystal may be thought of two interpenetrating fcc lattices, one for arsenic the other for gallium, with their origins displaced by one quarter along a body diagonal. Ga occupies lattice corners and fcc positions and As atoms occupy alternate tetrahedral sites.

15.2.4 Wurzite Type (ZnS) Phases

Examples of intermetallic phases with Wurzite type crystal structure are ZnTe, MnSe, AlN, GaN, InN, TlN, etc. Wurzite is a more open structure with high lattice energy than zinc blende type structure. These structures are thermodynamically less stable and tends convert to zinc blende type structure. They have higher band gap compared to zinc blend type phase.

15.2.5 Nickel Arsenide (NiAs) Phase

This structure type is commonly formed by the transition metal alloyed with the metalloid of group 15 and 16 such as As, Bi, Sb, Se and Te forming *chalcogenides*, *arsenides*, *antimonides* and **bismuthides** of *transition metals*. The structure of these compounds is hcp with sequence of layers of metal and metalloid atoms stacked alternatively. These phases exhibit wide range of solubility. Examples of compounds having NiAs type structure are: NiSb, NiSn, FeSb, PtSn, MnAs, MnBi, PtBi, NiS, NiSe, NiTe, FeS, FeSe, FeTe, CoS, CoSe, CoTe, CrSe, CrTe, MnTe, etc.

15.2.6 Electron Phases

The intermetallic phases formed at definite electron concentrations are called electron phases. In these phases, the electron concentration determines their stability. The phases are also known as Hume Rothery phases in the name of their discoverer. These phases show high degree of solubility of the component elements. Electron phases are formed at fixed values of valence electron to atom ratio in the alloy phase, i.e. 3:2, 21:13 and 7:4. Some examples of electron phases are CuZn (3:2), Cu_5Zn_8(21:13) and $CuZn_3$(7:4).

15.2.7 Laves Phases

The laves phases denote intermetallic phases with general chemical formula AB_2. Examples of three prototype structures are: (a) $MgCu_2$, (b) $MgZn_2$ and (c) $MgNi_2$. Out of these, $MgCu_2$ is cubic while $MgZn_2$ and $MgNi_2$ are hexagonal. A large number of intermetallic compounds are iso-structural with the above Mg-based compounds. Table 15.2 gives the examples of laves phases iso-structural with $MgCu_2$, $MgZn_2$ and $MgNi_2$.

Table 15.2 Examples of laves phases iso-structural with $MgCu_2$, $MgZn_2$ and $MgNi_2$ type phases

$MgCu_2$ structure type	$MgZn_2$ structure type	$MgNi_2$ structure type
$CuBe_2$	$MnBe_2$	$MgNi_2$
$CeAl_2$	$CaMg_2$	$MgPt_2$
UAl_2	$ZrCr_2$	$U(Fe, Ni)_2$
$BiAl_2$	$TiMn_2$	$U(Mn, Ni)_2$
$CeCO_2$	UNi_2	$U(Mg, Zn)_2$
UMn_2	CoCrTa	

In laves phase, the atom 'A' is generally larger compared to atom 'B'. The formation of these phases is favoured when the ratio of the atomic radii of constituent atoms (r_A and r_B) is close to 1.225 (ranging from 1.1 to 1.6).

15.2.8 Interstitial Phases

Interstitial alloy refers to a metal lattice in which the crystal lattice is formed by metal–metal bond and the metal/non-metallic atoms of small sizes occupy interstitial lattice positions without, or with only a limited degree of, distortion from crystal symmetry. An interstitial alloy is formed when atoms of sufficiently small radii like hydrogen, boron, carbon and nitrogen occupy interstitial voids in a metal lattice. The some important examples of interstitial alloys are: Fe–C and Fe–N alloy. Metals which have close packed structures, e.g. fcc or bcc, have tetrahedral or octahedral voids. The smaller atoms are occupied in these voids. The formation of interstitial phases is favoured when the electronegativity difference between the constituent atoms is small, difference in the atomic radii of the metal atoms and the smaller atoms is less than 15% and the crystal structure and the valency of the atoms are same. The number of smaller atoms present in the interstitial positions is generally much smaller compared to the available interstitial sites.

15.2.9 Sigma Phases

The formation of sigma phases in an alloy is deleterious as they reduce the corrosion resistance and toughness of the material. Sigma phases are tetragonal structured compounds (involving transition metals) having 30 atoms per unit cell. These 30 atoms occupy 5 non-equivalent crystallographic positions, viz. (a), (f), (ic), (id) and (j) in the unit cell. The atoms occupying the above crystallographic positions are designated as A, B, C, D and E. There are two atoms in the position (a), 4 atoms in the position (f), 8 atoms in position (ic), 8 atoms in position (id) and 8 atoms in position (j). These phases have broad homogeneity range. For different systems composition and temperature stability ranges of these sigma phases are different. Cr–Co phase diagram [17] showing the presence of sigma phase is given in Fig. 15.1

Some examples of sigma phases with their composition range and decomposition temperature are given in Table 15.3.

The formation and the stability of sigma phases depend on factors like atomic size and the electronic configuration of constituent atoms.

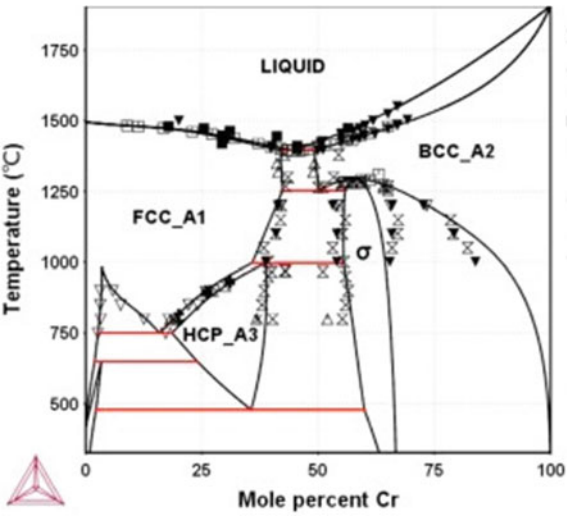

Fig. 15.1 Cr–Co phase diagram showing the presence of sigma phase (Reproduced with permission from Elsevier, Calphad 52 (2016), 7)

Table 15.3 Examples of sigma phases with their composition range and decomposition temperature

Sigma phases	Composition range	Decomposition temperature (°C)
Cr–Mn	16–24 at % Cr	1000
Cr–Fe	43–49 at % Fe	600
Cr–Co	58.6–63 at % Cr	1200
Mn–V	13.4–24.5 at % V	1000

15.2.10 Zintl Phases

These are intermetallic compounds formed by reaction of group 1 or group 2 elements with any metalloid (p block elements). It is named after the scientist who investigated them in the 1930s (German chemist Eduard Zintl). They are electronically balanced or closed-shell compounds having very narrow or no homogeneity range. Zintl phases are brittle in nature and exhibit diamagnetism or very weak temperature independent paramagnetism. Zintl phases are air and moisture sensitive. Therefore, their synthesis and handling is carried out in vacuum or inert atmosphere.

15.2.11 Nanoalloys (NAs)

Nanoalloys (NAs) are metallic systems where properties of material are significantly modified by the synergistic effects of multi-elements in the nanoform. The variations in structure, composition and properties of NAs have led to their extensive applications in catalysis and other engineering fields. The physical and chemical

properties of NAs can be fine-tuned by altering the chemical composition, ordering of atoms and varying the size of the clusters. Surface morphology, chemical compositions and particle size play an important role in fixing their chemical reactivity with respect to catalysis [18, 19]. Bimetallic NAs sometimes exhibit synergism in catalysis compared to the bulk alloys owing to nanosize effects [20].

The extent of mixing or segregation of atoms in binary alloys (X, Y) depends on factors like relative strengths of X–X, Y–Y and X–Y bonds, excess surface energies of constituent phases, relative atomic sizes, extent of charge transfer and strength of bonding. Higher inter atomic (X–Y) bond energy and easier electron transfer from less electronegative atom to more electronegative atom favour the mixed phase formation. The atoms forming strong homonuclear bonds generally remain at the centre of the core–shell structure [21]. Similarly, element with smallest surface energy prefers to move to the surface of the alloy while the smaller atoms prefer sterically confined central region. In case of supported cluster alloy systems, strongly bonded element is generally pushed towards the surface. In addition to the above factors, the atomic arrangement for binary NAs also depends on the method of their preparation and other experimental conditions.

Nanoalloy phases can be deposited onto substrates like graphite, silicon or any other inorganic oxide from solution or the gas phase adopting different techniques. In such experiments, controlling the geometric or electronic structure of clusters is somewhat difficult. However, it is possible to perturb the geometry by changing the substrate and sometimes by application of electric or magnetic field.

15.2.12 Magnetic Alloys

Magnetic alloys and intermetallics are material that produces a constant permanent magnetic field under normal condition. Magnets can be of two types: hard magnets and soft magnets. Hard magnets have a high coercivity and are called as permanent magnet, whereas soft magnets have a low coercivity. Permanent magnets are intermetallic phases that can be *magnetized* and create their own persistent magnetic field. The materials are strongly resistant to demagnetization after they get magnetized. They have coercivities ranging from 10 to 100 kA/m. Fe, Ni, Co and rare earth metals are among the few elements which form permanent magnets. Rare earth based magnets such as $SmCo_5$ and $Nd_2Fe_{14}B$ are among the strongest permanent magnets that produce the largest magnetic flux with smallest mass [22]. Examples of non-rare earth permanent magnets are Fe–Co, $Fe_{0.3}Cr_3Co_3$, $Fe_{6.3}Cr_{2.5}Co_{12}$, Mn–Al–C, Co–Pt.

15.2.13 Coloured Intermetallic Phases

Out of large number of reported intermetallic phases, only few phases exhibit colour. Some example of coloured intermetallic phases are: Cu_5Sn—golden-yellow; NiAl—blue; CoAl—yellow; CoGa—yellow; $AuGa_2$ and $AuIn_2$—blue; $CoSi_2$ dark blue, $NiSi_2$—blue grey, $AuAl_2$—purple and PdIn—red. The origin of colour in intermetallic species can be explained due to the existence of both metallic as well as strong covalent bonds between different metals.

Gold-based intermetallic phase is among the most popular coloured alloys. In addition to bright golden colours, these phases can be synthesized in various other colours including blue, purple and black. Reddish colour gold alloys can be produced by mixing gold with copper. Example of other coloured intermetallic gold compound is $AuAl_2$ (golden), $AuIn_2$ (blue colour). In turbine blade, some of the precious coloured intermetallic compounds are used as coating material for preventing high-temperature oxidation/corrosion.

15.2.14 High-Entropy Alloys (HEAs)

High-entropy alloys (HEAs) are intermetallic phases consist of five or more major elements having concentration ranging between 5 and 35 at.%. HEAs can also include some minor elements for modifying base alloy properties [23]. These are relatively new class of alloys that explore the influence of phase stability of solid solution through the control of configurational entropy. Due to multi-principal elemental compositions, HEAs exhibit many special properties including high strength/hardness, outstanding wear resistance, exceptional high-temperature strength, good structural stability, good corrosion and oxidation resistance. Many of these properties of HEAs are not commonly observed in other alloys.

The existing knowledge of phase diagram and physical metallurgy studies suggest that employing multiple elements for alloy making can lead to the formation of large numbers of intermetallic compounds and phases, resulting in formation of discrete and brittle microstructures which have limited practical utility. In contrast, the experimental results indicate HEAs have simple structures and less number of phases than expected.

The mass production HEAs can be easily achieved with normal processing equipments, with prevailing technologies. The two important aspects for the formation of HEAs are the core effects and formation of intermetallic phases. The ‘core effects’ employed to portray HEAs are: sluggish diffusion, lattice distortion, cocktail and higher entropy effects. The description of these effects is given below.

The high degree of disorderness is responsible for the increase in configurational entropy in HEAs that favours solid solution phase formation. The higher configurational entropy decreases the Gibbs free energy HEAs and favours their formation, at high temperatures [21–27]. It is generally observed that in HEAs, the total number of

phases observed is much smaller than the expected number phases due to high degree of mutual solubility of constituent elements. However, in some cases, the enthalpy of formation of intermetallic compounds dominates over the thermodynamic stability achieved through configurational entropy leading to precipitation of ordered phases.

The lattice of HEAs consists of a large number of elements with different sizes causes lattice distortion. In such cases, bigger atoms occupy the normal lattice positions, whereas the smaller atoms occupy the interstitial positions that lead to distortion of lattice structure. The lattice strain arising due to the distortion increases the total free energy and affects its properties. This lattice distortion hinders the movement of dislocations and strengthens the solid solution. The lattice strain is also responsible for higher scattering of electrons and phonons, those results in lowering of thermal and electrical conductivity [28].

In HEAs, it is assumed that the phase transformation and diffusion kinetics are more sluggish than the conventional alloy phases [29]. This may be understood by the fact that in HEAs, neighbouring atoms in each lattice site are different from each other. Hence, neighbouring atoms prior and after the migration to a vacancy are not same. This leads to a new atomic rearrangement with different binding energy in local structure. In cases where an atom migrates to a site having lower energy, it gets 'trapped', similarly when the atom migrates a site with higher energy; it hops back to its lower energy site. Both these phenomena decrease the rate of diffusion in the matrix. The effect of the above local energy fluctuations in diffusion process has been calculated by Tsai et al. employing seven-bond model. The authors have shown that the difference in average potential energy among lattice sites in HEAs is generally 50% higher than that of normal alloys. This energy difference leads to a significantly longer occupation time at low-energy sites. The slow kinetics in HEAs allows readily attainable supersaturated state and nano-sized precipitates, even in casting stage [30–33], which contributes to the excellent performance of HEA coatings as diffusion barrier materials.

The constituent elements influence the HEAs properties to a great extent. Besides the properties of the component constituent atoms, the mutual interaction among them also influences the overall properties of HEAs. Figure 15.2 depicts the increase in hardness of $Al_xCoCrCuFeNi$ HEAs by addition of Al atoms [34].

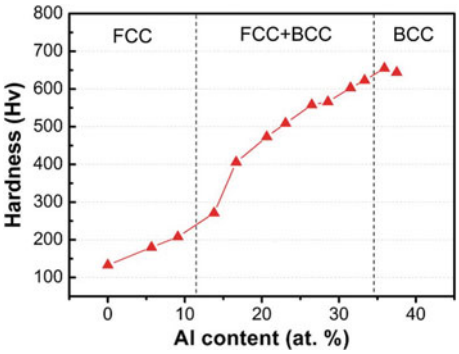

Fig. 15.2 Influence Al content on micro-hardness of $Al_xCoCrCuFeNi$ HEA (Reproduced with permission from Taylor and Francis; Mater Res. Lett., 2 (2014) 107–123)

The figure shows that addition of Al significantly increases the hardness of the $Al_xCoCrCuFeNi$ HEA. This could be due to formation of strong cohesive bonding between constituent elements with Al atom and formation of a hard BCC phase. Hence, the properties of HEAs can be assumed to the average properties of constituent elements. The average HEA properties also depend on the interaction energy of the component elements and the distortion of the lattice structure.

15.3 Bonding in Intermetallic Phases

The nature of bonding in intermetallic phases is similar to that of metallic alloys. In these phases, the metallic bonding is governed by concentration of electron 'e/a' (i.e. number of valence electrons per atom). In addition, in these phases, some extent of other type of bonding also exists between the constituent elements. Intermetallic phases can be very well described by mixed bonding pattern, viz. partially covalent, ionic and metallic bonding [35]. For example, the compounds like Mg_2Zn and Mg_2Pb possess both ionic and metallic characters. Mg_2Sn has high electrical conductivity indicating metallic bonding in the compound. However, it is not possible to quantify the % of metallic and non-metallic bonding character in this compound.

For intermetallic phases, the concept of valence is somewhat complicated, possibly due to the existence of extensive solid solubility and occurrence of non-stoichiometric compositions. For example, the compound KHg_{11} does not seem to follow the rules of chemical valency as in this case the net charge on each Hg atom is 1/11. Hence, the notion of valence needs careful interpretation of bonding in intermetallic phases.

The formation of intermetallic phases can sometimes show exothermic effect due to ionic, covalent and Van der Waals type bonds. However, due to predominantly metallic bonding, the heat of formation in intermetallic compounds is generally low. The Pauling equation for the heat of formation in AB type phases is:

$$\Delta H\,(\mathrm{kJ/mol}) = -96.5 \times Z(AE_a - BE_b)^2$$

where Z is number of valence bonds and E_a and E_b are the electronegativities of the component atoms. The above equation based on electronegativity becomes less applicable where covalent and metallic bonds are gradually replaced by ionic bonds.

The Lewis acid–base interaction between the constituent metal atoms is another concept in describing the formation of intermetallic compounds. In intermetallic phases containing transition elements, the d-d interaction plays vital role in the formation of stable bonds. It was observed that on heating, Pt metal reacts with ZrC, which is a highly stable compound, to form $ZrPt_3$ compound. It indicates that the standard molar enthalpy of formation of $ZrPt_3$ is more negative than the enthalpy of formation of ZrC. Similarly, when the mixture containing Hf and Pt powders is heated at 1000 °C, an explosive reaction takes place due to spontaneous evolution of excess

energy. The enthalpy of formation of $HfPt_3$ measured by calorimetric measurements confirms evolution of high amount of energy, i.e. -548.7 kJ mol^{-1}.

Zirconium has outermost electronic configuration d^2s^2 and Pt has outermost electronic configuration d^9s^1. When Zr and Pt combine, the partly filled orbitals of Pt overlap with partly filled d-orbitals of zirconium to form stable fully filled d-orbital. This leads to strong bonding in intermetallics having transition metals as component metals.

The strength of the acid–base interaction depends upon the degree of localization of d-orbital. As nuclear charge increases along a group, s and p-electrons get attracted more towards the nucleus than the d-electron due to greater penetrative power of s and p orbital. Thus, ongoing down the group d-orbital gets more exposed, resulting stronger intermetallic bonds. For right 3-d metals, the electrons are more localized due to reduced size and hence are less basic than the left 3-d metals. Base strength of metals with incomplete d-orbitals increases down the group.

In compounds $ZrPt_3$ or $HfPt_3$, the electrons are transferred from Pt to a more electropositive atom Zr or Hf. The factor that determines the direction of transfer of electron is the availability of orbital and non-bonding electrons. The electronegativity difference then determines the electron distribution in bond after their transfer. In general, larger the difference in the electronegativity among the constituent atoms, greater is the tendency to form compounds and they are relatively more ordered compared to the other alloys. The crystal field effects in the transition element also influence the strength of bonding in intermetallic compound.

15.4 Role of Phase Diagram in the Synthesis of Intermetallic Phases

Since the properties of intermetallic phases are dependent to a large extent on the type, number, amount and crystallographic form of the phases present, it is imperative to know the conditions of existence and transformation of these phases. A phase diagram gives the number of phases which coexist with each other under equilibrium conditions. Phase diagram provides a pictorial representation of conditions including temperature, pressure and compositions for the formation of a given phase.

For example, crystals of A in a binary metallic system A-B (Fig. 15.3a) can be grown at temperature T (which is below the melting point of A) by adding small amount of second component 'B' that reduces the melting point of A drastically. In order to obtain the crystals of 'A', the mixture with composition X should be cooled slowly from T_F to T_E (eutectic temperature). On subsequent cooling to room temperature, the remaining liquid will crystallize in fine grains of A and B crystal.

Figure 15.3b gives another example, where phase diagram of a complex binary system provides guidance for the crystallization of intermetallic phase AB from binary melt. The phase diagram indicates crystallization of AB-phase from the melt with molar ratio of A and B equals to 1:1 is not possible. Under such situation, phase

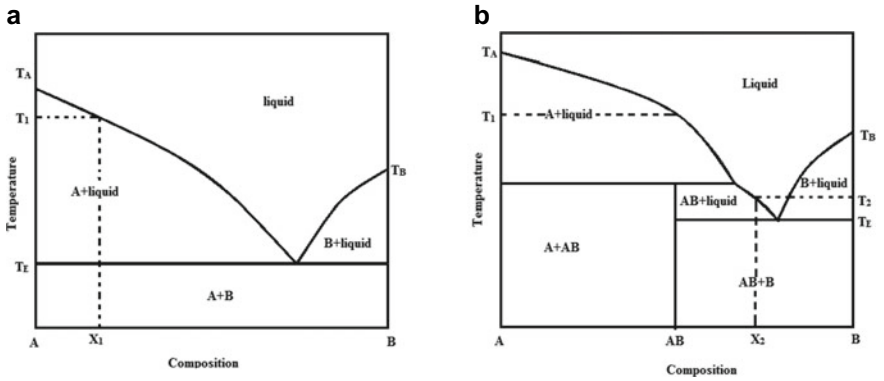

Fig. 15.3 **a** Phase diagrams of simple binary eutectic system, **b** phase diagram of binary system having an intermediate compound

'A' will crystallize. Phase diagram dictates that the composition should be more B-rich (composition range $\times 1$ and $\times 2$) in order to crystallize AB phase.

Apart from predicting crystallization process, phase diagram provides wealth of information on number of phases that can be formed under given set of composition, temperature and pressure. It also provides information on crystallographic phase transition temperature of the pure phases, their melting points, peritectic decomposition temperature if any, solidus liquidus phase boundary, homogeneity range of stability, etc. All the information is the first hand information needed for synthesis of a desired product. Phase diagram is extremely important to understand various stages of intermetallic phase processing.

15.5 Synthesis of Intermetallic Phases

Intermetallic phases are prepared by different techniques such as heating in furnaces, mechanical alloying, electrolysis methods, and chemical and vapour deposition methods. A brief description of these methods of preparation is given below.

15.5.1 Furnace Heating Methods

15.5.1.1 Resistance Heating Furnace

Preparation of intermetallic phases by heating the intimate mixture of metals in the form powders, chips or small pieces is the most common method adopted worldwide. Heating of the reaction mixture can be carried out in a normal resistance furnace, induction furnace or arc melting furnace. Resistance furnaces can be tubular or

box type. The heating elements of the furnace can vary depending upon maximum operating temperature.

Since most of the metals readily react with oxygen on heating, synthesis of intermetallic phases is generally carried out under the flow of high pure inert gas, viz. nitrogen, argon or helium or under high vacuum conditions. Metallic samples are generally heated in quartz/recrystallized alumina tube under the flow of inert gas. The partial pressure of oxygen required for the synthesis of an intermetallic phase depends on the nature of constituent metals to be heated. Metals with higher reduction potential get easily oxidized and are difficult to prepare by long heating cycle. They require stringent control of oxygen partial pressure in the reaction cell. In such cases, the carrier gases used for maintaining inert gas atmosphere are purified by passing over oxygen getters. The oxygen impurity in the carrier gas is controlled by passing the gas over copper turning heated at 500 °C or titanium sponges heated at 900 °C. In addition to these metals, calcium, zirconium or sometimes uranium can be used to effectively remove oxygen impurity in the gas.

In order to minimize the oxidation, the metallic samples are mostly sealed in evacuated quartz ampoules under dynamic vacuum condition. In this case, the oxidation of sample takes place only by the oxygen diffused through quartz, which is negligible. Proper care should be taken to make sure that the reactive metal does not reduce silica, which can lead to the leak in the quartz ampoule. In case of reactive metals, an inert liner of high melting metals like tungsten, tantalum or graphite is provided between the sample and the silica. Sometimes to prevent any oxidation and to maintain the desired oxygen partial pressure, oxygen getters can be sealed along with sample in the ampoule in a separate location. In addition to prevent the oxidation of the sample, heating metallic samples in the quartz ampoules also help in fixing the composition during heating. The process prevents vaporization loss during heating and annealing.

Control atmosphere furnaces and vacuum sealing techniques are limited to small-scale laboratory synthesis of intermetallic phases with small sample volumes. However, in industries which involve synthesis of large volume of intermetallic phases, vacuum furnaces are employed. For vacuum furnaces, high-temperature alloys like SS 316, inconel, hastelloys are used as reaction tubes. The provisions for flow of inert gas and water cooling for end coupling of working tube are required for these furnaces. In order to prevent corrosion of working tube wall by the metal vapour, sometimes high-temperature ceramics compatible to the furnace and the sample are used as liner between the two. Since large volume of reactive metal samples is heated in vacuum furnaces, the control of residual oxygen is taken care by sample itself, provided the system is leak tight.

15.5.1.2 Induction Heating

Induction heating is a very convenient method to synthesize intermetallic phases in pure form. The method provides many distinct advantages over heating the samples in resistance furnace or by arc melting furnace. The most important advantages of

induction heating method include fine control of atmosphere over the sample, fast and localized heating, efficient energy consumption.

Principle of Induction Heating

In induction process, an electrically conducting object called susceptor is heated by transfer of energy from the inductor to the susceptor through electromagnetic field. The eddy current induced by the rapidly changing electromagnetic field produced by the flow of high frequency AC current through coil causes the heating effect. The induction coil functions as a primary coil of the transformer, whereas the susceptor behaves as the secondary coil of the transformer. The rate at which the susceptor is heated depends on the frequency and intensity of induced current, and specific heat, magnetic permeability and the resistance of the material. In this process, only a limited area is heated due to skin and proximity effects, and there is no direct contact between the susceptor and the coil carrying high frequency AC current. In the skin effect, the RF current flows through a limited area of the conducting surface, whereas in the proximity effect, the primary current flows through the inductor and the secondary current flow though a limited area of the susceptor material.

The oxygen partial pressure around the sample can be controlled by evacuation and purging of the high purity inert gas like argon or helium. The residual oxygen in ppm level present in the inert gas can be purified by passing the carrier gas over oxygen getter such as titanium sponge maintained at 900 °C.

In order to arrest the change in composition of the sample particularly for the volatile materials, sample is usually sealed in a tantalum tube. For sample preparation at low temperature, sealed quartz ampoules can be used. In such cases, care should be taken to make sure that the sample components do not react with container of the sealed tube. The proper mixing of the sample during heating process is possible by levitation technique, where the sample holder can be rotated to a certain extent.

Induction heating is a very efficient method for the preparation of air sensitive metallic sample. In addition to the synthesis of metallic phases, it can be used for other heat treatments, e.g. hardening, annealing, tempering, brazing, etc. Figure 15.4 shows the picture of a 12 kW Induction furnace with accessories used in authors laboratory.

15.5.1.3 Arc Melting Set-Up

Arc melting is a preferred technique for the synthesis of alloys and intermetallic phases, where the material to be heated has sufficient conductivity. In this technique, the heat generated by the electric arc struck between the electrodes is used for melting the sample. Arc melting equipment essentially consists of two electrodes, i.e. one water cooled copper block (hearth) with a cavity to hold sample and a tungsten electrode. Both these electrodes are housed in an air tight vessel. The copper acts as positively charged electrode while the tungsten rod acts as negatively charged electrode. The atmosphere inside the vessel housing the electrodes is maintained inert by evacuation and purging of the inert gases like argon or helium. The system

Fig. 15.4 Picture of a 12 kW induction furnace with accessories (in house fabricated)

is fitted with high vacuum pump, vacuum gauges, valves for inert gas inlet and outlet and cooling water lines. Schematic diagram of arc melting system is described in Fig. 15.5.

For preparation of intermetallic phases, homogenous mixture of two or more metals to be melted is kept in the cavity of the copper electrode and the tungsten electrode is slowly brought close (about 1–2 mm) to the sample. Voltage across the positively charged (copper block) electrode and the negatively charged electrode (tungsten electrode) is slowly increased till a fine arc is produced. The voltage is then increased till the entire metal charge is fully melted. The typical voltage across the electrodes and the current which can be passed through the sample can vary from 0 to 70 V and 10–400 A, respectively. High current passing through the sample is responsible for its melting. In order to prevent the copper hearth melting and contaminating the sample, chilled water is circulated through it. To homogenize the molten mass, the sample is turned upside down and re-melted after sufficient cooling.

Arc melting method is suitable for preparation of metallic samples having sufficient conductivity. This method of preparation is quite fast, and in this method, the exposure time for the oxidation of the sample is short. The method gives better product when the melting points of the constituent metals are close. If the melting points differ significantly, it is always possible that more volatile component (low

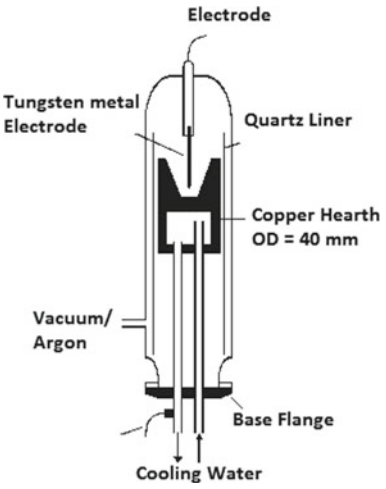

Fig. 15.5 Sketch diagram of arc melting apparatus

melting metal) vaporize during melting forming undesired product. In such cases, the volatile component is taken in excess amount to compensate for the loss.

15.5.1.4 Vacuum Plasma Heating

Vacuum plasma heating (VPH) technique has several applications in thin layer and multi-layer coating of metals. In this technique, the metal particles of dimensions 10–100 μm are accelerated by plasma gas towards the substrate, where they get deposited and solidify to form thin layer of metals. The plasma is formed by passing electric arc in flowing argon by applying high voltage across positive and negative electrodes. High temperature of the order of several thousand degrees Celsius is achieved in the argon plasma, which causes ionization of atom forming positive ions, electrons and neutral atoms. The fine metal powders are injected to the plasma where they get heated, ionized and accelerated towards the substrate. Detail mechanism of the plasma heating process for the formation of alloys and composites is described in the literature [36]. Lee et al. suggested inductively coupled plasma for low temperature deposition of metals or alloys [37]. The principle of inductively coupled plasma heating is similar to the inductive heating where eddy current is responsible for generating heat. In this technique, highly dense ion beam (10^{11}–10^{12} ions/cc) and large number of electrons are generated which are responsible for formation of higher density products compared to the normal plasma deposition technique. High density plasma can be used to lower the substrate temperature and improve the quality of metal/alloy films.

15.5.1.5 Electron Beam Furnace

The electron beam melting technique was first developed by Von Pirani in 1907. This technique is useful for melting refractory metals like tantalum, niobium and tungsten. In this technique, a beam of high-energy electrons strikes at metal target, where its kinetic energy converts into heat energy. This process needs to be performed in vacuum; else electron collision with air molecule could lead to loss of its energy before it could collide with the working material. This heat energy produced by the bombardment of high-energy electrons is sufficient to melt metals forming the desired products. The combination of electron beam melting and vacuum processing is very powerful technique to synthesize material that is otherwise difficult to synthesize employing other techniques.

The electron beam melting unit essentially consists of electron gun, annular biased grids, magnetic lenses and deflecting coils, work piece and holding devices. Development of high-energy electron gun and the associated vacuum technique is a challenge for electron beam melting technology. Sketch diagram of electron beam melting equipment is given in Fig. 15.6.

The electron beam melting method can be classified into drip melting and cold-hearth melting categories. In drip melting, the refractory metals are drip melted in water cooled mould, whereas in cold-hearth melting, the molten metal flows along the water cooled hearth and stored in water cooled mould. In drip melting method, it is possible to remove dissolved gases and volatile materials from the metals, which is not so in cold-hearth technique.

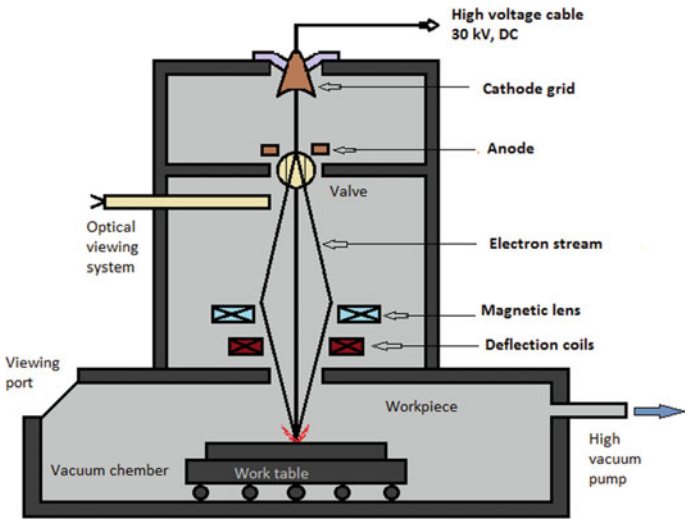

Fig. 15.6 Sketch diagram of electron beam melting equipment

15.5.2 Mechanical Alloying Method

Conventional methods used for synthesis of intermetallic phases are generally combination of melting, casting followed by annealing, sintering, grinding and hot pressing. However, the melting and casting method is not a suitable method to synthesize intermetallic phases having constituent elements differing significantly in their melting points [38]. Mechanical alloying (MA) is a powerful method for the synthesis of stable and metastable intermetallic phases without involving heat treatment. In this technique, the sample is prepared by grinding the components by impact, attrition and compression techniques which causes strain in the sample and provides activation energy for transformation. Intermetallic phases produced by this method can be either in crystalline or quasi-crystalline form. A large number of intermetallic phases including iron, nickel, titanium and aluminium have been synthesized by this method. This process is highly reliable, cheap, simple and easy to operate [39–41]. It is essentially a ball milling process for producing nanostructured and metastable materials employing mechanical energy at very low temperatures [42].

In mechanical alloying method, metals in form of small pieces are crushed into fine powder. In this process, the particles are fractured, deformed and cold welded. Due to such induced fracturing deformation and cold welding, a large number of lattice defects such as dislocations, stacking faults are introduced into the samples. As a result, free energy of the material increases [43]. The process of minimization of excess energy leads to form an ordered phase. However, detail mechanism explaining the formation of intermetallic phases by mechanical alloy technique has not been investigated in depth. It could be presumed that there is a competition between disordering of atoms induced by MA and reordering by thermal activation that results in the formation of ordered or disordered phases. When the energy difference between disordered and ordered states is less, a disordered alloy is formed, and when it is large, an ordered alloy is formed [44]. The free energy change due to milling ΔG (milling) = free energy change due to disordering ΔG (disordering) + free energy change due to formation of grain boundaries ΔG (grain boundaries) [29]. Miedema analysis suggests that, when ΔG (milling) is greater than ΔG (disorder + grain boundaries), it leads to the formation of a complete amorphous phase. On the other hand, a solid solution is formed when ΔG (milling) is less than ΔG (disorder + grain boundaries) [45].

Depending on types of mills used, ball milling can be of ‘low-energy’ and ‘high-energy’ type. Ball mills of different volume, acceleration field, milling efficiency and having provisions for control atmosphere during milling are available. The nature of the products formed is dependent on material, shape and internal design of the milling container and most importantly on milling speed. Varieties of hardened steels are used as container and bearing materials. By increasing the milling speed, the efficiency of the process increases. It is observed that the milling speed should be limited to below a critical speed. At critical speed, balls start pinning to the inner walls of container adding impurity due to structural material. For getting phases of desired microstructure, milling should be done for proper span of time.

In addition to milling speed, the quality of products also depends on ball to powder weight ratio and temperature of the milling process [43]. Alloying process becomes more efficient with higher ball to charge ratio due to higher number of collisions [46–48]. For an optimum yield of the product, the volume of charge should be about 50% of cavity volume of the milling machine. Smaller volume will lead to lower yield, whereas charge volume higher than 50% may result in incompletion of reaction. For reactive phases, the atmosphere in the milling cavity should be inert. The prevailing atmosphere in the milling cavity sometimes affects the kinetics of formation of intermetallic phases.

For preparation of metal nitrides and hydrides, N_2, NH_3 or H_2 atmosphere is maintained. The temperature is an important experimental parameter particularly for high-energy ball milling process. During milling, there can be local rise in temperature because of ball collisions and global temperature rise in the cavity of the ball mill [43]. In general, ball has to be interrupted between milling process to keep temperature of the cavity to an optimum level.

The ball milling of solid and liquid, based on coupling effect (arising due to thermochemistry and mechanochemistry), has been adopted for the synthesis of intermetallic phases. Mechanochemistry approach has several distinct advantages over traditional mechanical alloying like smaller particle size of the products with higher purity and faster kinetics of formation of alloy phases. Large number of intermetallic phases in Al–Cu–M (M=Co, Fe and Ni) systems, i.e. Al_7Cu_2Fe, $Al_{13}Cu_4Fe_3$, $Al_{65}Cu_{20}Fe_{15}$, $Al_{65}Co_{15}Cu_{20}$, $Al_{69}Co_{25}Cu_6$, $Al_{17}Cu_4Ni$ and $Al_{0.28}Cu_{0.69}Ni$ have been successfully synthesized by this technique [49–51].

Mechanical milling (MM) on the other hand is yet another powerful technique to prepare disordered intermetallic phases by inflicting heavy deformation in the ordered phases. During mechanical milling, the ordered polymorphs undergo transformations [52–54] like grain refinement down to the nanocrystalline regime, disappearance of long-range order and decrease in short-range order leading to formation of random solid solution [55]. During these processes the grain size, microstructure, composition and morphology of the phases undergo drastic modifications [56, 57].

15.5.3 Electrolysis Method

Molten salt electrolysis process is an attractive method for synthesis of pure metals and intermetallic phases. This process is being adopted for large-scale production of a number of reactive metals and alloys due to low production cost, easy operational procedure, large batch size and better purity of the products. Electrolysis is highly attractive method for the large-scale production of light rare earth (RE) metals and their alloys [58]. The electrolytes employed in these processes are mostly mixtures of RE metal and alkali or alkaline chlorides. Alkali or alkaline chlorides eutectic mixtures such as LiCl–KCl or NaCl–KCl are the most commonly used electrolytes for electrolytic production of RE metals [59]. **Low current efficiency is**

the major concern for molten salt electrolysis process that limits its application. The current efficiency in the electrowinning of metals is highly dependent on molten salt-electrode reaction kinetics. Large number of studies have been reported on electrochemical investigations of RE (La, Ce, Pr and Nd) chloride electrolytes [60–66]. Sahoo et al. have recently investigated the electrochemical behaviour of RE ions in molten LiCl–KCl and NaCl–KCl electrolytes [67] employing molybdenum and tungsten metal electrodes. For the quantitative production of intermetallic phases by molten salt electrolysis process, information on reaction mechanism and kinetic parameters such as exchange current densities and diffusion coefficient is required.

In electrolysis process, the starting materials generally in the form of chlorides are thoroughly dehydrated by heating the salt mixtures under dynamic vacuum of 0.1 mbar in the temperature range 200–300 °C for sufficiently long time to completely remove adsorbed water and water of crystallization. Similar procedure is followed to dehydrate the electrolyte materials, viz. LiCl–KCl and NaCl–KCl. The chloride mixtures are then melted in a cell which is compatible to the electrolytes. The temperature of the electrolytic cell is measured with a protected thermocouple.

Electrolytic Cell

In the molten salt electrolysis process, pure metal is deposited at the cathode by electrolytic decomposition of its compound dissolved in a molten salt media. The metallic salt which is to be reduced to the metal is known as functional electrolyte whereas the salt mixture which acts as solvent for the metal salt is called as the carrier electrolyte. The carrier electrolytes must have suitable properties like (i) high solubility for the functional electrolyte, (ii) greater stability at working temperature than functional electrolyte, (iii) suitable physiochemical properties like low melting point, high conductivity, low viscosity and low vapour pressure. Alkali /alkaline earth fluorides/chlorides or their mixtures satisfy all above properties.

The electrolysis process for production of reactive metals is generally carried out under the cover of inert gas like argon or nitrogen employing a specially designed electrochemical cell. The electrochemical cell consists of a vacuum tight retort having provisions for placing the reference electrode, counter electrode, working electrode and temperature measurement device, i.e. thermocouple. Electrolytic mixture is placed in the crucible inside a retort and the assembly is equilibrated inside a furnace. Schematic of a typical electrolytic set-up is shown in Fig. 15.7.

Electrochemical measurements are generally carried out on a three electrode system, viz. reference, counter and the working electrode. Cyclic voltammetry plots are obtained by dipping the working electrode to different depths. The current for corresponding depth is measured while keeping all other experimental parameters like temperature, concentration of the electrolyte and value of applied potential constant.

The reduction behaviour of metal ions in LiCl–KCl or NaCl–KCl systems can be understood employing cyclic voltammetry technique. Detailed mechanism of electrolysis method is explained by deposition of La metal as given below. The comparison between the voltammograms for LiCl–KCl electrolyte before and after addition of metal ions can be used to understand the reduction process. Figure 15.8

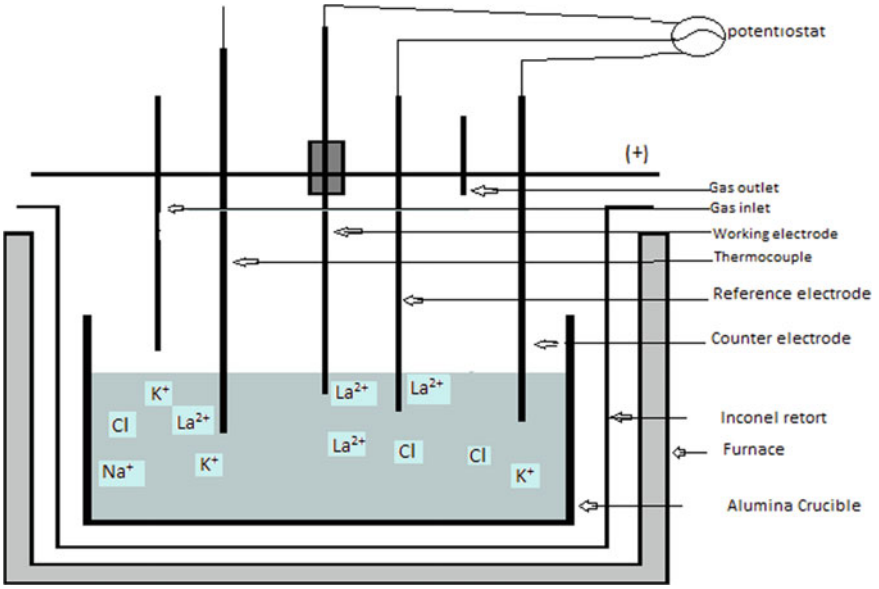

Fig. 15.7 Schematic of the electrochemical set-up used for molten salt electrolysis

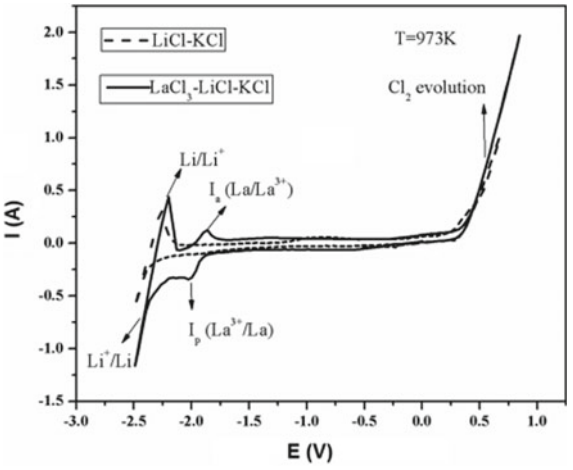

Fig. 15.8 Comparison of the cyclic voltammogram for pure LiCl–KCl melt and $LaCl_3$–LiCl–KCl melt in the potential range of 1 to −2.5 V. Working electrode: molybdenum, apparent electrode area: 0.77 cm^2, Temperature: 973 K, Conc.:2.5×10^{-4} mol/cc, scan rate: 0.1 V s^{-1}

compares the cyclic voltametric curves for eutectic LiCl–KCl melt (dashed curve) and LiCl–KCl melt loaded with $LaCl_3$ salt (solid curve). The anodic discharge observed at 0.5 V is due to the evolution of Cl_2 gas; thus, 0.5 V is the anodic limit of the melt. Similarly, cathodic discharge at −2.4 V is due to the deposition of Li ion which is assigned to the cathodic voltage limit of the melt. The cathodic and the anodic peaks (I_c) and (I_a) are at −2.04 V and −1.87 V, respectively. The observed pair of peaks

is attributed to deposition and dissolution of lanthanum metal. Sharp anodic peak observed in the reverse scan is a signature of dissolution of deposited metal. The product obtained was then characterized by different analytical methods.

15.5.4 High-Temperature Reduction Process

Simultaneous reduction and phase formation through chemical reaction from mixtures of oxides is a shorter route to synthesize intermetallic phases and alloys. The synthesis of intermetallic phases by reduction process involves minimum number of steps and has proven to be economical and environmental friendly. The reduction process is generally carried out by using carbon, hydrogen, natural gas and many electropositive elements. The reducibility of the oxides can be correlated to their thermodynamic stabilities, which in other words depends on the reduction potential of the ions. Ellingham diagram is generally used to fix the reductant and reduction temperature for reducing a given metal oxide to its corresponding metal. Using the Ellingham diagram, the relative ease in reducing a particular metal oxide into metal by another reducing metal can be predicted. For example, calcium metal can be used to reduce all other oxides lying above in the Ellingham diagram to produce corresponding metal. Bavbande et al. [68] reported the reduction of TiO_2 and simultaneous synthesis of TiC using calciothermic reduction of titanium oxide in presence of fine powder of carbon. Other low cost elements like H, C, Mg, and Al are the most important reducing elements widely used for preparing metals and intermetallic phases in the large scale. The carbon in particular is extensively used for the reduction of iron oxide to iron metal in presence of CaO and SiO_2.

15.5.5 Synthesis of Nanoalloys

The physical and electronic properties of alloys in their nanoform differ significantly from those of their respective bulk materials. In nanoalloy, the percentage of atoms present at surface is much high compared to the corresponding bulk alloys. Hence, nanoalloys always have excess surface energy compared to the bulk alloys. This excess surface energy of nanomaterials plays significant role in defining their physical properties [69–72]. The melting temperature of the nanoalloy phase decreases with decrease in their particle size. The quantitative relationships between the particle size and melting temperature have been discussed at length in the literature [73–81]. Similarly, decrease in Curie temperature and magnetic moments, rise in magnetocaloric effect have been reported for many magnetic nanoparticles [82–84]. The band gap in semiconductors is found to increase with decrease of particle size. The band gap becomes very high, when particle size becomes comparable or smaller than the Bohr exciton radius [85, 86]. The nature and particle size of the nanoalloys are highly dependent on mode of synthesis.

Alloys, in general, are prepared by high-temperature synthesis methods employing different types of furnaces as discussed earlier under controlled atmosphere. These alloys are generally obtained in the form of ingots. Synthesis of alloy in the form of nanoparticles with desired properties needs fine control of conditions for synthesis. For such synthesis, a variety of soft chemical methods are adopted, viz. chemical reduction method, micro-emulsion template, laser irradiation, thermal decomposition of metal complexes, molecular beams and biosynthesis techniques.

15.5.5.1 Chemical Reduction Method

Synthesis of nanoalloys by chemical reduction process using reducing agents like ammonia, alcohol, amines, $NaBH_4$, hydrazine, NaH, MgH_2 and super hydrides, i.e. lithium (ethyl)$_2$borohydrides, has reported [87]. For example, Mishra et al. have synthesized Sn and Sn-rich Ni–Sb–Sn nanoalloys [88] using dilute solutions of $SnCl_2$, $SbCl_3$ and $NiCl_2$ employing $NaBH_4$ as reducing agent. In this method, appropriate volume of the above metal chloride solutions was mixed together. The resulting solution was added with required amount of 1 M solution of tri-sodium citrate (chelating reagent). A second stock solution containing 0.5 M $NaBH_4$ at a pH 14 was prepared. The aqueous solutions were cooled to 0 °C. A known volume of metal chloride solution was then added to the solution containing excess amount of $NaBH_4$ drop wise with magnetic stirring. The black suspension formed was stirred for another 30 min in ice water. The resultant suspensions were separately washed and dried to get nanoalloys.

Modified polyol method can also be used for the synthesis of nanoalloys. In this method, polyethylene glycol (PEG) was used as a reducing agent, while oleyl amine and oleic acid act as surfactants. In a typical procedure, metal acetyl acetonate solution mixed with diphenyl ether was heated at 140 °C in the presence of reducing agent and surfactants. The reaction solution was heated isothermally at 140 °C for 10 min and then slowly temperature was raised to 260 °C. The dispersed products in nanoform were then extracted by centrifugation of solution. Monodispersed 3 nm fcc-FePd particles have been synthesized employing this method by Gajbhiye et al. [89].

15.5.5.2 Micro-emulsion Template

Water pool reversed (w/o) micro-emulsion process is another interesting method for the synthesis of tailor made well-defined nanoalloys employing surfactants [90, 91]. The phase formed by dispersing nano-sized droplets of oil in water is called as micro-emulsions, whereas when water droplets are trapped into oil (w/o), the phase formed is called as reversed micro-emulsion. These micro-emulsion droplets are under continuous dynamic fusion or dispersion process resulting in the formation of

smaller or bigger spheres. Metallic nanoparticles are formed by combining micro-emulsion containing a reductant with w/o micro-emulsion containing metal salt solution(s). The reductants can be either hydrazine (N_2H_4) [92] or sodium borohydride ($NaBH_4$) [93]. Catalytically active bimetallic Pd–Ag nanoparticles were synthesized by Ström et al. [94] using the water pools of a reversed micro-emulsion template and methanol as a reducing agent. Pd–Ag nanoparticles were synthesized using w/o reversed micro-emulsions containing 75 wt.% n-heptane, 20 wt.% dioctyl sulfosuccinate sodium salt and 5 wt.% water as surfactant and dilute aqueous solutions of $AgNO_3$, $Pd(NO_3)_2$ containing 2 wt.% metal ion as water phases by the authors.

15.5.5.3 Laser Irradiation Technique

An efficient, versatile, surfactant-free top-down approach for obtaining multi-element nanoalloys (NAs) is by irradiating the material with high-energy intense laser pulses. In this technique, the matrix containing mixture of metal oxides is irradiated with intense laser pulses. The interaction of high-energy photons with the metal oxides causes significant lattice disorder resulting in the migration of metal ions from lattice sites to the surface and subsequently to the plasma plume. Reduction of the metal ions occurs in the plasma plume because electrons and metal ions coexist under extreme pressure and temperature. During this reduction process, nucleation and growth of the alloy occur in a controlled manner. Synthesis of NAs by laser irradiation technique has been investigated by many authors in recent past [95–99]. Machado et al. have reported synthesis of Ag–Bi nanoalloys by irradiating mixture of Ag_2WO_4 and $NaBiO_3$ target with femto second laser without using any reducing agents or solvent [100].

15.5.5.4 Thermal Decomposition of Metal Complexes

Formation of nanomaterials at relatively low temperature is achieved by thermal decomposition of the single molecular precursor. The synthesis of a large number of mono and bimetallic nanoparticles, i.e. low-valent transition metal or noble metals, has been carried out by thermally decomposing the organometallic complexes involving these metal ions [101–104]. Interesting results were obtained when thermolysis was carried out in the presence of stabilizing ligands such as polyvinylpyrrolidone (PVP) [105], where the PVP serves as surface stabilizer, growth modifier, particle dispersant and reducing agent. Many bimetallic NAs, viz. Ru_6Pd_6, $Ru_{10}Pt_2$, Ru_6Sn, $Ru_{12}Cu_4$, Ru_5Pt and $Ru_{12}Ag_4$, have been synthesized by this method. Organometallic complex precursors of these metal ions, typically containing carbonyl and phosphine ligands anchored on silica, were thermally decomposed at 200 °C in vacuum for 2 h [105].

Similarly, binary NAs like Ni–Pd, Ni–Cu, Cu–Pd and Ag–Au phases were synthesized by thermally evaporating the mixture of corresponding metal complexes under vacuum. For example, Kolay et al. have synthesized single phasic nanointermetallic

phase $Pd_{17}Se_{15}$ by thermal decomposition of metal chalcogen complex $[Pd_2(\mu\text{-}Cl)_2\{MesSeC_6H_2(Me_2\text{-}4,6)CH_2\}_2]$ at ~280 °C under inert atmosphere condition [106].

15.5.5.5 Molecular Beams

The molecular beam technique for the synthesis of intermetallic phases generates cluster of atoms. The process involves vaporization of metal atoms, nucleation of these metal atoms to form a cluster nucleus, growth of this nucleus and then aggregation of small clusters to form big clusters. In many molecular beam experiments, a narrow beam of clusters was generated using supersonic and adiabatic expansion of the initially generated clusters. The type of sources to be used for the synthesis metal clusters depends largely on nature of metal atoms. The size distribution of the clusters depends largely on the nature and conditions of the source prevailing during their synthesis.

The metal cluster can be formed by the techniques like pulsed arc vaporization, laser evaporation, sputtering by ions and magnetron methods. Laser beam vaporization technique is very useful for the synthesis of metallic nanoparticles and mixed metallic nanopowders. In the pulsed arc technique, an intense electrical discharge applied between constituent metals of alloy to be synthesized to prepare mono or bimetallic targets. In the ion sputtering technique, high-energy inert gas ions such as Kr^+ or Xe^+ with energy ranging from 10 to 30 keV corresponding to 10 mA currents are bombarded on metal targets to produce intermetallic clusters. Similarly in magnetron sputtering technique, a plasma containing Ar^+ ions is bombarded on a target under magnetic field to form metal cluster. Sketch diagram of molecular beam epitaxy (MBE) experimental technique is shown in Fig. 15.9.

15.5.5.6 Biosynthesis Method

Synthesis of many nanoalloy phases has been reported in the literature by mimicking biological processes [107, 108]. Various biological systems like proteins, polysaccharides, DNA have been successfully deployed for the growth of nanoparticles [109]. Rotello et al. have reported the synthesis of nanoalloy phase, i.e. composites of FePt involving DNA [110]. It is well known that some microbes have the ability to reduce metal ions to the corresponding metal (zero oxidation state) [111]. For example, Macaskie et al. synthesized palladium nanoparticles from Pd(II) aqueous solutions [112] using hydrogenases bacteria. The Pd nanoparticles obtained by this technique exhibited ferromagnetism and high catalytic activity for hydrogenation. This technique can be readily used for bioremediation various types industrial wastes and retrieving precious metals such as gold palladium and platinum.

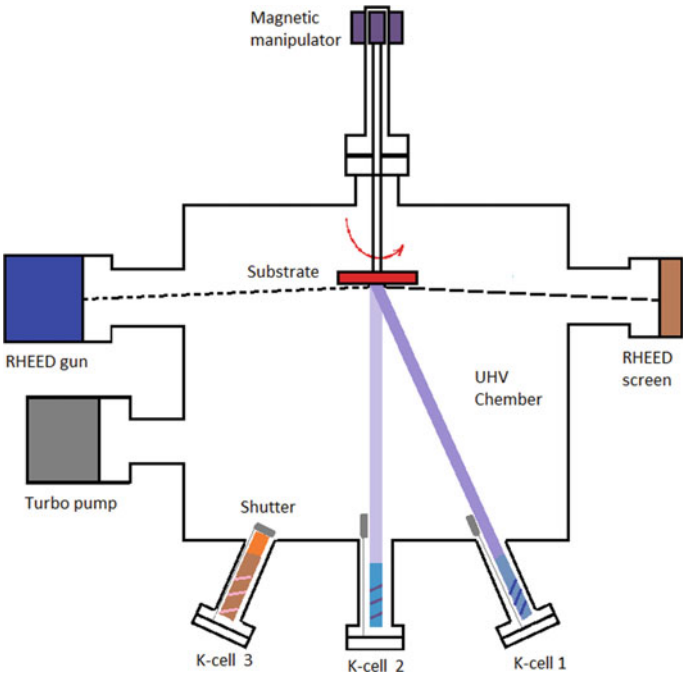

Fig. 15.9 Sketch diagram of molecular beam epitaxy (MBE) experimental technique

15.5.5.7 Radiolysis Method

Radiolysis is yet another modern technique that can be used to synthesize small quantity of metallic cluster from the aqueous solutions containing the metal ions. This method has been employed for the synthesis Ag–Au, Cu–Ag, Pd–Ag, Pt–Ag, Pd–Au, Pt–Au, Cu–Pd and Ni–Pt nanoalloys [113–118]. In this method, water is irradiated by γ-rays to form solvated electrons that subsequently reduce metal ions to metal, which then coalesce to form clusters. When aqueous solution containing two dissimilar metal ions are subjected to radiolysis, metal which nobler is reduced first. Formation of nanoparticles of an alloy phase depends largely on relative concentrations of metal ions, intensity of radiation and kinetics of electron transfer process. The yield of the products is also dependent on nature of ligand molecules attached to the metal ion. Higher dose rates favour mixing over core–shell formation. In some binary alloy systems such as copper-palladium, nickel-platinum and platinum-silver, formation of alloy and ordering of atoms has been reported by exposing the aqueous solution to a moderately low dose rates. Radiolysis can be employed for grafting binary metal clusters such as Pt–Ru, Ni–Ru over titanium or nickel plates. A number of radiolytically alloyed bi and trimetallic clusters (e.g. Cu–Au, Ni–Pt, Ag–Au, Cu–Ag and Cu–Pd–Ag) deposited on silver halide emulsions have shown good activity as development centres for high-resolution photography.

15.5.6 Synthesis of Porous Intermetallic Phases

Porous intermetallics are relatively a new form of phases which are being considered for various technological applications [6, 119, 120]. They have excellent resistance to thermal shock, favourable mechanical properties, high structural strength, superior thermal conductivity, machinability and electrical conductivity. These alloys can be utilized as potential structural and engineering materials [121–125]. The formation of porous intermetallic phases is based on differences in the rate of self-diffusion between elements called Kirkendall effect. The pore structures in such phases have regular pattern which can be controlled during their synthesis [119]. Synthesis of porous intermetallic phases using mixed metal powders is based on self-propagating reaction at high temperature having distinctly different self-diffusion coefficient [126, 127].

15.5.7 Synthesis of HEAs

Synthesis of high-entropy alloys with more than four principal elements with desired properties is quite tricky. During the synthesis the alloy, mixture tends to form a large number of intermetallic phases resulting complicated microstructures. HEAs are generally prepared using arc melting and casting techniques [128, 129]. In addition to these well-established preparation methods, large number of novel synthesis methods is being explored. Some of the new synthesis procedures are described below.

(a) **Ball Milling Method**

In this method, high pure metal powders are mechanically alloyed in a tungsten carbide ball milling set-up. During the mixing process, the ratio of weight of ball to powder is generally maintained high, i.e. 10:1, and some organic solvents like benzene, toluene are used as process controlling agent (PCA) to avoid excess cold welding. The PCA is also acts as protective medium to evade oxidation of alloy phases [130, 131].

In the ball milling process, a rotational speed of the range 300–500 rpm is maintained for several hours to synthesize the products. The resulting powder is hot compacted by hydraulic press and sintered at appropriate temperature under controlled atmosphere. Kumar et al. [132] synthesized $Al_XFe_{1.5}CrMnNi_{0.5}$ ($x = 0.3$, 0.5) HEAs by ball milling method.

(b) **Ion Beam Sputter-Deposition Technique**

Thin films of HEAs can be very well-synthesized employing ion beam sputter-deposition technique. High-energy Ar ions with the energy in the range keV are used to sputter the elements and deposit on the Si substrate. During the ion bombardment process, substrate is kept at a constant desired temperature. A high

vacuum of the order 10^{-10} atm is maintained during deposition of metal atoms. The shape/geometry of target metals exposed to the sputtering ions are suitably adjusted to achieve required atomic compositions. Tunes et al. have reported synthesis and characterization of thin films of quaternary FeCrMnNi phase employing ion beam sputter-deposition method [133].

(c) **Combustion Synthesis Under High Gravity**

In this method, stoichiometric mixture of metals oxides with uniform particle size is mixed with reducing elements like Al by ball milling in organic solvent, i.e. ethanol medium. The dried mixture was then cold pressed into pellet and loaded into graphite crucible mounted on a Ni-based container. The entire assembly is evacuated to 10^{-5} atm and ignited with the W wire with centrifuge. Under the influence of heat of reaction and high gravitational energy, the reaction mixtures melt and the metal in the form liquid get separated from oxide slag due to density difference. This leads to the formation of glass ceramics and HEAs. Li et al. [134] have synthesized HEAs using combustion synthesis under high-gravity.

(d) **Laser Coating Method**

Laser coating is another fast developing surface modification method for the synthesis of HEAs. This technique has distinct advantages of using high-energy density, fast solidification rate. Moreover, coatings of metal vapours by laser vaporization can lead to the fine control of microstructure, strong bonding and intermixing with the substrate [135, 136]. These properties have made the laser coating method, an attractive method for synthesis of HEAs. In this technique, equiatomic metal powder mixtures prepared by mechanically mixing are used as the coating material. The mixed metal powders are then pre-placed on metal substrate by plasma spray to form a powder bed with required thickness. A series of optimization runs with different processing parameters such as radiation wavelength, power, beam diameter and scanning speed are carried out. The coatings are then vacuum sealed and annealed at high temperature to form HEAs. Mina Zhang et al. [137] and Qiu et al. [138] have synthesized TiZrNbWMo and $Al_2CrFeCoCuTiNi_x$ HEAs on Q235 steel by laser coating method.

15.6 Heat Treatment Processes

Heat treatment is a process for improving the properties of materials. The phase purity, crystal structure, mechanical strength, shear modulus, micro-hardness of intermetallic phases largely depend on the nature of heat treatment. Depending on requirements, intermetallic phases are either cooled slowly or quenched from high temperature to the room temperature. Often these phases are annealed for sufficiently long time at temperatures lower than their melting points. Some of the common heat treatment processes are listed below.

15.6.1 Annealing

Annealing is a heat treatment process in which metal or alloy phases heated at an appropriate temperature for a certain period and then very slowly cooled in the furnace. The purpose of annealing is to alter the physico-chemical properties of a material through heat treatment. Annealing reduces micro-hardness of the intermetallic phases and improves their plasticity and ductility. It facilitates the machinability, relieves the internal stresses and prevents deformation or cracking of alloy phases. In addition, annealing process homogenizes the chemical composition, reorganize and refine the grain boundary. Depending on requirements, annealing can be of following types: complete annealing, diffusion annealing, spheroidizing annealing, recrystallization annealing, stress relief annealing and process annealing.

In complete annealing, the phases are heated above the upper critical temperature and then slowly furnace cooled to room temperature. For example, hypoeutectoid steel is heated above the critical temperature and then furnace cooled very slowly, where the austenite steel is transformed to the coarse pearlite phase within 50 °C of eutectoid temperature. As the complete annealing requires prolonged heat treatment, the process is quite expensive. The time for the transformation can be curtailed by transferring austenitized components to an isothermal furnace maintained below its eutectoid temperature.

In spheroidizing annealing, the material is heated just below the critical temperature (temperature at which austenite begins to form during heating) or thermal cycled in a narrow temperature interval around the eutectoid temperature in Fe–C system. By this process, the cementite lamellae in pearlite phase tends to become spheres and thereby reduces its surface area. On prolonged heat treatment, spheroidized particle become fewer in number and more widely spaced. This process softens the alloy phases. For example, in carbon and low alloy structure steel, the optimum machinability corresponds to the sample having 50% spheriodized and 50% lamellar in the microstructure.

15.6.2 Sintering

Sintering is an important step in the processing of intermetallic phases processing, where the particles bind together by heating at a temperature lower than the melting points (generally 2/3rd of its melting temperature) of the species. Sintering takes place by the mass transport of atoms or ions through small range of distance across the grain boundaries. The model describing the sintering process was first proposed by Frenkel [128] and later by many authors.

Pressure less sintering is a form of material transport involving diffusion of labile species influenced by surface energy. Its magnitude ranges from 0.1 to a few J m^{-2}. The diffusion in sintering can be theoretically estimated or experimentally determined. The technique for visualization and measurement of surface energy is known

as *zero-creep* technique. Depending on volume and dispersion of porosity within a sample, the excess surface energy can be in the range 0.1–100 J mol^{-1}. The energy at the grain boundary usually imparts back-driving force at beginning of sintering, when fresh grain boundaries are created and the particle contacts are filled. As the grain-boundary energy is smaller by a factor of three compared to the surface energy, this makes back-driving effect less dominant for sintering. Hoge and Pask [130] pointed out that the material transport taking place during sintering can cease due to local equilibrium between grain boundary. If γ is the isotropic surface energy per unit area, ΔA is the change in surface area, r_1 and r_2 are the radii of curvature before, and after sintering, the ratio of change in energy (ΔE) to change in volume (ΔV) can be expressed as:

$$\frac{\Delta E}{\Delta V} = \gamma \frac{\Delta A}{\Delta V} = \gamma \left(\frac{1}{r_1} - \frac{1}{r_2}\right)$$

The ratio $\frac{\Delta E}{\Delta V}$ corresponds to the thermal stress σ, generated during sintering process which can be represented by Laplace equation $\sigma = \gamma(\frac{1}{r_1} - \frac{1}{r_2})$. The stress which is tensile for concave and compressive for convex creates stress gradient between interior particle and the particles at the neck. Due to the stress gradient, the metal atom is transported though surface and grain boundaries. The chemical potential developed due to concentration gradient is usually much higher than the surface energy. This is evident from the numerical values of molar surface energy and the enthalpy of mixing or formation enthalpy of intermetallic phases. The chemical potential which plays a major role in most of the intermetallic systems can be clearly differentiated from ideal surface energy controlled sintering process.

In practice, high temperature is required to have appreciable sintering rates. In addition, sintering rate is dependent on factors like particle size, non-stoichiometry, presence of impurity, enveloping gas atmosphere, magnetic and electric field, etc. Therefore, it is necessary to control the experimental conditions to obtain the desired products. Numerous experimental methods are available to monitor the sintering process and to establish the mechanism of sintering. Table 15.4 gives summary of frequently used techniques for sintering studies.

15.6.3 Recrystallization

In recrystallization process, the deformed grains are slowly replaced by an un-deformed grains. The process continues until the entirely deformed grains are replaced with fresh un-deformed grain. Recrystallization annealing is generally carried out at a subcritical temperature. This heat treatment process removes the heavy plastic deformation. The rerystallization annealing is effective when applied to harden and recrystallize the structure to form new ferrite grains. Rerystallization

Table 15.4 Techniques for sintering studies

Methods	Measured quantity	Remarks
Dilatometry	Change in length	Shrinkage may vary in different directions. Relative precision is of the order 10^{-6} of sample length
Buoyancy	Density	Impregnations of pore sealing necessary. Relative precision is of the order 10^{-3} of sample length
Indirect method	Physical properties	Measures change in physical properties which can be correlated to the degree of sintering
Quantitative microscopy	Direct geometrical parameters	Tedious, but most effective method for complete characterization of sintering process

normally reduces the strength, hardness and at the same time increases the ductility of material.

Stress relieving is a process in which metal or alloys are heated to a predetermined temperature below its lowest transformation temperature followed by natural cooling. In this process, the annealing recovery of alloys occurs without recrystallization. The primary purpose of the stress relief cooling is to relieve stresses that have been formed due to forming, straightening, machining or rolling. Process annealing is a subcritical treatment given to metals to soften them during mechanical processing. It may or may not involve full recrystallization of the cold work metals.

Rerystallization of intermetallics is a widely used process, where the orientation of the crystal is altered by thermal process, producing materials with high grain boundaries angle. New grain structures inside the deformed materials are formed via creation and movement of high angle grain boundaries (angle is more than 10°–15° mis-orientation) facilitated by the excess deformation energy. The nucleation grain growth takes place at the grain boundary of deformed material. The grain starts growing at the cost of deformed structure until they get completely consumed. The grain growth is uniform in all direction that results in uniform size of the crystal. Such type of recrystallization is called primary crystallization.

However, if the grain growth is restricted to minority boundaries, where grain growth is large compared to others the process, this results in non-uniform distribution of grain size. This is termed as secondary recrystallization, which may also called as coarsening and exaggerated grain growth. *Secondary recrystallization* takes place when there is selective grain growth taking place along {110} and {001} crystal plains, at the expense of primary recrystallized grains.

In many cases, boundaries of deformed structures migrate over a short distance leaving their wake crystal in the same geometric orientation as that of the growing crystal. The regions covered by the grain boundary are considerably free of dislocations. Such phenomena are known as strain-induced migration of grain boundary. Recrystallization occurring during deformation is called dynamic recrystallization,

whereas the event taking place after deformation is called static recrystallization. In addition, there can be discontinuous recrystallization, where new distinct grains are nucleated and grow, not in a continuous manner.

The mechanisms by which recrystallization takes place are quite complex and have not been fully understood. Based on a large number of experimental information on primary crystallization, over several years of research, various empirical laws of recrystallization have been proposed. The statements of these empirical laws are: (a) Initiation of crystallization process requires a minimum critical concentration of deformation, (b) the rate of nucleation and growth of recrystallized grains depends on annealing temperature, (c) recrystallization necessitates a minimum temperature for the initiation atomic movement, (d) the final grain size largely depends on extent of deformation and to a smaller extent on annealing temperature.

15.7 Strategies for Improving Ductility of Ordered Intermetallics

Defect free ordered intermetallic phases are widely envisaged as potential high-temperature structural materials. In conventional alloys, the yield strength generally decreases with temperature, whereas in ordered intermetallic phases, it increases with increasing temperature. The long-range ordered intermetallic phases have stronger bond strength and closer packing of atoms. This helps in restricting atom movement which leads to the better creep resistance properties of intermetallics [130]. However, in practice, most of the intermetallic phases are brittle and exhibit low tensile ductility at room temperature. For this reason, their use as structural materials [134] is severely restricted.

A lot of research work has been published to explain and understand the mechanism of embrittlement in intermetallic phases. The intrinsic and extrinsic factors that cause embrittlement in intermetallic phases have been identified which has led to the substantial improvement in ductility of ordered intermetallic phase. The processes like controlling crystal structures, engineering the grain boundary, tuning the chemistry of compound formation, removing environmental embrittlement, optimizing the microstructure and controlling the phase stability are among the strategies adopted for the improvement of ductility of intermetallic phases.

Low symmetry crystal structure is one of the important impediments for poor tensile ductility at room temperature in many ordered intermetallic phases. This is due to presence of inadequate number of independent slip systems. Hence, ductility in these phases can be improved considerably by changing the crystal structure from low symmetry to high symmetry by modifying the composition. The crystal structure on the other hand can be modified by changing e/a (number of valence electron to number of atom). For example, in ordered A_3B type intermetallic, crystal structure can be changed from predominantly cubic to predominantly hexagonal stacking by changing the e/a value.

15.8 Applications of Intermetallic Phases

15.8.1 High-Temperature Alloys

15.8.1.1 Structural Alloys

High-temperature alloys are being used in large number of industries including aerospace, steel, chemical, petrochemical, nuclear and thermal power production, etc. Air craft turbine blades which experience extreme pressure and temperature conditions use nickel-based super alloys. Heat exchangers of coal-based power plants and nuclear power plants use ferritic steels, viz. 2.25Cr–lMo, niobium stabilized 2.25Cr–lMo and modified 9Cr–lMo (Grade 91) high-temperature alloys. Inter granular stress, fatigue, pitting and erosion corrosion are the major factors which create defects in these alloys. The addition of carbon in Fe, Ni and Co-based alloys forms various types of carbide precipitates, e.g. $M_{23}C_6$, MC, M_6C, M_7C_3 (M is refractory element, viz. Mo, W, V, Nb or Cr), which contribute to the strengthening of these alloys [139]. Oxide dispersion strengthened ferritic steels (ODS) show excellent performance in high-temperature conditions. In this type of alloy, oxide particles such as Y_2O_3, ThO_2 or ZrO_2 are dispersed homogeneously in the alloy matrix. These oxide particles do not get coarsen at high temperatures due to their extremely low solubility in the matrix. Other examples of high-temperature alloys used extensively in various industries are: Inconel, Hastelloy etc.

15.8.1.2 Heating Elements

Alloys are generally preferred as heating elements over the constituent metals due to higher electrical resistance. For example, $MoSi_2$, is primarily used as heating element instead of pure molybdenum. At high temperature, $MoSi_2$ forms a passive silicon dioxide layer that protects the heating element from getting oxidized further. The furnace with $MoSi_2$ heating element can be operated up to 2000 °C and can be used for sintering and heat treatment processes.

For low temperature applications (300–400 °C) copper-nickel (CuNi), alloys are used as heating element. Most of the resistive furnaces use an alloy containing 80% nickel and 20% chromium (nichrome 80/20) in the form of wire, ribbon or strip as heating element. Nichrome 80/20 (melting point 1400 °C) forms a protective layer of chromium oxide on the surface when heated for the first time that prevents it from further oxidation. Maximum temperature of operation of nichrome is up to 900–1000 °C. NiCr-based alloys have very good mechanical properties even at high temperatures as well as good oxidation and corrosion properties. Tubular (sheathed) elements used for heating purpose consist of a fine nichrome resistance heating coil located inside the metallic tube (SS alloy or inconel). Magnesium oxide powder provides insulation between nichrome and metallic tube. Another alloy Kanthal (FeCrAl) in the form of wire or strip is commonly employed in heating devices

such as furnaces for industrial heating, toasters and hair dryers. They can be used till 1400 °C safely.

15.8.2 Super Alloys

Super alloys are a group of nickel, nickel–iron based alloys. They play an important role in high-temperature applications. Nickel-based super alloys have proven to be the alloy of choice for various technological applications. The properties of these super alloys can be tuned as per the demand by alloying with other elements like iron, chromium, cobalt, molybdenum, aluminium, silicon, titanium, tungsten, tantalum, yttrium, vanadium, carbon, boron, etc. [140]. The γ'-Ni_3(Al, Ti) phase present in the nickel-based super alloys prevents dislocation motion and increases its creep resistance. Addition of aluminium and titanium promotes the formation of γ' phase. The size of this γ' phase can be controlled precisely by precipitation strengthening through heat treatment.

Due to their high strength, structural reliability and good oxidation resistance properties at high temperature, nickel-based super alloys are extensively used in combustion chambers and exhaust section of an aircraft. They are also commonly used in pressure vessels, rocket engines, gas turbine blades, turbine discs, etc. Ni-based super alloys have exceptional creep resistance and stress-rupture properties. Nickel-based alloys (36% Ni) are also employed for construction of measuring devices, components for laser sources, tanks and piping for liquefied gas storage. However, high cost of these super alloys is major constraint in meeting the demand. It is, therefore, required to emphasize on new methods for their preparation and processing.

15.8.3 Soft Alloys

Brass, an alloy of zinc and copper, is a perfect example of soft alloy. In this alloy, the amount of copper and zinc can be varied to achieve desired material properties. Due to its bright gold like appearance, this alloy is also employed for decorative purposes. Brass is extensively used for making locks, gears, bearings, zippers, ammunition casings and valves, etc. The brass is often alloyed with 2 atom % lead to enhance its machinability. Similarly, small amount of aluminium is added to brass to make it more strong and corrosion resistant.

Brass is used for the construction of acoustic resonators in long musical instruments, viz. harmonica, organ pipes, electric guitars, bells, saxophones, etc. Depending on the relative amount of copper and zinc, brass can be of red and yellow colour. DZR-brass (dezincification resistant) is excellent in water boiler systems. To further reduce the rate of corrosion in water boilers, about 0.03 atom % arsenic is added.

15.8.4 Superconducting Alloys

Niobium family of intermetallic compounds such as NbTi, Nb_3Sn, NbZr, Nb_3Al, Nb_3Ge are the examples most commonly used superconductors. They exhibit zero resistance at temperatures below critical temperatures. Most superconducting alloys come under the category of type II superconductors. Among these, only a few alloys have high critical fields. The critical field limits the value of critical current.

Nb–Ti alloys are used in fabrication of super magnets which are capable of generating magnetic fields up to about 10 teslas [141]. Hence, they are used in magnetic resonance imaging, superconducting magnetic energy storage, nuclear magnetic resonance and particle accelerators. In MRI machines, powerful magnetic field is employed to create radio signal inside the body, to generate pictures of various organs such as bones and tissue. Nb–Ti containing super magnets are being in use in bubble chamber in Argonne National Laboratory (ANL), tevatron accelerator in Fermilab, relativistic heavy ion collider, large hadron collider particle accelerator, alpha magnetic spectrometer-international space station.

15.8.5 Magnetic Alloys

Permanent magnets are widely used in motors, dynamos, loud speaker, etc. In recent times, neodymium-based magnets like $Nd_2Fe_{14}B$ are in the focus of attention due to their comparable magnetic strength and low cost. Magnets are principal component of electric generators that convert mechanical energy into electricity. Magnets are used in mines for separating useful magnetic ores from crushed rock. Similarly in food processing industries, magnets are used for removing small magnetic metal pieces from food grains and other food materials. Magnets also find extensive applications in house hold equipments like refrigerator, paper holder, bottle openers, etc. Magnetic needle compass has been used for centuries for navigation. The magnetic strip on a credit card is used to store data. The electric motors inside the washing machines, vacuum cleaners, blenders work by magnetic principles.

15.8.6 Electronic/Electric Alloys

Alloy applications in electronic industry range from very large part to nanoscale. In most of the key components of electronic industry, nickel-containing materials are used. Mostly nickel-based alloys, i.e. nickel irons, stainless steels, nickel-containing copper alloys find their application in electronic industry. Commercially pure nickel is an exceptional choice for electronic applications due to its superb mechanical properties, good thermal and electrical conductivity and excellent corrosion resistance. These alloys find applications as anode material, lead wires and battery casings.

Nickel alloys are used as aerospace electrical components, sensitive wiring in electronic industry, construction of electrode and grids for electronic valves, battery cases, magnetostrictive transducers and electrical resistance thermometers.

ASTM F15 ALLOY (Ni 29%, Co 17%, Fe 53%, C 0.02%, Si 0.20%, and Cr 0.20%) finds its extensive use in telecommunications industry. This includes wavelength add/drop multiplexer (WADM) modules, pump lasers, transistors, amplifiers, modulators, diodes, attenuators, image sensors, integrated and hybrid circuits. This alloy is used in cables which are used for transmitting voice, video and internet data. This is most popular alloy used to create metal to glass hermetic seals because of its controlled expansion property.

15.8.7 Biological Alloys

Till 1940, stainless steel and cobalt-chromium alloys (Vintallium) [142] were mostly used for surgical implants. There was continuous search for better alloy for biomedical applications. The most desired properties of alloys to be used for fabrication of implants are: biocompatibility and corrosion resistance. Titanium, because of, its favourable mechanical and biocompatibility character, has been the most desired material for biological applications. Ti and Ti-based alloys are employed in implant devices such as artificial hip and knee joints, artificial heart, bone plate, screws for fracture fixation, cardiac valve prostheses, pace makers for replacing the failed hard tissue. Ti–6Al–4 V alloy has been used extensively for biomedical applications. However, these alloys cannot be used for permanent implant applications because of toxic effect due to released vanadium and aluminium [143]. For this reason, alloys free from Al and V, viz. Ti–13Nb–13Zr, Ti–12Mo–6Zr, have been introduced for implant applications.

Properties of Ti alloys, i.e. low electronic conductivity, highly corrosion resistant, thermodynamically stable at physiological pH values and low ion formation tendency in aqueous environments, comparable dielectric constant to that of water make these alloys most desirable for biomedical applications. Titanium alloys are also used for dentistry devices, viz. dental implants, crowns, bridges, over dentures, etc. [144].

15.9 Conclusions

Inter metallic phases are extensively used in a wide variety of applications due to their high specific strength, high corrosion resistance and good ductility. The properties of intermetallic phases are largely governed by the nature of their synthesis and the level of impurity phases present and can be tuned by varying the compositions and experimental conditions like heat treatment procedure and the reaction environment. In this chapter, detail classifications of different types of intermetallic phases with their structure have been discussed. The role of phase diagram in the synthesis of

intermetallic phases in pure form has been discussed. Different synthesis approaches like heating under control atmosphere, mechanical alloying, electrolytic method and chemical reduction methods have been elaborated. Synthesis of various types alloy phases in the nanoform by chemical reduction, micro-emulsion, laser irradiation, thermal decomposition, molecular beam deposition and biosynthesis methods have been described. Various heat treatment methods such as annealing, sintering, recrystallization and zone refining for processing as of intermetallic phases have been presented. At the end, applications of intermetallic phases as high-temperature alloys for structural and heating elements, as soft alloys, electrical or electronic alloys and biomedical alloys have been presented.

References

1. Mehrer H (2007) Diffusion in solids: fundamentals, methods, materials, diffusion- controlled processes. In: Springer series in solid-state sciences, vol 155. Springer, Berlin, Heidelberg, New York
2. Westbrook JH (1993) Structural intermetallics. In: Dariola R, Lewendowski JJ, Liu CT, Martin PL, Miracle DB, Nathal MV (eds) TMS, Warrendale, PA, pp 87–96
3. Sauthoff G (1995) Intermetallics. Wiley – VCH Verlag GmbH, Weinheim, Germany
4. Horton JA, Liu CT, George EP (1995) Shape memory properties of a two-phase NiAl plus Fe alloy. Mat Sci Eng A,192–193:873–880
5. Pike LM, Anderson IM, Liu CT, Chang YA (2002) Site occupancies, point defect concentrations, and solid solution hardening in B2 (Ni, Fe)Al. Acta Mater 50:3859–3879
6. He YH, Jiang Y, Xu NP, Zou J, Huang BY, Liu CT, Liaw PK (2007) Fabrication of Ti–Al micro/nanometer-sized porous alloys through the Kirkendall effect. Adv Mater 19:2102–2106
7. Cahn RW (1996) Multiphase intermetallics. In: Cahn RW, Evans AG, McLean M (eds) High-temperature structural materials. Springer, Dordrecht, pp 79–91
8. Adeva P (1999) Revista de la Asociacion Espanola de Cientificos 1:1
9. Kurnakov SFZNS, Zasedatelev M (1916) J Inst Met 15:305
10. Aoki K, Izumi O (1979) Flow and fracture behaviour of Ni3(Al·Ti) single crystals tested in tension. J Mater Sci 14:1800–1806
11. He Y, Liu Y, Huang B, Qu X, Lei C (1994) Grain refiner for TiAl intermetallic compounds. J Mater Sci Technol 10:205–208
12. Nieh TG, Wadsworth J, Liu CT (2011) Mechanical properties of nickel beryllides. J Mater Res 4:1347–1353
13. Takeyama M, Liu CT (1989) Grain-boundary contamination and ductility loss in boron-doped Ni3Al. Metall Trans A 20:2017–2023
14. Bewlay BP, Weimer M, Kelly T, Suzuki A, Subramanian PR (2013) The science technology, and implementation of TiAl alloys in commercial aircraft engines. MRS Proc 1516:49–58
15. Xiao CB, Han YF, Li SS, Song JX (2003) Development of directionally solidified Ni-Al-Mo-B-Y alloy IC6A. Mater Sci Technol 19:1677–1680
16. Jackson AG (1991) Handbook of Crystallography: for electron microscopists and others. Spinger, New York
17. Li Z, Mao H, Korzhavyi PA, Selleby M (2016) Thermodynamic re-assessment of the Co–Cr system supported by first-principles calculations. Calphad 52:7
18. Schmid G (1999) Metal clusters in Chemistry, Braunstein P, Oro LA, Raithby PR (eds), vol 3, pp 1325
19. Andrews MP, O'Brien SC (1992) Gas-phase "molecular alloys" of bulk immiscible elements: iron-silver (FexAgy). J Phys Chem 96:8233–8241

20. Yeh JW (2006) Recent progress in high-entropy alloys. Ann Chim Sci Mat 31:633–648
21. Tong C-J, Chen M-R, Yeh J-W, Lin S-J, Chen S-K, Shun T-T, Chang S-Y (2005) Mechanical performance of the AlxCoCrCuFeNi high-entropy alloy system with multiprincipal elements. Metall Mater Trans A 36:1263–1271
22. Herbst JF (1993) Permanent magnets. Am Sci 81:9
23. Li XZ (2009) Thermodynamic analysis of the simple microstructure of AlCrFeNiCu high-entropy alloy with multi-principal elements. Acta Metall Sinica 22:219–224
24. Tong C-J, Chen Y-L, Yeh J-W, Lin S-J, Chen S-K, Shun T-T, Tsau C-H, Chang S-Y (2005) Microstructure characterization of AlxCoCrCuFeNi high-entropy alloy system with multiprincipal elements. Metall Mater Trans A 36:881–893
25. Senkov ON, Wilks GB, Miracle DB, Chuang CP, Liaw PK (2010) Refractory high-entropy alloys. Intermetallics 18:1758–1765
26. del Grosso MF, Bozzolo G, Mosca HO (2012) Determination of the transition to the high entropy regime for alloys of refractory elements. J Alloys Comp 534:25–31
27. Chun Ng, Guo S, Luan J, Shi S, Liu CT (2012) Entropy-driven phase stability and slow diffusion kinetics in an $Al_{0.5}$CoCrCuFeNi high entropy alloy. Intermetallics 31:165–172
28. Tsai M-H (2013) Physical properties of high entropy alloys. Entropy 15:5388–5345
29. Cheng K-H, Lai C-H, Lin S-J, Yeh J-W (2006) Recent progress in multi-element alloy and nitride coatings sputtered from high-entropy alloy targets. Ann Chim Sci Mat 31:723–736
30. Chen Y Y, Duval T, Hong U T, Yeh J W, Shih H C, Wang L H, Oung J C (2007) Corrosion properties of a novel bulk Cu0.5NiAlCoCrFeSi glassy alloy in 288 °C high-purity water. Mater Lett 61:2692–2696
31. Singh S, Wanderka N, Murty BS, Glatzel U, Banhart J (2011) Decomposition in multi-component AlCoCrCuFeNi high-entropy alloy. Acta Mater 59:182–190
32. Tsai M-H, Yeh J-W, Gan J-Y (2008) Diffusion barrier properties of AlMoNbSiTaTiVZr high-entropy alloy layer between copper and silicon. Thin Solid Films 516:5527–5530
33. Tsai M-H, Wang C-W, Tsai C-W, Shen W-J, Yeh J-W, Gan J-Y, Wu W-W (2011) Thermal stability and performance of NbSiTaTiZr High-entropy alloy barrier for copper metallization. J Electrochem Soc 158:H1161
34. Tsai M-H, Yeh J-W (2014) High-entropy alloys: a critical review. Mater Res Lett 2:107–123
35. Williams SH (2009) PhD thesis, University of Iowa
36. Azami F (2005) Adv Mater Process 163:37
37. Lee S-H, Jung D-H, Jung S-J, Hong S-C, Lee J-J (2006) Low temperature deposition with inductively coupled plasma. Z Met 97:475–479
38. Yeh CL, Yeh CC (2005) Preparation of CoAl intermetallic compound by combustion synthesis in self-propagating mode. J Alloy Compd 388:241–249
39. Pithawalla YB, El Shall MS, Deevi SC (2000) Synthesis and characterization of nanocrystalline iron aluminide particles. Intermetallics 8:1225–1231
40. Rajan S, Shukla R, Kumar A, Vyas A, Brajpuriya R (2014) Structural and magnetic evolution of ball milled nanocrystalline Fe-50 at.% Al alloy. Int J Mater Res 106:114–126
41. Khan RBS, Vyas A, Kumar A (2015) Int J Sci Res 4:1243
42. Suryanarayana C (2005) Mechanical alloying and milling. Adv Mater 17:2893–2894
43. Suryanarayana C (2001) Mechanical alloying and milling. Prog Mater Sci 46:1–184
44. Suryanarayana C (1996) Recent advances in the synthesis of alloy phases by mechanical alloying/milling. Met Mater 2:195–209
45. Simhadri D (2003) Determination of phase fraction, lattice parameters and crystallite size in mechanically alloyed Fe-Ni powders. University of New Orleans Theses and Dissertations. 56
46. Azzaza MBS, Aliofkhazraci M (eds) (2016) Hand book of mechanical nanostructuring, 1st edn. Wiley-VCH Verlag GmbH & Co, KGaA
47. Chin ZH, Perng TP (1996) Amorphization of Ni-Si-C ternary alloy powder by mechanical alloying. Mater Sci Forum 235–238:121–126
48. Maziarz W, Dutkiewicz J, Senderski J (2004) Processing of nanocrystalline FeAlX (X = Ni, Mn) intermetallics using a mechanical alloying and hot pressing techniques. J Mater Sci 39:5425–5429

49. Chen D, Chen J, Yan H, Chen Z (2007) Synthesis of binary and ternary intermetallic powders via a novel reaction ball milling technique. Mater Sci Eng A 444:1–5
50. Chen D, Chen Z, Cai J, Chen Z (2008) Preparation of W-Al intermetallic compound powders by a mechanochemical approach. J Alloys Compd 461:L23–L25
51. Chen D, Chen G, Ni S, Chen G, Yan H, Chen Z (2008) Phase formation regularities of ultrafine TiAl, NiAl and FeAl intermetallic compound powders during solid–liquid reaction milling. J Alloys Compd 457:292–295
52. Bakker H, Zhou GF, Yang H (1995) Mechanically driven disorder and phase transformations in alloys. Prog Mater Sci 39:159–241
53. Negri D, Yavari AR, Deriu A (1999) Deformation induced transformations and grain boundary thickness in nanocrystalline B2 FeAl. Acta Mater 47:4545–4554
54. Yavari AR (1997) Ann Chim Sci Mater 22
55. Yavari AR (1993) Reordering kinetics and magnetic properties of mechanically disordered nanocrystalline Ll2-type Ni3Al + Fe alloys. Acta Metall Mater 41:1391–1403
56. Benameur T, Yavari AR (2011) Disordering and amorphization of L12-type alloys by mechanical attrition. J Mater Res 7:2971–2977
57. Yavari AR, Gialanella S, Benameur T, Cahn RW, Bochu B (2011) On the bcc, fcc, hcp, and amorphous polymorphs of Zr3Al. J Mater Res 8:242–244
58. Singh S, Pappachan AL, Gadiyar HS (1986) Electroproduction of cerium and Ce-Co alloy. J Less Common Metals 120:307–315
59. Singh S, Pappachan AL (1990) Electrodeposition of lanthanum metal from fused chloride bath. Bull Electrochem 6:97–100
60. Lantelme FDR, Cartailler T, Berghoute Y, Hamdani M (2001) Physicochemical properties of lanthanide and yttrium solutions in fused salts and alloy formation with nickel. J Electrochem Soc 148:C604
61. Masset P, Konings RJM, Malmbeck R, Serp J, Glatz J-P (2005) Thermochemical properties of lanthanides (Ln=La,Nd) and actinides (An=U,Np,Pu,Am) in the molten LiCl–KCl eutectic. J Nucl Mater 344:173–179
62. Fusselman SP (1999) Thermodynamic properties for rare earths and Americium in pyropartitioning process solvents. J Electrochem Soc 146:2573
63. Gao F, Wang C, Liu L, Guo J, Chang S, Chang L, Li R, Ouyang Y (2009) Electrode process of La(III) in molten LiCl-KCl. J Rare Earths 27:986–990
64. Vandarkuzhali S, Gogoi N, Ghosh S, Prabhakara Reddy B, Nagarajan K (2012) Electrochemical behaviour of LaCl3 at tungsten and aluminium cathodes in LiCl–KCl eutectic melt. Electrochimica Acta 59:245–255
65. Tang H, Pesic B (2014) Electrochemical behavior of LaCl3 and morphology of La deposit on molybdenum substrate in molten LiCl–KCl eutectic salt. Electrochim Acta 119:120–130
66. Castrillejo Y, Bermejo MR, Pardo R, Martínez AM (2002) Use of electrochemical techniques for the study of solubilization processes of cerium–oxide compounds and recovery of the metal from molten chlorides. J Electroanal Chem 522:124–140
67. Sahoo DK, Satpati AK, Krishnamurthy N (2015) Electrochemical properties of Ce(iii) in an equimolar mixture of LiCl–KCl and NaCl–KCl molten salts. RSC Adv 5:33163–33170
68. Bavbande DV, Mishra R, Juneja JM (2004) Studies on the kinetics of synthesis of TiC by calciothermic reduction of TiO2 in presence of carbon. J Thermal Anal Calorimetry 78:775–780
69. Ahmed HM, Viswanathan NN, Seetharaman S (2016) Gas-condensed phase reactions – a novel route to synthesize slloys and intermetallics involving refractory metals. Mater Today Proc 3(9):2951–2961
70. Gleiter H (1989) Nanocrystalline materials. Prog Mater Sci 33:223–315
71. Dingreville R, Qu J, Mohammed C (2005) Surface free energy and its effect on the elastic behavior of nano-sized particles, wires and films. J Mech Phys Solids 53:1827–1854
72. Ningthoujam RS, Sudhakar N, Rajeev KP, Gajbhiye NS (2002) Electrical resistivity study of La, B doped nanocrystalline superconducting vanadium nitride. J Appl Phys 91:6051–6056

73. Sambles JR, Blackman M (1971) An electron microscope study of evaporating gold particles: the Kelvin equation for liquid gold and the lowering of the melting point of solid gold particles. Proc Roy Soc London. A. Math Phys Sci 324:339–351
74. Goldstein AN, Echer CM, Alivisatos AP (1992) Melting in semiconductor nanocrystals. Science 256:1425
75. Sheng HW, Lu K, Ma E (1998) Melting of embedded Pb nanoparticles monitored using high-temperature in situ XRD. Nanostruc Mater 10:865–873
76. Peters KF, Cohen JB, Chung Y-W (1998) Melting of Pb nanocrystals. Phys Rev B 57:13430–13438
77. Cleveland CL, Luedtke WD, Landman U (1999) Melting of gold clusters. Phys Rev B 60:5065–5077
78. Pawlow P (1909) Ober die Abhängigkeit des Schmelzpunktes von der Oberflächenenergie eines festen Körpers (Zusatz.). Z Phys Chem 65:545–548
79. Buffat P, Borel JP (1976) Size effect on the melting temperature of gold particles. Phys Rev A 13:2287–2298
80. Borel JP (1981) Thermodynamical size effect and the structure of metallic clusters. Surf Sci 106:1–9
81. Dick K, Dhanasekaran T, Zhang Z, Meisel D (2002) Size-dependent melting of silica-encapsulated gold nanoparticles. J Am Chem Soc 124:2312–2317
82. Du YW, Xu MX, Wu J, Shi YB, Lu HX, Xue RH (1991) Magnetic properties of ultrafine nickel particles. J Appl Phys 70:5903–5905
83. Zhang D, Klabunde KJ, Sorensen CM, Hadjipanayis GC (1998) Magnetization temperature dependence in iron nanoparticles. Phys Rev B 58:14167–14170
84. Shir F, Yanik L, Bennett LH, Della Torre E, Shull RD (2003) Room temperature active regenerative magnetic refrigeration: magnetic nanocomposites. J Appl Phys 93:8295–8297
85. Castillo JD, Rodríguez VD, Yanes AC, Méndez-Ramos J, Torres ME (2005) Luminescent properties of transparent nanostructured Eu3+doped SnO2–SiO2 glass-ceramics prepared by the sol–gel method. Nanotechnology 16:S300–S303
86. Yanes AC, Del Castillo J, Torres M, Peraza J, Rodríguez VD, Méndez-Ramos J (2004) Nanocrystal-size selective spectroscopy in SnO2:Eu3+ semiconductor quantum dots. Appl Phys Lett 85:2343–2345
87. Yang R, Huang J, Zhao W, Lai W, Zhang X, Zheng J, Li X (2010) Bubble assisted synthesis of Sn–Sb–Cu alloy hollow nanostructures and their improved lithium storage properties. J Power Sources 195:6811–6816
88. Mishra R, Zemanova A, Kroupa A, Flandorfer H, Ipser H (2012) Synthesis and characterization of Sn-rich Ni–Sb–Sn nanosolders. J Alloys Compounds 513:224–229
89. Gajbhiye NS, Sharma S, Ningthoujam RS (2008) Synthesis of self-assembled monodisperse 3 nm FePd nanoparticles: phase transition, magnetic study, and surface effect. J Appl Phys 104:123906
90. Holmberg K (2004) Surfactant-templated nanomaterials synthesis. J Colloid Interf Sci 274:355–364
91. Holmberg K, Jönsson B, Kronberg B, Lindaman B (2003) Surfactants and polymers in aqueous solutions, 2nd edn. Wiley, Chichester
92. Sanchez-Dominguez M, Koleilat H, Boutonnet M, Solans C (2011) Synthesis of Pt nanoparticles in oil-in-water microemulsions: phase behavior and effect of formulation parameters on nanoparticle characteristics. J Dispersion Sci Technol 32:1765–1770
93. US EPA (2002) Health and environmental effects profile for hydrazine and hydrazine sulfate. report no. EPA/600/X-84/332 (NTIS PB88161963), U.S. Environmental Protection Agency: Washington, D.C. (Accessed April 15, 2018)
94. Ström L, Ström H, Carlsson P-A, Skoglundh M, Härelind H (2018) Catalytically active Pd–Ag alloy nanoparticles synthesized in microemulsion template. Langmuir 34:9754–9761
95. Nandini P, Akash K, Rohit G, Vipul S, Palani IA (2017) Investigations on the influence of liquid-assisted laser ablation of NiTi rotating target to improve the formation efficiency of spherical alloyed NiTi nanoparticles. J Mater Eng Perform 26:4707–4717

96. Chen Q, Song H, Zhang F, Zhang H, Yu Y, Chen Z, Wei R, Dai Y, Qiu J (2017) A strategy for fabrication of controllable 3D pattern containing clusters and nanoparticles inside a solid material. Nanoscale 9:9083–9088
97. Fujita Y, Aubert R, Walke P, Yuan H, Kenens B, Inose T, Steuwe C, Toyouchi S, Fortuni B, Chamtouri M, Janssen KPF, De Feyter S, Roeffaers MBJ, Uji-i H (2017) Highly controllable direct femtosecond laser writing of gold nanostructures on titanium dioxide surfaces. Nanoscale 9:13025–13033
98. Sarker MSI, Nakamura TZ, Herbani Y, Sato S (2013) Fabrication of Rh based solid-solution bimetallic alloy nanoparticles with fully-tunable composition through femtosecond laser irradiation in aqueous solution. Appl Phys A 110:145–152
99. Assis M, Cordoncillo E, Torres-Mendieta R, Beltrán-Mir H, Mínguez-Vega G, Oliveira R, Leite ER, Foggi CC, Vergani CE, Longo E, Andrés J (2018) Towards the scale-up of the formation of nanoparticles on α-Ag2WO4 with bactericidal properties by femtosecond laser irradiation. Sci Reports 8:1884
100. Machado TR, Macedo NG, Assis M, Doñate-Buendia C, Mínguez-Vega G, Teixeira MM, Foggi CC, Vergani CE, Beltrán-Mir H, Andrés J, Cordoncillo E, Longo E (2018) From complex inorganic oxides to Ag–Bi nanoalloy: synthesis by femtosecond laser irradiation. ACS Omega 3:9880–9887
101. Bönnemann H, Richards RM (2001) Nanoscopic metal particles—synthetic methods and potential applications. Eur J Inorg Chem 2455–2480
102. Braunstein JRP (1999) Metal clusters in Chemistry, Braunstein P, Oro LA, Raithby PR (eds), Wiley-VCH: Weinheim, vol 2, p 616
103. Esumi K, Tano T, Torigoe K, Meguro K (1990) Preparation and characterization of bimetallic palladium-copper colloids by thermal decomposition of their acetate compounds in organic solvents. Chem Mater 2:564–567
104. Bradley JS, Via GH, Bonneviot L, Hill EW (1996) Infrared and EXAFS study of compositional effects in nanoscale colloidal palladium−copper alloys. Chem Mater 8:1895–1903
105. Thomas JM, Johnson BFG, Raja R, Sankar G, Midgley PA (2003) High-performance nanocatalysts for single-step hydrogenations. Acc Chem Res 36:20–30
106. Kolay S, Kumar M, Wadawale A, Das D, Jain VK (2014) Cyclopalladation of telluro ether ligands: synthesis, reactivity and structural characterization. Dalton Trans 43:16056–16065
107. Mann S (2001) Biomineralization: principles and concepts. In: Bioinorganic materials Chemistry. Oxford University Press, Oxford
108. Mann S (1996) Biomimetic materials Chemistry. VCH, New York
109. Brayner R, Coradin T, Fiévet-Vincent F, Livage J, Fiévet F (2005) Algal polysaccharide capsule-templated growth of magnetic nanoparticles. New J Chem 29:681–685
110. Srivastava S, Samanta B, Arumugam P, Han G, Rotello VM (2007) DNA-mediated assembly of iron platinum (FePt) nanoparticles. J Mater Chem 17:52–55
111. Lloyd JR, Lovley DR (2001) Microbial detoxification of metals and radionuclides. Current Opinion in Biotechnol 12:248–253
112. Macaskie LE, Baxter-Plant VS, Creamer NJ, Humphries AC, Mikheenko IP, Mikheenko PM, Penfold DW, Yong P (2005) Applications of bacterial hydrogenases in waste decontamination, manufacture of novel bionanocatalysts and in sustainable energy. Biochem Soc Trans 33:76–79
113. Remita S, Mostafavi M, Delcourt MO (1996) Bimetallic Ag-Pt and Au-Pt aggregates synthesized by radiolysis. Radiat Phys Chem 47:275–279
114. Belloni MMJ, Remita H, Marignier J-L, Delcourt M-O (1998) Radiation-induced synthesis of mono- and multi-metallic clusters and nanocolloids. New J Chem 22:1239–1255
115. Belloni MMJ (1999) Metal clusters in Chemistry, Braunstein P, Oro LA, Raithby PR (eds) vol 2. Wiley-VCH, Weinheim, p 1213
116. Treguer M, de Cointet C, Remita H, Khatouri J, Mostafavi M, Amblard J, Belloni J, de Keyzer R (1998) Dose rate effects on radiolytic synthesis of gold−silver bimetallic clusters in solution. J Phys Chem B 102:4310–4321

117. Doudna CM, Bertino MF, Tokuhiro AT (2002) Structural investigation of Ag−Pd clusters synthesized with the radiolysis method. Langmuir 18:2434–2435
118. Doudna CM, Bertino MF, Blum FD, Tokuhiro AT, Lahiri-Dey D, Chattopadhyay S, Terry J (2003) Radiolytic synthesis of bimetallic Ag−Pt nanoparticles with a high aspect ratio. J Phys Chem B 107:2966–2970
119. Jiang Y, He YH, Xu NP, Zou J, Huang BY, Liu CT (2008) Effects of the Al content on pore structures of porous Ti–Al alloys. Intermetallics 16:327–332
120. Jiang Y, Deng C, He Y, Zhao Y, Xu N, Zou J, Huang B, Liu CT (2009) Reactive synthesis of microporous titanium-aluminide membranes. Mater Lett 63:22–24
121. Liang W, Jiang Y, Hongxing D, He Y, Xu N, Zou J, Huang B, Liu CT (2011) The corrosion behavior of porous Ni3Al intermetallic materials in strong alkali solution. Intermetallics 19:1759–1765
122. Dong HX, Jiang Y, He YH, Zou J, Xu NP, Huang BY, Liu CT, Liaw PK (2010) Oxidation behavior of porous NiAl prepared through reactive synthesis. Mater Chem Phys 122:417–423
123. Gao HY, He YH, Shen PZ, Zou J, Xu NP, Jiang Y, Huang BY, Liu CT (2011) Congenerous and heterogeneous brazing of porous FeAl intermetallics. Powder Metall 54:142–147
124. Liu X, Jiang Y, Zhang H, Yu L, Kang J, He Y (2015) Porous Ti3SiC2 fabricated by mixed elemental powders reactive synthesis. J Eur Ceram Soc 35:1349–1353
125. Wu L, He Y-H, Jiang Y, Zeng Y, Xiao Y-F, Nan B (2014) Effect of pore structures on corrosion resistance of porous Ni3Al intermetallics. Trans Nonferrous Met Soc China 24:3509–3516
126. Jiang Y, He YH, Huang BY, Zou J, Huang H, Xu NP, Liu CT (2011) Criterion to control self-propagation high temperature synthesis for porous Ti–Al intermetallics. Powder Metall 54:404–407
127. Chen MR, Jiang Y, He YH, Lin LW, Huang BY, Liu CT (2012) Pore evolution regulation in synthesis of open pore structured Ti–Al intermetallic compounds by solid diffusion. J Alloys Compd 521:12–15
128. Frenkel JJ (1945) Viscous flow of crystalline bodies under the action of surface tension. J Phys 9:385–391
129. Ristic MM, Milosević SĐ (2006) Frenkel's theory of sintering. Sci Sinter 38:7–11
130. Hoge CE, Pask JA (1977) Thermodynamic and geometric considerations of solid state sintering. Ceramurg Int 3:95–99
131. Maulik O, Kumar V (2015) Synthesis of AlFeCuCrMgx (x=0, 0.5, 1, 1.7) alloy powders by mechanical alloying. Mater Charact 110:116–125
132. Kumar S, Kumar D, Maulik O, Pradhan AK, Kumar V, Patniak A (2018) Synthesis and air jet erosion study of AlXFe1.5CrMnNi0.5 (x = 0.3, 0.5) high-entropy alloys. Metall Mater Trans A 49:5607–5618
133. Tunes MA, Vishnyakov VM, Donnelly SE (2018) Synthesis and characterisation of high-entropy alloy thin films as candidates for coating nuclear fuel cladding alloys. Thin Solid Films 649:115–120
134. Li RX, Liaw PK, Zhang Y (2017) Synthesis of AlxCoCrFeNi high-entropy alloys by high-gravity combustion from oxides. Mater Sci Eng A 707:668–673
135. Ye X, Ma M, Cao Y, Liu W, Ye X, Gu Y (2011) The property research on high-entropy alloy AlxFeCoNiCuCr coating by laser cladding. Phys Procedia 12:303–312
136. Zeng C, Tian W, Liao WH, Hua L (2016) Microstructure and porosity evaluation in laser-cladding deposited Ni-based coatings. Surf Coat Technol 294:122–130
137. Zhang M, Zhou X, Yu X, Li J (2017) Synthesis and characterization of refractory TiZrNbWMo high-entropy alloy coating by laser cladding. Surf Coat Technol 311:321–329
138. Qiu X-W, Zhang Y-P, He L, Liu C-G (2013) Microstructure and corrosion resistance of AlCrFeCuCo high entropy alloy. J Alloys Compd 549:195–199
139. Basuki EA, Prajitno DH, Muhammad F (2017) Alloys developed for high temperature applications. AIP Conf Proc 1805:020003-1–020003-15
140. Mouritz AP (2012) Superalloys for gas turbine engines. In: Mouritz AP (ed) Introduction to aerospace materials. Woodhead Publishing, pp 251–267

141. Mousavi T, Hong Z, Morrison A, London A, Grant P S, Grovenor, Speller S C (2017) A new approach to fabricate superconducting NbTi alloys. Supercond Sci Technol 30:09001
142. Narushima T., Ueda K., Alfirano (2015) Co-Cr Alloys as Effective Metallic Biomaterials. In: Niinomi M., Narushima T., Nakai M. (eds) Advances in Metallic Biomaterials. Springer Series in Biomaterials Science and Engineering, vol 3. Springer, Berlin, Heidelberg
143. Elias C.N., Lima J.H.C., Valiev R. Meyers M A (2008) Biomedical applications of titanium and its alloys. JOM 60:46–49
144. do Prado RF, Esteves GC, Santos ELDS, Bueno DAG, Cairo CAA, Vasconcellos LGOD (2018) In vitro and in vivo biological performance of porous Ti alloys prepared by powder metallurgy. PLoS ONE 13(5): e0196169

Chapter 16
Synthesis and Characterization of Metal Hydrides and Their Application

Seemita Banerjee and Priyanka Ruz

Abstract Solid-state metal hydrides provide a safe and efficient method for hydrogen storage. In this chapter, fundamental mechanism of metal–hydrogen interaction, the thermodynamic and kinetic aspects of hydride formation and the factors affecting them are provided. Metal hydrides are formed by dissociative chemisorption of hydrogen on metals at definite temperature and pressure. A brief description of volumetric and gravimetric set-up required for gas phase hydrogen absorption measurement is presented. Loading of hydrogen on metal can also be realized electrochemically by splitting of water, which is the main concept of metal hydride battery. Representative preparation techniques of different systems such as intermetallic hydrides, light metal hydrides and complex hydrides are illustrated. The techniques employed for characterization of metal hydrides are discussed. Current researches on various applications of metal hydrides are also discussed.

Keywords Metal hydride · Thermodynamic properties · Kinetics · Applications

16.1 Introduction

In 1671, Robert Boyle first reported the formation of gas bubbles by reaction between iron and acid [1], and later, Cavendish distinctly differentiated hydrogen from other gases and demonstrated that, when it is burnt in presence of oxygen, it produces water [2]. The above discovery motivated Lavoisier to term the new substance as 'hydro-gen', which means water-former [3]. In 1800, Nicholson and Carlisle (shortly followed by Ritter) managed to decompose water electrochemically to produce

S. Banerjee (✉) · P. Ruz
Chemistry Division, Bhabha Atomic Research Centre, Mumbai 400085, India
e-mail: seemita@barc.gov.in

P. Ruz
e-mail: pdas@barc.gov.in

S. Banerjee
Homi Bhabha National Institute, Mumbai 400094, India

A. K. Tyagi and R. S. Ningthoujam (eds.), *Handbook on Synthesis Strategies for Advanced Materials*, Indian Institute of Metals Series,
https://doi.org/10.1007/978-981-16-1892-5_16

hydrogen. Hydrogen is abundant in bound form and environmental friendly as its oxidation product is only water. In the universe, total estimated hydrogen accounts for 90% of all the atoms. Free hydrogen gas is limited in earth's atmosphere as any hydrogen gas entering into the earth atmosphere rapidly escapes the earth's gravity. The oxidation states of hydrogen vary from −1 (hydride), through 0 (elemental), to +1 (proton). Hydrogen in the molecular form is quite inert due to its close shell structure; H anion and cation are very strong reducer and oxidizer, respectively. Again, H^- is very strong base, whereas H^+ is a voracious acid. Hydrogen gas is very promising as a fuel and excellent energy carrier due to its ultrahigh energy density. For practical applications, however, it must be stored either in a compressed state, liquefied state or inside some solid matrix. Absorption of hydrogen by Pd metal was observed by Graham [4] in 1866 where he showed that 1 vol. of Pd metal can absorb 643.3 volumes of hydrogen. He has described the reaction as $Pd + H_2 \rightarrow PdH_x$ where Pd forms non-stoichiometric hydride. Hydrogen goes into the interstitial sites of the metal lattice and forms solid solutions. The finding opens up scientific curiosities, and over several years, tremendous amount of work was performed on different metal hydride systems to study their thermodynamics and kinetics of hydride formation, thermo physical properties. The results categorize metals according to their hydrogen forming ability [5], and it is found that Ni, Co, Pd, Cu, etc., and various rare earths interact with hydrogen, whereas Zn, Sn, Au, Ag, Cd, etc., remain inert (Fig. 16.1). Apart from the basic understanding in properties, later on, research on metal hydride got enormous attention due to their several important nuclear and energy applications. First of all, in water cooled nuclear reactor, Zr metal reacts with hydrogen, and ZrH_2 precipitates out, which causes embrittlement of the structural material. Therefore, for development of nuclear materials, parallel studies on metal hydride

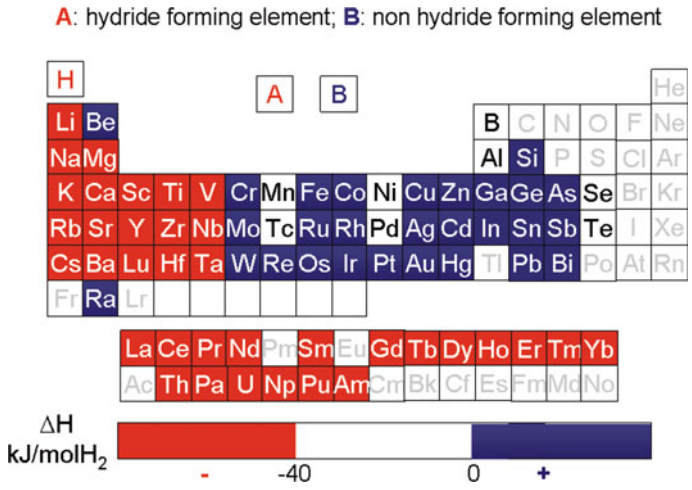

Fig. 16.1 Hydride and non-hydride-forming elements in the periodic system of elements (Reproduced from Ref. [5] with Licensee IntechOpen)

systems of all the structural materials have become important. Secondly, due to good mechanical properties and high hydrogen retention capability of metal hydride, they can be used as moderator, reflector and shielding materials for high temperature reactors. Search of new appropriate hydride material gains lots of importance, and for the first time, Libowitz et al. [6] developed ZrNi-based intermetallic hydride, $ZrNiH_3$, in 1953. But it took years together to explore other possibilities of metal hydride with various compositions [7]. Third and most important aspect is that, due to its great abundance, renewable nature and high energy density, hydrogen has been proposed as an alternative energy carrier. Among different methods of hydrogen storage, solid-state storage in the form of metal hydride got impressive consideration due to its unparallel safety features [8]. Because of the high cost and scarcity of Pd metal, research is focused on finding new materials with similar thermodynamic and kinetic properties with Pd, but with lower cost and higher hydrogen storage capacity. Subsequently, different intermetallic compounds and alloy were discovered, and their structure, hydrogen storage properties and other physicochemical properties were evaluated. First practical hydrogen storage material was accidentally synthesized during research on $SmCo_5$ to develop permanent magnet in 1960s [9]. Later, it has been found that $SmCo_5$ can absorb and desorb hydrogen to form $SmCo_5H_{2.5}$ with slight variation of pressure at ambient temperature [10]. In 1970, scientists of Philips Research laboratories showed that some other intermetallic compounds can absorb hydrogen reversibly and form reversible hydride [11]. Afterwards more promising materials came up from different laboratories, and the most studied one till now is $LaNi_5$ [12], which can form hydride with formula $LaNi_5H_{6.5}$ at room temperature and 1 atm. pressure. After discovery of the alloy, it was used immediately in Ni/MH battery due to its tremendous potential. Many other AB_5 type of intermetallics which are studied later on includes $MmNi_5$ (Mm = Mischmetal), $MmNi(Co, Mn, Al)_5$ and led to first mass production of nickel–metal hydride battery-powered vehicles, which launched in Japan in 1997 [13]. Apart from battery application, stationary storage of hydrogen is also another thrust area of research. It has been proposed that, in the off-peak hours, the energy produced in power plants can be stored in form of hydrogen in hydrogen storage materials, and subsequently, it can be used during the peak hours. 400 kg of FeTi-based materials (AB type) are being studied as prototype hydrogen storage unit built by New Jersey electricity unit, Public Service Electric and Gas Co. [14, 15]. Though AB_5 and AB_2 types of metal hydrides have remarkable potential for metal hydride battery [16] and stationary storage, but they are too heavy for mobile application for hydrogen-fuelled car. Several hydrogen storage alloys with body-centred cubic (BCC) structure have been developed with higher hydrogen storage capacity, and more attention has been given to light metal hydride to increase the hydrogen storage capacity [17–23]. The recent developments in this area will be discussed later in this Chapter. Before that, we focus on fundamental mechanism of metal–hydrogen interaction, the thermodynamic and kinetic aspects of hydride formation and the factors affecting them.

16.2 Metal Hydrides

Binary hydrides can be broadly classified as ionic, covalent and metallic hydrides though the delineation between them is not very sharp, and they merge into each other. Alkali and alkaline earth metal hydrides are strongly ionic, hydrogen being the negatively charged atom with a charge ~(−1), so in that sense it is a 'true' metal hydride. Due to presence of even number of valence electrons, the hydrides are semiconductor with large Brillouin zone gaps. Alkali metal hydrides are analogues to halide and found to have NaCl type of structure. Most of the alkaline earth metals are found to have $PbCl_2$ type of structure except BeH_2, which have BeH_4 tetrahedral network structure and MgH_2 having rutile structure [6, 24–28]. Due to strong ionic interaction between metal and hydrogen in the ionic hydride, they are very stable except MgH_2. Magnesium hydride is found to be relatively unstable, and it falls between the ionic and covalent hydride. The classic example of covalent hydride is CH_4. Other covalent hydrides are SnH_4, BeH_2, BH_3, AlH_3, where the molecules are held together by weak van der Waals interaction and mostly liquid or gaseous at room temperature.

The binary hydrides of transition metal elements are conventionally referred as metallic hydride due to their metallic nature. These hydrides possess a metallic or graphite-like appearance, have high surface energy, and they are found to be good conductors of electricity and heat. Metal hydrides are not true chemical hydride formed by true chemical reaction between metal and hydrogen in these hydrides. They are also referred as interstitial hydride due to their typical lattice structure, where hydrogen atoms occupy interstitial sites of the metal. Initially, hydrogen atom occupies tetrahedral hole formed by four metal atoms, and in the latter stage, they occupy octahedral hole by getting surrounded by six metal atoms. In metallic hydride, hydrogen carries a partial negative charge depending on the electronegativity of metal atom, and the stoichiometry of a covalent metal hydride is not restricted by requirements of charge neutrality. As a result, most of the metal hydrides are found to be non-stoichiometric. In the present chapter, more emphasis will be given on metallic and ionic hydrides due to their importance in hydrogen storage application.

There is a general (but not universal) tendency of decrease in affinity towards hydrogen with increasing group number of the transition metal elements in the periodic table. Starting from group 6 (Cr) up to group 11 (Cu), a substantial 'hydride gap' is observed in the periodic table, where the elements do not form stable hydride. Within the hydride gap, only stable hydride is palladium hydride ($PdH_{0.7}$). Due to limited choice of binary metal hydride in the periodic table, more interesting are intermetallic hydrides, where the properties of hydride can be tailored by changing elements. Simplest ternary hydride system is represented as AB_xH_n, where A mostly tends to form a stable hydride (such as Mg, Ti, Zr, Sc, Nd and Sm), and B element is mostly a transition metal and forms unstable hydrides (such as A1, Fe, Cu and Ni).

When hydrogen occupies the interstitial sites, deformation of the lattice occurs, which does not necessarily involve drastic changes in the arrangement of metals in the lattice. Upon hydrogenation, the lattice volume expanded generally in the

Table 16.1 Different classes of intermetallic compounds and hydride having technological importance

Compound	A	B	Intermetallic	Hydride	Structure/Type
AB_5	Ca, La, Rare Earth	Ni, Cu, Co, Pt, Fe	$CaNi_5$, $LaNi_5$, $LaCu_5$, $LaPt_5$, $LaFe_5$	$LaNi_5H_6$	Haucke phases, Hexagonal
A_6B_{23}	Y	Fe, Co, Ni	Y_6Fe_{23}	$Ho_6Fe_{23}H_{12}$	Th_6Mn_{23}-type
A_2B_7	Y, Th	Ni, Co, Fe	Y_2Ni_7, Th_2Fe_7	$Y_2Ni_7H_3$	Hexagonal, Ce_2Ni_7-type
AB_3	$CeNi_3$, La, Y, Mg	Ni, Co	$CeNi_3$, $LaCo_3$,YNi_3,$LaMg_2Ni_9$	$CeNi_3H_4$	Hexagonal, $PuNi_3$-type
AB_2	Zr, Ti, Y, La	V, Cr, Mn, Fe, Ni	$LaNi_2$, YNi_2,YMn_2, $ZrCr_2$, $ZrMn_2$,ZrV_2, $TiMn_2$, $ZrMn_2$,	$ZrV_2H_{5.5}$	Laves phases, hexagonal or cubic
AB	Ti, Zr	Ni, Fe	TiFe, ZrNi, TiNi,	$TiFeH_2$	Cubic, CsCl-type
A_2B	Mg, Zr, Ti	Ni, Fe, Co	Mg_2Ni, Ti_2Ni, Mg_2Co, Zr_2Fe	Mg_2NiH_4	Cubic, $MoSi_2$ or Ti_2Ni-type

range of 2–3 $Å^3$/H atom. There are rare cases also where lattice contraction occurs. In cubic di, tri-hydrides, the volume decreases or remains constant with hydrogen concentration. The most well-known example where lattice contraction is observed is $ThNi_2$ (-2.2% for $ThNi_2D_2$). In many of the systems such as TiFe, Mg_2Ni, $CaNi_5$ and $LaNi_5$, structural changes of metal sublattices also can occur. The structural parameters of some of the technologically important alloy representative of each structural group are listed in Table 16.1.

16.2.1 Different Classes of Intermetallic Hydride

Table 16.1 shows different classes of intermetallic compounds, which form interesting hydrides [29]. Many of the binary and pseudo-binary hydrides consist of hydride-forming metal with large metallic radius (A) and non-hydride-forming metal with small metallic radius (B). Some typical combinations are AB, AB_2, AB_5, A_2B_7, AB_3 and A_6B_{23}, among which the first three are more common. The properties of the binary hydrides can be tuned very easily by different substitutions in A and B place.

16.2.1.1 AB Interstitial Hydrides

AB types of compounds crystallize in the W-type structure or CsCl-type structure. Mostly AB types of alloys are made up of two 3d transition metals, and they do not differ much in size. The most common example is $TiFeH_x$. A CsCl type of cubic structure has higher interstitial space compared to face-centred cubic (FCC), and hexagonal close-packed (HCP) structures thus are more attractive towards hydrogen storage application.

16.2.1.2 AB_2 Interstitial Hydrides

The Laves phase intermetallic compounds are in general represented by a common formula AB_2 [30, 31]. The ideal size ratio of two metal atoms (considering perfect sphere) is $\sqrt{(3/2)} = 1.225$ with an overall packing density 0.71. The Laves phase compounds can be classified into three major types where Friauf polyhedra are stacked in different ways. Cubic C15 (typical example is $MgCu_2$), Hexagonal C14 (typical example is $MgZn_2$) and Hexagonal C36 (Typical example is $MgNi_2$) are shown in Fig. 16.2.

16.2.1.3 AB_5 Interstitial Hydrides

AB_5 type of interstitial hydrides crystallizes in $CaCu_5$-type structure and mostly formed by a hydride-forming metal usually a rare-earth metal (La, Ce, Nd, Pr, Y or their mixture known as Mischmetal) combined with transition metal Ni/Co (B). Here also, like Laves phase, the structure consists of stacking of polyhedra built from AB_4

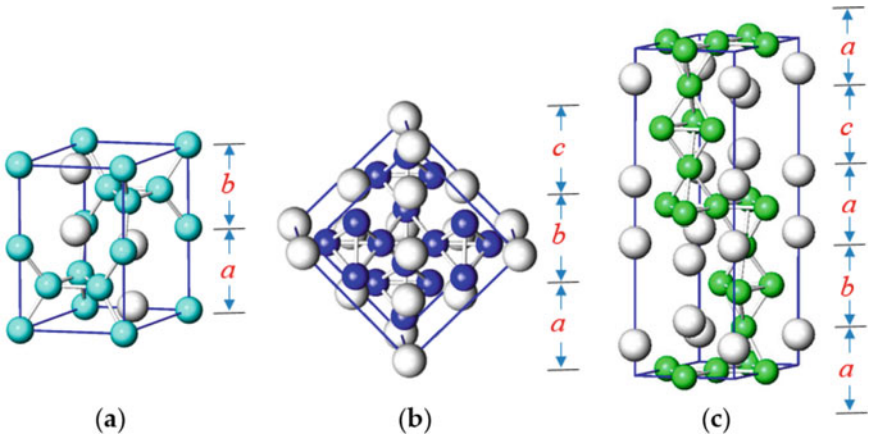

Fig. 16.2 Schematic of **a** C14 (hexagonal), **b** C15 (cubic) **c** and C36 (rhombohedral) crystal structures (Reproduced from Ref. [30] with Creative Commons Attribution License (CC-BY))

tetrahedra. The most common example of AB_5 hydrides is $LaNi_5$ and its substituted counterparts. Ni can be doped with different other metals, like Co, Sn or Al, to adjust its hydrogen storage properties and improve stability.

16.2.1.4 AB_3 Interstitial Hydride

The AB_3 compounds mostly have $PuNi_3$ type of rhombohedral lattice (Fig. 16.3). Some of the AB_3 compounds form $CeNi_3$ type of hexagonal structure (P63/mmc), where the third $CaCu_5$-type layer is directly above the first. In $PuNi_3$ type of AB_3 structure, the third $CaCu_5$-type layer is displaced 1/3, 2/3, 2/3 above the first $CaCu_5$-type layer. Certain A_2B_7 alloys show similar structure and are identified as pseudo AB_3 alloy. Their structure is similar to $LaNi_3$ structure and has two $CaCu_5$-type units stacked with one $MgZn_2$-type unit.

16.2.1.5 Zintl Phase Hydrides

Another very interesting class of metal hydrides are Zintl phases which are formed by combining electropositive alkali, alkaline earth or rare-earth metals with a complex ion of electronegative p-block metals which are bound to fulfil the octet rule. In Zintl phase hydride, the hydride ions (H^-) are located in interstitial positions surrounded by the electropositive metal ion, and the hydrogen atoms are covalently bound to the complex ion forming complex hydride [33–36]. For recent developments on Zintl phase compounds, the readers should see the reference [37]. Typical examples of these types of compounds are A_5B_3H (A = alkaline earth metal, B = As, Sb, Bi) A_5T_3H (T = Si, Ge, Sn, Pb).

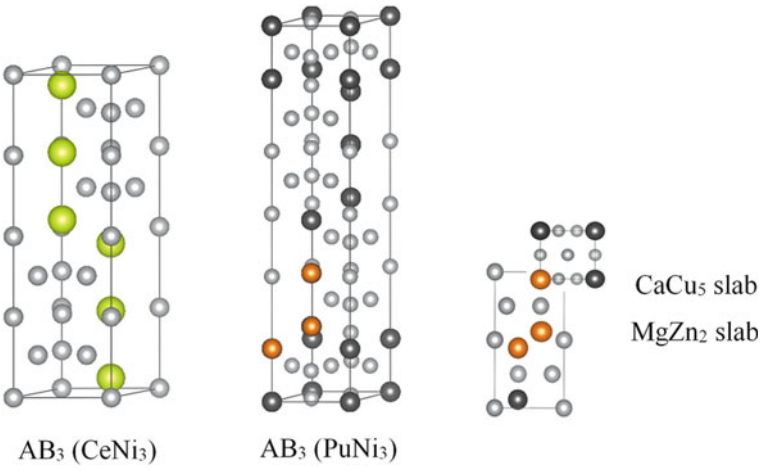

Fig. 16.3 Structures of AB_3 type of intermetallic compounds (Reproduced from Ref. [32] with the permission of Elsevier publishes)

16.3 Mechanism of Metallic Hydride Formation

Many transition metal elements form metallic hydrides, where H atoms occupy interstitial sites of the crystal structures. As we have already discussed, mostly the metallic hydride systems are non-stoichiometric, with variable amounts of H atoms in the lattice [38, 39]. The early transition metal elements show more tendencies for hydride formation, and it decreases from left to the right in the series. A detailed analysis of the changes in band structure and electron density before and after the formation of hydride indicate that there are actually three major contributing factors, which determine the stability of the hydride [40]. First contribution comes from the energy involved for changing the crystal structure from metal to the corresponding hydride. For example, most of the BCC metals like V, Cr transform to FCC structure upon hydrogenation, which significantly lowers the driving force for hydride formation. The second contribution is the loss of cohesive energy due to the expansion of metal lattice after hydride formation. This effect predominates for the late transition metal elements, where the cohesive energy is very high, and this is one of the major barriers for formation of stable hydride. The final and most important contribution which favours the formation of metal hydride is the chemical bonding between the hydrogen and metal. The bond energy grows positive across the transition metal series, thus destabilizes the hydride. So for designing metal hydride with better stability, one should try to modify the alloy composition to tailor the density of state at the Fermi level and to decrease the cohesive energy. Phase transition and decomposition behaviour of different light metal hydrides, complex hydrides and alanates of first and second group elements have been reviewed in detail in reference [41]. It has been found that the decomposition temperatures of alkali borohydrides increase with molar volume and the size of alkali metals.

Several fundamental steps are involved for formation of interstitial hydrides [42, 43]. The dissociation energy of molecular hydrogen in free state is E_D = 435.99 kJ mol^{-1}. Initially, when hydrogen molecule approaches towards the metal surface, it gets physisorbed on the surface by weak van der Waals force ($E_{Phys} \approx$ 10 kJ^{-1}) at a distance approximately one hydrogen molecule radius ($\approx$ 0.2 nm). For formation of metal–hydrogen bond, hydrogen molecule has to overcome an activation barrier for dissociation. The step is called dissociative chemisorptions, where hydrogen molecule dissociates on the metal surface and subsequently gets chemisorbed. The activation energy for the dissociation of hydrogen molecule depends on the nature of the metal surface [44–47]. After dissociation, the chemisorbed ($E_{Chem} \approx$ 50 kJ^{-1} H_2) hydrogen may remain on the metal surface and interact with each other, may penetrate into the subsurface layer and diffuse towards the lattice interstitial sites of the host metal to form solid solution, as depicted in Fig. 16.4. The solid solution is called *α-phase,* and here, the lattice parameter increases compared to the parent metal system.

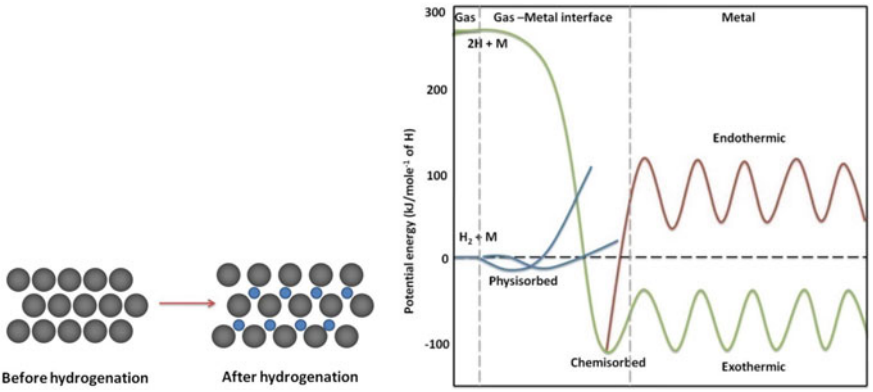

Fig. 16.4 Mechanism of hydride formation

16.4 Thermodynamics of Metal Hydride Formation: Pressure Composition Isotherm

Thermodynamics of metal hydride formation can be best explained by pressure composition isotherm (PCI), which is characteristic of a metal (alloy/intermetallic compound) hydride system and gives fundamental information about the thermodynamic stability and hydrogen storage capacity of that particular metal hydride system. A detail discussion on thermodynamics of metal hydride could be found elsewhere [5, 48], and here, the fundamentals of thermodynamic feature of intermetallic compound hydrogen system are briefly outlined.

In typical pressure composition isotherm (PCI) diagram (Fig. 16.5), equilibrium hydrogen pressure is plotted as a function of hydrogen to metal ratio (H/M) at a

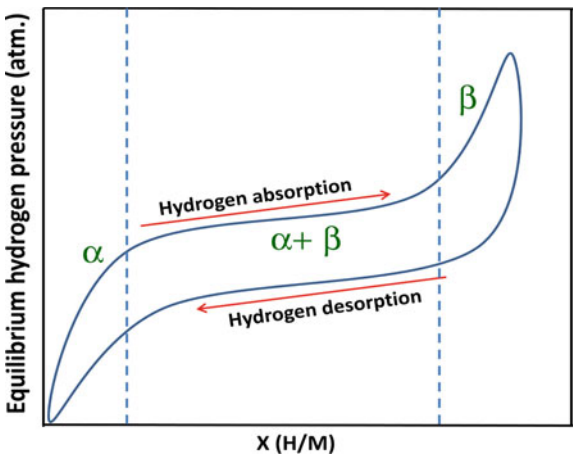

Fig. 16.5 Pressure composition isotherm (PCI) of metal hydride

constant temperature. Initially, small amount of hydrogen (<0.3 wt%) goes into interstitial positions of metals forming solid solution (α phase), and the equilibrium hydrogen pressure increases sharply with H/M ratio. With further increase in the hydrogen pressure, the solubility limit of hydrogen exceeds, and precipitation of hydride phase (β phase) starts. In plateau region of the PCI diagram both α and β phases and coexists the equilibrium pressure remains almost constant. After complete formation of hydride phase (β phase), the equilibrium pressure again increases sharply as no further hydrogen absorption occurs. Here, only very little amount of hydrogen goes into the interstitial position forming solid solution of hydrogen in β hydride phase. The width of the plateau region determines the amount of hydrogen that could be stored reversibly at that particular temperature with very small pressure variation, so in other work, it decides the reversible hydrogen storage capacity of a metal hydride. The plateau pressure determines the stability of the metal hydride. Lower the plateau pressure, more stable is the hydride. The existence of the absorption and desorption plateau in the PCI diagram can be explained according to the Gibbs phase rule, $F = C - P + 1$, (at fixed temperature), where F, P and C are number of degrees of freedom, number of phases, number of components, respectively. In the plateau region, the number of components is 2 (H, metal), and two phases are in (presumed) equilibrium (α, β). So, as per the phase rule, the ideal metal hydride system can have only one degree of freedom (F). But contrary to the ideal case, in most of the cases, plateau shows sloping behaviour due to presence of localized defects, strains and surface inhomogenities in the structure. Upon hydrogenation, large expansion of lattice parameter occurs in most of the hydrides (10–20% of the metal lattice), and in some cases, symmetry may also change. Due to substantial volume expansion, a large stress builds up at the grain boundaries and often leads to a decrepitation of brittle host metals. Figure 16.6 shows a typical picture of a typical Ti-based intermetallic alloy before and after hydrogen absorption. The final hydride is a powder with a typical particle size of 10–100 μm.

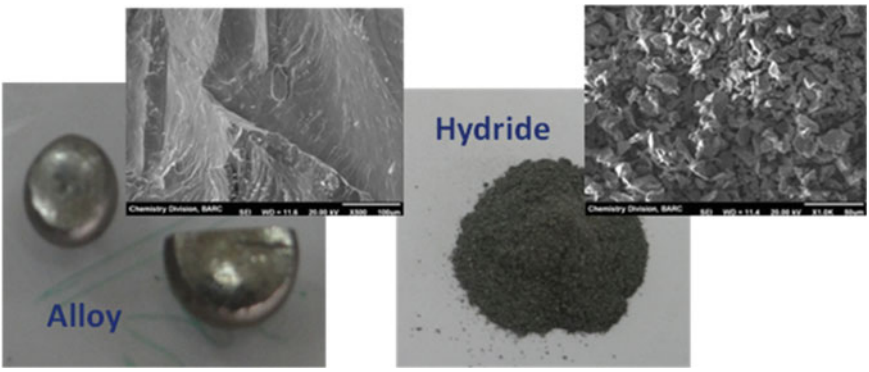

Fig. 16.6 Ti-based alloy and its hydride after complete hydrogen absorption and their SEM pictures

More than one plateau region can exist in a PCI diagram due to presence of more than one metal hydride phases. The pressure composition isotherms of $LaNi_5$-H_2 system isotherms measured at a temperature higher than 80 °C clearly show two plateaux on desorption [49, 50]. Another typical example of coexistence of different hydride phases is found in the $CaNi_5$-H_2 system. There are four different hydride phases exist in this system [51, 52]. Initially, in α-phase, hydrogen solid solution is formed within the hexagonal $CaNi_5$. At a composition of $CaNi_5H_1$, the β-phase is formed with deformed orthorhombic structure. In the γ-phase ($CaNi_5H_5$), deformation in orthorhombic structure occurs in such a way that it becomes close to the original hexagonal structure. The hydrogen saturated phase ($CaNi_5H_6$) is δ-phase, where the structure is same as the original hexagonal $CaNi_5$ structure with increased lattice parameters. AB type of alloy like FeTi forms β and γ hydride phases at H/M = 0.5 and 1, respectively. As a result, the PCI profile of FeTi system shows two-stepped plateau and relatively extensive hysteresis.

In many of the metal–hydrogen systems, desorption curve does not follow the same path as absorption, and the equilibrium plateau pressure of desorption is usually lower than that of the absorption. The difference between absorption and desorption curves is known as hysteresis, which arises mainly due to irreversible plastic deformation caused by hydride formation and quantified by $\ln(P_a/P_d)$. The largest hysteresis reported so far is for U-Nb alloy [53] where the hydrogen absorption pressure is almost 50 times greater than that of desorption pressure.

The enthalpy (ΔH) and entropy (ΔS) of hydride formation of a particular hydride system can be determined conveniently from the value of equilibrium plateau pressures at different temperatures by applying van't Hoff relation. The effect of temperature on plateau pressure is shown in Fig. 16.7. With increase in temperature, the width of the plateau decreases, and the plateau pressure increases. At a critical temperature (T_c), plateau region disappears, and spontaneous conversion of α phase to β phase occurs.

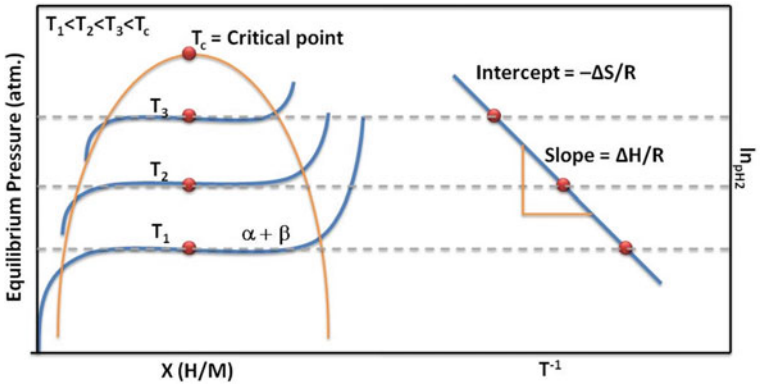

Fig. 16.7 Determination of enthalpy and entropy of hydride formation using van't Hoff relation

The reaction between a metal and hydrogen gas can be represented by the following equation:

$$M + \frac{x}{2} H_2 = MH_x \tag{16.1}$$

where M is metal (alloy/intermetallic compound), and x indicates the molar ratio of hydrogen to metal.

Now, the change in standard Gibbs free energy at equilibrium condition is represented by

$$\Delta G = -RT \ln K \tag{16.2}$$

K is the equilibrium constant and given by $K = P_{H_2}^{-1}$, where P_{H_2} denotes equilibrium plateau pressure. R is the gas constant 8.314 J mol^{-1} K^{-1}, and T is absolute temperature. So,

$$\Delta G = RT \ln P_{H_2} = \Delta H - T\Delta S \tag{16.3}$$

$$\ln P_{H_2} = \frac{\Delta H}{RT} - \frac{\Delta S}{R} \tag{16.4}$$

where ΔH and ΔS are the change in enthalpy and entropy, respectively, during the hydrogenation of metal. The above equation is known as van't Hoff relation. Figure 16.7 shows a typical van't Hoff plot where logarithm of pressure ($\ln P_{H_2}$) is plotted versus reciprocal temperature ($1/T$). From the slope ($-\Delta H/R$) and intercept ($\Delta S/R$) of the plot, the change in enthalpy (ΔH) and entropy (ΔS) can be calculated. ΔH varies widely for different metal–hydrogen systems, whereas the entropy change is almost independent of the host metal or compound and equal to ~130 J K^{-1} mol^{-1} H_2. The change in entropy corresponds to the loss of entropy of gaseous hydrogen upon absorption in solid matrix. The other entropy terms like vibrational entropy of hydrogen in host lattice, configurational entropy, etc., are very negligible. Due to the factor that there is almost constant entropy change in different metal hydride system, the entropy term (ΔH) largely determines the stability of metal–hydrogen bond. For a stable hydride, where equilibrium hydrogen pressure lies below 1 atm., the enthalpy should be more negative than that of −39 kJ/mole. The plateau pressure and reaction kinetics fix the reaction temperature of metal and hydrogen. Dissociation pressure of some of the important metal hydride as a function of temperature is shown in Fig. 16.8.

The hydrogen storage capacity of a metal hydride is defined either by *H/M* ratio (H = number of hydrogen atom, M = number of metal atoms) or by weight percentage. The weight percentage (H_w) is calculated by the weight ratio of hydrogen and hydride.

$$H_w = \left(m_H / m_{\text{Hydride}}\right) \times 100, \text{ where } m_{\text{hydride}} = \text{mass of metal} + \text{hydrogen}.$$

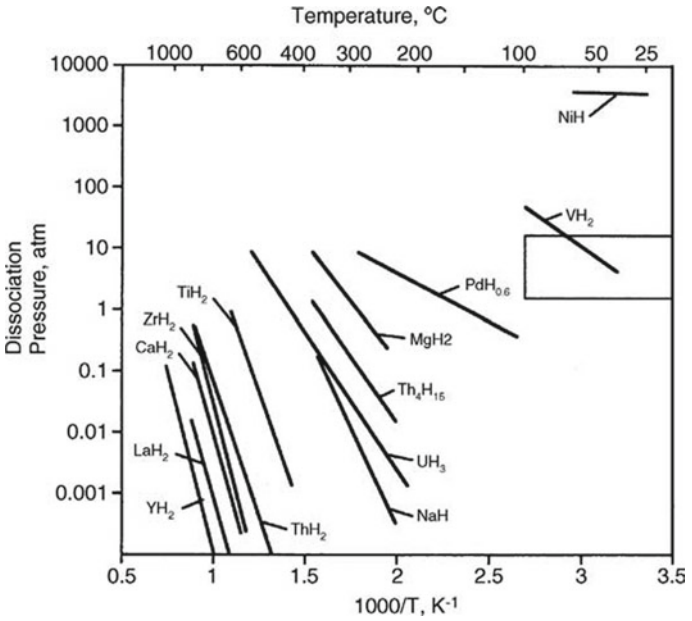

Fig. 16.8 Dissociation pressure of different hydrides as a function of temperature (Reproduced from Ref. [52] with the permission of Elsevier publishes)

In technological point of view, weight percentage is very important parameter to choose a particular metal hydride for practical application, especially for vehicular hydrogen storage, which will be discussed later in this chapter.

16.5 Kinetics of Interstitial Hydride Formation

The kinetics of hydrogen absorption and desorption is also important for practical application as it limits the lower temperature of hydriding. Considering the many steps involved in hydride formation mechanism, the overall rate is governed by rate of the following steps:

(i) Physisorption of hydrogen molecule at metal surface.
(ii) Dissociation of hydrogen molecule to hydrogen atom at the metal surface.
(iii) Chemisorption of hydrogen at the surface.
(iv) Rate of diffusion of hydrogen atoms through the bulk.
(v) Rate of nucleation and growth of β-phase hydride.

As the hydride formation reaction is controlled by a number of factors [54], practically it is very difficult to numerically find out the rate constants of individual steps following conventional methods. Hence, there is a practice to employ different

Table 16.2 List of some of the kinetic models from literature [58–63]

Model	Kinetic equation
Zero-order chemical reaction	$\xi = \mathrm{k}t$
First-order chemical reaction	$-\ln(1-\xi) = \mathrm{k}t$
Second-order chemical reaction	$[1/(1-\xi)] - 1 = \mathrm{k}t$
One-dimensional diffusion	$\xi^2 = \mathrm{k}t$
2-D diffusion	$(1-\xi)\ln(1-\xi) + \xi = \mathrm{k}t$
Ginsling–Braunshteinn model	$1 - 2/3\xi - (1-\xi)^{2/3} = \mathrm{k}t$
Jander diffusion model	$[1-(1-\xi)^{1/3}]^2 = \mathrm{k}t$
Kolmogorov–Johnson–Mehl–Avrami	$\ln(-\ln(1-\xi)) = \mathrm{nlnk} + \mathrm{nln}t$
2-D contracting area	$1-(1-\xi)^{1/2} = \mathrm{k}t$
3-D contracting volume	$1-(1-\xi)^{1/3} = \mathrm{k}t$

standard mathematical kinetic models to identify the rate limiting step and determine the apparent rate constants [55, 56]. Same is also true for dehydrogenation kinetics.

A mathematical kinetic model is a mathematical representation of experimentally observed kinetics data. When a set of experimental kinetics data (applicable for both hydrogenation and dehydrogenation) can be fitted with a model within error limit, it is assumed that the hydrogenation/dehydrogenation follows the mechanism based on which the model was derived. Several kinetic models are reported in the literature, and some of them are listed in Table 16.2.

This section briefly describes the general procedure for finding rate constants and activation energies using kinetic models.

The rate of a solid–gas reaction is in general expressed by

$$\frac{\mathrm{d}\xi}{\mathrm{d}t} = k \cdot f(\xi) \tag{16.5}$$

where ξ is the reacted fraction at time t, k is apparent rate constant, and $f(\xi)$ is a function determining the mechanism of reaction. It can also be written in the integrated form

$$g(\xi) = \int \frac{\mathrm{d}\xi}{\mathrm{d}t} = kt \tag{16.6}$$

where $g(\xi)$ is the integral form of $f(\xi)$.

For a volumetric hydrogen storage measurement, ξ is given by

$$\xi = \frac{P(0) - P(t)}{P(0) - P(\infty)} \tag{16.7}$$

where $P(0)$ is initial hydrogen pressure; $P(t)$ and $P(\infty)$ are the hydrogen pressures at time 't' and after reaching the final equilibrium, respectively. The kinetic equation with largest co-relation coefficient (R^2) is considered as the best fitting model to describe the kinetics of hydrogen absorption/desorption for that particular system. Using the best fitting model, the rate constants "k" are determined at different temperatures. Gérard et al. [57] summarize the kinetic results of hydrogen absorption and desorption for AB_5, ($LaNi_5$ type), magnesium alloys, FeTi and the Laves phases.

16.5.1 Calculation of Activation Energy

Activation energy of absorption and desorption of hydrogen can be calculated both by kinetic model fitting and by Kissinger method.

16.5.1.1 Kinetic Model Fitting

Activation energy of absorption and desorption of hydrogen can be found out using the Arrhenius equation by calculating the rate constant of reaction at different temperature by kinetic model fitting [64, 65]. The Kolmogorov–Johnson–Mehl–Avrami (KJMA) model of hydrogenation reaction is based on the nucleation, growth theory of hydride and is most frequently used and popular model for determining the activation energy of hydriding reaction [58], and we are concentrating our discussion within this model only. KJMA model is applied when random nucleation occurs throughout the sample and the bulk and homogeneous growth takes place thereafter.

The linear form of KJMA model is

$$\ln(-\ln(1-\xi)) = \mathrm{nlnk} + \mathrm{nln}t \tag{16.8}$$

where ξ is the reacted fraction, k is rate constant, t is time, and n is Avrami constant. Avrami constant gives idea about the dimensionality of the reaction and thus put light on reaction mechanism.

If $\ln(-\ln(1-\xi))$ is plotted against $\ln t$, then from the slope, Avrami constant can be determined, and using that in the intercept value, the rate constant can be evaluated. The apparent activation energy of hydrogen absorption/desorption is calculated using the Arrhenius equation:

$$\mathrm{lnk} = \ln A - \frac{E_\mathrm{a}}{RT} \tag{16.9}$$

where k is the rate constant, A is pre-exponential factor, E_a in the activation energy, T is the temperature, and R is the universal gas constant (8.314 J mol^{-1} K^{-1}).

16.5.1.2 Activation Energy by Kissinger Method

The activation energy can also be determined directly by Kissinger plot based on the following equation:

$$\ln\left(\frac{\varnothing}{T^2}\right) = -\frac{E_a}{RT} + \ln\left(\frac{AR}{E_a}\right) \tag{16.10}$$

T is the peak temperature of hydrogen absorption/desorption, φ is the heating rate, E_a is the activation energy, and R is the universal gas constant. This plot between $\ln(\varphi/T^2)$ versus T^{-1} at different heating rate should give a straight line, which yields the apparent activation energy of the absorption or desorption process (E_a) [66, 67].

16.6 Hydrogenation of Intermetallic Phases

16.6.1 Reaction Between Hydrogen Gas and Metals at Convenient Pressure and Temperature

Metal, intermetallics and alloys can be hydrogenated by simply exposing the sample in hydrogen atmosphere at suitable temperature and pressure. After hydrogen absorption, mostly the intermatallic phase remains stable except in some cases, where disproportionation occurs. One of the classic examples of such type of system is Mg_2Cu [68]. Upon hydrogenation, it forms Mg_2CuH_4 which readily disproportionate into $MgCu_2$ and MgH_2. In La_7Ni_3 also, after hydrogenation bimetallic alloy ($LaNi_5$) and elemental hydride (LaH_3) segregates [69]. Again, there are some intermetallic which can only exist in presence of hydrogen. For example, Mg and Fe metals are almost immiscible, but Mg_2FeH_6 is quite stable [70–73].

Diffusion of hydrogen in metal hydride is generally very slow which is evident from lower diffusion coefficient value of hydrogen in metal hydride. But as alloy starts to absorb hydrogen, mostly there is large expansion in the lattice parameter, so it cannot accommodate plastic deformation and decrepitates. As a result of that, new fresh surface is created in the alloy, and also, the diffusion path length decreases. During hydrogenation, several precautions should be taken as mostly all the intermetallic compounds are reactive towards air and moisture.

1. The purity of the hydrogen should be very high.
2. The reaction chamber should be leak proof and should have very low degassing rate.
3. The chamber should be attached with ultrahigh vacuum to eliminate traces of contamination.

16.6.2 Electrochemical Charging and Discharging of Metal Hydride

Another way of charging and discharging of metal hydride at room temperature is by electrochemical route. This is also basic principle of Ni metal hydride battery. Here, negative metal hydride electrode (anode) is combined with positive nickel hydride electrode (cathode) in an electrochemical cell [18, 74]. The reaction is fully reversible and can be represented as

$$MH_x + xOH^- \leftrightarrow M + xH_2O + xe^- \tag{16.11}$$

$$NiOOH + H_2O + e^- \leftrightarrow Ni(OH)_2 + OH^- \tag{16.12}$$

Schematic diagram of metal hydride electrode is presented in Fig. 16.9.

16.6.3 Mechanical Milling for Metal Hydride Formation

Ball milling has become one of the most utilized preparation methods for metal hydrides though till now it is significantly unexplored. Mechanical milling can be utilized in several ways for metal hydride formation.

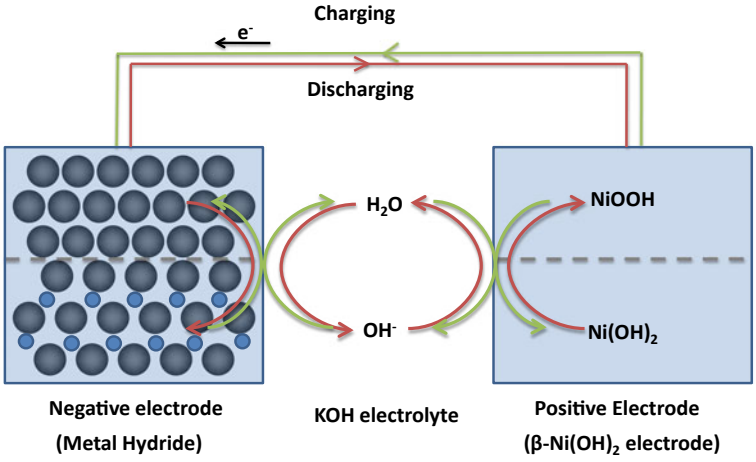

Fig. 16.9 Schematic diagram of metal hydride electrode

16.6.3.1 Mechanical Milling

Some metals and alloys do not absorb (or absorb very slowly) hydrogen in gas phase when prepared by arc melting or induction heating but they can when prepared by mechanical milling route. Although the diffusion rate of hydrogen in early transition metals is quite high due to the presence of vacant d orbital, but practically, it is limited by the presence of surface oxides. By mechanical milling, there can be a tremendous increase in the hydrogen absorption rate of such systems. The greatly increased diffusion rates observed during ball milling are due to several factors. Firstly, by milling, large amount of oxide-free metal surface is exposed towards hydrogen, and thus, the dissociation barrier of hydrogen molecules towards hydrogen atom decreases. Again, ball milling lowers the particle size and grain size, thus the surface area increases and gain boundary concentration increases as a result hydrogen diffusion length decreases. Again, ball milling introduces significant lattice defects and stress in the material, and thus, the reactivity of metal increases.

A very important alloy which has been synthesized by ball milling and explored due to high gravimetric hydrogen storage capacity is Mg-based BCC alloys. An interesting fact is that magnesium itself is having HCP structure, but by reactive ball milling, BCC phase of magnesium can be stabilized in presence of certain transition metals such as Ti, Co and Ni [75–81]. Study shows that BCC Mg50Ti50 alloy with crystalline size of 3 nm can be prepared by ball milling a mixture of Mg and Ti powder in a Fritsch P5 planetary ball mill for 150 h at a rotation speed of 200 rpm [76].

By mechanical milling, amorphous alloys also can be synthesized, which are very difficult to get by conventional methods. Ni-Ti, Y-Co-based amorphous materials have been synthesized successfully by mechanical milling [82, 83]. For grinding alkali metals, extreme precautions are needed, and inert conditions (mostly under Ar atmosphere) and nonreactive diluting agents such as iron powder, sodium carbonate or alkali metal chlorides or hydrides are primary requirements [84].

16.6.3.2 Reactive Mechanical Milling

In some cases, metal nano hydride could be directly formed by mechanical milling of metal powder under hydrogen atmosphere, where the reaction is accompanied both by particle and grain size reduction. The method is called reactive mechanical milling. This method considerably lowers down the reaction temperature and overcomes the issues related to slowing down of the reaction due to the formation of hydride layer over the metal surface. During mechanical milling, the clean metal surface continuously gets exposed towards hydrogen, enabling reaction to go towards the completion.

TiH_2 is conventionally prepared by exposing Ti metal in hydrogen atmosphere (1 atm) at around 400 °C for several hours, and several hydrogen absorption desorption cycle is required to attain the maximum hydrogen storage capacity. Titanium hydride could be synthesized at room temperature by ball milling Ti powder under

hydrogen atmospheres. Study shows that the hydride formed by the milling process shows lower desorption temperature compared to the conventional route [85].

Reactive ball milling is found to be excellent preparation route for producing alkali metal hydride at near ambient temperatures and have high opportunity for scaling up. The synthesis of alkali metal hydrides by direct hydrogenation is generally very energy-intensive process, and in many of the cases, the reaction temperature are above their melting point. By and large, they require additional catalyst also [86, 87]. For example, lithium monohydride is typically synthesized at 700–900 °C by reaction of molten lithium metal and gaseous hydrogen. Mechano-chemical synthesis of AHs (A = Na, K, Rb, and Cs) can be achieved by ball milling the respective metals under hydrogen pressure without any additive agent or catalyst. Though for completion of reaction, around 120 °C temperature is needed [88]. A recent study demonstrates that in presence of process control agent such as corresponding metal monohydride the reaction can go towards the completion at room temperature only [89].

Magnesium hydride is formed by the reaction of hydrogen gas with Mg powder at temperatures around 700 K with hydrogen pressures in the range 78 MPa for several hours. The natural inertness of magnesium metal towards hydrogen comes due to the following factors. (1) In normal condition, magnesium metal remains covered with thick oxide layer, which acts as the barrier for hydrogen dissociation and diffusion. (2) Due to high activation barrier for dissociation of hydrogen molecule and slow diffusion rate of hydrogen through magnesium and magnesium hydride lattice. However, MgH_2 formation can be achieved near room temperature using high-pressure reactive ball milling with a ball-to-powder weight ratio of 10:1 at 500 rpm and hydrogen pressures of 1, 4 and 9 MPa [90].

16.6.3.3 Reactive Mechanical Alloying

In reactive mechanical alloying, different metal powders can be milled together under hydrogen atmosphere to produce ternary and higher hydride.

$$aA + bB + (x/2)H_2 \rightarrow A_aB_bH_x \tag{16.13}$$

Similarly, ternary hydride can also be formed by mechanical milling of metal hydride with another metal in presence of hydrogen. One of the classic examples is synthesis of sodium alanate.

$$NaH + Al + 3/2\ H_2 \rightarrow NaAlH_4 \tag{16.14}$$

Several complex hydrides have been prepared successfully using reactive mechanical milling under hydrogen atmosphere. For example, Mg_2FeH_6 and $Mg(BH_4)_2$ are prepared, by reacting Mg or MgH_2 with Fe, and MgB_2, respectively, under hydrogen gas [91, 92].

Precautions During Ball Milling

The reactivity of metal alloy and hydrogen absorption kinetics depends on several milling parameters such as powder-to-ball weight ratio, milling speed, milling time, milling container and ball composition, diameter and density of the starting material, temperature and hydrogen pressure, and to get desired product, each of the parameters should be optimized and controlled [93]. During ball milling, heat is produced due to friction, which may lead to thermal decomposition of the sample after prolonged milling, and necessary safety precautions should be taken into account (especially when hydrogen is being handled). A routine procedure is to give short intervention time in between the milling processes to allow the intrinsic heat to dissipate. Again the milling time and the interval time optimization are crucial for successful synthesis. A very effective way to make unstable hydride is cryogenic ball milling, where the milling is done under liquid nitrogen temperature.

16.7 Stability of Intermetallic Hydride

The stability of a ternary hydride can be determined by Miedema model which explains the stability of ternary hydrides in terms of the enthalpy of formation of a ternary hydride from knowledge of enthalpy of formation values for the corresponding binary hydrides and binary intermetallic compounds [94]. The model states that

1. The interstitial hydrogens are considered to be metallic in nature.
2. The stability of hydride is explained in terms of only enthalpy of formation as the contribution from the entropy term is fixed. The standard entropy loss is 130 JK^{-1} mol^{-1} for gaseous hydrogen after absorption in metal hydride. Therefore, the criterion of a stable metal hydride at an equilibrium pressure below 1 atm. and at room temperature is that the formation of enthalpy should be more than 40 kJ mol^{-1}.
3. The intermetallic compound containing at least one stable hydride-forming metal can absorb large quantity of hydrogen thermodynamically.
4. The heat of formation of a ternary hydride (AB_nH_{2m}) can be approximately estimated by the following equation

$$\Delta H(AB_nH_{2m}) = \Delta H(AH_m) + \Delta H(B_nH_m) - \Delta H(AB_n), \tag{16.15}$$

where $n > 1$, A is hydride-forming metals, and B is an arbitrary transition metal. It is also called the rule of reverse stability. According to this rule, more stable is the alloy, and less stable is the hydride.

For example, in case of $LaNi_5$, the relation (16.15) becomes

$$\Delta H(LaNi_5H_6) = \Delta H(LaH_3) + \Delta H(Ni_5H_3) - \Delta H(LaNi_5) \tag{16.16}$$

The values of the terms in the right hand side of the above equation are –252, +4, and +168 kJ/mol alloy, respectively. The left-hand side of Eq. (16.16) is then calculated to be –80 kJ/mol alloy (–27 kJ/mol H_2), which agrees well with the observed value, –32 kJ/mol H_2. $LaCo_5$ is one of the alloys of the same series but less stable than $LaNi_5$. It clearly proves that these AB_5-type hydrides obey the rule of reversed stability [95].

The model assumes that the crystal structure of the intermetallic compound is not important for determining thermodynamic stability of hydride. Afterwards many scientists have improved the Miedema model by including different terms in the simple model which can give better prediction of enthalpy of formation of the metal hydride. For example, Wang and Northwood have proposed modified Miedema model [96] where they have taken account of the fact that both the electron density and electronegativity of hydrogen vary with the size of the interstices of the host metal. The model also can predict the site occupancy and energy of hydrogen in tetrahedral (T) or octahedral (Oh) sites in metal hydride.

Another model which can predict the hydride formation energy close to the experimental value is the semi-empirical band structure model proposed by Griessen and Driessen [97, 98]. They have proposed that the heat of formation of metal hydride can be given by

$$\Delta H = \frac{n}{2}\left[\alpha\left(E_f - E_s\right)\right] - \beta], \tag{16.17}$$

where E_f and E_s are the Fermi energy and the energy of lowest conduction band, respectively.

16.8 Interstitial Site Occupancy of Hydrogen in Intermetallic Hydride

The two models have been widely accepted to predict the interstitial site occupancy in intermetallic compounds, namely Westlake's geometrical model [99, 100] and local heat ΔH of formation model by Shaltiel [101].

16.8.1 Westlake's Geometrical Model

The model states that

(i) For an interstitial site to be occupied by a H atom, its hole radius should be 0.4 Å or greater.

(ii) The distance between the two occupied interstitial sites should be 2.1 Å or greater.

(iii) The interstitial sites with larger hole radii are occupied first.

The postulate is of totally geometric origin, and it completely ignores the relative hydrogen affinity of the metal atoms forming the interstitial site. It cannot predict phase transformation of metal upon hydrogenation or high-pressure phase when much more hydrogen in involved. However, as Westlake reported for several systems like $LaNi_5D_6$, $LaNi_4AlD_{4.5}$, ZrV_2D_6, $ZrMn_2D_{2.75,}$ etc., the postulate is in good agreement with observed site occupancy of hydrogen.

16.8.2 Local Heat of Formation Model

Local heat of hydride formation (ΔH) energy is calculated empirically by adding the formation energy of elementary binary hydrides formed by the H and metal atoms. Thus, the sites with more number of neighbours, with high H affinity, are predicted to be preferentially occupied. It is clear that this model completely ignores the geometry and size of the interstitial hole and the emphasis is mainly on the relative affinity of the constituent metal atoms towards hydrogen. It is established that hydrogen prefers to occupy interstitial sites surrounded by at least one atom of stable hydride-forming metals. As an example, in $TiFeD_{1.9}$, hydrogen atoms occupy the sites [Ti4Fe2] and [Ti2Fe4], where at least one Ti atom is there. In Laves phase hydride such as $ZrMn_2$, hydrogen atoms have a tendency to occupy the sites [Zr3Mn] and [Zr2Mn2].

As both the models have their own advantages and disadvantages, so both should be considered together for the prediction of hydrogen site occupancy in an intermetallic hydride.

16.9 Isotope Effect

The changes in free energy upon absorption of *H* and *D* in metal can be different due to differences in enthalpy and entropy of the two gases and those of the hydride/deuteride phases. At room temperature, the difference between the enthalpies of H_2 and D_2 gas is 4 kJ/mol. Because of the higher atomic mass, D_2 molecule has lower optical frequency, and as a result, it leads to lower zero-point energies. Therefore, it is expected that at sufficiently lower temperature deuteride will be more stable than the corresponding hydride. But at elevated temperature the entropy effect predominates, and hydride tends to become more stable than the corresponding deuteride. The entropy difference between gaseous D_2 and H_2 is 14 JK^{-1} at room temperature. For each hydride, there should be a crossover temperature above which the hydride becomes more stable. Fort V-H system, the crossover temperature is found to be 137 °C. An example of more stable deuteride is given by Wiswall et al. [102]. In the absorption reaction between the first and the second hydride phase in the vanadium-hydrogen system, the absorption pressure for H_2 exceeds that for D_2

by a factor of 3. $CaNi_5$ shows very unusual isotope effect as it shows different effect for different plateau region. For β to α [103], the deuteride plateau is higher than the corresponding hydride indicating normal isotope effect. Intermediate plateau (γ to β) shows no detectable isotope effect. Whereas δ to γ transition shows prominent inverse isotope effect, and deuteride exhibits 1/3 of the plateau pressure of that of the hydride.

16.10 Characterization of Metal Hydrides

16.10.1 Hydrogen Sorption Measurement Techniques

For different classes of metal hydride, it is important to accurately quantify the total hydrogen loading in metal at different pressures and temperature. Accurate measurement of hydrogen gas uptake in solid sample is central characterization technique for number of research areas including hydrogen storage, carbon dioxide sequestration, catalysis, environmental protection, including among others. Precise determination of quantity of gas absorbed or adsorbed by a solid material and pressure composition isotherm can be done in several ways that are in principle very simple, but achieving accurate, reproducible results is not that straightforward. Broadly, there are three main methods (gravimetric, volumetric and temperature-programmed desorption) are being applied to determine hydrogen loading at different temperatures and pressure and also to determine the thermodynamics and kinetics of hydrogen loading. The three methods with their typical advantages and disadvantages are briefly summarized here.

16.10.1.1 Gravimetric Hydrogen Storage Set-up

In the gravimetric method, the amount of hydrogen absorbed is directly measured by change in the weight of sample during hydrogen absorption desorption cycle. Block diagram for simplified gravimetric set-up is given in Fig. 16.10. The heart of the apparatus is electronic microbalance for high-pressure applications including the balance housing. The other components are gas supply system (hydrogen as the reactive gas and helium as reference gas), an evacuation system consisting of a turbo molecular pump backed up by a roughing pump, a heater and data acquisition system.

To determine total hydrogen uptake, minimum possible amount of sample is loaded in the stainless steel sample crucible, and same weight (±1 mg) of reference material is loaded into the reference crucible. Before starting, the whole system is evacuated using turbo vacuum, and the sample is heated to the desired temperature. When the desired temperature is reached, certain pressure of hydrogen gas is introduced in the chamber, and amount of absorbed hydrogen is determined from the weight difference between the sample and the reference material.

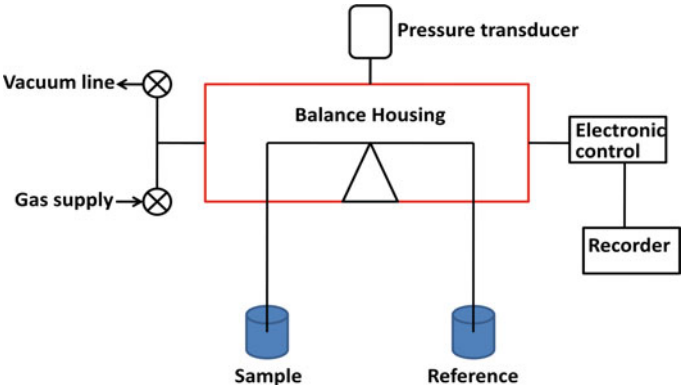

Fig. 16.10 Schematic diagram of gravimetric set-up for hydrogen uptake measurement

The major advantage of gravimetric hydrogen uptake measurement system is that it is direct method as here the hydrogen uptake is directly measured from the weight difference between the sample and reference materials after exposure to hydrogen at a particular temperature and pressure. So, several complications can be avoided due to volume calibration, adiabatic expansion of hydrogen gas, sample volume and density, etc., which are present in volumetric set-up (will be discussed in detail later). As the minute weight changes during absorption, desorption cycle is measured using a microbalance, so to get accurate result, optimized amount of sample should be loaded in thermo-gravimetric apparatus, and the sample amount is limited by the resolution and capacity of microbalance. In principle, this method is sensitive to all gasses absorbed in the materials, and as very small sample amount is used for the measurements, only high hydrogen absorbing materials give accurate results by this measurement. Buoyancy correction and highly sensitive microbalance are must for gravimetric measurement. Therefore, the method is best suited for chemical and metallic hydrides with high hydrogen storage capacities. To avoid buoyancy, the volume of the sample and the reference should be similar and at best the same.

16.10.1.2 Volumetric Hydrogen Storage Set-up

The volumetric method is indirect way of determining the total amount of hydrogen absorbed, by measuring the hydrogen pressure drop resulting from adsorption of hydrogen after exposing the sample to a particular hydrogen pressure at a constant volume and temperature. This approach is also called Sieverts approach, and the set-up is called Sieverts-type set-up. A schematic diagram of typical Sieverts type of set-up is presented in Fig. 16.11a. Different parts of this apparatus are a reactor, whose temperature is controlled by a temperature controller, heater, pressure monitoring system, vacuum system and gas inlet. The volume of the reactor and the manifold part should be well calibrated initially. To determine PCT curve and hydrogen

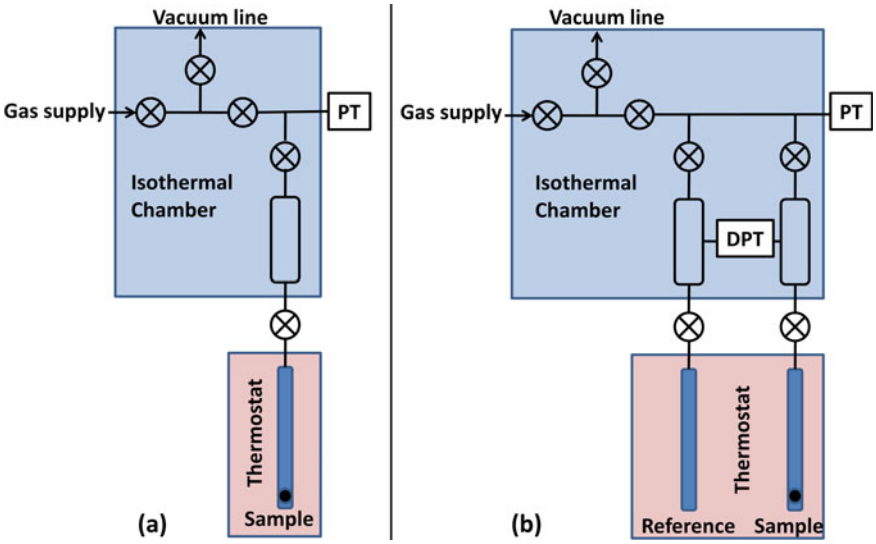

Fig. 16.11 **a** Schematic diagram of Sieverts-type apparatus. **b** Schematic of high-pressure differential pressure sorption apparatus. PT = pressure transducer, DPT = differential pressure transducer

storage capacity, the precise mass of the sample is required. Before starting experiment, the whole set-up is evacuated, and the temperature is increased up to working temperature. After that, the manifold region is charged with certain hydrogen pressure, and the absolute pressure is measured by pressure transducer. After stabilization of pressure and temperature, hydrogen gas is allowed to expand in sample chamber. As all the volumes are well calibrated, so from the pressure change in the absolute transducer, the total amount of absorbed hydrogen can be calculated. At a particular temperature, the gradual change in pressure gives the hydrogen sorption kinetics at the particular temperature and pressure.

The quantity of absorbed hydrogen is estimated, based on ideal gas low:

$$\Delta n = n1 - n2 = \Delta P(V/RT) \tag{16.18}$$

ΔP is difference between initial and final gas pressure, V = volume, n = number of moles of gas absorbed/desorbed, R = universal gas constant (8.314 J mol^{-1} K^{-1}), and T = absolute temperature.

The accuracy of volumetric hydrogen measurements set-up is highly dependent on the accuracy of initial volume calibration and the pressure transducers and their ability to provide both wide range and high-resolution measurements. The main advantage of this method is that here the conditions directly mimic that of high-pressure tank and the amount of sample can be increased to get sufficiently accurate results. In Sieverts-type apparatus, the uptake is measured by change in pressure of

the adsorbate within confined volume, so any factor which can affect pressure of the system will lead to error. Pressure measurement is very sensitive to (a) temperature fluctuations, (b) leaks and additional pressure effects caused by expanding the hydrogen from the reservoir to the sample cell. The other sources of error in volumetric measurement are discussed in detail by Broom [104] and others [105] which are issues related to internal volume calibrations, temperature and pressure measurements, sample amount and temperature gradients, equilibrium wait times, gas purity, sample degassing, thermal transpiration and leaks, sample density and volume, knowledge of the sample preparation and history and the compressibility of the gas. The volumetric technique is very sensitive to uncertainty in the sample volume, and it accumulates in each step. One of the ways to take care of sample volume is to do pycnometry correction with He gas. Again the design of Sieverts-type apparatus may be optimized for least uncertainty by having similar volumes for the reference and cell volumes which are both as small as practical [106]. Volumetric differential pressure hydrogen adsorption set-up has been designed by some researchers to minimize the additional pressure effects caused by expanding the hydrogen from the reservoir to the sample cell. A schematic diagram of such system is presented in Fig. 16.11b. Here, two identical vessels are connected to the sides of a differential pressure transducer. The sample is put in the reaction vessel, while a similar volume non-interacting reference material is placed in the reference vessel. At each step of the hydrogen absorption, the manifold sections are charged with hydrogen gas, and the gas pressure is measured by pressure transducer. After that, the gas in two manifold sections was simultaneously expanded into the cells (sample and reference). The difference between the pressures of the sample cell and the reference cell is measured by differential pressure transducer, and it represents the gas uptake by the adsorbent [107, 108]. The uncertainties of hydrogen capacity measurement can also be minimized by minimizing the reservoir volume, taking higher mass of loaded sample, using high accuracy pressure and temperature transducer and giving adequate thermal equilibration time [109]. Though total hydrogen storage capacity of metallic and chemical hydride can be determined very accurately by the above-mentioned methods, but for hydrogen storage capacity measurement of physisorbed materials (specially high surface area carbon based materials) at high pressure (>10 MPa), utmost care should be taken to obtain satisfactory degree of accuracy and reproducibility [110].

At higher hydrogen gas pressure (>5 MPa), errors in volumetric measurement come due to the deviation from ideal gas law as in that the interaction between the gas molecules is important. In that case, the ideal gas law should be corrected by van der Waals gas equation

$$\left(P + \frac{n^2 a}{V^2}\right)(V - nb) = nRT \tag{16.19}$$

where a and b are 0.2476 L^2 bar mol^{-1} and 0.2661 L mol^{-1} for hydrogen.

Again in hydrogen measurement set-up, in order to load samples, exposure towards air is inevitable. So, it is very difficult to characterize air-sensitive metals like magnesium, sodium for their hydrogen storage properties. For these cases, experimental setup with a detachable reactor is needed to load the sample under protective atmosphere if needed.

16.10.1.3 Temperature-Programmed Desorption

Temperature-programmed desorption (TPD) is an indirect technique to measure the amount of hydrogen in a metal hydride where a pre-hydrided sample is subjected to a temperature ramp, and the amount of hydrogen desorbed from the sample as a function of temperature is measured using a calibrated detector (quadrupole mass spectrometer/thermal conductivity detector). Here, very little amount of sample can be used and limited only by the sensitivity of the detector.

For thin film samples, conventional volumetric and gravimetric methods are not well suited for determining the total hydrogen storage capacity. For these cases, Robin Gremaud et al. [111] have recently proposed an innovative approach using optical combinatorial method to determine hydrogen absorption and desorption which is called hydrogenography. Using this approach, the P-C-T diagram at different temperature and enthalpy of hydrogen formation for several thin films has been determined successfully and is applicable for alloys which show appreciable change in the electronic structure after hydrogenation.

16.10.2 X-ray Diffraction and Neutron Diffraction

There are several techniques for determining site occupancy of H/D in metal hydride or deuteride. For structural determination of metal hydride, the most widely used technique is diffraction technique which is quite useful for ordered metal hydrides. Because of low atomic number of hydrogen, it cannot be located in metal hydride by X-ray diffraction, but neutron diffraction is very successful in this regard. In neutron diffraction, the position of both the metal atom and hydrogen can be determined by analysing the diffraction data [111, 113]. Neutron diffraction is mostly performed on metal deuteride because of favourable ratio between coherent and incoherent cross section of deuterium compared to that of hydrogen [114]. Neutron diffraction also helps to study the phase transformation of metal hydride with temperature [115]. A comprehensive review on neutron diffraction study of metal hydride can be found elsewhere [116], and detail of this will not be discussed in the present book chapter. Three major drawbacks of neutron diffraction measurement for structural determination are as follows:

(1) As relatively large amount of sample is needed, so sample homogeneity is a major limiting factor.

(2) In case of hydride, loss of crystallinity during hydriding leads to difficulty in structural determination.
(3) Due to lack of single crystal, mostly all the neutron diffraction studies have been done on powder sample, limiting the accuracy.

Hydrogen has the largest scattering interaction with neutrons of all the elements in the periodic table. Hence, neutron scattering technique is ideal for characterizing the structure and dynamics of these materials during hydrogen uptake [117]. Neutron scattering in combination with density functional theory provides fundamental information on host hydrogen interaction, dynamics process and the nature of the hydrogen containing species [118–123].

16.10.3 Nuclear Magnetic Resonance (NMR)

The chemical environment of hydrogen/deuterium in metal hydride and their mobility inside the host matrix can be determined using magic angle spinning (MAS) $^{1}H/^{2}D$ NMR and is used successfully nowadays to investigate metal hydride [124–126]. The magic angle spinning (MAS) in NMR reduces the line broadening of NMR signal, and thus, the resolution increases. This technique involves rotating the sample at an angular velocity around an axis inclined at a magic angle of 54.74° with respect to the magnetic field, which averages the anisotropic parts of the interactions that depend on the crystalline orientation in the magnetic field. Solid-state NMR also offers a better insight into reaction kinetics, reversibility and effect of catalysts by studying various steps leading to the formation of hydride [127]. It can be noted that deuteride gives better spectral resolution in MAS NMR than that of metal hydride at same rotation speed due to smaller magnetic moment of deuterium. Adolphi et al. have demonstrated that MAS NMR of YD_x yields spectrally resolved lines for D atoms at three non-equivalent deuterium sites, namely tetrahedral (T), octahederal (Oh) and tetrahedral sites with one or more occupied nearest neighbour octahedral site (T_{Oh}) [128]. In another similar study [129], Adolphi et al. have confirmed two equivalent deuteride sites in $ZrNiD_{3.0}$, in 2:1 ratio, using both static- and frequency-dependent MAS ^{2}D nuclear magnetic resonance spectroscopy. Manivasagam et al. [129] have investigated chemical environment of deuterium in electrochemically loaded $Mg_{0.65}Ti_{0.35}D_{1.2}$ using solid-state NMR, and from the chemical shift value, they could identify whether D is in Mg-rich or Ti-rich nano-domain.

16.11 Electronic and Magnetic Structure of Metal Hydride

The electronic structure and formation energy of many hydrides have been systematically investigated by several researchers [130].

Figure 16.12 explains the electronic band structure of metal hydride. In the electronic structure of transition metal or alloy, highly localized d band and delocalized s, p bands are prominent. When hydrogen gets absorbed in transition metal, it donates electron depending on the electronegativity of the metal atom. Insertion of hydrogen in metals introduces hydrogen s band with prominent hydrogen character below the Fermi level. After interaction, primarily electrons occupy the metal d band, and some electrons get localized to the hydride band, consuming electrons from the s and p band of metal. From the electronic structure, it is established that hydrogen remains in anionic form in metal hydride and causes electron promotion to the Fermi surface. The effect of hydrogen concentration on the electronic structure also has been studied in detail [131]. For LaH_x, $x \simeq 2$, the hydrogen-induced s band is centred ~5 eV below the Fermi level. With increase in hydrogen concentration, the d bands concentration near Fermi level decreases, and the hydrogen s band shifts to higher binding energy [132].

Using first principle calculation, the electronic structures of the complex hydrides Li_3AlH_6, Na_3AlH_6, $LiAlH_4$, $NaAlH_4$ and $Mg(AlH_4)_2$ have also been studied. All compounds are found to be large band gap insulators where the valence bands are dominated by the hydrogen atoms, and the conduction bands have mixed contributions from hydrogen and metal cationic states [133].

When lanthanides are hydrogenated up to the saturation value, they lose their electrical conductivity and magnetic ordering due to the depopulation of conduction band of the host metal. In the lanthanides and their hydrides, the magnetism originates due to the presence of partially filled f orbital [134]. Due to the restricted special extension of f orbital, no significant overlap occurs with neighbouring atom, and conduction electrons are responsible for magnetism. With hydrogenation, the conduction band of lanthanides depopulates, and on saturation, a complete depopulation of conduction band occurs, which suppresses its magnetism. In the intermetallic

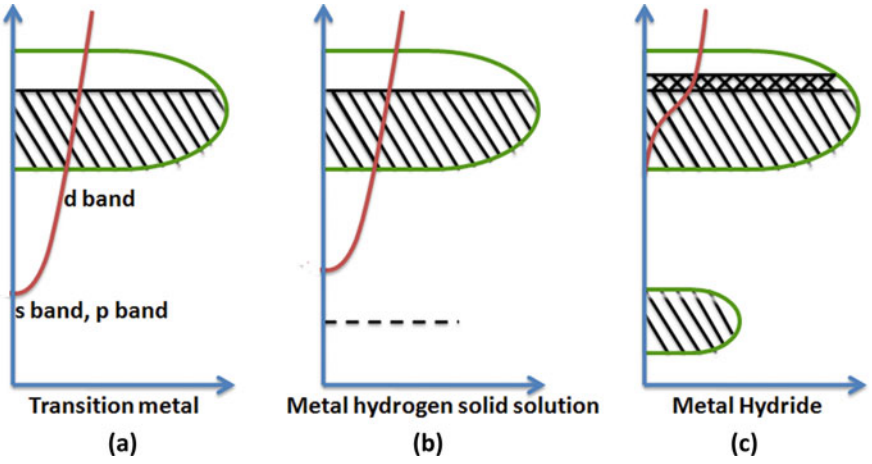

Fig. 16.12 Electronic band structure of hydrides

compounds between lanthanides and transition metal element, interesting observations are noted in magnetic structure after hydrogen loading and are considered to be one of most fascinating magnetic systems. A paramagnetic system (Th_6Mg_{23}) can transform into a ferromagnetic system upon hydrogenation due to straightening of magnetic ordering, suppression of ferromagnetism can occur (Y_6Mn_{23}), a superconducting alloy can get transformed into ferromagnet upon hydrogen absorption (Th_7Fe_3), and also, hydrogenation can lead to spin glass system (Er_6Mn_{23}). In most of the alloys, the lanthanides transfer its electrons to the d orbital of transition metal changing its magnetic behaviour.

16.12 Applications of Metal Hydride

From practical application point of view, metal hydrides are interesting candidates in scientific and engineering communities since their discovery in 1866 [135, 136]. Most researches in metal hydrides are intended for two types of applications: Ni-MH rechargeable battery and hydrogen storage. Its battery application is widely exploited as a good replacement for conventional Ni-Cd batteries. However, the metal hydride as hydrogen storage material is still challenging because of some technical issues. Some of the other applications of metal hydrides are thermochemical devices, hydrogen purification and separation, hydrogen gettering, hydrogen sensor, switchable mirror, electrochemical application, isotope separation, etc.

16.12.1 Hydrogen Storage

The first studies on metal hydrides as hydrogen storage materials for vehicular application were made by German automobile manufacturer Daimler Benz by combining metal hydride tanks with combustion engines in mini vans [137]. Since then, a number of alloys/intermetallics have been designed for hydrogen storage application [52, 138]. Safety-wise they are considered as the most relevant class of hydrogen storage materials because they can store hydrogen at relatively lower pressure. It is desirable to have high gravimetric hydrogen storage capacity for the metal hydride to deliver satisfactory driving range between refuelling. The other crucial parameters (as set by Department of Energy, United States) that determine the performance of metal hydrides for on-board vehicular application are listed in Table 16.3.

Among different types of intermetallic compounds, $LaNi_5$-based systems are attractive candidates for hydrogen storage due to easy activation, ability to store hydrogen at ambient condition, fast hydriding/dehydriding kinetics, tolerance towards gas impurities and low hysteresis [140]. Another advantage of these systems is that the absorption/desorption thermodynamics can be altered just by varying the composition or by partial substitution with other elements like Ce (in La site), Al, Cu, Cr, Sn, Fe, Co, Mn, Rh, Ir, Pt or Au, etc. (in Ni site) [141–143]. However,

Table 16.3 Targets set by department of energy DOE for hydrogen storage system (vehicular application) [139]

Parameters	Unit	2020 target	Ultimate target
Gravimetric capacity	kg H_2/Kg system	0.055	0.075
Volumetric capacity	kg H_2/L system	0.04	0.070
Min/Max delivery temperature	°C	−40/85	−40/85
Cycle life	Cycles	1500	1500
System fill time for 5 kg fill	Min	3.3	2.5

the gravimetric hydrogen storage capacity of $LaNi_5$-based systems is intrinsically low because of its $CaCu_5$-type hexagonal structure [144]. Moreover, for practical applications, a long-term cycling stability is required. Borzone et al. [145, 146] have shown that the partial substitution of Ni by Sn reduces the cyclic degradation of $LaNi_5$-based intermetallic compounds. Al substitution is also effective in improving the cyclic stability of [147] La-based metal hydrides.

TiFe is another well-known intermetallic compound which is much cheaper than $LaNi_5$-based hydrogen storage systems [148]. They exist in cubic CsCl-type structure and possess reversible hydrogen storage capacity of 1.9 wt.% [149]. TiFe alloys are capable of absorbing hydrogen provided proper activation is done prior to hydrogenation. TiFe-based systems are highly sensitive to gas impurities. Moreover, they suffer from poor hydrogen reaction kinetics and high equilibrium plateau pressure. Ćirić et al. [149] have reported that partial substitution of Fe with Ni results in lower equilibrium pressure and enhances the hydrogen absorption–desorption kinetics. However, the maximum hydrogen storage capacity decreases with increase in Ni content. Other substituents such as Mn, Cr and V are also effective in reducing the plateau pressure and improving the activation performance [150, 151]. Manganese has been proven to enhance the tolerance towards gas impurities.

Apart from TiFe, another cost-effective intermetallic hydrides are Laves phase compounds with AB_2-type structure where A is either Ti or Zr, and B represents transition metal. Vanadium (V) is an important modifier used to increase the hydrogen storage capacity of Zr-based Laves phase compound [152]. Actually, the hydrogen uptake increases with decrease in outer shell occupation number in the 3d series. Banerjee et al. have found that the partial substitution of Fe by V can remarkably increase the hydrogen storage capacity of $ZrFe_2$-based Laves phase compound [153]. However, an increase in V content increases the stability of the hydride indicating that the enthalpy of hydride formation increases with increase in V concentration. The compound with $ZrFe_{1.2}V_{0.8}$ composition was found to absorb 3.78 H/formula unit with a formation enthalpy of −41.8 kJ/mol by this research group. Recently, Rabahi et al. [154] have used density functional theory (DFT) pseudo-potential method to investigate the atomic hydrogen absorption trends in the cubic C15-$ZrFe_2$ Laves

phase compound in presence of third elements. They have found that compounds with Be, V, Cr, Mn, Y and Tc at the Fe sites can absorb up to 6H/*formula unit.*

Titanium (Ti)-based solid solution alloys with BCC structure are reported to have higher hydrogen storage capacities compared to conventional intermetallic compounds. Some of the recent reports show that the room temperature gravimetric hydrogen storage capacity may reach up to 4 wt.% [22, 155]. However, two major drawbacks of these alloys are as follows: difficult initial activation and comparatively higher desorption temperature. Extensive researches have been conducted by implementing methods such as elemental substitution, composite formation and annealing. Fe substitution is reported to improve the activation performance of Ti-based BCC alloys [156, 157]. Recently, Kamble et al. have suggested that tuning the chemical composition is the most efficient way to improve the activation characteristic of Ti-Cr-V-based hydrogen storage alloys [158]. The most critical feature in the activation procedure of these alloys is longer incubation period. This incubation time can be reduced by addition of elements such as Zr and Mn which are known to promote Laves phase formation [20, 64, 65, 159, 160]. In these Laves phase-related BCC solid solution, it acts as the penetration path for H atoms to enter into the main hydrogen absorbing BCC phase and thus catalyses the hydrogenation process. However, they absorb less amount of hydrogen compared to pure BCC phase. Zr, being a good hydrogen getter, is effective to improve the cyclic stability of Ti-Cr-V-based BCC alloys [64]. The presence of Zr-based Laves phase in BCC matrix was found to reduce the desorption temperature remarkably [65].

Although a number of alloys and intermetallic compounds have been investigated for their prospective as hydrogen storage materials, very few of them have proper combination of properties to allow for automobile application. Some of the hydrides (of alloys/ intermetallic compounds) used as hydrogen storage tanks to run vehicles by some major automobile companies are listed in Table 16.4.

In India, 2/3-wheelers (primarily responsible for terribly poor air quality in cities) fuelled by hydrogen from metal hydride storage tanks have been demonstrated successfully by the group led by Professor O. N. Srivastava at Banaras Hindu University [162]. For running these hydrogen-fuelled 2/3-wheelers by internal combustion engine, mischmetal (Mm)-based AB_5-type alloy with a reversible hydrogen storage capacity of 1.8 wt.% was developed by this group.

Table 16.4 Metal hydride-based automobiles (already demonstrated) [161]

Manufacturer	Type of vehicle	Power	Alloy/Intermetallics	Year
SRTC Bus	Augusta	Internal combustion engine	$Lm(Ni, Al)_5$	1996
John Deere	Gator 1	Fuel cell	Mm(Ni, Al)	1998
John Deere	Gator 2	Fuel cell	Ti(Fe, Mn)	1998
FCPI /SNL	Mine Locomotive	Fuel cell	(Ti, Zr)(Mn, V, Cr, Fe)	2001
ECD	Motor Scooter	Hybrid internal combustion engine	ECD	2002

16.12.2 Thermochemical Devices

16.12.2.1 Heat Storage

Formation of reversible metal hydride is associated with heat release which is exploited in utilizing metal hydrides as thermochemical heat storage systems. The main advantage of metal hydride (MH)-based heat storage systems (over the latent heat storage systems using phase change materials) is that they can store heat for a longer time without any thermal insulation, thereby greatly increasing overall system efficiency. They are characterized by high energy density and nearly constant heat delivery temperature. A wide range of operating temperature is available with MH-based thermochemical energy storage systems [163]. For example, Mg-based metal hydride systems can provide heat energy with density as high as 2814 kJ kg^{-1} of hydride [164].

When a metal hydride is gradually heated in a closed system, the hydride will dissociate into corresponding metal and H_2. For the operation of MH-based heat storage system, a prior knowledge of the equilibrium hydrogen pressure at different temperatures (which is usually obtained from van't Hoff plot) is required. By choosing the hydrogen pressure, it is possible to find out the appropriate temperature level for release of stored heat. Hence, a proper selection of hydride-forming metal/alloy/intermetallic compound assures maximum performance within the desired range of operation. Metal hydrides with high enthalpy of hydride formation and relatively lower value of hydride dissociation pressure are attractive as heat storage materials. For an optimal heat storage system, it is desirable that the hydrogen absorption/desorption reaction should be faster enough compared to heat transport so that heat transport will govern the overall dynamics of the system. In addition, it is necessary that the metal should have easy activation, low hysteresis, good reversibility and high melting point.

16.12.2.2 Heat Pump

Conventional refrigerants and air conditioners use chlorofluorocarbons (CFC) which are responsible for damaging ozone layer. Thermally driven metal hydride-based heat pumps seem to be a promising alternate because it uses environment-friendly hydrogen as refrigerant [165]. They provide wide operating temperature ranges by changing the MH composition. They utilize low grade waste heat (industrial waste heat, exhaust gas of automobile, etc.) without using any mechanical moving part.

16.12.2.3 Hydrogen Compressor

Another practical application of metal hydride which exploits pressure–temperature response of reversible hydrogenation dehydrogenation reactions is hydrogen

compressor. This thermally driven MH hydrogen compressor is a good alternative to conventional mechanical hydrogen compressor [166]. MH hydrogen compressor offers several advantages such as simple design, easy operation, compactness, safety and reliability, absence of moving parts and possibility to consume waste heat instead of electricity. The performance of a MH hydrogen compressor is largely dependent on the thermodynamics and kinetics of metal hydride formation reaction. Apart from that, structural and morphological aspects of metal and its corresponding hydride determine the overall performance of the hydrogen compressor. For better performance of hydrogen compressor, several features such as synchronization of plateau pressure for multi-stage compressors, minimizing the slope of the isotherms and hysteresis, increase of cycling stability and minimal dilatation should be attained. Again, the efficiency can be improved by reducing the mass of MH reactors together with auxiliary elements such as heat exchangers and filters. For better productivity of hydrogen compressor, heat transfer performance of the MH reactor has to be improved. Application of MH as hydrogen compressor requires compromisation between thermal energy for hydrogen desorption and high compression ratio. This imposes a medium heat effect requirement for MH materials ($\triangle H$ = 20–30 kJ/mol H_2).

Several applications of MH-based H_2 compressors include laboratory facilities, cryogenics, utilization of industrial waste heat, space application, H_2 filling stations, temperature sensors and actuators.

16.12.3 Hydrogen Purification and Separation

Metal hydride-based hydrogen separation and purification technology mainly depend on the selective absorption of hydrogen by hydrogen storage materials [167–169]. When a mixture of gases containing hydrogen is allowed to flow through a hydrogen storage bed, hydrogen reacts with the metal/alloy to form a metal hydride (provided hydrogen partial pressure is higher than equilibrium plateau pressure). All other gas contents in the mixture (which do not react with metal/alloy) flow out from the bed. Thermal ballast is used in order to control temperature change in the hydriding–dehydriding cycle of the hydrogen separation and purification system [170]. However, Saitou et al. [171] have reported hydrogen purification employing $FeTi_{0.95}Mm_{0.08}$-based alloy in the temperature range of 25–90 °C. The main problem in the successful application of metal hydride-based hydrogen purification from mixed gases is the extreme sensitivity of the metal/alloy surface to different impurities. For example, carbon monoxide (CO) forms a layer on the surface of metal hydride. As a result, the metal hydride loses its ability to absorb hydrogen. Miura et al. have introduced some CO absorbent in the initial stage of purification to eliminate its poisoning effect and then passed the gas mixture through AB_5-type metal hydride bed [172] and ultimately obtained 83% hydrogen recovery.

16.12.4 Hydrogen Gettering

Hydrogen gettering is based on the ability of certain metals/alloys to absorb free hydrogen gas leading to metal hydride formation. Transition metals such as zirconium, titanium and their alloys are used as potential hydrogen getters and maintain a low equilibrium hydrogen pressure [173]. The technological importance of getter materials is realized in different fields including particle accelerators, ultrahigh vacuum (UHV) systems, space probes, semiconductor manufacturing and plasma physics experiments [174]. Hydrogen exists as main residual gas component in an ultrahigh vacuum system. Pumping of hydrogen by metal/alloy-based getter materials involves dissociation of hydrogen molecules into hydrogen atoms (H) on the metal/alloy surface at lower atmospheric pressure, intrusion of nascent H atoms into the material and formation of a stable M–H bond irreversibly. The performance of a metal/alloy as gettering material is governed by its pumping speed, absorption capacity and thermodynamic property. Ghezzi et al. [175] have investigated the effect of grain size distribution on the thermodynamics of $Zr(Fe_{0.5}Mn_{0.5})_2$ getter alloy and found that the small grain distribution resulted in H_2 pressure values close to equilibrium plateau pressure. They have shown the importance of grain size distribution study to scrutinize the possibility of this alloy for practical use as getter material without performing cycling test.

16.12.5 Hydrogen Sensor

In a hydrogen-based economy, hydrogen sensor will become an essential part of the infrastructure to provide safe operation by detecting hydrogen leaks from storage tanks, gas lines, etc. Thus, it will be able to prevent ignition or explosion of highly flammable/explosive H_2. Apart from hydrogen-based future economy, nowadays hydrogen is mostly used in chemical industry such as production of ammonia, petrochemical industry, food industry and pharmaceutical industry. Thus, hydrogen sensors are required for these applications to monitor and control hydrogen partial pressure.

Some of the metal hydrides possess interesting optical and electrical properties which can be exploited for the design and development of hydrogen sensor. Mg- or Pd-based thin films have shown good hydrogen sensing property at room temperature [176, 177]. Palmisano et al. [178] have investigated the H_2 gas sensing ability of Pd capped Mg-based thin film device and shown one to one relationship between hydrogen partial pressure and the visible optical change along the layers of the thin film. Apart from optical and electrical properties, lattice expansion of alloys upon hydrogen exposure has also been employed for fabrication of H_2 gas sensor [179].

16.12.6 Switchable Mirror

Switchable mirrors based on reversible uptake of hydrogen by rare-earth alloy films (yttrium or lanthanum thin film) were discovered by Huiberts et al. [180]. Upon exposure to hydrogen gas, the alloy film switches from reflecting metallic state (mirror) to the transparent hydride phase. Subsequently, rare-earth magnesium alloy-based films were found to be better compared to pure lanthanide films relating to maximum transparency and mirror-state reflectivity. Mg-Ni-based switchable mirrors are beneficial over rare-earth hydrides due to larger optical contrast [181]. The reversible conversion from mirror state to transparent state may also happen by cathodic polarization in electrochromic switchable mirrors [182]. Electrochemical switching is usually carried out in alkaline electrolyte with in situ measurement of optical transmission spectra. A room equipped with smart window (window impregnated with switchable mirror sheet) requires less cooling power compared to the room equipped with normal transparent window [183].

16.12.7 Electrochemical Application

One of the major electrochemical applications of metal hydride is in Ni-MH batteries [18, 184]. It is already mentioned that Ni-MH battery is a good alternate to Ni-Cd battery to replace the toxic Cd electrode. Hydrogen storage alloy is used as negative electrode in Ni-MH battery. Improvement of hydrogen storage capacity of the alloy results in high energy density of the Ni-MH battery, and many of the Ni-MH batteries are available in market [185, 186]. First commercial Ni-MH battery was discovered in 1989 by Ovonic Battery Company, Sanyo and Matsushita with AB_2 and AB_5 alloys. Some of the required properties of the alloys used in Ni-MH batteries are as follows: an appropriate equilibrium hydrogen pressure (0.1–1 atm); an appropriate equilibrium potential (~−0.9324 V vs. Hg/HgO); fast mass and charge transfer, good corrosion resistance (for better cyclic life of the battery). The important processes that take place in the metal hydride-based batteries can be represented with the following charge and discharge reactions:

Charge

During electrochemical charge, water in the electrolyte generates proton at the metal/electrolyte interface under an applied electric field. These protons are absorbed in the matrix of metal to form corresponding metal hydride (MH). The charging process is depicted by the half reaction:

$$M + H_2O + e^- \rightarrow MH + OH^-$$

At the positive electrode, nickel hydroxide ($Ni(OH)_2$) gets oxidized into nickel oxy-hydroxide (NiOOH) as follows:

$$Ni(OH)_2 + OH^- \rightarrow NiOOH + H_2O + e^-$$

Thus, the positive electrode is oxidized, and the negative electrode is reduced during charge.

Discharge

During discharge, proton in the MH leaves the surface of negative electrode and recombines with the hydroxyl ion in the alkaline electrolyte to form water. The discharge process is characterized by the half reaction:

$$MH + OH^- \rightarrow M + H_2O + e^-$$

At the positive electrode, nickel oxy-hydroxide is reduced to nickel hydroxide.

$$NiOOH + H_2O + e^- \rightarrow Ni(OH)_2 + OH^-$$

Both charging and discharging reactions take place in an alkaline medium (usually KOH solution) because in acid solution vigorous etching of the metal-based negative electrode occurs. Moreover, $Ni(OH)_2$ is unstable in acidic solution.

16.12.8 Isotope Separation

Metal–hydrogen interaction is extensively employed for isotope separation using isotope-dependent properties. Metal-based alloys with large difference in plateau pressures for different isotopes of hydrogen are used for this purpose [187, 188]. The isotope effect is more prominent in the presence of magnetic field for a ferromagnetic hydrogen storage material. Ito et al. have reported that the isotope separation ability of $LaCo_5$, a ferromagnetic material is remarkably enhanced when it is placed inside the core of a superconducting magnet [189].

Apart from the above-mentioned applications, metal hydrides can also be used as efficient moderator, reflector, shielding materials in nuclear reactors [190]. In powder metallurgy, hydrides of transition metal-based alloys are commonly used as attractive starting material for obtaining alloy powder [191]. The concept of metal hydride integrated hydrogen-powered actuators is getting popularity due to its unique characteristics such as compact design, biomimeticity and high force to mass ratio [192, 193].

16.13 Conclusion

The present chapter discussed about the rapid development of metal hydride since 1970s and its importance both in fundamental research as well as for various practical applications. Many of metal or alloys can form hydride under hydrogen pressure, and the pressure of hydrogen absorption solely depends on the thermodynamic parameter. By reducing the pressure or increasing the temperature, absorbed hydrogen can be released from the hydride system. The kinetic analysis of metal hydride is very complicated and gets affected by surface impurity, particle size, impurity in gas, etc. Different metal hydrides like $LaNi_5H_6$, FeTi, MgH_2 and $NaAlH_4$ have shown very high promises for on-board storage, but till now, there is no ideal hydrogen storage material with adequate level of performance, which may be acceptable. During development of efficient metal hydride tank, typical influencing parameters are the thermal conductivity of metal as well as the hydride, heat of reaction and the apparent activation energy for hydrogen absorption and desorption. Thermal heat management, efficiency and reversibility of metal hydride are providing a lot of challenge, and tremendous amount of research is going on in these areas. The major issue with metal hydride is to increase the hydrogen storage capacity at room temperature, and they are expected to play an important role in the future 'hydrogen economy'.

Acknowledgements The authors would like to thank Dr. V. Sudarsan, Dr. K. Shahsikala and Dr. C. G. S. Pillai Chemistry Division, BARC, for their valuable advices and suggestions, and Mr. Asheesh Kumar for his constant help and support.

References

1. Webelements, Hydrogen historical information. Retrieved 27 Dec 2007
2. Cavendish H (2007) Philos Trans 56(1766):141–184. The University Press. https://doi.org/10.1098/rstl.1766.0019. The university press. Retrieved on 6 Nov 2007
3. Osiris JG (1994) Precision instruments and the demonstrative order of proof in Lavoisier's chemistry. Instruments 9:30–47. https://doi.org/10.1086/368728,jstor.org/stable/301997
4. Graham T (1866) On the absorption and dialysis separation of gases by colloid septa. Phil Trans Roy Soc (London) 156:399–349
5. Dornheim M (2011)Thermodynamics—interaction studies—solids, liquids and gases, book edited by Pirajáan JCM. ISBN 978-953-307-563-1, Published: November 2, 2011 under CC BY Chapter 33, Thermodynamics of metal hydrides: tailoring reaction enthalpies of hydrogen storage materials. Wiley, New York
6. Libowitz GG, Hayes HF, Gibb TRP (1958) The system zirconium–nickel and hydrogen. J Phys Chem 62:76–79
7. Dantzer P (1997) Topics in applied physics hydrogen in metals III, metal-hydride technology. Crit Rev 73:279–340
8. Lim KL, Kazemian H, Yaakob Z, Daud WRW (2010) Solid-state materials and methods for hydrogen storage: A critical review. Chem Eng Technol 33:213–226
9. Strnat K, Hoffer G, Olson J, Ostertag W, Becker JJ (1967) A family of new cobalt-base permanent magnet materials. J Appl Phys 38:1001–1002

10. Zijlstra H, Westendorp FF (1969) Influence of hydrogen on the magnetic properties of SmCo5. Solids State Comm 7:857–859
11. Williems JJG, Buschow KHJ (1987) From permanent magnets to rechargeable hydride electrodes. J Less-Common Met 129:13–30
12. Buschow KHJ, Gschneidner KA, Eyring JrL (Eds.) (1984) Handbook on the physics and chemistry of rare earths 6:1–574
13. Kempton W, Kubo T (2000) Energy policy, electric-drive vehicles for peak power in Japan. Energy policy 28:9–18
14. Kiley D (2004) The ultimate hydrogen future in Driven: Inside BMW, the most admired car company in the world. Hoboken, New Jersey, John Wiley & Sons, Inc. ISBN: 978–0–471–26920–5. Pp. 289–90
15. Samuel L (2016) Review of the prospects for using hydrogen as a fuel source in internal combustion engines. H2FC Working Paper 2(2)
16. Bowman RC, Fultz JrB, Bulletin MRS (2002) Hydrogen storage. 27(9):688–693
17. Yu XB, Feng SL, Wu Z, Xia BJ, Xu NX (2005) Hydrogen storage performance of Ti–V-based BCC phase alloys with various Fe content. J Alloys Compd 393:128–134
18. Young K, Nei J (2013) The current status of hydrogen storage alloy development for electrochemical applications. Mater 6:4574–4608
19. Yu X, Wu Z, Xia B, Huang T, Chen J, Wang Z, Xu N (2003) Hydrogen storage in Ti–V-based body-centered-cubic phase alloys. J Mater Res 18:2533–2536
20. Shashikala K, Banerjee S, Kumar A, Pai MR, Pillai CGS (2009) Improvement of hydrogen storage properties of TiCrV alloy by Zr substitution for Ti. Int J Hydrogen Energy 34:6684–6689
21. Basak S, Shashikala K, Kulshreshtha SK (2008) Hydrogen absorption characteristics of Zr substituted Ti0. 85VFe0. 15 alloy. Int J Hydrogen Energy 33:350–355
22. Kumar A, Shashikala K, Banerjee S, Nuwad J, Pillai CGS (2012) Effect of cycling on hydrogen storage properties of Ti2CrV alloy. Int J Hydrogen Energy 37:3677–3682
23. Basak S, Shashikala K, Sengupta P, Kulshreshtha SK (2007) Hydrogen absorption properties of Ti–V–Fe alloys: Effect of Cr substitution. Int J Hydrogen Energy 32:4973–4977
24. Switendick AC (1978) In Hydrogen in Metals I. Topics in Applied Physics, Vol. 28. Alefeld G and Völkl J (Eds). Berlin: Springer
25. Smith GS, Johnson QC, Smith DK, Cox DE, Snyder RL, Zhou RS, Zalkin A (1988) The crystal and molecular structure of beryllium hydride. Solid State Comm 67:491–494
26. Bergsma J, Loopstra BO (1962) The crystal structure of calcium hydride. Acta Crystallogr A 15:92–93
27. Brese NE, O'Keeffe M, Von Dreele RB (1990) Synthesis and crystal structure of SrD2 and SrND and bond valence parameters for hydrides. J Solid State Chem 88:571–576
28. Noritake T, Towata S, Aoki M, Seno Y, Hirose Y, Nishibori E, Takata M, Sakata M (2003) Charge density measurement in MgH2 by synchrotron X-ray diffraction. J Alloys and Compd 356–357:84–86
29. Rittmeyer P, Wietelmann U Chap: Hydrides, ullmann's encyclopedia of industrial chemistry, fifth, completely revised Edition. Vol. A13. VCH, pp. 199–226
30. Young KH, Chang S, Lin X (2017) Chap: C14 Laves phase metal hydride alloys for Ni/MH batteries application in book "Nickel Metal Hydride Batteries 2017". Young KH (ed.) MDPI. http://www.mdpi.com/journal/batteries/special_issues/ni_mh_batteries2017.
31. Lundin CE, Lynch FE, Magee CB (1977) A correlation between the interstitial hole sizes in intermetallic compounds and the thermodynamic properties of the hydrides formed from those compounds. J Less-Common Met 56:19–37
32. Liu W, Webb CJ, Gray EM (2016) Review of hydrogen storage in AB3 alloys targeting stationary fuel cell applications. Int J Hydrogen Energy 41:3485–3507
33. Gingl F, Vogt T, Akiba E (2000) Trigonal SrAl2H2: the first Zintl phase hydride. J Alloys Compd 306:127–132
34. Huang B, Corbett JD (1997) Intermetallic hydrides as Zintl phases: A3TtH2 Compounds (A = Ca, Yb; Tt = Sn, Pb) and their structural relationship to the corresponding oxides. Inorg Chem 36:3730–3734

35. Auer H, Guehne R, Bertmer M, Weber S, Wenderoth P, Hansen TC, Haase J, Kohlmann H (2017) Hydrides of Alkaline Earth–Tetrel (AeTt) Zintl Phases: Covalent Tt–H Bonds from Silicon to Tin. Inorg Chem 56:1061–1071
36. Auer H, Schlegel R, Oeckler O, Kohlmann H (2017) Structural and electronic flexibility in hydrides of zintl phases with tetrel–Hydrogen and tetrel–Tetrel bonds. Angew Chem Int Ed Engl 56:12344–12347
37. Zintl Phases: Principles and recent developments. Springer, edited by Thomas F. Fässler
38. Libowitz GG (1963) Advances in chemistry, nonstoichiometry in metal hydrides. Ch. 7, 39:74–86
39. Gibb TRP (1963) Nonstoichiometric hydrides interstitial-atom, proton, and hydride-anion models, advances in chemistry. 39:pp 99–110
40. Smithson H, Marianetti CA, Morgan D, Van der Ven A, Predith V, Ceder G (2002) First-principles study of the stability and electronic structure of metal hydrides. Phy Rev B 66:144107(1)- 144107(10)
41. George L, Saxena SK (2010) Structural stability of metal hydrides, alanates and borohydrides of alkali and alkali-earth elements: A review. Int J Hydrogen Energy 35:5454–5470
42. Sakintuna B, Lamari-Darkrim F, Hirscher M (2007) Metal hydride materials for solid hydrogen storage: a review. Int J Hydrogen Energy 32:1121–1140
43. Borgschulte A, Gremaud R, Griessen R (2008) Interplay of diffusion and dissociation mechanisms during hydrogen absorption in metals. Phys Rev B 78:094106(1)–094106(16)
44. Banerjee S, Pillai CGS, Majumder C (2009) Dissociation and diffusion of hydrogen on the Mg (0001) surface: catalytic effect of V and Ni double substitution. J Phys Chem C 113:10574–10579
45. Banerjee S, Pillai CGS, Majumder C (2008) First-principles study of the interaction with transition metal (Ti, V, Ni) doped Mg(0001) surface: Implications for H-storage materials. J Chem Phys 129:174703(1)–174703(6)
46. Pozzo M, Alfe D (2009) Hydrogen dissociation and diffusion on transition metal (= Ti, Zr, V, Fe, Ru, Co, Rh, Ni, Pd, Cu, Ag)-doped Mg (0001) surfaces. Int J Hydrogen Energy 34:1922–1930
47. Pozzo M, Alfè D, Amieiro A, French S, Pratt A (2008) Hydrogen dissociation and diffusion on Ni-and Ti-doped Mg (0001) surfaces. J Chem Phy 128:094703
48. Wiswall R (1978) Hydrogen storage in metals, Hydrogen in metals II. (eds G. Alefeld and J. V€olkl), Top Appl Phys Springer-Verlag, Berlin, 29 (1978) 201–242
49. Ono S, Nomura K, Akiba E, Uruno H (1985) Phase transformations of the LaNi5-H2 system. J Less-Common Met 113:113–117
50. Akiba E, Nomura K, Ono S (1987) A new hydride phase of LaNi5H3. J Less-Common Met 129:159–164
51. Sandrock GD, Murray JJ, Post ML, Taylor JB (1982) Hydrides and deuterides of CaNi5. Mat Res Bull 17:887–894
52. Sandrock GD (1999) A panoramic overview of hydrogen storage alloys from a gas reaction point of view. J Alloys Compd 293–295:877–888
53. Katz OM, Gulbransen EA (1962) Some observations on the uranium-niobium hydrogen system. J Nucl Mater 5:269–279
54. Bloch J, Mintz MH (1997) Kinetics and mechanisms of metal hydrides formation—a review. J Alloys Compd 253–254:529–541
55. Schur DV, Lavrenko VA, Adejev VM, Kirjakova IE (1994) Studies of the hydride formation mechanism in metals. Int J Hydrogen Energy 19:265–268
56. Efron A, Lifshitz Y, Lewkowicz I, Mintz MH (1989) The kinetics and mechanism of titanium hydride formation. J Less-Common Met 153:23–34
57. Gérard N, Ono S, Hydride formation and decomposition kinetics Hydrogen in intermetallic compunds II pp 165–195 Hydride formation and decomposition kinetics.
58. Khawam A, Flanagan DR (2006) Solid-state kinetic models: basics and mathematical fundamentals. J Phys Chem 110:17315–17328

59. Hancock JD, Sharp JH (1972) Method of Comparing Solid-State Kinetic Data and Its Application to the Decomposition of Kaolinite, Brucite, and $BaCO_3$. J Am Ceram Soc 55:74–77
60. Sharp JH, Brindley GW, Achar BNN (1966) Numerical data for some commonly used solid state reaction equations. J Am Ceram Soc 49:379–382
61. Ginstling AM, Brounshtein BI (1950) Concerning the diffusion kinetics of reactions in spherical particles. J Appl Chem USSR 23:1327–1338
62. Muthukumar P, Satheesh A, Linder M, Mertz R, Groll M (2009) Studies on hydrating kinetics of some La-based metal hydride alloys. Int J Hydrogen Energy 34:7253–7262
63. Avrami M (1939) Close kinetics of phase change. J Chem Phys 7:1103–1112
64. Ruz P, Banerjee S, Halder R, Kumar A, Sudarsan V (2017) Thermodynamics, kinetics and microstructural evolution of Ti0. 43Zr0. 07Cr0. 25V0. 25 alloy upon hydrogenation. Int J Hydrogen Energy 42:11482–11492
65. Banerjee S, Kumar A, Ruz P, Sengupta P (2016) Influence of Laves phase on microstructure and hydrogen storage properties of Ti–Cr–V based alloy. Int J Hydrogen Energy 41:18130–18140
66. Leardini F, Ares JR, Bodega J, Fernandez JF, Ferrer IJ, Sanchez C (2010) Reaction pathways for hydrogen desorption from magnesium hydride/hydroxide composites: bulk and interface effects. Phys Chem Chem Phys 12:572–577
67. Ferrizz RM (2006) Erbium hydride decomposition kinetics. J Alloys Compd 419:40–44, SANDIA REPORT SAND2006-7014
68. Genossar J, Rudman PS (1979) The Catalytic Role of Mg2 Cu in the Hydrating and Dehydrating of Mg. Z Phys Chem 116:215–224
69. Hälg FW, Schlapbach L, Yvon K (1978) Neutron and X-Ray Diffraction Investigation of Deuterium Storage in La7Ni3. J Less-Common Met 60:1–9
70. Gennari FC, Castro FJ, Andrade Gamboa JJ (2002) Synthesis of Mg2FeH6 by reactive mechanical alloying: formation and decomposition properties. J Alloys Compd 339:261–267
71. Retuerto M, Sánchez-Benítez J, Rodríguez-Cañas E, Serafini D, Alonso JA (2010) High-pressure synthesis of Mg2FeH6 complex hydride. Int J Hydrogen Energy 35:7835–7841
72. Zhang X, Tian W, Yang J, Yang R, Zheng J, Li X (2011) Synthesis and hydrogen storage behaviour of pure Mg2FeH6 at nanoscale. Mater Trans 52:618–622
73. Danaie M, Asselli AAC, Huot J, Botton GA (2012) Formation of the ternary complex hydride Mg2FeH6 from magnesium hydride (β-MgH2) and iron: An electron microscopy and energy-loss spectroscopy study. J Phys Chem C 116:25701–25714
74. Kleperis J, Wójcik G, Czerwinski A, Skowronski J, Kopczyk M, Beltowska-Brzezinska M (2001) Electrochemical behavior of metal hydride. J Solid State Electrochem 5:229–249
75. Asano K, Enoki H, Akiba E (2009) Synthesis of HCP, FCC and BCC structure alloys in the Mg–Ti binary system by means of ball milling. J Alloys Compd 480:558–563
76. Asano K, Enoki H, Akiba E (2009) Synthesis of Mg–Ti FCC hydrides from Mg–Ti BCC alloys. J Alloys Compd 478:117–120
77. Zhang Y, Tsushio Y, Enoki H, Akiba E (2005) The hydrogen absorption–desorption performances of Mg–Co–X ternary alloys with BCC structure. J Alloys Compd 393:185–193
78. Zhang Y, Tsushio Y, Enoki H, Akiba E (2005) The study on binary Mg–Co hydrogen storage alloys with BCC phase. sJ Alloys Compd 393:147–153
79. Shao HY, Asano K, Enoki H, Akiba E (2009) Preparation and hydrogen storage properties of nanostructured. Mg-Ni BCC alloys. Scr Mater 60:818–821
80. Shao H, Asano K, Enoki H, Akiba E (2009) Preparation and hydrogen storage properties of nanostructured Mg–Ni BCC alloys. J Alloys Compd 477:301–306
81. Shao H, Asano K, Enoki H, Akiba E (2009) Fabrication and hydrogen storage property study of nanostructured Mg–Ni–B ternary alloys. J Alloys Compd 479:409–413
82. Kishimura H, Matsumoto H (2011) Fabrication of Ti–Cu–Ni–Al amorphous alloys by mechanical alloying and mechanical milling. J Alloys and Compd 509:4386–4389
83. Enayati MH, Mohamed FA (2014) Application of mechanical alloying/milling for synthesis of nanocrystalline and amorphous materials. Int Mater Reviews 59:394–416

84. Kloepfer H, Freudenberg H (1931) Freudenberg, Process of manufacture of alkali-metal hydrides. US Pat., 1,796, 265 A, 1931
85. Zhang H, Kisi EH, Phys J (1997) Formation of titanium hydride at room temperature by ball milling. Condensed Matter 9:L185–L190
86. Chu H, Qiu S, Sun L, Huot J (2015) Enhancement of the initial hydrogenation of Mg by ball milling with alkali metal amides MNH 2 (M= Li or Na). Dalton Trans 44:16694–16697
87. Smith RL, Miser JW (1963) Compilation of the properties of lithium hydride, NASA
88. Elansari L, Antoine L, Janot R, Gachon JC, Kuntz JJ, Guerard D (2001) Preparation of alkali metal hydrides by mechanical alloying. J Alloys Compd 329:L5–L8
89. Hlova IZ, Castle A, Goldston JF, Gupta S, Prost T, Kobayashi T, Chumbley LS, Pruski M, Pecharsky VK (2016) Solvent-and catalyst-free mechanochemical synthesis of alkali metal monohydrides. J Mater Chem A 4:12188–12196
90. Doppiu S, Schultz L, Gutfleisch O (2007) In situ pressure and temperature monitoring during the conversion of Mg into MgH2 by high-pressure reactive ball milling. J Alloys Compd 427:204–208
91. Baum LA, Meyer M, Mendoza-Zelis L (2008) Complex Mg-based hydrides obtained by mechanosynthesis: characterization and formation kinetics. Int J Hydrogen Energy 33:3442–3446
92. Gupta S, Hlova IZ, Kobayashi T, Denys RV, Chen F, Zavaliy IY, Pruski M, Pecharsky VK (2013) Facile synthesis and regeneration of Mg (BH 4) 2 by high energy reactive ball milling of MgB2. Chem Commun 49:828–830
93. Huot J, Ravnsbæk DB, Zhang J, Cuevas F, Latroche M, Jensen TR (2013) Mechanochemical synthesis of hydrogen storage materials. Prog Mater Sci 58:30–75
94. Miedema AR, Buschow KHJ, van Mal HH (1976) Which intermetallic compounds of transition metals form stable hydrides?. J Less-Common Met 49:463–472
95. ENERGY CARRIERS AND CONVERSION SYSTEMS – Vol. II - Physics of Metal Hydrides – E. Akiba
96. Wang YB, Northwood DO (1987) Calculation of the enthalpy of metal hydride formation. J Less-Common Met 135:239–245
97. Griessen R, Driessen A (1984) Heat of formation and band structure of binary and ternary metal hydrides. Phys Rev B 30:4372–4381
98. Griessen R (1988) Heats of solution and lattice-expansion and trapping energies of hydrogen in transition metals. Phys Rev B 38:3690–3698
99. Westlake DG (1980) Stoichiometries and interstitial site occupation in the hydrides of ZrNi and other isostructural intermetallic compounds. J Less-Common Met 75:177–185
100. Westlake DG, Shaked H, Mason PR, McCart BR, Mueller MH, Matsumoto T (1982) Interstitial site occupation in ZrNiH. J Less-Common Met 88:17–23
101. Jacob I, Bloch JM, Shaltiel D, Davidov D (1980) On the occupation of interstitial sites by hydrogen atoms in intermetallic hydrides: A quantitative model. Solid State Commun 35:155–158
102. Wiswall RH, Reilly JJ (1972) Inverse Hydrogen Isotope Effects in Some Metal Hydride Systems. Inorg Chem 11(7):1691–1696
103. Sandrock GD, Murray JJ, Post ML, Taylo JB (1982) Hydrides and deuterides of $CaNi_5$. Mat Res Bull 17:887–894
104. Broom DP (2007) The accuracy of hydrogen sorption measurements on potential storage materials. Int J Hydrogen Energy 32:4871–4888
105. Gray EM (2008). In: Walker G (ed) Solid-state hydrogen storage. Woodhead Publishing Ltd., Cambridge, pp 174–204
106. Webb CJ, Gray EM (2014) Analysis of the uncertainties in gas uptake measurements using the Sieverts method. Int J Hydrogen Energy 39:366–375
107. Blackman JM, Patrick JW, Snape CE (2006) An accurate volumetric differential pressure method for the determination of hydrogen storage capacity at high pressures in carbon materials. Carbon 44:918–927

108. Qajar A, Peer M, Rajagopalan R, Foley HC (2012) High pressure hydrogen adsorption apparatus: Design and error analysis. Int J Hydrogen Energy 37:9123–9136
109. Demirocak DE, Srinivasan SS, Rama MK, Goswami DY, Stefanakos EK (2013) Volumetric hydrogen sorption measurements – Uncertainty error analysis and the importance of thermal equilibration time. Int J Hydrogen Energy 38:1469–1477
110. Broom DP, Hirscher M (2016) Irreproducibility in hydrogen storage material research. Energy Environ Sci 9:3368–3380
111. Gremaud R, Broedersz CP, Borsa DM, Borgschulte A, Mauron P, Schreuders H, Rector JH, Dam B, Griessen R (2007) Hydrogenography: An optical combinatorial method to find new light-weight hydrogen-storage materials. Adv Mater 19:2813–2817
112. Paul-Boncour V, Bourée-Vigneron F, Filipek SM, Marchuk I, Jacob I, Percheron-Guégan A (2003) Neutron diffraction study of ZrM2Dx deuterides (M=Fe, Co). J Alloys Compd 356–357:69–72
113. Retuerto M, Sánchez-Benítez J, Alonso JA, Leardini F, Ares JR, Fernández JF, Sánchez C (2011) Deuteration properties of CaNi5−xCux system. J Power Sources 196:4342–4346
114. Yartys VA, Denys R, Maehlen JP, Webb J, MacA Gray E, Blach TP, Poletaev AA, Solberg JK, Isnard O (2010) In (Ed.) MRS Proceedings, Cambridge University Press, San Francisco, California, 1262:pp. 1–11
115. MacA Gray E, Kisi EH, Smith RI (1999) Observation of a continuous phase transformation in LaNi5–D. J Alloys Compd 293–295:135–139
116. Asano H, Hirabayashi M, Bambakidis G (ed.) (1981) Metal Hydrides, Springer Science Business Media New York 1981, pp 81–103
117. Ramirez-Cuesta AJ, Jones MO, David WIF (2009) Neutron scattering and hydrogen storage. Mater Today 12:54–61
118. Schimmel HG, Johnson MR, Kearley GJ, Ramirez-Cuesta AJ, Huot J, Mulder FM (2005) Structural information on ball milled magnesium hydride from vibrational spectroscopy and ab-initio calculations. J Alloys Compd 393:1–4
119. Schimmel HG, Huot J, Chapon LC, Tichelaar FD, Mulder FM (2005) Hydrogen cycling of Niobium and Vanadium Catalyzed Nanostructured Magnesium. J Am Chem Soc 127:14348–14354
120. Schimmel HG, Johnson MR, Kearley GJ, Ramirez-Cuesta AJ, Huot J, Mulder FM (2004) The vibrational spectrum of magnesium hydride from inelastic neutron scattering and density functional theory. Mater Sci Eng B-Solid State Mater Adv Technol 108:38–41
121. Hartman MR, Rush JJ, Udovic TJ, Bowman RC Jr, Hwang SJ (2007) Structure and vibrational dynamics of isotopicallylabeled lithiumborohydride using neutron diffraction and spectroscopy. J Solid State Chem 180:1298–1305
122. F. Buchter, Z. Łodziana, Ph. Mauron, A. Remh**o**f, O. Friedrichs, A. Borgschulte, A. Züttel, D. Sheptyakov, Th. Strässle, and A. J. Ramirez-Cuesta, Dynamical properties and temperature induced molecular disordering of LiBH4 and LiBD4. Phy Rev B 78094302 (1–9)
123. Buchter F, Łodziana Z, Remhof A, Friedrichs O, Borgschulte A, Mauron Ph, Zuttel A, Sheptyakov D, Barkhordarian G, Bormann R, Chłopek K, Fichtner M, Sorby M, Riktor M, Hauback B, Orimo S (2008) Structure of Ca(BD4)2 β-Phase from Combined Neutron and Synchrotron X-ray Powder Diffraction Data and Density Functional Calculations. J Phys Chem B 112:8042–8048
124. Manivasagam TG, Magusin PCMM, Iliksu M, Notten PHL (2014) Influence of Nickel and Silicon Addition on the Deuterium Siting and Mobility in fcc Mg–Ti Hydride Studied with 2H MAS NMR. J Phys Chem C 118:10606–10615
125. Manivasagam TG, Magusin PCMM, Srinivasan S, Krishnan G, Kooi BJ & Notten PHL (2014) Electrochemical deuteration of metastable MgTi alloys: an effective way to inhibit phase segregation. Adv Energy Mater 4(1300590):(1–7)
126. Srinivasan S, Magusin PCMM, Kalisvaart WP, Notten PHL, Cuevas F, Latroche M, van Santen RA (2010) Nanostructures of Mg0.65Ti0.35Dxstudied with x-ray diffraction, neutron diffraction,and magic-angle-spinning 2H NMR spectroscopy. Phy Rev B: Solid State 81 054107:1–10

127. Conradi MS, Mendenhall MP, Ivancic TM, Carl EA, Browning CD, Notten PHL, Kalisvaart WP, Magusin PCMM, Bowman RC Jr, Hwang SJ, Adolphi NL (2007) NMR to determine rates of motion and structures in metal-hydrides. J Alloys Compd 446–447:499–503
128. Adolphi NL, Balbach JJ, Conradi MS, Market JT, Cotts RM, Vajda P (1996) Deuterium site occupancy in YDx by magic-angle-spinning NMR. Phys Rev B 53:15054–15062
129. Adolphi NL, Badola S, Browder LA, Bowman RC (2001) Bowman, Magic-angle spinning NMR study of deuterium site occupancyand dynamics in ZrNiD1.0 and ZrNiD3.0. Phys Rev B 65(024301):1–9
130. Smithson H, Marianetti CA, Morgan D, Van der Ven A, Predith A, Ceder G (2002) First-principles study of the stability and electronic structure of metal hydrides. Phy Rev B 66(144107):1–10
131. Peterman DJ, Weaver JH, Peterson DT (1981) Electronic structure of metal hydrides. V. x-dependent properties of LaHx (1.9<~x<~2.9) and NdHx (2.01<~x<~2.27). Phys Rev B 23:3903–3913
132. Hood DM, Pitzer RM, Schaefer HF III (1979) Schaefer III, Electronic structure of homoleptic transition metal hydrides: TiH4, VH4, CrH4, MnH4, FeH4, CoH4, and NiH4. J Chem Phys 71:705–712
133. van Setten MJ, Popa VA, Popa VA, De Wijs GA, Brocks G (2007) Electronic structure and optical properties of lightweight metal hydrides. Phy Rev B: Condensed matter and materials physics 75(035204):1–13
134. Buschow KHJ (2007) Handbook of magnetic materials. Vol. 17, Elsevier, 15-Dec-2007
135. Mueller WM, Blackledge JP, Libowitz GG (eds) (1968) Metal Hydrides. Academic Press, New York
136. Bowman RC, Sandrock G (2003) Proceedings of GLOBAL 2000 atoms for prosperity, American Nuclear Society meeting, New Orleans, LA; Nov. 16–20
137. Buchner H, Povel R (1982) Int J Hydrogen Energy 7:259–266
138. Schlapbach L (1988) Topics in Applied Physics Vol. 63: (Berlin: Springer Verlag, 1988)
139. http://energy.gov/eere/fuelcells/doe-technical-targets-onboard-hydrogen-storage-light-duty-vehicles
140. Sharma VK, Kumar EA (2014) Effect of measurement parameters on hydrogen storage and thermodynamic properties of La – based metal hydrides. Int J Hydrogen Energy 39:5888–5898
141. Prigent J, Joubert JM, Gupta M (2012) Modification of the hydrogenation properties of LaNi5 upon Ni substitution by Rh, Ir, Pt or Au. J Alloys Compd 511:95–100
142. Corré S, Bououdina M, Fruchart D, Adachi G (1998) Stabilisation of high dissociation pressure hydrides of formula La1−xCexNi5 (x=0–0.3) with carbon monoxide. J Alloys Compd 275–277:99–104
143. An XH, Li LG, Zhang JY, Li Q (2012) Comparison of dehydriding kinetics between pure LaNi5 and its substituted system. J Alloys Compd 511:154–158
144. Pan H, Liu Y, Gao M, Zhu Y, Lei Y (2003) The structural and electrochemical properties of La0.7Mg0.3(Ni0.85Co0.15)x (x = 3.0–5.0) hydrogen storage alloys. Int J Hydrogen Energy 28:1219–1228
145. Borzone EM, Baruj A, Blanco MV, Meyer GO (2013) Dynamic measurements of hydrogen reaction with LaNi5− xSnx alloys. Int J Hydrogen Energy 38:7335–7343
146. Borzone EM, Blanco MV, Baruj A, Meyer GO (2014) Stability of LaNi5− xSnx cycled in hydrogen. Int J Hydrogen Energy 39:8791–8796
147. Dhaou MH, Belkhiria S, Sdiri N, Mallah A et al (2017) Thermodynamic and electric study of the LaNi3, 6Al0, 4Co0, 7Mn0, 3 alloy. Int J Hydrogen Energy 42:2209–2214
148. G. Principi, F. Agresti, A. Maddalena, S. Lo Russo (2009) The problem of solid state hydrogen storage. Energy 34:2087–2091
149. Ćirić KD, Kocjan A, Gradišek A, Koteski VJ, Kalijadis AM et al (2012) A study on crystal structure, bonding and hydriding properties of Ti–Fe–Ni intermetallics – Behind substitution of iron by nickel. Int J Hydrogen Energy 37:8408–8417
150. Gueguen A, Latroche M (2011) Influence of the addition of vanadium on the hydrogenation properties of the compounds TiFe0.9Vx and TiFe0.8Mn0.1Vx (x = 0, 0.05 and 0.1). J Alloys Compd 509:5562–5566

151. Lee SM, Perng TP (1994) Effect of the second phase on the initiation of hydrogenation of TiFe1−xMx (M = Cr,Mn) alloys. Int J Hydrogen Energy 19:259–263
152. Young M, Chang S, Young K, Nei J (2013) Hydrogen storage properties of ZrVxNi3.5−x (x = 0.0–0.9) metal hydride alloys. J Alloys Compd 580:S171-174
153. Banerjee S, Kumar A, Pillai CGS (2014) Improvement on the hydrogen storage properties of ZrFe2 Laves phase alloy by vanadium substitution. Intermetallics 51:30–36
154. Rabahi L, Gallouze M, Grosdidier T, Bradai D, Kellou A (2017) Energetics of atomic hydrogen absorption in C15-Fe2Zr Laves phases with ternary additions: A DFT study. Int J Hydrogen Energy 42:2157–2166
155. Shashikala K, Kumar A, Betty CA, Banerjee S, Sengupta P, Pillai CGS (2011) Improvement of the hydrogen storage properties and electrochemical characteristics of Ti0. 85VFe0. 15 alloy by Ce substitution. J Alloys Compd 509:9079–9083
156. Yu XB, Yang ZX, Feng SL, Wu Z, Xu NX (2006) Influence of Fe addition on hydrogen storage characteristics of Ti–V-based alloy. Int J Hydrogen Energy 31:1176–1181
157. Ruz P, Kumar A, Banerjee S, Meena SS, Pillai CGS (2014) Hydrogen absorption characteristics and Mössbauer spectroscopic study of Ti0.67Nb0.33−xFex (x = 0.00, 0.13, 0.20) alloys. J Alloys Compd 585:120–128
158. Kamble A, Sharma P, Huot J (2017) Effect of doping and particle size on hydrogen absorption properties of BCC solid solution 52Ti-12V-36Cr. Int J Hydrogen Energy 42:11523–11527
159. Akiba E, Iba H (1998) Hydrogen absorption by Laves phase related BCC solid solution. Intermetallics 6:461–470
160. Mouri T, Iba H (2002) Hydrogen-absorbing alloys with a large capacity for a new energy carrier. Mater Sci Eng A 329–331:346–350
161. Bowman RC Jr, Sandrock G (2003) Gas-based hydride applications: Recent progress and future needs. J Alloys Compd 356–357:794–799
162. Hudson MSL, Dubey PK, Pukazhselvan D, Pandey SK, Singh RK, Raghubanshi H, Shahi RR, Srivastava ON (2009) Hydrogen energy in changing environmental scenario:Indian context. Int J Hydrogen Energy 34:7358–7367
163. Dong D, Humphries TD, Sheppard DA, Stansby B, Paskevicius M, Sofianos MV, Chaudhary A-L, Dornheim M, Buckley CE (2017) Thermal optimisation of metal hydride reactors for thermal energy storage applications. Sustain Energ Fuels 1:1820–1829
164. Reiser A, Bogdavonic B, Schliche K (2000) Application of Mg-based metal-hydrides as heat energy storage systems. Int J Hydrogen Energy 25:425–430
165. Kim KJ, Feldman KT Jr, Lloyd G, Razani A (1997) Compressor-driven metal-hydride heat pumps. Appl Thermal Eng 17:551–560
166. Lototskyy MV, Yartys VA, Pollet BG, Bowman RC Jr (2010) Metal hydride hydrogen compressors: A review. Int J Hydrogen Energy 39:5815–5851
167. Fujisawa A, Miura S, Mitsutake Y (2013) J Alloys Compd 580(S1):S423–426
168. Block FR, Dey A, Kappes H, Reith K (1987) Hydrogen purification with metal hydrides in a new kind of reactor. J Less-Common Met 131:329–335
169. Wang ZM, Li V, Chan SLI (2005) Review of alloy membranes/film for hydrogen separation or purification. J Rare Earth 23:611–616
170. Rudman PS, Sandrock GD, Goodell PD (1983) Hydrogen separation from gas mixtures using LaNi5 pellets. J Less-Common Met 89:437–446
171. Saitou T, Sugiyama K (1995) Hydrogen purification with metal hydride sintered pellets using pressure swing adsorption method. J Alloys Compd 231:865–870
172. Miura S, Fujisawa A, Ishida M (2012) A hydrogen purification and storage system using metal hydride. Int J Hydrogen Energy 37:2794–2799
173. Ichimura K, Inoue N, Watanabe K, Takeuchi T (1984) Absorption and desorption of hydrogen, deuterium, and tritium for Zr–V–Fe getter. J Vac Sci Technol A: Vacuum, Surfaces, and Films 2:1341–1347.
174. Knize RJ, Cechi JL (1983) Theory of bulk gettering. J Appl Phys 54:3183–3189
175. Ghezzi F, De Angeli M (2002) On the dependence of true hydrogen equilibrium pressure on the granular size distribution of the $Zr(Fe0.5Mn0.5)^2$ getter alloy. J Alloys Compd 330:76–80

176. Slaman M, Dam B, Schreuders H, Griessen R(2008) Optimization of Mg-based fiber optic hydrogen detectors by alloying the catalyst. Int J Hydrogen Energy 33:1084–1089
177. DiMeo F Jr, Chen I, Chen P, Neuner J, Roerhl A, Welch J (2006) MEMS-based hydrogen gas sensors. Sens Actuator B-Chem. 117:10–16
178. Palmisano V, Filippi M, Baldi A, Slaman M, Schreuders H, Dam B (2010) An optical hydrogen sensor based on a Pd-capped Mg thin film wedge. Int J Hydrogen Energy 35:12574–12578
179. Kirby DJ, Chang DT, Stratton FP (2009) A differential capacitive thin film hydrogen sensor. Sens Actuator B-Chem. 141:424–430
180. Huiberts JN, Griessen R, Rector JH, Wijngaarden RJ, Dekker JP, de Groot DG, Koeman NJ (1996) Yttrium and lanthanum hydride films with switchable optical properties. Nature (London) 380:231–234
181. Richardson TJ, Slack JL, Armitage RD, Kostecki R, Farangis B, Rubin MD (2001) Switchable mirrors based on nickel–magnesium films. Appl Phys Lett 78:3047–3049
182. Armitage R, Rubin M, Richardson T, O'Brien N, Chen Y (1999) Solid-state gadolinium–magnesium hydride optical switch. Appl Phys Lett 75:1863–1865
183. Yoshimura K, Yamada Y, Bao S, Tajima K, Okada M (2009) Preparation and characterization of gasochromic switchable-mirror window with practical size. Sol Energy Mater Sol Cells 93:2138–2142
184. Feng F, Geng M, Northwood DO (2001) Electrochemical behaviour of intermetallic-based metal hydrides used in Ni/metal hydride (MH) batteries: a review. Int J Hydrogen Energy 26:725–734
185. Hong K (2001) The development of hydrogen storage electrode alloys for nickel hydride batteries. J Power Sources 96:85–89
186. Cuevas F, Joubert JM, Latroche M, Percheron-Guégan A (2001) Intermetallic compounds as negative electrodes of Ni/MH batteries. Appl Phys A 72:225–238
187. Fukada S, Fuchinoue K, Nishikawa M (1995) Isotope separation factor and isotopic exchange rate between hydrogen and deuterium of palladium. J Nucl Mater 226:311
188. Reddy B, Mistry K, Kumar R, Mohan S, Mahajani S (2016) Recovery of deuterium from hydrogen–deuterium mixture using palladium. Sep Sci Technol 51:784–796
189. Ito Y, Takahashi R, Mizusaki S, Yamamoto I, Yamaguchi M (2006) Magnetic field effects on the hydrogen isotope separation with metal hydrides. Sci Technol Adv Mater 7:369–372
190. Vetrano JB (1970) Hydrides as neutron moderator and reflector materials. Nucl Eng Des 14:390–412
191. Azevedo CRF, Rodrigues D, Beneduce Neto F (2003) Ti-Al-V powder metallurgy (PM) via the hydrogenation-dehydrogenation (HDH) process. J Alloys and Compd 353:217–227
192. Vanderhoff A, Kwang JK (2009) Experimental study of a metal hydride driven braided artificial pneumatic muscle, Smart Mater. Struct 18:125014
193. Sato M, Hosono M, Yamashita K (2011) Solar or surplus heat-driven actuators using metal hydride alloys, Sens. Actuator B-Chem. 156:108–113

Chapter 17
Synthesis Strategies for Si-Based Advanced Materials and Their Applications

S. P. Koiry and A. K. Chauhan

Abstract Silicon compounds are very important owing to their stability, non-toxicity, and high natural abundance of silica in earth crust. These materials have been studied for more than a century, and a vast literature on their synthesis and application is available. These are utilized in various forms in organometallics, polymers, material science, and microelectronics, and have immense potential for their application in organic and hybrid electronic devices. Thus, a comprehensive review on synthesis, processing, and potential applications of silicon-based materials was a need of the time. In this chapter, the synthesis of silane, methods of extracting elemental silicon, and their use in the growth of single crystals are discussed. In addition, synthesis strategies of various silicon compounds which include organosilane, silicone, polysilane, and silicene are described and their applications are discussed.

Keywords Silane · Silicone · Polysilane · And silicene

17.1 Introduction

Silicon and carbon both belong to the group IV of the periodic table. Thus, like carbon, silicon also forms compounds similar to alkane which are called silanes [1–3]. These silanes are very important starting material for synthesizing silicon compounds, silicon polymer, and semiconductor grade Si [3, 4]. The simplest silane is SiH_4, an analogous to methane [1, 3, 4]. Like alkane, silanes also contain Si–Si saturated bonds. Unlike alkane, Si–Si cannot construct a long stable chain. But when hydrogen atoms of silane are replaced by Cl, then chain of up to 25 silicon atoms can be obtained [1]. If Cl is substituted by alkyl or aryl groups, the number of Si atoms in a chain is further increased because of the strengthening of Si–Si bonds [1]. These hydrocarbon-substituted silanes are called organosilane [1, 5, 6]. These

S. P. Koiry · A. K. Chauhan (✉)
Technical Physics Division, Bhabha Atomic Research Centre, Trombay, Mumbai 400085, India
e-mail: akchau@barc.gov.in

Homi Bhabha National Institute, Anushaktinagar, Mumbai 400094, India

A. K. Tyagi and R. S. Ningthoujam (eds.), *Handbook on Synthesis Strategies for Advanced Materials*, Indian Institute of Metals Series,
https://doi.org/10.1007/978-981-16-1892-5_17

silanes can undergo polymerization which leads to organometallic polymers [1–3]. The polymers which contain Si–O–Si repeating unit are called silicones, whereas Si–Si repeated units containing polymer are called polysilane [2, 6–8]. The silane and their polymers are widely used in many industrial applications. For example, smaller silane molecules like chlorosilane and its derivatives are used for producing semiconductor grade silicon for microelectronics and photovoltaic applications [4]. Silanes are also used in pharmaceuticals industries as protecting group of organic functional groups [3]. Organosilane and silicone are widely used for water repellent, adhesive, surface modification, surface coating, and coupling agents for adhesion promotion between two dissimilar materials, thermal and electrical resistant, sealant, adhesive, encapsulator, antifoaming agent, etc [5, 6]. Recently, organosilane also found wide acceptability in the development of organic electronics to make devices portable, large scale, thin, stretchable, and flexible [9]. The recognition of silane arises from its properties to form bonds with substrates, self-polymerization, and the possibility to modify carbon chain of silane by surface chemistry [10–12]. From electronic application point of view, electronic properties of silane have been studied by depositing mono-/multilayer of silane on Si. Any positive result of these studies has direct application to Si industry without altering basic structure of the present electronic devices [11, 13, 14]. Moreover, the monolayer of organosilane is the assembly of single molecules, and its electrical properties would give an idea of single molecular electrical properties which will be useful for the development of single-molecule-based electronic devices [12]. For polymer electronics, polysilane has been investigated as a hole transporting layer in the organic light-emitting diode, field-effect transistor, and organic photovoltaic [7, 15–17]. Recently, silicene, Si analogue of graphene, has emerged as a next-generation energy storage material [18, 19].

This chapter is mainly focused on the synthesis of silane from SiO_2 and their use in the growth of the single crystal, the synthesis of silane, organosilane, silicone, polysilane, and silicene. Along with the synthesis, the important electronic applications of each silicon compound are also discussed. This chapter provides an overview of synthesis of important silicon compounds so that it can act as single point information source for the silicon-based materials.

17.2 Synthesis of Small Silane Molecules

Silanes are important and generally used as precursors for the production of Si bulk material or thin film of silicon for semiconductor applications [4, 20–23]. Among other, trichlorosilane ($SiHCl_3$) is the precursor for industrial production of the polycrystalline silicon (polysilicon) that is converted into single crystalline ingots via Czochralski or float-zoning methods of crystal growth [4, 20, 22, 23]. Thin-film silicon is deposited from dichlorosilane (SiH_2Cl_2), $SiHCl_3$, tetrachlorosilane ($SiCl_4$),

and silane (SiH_4) by various chemical vapor deposition processes [4, 20–22]. In addition to the production of element silicon, these silanes are the precursor for synthesizing other functional silane; for example, organosilane is obtained by replacing H of $HSiCl_3$ with alkyl function group. Therefore, this section begins with the discussion of synthesizing chlorosilane as it is the starting materials for many functional silanes/Si.

17.2.1 Trichlorosilane

The synthesis of chlorosilane is a two-step process [22]. The steps involved are as follows

Step 1. Production of metallurgical grade Si from silica.

Silica, SiO_2, is the main source of silicon which is available in abundant in the earth crust. It is reduced to Si by carbothermic method as shown by overall reaction.

$$SiO_2(s) + C(s) \rightarrow Si(I) + 2CO(g) \tag{17.2.1}$$

The source of carbon is coke, coal, or wood chips. Si produced in this method is 98–99% pure [4].

Step 2: The Si produced in step 1 is reacted with HCl to produce trichlorosilane [6, 24].

$$Si(s) + 3HCl(g) \rightarrow SiHCl_3(g) + H_2(g) \tag{17.2.2}$$

For this purpose, Si is ball milled to produced fine Si particles of size <40 micron. These particles are allowed to react with anhydrous hydrogen chloride in a fluidized bed reactor at 575 K under exothermic conditions [4]. The reaction yield is 90%, and the remaining is tetrachlorosilane ($SiCl_4$). Since both these chlorosilanes ($SiHCl_3$ and $SiCl_4$) have different boiling points, $SiHCl_3$ is purified by fractional distillation [4, 25]. Additional impurities that come with Si, like BCl_3, can be removed by water treatment. Boron and phosphorus are reduced to **<1** ppb by complexing them with $SiHCl_3$ [4, 25].

Trichlorosilane can also be prepared in a fluidized bed of Si by heating the mixture of $SiCl_4$ and H_2 in the presence of a copper catalyst [6, 26]:

$$3SiCl_4(g) + 2H_2(g) + Si \xrightarrow{Cu} 4SiHCl_3(g) \tag{17.2.3}$$

17.2.2 Tetrachlorosilane

As discussed above, $SiCl_4$ is produced as a by-product during synthesis of trichlorosilane.

$SiCl_4$ is also produced during the production of Si from $SiHCl_3$ by Siemens process [27].

$$SiHCl_3(g) + H_2(g) \xrightarrow{1375K} Si(g) + 3HCl \tag{17.2.4}$$

By−product

$$SiHCl_3(g) + HCl(g) \rightarrow SiCl_4(g) + H_2 \tag{17.2.5}$$

Overallreaction

$$3SiHCl_3(g) \xrightarrow{1375K} Si(s) + 2SiCl_4(g) + HCl(gl + H_2(g)) \tag{17.2.6}$$

$SiCl_4$ is separated from other gaseous products by distillation process.

Tetrachlorosilane can be produced from chlorination of silicon carbide:

$$SiC(s) + 2Cl_2(g) \rightarrow SiCl_4(g) + C(s) \tag{17.2.7}$$

As obtained, $SiCl_4$ is purified by distillation.

$SiCl_4$ is also produced as the by-product during synthesis of $TiCl_2$ and $ZrCl_2$ in a fluidized bed reactor. The by-product arises from chlorination of SiO_2 present in the ore of Ti and Zr [4].

For example:

$$TiO_2(s) + 2Cl_2(g) + 2C(s) \xrightarrow{1175K} SiCl_4(g) + CO(g) \tag{17.2.8}$$

$$SiO_2(s) + 2Cl_2(g) + 2C(s) \xrightarrow{1175K} SiCl_4(g) + CO(g) \tag{17.2.9}$$

17.2.3 Dichlorosilane

Dichlorosilane can be readily produced from $SiHCl_3$ by rearrangement reaction in the presence of polymeric resins as a catalyst at a temperature of about 350 K [4].

$$2SiHCl_3(g) \xrightarrow[\text{Cat.resin}]{350K} SiH_2Cl_2(g) + SiCl_4(g) \tag{17.2.10}$$

Around 0.3% SiH_3Cl (monochlorosilane) is also generated during the rearrangement reaction of SiH_2C1_2

$$2SiH_2Cl_2(g) \rightarrow SiH_3Cl(g) + SiHCl_3(g) \tag{17.2.11}$$

17.2.4 Silane (SiH_4)

Silane is produced by reducing $SiCl_4$ by metal hydride (LiH) in LiCl/KCl melt [4].

$$4LiH(I) + SiCl_4 \xrightarrow{675K} SiH_4(g) + 4LiCl(l) \tag{17.2.12}$$

The by-product LiCl (l) is recycled back to Li by electrolysis as

$$4LiCl(I) \rightarrow 4Li(I) + 2Cl_2(I) \tag{17.2.13}$$

Magnesium silicide produced from elemental silicon is also used to produce larger quantities of SiH_4 (17.2.14). The reaction occurs at −33 °C in liquid ammonia.

$$4Mg_2Si + 4NH_4Br \rightarrow SiH_4 + 2MgBr_2 + 4NH_3 \tag{17.2.14}$$

For industrial production of silane, two processes have been discussed: (1) the Union Carbide process from chlorosilane and (2) Ethyl Corporation process from fluorosilicic acid on fluidized bed technology [4]. The steps involve as follows.

From chlorosilane:

$$3SiCl_4(g) + 2H_2(g) + Si \xrightarrow{Cu} 4SiHCl_3(g) \tag{17.2.15}$$

$$2SiHCl_3(g) \rightarrow SiH_2Cl_2(g) + SiCl_4(g) \tag{17.2.16}$$

$$2SiH_2Cl_2(g) \rightarrow SiH_3Cl(g) + SiHCl_3(g) \tag{17.2.17}$$

$$2SiH_3Cl(g) \rightarrow SiH_4(g) + SiH_2Cl_2(g) \tag{17.2.18}$$

From fluorosilicic acid: In this process, the raw material is not metallurgical grade silicon for silane but fluorosilicate which is generated as by-product in fertilizer industry. The steps involve

$$H_2SiF_6 + H_2SO_4 \rightarrow SiF_4 + 2HF \tag{17.2.19}$$

$$SiF_4 + 4LiH \rightarrow SiH_4 + 4LiF \quad (17.2.20)$$

The hydride forms at 500 K at ambient pressure.

The silane can undergo decomposition reaction to produce pure Si in a Siemens-type reactor/fluidized bed reactor according to the reaction

$$SiH_4(g) \rightarrow Si(s) + 2H_2 \quad (17.2.21)$$

17.2.5 Application of Chlorosilane

Semiconductor grade silicon has twelve 9 purity [4]. Although Si can be produced from silica by reduction process, it is not possible to reduce impurity to ppb level. The alternative method is the production of Si from chlorosilane where Si is produced by gas phase reaction. Among other chlorosilane, trichlorosilane (TCS) is found to be met ppb-level purity requirement [4, 22]. Thus, TCS is used as the precursor for the production of polysilicon which is used for semiconductor grade Si crystal. The early days' suppliers of semiconductor grade (TCS) among other were Union Carbide, Dynamite Nobel, Wacker, Dow Corning, Chisso, Hills, Osaka Titanium, Shin-Etsu Handotai, Tokuyama Soda, Chinese Companies, etc [4].

Recently, the demand for semiconductor grade Si has been increased tremendously because of the astronomical rise in the use for the fabrication of solar cells [21, 27, 28]. At present, the production cost of Si from TCS contributes approximately to 25–33% of the overall cost of the solar panels [21, 28]. It requires about 30–40% of the total energy in their fabrication which is because chlorosilane method has low efficiency, high production costs, and high energy consumption [21, 28]. Therefore, the need is to increase the production of Si and to reduce the cost of Si/kg. Scientist and engineers have been improving present method to make it cost-effective and at the same time exploring an alternative method for Si production [20, 28]. One of the alternative methods is the decomposition of SiH_4 [21, 28]. The advantage over chlorosilane is that the deposition temperatures of polysilicon from SiH_4 are lower than that with TCS which is reducing energy consumption [21]. Moreover, SiH_4 can be purified to higher levels than any of the chlorosilanes [21]. However, there are limitations too. SiH_4 decomposition results in amorphous silicon powders or dust [21]. It is undesirable in polysilicon production and requires additional process to recover Si [21]. However, this fine powder is nanocrystal which has been explored for photovoltaic applications [21].

17.2.5.1 Production of Si Crystal

In 1952, Teal and Buehler reported the Si single crystal ingot growth by Czochralski (Cz) method [4, 22, 29, 30]. This method is still used by the semiconductor industry

[22, 29]. The ingots are grown from the melt of semiconductor grade Si which is obtained from silane as discussed above. The growing of Si crystal is described here briefly [22]. The polycrystalline silicon charge is melted by heating above its melting point to form a complete liquid in the crucible. For initiating the crystal growth, the temperature is reduced until the center of the melt surface achieves the melting point. Then, a single crystal seed is dipped into the melt. Crystal pulling is started by lowering melt temperature further. Once the freezing begins at the seed crystal, it is withdrawn gradually to develop as an ingot.

17.3 Organosilane

The silane that introduced in the previous section is small molecules which are the precursors for different silicon derivatives [6]. Organosilane is one such derivative which contains one or more organic moiety attached to Si [1, 31, 32]. These silanes are widely used in industry as surface modifiers, coating, and coupling agents [5, 33]. The synthesis of a few important organosilane and their applications is discussed in this section.

17.3.1 Formation of Alkyl Chlorosilane

(a) From trichlorosilane: It is prepared by heating the mixture of trichlorosilane and alkene or acetylene in gas or liquid phase. The reaction is carried out between 200 and 600 °C at different pressures depending on the nature of the olefin. If the reaction is carried out in the presence of catalysts such as peroxides, tertiary bases, or platinum salts or UV light [5], the reaction occurs at mild reaction condition such as by simply refluxing [5]

$$Cl_3SiH + CH_2 = CH - R \rightarrow Cl_3SiH\ CH_2CH_2 - R \tag{17.3.1}$$

If organic moiety contains active functional group, the reaction is carried out in the presence of catalysts such as peroxides, tertiary bases, or platinum salts [5].

Benzene and its derivatives can also be added to silane at 350 °C

$$Cl_3SiH + C_6H_6 \xrightarrow{350\ ^\circ C} Cl_3SiH + C_6H_5SiCl_3 \tag{17.3.2}$$

(b) From tetrachlorosilane: The reaction between tetrachlorosilanes with organozinc yields organochlorosilane [6]

$$SiCl_4 + n/_2ZnR_2 \rightarrow R_2SiCl_{4-n} + n/_2ZnCl_2 \tag{17.3.3}$$

17.3.2 Preparation of Alkoxysilane

The alkoxysilane is prepared by warming chlorosilane with orthoformate ester in the presence of alcohol [34].

$$\mathrm{ClSiH_3 + HC(OR)_3 \xrightarrow{ROH} H_3Si(OR) + RCl + HCOOR} \tag{17.3.4}$$

However, haloalkane reacts directly with alcohol, but in that reaction HCl is evolved which acceptors like tertiary amines or sodium alkoxides remove.

To exchange one alkoxy group with other different alkoxy groups requires a catalyst and moderates temperature [34].

17.3.3 Acetoxysilanes

It is synthesized by the acylation of chlorosilane with sodium acetate in an anhydrous acetic solvent [5].

$$\mathrm{RSiCl_3 + 3NaAc \rightarrow RSi(OAc)_3 + 3NaCl} \tag{17.3.5}$$

The acetic anhydride solvent is used to avoid the formation of precipitated salt

$$\mathrm{RSiCl_3 + 3Ac_2O \rightarrow RSi(OAc)_3 + 3AcCl \uparrow} \tag{17.3.6}$$

17.3.4 Organofunctional Silane

The previous section has mainly discussed the addition of functional groups to Si atom in silane. The most significant advantage of organosilane over other silane is that the addition of functional groups is not limited to Si only. In such silane, organic moiety can also be functionalized, which makes organosilane more attractive for industrial applications. Therefore, in this section the preparation of many organofunctional silanes will be discussed.

17.3.4.1 Haloalkylsilane

The chlorofunctional organosilane is used as a precursor for synthesizing other organofunctional silanes.

Preparation: Chloromethyltrichlorosilane may be obtained by chlorination of methyltrichlorosilane in the presence of UV [35].

$$CH_3SiCl_3 + Cl_2 \xrightarrow{UV} ClCH_2SiCl_3 \tag{17.3.7}$$

This methylchlorosilanes are used as protecting agents for intermediates in pharmaceutical syntheses.

Chloro-/bromo-functional group is added by the reaction between trichlorosilane and allylbromide/chloride [32].

$$Cl_3SiH + CH_2 = CH - Br \rightarrow Cl_3SiHCH_2CH_2 - Br \tag{17.3.8}$$

This bromosilane is widely used in analytical studies because of the clear signal given by bromine in X-ray fluorescence [5].

Iodoalkylsilanes are obtained by replacement reactions of chloroalkylsilanes with NaI:

$$(MeO)_3SiCH_2CH_2CH_2Cl + NaI \xrightarrow{Acetone} (MeO)_3SiCH_2CH_2CH_2I \tag{17.3.9}$$

Haloarylsilanes is prepared by halogenation of aromatic silane (17.3.10). These haloarylsilanes are incorporated into silicone polymers to increase lubricity.

$$Cl_3SiC_6H_5 + Cl_2 \xrightarrow{Fe} Cl_3SiC_6H_4Cl \tag{17.3.10}$$

The haloalkylsilane is the precursor for another functional silane. For example, amino functional silanes are readily prepared by reacting chloroalkylsilane with ammonia or amine [36].

$$\begin{aligned}&(MeO)_3SiCH_2CH_2CH_2Cl + 2H_2NR\\ &\rightarrow (MeO)_3SiCH_2CH_2CH_2NHR\\ &+ RNH_2 - HCl\end{aligned} \tag{17.3.11}$$

Haloalkylsilanes form ether with alkoxide:

$$(MeO)_3SiCH_2CH_2CH_2Cl + NaOR \rightarrow (MeO)_3SiCH_2CH_2CH_2OR + NaCl \tag{17.3.12}$$

The ester group is added to haloalkylsilanes by alkali or tertiary amine salts of carboxylic acids.

$$\begin{aligned}&(MeO)_3SiCH_2CH_2CH_2Cl + CH_2C(CH_3)COOH\\ &\xrightarrow{R_3N} (MeO)_3SiCH_2CH_2CH_2COO(CH_3)CCH_2\end{aligned} \tag{17.3.13}$$

Thus, haloalkylsilane is a versatile reagent for the production of organofunctional silanes.

17.3.4.2 Aminopropylsilane

Amino silane is prepared by hydrogenation of cyanoethylsilanes (17.3.14) or by reaction between chloropropyltrimethoxysilane and ammonia or amines (17.3.11) [6, 37, 38].

$$(EtO)_3SiCH_2CH_2CH_2CN + H_2 \rightarrow (MeO)_3SiCH_2CH_2CH_2NH_2 \qquad (17.3.14)$$

The amino functional silanes act as coupling agents with condensation-thermosetting polymers, e.g., epoxides, phenolics, melamines, furanes, isocyanates, etc [6, 39, 40]. Furthermore, aminosilane readily forms self-assembled monolayer on hydroxylated Si [12, 41, 42]. These aminosilane-coated Si substrates are used for further functionalization of Si surface; e.g., amino groups act as an anchoring site in the synthesis of polyaniline crystal on Si substrate. The multilayer of aminosilane on Si substrate exhibits resistive random memory characteristics which will be discussed in detail in the application subsection of this section.

17.3.4.3 Etherification and Esterification of Chlorosilane Derivatives

With sodium alkoxide, chlorosilane forms ethers. Alkali or tertiary amine salts of carboxylic acids react with haloalkylsilanes to form esters (17.3.13).

17.3.4.4 Addition of Sulfur Group

Mercaptoalkylsilanes are synthesized from chloroalkylsilanes and ammonium salts of hydrogen sulfide [6, 43, 44].

$$\begin{aligned}&(MeO)_3SiCH_2CH_2CH_2Cl + H_2NCH_2CH_2NH_2H_2S \rightarrow \\ &(MeO)_3SiCH_2CH_2CH_2SH + H_2NCH_2CH_2NH_2 - HCl\downarrow\rightarrow\end{aligned} \qquad (17.3.15)$$

The reaction between thiourea and chloroalkylsilanes readily forms isothiouronium salts which are cleaved by ammonia to form mercaptoalkylsilanes free of dialkylsulfide by-products [44].

$$\begin{aligned}(MeO)_3SiCH_2Cl + (H_2N)_2CS &\rightarrow (MeO)_3SiCH_2HNC(NH_2)S - HCl \\ &+ NH_3 \rightarrow (MeO)_3SiCH_2SH + NH_4Cl\end{aligned} \qquad (17.3.16)$$

Alkenylsilane: Vinyl-terminated silane is prepared by the addition of acetylene to chlorosilane. It is also prepared from allyl chloride or vinyl chloride at high temperatures [5].

$$Cl_3SiH + HC \equiv CH \rightarrow Cl_3Si\,CHCH_2 \tag{17.3.17}$$

$$Cl_3SiH + CH_2 = CHCl \xrightarrow{550^\circ C - 650^\circ C} Cl_3SiCH = CH_2 \tag{17.3.18}$$

Vinyl-terminated silanes are widely used as a coupling agent for unsaturated polyesters; for example, styrene-functional cationic silanes are used extensively as coupling agents with almost all thermoset resins and thermoplastic resins.

17.3.4.5 Applications

Organosilane contains two reactive functional groups: (1) hydrolyzable groups (*X*) and (2) organofunctional moiety (*Y*) in compounds of the structure X_3SiRY. *X* is generally –Cl, ethoxy, methoxy, and acetoxy groups which undergo hydrolysis in the presence of even moisture to silanol (Si–OH). These silanol groups can form a polymer network of Si–O–Si by condensation of Si–OH with other OH groups. The bond formation of Si–OH with other OH has been utilized for surface modification or surface coating of virtually any material. If the organic group (*Y*) contains only alkyl chain, then silane-coated surface becomes hydrophobic and even corrosion resistive [5]. If Y includes a functional group such as a vinyl group, it can form a bond with other unsaturated chains present in resin or epoxy in the presence of heat or light. The application of silane as coupling and surface coating agents is well known, and the vast literature is available [45–48]. The relatively new application of organosilane that emerged is the use of silane mono-/multilayer as an electronic component for organic electronic that will be discussed in detail [9, 12, 49–54].

Application of Silane in Organic/Molecular Electronics

Silane undergoes spontaneous condensation reaction in the presence of moisture which is fast and thermodynamically favorable. This spontaneous condensation of organosilane on Si substrates is called self-assembly of silane or silanization of Si [55, 56]. Thus to explore the possibility to use organic molecules in futuristic electronic devices, the electrical properties of organosilane are studied by depositing its monolayer on Si. The silane $R(CH_2)nSiX_3$ that is used for silanization contains hydrolyzable groups such as X = chloro, ethoxy, methoxy. The R groups are chosen depending upon the application, for example, R = alkyl chain for dielectric properties and π-conjugated molecule or polymer for semiconductor/metallic behaviors. Since silane forms an intermolecular bond by self-condensation in the presence of moisture and oxygen, the monolayer of silane is generally prepared in a glove box

having relative humidity (<1%) and oxygen (<1%) [51]. In addition to the controlled environment, the monolayer formation depends on silane concentration, duration of time, temperature, and presence of moisture at solvent.

(a) **Mono-/multilayer deposition techniques**:

For silanization, Si substrate has to be pretreated to make hydroxy terminated which has been done in the following method. The Si wafers usually have a layer of native oxide (about 1–1.5 nm thickness) or thermally grown SiO_2. The top surface of the SiO_2 layer is hydroxylated which is achieved by dipping the Si substrates into piranha solution (a mixture of concentrated sulfuric acid and hydrogen peroxide 1:1 by volume) for 10 minutes [12, 42]. Thereafter, the piranha-treated Si substrates are washed thoroughly by deionized water, after that it is dried under a stream of inert gas.

Formation of monolayer and multilayer [52–54, 57]: The monolayer of silane is prepared by dipping hydroxylated Si substrate into a micromolar solution of silane prepared in anhydrous hexane, toluene, and ethanol depending on the type of silane [12]. The time required for the formation of monolayer depends on solvent polarity, dipping time, and alkyl chain. Silane monolayers can also be deposited on hydroxylated substrate by controlled evaporation in a jar under the inert atmosphere.

Since self-assembly method is highly dependent on the environment, there is no control over the film formation[[52, 54]. For overcoming these limitations, the electrochemical method has been developed for grafting silane monolayer on Si. In this method, silane is grafted by applying cathodic potential. Thus, the deposition method is controlled by applied potential, and it is possible to check the deposition in situ by observing the deposition current under applied potential. In the electrochemical method, Si substrate is hydrogenated by treating with 40% NH_4F for Si(111) and 1–2% HF for Si(100) to obtain monohydrated Si surface which has been used a working electrode for deposition. The silane that has to be grafted should be terminated with halo or other such cleavable groups.

For deposition of multilayer, the layer-by-layer self-assembly method has been reported. In this method, the alkyl chain of silane should be terminated with group that can form a bond with silanol groups of silane after the first layer of silane is formed. Such multilayer deposition has been shown with aminopropylsilane in which propyl chain is terminated with amino group which can form hydrogen bond with the Si–OH groups of silane [53, 57]. If the proper control is not maintained, aminopropylsilane undergoes spontaneous polymerization to form a thick polymer film on any substrate in ambient condition [53, 57].

(b) **Characterization**:

The thickness of monolayer is in the range of 0.7–5 nm [53, 57]. Therefore, it is required special characterization tools. The thickness of the film is measured by an ellipsometer; functional groups are characterized by Fourier transform infrared (FTIR) spectrophotometer. X-ray photoelectron spectroscopy (XPS) is used for elemental analysis. The surface morphology is studied by atomic force microscope (AFM). The wettability of the film is measured by the contact angle measurement

system. For measuring the electrical properties of these monolayers/multilayers, metal contacts are required to deposit on the top of the layer. Making reliable and reproducible contacts is not an easy task and is an open challenge until today. Some of the most used methods are thermal evaporation method, conductive probe atomic force microscope (c-AFM), scanning tunneling microscope (STM) method, liquid metal (Hg) or InGa eutectic mixture as contact, soft lithography methods [12, 52–54, 57].

(iii) **Electrical characterization:**

(1) **Alkane monolayers as dielectrics**: The energy-level gap between the highest occupied molecular orbital (HOMO) and the lowest unoccupied molecular orbital (LUMO) of an alkane is 6–8 eV [12]. The high energy gap is analogous to the band gap of inorganic dielectric materials. Therefore, alkane monolayers of silane on Si/SiO_2 surface have been investigated to elucidate their dielectric properties by applying a high electric field on the silane monolayer till its irreversible breakdown. The physical definition of the electrical breakdown is the irreparable destruction of the bonding structure of insulating materials which leads to high leakage current. It is reported that electrical breakdown field for monolayer (thickness ~ 0.7 nm) of mercaptopropyl silane (MCPS) SiO_2 is ~ 16 MV/cm when monolayer was deposited on native SiO_2 [58]. The measurement was carried out in sandwich geometry where Si was the bottom contact, and for the top contact, the liquid, Hg drop, was used on the monolayer. The breakdown voltage for alkane chains (no. of carbon atoms > 10) has also been studied, and it is reported relatively high breakdown voltage in the range 12–20 MV/cm [59]. Diebold et al. reported that the addition of fluorine-substituted alkane silane has improved the breakdown strength of native SiO_2 by 158% [60]. This increase in strength is attributed to electron trapping, scattering, or attachment processes inherent to the fluorinated moieties. They used c-AFM for top contact for their measurements, and 5 nA leakage current was considered as the breakdown threshold. The rationale behind this current level is three orders higher than the current observed at low voltage. This low leakage current also helps to preserve the integrity of the c-AFM tip over multiple tests. The high breakdown voltage of silane of thickness < 2 nm is the reason to consider silane monolayer for transistor gate for reducing the size of the transistor. The reduction of gate length would help to increase the number of transistors per chip. The application of silane as a gate in field-effect transistor (FET) will be discussed later.

(2) **Resistive random access memory:** Recently, resistive random access memory (RRAM) has emerged as a next-generation storage element which has high operational speed (sub ns), low operational energy (<0.1 pJ) voltage, and high endurance. The RRAM is a two-terminal device in which memory material is sandwiched between two metal contacts. In such devices, the resistance of the memory material changes under applied voltage which leads to two conduction states (high and low) [53, 57]. The one way of obtaining such electrical properties is to introduce trap states in an insulating/semiconducting material.

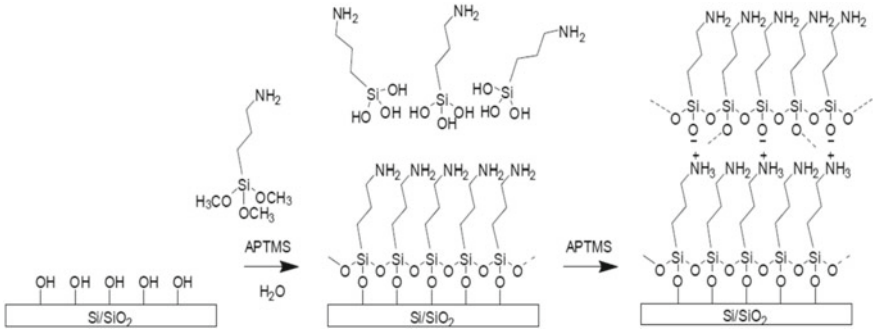

Fig. 17.1 Detail of layer-by-layer deposition of organosilane [53, 57]. *Reproduced with the permission from [Springer Nature Customer Service Centre GmbH]: [Springer] [Resistive memory effect in self-assembled 3-aminopropyltrimethoxysilane molecular multilayers. Physica Status Solidi, AK Chauhan, DK Aswal, SP Koiry, N Padma, V Saxena, SK Gupta, and JV Yakhmi [COPYRIGHT] (2008)*

Chauhan et al. explored the possibility of RRAM characteristics in the mono-/multilayer of aminopropyltrimethoxysilane (APTMS) layer which contains trap states (NH^{3+}) as shown in Fig. 17.1 [53, 57]. Typical J–V characteristics of various APTMS samples recorded are shown in Fig. 17.2. The voltage was cycled as $-V_{max} \rightarrow 0\,V \rightarrow +V_{max} \rightarrow 0\,V \rightarrow -V_{max}$, at the scan speed of 5 mV/s. It is seen that the multilayer exhibits negative differential resistance (NDR), i.e., decreasing current with increasing voltage in particular voltage ranges which is the property of a tunnel diode. Such characteristics are needed for the realization of memory circuits.

For elucidating memory characteristics, a sequence of write–read–erase–read voltage pulses was applied where + 3 V (write) and −5 V (erase) pulses are for 10 s and −4 V pulse to read these states. As shown in Fig. 17.3, the "read" current for high conduction state (write state) is high as compared to that for the low-conducting state. Thus, two conduction states are electronically accessible that is the requirement for rewritable random access memory devices. The reported stability of these devices is up to 7 months at ambient temperature (25–35 °C) and humidity >60%.

(3) **Organic field-effect transistor (OFET):** In recent time, OFET attracts immense attention because of its capability to be used in large-scale, portable, foldable electronic devices [61]. OFET comprises three terminals: drain, source, and gate [61]. The current is measured between the source and drain through organic semiconducting channel lying between these two terminals. Its flow is controlled by a gate which is separated from the organic layer by a dielectric material [62]. The interface between the semiconducting channel and dielectric plays an important role. For example, the hydrophobicity of the dielectric materials or surface groups attached to the dielectric material influences the ordering and crystallinity of organic layer which influences the mobility of the charge carrier [62–64]. Even, the surface modification lowers

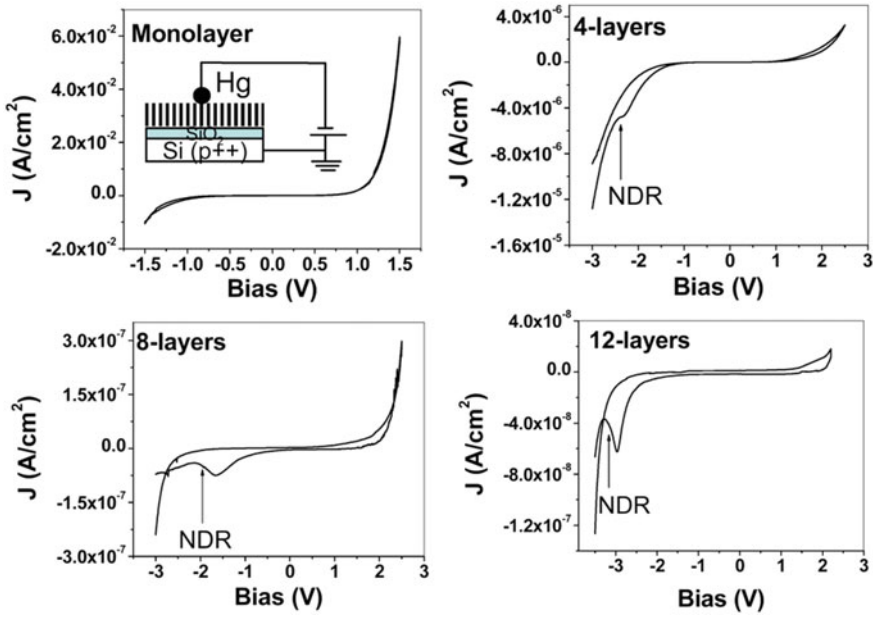

Fig. 17.2 Current–voltage (*J–V*) characteristics recorded for different APTMS samples by scanning the applied bias in the sequence: $-V_{max} \rightarrow 0\,V \rightarrow +V_{max} \rightarrow 0\,V \rightarrow -V_{max}$. The inset shows the schematic of the device structure used for the *J–V* measurements. Current peak (NDR) is marked in the figure [57]. *Reprinted by permission from [Springer Nature Customer Service Centre GmbH]: [Springer] [Resistive memory effect in self-assembled 3-aminopropyltrimethoxysilane molecular multilayers. Physica Status Solidi, AK Chauhan, DK Aswal, SP Koiry, N Padma, V Saxena, SK Gupta, and JV Yakhmi [COPYRIGHT] (2008)*

the leakage current through the dielectric and improves the dielectric property of the material. There are many dielectric materials which have been tried to get the better result. Among those, SiO_2 has been widely investigated for OFET because of its good dielectric properties and excellent reproducibility in device fabrication and performance. One more factor that makes SiO_2 popular dielectric for OFET is the ease of its surface modification by self-assembly of silane as discussed above. The silanization of SiO_2 shows significant improvement of FET behaviors in comparison with bare SiO_2 [63]. Yanlian Lei et al. reported the effect of silane modification of SiO_2 gate on OFET properties in detail [62]. They employed four silanes for this study, namely methyltrichlorosilane (MTS), phenyltrichlorosilane (PTS), octyltrichlorosilane (OTS-8), and octadecyltrichlorosilane (OTS-18). The effects of surface modification by these silanes were investigated on the performance of OFET which had a bottom-gate, top-contact configuration. The semiconducting channel

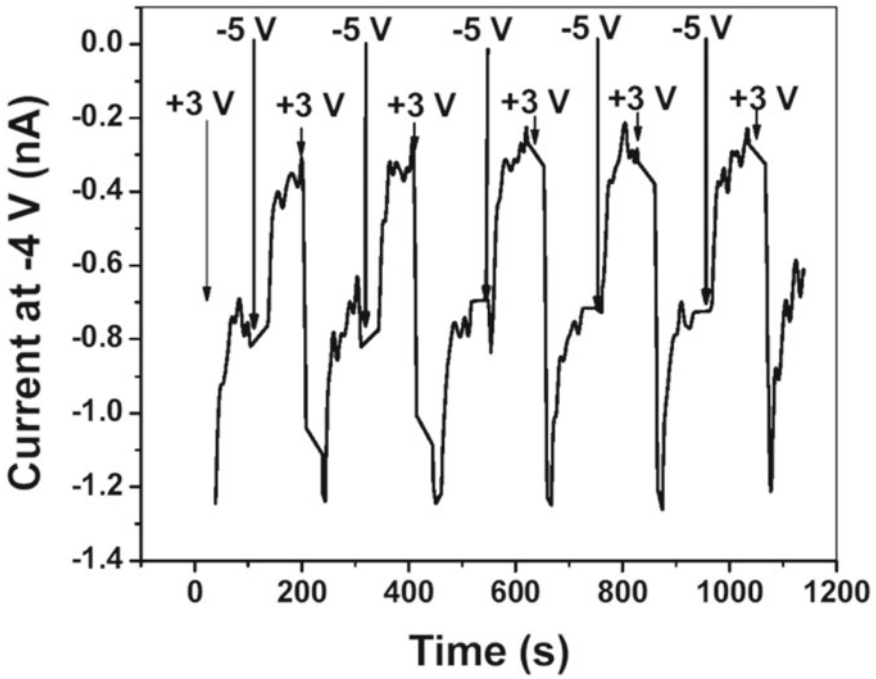

Fig. 17.3 Memory effect in Hg/APTMS multilayer/Si(p^{++}) device. The "write–read–erase–read" operations were performed by 10 s pulsing of + 3 V and −5 V, consecutively. The device was read 50 times at −4 V after each write (+3 V) and erase (−5 V) pulse [57]. *Reproduced with the permission from John Wiley and Sons*

that used in this OFET structure was polymeric materials: diketopyrrolopyrrole–dithienylthieno[3,2-b]thiophene (DPP–DTT) and regioregular poly(3-hexylthiophene) (regio-P3HT) (II). Their results demonstrate that OTS-18-modified SiO_2 gate dielectrics exhibit high field-effect mobility, but the on/off ratio is comparatively low. On the contrary, OTS-8 or PTS modification results in a higher on/off ratio, but lower field-effect mobility. These results show that long chain and short chain are complementary to each other in regard to OFET properties. Therefore, the mixture of long and short silanes was investigated which showed both high mobility and high on/off ratio in OFETs.

17.4 Silicone

Silicone is a class of silicon polymer that constitutes of–$(R)_2$Si–O repeated unit, where R is an organic group [8, 65]. First, Kipping described the synthesis of new silicon compounds and coined their name as silicone in 1901 [65–67]. Three decades later, Hyde of Dow Corning demonstrated commercial potential of silicone resins as thermal and electrical insulators [66]. The industrial production of silicone was started after the invention of a direct synthesis method by Rochow of General Electric from Si and MeCl in 1941 [68–70].

Nomenclature: The bonding structure of silicone is complex and of 3D nature which arises due to the tetrahedral arrangement of Si–O bonds. For ease of naming such 3D structures, silicone chain is divided into units depending on the number of O atoms bonded to Si [8, 70]. If Si is bonded to one oxygen atom and rest are with other organic groups (R_3Si-O), such unit is designated as M which signifies mono-functional, similarly bifunctional as D (R2SiO_2/2), trifunctional as T ($RSiO_3$/2), and tetrafunctional as Q (SiO4/2) [65].

17.4.1 Direct Synthesis Method

Rochow synthesized polydimethylsiloxane (PDMS) by reacting methylmagnesium bromide with $SiCl_4$ at −30 °C in ether solvent followed by hydrolysis [68, 71, 72]. He also reported the preparation of PDMS by hydrolysis of methyl chlorosilanes [68]. Based on this, the industrial method is developed for PDMS where the reaction is carried out in a fluidized bed of silicon metal powder under the stream of methyl chloride at temperatures of 250 to 350 °C and pressures of 1 to 5 bar in the presence of Cu catalyst [65]. A mixture of chlorosilane is produced which is separated by distillation.

$$\mathrm{Si} + \mathrm{CH_3Cl} \xrightarrow{\mathrm{Cu}} (\mathrm{CH_3})_2\mathrm{SiCl_2} \quad \text{Yield} > 50\% \tag{17.4.1}$$

Dimethylchlorosilane collected by distillation is hydrolyzed to obtain PDMS.

Polymerization: Dimethylchlorosilane reacts with excess water producing disilanol which readily condenses to form linear and cyclic oligomers of silicone according to the reaction as follows [65, 70, 73–75].

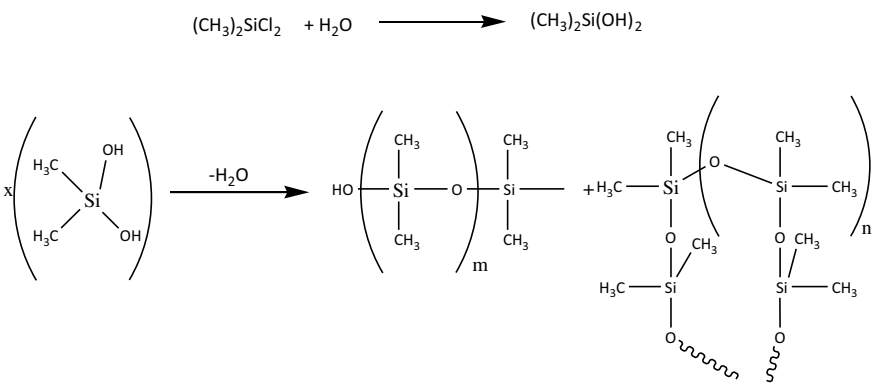

(17.4.2)

The rate of the reaction depends on pH, and the ratio of linear to cyclic oligomers depends on the pH, solvent, and concentrations [76]. For example, if the reaction is carried out in an organic solvent, cyclic oligomer dominates [71, 77, 78]. These silicone oligomers are of low molecular weight and have short molecular chains which hinder their direct use. Therefore, these oligomers are further polymerized to obtain large molecular weight. The linear oligomer can undergo condensation to form a polymer in the presence of a catalyst such as phosphonitrilehalide, n-hexylammonium 2-ethyl caproate [71, 78, 79]. The cyclic oligomers are condensed by opening ring using a strong acid/base which gives equilibrium mixture of cyclic oligomers and a linear polymer of longer chains [77]. The linear polymers are separated by evaporation [65, 71, 80]. The extent of polymerization depends on the end group present in the chain. If the polymerization is carried out in the presence of a base such as KOH, the end group is OH which can go further polymerization [80]. For terminating the chain, oligomers like $(Me_3SiO)_2$ are added during polymerization to obtain chain with end group (Me_3SiO) which blocks further catenation [65, 71, 80]. The preparation method discussed above is not limited to PDMS, and silicone can be prepared from different organosilanes such as ethyl methyl dichlorosilane, phenyl silane, alkoxysilane, and vinyl silane. Synthesis of all these silanes is discussed in Sect. 17.2. Silicone can also be synthesized from sodium silicate in which silicate is first hydrolyzed to silanol, and then it is reacted with trimethylchlorosilane or hexamethyldisiloxane.

Silicone can be designed to undergo interchain condensation (cross-linking) to make a 3D network [5]. For example, if a silicone contains vinyl groups, it may undergo cross-linking with other organic radical generated in the chain by peroxide or UV light. Another method of cross-linking is mixing silicone with end group OH and excess hydrolyzable silane (alkoxysilane) which undergo cross-linking when exposing to moisture. Such a mixture is used as a sealant. In addition to these methods, there are different ways to cross-link the silicone chain, such as the addition of SiH-terminated silicone with vinyl-terminated silane in the presence of metal catalyst.

17.4.2 Application

Silicone is widely used in our day-to-day life as which includes but not limited to insulator, sealant, adhesive, encapsulator, antifoaming agent, water repellant, a surface modifier [81]. A specific application in daily usage is the use of silicone to control the foam formation in detergent and shampoo [82–84]. Although silicone is invented at the beginning of the twentieth century, the field of synthesis of new silicone is still exciting and open for research and development (R&D) for newer applications. The R&D activities on silicone can be understood from more than 100 numbers of patents filed and articles published on the synthesis of new silicone in 2018 alone [8]. For further reading, those literatures may be concerned. Here, two emerging applications of silicone in (1) organic electronics and (2) fluorescent imaging are discussed.

17.4.2.1 Silicone Matrix for Electronic and Imaging

(a) **Silicone matrix for memory application**: Resistive random access memory (RRAM) characteristics can be obtained by electrochemical oxidation and reduction in the solid state [85–87]. Such characteristics have been shown in redox switching memory devices which have metal–insulator–metal (M–I–M) structures with I being metal oxides. For example, the switching behavior in Ag/SiO_2/Pt devices is attributed to oxidation and reduction of Ag^+ in the presence of OH^- ions. The Ag^+ and OH^- ions are generated from Ag electrode and moisture present within the SiO_2 film under the applied electric field, respectively [88]. Owing to the electrochemical oxidation and reduction of Ag^+, these Ag/SiO_2/Pt devices exhibit an open-circuit voltage (OCV) in hundreds of mV and a short-circuit current (Jsc) in hundreds of pA [88]. It has been demonstrated the memory characteristic of such device by using OCV to read on/off states as on states are set by one polarity voltage and off states are reset by reversed polarity voltage [88].
These properties have been replicated in silicone matrix obtained by condensation of aminopropyltrimethoxysilane (APTMS) [89]. Silicone matrix has –O–Si–O– network which can facilitate the proton (H^+ and OH^-) generation from absorbed moisture in the film [90]. These protons are exploited for resistive switching analogous to SiO_2-based RRAMs [91]. For this purpose, 5,10, 15, 20-tetrakis(4-hydroxyphenyl)-21H, 23H-porphine and 5, 10, 15, 20-tetra(4-pyridyl)-21H, 23H-porphine are embedded in (3-aminopropyl) trimethoxysilane film for controlling protons in the film. The current–voltage (I–V) characteristics of the films sandwiched between gold electrodes show OCV(~ ± 0.8 V) and Jsc (~ ± 6 μA) [89]. This characteristic has been explained from quasi-reversible oxidation and reduction of moisture in the polymer matrix. It is demonstrated that OCV could be used for nonvolatile flexible memory application.

(b) **Silicone as semiconductor**: The semiconducting properties are imparted into silicone network by incorporating semiconductor material by hydrosilylation, Piers–Rubinsztajn reaction, and Mizoroki–Heck reaction [92]. Another way of incorporation of semiconductor material is polycondensation of alkoxy groups attached to organic semiconductor. Such polycondensation is very useful for the devices, which have multilayer structure deposited on top of one another by solution process. Because of polycondensation, each organic layer becomes insoluble, and subsequent layers do not disturb the interface of the previous layer [92]. This polycondensation has been exploited for the organic light-emitting diode (OLED) which has a multilayer structure: (1) electron transporting, (2) light emitting, and (3) hole transporting layer. There are several reports on the use of semiconductor-incorporated silicone in OLED [92].

(c) **Silicone as fluorescent materials**: Fluorescent materials are being investigated for bioimaging, a topographic image of tissues and drug delivery [93]. There are lots of advancement occurred in this direction. The advantage of silicone is that such materials can be synthesized with desired terminal groups to which fluorescent materials can be bonded. Silicones such as polydimethylsiloxane (PDMS) being nontoxic and biocompatible have been used to incorporate fluorescent materials. WiktorKasprzyk et al. reported such incorporation in which fluorescent molecule constituted of 5-oxo-1,2,3,5-tetrahydroimidazo[1,2-a]pyridine-7-carboxylic acid was chemically bonded to PDMS through its NH_2-terminated groups [94].

17.5 Polysilane

Polysilane is another class of silicon polymers which differ from silicone in bonding structure. In the polysilane, the backbone is Si–Si that is analogous to C–C bonds in the alkane. However, the chain formation property of Si is vastly different from C. This may be attributed to the difference in the number of electronic shells ($n = 2$ for C and $n = 3$ for Si), bigger in size, low electronegativity (Si-1.8 and C-2.5) [1]. These differences make the Si bond more labile; for example, Si–X halogen bond is more polar than C–X bond which makes Si–X more susceptible to a reaction. In the case of Si–H, its bond energy (~ 80 kcal/mole) is lower than that of the C–H bond (98 kcal/mol). Moreover, in Si–H bond H is negative which causes high reactivity of Si–H moiety. However, if hydrogen is replaced by alkyl or phenyl group, the reactivity of Si–C bond decreases. Therefore, the polysilane is divided into two groups depending on the groups attached to Si–Si skeleton: Hydrogen substituted is called inorganic polysilane or polyhydrosilane and organic functional group substituted as poly(organosilane).

The synthesis of polysilane was first reported by Kipping and Sands in 1921 [95–97]. They synthesized phenyl-substituted crystalline polysilane compounds (SiPh2)n = 2 to 6. In 1949, Burkhard reported the synthesis of methyl-substituted polysilane

using the same synthetic method as described by Kipping [98, 99]. Both polysilanes were insoluble in common solvents and were poorly investigated due to which further development of polysilane got hindered. Thus, this field was remained dormant until the report of polysilane as the precursors for SiC fibers in 1978 which surged the interest in the polysilane synthesis [100, 101]. Another factor that attracts much attention in polysilane is its UV absorption property [101–103]. The absorption of UV by a sigma-bonded polysilane is unusual optical property because such absorption is generally expected from pi-conjugated systems [99, 104]. Therefore, many theoretical studies have been carried out to understand the optical properties of polysilane, which is eventually explained by delocalization of σ-electrons along the Si–Si chain. Along with the theoretical studies, many new soluble polysilanes and their derivatives have been synthesized which show unusual electronic, optical, and photophysical properties [104, 105]. Only recently, these unique properties of polysilane have found practical applications for futuristic devices such as UV OLED, hole transporting layer in organic solar cells, and semiconducting materials for field-effect transistor [7].

17.5.1 Synthesis: Wurtz-Type Coupling of Dichlorosilanes

As mentioned above, Kipping first reported the synthesis of polysilane by refluxing diphenyldichlorosilane with sodium in inert solvent toluene or xylene according to the following reaction [96–99, 101, 103, 104, 106].

$$Ph_2SiCl_2 \xrightarrow[\text{Reflux}]{\text{Na}} (Ph_4Si_2)_n + NaCl \tag{17.5.1}$$

This reaction is considered as a general method of synthesizing different polysilanes depending on the substituents attached to dichlorosilane; for example, alkyl-substituted polysilane can be prepared using dialkyldichlorosilane. The drawbacks of this reaction are: (1) Only robust functional groups such as phenyl, alkyl, silyl, and a few intrinsically stable substituents can withstand extreme reductive and high-temperature reaction condition. Therefore, getting functional polysilanes is required new strategy. (2) Other than the ability to sustain reaction condition, the polymerization is also sensitive to the size of the substituent. (3) The product of the reaction has trimodal mass distributions comprised of low, intermediate, and high mass fractions. The low mass contains mainly cyclic oligomers and can be separated by solvent extraction, but intermediate and high molecular mass requires effort to separate. Moreover, it is also observed that the yield of the polymer depends on the temperature and solvent used. Thus, synthesis of polysilane homopolymer is a challenging task and attracts much attention.

For overcoming the drawbacks, a few strategies have been developed. For synthesizing polysilane with a desired functional group that is sensitive to reaction condition, the strategy is to use a protecting group, which can withstand harsh reaction

condition, and after polymerization, the group is removed to obtain desired functionality. Since the temperature influences the yield by changing the length of the polymer chain in turn mass distribution, the lowering of temperature gives a more homogeneous polymer [107]. Thus, the synthesis has been carried out at low temperature using low boiling point solvent such as THF [108]. The optically active chiral solvent has been tested to obtain high molecular mass at low temperature. Richard et al. reported a new reductive graphite potassium intercalates (C_8K) to produce polysilane. The use of the graphite potassium brings down the reaction temperature to −79 °C [7].

$$\mathrm{PhMeSiCl_2} \xrightarrow[>0^{\circ}\mathrm{C}]{\mathrm{C_8K}} -(\mathrm{PhMeSi_2})_n- + \mathrm{NaCl} + \mathrm{Graphite} \qquad (17.5.2)$$

In addition to changing the temperature and solvent, sequestering the sodium species such as 15-crown-5 controls the coupling reaction by stabilizing silyl anions, the active species for the propagation of polymerization, which in turn control the yield and mass distribution [109]. These polysilanes have more isotactic content than that formed by the method described above. Other than Na and K, alternative reducing agents have been reported which include yttrium and pyrophoric lead [110]. However, the yield of the polymer obtained by using these reducing agents is low.

Since the Wurtz-type coupling is widely used for synthesizing new polymer, it is essential to understand its reaction mechanism, which would help to design new synthetic route. Briefly, this coupling reaction is a heterogeneous reaction, where coupling reaction takes place on alkali metal surface. In chain propagation steps, alkali metal, for example, Na, transfers an electron to more electrophilic Si to form silyl anion (reaction 5.3: steps (a) and (b)) and NaCl. In the next step, the silyl anion and monomer undergo S_N2 reaction to continue the chain reaction (c) [106, 107, 109].

Chain propagation:

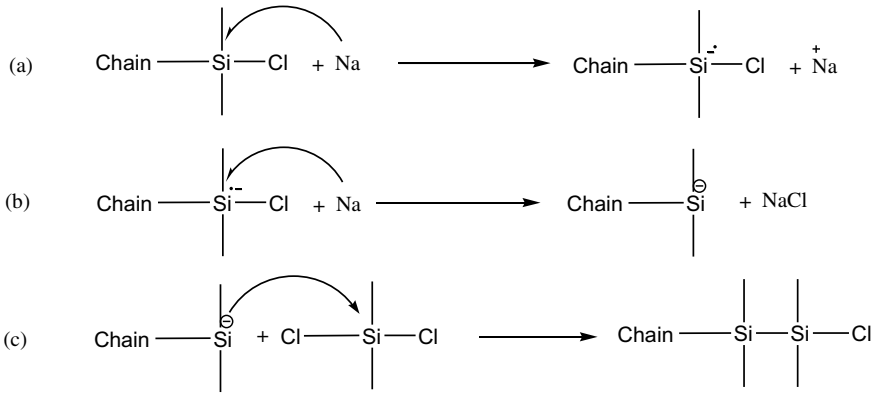

(17.5.3)

Copolymer: The homopolymer is intractable crystalline solid and thus has limited processability. In 1978, West et al. reported first meltable polysilane which was a

copolymer synthesized by co-condensation of dimethyl dichlorosilane and phenyl methyl dichlorosilane in the ratio 10:1 to 3:1 [99, 101]. By changing the ratio to 1:1, they later produced amorphous polysilane:

$$Ph_2SiCl_2 + PhMeSiCl_2 \xrightarrow[90-100^\circ C]{Na} -(PhMeSi)_x(Me_2Si)_y- + NaCl \qquad (17.5.4)$$

These polymers are fusible at 200 °C and are soluble in many common organic solvents such as benzene, toluene, chlorocarbons, and tetrahydrofuran. They reported that these polymers were initially insulator, conductivity $<10^{-11}\Omega^{-1}$ cm^{-1} which became semiconducting (~0.5 Ω^{-1} cm^{-1}) after doping with AsF_5 [99, 101]. Such co-condensation expedited synthesis of polysilane due to the limitless possibility of variation in monomer selections and ratios of the two monomers [104].

17.5.2 Other Than Wurtz-Type Reaction

Since Wurtz-type reaction has limitations, other new approaches have been developed. Among them are dehydrocoupling of hydrosilanes by transition metals, the catalytic disproportionation of alkoxysilanes, the ring-opening polymerization of cyclooligosilanes, and the anionic polymerization of masked disilenes [7, 104, 107, 111].

17.5.2.1 Dehydrocoupling

The name itself suggests the removing of hydrogen and then the formation of Si–Si bonds. Thus for this type of reactions, silane monomers should contain at least two Si–H instead of two Si-Cl in Wurtz-type reaction [7, 112].These Si–H bonds undergo disproportionate reaction to give Si–Si and H–H bonds in the presence of transition metal catalysts.

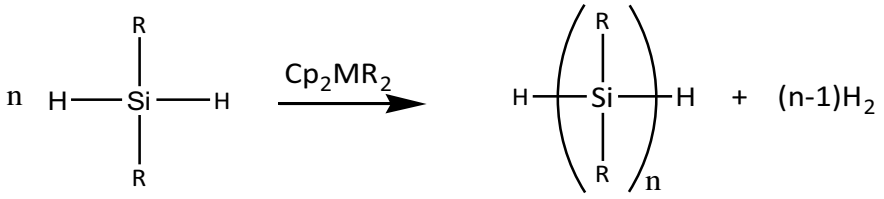

(17.5.5)

The transition metal catalysts are metallocene derivative of group (IV) metal of structure $CpMR_2$ where Cp = C_6H_5, M = Ti, Zr, Hf, and R = alkyl and aryl.

The polymer yield depends upon the metal M, ring substituents on Cp, and type of R. For example, $CpZrMe_2$ produces 20 Si unit long chain from phenylsilane,

whereas $CpTiMe_2$-catalyzed coupling reaction of the same silane has 10 unit long chain. This difference is attributed to the dependence of catalytic activity on atomic number [111].

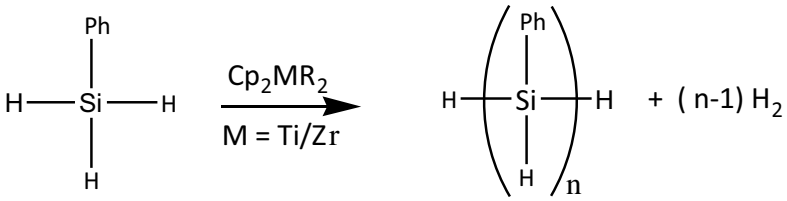

DP= 10 for Ti and DP= 20 for Zr, DP= degree of polymeriztion

(17.5.6)

The reaction that is discussed above is an early report of dehydrocoupling reaction of silanes. After that, many strategies have been adopted to increase degree of polymerization. It is shown that the catalyst $CpCp^*MR_2$ in which the ring of one Cp is slightly modified by methyl groups (designated as Cp^*) produces a long chain of Si of 100 unit for the reaction above. The time required for polymerization is shown to be dependent on the R group. If one Me of $CpCp^*ZrMe_2$ is changed to $Si(SiMe_3)_3$, this leads to faster chain growth for comparable molecular weights (for $CpCp^*MMe_2$; Mn = 4,240 in 52 h: $CpCp^*$Zr[Si(SiMe3)3]Me; Mn = 4230 in 24h) [7, 111].

Ansa-metallocenes (ansa is bridged) were also investigated for dehydrocoupling reaction for silane because such metallocenes are widely used in olefin polymerization. However, the polymerization by ansa-metallocene was not encouraging as the yield was either less than or comparable to normal metallocenes [111].

Other non-group (IV) metal-based metallocenes have been investigated and were found to be mostly ineffective or producing dimer or trimer. The actinide complexes Cp*2UMe2 and Cp*,ThMe2 were found to be active only for $PhSiH_3$ which after dehydrocoupling produce dimers and other low molecular weight materials at room temperature [111]. However, the reasonably good polymer species are produced by Pt-, Pd-, and Rh-based catalyst; for instance, Pt-based catalyst dehydrocouples Et_2SiH_2 to a polymer of Mw = 2,100–31000 [111].

The choice of silane monomer is also crucial for reaction yield. The order of reactivity in the presence of the group IV metallocene catalyst is primary silane, $RSiH_3$ (R = alkyl or aryl) > secondary silane (R_2SiH3 (R = alkyl/aryl or both) > R3SiH (unreactive). Such order of reactivity is attributed to steric hindrance. This is why the secondary silane requires elevated temperature for dehydrocoupling reaction; for example, MeSiH2 with a Cp_2TiPh_2 catalyst undergoes dehydrocoupling reaction at 90 °C [111]. Moreover, the dehydrocoupling secondary silane produces only dimer/trimer rarely any higher polymer because of the steric hindrance. Although

the dehydrocoupling reaction is ineffective to many reactive groups, it could polymerize the monomers that would not survive a Wurtz-type coupling such as fluorine-substituted monomers and halogenated aryl silanes $H_3Si(P–C_6H_4X)$ (X = F, CI, Br).

17.5.2.2 Catalytic Disproportion Reaction

Nagai et al. first reported the cleavage of the Si–Si bond of methyl methoxydisilane compound by sodium ethoxide to form silyl anions, a disproportion reaction [112]:

$$MeO(SiMe_2)_2OMe \xrightarrow{NaOEt} (MeO)Me_2Si^-Na^+ + (MeO)_2SiMe_2 \qquad (17.5.7)$$

Later, the authors utilized this disproportionate reaction to produce cyclic or linear oligosilanes at moderate temperature ($MeO(SiMe_2)_nOMe$ where $n \geqslant 3$ and cyclic polysilane $(Me_2Si)_n$ where $n = 5–7$ in the presence of catalytic amount of NaOEt [112]:

$$MeO(SiMe_2)_2OMe \xrightarrow{NaOEt,cat.} \begin{matrix} MeO(SiMe_2)_nOMe \\ n = 3, 4, 5 \\ \text{Major product} \end{matrix} \qquad (17.5.8)$$

Imai et al. prepared the network of methylethoxypolysilane containing various substituents such a hexyl, phenyl, ethylene, hexamethylene, phenylene, and thiophene groups by a disproportionation reaction of 1,1,2,2-tetraethoxy-1,2-dimethylsilane in the presence of the corresponding substituted alkoxysilanes [113]. The yields of the polysilanes were quite high, and the polymer had molecular mass more than 7000.

17.5.2.3 Ring Opening of Silacycles

Strained cyclopolysilane undergoes ring-opening reaction to produce linear polysilane. The final product depends on the monomer structure, catalysts, and initiator [7, 112]. Therefore, this method provides total control on the end product, thus low polydispersities. Matyjaszewski et al. first reported the ring-opening polymerization of strained 1,2,3,4-tetramethyl-1,2,3,4-tetraphenylcyclotetrasilane (1) by nucleophilic reagents such as BuLi.

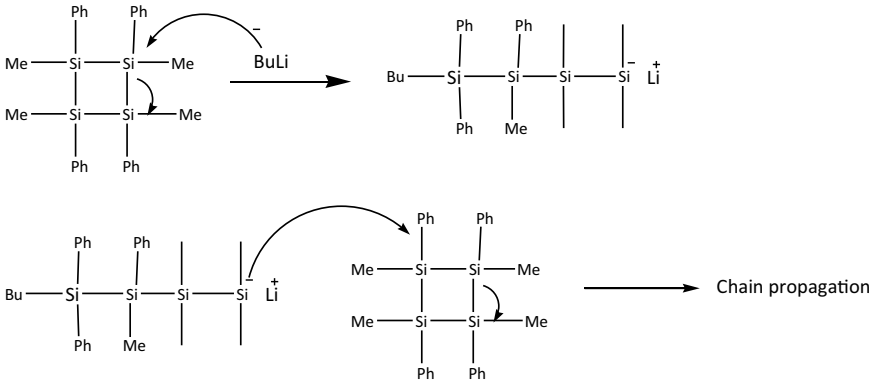

(17.5.9)

The ring opening of all trans (1) using $(PhMe_2Si)_2Cu(CN)Li_2$ produced polymer in nearly quantitative yield [7, 112]. The microstructure of the polymer consists of 75% heterotactic and 25% isotactic triads that were confirmed by [29] Si NMR spectroscopy. Molecular weights were obtained up to 30,000. This type of ring-opening polymerization has been extensively used to produce many functional polysilanes such as ring-opening copolymerization of cyclotetrasilane with silicon-bridged ferrocenophane to give polysilane-poly(ferrocenylsilane) random copolymers [7, 112].

17.5.2.4 Masked Disilene

Disilene, Si–Si double-bonded spices, is unstable except for those with very bulky substituents. Roark and Peddle reported for the first time the generation of tetramethylsilane by thermolysis of 7,7,8,8-tetramethyl-I-phenyl-7,8-disilabicyclo[2.2.2]octa-2,5-diene which became a source of disilene for both thermal and photochemical reactions [114].

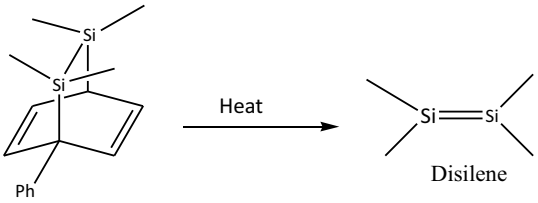

(17.5.10)

Based on these facts, Sakurai and co-workers developed a new method of preparing polysilanes through polymerization of masked disilenes [112]. Here, a masked disilene is a highly reactive disilenes which can temporarily be masked by adding a suitable auxiliary group just as in the case of 7,7, 8,8-tetramethyl-I-phenyl-7,8-disilabicyclo[2.2.2]octa-2,5-diene shown above. For polymerization,

Sakurai et.al developed a new masked disilene l-phenyl-7,8-disilabicyclo[2.2.2]octa-2,5-dienes [112]. These monomers are used to polymerize with a catalytic amount of anionic initiators, such as organolithium compounds or alkali metal alkoxides. Termination is accomplished by adding alcohol.

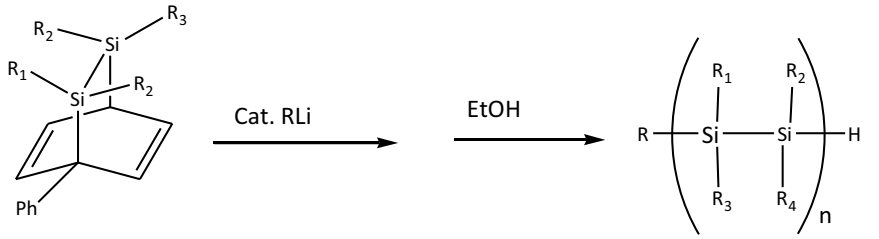

(17.5.11)

The highly ordered polymer structures are obtained by this method. Although this polymerization process has the potential for high yield, the reaction conditions for the preparation of the masked disilenes are as harsh as those of the Wurtz-type reductive coupling reaction. Moreover, the introduction of functional groups is a multistep process.

17.5.2.5 Other Alternatives

Electrochemical polymerization of diorganodichlorosilanes has also been investigated which generally yield oligomers [7, 115]. Ishifuna and co-workers were able to obtain polymethylphenylsilane with an *M*n of 3600 and a PDI of 2.3 from a dichlorotrisilane using ultrasonic electrochemical reduction. The advantage of this technique is the possibility of producing a monomodal weight distribution [116].

17.5.3 Applications

As discussed at the beginning of this section, polysilanes have unusual optical, electronic, and photophysical properties due to the delocalization of σ-electrons along the silicon chain. The delocalization of σ-electrons can be explained from molecular orbital theory. The head-on overlapping of sp3 hybrid orbital of each Si atom forms the Si–Si bond of the polymer chain. *d*-orbitals do not contribute to the formation of the bonds. The overlapping of hybrid orbitals leads to bonding σ- and antibonding σ^* molecular orbitals responsible for the σ-conjugation along the main silicon chain. The energy levels of these molecular orbitals are dependent on the chain length and the substituents attached [7]. This delocalization of σ-electrons is analogous to the delocalization of π-electrons in conjugated C–C system. Moreover, like π-conjugated C–C system, polysilane shows electrical conductivity and optical absorption property.

Therefore, the polysilanes have been investigated for polymer-based optoelectronic applications similar to the organic polymer. A few applications are discussed here.

17.5.3.1 Polysilane in Organic Light-Emitting Diode (OLED)

Suzuki et al. have reported the application of polymethylphenylsilane (PMPS) as a hole transporting layer in OLEDs which have hole mobility up to 10^{-3}cm^2/Vs at room temperature [17]. Polysilanes have also been reported as light-emitting layers when its chain contains metal complex. Since polysilane absorbs UV light depending upon the substituent attached, it has been investigated as UV emitter for OLED. The first UV emission was reported in PMPS, but the electroluminescence was only detectable at-77 K[7]. Room-temperature UV OLED was demonstrated by linear high molecular weight (Mw $> 5 \times 10^5$gmol^{-1}) polymethylphenylsilane and poly(bis(4-butylphenyl) silane. However, the lifetime of such OLED is less than the state of the art of OLED [7].

17.5.3.2 Organic Solar Cell

Similar to OLED, polysilane has also been tried as a hole transporting layer in the organic solar cell [117–119]. The results are not encouraging, and it requires new material designing [7, 119].

17.5.3.3 Field-Effect Transistor

Because of semiconducting nature, polysilane has also been proposed for FET application. Since pure polysilane has poor hole mobility, it attracts less attention as a semiconductor in FET [7]. However, the mixtures of polysilane with other polymer have been investigated as a semiconducting layer in FET [120]. The use of polysilane as a semiconductor requires new concept such as the addition of new substituents on polymer chain or copolymerization to enhance charge carrier mobilities to make it suitable for OFETs.

17.6 Silicene

Silicene is a 2D silicon monolayer similar to graphene [18, 19, 121]. The most fascinating property of graphene is that the electrons behave as if they are massless or relativistic electrons (so-called Dirac electrons) [18]. Thus, the electron mobility is a hundred time faster for graphene than that for silicon because of which graphene is emerged as next-generation material for faster electronics. After the discovery of graphene and realization of its immense technological potential, the curiosity

has been raised to obtain silicene, silicon analogue of graphene. Like C, silicon cannot form double bond and triple bond. Therefore, many theoretical studies have been carried out to obtain the exact structure of silicene. Since Si is sp3-hybridized, silicon atoms are lying on two different plans rather than single plan like graphene. Such structure is referred to as a buckled 2D sheet which is similar to Si (111) plan. However, theoretical calculation predicts similar electronic property as graphene [122].

Although the possible existence of Si analogue of graphene had been predicted theoretically in 1994 [121], after 16 years of the prediction, Bernard et al. revealed epitaxial growth of silicene ribbon on the anisotropic silver (110) surface [123]. Since then, the activity for the synthesis of silicene has increased exponentially.

17.6.1 Synthesis of Silicene

Silicon does not have graphite-like materials for obtaining silicene by mechanical exfoliation technique. Therefore, different approaches are adopted.

17.6.1.1 Vacuum Deposition

First report for the synthesis of silicene sheet appeared in 2012. In this report, silicene sheet was grown by epitaxially on silver single crystal [18, 19, 124]. In this method, Si was deposited by sublimation of a piece of silicon wafer in the ultra-high vacuum on the Ag(111) surface held at ~220 °C with a 4 × 4 periodicity concerning primitive Ag(111) which is confirmed by 1 × 1 in LEED patterns and STM images [18, 19]. The structure of this silicon superstructure has been found dependent on substrate temperature. At present, silicene sheet has been successfully fabricated on an Ag (111) substrate held at 150−300 °C and at a slow deposition rate of Si below 0.1 monolayer per minute. Silicene has also been reported to form on Ag(110), Ag(001), Ag(111), Au(110), ZrBr2, ZrC(111), Ir(111), and MoS2 surfaces [125, 126]. Among these substrates, silver has emerged as an ideal substrate for silicene fabrication because Si does not react with Ag and Ag has matching crystal lattice parameters. However, the freestanding silicene is yet to be fabricated.

17.6.1.2 Functionalized Silicene

Although pure silicene is desirable, adding different functional groups introduces other desirable properties [19]. The functionalized silicene is generally obtained from $CaSi_2$ [127]. Calcium disilicide (CaSi2) is an intermetallic compound in which silicon is the anionic part of the structure. The anionic Si is interconnected to form 2D silicon sub-network resembling buckled Si(111) planes. These Si polyanion layers are separated by planar monolayers of Ca^{2+}. Thus to obtain Si 2D network, Ca^{2+} is

deintercalated by concentrated HCl which produces layered siloxene ($Si_6H_3(OH)_3$) as described below

$$Ca(Si)_2 + HCl + H_2O \rightarrow Si_6H_3(OH)_3 + CaCl_2 + H_2 \quad (17.6.1)$$

The layered $Si_6H_3(OH)_3$ can be chemically exfoliated into individual sheets using a surfactant, such as sodium dodecyl sulfate (SDS: $C_{12}H_{25}OSO_3Na$). In place of water, if a solution of HCl and methanol, ethanol, butanol, $C_{12}H_{25}$, benzyl alcohol, or CH_2COOMe are used, then corresponding alkoxide-terminated organosiloxenes (Si_6H_5OR, where R = methanol, ethanol, butanol, $C_{12}H25$, benzyl alcohol, or CH2COOMe) were also obtained.

At −30 °C, this chemical exfoliation results in Si_6H_6

$$Ca(Si)_2 + HCl \rightarrow Si_6H_6 + CaCl_2 \quad (17.6.2)$$

The structure of $Si_6H_3(OH)_3$ and Si_6H_6 is same, but in Si_6H_6 all Si atoms are terminated with H only [18, 19]. Since Si–H bond is polarized, it is susceptible to a chemical reaction. Thus, hydrogenated silicene is the starting material for adding functional groups. For example, in Pt-catalyzed hydrosilylation reaction, Si_6H_6 was functionalized with 1-hexene to produce a stable colloidal silicene suspension. Recently, silicene quantum dots (SiQDs) of 2 nm in diameter and 4 atomic layers of silicone were synthesized by using fine powders of $CaSi_2$ as raw materials, and PtO_2 powders, as the hydrosilylation catalyst and olefin/acetylene derivatives as a stabilizer [128]. Phenyl-terminated silicene was obtained from the reaction between Si_6H_6 and Grignard reagent. The obtained product is soluble in a number of a solvent such as hexane, chloroform, acetone, or ether. Lithiated silicene is prepared by milling Li with Si_6H_6 layer for 30 min. In this mechanochemical reaction, Li replaces H from Si_6H_6 by releasing hydrogen gas.

17.6.1.3 Silicene Nanoribbon

In 2009–2010, the first reported silicene was nanoribbons which were grown on Ag surface [123]. Now such ribbon has been grown on Au, too [124–127]. The nanoribbons have high uniformity and are more stable to molecular oxygen than bulk Si [124–127]. The electronic properties of freestanding silicene depend on its structure [124–127]. The armchair silicone nanoribbons (ASiNRs) are reported to be nonmagnetic but could be metals or semiconductors. The zigzag silicone nanoribbons (ZSiNRs) show antiferromagnetic semiconducting ground state. Here, armchair and zigzag describe nanoribbons with two different shapes of edges [121, 124–127].

17.6.2 Applications

Since silicene imitates graphene, it is expected the same potential applications of graphene for silicene. At the present stage, the field of silicene is infancy and much more studies are needed to elucidate its properties. Still, conceptual silicene-based transistor has been demonstrated. Recently, electrostatic measurement data of silicene device are reported which reveal field-effect mobility of 100 and 200 cm^2V^{-1} for single-layer and multilayer silicene, respectively [19]. However, the predicated mobility is 1000 cm^2V^{-1} for single-layer silicene [19]. Energy storage is another field that attracts much interest. In this respect, multilayer lithiated would enable intercalation/deintercalation of lithium atoms during charge/discharge of the cell similar to graphite and has been shown the exceptionally high specific capacity (4200 mA h g^{-1}) against graphite (~371 mA h g^{-1}) [19]. Among others, one of the most touted applications is silicene for topology-based electronics which is still in the conceptual level [19].

17.7 Conclusions

In this chapter, an overview of synthesis of important silicon compounds, present status, and future outlook has been presented. The methods for extraction of elemental silicon from SiO_2 and conversion of elemental Si to crystal, silane, and polymer have been discussed. Like carbon, silicon can form different compounds with other elements such as C and O and can also undergo polymerization, and therefore, it is possible to engineer novel silicon compounds. This is one of the reasons for a tremendous development in designing and synthesizing silicon compounds for different applications. A relatively newer entry of silicon polymer is polysilane, which shows hole transporting properties and has found its acceptability for fabrication of UV organic light-emitting diode, etc. However, the hole mobility in polysilane is low and requires new synthetic strategies. More recently, the synthesis of silicene, a silicon analogue of graphene, has generated considerable interest because of its potential applications.

References

1 Petrov BFMAD, Ponomarenko VA, Chernyshev EA (1964) Synthesis of organosilicon monomers. Consultants Bureau, New York
2 Semenov VV (2011) Preparation, properties and applications of oligomeric and polymeric organosilanes. Russ Chem Rev 80(4):313–339
3. Brook MA (1999) Silicon in organic, organometallic, and polymer chemistry. Wiley
4. O'Mara WC, Herring RB, Hunt LP (1990) Handbook of semiconductor silicon technology. Noyes Publications
5. Plueddemann EP (2013) Silane coupling agents. Springer, US

6. Moriguchi K, Utagawa S (2012) Silane: chemistry, applications and performance. Nova Publishers
7. Muzafarov AM (2010) Silicon polymers. Springer, Berlin Heidelberg
8 Robeyns C, Picard L, Ganachaud F (2018) Synthesis, characterization and modification of silicone resins: an "Augmented Review." Prog Org Coat 125:287–315
9 Su TA, Li H, Klausen RS, Kim NT, Neupane M, Leighton JL, Steigerwald ML, Venkataraman L, Nuckolls C (2017) Silane and Germane Molecular Electronics. Acc Chem Res 50(4):1088–1095
10 Lee B, Chen Y, Duerr F, Mastrogiovanni D, Garfunkel E, Andrei EY, Podzorov V (2010) Modification of electronic properties of graphene with self-assembled monolayers. Nano Lett 10(7):2427–2432
11 Puniredd SR, Jayaraman S, Yeong SH, Troadec C, Srinivasan MP (2013) Stable organic monolayers on oxide-free silicon/germanium in a supercritical medium: a new route to molecular electronics. J Phys Chem Lett 4(9):1397–1403
12 Aswal DK, Lenfant S, Guerin D, Yakhmi JV, Vuillaume D (2006) Self assembled monolayers on silicon for molecular electronics. Anal Chim Acta 568(1):84–108
13 Rakshit T, Liang G-C, Ghosh AW, Datta S (2004) Silicon-based molecular electronics. Nano Lett 4(10):1803–1807
14 Guisinger NP, Greene ME, Basu R, Baluch AS, Hersam MC (2004) Room temperature negative differential resistance through individual organic molecules on silicon surfaces. Nano Lett 4(1):55–59
15 Okumoto H, Yatabe T, Richter A, Peng J, Shimomura M, Kaito A, Minami N (2003) A strong correlation between the hole mobility and silicon chain length in oligosilane self-organized thin films. Adv Mater 15(9):716–720
16 Surampudi S, Yeh ML, Siegler MA, Hardigree JFM, Kasl TA, Katz HE, Klausen RS (2015) Increased carrier mobility in end-functionalized oligosilanes. Chem Sci 6(3):1905–1909
17 Suzuki H, Meyer H, Simmerer J, Yang J, Haarer D (1993) Electroluminescent devices based on poly (methylphenylsilane). Adv Mater 5(10):743–746
18. Yan Voon LCL, Guzmán-Verri GG (2014) Is silicene the next graphene?. MRS Bull 39(4):366–373
19 Molle A, Grazianetti C, Tao L, Taneja D, Alam MH, Akinwande D (2018) Silicene, silicene derivatives, and their device applications. Chem Soc Rev 47(16):6370–6387
20 Li X-G, Xiao W-D (2016) Silane pyrolysis to silicon rod in a bell-jar reactor at high temperature and pressure: modeling and simulation. Ind Eng Chem Res 55(17):4887–4896
21 Zhang P, Duan J, Chen G, Li J, Wang W (2018) Production of polycrystalline silicon from silane pyrolysis: a review of fines formation. Sol Energy 175:44–53
22 Shimura F (2017) Single-crystal silicon: growth and properties. In: Kasap S, Capper P (eds) Springer handbook of electronic and photonic materials. Springer International Publishing, Cham, pp 1–1
23 Hoshikawa K, Huang X, Taishi T, Kajigaya T, Iino T (1999) Jpn J Appl Phys 38(Part 2, No. 12A):L1369–L1371
24. Barker Jr TH (1986) Process for preparing chlorosilanes from silicon and hydrogen chloride using an oxygen promoter. Google Patents
25. Ingle WM, Darnell RD (1985) Oxidative purification of chlorosilane silicon source materials. J Electrochem Soc 132(5):1240–1243
26. Ingle WM, Peffley MS (1985) Kinetics of the hydrogenation of silicon tetrachloride. J Electrochem Soc 132(5):1236–1240
27 Alcántara-Avila JR, Sillas-Delgado HA, Segovia-Hernández JG, Gómez-Castro FI, Cervantes-Jauregui JA (2015) Optimization of a reactive distillation process with intermediate condensers for silane production. Comput Chem Eng 78:85–93
28 Filtvedt WO, Holt A, Ramachandran PA, Melaaen MC (2012) Chemical vapor deposition of silicon from silane: review of growth mechanisms and modeling/scaleup of fluidized bed reactors. Sol Energy Mater Sol Cells 107:188–200

29 Friedrich J, von Ammon W, Müller G (2015) 2 - Czochralski growth of silicon crystals. In: Rudolph P (ed) Handbook of crystal growth (Second Edition). Elsevier, Boston, pp 45–104
30 Uecker R (2014) The historical development of the Czochralski method. J Cryst Growth 401:7–24
31 West R, Barton TJ (1980) Organosilicon chemistry: part I. J Chem Educ 57(3):165
32 Deschler U, Kleinschmit P, Panster P (1986) 3-chloropropyltrialkoxysilanes—key intermediates for the commercial production of organofunctionalized silanes and polysiloxanes. Angew Chem Int Ed Engl 25(3):236–252
33 Sterman S, Marsden JG (1966) Silane coupling agents. Ind Eng Chem 58(3):33–37
34. Shorr LM (1955) Method of preparing alkoxysilicon compounds. Google Patents
35. Speier JJL (1950) Chlorination of organosilicon compositions. Google Patents
36 Speier JL, Roth CA, Ryan JW (1971) Syntheses of (3-aminoalkyl) silicon compounds. J Org Chem 36(21):3120–3126
37. Reichel S (1972) Process for preparing gamma-aminopropylalkoxy-silanes and gamma-aminopropylalkylalkoxysilanes. Google Patents
38 Sommer LH, Rockett J (1951) The polar effects of organosilicon substituents in aliphatic amines 1,2. J Am Chem Soc 73(11):5130–5134
39. Plueddemann EP (1969) Alkoxyalkarylsilanes and condensates thereof. Google Patents
40 Kricheldorf HR (1996) Chemical modification of polymers and surfaces. In: Kricheldorf HR (ed) Silicon in polymer synthesis. Springer, Berlin Heidelberg, pp 404–457
41 Zeng X, Xu G, Gao Y, An Y (2011) Surface wettability of (3-aminopropyl) triethoxysilane self-assembled monolayers. J Phys Chem B 115(3):450–454
42. Siqueira Petri DF, Wenz G, Schunk P, Schimmel T (1999) An improved method for the assembly of amino-terminated monolayers on sio2 and the vapor deposition of gold layers. Langmuir 15(13):4520–4523
43. Omietanski G, Petty H (1974) Process for reacting weak acids with chloroalkyl substituted silicon compounds. Google Patents
44. Le Grow GE (1971) Method of preparing mercaptoalkyl alkoxy silanes. Google Patents
45 Xie Y, Hill CAS, Xiao Z, Militz H, Mai C (2010) Silane coupling agents used for natural fiber/polymer composites: a review. Compos A Appl Sci Manuf 41(7):806–819
46 Plueddemann EP (1983) Silane adhesion promoters in coatings. Prog Org Coat 11(3):297–308
47 Plueddemann EP (1983) Silane adhesion promoters for polymeric coatings. In: Mittal KL (ed) Adhesion aspects of polymeric coatings. Springer, US, Boston, MA, pp 363–377
48 Child TF, van Ooij WJ (1999) Application of silane technology to prevent corrosion of metals and improve paint adhesion. Transactions of the IMF 77(2):64–70
49. Klauk H (2006) Organic electronics: materials, manufacturing, and applications. Wiley
50. Wöll C (2009) Physical and chemical aspects of organic electronics: from fundamentals to functioning devices. Wiley
51. Lyshevski SE (2018) Nano and molecular electronics handbook, CRC Press
52 Aswal DK, Koiry SP, Jousselme B, Gupta SK, Palacin S, Yakhmi JV (2009) Hybrid molecule-on-silicon nanoelectronics: electrochemical processes for grafting and printing of monolayers. Phys E 41(3):325–344
53 Chauhan AK, Aswal DK, Koiry SP, Gupta SK, Yakhmi JV, Sürgers C, Guerin D, Lenfant S, Vuillaume D (2008) Self-assembly of the 3-aminopropyltrimethoxysilane multilayers on Si and hysteretic current–voltage characteristics. Appl Phys A 90(3):581–589
54. Koiry SP, Aswal DK, Saxena V, Padma N, Chauhan AK, Joshi N, Gupta SK, Yakhmi JV, Guerin D, Vuillaume D (2007) Electrochemical grafting of octyltrichlorosilane monolayer on Si. Appl Phys Lett 90(11):113118
55 Zheng K, Sun F, Zhu J, Ma Y, Li X, Tang D, Wang F, Wang X (2016) Enhancing the thermal conductance of polymer and sapphire interface via self-assembled monolayer. ACS Nano 10(8):7792–7798
56. Kim J (2011) Formation, structure, and reactivity of amino-terminated organic films on silicon substrates. In: Interfaces and Interphases in Analytical Chemistry. American Chemical Society, pp 141–165

57 Chauhan AK, Aswal DK, Koiry SP, Padma N, Saxena V, Gupta SK, Yakhmi JV (2008) Resistive memory effect in self-assembled 3-aminopropyltrimethoxysilane molecular multilayers. Phys Status Solidi A 205(2):373–377
58 Aswal DK, Lenfant S, Guerin D, Yakhmi JV, Vuillaume D (2005) A tunnel current in self-assembled monolayers of 3-Mercaptopropyltrimethoxysilane. Small 1(7):725–729
59 Zhao J, Uosaki K (2003) Dielectric properties of organic monolayers directly bonded on silicon probed by current sensing atomic force microscope. Appl Phys Lett 83(10):2034–2036
60 Diebold RM, Gordon MJ, Clarke DR (2014) Effect of silane coupling agent chemistry on electrical breakdown across hybrid organic–inorganic insulating films. ACS Appl Mater Interfaces 6(15):11932–11939
61 Sirringhaus H (2014) 25th anniversary article: organic field-effect transistors: the path beyond amorphous silicon. Adv Mater 26(9):1319–1335
62 Lei Y, Wu B, Chan W-KE, Zhu F, Ong BS (2015) Engineering gate dielectric surface properties for enhanced polymer field-effect transistor performance. J Mater Chem C 3(47):12267–12272
63 Liu D, Miao Q (2018) Recent progress in interface engineering of organic thin film transistors with self-assembled monolayers. Mater Chem Front 2(1):11–21
64 Lei Y, Deng P, Lin M, Zheng X, Zhu F, Ong BS (2016) Enhancing crystalline structural orders of polymer semiconductors for efficient charge transport via polymer-matrix-mediated molecular self-assembly. Adv Mater 28(31):6687–6694
65. Colas A (2005) Silicones: preparation, properties and performance. Dow corning, life sciences
66. Modjarrad K, Ebnesajjad S (2013) Handbook of polymer applications in medicine and medical devices. Elsevier Science
67. Kipping FS, Lloyd LL (1901) XLVII.—Organic derivatives of silicon. Triphenylsilicol and alkyloxysilicon chlorides. J Chem Soc Trans 79:449–459
68 Rochow EG, Gilliam WF (1941) Polymeric methyl silicon oxides1. J Am Chem Soc 63(3):798–800
69. Rochow EG (1941) Methyl silicones and related products. US
70. Noll W (2012) Chemistry and technology of silicones. Elsevier Science
71. Jones RG, Ando W, Chojnowski J (2013) Silicon-containing polymers: the science and technology of their synthesis and applications. Springer, Netherlands
72 Patnode W, Wilcock DF (1946) Methylpolysiloxanes1. J Am Chem Soc 68(3):358–363
73. Lane TH, Burns SA (1996) Silica, silicon and silicones...Unraveling the mystery. Springer, Berlin, Heidelberg
74. Bokerman GN, Freeburne SK, Schuelke LM, VanKoevering DG (1991) Anhydrous hydrogen chloride evolving one-step process for producing siloxanes. US
75 Burger C, Kreuzer F-H (1996) Polysiloxanes and polymers containing siloxane groups. In: Kricheldorf HR (ed) Silicon in polymer synthesis. Springer, Berlin, Heidelberg, pp 113–222
76. Panchenko BI, Gruber VN, Klebanskii AL (1969) Study of the hydrolytic polycondensation of dimethyldichlorosilane in concentrated hydrochloric acid. Polym Sci U.S.S.R. 11(2):496–501
77. Lambert JB, Kania L, Schulz Jr WJ (1993) Redistribution of cyclosiloxanes to favor formation of decamethylcyclopentasiloxane. J Polym Sci Part A: Polym Chem 31(7):1697–1700
78. Sandler SR, Karo W (eds) (1977) Chapter 4 - Silicone Resins (Polyorganosiloxanes or Silicones). In: Organic chemistry, Elsevier, pp 114–139
79 Cypryk M, Apeloig Y (2002) Mechanism of the acid-catalyzed Si−O bond cleavage in siloxanes and siloxanols. A theoretical study. Organometallics 21(11):2165–2175
80. Wicht MBJCCDWGGRKJLLLSRSRFSJSJWD (2003) Silicones. In: Encyclopedia of polymer science and technology, vol. 11, pp. 765–776
81. Andriot M, Chao S, Colas A, Cray S, DeBuyl F, DeGroot J, Dupont A, Easton T, Garaud J, Gerlach E (2007) Silicones in industrial applications. Inorg Polym 61–161
82 Cornwell PA (2018) A review of shampoo surfactant technology: consumer benefits, raw materials and recent developments. Int J Cosmet Sci 40(1):16–30
83. L'hostis J, Renauld F, Sawicki G (2003) Silicone foam control agent. US Patent

84 Sawicki GC (1988) Silicone polymers as foam control agents. J Am Oil Chem' Soc 65(6):1013–1016
85 Waser R, Dittmann R, Staikov G, Szot K (2009) Redox-based resistive switching memories – nanoionic mechanisms, prospects, and challenges. Adv Mater 21(25–26):2632–2663
86. Sugiyama I, Shimizu R, Suzuki T, Yamamoto K, Kawasoko H, Shiraki S, Hitosugi T (2017) A nonvolatile memory device with very low power consumption based on the switching of a standard electrode potential. APL Mater. 5(4):046105
87. Valov I, Waser R, Jameson JR, Kozicki MN (2011) Electrochemical metallization memories—fundamentals, applications, prospects. Nanotechnology 22(25):254003
88 Valov I, Linn E, Tappertzhofen S, Schmelzer S, van den Hurk J, Lentz F, Waser R (2013) Nanobatteries in redox-based resistive switches require extension of memristor theory. Nat Commun 4:1771
89 Koiry SP, Jha P, Putta V, Saxena V, Chauhan AK, Aswal DK, Gupta SK (2015) Memory and ferroelectric photovoltaic effects arising from quasi-reversible oxidation and reduction in porphyrin entrapped aminopropyl-silicate films. Org Electron 25:143–150
90 Chandra S, Sekhon SS, Srivastava R, Arora N (2002) Proton-conducting gel electrolyte. Solid State Ion 154–155:609–619
91 Valov I (2014) Redox-Based Resistive Switching Memories (ReRAMs): electrochemical systems at the atomic scale. Chem Electro Chem 1(1):26–36
92 Kamino BA, Bender TP (2013) The use of siloxanes, silsesquioxanes, and silicones in organic semiconducting materials. Chem Soc Rev 42(12):5119–5130
93 Mehwish N, Dou X, Zhao Y, Feng C-L (2019) Supramolecular fluorescent hydrogelators as bio-imaging probes. Mater Horizons 6(1):14–44
94 Kasprzyk W, Krzywda P, Bednarz S, Bogdał D (2015) Fluorescent citric acid-modified silicone materials. RSC Adv 5(110):90473–90477
95. Fs K (1923) J Chem Soc 125:2291
96. Kipping FS, Sands JE (1921) XCIII.—Organic derivatives of silicon. Part XXV. Saturated and unsaturated silicohydrocarbons, Si4Ph8. J Chem Soc Trans 119(0):830–847
97. Kipping FS (1924) CCCVIII.—Organic derivatives of silicon. Part XXX. Complex silicohydrocarbons [SiPh2]n. J Chem Soc Trans 125(0):2291–2297
98. Burkhard CA, J Am Chem Soc 71:963
99 West R, David LD, Djurovich PI, Stearley KL, Srinivasan KSV, Yu H (1981) Phenylmethylpolysilanes: formable silane copolymers with potential semiconducting properties. J Am Chem Soc 103(24):7352–7354
100. Yajima SH, Hayashi Y, Iimura MM (1978) J Mater Sci 13
101 West R (1986) The polysilane high polymers. J Organomet Chem 300(1):327–346
102 Naito M, Fujiki M (2008) Polysilanes on surfaces. Soft Matter 4(2):211–223
103. Semenov VV (2011) Preparation, properties and applications of oligomeric and polymeric organosilanes. Russ Chem Rev 80
104 Miller RD, Michl J (1989) Polysilane high polymers. Chem Rev 89(6):1359–1410
105 Jovanovic M, Michl J (2018) Understanding the Effect of Conformation on Hole Delocalization in Poly(dimethylsilane). J Am Chem Soc 140(36):11158–11160
106 Jones RG, Holder SJ (2006) High-yield controlled syntheses of polysilanes by the Wurtz-type reductive coupling reaction. Polym Int 55(7):711–718
107. Jones RG, Ando W, Chojnowski J (eds) (2013) Silicon-containing polymers: the science and technology of their synthesis and applications. Springer Netherlands, pp 365–375
108. Jones RG, Budnik U, Holder S, Wong WKC (1996) Reappraisal of the origins of the polymodal molecular mass distributions in the formation of poly(methylphenylsilylene) by the Wurtz reductive-coupling reaction, vol 29
109 Jones RG, Benfield RE, Cragg RH, Swain AC, Webb SJ (1993) Evaluation of the synthesis of polysilanes by the reductive-coupling of dihaloorganosilanes. Macromolecules 26(18):4878–4887
110. Robert RHC, Benfield E, Jones RG, Swain AC (1992) Alternative reducing agents for the Wurtz synthesis of polysilanes. J Chem Soc Chem Commun 1022–1024:1

111. Gray GM, Corey JY (2013) Silicon-containing polymers: the science and technology of their synthesis and applications. In (eds) Jones RG, Ando W, Chojnowski J. Springer, Netherlands, pp 402–416
112. Sakurai H, Yoshida S (2013) Silicon-containing polymers: the science and technology of their synthesis and applications. In: Jones RG, Ando W, Chojnowski J (eds) Springer, Netherlands, pp 375–399
113. Kabeta K, Wakamatsu S, Imai T (1996) Preparation of substituted network polysilanes by a disproportionation reaction of alkoxydisilanes in the presence of alkoxysilanes. J Polym Sci Part A: Polym Chem 34(14):2991–2998
114 Roark DN, Peddle GJD (1972) Reactions of 7,8-disilabicyclo[2.2.2]octa-2,5-dienes. Evidence for the transient existence of a disilene. J Am Chem Soc 94(16):5837–5841
115 Kashimura S, Ishifune M, Yamashita N, Bu H-B, Takebayashi M, Kitajima S, Yoshiwara D, Kataoka Y, Nishida R, Kawasaki S-I, Murase H, Shono T (1999) Electroreductive synthesis of polysilanes, polygermanes, and related polymers with magnesium electrodes1. J Org Chem 64(18):6615–6621
116 Ishifune M, Kashimura S, Kogai Y, Fukuhara Y, Kato T, Bu H-B, Yamashita N, Murai Y, Murase H, Nishida R (2000) Electroreductive synthesis of oligosilanes and polysilanes with ordered sequences. J Organomet Chem 611(1):26–31
117. Nakagawa J, Oku T, Suzuki A, Akiyama T, Tokumitsu K, Yamada M, Nakamura M (2012) Fabrication and characterization of polysilane/C60thin film solar cells. J Phys Conf Ser 352:012019
118. Iwase M, Oku T, Suzuki A, Akiyama T, Tokumitsu K, Yamada M, Nakamura M (2012) Fabrication and characterization of poly[diphenylsilane]-based solar cells. J Phys Conf Ser 352:012018
119. Oku T, Nakagawa J, Iwase M, Kawashima A, Yoshida K, Suzuki A, Akiyama T, Tokumitsu K, Yamada M, Nakamura, M (2013) Microstructures and photovoltaic properties of polysilane-based solar cells. Jpn J Appl Phys 52(4S):04CR07
120. Acharya A, Seki S, Saeki A, Tagawa S (2006) Photoconductivity in fullerene-doped polysilane thin films. 156:293–297
121. Lew Yan Voon L, Guzmán-Verri GG (2014) Is silicene the next graphene?. 39
122. Kara A, Enriquez H, Seitsonen AP, Lew Yan Voon LC, Vizzini S, Aufray B, Oughaddou H (2012) A review on silicene — new candidate for electronics. Surf Sci Rep 67(1):1–18
123. Aufray B, Kara A, Vizzini S, Oughaddou H, Léandri C, Ealet B, Lay GL (2010) Graphene-like silicon nanoribbons on Ag(110): a possible formation of silicene. Appl Phys Lett 96(18):183102
124. Bernard Aufray BE, Jamgotchian H, Hichem Maradj J-YHAJ-PB (2016) Silicene: structure, properties and applications. In: Spencer M, Morishita T (eds) Springer International Publishing, Switzerland, pp 183–185
125. Paola De Padova BO, Quaresima C, Ottaviani AC. Silicene: structure, properties and applications. In: Spencer M, Morishita T, Springer International Publishing, pp 143–146
126. Houssa M, Dimoulas A, Molle A (2015) Silicene: a review of recent experimental and theoretical investigations. J Phys Condens Matter 27(25):253002
127. Nakano H, Ohashi M (2016) Silicene: structure, properties and applications. In: Spencer M, Morishita T (eds) Springer International Publishing, Switzerland
128 Hu P, Chen L, Lu J-E, Lee H-W, Chen S (2018) Silicene quantum dots: synthesis, spectroscopy, and electrochemical studies. Langmuir 34(8):2834–2840

Chapter 18
Synthesis and Processing of Li-Based Ceramic Tritium Breeder Materials

Biranchi M. Tripathi, A. K. Tyagi, and Deep Prakash

Abstract Fusion energy has undisputable potential to cope with the challenges of increasing global energy demand and to protect the environment from global warming. The construction of a fusion reactor based on the D–T fuel cycle has been at the forefront of fusion energy research. Due to insufficient availability of tritium in nature and limited global inventory, the fusion reactors ought to breed their tritium. Tritium is produced in a blanket containing Li-based compounds called tritium breeding blanket surrounding the fusion reactor. Li-based ceramics are candidate materials for the fabrication of tritium breeding blankets. In order to attain tritium self-sufficiency, the blanket must produce enough tritium so as to maintain the tritium breeding ratio (TBR) greater than 1. The present chapter reviews R&D results of powder synthesis, consolidation to form shapes and sintering of Li-based ceramics. Further, this chapter summarizes the challenges and opportunities concerning the processing of Li-based ceramic tritium breeding materials.

Keywords Nuclear fusion · ITER · Tritium breeding blanket · Ceramic · Sintering

B. M. Tripathi (✉) · D. Prakash
Powder Metallurgy Division, Bhabha Atomic Research Centre, Vashi Complex, Navi, Mumbai 400705, India
e-mail: biranchi@barc.gov.in

A. K. Tyagi
Chemistry Division, Bhabha Atomic Research Centre, Trombay, Mumbai 400085, India

B. M. Tripathi · A. K. Tyagi · D. Prakash
Homi Bhabha National Institute, Mumbai 400094, India

A. K. Tyagi and R. S. Ningthoujam (eds.), *Handbook on Synthesis Strategies for Advanced Materials*, Indian Institute of Metals Series,
https://doi.org/10.1007/978-981-16-1892-5_18

18.1 Introduction

18.1.1 Global Energy Demand and Role of Thermonuclear Fusion

Energy is recognized as an essential stimulus for fostering the standard of living of citizens of any country. Due to the continuous increase in the global population, better living standards and expanding economies, the demands for all forms of energy will continue to rise. No single energy source and technology can fulfil the huge global energy demand expected in the coming decades as each of them has strengths and weaknesses [1–5]. In this scenario, a mix of energy sources will be the most viable option.

Nuclear energy, in view of the present global concern on energy security, sustainable development and greenhouse effect (a major culprit of climate change), has recently returned to centre stage. Nuclear fusion is nature's fundamental source of energy which we witness in everyday life in the form Sun [6, 7]. Fusion power, due to attractive characteristics such as no greenhouse gas emission, abundant and word-wide distributed fuel resources, no long-lived radioactive waste generation and inherent safety, is a potential source of base-load electricity [8–11]. In fusion reactions, the specific energy is much higher as compared to the normal chemical reactions such as the combustion of coal [10].

18.2 Nuclear Fusion as an Energy Source

In nuclear fusion, light nuclei are brought intimately together to a distance comparable to their size to form heavier ones. In this process, a small mass defect arises that is converted into equivalent amount of energy invoking Einstein's renowned mass-energy relationship ($E = mc^2$, where c is the speed of light and m is the mass defect). The mass defect is difference in mass between the initial and the final reaction products. As the speed of light is a large number, the energy equivalent to a small quantity of mass defect is quite large. For example, some of the fusion reactions of interest with respective values of energy released (Q value) are given in Table 18.1 [12].

For the occurrence of a fusion reaction, the fusing nuclei need to be imparted sufficient kinetic energy to circumvent the repulsive electrostatic force (Coulomb barrier). The cross-section of a fusion reaction is used to express the probability of its successful occurrence. Fusion reactivity is defined as average cross sections (σ) times the relative speed (v) of the reacting nuclei. The fusion reactivity as a function of temperature plot for the three most probable fusion reactions is depicted in Fig. 18.1 [12]. The fusion of elements with higher charges takes place with an increasingly lower probability and requires higher temperatures/kinetic energy. It is because, with an increase in electrical charge, the fusing nuclei have to experience an

Table 18.1 Some of the fusion reactions of interest

$D + T \rightarrow \alpha + n$	$Q = 17.59$ MeV	(R1)
$D + D \rightarrow T + p$	$Q = 4.04$ MeV	(R2)
$\rightarrow {}^{3}He + n$	$Q = 3.27$ MeV	(R3)
$\rightarrow \alpha + \gamma$	$Q = 23.85$ MeV	(R4)
$T + T \rightarrow \alpha + 2n$	$Q = 11.33$ MeV	(R5)
$D + {}^{3}He \rightarrow \alpha + p$	$Q = 18.35$ MeV	(R6)
${}^{3}He + {}^{3}He \rightarrow \alpha + 2p$	$Q = 12.86$ MeV	(R7)
$p + {}^{6}Li \rightarrow \alpha + {}^{3}He$	$Q = 4.02$ MeV	(R8)
$p + {}^{7}Li \rightarrow 2\alpha$	$Q = 17.35$ MeV	(R9)
$p + {}^{11}B \rightarrow 3\alpha$	$Q = 8.68$ MeV	(R10)

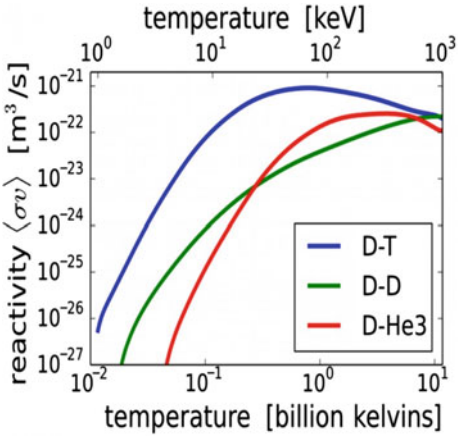

Fig. 18.1 Plot of the fusion reactivity as a function of temperature. Under CC-BY License from [13]

increasingly more repulsive Coulomb barrier. The rate of fusion reaction increases sharply with temperature until the attainment of maximum and subsequently drops off gradually.

The D–T fusion rate maximizes at a lower temperature (~70 keV/or 700 million kelvins) with higher reactivity value than other reactions. Because of these reasons, D–T fusion has been the reaction of choice to date for fusion energy. In order to realize D–T fusion, the fuel comprising of these gases must be heated to temperature of around 20 keV or 20×10^{7} °C. At such extremely high temperatures, the fuel turns into plasma.

The fusion of deuterium and a tritium nucleus produces a helium nucleus and a neutron with liberation of total energy of 17.6 meV (Fig. 18.2).

The alpha particle carries 20% (3.5 meV), and the neutron 80% (14.1 meV) of the total energy [6, 12]. In fusion reactor, the energy of neutron will be dissipated as heat and further, the dissipated heat will be converted into electricity. The positively charged alpha particle is entrapped by the magnetic field and its energy can be utilized for plasma heating purpose. For a self-sustaining fusion reaction, initially, an external

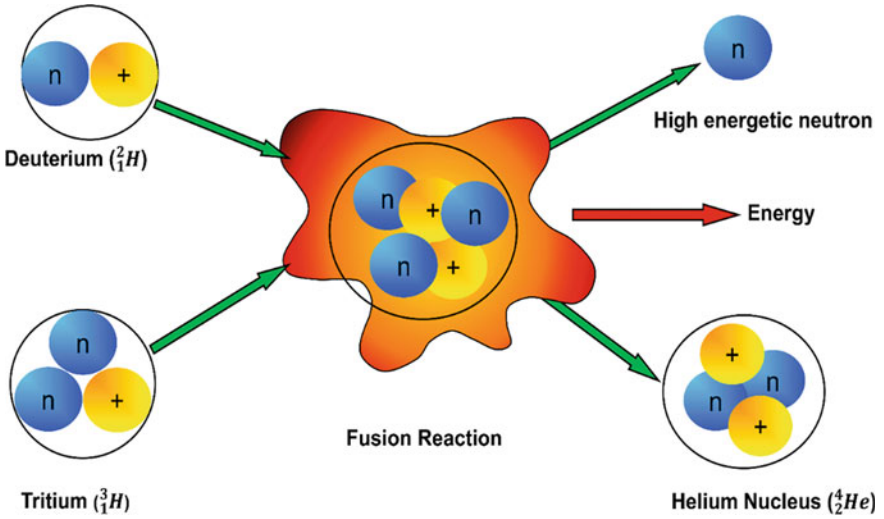

Fig. 18.2 D–T fusion reaction-schematic

energy source with minimal thermal loss is required to raise the plasma temperature over 100 million Kelvin [6, 12].

However, the fraction of heating power contributed by the alpha particles towards total power required for the plasma heating increases with increase in the rate of fusion reaction. Therefore, at some point called ignition, the heating power provided by the alpha particle itself is adequate to sustain the D–T fusion. The isolation of hot plasma from the reactor walls is essential to protect the structural materials at such a high temperature. This is achieved through different confinement techniques and one such technique is magnetic confinement. In magnetic confinement, a strong magnetic field is applied to confine the motion of alpha particles into a circular trajectory away from the reactor walls by creating a magnetic cage [6, 14].

To generate more energy from D–T magnetic confinement fusion reaction than the input energy, Lawson's criterion developed by John D. Lawson (a Physicist at the UK Atomic Energy Establishment at Harwell) in 1955 need to be satisfied. The Lawson criterion was derived by equating the alpha particle heat to the rate at which the energy is lost from the plasma. This criterion is expressed as triple product of plasma temperature (T), density (n) and confinement time (τ): $nT\tau_E > 3 \times 10^{21}$ keVm^{-3} s^{-1}[15]. According to this criterion, a minimum temperature (ideal ignition temperature) needs to be exceeded for the D–T fusion reaction to serve as an energy source. Moreover, a trade-off between the required density (n) and confinement time (τ) exists according to which higher density requires lower confinement time and vice versa. The Lawson criterion constituted a scientific Holy Grail for researchers working in the area of fusion energy.

18.2.1 Conceptual Design of a Fusion Reactor

To harness energy from nuclear fusion many attempts have been made to mimic thermonuclear action of the sun and the stars and develop fusion power stations. The conceptual design of a fusion power station is depicted in Fig. 18.3 [16]. The design is similar to a contemporary thermal power station. The dissipated heat generated due to slowing down of neutrons in the blanket material of fusion reactor will be converted into steam and steam will be further used to drive turbines and generate electrical power.

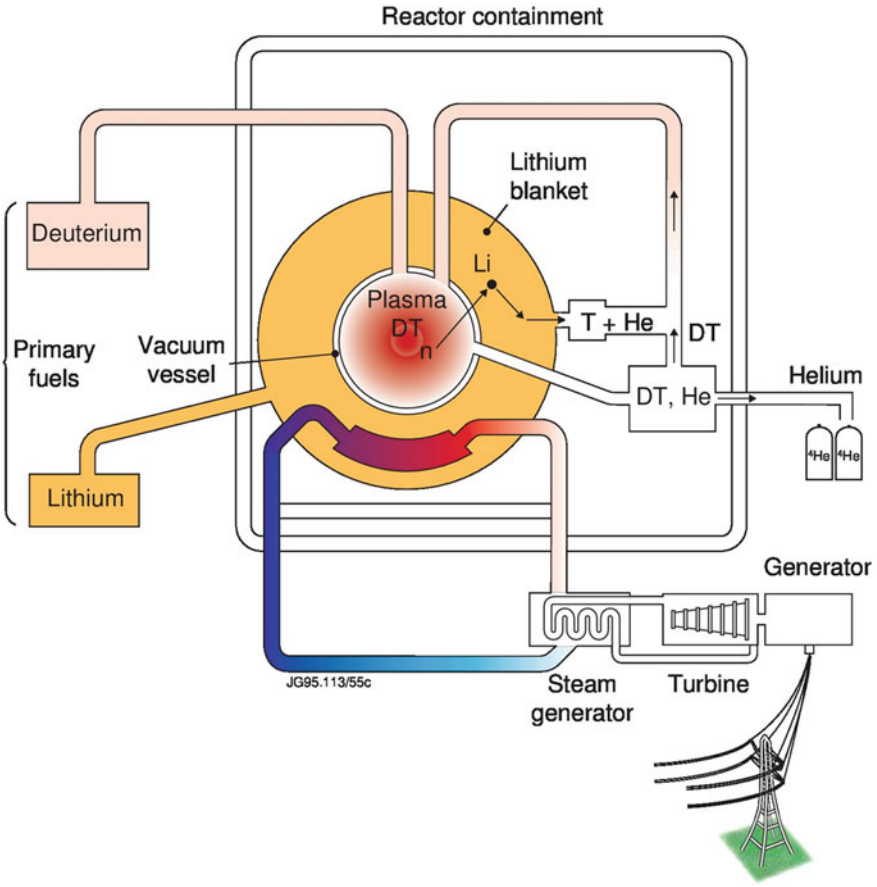

Fig. 18.3 Schematic design of a D–T nuclear fusion power plant. Courtsy JET-EFDA [16]

18.3 International Thermonuclear Experimental Reactor (ITER)

ITER means The Way in Latin. The ITER project is directed towards the development of commercial fusion reactor [17–19]. Its programmatic objective, as defined in the ITER EDA Agreement, is to demonstrate the scientific and technological feasibility of fusion energy for peaceful purposes [20]. The participant countries in this mega project are: China, the European Union, India, Japan, South Korea, Russia and the United States of America. ITER will be the first thermonuclear fusion device that aims to produce net energy by sustaining fusion for long periods. ITER will also provide an opportunity to test the integrated technologies, materials and physics regimes necessary for the development of commercial fusion power reactors. The ITER project site is located at Cadarache in southern France.

The ITER Tokamak cutaway is shown in Fig. 18.4 [20]. The ITER primarily has been designed to achieve the following objectives [20];

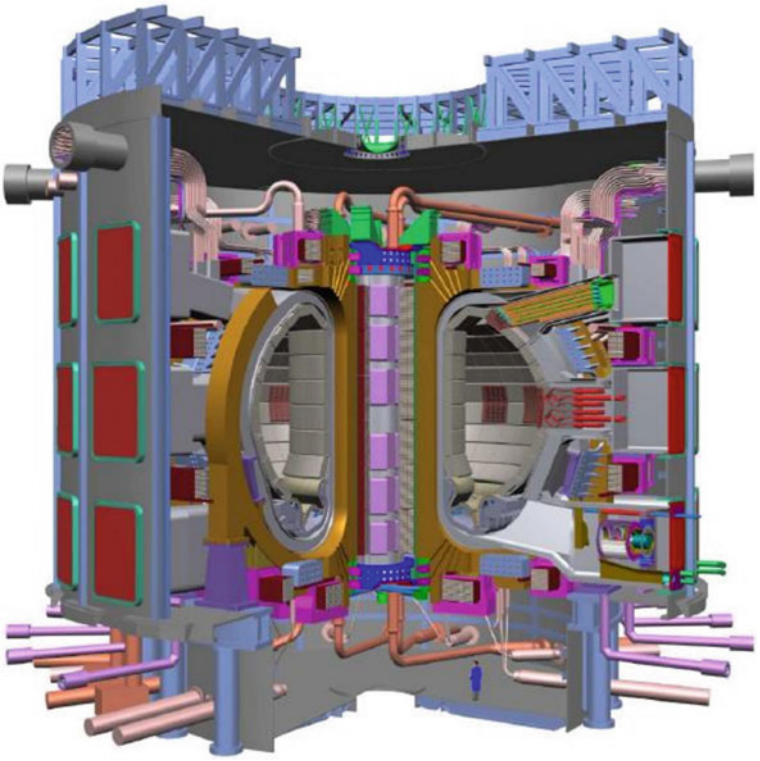

Fig. 18.4 A cutaway view of ITER Tokamak [20]

- Demonstrate release of 500 MW of fusion power from 50 MW of input power (i.e. energy gain factor Q = 10) for up to 500 s.
- Demonstrate integrated operation of technologies for a fusion power plant.
- Demonstrate the feasibility of heating a large volume of deuterium-tritium plasma and sustain fusion reaction through internal heating.
- Demonstrate endurance of candidate fusion reactor materials against irradiation by high energy neutrons and radiations, high thermal stresses and intense interactions with D and T in the fusion reactor environment.
- Demonstrate the feasibility of tritium breeding within the vacuum vessel.
- Demonstrate the safety characteristics of a fusion device.

18.3.1 Necessity of Tritium Breeding for Fusion Reactor

For the operation of a commercial fusion power plant based on the D–T fuel cycle, an uninterrupted supply of fuels (D and T) is required to be maintained into the reactor core. Although adequate quantity of deuterium is available in nature as heavy water (D_2O), however, quantity, as well as the concentration of the naturally occurring tritium is insufficient for use as a fuel. Hydrogen composed of three naturally occurring isotopes, namely ^{1}H (protium or H), ^{2}H (deuterium or D) and ^{3}H (tritium or T), is the most abundant element in the solar system, around 91% of all the atoms are hydrogen. Among hydrogen isotopes, H is the most abundant in nature and natural abundance of other isotopes, D and T are 0.0156 atom% (156 ppm) and 1TU (1 atom per 10^{18} atoms of hydrogen), respectively [12]. In addition to extremely low natural abundance, tritium is also exhausted owing to its radioactive nature (beta decay with half-life of 12.3 years) [12].

Projections for world tritium supply (Fig. 18.5) available to fusion reveals serious problems [21, 22]. The maximum global tritium inventory is around 30 kg [22]. The estimated tritium consumption in commercial D–T fusion reactor is high (55.8 kg per 1000 MW fusion power per year). According to this projection, if ITER were to run at 1000 MW fusion power with 10% availability, the world tritium supply would be exhausted by the year 2025 [21, 22]. The estimated "start-up" tritium inventory for ITER DEMO is about 5–10 kg [21, 22]. Therefore, commercial D–T fusion reactor must breed their tritium from other sources.

This chapter describes synthesis and processing of Li-based ceramic tritium breeding materials. The various routes employed or investigated for Li-based ceramic powder synthesis and fabrication of shapes is described. The issues concerning sintering and microstructural control in relation to tritium retention and release characteristics of tritium breeding materials is described. Summary of the properties and R&D results for a number of Li-based ceramic tritium breeding materials is presented.

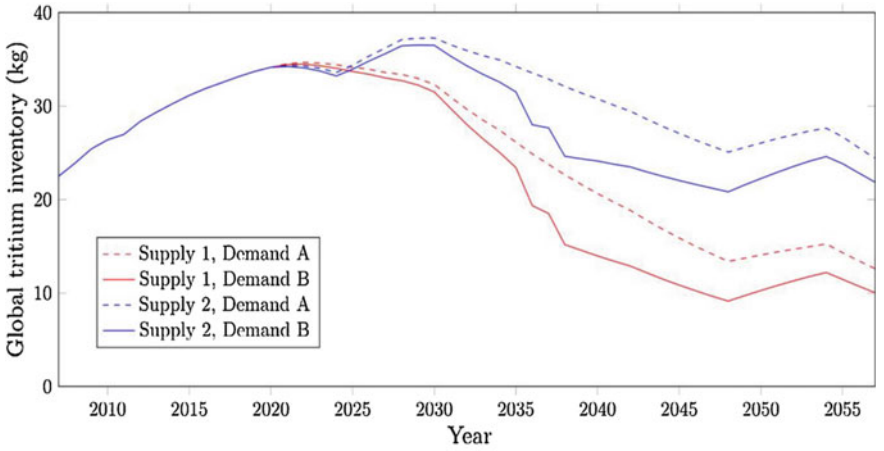

Fig. 18.5 Available global tritium inventory adjusted for fusion demands. Courtsy [22]

18.4 Concept of Tritium Breeding

Lithium, by irradiation of neutrons, can be used to produce tritium. Natural lithium is composed of two stable isotopes viz. ^{6}Li and ^{7}Li with isotopic composition of 7.4% and 92.6% respectively [12, 23]. The isotopes of lithium, because of low nuclear binding energy per nucleon, are used to produce tritium by the following nuclear reactions:

$$^{6}_{3}\mathrm{Li} + {}^{1}_{0}n \rightarrow {}^{3}_{1}\mathrm{H} + {}^{4}_{2}\mathrm{He} + 4.78\,\mathrm{MeV}$$
$$^{7}_{3}\mathrm{Li} + {}^{1}_{0}n \rightarrow {}^{3}_{1}\mathrm{H} + {}^{4}_{2}\mathrm{He} + {}^{1}_{0}n - 2.47\,\mathrm{MeV}$$

The tritium production cross-section as a function of neutron energy for the above reactions is depicted in Fig. 18.6 [24, 25].

The reaction of ^{6}Li isotope with neutron is exoergic and has a high cross-section for low energy neutrons. In contrast, the reaction of ^{7}Li is a threshold reaction (endoergic) that requires an incident neutron energy over 2.47 meV. Moreover, because of the Coulomb barrier, the cross-section of this reaction is considerably low above the threshold energy (2.5 meV). Therefore, ^{6}Li enrichment of the selected tritium breeding material is always required to achieve target tritium breeder ratio to satisfy tritium self-sufficiency. The effective ^{6}Li density can be increased to any desired value through the use of isotope enrichment process. However, the neutrons with energy of 14 meV generated from the primary fusion reaction can promptly cause^{7}Li reaction and the decelerated neutron can produce another tritium atom by the ^{6}Li reaction. Therefore, two tritium atoms can be produced from single neutron.

The availability of Li is very important for generation of fusion energy at large scale. According to the US Geological Survey, the worldwide known reserves of Li (in

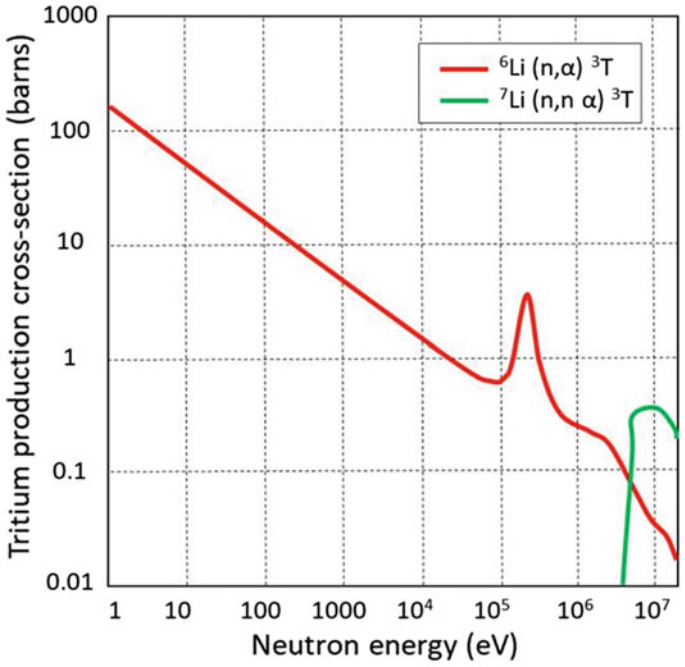

Fig. 18.6 Tritium production cross-section as function of neutron energy. Courtsy [24, 25]

year 2011) were estimated as 13 million tonnes [26, 27]. The Li extraction from ocean sea is the last important fuel source which is uniformly distributed worldwide [28].

18.4.1 Breeding Blankets

Tritium breeding blanket is a critical component of the magnetic confinement-based D–T fusion reactor. In addition to tritium breeding, it also functions as the heat exchanger and shields for the adjacent reactor components from the irradiation of neutrons and radiations [23, 29–31]. The tritium breeding blanket is schematically depicted in Fig. 18.7. The blanket should produce adequate tritium to achieve the condition of 'tritium self-sufficiency', i.e. the tritium production rate is at least equal to its consumption rate plus tritium decay and losses at scheduled or unscheduled plant outages. For effective tritium production, the Li compounds should be located in such a way that allows capture of maximum number of D–T neutrons in the tritium breeding blanket. However, some portion of the plasma facing area is utilized to incorporate necessary tools for plasma heating, plasma diagnostics, plasma control and fuel exhaust. Therefore, use of neutron multipliers is often required in the blanket for effective tritium breeding. The required tritium breeding ratios (TBRs) for tritium self-sufficiency is around 1.05–1.1.

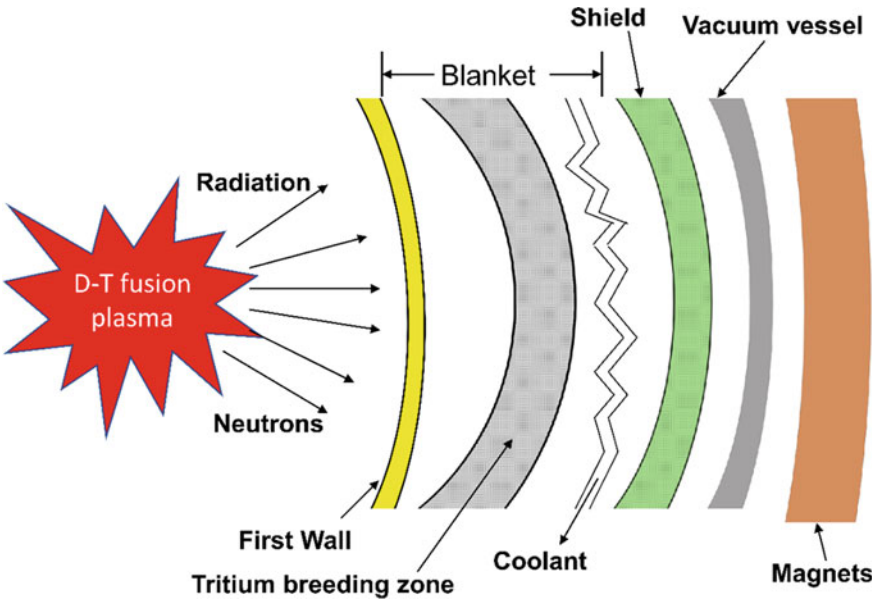

Fig. 18.7 Schematic configuration of tritium breeding blanket

18.4.2 Prospective Li-Based Ceramic Tritium Breeding Materials

The tritium breeding materials should meet certain prerequisites for use in blanket design of magnetic confinement-based fusion reactor. Tritium breeding materials should.

- Provide high tritium production rate in small volume.
- Release tritium in such a way that permits fast processing into the plasma fuelling system.
- Have required high temperature physical and chemical stability.
- Exhibit adequate irradiation behaviour.
- Be compatible with the adjacent structural materials and other components
- Have either no or nuclear activation characteristics that allow generation of only low-activity nuclear waste.
- Not lead to specific safety risks under off-normal and accidental scenarios.

Lithium-based ceramics, owing to their inherent thermal stability and chemical inertness are acknowledged as attractive tritium breeding materials.

The research activity initially focussed on γ-$LiAlO_2$, Li_2O, Li_2SiO_3, and Li_2ZrO_3. [32–37]. Later work involved Li_4SiO_4, Li_8ZrO_6, and Li_2TiO_3. Currently, most blanket concepts utilize Li_4SiO_4 or Li_2TiO_3 [38]. Recently, work on other systems

including Li_3TaO_4, Li_8PbO_6, and composites of Li_2TiO_3 with Li_2O or Li_4TiO_4 additives have been reported [32, 39]. The list of few lithium compounds considered as breeding material and some of their key basic properties are summarized in Table 18.2 [12].

From the sole consideration of tritium breeding, the best breeder material would be the one containing highest lithium atom density. Although Li and Li-Pb, offers the highest tritium breeding ratios (TBR), however, high chemical reactivity of metallic Li (particularly in the molten state) and associated fire hazard if Li comes in contact with air or water during the off-normal or accidental scenarios are serious disadvantages. Moreover, since the molten liquid metals are electrically conducting, it often poses difficulties in pumping the liquid metals at high rates across the existing strong magnetic [29–31, 40]. In order to circumvent these problems, alternative blanket concepts utilizing Li-based ceramics solid tritium breeders has been developed.

Table 18.2 Properties of candidate Li-based ceramic tritium breeders. Adopted from [12]

Properties	Preferable	Li_2O	Li_2TiO_3	Li_2ZrO_3	Li_4SiO_4	γ-$LiAlO_2$
Melting point [K]	Higher	1692	1808	1888	1523	1883
Density [g/cm^3]	Lower	2.02	3.43	4.15	2.21	2.55
Li density [g/cm^3]	Higher	0.94	0.43	0.38	0.51	0.27
Thermal conductivity at 500 °C [W/m/°C]	Higher	4.7	1.8	0.75	2.4	2.4
Thermal expansion at 500 °C, [dL/L_0%]	Smaller	1.25	0.8	0.50	1.15	0.54
Reactivity with water	Lower	High	Stable	Stable	Low	Low
Tritium retention time at 400 °C [h]	Shorter	8.0	2.0	1.1	7.0	50
Swelling [dV/V_0%]	Lower	7.0	–	<0.7	1.7	<0.5
Activated products by neutron absorption	Less	^{16}O(n, p): 7 s	^{46}Ti(n, p): 84 d ^{47}Ti(n, p): 3.4 d ^{48}Ti(n, p): 1.8 d	^{90}Zr(n, p): 64 h ^{91}Zr(n, p): 57 d ^{94}Zr(n, 2n): 106 y ^{96}Zr(n, 2n): 64 d	^{28}Si(n, 2n): 4 s ^{29}Si(n, p): 6 m ^{30}Si(n, α): 9 m	^{27}Al(n, 2n): 6 s ^{27}Al(n, p): 9.5 m ^{27}Al(n, α): 15 h

Lithium oxide, due to very high lithium atom density and good thermal conductivity was given preference in the initial blanket concepts. However, strong moisture sensitivity and the evidence of irradiation induced swelling are its biggest disadvantages [34, 36, 41].

The most widely studied silicates include Li_2SiO_3 andLi_4SiO_4 in which often the traces of Li_2SiO_5 or $Li_6Si_2O_7$ can be found as well. A variety of lithium zirconates such as metazirconate Li_2ZrO_3 and Li_8ZrO_6 octazirconate have also been studied by Roux and co-workers [31, 35, 41]. However, because of activation issues of Zr, these compounds became less attractive.

Lithium titanate (Li_2TiO_3), have shown promising results in early tritium release experiments. Hoshino et al. found that lithium titanate forms oxygen-deficient defects in reducing atmosphere (hydrogen). Moreover, it also forms lithium-deficient defects when atmosphere is changed from reducing to oxidizing and as result the formation of doubly nonstoichiometric composition, $Li_{2-x}TiO_{3-y}$, has been confirmed [31, 35, 41, 42].

Most of the studies on lithium aluminates focussed on γ-$LiAlO_2$ [43–46]. However, this material has started receiving less consideration due to its low lithium atom density, modest tritium release performance and activation characteristic of Al.

18.5 Phase Diagrams of Li-Based Ceramic Tritium Breeders

18.5.1 Lithium Titanate (Li_2TiO_3)

The phase diagram reveals four ternary oxides (Li_4TiO_4, Li_2TiO_3, $Li_4Ti_5O_{12}$), and the high temperature phase $Li_2Ti_3O_7$ in the binary Li_2O–TiO_2 system. The phase diagram is depicted in Fig. 18.8 [47, 48].

There are three allotropic modifications of phase Li_2TiO_3: α, β and γ. The α-modification is a metastable phase. Upon heating at temperature of more than 300 °C, the α-phase monotropically transforms to β-phase. The low-temperature β-phase has narrow homogeneity range and a monoclinic crystal structure. It crystallizes in the Li_2SnO_3-type structure with the space group C2/c (No. 15), Z = 8. The lattice parameters are: a = 504.1 pm, b = 880.6 pm, c = 972.7 pm and β = 100.08°. The high temperature γ-phase crystallizes in the NaCl-type structure (Z = 4/3). The γ-phase has cubic crystal structure with the room temperature lattice parameter a = 415.05 pm.

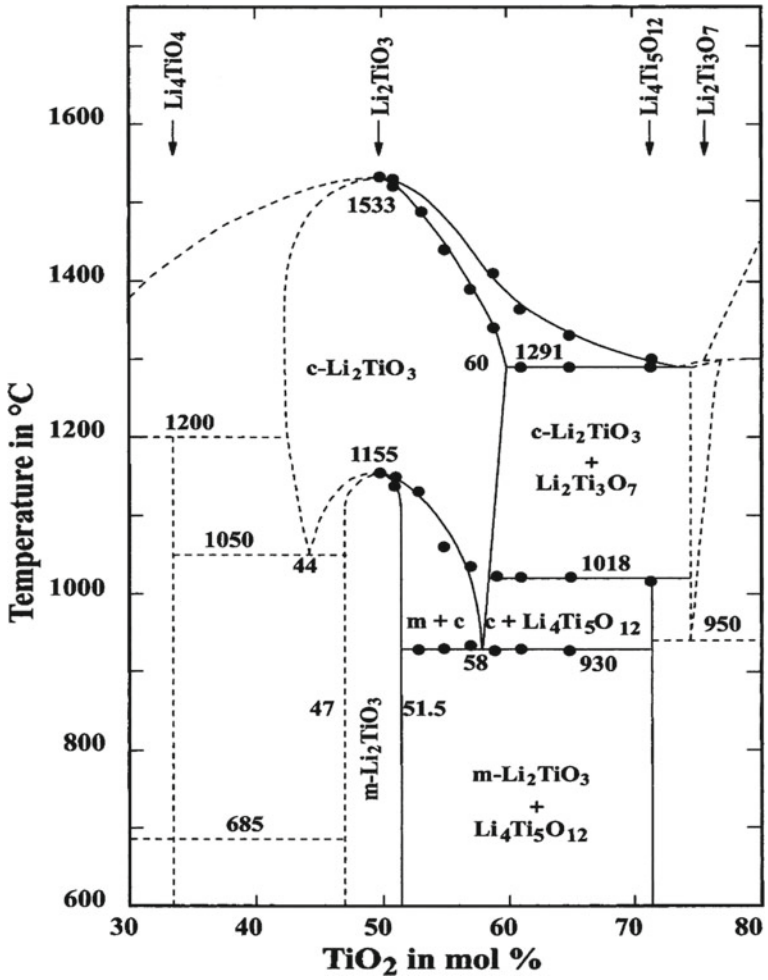

Fig. 18.8 Phase diagram of Li_2O–TiO_2 system (Reproduced from [47] with permission of Elsevier)

18.5.2 Lithium Zirconate (Li_2ZrO_3)

Several compounds in Li_2O–ZrO_2 system (e.g. Li_8ZrO_6, $Li_6Zr_2O_7$ and Li_2ZrO_3) has been considered for tritium breeding. The phase diagram of Li_2O-ZrO_2 system is presented in Fig. 18.9 [49]. The Li_2ZrO_3 has monoclinic crystal structure with space group C2/c (No. 15), Z = 4. The lattice parameters are: a = 542.2 pm, b = 902.2 pm and c = 541.9 pm and β = 112.709°. It crystallizes in NaCl-type structure.

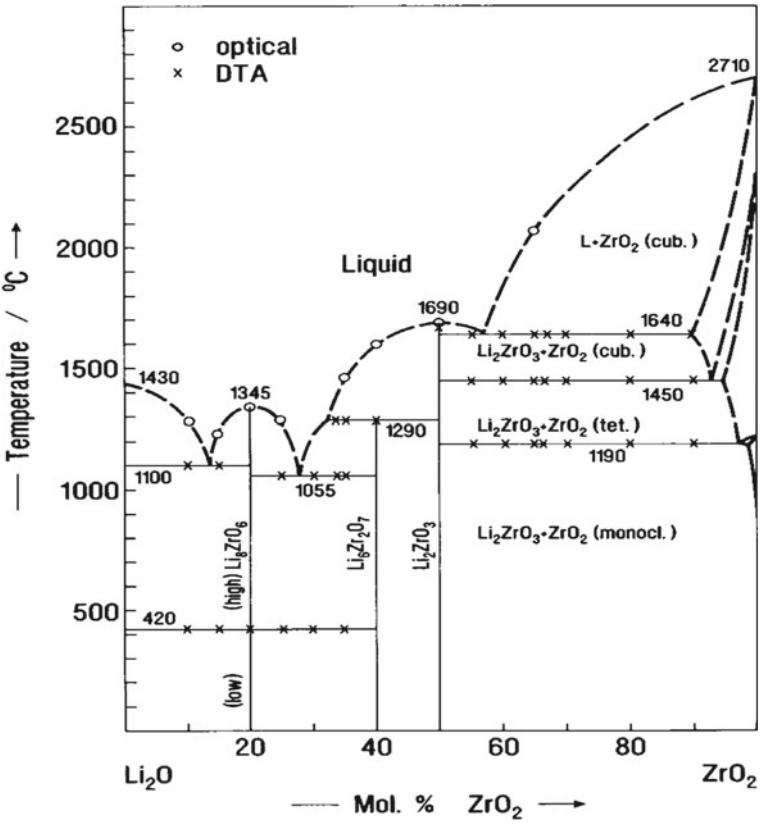

Fig. 18.9 Phase diagram of Li_2O–ZrO_2 system (Reproduced from [49] with permission of Elsevier)

18.5.3 Lithium Aluminate ($LiAlO_2$)

Although six polymorphs of $LiAlO_2$ have been announced so far, however, only three modifications which are referred to in the literature as α-phase, β-phase and γ-phase have been synthesized and their structures have been thoroughly established using diffraction technique [50–52]. The α-$LiAlO_2$ has a hexagonal crystal structure. The density of α-phase (3.401 g cm^{-3}) is the highest among the three phases. Therefore, this phase is the most stable at high pressure [53, 54]. The β-$LiAlO_2$has an orthorhombic crystal structure with density of 2.61 g cm^{-3} [53]. The γ-$LiAlO_2$ is preferred in various applications because it is the most stable phase among all the polymorphs under ambient conditions. Therefore, α-$LiAlO_2$ and β-$LiAlO_2$phases transform into γ-$LiAlO_2$phase at temperature above 750 °C. The γ-$LiAlO_2$ has a tetragonal crystal structure with the space group $P4_12_12$ (No. 92), Z = 4 and the lattice parameters: a = 522.4 pm and c = 629.7 pm [53]. The phase diagram of Li_2O-Al_2O_3 system is shown in Fig. 18.10 [49].

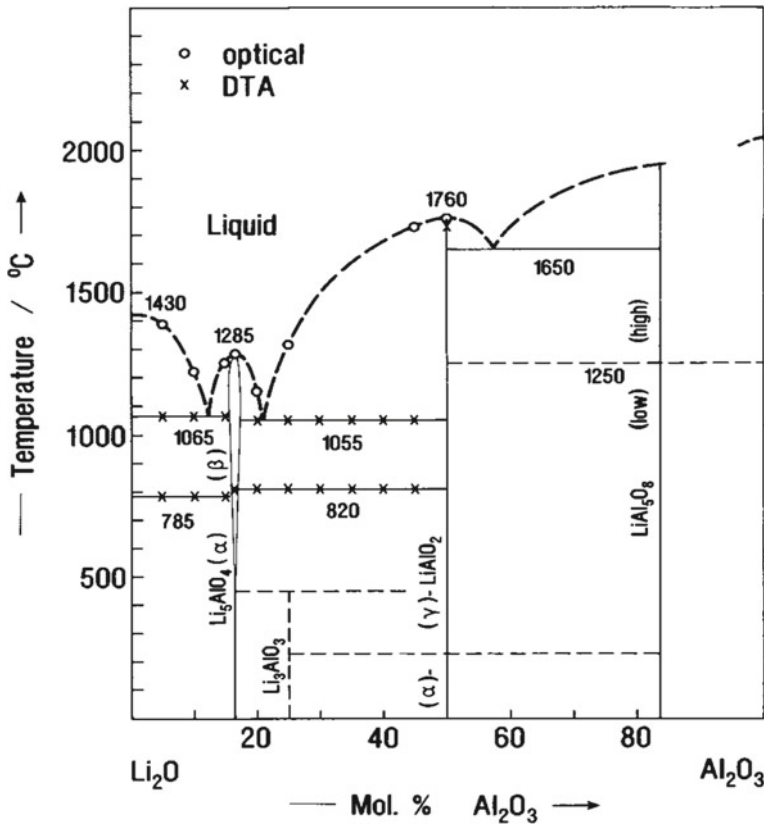

Fig. 18.10 Phase diagram of Li_2O–Al_2O_3 system (Reproduced from [49] with permission of Elsevier)

18.5.4 Lithium Orthosilicate (Li_4SiO_4)

Several compounds in Li_2O–SiO_2 system including Li_4SiO_4, Li_6SiO_5, Li_8SiO_6, Li_2SiO_3 and $Li_2Si_2O_5$with different Li_2O content is considered as tritium breeding material. The phase diagram (Fig. 18.11) shows different phases of lithium silicates [55–57].

18.5.5 Processing of Tritium Breeding Materials

Processing has a critical role in determining performance of Li-based ceramics as tritium breeding materials. The processing of tritium breeding materials broadly

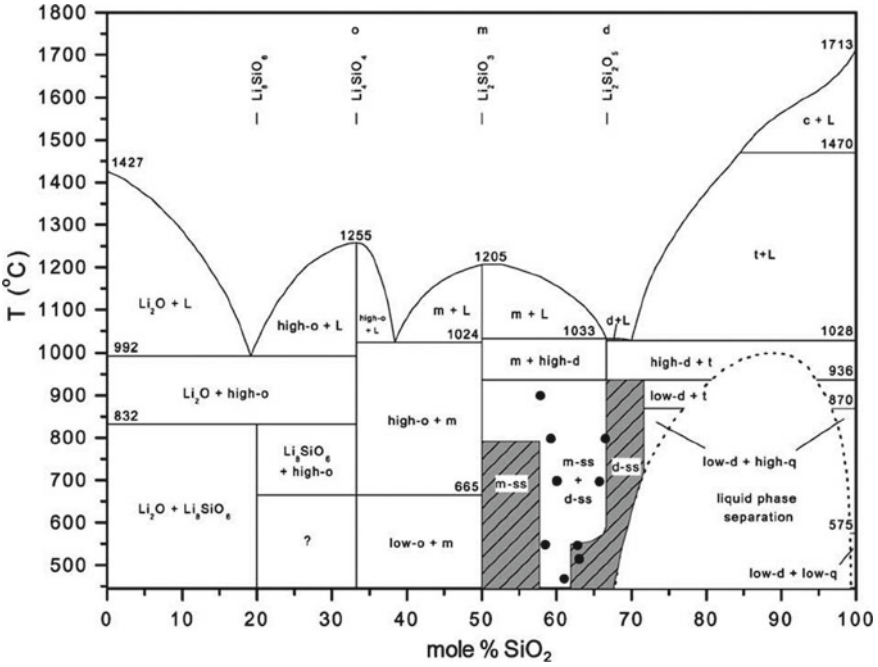

Fig. 18.11 Phase diagram of Li_2O–SiO_2 system (Reproduced from [57] with permission of Elsevier)

involves three steps (i) powder synthesis, (ii) powder consolidation/shaping and (iii) sintering. The general preparation scheme is outlined in Fig. 18.12.

18.6 Powder Synthesis

18.6.1 Solid-State Synthesis Method

Earlier, the solid-state reaction method was widely reported for the synthesis of Li-based ceramic powders. The simplicity is the main attractive feature and reason behind the extensive use of solid-state method for synthesis of ceramic powders. Solid-state synthesis of Li_2TiO_3 commonly utilizes lithium carbonate (Li_2CO_3) and titanium oxide (TiO_2) as precursors. The synthesis temperature and time were reported as 750–800 °C and 5–10 h respectively [58–63]. Sometimes even higher temperature of 900–1100 °C and time of several days were reported [64, 65]. However, TGA/DTA curve (Fig. 18.13) of precursor mixture (Li_2CO_3 + TiO_2) revealed synthesis temperature of about 650–800 °C [60]. The XRD pattern confirmed formation of $Li_2TiO_3$by solid-state method at 700 °C (Fig. 18.14) [60].

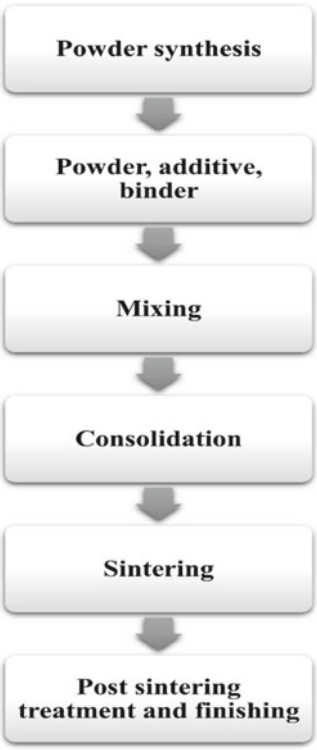

Fig. 18.12 General processing scheme for preparation of ceramic breeder

S. Sonak et al. investigated kinetics of lithium titanate formation via solid-state reaction of Li_2CO_3 and TiO_2using non-isothermal thermogravimetric technique. The average activation energy for Li_2TiO_3 formation was determined to be 243 kJ/mol K [62, 66].

Recently our group developed a novel urea-assisted solid-state synthesis method to synthesize pure phase monoclinic Li_2TiO_3 nano-crystalline powder. A single phase and well crystalline powder were synthesized at 700 °C and shorter duration (2 h) as compared to the conventional solid-state method (Fig. 18.15). The crystallite size of Li_2TiO_3 powder was observed to be 15–80 nm [67].

Solid-state synthesis of Li_2ZrO_3 was often reported using Li_2CO_3 and ZrO_2 as precursor at temperature of about 800–1000 °C and time duration of 2-6 h [68–74]. The metastable tetragonal phase of Li_2ZrO_3 is first formed at temperature of about 800-850 °C which transformed into stable monoclinic phase at temperature close to 1000 °C (Fig. 18.16) [75].

Solid-state synthesis of $LiAlO_2$ using mixture of Li_2CO_3 and Al_2O_3/or $Al(OH)_3$ was reported at temperature of about 700–1000 °C and time duration about 2-4 h [43, 44, 76–80]. During the synthesis of $LiAlO_2$, often α-phase (hexagonal) is first

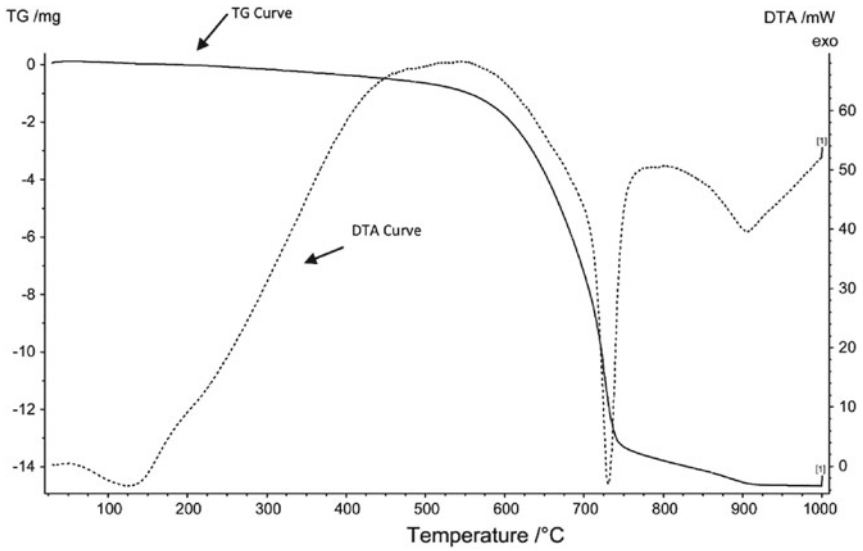

Fig. 18.13 TG–DTA of mixture ($Li_2CO_3 + TiO_2$) for solid-state synthesis of Li_2TiO_3 (Reproduced from [60] with permission of Elsevier)

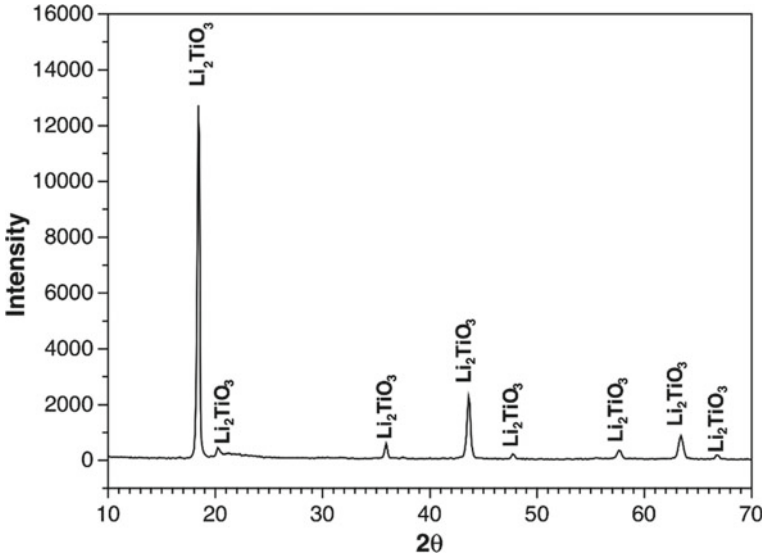

Fig. 18.14 XRD pattern of Li_2TiO_3 synthesized by solid-state method (Reproduced from [60] with permission of Elsevier)

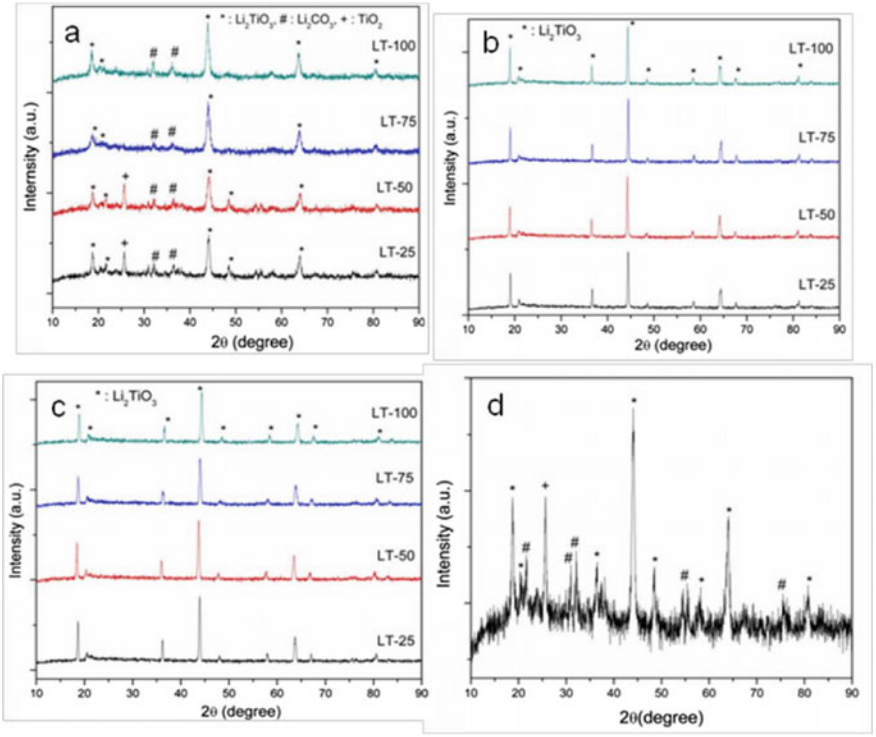

Fig. 18.15 XRD patterns of Li_2TiO_3 **a** 600 °C **b** 700 °C **c** 800 °C **d** solid-state route without urea at 1000 °C (Reproduced from [67] with permission of Elsevier)

formed at lower temperature (500–550 °C) which is transformed into stable γ-phase (tetragonal) after annealing at 700–800 °C [80–88].

Solid-state synthesis of Li_4SiO_4 often utilizes Li_2CO_3 and SiO_2 as precursors. In some reports, lithium nitrate and lithium hydroxide were also used as precursors. The synthesis temperature was reported about 700–900 °C and time duration 4–6 h (Fig. 18.17) [89–94]. The synthesis of often reported to proceed via intermediate formation of lithium metasilicate (Li_2SiO_3), due to which often mixture of meta- and orthosilicates is formed. In order to synthesize pure phase lithium orthosilicate (Li_4SiO_4), it is required to carefully optimize the reaction temperature and time.

The inconsistency in reported synthesis temperature and time duration of Li-based ceramics could be due to inhomogeneity in precursor mixture and lack of process optimization. Due to high synthesis temperature and prolonged reaction, the solid-state synthesis method most often produces ceramic powders with large particle sizes and hard particle aggregates. Therefore, extensive mechanical milling is required to make fine powders.

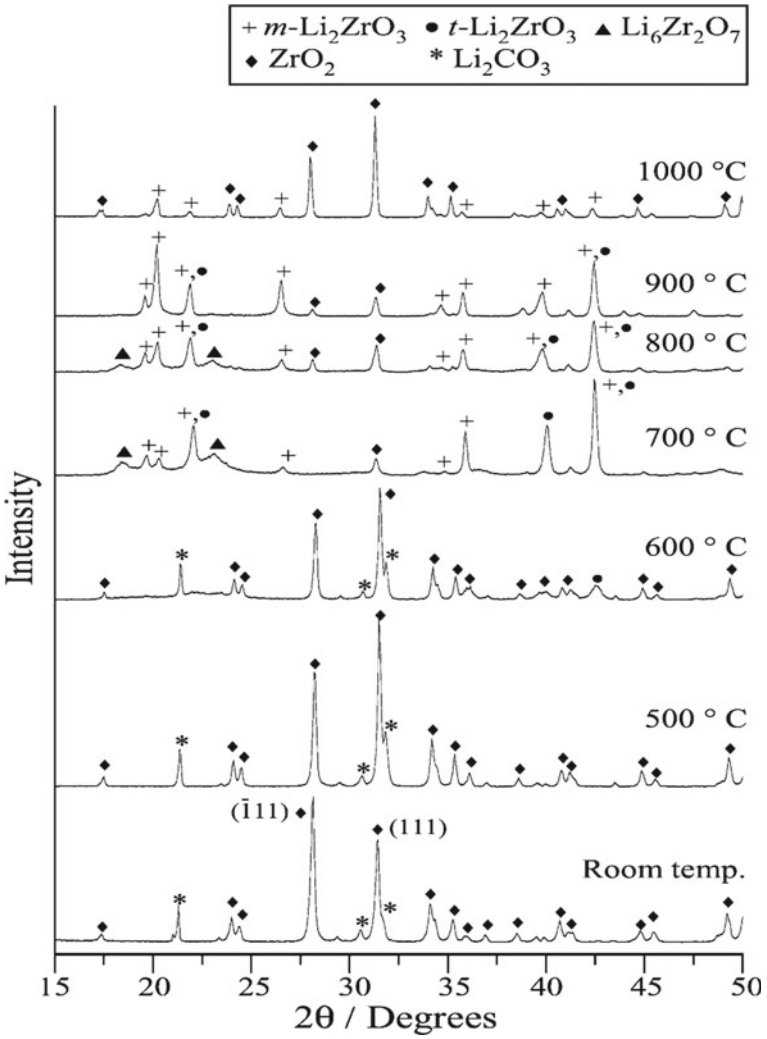

Fig. 18.16 XRD patterns of pellet ($Li_2CO_3 + ZrO_2$) heat treated for 4 h at different temperatures (Reproduced from [75] with permission of Elsevier)

18.6.2 Wet Chemical Methods

The wet chemical methods refer to a group of chemical syntheses in which precursors for synthesis of Li-based ceramics are mixed in solutions. Therefore, unlike in the solid-state synthesis where inhomogeneity in solid-state mixing of precursors is a cause of serious concern, in wet chemical methods, the precursors are mixed at the molecular level that results in the formation of homogeneous products. Moreover, wet chemical methods often result in soft-agglomerated ceramic powders

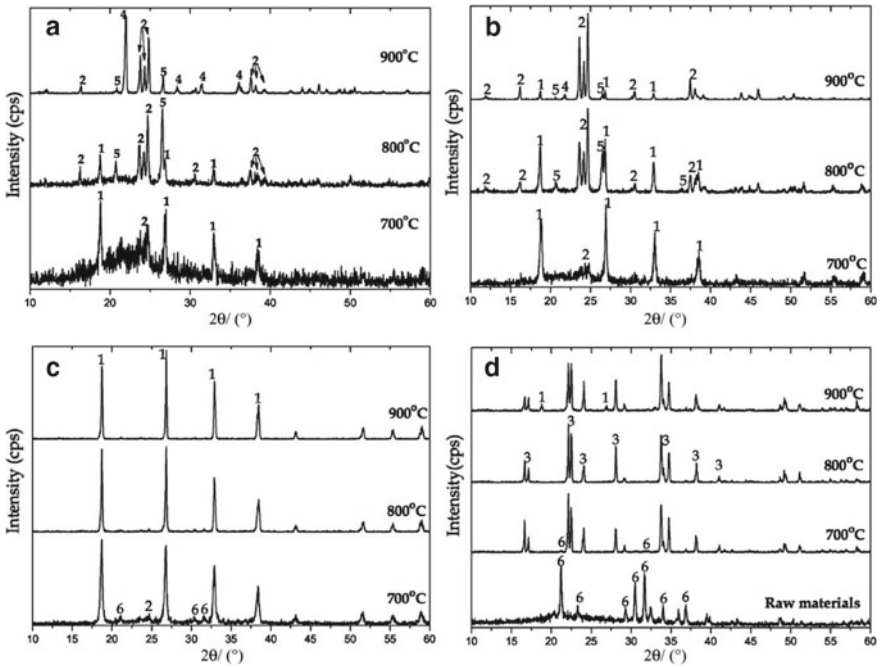

Fig. 18.17 XRD patterns of powders for different Li/Si molar ratios and reaction temperatures. (**a**, **b**, **c** and **d** represents Li/Si molar ratio of 0.5, 1, 2 and 4, respectively; 1-Li_2SiO_3, 2-$Li_2Si_2O_5$, 3-Li_4SiO_4, 4-cristobalite, 5-quartz and 6-Li_2CO_3) (Reproduced from [89] with permission of Elsevier)

with relatively small particle sizes. In view of these advantages, many wet chemical methods including sol-gel, hydrothermal and solution combustion were developed for synthesis of Li-based ceramic powders [95–106].

18.6.3 Solution Combustion Synthesis (SCS)

C.-H. Jung et al. reported solution combustion synthesis of nanoscale powders of Li_2TiO_3 with high surface area (14–30 m^2/g) utilizing aqueous solutions of lithium nitrate ($LiNO_3$) and titanium oxynitrate $TiO(NO_3)_2$ as precursors and different organic fuels (citric acid, urea and glycine) (Fig. 18.18) [104, 107, 108].

The SEM micrograph (Fig. 18.18) showed porous microstructure of powder which may be formed by the evolved gases during combustion. The SAED ring patterns of the TEM micrograph confirmed formation of very fine nano-size crystals.

Q. Zhou et al. synthesized Li_2TiO_3 by SCS under different fuel-to-oxidizer ratios to synthesize powders with different morphologies [109]. A flash microwave-induced solution combustion synthesis of nano-crystalline Li_2TiO_3 powder was performed by Zhou et al. using titanyl nitrate ($TiO(NO_3)_2$) and lithium nitrate ($LiNO_3$) as oxidizer

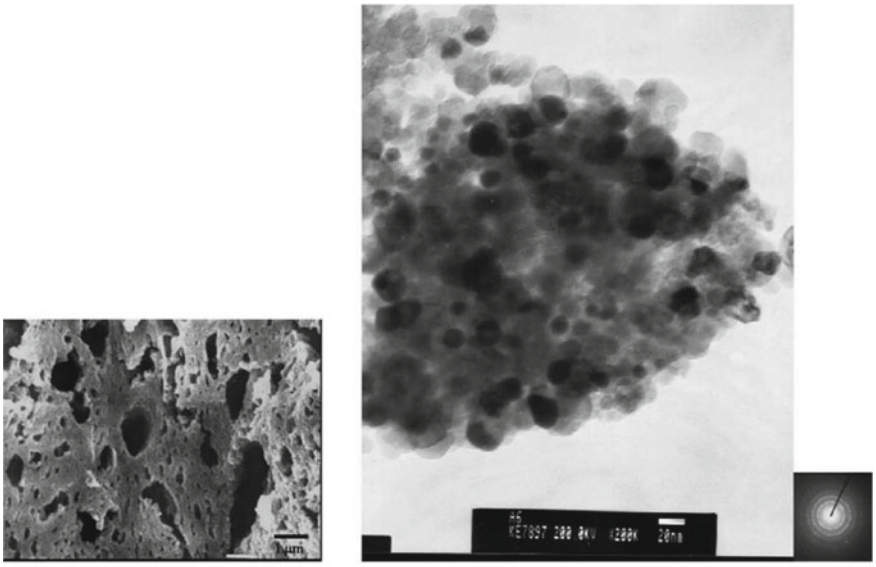

(a) SEM micrograph (b) TEM micrograph

Fig. 18.18 SEM micrograph **a** and Bright-field TEM image and SAD pattern **b** of as-synthesized Li_2TiO_3 powders (Reproduced from [107] with permission of Elsevier)

and urea ($CO(NH_2)_2$) as fuel. Urea also functions as a complexing agent [110]. Sinha et al. synthesized high purity monoclinic $Li_2TiO_3$by solid–liquid combustion synthesis directly from the combustion without any further heat treatment for phase formation [111].

Xiao et al. synthesized nanoscale powder of Li_2ZrO_3 by solution combustion using zirconium oxynitrate [$ZrO(NO_3)_2.2H_2O$] and lithium nitrate ($LiNO_3$) as precursors/oxidizers and citric acid ($C_6H_8O_7$) and urea [$CO(NH_2)_2$] as fuels [112–115].

Recently, our group reported synthesis of pure monoclinic Li_2ZrO_3 nanocrystalline powder by SCS route followed by calcination. The mixture of zirconium oxynitrate and lithium nitrate was used as oxidants and glycine as fuel [116]. Annealing of as-synthesized powders (under fuel-rich as well as fuel-lean conditions) at temperature of 700 and 750 °C produced mixture of monoclinic and tetragonal phases as revealed by XRD pattern (Fig. 18.19) [116]. Pure monoclinic phase was obtained after annealing the powder at 800 °C with crystallite size in the range of 18-40 nm. The synthesized powder comprised of agglomerated, highly porous and voluminous particles. The shape of agglomerated powder was irregular flake type and the particle size was in the broad range of 5–30 μm (Fig. 18.20) [116].

F. Li et al. [117] attempted to synthesize γ-lithium aluminate by SCS method using lithium nitrate and aluminium nitrate as oxidants and different reductants (urea, glycine carbohydrazide, alanine and citric acid) (Fig. 18.21). Although all the

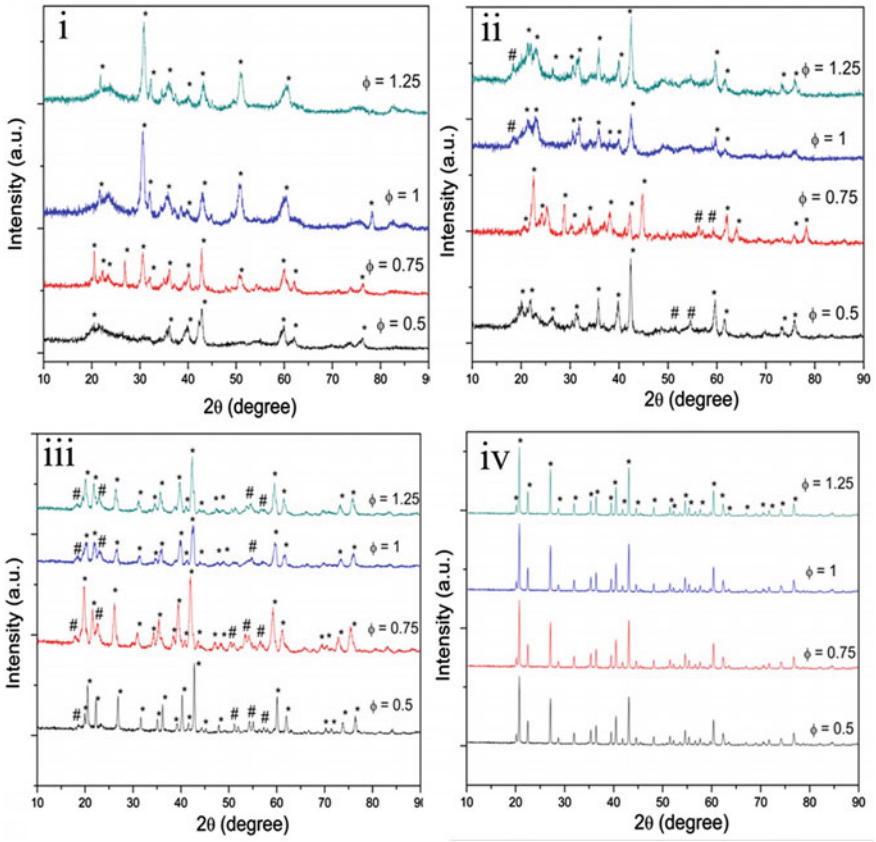

Fig. 18.19 XRD pattern of Li_2ZrO_3 powder synthesized at varying fuel-to-oxidizer ratios and temperatures (* = Monoclinic phase, # = Tetragonal phase) **i** 600 °C **ii** 700 °C **iii** 750 °C **iv** 800 °C (Reproduced from [116] with permission of Elsevier)

mixtures of nitrate and fuel could be ignited at 450 °C, only the mixture containing urea and carbohydrazide resulted in pure γ-$LiAlO_2$.

Choudhary et al. synthesized $Li_4SiO_4$by SCS using $LiNO_3$ and Rice husk (source of SiO_2) as precursors and citric acid as fuel. The citrate-to-metal (C/M) ratio of the solution was varied (Fig. 18.22) [118, 119]. The powder synthesized at C/M of 1.4 after calcination at 700–750 °C produced pure Li_4SiO_4 phase (Fig. 18.23) [118].

18.6.4 Sol-gel Synthesis

X. Wu et al. synthesized pure monoclinic Li_2TiO_3phase nanoscale powder by aqueous sol-gel method at considerably low temperature (500 °C). $LiNO_3$ and

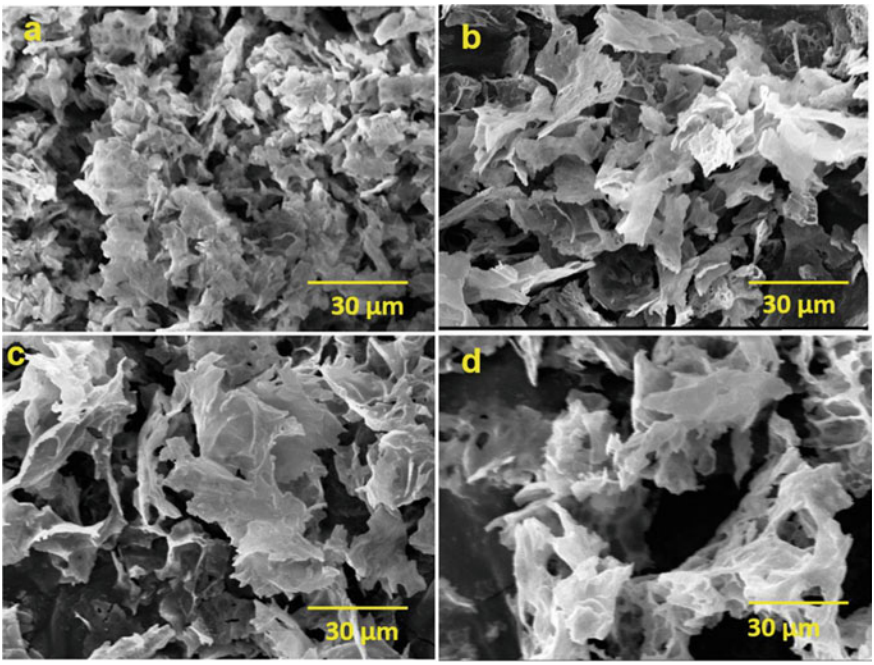

Fig. 18.20 SEM images of Li_2ZrO_3 powder after calcination at 800 °C and fuel-to-oxidizer ratio **a** = 0.5, **b** 0.75, **c** = 1, **d** = 1.25 (Reproduced from [116] with permission of Elsevier)

$Ti(C_6H_6O_7)_2$were used as starting materials (Fig. 18.24). Due to high surface area of nanoparticles, the agglomerated powder was obtained (Fig. 18.25a). The size of primary particles in the agglomerated powder was smaller than 50 nm (Fig. 18.25b) [95]

18.6.5 Hydrothermal Method

A. Laumann et al. developed hydrothermal method to synthesize cubic Li_2TiO_3.Lithium hydroxide and TiO_2 (rutile + anatase) were used as starting materials and the hydrothermal reaction was conducted at 180 °C for 18 h. Further annealing at 800 °C resulted in monoclinic Li_2TiO_3[102].

C.-L. Yu et al. exploited $LiOH.H_2O$ and anatase TiO_2 as precursors and synthesized pure phase Li_2TiO_3 nanoparticles via hydrothermal reaction at 200 °C for 2–10 h. TEM micrograph and particle size analysis indicated general particle size around 114 nm. The hydrothermal reaction resulted in a metastable cubic phase which transformed into stable monoclinic phase after calcinations above 500 °C for 6 h in air [120].

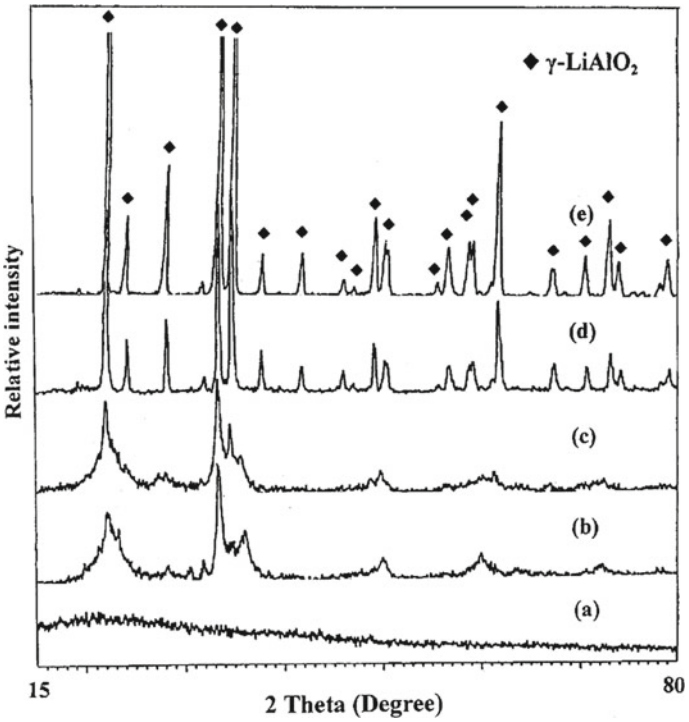

Fig. 18.21 XRD patterns of the as-synthesized powders using various fuels: **a** citric acid, **b** alanine, **c** glycine, **d** carbohydrazide and **e** urea (Reproduced from [117] with permission of Elsevier)

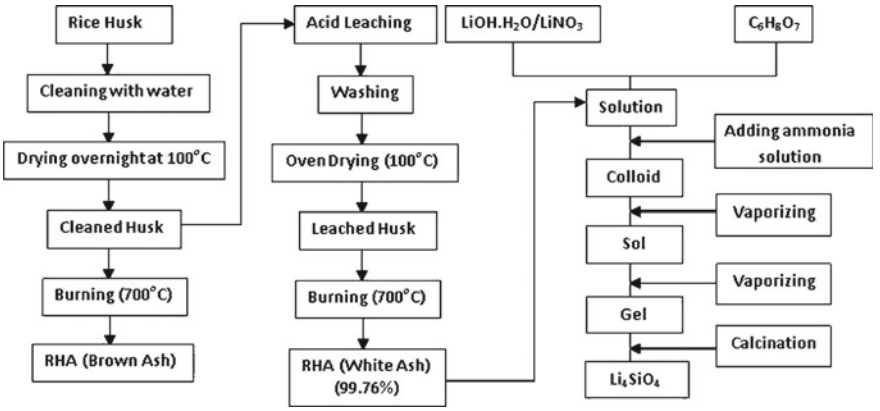

Fig. 18.22 Preparation of white RHA and Li_4SiO_4 powders using SCS (Reproduced from [119] with permission of Elsevier)

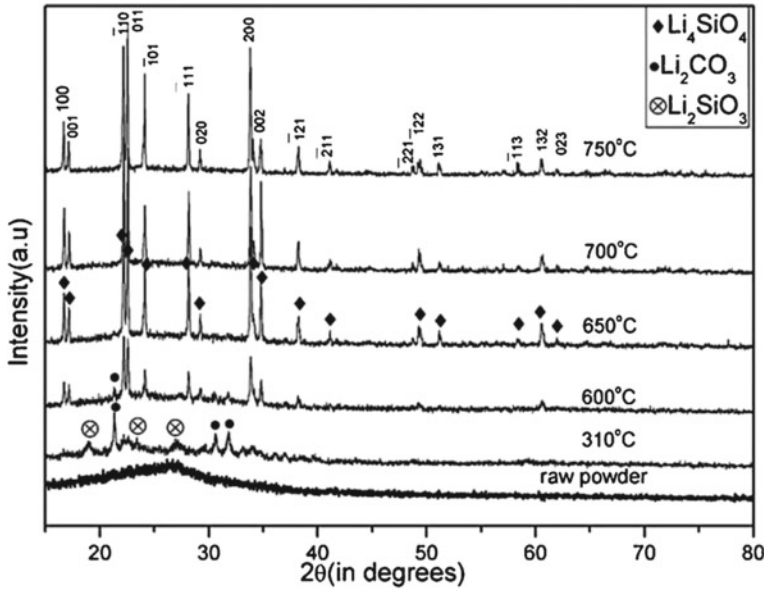

Fig. 18.23 XRD pattern of Li_4SiO_4 powder with C/M = 1.4 (Reproduced from [119] with permission of Elsevier)

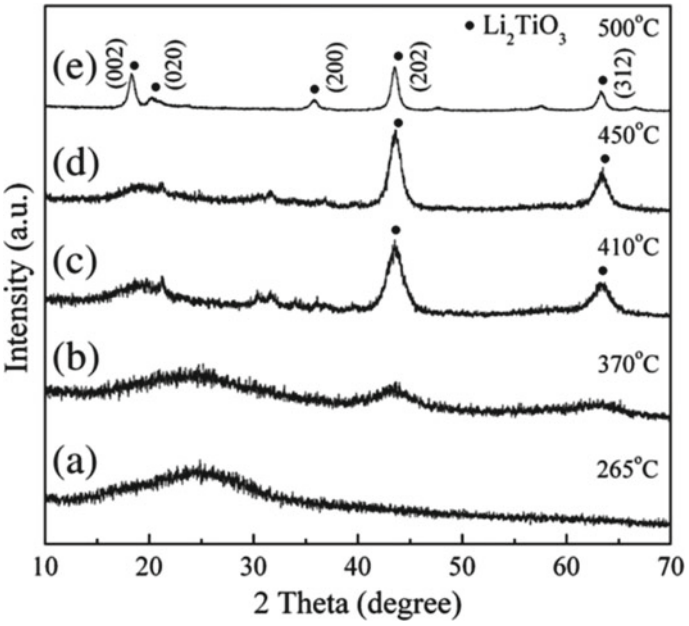

Fig. 18.24 XRD patterns of the gel treated at different temperatures (Reproduced from [95] with permission of Elsevier)

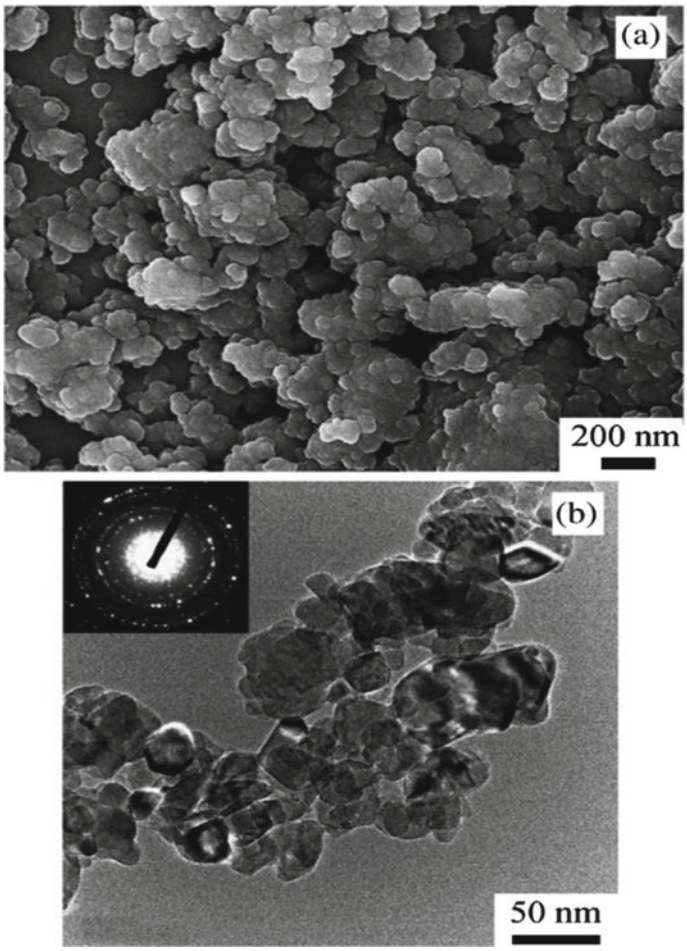

Fig. 18.25 SEM **a** and TEM **b** micrographs of the Li_2TiO_3 powder synthesized by sol-gel method (Reproduced from [95] with permission of Elsevier)

18.6.6 Consolidation and Fabrication of Shapes

In the initial concepts of ceramic breeding blankets, block or plate shape Li-based ceramics were used as tritium breeding materials and afterwards designs based on pellet shape ceramics emerged [35, 70, 77, 90, 121, 122]. Recent breeding blanket concepts often utilize pebble shape ceramics. It is mainly because the pebble-bed concepts minimize thermal stresses, swelling and embrittlement and thereby protect the structural integrity of the larger breeder component [123–125].

Pellets or blocks of Li-based ceramic tritium breeders are fabricated by a well-established, widely used and cost-effective pressing and sintering process of ceramic powders. Many research groups have reported the fabrication of pellets of $LiAlO_2$,

Li_2ZrO_3 and Li_2TiO_3 with desired dimension, microstructure and purity [46, 71]. Pellets of Li_4SiO_4, Li_2SiO_3 and $LiAlO_2$, with around 10 mm diameter and different heights (5, 10 and 14 mm) were fabricated by Kapychev et al. [126].

For the fabrication of pebbles of Li-based ceramic tritium breeders, the currently used processes are as follows:

- **Melting–spraying process**: This process was used for fabrication of Li_4SiO_4 and Li_4SiO_4–SiO_2 pebbles. This process is schematically depicted in Fig. 18.26 [127]. In this process, molten silicates are sprayed through a nozzle and the droplets are allowed to cool to form pebbles. After annealing, spherical pebbles of relative density 95–96% with satisfactory mechanical strength was obtained. Knitter et al. developed a modified process utilizing lithium hydroxide in place of carbonate and produced pebbles with somewhat lower density. The mixture of Li_4SiO_4 + 2.5 wt% SiO_2resulted in biphasic mixture (Li_4SiO_4 + $Li_6Si_2O_7$) in as-melted condition and $Li_4SiO_4 + Li_2SiO_3$ after annealing. This process is often not suitable for pebble fabrication of Li-based ceramics with high melting points (Li_2TiO_3, Li_2ZrO_3 and $LiAlO_2$).
- **Sol-gel type processes**: Many variants of sol-gel type processes have been developed for fabrication of Li-based ceramic pebbles [96, 97, 128–133]. A typical sol-gel process for the fabrication of spherical pebbles of Li_2TiO_3 is depicted in Fig. 18.27 [134]. The variants of this process mainly utilize different solvents and binders to tailor pebble morphology and sintered microstructure. The sol-gel processes have been developed for pebble fabrication of various Li-based ceramics and compositions.

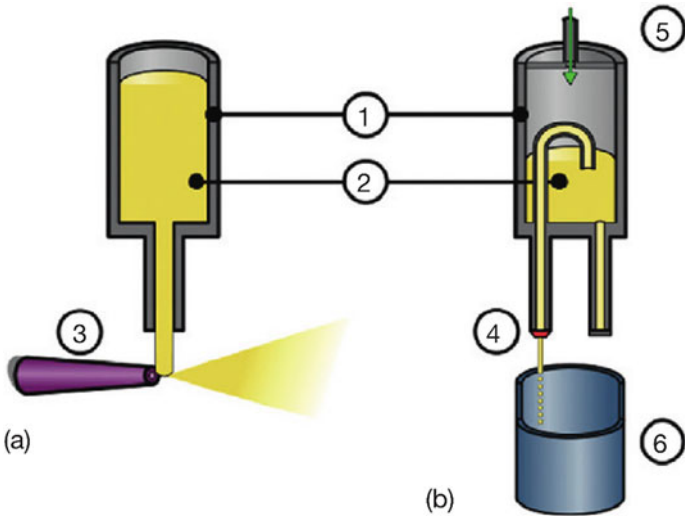

Fig. 18.26 Illustration of the melt spraying processes (Reproduced from [127] with permission of Elsevier). (**1**) Platinum alloy crucible; (**2**) Molten silicate; (**3**) Air spray gun; (**4**) Nozzle; (**5**) Piston; (**6**) Droplet solidification

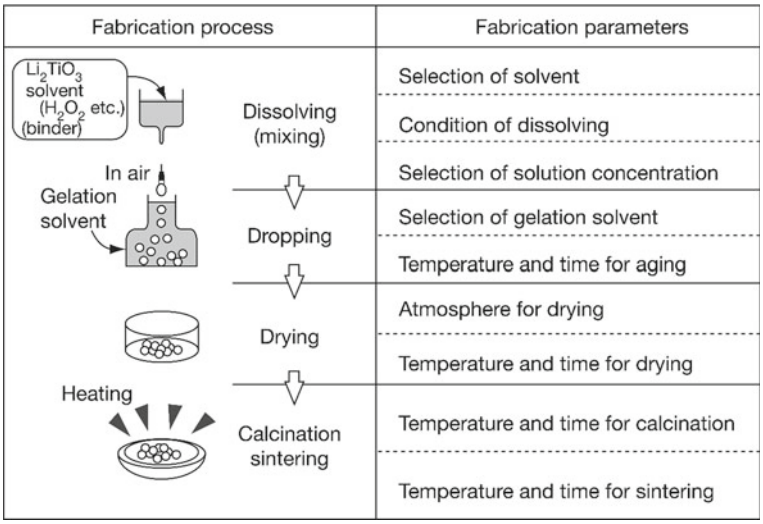

Fig. 18.27 Fabrication process and parameters of Li_2TiO_3 pebbles in the direct wet-process (Reproduced from [134] with permission of Elsevier)

- **Extrusion-spheronization process**: This technique has, for many years, been used to produce pebbles of $LiAlO_2$, Li_2ZrO_3 and $Li_2TiO_3$with different sizes and relative densities of around 80–90% range [60, 123, 124, 135].
- **Agglomeration-sintering process**: This process has been used for producing Li_2O, Li_4SiO_4 and Li_2ZrO_3 pebbles of size about 1 mm. Pebbles with relative densities of around 90% were obtained with good mechanical strength [123].
- **Graphite-bed process**: M. Hong et al. recently developed a graphite bed method as a new technique to fabricate Li_2TiO_3(size 1–1.2 mm) with relative density of around 85–90% and grain size of 4–14 μm. M. Hong et al. also fabricated Li_4SiO_4 pebbles (average diameter 1.5 mm) with relative density of around 85–90%, grain size of 3–6 μm and good mechanical strength [136, 137].
- Several other wet chemical methods including gel-casting, agar method, dry-granulation, etc. have been reported for fabrication of Li-based ceramic pebbles [96, 107, 138–141].

18.6.7 Sintering

Sintering is the final and important processing step of Li-based ceramic tritium breeding materials irrespective of powder synthesis method and shape of the consolidated powder (pellet, block, pebble or foam).

Sintering is a process of bonding individual powder particles into a coherent, predominantly solid structure by the application of heat. Heat enables the mass transport phenomena that often occur on the atomic scale leading to inter-particle

bonding that results in improved strength and lower system energy [142]. The driving force for sintering is reduction of the total interfacial energy by the reduction of surface area of the powder. Reduction of total interfacial energy of a powder compact can be expressed as follows: [143, 144]

$$\Delta(\gamma A) = \Delta\gamma A + \gamma \Delta A$$

where γ is the specific surface energy and A, the total surface area of the compact. The reduction of total interfacial energy of the powder compact can occur by two often competing processes, densification ($\Delta\gamma$) and grain growth/coarsening (ΔA) as schematically shown in Fig. 18.28 [143, 144].

The resulting microstructure comprised of relative density, grain size, porosity and distribution of other phases plays significant role in controlling tritium retention and release characteristics of ceramic breeder. Therefore, for optimum tritium release and retention characteristics as well as mechanical properties of sintered tritium breeders, the microstructure needs to be carefully controlled by controlling the sintering variables (Fig. 18.29).

The mechanisms involved in transport of tritium through the microstructure of the single sintered ceramic breeder pebble is schematically depicted in Fig. 18.30 [29, 145–148].

Firstly, tritium generated from nuclear transmutation of Li by neutron capture is transported to the grain boundary by intragranular (lattice) diffusion. The bulk diffusion and trapping of tritium within the grains are affected by the neutron and

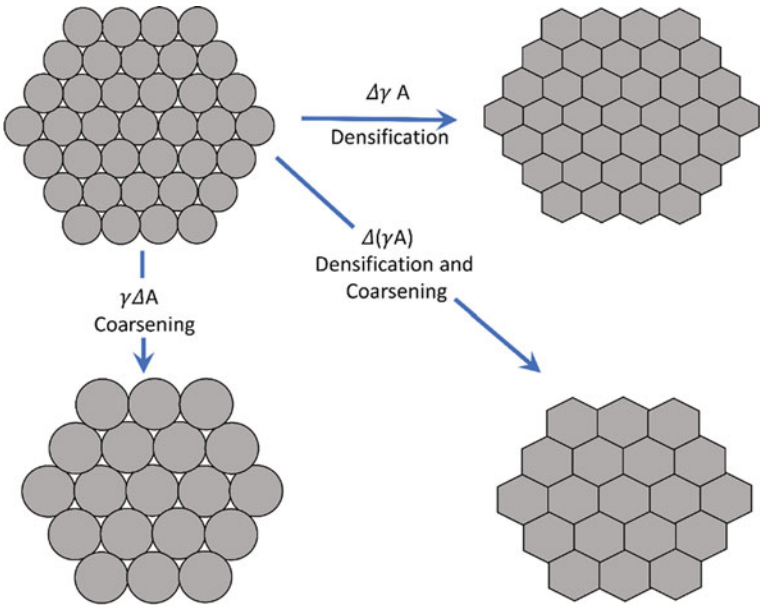

Fig. 18.28 Schematic demonstration of phenomena occurring during sintering

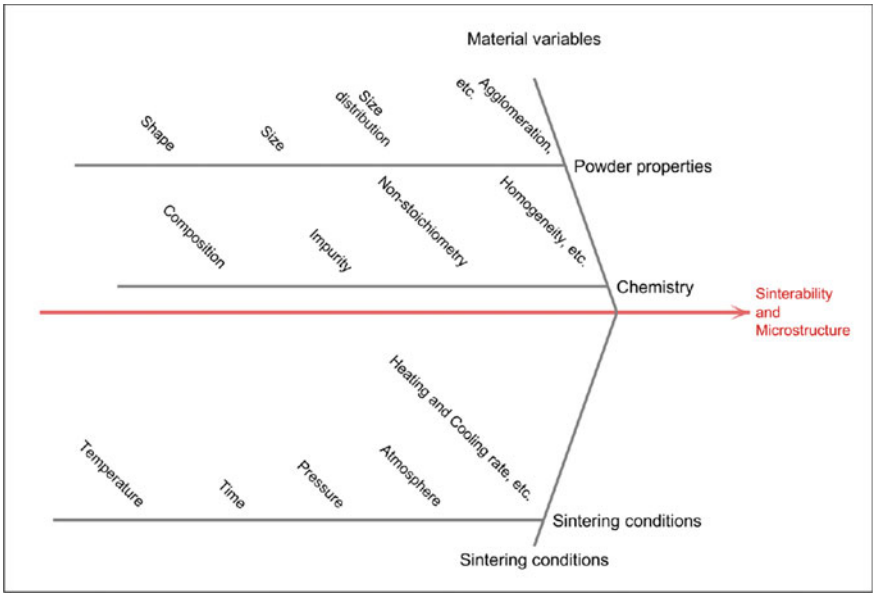

Fig. 18.29 Sintering variables: factors and effects

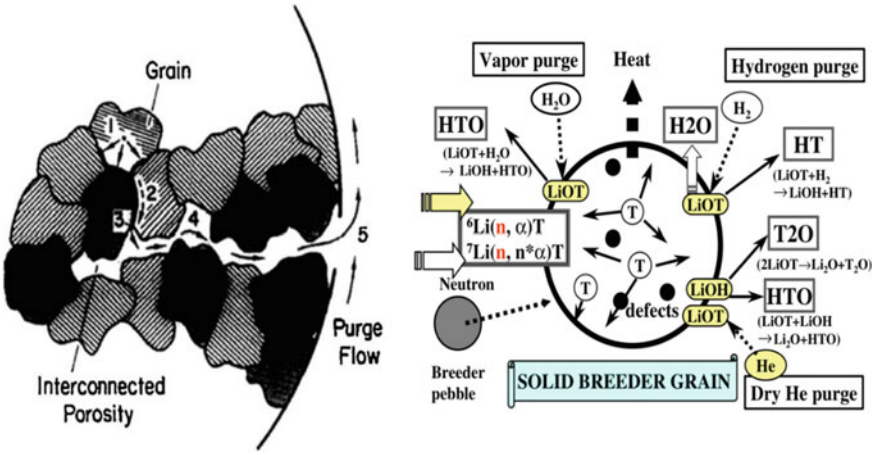

Fig. 18.30 Schematic illustration of the tritium transport mechanism in the ceramic breeder (**1**: intragranular diffusion, **2**: grain boundary diffusion, **3**, **4**: pore diffusion and **5**: purge flow convection (Reproduced from [148, 149] with permission of Elsevier)

radiation-induced defects. Subsequently, tritium diffuses along the grain boundary pathways existing between the adjacent grains to the solid/gas interface (open and closed porosity. The fraction of closed porosity provides another means to build up inventory in the material. At the surface, various processes take place involving isotope exchange with hydrogen (H_2) and water (H_2O) leading to desorption of tritium in chemical forms of HT and HTO, respectively. Further, the tritium bearing species (HT, HTO and T_2O) is transported via interconnected pores and enters the flow of the purge gas. The assessment of tritium retention in the breeder requires knowledge of rate determining steps and the most relevant operation as well as microstructural parameters that facilitate the tritium release. In summary, the entire tritium transport mechanisms can be divided into the following steps: intragranular diffusion; grain boundary diffusion; surface adsorption/desorption; pore diffusion and purge flow convection. The microstructure of sintered tritium breeder mainly affect the intragranular diffusion, grain boundary diffusion and pore diffusion and thereby influences the tritium transport process. Grain size is an important parameter affecting the tritium release properties of tritium breeding ceramics. The average residence time (θ_D) of tritium in the crystal grain under diffusion is related to the grain size (d_p) and effective diffusion coefficient of tritium within the grain by the following relation [150].

$$\theta_D = \frac{d_p^2}{60 D_T}$$

The above relation clearly shows that release rate of tritium can be accelerated by decreasing grain size which has been confirmed by the out-of-pile tritium annealing studies on sintered Li ceramic pebbles. It is because the activation energy for intragranular diffusion is higher as compared to grain boundary diffusion. Annealing studies and in-pile tests clearly demonstrated that, in case of small grained microstructure, tritium release is faster compared to large grained [44, 151–153]. The tritium retention (i.e. residence time) θ_D in sintered Li ceramic with large grain size is much longer than for the small grain size. Moreover, microstructure has a significant effect on mechanical properties of the breeder. The mechanical properties and radiation resistance can be augmented by increasing relative density and decreasing grain size. Therefore, fragmentation of Li ceramic breeders due to swelling and embrittlement in fusion reactor environments can be effectively controlled [71, 93, 154–156].

18.6.8 Desired Microstructure of Sintered Tritium Breeder

The central theme in the processing of Li ceramic breeders is to enhance densification while limiting grain growth. For the optimum performance of tritium breeding materials, the desired characteristics often include high Li atom density (no evaporative loss of Li), the relative sintered density in the range of 80–90%, the grain size 1-5μ and about 5–15% of interconnected open porosity [96, 101, 157].

18.7 Challenges in Achieving Desired Microstructure

The challenges in processing of Li-based ceramic tritium breeding materials mainly include i) evaporative loss of Li and ii) uncontrolled grain growth [125, 158–162]. These problems were often experienced when the processing temperature exceeds 1000 °C either during the powder synthesis or sintering steps [67, 116]. Due to these factors, it is often quite challenging to achieve required density and small grain size at the same time while maintaining the high Li atom density. Loss of Li has a detrimental effect on tritium breeding as the breeder in the blanket must have a high lithium atom density to achieve tritium self-sufficiency. The large grain size arising due to uncontrolled grain growth could dampen the tritium release process through the breeder microstructure. It would decrease tritium breeding ratio and also allow accumulation of tritium inventory in breeders, which has serious concern with regard to D–T fusion reactor safety. In order to circumvent these issues, sinterability of Li-based ceramic powders needs to be enhanced so as to reduce the sintering temperature and/or time.

18.8 Approaches to Sinterability Enhancement

There are many methods to improve the sinterability of ceramic powders. The widely used methods are (i) use of fine (sub-micron to nanoscale) powders, (ii) addition of sintering aids and (iii) aliovalent doping. Among these methods, the one utilizing the fine powders could be the most useful approach for Li ceramics. The other methods, (addition of sintering aid and aliovalent doping), have only limited scope, in view of the strict chemical purity (nuclear grade) desired in Li-based ceramic tritium breeders. This imposes restrictions on the addition of many foreign elements, particularly those which can act as a neutron absorber or give rise to activation products upon neutron irradiation.

Nanoscale ceramic powders often exhibit higher rate of densification. It is mainly due to high surface area of nanoscale powders (i.e. large driving force for sintering), reduced diffusion lengths and increased grain boundary areas. These effects can be explained by a general densification rate equation given below [163].

$$\frac{d\rho}{dt} = \frac{1}{G^{\mathrm{n}}}\exp\left(\frac{-E_a}{RT}\right)$$

According to this equation, the rate of densification (dρ/dt) is inversely proportional to the nth power of grain size (G). The value of n depends on which mechanism dominates the sintering process. If surface diffusion is dominating then $n = 3$ and in case of grain boundary diffusion is dominant mechanism the value of $n = 4$. This implies that sintering temperature and/or time duration necessary to attain required density could be drastically reduced.

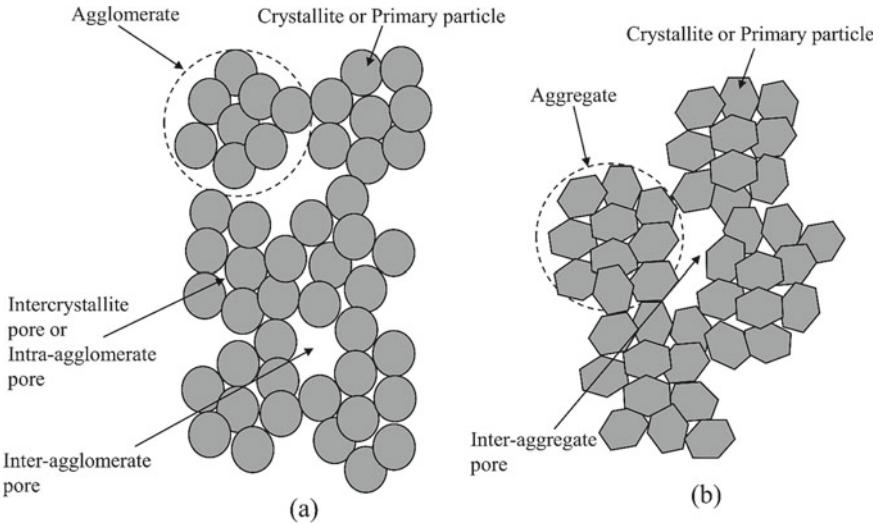

Fig. 18.31 Schematic illustration of **a** agglomerate and **b** aggregate

However, there are some issues in compaction and sintering of nanoscale ceramic powders which mainly arise because considerable agglomeration of nanoscale powders under the influence of Van der Waals attraction forces. The agglomeration often takes place during the synthesis, handling and particularly drying. Agglomeration leads to two types of pores in the green body (the powder compacts prior to sintering); inter-agglomerate pores and smaller inter-crystalline pores within the agglomerate; as shown in Fig. 18.31 [163]. The removal of the inter-agglomerate pores generally requires high temperatures during sintering, which also encourages grain growth which makes it challenging to maintain nanoscale grain size in sintered components. The removal of agglomeration so as to achieve dense packing free from cracks, pores and density gradients in the green powder compact is of serious concern in consolidation of nanoscale powders. The uniform particle packing is an effective means of achieving higher densification of the green body during sintering.

18.9 Comparison of Sinterability of Li-Based Ceramic Powders Synthesized by Different Methods

C.-H. Jung et al. investigated the sinterability of Li_2TiO_3 powder synthesized by solution combustion synthesis and other methods by dilatometry. As shown by dilatometric curves (Fig. 18.32), pellet prepared using combustion synthesized powder experienced fast-linear shrinkage above 600 °C, however, pellet prepared using commercial and solid-state synthesized powder experienced shrinkage at around 850 °C [108]. Therefore, sintering of the combustion synthesized pellet occurred

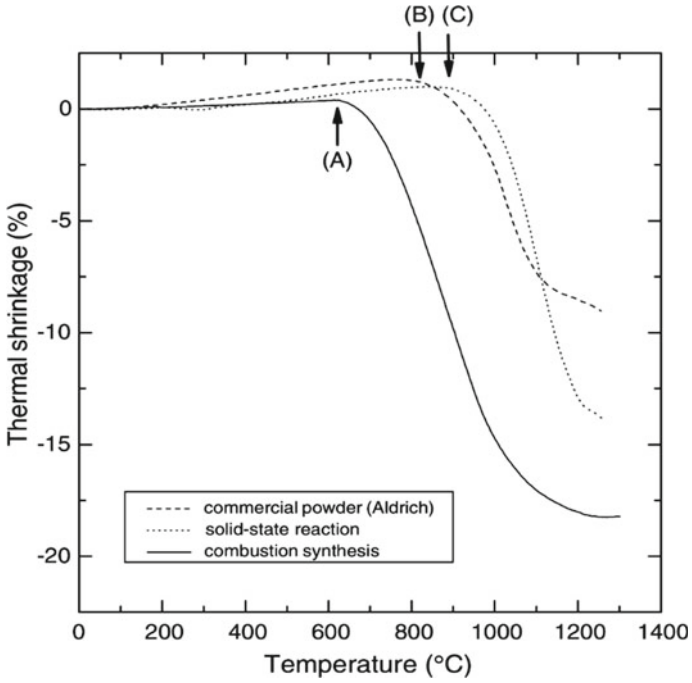

Fig. 18.32 Shrinkage (%) curves of Li_2TiO_3 pellets in air atmospheres (Reproduced from [108] with permission of Elsevier)

between 600 and 1200 °C with 20% of linear shrinkage (A in Fig. 18.32). However, in case of commercial (B in Fig. 18.32) and solid-state synthesized powder (C in Fig. 18.32), densification could not be achieved even at temperatures as high as 1300 °C. The powder synthesized by SCS method could be sintered to high density at lower temperature and short duration as compared to powder synthesized by solid-state reaction and commercial powders. It indicates the relatively more reactive nature of the combustion-derived powders (Fig. 18.33) [108]. The higher sintering temperature and longer sintering duration often led to large grain size in solid-state derived powder compacts. Li-based ceramic pebbles fabricated using powder derived from solid-state method often sintered at temperatures around 1100–1200 °C for 4–10 h duration to achieve 80–85% of relative density with grain size in 5-20 μm.

Enhanced sinterability of combustion-derived powders is due to small particle size, high surface area, soft-agglomeration and high porosity compared to powders derived from solid-state reaction or commercial powders.

Q. Zhou et al. reported excellent sinterability of solution combustion-derived Li_2TiO_3 powder compact. Relative density of the compact reached 90.7% at temperatures as low as 800 °C (Fig. 18.34). Further increase of sintering temperature considerably increases the grain size, however, the relative density remained nearly unchanged (Fig. 18.35) [109].

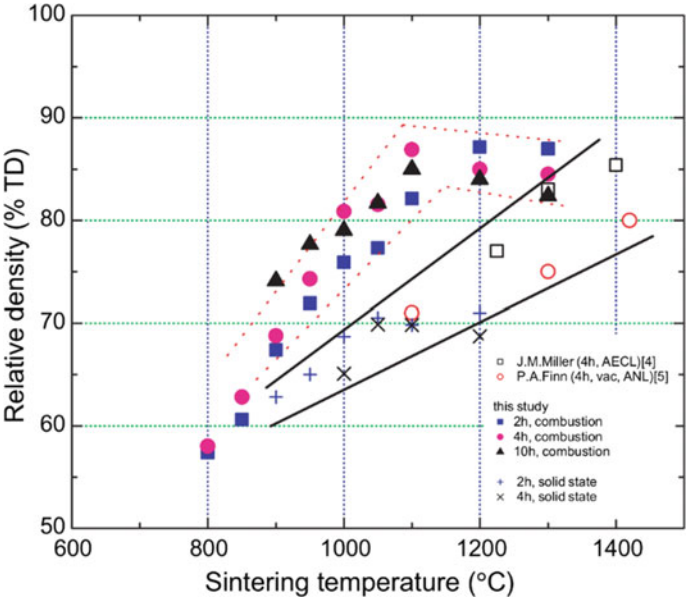

Fig. 18.33 Relative density of Li_2TiO_3 pellets synthesized by the various processes (Reproduced from [108] with permission of Elsevier)

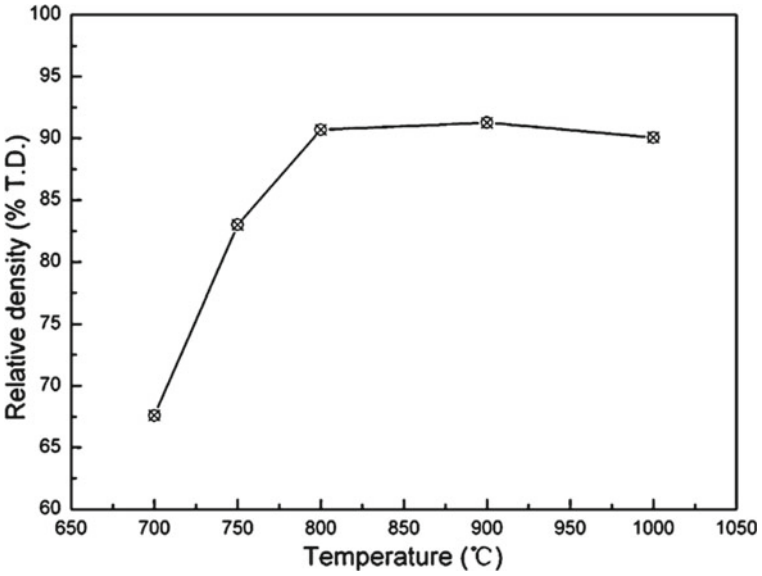

Fig. 18.34 Curve of relative density of Li_2TiO_3 ceramic against sintering temperatures (Reproduced from [109] with permission of Elsevier)

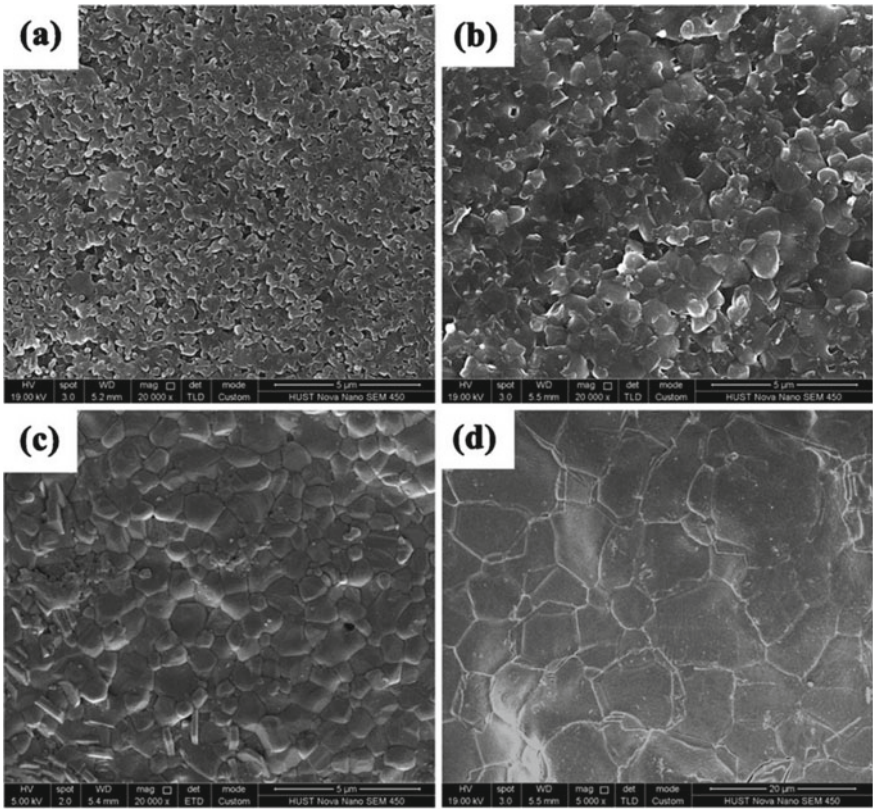

Fig. 18.35 SEM images of the surface of the Li_2TiO_3 ceramic sintered at **a** 700 °C **b** 750 °C **c** 800 °C **d** 900 °C (Reproduced from [109] with permission of Elsevier)

Li_2TiO_3 powder pellet prepared using powder synthesized by urea-assisted solid-state method, recently developed by our group, displayed excellent sinterability. The pellet achieved relative density of more than 90% at temperatures as low as 850 °C Fig. 18.36. The relative density further approached around 98% at 950 °C Fig. 18.36. Upon further increasing the sintering temperature up to 1000 °C, rapid grain growth occurred without any considerable increase in relative density. The grain size in pellet sintered at 900–950 °C was in 2–3 μm range (Fig. 18.37).

Pellet of Li_2ZrO_3 fabricated using the powder derived from glycine-nitrate solution combustion (recently developed by our group), displayed remarkable sinterability. The relative density of the pellets increased to around 90% at temperatures as low as 950 °C and steeply increased to around 98% at 1000 °C (Fig. 18.38) [116]. The grain size at sintering temperature of 1000 °C was in the range of 1–2 μm. Further increasing sintering temperature up to 1050 °C results in rapid grain growth (grain size >25 μm) with large number of closed pores (Fig. 18.39) [116].

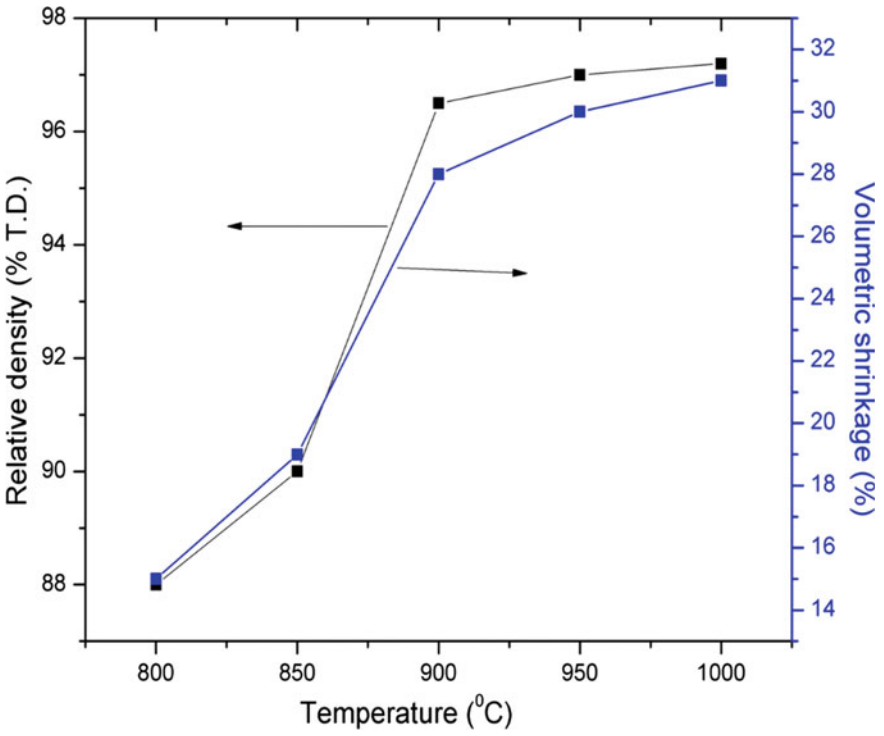

Fig. 18.36 Relative density and volumetric shrinkage of Li_2TiO_3 pellet as a function of sintering temperature (Reproduced from [67] with permission of Elsevier)

In general, the Li-based ceramic compacts (pellets or pebbles) fabricated using powders synthesized by wet chemical methods, particularly solution combustion method exhibited significant improvement in sinterability manifested by reduction of sintering temperature and sintering time. Reduction of sintering temperature can be an effective way to produce Li-based ceramic tritium breeding materials with desired density, small grain size and circumvent the loss of Li. Moreover, it will also facilitate incorporation of desired interconnected porosity in the sintered tritium breeding materials. Tritium breeding materials with all of these desired microstructural features can produce tritium at high rate leading to the attainment of tritium self-sufficiency condition for fusion reactors.

18.10 Conclusion

- Fusion is a potential source of energy to meet increasing global energy demand and also combat global warming which is the primary culprit of climate change.

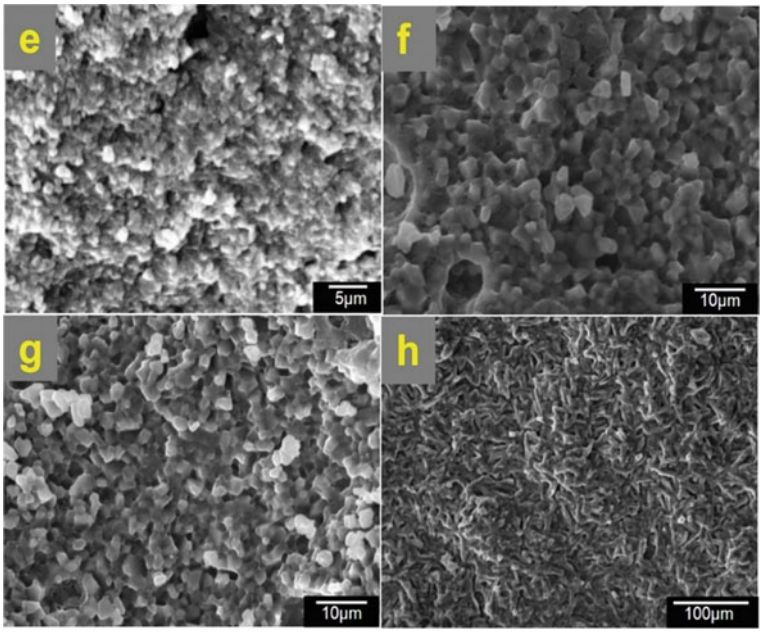

Fig. 18.37 Fracture surface SEM images of Li_2TiO_3 sintered at **e** 850 °C **f** 900 °C **g** 950 °C and **h** 1000 °C (Reproduced from [67] with permission of Elsevier)

- Fusion reactors based on D–T fuel cycle need to breed sufficient tritium to achieve tritium self-sufficiency condition.
- Li-based ceramics are potential candidates tritium breeding blanket materials.
- Microstructure including density, grain size and porosity has significant influence on tritium release and retention characteristics of sintered tritium breeding materials.
- Sinterability of Li-based ceramics need to be improved to produce tritium breeding materials with designed microstructure (optimum density, small grain size and interconnected porosity) for high tritium production rate.
- Improvement in sinterability will significantly reduce the large scale processing cost of Li-based ceramic tritium breeding materials.
- Processing of tritium breeding materials starting with sub-micron to nanoscale powders is advantageous for augmenting the sinterability of Li-based ceramics.
- Processing parameters need to be optimized for large scale production of fine Li ceramic powders using wet chemical routes and fabrication of sintered tritium breeding materials with desired microstructure.

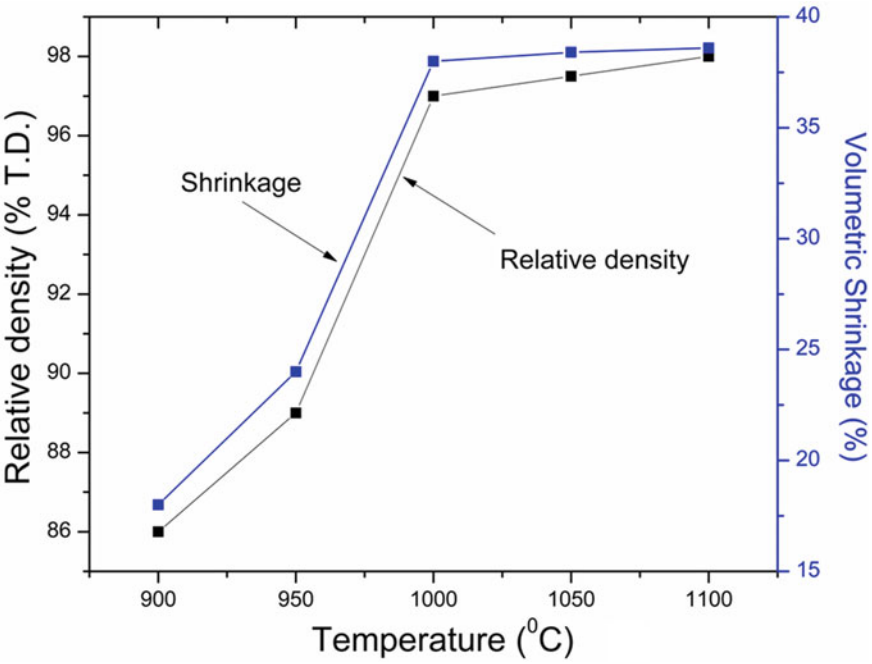

Fig. 18.38 Relative density and volumetric shrinkage of Li_2ZrO_3 pellet as a function of sintering temperature (Reproduced from [116] with permission of Elsevier)

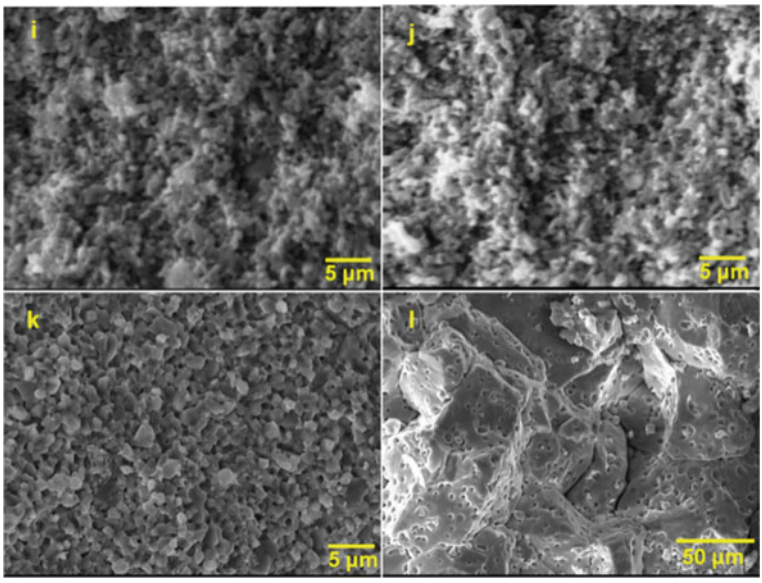

Fig. 18.39 Fracture surface SEM images of Li_2ZrO_3 sintered at **i** 900 °C **j** 950 °C **k** 1000 °C and **l** 1050 °C (Reproduced from [116] with permission of Elsevier)

References

1. IEA (2020) India 2020 policy energy review. www.Iea.Org 4:1–14
2. International renewable energy agency (IRENA) (2018) Global energy transformation: a roadmap to 2050
3. IEA—international energy agency (2013) Redrawing the energy-climate map: world energy outlook special report. 134
4. Krey V, Clarke L (2011) Role of renewable energy in climate mitigation: a synthesis of recent scenarios. Clim Policy 11:1131–1158
5. Höök M, Tang X (2013) Depletion of fossil fuels and anthropogenic climate change—a review. Energy Policy 52:797–809
6. Garry McCracken PS (1902) Fusion the energy of the universe. https://doi.org/10.1016/s0016-0032(02)90233-4
7. Clery D (2013) A piece of the sun: the quest for fusion energy. Overlook Duckworth
8. Mohan A (2016) The future of nuclear energy in India. Obs Res Found
9. Bradshaw AM, Hamacher T, Fischer U (2011) Is nuclear fusion a sustainable energy form? Fusion Eng Des 86:2770–2773
10. Toschi R (1997) Nuclear fusion, an energy source. Fusion Eng Des 36:1–8
11. Smith CL (2005) The need for fusion. Fusion Eng Des 74:3–8
12. Tanabe T (2016) Tritium: fuel of fusion reactors. https://doi.org/10.1007/978-4-431-56460-7
13. Dstrozzi, Own work, CC-BY 2.5 web page: https://commons.wikimedia.org/w/index.php?curid=2351259
14. Zarnstorff MC, Goldston RJ (2016) Magnetic fusion energy. https://doi.org/10.1142/9789814689205_0006
15. Lawson JD (1957) Some criteria for a power producing thermonuclear reactor. Proc Phys Soc (London) B70(6)
16. Conceptual design of fusion reactor, figure supplied courtesy of JET-EFDA publications copyright Euratom. http://figures.euro-fusion.org/Images/JG95.113-55c1500.1500.jpg
17. What will ITER do ? https://www.iter.org/sci/Goals
18. Overview|ITER-India, https://www.iter-india.org/index.php/overview. Accessed June 30, 2020
19. Aymar R (1997) Overview of the ITER project. In: Haruyama T, Mitsui T, KBT-P. of the S.I.C.E.C.C.M.C. Yamafuji K (eds) Elsevier Science, Oxford, pp 53–59. https://doi.org/10.1016/B978-008042688-4/50013-2
20. ITER EDA documentation series no. 22 (2001) International, international thermonuclear experimental reactor (ITER), Int At energy agency
21. Ni M, Wang Y, Yuan B, Jiang J, Wu Y (2013) Tritium supply assessment for ITER and demonstration power plant. Fusion Eng Des 88:2422–2426. https://doi.org/10.1016/j.fusengdes.2013.05.043
22. Pearson RJ, Antoniazzi AB, Nuttall WJ (2018) Tritium supply and use: a key issue for the development of nuclear fusion energy. Fusion Eng Des 136:1140–1148. https://doi.org/10.1016/j.fusengdes.2018.04.090
23. Rubel M (2019) Fusion neutrons: tritium breeding and impact on wall materials and components of diagnostic systems. J Fusion Energy 38:315–329. https://doi.org/10.1007/s10894-018-0182-1
24. Giegerich T, Day C, Knitter R, Osman N (2016) Lithium enrichment issues in the sustainable supply chain of future fusion reactors, Kit. pp 1–21. https://nucleus.iaea.org/sites/fusionportal/Technical Meeting Proceedings/1st IAEA TM on Fusion Power Plant Safety/Presentations/Giegerich.pdf
25. Biel W (2014) Tritium breeding and blanket technology, pp 1–24. https://www.dpg-physik.de/veranstaltungen/2014/biel2.pdf
26. Mohr SH, Mudd GM, Giurco D (2012) Lithium resources and production: critical assessment and global projections. Minerals 2:65–84. https://doi.org/10.3390/min2010065

27. Kavanagh L, Keohane J, Cabellos GG, Lloyd A, Cleary J (2018) Global lithium sources-industrial use and future in the electric vehicle industry: a review. Resources 7. https://doi.org/10.3390/resources7030057
28. Grosjean C, Herrera Miranda P, Perrin M, Poggi P, (2012) Assessment of world lithium resources and consequences of their geographic distribution on the expected development of the electric vehicle industry. Renew Sustain Energy Rev 16:1735–1744. https://doi.org/10.1016/j.rser.2011.11.023
29. Abdou M, Morley NB, Smolentsev S, Ying A, Malang S, Rowcliffe A, Ulrickson M (2015) Blanket/first wall challenges and required R&D on the pathway to DEMO. Fusion Eng Des 100:2–43. https://doi.org/10.1016/j.fusengdes.2015.07.021
30. Raffray A, Akiba M, Chuyanov V, Giancarli L, Malang S (2002) Breeding blanket concepts for fusion and materials requirements. J Nucl Mater 307–311:21–30. https://doi.org/10.1016/S0022-3115(02)01174-1
31. Proust TKE, Anzidei L, Dalle Donne M, Fischer U (1991) Solid breeder blanket design and tritium breeding. 16:73–84
32. Hernández FA, Pereslavtsev P (2018) First principles review of options for tritium breeder and neutron multiplier materials for breeding blankets in fusion reactors. Fusion Eng Des 137:243–256. https://doi.org/10.1016/j.fusengdes.2018.09.014
33. Johnson CE (1991) Ceram Breeder Materialst 17:253–258
34. Roux N, Hollenberg G, Johnson C, Noda K, Verrall R (1995) Fusion engineering and design summary of experimental results for ceramic breeder materials. 27:154–166
35. Rasneur B, Mougin J, Roux N (1994) Study of the thermomechanical and tritium release behaviour of Li_2ZrO_3 as tritium breeding ceramic for the European BIT blanket concept. J Nucl Mater 212–215:923–926. https://doi.org/10.1016/0022-3115(94)90970-9
36. Ehrlich K (2001) Materials research towards a fusion reactor. Fusion Eng Des 56–57:71–82. https://doi.org/10.1016/S0920-3796(01)00236-8
37. Rasneur B (1985) Tritium breeding material: γ $LiAlO_2$ Fusion Technol. 8. https://doi.org/10.13182/FST85-A40040
38. Knitter R, Chaudhuri P, Feng YJ, Hoshino T, Yu I-K (2013) Recent developments of solid breeder fabrication. J Nucl Mater 442:S420–S424. https://doi.org/10.1016/j.jnucmat.2013.02.060
39. Li K, Yang W, Ma ZB, Li YT (2020) First-principles study of tritium diffusion in the Li_3TaO_4 crystal. ACS Omega 5:851–858. https://doi.org/10.1021/acsomega.9b03700
40. Cismondi F (2010) Solid and liquid breeding blankets, presentation. https://staff.polito.it/roberto.zanino/sub1/teach_files/current_topics/lect_cismondi_2.pdf
41. Roux N, Johnson C, Noda K (1992) Properties and performance of tritium breeding ceramics. J Nucl Mater 191–194:15–22. https://doi.org/10.1016/S0022-3115(09)80005-6
42. Hoshino T, Kawamura H, Dokiya M, Takahashi Y, Terai T, Yamawaki M (2004) Non-stoichiometry of Li_2TiO_3 under hydrogen atmosphere conditions. J Nucl Mater 329–333:1300–1304. https://doi.org/10.1016/j.jnucmat.2004.04.226
43. Roth E, Abassin JJ, Botter F, Briec M, Chenebault P, Masson M, Rasneur B, Roux N (1985) Irradiation of lithium aluminate and tritium extraction. J Nucl Mater 133–134:238–241. https://doi.org/10.1016/0022-3115(85)90142-4
44. Briec M, Botter F, Abassin JJ, Benoit R, Chenebault P, Masson M, Rasneur B, Sciers P, Werle H, Roth E (1986) In and out-of-pile tritium extraction from samples of lithium aluminates. J Nucl Mater 141–143:357–363. https://doi.org/10.1016/S0022-3115(86)80065-4
45. Botter F, Cherquitte D, Roux N (1986) Out of pile tritium release from various lithium materials. In: Fusion technol. Pergamon, pp 1537–1544. https://doi.org/10.1016/B978-1-4832-8376-0.50214-X
46. Charpin J, Botter F, Briec M, Rasneur B, Roth E, Roux N, Sannier J (1989) Investigation of γ lithium aluminate as tritium breeding material for a fusion reactor blanket. Fusion Eng Des 8:407–413. https://doi.org/10.1016/S0920-3796(89)80140-1
47. Kleykamp H (2002) Phase equilibria in the Li–Ti–O system and physical properties of Li_2TiO_3. Fusion Eng Des 61–62:361–366. https://doi.org/10.1016/S0920-3796(02)00120-5

48. Izquierdo G, West AR (1980) Phase equilibria in the system Li_2O–TiO_2. Mater Res Bull 15:1655–1660. https://doi.org/10.1016/0025-5408(80)90248-2
49. Skokan A (1990) Phase stability investigations in the ceramic breeder systems Li_2O–Al_2O_3 and Li_2O-ZrO_2. Fusion Technol 1991:772–776. https://doi.org/10.1016/b978-0-444-88508-1.50139-0
50. Wiedemann D, Nakhal S, Rahn J, Witt E, Islam MM, Zander S, Heitjans P, Schmidt H, Bredow T, Wilkening M, Lerch M (2016) Unravelling ultraslow lithium-ion diffusion in γ-$LiAlO_2$: experiments with tracers, neutrons, and charge carriers. Chem Mater 28:915–924. https://doi.org/10.1021/acs.chemmater.5b04608
51. Bianchini F, Fjellvåg H, Vajeeston P (2018) A first principle comparative study of the ionic diffusivity in $LiAlO_2$ and $NaAlO_2$ polymorphs for solid-state battery applications. Phys Chem Chem Phys 20:9824–9832. https://doi.org/10.1039/c8cp00715b
52. Jia T, Zeng Z, Paudel H, Senor DJ, Duan Y (2019) First-principles study of the surface properties of γ-$LiAlO_2$: stability and tritium adsorption. J Nucl Mater 522:1–10. https://doi.org/10.1016/j.jnucmat.2019.05.007
53. Lei L, He D, Zou Y, Zhang W, Wang Z, Jiang M, Du M (2008) Phase transitions of $LiAlO_2$ at high pressure and high temperature. J Solid State Chem 181:1810–1815. https://doi.org/10.1016/j.jssc.2008.04.006
54. Singh B, Gupta MK, Mittal R, Chaplot SL (2018) Phonons, phase transitions and thermal expansion in $LiAlO_2$: an: ab initio density functional study. Phys Chem Chem Phys 20:12248–12259. https://doi.org/10.1039/c8cp01474d
55. Khacek FC (1930) The binary system Li_2O–SiO_2. J Phys Chem 34:2641–2650
56. Wedemeyer H, Ritzhaupt-Kleissl H-J, Günther E, Werle H (1990) Fabrication of grain-size controlled lithium Orthosilicate. Fusion Technol 1991:877–880. https://doi.org/10.1016/b978-0-444-88508-1.50160-2
57. Soares PC, Zanotto ED, Fokin VM, Jain H (2003) TEM and XRD study of early crystallization of lithium disilicate glasses. J Non Cryst Solids 331:217–227. https://doi.org/10.1016/j.jnoncrysol.2003.08.075
58. Hong M, Zhang Y, Mi Y, Xiang M, Zhang Y (2014) Fabrication and characterization of Li_2TiO_3 core–shell pebbles with enhanced lithium density. J Nucl Mater 445:111–116. https://doi.org/10.1016/j.jnucmat.2013.10.055
59. Ramaraghavulu R, Buddhudu S, Bhaskar Kumar G (2011) Analysis of structural and thermal properties of Li_2TiO_3 ceramic powders. Ceram Int 37:1245–1249. https://doi.org/10.1016/j.ceramint.2010.12.007
60. Mandal D, Sathiyamoorthy D, Rao VG (2012) Preparation and characterization of lithium–titanate pebbles by solid-state reaction extrusion and spherodization techniques for fusion reactor. Fusion Eng Des 87:7–12. https://doi.org/10.1016/j.fusengdes.2011.08.006
61. Mandal D, Shenoi MRK, Ghosh SK (2010) Synthesis and fabrication of lithium-titanate pebbles for ITER breeding blanket by solid state reaction and spherodization. Fusion Eng Des 85:819–823. https://doi.org/10.1016/j.fusengdes.2010.06.018
62. Sonak S, Jain U, Sahu AK, Kumar S, Krishnamurthy N (2015) Thermogravimetric analysis and kinetic study of formation of lithium titanate by solid state route. J Nucl Mater 457:88–93. https://doi.org/10.1016/j.jnucmat.2014.11.016
63. Sathiyamoorthy D, Ghanwat SJ, Tripathi BM, Danani C (2011) Novel mixed-oxide ceramic for neutron multiplication and tritium generation. J Nucl Mater 417:775–779. https://doi.org/10.1016/j.jnucmat.2010.12.138
64. Castellanos M, West AR (1979) Order-disorder phenomena in oxides with rock salt structures: the system Li_2TiO_3–MgO. J Mater Sci 14:450–454. https://doi.org/10.1007/BF00589838
65. Aguas MD, Coombe GC, Parkin IP (1998) New solid state routes to lithium transition metal oxides via reactions with lithium oxide. Polyhedron 17:49–53. https://doi.org/10.1016/S0277-5387(97)00257-X
66. Kumar S, Mukherjee A, Sonak S, Krishnamurthy N (2013) Studies on the interaction of hydrogen with Li_2TiO_3 pebbles and pellets. J Nucl Mater 443:207–211. https://doi.org/10.1016/j.jnucmat.2013.07.045

67. Tripathi BM, Mohanty T, Prakash D, Tyagi AK, Sinha PK (2017) Monoclinic β-Li_2TiO_3 nanocrystalline particles employing novel urea assisted solid state route: synthesis, characterization and sintering behavior. J Nucl Mater 490:167–173. https://doi.org/10.1016/j.jnucmat.2017.04.022
68. Miller JM, Hamilton HB, Sullivan JD (1994) Testing of lithium titanate as an alternate blanket material. J Nucl Mater 212:877–880. https://doi.org/10.1016/0022-3115(94)90961-X
69. Van Der Laan JG, Kawamura H, Roux N, Yamaki D (2000) Ceramic breeder research and development: progress and focus. J Nucl Mater 283:99–109. https://doi.org/10.1016/S0022-3115(00)00352-4
70. Roux N, Mougin J, Rasneur B, Proust E, Giancarli L, Salavy JF (1994) Current material and design studies for the utilization of Li_2ZrO_3 in the BIT blanket concept. J Nucl Mater 212–215:862–867. https://doi.org/10.1016/0022-3115(94)90958-X
71. Rasneur B, Thevenot G, Bouilloux Y (1992) Irradiation behavior of $LiAlO_2$ and Li_2ZrO_3 ceramics in the ALICE 3 experiment. J Nucl Mater 191–194:243–247. https://doi.org/10.1016/S0022-3115(09)80043-3
72. Taddia M, Modesti P, Albertazzi A (2005) Determination of macro-constituents in lithium zirconate for tritium-breeding applications. J Nucl Mater 336:173–176. https://doi.org/10.1016/j.jnucmat.2004.09.011
73. Roth E, Charpin J, Roux N (1989) Prospects of ceramic tritium breeder materials. Fusion Eng Des 11:219–229. https://doi.org/10.1016/0920-3796(89)90020-3
74. Ichi-Ida J, Xiong R, Lin YS (2004) Synthesis and CO_2 sorption properties of pure and modified lithium zirconate. Sep Purif Technol 36:41–51. https://doi.org/10.1016/S1383-5866(03)00151-5
75. Pfeiffer H (2004) Reaction mechanisms and kinetics of the synthesis and decomposition of lithium metazirconate through solid-state reaction. J Eur Ceram Soc 24:2433–2443. https://doi.org/10.1016/S0955-2219(03)00630-7
76. Wen Z, Wu X, Xu X, Lin J, Gu Z (2010) Research on the preparation of ceramic tritium breeders in SICCAS. Fusion Eng Des 85:1551–1555. https://doi.org/10.1016/j.fusengdes.2010.04.037
77. Tanaka S, Kawamoto A, Yamawaki M, Terai T, Takahashi Y, Kawamura H, Saito M (1989) In-situ tritium release experiments from solid breeding materials (TTTEx)—tritium diffusion coefficients and surface reaction on lithium aluminate. Fusion Eng Des 8:155–160. https://doi.org/10.1016/S0920-3796(89)80100-0
78. Rakshit SK, Naik YP, Parida SC, Dash S, Singh Z, Sen BK, Venugopal V (2008) Synergistic use of Knudsen effusion quadrupole mass spectrometry, solid-state galvanic cell and differential scanning calorimetry for thermodynamic studies on lithium aluminates. J Solid State Chem 181:1402–1412. https://doi.org/10.1016/j.jssc.2008.03.003
79. Asou M, Terai T, Takahashi Y (1990) Enthalpy and heat capacity of $Lialo_2$ and Li_2SnO_3 from 300 to 1000 K. J Nucl Mater 175:42–46. https://doi.org/10.1016/0022-3115(90)90267-Q
80. Lin J, Wen Z, Xu X, Gu Z (2010) Processing and microstructure of γ-$LiAlO_2$ ceramics. Ceram Int 36:2221–2225. https://doi.org/10.1016/j.ceramint.2010.03.032
81. Kinoshita K, Sim JW, Ackerman JP (1978) Preparation and characterization of lithium aluminate. Mater Res Bull 13:445–455. https://doi.org/10.1016/0025-5408(78)90152-6
82. Jimenez-Becerril J, Bosch P, Bulbulian S (1991) Synthesis and characterization of γ-$LiAlO_2$. J Nucl Mater 185:304–307. https://doi.org/10.1016/0022-3115(91)90520-H
83. Isupov VP, Eremina NV (2012) Effect of mechanical activation of $Al(OH)_3$ on its reaction with Li_2CO_3. Inorg Mater 48:918–924. https://doi.org/10.1134/S0020168512080055
84. Schulz B, Wedemeyer H (1986) Preparation, characterization and thermal diffusivity of γ-$LiAlO_2$. J Nucl Mater 139:35–41. https://doi.org/10.1016/0022-3115(86)90161-3
85. Chatterjee M, Naskar MK (2003) Novel technique for the synthesis of lithium aluminate ($LiAlO_2$) powders from water-based sols. J Mater Sci Lett 22:1747–1749. https://doi.org/10.1023/B:JMSL.0000005411.77240.9b
86. Gao J, Shi S, Xiao R, Li H (2016) Synthesis and ionic transport mechanisms of α-$LiAlO_2$. Solid State Ionics 286:122–134. https://doi.org/10.1016/j.ssi.2015.12.028

87. Wen Z, Gu Z, Xu X, Zhu X (2004) Research on the preparation, electrical and mechanical properties of γ-$LiAlO_2$ ceramics. J Nucl Mater 329–333:1283–1286. https://doi.org/10.1016/j.jnucmat.2004.04.230
88. Jiménez-Becerril J, García-Sosa I (2011) Synthesis of lithium aluminate by thermal decomposition of a lithium dawsonite-type precursor. J Ceram Process Res 12:52–56
89. Tang T, Zhang Z, Meng J-B, Luo D-L (2009) Synthesis and characterization of lithium silicate powders. Fusion Eng Des 84:2124–2130. https://doi.org/10.1016/j.fusengdes.2009.02.017
90. Löbbecke B, Knitter R, Rohde M, Reimann J (2009) Thermal conductivity of sintered lithium orthosilicate compacts. J Nucl Mater 386–388:1068–1070. https://doi.org/10.1016/j.jnucmat.2008.12.281
91. Smaihi M, Boilot JP, Botter F, Mougin J, Boncoeur MJ (1991) Out-of-pile tritium extraction from lithium orthosilicate-based ceramics. J Nucl Mater 185:19–28. https://doi.org/10.1016/0022-3115(91)90361-A
92. Carella E, Hernandez MT (2014) High lithium content silicates: a comparative study between four routes of synthesis. Ceram Int 40:9499–9508. https://doi.org/10.1016/j.ceramint.2014.02.023
93. Hollenberg GW, Knight RC, Densley PJ, Pember LA, Johnson CE, Poeppel RB, Yang L (1986) The FUBR-1B experiment—irradiation of lithium ceramics to high burnups under large temperature gradients. J Nucl Mater 141–143:271–274. https://doi.org/10.1016/S0022-3115(86)80049-6
94. Kurasawa T (1994) The VOM/JRR-2 experiments; performance of in-situ tritium release from the lithium ceramics. J Nucl Mater 212–215:937–941. https://doi.org/10.1016/0022-3115(94)90973-3
95. Wu X, Wen Z, Lin B, Xu X (2008) Sol–gel synthesis and sintering of nano-size Li_2TiO_3 powder. Mater Lett 62:837–839. https://doi.org/10.1016/j.matlet.2007.06.073
96. Hong M, Zhang Y, Mi Y, Jiang Y, Xiang M (2014) Synthesis of Li_2TiO_3 by sol–gel combustion method and its gel-casting formation. J Nucl Mater 455:311–315. https://doi.org/10.1016/j.jnucmat.2014.06.054
97. Tsuchiya K, Kawamura H, Fuchinoue K, Sawada H, Watarumi K (1998) Fabrication development and preliminary characterization of Li_2TiO_3 pebbles by wet process. J Nucl Mater 258–263:1985–1990. https://doi.org/10.1016/S0022-3115(98)00229-3
98. Xu C, Li Y, Li L, Wang X, Han Q, Ren M, Ye W (2014) Effect of Cl^- on the properties of Li_2TiO_3 ceramic powders synthesized by in-situ hydrolysis. Ceram Int 40:7213–7218. https://doi.org/10.1016/j.ceramint.2013.12.060
99. Abbasian MR, Rahimipour M, Hamnabard Z (2019) Sintering behavior of lithium meta titanate nanocrystallites. Iran J Mater Sci Eng 16:43–52. https://doi.org/10.22068/ijmse.16.4.43
100. Zhang DR, Liu HL, Jin RH, Zhang NZ, Liu YX, Kang YS (2007) Synthesis and characterization of nanocrystalline $LiTiO_2$ using a one-step hydrothermal method. 13:92–96
101. Zhang W, Zhou Q, Xue L, Yan Y (2015) Fabrication of Li_2TiO_3 pebbles with small grain size via hydrothermal and improved dry-rolling methods. J Nucl Mater 464:389–393. https://doi.org/10.1016/j.jnucmat.2015.01.044
102. Laumann A, Fehr KT, Wachsmann M, Holzapfel M, Iversen BB (2010) Metastable formation of low temperature cubic Li_2TiO_3 under hydrothermal conditions—its stability and structural properties. Solid State Ionics 181:1525–1529. https://doi.org/10.1016/j.ssi.2010.08.017
103. Jung C, Jin S, Kriven WM, Park J, Ryu W (2008) A polymer solution technique for the synthesis of nano-sized Li_2TiO_3 ceramic breeder powders. 373:194–198. https://doi.org/10.1016/j.jnucmat.2007.05.050
104. Jung CH (1998) Synthesis of Li_2TiO_3 ceramic breeder powders by the combustion process
105. Kim D, Cho K, Park JY, Kim YS (1999) Combustion synthesis of gamma-lithium aluminate. Key Eng Mater 161–163:87–90. www.scientific.net/kem.161-163.87
106. Renoult O, Boilot JP, Korb JP, Petit D, Boncoeur M (1995) Sol-gel lithium aluminate ceramics and tritium extraction mechanisms. J Nucl Mater 219:233–239. https://doi.org/10.1016/0022-3115(94)00399-8

107. Jung C-H, Park J-Y, Kim W-J, Ryu W-S, Lee S-J (2006) Characterizations of Li_2TiO_3 prepared by a solution combustion synthesis and fabrication of spherical particles by dry-rolling granulation process. Fusion Eng Des 81:1039–1044. https://doi.org/10.1016/j.fusengdes.2005.08.085
108. Jung C-H (2005) Sintering characterization of Li_2TiO_3 ceramic breeder powders prepared by the solution combustion synthesis process. J Nucl Mater 341:148–152. https://doi.org/10.1016/j.jnucmat.2005.01.022
109. Zhou Q, Mou Y, Ma X, Xue L, Yan Y (2014) Effect of fuel-to-oxidizer ratios on combustion mode and microstructure of Li_2TiO_3 nanoscale powders. J Eur Ceram Soc 34:801–807. https://doi.org/10.1016/j.jeurceramsoc.2013.10.004
110. Zhou Q, Tao L, Gao Y, Xue L, Yan Y (2014) Flash synthesis of Li_2TiO_3 powder by microwave-induced solution combustion. J Nucl Mater 455:101–105. https://doi.org/10.1016/j.jnucmat.2014.05.019
111. Sinha A, Nair SR, Sinha PK (2010) Single step synthesis of Li_2TiO_3 powder. J Nucl Mater 399:162–166. https://doi.org/10.1016/j.jnucmat.2010.01.013
112. Xiao Q, Tang X, Liu Y, Zhong Y, Zhu W (2013) Comparison study on strategies to prepare nanocrystalline Li_2ZrO_3-based absorbents for CO_2 capture at high temperatures. Front Chem Sci Eng 7:297–302. https://doi.org/10.1007/s11705-013-1346-1
113. Xiao Q, Tang X, Liu Y, Zhong Y, Zhu W (2011) Citrate route to prepare K-doped Li_2ZrO_3 sorbents with excellent CO_2 capture properties. Chem Eng J 174:231–235. https://doi.org/10.1016/j.cej.2011.09.005
114. Xiao Q, Liu Y, Zhong Y, Zhu W (2011) A citrate sol-gel method to synthesize Li_2ZrO_3 nanocrystals with improved CO_2 capture properties. J Mater Chem 21:3838–3842. https://doi.org/10.1039/c0jm03243c
115. Xiao Q, Liu Y, Zhong Y, Zhu W (2011) A citrate sol–gel method to synthesize Li_2ZrO_3 nanocrystals with improved CO_2 capture properties. J Mater Chem 21:3838. https://doi.org/10.1039/c0jm03243c
116. Tripathi BM, Mohanty T, Prakash D, Tyagi AK, Sinha PK (2020) Glycine-nitrate solution combustion synthesis of lithium zirconate: effect of fuel-to oxidant ratio on phase, microstructure and sintering. J Eur Ceram Soc 40:136–144. https://doi.org/10.1016/j.jeurceramsoc.2019.09.008
117. Li F, Hu K, Li J, Zhang D, Chen G (2002) Combustion synthesis of γ-lithium aluminate by using various fuels. J Nucl Mater 300:82–88. https://doi.org/10.1016/S0022-3115(01)00710-3
118. Choudhary A, Mazumder R, Bhattacharyya S, Chaudhuri P (2014) Synthesis and characterization of Li_4SiO_4 ceramics from rice husk ash by a solution-combustion method. Fusion Sci Technol 65:273–281. https://doi.org/10.13182/FST13-666
119. Choudhary A, Sahu BS, Mazumder R, Bhattacharyya S, Chaudhuri P (2014) Synthesis and sintering of Li_4SiO_4 powder from rice husk ash by solution combustion method and its comparison with solid state method. J Alloys Compd 590:440–445. https://doi.org/10.1016/j.jallcom.2013.12.084
120. Yu C-L, Yanagisawa K, Kamiya S, Kozawa T, Ueda T (2014) Monoclinic Li_2TiO_3 nanoparticles via hydrothermal reaction: processing and structure. Ceram Int 40:1901–1908. https://doi.org/10.1016/j.ceramint.2013.07.097
121. Jakhar S, Abhangi M, Rao CVS, Basu TK, Bhade SPD, Reddy PJ (2012) Measurement of tritium production rate distribution in natural lialo 2/HDPE assembly irradiated by D–T neutrons. Fusion Eng Des 87:184–187. https://doi.org/10.1016/j.fusengdes.2011.12.017
122. Tanaka S, Kawamoto A, Yamaki D, Yamaguchi K, Yamawaki M (1991) In situ tritium release experiments from solid breeding materials (TTTEx)—surface reaction on Li_2O and $LiAlO_2$ for sweep gases of He^+ H_2 and He^+ H_2O. J Nucl Mater 179–181:867–870. https://doi.org/10.1016/0022-3115(91)90226-W
123. Lulewicz JD, Roux N (1998) First results of the investigation of Li_2ZrO_3 and Li_2TiO_3 pebbles. Fusion Eng Des 39–40:745–750. https://doi.org/10.1016/S0920-3796(98)00328-7

124. Lulewicz JD, Roux N, Piazza G, Reimann J, van der Laan J (2000) Behaviour of Li_2ZrO_3 and Li_2TiO_3 pebbles relevant to their utilization as ceramic breeder for the HCPB blanket. J Nucl Mater 283–287:1361–1365. https://doi.org/10.1016/S0022-3115(00)00298-1
125. Hoshino T, Yasumoto M, Tsuchiya K, Hayashi K (2006) Vapor species evolved from Li_2TiO_3 heated at high temperature under various conditions. Fusion Eng Des 81:555–559. https://doi.org/10.1016/j.fusengdes.2005.10.004
126. Kapychev V, Tebus V, Frolov V (2002) Influence of neutron irradiation on the strength characteristics of lithium ceramic pellets for fusion reactor blankets. J Nucl Mater 307–311:823–826. https://doi.org/10.1016/S0022-3115(02)01299-0
127. Kolb MHH, Knitter R, Kaufmann U, Mundt D (2011) Enhanced fabrication process for lithium orthosilicate pebbles as breeding material. Fusion Eng Des 86:2148–2151. https://doi.org/10.1016/j.fusengdes.2011.01.104
128. Wu X, Wen Z, Xu X, Liu Y (2010) Fabrication of Li_4SiO_4 pebbles by a sol-gel technique. Fusion Eng Des 85:222–226. https://doi.org/10.1016/j.fusengdes.2010.01.018
129. Wu X, Wen Z, Han J, Xu X, Lin B (2008) Fabrication of Li_2TiO_3 pebbles by water-based sol-gel method. Fusion Eng Des 83:112–116. https://doi.org/10.1016/j.fusengdes.2007.09.005
130. Vittal Rao TV, Bamankar YR, Mukerjee SK, Aggarwal SK (2012) Preparation and characterization of Li_2TiO_3 pebbles by internal gelation sol–gel process. J Nucl Mater 426:102–108. https://doi.org/10.1016/j.jnucmat.2012.03.003
131. Deptuła A, Brykała M, Łada W, Olczak T, Sartowska B, Chmielewski AG, Wawszczak D, Alvani C (2009) Preparation of spherical particles of Li_2TiO_3 (with diameters below 100 μm) by sol-gel process. Fusion Eng Des 84:681–684. https://doi.org/10.1016/j.fusengdes.2008.12.077
132. Hoshino T (2013) Development of fabrication technologies for advanced tritium breeder pebbles by the sol–gel method. Fusion Eng Des 88:2264–2267. https://doi.org/10.1016/j.fusengdes.2013.05.025
133. Yu X, Yang M, Lu T, Wei N, Wei J, Shi Y, Huang Z, Xiang X, Zhang Q, Zhang W (2015) Fabrication of Li_4SiO_4 pebbles by wet method with modified powders synthesized via sol–gel process. J Nucl Mater 456:455–460. https://doi.org/10.1016/j.jnucmat.2014.10.030
134. Tsuchiya K, Kawamura H, Uchida M, Casadio S, Alvani C, Ito Y (2003) Improvement of sintered density of Li_2TiO_3 pebbles fabricated by direct-wet process. Fusion Eng Des 69:449–453. https://doi.org/10.1016/S0920-3796(03)00097-8
135. Lulewicz JD, Roux N, Piazza G, Reimann J, van der Laan J (2000) Section 12. Blanket materials and engineering behaviour of Li_2ZrO_3 and Li_2TiO_3 pebbles relevant to their utilization as ceramic breeder for the HCPB blanket. 287:1361–1365. www.elsevier.nl/locate/jnucmat
136. Hong M, Zhang Y, Mi Y, Fu B (2013) Characterization of Li_2TiO_3 pebbles by graphite bed process. J Nucl Mater 441:390–394. https://doi.org/10.1016/j.jnucmat.2013.06.024
137. Hong M, Zhang Y, Xiang M, Liu Z (2015) Preparation and characterization of Li_4SiO_4 ceramic pebbles by graphite bed method. Fusion Eng Des 95:72–78. https://doi.org/10.1016/j.fusengdes.2015.04.039
138. Xiang M, Zhang Y, Zhang Y, Wang C, Yu Y (2015) Effect of the fabrication process of ceramic pebbles on the porosity of Li_2TiO_3 tritium breeder. J Fusion Energy 34:1423–1432. https://doi.org/10.1007/s10894-015-9991-7
139. Xu X, Wen Z, Wu X, Lin J (2009) Preparation of γ-$LiAlO_2$ green bodies through the gel-casting process. Ceram Int 35:1429–1434. https://doi.org/10.1016/j.ceramint.2008.07.012
140. Xu X, Wen Z, Wu X, Lin J, Wang X (2009) Rheology and chemorheology of aqueous γ-$LiAlO_2$ slurries for gel-casting. Ceram Int 35:2191–2195. https://doi.org/10.1016/j.ceramint.2008.11.033
141. Xu X, Wen Z, Lin J, Li N, Wu X (2010) An aqueous gel-casting process for γ-$LiAlO_2$ ceramics. Ceram Int 36:187–191. https://doi.org/10.1016/j.ceramint.2009.07.017
142. German R (2014) Sintering: from empirical observations to scientific principles. https://doi.org/10.1016/C2012-0-00717-X
143. Kang S-JL s(n.d.) Sintering densification, grain growth, and microstructure

144. Rahaman MN (1996) Ceramic processing and sintering. Int Mater Rev 41:36–37. https://doi.org/10.1179/095066096790151286
145. Federici G, Raffray AR, Abdou MA (1990) Mistral: a comprehensive model for tritium transport in lithium-base ceramics. Part I: theory and description of model capabilities. J Nucl Mater 173:185–213. https://doi.org/10.1016/0022-3115(90)90257-N
146. Kinjyo T, Nishikawa M, Yamashita N, Koyama T, Tanifuji T, Enoeda M (2007) Chemical form of released tritium from solid breeder materials under the various purge gas conditions. Fusion Eng Des 82:2147–2151. https://doi.org/10.1016/j.fusengdes.2007.07.002
147. Nishikawa M, Kinjyo T, Nishida Y (2004) Chemical form of tritium released from solid breeder materials. J Nucl Mater 325:87–93. https://doi.org/10.1016/j.jnucmat.2003.11.001
148. Nishikawa M, Kinjyo T, Ishizaka T, Beloglazov S, Takeishi T, Enoeda M, Tanifuji T (2004) Release behavior of bred tritium from $LiAlO_2$. J Nucl Mater 335:70–76. https://doi.org/10.1016/j.jnucmat.2004.07.032
149. Abdou M, Morley NB, Smolentsev S, Ying A, Malang S, Rowcliffe A, Ulrickson M (2015) Blanket/first wall challenges and required R&D on the pathway to DEMO. Fusion Eng Des 100:2–43. https://doi.org/10.1016/j.fusengdes.2015.07.021
150. Tanifuji T, Yamaki D, Nasu S, Noda K (1998) Tritium release behavior from neutron-irradiated Li2TiO3 single crystal. J Nucl Mater 258–263:543–548. https://doi.org/10.1016/S0022-3115(98)00103-2
151. Briec M, Abassin JJ, Masson M, Roth E, Sciers P, Werle H (1988) In-pile tritium extraction from ample of lithium aluminate. J Nucl Mater 155:549–552. https://doi.org/10.1016/0022-3115(88)90308-X
152. Botter F, Tistchenko S, Briec M, Kopasz JP (1991) Progress in the knowledge of the mechanism of tritium release from lithium ceramics. Fusion Eng Des 17:49–54. https://doi.org/10.1016/0920-3796(91)90035-O
153. Debarberis L, Moretto P (1993) In-pile tritium release rate limiting process study. Fusion Eng Des 23:43–48. https://doi.org/10.1016/0920-3796(93)90109-U
154. Carella E, Hernández T (2015) The effect of γ-radiation in Li_4SiO_4 ceramic breeder blankets. Fusion Eng Des 90:73–78. https://doi.org/10.1016/j.fusengdes.2014.11.010
155. Hollenberg GW (1984) Fast neutron irradiation results on Li_2O, Li_4SiO_4, Li_2ZrO_3 and $LiAlO_2$. J Nucl Mater 123:896–900. https://doi.org/10.1016/0022-3115(84)90189-2
156. Miller JM, Verrall RA (1994) Performance of a Li_2ZrO_3 sphere-pac assembly in the CRITIC-II irradiation experiment. J Nucl Mater 212–215:897–901. https://doi.org/10.1016/0022-3115(94)90965-2
157. Mandal D, Jadeja MC, Ghuge NS, Sen D, Mazumder S (2016) Effect of excess lithium on sintering behaviour of lithium-titanate pebbles: modifications of microstructure and pore morphology. Fusion Eng Des 112:520–526. https://doi.org/10.1016/j.fusengdes.2016.05.041
158. Shin-mura K, Otani Y, Ogawa S, Hoshino T, Sasaki K (2017) Li vaporization properties of candidate materials for tritium breeder with high Li density. Fusion Eng Des 124:762–766. https://doi.org/10.1016/j.fusengdes.2017.04.053
159. Hoshino T, Yasumoto M, Tsuchiya K, Hayashi K, Nishimura H, Suzuki A, Terai T (2007) Non-stoichiometory and vaporization characteristic of $Li_{2.1}TiO_{3.05}$ in hydrogen atmosphere. Fusion Eng Des 82:2269–2273. https://doi.org/10.1016/j.fusengdes.2007.07.005
160. Ogawa S, Masuko Y, Kato H, Yuyama H, Sakai Y, Niwa E, Hashimoto T, Mukai K, Hosino T, Sasaki K (2015) Li vaporization property of two-phase material of Li_2TiO_3 and Li_2SiO_3 for tritium breeder. Fusion Eng Des 98–99:1859–1863. https://doi.org/10.1016/j.fusengdes.2015.01.042
161. Asano M, Kato Y, Harada T, Mizutani Y (1996) Vaporization and thermochemical properties of Li_8ZrO_6 and comparison with other lithium-containing complex oxides. J Nucl Mater 230:110–115. https://doi.org/10.1016/0022-3115(96)00171-7
162. Yamawaki M (1996) Sweep gas chemistry effect on vaporization of $LiAlO_2$. J Nucl Mater 233–237:1452–1456. https://doi.org/10.1016/s0022-3115(96)00252-8
163. Mayo MJ (1996) Processing of nanocrystalline ceramics from ultrafine particles. Int Mater Rev 41:85–115. https://doi.org/10.1179/imr.1996.41.3.85